

**Polymer Vol. 52, No. 2, 21 January 2011**

**Contents**

**FEATURE ARTICLE**

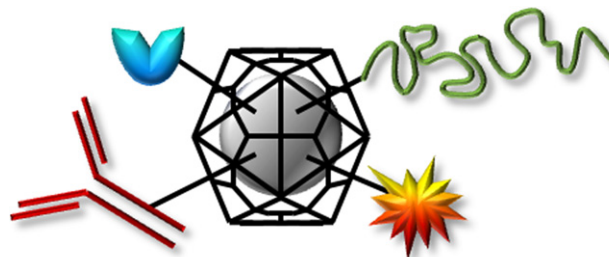
**Bionanoparticles as functional macromolecular building blocks – A new class of nanomaterials**

pp 211–232

Günther Jutz<sup>a</sup>, Alexander Böker<sup>b,\*</sup>

<sup>a</sup>Physikalische Chemie II, Universität Bayreuth, 95440 Bayreuth, Germany

<sup>b</sup>DWI an der RWTH Aachen e. V., Lehrstuhl für Makromolekulare Materialien und Oberflächen, RWTH Aachen University, 52056 Aachen, Germany



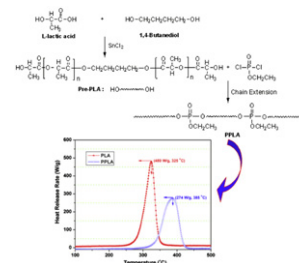
**POLYMER COMMUNICATIONS**

**A novel phosphorus-containing poly(lactic acid) toward its flame retardation**

pp 233–238

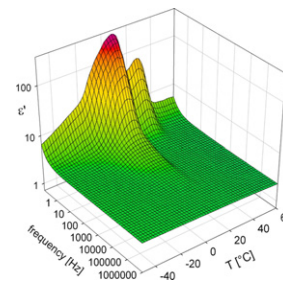
De-Yi Wang, Yan-Peng Song, Ling Lin, Xiu-Li Wang, Yu-Zhong Wang\*

Center for Degradation and Flame-Retardant Polymeric Materials, College of Chemistry, State Key Laboratory of Polymer Materials Engineering, National Engineering Laboratory of Eco-Friendly Polymeric Materials (Sichuan), Sichuan University, Chengdu 610064, China



## Exploiting interfacial polarization to detect phase transitions in dilute solutions: Crystallization and melting of P3HT in toluene down to ppm contents

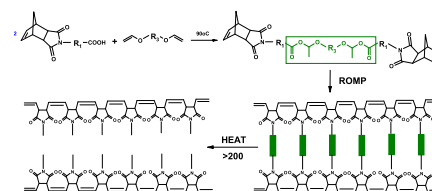
pp 239–242

Isabelle Monnaie<sup>a,b</sup>, Simone Napolitano<sup>c,\*</sup>, Erik Nies<sup>a,d,\*\*</sup>, Michael Wübbenhorst<sup>c</sup><sup>a</sup> Katholieke Universiteit Leuven, Polymer Research Division, Department of Chemistry, Celestijnenlaan 200F, B-3001 Leuven, Belgium<sup>b</sup> Eindhoven University of Technology, Laboratory of Materials and Interface Chemistry, Department of Chemical Engineering and Chemistry, P.O. Box 513, 5600MB Eindhoven, The Netherlands<sup>c</sup> Katholieke Universiteit Leuven, Acoustic and Thermal Physics, Department of Physics and Astronomy, Celestijnenlaan 200D, B-3001 Leuven, Belgium<sup>d</sup> Eindhoven University of Technology, Laboratory of Polymer Technology, Department of Chemical Engineering and Chemistry, P.O. Box 513, 5600MB Eindhoven, The Netherlands

## POLYMER PAPERS

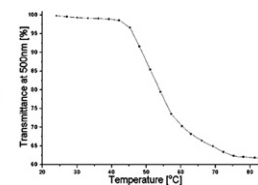
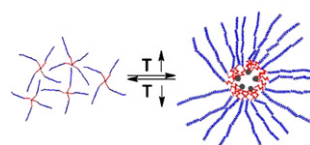
### Thermosetting ROMP materials with thermally degradable linkages

pp 243–249

Ezat Khosravi<sup>a,\*</sup>, Favaad Iqbal<sup>a</sup>, Osama M. Musa<sup>b</sup><sup>a</sup> Interdisciplinary Research Centre in Polymer Science and Technology, Chemistry Department, Durham University, Durham DH1 3LE, UK<sup>b</sup> International Specialty Products, 1361 Alps Road, Wayne, NJ 07470, USA

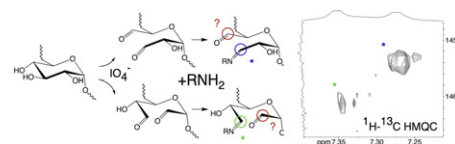
### Synthesis and thermoresponsive properties of four arm, amphiphilic poly(*tert*-butyl-glycidylether)-block-polyglycidol stars

pp 250–257

Marcin Libera<sup>a</sup>, Barbara Trzebicka<sup>a</sup>, Agnieszka Kowalczyk<sup>a</sup>, Wojciech Wałach<sup>a</sup>, Andrzej Dworak<sup>a,b,\*</sup><sup>a</sup> Centre of Polymer and Carbon Materials, Polish Academy of Sciences, M. Curie-Skłodowskiej 34, 41-819 Zabrze, Poland<sup>b</sup> University of Opole, Institute of Chemistry, Oleska 48, 45-052 Opole, Poland

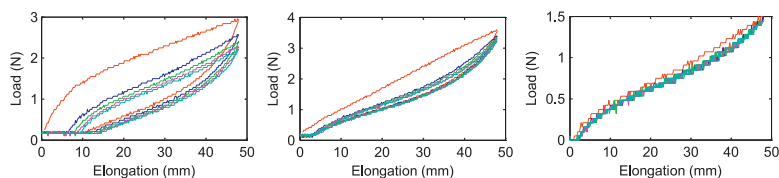
### Insight on the periodate oxidation of dextran and its structural vicissitudes

pp 258–265

João Maia<sup>a,\*</sup>, Rui A. Carvalho<sup>b,c</sup>, Jorge F.J. Coelho<sup>a</sup>, Pedro N. Simões<sup>a</sup>, M. Helena Gil<sup>a</sup><sup>a</sup> Chemical Engineering Department, Rua Silvio Lima, Polo II, FCTUC, 3030-790 Coimbra, Portugal<sup>b</sup> Life Sciences Department of the Faculty of Sciences and Technology of the University of Coimbra, Coimbra, Portugal<sup>c</sup> Center of Neurosciences and Cell Biology, Coimbra, Portugal

**Influence of soft segment molecular weight on the mechanical hysteresis and set behavior of silicone-urea copolymers with low hard segment contents**

pp 266–274

Iskender Yilgor<sup>a,\*</sup>, Tugba Eynur<sup>a</sup>, Sevilay Bilgin<sup>a</sup>, Emel Yilgor<sup>a</sup>, Garth L. Wilkes<sup>b</sup><sup>a</sup> Koc University, Chemistry Department, Sariyer 34450, Istanbul, Turkey<sup>b</sup> Department of Chemical Engineering, Virginia Tech, Blacksburg, VA 24061-0211, USA**Living/controlled hex-1-ene polymerization initiated by nickel diimine complexes activated by non-MAO cocatalysts: Kinetic and UV-vis study**

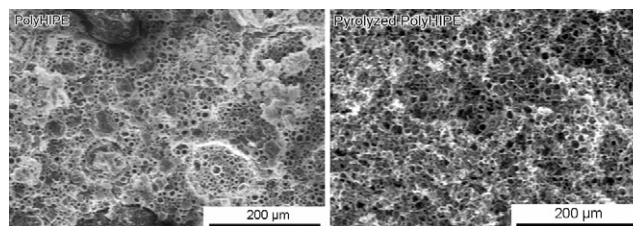
pp 275–281

Jan Peleška<sup>a</sup>, Zdeněk Hošťálek<sup>b</sup>, Darja Hasalíková<sup>b</sup>, Jan Merna<sup>b,\*</sup><sup>a</sup> Institute of Materials Chemistry, Brno University of Technology, Purkyňova 118, 612 00 Brno, Czech Republic<sup>b</sup> Institute of Chemical Technology, Prague, Department of Polymers, Technická 5, 166 28 Prague 6, Czech Republic**Synthesis of emulsion-templated porous polyacrylonitrile and its pyrolysis to porous carbon monoliths**

pp 282–287

Noa Cohen, Michael S. Silverstein<sup>\*</sup>

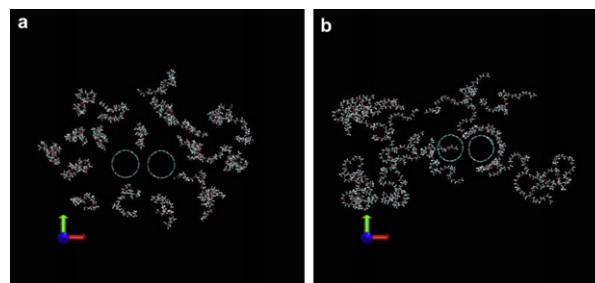
Department of Materials Engineering, Technion - Israel Institute of Technology, Haifa 32000, Israel

**Molecular dynamics simulations of the interactions and dispersion of carbon nanotubes in polyethylene oxide/water systems**

pp 288–296

Nasir M. Uddin, Franco M. Capaldi, Bakhtier Farouk<sup>\*</sup>

Department of Mechanical Engineering and Mechanics Drexel University, Philadelphia, PA 19104, USA



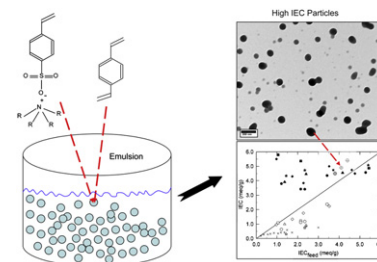
### Synthesis of high proton conducting nanoparticles by emulsion polymerization

pp 297–306

Emmanuel Pitia<sup>a,\*</sup>, M.T. Shaw<sup>b</sup>, R.A. Weiss<sup>a,\*</sup>

<sup>a</sup> University of Akron, Department of Polymer Engineering, Polymer Engineering Academic Center, 250 South Forge Street, Akron, OH 44325-0301, USA

<sup>b</sup> University of Connecticut, Polymer Program and Department of Chemical Engineering, Institute of Materials Science, 97 North Eagleville Road, Storrs, CT 06269-3136, USA



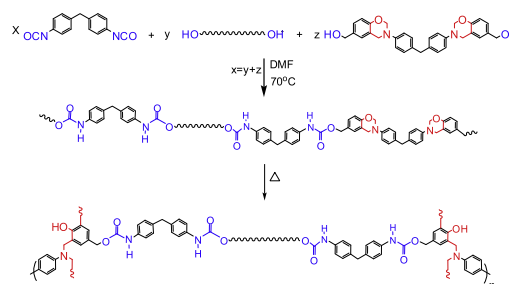
### Poly(benzoxazine-co-urethane)s: A new concept for phenolic/urethane copolymers via one-pot method

pp 307–317

Mohamed Baqar<sup>a</sup>, Tarek Agag<sup>b,\*</sup>, Hatsuo Ishida<sup>b</sup>, Syed Qutubuddin<sup>a,b</sup>

<sup>a</sup> Department of Chemical Engineering, Case Western Reserve University, Cleveland, OH 44106-7202, USA

<sup>b</sup> Department of Macromolecular Science and Engineering, Case Western Reserve University, Cleveland, OH 44106-7202, USA



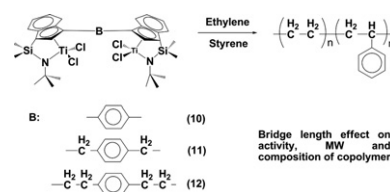
### Bridge length effect of new dinuclear constrained geometry catalysts on controlling the polymerization behaviors of ethylene/styrene copolymerization

pp 318–325

Thi Dieu Huyen Nguyen<sup>a</sup>, Thi Le Thanh Nguyen<sup>a</sup>, Seok Kyun Noh<sup>a,\*</sup>, Won Seok Lyoo<sup>b</sup>

<sup>a</sup> School of Display and Chemical Engineering, Yeungnam University, 214-1 Daedong, Gyeongsan, Gyeongbuk 712-749, Republic of Korea

<sup>b</sup> School of Textiles, Yeungnam University, 214-1 Daedong, Gyeongsan, Gyeongbuk 712-749, Republic of Korea



### Bulky side-chain density effect on the photophysical, electrochemical and photovoltaic properties of polythiophene derivatives

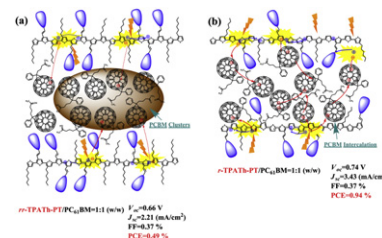
pp 326–338

Hsing-Ju Wang<sup>a</sup>, Li-Hsin Chan<sup>b,\*</sup>, Chih-Ping Chen<sup>c</sup>, Shin-Lei Lin<sup>c</sup>, Rong-Ho Lee<sup>a</sup>, Ru-Jong Jeng<sup>a,\*\*</sup>

<sup>a</sup> Department of Chemical Engineering, National Chung Hsing University, Taichung, Taiwan

<sup>b</sup> Department of Applied Materials and Optoelectronic Engineering, National Chi Nan University, Puli, Taiwan

<sup>c</sup> Material and Chemical Laboratories, Industrial Technology Research Institute, Hsinchu, Taiwan



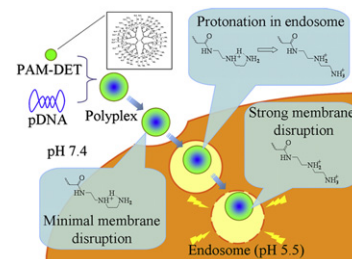
**PAMAM dendrimer with a 1,2-diaminoethane surface facilitates endosomal escape for enhanced pDNA delivery**

pp 339–346

Geun-woo Jin<sup>a</sup>, Heebeom Koo<sup>b</sup>, Kihoon Nam<sup>a</sup>, Heejin Kim<sup>a</sup>, Seonju Lee<sup>a</sup>, Jong-Sang Park<sup>a,\*</sup>, Yan Lee<sup>a,\*</sup>

<sup>a</sup> Department of Chemistry, Seoul National University, 599 Gwanak-ro, Gwanak-gu, Seoul 151-747, Republic of Korea

<sup>b</sup> Biomedical Research Center, Korea Institute of Science and Technology, 39-1 Hawolgok-dong, Seongbuk-gu, Seoul 136-791, Republic of Korea

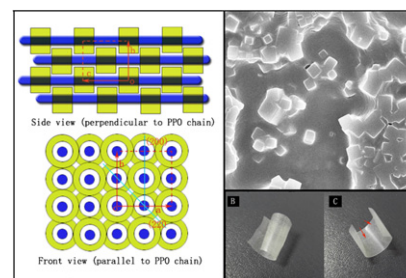


**Novel polyrotaxanes comprising  $\gamma$ -cyclodextrins and Pluronic F127 end-capped with poly(*N*-isopropylacrylamide) showing solvent-responsive crystal structures**

pp 347–355

Jin Wang, Peng Gao, Pei-jing Wang, Lin Ye, Ai-ying Zhang, Zeng-guo Feng<sup>\*</sup>

School of Materials Science and Engineering, Beijing Institute of Technology, Beijing 100081, People's Republic of China



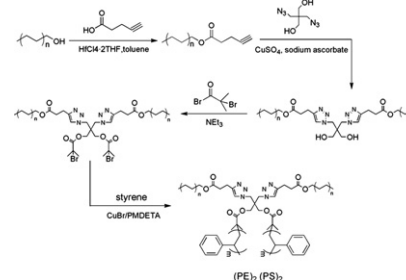
**Synthesis and self-assembly of miktoarm star copolymers of (polyethylene)<sub>2</sub>–(polystyrene)<sub>2</sub>**

pp 356–362

Ran Liu<sup>a</sup>, Zhiyun Li<sup>a</sup>, Dan Yuan<sup>a</sup>, Chunfeng Meng<sup>a</sup>, Qing Wu<sup>a,b</sup>, Fangming Zhu<sup>a,b,\*</sup>

<sup>a</sup> Institute of Polymer Science, School of Chemistry and Chemical Engineering, Sun Yat-Sen University, Guangzhou 510275, China

<sup>b</sup> Laboratory of Synthesis Design and Application of Polymer Materials, School of Chemistry and Chemical Engineering, Sun Yat-Sen University, Guangzhou 510275, China



**A fluorescence sensor based on chiral polymer for highly enantioselective recognition of phenylalaninol**

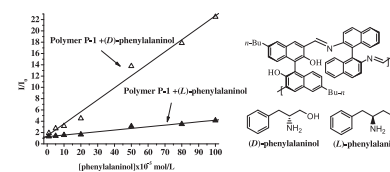
pp 363–367

Jie Meng<sup>a</sup>, Guo Wei<sup>a</sup>, Xiaobo Huang<sup>a,c</sup>, Yu Dong<sup>a</sup>, Yixiang Cheng<sup>a,\*</sup>, Chengjian Zhu<sup>b,\*\*</sup>

<sup>a</sup> Key Lab of Mesoscopic Chemistry of MOE, School of Chemistry and Chemical Engineering, Nanjing University, Nanjing 210093, China

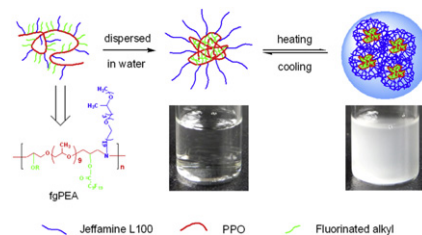
<sup>b</sup> State Key Laboratory of Coordination Chemistry, School of Chemistry and Chemical Engineering, Nanjing University, Nanjing 210093, China

<sup>c</sup> College of Chemistry and Materials Engineering, Wenzhou University, Wenzhou 325027, China



**Well-defined multi-stimuli responsive fluorinated graft poly(ether amine)s (fgPEAs)**

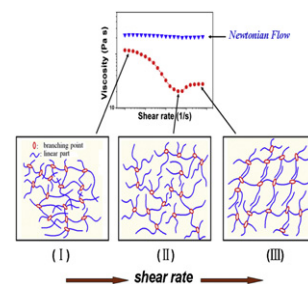
pp 368–375

Rui Wang<sup>a</sup>, Xuesong Jiang<sup>a,\*</sup>, Guilin Yin<sup>b</sup>, Jie Yin<sup>a,\*</sup><sup>a</sup> School of Chemistry & Chemical Technology, State Key Laboratory for Metal Matrix Composite Materials, Shanghai Jiao Tong University, Shanghai, China<sup>b</sup> National Engineering Research Center for Nanotechnology, Shanghai 200240, People's Republic of China**Hyperbranched poly(methyl methacrylate)s prepared by miniemulsion polymerization and their (non)-Newtonian flow behaviors**

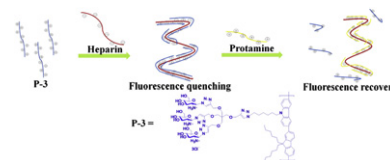
pp 376–382

Chaolong Li, Hao Jiang, Yu Wang, Yuechuan Wang<sup>\*</sup>

State Key Laboratory of Polymer Materials Engineering, College of Polymer Science and Engineering, Sichuan University, Chengdu 610065, PR China

**Water-soluble conjugated polyelectrolyte with pendant glycocluster: Synthesis and its interaction with heparin**

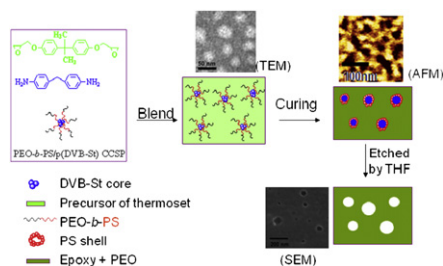
pp 383–390

Qi Chen<sup>a</sup>, Yi Cui<sup>a,b</sup>, Jie Cao<sup>c</sup>, Bao-Hang Han<sup>a,\*</sup><sup>a</sup> National Center for Nanoscience and Technology, Beijing 100190, China<sup>b</sup> Graduate University of Chinese Academy of Sciences, Beijing 100049, China<sup>c</sup> Department of Chemistry, Beijing Institute of Technology, Beijing 100081, China**Thermosets with core-shell nanodomain by incorporation of core crosslinked star polymer into epoxy resin**

pp 391–399

Yuan Meng, Xing-Hong Zhang<sup>\*</sup>, Bin-Yang Du, Bo-Xuan Zhou, Xin Zhou, Guo-Rong Qi

Key Laboratory of Macromolecular Synthesis and Functionalization of the Ministry of Education, Department of Polymer Science and Engineering, Zhejiang University, Hangzhou 310027, China

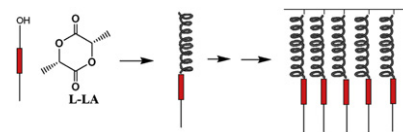


**Synthesis and characterization of side chain polymer with helical PLLA segments containing mesogenic end group**

pp 400–408

Hongru Chen, Qingbin Xue\*, Zhuohua Li, Lingmin Sun, Quanxuan Zhang

Key lab of Colloid and Interface Chemistry, Ministry of Education, Chemistry and Chemical Engineering College, Shandong University, Shanda South Road No. 27, Jinan 250100, China

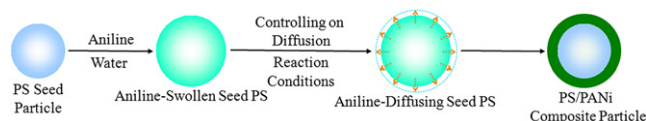
**Controlling the morphology of micrometre-size polystyrene/polyaniline composite particles by Swelling–Diffusion–Interfacial-Polymerization Method**

pp 409–414

Yunxing Li<sup>a</sup>, Zhaoqun Wang<sup>a,\*</sup>, Chunjian Wang<sup>a</sup>, Zhen Zhao<sup>a</sup>, Gi Xue<sup>a,b</sup>

<sup>a</sup> Department of Polymer Science and Engineering, School of Chemistry and Chemical Engineering, Nanjing University, Nanjing 210093, China

<sup>b</sup> State Key Laboratory of Coordination Chemistry, Nanjing National Laboratory of Microstructures, Nanjing University, Nanjing 210093, China

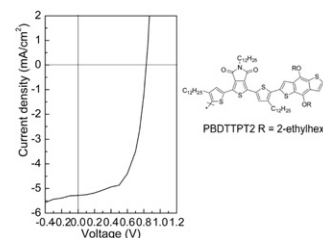
**Low bandgap polymers with benzo [1,2-b:4,5-b'] dithiophene and bithiophene-dioxypyrrrolothiophene units for photovoltaic applications**

pp 415–421

Guobing Zhang<sup>a</sup>, Yingying Fu<sup>b</sup>, Zhiyuan Xie<sup>b,\*</sup>, Qing Zhang<sup>a,\*</sup>

<sup>a</sup> Department of Polymer Science and Engineering, School of Chemistry and Chemical Engineering, Shanghai Jiao Tong University, Shanghai 200240, China

<sup>b</sup> State Key Laboratory of Polymer Physics and Chemistry, Changchun Institute of Applied Chemistry, Chinese Academy of Science, Changchun 130022, China

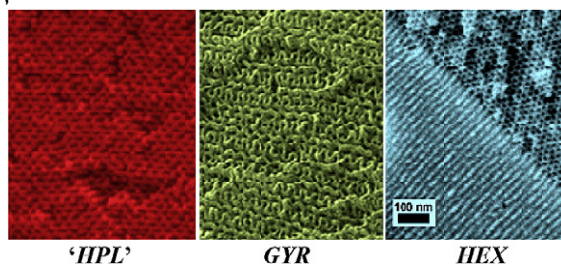
**Nanoporous materials from stable and metastable structures of 1,2-PB-*b*-PDMS block copolymers**

pp 422–429

Lars Schulte<sup>a</sup>, Anne Grydgaard<sup>b</sup>, Mathilde R. Jakobsen<sup>b</sup>, Piotr P. Szczykowski<sup>a,b</sup>, Fengxiao Guo<sup>a,b</sup>, Martin E. Vigild<sup>b</sup>, Rolf H. Berg<sup>a</sup>, Sokol Ndoni<sup>a,\*</sup>

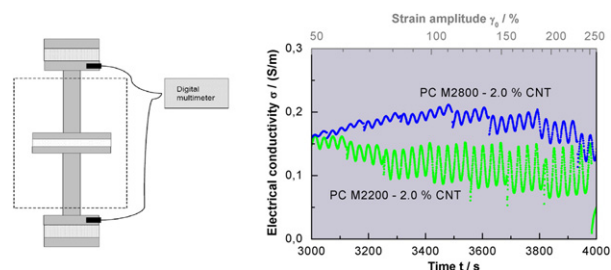
<sup>a</sup> Department of Micro and Nanotechnology, Technical University of Denmark, Frederiksborgvej 399, Build 124, DK-4000 Roskilde, Denmark

<sup>b</sup> Danish Polymer Centre, Department of Chemical and Biochemical Engineering, Technical University of Denmark, DK-2800 Kgs. Lyngby, Denmark



## Influence of molar mass and temperature on the dynamics of network formation in polycarbonate/carbon nanotubes composites in oscillatory shear flows

pp 430–442

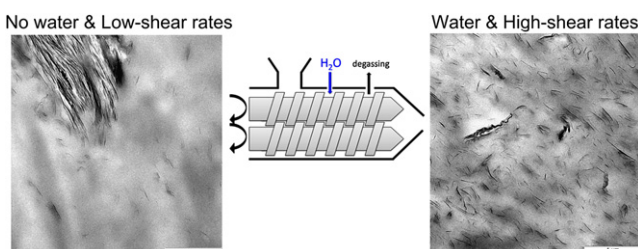
R. Zeiler<sup>a,b</sup>, U.A. Handge<sup>b,\*</sup>, D.J. Dijkstra<sup>a</sup>, H. Meyer<sup>c</sup>, V. Altstädt<sup>b</sup><sup>a</sup> Bayer MaterialScience AG, CAS-INN-Physics, 51368 Leverkusen, Germany<sup>b</sup> Department of Polymer Engineering, Faculty of Engineering Science, University of Bayreuth, Universitätsstrasse 30, 95447 Bayreuth, Germany<sup>c</sup> Bayer MaterialScience AG, CAS-INN-CNT, 51368 Leverkusen, Germany

## Water-assisted extrusion of polypropylene/clay nanocomposites: A comprehensive study

pp 443–451

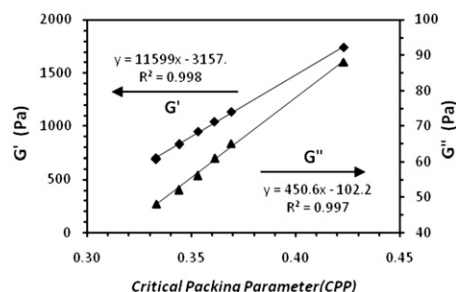
Dimitri D.J. Rousseaux, Naïma Sallem-Idrissi, Anne-Christine Baudouin, Jacques Devaux, Pierre Godard, Jacqueline Marchand-Brynaert<sup>\*\*</sup>, Michel Sclavons<sup>\*</sup>

Institute of Condensed Matter and Nanosciences (IMCN), Université Catholique de Louvain, Place Louis Pasteur 1, Bâtiment Lavoisier, B-1348 Louvain-la-Neuve, Belgium



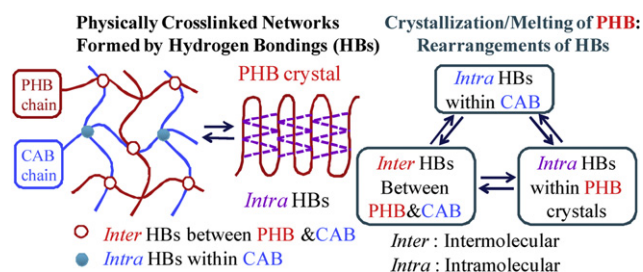
## An experimental study of interaction between surfactant and particle hydrogels

pp 452–460

Yongfu Wu<sup>a</sup>, Tingji Tang<sup>a</sup>, Baojun Bai<sup>a,\*</sup>, Xiaofen Tang<sup>b</sup>, Jialu Wang<sup>b</sup>, Yuzhang Liu<sup>b</sup><sup>a</sup> Department of Geological Science and Engineering, Missouri University of Science and Technology, 129 McNutt Hall, 1400N Bishop Avenue, Rolla, MO 65409, USA<sup>b</sup> Research Institute of Petroleum Exploration and Development, PetroChina, 20 Xueyuan Road, Beijing 100083, China

## Intermolecular interactions and crystallization behaviors of biodegradable polymer blends between poly (3-hydroxybutyrate) and cellulose acetate butyrate studied by DSC, FT-IR, and WAXD

pp 461–471

Nattaporn Suttiwijitpukdee<sup>a</sup>, Harumi Sato<sup>a,\*</sup>, Jianming Zhang<sup>b</sup>, Takeji Hashimoto<sup>a,c</sup>, Yukihiro Ozaki<sup>a,\*</sup><sup>a</sup> Department of Chemistry, School of Science and Technology and Research Center for Environment Friendly Polymers, Kwansei-Gakuin University, Sanda 669-1337, Japan<sup>b</sup> Key Laboratory of Rubber-plastics, Ministry of Education, Qingdao University of Science and Technology, Qingdao City 266042, People's Republic of China<sup>c</sup> Professor Emeritus, Kyoto University, Kyoto 606-8501, Japan

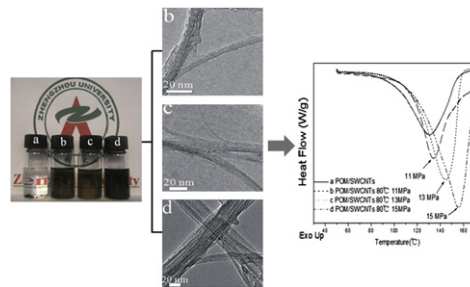


**High-crystallization polyoxymethylene modification on carbon nanotubes with assistance of supercritical carbon dioxide: Molecular interactions and their thermal stability**

pp 472–480

Ning Yu, Linghao He, Yuanyuan Ren, Qun Xu\*

College of Materials Science and Engineering, Zhengzhou University, Zhengzhou 450052, People's Republic of China



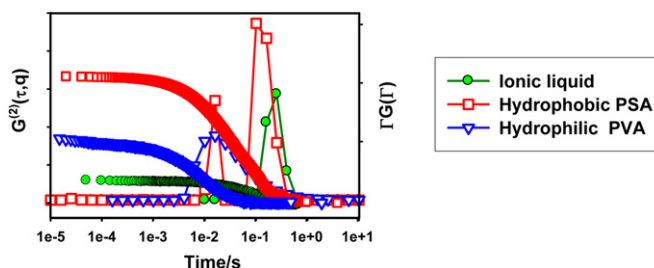
**Solubility of neutral and charged polymers in ionic liquids studied by laser light scattering**

pp 481–488

Ye Chen<sup>a,b</sup>, Yumei Zhang<sup>a</sup>, Fuyou Ke<sup>b</sup>, Jihan Zhou<sup>b</sup>, Huaping Wang<sup>a,\*\*</sup>, Dehai Liang<sup>b,\*</sup>

<sup>a</sup>State Key Laboratory for Modification of Fiber Materials, College of Material Science and Engineering, Donghua University, Shanghai 201620, China

<sup>b</sup>Beijing National Laboratory for Molecular Sciences and the Key Laboratory of Polymer Chemistry and Physics of Ministry of Education, College of Chemistry and Molecular Engineering, Peking University, Beijing 100871, China

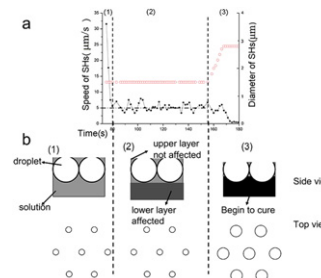


**In situ optical microscopy observation of the growth and rearrangement behavior of surface holes in the breath figure process**

pp 489–496

Hengyu Ma, Ye Tian, Xiaolin Wang\*

State Key Laboratory of Chemical Engineering, Department of Chemical Engineering, Tsinghua University, Beijing 100084, China



**Interface-tuned epoxy/clay nanocomposites**

pp 497–504

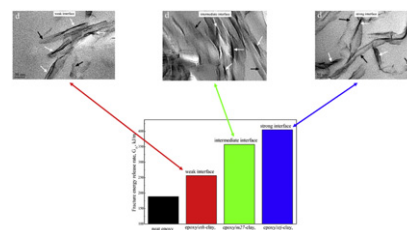
Izzuddin Zaman<sup>a,b</sup>, Quyen-Huyen Le<sup>a</sup>, Hsu-Chiang Kuan<sup>c</sup>, Nobuyuki Kawashima<sup>d</sup>, Lee Luong<sup>a</sup>, Andrea Gerson<sup>d</sup>, Jun Ma<sup>a,\*</sup>

<sup>a</sup>School of Advanced Manufacturing and Mechanical Engineering, University of South Australia, Mawson Lakes, SA 5095, Australia

<sup>b</sup>Faculty of Mechanical Engineering and Manufacturing, University of Tun Hussein Onn Malaysia, 68400 Batu Pahat, Malaysia

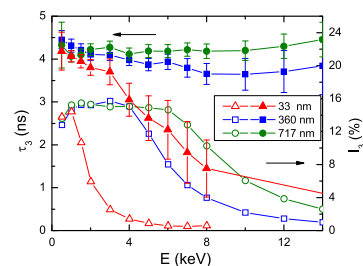
<sup>c</sup>Department of Energy Application Engineering, Far East University, Tainan County 744, Taiwan, ROC

<sup>d</sup>Applied Centre for Structural and Synchrotron Studies, University of South Australia, SA 5095, Australia



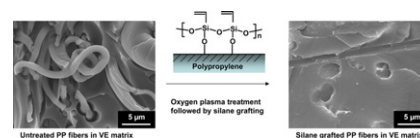
### Free volume distribution at the Teflon AF<sup>®</sup>/silicon interfaces probed by a slow positron beam

pp 505–509

Stephan Harms<sup>a</sup>, Klaus Rätzke<sup>a,\*</sup>, Vladimir Zaporozhchenko<sup>a</sup>, Franz Faupel<sup>a</sup>, Werner Egger<sup>b</sup>, Luca Ravelli<sup>b</sup><sup>a</sup> Institut für Materialwissenschaft – Materialverbunde, Technische Fakultät, Christian-Albrechts Universität zu Kiel, 24143 Kiel, Germany<sup>b</sup> Institut für Angewandte Physik und Messtechnik, Universität der Bundeswehr München Werner Heisenberg-Weg 39, 85577 Neubiberg, Germany

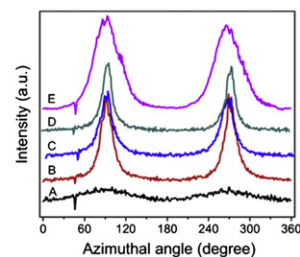
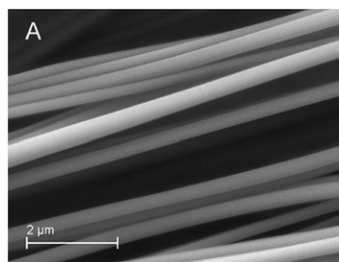
### Toughening vinyl ester networks with polypropylene meso-fibers: Interface modification and composite properties

pp 510–518

Y. Liang<sup>a</sup>, R.E. Jensen<sup>b</sup>, D.D. Pappas<sup>b</sup>, G.R. Palmese<sup>a,\*</sup><sup>a</sup> Department of Chemical and Biological Engineering, Drexel University, Philadelphia, PA 19104, USA<sup>b</sup> U.S. Army Research Laboratory, Aberdeen Proving Ground, MD 21005, USA

### Investigation of post-spinning stretching process on morphological, structural, and mechanical properties of electrospun polyacrylonitrile copolymer nanofibers

pp 519–528

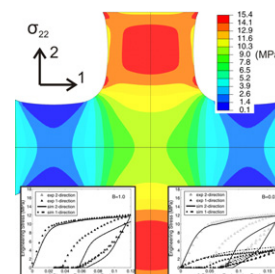
Chuilin Lai<sup>a</sup>, Ganji Zhong<sup>b</sup>, Zhongren Yue<sup>c</sup>, Gui Chen<sup>d</sup>, Lifeng Zhang<sup>a</sup>, Ahmad Vakili<sup>c</sup>, Ying Wang<sup>d</sup>, Lei Zhu<sup>b,\*</sup>, Jie Liu<sup>d,\*\*</sup>, Hao Fong<sup>a,\*\*\*</sup><sup>a</sup> Department of Chemistry, South Dakota School of Mines and Technology, Rapid City, SD 57701, USA<sup>b</sup> Department of Macromolecular Science and Engineering, Case Western Reserve University, Cleveland, OH 44106, USA<sup>c</sup> Department of Materials Science and Engineering, University of Tennessee Space Institute, Tullahoma, TN 37388, USA<sup>d</sup> Key Laboratory of Carbon Fiber and Functional Polymers, Ministry of Education, Beijing University of Chemical Technology, Chao-Yang District, Beijing 100029, China

### Biaxial elastic–viscoplastic behavior of Nafion membranes

pp 529–539

Meredith N. Silberstein, Priam V. Pillai, Mary C. Boyce<sup>\*</sup>

MIT Department of Mechanical Engineering, 77 Massachusetts Avenue, Cambridge, MA 02139, USA



**Charge dynamics and bending actuation in Aquivion membrane swelled with ionic liquids**

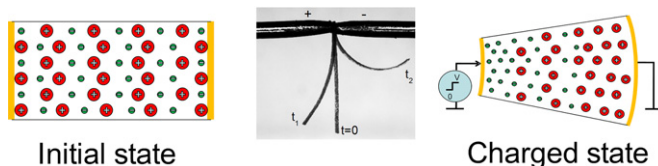
pp 540–546

Junhong Lin<sup>a,b</sup>, Yang Liu<sup>b,c,\*</sup>, Q.M. Zhang<sup>a,b,c</sup>

<sup>a</sup> Department of Materials Science and Engineering, The Pennsylvania State University, University Park, PA 16802, USA

<sup>b</sup> Materials Research Institute, The Pennsylvania State University, University Park, PA 16802, USA

<sup>c</sup> Department of Electrical Engineering, The Pennsylvania State University, University Park, PA 16802, USA



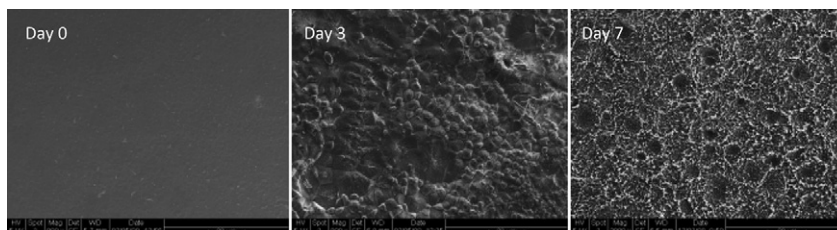
**Anaerobic biodegradation of the microbial copolymer poly(3-hydroxybutyrate-co-3-hydroxyhexanoate): Effects of comonomer content, processing history, and semi-crystalline morphology**

pp 547–556

Margaret-Catherine Morse<sup>a</sup>, Qi Liao<sup>b</sup>,  
Craig S. Criddle<sup>a,\*</sup>, Curtis W. Frank<sup>b,\*\*</sup>

<sup>a</sup> Department of Civil and Environmental Engineering, Stanford University, Stanford, CA 94305, USA

<sup>b</sup> Department of Chemical Engineering, Stanford University, Stanford, CA 94305, USA

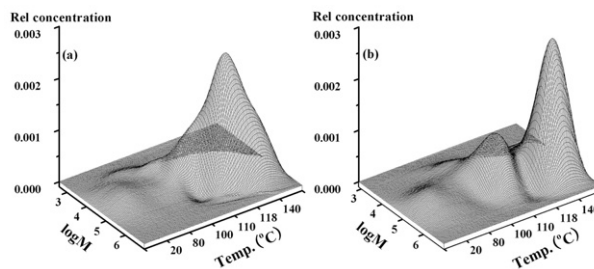


**Microstructure of two polypropylene homopolymers with improved impact properties**

pp 557–563

Yandi Fan, Chunyu Zhang, Yanhu Xue, Xuequan Zhang, Xiangling Ji<sup>\*</sup>,  
Shuqin Bo<sup>\*</sup>

State Key Laboratory of Polymer Physics and Chemistry, Changchun Institute of Applied Chemistry, Chinese Academy of Sciences, Changchun 130022, PR China

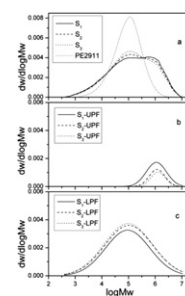


**Fracture behavior of bimodal polyethylene: Effect of molecular weight distribution characteristics**

pp 564–570

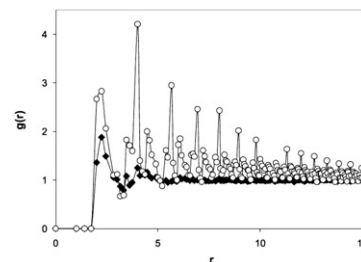
Xin Sun, Hongwang Shen, Banghu Xie<sup>\*</sup>, Wei Yang, Mingbo Yang

College of Polymer Science and Engineering, Sichuan University, State Key Laboratory of Polymer Materials Engineering, Chengdu 610065, Sichuan, China

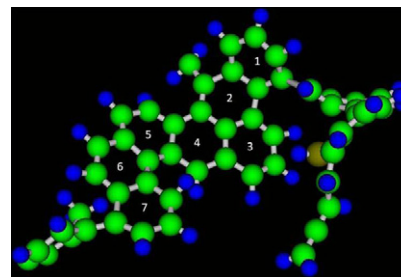


**Semicrystalline ordering in polymeric systems simulated by Bond Fluctuation Model**

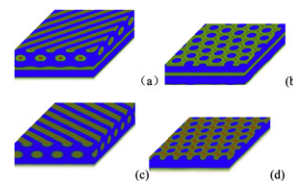
pp 571–576

J. Molina-Mateo<sup>a,\*</sup>, M. Arnoult<sup>b</sup>, J.M. Saiter<sup>c</sup>, J.M. Meseguer-Dueñas<sup>a</sup>, J.L. Gómez-Ribelles<sup>a</sup><sup>a</sup> *Universidad Politécnica de Valencia, Center for Biomaterials and Tissue Engineering, Camino de Vera s/n, 46022 Valencia, Spain*<sup>b</sup> *University of Nebraska-Lincoln, Department of Engineering Mechanics, W316 Nebraska Hall, Lincoln, NE 68588-0526, USA*<sup>c</sup> *Laboratoire d'Etude et Caractérisation des Amorphes et des Polymères, Université de Rouen, Rouen, France***Modeling initial stage of phenolic pyrolysis: Graphitic precursor formation and interfacial effects**

pp 577–585

Tapan G. Desai<sup>a,\*</sup>, John W. Lawson<sup>b</sup>, Pawel Koblinski<sup>c</sup><sup>a</sup> *Advanced Cooling Technologies, Inc., Lancaster, PA 17601, USA*<sup>b</sup> *Thermal Protection Materials Branch, NASA Ames Research Center, Moffett Field, California 94035, USA*<sup>c</sup> *Department of Materials Science and Engineering, Rensselaer Polytechnic Institute, Troy, NY 12180, USA***Hetero-structure of ABC triblock copolymer thin film on polymer-coated substrate**

pp 586–592

Rong Wang<sup>\*</sup>, Shanning Zhang, Yudong Qiu*Department of Polymer Science and Engineering, State Key Laboratory of Coordination Chemistry, Nanjing National Laboratory of Microstructures, School of Chemistry and Chemical Engineering, Nanjing University, Nanjing 210093, China*

(a) C+L : Cylindrical and lamellar phase  
 (b) PL+L : Perforated lamellar and lamellar phase  
 (c) Chex : Hexagonally packed cylindrical phase  
 (d) PL : Perforated lamellar phase

\*Corresponding author

Full text of this journal is available, on-line from **ScienceDirect**. Visit [www.sciencedirect.com](http://www.sciencedirect.com) for more information.

Abstracted/indexed in: AGRICOLA, Beilstein, BIOSIS Previews, CAB Abstracts, Chemical Abstracts, Current Contents: Life Sciences, Current Contents: Physical, Chemical and Earth Sciences, Current Contents Search, Derwent Drug File, Ei compendex, EMBASE/Excerpta Medica, Medline, PASCAL, Research Alert, Science Citation Index, SciSearch. Also covered in the abstract and citation database SCOPUS<sup>®</sup>. Full text available on ScienceDirect<sup>®</sup>

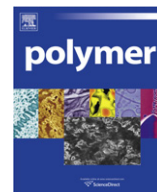


ELSEVIER

ISSN 0032-3861

## Author Index

- Agag, T. 307  
 Altstädt, V. 430  
 Arnoult, M. 571  
  
 Bai, B. 452  
 Baqar, M. 307  
 Baudouin, A.-C. 443  
 Berg, R. H. 422  
 Bilgin, S. 266  
 Bo, S. 557  
 Böker, A. 211  
 Boyce, M. C. 529  
  
 Cao, J. 383  
 Capaldi, F. M. 288  
 Carvalho, R. A. 258  
 Chan, L.-H. 326  
 Chen, C.-P. 326  
 Chen, G. 519  
 Chen, H. 400  
 Chen, Q. 383  
 Chen, Y. 481  
 Cheng, Y. 363  
 Coelho, J. F. J. 258  
 Cohen, N. 282  
 Criddle, C. S. 547  
 Cui, Y. 383  
  
 Desai, T. G. 577  
 Devaux, J. 443  
 Dijkstra, D. J. 430  
 Dong, Y. 363  
 Du, B.-Y. 391  
 Dworak, A. 250  
  
 Egger, W. 505  
 Eynur, T. 266  
  
 Fan, Y. 557  
 Farouk, B. 288  
 Faupel, F. 505  
 Feng, Z.-g. 347  
 Fong, H. 519  
 Frank, C. W. 547  
 Fu, Y. 415  
  
 Gao, P. 347  
 Gerson, A. 497  
 Gil, M. H. 258  
 Godard, P. 443  
 Gómez-Ribelles, J. L. 571  
 Grydgaard, A. 422  
 Guo, F. 422  
  
 Han, B.-H. 383  
 Handge, U. A. 430  
 Harms, S. 505  
 Hasalíková, D. 275  
 Hashimoto, T. 461  
 He, L. 472  
 Hošťálek, Z. 275  
 Huang, X. 363  
  
 Iqbal, F. 243  
 Ishida, H. 307  
  
 Jakobsen, M. R. 422  
 Jeng, R.-J. 326  
 Jensen, R. E. 510  
 Ji, X. 557  
 Jiang, H. 376  
 Jiang, X. 368  
 Jin, G.-w. 339  
 Jutz, G. 211  
  
 Kawashima, N. 497  
 Ke, F. 481  
 Keblinski, P. 577  
  
 Khosravi, E. 243  
 Kim, H. 339  
 Koo, H. 339  
 Kowalczyk, A. 250  
 Kuan, H.-C. 497  
  
 Lai, C. 519  
 Lawson, J. W. 577  
 Le, Q.-H. 497  
 Lee, R.-H. 326  
 Lee, S. 339  
 Lee, Y. 339  
 Li, C. 376  
 Li, Y. 409  
 Li, Z. 356, 400  
 Liang, D. 481  
 Liang, Y. 510  
 Liao, Q. 547  
 Libera, M. 250  
 Lin, J. 540  
 Lin, L. 233  
 Lin, S.-L. 326  
 Liu, J. 519  
 Liu, R. 356  
 Liu, Y. 452, 540  
 Luong, L. 497  
 Lyoo, W. S. 318  
  
 Ma, H. 489  
 Ma, J. 497  
 Maia, J. 258  
 Marchand-Brynaert, J. 443  
 Meng, C. 356  
 Meng, J. 363  
 Meng, Y. 391  
 Merna, J. 275  
 Meseguer-Dueñas, J. M. 571  
 Meyer, H. 430  
 Molina-Mateo, J. 571  
 Monnaie, I. 239  
 Morse, M.-C. 547  
 Musa, O. M. 243  
  
 Nam, K. 339  
 Napolitano, S. 239  
 Ndoni, S. 422  
 Nguyen, T. D. H. 318  
 Nguyen, T. L. T. 318  
 Nies, E. 239  
 Noh, S. K. 318  
  
 Ozaki, Y. 461  
  
 Palmese, G. R. 510  
 Pappas, D. D. 510  
 Park, J.-S. 339  
 Peleška, J. 275  
 Pillai, P. V. 529  
 Pitia, E. 297  
  
 Qi, G.-R. 391  
 Qiu, Y. 586  
 Qutubuddin, S. 307  
  
 Rätzke, K. 505  
 Ravelli, L. 505  
 Ren, Y. 472  
 Rousseaux, D. D. J. 443  
  
 Saiter, J. M. 571  
 Sallem-Idrissi, N. 443  
 Sato, H. 461  
 Schulte, L. 422  
 Sclavons, M. 443  
 Shaw, M. T. 297  
 Shen, H. 564  
 Silberstein, M. N. 529  
 Silverstein, M. S. 282  
  
 Simões, P. N. 258  
 Song, Y.-P. 233  
 Sun, L. 400  
 Sun, X. 564  
 Suttiwijitpukdee, N. 461  
 Szewczykowski, P. P. 422  
  
 Tang, T. 452  
 Tang, X. 452  
 Tian, Y. 489  
 Trzebicka, B. 250  
  
 Uddin, N. M. 288  
  
 Vakili, A. 519  
 Vigild, M. E. 422  
  
 Watach, W. 250  
 Wang, C. 409  
 Wang, D.-Y. 233  
 Wang, H. 481  
 Wang, H.-J. 326  
 Wang, J. 347, 452  
 Wang, P.-j. 347  
 Wang, R. 368, 586  
 Wang, X. 489  
 Wang, X.-L. 233  
 Wang, Y. 376, 519  
 Wang, Y.-Z. 233  
 Wang, Z. 409  
 Wei, G. 363  
 Weiss, R. A. 297  
 Wilkes, G. L. 266  
 Wu, Q. 356  
 Wu, Y. 452  
 Wübbenhorst, M. 239  
  
 Xie, B. 564  
 Xie, Z. 415  
 Xu, Q. 472  
 Xue, G. 409  
 Xue, Q. 400  
 Xue, Y. 557  
  
 Yang, M. 564  
 Yang, W. 564  
 Ye, L. 347  
 Yilgor, E. 266  
 Yilgor, I. 266  
 Yin, G. 368  
 Yin, J. 368  
 Yu, N. 472  
 Yuan, D. 356  
 Yue, Z. 519  
  
 Zaman, I. 497  
 Zaporojtchenko, V. 505  
 Zeiler, R. 430  
 Zhang, A.-y. 347  
 Zhang, C. 557  
 Zhang, G. 415  
 Zhang, J. 461  
 Zhang, L. 519  
 Zhang, Q. 400, 415  
 Zhang, Q. M. 540  
 Zhang, S. 586  
 Zhang, X. 557  
 Zhang, X.-H. 391  
 Zhang, Y. 481  
 Zhao, Z. 409  
 Zhong, G. 519  
 Zhou, B.-X. 391  
 Zhou, J. 481  
 Zhou, X. 391  
 Zhu, C. 363  
 Zhu, F. 356  
 Zhu, L. 519



## Feature Article

# Bionanoparticles as functional macromolecular building blocks – A new class of nanomaterials

Günther Jutz<sup>a</sup>, Alexander Böker<sup>b,\*</sup><sup>a</sup> *Physikalische Chemie II, Universität Bayreuth, 95440 Bayreuth, Germany*<sup>b</sup> *DWI an der RWTH Aachen e. V., Lehrstuhl für Makromolekulare Materialien und Oberflächen, RWTH Aachen University, 52056 Aachen, Germany*

## ARTICLE INFO

*Article history:*

Received 3 August 2010

Received in revised form

22 November 2010

Accepted 25 November 2010

Available online 7 December 2010

*Keywords:*

Bionanoparticle

Ferritin

Biopolymer conjugate

## ABSTRACT

We would like to introduce bionanoparticles with their unique multifunctional and self-assembling properties. Particularly, protein cages like plant viruses or ferritin but also other well-defined self-assembling protein structural motifs are valuable building blocks with great potential in (bio-) nanotechnology. A steeply increasing number of research works present promising results and applications in biomedicine, diagnostics and analytics as well as nanoelectronics. However, the use of bionanoparticles for hybrid and soft protein–polymer composite materials has not received high attention yet. The article will first introduce the structural principles of well-defined protein complexes and exemplarily describe the structure of a few selected plant viruses and ferritin. Then, the recent progress in chemical or genetically programmed functionalization and the use of the modified bionanoparticles for the production of novel nanostructured (hybrid) materials will be presented. An updated overview of grafting-onto and grafting-from polymerization methods for the modification of proteins and protein complexes will be given as well. The feature closes with some exciting examples in which bio (in-) organic nanoparticles are employed in analytics, for catalysis and biomedical applications.

© 2010 Elsevier Ltd. All rights reserved.

## 1. Introduction

Miniaturization towards nanoscale structured materials and devices have become a leading trend in the beginning of this century. The generation of small structures was traditionally a top-down process: The application of masks, illumination and etching steps generated the desired structures on an initially unpatterned material. To generate even smaller structures than currently possible with commercially competitive lithographic methods, bottom-up approaches, i.e. the generation of complex nanoscale patterns which start from nanoscaled building blocks, have been developed. By now, an astonishing multitude of materials, ranging from inorganic to polymeric nanoparticles, biological building blocks and nanostructured thin films with many different electronic, magnetic, optical and (bio-) chemical properties have been synthesized and characterized in great detail. The pivotal point is the directed assembly or self-assembly of these systems into hierarchically ordered and/or arbitrarily defined structures [1]. Such

structures can be used in high-resolution soft lithography to produce next-generation nanoelectronic devices [2,3]. The production and use of nanostructured and nanoscaled materials became a key technology in many more fields e.g. pharmacy [4], regenerative medicine [5], diagnostics [6], cosmetics [7] or food technology [8,9].

Progress in nanotechnology is not only aiming at miniaturization but also at systems with increased complexity. This is not just a matter of geometrical structurization but also a matter of specific functionalities that are positioned at discrete locations and in defined distances. Nature and its highly precise mechanisms of life, mainly based on two classes of biomacromolecules, proteins or polypeptides and polynucleic acids, set the benchmark for functional structures down to atomic scales. Thus, the use of biomolecules is considered as an obvious step in the synthesis and construction of next-generation nanomaterials and devices. A whole new branch termed bionanotechnology seeks for scientific as well as economic breakthroughs in the development of bio-inorganic nanomaterials with novel properties for computation and nanotechnology, new methods in diagnosis and analytics or new drugs and drug delivery systems [10,11]. While protein or polynucleic acid scaffolds provide structural and chemical functions, nanoparticles may contribute electronic, luminescent or magnetic

\* Corresponding author. Fax: +49 241 8023301.

E-mail addresses: [guenther.jutz@uni-bayreuth.de](mailto:guenther.jutz@uni-bayreuth.de) (G. Jutz), [boeker@dwi.rwth-aachen.de](mailto:boeker@dwi.rwth-aachen.de) (A. Böker).

properties to such hybrid assemblies [12]. Ligand systems on nanoparticles can introduce further functionalities for recognition and affinity processes or change the solution properties. Attached polymers change pharmacokinetic properties, mediate solubility or can be used as the bulk material in blends, providing a matrix for the embedded or surface-immobilized (bio-) nanoparticles (Fig. 1).

This feature focuses on protein complexes which can be used as valuable macromolecular building blocks for functional assemblies, as size-constrained reaction vessels, for the construction of bio-(in)organic nanostructured hybrid materials and biocompatible scaffolds for potential applications in bionanotechnology. Self-assembled natural protein complexes, protein cage architectures and particularly ferritin and some plant viruses have been extensively used in the last few years as building blocks and templates in bionanochemistry and bionanotechnology [13–15]. They are robust assemblies and can be obtained from biological sources or through *in vitro* expression and self-assembly. The combination of protein complexes with inorganic nanoparticles has resulted in materials with a number of interesting properties and applications and received already considerable attention from applied research. With increasing understanding and progress in modification of such systems, multifunctional systems can be constructed. Among the plurality of biological entities which can be used in bionanotechnology, this feature presents mainly examples of Cowpea Mosaic Viruses (CPMV), Tobacco Mosaic Virus (TMV) and ferritin. They have been used as model systems for the development of new compounds and as reference systems to test new (bio-) chemical analytical techniques since decades. Their peculiar properties make them ideal workhorses and they have routinely been used to show a proof of principle. Additionally, Turnip Yellow Mosaic Virus (TYMV) is presented, an icosahedral virus with properties similar to CPMV. This serves to illustrate the applicability of the concepts derived from e.g. CPMV to other similar systems.

We aim to highlight recent developments in the area of defined, self-assembled bionanoparticles, starting with their structural design, methods for modification by chemical and genetic means and finally, their use in the synthesis of novel nanomaterials. Many different disciplines have to contribute to the development of these nanosystems in bioengineering and biomedicine. The section on the recent progress in the synthesis of well-defined functional polymer–protein conjugates aims to inspire new ideas for future contributions of macromolecular chemistry to the construction of materials derived from bio-(in)organic macromolecular building blocks.

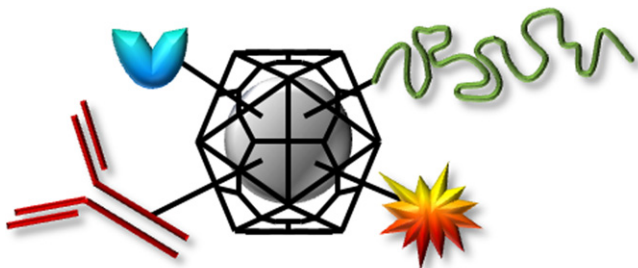


**Fig. 1.** Schematic picture of a multifunctional bionanoparticle with different labels, e.g.: antibodies that mediate cell-specific interactions; enzymes that perform catalytic biological functions; polymers that shield and/or modify solution and pharmacokinetic properties; fluorescent dyes that allow tracking and visualizing the nanoparticle distribution in cells or tissues. The interior of the protein cage can be used to load nanoparticles for therapeutic (e.g. radio therapy) or diagnostic purposes (e.g. tracking by magnetic resonance).

## 2. Complexity and symmetry

In the last two decades groundbreaking developments in biochemistry and microbiology led to tools for the analysis and synthesis of polynucleic acids. Facile cloning and rapid PCR techniques allow the design and high yield production of this class of biopolymers. DNA and RNA nanotechnology have become an established field in science and complex architectures have been obtained by assembling DNA and RNA functionalized materials through primarily sticky-ends of complementary base pair sequences.

While programmed assembly of polynucleic acid strands has become a standard technique in bionanotechnology, the design of self-assembling polypeptide or protein complexes is still a considerable challenge [16,17]. Proteins have – unlike most synthetic polymers – a more or less fixed three-dimensional conformation through covalent bonds or non-covalent interactions. This structural rigidity and the highly functional surface of proteins can drive self-assembly of protein subunits in solution to oligomeric filamentous, cage-like or tubular structures and to regular patterns on various surfaces and interfaces [18]. Symmetry plays an important role in the assembly process [19]. Binding sites and functional groups on such complexes are held at precisely defined positions and orientations. While protein crystals are rare *in vivo*, many examples of symmetric protein complexes have been found and characterized with the advance of electron microscopy and X-ray crystallography. The helical symmetry in the protein shell of tobacco mosaic virus and the cubic symmetry of spherical viruses were already described in the mid 1950s and the regular geometry and structure of many viruses is known today in great detail [20]. The quasi-equivalent assembly of protein subunits in icosahedral virus capsids is a particularly early recognized and well investigated, yet complex example of protein assembly [21,22].

The *de novo* design of peptides with predetermined geometric structures requires detailed knowledge of structure-forming principles. Analysis of the genomic pattern of known supramolecular assemblies can help to make predictions for potentially self-assembling proteins [23]. Short oligopeptides and simple tertiary structures like beta-sheet forming amphiphilic peptides can be synthesized by classical stepwise solution synthesis or chosen from combinatorial libraries of structure-forming amino acid sequences. Their manifold assembling capabilities were explored in detail [24,25]. Although peptides which self-assemble to large extended sheets, tubes or fibers are nowadays well-known, novel particulate architectures which were constructed by playing some sort of “peptide Lego<sup>®</sup>” are still rare. Exploiting geometrical principles, a few novel self-assembled protein complexes have been constructed by rational design of peptide building blocks [26,27]. Padilla and co-workers and Matsuura and co-workers created polyhedral cages through programmed self-assembly of designed peptides [18,28]. Cloning techniques allow the expression of fusion peptides in which different block sequences form various structures. Sugimoto reported about the construction of a protein ball-spike supramolecule by fusing the  $\beta$ -helix forming gp5 protein of the T4-bacteriophages to the cage-forming subunits of *Listeria*-Dps (DNA-binding proteins from starved cells) at the corresponding symmetry axis. The protein self-assembly leads to the formation of a tetrahedral arrangement of the four helical spikes with the Dps cage in the middle [29]. Such proteins can assemble to new architectures for which nature delivers the construction kit. The rational design of the conformation of protein complexes to build novel enzymatic and other biological complexes seems not out of reach (Fig. 2).

Proteins can display a vast variety of functions. Enzymatic and immunospecific reactions etc. are the natural working domain of

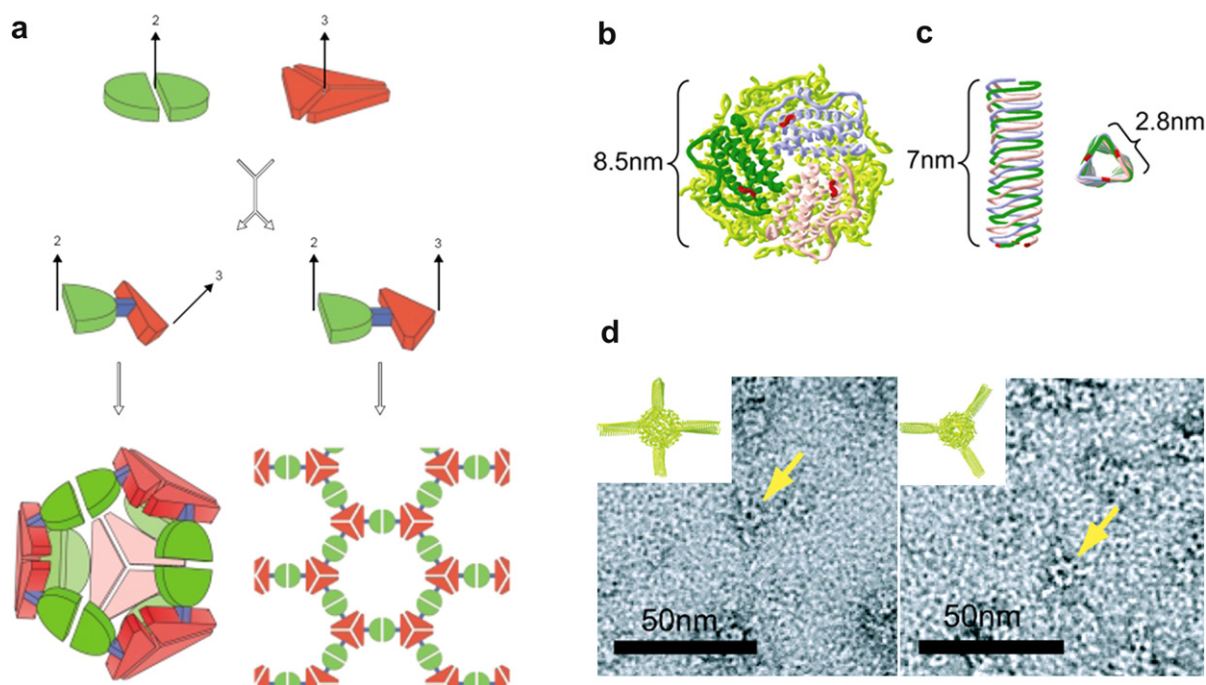


**Fig. 2.** a) Design principle for self-assembling cage or layer forming fusion protein. The formed nanostructure depends on the geometry of the linker between the symmetrical self-assembling subunits [26]. (Reprinted from Current Opinion in Structural Biology 12, Yeates and Padilla, Designing supramolecular protein assemblies, 464–470, Copyright 2002, with permission from Elsevier) b)–d) Realization of a ball- and spikes- protein supramolecular assembly: b) The dodecahedron cage of the ferritin-like protein Dps from *Listeria innocua* along the three-fold axis with the three subunits surrounding the axis in different colours. c) Schematic drawing of the subunit and self-assembly of the  $\beta$ -helix domain of bacteriophage T4 (gp5 C). d) Model of self-assembled Dps-gp5 C fusion protein which was constructed by fusion of the N-terminus of the Dps subunits (depicted in b) in red) with the C-terminus of the gp5 C protein (depicted in c) in red) via a flexible 22 residue linker at the corresponding three-fold symmetry axes. Two orientations along different symmetric axis are shown and with examples indicated in the corresponding images from negatively stained transmission electron microscopy [29] (Sugimoto et al. Construction of a ball-and-spike protein supramolecule. *Angewandte Chemie – International Edition* 2006, 45, 2725–2728. Copyright Wiley-VCH Verlag GmbH & Co. KGaA. Reproduced with permission.)

proteins. However, peptides can also interact with metal or other inorganic substrates, a domain which only recently came into focus [30–32]. Through modern biomolecular techniques, peptides with non-natural and previously unknown functions can be selected and identified. The display technologies are an elegant example of evolutionary screening principles to identify substrate-specific binding properties [33]. Many different aptamers, protein sequences which show specific affinities, have been identified by this route [34,35]. The approach shows that the use of biomolecules is not restricted to native conditions and natural working fields but can be engineered for their use in hybrid structures and devices, which is an invaluable advantage [36].

### 3. Bionanoparticles

Meanwhile, a number of different protein cage architectures are known and characterized to great detail. In this section, we will introduce some prominent examples, including icosahedral and rod-like plant viruses and ferritin, which have all been used by many research groups during the last decade. They are commercially available or can be produced by rather simple biological procedures. This section should give the reader who is unfamiliar with the matter a general idea about protein cage architectures.

The robust nature and easy accessibility made cowpea mosaic virus (CPMV) one of the best investigated viruses and most widely used plant virus in bionanotechnology [37]. It is an isometric plant virus with pseudo- $T=3$  icosahedral symmetry and a diameter of approximately 30 nm (Fig. 3a) [38]. The crystal structure is refined at 2.8 Å resolution [39] and the bipartite genome is fully sequenced [40]. The 60 small capsid proteins (S, domain A) are arranged as 12 pentamers at the 5-fold axis and the 60 large ones (L, domains B and C) as trimers at the 3-fold axis. The natural host range is

restricted to legumes. Infection leads to chlorotic mottling and yellow mosaic pattern. Experimentally, high yields of virus can be obtained from infected leaves of black-eyed pea plants (*Vigna unguiculata*) after mechanical transmission. Typically 100 g fresh leaves deliver 100–200 mg of virus [41,42].

Turnip yellow mosaic virus (TYMV) is the type species of the genus *Tymovirus* (family *Tymoviridae*) [43]. Their capsid exhibits  $T=3$  icosahedral symmetry with a diameter of approximately 30 nm. The protein shell is made up of 180 chemically identical subunits and is specially stabilized through hydrophobic protein–protein interactions. TYMV particles show distinct and clearly visible surface structures (Fig. 3b) [44]. There are two main sedimenting components, the protein shell with no or little amount of RNA (T-component) and the capsid containing the single infectious virus genome as (+) ssRNA (B-component). The host range is restricted to dicots. Chinese cabbage (*Brassica campestris ssp. chinensis* and *ssp. pekinensis*) is found to be a useful host for propagation from which it can be obtained in large amounts and good yields [45]. TYMV and its crystalline assemblies have been investigated and characterized in great detail by atomic force microscopy with high resolution [46,47].

Tobacco mosaic virus (TMV) was the first virus that was isolated (Stanley 1935, Nobel Prize 1946) [48], and since then, TMV has been connected with many scientific milestones in biochemistry in general and virology in particular [49,50]. The tobacco mosaic virus (*tobamovirus*; unassigned genus), is a rod-shaped virus with helical symmetry [51]. The rigid tubes of approximately 18 nm  $\times$  300 nm have a central hollow core of 4 nm. 2100 subunits of a single coat protein enclose the single RNA genome in form of a right-handed helix (Fig. 3c). Distinct contacts between each subunit with three nucleotides lead to an *in vivo* and *in vitro* self-assembly of purified coat protein with viral RNA into infectious particles. As most



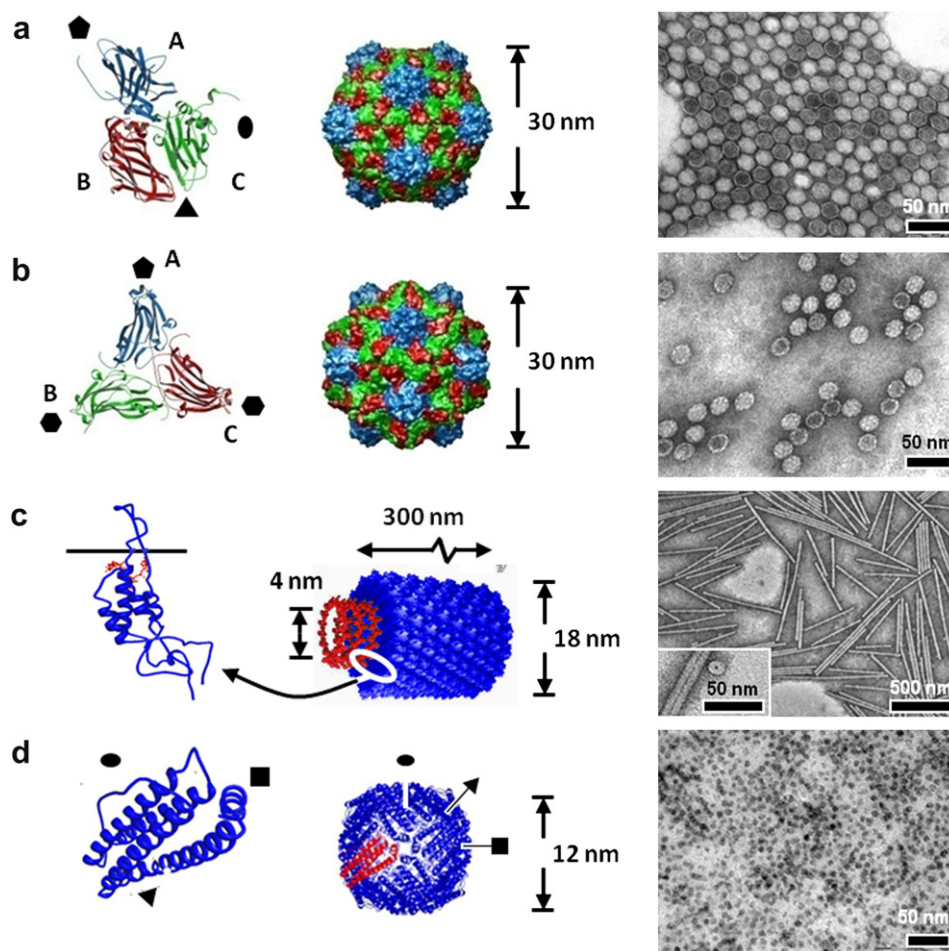


**Fig. 3.** Examples of bionanoparticles and their images in transmission electron microscopy (virus samples negatively stained with phosphotungstic acid). a) Cowpea mosaic virus (CPMV): Ribbon diagram of the coat protein subunits (BC and A) and domains (A, B and C) and contour surface plot with corresponding colour coding. The axes of the icosahedral pseudo-T3 symmetry are indicated. b) Turnip yellow mosaic virus (TYMV): Ribbon diagram of the identical coat protein subunits and domains (A, B and C) and contour surface plot with corresponding colour coding. The axes of the icosahedral T3 symmetry are indicated. The TEM image shows the distinct surface morphology of the protein capsid. c) Tobacco mosaic virus (TMV): Ribbon diagram of the coat protein subunit and biological molecule. The identical subunits (blue) arrange in a helical manner with distinct contacts around the DNA (red) in the inner cavity. The black line indicates the axis of the rod. The TEM shows a high magnification insert of a lying rod and a perpendicular disc. d) Ferritin: Ribbon diagram of the protein subunit and biological molecule. One of the 24 identical subunits is labelled in red. The symmetry axes of the rhombic dodecahedral arrangement are indicated. The ferritin sample was not stained and only the mineral cores can be seen [20].

filamentous molecular assemblies, TMV does not crystallize. Today, the structure is resolved to 2.9 Å and 5 Å by fiber X-ray diffraction [52] and electron microscopy [53,54], respectively. The coat protein alone assembles into small disks and short helix structures depending on pH, temperature and ionic strength as reviewed by Klug [55]. The unique highly anisotropic shape and easy production [41,56] made TMV for many years a model system of choice for many investigations in analytics and surface science, e.g. scattering techniques [57,58].

Ferritin represents a family of proteins with widespread biological importance [59], however, most of the time ferritin from horse spleen (HSF) is used. 24 protein subunits self-assemble to form a cage with an outer diameter of approximately 12 nm and an inner cavity of approximately 8 nm that is filled with hydrated ferric oxide (ferrihydrite  $\text{Fe}_2\text{O}_3 \times n\text{H}_2\text{O}$ ) (Fig. 3d) [60,61]. Ferritin preparations from natural sources possess some heterogeneity, arising from irreversibly aggregated dimers and trimers (polymeric forms) as well as from different iron contents which can vary from a few Fe-atoms to clusters with up to 4500 Fe-atoms. The protein shell is usually heterogeneous, too, and consists of a mixture of two different subunits, termed H for heavy and L for light chain. The ratio of H and L varies between organisms as well as between different tissues

within an organism. Each subunit protein forms a four-helix bundle that is arranged in 12 anti-parallel pairs to build a roughly rhombic dodecahedron shape [62,63]. The resulting three-fold channel is hydrophilic in nature and considered as the entrance for cations to form the mineral core while the fourfold channel is hydrophobic in nature. Both have a diameter of 0.3 nm. The formation of the mineral core is a catalytic multi-step process whose mechanism has been investigated in great detail and is quite well understood [61,64,65]. The sequences of different subunit chains are known and have been cloned and expressed in *Escherichia coli* to form recombinants devoid of the natural subunit heterogeneity of ferritin [66,67]. The subunits self-assemble *in vitro* to a 24-mer shell but only those subunits incorporating the H-chain with the ferroxidase center can be fully reconstituted with an iron core under native conditions [68].

#### 4. Self-assembling protein materials in nano- and biotechnology

##### 4.1. Overview

The chemically well-defined and monodisperse particulate nature of biomolecules is the basis for using them as self-assembling

building blocks for hierarchically nanostructured materials and for the production of bio-(in)organic nanoparticles [69]. The outer surface of proteins and protein cages has been employed as polyvalent scaffold similarly to dendrimers or multiple antigene peptides. Besides site-specific chemical conjugation reactions, biomolecules can be produced under genetic control which allows *a priori* ultimate control of the chemical structure and functionality. Such modified protein materials have been used e.g. as nanoscale building blocks with novel functionality or as vaccines. The interior cavity has been utilized as size-constrained reaction vessel for the production of nanomaterials or for encapsulation of drugs and labels for theragnostic applications in biomedicine. The self-assembling properties can be used for the construction of ordered functional arrays or nanowires. Fig. 4 gives a schematic categorization of fields in which self-assembling proteins and bionanoparticles have been used in the fabrication of hybrid materials.

#### 4.2. Polyvalent scaffolds

Recently, the topological analogy of plant viruses to dendrimers has been exploited in a number of organic reactions (overview [70]; selected examples [71–73]). Many researchers made use of the unique dendrimer-like polyvalent properties of the protein capsid for the synthesis of monodisperse and highly functional bionanoparticles. The close proximity of different labels could be shown by fluorescence resonance energy transfer (FRET) of differently introduced fluorescein and rhodamine dyes [74,75]. The advantage of symmetric protein complexes over dendrimers is that their structure is defined and can be known with atomic resolution. Labels can be introduced either on the assembled bionanoparticle or on the disassembled protein subunits. Care has to be taken then to direct the modifications to sites which are not involved into the self-assembly process and may impede the formation of the bionanoparticle.

A vast literature emerged from the first report about using cowpea mosaic virus particles as addressable nanoscale building blocks [76]. Besides carboxylic groups [77], especially uniquely addressable amino groups from lysine residues have been used in

conjugation reactions on the CPMV capsid's exterior [78]. The number of attached labels can be controlled through the excess amount and the conjugation chemistry. Thus, e.g. FITC reacts exclusively at one lysine amino group on the small subunit (KS38) while up to four lysine amino groups per asymmetric unit can be addressed with *N*-hydroxysuccinimidyl (NHS)-activated fluorescein if the dye/protein subunit ratio is increased up to 2000. Under less forcing conditions only KS38 is usually labelled. Many different labels, e.g. dyes, polymers, quantum dots or antigens have been introduced on the surface of CPMV using well-established chemical crosslinking procedures which employed either direct activation or bifunctional crosslinking agents. An exhaustive and current overview over the surface reactivity of CMPV is given by Steinmetz et al. [79,80]. Limited stability of the virus in aqueous organic solvents seems to be the only restriction for conjugation reactions (stability for up to 50% DMSO in buffered solution at pH = 3–9 and room temperature for prolonged time or at 60 °C for at least an hour was reported). Functional groups can be introduced on the virus surface by chemical conjugation strategies or through site-directed and insertional mutagenesis in clones. While the first offers larger variability of modifications the latter allows ultimate control of composition and location. As an example, hexahistidine-metal affinity ligands have been introduced by both ways [81,82].

An extremely powerful orthogonal method for (bio-) conjugation reactions is copper-catalyzed azide-alkyne cycloaddition (CuAAC), also descriptively called click-chemistry [83,84]. In a unique and highly selective reaction, alkynes and azides react in a [3 + 2] cycloaddition to form a triazol without interference from other functional groups of biomolecules. The proper choice of the copper catalyst and ligand greatly enhances the performance and applicability of the reaction to various substrates and scaffolds [71,85]. Installing the necessary azide or alkine groups on the biological scaffold can be done by conventional strategies, e.g. NHS-activated esters or by genetic engineering with non-canonical amino acids (see Fig. 18, 20). Click-chemistry has proven as the currently most efficient coupling strategy which allows single-site conjugation reactions also with large macromolecules. For example, Sen Gupta et al. managed to decorate CPMV with up to 125 alkyne-terminal side-chain glycopolymers with an average molecular weight of 13 kg/mol [86]. Previously, the attachment of e.g. PEG was limited to short polymer lengths and low labelling ratios. Under forcing conditions, up to 70 NHS-activated PEG-2000 but no more than 29 PEG-5000 could be attached per virus particle. The glycopolymer was additionally end-functionalized with a fluorescent dye which allowed convenient estimation of the number of bound polymer chains after separation from excess polymer. Another convenient feature of the click-reaction is the formation of fluorescent moieties upon formation of the triazol from non-fluorescent starting materials [87]. “Fluorogenic” reactions greatly facilitate the tracking and analysis of the conjugation reactions without further labelling or chemical quantification reactions [88,89].

Recently, also other plant viruses were employed as a polyvalent scaffold, particularly turnip yellow mosaic virus (TYMV), an icosahedral virus with a diameter of approximately 30 nm and a shell composed of 180 identical subunits. Reactions with dyes under NHS/EDC (1-(3-dimethylaminopropyl)-3-ethylcarbodiimide hydrochloride)-activation were used to address lysine amino groups and carboxylic groups [90]. The close proximity of orthogonal addressable amino and carboxylic groups was shown by dual labelling with terbium complexes as donor and Alexa-488 fluorophore as acceptor by time-resolved fluoroimmuno assay (Fig. 5) [91]. TYMV worked as a prototype protein scaffold for sensor development because the fluorophore was anchored via specific ligand–receptor (biotin–avidin) binding.

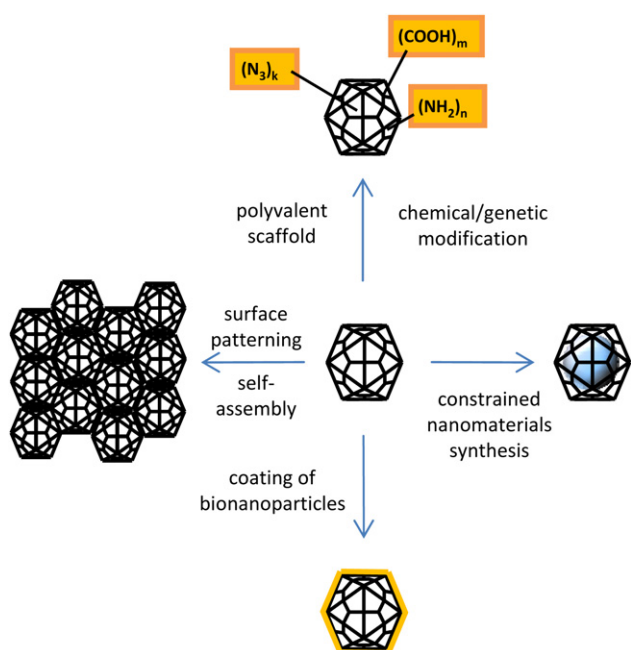
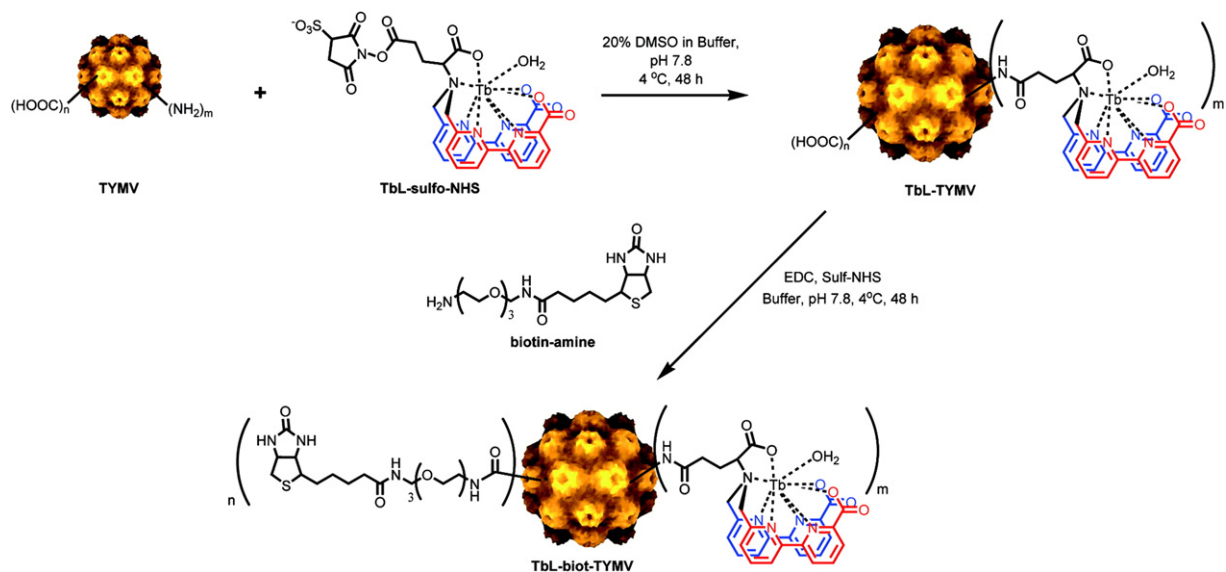


Fig. 4. Schematic overview of different uses of bionanoparticles in bionanotechnology.



**Fig. 5.** Example for orthogonal labelling of bionanoparticles: Dual labelling of turnip yellow mosaic virus (TYMV) with an NHS-activated terbium complex ligand and biotinyne-amine after activation of the surface accessible carboxylic acid groups of the virus coat protein with sulfo-NHS/EDC [91].

Few organic conjugation reactions have been reported for TMV because the commonly functional groups targeted for bioconjugation are not available on the exterior protein surface of TMV. Endo and co-workers used a genetically engineered TMV coat protein for the conjugation of porphyrin-maleimide. Self-assembly of the modified coat proteins to discs and rods leads to the formation of light harvesting arrays [92]. The same strategy was followed by Miller et al. who installed different fluorescent chromophores on the coat protein to achieve broad spectrum light collection with high efficiency [93]. The work of Schlick et al. significantly broadened the range of modifications [94]. They introduced the modification of the tyrosine-139 residue using diazonium salts; the robust protein assembly allowed also harsh conditions. Click-chemistry was used successfully for modification of the virus as well [95].

Modification of ferritin is of special interest because it enables to change the surface-assembling properties of the particles. Ferritin with its unique cavity is able to house many different inorganic materials and offers thus the chance to produce functional assemblies from the hybrid nanoparticles with interesting electronic, magnetic and optical properties (see below). Ferritin particles with reversed overall charge ('cationic ferritin') [96] and hydrophobic solution properties ('hydrophobic ferritin') [97,98] were prepared. Conjugating PEG-chains to the protein capsid produced ferritin that could be stably dissolved in organic solvents [99]. Zheng et al. functionalized ferritin with a number of initiating sites for ATRP polymerization and subsequently grafted oligo ethyleneglycol methacrylate-polymer chains from the ferritin protein shell [73]. This conjugate was also shown to be soluble in dichloromethane. In all these works, surface exposed carboxylic groups were addressed through carbodiimide-mediated amide formation.

A major advantage of proteins is their ultimate precision regarding composition (primary structure) as well as conformation (secondary – structure). An elegant way to alter the amino acid sequence and chemical structure is genetic engineering. Thus, the expression of coat proteins and *in vitro* self-assembly of the subunits allow the synthesis of non-natural virus capsids (virus-like particles, VLP). Substitution with non-natural amino acids provides protein complexes with novel desired functionalities at locations with ultimate precision. Finn and co-workers demonstrated the synthesis of virus-like particles derived from hepatitis B virus (HBV)

and bacteriophage Q $\beta$  which contained azidohomoalanine and homopropargyl glycine [100]. The VLPs could be labelled post-translationally with dyes, linkers, metal complexes or proteins through CuAAC (see Fig. 17). Ferritin chains were cloned and expressed in *E. coli* and self-assembled readily *in vitro* to intact cages [67]. The introduction of specific binding sequences is of particular interest in bionanotechnology. Combinatorial phage display technology is a valuable tool to identify and isolate binding motifs on the coat protein of bacteriophages [33]. Libraries of random peptides as part of the phage coat protein are screened in a few rounds of selection for binding affinity to different inorganic materials [30,101]. Identified peptide sequences can be incorporated into the *E. coli* expression vector for the ferritin subunit. Kramer et al. fused a sequence to the C-terminus of the coat protein which binds specifically to silver nanoparticles and directed thus the formation of silver nanoparticles to the interior of the ferritin cage (Fig. 6) [102]. Antigen or other sequences which are fused to the N-terminus of the subunit will be displayed on the exterior surface and yielded functional particles for cell targeting, diagnostic purposes or affinity for inorganic materials [103,104]. Both insertions do not hamper the self-assembly properties of the subunits to intact particles.

The presented plant viruses and ferritin have an intrinsic symmetry and thus the chemical functionalities are distributed over the particles' surface in a regular manner. Chemical means have to be employed to break the symmetry. Young, Douglas and co-workers used a solid-phase synthetic approach [105,106]. LiDps, the DNA-binding protein from *Listeria innocua*, consists of 12 subunits that self-assemble into a hollow protein cage with an outer diameter of 9 nm, was first bound to solid-phase support particles via disulfide linkages. Three out of 12 of the functional groups on the outside of the protein cage remain unoccupied and can be labelled. Cleaving LiDps from the support left the other nine free cysteine groups for reaction with a second label. Unsymmetrically functionalized particles tend to much less crosslinking phenomena than Janus-like particles. The *in vitro* self-assembling properties of bionanoparticle subunits allow also another approach, namely the mixed self-assembly of differently functionalized subunits. This has been shown e.g. for the Cowpea chlorotic mottle virus or ferritin [107,108]. Labels can also impeded the self-assembly properties. Mueller et al. show a nice example for differently modified TMV coat proteins [109].

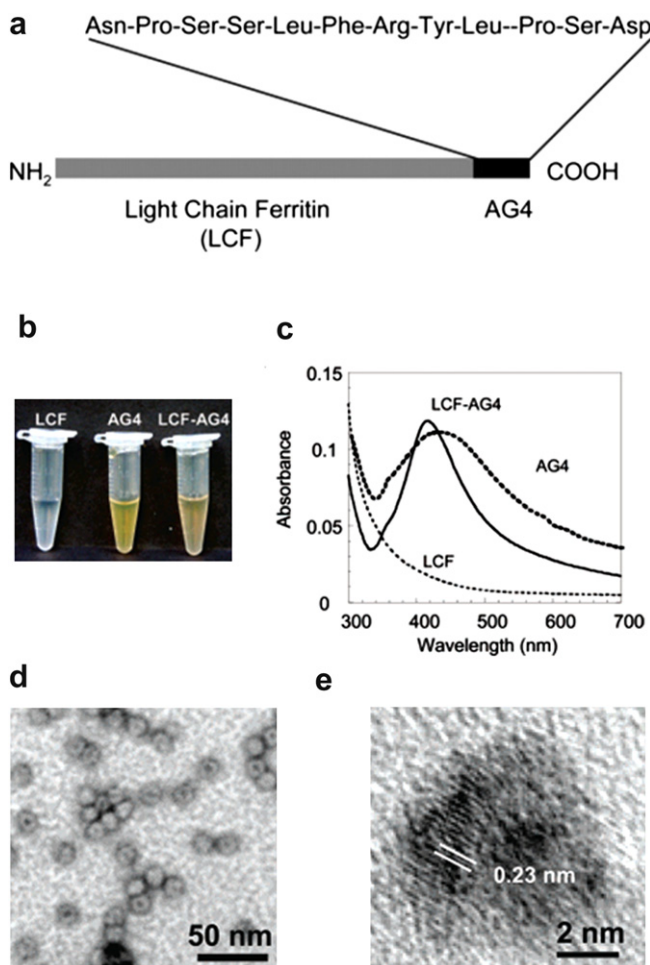


**Fig. 6.** a) Gene construction of a ferritin subunit with silver binding peptide for display on the interior of the assembled cavity. b) Incubation of non-modified ferritin, silver binding peptide and engineered ferritin and c) the corresponding UV–Vis spectra. d) Uranyl-stained TEM image of assembled engineered ferritin particles with silver cores. e) High-resolution image of a silver core showing lattice fringes. Reprinted with permission from Ref. [102]. Copyright 2004 American Chemical Society.

#### 4.3. Protein cages as templates for constrained nanomaterials synthesis

When in the beginning of the 1990s research was focusing on the preparation of well-defined nanoparticles, Mann and Meldrum were the first who made use of the cage structure of the iron-storage protein ferritin as size-constrained reaction vessel [110,111]. The interest went well beyond understanding biomineralization but was looking to use bio-nanoreactors for the production and encapsulation of non-native technologically relevant inorganic materials.

Ferritin became the prototype of a bio-inorganic composite nanoparticle [15]. Since then, numerous different inorganic cores have been synthesized inside the capsid, e.g. semiconductor nanoparticles of CdS [112], CdSe [113], ZnSe [114] and PbS [115] or metallic nanoparticles of Pd [116] and Ag [117] and many more but to name a few (Fig. 8). Various fields of applications have been demonstrated for these bio-inorganic particles in parallel [118,119]. Two approaches have been mainly followed for the templated nanoparticle synthesis: Either reassembly of the protein cage from the subunits in presence of the material which should be encapsulated or incubation of the empty and intact apoferritin with the respective metal ions, followed by conditions inducing slowly the

mineral precipitation (Fig. 7). The accessibility of the interior is restricted by the size of the hydrophilic channels in the protein cage. The directed mineralization inside the capsid is prerequisite for the controlled synthesis of nanoscale materials without non-specific bulk precipitation. *In vivo*, the formation of the ferrihydrite core is enzymatically controlled through the ferroxidase site at the interior protein surface. For non-ferroxidase substrates or for mineralization in virus capsids which is not assisted by specific proteins, the spatial selectivity is controlled by charged nucleation sites at the protein interface. Previously unknown ferritins from life-forms in extreme conditions, e.g. the hyperthermophile *Pyrococcus furiosus*, allow expanding the synthetic conditions for preparation of hybrid materials e.g. to high temperatures [120]. An expanded temperature range can be of importance when nanoparticles with different crystalline phases and e.g. better magnetic properties are desired.

Only the maximum loading of the protein cage gives a good uniform size distribution of the formed nanoparticles and thus, the interior dimensions of the protein cage dictate the final size of the core. Other ferritin cages with smaller cavity sizes have to be chosen for the bio-templated preparation of smaller inorganic nanoparticles. For example, the 5 nm cavity of the dodecameric bacterioferritin from *L. innocua* shares structural features with ferroxidase sites [121]. Cobalt oxide nanoparticles or ultrasmall platinum clusters were successfully prepared [122,123].

The approach was also expanded to plant viruses and many other protein cage systems, e.g. heat shock proteins [118,124,125].

#### 4.4. Bionanoparticles as scaffolds and templates for materials synthesis

Viruses can serve as building blocks or can be used themselves as scaffolds for the fabrication of novel bio-(in-)organic nanoscale and nanostructured materials [124]. Of particular interest are one-dimensional conducting nanostructures that can be used to build nanoelectronic devices. Phospholipid tubes or microtubules are classical templates for filamental or rod-like structures [126]. However, both suffer from limited stability because they are non-covalent assemblies and sensitive to solution conditions. The highly functional, negatively charged DNA has been routinely utilized for decoration with nanoparticles or deposition of conducting metal layers [127]. Polypeptides which form preferably highly stable structures like  $\beta$ -sheets can also form considerably stable fibers which provide a robust and highly functional template for metalization [128,129].

The M13 bacteriophage has a filamentous shape with a length of over 800 nm. The coat proteins are very amenable to changes via genetic engineering. Particularly, the easy genetic manipulation enabled the development of the above mentioned phage display technology. With this technology, specific binding sequences of inserted peptide libraries on the virus protein coat can be identified. Thus, it was an evident step to engineer phages and produce bio-inorganic hybrid assemblies. Insertion and expression of specific binding sequences can be achieved either for the coat protein only at the ends or along the whole virus capsid [130,131]. Annealing of the phages with ZnS or CdS nanocrystals aligned along the virus yielded long single crystalline semiconductor nanowires [132]. The two-dimensional assembly of the phages on electrostatically cohesive films of polyelectrolytes on macroscopic length scales represents an interesting approach for novel nanostructured and functionalized polymer surfaces for sensor or battery applications [131,133].

The rod-like tobacco mosaic viruses (TMV) have the additional advantage of being rigid and shape persistent. Thus, TMV is an attractive template and utilized in wild-type or genetically engineered form in a number of approaches to synthesize nanowires

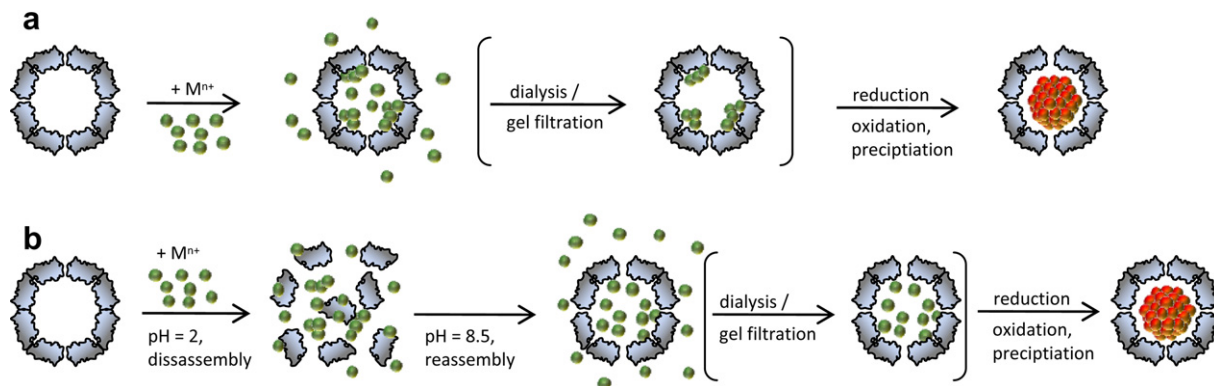


**Fig. 7.** Ferritin for the template synthesis of inorganic nanoparticles. a) Ferritin as nanoreactor. b) Synthesis of nanoparticles by the disassembly/reassembly route. Removal of excess salt by dialysis or gel filtration is optional as the ferritin cavity provides for some reactions a specific reaction environment over the surrounding.

[134]. Improved synthetic protocols enable the synthesis of virus rods which were homogeneously and densely coated with e.g. gold nanoparticles or platinum clusters [135,136]. However, the conductivity of such rods is poor because the single nanoparticles are electrically isolated. Royston et al. introduced a procedure in which they stabilized the TMV template with a thin silica shell before metal deposition. Polyaniline-coated TMV was sufficiently stable to withstand harsh Stöber conditions. TMV-silica composite rods were then successfully coated in silver, gold, palladium or platinum salt solution upon reduction with dimethylaminoborane [137]. In another similar approach, conducting poly(styrenesulfonate)-doped TMV-poly(aniline) fibers were coated with in sol-gel process with titania [138]. Such fibers could find application in nano-sensor devices because they combine inherent conductivity with a nanoscale catalytic surface. TMV with an additional inserted cysteine in the coat protein could readily be metalized with nickel

or cobalt through an electrodeless plating procedure [139]. Interestingly, if the reaction were done in the presence of gold-coated silicon substrates, the virus would have ordered perpendicular to the surface. Such assemblies had a very high surface area and could be suitable for the fabrication of microbatteries [140,141].

TMV was also used as template for the preparation of organic conducting nanofibers (Fig. 9). In a typical synthesis, aniline was oxidatively polymerized at room temperature in aqueous solutions of TMV [142–145]. At near neutral pH-values, long fibers with few ten micrometers in length and 21 nm in diameter (measured by TEM) were formed through the head-to-tail self-assembly capabilities of TMV. The assembly process was further enhanced by the surface polymerization of aniline. The electrostatic interaction of aniline/polyaniline with the negatively charged coat protein surface restricted the polymerization reaction exclusively to the virus surface. Bruckman et al. investigated the formation of fibers after functionalization of TMV [143]. The uncharged coating prevented interaction with aniline and no surface polymerization was observed. However, introducing sulphate groups on the tyrosine moieties of the subunits increased interaction and prevented the formation of long fibers because head-to-tail assembly was hindered. In contrast, ammonium thiophene could be polymerized successfully in presence of unmodified TMV at near neutral pH, similarly like aniline. The reaction pH influenced the morphology of the final product as well: Only single tobacco mosaic viruses could be observed at low pH < 2.5. At intermediate acidic pH = 4, initially formed single composite fibers tended to aggregate during the course of the reaction to form fiber bundles. Long and well dispersed single fibers were obtained only at near neutral pH [145]. The non-conducting fibers of branched polyaniline which formed at near neutral pH could be converted to conducting and well water-soluble fibers when aniline is polymerized in a second step at low pH in presence of polystyrenesulfonate [142].

#### 4.5. Surface patterning with self-assembled bionanoparticles

##### 4.5.1. Decoration of solid surfaces with bionanoparticles

The monodisperse nature of proteins and bionanoparticles makes them readily crystallizing in regular patterns on surfaces [146,147]. The adsorption and manipulation of two-dimensional arrays of ferritin on various surfaces and interfaces has been investigated intensively and in great detail [148–150]. Bacterial surface layers (termed S-layers) are a prominent example of ordered two-dimensional arrays of proteins at interfaces [151,152]. The protein sheets exhibit almost pure crystalline symmetry and are oriented with a different top and bottom side.

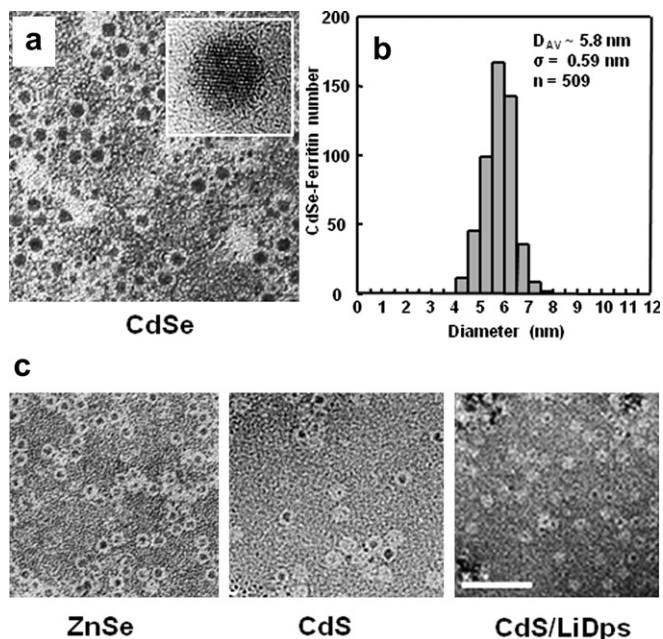


**Fig. 8.** Ferritin templated synthesis of nanoparticles. a) TEM image of CdSe nanoparticles formed in apoferritin. The insert shows a high-resolution image of a single CdSe nanodot. b) Size distribution of CdSe cores obtained from TEM. c) A gallery of various semiconductor/ferritin bionanodots. Dps from *Listeria* yields smaller particles. All images were stained with aurothioglucose [118]. Reproduced by permission of The Royal Chemical Society.

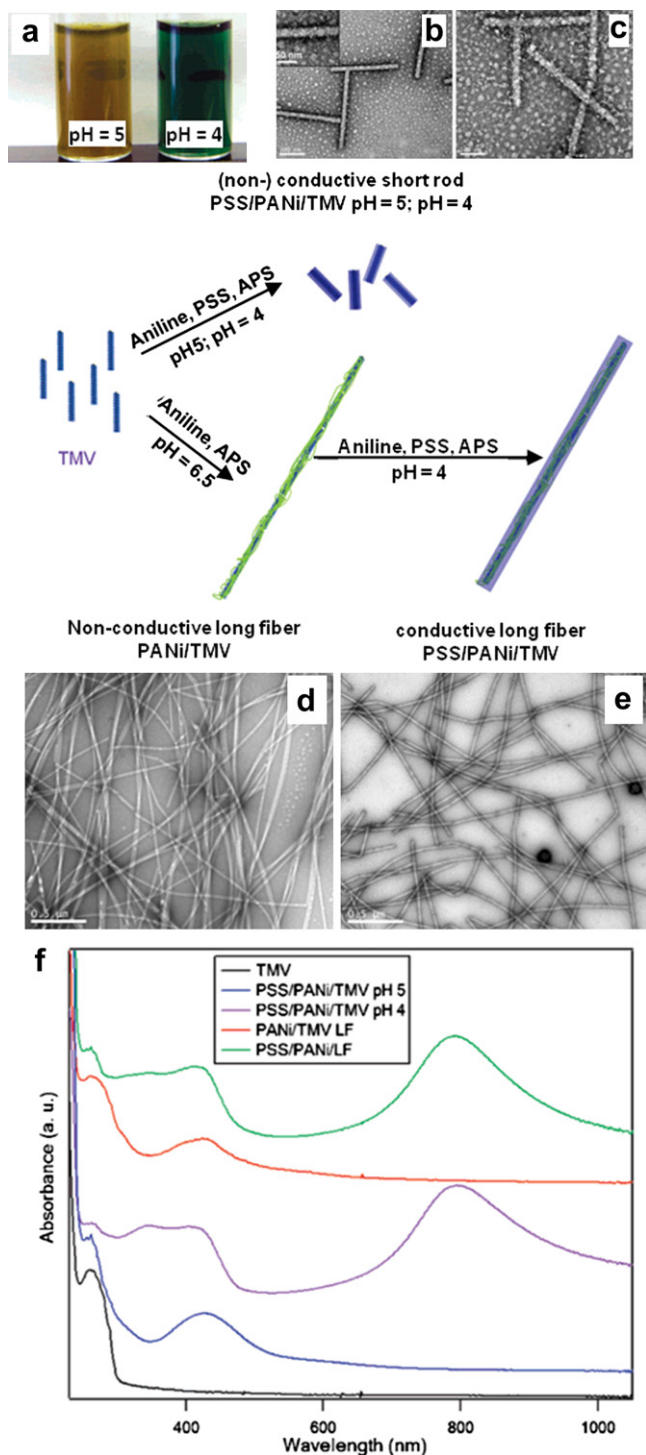


**Fig. 9.** Synthesis and TEM images of a)–c) short PSS/PANI/TMV rods (pH = 5 non-conducting; pH = 4 conducting) and of d)–e) long fibers PANi/TMV (non-conducting) and PSS/PANI/TMV (conducting). f) UV–Vis spectra of native TMV and the polymer/TMV composite rods and fibers. The three absorption peaks at ~420, 320 and 825 nm indicate the formation of conducting emeraldine salt form of PANI. Adapted in part with permission from Ref. [142]. Copyright 2007 American Chemical Society.

The formation of regular 2D-arrays of viruses or ferritin on liquid interfaces depends critically on solution conditions and the presence of e.g. cadmium ions or adsorptive layers, either formed through initially spread proteins, charged polypeptides or surfactants. After pick-up on a hydrophobically coated silicon wafer, 2D-crystalline ferritin arrays could be thermally treated to remove

the protein shell and fix the iron-oxide core on the substrate [149]. The possibility to fill the ferritin cavity with different inorganic materials makes it a versatile platform for nanoparticle arrays. Although the formation of 2D-crystalline arrays is experimentally still a delicate task, Yoshimura and co-workers have managed to produce excellent arrays of ferritin and Dps loaded with inorganic minerals over large areas (Fig. 10) [153,154]. Unfortunately, the experimental difficulty of this procedure makes the fabrication of arrays by this method unsuitable for robust device production. The surface crystal growth from a three-phase contact line has been proposed by Ikezoe et al. as an appealing simple method to prepare very large scale, well ordered and dense two-dimensional assemblies [155]. Selective nanoscale positioning of ferritin was realized by target-specific peptides that had been fused to the surface exposed N-terminus. Such modified ferritins bind with good selectivity to the respective inorganic surface and thus allow the formation of nanodot-arrays on arbitrarily lithographically pre-structured surfaces [156]. A printing method based on lithography controlled dewetting has been used to produce single lines of assembled ferritins [157]. Strong covalent binding yields dense but usually irregular assemblies. For example, gold surfaces were activated towards amide bond formation by a self-assembled layer of disulfides, carrying a succinimidyl moiety. Ferritin formed irregular assemblies with occasional formation of aggregates on such surfaces [158]. The same was observed when ferritin was thiolated with 2-iminothiolane hydrochloride and covalently immobilized on gold surfaces [159]. Electrostatic adsorption of ferritin can be achieved with appropriately chosen surface potential and ferritin particle charge. The electrostatic interaction potential can be adjusted through the buffer strength, thus varying the Debye length, i.e. the distance over which electrostatic interactions are greatly attenuated. Calculation of the spatial distribution of the total interaction free energy was performed for regular 15 nm disc pattern of 3-aminopropyltriethoxysilane (APTES) on a silicon wafer [160]. Single ferritin particles could be deposited on the APTES islands under optimized electrostatic conditions. Such selectively deposited nanodots can be part of a more sophisticated nano-electronic system. For example, the mineral cores can work as catalyst for carbon nanotube growth [161]. For applications in nanoelectronics where irregular quantum dot arrays are sufficient, simple droplet evaporation methods, convective assembly or spin-coating on polyelectrolyte layers can be done. They yield dense arrays without crystalline order [162–164].

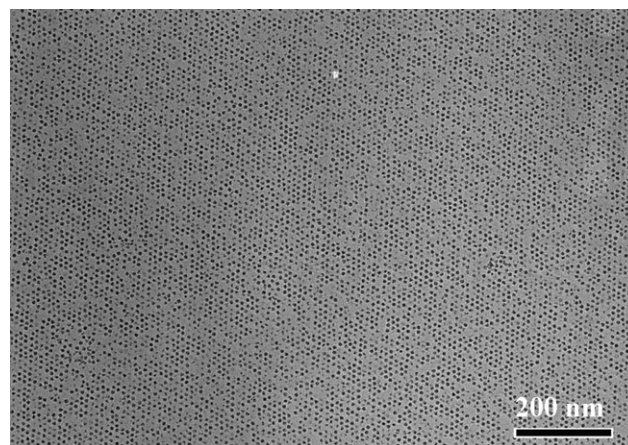


**Fig. 10.** Unstained TEM image of ferritin array on carbon film. The ferritin array was transferred from the water–air interface to a holey carbon grid and reinforced by carbon coating. Reprinted with permission from Ref. [154]. Copyright 2006 American Chemical Society.

Functional nanoarrays of adsorbed plant viruses have been achieved through electrostatic adsorption [165], covalent immobilization [166–168] or specific binding. Covalent immobilization yields usually irregular multilayers due to strong and irreversible virus–substrate and inter-viral interactions [166]. The formation of such assemblies thus depends on virus concentration, solution conditions and additives like PEG [167]. Chemo-selective binding to line patterns on a substrate was achieved by nickel-mediated interaction between the nitrilotriacetic acid-functionalized substrate and the genetically modified CPMV to present a hexahistidine tag on its capsid [169]. Soft polymer surfaces led to denser and more regular patterns than hard surfaces.

Virus layers with their inherent immunological properties and multifunctional surface were considered as building blocks for the construction of diagnostic arrays. For example, Steinmetz et al. investigated the formation of CPMV-multilayer arrays on solid supports via biospecific recognition. Biotin-functionalized CPMV was dual labelled with fluorescent dyes and immobilized on streptavidin-functionalized surfaces. The layer formation was monitored by quartz crystal microbalance or fluorescence microscopy [170,171]. The adsorption of non-modified plant viruses and proteins on surfaces in aqueous buffered solution is mainly governed by electrostatic interactions. The formation of virus layers depends therefore on the isoelectric point (pI) and the surface charge of the particle. At solution conditions below pI, viruses should adsorb strongly to negatively charged surfaces and weakly on positively charged surfaces; for solution conditions above pI the reverse should hold true. The largest amount of virus can be deposited at the pI itself because there is the balance between the opposing trends of particle–substrate attraction and particle–particle-repulsion [172]. However, particle charge is not the only factor which governs the layer-by-layer assembly of virus capsids and polyelectrolytes. Steinmetz et al. observed different architectures for spherical and rod-like viruses in multilayer assemblies. While icosahedral CPMV was readily incorporated into multilayers in the expected alternating manner, rod-like TMV was floating atop of the polyelectrolyte surface with spontaneous ordering [173]. A similar effect was also observed earlier for filamental bacteriophages [133].

The formation of one-dimensional structures is of special interest for the construction of nanowires and other structures in nanoelectronics. Thus, the controlled deposition and alignment of conductive wires from TMV is a topic of current investigations. For example, Velev and co-workers reported the formation of conducting fibers from flow-aligned tobacco mosaic viruses and covalently attached gold nanoparticles [174]. Silver enhancement was applied to finally achieve a continuous conducting metal layer. Micrometers long, end-to-end assembled TMV with single-virus width were printed on adhering surfaces from structured hydrophilic PDMS stamps and would form viable templates for the preparation of virus nanowires after metallization [175]. Complex patterns on a single-particle level were generated on carboxylic acid functional surfaces by metal-ion mediated selective adsorption. AFM-based dip-pen lithography was used to generate the chemical pattern for the precise and oriented deposition of single TMV [176]. Previously, the first report on TMV assemblies perpendicular to the surface was published [139]. A TMV mutant was created by insertion of an additional cysteine at the amino terminus of the coat protein. Since this cysteine is only sufficiently exposed at the end of the virus which contains the 3' end of the genome sequence, preferred vertical arrangement of the virus rods was observed on gold surfaces.

#### 4.5.2. Adsorption of bionanoparticles to liquid interfaces and soft polymeric surfaces

Liquid–liquid interfaces have been proposed to be “the emerging horizon for self-assembly of nanoparticles” [177]. Solid-

stabilized emulsions, known as Pickering Emulsions, and protein-stabilized emulsions are of considerable technological importance and have been investigated for decades. However, the field experienced a renaissance after stimulating reports from the group of Russell and co-workers [178,179]. Soon it was assumed that bionanoparticle stabilized emulsions could have interesting applications in drug delivery or as functional surfaces and interfaces. In a pioneering report, Russell et al. described the preparation of an emulsion of perfluorodecalin droplets in water which were stabilized by a monolayer of CPMV viruses (Fig. 11) [180]. Detailed investigations of the bionanoparticle covered interface showed that the virus cage is not des-integrating upon their adsorption. Similarly, TMV and TYMV were employed and the formation of the interfacial assembly kinetically and structurally investigated [181,182]. Particularly, the anisotropic rod-like TMV assembled either parallel or perpendicular to the surface, depending on the solution ionic strength or TMV concentration [181]. While modelling of respective surface tension curves indicated that “normal” proteins like BSA are – at least partially – unfolded at the interface, direct experimental results are difficult to obtain and sometimes contradictory. Bionanoparticles with their more distinct shape and robust structure are better amenable to microscopic investigations. Scanning force microscopy (SFM) and electron microscopy techniques were applied to image the bionanoparticles assembly at the interface of a liquid polymer precursor (poly(dimethyl siloxane), PDMS) which could be crosslinked by UV-light. By this trick, the equilibrium assemblies of bionanoparticles could be preserved and investigated in detail. In Fig. 11 it can be seen that the particles form a dense, although not regular assembly at the interface. Moreover, TMV was not forming liquid-crystalline arrays with parallel rods. The emulsions could be washed to remove excess nanoparticles

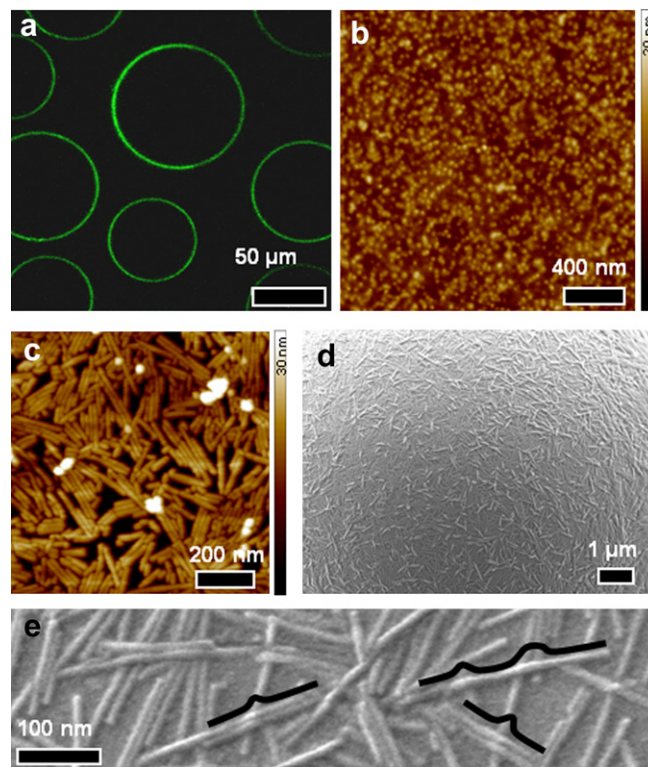


**Fig. 11.** a) Confocal laser scanning microscopy of a perfluorooctane-in-water emulsion, stabilized by fluorescein-tagged CPMV. b) AFM image of a CPMV stabilized poly (dimethyl siloxane, PDMS) surface after UV-crosslinking. c) AFM image of a TMV stabilized PDMS surface after UV-crosslinking. d), e) SEM image of the sample in c). Black lines should guide the eye.

and the droplets still did not coalesce. Thus, similarly to proteins, the bionanoparticles are irreversibly trapped at the interface.

A detailed investigation of the TMV adsorbed at the interface indicated that the rod was forming strongly curved bends when crossing each other (Fig. 11). This indicates the strong attraction to the interface but also a probable softening of the viral nucleoprotein by surface denaturing upon contact with the oil phase. Such thin biopolymer monolayer arrays can retain its function. For example, Zhu and Wang showed that a conjugate of  $\beta$ -galactosidase with polystyrene which was able to self-assemble at the interface had an increased stability and was active in the enzymatic interfacial transformation of lactose to octyl galactoside [183]. Further, the protein covered interface forms a viable template for biomineralization. Jutz and Böker used bovine serum albumin (BSA) and ferritin to stabilize oil-in-water emulsions. After exchange of the water phase with aqueous calcium phosphate solutions, slow and steady growth of mineral shells was observed [184].

Bionanoparticles were also used to stabilize polymer particles by assembling at the surface. When poly(4-vinyl pyridine) (PV4P) in dimethyl formamide was co-dissolved in an aqueous solution of CPMV, the bionanoparticles enabled solubilisation of the fairly hydrophobic polymer at pH > 5. Well-defined, sub-micron polymer spheres were produced upon slow dialysis against water. The polymer was becoming less soluble but the virus was assembling at the interface and kept it from phase separation and precipitation. Upon equilibration, a regular and dense assembly of CPMV on the polymer colloid surface was obtained finally, much of the imagination of a raspberry (Fig. 12) [185]. It was proposed that the final product was thermodynamically controlled and a simple geometrical model of the virus size and a hexagonal pattern could explain the decreasing colloid size with increasing virus mass to polymer mass-ratio [186]. The approach worked as well for TYMV, ferritin and rod-like viruses like TMV and bacteriophage [185–187]. The concept can be considered as an approach to produce responsive drug carriers. The polymer–bionanoparticle colloids can be redissolved at pH < 4, releasing the surface trapped proteins and therapeutic or diagnostic species which are conjugated or entrapped in the polymeric core.

Materials and surfaces with immobilized or “imprinted” proteins and bionanoparticles can work as viable scaffolds for chemical selective separations, biomimetic sensors and the development of biomedical devices and materials, e.g. artificial antibodies [188,189].

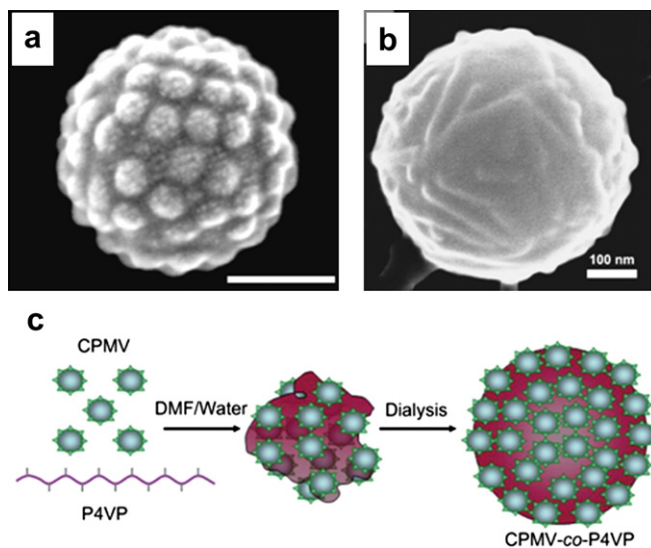


**Fig. 12.** a) CPMV and b) TMV assembled at the surface of P4VP particles after dialysis of the bionanoparticle–polymer mixture against water which lead to desolvation and phase separation of the polymer. The process is schematically shown in c) [185].

Molecular imprinting of bulk materials with large biopolymers has faced limitations because removal of the templating molecules is as difficult as the later access of the large analyte molecules. Recent developments in imprinting surfaces with protein-recognition sites have solved this problem [190,191]. Suitable protective layers, e.g. disaccharides and fluoropolymers, mediate the bionanoparticles' chemical and structural information to the interface and transfer the complementary chemical functionalities and shape to the matrix.

Bionanoparticles can usually not directly be mixed with polymers due to solvent incompatibility. Many polymers are only soluble in organic solvents and strong polar organic solvents usually denature proteins if not used in aqueous mixtures with a low solvent-to-water ratio. Thus, the first step to prepare protein or bionanoparticle–polymer blends is to find a common solvent or to modify the bionanoparticles appropriately. Alkylated [97,98] or PEGylated ferritin [73,99] shows good solubility in dichloromethane. TEM confirmed that the protein cage did not disassemble. Such modified ferritin could be dissolved in polymer blends. After the initial stimulating report by Russell and co-workers only marginal progress has been achieved. Russell showed that the presence of nanoparticles changes the morphology of micro-phase-separated block copolymers. For example, lamella-forming poly(2-vinylpyridine)-*b*-poly(ethylene glycol) changed the orientation from parallel to perpendicular to the surface in presence of PEG-ferritin but the localization of ferritin was difficult [192]. In thin films of polystyrene–poly(ethylene oxide) block copolymers, poly(PEG methacrylate) modified ferritin was directed to the cylinder phase because of the solubility [193]. Wild-type and modified ferritin were also used for phase-selective adsorption in phase-separated polymer blends [194]. Due to its multifunctional surface, the ferritin protein cage can interact with polymer chains and efficiently mediate load bearings to the matrix. For example, fibers from water-soluble poly(vinyl alcohol) which have been electrospun from polymer–ferritin mixtures had markedly increased toughness (Fig. 13) [195]. This is also seen in an absolute absence of creep during pH-triggered actuation of the nanofibrous composite hydrogels [196]. The composite hydrogels are stable in a wide range of pH-values and applicable to magnetic resonance imaging-based detectable cell culture scaffolds due to the superparamagnetic iron-oxide core [197]. Acid-treated carbon nanotubes which were functionalized with ferritin were readily dispersed in PVA matrices and the elastic modulus increased dramatically compared to composites prepared with pristine carbon nanotubes [198].

#### 4.6. Synthesis of polymer–bionanoparticle conjugates

Evidently, bio-(inorganic) nanoparticles exhibit interesting properties which could add valuable functions and functionalities to various other materials, surfaces and interfaces or function as therapeutic or diagnostic agents by themselves. Biomacromolecules can be covalently linked to polymers, used in blends or immobilized on functional polymeric surfaces. The covalent conjugation to polymers and (polymeric) surfaces is particularly important modification processes to prepare proteins and protein complexes for use in applications, as in biomedicine or as molecular sensors in diagnostic assays. We will focus here primarily on the preparation of well-defined site-specific conjugation reactions. Polymer–protein hybrid materials are still a niche although they gained steeply increasing interest in the last years. Undoubtedly, this is connected with excellent progress in the preparation of well-defined functional polymers via controlled radical polymerization techniques.

Until recently, mostly water-soluble poly(ethylene glycols) (PEG) were conjugated to proteins. A portfolio of suitably end-functionalized and activated PEGs of different chain lengths is commercially available [199]. This is attributed to the change in pharmaceutical



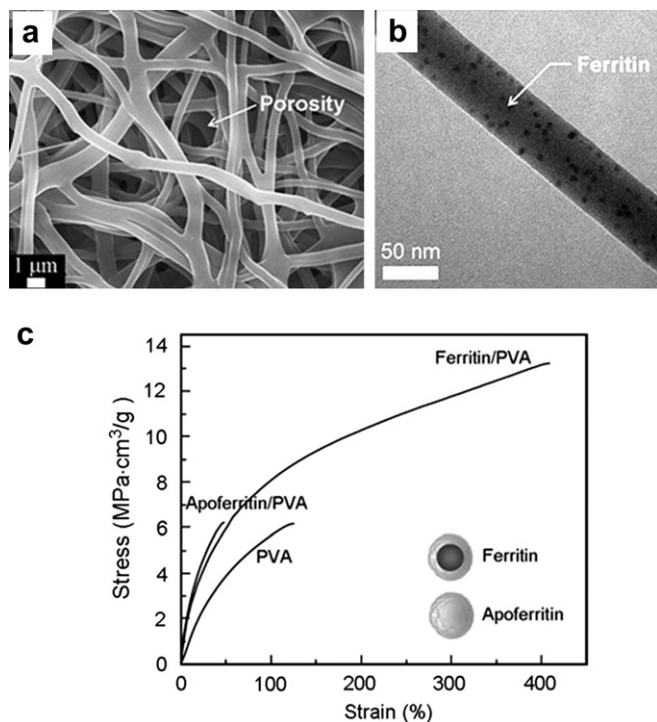


**Fig. 13.** a) PVA/ferritin composite fibrous hydrogel from electrospinning. b) Detail of a fiber showing the dispersed ferritin particles. c) Stress–strain curve showing the markedly increased toughening of composite fibers [195]. Reprinted with permission from Shin, Kim et al.: *Appl. Phys. Lett.* 93 (2008), 163902. Copyright 2008, American Institute of Physics.

research from mainly small molecules to therapeutic biomolecules, often collectively named biologics. The modification of macromolecular biological drugs and drug delivery systems with poly(ethylene glycol) (PEGylation) is a well-established and -investigated method to enhance blood circulation time and stability, decrease non-specific binding and immunogenicity etc. [200,201]. Other polymers are rarely used for the preparation of polymer–protein block copolymers, certainly also because of regulatory issues in the field of biomedicine [202,203]. However, they are considered important for further improving the pharmacokinetic performance of conjugates [202,204,205].

The advancements in the preparation of well-defined functional polymers, particularly the newly developed methods of controlled radical polymerization, e.g. reversible addition fragmentation chain transfer (RAFT) radical polymerization or atom transfer radical polymerization (ATRP) allow conducting controlled polymerizations in aqueous solutions at ambient conditions [206,207]. The basic strategy of controlled radical polymerization techniques relies on the establishment of a large pool of dormant radicals which can be easily reactivated and are in equilibrium with propagating species. Most important, they tolerate the presence of a wide variety of functional groups. Thus, these polymerization techniques are particularly well suited for the preparation of polymer–protein block copolymers, either by grafting-onto or grafting-from methods. Grafting-onto strategies (convergent synthesis) build on the preparation of defined functional polymers which are conjugated to the biopolymer via reactive groups and established crosslinking chemistries [208]. For the grafting-from strategy (divergent synthesis), biopolymers or biological scaffolds are suitably functionalized with initiators or transfer agents and the polymer chain is grown directly from the biomaterial. The different approaches have been reviewed recently by Haddleton and Klok [209,210]. Since then,

new exciting results have been reported, particularly on grafting-from approaches under very mild conditions. Figs. 14 and 16 give a schematic overview over polymerization reactions and functional versatility. The table is not meant to be exhaustive but limited to the most recently reported progress.

End-functional polymers for grafting-onto can be synthesized by starting with a suitable functional initiator (optionally protected) or by modification of end groups after polymerization (Figs. 14 and 16). For example, Haddleton and co-workers used a 2-bromoisobutryl ester with a protecting acetal as initiator for ATRP (Fig. 14). After polymerization of poly(ethylene glycol) methacrylate (PEGMA) and deprotection under acidic conditions, aldehyde end-functional polymers were obtained [211]. Samanta et al. synthesized unprotected benzaldehyde-functional ATRP-initiators for the preparation of poly(methacryloyloxyethyl phosphorylcholine) (PMPC), a hydrophilic and biocompatible zwitterionic polymer [212]. Aldehydes are suitable for conjugation to protein-amino groups via imine-formation. A second reduction step is necessary to yield stable secondary amines. *N*-hydroxysuccinimidyl (NHS) activated esters are most popular for conjugation reactions to amino groups. However, side reactions and decreased stability in neutral and alkaline aqueous solution constitute major drawbacks and result in low conjugation ratios for difficult reactions i.e. with few accessible amino groups or long polymer chains. *N*-hydroxysuccinimidyl esters of 2-bromo-2-methylpropionate or 2-bromoisobutyrate were used to polymerize PEG methacrylate or MPC [212–214]. No conjugation or only low ratios could be achieved for conjugation of MPC with lysozyme or interferon- $\alpha$ 2a. Click-chemistry was considered as a suitable alternative because of the high stability of the involved functional groups, their strict bio-orthogonality and exceptionally high efficiency (see as an example Fig. 15). In the most simple case, the azide group can be introduced through azide-bromine exchange after polymerization with any conventional ATRP-initiator [215]. To eliminate this step, Shi et al. used an azide-functional 2-bromoisobutryl ester for the polymerization of *tert*-butyl methacrylate. The polymer was conjugated to alkyne-functional biotin or via a dialkyne linker to azide-functionalized BSA. Side-chain modifications with glucosamine and a near infrared fluorescence dye produced multifunctional polymer–protein conjugates [216]. Glycopolymers with an azide endgroup were prepared by Sen Gupta et al. and conjugated to CPMV (Fig. 15) [86].

Native free cysteines which are not involved in structure-stabilizing disulfide bridges are less abundant than amines and represent therefore very interesting targeting sites. Popular coupling strategies make use of Michael-addition of the thiol group to maleimides or the formation of disulfides. Bontempo and Maynard prepared a pyridyl disulfide-functionalized bromoisobutryl ester as initiator for the controlled polymerization of hydroxyethyl methacrylate [217]. Around 90% of the polymers contained the disulfide endgroup which were directly usable for conjugation to BSA. The non-covalent, yet very stable avidin–biotin interaction was also employed to prepare bioconjugates. Biotin-end-functional poly(*N*-isopropyl acrylamide) (PNIPAm) was synthesized directly with a biotinylated ATRP-initiator by Heredia et al. [218]. Ferritin which was covalently functionalized with thermoresponsive PNIPAm showed reversible aggregation to raspberry like colloids at temperatures above the cloud point at 30 °C [219].

The RAFT technique also presents possibilities for a convergent strategy (Fig. 16). Pound et al. reported that the dithioester-endgroup of poly(*N*-vinylpyrrolidone) prepared by RAFT easily converted to an aldehyde function post-polymerization [220]. The quantitative reaction was shown by NMR, gradient polymer elution chromatography as well as MALDI-TOF mass spectrometry. The functional polymer reacted with lysozyme and formed a covalent conjugate after reduction with sodium cyanoborohydride. The

Functional initiator	End-functional polymer	Target group/ resulting bond	ref.
		NH <sub>2</sub> /sec. amine (after reduction)	[211]
		NH <sub>2</sub> /sec. amine (after reduction)	[212]
		NH <sub>2</sub> /amide	[212- 214]
		SH/disulfide	[216]
		alkyne/triazol („click chemistry“)	[217]
		streptavidin/ non-covalent interaction	[218]

Fig. 14. Reactive end-functional polymers for grafting-onto to biomolecules via ATRP.

actual number of grafts was not determined. A RAFT agent with an NHS-activated ester group was prepared for the synthesis of other functional RAFT agents but not used itself for the preparation of NHS-terminal polymers [221]. Theato and co-workers presented the use of a pentafluorophenyl active ester of a dithiobenzoic acid chain transfer agent (CTA) for the RAFT polymerization of poly(diethylene glycol methyl ether methacrylate) [222]. Reaction of the active ester with thyroxin and reduction of the thiocarbonyl moiety and subsequent reaction with a thiosulfonate derivative of biotin yielded heterobifunctional polymers [223]. Maynard and co-workers used the unique single free cysteine of V131C T4 lysozyme for conjugation of maleimide-end-functional poly(PEG acrylate) (poly(PEGA)) [224]. The endgroup was obtained from a furan-protected maleimide CTA. Conjugation with up to 50% conversion was shown by SEC and SDS-PAGE. The same chemistry was used to prepare hetero-telechelic poly(*N*-isopropyl acrylamide) (PNIPAM) by using a biotin-functional chain transfer agent. The trithiocarbonate group was exchanged with the furan-protected maleimide in a radical reaction. After deprotection, conjugation to two different proteins, streptavidin via non-covalent binding and BSA via its single free thiol group, was successful [225,226]. A homodimeric lysine conjugate was prepared, too [227]. Previously, the authors reported also on the RAFT synthesis of poly(PEGA) with a pyridyl disulfide endgroup [228]. Deprotected siRNA with a 5'-thiol group was chosen as model compound and successful conjugation was verified through PAGE by the shift of the bands to higher molecular weights. Upon reduction, the conjugate band disappeared and a band at the identical position of the original siRNA was regained. Sumerlin and co-workers prepared an azido-

functional trithiocarbonate CTA and conjugated such prepared PNIPAM via click-chemistry to BSA whose cysteines were modified with a maleimide-functional terminal alkyne [229]. Upon reduction of BSA, a disulfide bridge was reduced and, additionally to the sulfhydryl group of the single native free cysteine, two more cysteines were amenable to modification. In the latter two examples the second possible functionality originates from the post-polymerizational reduction of the thiocarbonyl group of the chain transfer agent. Boyer et al. prepared a truly bifunctional RAFT chain transfer agent. They modified a trithiocarbonate unsymmetrically with an azide- and dithiopyridyl-group bearing moiety [230]. A careful assessment of the click-reaction conditions which do not cleave the thiocarbonate group is necessary; copper(II) sulphate, and sodium ascorbate in water/isopropanol (1/1 v/v) proved to be suitable. Conjugation of the hetero-telechelic PNIPAM was done to alkyne-bearing biotin and, on the disulfide side, to glutathione or BSA.

The grafting-onto-approach has intrinsic limitations. Steric hindrance and/or low stability of the reactive functional group during long reaction times can hamper conjugation with very long polymer chains. Further, a distribution in the number of polymer grafts will result from multiple attachment sites which again may depend on the graft length. More uniform conjugates can be obtained, if the polymer is directly synthesized with a protein-macroinitiator (grafting-from or divergent approach). Lysine amino groups can be smoothly modified with 2-bromoisobutyryl bromide. The installation of a precise number of initiating sites at the protein is the crucial step in the formation of polymer–protein conjugates with a well-defined number of attached polymer chains.

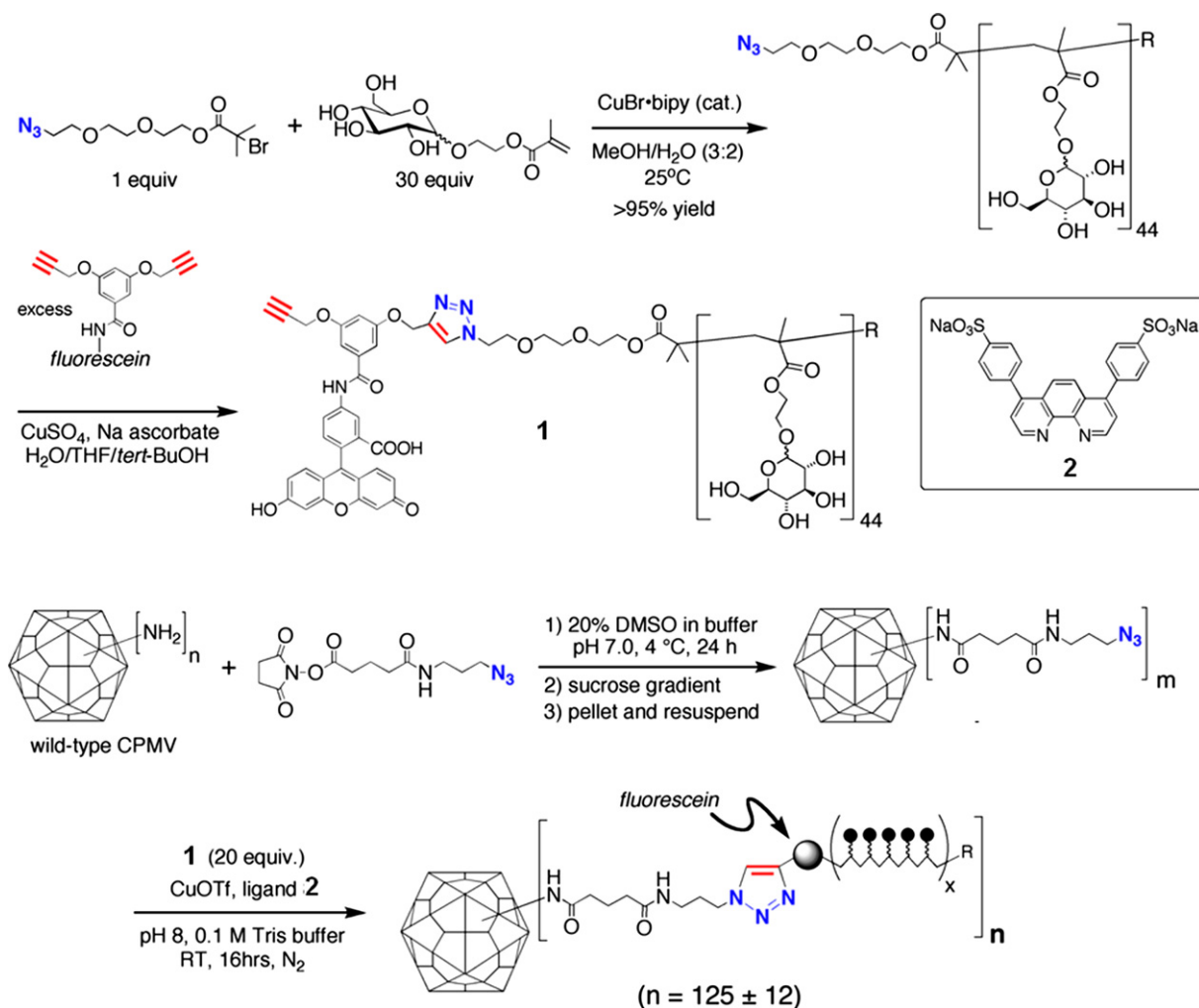


Fig. 15. Click-chemistry for grafting-from of fluorescently labelled glycopolymers on a viral scaffold [86]. Reproduced by permission of The Royal Society of Chemistry.

Differences in reactivity and the appropriate excess of reactive initiator can be used to limit the number of initiating sites. Lele and co-workers showed that precisely defined conjugates can be obtained in the case of a single initiating site. However, increasing the initiator to protein ratio led to a variable number of initiating sites. This results in a variable number of polymer chains [231]. Moreover, an increased steric crowding led to lower monomer conversion. Magnusson et al. conjugated the ATRP-initiator via a succinimide active ester to recombinant human growth hormone. The oligoethylene glycol spacer helped to achieve full reaction with free protein-amino groups and to reduce steric crowding in the subsequent polymerization of OEGMA [232]. Le Droumaguet and Velonia chose the unique single free cysteine Cys-34 of BSA as site for the grafting-from polymerization of NIPAM. The macroinitiator was prepared by conjugation of a maleimide terminal isobutyl bromide ester. Polymerization of styrene in a suitable DMSO/water mixture resulted in giant polystyrene-BSA amphiphiles [233]. The group of Chilkoti achieved recently the modification of only the C-terminus of green fluorescent protein with an ATRP-initiator and the synthesis of well-defined protein-poly(oligo(ethylene glycol) methyl ether methacrylate) conjugates [234]. Similarly, grafting-from polymerizations with the RAFT technique were reported. For example, Davis and co-workers used a dithiopyridyl functional trithiocarbonate to prepare a monofunctional BSA-macroinitiator for the polymerization of PEGA or NIPAM while De et al. chose

a maleimide-functional CTA [235,236]. Fully synthetic oligopeptide-RAFT agents were prepared on solid supports [237].

Particularly, for multivalent scaffolds with closely located sites, conjugation of long polymer chains has been difficult [238]. Wang and co-workers used therefore the grafting-from approach to decorate ferritin particles with polymer chains. The ferritin protein cage was functionalized with bromoisobutyrate and served as multivalent initiator for ATRP polymerization of water-soluble PEG-240 methacrylate [73]. The number of grafts, i.e. number of initiating sites, was not determined but experiments with similar small reagents like bromoisobutyrate showed that all four surface exposed lysine residues K83, K97, K104 and K143 can be labelled. The poly(PEGMA)-ferritin conjugate was soluble but aggregated in both, water and organic solvents. Modification with polymers is a valuable contribution to develop ferritin as novel drug delivery system as it combines the great potential of ferritin-like particles for theragnostic purposes and the advantageous pharmacokinetic properties of PEGylated proteins.

There are few useful functional groups in peptides and proteins which allow reactions with sufficient efficiency. The  $\epsilon$ -amino group of lysine is very popular because it is often surface exposed and good accessible. The drawback is their quite high abundance which makes selective conjugations difficult. The cysteine thiol group is more reactive but often involved in disulfide bridges with significant importance for the structure and must be reduced to the free

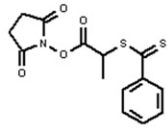
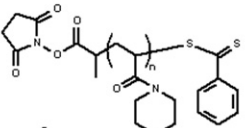
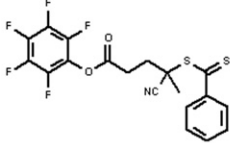
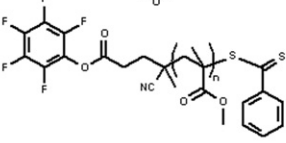
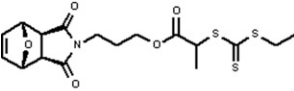
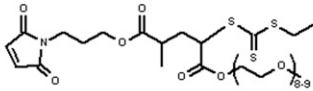
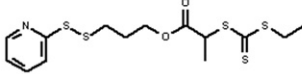
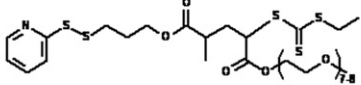
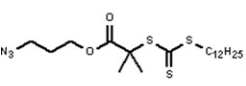
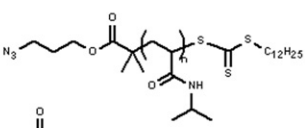
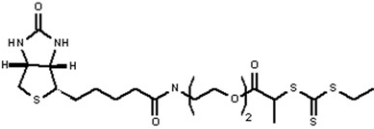
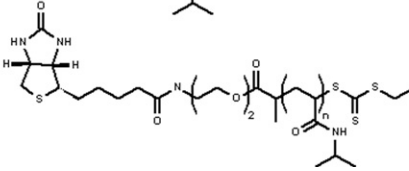
Functional chain transfer agent	End-functional polymer	Target group/ resulting bond	ref.
		NH <sub>2</sub> /amide	[220]
		NH <sub>2</sub> /amide	[222] [223]
		SH/sulfide	[224]
		SH/disulfide	[218]
		alkyne/triazol („click chemistry”)	[219]
		streptavidin/non-covalent interaction	[225] [226]

Fig. 16. Reactive end-functional polymers for grafting-onto to biomolecules via RAFT polymerization.

thiol before any reactions. Other amino acids need special reaction conditions and reagents and have limited value for general conjugation reactions. Ultimate goal would be therefore a residue- and site-specific functionalization strategy of arbitrary choice. The use of non-canonical amino acids can be a solution for this [239]. Incorporation of amino acids with non-natural functional groups can be achieved by various chemical or biological pathways. The introduction of chemo-selective handles and functionalities which are orthogonal to that of other amino acids in the protein is particularly valuable. For example, virus-like particles derived from hepatitis B virus (HBV) or bacteriophage Q $\beta$  were labelled with alkyne-derivatives of e.g. fluorescein, biotin, a gadolinium complex or transferrin by click-chemistry [100] (Fig. 20). The necessary azido-groups on the virus capsid were engineered by reassignment of the sense codon of methionine for an azide-bearing analog, azidohomoalanine. Global replacement of all methionines was achieved. As the Q $\beta$ -protein does not contain any methionine (except eventually at position 1 from bacterial expression), mutants with methionines at the most exposed position K16 and/or at an interior position T93 were generated. The coat protein sequences were cloned into plasmids and expressed in methionine auxotroph *E. coli* strains. The replacement did not hamper the self-assembly of the protein subunits to intact particles which were indistinguishable in their physical properties from their native analogs as seen in the TEM images. HBV was however sensitive to the introduction of the different labels and low recovery of intact particles was observed. The Q $\beta$ -bacteriophage was much less sensitive and near-quantitative labelling of the 180 subunits with fluorescein and high recoveries of intact particles (>70%) could be obtained. Moreover, the conjugation of even very large proteins like the 80 kDa transferrin, an iron transport protein, was successful. Both reactions

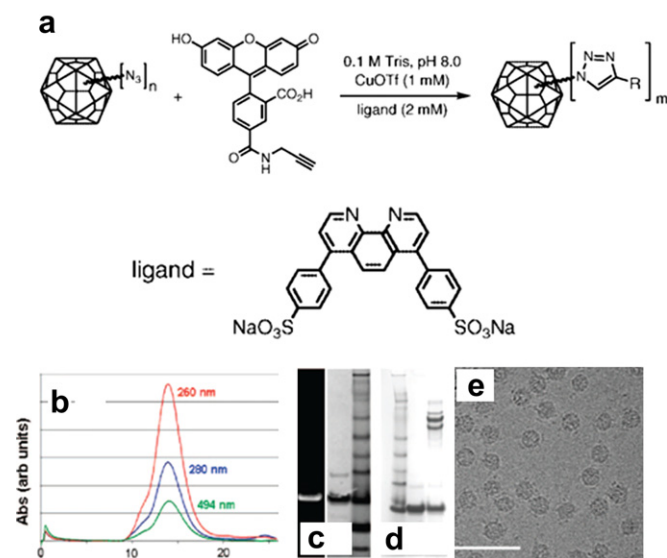
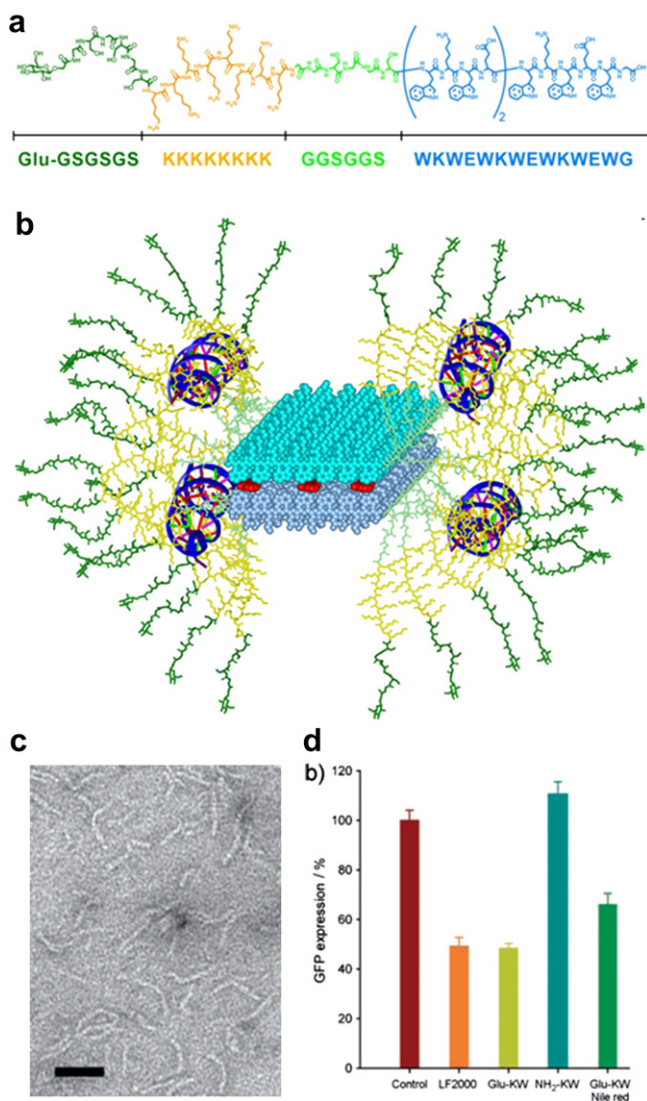


Fig. 17. a) Copper-catalyzed azide-alkyne cycloaddition (“click-reaction”) of homo-azidoalanine substituted virus-like particle (bacteriophage Q $\beta$ ) with alkyne-functional fluorescein. b) Size-exclusion chromatography of intact, dye-labelled Q $\beta$  capsids (fluorescein-absorption at 494 nm co-eluting at the elution volume of the intact capsid at 14 ml). c) SDS-PAGE showing the band of fluorescein labelled Q $\beta$ -protein: UV-illumination (lane E), Coomassie staining (lane F). d) SDS-PAGE of Q $\beta$ -transferrin conjugate: lane G same as lane F; lane H showing the high molecular weight bands of the conjugate. e) TEM image of the intact Q $\beta$ -transferrin conjugates [100].



**Fig. 18.** a) Designed multi-block polypeptide with a  $\beta$ -sheet forming sequence and a cationic oligo-lysine block for binding of polynucleic acids. b) Schematic model of the  $\beta$ -ribbon, intercalated dye and siRNA. c) TEM image of  $\beta$ -ribbon/GFP siRNA complexes; scale bar 50 nm. d) Knock-down experiment performed with 40 pmol GFP siRNA in the presence of 10% serum [247].

were analysed by size-exclusion chromatography which showed the coelution of fluorescein at the elution volume of the intact particles or by SDS-PAGE (Fig. 20). Mehl and co-workers succeeded recently in introducing a bromoisobutyramido functionalized phenylalanine into green fluorescent protein on a single site and polymerizing oligo(ethylene oxide) monomethyl ether methacrylate with this protein-macroinitiator in aqueous solution [240]. The global replacement of amino acids has become a feasible approach to proteins with non-natural amino acids. However, site-specific replacements represent still a major challenge and overcoming it will be a challenging next step in chemical biology.

#### 4.7. Applications

Bio-(in)organic nanomaterials cover a wide range of potential applications. Functional nanostructures from self-assembling bio-active building blocks will find use in various fields in biomedicine [241,242]. Particularly, fiber forming peptide amphiphiles were used as soft biomimetic scaffolds for tissue engineering [243,244] or as

scaffolds for the mineralization and repair of critical size bone defects [245,246]. Such molecular assemblies cannot only present binding sequences and growth factors on their outer surface but also function as efficient drug and gene carriers if they are stabilized as small virus-like particles. For example, Lim et al. designed a multi-block polypeptide which self-assembled to small  $\beta$ -ribbon filaments. Small interfering RNA (siRNA) for sequence specific post-translational gene silencing (RNA interference, RNAi) formed an interpolyelectrolyte complex with an oligo-lysine block which was presented on the surface of the particles (Fig. 20) [247]. The discrete supramolecular assemblies showed excellent transfection efficiencies in green fluorescent protein knock-down experiments with HeLa cells. Moreover, hydrophobic dyes could be intercalated within the hydrophobic space of the  $\beta$ -ribbon bilayer to track the intracellular distribution with confocal laser scanning microscopy. Localization of the complex in the nucleus proved that this nanomaterial may be a potent artificial virus for gene and drug delivery. Interesting to note, a multivalent presentation of a charge-neutral carbohydrate moiety is needed as the outermost layer. It prevents aggregation via interparticle crosslinking upon adsorption of the siRNA and ensures high transfection efficiencies. Conjugation of side-chain functional polymers could render particles with even stronger binding efficiencies or improved pharmacokinetic properties.

Nowadays, biomedical nanotechnology is one of the fastest progressing fields in nanotechnology, proposing most promising applications yet within realistic expectations. Viruses and other protein cages have been used in a variety of applications, like cell targeting, gene delivery, drug encapsulation and release, vaccine development and immune modulation. The rigid scaffold and geometrical constraints of the bionanoparticles are of high importance for the multivalent presentation of foreign epitopes. Often, free small peptides exhibit low immunogenicity. The presentation as fusion peptides on a macromolecular scaffold as carrier of the antigenic determinant can strongly stimulate immunogenic reactions and enhance the production of antibodies. Such virus-like particles (VLPs) which mimic the structure of authentic virus particles represent a novel and promising class of vaccines [248,249]. Plant viral systems are of particular interest as they seem to be a safe and non-toxic platform for *in vivo* biomedical applications, e.g. investigated for CPMV by Singh et al. [250]. Thus, epitope-presenting systems based on CPMV and TMV have early been realized and investigated in detail [37,251]. Viruses displaying heterologous proteins can be constructed by genetic engineering of fusion proteins or by chemical conjugation. The choice of method is determined by strong differences in immunogenic properties of the resulting virus-like particles and not every conjugate can be produced by gene expression [251]. Few recent examples concern the production of carbohydrate based antitumor vaccines, based on CPMV glycan derivatives. For example, Miermont et al. conjugated Tn glycan analogs to CPMV capsids [252]. Tn glycan is overexpressed on many cancer cell surfaces but is a low immunogene itself. However, significantly increased antibody titers were observed for the analysed sera of mice that have been immunized with the CPMV conjugates. That points out the necessity of a highly organized display of Tn to elicit strong immune response. The produced antibodies recognized MCF-7 breast cancer cell surfaces as shown by Fluorescent Assisted Cell Sorting (FACS) with a fluorescein labelled anti-IgG secondary antibody. In another study, Kaltgrad et al. analysed the production of anti-glycan antibodies in chicken induced by CPMV-carbohydrate conjugates [253]. The binding and internalization of CPMV-based virus-like particles in antigen presenting cells like dendritic cells, macrophages and B-cells has been investigated in greater detail by Gonzales et al. [254]. VLPs can also be utilized as vectors to express valuable recombinant enzymes or

single-chain antibodies in plants – a very economical and productive source of biomacromolecular pharmaceuticals [255].

Considering the excellent packing of polynucleic acid in viruses, well shielded from the surrounding, protein cages render a stable, biocompatible coating around enclosed substances or nanoparticles. Such composite core-shell particles can work as excellent capsules for the delivery of drugs and/or carrier of labels for diagnostic purposes (theragnostics). For example, the comparatively small ferritin particles present less steric hindrance in *in vivo* applications than other polyvalent drug carriers and has been of interest for nuclear magnetic resonance imaging [256]. Upon reconstitution of recombinant human H-chain apoferritin with  $(\text{NH}_4)_2\text{Fe}(\text{SO}_4) \cdot 6 \text{H}_2\text{O}$  and hydrogen peroxide under alkaline conditions, crystalline iron-oxide cores of maghemite ( $\gamma\text{-Fe}_2\text{O}_3$ ) or magnetite ( $\text{Fe}_3\text{O}_4$ ) were obtained [257]. The magnetic resonance relaxivities  $R_1$  and  $R_2$  increased with higher iron loadings and came close to the values of clinically known iron-oxide contrast agents. As the uptake of the mineralized ferritin was significantly higher than the uptake of iron-oxide particles of other contrast agents, the macrophage cells incorporated higher total levels of iron. Gadolinium(III)-based contrast agents have been prepared as well. Similarly, excellent and higher relaxivities than with low molecular weight Gd-chelates were obtained [258]. Moreover, the protein shell can serve as a versatile platform for cell-specific targeting moieties or another therapeutic agent may be co-loaded into the protein cage. Covalently bound drugs can be released if triggerable linkers are used. Flenniken et al. bound the chemotherapeutic agent doxorubicin via the acid-labile hydrazone linker to the interior of the small heat shock protein of *Methanococcus jannaschii* [259]. The multivalent presentation of epitopes will enhance and maximize specific binding properties to tissues and cells and thus increase drug delivery efficiency. Destito et al. targeted tumor cells with folic acid derivatized cowpea mosaic viruses [260]. The folate receptor is specifically up-regulated on a variety of human tumor cells. The significant uptake of wild-type CPMV was inhibited by PEGylation; redirection to KB and HeLa tumor cell lines was achieved by PEG–folic acid conjugates [238,260]. Efficient synthesis via click-chemistry guaranteed the consistent synthesis of CPMV particles with varying ratios of folic acid bearing and non-derivatized PEG-chains. Tumor cell surface carbohydrates are another kind of potential target for immunotherapy. Finn and co-workers showed the preparation of virus-glycopolymer or -glycan derivatives of CPMV [252,261,262]. Such virus conjugates were found to bind e.g. to CD22, a receptor specifically expressed on B-cells and B lymphoma cells which need an effective polyvalent presentation of the respective glycan ligand [262]. However, there are also examples where uptake does not benefit from multivalent display of epitopes [263].

The main idea was further developed to ever more complex, multifunctional nanosystems that work at the interface of physical and life sciences [264]. Good examples are the multifunctional MR-theragnostics which Boyes and co-workers recently introduced. The core consisted of a gadolinium-metal-organic framework nanoparticle for magnetic resonance imaging. It was modified with biocompatible reactive polymers carrying a fluorescent tag for cellular-scale imaging and targeting ligands like GRGDS-oligo peptides or therapeutic agents like methotrexate, an antineoplastic drug [265]. Cage-like bionanoparticles offer an easier platform for such multifunctional nanosystems [70]. For example, viral behaviour was investigated by capsid enclosed CdSe-quantum dots in living cells [266]. In another study, Cotlet, Swanson and co-workers engineered the subunits of chaperonin, an 18 subunit double ring, with an oligo-his tag to accommodate water-soluble, dihydroliipoic acid-coated CdSe–ZnO quantum dots [267]. Nanoparticles of the appropriate size were well accommodated, forming defined 1:1

complexes with the protein ring. The histidine ligands were not only responsible for an efficient uptake of the nanoparticles but also for an increased photoluminescence. The potential targeting capabilities were shown with protein rings which had been assembled from mixed subunits, some of them carrying a biotin ligand.

The size uniformity of the particles and the homogeneous conformational orientation of target-binding probes on a scaffold are also critical for excellent detection sensitivity in bioassays. Assay sensitivity is further strongly enhanced by the multivalent display of epitopes and the high binding capabilities. Thus, an ferritin-based ultrasensitive detection system for the 65 kDa glutamate decarboxylase ( $\text{GAD}_{65}$ ) specific autoantibody, an early marker of Type I diabetes, was demonstrated with attomolar sensitivity [268]. Human ferritin heavy chain subunits were genetically engineered to present the respective epitope (H-FTN- $\text{GAD}_{65}$ ). The bound antibodies (anti- $\text{GAD}_{65}$  mAb) were then detected by a secondary CdSe-quantum dot labelled antibody through photoluminescence. The same amount of immobilized non-supramolecular antigene probes resulted in a detection sensitivity that was at least 6 orders of magnitude lower, which impressively points out the importance of a homogeneous scaffold for highest assay sensitivities (Fig. 19). The simultaneous detection of two analytes, a diabetes and hepatitis marker, with a mixture of the respective ferritin labels suggest that multiplexed detection techniques will be feasible. Encapsulated materials can also be used for direct fluorescence or electrochemical

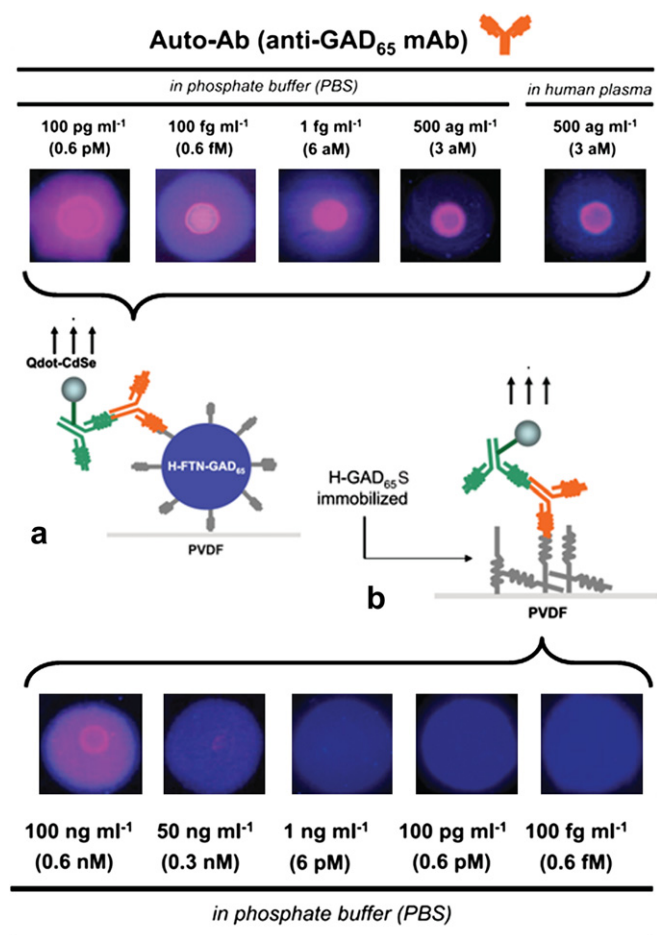


Fig. 19. Quantum dot-based detection of autoantibodies of Type I diabetes. Epitope presentation on a) genetically engineered multivalent ferritin particles results in much higher sensitivity than with b) non-supramolecular probes [268].

assays [103,269]. The encapsulation of different ions within the chemically identical shell or the assembly of the bionanoparticle shells from differently modified subunits extend the approach to multiplexed assays.

The unique versatility of ferritin but also other protein and viral cages to house a variety of useful inorganic materials and the possibility to control the surface chemistry and thus the assembling properties, make them a versatile nanoscale platform for the fabrication of ordered arrays for e.g. nanoelectronics [119]. Yamashita and co-workers were one of the first who broke the border between the well-separated fields of clean-room semiconductor based nanotechnology and wet biological materials for the fabrication of nanoscale electronic structures [149]. After the synthesis of nanoparticles inside the protein cavity, self-assembly on a surface and elimination of the protein moiety, the deposited nanodots could be reduced and burred in a silicon-dioxide layer (BioNanoProcess). Such assemblies worked as electron storage nodes in floating nanodot gate memory devices (FNGM) which are promising candidates for next-generation non-volatile memory applications. The structure is very similar to metal-oxide semiconductor field-effect transistors (MOSFET) but a nanodot array is additionally embedded above the channel. Injected charges from the gate electrode are stored and lead to a pronounced hysteresis of

the drain current–gate voltage curve [270]. Fig. 20 shows the dense, nevertheless irregular assembly of Co-filled ferritin on a silicon substrate before device fabrication. A cross-sectional TEM of the final MOS-structure reveals the monolayer formation on the substrate. During annealing of the device, partial reduction can be achieved to provide metal nanoparticles as seen with XPS. The observed hysteresis in the drain current–gate voltage curve indicated the charge confinement to the embedded nanodots. Large charge capacity, long charge retention time and good stress resistance were observed when the device was operated as non-volatile memory [271,272].

A further useful application of self-assembled ferritin bionanoparticles is the use as masks for lithography applications in nanoelectronics. In contrast to conventional colloidal particles, ferritin and its inorganic core exhibit absolute uniformity which is replicated in the image structure. Kubota et al. deposited ferrihydrite containing ferritin on a wafer. By etching the silicon support, they generated 7 nm columns which replicated the exact size of the deposited ferritin cores [274,275]. Stacked nanodisk structures were prepared with this technique that exhibited a staircase quantum effect. The single-electron charging effect was investigated by conductive AFM measurements and was observed even at room temperature [276].

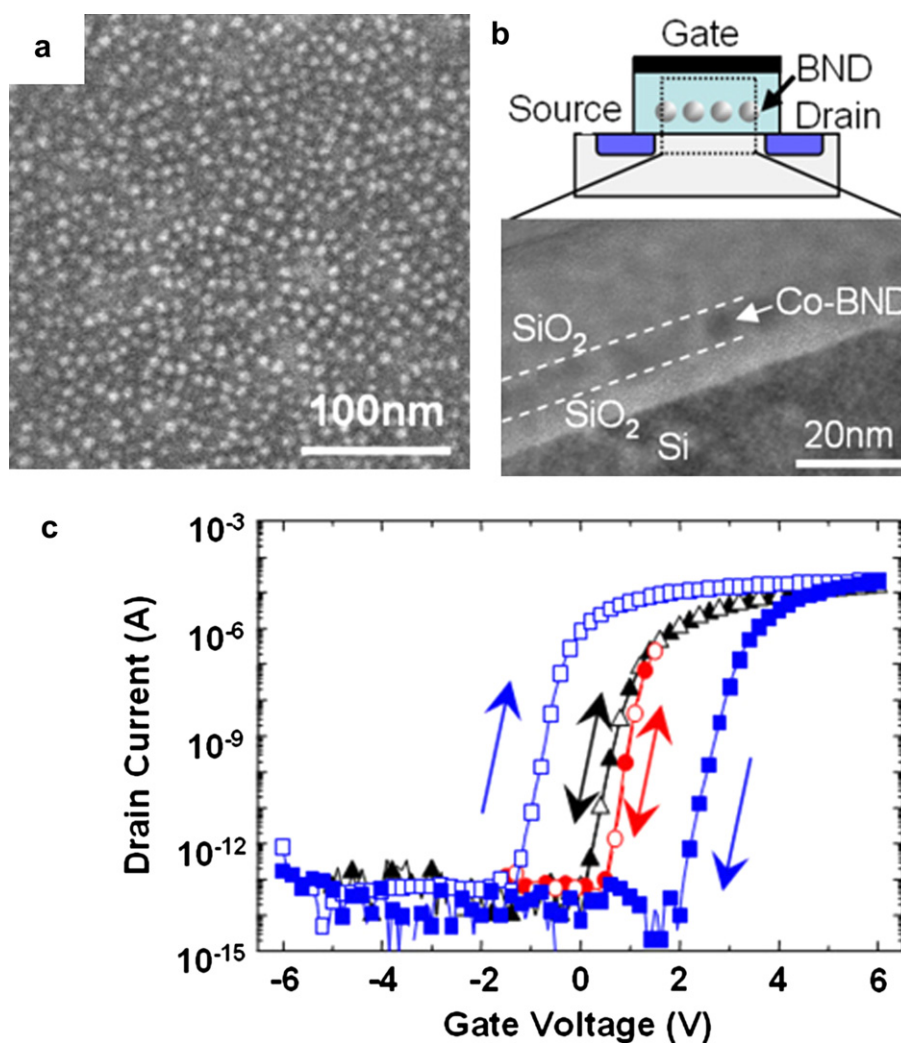


**Fig. 20.** a) Co<sub>3</sub>O<sub>4</sub> nanodot array on an SiO<sub>2</sub> surface. The nanodots were prepared in apoferritin and after deposition, the protein cage was eliminated by UV. b) The assembly was fabricated to be a part of a MOS field-effect transistor. The cross-sectional TEM shows the nanodots embedded in the MOS stacked structure. c) Typical transfer characteristics (drain current–gate voltage) of a control device (triangles), quasi-neutral scans (circles) and memory behaviour under +/-6 V gate voltage sweep (squares) [273].

The catalytic properties of entrapped nanoparticles were shown in a variety of research works. Metal or metal oxide filled ferritin promotes the growth of suspended, diameter-controlled single-walled carbon nanotubes. This enables the site-specific growth of carbon nanotubes for advanced nanoelectronic devices from surface deposited ferritin particles [161,277]. The native ferrihydrite core efficiently converted toxic chromium (VI) ions to chromium (III) in aqueous solution when irradiated with visible light [278]. Protein-stabilized and -shielded semiconductor catalysts may represent interesting candidates for biocompatible remediation. The small protein cages of the small heat shock protein from *Methanococcus jannaschii* and the Dps from *L. innocua* were mineralized with platinum [122,279]. In model reactions the efficient H<sub>2</sub>-production was shown for certain minimum platinum loadings. The exceptional temperature-stability of Hsp is important for the utility of such systems in real life applications.

## 5. Summary and perspectives

(Bio-) nanotechnology is at the frontier of biochemistry, polymer chemistry and material science. Previously separate fields come together to produce materials and build devices which combine the best properties of all the involved materials: (Bio-) organic functional ligands that mediate interactions with the surrounding, work as recognition tags or render them biocompatible; polymers that work as matrix, change solubility properties or add multiple functional groups; and finally, chemical material science that delivers nanoparticles with unprecedented optical, magnetic or catalytic properties or engineers organic and inorganic compounds to composites. Obviously, intelligent combination of these topics will mark a new era of nanomaterials with many possible applications in the field of catalysis, biomedical applications as diagnostic or therapeutic agents, in sensing devices or nanotechnology.

In this article, we outlined the rapidly increasing interest in and multiple uses of self-assembling proteins, particularly protein complexes and protein cages like ferritin, bacteriophages and plant viruses in bionanotechnology. Monodispersity, absolute definition of chemical (secondary) and geometrical (tertiary/quaternary) structure, easy and manifold possibilities for manipulation and the inherent biological functionality are a few aspects which constitute reasons for the strong advances in the field.

Understanding the structure-forming principles is the primary prerequisite for the *de novo* design of novel self-assembling biomolecules. Symmetric protein cages like ferritin or plant viruses or self-assembling peptide motifs like  $\beta$ -sheets are structures which are well understood today and give principal guidelines for the construction of complex artificial structures. Therefore, artificial systems from novel building blocks are investigated besides naturally occurring bionanoparticles as well.

Conjugation of bionanoparticles with dyes, polymers and other ligands or decoration with nanoparticles is done by chemical means. Specific peptide sequences with binding properties can be inserted by genetic engineering with ultimate precision and expressed in high yields. The self-assembled structures can work as reaction vessels for nanoparticle synthesis or as scaffolds for the synthesis of nanostructured bio-inorganic composite materials.

Conjugation of polymers to proteins has recently become a topic of strong interest. Particularly, the progress in the divergent synthesis of defined polymer–protein conjugates opens new opportunities for the preparation of novel soft materials in which both macromolecular blocks combine for the formation of structured and functional materials. The introduction of biological structural motifs will allow novel polymeric architectures. On the other hand, proteins will add novel functions into synthetic polymers. Fully synthetic and soluble materials will be necessary in the

further development of (printable) sensor chips or the construction of responsive or triggerable drug delivery systems. Incorporation of inorganic nanoparticles will add optical, electronic or magnetic properties which yields finally multifunctional molecular hybrid assemblies.

The preparation of multifunctional nanosystems like those for new theragnostic systems which have been realized only previously, is challenging and has to make use of many of the above mentioned principles. The progress in diagnosis and disease treatment will strongly demand those multifunctional nanosystems in the future. Polymer-modified, biopolymer encapsulated inorganic nanoparticles for drug delivery and cellular level imaging can be a solution – and yet represent only one challenge for the further advancements in bionanotechnology.

## Acknowledgement

The authors thank the SFB 481 (TP B10) and the Volkswagen-Stiftung for financial support.

## References

- [1] Grzelczak M, Vermant J, Furst EM, Liz-Marzan LM. ACS Nano 2010;4(7):3591–605.
- [2] Chowdhury D. Current Science 2009;96(7):923–32.
- [3] Zhang G, Wang DY. Chemistry – An Asian Journal 2009;4(2):236–45.
- [4] Rivera Gil P, Huehn D, del Mercato LL, Sasse D, Parak WJ. Pharmacological Research 2010;62(2, Sp. Iss. SI):115–25.
- [5] Engel E, Michiardi A, Navarro M, Lacroix D, Planell JA. Trends in Biotechnology 2008;26(1):39–47.
- [6] Ansari AA, Alhoshan M, Alsalmi MS, Aldwayyan AS. Sensors 2010;10(7):6535–81.
- [7] Mu L, Sprando RL. Pharmaceutical Research 2010;27(8):1746–9.
- [8] Weiss J, Takhistov P, McClements DJ. Journal of Food Science 2006;71(9):R107–16.
- [9] Sugiyama S, Ohtani T. Food Hygiene and Safety Science 2010;51(2):J201–5.
- [10] Niemeyer CM, Mirkin CA. Nanobiotechnology. More concepts and applications. Weinheim: Wiley-VCH; 2007.
- [11] Kumar CSSR. In: Kumar CSSR, editor. Nanotechnologies for the life sciences, vol. 1–10. New York: Wiley-VCH; 2005–2012.
- [12] Niemeyer CM. Angewandte Chemie, International Edition 2003;42(47):5796–800.
- [13] Manchester M, Steinmetz NF. Current Topics in Microbiology and Immunology; 2009:327.
- [14] Manchester M, Steinmetz NF. Viral nanoparticles: tools for materials science & biomedicine. Singapore: Pan Stanford Publishing; 2010.
- [15] Uchida M, Kang S, Reichhardt C, Harlen K, Douglas T. Biochimica et Biophysica Acta – General Subjects 2010;1800(8):834–45.
- [16] Tsai CJ, Zheng J, Aleman C, Nussinov R. Trends in Biotechnology 2006;24(10):449–54.
- [17] Tsai CJ, Zheng J, Zanuy D, Haspel N, Wolfson H, Aleman C, et al. Proteins-Structure Function and Bioinformatics 2007;68(1):1–12.
- [18] Padilla JE, Colovos C, Yeates TO. Proceedings of the National Academy of Sciences of the United States of America 2001;98(5):2217–21.
- [19] Bromley EHC, Channon K, Moutevelis E, Woolfson DN. ACS Chemical Biology 2008;3(1):38–50.
- [20] Carrillo-Tripp M, Shepherd CM, Borelli IA, Venkataraman S, Lander G, Natarajan P, et al. Nucleic Acids Research 2009;37:D436–42.
- [21] Johnson JE, Speir JA. Journal of Molecular Biology 1997;269(5):665–75.
- [22] Sinkovits RS, Baker TS. Journal of Structural Biology 2010;170(1):109–16.
- [23] Beeby M, Bobik TA, Yeates TO. Protein Science 2009;18(1):69–79.
- [24] Cavalli S, Albericio F, Kros A. Chemical Society Reviews 2010;39(1):241–63.
- [25] Yang YL, Khoe U, Wang XM, Horii A, Yokoi H, Zhang SG. Nano Today 2009;4(2):193–210.
- [26] Yeates TO, Padilla JE. Current Opinion in Structural Biology 2002;12(4):464–70.
- [27] Usui K, Maki T, Ito F, Suenaga A, Kidoaki S, Itoh M, et al. Protein Science 2009;18(5):960–9.
- [28] Matsuura K, Murasato K, Kimizuka N. Journal of the American Chemical Society 2005;127(29):10148–9.
- [29] Sugimoto K, Kanamaru S, Iwasaki K, Arisaka F, Yamashita I. Angewandte Chemie-International Edition 2006;45(17):2725–8.
- [30] Vallee A, Humblot V, Pradier CM. Accounts of Chemical Research 2010;43(10):1297–306.
- [31] Seker UOS, Wilson B, Sahin D, Tamerler C, Sarikaya M. Biomacromolecules 2009;10(2):250–7.
- [32] Slocik JM, Naik RR. Chemical Society Reviews 2010;39(9):3454–63.
- [33] Pande J, Szweczyk MM, Grover AK. Biotechnology Advances 2010;28(6):849–58.



- [34] Shiba K. *Current Opinion in Biotechnology* 2010;21(4):412–25.
- [35] Shiba K. *Chemical Society Reviews* 2010;39(1):117–26.
- [36] Tamerler C, Khatayevich D, Gungormus M, Kacar T, Oren EE, Hnilova M, et al. *Biopolymers* 2010;94(1):78–94.
- [37] Sainsbury F, Canizares MC, Lomonossoff GP. *Annual Review of Phytopathology* 2010;48:437–55.
- [38] Lomonossoff GP, Shanks M. *Comoviruses (Comoviridae)*. In: Granoff A, Webster RG, editors. *Encyclopedia of virology*, vol. 1. San Diego: Academic Press; 1999. p. 285–91.
- [39] Lin T, Chen Z, Usha R, Stauffacher CV, Dai J-B, Schmidt T, et al. *Virology* 1999;265(1):20–34.
- [40] Goldbach R, Kammen AV. Structure, replication, and expression of the bipartite genome of cowpea mosaic virus. In: Davies JW, editor. *Molecular plant virology*, vol. 2. Boca Raton: CRC Press, Inc.; 1985. p. 83–120.
- [41] Dijkstra J, Jager CPD. *Practical plant virology*. Berlin: Springer; 1998.
- [42] Wellink J. *Comovirus isolation and RNA extraction*. In: Foster GD, Taylor SC, editors. *Plant virology protocols*, vol. 81. Totawa: Humana Press; 1998. p. 205–9.
- [43] Gibbs A. *Tymoviruses*. In: Granoff A, Webster RG, editors. *Encyclopedia of virology*, vol. 3. San Diego: Academic Press; 1999. p. 1850–3.
- [44] Canady MA, Larson SB, Day J, McPherson A. *Nature Structural Biology* 1996;3(9):771–81.
- [45] Gibbs A, Mackenzie AM. *Tymovirus isolation and genomic RNA extraction*. In: Foster GD, Taylor SC, editors. *Plant virology protocols*, vol. 81. Totawa: Humana Press; 1998. p. 219–24.
- [46] McPherson A, Kuznetsov YG, Malkin A, Plomp M. *Journal of Structural Biology* 2003;142(1):32–46.
- [47] Kuznetsov YG, Malkin AJ, Lucas RW, Plomp M, McPherson A. *Journal of General Virology* 2001;82(9):2025–34.
- [48] Stanley WM. *Science* 1935;81:644–5.
- [49] Harrison BD, Wilson TMA. *Philosophical Transactions of the Royal Society of London, Series B: Biological Sciences* 1999;354(1383):521–9.
- [50] Scholthof K-BG, Shaw JG, Zaitlin M. *Tobacco mosaic virus: one hundred years of contributions to virology*. St. Paul, Minnesota, USA: American Phytopathological Society Press; 1999.
- [51] Lewandowski DJ, Dawson WO. *Tobamoviruses*. In: Granoff A, Webster RG, editors. *Encyclopedia of virology*, vol. 3. San Diego: Academic Press; 1999. p. 1780–3.
- [52] Namba K, Pattanayek R, Stubbs G. *Journal of Molecular Biology* 1989;208(2):307–25.
- [53] Sachse C, Chen JZ, Coureux P-D, Stroupe ME, Faendrich M, Grigorieff N. *Journal of Molecular Biology* 2007;371(3):812–35.
- [54] Clare DK, Orlova EV. *Journal of Structural Biology* 2010;171(3):303–8.
- [55] Klug A. *Annual Review of Biochemistry* 2010;79:1–35.
- [56] Chapman SN. *Tobamovirus isolation and RNA extraction*. In: Foster GD, Taylor SC, editors. *Plant virology protocols*, vol. 81. Totawa: Humana Press; 1998. p. 123–9.
- [57] Santos NC, Castanho MARB. *Biophysical Journal* 1996;71(3):1641–50.
- [58] Lehner D, Lindner H, Glatter O. *Langmuir* 2000;16(4):1689–95.
- [59] Arosio P, Ingrassia R, Cavadini P. *Biochimica Et Biophysica Acta-General Subjects* 2009;1790(7):589–99.
- [60] Chasteen ND, Harrison PM. *Journal of Structural Biology* 1999;126(3):182–94.
- [61] Harrison PM, Arosio P. *Biochimica et Biophysica Acta – Bioenergetics* 1996;1275(3):161–203.
- [62] Banyard SH, Stammers DK, Harrison PM. *Nature* 1978;271(5642):282–4.
- [63] Clegg GA, Stansfield RFD, Bourne PE, Harrison PM. *Nature (London, United Kingdom)* 1980;288(5788):298–300.
- [64] Lawson DM, Artymiuk PJ, Yewdall SJ, Smith JMA, Livingstone JC, Treffry A, et al. *Nature* 1991;349(6309):541–4.
- [65] Liu X, Theil EC. *Accounts of Chemical Research* 2005;38(3):167–75.
- [66] Jaaskelainen A, Harinen R-R, Lamminmaki U, Korpimaki T, Pelliniemi LJ, Soukka T, et al. *Small* 2007;3(8):1362–7.
- [67] Takeda S, Ohta M, Ebina S, Nagayama K. *Biochimica et Biophysica Acta – Gene Structure and Expression* 1993;1174(2):218–20.
- [68] Orino K, Harada S, Natsuhori M, Takehara K, Watanabe K. *BioMetals* 2004;17(2):129–34.
- [69] Soto CM, Ratna BR. *Current Opinion in Biotechnology* 2010;21(4):426–38.
- [70] Lee LA, Niu ZW, Wang Q. *Nano Research* 2009;2(5):349–64.
- [71] Sen Gupta S, Kuzelka J, Singh P, Lewis WG, Manchester M, Finn MG. *Bioconjugate Chemistry* 2005;16(6):1572–9.
- [72] Barnhill HN, Reuther R, Ferguson PL, Dreher T, Wang Q. *Bioconjugate Chemistry* 2007;18(3):852–9. Ref. in there.
- [73] Zeng Q, Li T, Cash B, Li S, Xie F, Wang Q. *Chemical Communications* 2007;14:1453–5.
- [74] Raja KS, Wang Q, Finn MG. *ChemBioChem* 2003;4(12):1348–51.
- [75] Fernandez B, Galvez N, Sanchez P, Cuesta R, Bermejo R, Dominguez-Vera JM. *Journal of Biological Inorganic Chemistry* 2008;13(3):349–55.
- [76] Wang Q, Lin T, Tang L, Johnson JE, Finn MG. *Angewandte Chemie – International Edition* 2002;41(3):459–62.
- [77] Steinmetz NF, Lomonossoff GP, Evans DJ. *Langmuir* 2006;22(8):3488–90.
- [78] Wang Q, Kaltgrad E, Lin T, Johnson JE, Finn MG. *Chemistry & Biology* 2002;9(7):805–11.
- [79] Steinmetz NF. *Tomorrow's Chemistry Today*; 2008:215–36.
- [80] Steinmetz NF, Evans DJ. *Organic & Biomolecular Chemistry* 2007;5(18):2891–902.
- [81] Blum AS, Soto CM, Wilson CD, Whitley JL, Moore MH, Sapsford KE, et al. *Nanotechnology* 2006;17(20):5073–9.
- [82] Medintz IL, Sapsford KE, Konnett JH, Chatterji A, Lin T, Johnson JE, et al. *Langmuir* 2005;21(12):5501–10.
- [83] Iha RK, Wooley KL, Nystrom AM, Burke DJ, Kade MJ, Hawker CJ. *Chemical Reviews* 2009;109(11):5620–86.
- [84] Best MD. *Biochemistry* 2009;48(28):6571–84.
- [85] Hong V, Presolski SI, Ma C, Finn MG. *Angewandte Chemie-International Edition* 2009;48(52):9879–83.
- [86] Sen Gupta S, Raja KS, Kaltgrad E, Strable E, Finn MG. *Chemical Communications* 2005;34:4315–7.
- [87] Xie F, Sivakumar K, Zeng Q, Bruckman MA, Hodges B, Wang Q. *Tetrahedron* 2008;64(13):2906–14.
- [88] Dirks AJ, Cornelissen J, Nolte RJM. *Bioconjugate Chemistry* 2009;20(6):1129–38.
- [89] Le Droumaguet C, Wang C, Wang Q. *Chemical Society Reviews* 2010;39(4):1233–9.
- [90] Barnhill HN, Reuther R, Ferguson PL, Dreher T, Wang Q. *Bioconjugate Chemistry* 2007;18(3):852–9.
- [91] Barnhill HN, Claudel-Gillet S, Ziessel R, Charbonniere LJ, Wang Q. *Journal of the American Chemical Society* 2007;129(25):7799–806.
- [92] Endo M, Fujitsuka M, Majima T. *Chemistry – A European Journal* 2007;13(31):8660–6.
- [93] Miller RA, Presley AD, Francis MB. *Journal of the American Chemical Society* 2007;129(11):3104–9.
- [94] Schlick TL, Ding Z, Kovacs EW, Francis MB. *Journal of the American Chemical Society* 2005;127(11):3718–23.
- [95] Bruckman MA, Kaur G, Lee LA, Xie F, Sepulveda J, Breitenkamp R, et al. *ChemBioChem* 2008;9(4):519–23.
- [96] Danon D, Goldstein L, Marikovsky Y, Skutelsky E. *Journal of Ultrastructure Research* 1972;38(5–6):500–10.
- [97] Wong KKW, Colfen H, Whilton NT, Douglas T, Mann S. *Journal of Inorganic Biochemistry* 1999;76(3–4):187–95.
- [98] Wong KKW, Whilton NT, Douglas T, Mann S, Colfen H. *Chemical Communications* 1998;16:1621–2.
- [99] Sengonul M, Ruzicka J, Attygalle AB, Libera M. *Polymer* 2007;48(13):3632–40.
- [100] Strable E, Prasuhn DE, Udit AK, Brown S, Link AJ, Ngo JT, et al. *Bioconjugate Chemistry* 2008;19(4):866–75.
- [101] Whaley SR, English DS, Hu EL, Barbara PF, Belcher AM. *Nature* 2000;405(6787):665–8.
- [102] Kramer RM, Li C, Carter DC, Stone MO, Naik RR. *Journal of the American Chemical Society* 2004;126(41):13282–6.
- [103] Jaaskelainen A, Harinen RR, Soukka T, Lamminmaki U, Korpimilki T, Virta M. *Analytical Chemistry* 2008;80(3):583–7.
- [104] Sano K, Ajima K, Iwahori K, Yudasaka M, Iijima S, Yamashita I, et al. *Small* 2005;1(8–9):826–32.
- [105] Kang S, Suci PA, Broomell CC, Iwahori K, Kobayashi M, Yamashita I, et al. *Nano Letters* 2009;9(6):2360–6.
- [106] Suci PA, Kang S, Young M, Douglas T. *Journal of the American Chemical Society* 2009;131(26):9164.
- [107] Gillitzer E, Suci P, Young M, Douglas T. *Small* 2006;2(8–9):962–6.
- [108] Zheng B, Uenuma M, Uraoka Y, Yamashita I. *Nanotechnology* 2010;21(44):445602.
- [109] Mueller A, Kadri A, Jeske H, Wege C. *Journal of Virological Methods* 2010;166(1–2):77–85.
- [110] Mann S, Meldrum F. *Advanced Materials* 1991;3(6):316–8.
- [111] Meldrum FC, Wade VJ, Nimmo DL, Heywood BR, Mann S. *Nature (London, United Kingdom)* 1991;349(6311):684–7.
- [112] Naito M, Iwahori K, Miura A, Yamane M, Yamashita I. *Angewandte Chemie-International Edition* 2010;49(39):7006–9.
- [113] Yamashita I, Hayashi J, Hara M. *Chemistry Letters* 2004;33(9):1158–9.
- [114] Iwahori K, Yoshizawa K, Muraoka M, Yamashita I. *Inorganic Chemistry* 2005;44(18):6393–400.
- [115] Hennequin B, Turyanska L, Ben T, Beltran AM, Molina SI, Li M, et al. *Advanced Materials* 2008;20(19):3592.
- [116] Ueno T, Suzuki M, Goto T, Matsumoto T, Nagayama K, Watanabe Y. *Angewandte Chemie – International Edition* 2004;43(19):2527–30.
- [117] Dominguez-Vera JM, Galvez N, Sanchez P, Mota AJ, Trasobares S, Hernandez JC, et al. *European Journal of Inorganic Chemistry* 2007;30:4823–6.
- [118] Yamashita I. *Journal of Materials Chemistry* 2008;18(32):3813–20.
- [119] Yamashita I, Iwahori K, Kumagai S. *Biochimica et Biophysica Acta* 2010;1800:846–57.
- [120] Parker MJ, Allen MA, Ramsay B, Klem MT, Young M, Douglas T. *Chemistry of Materials* 2008;20(4):1541–7.
- [121] Haikarainen T, Papageorgiou AC. *Cellular and Molecular Life Sciences* 2010;67(3):341–51.
- [122] Kang S, Lucon J, Varpness ZB, Liepold L, Uchida M, Willits D, et al. *Angewandte Chemie-International Edition* 2008;47(41):7845–8.
- [123] Resnick DA, Gilmore K, Idzerda YU, Klem MT, Allen M, Douglas T, et al. *Journal of Applied Physics* 2006;99(8).
- [124] Behrens SS. *Journal of Materials Chemistry* 2008;18(32):3788–98.
- [125] de la Escosura A, Nolte RJM, Cornelissen J. *Journal of Materials Chemistry* 2009;19(16):2274–8.
- [126] Diner BA, Harmer MA, Mitchell G. *Metalization of microtubules by reducing metal salts. Application. US USA*; 2004. 17 pp.

- [127] Pruneanu S, Olenic L, Al-Said SAF, Borodi G, Houlton A, Horrocks BR. *Journal of Materials Science* 2010;45(12):3151–9.
- [128] Scheibel T, Parthasarathy R, Sawicki G, Lin X-M, Jaeger H, Lindquist SL. *Proceedings of the National Academy of Sciences of the United States of America* 2003;100(8):4527–32.
- [129] Ghadiri MR, Granja JR, Milligan RA, McRee DE, Khazanovich N. *Nature* 1993;366(6453):324–7.
- [130] Lee S-W, Mao C, Flynn CE, Belcher AM. *Science* 2002;296(5569):892–5.
- [131] Nam KT, Kim D-W, Yoo PJ, Chiang C-Y, Meethong N, Hammond PT, et al. *Science* 2006;312(5775):885–8.
- [132] Mao C, Solis DJ, Reiss BD, Kottmann ST, Sweeney RY, Hayhurst A, et al. *Science* 2004;303(5655):213–7.
- [133] Yoo PJ, Nam KT, Qi J, Lee S-K, Park J, Belcher AM, et al. *Nature Materials* 2006;5(3):234–40.
- [134] Shenton W, Douglas T, Young M, Stubbs G, Mann S. *Advanced Materials* 1999;11(3):253–6.
- [135] Bromley KM, Patil AJ, Perriman AW, Stubbs G, Mann S. *Journal of Materials Chemistry* 2008;18(40):4796–801.
- [136] Gorzny ML, Walton AS, Evans SD. *Advanced Functional Materials* 2010;20(8):1295–300.
- [137] Royston ES, Brown AD, Harris MT, Culver JN. *Journal of Colloid and Interface Science* 2009;332(2):402–7.
- [138] Rong JH, Oberbeck F, Wang XN, Li XD, Oxshier J, Niu ZW, et al. *Journal of Materials Chemistry* 2009;19(18):2841–5.
- [139] Royston E, Ghosh A, Kofinas P, Harris MT, Culver JN. *Langmuir* 2008;24(3):906–12.
- [140] Gerasopoulos K, McCarthy M, Royston E, Culver JN, Ghodssi R. *Journal of Micromechanics and Microengineering* 2008;18(10).
- [141] Chen XL, Gerasopoulos K, Guo JC, Brown A, Wang CS, Ghodssi R, et al. *ACS Nano* 2010;4(9):5366–72.
- [142] Niu Z, Liu J, Lee LA, Bruckman MA, Zhao D, Koley G, et al. *Nano Letters* 2007;7(12):3729–33.
- [143] Bruckman MA, Niu Z, Li S, Lee LA, Varazo K, Nelson TL, et al. *Nano-Biotechnology* 2007;3(1):31–9.
- [144] Niu Z, Bruckman M, Kotakadi VS, He J, Emrick T, Russell TP, et al. *Chemical Communications* 2006;28:3019–21.
- [145] Niu Z, Bruckman MA, Li S, Lee LA, Lee B, Pingali SV, et al. *Langmuir* 2007;23(12):6719–24.
- [146] Lorber B, Adrian M, Witz J, Erhardt M, Harris JR. *Micron* 2008;39(4):431–46.
- [147] Aoyama K, Ogawa K, Kimura Y, Fujiyoshi Y. *Ultramicroscopy* 1995;57(4):345–54.
- [148] Matsui T, Matsukawa N, Iwahori K, Sano KI, Shiba K, Yamashita I. *Langmuir* 2007;23(4):1615–8.
- [149] Yamashita I. *Thin Solid Films* 2001;393(1,2):12–8.
- [150] Yoshimura H. *Advances in Biophysics* 1997;34:93–107. *Protein Array: An Alternative Biomolecular System*.
- [151] Schuster B, Pum D, Sleytr UB. *Biointerphases* 2009;3(2).
- [152] Tang J, Badelt-Lichtblau H, Ebner A, Preiner J, Kraxberger B, Gruber HJ, et al. *Chemphyschem* 2008;9(16):2317–20.
- [153] Okuda M, Kobayashi Y, Suzuki K, Sonoda K, Kondoh T, Wagawa A, et al. *Nano Letters* 2005;5(5):991–3.
- [154] Yoshimura H. *Colloids and Surfaces, A: Physicochemical and Engineering Aspects* 2006;282–283:464–71.
- [155] Ikezoe Y, Kumashiro Y, Tamada K, Matsui T, Yamashita I, Shiba K, et al. *Langmuir* 2008;24(22):12836–41.
- [156] Yamashita K, Kirimura H, Okuda M, Nishio K, Sano KI, Shiba K, et al. *Small* 2006;2(10):1148–52.
- [157] Martinez RV, Martinez J, Chiesa M, Garcia R, Coronado E, Pinilla-Cienfuegos E, et al. *Advanced Materials* 2010;22(5):588.
- [158] Dominguez-Vera J, Welte L, Galvez N, Fernandez B, Gomez-Herrero J, Zamora F. *Nanotechnology* 2008;19(2). 025302/025301-025302/025303.
- [159] Won K, Park MJ, Yoon HH, Kim JH. *Ultramicroscopy* 2008;108(10):1342–7.
- [160] Yoshii S, Kumagai S, Nishio K, Kadotani A, Yamashita I. *Applied Physics Letters* 2009;95(13).
- [161] Kumagai S, Ono T, Yoshii S, Kadotani A, Tsukamoto R, Nishio K, et al. *Applied Physics Express* 2010;3(1).
- [162] Kwon M, Choi H, Chang M, Jo M, Jung S-J, Hwang H. *Applied Physics Letters* 2007;90(19). 193512/193511-193512/193513.
- [163] Miura A, Uraoka Y, Fuyuki T, Kumagai S, Yoshii S, Matsukawa N, et al. *Surface Science* 2007;601(15):L81–5.
- [164] Yamada K, Yoshii S, Kumagai S, Fujiwara I, Nishio K, Okuda M, et al. *Japanese Journal of Applied Physics, Part 1: Regular Papers, Brief Communications & Review Papers* 2006;45(5A):4259–64.
- [165] Suci PA, Klem MT, Douglas T, Young M. *Langmuir* 2005;21(19):8686–93.
- [166] Klem MT, Willits D, Young M, Douglas T. *Journal of the American Chemical Society* 2003;125(36):10806–7.
- [167] Cheung CL, Camarero JA, Woods BW, Lin T, Johnson JE, De Yoreo JJ. *Journal of the American Chemical Society* 2003;125(23):6848–9.
- [168] Smith JC, Lee K-B, Wang Q, Finn MG, Johnson JE, Mrksich M, et al. *Nano Letters* 2003;3(7):883–6.
- [169] Cheung CL, Chung S-W, Chatterji A, Lin T, Johnson JE, Hok S, et al. *Journal of the American Chemical Society* 2006;128(33):10801–7.
- [170] Steinmetz NF, Bock E, Richter RP, Spatz JP, Lomonosoff GP, Evans DJ. *Biomacromolecules* 2008;9(2):456–62.
- [171] Steinmetz NF, Calder G, Lomonosoff GP, Evans DJ. *Langmuir* 2006;22(24):10032–7.
- [172] Lin Y, Su Z, Niu Z, Li S, Kaur G, Lee LA, et al. *Acta Biomaterialia* 2008;4(4):838–43.
- [173] Steinmetz NF, Findlay KC, Noel TR, Parker R, Lomonosoff GP, Evans DJ. *ChemBioChem* 2008;9(10):1662–70.
- [174] Kuncicky DM, Naik RR, Velev OD. *Small* 2006;2(12):1462–6.
- [175] Horn A, Hiltl S, Fery A, Boker A. *Small* 2010;6(19):2122–5.
- [176] Vega RA, Maspoch D, Salaita K, Mirkin CA. *Angewandte Chemie – International Edition* 2005;44(37):6013–5.
- [177] Wang D, Duan H, Moehwald H. *Soft Matter* 2005;1(6):412–6.
- [178] Lin Y, Skaff H, Boker A, Dinsmore AD, Emrick T, Russell TP. *Journal of the American Chemical Society* 2003;125(42):12690–1.
- [179] Lin Y, Skaff H, Emrick T, Dinsmore AD, Russell TP. *Science* 2003;299(5604):226–9.
- [180] Russell JT, Lin Y, Böker A, Su L, Carl P, Zettl H, et al. *Angewandte Chemie – International Edition* 2005;44(16):2420–6.
- [181] He JB, Niu ZW, Tangirala R, Wan JY, Wei XY, Kaur G, et al. *Langmuir* 2009;25(9):4979–87.
- [182] Kaur G, He JB, Xu J, Pingali SV, Jutz G, Böker A, et al. *Langmuir* 2009;25(9):5168–76.
- [183] Zhu GY, Wang P. *Journal of the American Chemical Society* 2004;126(36):11132–3.
- [184] Jutz G, Boker A. *Journal of Materials Chemistry* 2010;20(21):4299–304.
- [185] Li T, Niu ZW, Emrick T, Russell TR, Wang Q. *Small* 2008;4(10):1624–9.
- [186] Li T, Ye B, Niu ZW, Thompson P, Seifert S, Lee B, et al. *Chemistry of Materials* 2009;21(6):1046–50.
- [187] Li T, Wu LY, Suthiwangcharoen N, Bruckman MA, Cash D, Hudson JS, et al. *Chemical Communications* 2009;20:2869–71.
- [188] Birnbaumer GM, Lieberzeit PA, Richter L, Schirhagl R, Milnera M, Dickert FL, et al. *Lab on a Chip* 2009;9(24):3549–56.
- [189] Turiel E, Martin-Esteban A. *Analytica Chimica Acta* 2010;668(2):87–99.
- [190] Shi HQ, Tsai WB, Garrison MD, Ferrari S, Ratner BD. *Nature* 1999;398(6728):593–7.
- [191] Turner NW, Jeans CW, Brain KR, Allender CJ, Hlady V, Britt DW. *Biotechnology Progress* 2006;22(6):1474–89.
- [192] Lin Y, Böker A, He J, Sill K, Xiang H, Abetz C, et al. *Nature* 2005;434(7029):55–9.
- [193] Hu Y, Samanta D, Parelkar SS, Xiong SW, Wang Q, Russel TP, et al. *Advanced Functional Materials* 2010;20:3603–12.
- [194] Sengonul M, Sousa A, Libera M. *Colloids and Surfaces B-Biointerfaces* 2009;73(1):152–5.
- [195] Shin MK, Kim SI, Kim SJ, Kim BJ, So I, Kozlov ME, et al. *Applied Physics Letters* 2008;93(16).
- [196] Shin MK, Spinks GM, Shin SR, Kim SI, Kim SJ. *Advanced Materials* 2009;21(17):1712–5.
- [197] Shin MK, Kim SI, Kim SJ, Park SY, Hyun YH, Lee Y, et al. *Langmuir* 2008;24(21):12107–11.
- [198] Bhattacharyya S, Sinturel C, Salvétat JP, Saboungi ML. *Applied Physics Letters* 2005;86(11).
- [199] Pasut G, Veronese FM. *Progress in Polymer Science* 2007;32:933–61.
- [200] Jain A, Jain SK. *Critical Reviews in Therapeutic Drug Carrier Systems* 2008;25(5):403–47.
- [201] Pasut G, Veronese FM. *Advanced Drug Delivery Reviews* 2009;61(13):1177–88.
- [202] Vicent MJ, Dieudonne L, Carbajo RJ, Pineda-Lucena A. *Expert Opinion on Drug Delivery* 2008;5(5):593–614.
- [203] Gaspar R, Duncan R. *Advanced Drug Delivery Reviews* 2009;61(13):1220–31.
- [204] Vicent MJ, Duncan R. *Trends in Biotechnology* 2006;24(1):39–47.
- [205] Liechty WB, Kryscio DR, Slaughter BV, Peppas NA. *Annual Review of Chemical and Biomolecular Engineering* 2010;1(1):149–73.
- [206] Millard P, Mougín N, Böker A, Müller AHE. *Controlling the fast ATRP of N-isopropylacrylamide in water*. In: Matyjaszewski K, editor. *Controlled/living radical polymerization: progress in ATRP*. Washington, D.C.: American Chemical Society; 2009. p. 127–39.
- [207] Boyer C, Bulmus V, Davis TP, Ladmira V, Liu JQ, Perrier S. *Chemical Reviews* 2009;109(11):5402–36.
- [208] Hermanson GT. *Bioconjugate techniques*. San Diego: Academic Press; 1996.
- [209] Gauthier MA, Klok H-A. *Chemical Communications* 2008;23:2591–611.
- [210] Nicolas J, Mantovani G, Haddleton DM. *Macromolecular Rapid Communications* 2007;28(10):1083–111.
- [211] Tao L, Mantovani G, Lecolley F, Haddleton DM. *Journal of the American Chemical Society* 2004;126(41):13220–1.
- [212] Samanta D, McRae S, Cooper B, Hu YX, Emrick T. *Biomacromolecules* 2008;9(10):2891–7.
- [213] Lewis A, Tang YQ, Brocchini S, Choi JW, Godwin A. *Bioconjugate Chemistry* 2008;19(11):2144–55.
- [214] Zarafshani Z, Obata T, Lutz JF. *Biomacromolecules* 2010;11(8):2130–5.
- [215] Siegwart DJ, Oh JK, Gao HF, Bencherif SA, Perineau F, Bohaty AK, et al. *Macromolecular Chemistry and Physics* 2008;209(21):2180–93.
- [216] Shi W, Dolai S, Averick S, Fernando SS, Saltos JA, L'Amoreaux W, et al. *Bioconjugate Chemistry* 2009;20(8):1595–601.
- [217] Bontempo D, Maynard HD. *Journal of the American Chemical Society* 2005;127(18):6508–9.
- [218] Maynard HD, Heredia KL, Li RC, Parra DP, Vazquez-Dorbatt V. *Journal of Materials Chemistry* 2007;17:4015–7.

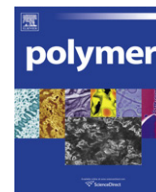
- [219] Mougou NC, Müller AHE, Böker A. *Polymeric Materials: Science and Engineering* 2008;99:713.
- [220] Pound G, McKenzie JM, Lange RFM, Klumperman B. *Chemical Communications* 2008;27:3193–5.
- [221] Bathfield M, D'Agosto F, Spitz R, Charreyre MT, Delair T. *Journal of the American Chemical Society* 2006;128(8):2546–7.
- [222] Wiss KT, Krishna OD, Roth PJ, Kiick KL, Theato P. *Macromolecules* 2009;42(12):3860–3.
- [223] Roth PJ, Jochum FD, Zentel R, Theato P. *Biomacromolecules* 2010;11(1):238–44.
- [224] Bays E, Tao L, Chang C-W, Maynard HD. *Biomacromolecules* 2009;10(7):1777–81.
- [225] Heredia KL, Grover GN, Tao L, Maynard HD. *Macromolecules* 2009;42(7):2360–7.
- [226] Heredia KL, Tao L, Grover GN, Maynard HD. *Polymer Chemistry* 2010;1(2):168–70.
- [227] Tao L, Kaddis CS, Loo RRO, Grover GN, Loo JA, Maynard HD. *Chemical Communications* 2009;16:2148–50.
- [228] Heredia KL, Nguyen TH, Chang CW, Bulmus V, Davis TP, Maynard HD. *Chemical Communications* 2008;28:3245–7.
- [229] Li M, De P, Gondi SR, Sumerlin BS. *Macromolecular Rapid Communications* 2008;29(12–13):1172–6.
- [230] Boyer C, Liu J, Bulmus V, Davis TP, Barner-Kowollik C, Stenzel MH. *Macromolecules* 2008;41(15):5641–50.
- [231] Depp V, Alikhani A, Grammer V, Lele BS. *Acta Biomaterialia* 2009;5(2):560–9.
- [232] Magnusson JP, Bersani S, Salmasso S, Alexander C, Caliceti P. *Bioconjugate Chemistry* 2010;21(4):671–8.
- [233] Le Droumaguet B, Velonia K. *Angewandte Chemie-International Edition* 2008;47(33):6263–6.
- [234] Gao WP, Liu WG, Christensen T, Zalutsky MR, Chilkoti A. *Proceedings of the National Academy of Sciences of the United States of America* 2010;107(38):16432–7.
- [235] Boyer C, Bulmus V, Liu JQ, Davis TP, Stenzel MH, Barner-Kowollik C. *Journal of the American Chemical Society* 2007;129(22):7145–54.
- [236] De P, Li M, Gondi SR, Sumerlin BS. *Journal of the American Chemical Society* 2008;130(34):11288–9.
- [237] Hentschel J, Bleek K, Ernst O, Lutz JF, Borner HG. *Macromolecules* 2008;41(4):1073–5.
- [238] Raja KS, Wang Q, Gonzalez MJ, Manchester M, Johnson JE, Finn MG. *Biomacromolecules* 2003;4(3):472–6.
- [239] Connor RE, Tirrell DA. *Polymer Reviews* 2007;47(1):9–28.
- [240] Peeler JC, Woodman BF, Averick S, Miyake-Stoner SJ, Stokes AL, Hess KR, et al. *Journal of the American Chemical Society* 2010;132(39):13575–7.
- [241] Lim YB, Moon KS, Lee M. *Chemical Society Reviews* 2009;38(4):925–34.
- [242] Ulijn RV, Woolfson DN. *Chemical Society Reviews* 2010;39(9):3349–50.
- [243] Cui HG, Webber MJ, Stupp SI. *Biopolymers* 2010;94(1):1–18.
- [244] Ma PX. *Advanced Drug Delivery Reviews* 2008;60(2):184–98.
- [245] Mata A, Geng YB, Henrikson KJ, Aparicio C, Stock SR, Satcher RL, et al. *Biomaterials* 2010;31(23):6004–12.
- [246] Gungormus M, Branco M, Fong H, Schneider JP, Tamerler C, Sarikaya M. *Biomaterials* 2010;31(28):7266–74.
- [247] Lim YB, Lee E, Yoon YR, Lee MS, Lee M. *Angewandte Chemie-International Edition* 2008;47(24):4525–8.
- [248] Roldao A, Mellado MCM, Castilho LR, Carrondo MJT, Alves PM. *Expert Review of Vaccines* 2010;9(10):1149–76.
- [249] Ludwig C, Wagner R. *Current Opinion in Biotechnology* 2007;18(6):537–45.
- [250] Singh P, Prasuhn D, Yeh RM, Destito G, Rae CS, Osborn K, et al. *Journal of Controlled Release* 2007;120(1–2):41–50.
- [251] McCormick AA, Palmer KE. *Expert Review of Vaccines* 2008;7(1):33–41.
- [252] Miermont A, Barnhill H, Strable E, Lu X, Wall KA, Wang Q, et al. *Chemistry – A European Journal* 2008;14(16):4939–47.
- [253] Kameta N, Masuda M, Minamikawa H, Mishima Y, Yamashita I, Shimizu T. *Chemistry of Materials* 2007;19(14):3553–60.
- [254] Gonzalez MJ, Plummer EM, Rae CS, Manchester M. *PLoS One* 2009;4(11). Article No.: e7981.
- [255] Smith ML, Fitzmaurice WP, Turpen TH, Palmer KE. *Plant-Produced Microbial Vaccines* 2009;332:13–31.
- [256] Cormode DP, Jarzyna PA, Mulder WJM, Fayad ZA. *Advanced Drug Delivery Reviews* 2010;62(3):329–38.
- [257] Uchida M, Terashima M, Cunningham CH, Suzuki Y, Willits DA, Willis AF, et al. *Magnetic Resonance in Medicine* 2008;60(5):1073–81.
- [258] Sanchez P, Valero E, Galvez N, Dominguez-Vera JM, Marinone M, Poletti G, et al. *Dalton Transactions* 2009;5:800–4.
- [259] Flenniken ML, Liepold LO, Crowley BE, Willits DA, Young MJ, Douglas T. *Chemical Communications (Cambridge, United Kingdom)* 2005;4:447–9.
- [260] Destito G, Yeh R, Rae CS, Finn MG, Manchester M. *Chemistry & Biology (Cambridge, MA, United States)* 2007;14(10):1152–62.
- [261] Kaltgrad E, Gupta SS, Punna S, Huang C-Y, Chang A, Wong C-H, et al. *ChemBioChem* 2007;8(12):1455–62.
- [262] Kaltgrad E, O'Reilly MK, Liao L, Han S, Paulson JC, Finn MG. *Journal of the American Chemical Society* 2008;130(14):4578–9.
- [263] Banerjee D, Liu AP, Voss NR, Schmid SL, Finn MG. *Chembiochem* 2010;11(9):1273–9.
- [264] Suh WH, Suh YH, Stucky GD. *Nano Today* 2009;4(1):27–36.
- [265] Rowe MD, Thamm DH, Kraft SL, Boyes SG. *Biomacromolecules* 2009;10(4):983–93.
- [266] Li F, Zhang ZP, Peng J, Cui ZQ, Pang DW, Li K, et al. *Small* 2009;5(6):718–26.
- [267] Xie H, Li YF, Kagawa HK, Trent JD, Mudalige K, Cotlet M, et al. *Small* 2009;5(9):1036–42.
- [268] Lee SH, Lee H, Park JS, Choi H, Han KY, Seo HS, et al. *FASEB Journal* 2007;21(7):1324–34.
- [269] Liu G, Wu H, Dohnalkova A, Lin Y. *Analytical Chemistry* 2007;79(15):5614–9.
- [270] Yamada K, Yoshii S, Kumagai S, Miura A, Uraoka Y, Fuyuki T, et al. *Japanese Journal of Applied Physics, Part 1: Regular Papers, Brief Communications & Review Papers* 2007;46(11):7549–53.
- [271] Ohara K, Yamashita I, Uraoka Y. *Japanese Journal of Applied Physics* 2010;49(4).
- [272] Miura A, Uraoka Y, Fuyuki T, Yoshii S, Yamashita I. *Journal of Applied Physics* 2008;103(7, Pt. 1). 074503/074501-074503/074510.
- [273] Miura A, Tsukamoto R, Yoshii S, Yamashita I, Uraoka Y, Fuyuki T. *Nanotechnology* 2008;19(25).
- [274] Kubota T, Baba T, Samukawa S, Kawashima H, Uraoka Y, Fuyuki T, et al. *Applied Physics Letters* 2004;84(9):1555–7.
- [275] Kubota T, Baba T, Saito S, Yamasaki S, Kumagai S, Matsui T, et al. *Journal of Vacuum Science & Technology B* 2007;25(3):760–6.
- [276] Kubota T, Hashimoto T, Takeguchi M, Nishioka K, Uraoka Y, Fuyuki T, et al. *Journal of Applied Physics* 2007;101(12).
- [277] Tempel H, Joshi R, Schneider JJ. *Materials Chemistry and Physics* 2010;121(1–2):178–83.
- [278] Kim I, Hosein H-A, Strongin DR, Douglas T. *Chemistry of Materials* 2002;14(11):4874–9.
- [279] Varpness Z, Peters JW, Young M, Douglas T. *Nano Letters* 2005;5(11):2306–9.



**Günther Jutz** studied Chemistry with Macromolecular Chemistry as a major subject at the University of Bayreuth. End of 2008, he received his Ph.D. under the supervision of Prof. Alexander Böker with a research work on mineralized bionanoparticle stabilized Pickering emulsions. His research interests reach from controlled polymerization techniques to viruses and proteins as building blocks in bionanotechnology and bio-(in)organic composite materials. After a visit in the group of Prof. José Carlos Rodríguez Cabello, University of Valladolid, Spain, he joined SGL Carbon GmbH, working now on the development of carbon and graphite materials for energy storage systems.



**Alexander Böker** is Full Professor at the RWTH Aachen University, holding the Chair for Macromolecular Materials and Surfaces and serving as Co-Director of the DWI an der RWTH Aachen e.V. He studied Chemistry at the Cornell University (Ithaca, NY, USA) and the University of Mainz, Germany, where he received his Diploma in Chemistry in 1999. In 2002 he completed his Ph.D. in Physical and Macromolecular Chemistry at the University of Bayreuth, Germany. From 2002 to 2004 he worked with Thomas P. Russell at the University of Massachusetts, Amherst, USA. After his return to Bayreuth, he was awarded a Lichtenberg-Professorship for Colloid Chemistry funded by the VolkswagenStiftung in 2006 and qualified as a professor for physical chemistry in 2007. His main research interests include guided self-assembly of block copolymer systems, hierarchical nanoparticle assemblies and the control of self-assembly processes via external fields.



## Polymer Communication

## A novel phosphorus-containing poly(lactic acid) toward its flame retardation

De-Yi Wang, Yan-Peng Song, Ling Lin, Xiu-Li Wang, Yu-Zhong Wang\*

Center for Degradation and Flame-Retardant Polymeric Materials, College of Chemistry, State Key Laboratory of Polymer Materials Engineering, National Engineering Laboratory of Eco-Friendly Polymeric Materials (Sichuan), Sichuan University, Chengdu 610064, China

## ARTICLE INFO

## Article history:

Received 30 May 2010

Received in revised form

3 November 2010

Accepted 13 November 2010

Available online 23 November 2010

## Keywords:

Flame retardance

Poly(lactic acid)

Chain extension

## ABSTRACT

An inherently flame-retardant poly(lactic acid) (PLA) was synthesized via the chain-extending reactions of dihydroxyl terminated pre-poly(lactic acid) (pre-PLA), which was synthesized by direct polycondensation of L-lactic acid using 1,4-butanediol as initiator and stannous chloride ( $\text{SnCl}_2$ ) as catalyst, using ethyl phosphorodichloridate as chain extender. The resulting phosphorus-containing poly(lactic acid) (PPLA) was characterized by gel permeation chromatography (GPC),  $^1\text{H}$  and  $^{31}\text{P}$  nuclear magnetic resonance ( $^1\text{H}$ ,  $^{31}\text{P}$  NMR) and homonuclear correlation spectroscopy (COSY) and inductively coupled plasma-mass (ICP). A comprehensive flame retardant property of PPLA was evaluated by microscale combustion calorimetry (MCC), limiting oxygen index (LOI), vertical burning test (UL-94) and cone calorimeter test (CCT). PPLA has excellent flame retardancy and also can be used as a flame retardant for commercial PLA. Only 5 wt.% of PPLA added into PLA can obtain good flame retardant properties. As the content of PPLA is further increased to 10 wt.%, PLA can have much better flame retardancy (LOI = 35 and UL-94 V-0 rating), lower peak heat release rate (pHRR) and longer ignition time (TTI) than neat PLA. All those results mean that this novel approach to impart flame retardancy to PLA is very effective.

© 2010 Elsevier Ltd. All rights reserved.

## 1. Introduction

Poly(lactic acid) (PLA) is one of the most promising candidates in the field of biobased polymers because it is biodegradable and can be produced from renewable resources (sugar beets, corn starch, etc.). Recently PLA has been considered as alternative in replacing petrochemical polymers due to its excellent mechanical properties, high degree of transparency, and ease of fabrication [1]. Usually, PLA can be synthesized by direct polycondensation of lactic acid, or chain extension after polycondensation and by ring-opening polymerization of lactide [2,3]. Currently, although the main use of PLA is still in biomedical application, its other applications are increasing because of its excellent potential properties. Actually, PLA has been used in electronic industries now, such as the housings of portable word processors [4]. Unfortunately, PLA is still as flammable as common synthetic thermoplastics, such as polyethylene, polyester, and so on owing to its own intrinsic chemical composition and molecular structures. Predictably, the flammability will limit its application and development, especially its potential wide application in the

electronic field. Therefore, the improvement of flame retardant performance of PLA has been an important and urgent task.

Unfortunately, so far few research reports have focused on flame retarded PLA in literatures. Several report employed ammonium phosphate, [5,6] melamine phosphate, [7] aluminium hydroxide, [8] silica gel [9] and compounds containing halogen and talc [10] as additive flame retardants for PLA matrix. Lately, Casetta and Bourbigot et al. evaluated the efficiency of intumescent formulations to flame-retardant PLA; those are composed of ammonium polyphosphate (APP), pentaerythritol (PER), lignin and starch [11]. The results show the flame retardancy of PLA has been improved greatly as the flame retardant reached a loading level of 40wt%. In our latest studies, a series of flame retardant toughened PLA composites have been prepared using poly(ethylene glycol) (PEG6000) and ammonium polyphosphate (APP) [12].

In the present study, we developed a novel approach to the preparation of flame-retardant PLA. We used a reactive flame retardant, ethyl phosphorodichloridate, as a chain extender to synthesize poly(lactic acid) containing phosphorus in the backbone (PPLA), shown in Scheme 1. The inherently flame-retardant PPLA has excellent flame retardancy, and can also be used as a flame retardant for PLA. The flame retardancy of PPLA and its blends with PLA has been investigated via microscale combustion calorimetry (MCC), limiting oxygen index (LOI), vertical burning test (UL-94) and cone calorimeter test (CCT).

\* Corresponding author. Tel./fax: +86 28 85410259.

E-mail address: [yzwang@scu.edu.cn](mailto:yzwang@scu.edu.cn) (Y.-Z. Wang).



**Table 1**  
Effect of reaction temperature and time on chain-extending reaction of PLA.

Samples	Temperature (°C)	Time (min)	Mn ( $\times 10^4$ ) (g/mol)	Mw ( $\times 10^4$ ) (g/mol)	Polydispersity
PPLA-1	160	10	2.6	24	9.1
PPLA-2	170	10	0.7	5.5	8.0
PPLA-3	180	10	1.7	18	11.1
PPLA-4	160	30	1.5	9.8	6.4
PPLA-5	160	60	1.4	1.7	1.2
PPLA-6	160	90	1.3	1.5	1.2

which would benefit the conduction of the following chain-extending reaction. The molecular weight data were measured by GPC. To determine the optimal conditions for preparing phosphorus-containing PLA (PPLA) via chain-extending reaction, a series of reaction conditions such as the feed molar ratio, reaction temperature and reaction time were studied. The molecular weights of pre-PLA and PPLA after chain extension were investigated by GPC.

Firstly, the effect of reaction temperature and time on chain extension behaviour of PLA was studied at a fixed  $-\text{OH}/-\text{P}(=\text{O})-\text{Cl}$  ratio of 1:1.2. From Table 1, it could be seen that the Mn of PPLA

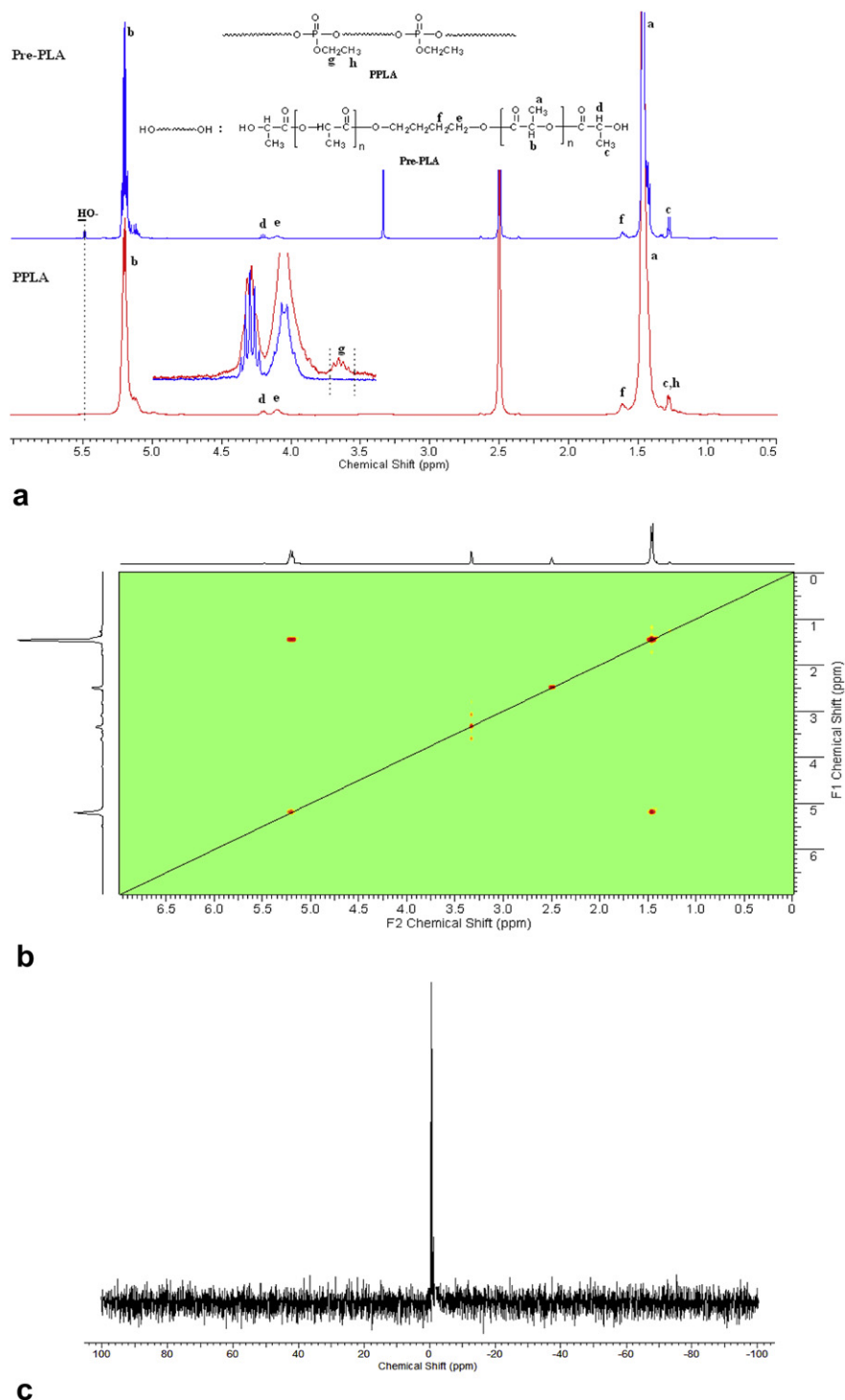


**Fig. 1.** Nuclear magnetic resonance spectra: (a)  $^1\text{H}$  NMR for PPLA and pre-PLA; (b) 2D-homonuclear correlation spectroscopy (COSY) for pre-PLA; (c)  $^{31}\text{P}$  NMR for PPLA.

decreased with the increase of reaction temperature from 160 °C to 180 °C, indicating that the higher reaction temperature could accelerate the chain degradation rather than chain extension. Meanwhile, a similar trend for Mn of PPLA was observed at longer reaction time. These results indicated that a reaction temperature of 160 °C and reaction time of 10 min seemed to be optimal for obtaining a high molecular weight of PPLA in this case. The theoretical values of P content for all samples can be calculated based upon the reactive mass ratio and the molecular weight of pre-PLA. For the veracity, the molecular weight of pre-PLA is calculated from  $^1\text{H}$  NMR (See Fig. 1(a)) and the value is 3500 g/mol.

Table 2 showed the effect of the molar ratio of  $-\text{OH}/-\text{P}(=\text{O})-\text{Cl}$  (mol/mol) on the chain-extending reaction of PLA when the reaction temperature and time were kept at 160 °C and for 10 min, respectively. The molar ratio of  $-\text{OH}/-\text{P}(=\text{O})-\text{Cl}$  (mol/mol) can be controlled between 1:1 to 1:1.75.

The results showed that although the Mn of PPLA did not have an obvious increase with increasing the chain extender, the phosphorus content in the PPLA had a corresponding increase. The phosphorus content in materials is an important factor to determine the flame retardancy of materials. Therefore, we used the high-phosphorus-content PPLA (PPLA-10) to conduct the relevant flame retardant studies in this paper. It was noted that the P contents measured by ICP were lower than the corresponding theoretical values. The possible reason for this is that the chain extender has a tiny loss in the low reaction pressure during the chain-extending reaction.

To confirm the structure of PPLA, the  $^1\text{H}$  NMR and  $^{31}\text{P}$  NMR of PPLA were measured, respectively. Furthermore, the assignment of the proton resonance with the structure of pre-PLA was also confirmed by a homonuclear correlation spectroscopy (COSY) 2D-NMR spectrum shown in Fig. 1(b), which provided  $^1\text{H}-^1\text{H}$  connectivity of neighbouring protons, showing a correlation between  $\text{H}^a$  and  $\text{H}^b$ . This correlation is in good agreement with the labelled pre-PLA structure in Fig. 1(a). The assignment of protons in Fig. 1(a):  $^1\text{H}$  NMR ( $d_6$ -DMSO,  $\delta = 2.53$  ppm [14]):  $\delta$  (ppm) = 1.47 (d,  $\text{H}^a$ ), 5.20 (m,  $\text{H}^b$ ), 1.27 (m,  $\text{H}^c$ ), 4.20 (m,  $\text{H}^d$ ), 4.10 (m,  $\text{H}^e$ ), 1.61 (m,  $\text{H}^f$ ), 3.93 (q,  $\text{H}^g$ ), 1.25 (m,  $\text{H}^h$ ), 5.48 (m,  $-\text{OH}$ ). Herein, comparing the spectrum of pre-PLA with that of PPLA in Fig. 1(a), we can notice that, actually, there mainly exist two differences between them. One is the position of 5.48 ppm, which is corresponding to the hydroxyl protons of the end group of pre-PLA, while it disappears in the spectrum of PPLA, indicating more hydroxyl groups are consumed in the chain extension.

The other is a new tiny quadruplicate peak at the position of 3.93 ppm appeared in the local magnification of PPLA spectrum, which corresponded to the methylene of the phosphorus-containing chain extender ( $(-\text{O}-)_2\text{P}(=\text{O})-\text{CH}_2\text{CH}_3$ ). Those differences just identify the structure of PPLA and prove the success of chain extension. Furthermore, more direct evidence comes from the  $^{31}\text{P}$  NMR spectrum of PPLA in Fig. 1(c), showing single peak at  $-2.2$  ppm corresponding to the phosphorus-containing unit [ $(-\text{O}-)_2\text{P}(=\text{O})-\text{OCH}_2\text{CH}_3$ ] in the PPLA structure. Therefore, we conclude that the PPLA, which contains phosphorus in the backbone, has been synthesized successfully by chain extension.

**Table 2**  
Effect of the molar ratio  $-\text{OH}/-\text{P}(=\text{O})-\text{Cl}$  on chain-extending reaction of PLA.

Samples	Molar ratio of $-\text{OH}/-\text{P}(=\text{O})-\text{Cl}$	Mn ( $\times 10^4$ ) (g/mol)	Mw ( $\times 10^4$ ) (g/mol)	Polydispersity	Theoretical content of P (wt.%)	Measured content of P (wt.%) by ICP
PPLA-7	1:1	0.7	1.4	2.0	0.86	0.65
PPLA-1	1:1.2	2.6	24	9.1	1.03	0.80
PPLA-8	1:1.25	0.9	1.6	1.8	1.07	0.78
PPLA-9	1:5	1.7	13	7.5	1.27	1.06
PPLA-10	1:1.75	1.9	9.6	5.1	1.46	1.18

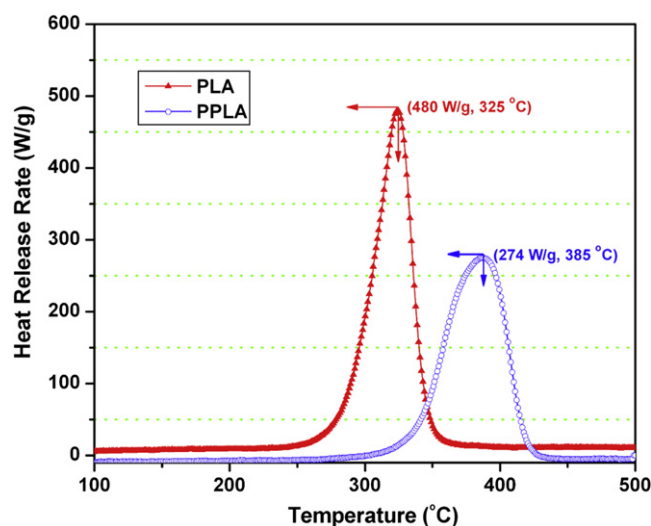


**Fig. 2.** Heat release rate (HRR) results of PLA and PPLA from microscale combustion calorimetry (MCC).

### 3.2. Flame retardancy of PPLA

In this section, a comprehensive flame retardancy of PPLA has been evaluated by microscale combustion calorimetry (MCC), cone calorimeter test (CCT), limiting oxygen index (LOI) and vertical burning test (UL-94), respectively, comparing with pure PLA. MCC is a smaller-scale flammability testing technique to screen polymer flammability prior to scale-up of a large size, which is a convenient and new technique developed in recent several years [15–18]. For MCC measurement, only 5–50 mg samples were needed. Like the cone calorimeter, MCC is also based on the principle of oxygen consumption. For PPLA and commercial PLA, their results of heat release rate (HRR) from MCC are shown in Fig. 2. Obviously, there is a significant difference between two samples. The peak heat release rate (pHRR) is generally regarded as an important parameter which can be used to evaluate the intensity of flames [19]. In the case of the neat commercial PLA, the curve shows a sharp HRR peak, and the value of pHRR is 480 W/g. The temperature corresponding to the pHRR ( $T_{\text{pHRR}}$ ) is 325 °C, which means that the maximum fuel produced by PLA decomposition at this temperature, and the initial fuel emergence temperature ( $T_{\text{initial fuel}}$ ) of PLA is about 270 °C. However, it can be seen from Fig. 2 that the HRR curve of PPLA is significantly different from that of PLA. Firstly, the pHRR value of PPLA is 274 W/g, which is only 57% pHRR of PLA. Secondly, the shape of HRR curve of PPLA looks a bit gentle compared with the sharp curve of PLA, meaning that the decomposition process of PPLA has been changed by introducing phosphorus into the backbone of PLA. More interestingly, the  $T_{\text{initial fuel}}$  and  $T_{\text{pHRR}}$  of PPLA are increased considerably to 325 °C and 385 °C, respectively. As we know, actually, only a small amount of phosphorus has been incorporated in the backbone of PPLA. Why can the so small

phosphorus content and structural difference lead to the significant difference in their flame retardancy? Although there has been no an exact answer to this question so far, undoubtedly, this should be a pioneering work and novel approach for preparing flame-retardant PLA. Also, if the result of this smaller-scale flammability test is assured, the flame retardancy of PPLA for scale-up flammability tests, such as LOI, UL-94 and cone calorimeter, might be predicted.

Owing to its excellent flame retardancy, PPLA also has a potential as a flame retardant for PLA. PPLA has the structure similar with PLA, therefore it can be expected to have more advantages than other additive flame retardants for PLA, which will be further studied in the future. Here only the flame retardancy of PPLA on a commercial PLA was investigated, that is, PPLA was added into the commercial PLA matrix to prepare flame-retardant PLA (FRPLA). The flame retardancy of FRPLA has been investigated via LOI, vertical burning (UL-94) and cone calorimeter. The effects of PPLA content on the LOI value and UL-94 rating of FRPLA were shown in Fig. 3.

From Fig. 3, we can see that PPLA shows high flame retardant efficiency to PLA. In comparison with the LOI value (LOI = 20) and UL-94 rating (no rating) of PLA, FRPLA had good flame retardant properties even if only 5 wt.% of PPLA was added into PLA. When the content of PPLA comes to 10 wt.%, FRPLA can reach a LOI value of 34 and UL-94 V-0 rating. Furthermore, the significant improvement in flame retardancy of FRPLA can also be seen from the following cone calorimeter test.

Compared with LOI and UL-94 test for evaluating the flammability of materials, the cone calorimeter provides a wealth of information on the burning behaviours and on its potential contribution in a flame [20]. Actually, it has been found that some cone calorimeter results have a good correlation with those obtained from large-scale flame test, even in real flame. Therefore, cone calorimeter is deemed as a powerful technique for investigating the flame retardancy of materials and flame behaviours. Fig. 4 presents the curves of HRR versus time of the FRPLA and PLA. For neat PLA, its peak heat release rate (pHRR) value is  $436 \text{ kW/m}^2$  and ignition time is 66 s.

In the case of FRPLA, the HRR curve presents significant difference from that of PLA. On the one hand, the ignition time has been prolonged from 66 s to 78 s. Generally, ignition of materials happens until the concentration of fuel from material degradation and releasing the pyrolysis gas reaches a limiting value. The prolonged ignition time is related to the reduction of decomposition of FRPLA under heating condition, which should be attributed to the

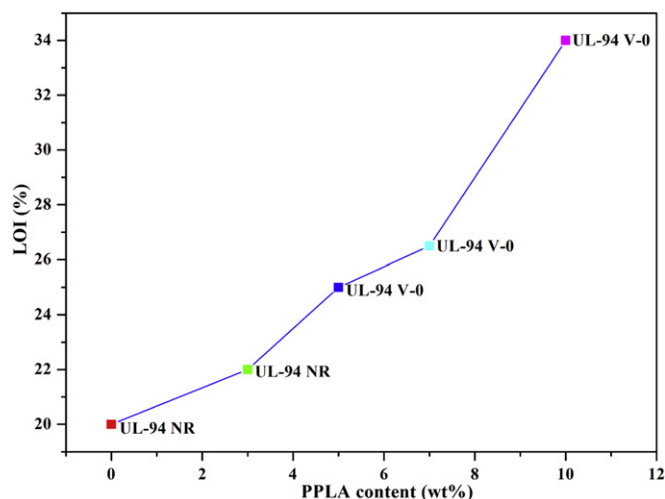


Fig. 3. The LOI values and UL-94 ratings of flame retarding PLA (FRPLA) when PPLA served as an additive for PLA.

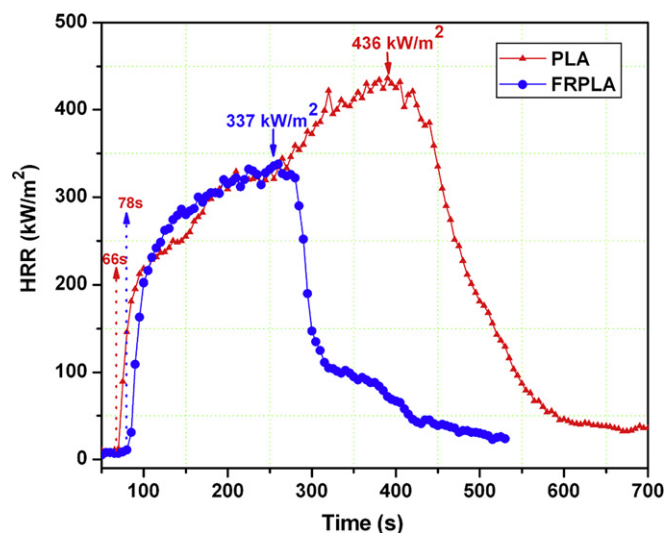


Fig. 4. Heat release rate (HRR) results of FRPLA and PLA from cone calorimeter test (CCT).

addition of PPLA. This result has a good agreement with the significant improvement of  $T_{\text{initial fuel}}$  of PPLA in the microscale combustion calorimeter measurement. On the other hand, the pHRR value of FRPLA is decreased from  $436 \text{ kW/m}^2$  to  $337 \text{ kW/m}^2$ , which means that the flame intensity degrades with the combustion of materials. Furthermore, some char residues are produced and left on the aluminium foil pool after combustion in the cone calorimeter for FRPLA, while there is nothing remaining for PLA after combustion. A systematic research on the exact reactive and flame-retardant mechanisms is underway.

As a consequence, it is an effective way to imparting PLA excellent flame retardancy to introduce phosphorus into the backbone of PLA by the chain-extending reaction of pre-PLA using phosphorus-containing chain extender. The approach will have a significant potential application in the future.

#### 4. Conclusions

A novel approach to the preparation of flame-retardant PLA is pioneered in this study. An inherently flame-retardant poly(lactic acid) has been synthesized successfully via the chain-extending reactions of dihydroxyl terminated pre-poly(lactic acid) using ethyl phosphorodichloridate as chain extender. The flame-retardant element phosphorus is incorporated into the backbone of PLA macromolecules. The resulting phosphorus-containing PLA (PPLA) exhibits excellent flame retardancy compared with commercial PLA and it can even be used as a flame retardant for commercial PLA. PPLA has much higher initial fuel emergence temperature ( $T_{\text{initial fuel}}$ ) and temperature of pHRR than neat PLA, and its pHRR value is remarkably reduced compared with that of neat PLA. As a flame retardant for PLA, only 5 wt.% of PPLA can impart PLA a good flame retardant property. When the content of PPLA is further increased to 10 wt.%, FRPLA has a LOI value of 35 and UL-94 V-0 rating and much lower pHRR value and longer TTI than neat commercial PLA. Therefore, this novel method for the flame retardation of PLA is very efficient and perspective.

#### Acknowledgements

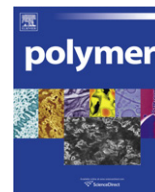
This research was supported by the National Science Foundation of China (50703026), the Key Project of the National Science Foundation of China (50933005), China Postdoctoral Science Foundation



funded project (20080440182, 200902615) and the International Foundation for Science (IFS, F/4285-2).

## References

- [1] SolarSKI S, Ferreira M, Devaux E. *Polymer* 2005;46:11187–92.
- [2] Dechy-Cabaret O, Martin-Vaca B, Bourissou D. *Chem Rev* 2004;104:6147–76.
- [3] Tim RC, Robson FS. *Macromolecules* 2008;41:655–62.
- [4] Kimura K, Horikoshi Y. *Fujitsu Sci Tech J* 2005;41(2):173–80.
- [5] Hata, Isamu. J.P.Pat. No. 2006335929.
- [6] Wang DY, Leuteritz A, Wang YZ, Wagenknecht U, Heinrich G. *Polym Degrad Stab* 2010;95(12):2474–80.
- [7] Ihara, Toshiaki; Tanaka, Masaki; Matsumura, Kazuyuki. E.P.Pat. No.1674551.
- [8] Oda, Tatsuki. J.P.Pat. No.2006077162.
- [9] Yamashita, Takehiko;Takeda, Kunihiko;Tani, Yoshiyuki; Hisazumi, Takao. PCT Pat. Appl. WO2005028558.
- [10] Chin, Hui. J.P.Pat. No.2004190025.
- [11] Reti C, Casetta M, Duquesne S, Bourbigot S, Delobel R. *Polym Adv Technol* 2008;19:628–35.
- [12] Song YP, Wang DY, Wang XL, Lin L, Wang YZ. *Polym Adv Technol*; 2010;. doi:10.1002/pat.1760.
- [13] Saunders BC, Stacey GJ, Wild F, Wilding IGE. *J Chem Soc*; 1948:695–9.
- [14] Greenwald M, Wessely D, Goldberg I, Cohe Y. *New J Chem*; 1999:337–44.
- [15] Schartel B, Pawlowshi KH, Lyon RE. *Thermochim Acta* 2007;462:1–14.
- [16] Ellzey KA, Ranganathan T, Zilberman J, Coughlin EB, Farris RJ, Emrick T. *Macromolecules* 2006;39:3553–8.
- [17] Ranganathan T, Zilberman J, Farris RJ, Coughlin EB, Emrick T. *Macromolecules* 2006;39:5974–5.
- [18] Hergenrother PM, Thompson CM, Smith JG, Connell JW, Hinkley JA, Lyon RE, et al. *Polymer* 2005;46:5012–24.
- [19] Lv P, Wang Z, Hu K, Fan W. *Polym Degrad Stab* 2005;90:523–34.
- [20] Price D, Liu Y, Hull TR, Milnes GJ, Kandola BK, Horrocks AR. *Polym Degrad Stab* 2002;77:213–20.



## Polymer Communication

## Exploiting interfacial polarization to detect phase transitions in dilute solutions: Crystallization and melting of P3HT in toluene down to ppm contents

Isabelle Monnaie<sup>a,b</sup>, Simone Napolitano<sup>c,\*</sup>, Erik Nies<sup>a,d,\*\*</sup>, Michael Wübbenhorst<sup>c</sup><sup>a</sup> Katholieke Universiteit Leuven, Polymer Research Division, Department of Chemistry, Celestijnenlaan 200F, B-3001 Leuven, Belgium<sup>b</sup> Eindhoven University of Technology, Laboratory of Materials and Interface Chemistry, Department of Chemical Engineering and Chemistry, P.O. Box 513, 5600MB Eindhoven, The Netherlands<sup>c</sup> Katholieke Universiteit Leuven, Acoustic and Thermal Physics, Department of Physics and Astronomy, Celestijnenlaan 200D, B-3001 Leuven, Belgium<sup>d</sup> Eindhoven University of Technology, Laboratory of Polymer Technology, Department of Chemical Engineering and Chemistry, P.O. Box 513, 5600MB Eindhoven, The Netherlands

## ARTICLE INFO

## Article history:

Received 9 November 2010

Received in revised form

23 November 2010

Accepted 3 December 2010

Available online 10 December 2010

## Keywords:

Dielectric spectroscopy

Phase transitions

P3HT

## ABSTRACT

Determination of phase diagrams of polymer solutions with conventional techniques, like differential scanning calorimetry (DSC), is limited to sufficiently high concentrations due to a low signal/noise ratio. Controlling the nanoscale morphology formation upon solution processing of dilute conjugated polymer solutions however requires this information. In this work, we introduce an experimental methodology able to detect phase transitions in solutions over a wide concentration regime, by means of dielectric spectroscopy. We tested the validity of our method for solutions of poly(3-hexylthiophene) in toluene. Apart from providing crystallization and melting temperatures consistent with DSC data for the overlapping sample concentrations, our method turned out to be able to detect phase transition down to trace level mass fractions as low as 10 ppm.

© 2010 Elsevier Ltd. All rights reserved.

## 1. Introduction

Poly(3-hexylthiophene) (P3HT) is a conjugated polymer widely used in the active layer of organic field effect transistors [1,2] and solar cells [3,4]. The final yield of these electronic devices strongly depends on the nanoscale morphology of the active layer [5], which is influenced by parameters like regioregularity [6] and molar mass [7] of its components as well as solvent of choice [8], and annealing conditions [9]. Increasing efficiently the performance of conjugated polymer electronics thus requires the knowledge of the phase behavior of the polymer in solution from the concentrated down to the dilute regime ( $\sim 1$  wt%), i.e. the starting point for layer deposition. Techniques like differential scanning calorimetry (DSC) and scattering methods fail at determining transition temperatures for mass fractions smaller than  $\sim 0.01$  because of a low signal/noise ratio (SNR); on the contrary, due to saturation effects, optical methods encounter difficulties with more concentrated solutions [10–12].

In this Communication we introduce an experimental methodology able to detect phase transitions in solutions over a wide concentration regime by means of dielectric spectroscopy (DS). At the state of the art, this technique allows characterization of molecular relaxations and crystallization events in bulk melts [13–17], in concentrated solutions [18], under elevated pressures [19–21] and in confined geometries [22,23]. Our approach is based on the temperature dependence of localized fluctuations of the dielectric constant and the conductivity within the solution. Aggregation of molecules at distances exceeding the path over which mobile charges screen out the effects of external electric fields (Debye length,  $l_D$ ) provokes interfacial polarization events affecting the apparent value of the dielectric constant.

Following Jonscher “universal” law [24,25], such a polarization grows with the inverse of the frequency, allowing an accurate detection of molecular reorganizations at crystalline contents lower than those detected by DSC.

## 2. Experimental section

## 2.1. Materials

Poly(3-hexylthiophene) (Plexcore OS1100,  $M_w = 49800$  g mol<sup>-1</sup>, PDI = 1.49 (GPC with PS standards in CHCl<sub>3</sub>), RR = 96% (NMR), data

\* Corresponding author. Tel.: +32 16 27167; fax: +32 16 327984.

\*\* Corresponding author. Katholieke Universiteit Leuven, Polymer Research Division, Department of Chemistry, Celestijnenlaan 200F, B-3001 Leuven, Belgium. Tel.: +32 16 327481; fax: +32 16 327990.

E-mail addresses: [simone.napolitano@fys.kuleuven.be](mailto:simone.napolitano@fys.kuleuven.be) (S. Napolitano), [erik.nies@chem.kuleuven.be](mailto:erik.nies@chem.kuleuven.be) (E. Nies).URL: <http://web.me.com/simone.napolitano>

as provided by the supplier, Plextronics) was mixed with toluene (HPLC grade 99.8%, Acros).

## 2.2. Experimental methods

Dielectric spectra in a frequency range from  $10^6$  Hz to 0.1 Hz were measured in isothermal conditions between  $60^\circ\text{C}$  and  $-50^\circ\text{C}$ , at an effective scanning rate of  $0.2^\circ\text{C min}^{-1}$ , with an Alpha High Resolution Analyzer (Novocontrol Technologies). Solutions were sealed in a parallel plate cell for investigation of liquids to avoid evaporation during experiments.

Differential scanning calorimetry was performed with a DSC-7 (PerkinElmer) TAC 7/DX. Samples were placed in stainless steel capsules and subjected to the following temperature profile: isothermal 10 min at  $80^\circ\text{C}$ , cooling ramp at  $-10^\circ\text{C min}^{-1}$  to  $-30^\circ\text{C}$ , isothermal 10 min and heating ramp to  $80^\circ\text{C}$ . Crystallization ( $T_c$ ) and melting temperatures ( $T_m$ ) were respectively determined as the onset of the exothermic and end point of the endothermic peaks.

## 3. Results and discussion

The temperature dependence of the dielectric constant ( $\epsilon'$ ) for solutions containing mass fractions of P3HT ranging from 0.05 to  $10^{-5}$  is shown in Fig. 1. Blue and red lines correspond to values of  $\epsilon'$

respectively obtained during cooling and subsequent heating scans; the response of pure toluene, appearing as a constant background over the whole temperature range investigated, is given in black.

Measurements on even more dilute solutions suffered from the increasing susceptibility to contaminations (e.g., from cell, sample preparation) that might alter the crystallization kinetics. We could promptly recognize contaminated samples, as the value of their dielectric constant at low and high temperatures deviated significantly from a flat response, see the lowest panel of Fig. 1. Nevertheless, regardless the reduction of the polarization intensity, analysis of isochronal plots at lower frequencies provides enough SNR to clearly observe transition phenomena at these extremely low concentrations.

During cooling, the temperature dependence of  $\epsilon'$  shows a frequency independent maximum in correspondence to the onset of crystallization measured by DSC,  $T_c$  (blue rectangle in Fig. 1).

The reduction of  $\epsilon'$  at lower temperatures could intuitively be ascribed to the immobilization of polymer chains and a decrease of the (mobile) dipole density in the samples, as expected during crystallization and observed in dry samples [14,22]. However, such a simplified picture cannot capture the enormous increase of the dielectric constant starting already  $15^\circ\text{C}$  before the onset of the exothermic peak in the calorimetric runs. The increase of  $\epsilon'$  preceding  $T_c$  suggests that this method is able to detect changes affecting the

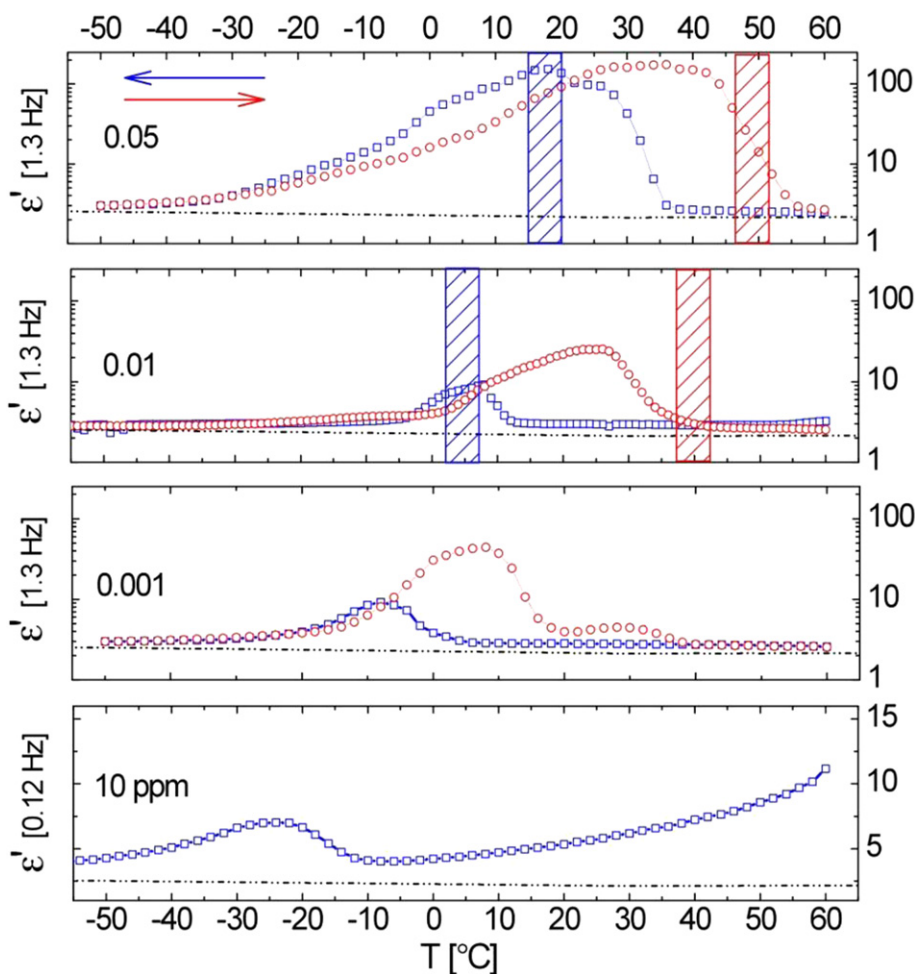


**Fig. 1.** Temperature dependence of the dielectric constant  $\epsilon'$  for solutions containing different mass fractions of P3HT in toluene. Cooling runs are represented in blue while subsequent heating scans are plotted in red. The measured dielectric response of pure toluene is given as a black dashed line. Similar transition temperatures are observed in the temperature dependence of the conductivity and of the dielectric loss (see Supporting information). Dashed rectangles indicate the transition temperatures measured by DSC, and their width includes the uncertainty ( $\pm 2.5$  K) due to the different scanning rate used.

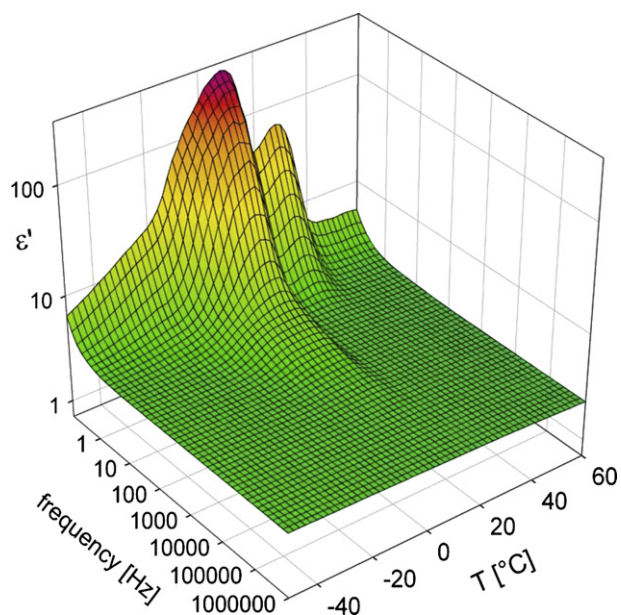


**Fig. 2.** Three-dimensional plot of the temperature and frequency dependence of the dielectric constant  $\epsilon'$  for a solution of toluene containing a mass fraction of P3HT of  $10^{-3}$ .

dielectric properties of the solution already at crystalline contents below the detection limit of DSC. This is in agreement with the scenario revealed by crystallization of poly( $\epsilon$ -caprolactone) [16], where perturbations in the dielectric properties were observed well before the onset of changes in the heat capacity or in neutron scattering, and thus attributed to precrystalline order.

Considering the temperature range being well above the glass transition temperature of the solution (corresponding to low viscosity  $\sim 1$  cP) as well as the relative low frequencies at which the phenomena appear, we can exclude dipolar fluctuations associated with the structural relaxation as a molecular origin.

On the other hand, electrode polarization, a common low-frequency process due to charge accumulation over macroscopic distances, can also be ruled-out because of the low conductivity of the sample [26]. Another argument disproving the role of “hidden” dipolar based relaxation mechanisms is the frequency independence of the maximum of the peak observed in  $\epsilon'(T)$ , see the three-dimensional plot of  $\epsilon'$  for a solution of toluene containing a mass fraction of P3HT of  $10^{-3}$  as a function of frequency and temperature

in Fig. 2. The most likely origin of the observed build-up of polarization is a Maxwell-Wagner (MW) process [15,17] due to charge accumulation over scales related to  $l_D$  ( $\sim 1 \mu\text{m}$ ).

A sketch of the possible scenario is given in Fig. 3. During the early stages of crystallization, a polarization proportional to the crystalline content is built up upon formation of agglomerates. This induces local anomalies in the ionic conductivity and the dielectric constant (1). In this specific case, it has been shown that poly-alkylthiophene chains undergo a coil-to-rod transition [27] upon decreasing temperature promoting crystalline lamellar organization, eventually leading to the formation of crystalline nanowire structures. At distances in between crystalline domains exceeding  $l_D$ , the strength of the MW process (and consequently of the value of  $\epsilon'$  in isochronal representations) grows with the ratio between the size of the nonconductive and the conductive species. The formation of sufficiently large domains with different dielectric constant ( $\epsilon_{\infty}^{\text{toluene}} = 2.5$ ,  $\epsilon_{\infty}^{\text{P3HT}} = 4\text{--}6.5$ , where  $\epsilon_{\infty}$  is the dielectric constant of the material in the limit of optical frequencies) provokes an effective charge accumulation at the borders of the nonconductive species (crystals) (2).

Further reduction of the temperature ( $T < T_c$ ) resulting in the formation of larger crystals, or crystalline aggregates, causes a reduction of the MW-polarization (3). The decrease of intensity of the process is the result of the reduction of the average distance between the crystalline species in solution. In this crystallization regime, when inter-particle distance drops below the Debye screening length, nearby or even associated crystals behave like single particles. Moreover, gelation, commonly observed in solutions of P3HT in toluene or xylene of similar concentration [28], could also take part in the decrease of  $\epsilon'(T)$ : the formation of a network, possibly by physical entanglements of nanowires, corresponds to a reduction of the overall surface/volume ratio and thus of the intensity of the MW-polarization.

As the molecular scheme described above is perfectly reversible, similar considerations can be made for the heating scans, where the increased chain mobility is finally associated to melting of the crystalline structure. The melting temperature, defined as the end point of the final endothermic transition in a DSC scan, corresponds to the end of the peak of  $\epsilon'$  (red rectangles in Fig. 1), proving that the transition to the isotropic liquid phase is accompanied by the disappearance of the investigated polarization process. At high concentrations, heating curves revealed relatively broad transition peaks, hinting to the presence of multiple non-resolved melting and recrystallization events, in agreement with calorimetric investigation [29]. The presence of two resolved peaks in the temperature

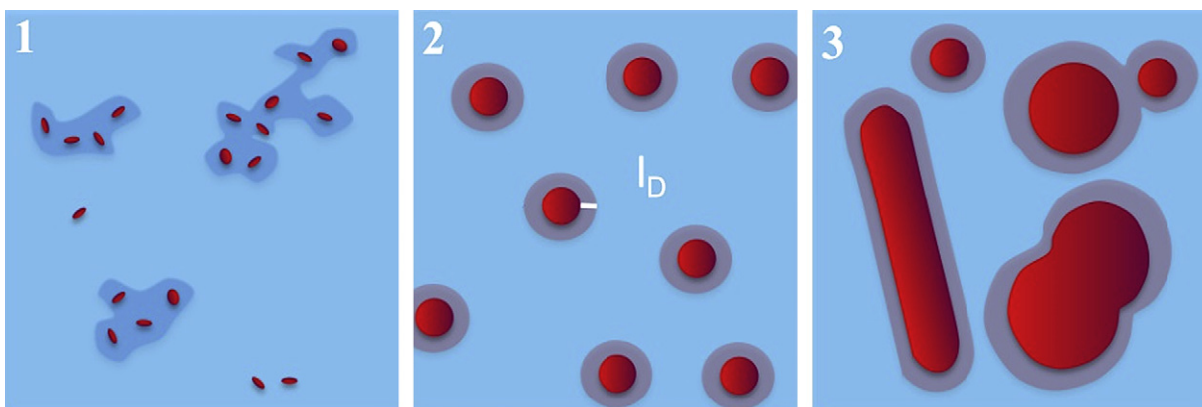


**Fig. 3.** Impact of crystalline morphology on the dielectric properties of a dilute solution. Presence of crystalline germs affects the local conductivity of the solution and introduces a polarization process raising the value of the dielectric constant at low frequencies. Due to a mismatch between the dielectric constants of the solvent (conductive) and the one of the crystals (nonconductive), an accumulation of charges at the borders of the nonconductive media increases the strength of the process. The effective polarization decreases upon aggregation (reduction of the surface/volume ratio), when the average distances between nonconductive domains get smaller than the Debye length.

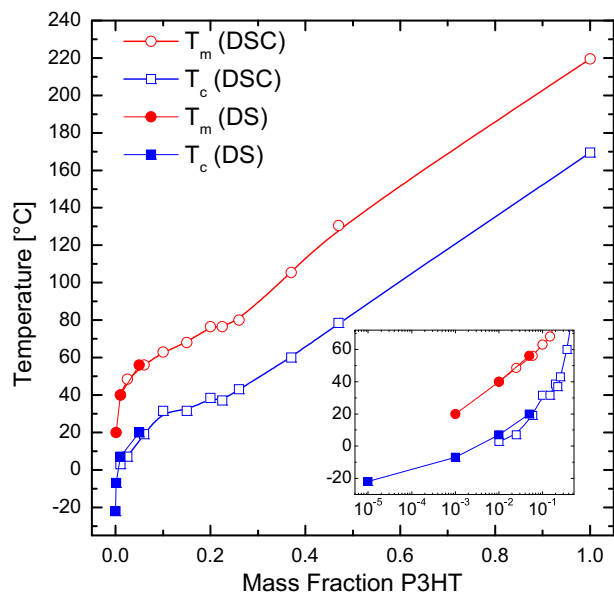


Fig. 4. Phase diagram of the melting and crystallization point for solutions of P3HT in toluene. In the inset, mass fractions are plotted in a logarithmic scale.

dependence of the dielectric constant at mass fractions of  $10^{-3}$  reinforces this interpretation. Moreover, part of the broadening could be attributed to convolution of molecular processes on the temperature dependence of the conductivity. The coil-to-rod transition preceding crystallization leads to significant loss of the main chain mobility, especially upon initial aggregation. However, local rearrangements within the hexyl side groups are not prohibited even after the phase transition takes place, hence smearing out the actual transition over a wider temperature domain. A phase diagram of the investigated solution is provided in Fig. 4, the points collected via the interfacial polarization method here described follow the trend in the data obtained via DSC extending the concentration range well below the limits of the calorimetric measurements. Finally, it is noteworthy highlighting that similar increases in the low-frequency response of the dielectric function were observed also in solutions of crude oils in mixtures of heptane and toluene [30]. The observation suggests that it might be possible to extend our approach to a larger number of materials.

#### 4. Conclusions

We described an experimental methodology to detect phase transitions in dilute polymer solutions by means of dielectric spectroscopy. We investigated crystallization and melting transitions in solutions of P3HT in toluene by means of the temperature dependence of the dielectric constant in the Hz and subHz region. In this frequency regime, formation of new species in solution gives rise to an interfacial polarization that allowed us to determine transition temperatures down to ppm contents. The method can be applied to different solute/solvent systems, pushing the

investigation of phase diagrams down to trace levels and providing a sensitive approach for the control of gelation and network formation in solution or the impact of contaminants on phase transitions.

#### Acknowledgements

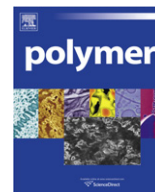
IM acknowledges the Dutch Polymer Institute (DPI), project #682, SN acknowledges FWO (Fonds Wetenschappelijk Onderzoek - Vlaanderen) for a postdoctoral scholarship. The authors acknowledge Joachim Loos (Department of Chemical Engineering and Chemistry, Eindhoven University of Technology) for providing the materials used in this work.

#### Appendix. Supporting information

Supplementary data related to this article can be found online at doi:10.1016/j.polymer.2010.12.010.

#### References

- [1] Siringhaus H, Tessler N, Friend RH. *Science* 1998;280:1741–4.
- [2] Bao Z, Lovinger AJ, Dodabalapur A. *Appl Phys Lett* 1996;69:3066–8.
- [3] Li G, Shrotriya V, Huang JS, Yao Y, Moriarty T, Emery K, et al. *Nat Mater* 2005;4:864–8.
- [4] Ma WL, Yang Y, Gong X, Lee K, Heeger AJ. *Adv Funct Mater* 2005;15:1617–22.
- [5] Bertho S, Oosterbaan WD, Vrindts V, D'Haen J, Cleij TJ, Lutsen L, et al. *Org Electron* 2009;10:1248–51.
- [6] Samitsu S, Shimomura T, Ito K. *Thin Solid Films* 2008;516:2478–86.
- [7] Ma W, Kim JY, Lee K, Heeger AJ. *Macromol Rapid Commun* 2007;28:1776–80.
- [8] Shaheen SE, Brabec CJ, Sariciftci NS, Padinger F, Fromherz T, Hummelen JC. *Appl Phys Lett* 2001;78:841–3.
- [9] Yang XN, Loos J, Veenstra SC, Verhees WJH, Wienk MM, Kroon JM, et al. *Nano Lett* 2005;5:579–83.
- [10] Balabin RM, Safieva RZ. *J Near Infrared Spectrosc* 2007;15:343–9.
- [11] Pochat-Bohatier C, Werapun W, Bouyer D, Chinpa W, Deratani A. *J Polym Sci B Polym Phys* 2010;48:1960–9.
- [12] Syunyaev RZ, Balabin RM, Akhatov IS, Safieva JO. *Energy Fuels* 2009;23:1230–6.
- [13] Kessairi K, Napolitano S, Capaccioli S, Rolla P, Wubbenhorst M. *Macromolecules* 2007;40:1786–8.
- [14] Sanz A, Jimenez-Ruiz M, Nogales A, Marero DMY, Ezquerro TA. *Phys Rev Lett* 2004;93:015503.
- [15] Napolitano S, Wubbenhorst M. *J Non-Cryst Solids* 2007;353:4357–61.
- [16] Wurm A, Soliman R, Schick C. *Polymer* 2003;44:7467–76.
- [17] Pluta M, Jeszka JK, Boiteux G. *Eur Polym J* 2007;43:2819–35.
- [18] Yoshizaki K, Urakawa O, Adachi K. *Macromolecules* 2003;36:2349–54.
- [19] Mierzwa M, Floudas G, Stepanek P, Wegner G. *Phys Rev B* 2000;62:14012–9.
- [20] Papadopoulos P, Peristeraki D, Floudas G, Koutalas G, Hadjichristidis N. *Macromolecules* 2004;37:8116–22.
- [21] Paluch M, Pawlus S, Roland CM. *Macromolecules* 2002;35:7338–42.
- [22] Napolitano S, Wubbenhorst M. *Macromolecules* 2006;39:5967–70.
- [23] Napolitano S, Pilleri A, Rolla P, Wubbenhorst M. *ACS Nano* 2010;4:841–8.
- [24] Syunyaev RZ, Balabin RM. *J Dispers Sci Technol* 2007;28:419–24.
- [25] Jonscher AJ. *Universal relaxation law*. Chelsea Dielectrics Press Ltd; 1995.
- [26] We further checked that during isothermal experiments (data not shown) the dielectric constant reaches a maximum at a crystallization time independent on the frequency of investigation. The evidence disproves the presence of an interfacial layer growing on the electrodes, see Ref. [16].
- [27] Yue S, Berry GC, McCullough RD. *Macromolecules* 1996;29:933–9.
- [28] Malik S, Jana T, Nandi AK. *Macromolecules* 2001;34:275–82.
- [29] Monnaie I. *Properties of P3HT in solution: Towards High-performance polymer solar cells by controlling Active Layer Morphology (Master Thesis)*, Katholieke Universiteit Leuven, 2009.
- [30] Vrålstad H, Spets Ø, Lesaint C, Lundgaard L, Sjöblom J. *Energy Fuels* 2009;23:5596–602.



## Thermosetting ROMP materials with thermally degradable linkages

Ezat Khosravi<sup>a,\*</sup>, Favaad Iqbal<sup>a</sup>, Osama M. Musa<sup>b</sup>

<sup>a</sup> Interdisciplinary Research Centre in Polymer Science and Technology, Chemistry Department, Durham University, Durham DH1 3LE, UK

<sup>b</sup> International Specialty Products, 1361 Alps Road, Wayne, NJ 07470, USA

### ARTICLE INFO

#### Article history:

Received 6 August 2010

Received in revised form

17 November 2010

Accepted 7 December 2010

Available online 15 December 2010

#### Keywords:

ROMP

Thermosetting materials

Degradable linkage

### ABSTRACT

Mono- and di-functional norbornene dicarboximide monomers containing acetal ester groups were synthesised. The ROMP of the di-functional monomer using Grubbs ruthenium first generation initiator at ambient temperature produced crosslinked material. Materials with various crosslink densities were prepared by the ROMP, under the same condition, of mixtures of the mono- and di-functional monomers. The FT-IR spectra clearly showed the presence of an acetal C–O band at  $1135\text{ cm}^{-1}$ . The TGA study of the crosslinked materials showed that they are stable to  $150\text{ }^{\circ}\text{C}$  and that they exhibit rapid breakdown at about  $200\text{ }^{\circ}\text{C}$ , as the result of the thermal decomposition of the acetal ester linkage. FT-IR analysis of the retrieved materials following TGA-MS showed that the intensity of acetal C–O band at  $1135\text{ cm}^{-1}$  was greatly reduced.

© 2010 Elsevier Ltd. All rights reserved.

### 1. Introduction

Thermosetting polymers exhibit excellent thermal and mechanical properties, and have been used in a wide range of applications [1–3]. However, the poor tractability, recyclability and biodegradability of thermosetting polymer limit their use in applications where reworkability, recycling and biodegradation are important [4,5].

Several research groups reported chemically breakable thermosetting materials by incorporating chemically cleavable linkages into their monomer systems [5–14]. Epoxy resins containing disulfide linkages were prepared and reported to exhibit reversible crosslinking behaviour through chemical reduction with triphenylphosphine [6–8]. Di-functional epoxy monomers incorporating chemically cleavable acetal and ketal linkages were prepared and the resulting thermoset network was reported to degrade slowly by applying acid-containing solvent mixtures [5]. Moreover, polymers containing acetal or ketal linkages in their backbone were prepared as pH-sensitive polymers for therapeutics and drug delivery applications [9,10]. The polymers were reported to degrade into low molecular weight compounds by acid-catalysed hydrolysis. Cationic polymerisation of diglycidylether of bisphenol A (DGEBA) with butyrolactone, using ytterbium triflate as initiator was also reported to yield degradable thermosets [11–13]. The ester groups formed during this copolymerisation reaction were reported to degrade by alkaline hydrolysis at  $80\text{ }^{\circ}\text{C}$ .

Although thermosetting materials incorporating chemically cleavable linkages may find some applications, the degradation process is unlocalised. In contrast, thermosetting materials with thermally breakable linkages are anticipated to offer the possibility of a localised degradation process. The syntheses of di-epoxide monomers containing cycloaliphatic ester groups were reported and the resulting thermosetting materials shown to degrade thermally at  $250\text{--}300\text{ }^{\circ}\text{C}$  [14–16]. Synthesis of a series of cycloaliphatic di-epoxide monomers containing carbamate linkages and their thermal degradation in the range of  $200\text{--}300\text{ }^{\circ}\text{C}$  was also reported [17,18]. The system is further complicated by the fact that the carbamate groups within the di-epoxides can act as an internal catalyst. Moreover, the syntheses of cycloaliphatic di-epoxides containing carbonate linkages were reported [17,19]. The cured materials were found to decompose at temperature slightly lower than of the cured samples of cycloaliphatic di-epoxide without carbonate linkages of  $350\text{ }^{\circ}\text{C}$ .

Ring opening metathesis polymerisation (ROMP) initiated by Grubbs well-defined ruthenium initiators has been demonstrated to results in the synthesis of well-defined polymers with controlled architectures, molecular weights, polydispersities, and terminal functionalities [20–28]. Moreover, we recently developed a ROMP processing technique for the synthesis of thermosetting materials with well-defined crosslinked networks from mixtures of mono-functional and di-functional norbornene dicarboximide monomers for applications in Resin Transfer Moulding (RTM) and Reaction Injection Moulding (RIM) [29,30]. We were able to demonstrate an excellent level of control over crosslink density by controlling the amount of added di-functional monomer to the reaction mixture. As the percentage of di-functional monomer was increased the  $T_g$  shifted to a higher temperature, and the plateau shear modulus above  $T_g$

\* Corresponding author. Tel.: +44 191 334 2014; fax: +44 191 334 2051.

E-mail address: [ezat.khosravi@durham.ac.uk](mailto:ezat.khosravi@durham.ac.uk) (E. Khosravi).

was increased. The resulting crosslinked materials showed values of yield strength and toughness which were either comparable to or better than the currently used engineering polymer materials, such as polycarbonates [30]. These ROMP thermosetting materials were thermally stable, degrading above 400 °C, and could be used only for applications where high temperature stability is required.

We recently started a programme of work to render these well-defined thermosetting ROMP materials thermally degradable, biodegradable and recyclable by introducing degradable linkages into the crosslinkable structures. The aim was to create opportunities in three interesting applications. First, the method of synthesis of these well-defined crosslinked ROMP materials is versatile and allows the introduction of functional groups such as OH and COOH into the monomer systems to promote adhesion to a wide range of substrates. This would be expected to lead to a potential application as reworkable adhesives, particularly in the electronics industry. Second, the decomposition of the thermally degradable linkage upon heating leads to a decrease in crosslinking density and modulus. The complete breakdown of all linkages is expected to result in the formation of linear thermoplastic materials, if the main chains remain intact. Doing so, would give the potential for recycling of thermosetting materials which is presently difficult to achieve. Third, the incorporation of biodegradable linkages into these thermosetting materials would result in materials which are tough and yet biodegradable leading to the breakdown of the bulk material. The benefit of developing recyclable and biodegradable thermosetting materials in an increasingly environmentally conscience society is obvious as it will render the thermosetting materials environmentally friendly [31].

Recently, acetal ester linkages were introduced into maleimides-based compounds which were polymerised by a thermally triggered process at 125 °C into highly crosslinked networks and the resulting thermosetting materials were reported to degrade at 225 °C [32]. However, the process requires thermally triggered polymerisation and, as it is expected for a free radical process, the curing reactions and the resulting thermosetting materials are ill-defined in terms of control over the degree of crosslinking and reproducibility.

The decomposition temperatures of the epoxy-based thermosetting materials containing esters, carbamates and carbonates linkages reported earlier are very close to that of epoxy resin without these linkages of 350 °C. Therefore, these linkages are unsuitable for our purpose. Moreover, the thermosetting materials containing esters, carbamates, carbonates and acetal esters exhibit 100% weight loss at temperature between 250 and 350 °C since these linkages are incorporated into the main chains. We became interested in developing well-defined thermosetting materials containing acetal ester linkages by an efficient, controllable and reproducible process at room temperature such as ROMP. The crucial part of the design of our thermosetting material is the thermal breakdown of only the linkages, leaving the main chains intact allowing the transition from thermosetting to thermoplastic facilitating the recycling. In the work presented here, we describe the synthesis of the first examples of thermosetting ROMP materials based on poly(norbornene dicarboximide) networks containing acetal ester linkages and report their thermal degradation behaviour. The combination of well-defined ROMP process, thermal degradation and biodegradability potential of acetal ester groups was anticipated to enable us to achieve the overall aims of the programme.

## 2. Experimental

### 2.1. Materials

6-aminocaproic acid (>99%), 1,4-butanediol divinyl ether (98%), 4-methoxyphenol (99%), Amberlyst A21 (free base), Grubbs' catalyst

first generation,  $\text{Cl}_2\text{Ru} = \text{CHPh}(\text{PCy}_3)_2$ , ethyl vinyl ether (99%) and butyl vinyl ether (98%) were purchased from Aldrich and used as received. Toluene, chloroform and dichloromethane were acquired from the departmental solvent purification system.

### 2.2. Measurements

All reactions were carried out under an atmosphere of nitrogen, or in a M-Braun 150B-G glove box. NMR spectra were either recorded on a Bruker Avance 400 spectrometer at 400.0 MHz ( $^1\text{H}$ ) and 100.6 MHz ( $^{13}\text{C}$ ); or a Varian Inova 500 spectrometer at 499.8 MHz ( $^1\text{H}$ , COSY, HSQC) and 125.7 MHz ( $^{13}\text{C}$ ); all chemical shifts were referenced to the residual proton impurity of the deuterated solvent,  $\text{CDCl}_3$  unless otherwise stated. Melting points were determined on Electrothermal 1A 9100 apparatus. Infrared spectra were recorded using a Perkin Elmer RX1 FT-IR machine. Elemental Analyses were carried out on an Exeter Analytical E-440 elemental analyser. Mass Spectra analyses were carried out on a micromass LCT using positive and negative ionisation electrospray modes as specified.

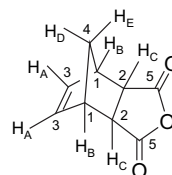
Thermogravimetric analysis-mass spectrometry (TGA-MS) measurements were performed using a Perkin Elmer Pyris 1 TGA in conjunction with a Hiden HPR20. For TGA-MS experiments 3.0–15.0 mg of sample was heated under Helium atmosphere (CP grade, 99.6% pure) from 25 to 400 °C at a heating rate of  $10^\circ\text{C min}^{-1}$ . Mass spectra were taken sequentially at intervals of 50 °C.

The gel fraction contents of crosslinked polymers **6–9** were determined by sol-gel extraction in boiling chloroform or dichloromethane, followed by thorough drying in a vacuum oven for one day at 50 °C. The gel fraction content (percent) was determined as a ratio of the final weight after extraction and drying,  $W_{\text{final}}$ , divided by the initial weight before extraction,  $W_{\text{initial}}$ :

$$\text{Gel content (\%)} = \frac{W_{\text{final}}}{W_{\text{initial}}} \times 100$$

### 2.3. Synthesis of *exo*-norbornene dicarboxylic anhydride (**1**)

A mixture of *endo*/*exo*-isomers of norbornene dicarboxylic anhydride was prepared according to the literature [30]. The mixture of *endo*/*exo*-norbornene dicarboxylic anhydride, containing 80% *exo*-isomer (27.33 g, 167 mmol) was placed in a round bottom flask (250 mL) fitted with a reflux condenser. Acetone (40 mL) was added and the mixture was refluxed until the solid was completely dissolved. The mixture was then left to recrystallise. The crystals were filtered and dried in a vacuum oven at room temperature. The final product **1** was obtained as white crystals in a 68% yield (18.71 g, 114 mmol).

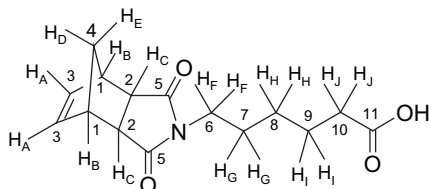


Mp 142–143 °C; IR (neat)  $\nu/\text{cm}^{-1}$ : 2886 (C–H), 1698 (C=O); NMR:  $\delta_{\text{H}}$  (400 MHz;  $\text{CDCl}_3$ ): 6.27 (2H, t,  $J_{\text{HAHB}} = 1.46$ ,  $\text{H}_A$ ), 3.39 (2H, m,  $\text{H}_B$ ), 2.93 (2H, d,  $J_{\text{HBHC}} = 0.89$ ,  $\text{H}_C$ ), 1.61 (1H, d,  $J_{\text{HDHE}} = 9.16$ ,  $\text{H}_D$ ), 1.40 (1H, d,  $J_{\text{HDHE}} = 9.16$ ,  $\text{H}_E$ );  $\delta_{\text{C}}$  (100 MHz;  $\text{CDCl}_3$ ): 171.52 ( $\text{C}^5$ ), 137.96 ( $\text{C}^3$ ), 48.77 ( $\text{C}^4$ ), 46.88 ( $\text{C}^2$ ), 44.11 ( $\text{C}^1$ ).

### 2.4. Synthesis of *N*-caproic acid-*exo*-norbornene dicarboximides (**2**)

*Exo*-norbornene dicarboxylic anhydride **1** (15.51 g, 94 mmol) and 6-aminocaproic acid (13.63 g, 103 mmol) were placed in a dry

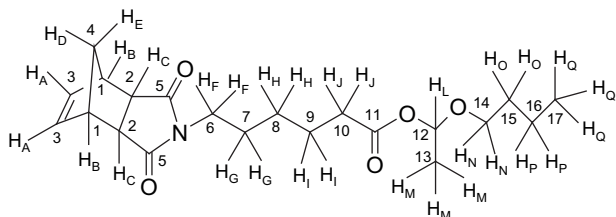
two necked round bottom flask (250 mL), fitted with a reflux condenser and kept under nitrogen. Toluene (dry, 65 mL) was added and the mixture was kept at 115 °C for 17 h. The reaction mixture was cooled to ambient temperature and toluene was removed under reduced pressure. The crude product was re-crystallised twice from ethyl acetate. The crystals were dried in a vacuum oven at ambient temperature. The product **2** was obtained as a white powder; 95% yield (25 g, 90 mmol).



Mp: 62–63 °C. IR (neat)  $\nu/\text{cm}^{-1}$ : 2886 (C–H), 1698 (C=O). Found: C, 64.93; H, 6.93; N, 5.03; O, 23.12%.  $\text{C}_{15}\text{H}_{19}\text{NO}_4$  requires C, 64.97; H, 6.91; N, 5.05; O, 23.08%. NMR:  $\delta_{\text{H}}$  (500 MHz;  $\text{CDCl}_3$ ): 10.46 (1H, broad, –OH), 6.22 (2H, t,  $J_{\text{HAHB}} = 1.46$ ,  $\text{H}_A$ ), 3.42 (2H, t,  $J_{\text{HFHG}} = 7.32$ ,  $\text{H}_F$ ), 3.20 (2H, m,  $\text{H}_B$ ), 2.64 (2H, d,  $J_{\text{HBHC}} = 1.00$ ,  $\text{H}_C$ ), 2.32 (2H, t,  $J_{\text{HJHI}} = 7.32$ ,  $\text{H}_J$ ), 1.61 (2H, m,  $\text{H}_I$ ), 1.57 (2H, m,  $\text{H}_G$ ), 1.48 (1H, d,  $J_{\text{HDHE}} = 9.76$ ,  $\text{H}_D$ ), 1.32 (2H, m,  $\text{H}_H$ ), 1.19 (1H, d,  $J_{\text{HDHE}} = 9.76$ ,  $\text{H}_E$ );  $\delta_{\text{C}}$  (126 MHz;  $\text{CDCl}_3$ ): 179.47 ( $\text{C}^{11}$ ), 178.40 ( $\text{C}^5$ ), 138.01 ( $\text{C}^3$ ), 48.00 ( $\text{C}^2$ ), 45.34 ( $\text{C}^1$ ), 42.92 ( $\text{C}^4$ ), 38.64 ( $\text{C}^6$ ), 34.03 ( $\text{C}^{10}$ ), 27.61 ( $\text{C}^7$ ), 26.55 ( $\text{C}^8$ ), 24.37 ( $\text{C}^9$ ); MS  $m/z$  (ES<sup>+</sup>): found: 300.3 [ $\text{M} + \text{Na}$ ]<sup>+</sup>, 100%. MS  $m/z$  (ES<sup>–</sup>): found: 276.3 [ $\text{M} - \text{H}$ ]<sup>–</sup>, 100%.

### 2.5. Synthesis of mono-functional norbornene dicarboximide monomer (**4**)

In a similar procedure to that in the literature [32], butyl vinyl ether **3a** (2.00 g, 20 mmol) and 4-methoxyphenol (0.016 g, 0.13 mmol) were added to a dry two necked round bottom flask (250 mL), fitted with a dry ice reflux condenser and kept under nitrogen. The mixture was heated to 75 °C and compound **2** (3.05 g, 11 mmol) was added in several portions over a period of 1 h. The mixture was stirred for an additional 10 h at 75 °C and was then allowed to reach the ambient temperature. Amberlyst A21 ion exchange resin (4.76 g) and toluene (dry, 20 mL) were added and the mixture was stirred for a further hr. The Amberlyst A21 was removed by filtration, and toluene was removed under reduced pressure. The product was dried under reduced pressure at ambient temperature. The product **4** was obtained as a viscous orange–brown liquid in a 50% yield (2.09 g, 5.5 mmol).

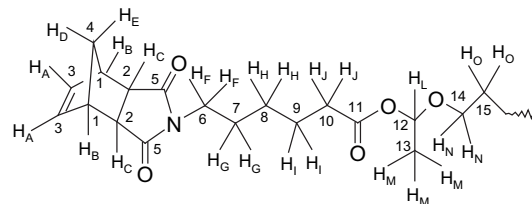


IR (neat)  $\nu/\text{cm}^{-1}$ : 2937 (C–H), 1694 (C=O), 1136 (acetal C–O). Found: C, 66.97; H, 8.34; N, 3.80; O, 20.89%.  $\text{C}_{21}\text{H}_{31}\text{NO}_5$  requires C, 66.82; H, 8.28; N, 3.71; O, 21.19%. NMR:  $\delta_{\text{H}}$  (500 MHz;  $\text{CDCl}_3$ ): 6.22 (2H, t,  $J_{\text{HAHB}} = 1.71$ ,  $\text{H}_A$ ), 5.87 (1H, q,  $J_{\text{HLHM}} = 5.25$ ,  $\text{H}_L$ ), 3.62–3.48 (2H, m,  $\text{H}_N$ ), 3.42 (2H, m,  $\text{H}_F$ ), 3.21 (2H, m,  $\text{H}_B$ ), 2.65 (2H, d,  $J_{\text{HBHC}} = 1.01$ ,  $\text{H}_C$ ), 2.32 (2H, t,  $J_{\text{HJHI}} = 7.69$ ,  $\text{H}_J$ ), 1.61 (2H, m,  $\text{H}_I$ ), 1.60 (2H, m,  $\text{H}_O$ ), 1.57 (2H, m,  $\text{H}_G$ ), 1.48 (1H, d,  $J_{\text{HDHE}} = 9.88$ ,  $\text{H}_D$ ), 1.36 (3H, d,  $J_{\text{HLHM}} = 5.25$ ,  $\text{H}_M$ ), 1.33 (2H, m,  $\text{H}_P$ ), 1.32 (2H, m,  $\text{H}_H$ ), 1.19 (1H, d,  $J_{\text{HDHE}} = 9.88$ ,  $\text{H}_E$ ), 0.89 (3H, t,  $J_{\text{HPHQ}} = 7.32$ ,  $\text{H}_Q$ );  $\delta_{\text{C}}$  (126 MHz;  $\text{CDCl}_3$ ):

178.23 ( $\text{C}^5$ ), 173.35 ( $\text{C}^{11}$ ), 138.02 ( $\text{C}^3$ ), 96.51 ( $\text{C}^{12}$ ), 69.19 ( $\text{C}^{14}$ ), 48.00 ( $\text{C}^2$ ), 45.36 ( $\text{C}^1$ ), 42.95 ( $\text{C}^4$ ), 38.66 ( $\text{C}^6$ ), 34.50 ( $\text{C}^{10}$ ), 31.77 ( $\text{C}^{15}$ ), 27.66 ( $\text{C}^7$ ), 26.65 ( $\text{C}^8$ ), 24.57 ( $\text{C}^9$ ), 21.02 ( $\text{C}^{13}$ ), 19.38 ( $\text{C}^{16}$ ), 14.04 ( $\text{C}^{17}$ ).

### 2.6. Synthesis of di-functional norbornene dicarboximide monomer (**5**)

In a similar procedure to that for the synthesis of the mono-functional monomer **4**, 1,4-butanediol divinyl ether **3b** (0.71 g, 5 mmol), and 4-methoxyphenol (0.016 g, 0.13 mmol) (inhibitor) were added to a dry two necked round bottom flask (250 mL), fitted with a reflux condenser and kept under nitrogen. The reaction mixture was heated to 90 °C and compound **2** (3.05 g, 11 mmol) was added in several portions over a period of 1 h, upon which the colourless mixture turned orange. The mixture was left to stir for further 10 h at 90 °C and was then allowed to reach ambient temperature. Amberlyst A21 ion exchange resin (4.76 g) and toluene (dry, 19 mL) were added and the mixture was stirred for an additional 2 h. The Amberlyst A21 was removed by filtration, and toluene was removed under reduced pressure. The product was then dried under reduced pressure at ambient temperature. The product **5** was obtained as a highly viscous orange–brown liquid in a 50% yield (1.741 g, 2.50 mmol).



IR (neat)  $\nu/\text{cm}^{-1}$ : 2942 (C–H), 1693 (C=O), 1133 (acetal C–O). Found: C, 65.26; H, 7.56; N, 3.96; O, 23.22%.  $\text{C}_{38}\text{H}_{52}\text{O}_{10}\text{N}_2$  requires C, 65.50; H, 7.52; N, 4.02; O, 22.96%. NMR:  $\delta_{\text{H}}$  (500 MHz;  $\text{CDCl}_3$ ): 6.22 (4H, t,  $J_{\text{HAHB}} = 1.59$ ,  $\text{H}_A$ ), 5.87 (2H, q,  $J_{\text{HLHM}} = 5.24$ ,  $\text{H}_L$ ), 3.62–3.48 (4H, m,  $\text{H}_N$ ), 3.42 (4H, t,  $J_{\text{HFHG}} = 7.44$ ,  $\text{H}_F$ ), 3.21 (4H, m,  $\text{H}_B$ ), 2.64 (4H, d,  $J_{\text{HBHC}} = 0.98$ ,  $\text{H}_C$ ), 2.32 (4H, t,  $J_{\text{HJHI}} = 7.32$ ,  $\text{H}_J$ ), 1.61 (4H, m,  $\text{H}_I$ ), 1.60 (4H, m,  $\text{H}_O$ ), 1.57 (4H, m,  $\text{H}_G$ ), 1.48 (2H, d,  $J_{\text{HDHE}} = 9.76$ ,  $\text{H}_D$ ), 1.36 (6H, d,  $J_{\text{HLHM}} = 5.24$ ,  $\text{H}_M$ ), 1.32 (4H, m,  $\text{H}_H$ ), 1.19 (2H, d,  $J_{\text{HDHE}} = 9.76$ ,  $\text{H}_E$ );  $\delta_{\text{C}}$  (126 MHz;  $\text{CDCl}_3$ ): 178.25 ( $\text{C}^5$ ), 173.33 ( $\text{C}^{11}$ ), 138.03 ( $\text{C}^3$ ), 96.44 ( $\text{C}^{12}$ ), 68.99 ( $\text{C}^{14}$ ), 48.00 ( $\text{C}^2$ ), 45.36 ( $\text{C}^1$ ), 42.95 ( $\text{C}^4$ ), 38.65 ( $\text{C}^6$ ), 34.46 ( $\text{C}^{10}$ ), 27.66 ( $\text{C}^7$ ), 26.65 ( $\text{C}^8$ ), 26.37 ( $\text{C}^{15}$ ), 24.55 ( $\text{C}^9$ ), 21.02 ( $\text{C}^{13}$ ).

### 2.7. Preparation of crosslinked material (**6**)

Ruthenium first generation catalyst (0.012 g, 0.014 mmol) was dissolved in dichloromethane (1.5 mL) in a sample vial containing a stirrer bar. Di-functional monomer **5** (0.546 g, 0.783 mmol) was dissolved in another sample vial in dichloromethane (1.5 mL). The monomer solution was added to the vial containing the initiator. An insoluble polymer was formed soon after the addition of initiator to monomer. The crosslinked product was filtered and dried in a vacuum oven at 50 °C for 18 h. A known amount of the product was subjected to a sol-gel extraction to remove any soluble fractions. TGA-MS analysis was performed on the dried material.

Monomer:Initiator ratio = 57:1; Gel Content: 89% ( $W_{\text{initial}}$ , 0.172 g;  $W_{\text{final}}$ , 0.153 g); IR before TGA (neat),  $\nu/\text{cm}^{-1}$ : 2937 (C–H), 1693 (C=O), 1133 (acetal C–O); IR after TGA (neat),  $\nu/\text{cm}^{-1}$ : 2937 (C–H), 1683 (C=O), 1146 (acetal C–O).

### 2.8. Preparation of crosslinked material (**9–7**)

**7**: Di-functional monomer **5** (0.274 g, 0.39 mmol) and mono-functional monomer **4** (0.049 g, 0.13 mmol) were dissolved in dichloromethane (4 mL) in a sample vial to obtain a molar ratio of



di-functional:mono-functional of 75:25. Ruthenium first generation initiator (0.008 g, 0.01 mmol) was dissolved in dichloromethane (1.5 mL) in another sample vial containing a small stirrer bar. The monomer solution mixture was added to the initiator and stirred for 2 h. The insoluble product was filtered and dried in a vacuum oven at 50 °C for 18 h. A known amount of the product was subjected to a sol-gel extraction to remove any soluble fractions. TGA-MS analysis was performed on the dried material.

Monomer:Initiator ratio = 57:1; Gel Content: 82% ( $W_{\text{initial}}$ , 0.222 g;  $W_{\text{final}}$ , 0.181 g); IR before TGA (neat),  $\nu/\text{cm}^{-1}$ : 2929 (C–H), 1692 (C=O), 1135 (acetal C–O); IR after TGA (neat),  $\nu/\text{cm}^{-1}$ : 2934 (C–H), 1695 (C=O), 1146.5 (acetal C–O).

**8:** Similar procedure using Di-functional monomer **5** (0.183 g, 0.26 mmol) and mono-functional monomer **4** (0.098 g, 0.26 mmol) to obtain a molar ratio of di-functional:mono-functional of 50:50.

Monomer:Initiator ratio = 57:1; Gel Content: 79% ( $W_{\text{initial}}$ , 0.202 g;  $W_{\text{final}}$ , 0.162 g); IR before TGA (neat),  $\nu/\text{cm}^{-1}$ : 2919 (C–H), 1692 (C=O), 1133 (acetal C–O); IR after TGA (neat),  $\nu/\text{cm}^{-1}$ : 2924 (C–H), 1694 (C=O), 1146 (acetal C–O).

**9:** Similar procedure using Di-functional monomer **5** (0.091 g, 0.13 mmol) and mono-functional monomer **4** (0.147 g, 0.39 mmol) to obtain a molar ratio of di-functional:mono-functional of 25:75.

Monomer:Initiator ratio = 57:1; Gel Content: 89% ( $W_{\text{initial}}$ , 0.144 g;  $W_{\text{final}}$ , 0.128 g); IR before TGA (neat),  $\nu/\text{cm}^{-1}$ : 2939 (C–H), 1691 (C=O), 1135 (acetal C–O); IR after TGA (neat),  $\nu/\text{cm}^{-1}$ : 2927 (C–H), 1693 (C=O), 1147 (acetal C–O).

### 3. Results and discussion

#### 3.1. Synthesis of monomers

Mono- and di-functional norbornene dicarboximide monomers **4** and **5**, containing acetal ester groups were synthesised following the reaction pathway shown in Scheme 1.

The reaction between *exo*-norbornene dicarboxylic anhydride **1** and 6-aminocaproic acid in refluxing toluene gave *N*-caproic acid-*exo*-norbornene dicarboximide **2** with 95% yield. The structures of intermediates **1** and **2** were confirmed by NMR Spectroscopy. The integration, in  $^1\text{H}$  NMR spectrum of **2**, of the  $\text{CH}_2$  next to Nitrogen ( $\text{N}-\text{CH}_2-$ ) at 3.42 ppm and that for the vinylic protons of norbornene at 6.22 ppm showed a ratio of 1:1 indicating the

attachment of one caproic acid chain per each norbornene moiety. The structure of **2** was further confirmed by mass spectroscopy and elemental analysis.

The reaction of **2** with butyl vinyl ether **3a** and 1,4-butanediol divinyl ether **3b** gave the mono-functional monomer **4** and the di-functional monomer **5**, respectively, both containing the acetal ester group. The structures of monomers **4** and **5** were confirmed by NMR spectroscopy. The clear indication for the formation of the acetal ester groups in monomers **4** and **5** is the appearance of the resonance due to the methyl of the acetal ester group at 1.36 ppm and 21.02 ppm in  $^1\text{H}$  and  $^{13}\text{C}$  NMR spectra, respectively. The integration, in  $^1\text{H}$  NMR spectrum of monomer **4**, of the single proton of the acetal group ( $\text{O}-\text{CH}(\text{CH}_3)-\text{O}$ ) at 5.87 ppm and that for the vinylic protons of norbornene at 6.22 ppm showed a ratio of 1:2, indicating the attachment of one acetal ester chain per each norbornene moiety. For the monomer **5**, the integration of the single protons in two acetal groups ( $\text{O}-\text{CH}(\text{CH}_3)-\text{O}$ ) at 5.87 ppm and that for the vinylic protons of two norbornene at 6.22 ppm showed a ratio of 2:4, indicating the attachment of one chain containing two acetal groups per two norbornene moieties. Furthermore, FT-IR spectra of monomers **4** and **5** clearly showed the presence of acetal C–O bonds at  $1135\text{ cm}^{-1}$ . Elemental analysis also confirmed the formation of monomers **4** and **5**.

#### 3.2. Synthesis of crosslinked materials

The di-functional monomer **5** was subjected to ROMP using Grubbs ruthenium first generation initiator to produce the cross-linked material **6**. Mixtures of di-functional **5** and mono-functional **4** monomers were also subjected to ROMP using Grubbs ruthenium first generation initiator to produce thermosetting materials with different degrees of crosslinking. Three materials were prepared using molar ratios of di-functional:mono-functional monomer of 75:25; 50:50, and 25:75, labelled **7**, **8** and **9**, respectively. Scheme 2 shows idealised structures for materials **6–9**, but the network may also contain some di-functional units which are incorporated through only one norbornene moiety [30].

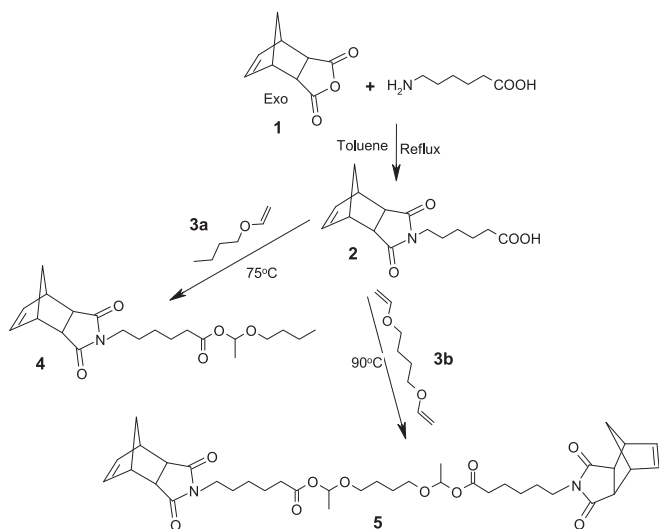
FT-IR spectra clearly showed the presence of an acetal C–O band at  $1135\text{ cm}^{-1}$ . The materials were all insoluble in common solvents. The sol-gel analysis of crosslinked materials **6–9** revealed gel contents of 79–89%, indicating the high efficiency of the ROMP crosslinking process.

#### 3.3. Thermal degradation

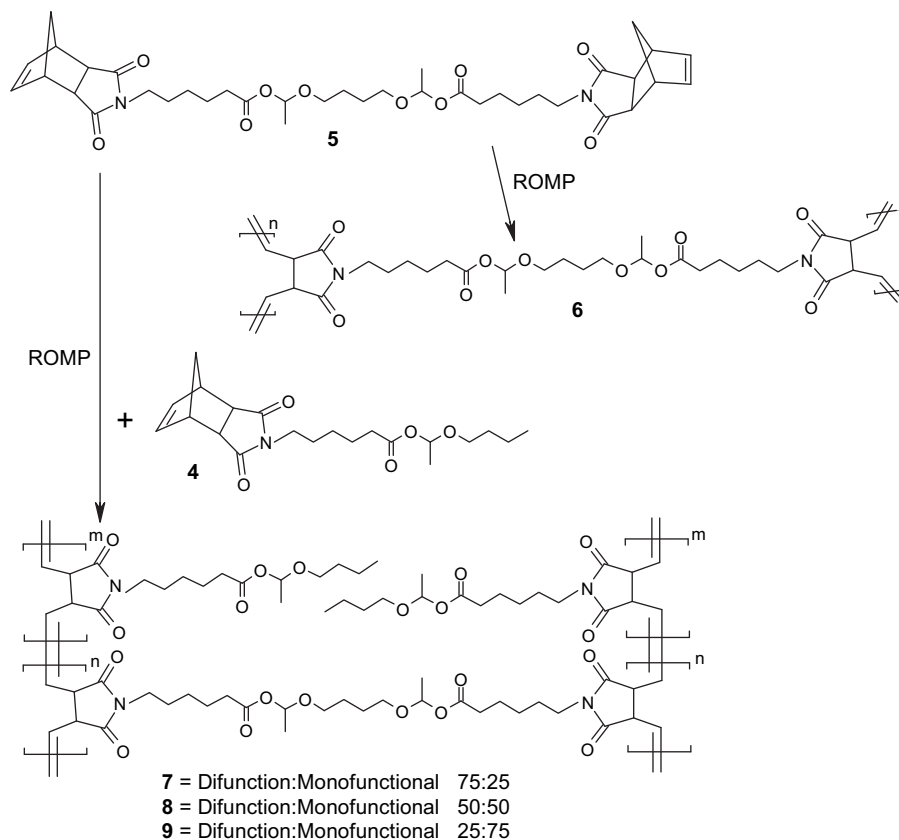
The thermal degradation of the materials **6** studied by TGA showed that the crosslinked material was stable to 150 °C and only a few percent weight loss was observed due to the moisture contaminant or residual solvent in the material, Fig. 1. However, the material showed weight loss of 13%, 36% and 44% at 200 °C, 250 °C and 300 °C, respectively, Table 1.

The thermal degradation of the materials **7–9** was also studied by TGA under the similar conditions to that for material **6**, Fig. 1. The weight loss was found to be 36%, 25%, 21% and 21%, respectively, for materials **6**, **7**, **8** and **9** at 250 °C. This behaviour is consistent with material **6** having the highest di-functional content, highest degree of crosslinking and hence higher weight loss; and material **9** having the lowest di-functional content, least degree of crosslinking and hence lower weight loss.

Materials **6–9** were also subjected to TGA-MS analysis to determine the fragments resulted from thermal decomposition of the materials by taking sequential mass spectrometric traces at 50 °C intervals. The fragments obtained from TGA-MS analysis are also presented in Table 1.



**Scheme 1.** Reaction pathway for the synthesis of mono- and di-functional norbornene dicarboximide monomers **4** and **5** containing acetal ester linkage.



**Scheme 2.** Synthesis of thermosetting materials **6–9** via ROMP using Grubbs first generation ruthenium initiator in chloroform at ambient temperature.

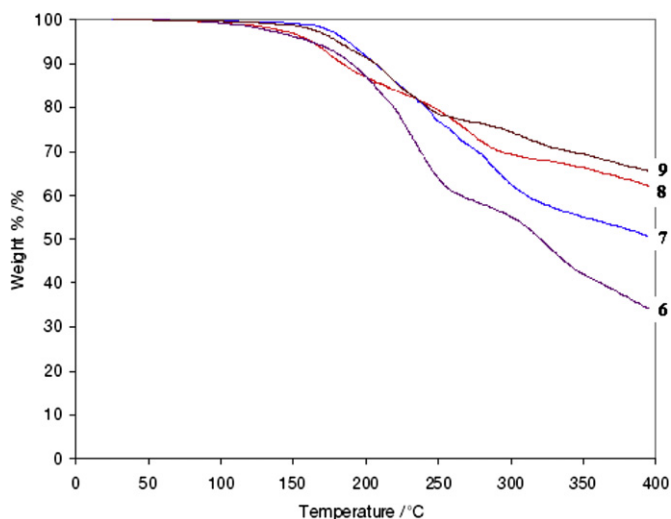


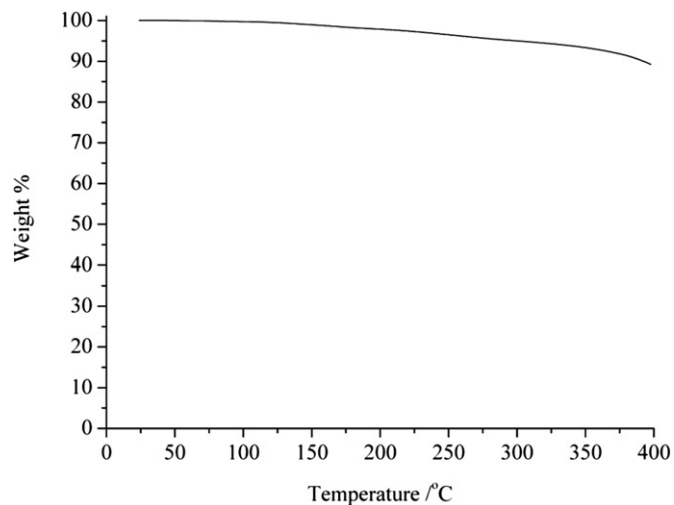
**Fig. 1.** TGA thermographs observed during the thermal degradation of materials **6–9**.

**Table 1**  
TGA and TGA-MS results for thermosetting materials **6–9**.

Temp. (°C)	Weight loss %				Fragments observed
	<b>6</b>	<b>7</b>	<b>8</b>	<b>9</b>	<i>m/z</i> ratio
100	0.5	0.5	1	1	44
150	3	1	3	1	44
200	13	9	14	9	44, 54, 72, 100
250	36	25	21	21	44, 54, 72, 100
300	44	37	30	26	44, 54, 72, 100
350	58	45	33	30	44

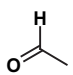
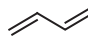
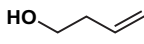
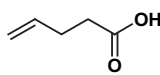
Thermal degradation studies on crosslinked materials from ROMP of mono-functional, *exo*-*N*-alkyl dicarboximide norbornenes, and di-functional bis(*exo*-*N*-alkylenedicarboximide norbornenes) reported earlier [30], showed that the resulting crosslinked material without acetal ester linkages is very stable to 400 °C, Fig. 2.

Therefore, the fragments observed during TGA-MS analysis must be the result of the thermal decomposition of the acetal ester linkage which is supported by considerable reductions in the intensity of C–O bands at 1135 cm<sup>-1</sup> in the FT-IR spectra observed for the retrieved materials.



**Fig. 2.** TGA thermographs observed during the thermal degradation of crosslinked materials without acetal ester linkages.

**Table 2**  
Fragment  $m/z$  ratios and corresponding structures.

Fragments $m/z$ ratio	Proposed corresponding structures
44	 Acetaldehyde
54	 Butadiene
72	 Butenyl alcohol
100	 Pentenoic acid

The most abundant fragments detected for the degradation of the material **6–9** were between 200 °C and 250 °C, possessed  $m/z$  ratios of 44, 54, 72 and 100 mass units, Table 1. These fragments and their proposed structures are shown in Table 2. The fragments with  $m/z$  ratios of 44, 54, 72, and 100 units, are believed to be corresponding to acetaldehyde, butadiene, butenyl alcohol and pentenoic acid, respectively.

The mechanisms by which these fragments are produced via thermal breakdown of the acetal ester linkages appear to be very complex. However, one plausible mechanism for the formation of these fragments is shown in Fig. 3. The FT-IR showed a considerable C–O shift when materials were heated, so it would be reasonable to suggest that one step involves the cleavage of the acetal C–O resulting in the formation of acetaldehyde **10** ( $m/z = 44$ ) along with compounds with terminal vinyl **11** and acid **12** groups. Further decomposition of the remaining acetal ester linkages is believed to

give butenyl vinyl ether **13** ( $m/z = 98$ ) and more **12**. The decomposition of **12** leads to the formation of pentenoic acid **14** ( $m/z = 100$ ). Butenol **15** ( $m/z = 72$ ) is formed from thermal degradation of **13**. The thermal dehydration of **15** then results in the formation of butadiene **16** ( $m/z = 54$ ).

The complete decomposition of all acetal ester linkages in thermosetting materials **6–9** was anticipated to result in the formation of soluble linear thermoplastic materials. However, the materials remained insoluble in common solvents after thermal treatment. It is not possible to determine accurately whether or not all the C–O bonds in the acetal ester in the crosslinking units have been broken upon heat treatment as the side chains also contain acetal ester groups. Considerable reductions in the intensity of C–O bands at  $1135\text{ cm}^{-1}$  in the FT-IR spectra is observed for the retrieved materials which is estimated to be about 70%. This extent of reduction in intensity is comparable to that reported for thermal degradation of maleimide resins containing acetal ester linkages [32]. The possibility of secondary crosslinking due to the thermal reactions between the double bonds of polynorbornene is ruled out since this secondary reaction has not been observed for polynorbornene-based thermosetting materials without acetal ester linkages. The possibility of thermal oxidation and hence crosslinking is also ruled out as the TGA experiments have been carried out under Helium atmosphere (CP grade, 99.6% pure). Our previous work on crosslinking behaviour of the thermosetting materials obtained from ROMP of mono- and di-functional norbornene dicarboximide monomers without acetal ester linkages revealed the chemical crosslinking as well as crosslinking due to physical entanglement [30]. Therefore, one plausible reason for the insolubility of materials **6–9** could be the presence of crosslinking due to the physical chain entanglement.

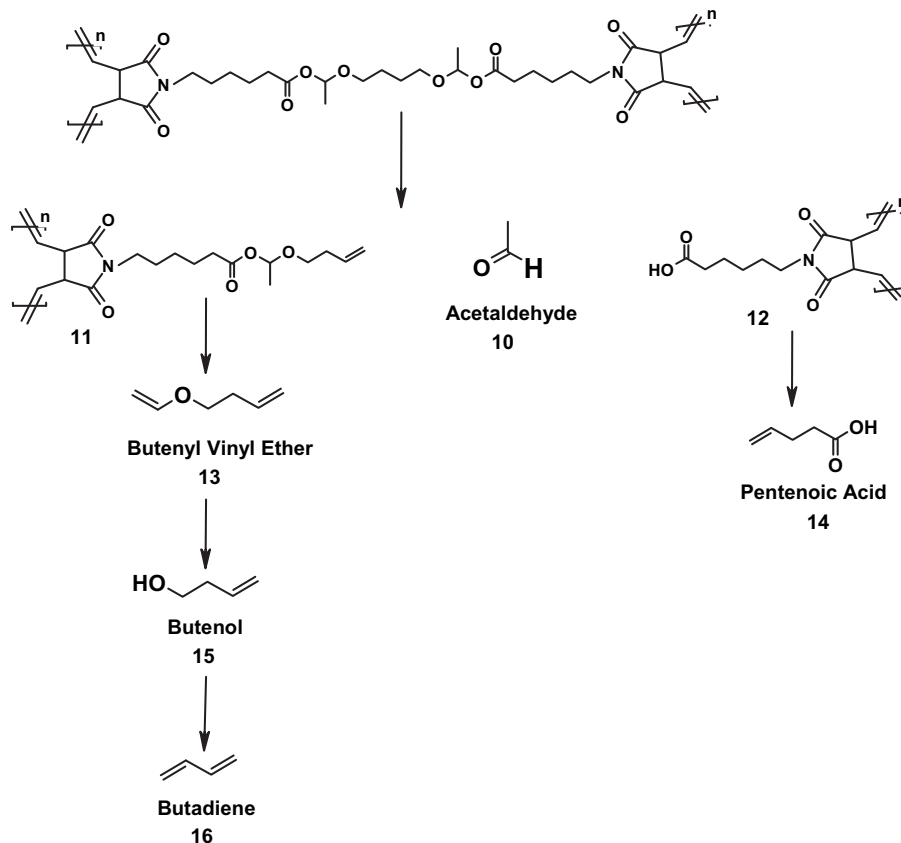


**Fig. 3.** A proposed mechanism for the thermal degradation of the acetal ester linkages in ROMP thermosetting materials.

Interestingly, the thermosetting ROMP materials containing acetal ester linkage reported here begin to breakdown around 200 °C, which is in the same region as the lead-free solder reflow temperature (217 °C). The crosslinked materials became very brittle after the heat treatment indicative of reduction in crosslinking density. This behaviour is extremely advantageous in the electronic industry, as it would allow easy chip removal and replacement, if these materials are used as adhesives.

#### 4. Conclusions

The mono- and di-functional norbornene dicarboximide monomer **4** and **5**, containing acetal ester groups were synthesised and fully characterised.

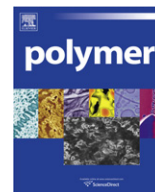
The ROMP of di-functional monomer **5** using Grubbs' ruthenium first generation initiator at ambient temperature produced cross-linked material **6**. Using the same condition, crosslinked materials **7**, **8** and **9** with various crosslink density were also prepared by the ROMP of mixtures of mono-functional monomer **4** with 75%, 50%, 25% molar ratios of di-functional monomer **5**, respectively. The FT-IR spectra clearly showed the presence of an acetal C–O band at 1135 cm<sup>-1</sup>.

The TGA study of the crosslinked materials **6–9** showed that they are stable to 150 °C, but exhibit rapid weight loss at 200 °C. The weight loss was found to be 36%, 25%, 21% and 21%, respectively, for materials **6**, **7**, **8** and **9** at 250 °C. This behaviour is consistent with material **6** having the highest di-functional content, highest degree of crosslinking and hence higher weight loss; and material **9** having the lowest di-functional content, least degree of crosslinking and hence lower weight loss.

The fragments obtained from TGA-MS analysis of materials **6–9** revealed that the most abundant fragments detected between 200 °C and 250 °C were acetaldehyde, butadiene, butenyl alcohol and pentenoic acid. These fragments are the result of the thermal decomposition of the acetal ester linkage which is supported by considerable reductions in the intensity of C–O bands at 1135 cm<sup>-1</sup> in FT-IR spectra observed for the retrieved materials.

#### References

- [1] Elias H-G. An introduction to polymer science. Weinheim, Germany: VCH; 1997.
- [2] Stepto RFT. Polymer networks. London: Blackie Academic & Professional; 1998.
- [3] Gosh SK. Functional coatings. Weinheim, Germany: Wiley-VCH; 2006.
- [4] Borchardt JK. Mater Today 2006;7:25.
- [5] Buchwalter SL, Kosbar LL. J Polym Sci A Polym Chem 1996;34:249.
- [6] Engelberg PI, Tesoro GC. Polym Eng Sci 1990;30:303–7.
- [7] Sastri VR, Tesoro GC. J Appl Polym Sci 1990;39:1439–57.
- [8] Tesoro GC, Sastri VR. J Appl Polym Sci 1990;39:1425–37.
- [9] Jain R, Standley SM, Fréchet JM. Macromolecules 2007;40:452.
- [10] Heffernan MJ, Murthy NJ. Bioconjugate Chem; 2005:1340.
- [11] Ramis X, Salla JM, Mas C, Mantecon A, Serra A. J Appl Polym Sci 2004;92:381.
- [12] Gimenez R, Fernandez-Francos X, Salla JM, Serra A, Mantecon A, Ramis X. Polymer 2005;46:10637.
- [13] Mas C, Ramis X, Salla JM, Mantecon A, Serra A. J Polym Sci A Polym Chem 2006;44:1711.
- [14] Yang S, Chem JS, Korner H, Breiner T, Ober CK, Poliks MD. Chem Mater 1998;10:1475–82.
- [15] Chen J-S, Ober CK, Poliks MD. Polymer 2002;43:131–9.
- [16] Li H, Wang L, Jacob K, Wong CP. J Polym Sci A Polym Chem 2002;40:1796.
- [17] Wang LJ, Li HY, Wong CP. J Polym Sci A Polym Chem 2000;38:3771–82.
- [18] Wang LJ, Wong CP. J Polym Sci A Polym Chem 1999;37:2991–3001.
- [19] Jansen JC. Side-chain liquid crystalline polycarbonates. Stevinweg, The Netherlands: Delft University Press; 1996. p. 9.
- [20] Schwab P, Grubbs RH, Ziller JW. J Am Chem Soc 1996;118:100–10.
- [21] Bielawski CW, Grubbs RH. Angew Chem 2000;112:3025–8.
- [22] Love JA, Morgan JP, Trnka TM, Grubbs RH. Angew Chem Int Ed 2002;41:4035–7.
- [23] Khosravi E. In: Grubbs RH, editor. "Block copolymers," A chapter in handbook of metathesis, vol. 3. VCH-Wiley; 2003. p. 72.
- [24] Grubbs RH. Handbook of metathesis. Weinheim, Germany: Wiley-VCH; 2003.
- [25] Hutchings LR, Khosravi E, Castle TC. Macromolecules 2004;37:2035–40.
- [26] Grubbs RH, Khosravi E. In: Schluter AD, editor. Synthesis of polymers – a volume of materials science and technology series. Wiley-VCH; 1998. p. 63–104.
- [27] Castle TC, Khosravi E, Hutchings LR. Macromolecules 2006;39:5639.
- [28] Czelusniak I, Khosravi E, Kenwright AM, Ansell CWG. Macromolecules 2007;40:444.
- [29] Khosravi E, Al-Hajaji AA. Eur Polym J 1988;34:153.
- [30] Hine PJ, Leejarkpai T, Khosravi E, Duckett RA, Feast WJ. Polymer 2001;42:9413.
- [31] Layman PL. Chem Eng News 1993;71:11.
- [32] Zhang X, Chen G-C, Collins A, Jacobson S, Morganelli P, Dar YL, et al. J Polym Sci 2008;47:1073–84.



## Synthesis and thermoresponsive properties of four arm, amphiphilic poly(*tert*-butyl-glycidylether)-block-polyglycidol stars

Marcin Libera<sup>a</sup>, Barbara Trzebicka<sup>a</sup>, Agnieszka Kowalczyk<sup>a</sup>, Wojciech Wałach<sup>a</sup>, Andrzej Dworak<sup>a,b,\*</sup>

<sup>a</sup>Centre of Polymer and Carbon Materials, Polish Academy of Sciences, M. Curie-Skłodowskiej 34, 41-819 Zabrze, Poland

<sup>b</sup>University of Opole, Institute of Chemistry, Oleska 48, 45-052 Opole, Poland

### ARTICLE INFO

#### Article history:

Received 16 August 2010

Received in revised form

26 October 2010

Accepted 2 December 2010

Available online 9 December 2010

#### Keywords:

Amphiphilic block stars

Thermosensitivity

Aggregation

### ABSTRACT

A series of four arm stars with copolymer arms composed of poly(*tert*-butyl-glycidylether)-*b*-polyglycidol were prepared using a multi-step process based on anionic ring-opening polymerization. Control of the length of the arms and the number of functional (hydroxyl) reactive groups was achieved by anionic polymerization. Stars with molar masses up to 12200 g/mol were prepared. The amphiphilic character of the star structure was varied using different polyglycidol block lengths. The star structure and molar mass of the obtained stars were characterized by SEC–MALLS and NMR spectroscopy.

The temperature behavior of an aqueous solution of the obtained polymers was also investigated. The phase transition temperature was strongly dependent on the hydrophilic–hydrophobic balance of the star structure and varied in the range of 25–59 °C. As shown by DLS and SEM, the stars formed temperature-sensitive spherical aggregates in aqueous solution. The aggregates may be used for controlled transport and release of active compounds.

© 2010 Elsevier Ltd. All rights reserved.

### 1. Introduction

Polymers with nonlinear topology have been extensively described in the literature [1–5]. Studies have focused on the synthesis, characterization and application of branched polymers.

Star polymers are macromolecules containing a single branch point from which arms spread out, forming macromolecules with a spherical architecture. The properties of star macromolecules are significantly different than those of linear chains of the same composition and molar mass. The preparation methods and properties of star polymers have been widely reviewed [2,6–10].

The classification of star polymers is frequently related to the structure of their arms. The simplest star structures contain chemically identical chains emanating from a central point. The arms of the stars may consist of the homopolymer chains ( $A_n$  type stars) or block copolymer  $(AB)_n$  type stars. The stars consisting of chemically different arms are called miktoarm or heteroarm stars. Among all types of stars, symmetric and asymmetric stars are also distinguished. The asymmetric ones have arms of different molar mass, functional groups or topology.

There are two main synthetic methods used to obtain star polymers: “core-first” and “arm-first”. The “core-first” method is based upon the polymerization of a monomer, initiated by a polyfunctional core. The length of the star arms increases during polymerization. The “arm-first” method is based upon the synthesis of living macromolecular chains (the prospective arms of the star) and their termination with a multifunctional terminating agent, the core [8].

The number of initiation centers on the branch point of a star has to be higher than 2. The branch point can be composed of a multifunctional low molar mass compound [11–16], a dendrimer [17,18], a hyperbranched polymer [3,19–22], an arborescent structure [23,24] or a microgel [25,26]. When the core is big enough, the stars obtained are called core–shell structures. They exhibit interesting properties, especially when the internal and external parts are chemically different. The hydrophilic–hydrophobic balance between the core and shell may be controlled, when the arms of the star are generated using living polymerization techniques.

The formation of a micellar structure from star polymers in solvents with different selectivity for the blocks of star arms was reported [27–30]. The self-assembly of amphiphilic four arm stars with poly( $\epsilon$ -caprolactone)-block-poly(*N*-(2-hydroxypropyl)methacrylamide) arms in aqueous solution was investigated by Leroux [27]. The critical aggregation concentration and size of particles formed were measured as a function of copolymer composition and solution concentration. The micellization of four arm stars consisting of poly(acrylic acid)-*b*-polystyrene was reported by Monteiro [28].

\* Corresponding author. Centre of Polymer and Carbon Materials, Polish Academy of Sciences, M. Curie-Skłodowskiej 34, 41-819 Zabrze, Poland. Tel.: +48 32 27 16 077; fax: +48 32 23 12 831.

E-mail address: [adworak@cmpw-pan.edu.pl](mailto:adworak@cmpw-pan.edu.pl) (A. Dworak).

The stars aggregated in water, forming core–shell micelles with sizes that increased with the length of the hydrophobic inner block. In DMF, a good solvent for both blocks no aggregation was observed. Micelle formation by other amphiphilic stars with poly(ethylene oxide)-*b*-poly( $\epsilon$ -caprolactone) or poly(ethylene oxide)-*b*-polylactide arms and PEO as an inner block were also presented [29]. Pispas et al. [30] reported the synthesis and micellization properties of eight arm polyisoprene-*b*-polystyrene stars that were prepared by anionic polymerization. The sizes and aggregation numbers of micelles depended on solvent selectivity.

The polymers of glycidol, which are hydrophilic polyethers that contain hydroxyl groups in their structures, have been intensively studied [31–35]. Polyglycidols with linear topology [31] and such of branched structures [32–35] were investigated. The anionic ring-opening polymerization of glycidol, with the use of slow monomer addition, leads to a branched polyether structure. Control of the molar mass and molecular structure of polyglycidol can be achieved by anionic polymerization of glycidol with a protected hydroxyl group [31–34].

Amphiphilic block copolymers, based upon glycidol and other oxiranes with different topologies, are investigated as new water soluble biocompatible materials [20,24,36–39]. The investigation uses highly branched copolymers of polyglycidol as biocompatible unimolecular micelles [20,24,36,37]. Linear copolymers of polyglycidol and other oxiranes that form micelles in water solutions were studied [38,39]. The relationship between the composition of the block copolymers and their association properties were investigated [39]. The modification of hydroxyl groups of polyglycidol to create amphiphilicity in this material was also investigated [38].

The precise synthesis of polyoxiranes with *tert*-butyl-glycidylether as a comonomer was reported recently [40,41]. The authors described the kinetics of the copolymerization of *tert*-butyl-glycidylether and allyl-glycidylether. The obtained copolymers were used to study the reaction condition for selective removal of the *tert*-butyl group [40]. The copolymer of *tert*-butyl-glycidylether and glycidol were used to functionalize hydroxyl groups with alkyl isocyanates [41].

Previous studies [24] of the copolymerization of ethylene oxide with 1-ethoxyethyl-glycidylether, and subsequent removal of 1-ethoxyethyl groups to recover the polyglycidol hydroxyl groups, has opened a route for preparing branched polyoxiranes with controllable molar masses and high hydroxyl group content.

Here we report the synthesis of four arm star block copolymers with well-defined amphiphilic arms of poly(*tert*-butyl-glycidylether)-block-polyglycidol with different polyglycidol block lengths. A multi-step process, based on anionic ring-opening polymerization, was used for synthesis. The sensitivity of the star to temperature changes, accompanied by their aggregation behavior, is also described.

## 2. Experimental section

### 2.1. Materials

*tert*-Butyl-glycidylether (Aldrich) was dried for several days over CaH<sub>2</sub> and distilled before use. 1-Ethoxyethyl glycidylether was synthesized according to Fitton et al. [42], distilled several times under reduced pressure, stored over CaH<sub>2</sub> and distilled before polymerization. A fraction of 99.98% purity was used. Dimethyl sulfoxide (DMSO, POCh) was distilled over calcium hydride, stirred under argon with barium oxide for several days, and then distilled into an ampoule equipped with a Rotaflo glass–teflon valve. Tetrahydrofuran (THF, POCh) was dried over CaH<sub>2</sub>, refluxed over Na/K alloy and distilled prior to use. Pentaerythritol (PENT, Aldrich) was crystallized from water and dried under high vacuum for several days. Potassium *tert*-butoxide (Fluka), formic acid and trichloroacetyl isocyanate (TCAI) were used as received.

**Table 1**  
The molar ratios of monomers and yields of synthesis.

S-[(BGE) <sub>n</sub> -b-(EGE) <sub>m</sub> ] <sub>4</sub>			S-[(BGE) <sub>n</sub> -b-(G) <sub>m</sub> ] <sub>4</sub>		Ratio of blocks in arms <sup>c</sup>	
Monomer used [mol]			Conversion (%) <sup>a</sup>	Yield (%) <sup>b</sup>	Before hydrolysis (BGE)/(EGE)	After hydrolysis (BGE)/(G)
PENT	BGE	EGE				
1.47 × 10 <sup>-3</sup>	0.058	0.041	99.9	88.3	1.38	1.44
1.61 × 10 <sup>-3</sup>	0.064	0.077	99.8	87.6	0.82	0.79
1.79 × 10 <sup>-3</sup>	0.079	0.108	99.9	89.2	0.72	0.69
1.22 × 10 <sup>-3</sup>	0.048	0.083	99.9	90.5	0.59	0.56
1.34 × 10 <sup>-3</sup>	0.053	0.113	99.8	87.7	0.47	0.45

<sup>a</sup> Measured by GC.

<sup>b</sup> Product after hydrolysis.

<sup>c</sup> Estimated after <sup>1</sup>H NMR analysis.

### 2.2. Synthesis of four arm [poly(*tert*-butyl-glycidylether)-block-polyglycidol]<sub>4</sub> stars S-[(BGE)<sub>n</sub>-b-(G)<sub>m</sub>]<sub>4</sub>

#### 2.2.1. Synthesis of potassium pentaerythritolate – initiator

Potassium alcoholate of pentaerythritol was prepared in DMSO. Dry pentaerythritol (1.47 mmol, 0.2 g) was placed in the reactor under argon atmosphere, additionally dried under a high vacuum, dissolved in DMSO (30 mL). All DMSO was removed under reduced pressure to remove adventitious water. The new portion of 30 mL of dry DMSO was added to the reactor along with the solution of potassium *tert*-butoxide (1.18 mmol, 0.13 g) in 20 mL DMSO. Nascent *tert*-butanol and almost all of the DMSO were removed by distillation under reduced pressure and the mixture was dissolved in 30 mL of dry DMSO. To avoid precipitation of the initiator from the solution, only up to 20% of all hydroxyl groups were ionized.

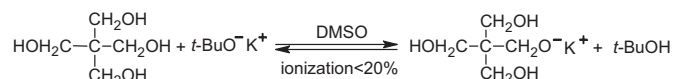
#### 2.2.2. Synthesis of four arm [poly(*tert*-butyl-glycidylether)-block-poly(1-ethoxyethyl-glycidylether)]<sub>4</sub> stars S-[(BGE)<sub>n</sub>-b-(EGE)<sub>m</sub>]<sub>4</sub>

All syntheses of star copolymers were carried out using a high-vacuum technique or dry argon atmosphere in reactors and ampoules equipped with glass–teflon valves. The proper molar ratios of the monomers used for star syntheses are placed in Table 1.

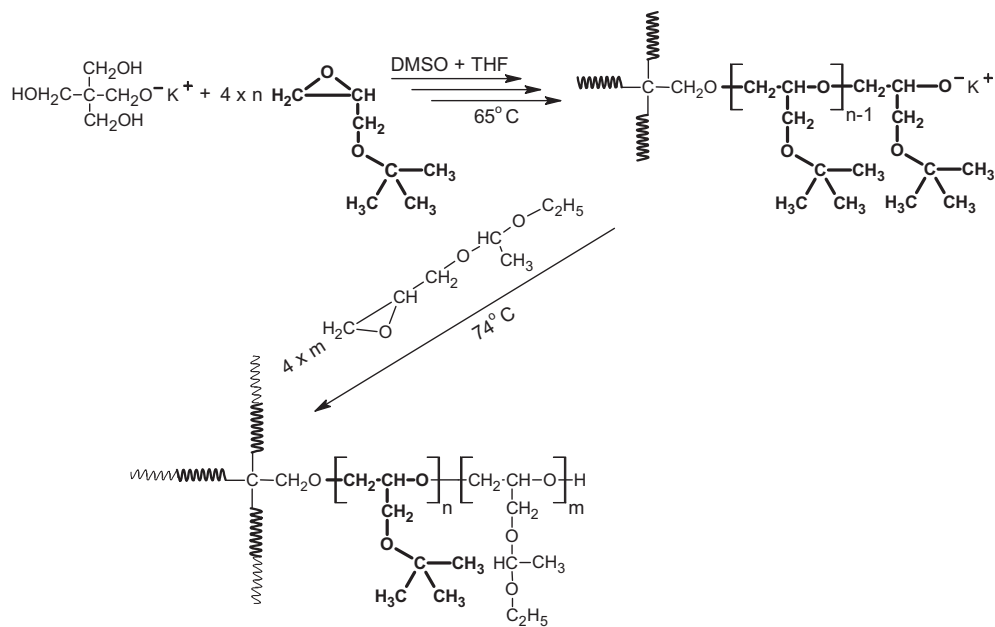
*tert*-Butyl-glycidylether (0.058 mol, 7.64 g) was distilled under high vacuum and placed in a reactor with a freshly prepared solution of potassium pentaerythritolate (partly ionized) (1.47 mmol) in 30 mL of DMSO. The reactor was placed in the oil bath and the mixture was stirred at 65 °C. After 24 h, freshly distilled THF (30 mL) was added to the reactor to keep the reaction mixture homogeneous. The polymerization was carried out at 74 °C. After 72 h, the conversion of *tert*-butyl-glycidylether was 100% (GC analysis). Freshly distilled 1-ethoxyethyl-glycidylether (0.041 mol, 5.99 g) was then added to the reactor. The reaction mixture was stirred at 74 °C for 72 h until complete conversion of the second monomer was achieved. The polymerization was terminated by adding water. After polymerization, the solvents were removed under reduced pressure, and the crude star block copolymer S-[(BGE)<sub>n</sub>-b-(EGE)<sub>m</sub>]<sub>4</sub> was analyzed by SEC–MALLS and <sup>1</sup>H NMR.

#### 2.2.3. Deprotection of hydroxyl groups in the (EGE)<sub>m</sub> block

Each star S-[(BGE)<sub>n</sub>-b-(EGE)<sub>m</sub>]<sub>4</sub> (13.5 g) was dissolved in formic acid (30 mL). After dissolution, the formic acid was removed under reduced pressure and the remaining material was dissolved in 1,4-dioxane (100 mL). A solution of potassium hydroxide (6.5 g) in



**Scheme 1.** The synthesis of potassium pentaerythritolate.



**Scheme 2.** The synthesis of an S-[(BGE)<sub>n</sub>-b-(EGE)<sub>m</sub>]<sub>4</sub> star.

methanol (100 mL) was added to the polymer solution for saponification. The mixture was stirred 24 h at room temperature and the solvents were removed under reduced pressure. The crude product was dissolved in methanol and desalinated through dialysis using a Spectra/Pore MWCO:3500 membrane against methanol at room temperature for two weeks. The methanol was changed two times per day. After dialysis, the methanol was removed under reduced pressure and a viscous, light yellow transparent product (6 g) was dried under high vacuum ( $1 \times 10^{-6}$  mbar) at 60 °C for several days.

The procedure yielded four arm [poly(*tert*-butyl-glycidylether)-block-polyglycidol]<sub>4</sub>, S-[(BGE)<sub>n</sub>-b-(G)<sub>m</sub>]<sub>4</sub> stars.

### 2.3. Measurements

#### 2.3.1. Gas chromatography

Gas chromatography measurements were performed to determine the residual monomer content in the reaction mixture. A gas chromatograph VARIAN 3400 equipped with an FID detector and a J&W Scientific DB-5 (30 m × 0.32 mm) column was used.

#### 2.3.2. NMR

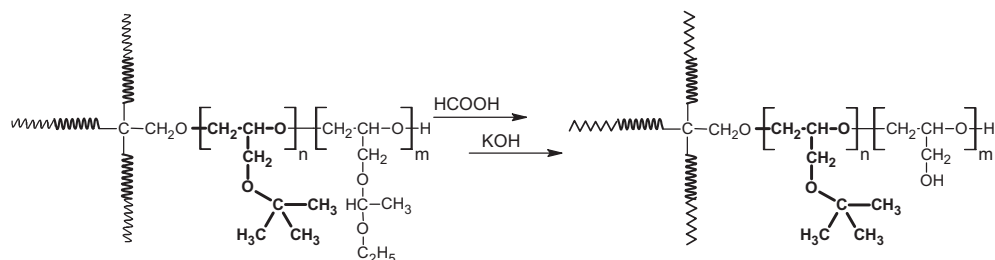
<sup>1</sup>H NMR spectra were recorded on a Varian UNITY-INOVA spectrometer operating at 300 MHz and a Bruker 600 Ultra Shield Plus spectrometer operating at 600 MHz. Either CDCl<sub>3</sub> or DMSO-*d*<sub>6</sub> with tetramethylsilane (TMS) as an internal standard were used as solvents. Trichloroacetyl isocyanate was added directly to the NMR tube to determine the number of hydroxyl groups.

#### 2.3.3. Size exclusion chromatography (SEC–MALLS)

The molar mass and dispersity of the polymers were determined using gel permeation chromatography with a refractive index detector and a multiangle laser light scattering detector. SEC measurements of the products before deprotection were carried out in THF at 35 °C using a PSS-SDV set of columns:  $1 \times 10^3$ ,  $1 \times 10^5$ ,  $2 \times 100$  Å. The refractive index increment of poly(*tert*-butyl-glycidylether) and poly(1-ethoxyethyl-glycidylether) was measured separately in THF ( $dn/dc = 0.057$  mL/g,  $dn/dc = 0.045$  mL/g respectively). The products, after deprotection, were analyzed in DMF (5 mmol/L solution of LiBr). Measurements were carried out at 45 °C using a set of columns:  $1 \times$  GRAM 100A (Polymer Standards Service) +  $2 \times$  Mixed-C (Polymer Laboratories). A refractive index detector Δn-2010 RI (WGE Dr. Bures) and a multiangle laser light scattering detector DAWN HELEOS of Wyatt Technologies ( $\lambda = 658$  nm) were used to determine the concentration and molar mass of the polymers. Measurements were performed with a nominal flow rate of 1 mL/min. The refractive index increment of poly(*tert*-butyl-glycidylether) was measured in DMF ( $dn/dc = 0.028$  mL/g). SEC results were collected and evaluated by ASTRA software from Wyatt Technologies.

#### 2.3.4. UV–VIS spectroscopy

Cloud point measurements of star aqueous solutions were performed using a Jasco V-530 UV–VIS spectrophotometer equipped with a programmable Medson MTC-P1 thermocontroller. The polymer concentration in aqueous solutions varied in the range of 1–10 g/L. The transmittance was measured at 500 nm. A heating



**Scheme 3.** Hydrolysis of (EGE)<sub>m</sub> blocks in an S-[(BGE)<sub>n</sub>-b-(G)<sub>m</sub>]<sub>4</sub> star.

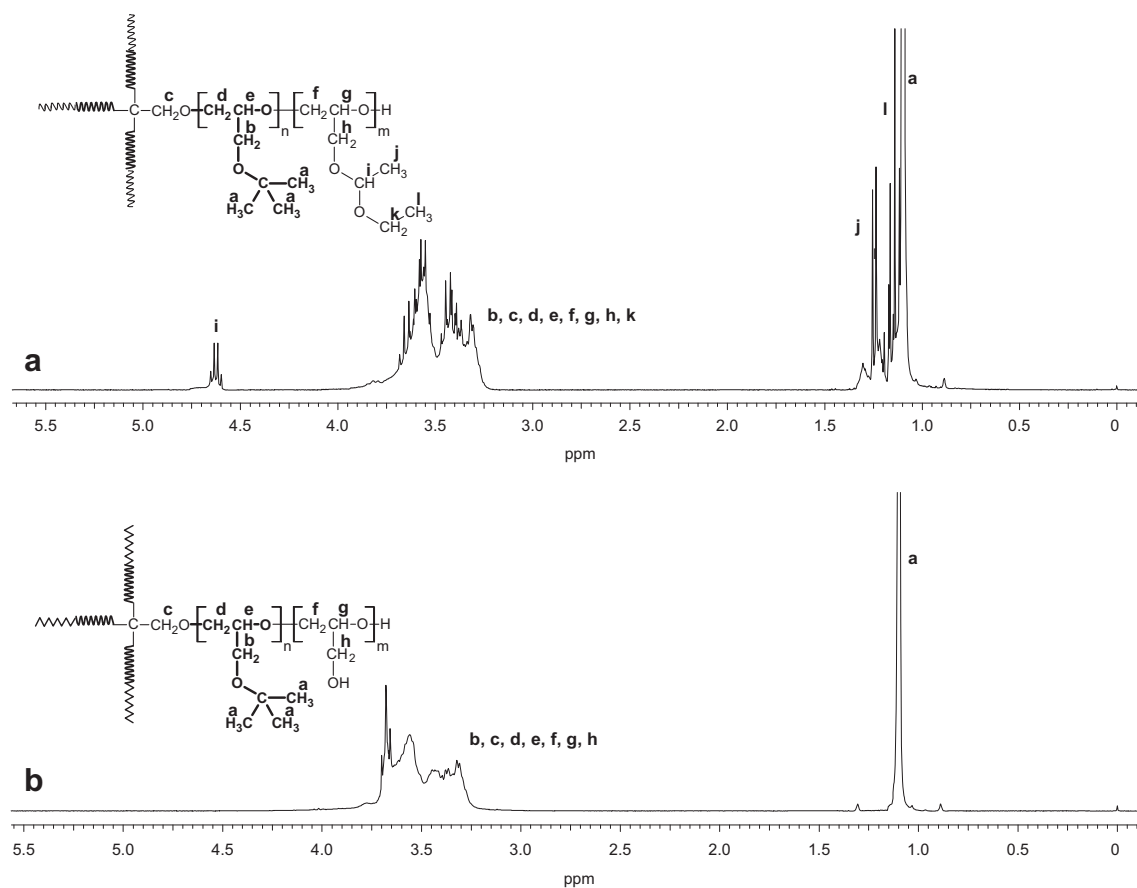


Fig. 1.  $^1\text{H}$  NMR spectrum of a)  $S-[(\text{BGE})_{10}-(\text{EGE})]_7$  star after polymerization and b) after hydrolysis of an  $S-[(\text{BGE})_{10}-(\text{G})]_7$  star (300 MHz,  $\text{DMSO}-d_6$ , 25 °C, TMS).

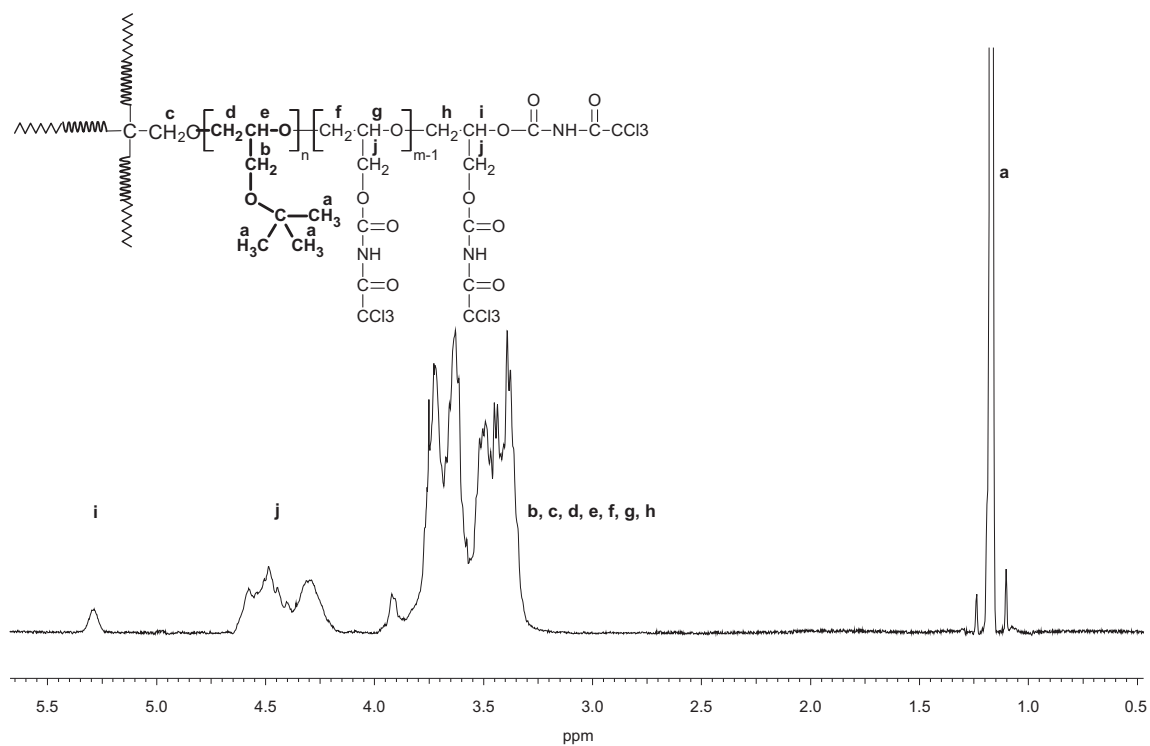


Fig. 2.  $^1\text{H}$  NMR spectrum of a 2- $S_4$  star after reaction with trichloroacetyl isocyanate (600 MHz,  $\text{DMSO}-d_6$ , 25 °C, TMS).



rate of 0.05 °C/min was applied. The data were collected every 2 °C 0.5 min after temperature stabilization. The cloud point was defined as the temperature where the polymer solution reached 50% transmittance.

### 2.3.5. Light scattering measurements

DLS measurements were performed on a Brookhaven BI-200 goniometer with vertically polarized incident 632.8 nm wavelength light supplied by a helium–neon laser operated at 35 mW and a Brookhaven BI-9000 AT digital autocorrelator. The polymer concentrations in the solutions used for measurements were from 2 to 10 g/L. Measurements were made at different angles  $\Theta$  from 60° to 120° at temperatures in the range between 15 and 40 °C for one polymer, and in the range 15–85 °C for the other. Calculations of the obtained results were made using a CONTIN algorithm to obtain distributions of the decay rates ( $\Gamma$ ). The apparent diffusion coefficients ( $D_{app}$ ) were calculated from the angular dependence of  $\Gamma$ :  $D_{app} = \Gamma/q^2$ , where  $q$  is the magnitude of the scattering vector  $q = (4\pi n/\lambda)\sin(\Theta/2)$ ,  $n$  is the refractive index of the solvent, and  $\lambda$  is the wavelength of the light source in vacuum. The apparent hydrodynamic radii were obtained from the Stokes–Einstein equation  $R_h^{app} = kT/(6\pi\eta D_{app})$ , where  $k$  is the Boltzmann constant and  $\eta$  is the viscosity of water at temperature  $T$ . The values of  $D$  for polymers below the phase transition temperature were plotted against concentration and extrapolated to zero concentration  $D_0 = \lim D$ . The hydrodynamic radii  $R_h$  for polymers below the phase transition temperature were obtained, taking into account the diffusion coefficient  $D_0$ .

The values of the apparent radii of gyration,  $R_g$ , were obtained from partial Berry plots, given by the following equation:

$$\sqrt{1/I_{ex}(q)} = C \left[ 1 + \left( R_g^2 q^2 \right) / 6 \right]$$

where  $I_{ex}$  is the excess of the scattered light.

### 2.3.6. SEM measurements

The star polymer aggregates were observed by scanning electron microscopy (SEM). SEM was performed on a Quanta 250 ESEM FEG Scanning Electron Microscope (FEI Company). A star polymer water solution was heated above its cloud point and dropped on a hot glass cover slide. After drying, the probe was coated with a gold film (5 nm) using a Leica EM SCD050 vacuum sputtering device.

## 3. Results and discussion

### 3.1. Synthesis of four arm [poly(*tert*-butyl-glycidylether)-block-polyglycidol]<sub>4</sub> S-[(BGE)<sub>n</sub>-b-(G)<sub>m</sub>]<sub>4</sub> stars

Four arm amphiphilic (AB)<sub>n</sub> type stars with hydrophobic poly(*tert*-butyl-glycidylether) internal parts and hydrophilic polyglycidol external blocks were synthesized using the “core-first” method.

**Table 2**  
Characteristics of S-[(BGE)<sub>n</sub>-b-(G)<sub>m</sub>]<sub>4</sub> stars.

Stars	S-[(BGE) <sub>n</sub> -b-(G) <sub>m</sub> ] <sub>4</sub>		$M_n$ (g mol <sup>-1</sup> )				Mass ratio <sup>a</sup> of PG (%)
	<i>n</i> : <i>m</i>	From feed	From feed			$M_w/M_n$	
			NMR	From feed	NMR		
1-S <sub>4</sub>	10:7	9.2:6.2	7400	6800	8200	1.02	27
2-S <sub>4</sub>	10:12	9:11.5	8900	8200	9100	1.01	41
3-S <sub>4</sub>	11:15	10.6:15	10300	10100	11400	1.03	44
4-S <sub>4</sub>	10:17	9.5:16.9	10400	10100	11600	1.03	50
5-S <sub>4</sub>	10:21	9:20.3	11550	10800	12200	1.03	56

<sup>a</sup> PG(%) =  $(4 \times 74)m/M_n$ . The “*m*” and “*M<sub>n</sub>*” values were calculated from <sup>1</sup>H NMR spectrum.

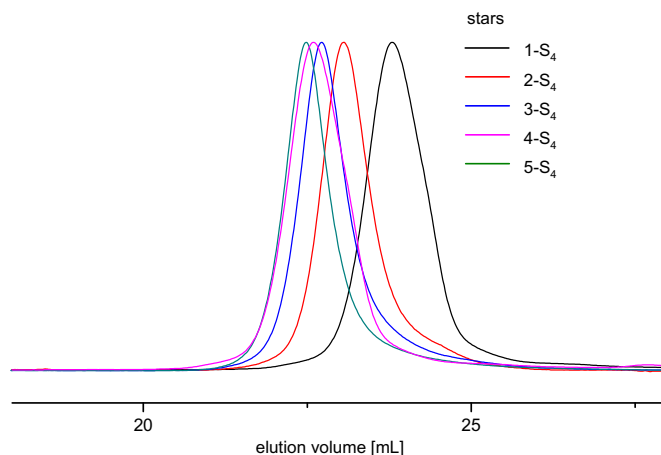


**Fig. 3.** Chromatograms (RI traces) of S-[(BGE)<sub>n</sub>-b-(G)<sub>m</sub>]<sub>4</sub> stars (DMF/5 mmol LiBr, 1 mL/min, 45 °C).

The potassium alcoholate of pentaerythritol was used as the initiator in the polymerization process. Synthesis of the initiator with hydroxyl active groups is shown in Scheme 1.

*tert*-Butanol was distilled off to shift the equilibrium. The *tert*-butanol hydroxyl group might act as a transfer agent. Therefore, the complete removal of *tert*-butanol was important to prevent the formation of linear chains.

Anionic living polymerization was applied to form arms with precise control over the arm's length and the structure of the star block copolymer.

In the first step, ionization of the pentaerythritol hydroxyl groups was accomplished by reaction with potassium *tert*-butoxide, taking into account that the final amount of ionized hydroxyl groups of pentaerythritol has to be lower than 20% to prevent precipitation of the initiator in DMSO [24]. The exchange reaction between the hydroxyl group and alcoholate active centers is much faster than the initiation reaction, which leads to simultaneous arm growth. The first monomer was added to the freshly prepared initiator. The synthesis of [poly(*tert*-butyl-glycidylether)-block-poly(1-ethoxyethyl-glycidylether)]<sub>4</sub> S-[(BGE)<sub>n</sub>-b-(EGE)<sub>m</sub>]<sub>4</sub> is shown in Scheme 2.

After initiation of *tert*-butyl-glycidylether polymerization and progressive growth of the polymer chain, the hydrophobic star polymer S-[(BGE)<sub>n</sub>]<sub>4</sub> precipitated in DMSO. However, the subsequent addition of THF kept the reaction mixture homogeneous. A full

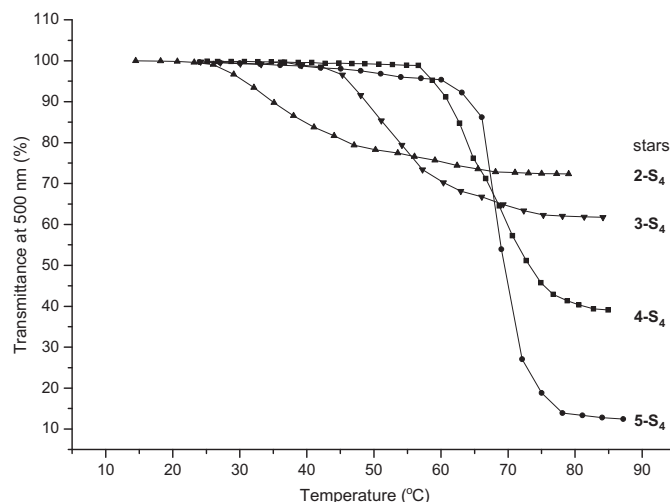


**Fig. 4.** Clouding curves of star polymer water solutions (2 g/L).

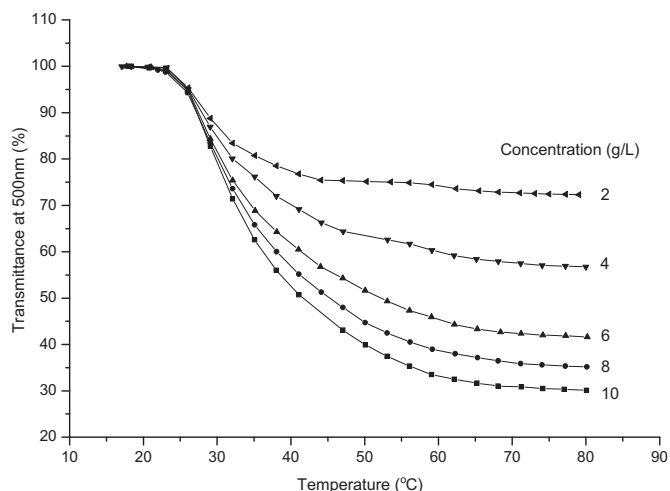


Fig. 5. Clouding curves of 2-S<sub>4</sub> star for different solution concentrations.

conversion of *tert*-butyl-glycidylether was obtained after 74 h of reaction at 65 °C. The second monomer, 1-ethoxyethyl-glycidylether, was subsequently added to the reaction mixture. A full conversion of the second monomer was obtained after 96 h at 74 °C. Control of the monomer conversion was verified by gas chromatography.

In the second step, the polyglycidol block hydroxyl groups were recovered by hydrolysis of the acetal linkages in the poly(1-ethoxyethyl-glycidylether) block. The acetal groups were converted to formates using formic acid and then saponified using KOH in methanol. The hydrolysis is shown in Scheme 3.

Completeness of the hydrolysis was checked by NMR. As an example, the spectrum of the star before and after hydrolysis is shown in Fig. 1.

The characteristic signal of methine protective group protons in a poly(1-ethoxyethyl-glycidylether) block (Fig. 1a, signal “i” at 4.68–4.58 ppm) is not visible in the NMR spectrum after hydrolysis. Complete hydrolysis of the protective groups was confirmed by NMR spectroscopy for all synthesized polymers. The average ratio of blocks estimated from the <sup>1</sup>H NMR for polymers after hydrolysis are in good agreement with the polymers before hydrolysis, which indicates that no degradation of the arms took place.

The molar ratios between the initiator and monomers used for polymerization of all the stars are presented in Table 1. Complete monomer conversion after each step is important for controlling

block length. Total monomer conversion, as measured by gas chromatography, is higher than 99.8% in all cases. The yield of stars after hydrolysis and purification by dialysis is higher than 87% in all cases.

The length of the blocks in the star arms, “m” and “n,” was estimated after the quantitative reaction of the hydroxyl groups of polyglycidol with trichloroacetyl isocyanate (TCAI) by NMR spectroscopy. For example, the spectrum of the 2-S<sub>4</sub> star after the reaction with TCAI is shown in Fig. 2. The results are collected in Table 2.

Signals from methine end group and methylene group protons of the obtained urethanes and protons of the *tert*-butyl groups were used to calculate the length of the glycidol “m” and *tert*-butyl-glycidylether “n” blocks. The ratio of the signal areas derived from polyglycidol pendant CH<sub>2</sub> group protons (Fig. 2, signal “j” at  $\delta = 4.65\text{--}4.20$  ppm) to the CH end group protons (Fig. 2, signal “i” at  $\delta = 5.30$  ppm) was used to determine the DP of the polyglycidol blocks. Similarly, the ratio of the signal area derived from the *tert*-butyl group CH<sub>3</sub> protons (Fig. 2, signal “a” at  $\delta = 1.17$  ppm) to the CH end group protons (Fig. 2, signal “i” at  $\delta = 5.30$  ppm) was used to determine the DP of the poly(*tert*-butyl-glycidylether) block. The results are collected in Table 2. Table 2 also contains the DP ratio of the poly(*tert*-butyl-glycidylether) block to the polyglycidol block, estimated from the feed. Both results are in good agreement, which verifies the structure of the obtained amphiphilic stars.

The molar masses and their dispersities for all obtained stars were determined using SEC–MALLS. Chromatograms of all star polymers are monomodal (Fig. 3). The dispersity of molar masses did not exceed 1.03. The refractive index increments (dn/dc) of the stars were estimated from the weight ratio of the comonomers and refractive index of polyglycidol in DMF (0.055 L/g) and poly(*tert*-butyl-glycidylether) in DMF (0.028 L/g). The value of dn/dc for both polymers was measured separately. The absolute molar masses obtained from SEC–MALLS (Table 2) are in good agreement with the molar masses calculated from NMR and with the values calculated from the feed.

The obtained results proved that the anionic polymerization of oxiranes lead to star shaped polymers with well controlled architectures.

### 3.2. Thermoresponsive behavior of stars

The [poly(*tert*-butyl-glycidylether)<sub>m</sub>-b-(polyglycidol)<sub>n</sub>]<sub>4</sub> are (except for the insoluble 1-S<sub>4</sub>) temperature sensitive. Their behavior resembles that of the linear amphiphilic block copolymers poly(ethylene oxide)-b-poly(*n*-alkyl glycidyl carbamates) [38,39] or poly(ethylene oxide)-b-poly(glycidyl acetates) [44]. These copolymers

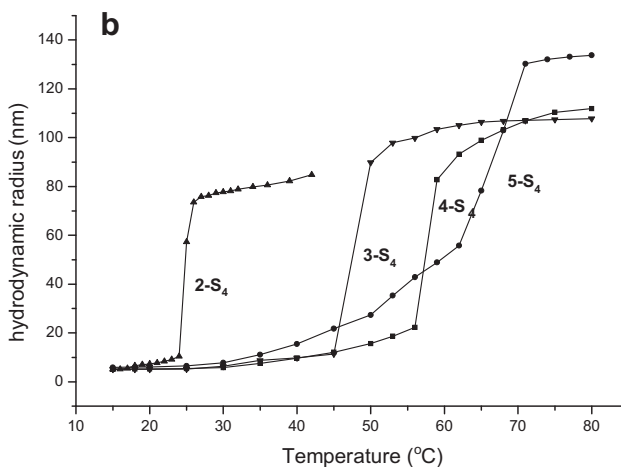
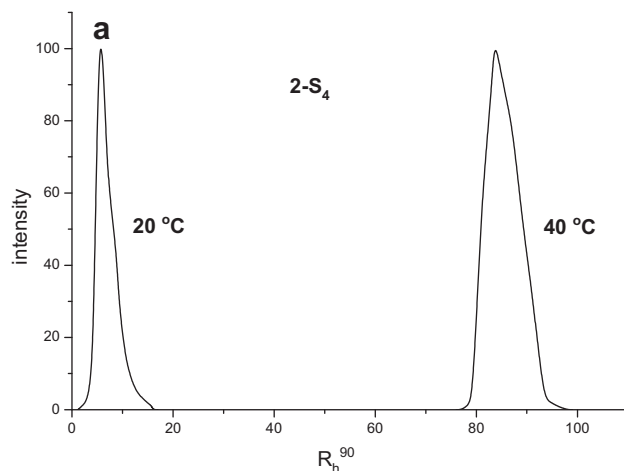


Fig. 6. Hydrodynamic radius a)  $R_h^{90}$  distribution of the star polymer 2-S<sub>4</sub> at 20 °C and 40 °C (solution concentration 2 g/L), b)  $R_h$ ,  $R_h^{90}$  of star polymers as a function of temperature (above phase transition the value of  $R_h^{90}$  for solution concentration of 2 g/L is given).

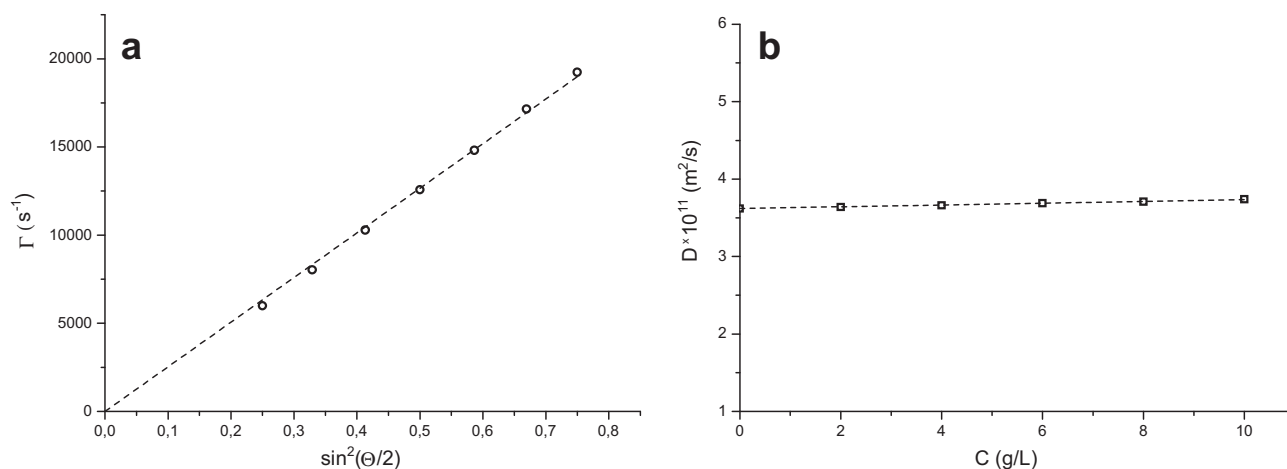


Fig. 7. a) Relaxation rate as a function of  $\sin^2(\Theta/2)$  and b) diffusion coefficient as a function of concentration for 2-S<sub>4</sub> stars at 15 °C. The dashed lines are the linear fit.

form at room temperature micelles above cmc and aggregates at elevated temperatures, which precipitate from water solutions.

Star block copolymers [poly(*tert*-butyl-glycidylether)<sub>m</sub>-b-(polyglycidol)<sub>n</sub>]<sub>4</sub> with polyglycidol block lengths of 12, 15, 17 and 21 monomer units were all water soluble at room temperature. After heating solutions of 2-S<sub>4</sub>, 3-S<sub>4</sub> and 4-S<sub>4</sub> became opalescent, the solution of 5-S<sub>4</sub> was opaque. The cloud point temperature of 2 g/L water solutions of these polymers measured as the changes in transmittance at a wavelength of 500 nm are shown in Fig. 4.

In no case did the transmittance fall to zero. The breadth of the transition range was narrowed with increasing hydrophilic polyglycidol block length.

Extension of the hydrophilic block shifts the transition temperature towards higher values. Changing the hydrophilic/hydrophobic ratio (the ratio of the block lengths of the polyglycidol and poly(*tert*-butyl-glycidylether) blocks) makes control of the transition temperature possible within wide limits.

The influence of the polymer concentration, in the range from 2 g/L to 10 g/L, on the cloud point temperature and the breadth of the transition range was also studied (Fig. 5). The cloud point temperature, measured as the value at which the transmittance falls to 50% of its final value, does not practically depend upon concentration. The final transmittance, however, does depend upon the concentration. The lower the concentration, the higher the final value of transmittance.

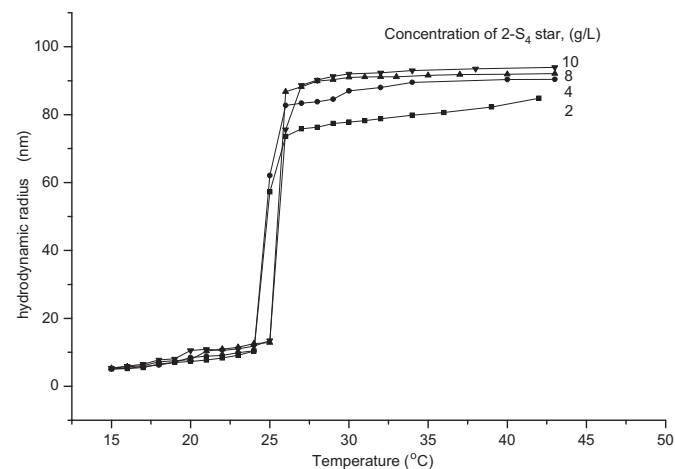


Fig. 8. Hydrodynamic radius of a 2-S<sub>4</sub> star for different solution concentrations as a function of temperature (above phase transition the value of  $R_h^{\text{app}}$  is given).

The sizes of the structures formed by the star polymers [poly(*tert*-butyl-glycidylether)<sub>m</sub>-b-(polyglycidol)<sub>n</sub>]<sub>4</sub> were investigated using static and dynamic light scattering as a function of temperature.

Dynamic light scattering (DLS) was used to follow how the hydrodynamic dimensions of the particles change with temperature. The measurements were carried out for solutions ranging from 2 g/L to 10 g/L. The dispersion of the particle sizes is expressed as  $\mu_2/\bar{T}^2$ , where  $\bar{T}$  is the average relaxation rate and  $\mu_2$  is the second moment of the  $I$  function [43]. For all systems, the  $I$  function was monomodal and diffuse in character. Examples of the distribution of the hydrodynamic radii at 20 °C (before the cloud point) and 40 °C (above cloud point), for the star 2-S<sub>4</sub>, measured at the light scattering angle of 90°, are shown in Fig. 6a.

Changes in the hydrodynamic radii for all stars as a function of temperature are shown in Fig. 6b. Below the phase transition, the diffusion coefficient, determined from the slope of the linear fit of relaxation time  $T$  versus the scattering angle expressed as  $\sin^2(\Theta/2)$  (Fig. 7a), was practically concentration independent (Fig. 7b). The extrapolation of  $D = f(c)$  to zero yields  $D_0$ , so the hydrodynamic radii below the phase transition are therefore given as  $R_h = kT/(6\pi\eta D_0)$ , (Fig. 6b).

However, above the transition temperature, the diffusion coefficients obtained by the extrapolation of  $T$  fall significantly with increasing concentration. It cannot be dismissed that this was caused by an increase in the particle sizes with an increasing concentration of aggregates. Therefore, in Fig. 6b, above the phase transition, the apparent values  $R_h^{\text{app}}$  of the hydrodynamic radii are given, as measured from  $R_h^{\text{app}} = kT/(6\pi\eta D)$  for 2 g/L.  $D$  was calculated from the slope of  $I(q^2)$ . Fig. 8 shows how the radii change with temperature at different concentrations.

The apparent hydrodynamic radii of the aggregates above the phase transition grow with increasing concentration from 80 nm to

Table 3  
Characteristics of thermoresponsive behavior of poly(*tert*-butyl-glycidylether)-block-polyglycidol stars in aqueous solution.

Stars	$T_{\text{cp}}$ (°C)	$R_h$ (nm) (15 °C)	$\mu_2/\bar{T}^2$	$R_h^{\text{app}}$ (nm) <sup>a</sup> (75 °C)	$\mu_2/\bar{T}^2$	$R_g$ (nm) (75 °C)	$\rho$
2-S <sub>4</sub>	26.1	5.1	0.07	80 <sup>b</sup>	0.13 <sup>b</sup>	63 <sup>b</sup>	0.79
3-S <sub>4</sub>	51.1	5.2	0.07	107	0.08	82	0.77
4-S <sub>4</sub>	62.8	5.4	0.06	110	0.07	85	0.77
5-S <sub>4</sub>	69.0	6.5	0.04	132	0.14	104	0.79

<sup>a</sup> Measured for 2 g/L solution concentration.

<sup>b</sup> Measured at 40 °C.

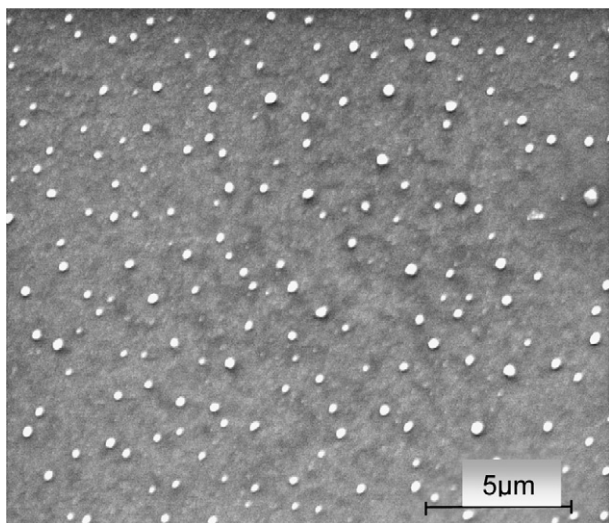


Fig. 9. SEM images of 5-S<sub>4</sub> star aggregates.

93 nm for 2-S<sub>4</sub>, from 107 nm to 124 nm for 3-S<sub>4</sub>, from 111 nm to 132 nm for 4-S<sub>4</sub> and from 133 nm to 167 nm for 5-S<sub>4</sub>. At constant concentration (Fig. 6b) the sizes of the aggregates depend upon the length of the hydrophilic block.

In contrary to what was observed for the thermosensitivity of linear amphiphilic block copolymers [38,39,44] the aggregates formed above 27 °C by the stars described here are stable and do not change up to 95 °C.

The values of the hydrodynamic radius of the stars measured below the phase transition point indicate that, for the studied range of concentrations, the stars in the solution do not exist as unimers, but form micelles. Micellization of the amphiphilic star block copolymers has been observed for several systems, as discussed in the introduction [27–30]. For four arm poly(acrylic acid)-block-polystyrene stars with much higher molar mass lower values of hydrodynamic radii (ca. 3 nm) were measured in a good solvent, which prevented micellization [28]. So here even smaller structures should be observed for star unimers, as the strongly hydrophobic core should be collapsed in water, thus lowering the size of the separate star.

DLS measurements of the studied stars in DMF, a good solvent for both blocks, indicated only a very low scattering intensity. Although the radii could not be measured with sufficient accuracy, this proves that the sizes of the structures in DMF are much smaller, probably corresponding to separate stars.

The radii of gyration,  $R_g$ , of the structures formed in water above the cloud point were measured by static light scattering (Table 3). The knowledge of both the hydrodynamic radius and the radius of gyration makes the shape factor  $\rho = R_g/R_h$  available. The value of  $\rho$  is close to 0.775, which indicates that the aggregates assume the structure of a dense sphere [1,45]. The data are collected in Table 3.

Aggregates of the star block copolymers were visualized using scanning electron microscopy. Sample 20 mg/L were heated above the cloud point and dispersed on a heated glass plate. After drying, the plate was covered with gold (ca. 3 nm) and measured by SEM under high vacuum. Fig. 9 shows the images. The structures are of spherical shape. The diameters vary from 240 to 300 nm.

#### 4. Conclusions

The anionic sequential polymerization of *tert*-butyl-glycidylether and 1-ethoxyethyl-glycidylether, initiated by partially ionized pentaerythritol, leads to four arm stars with block copolymer

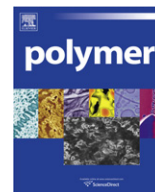
arms of controlled length. <sup>1</sup>H NMR spectroscopy and SEC–MALLS measurements confirm the structure of stars. The amphiphilic character of the star arms causes temperature sensitivity in water solution. The adjustment of the length of the hydrophobic and the hydrophilic blocks permits control of the phase transition temperature in a broad range. Above the phase transition, stars formed in water stable aggregates of 60–100 nm radius and of low size dispersities. The thermosensitivity of synthesized stars and their amphiphilic character makes them a prosperous tool for temperature controlled delivery of active compounds.

#### Acknowledgements

This work was supported by the Polish Ministry of Science and Higher Education, grant NN 209 100 237.

#### References

- [1] Burchard W. *Adv Polym Sci* 1999;143:113–94.
- [2] Grest GS, Fetters LJ, Huang JS, Richter D. *Adv Chem Phys* 1996;94:67–163.
- [3] Roovers J, Zhou LL, Toporowski PM, van der Zwan M, Iatrou H, Hadjichristidis N. *Macromolecules* 1993;26:4324–31.
- [4] Hult A, Johansson M, Malmström E. *Adv Polym Sci* 1999;143:1–34.
- [5] Matthews OA, Shipway AN, Stoddart JF. *Prog Polym Sci* 1998;23:1–56.
- [6] Salamone JC, editor. *Polymeric materials encyclopedia*. Boca Raton, FL: CRC Press; 1996.
- [7] Hadjichristidis N, Pitsikalis M, Pispas S, Iatrou H. *Chem Rev* 2001;101:3747–92.
- [8] Mishra M, Kobayashi S, editors. *Star and hyperbranched polymers*. Basel, New York: Marcel Dekker Inc; 1999.
- [9] Gao H, Matyjaszewski K. *Prog Polym Sci* 2009;34:317–50.
- [10] Blencowe A, Tan JF, Goh TK, Qiao GG. *Polymer* 2009;50:5–32.
- [11] Eschwey H, Hallensl ML, Burchard W. *Macromol Chem* 1973;173:235–9.
- [12] Cloutet E, Fillaut JL, Gnanou Y, Astruc D. *J Chem Soc Chem Commun* 1994;21:2433–4.
- [13] Angot S, Taton D, Gnanou Y. *Macromolecules* 2000;33:5418–26.
- [14] Ohno K, Wong B, Haddleton DM. *J Polym Sci Part A Polym Chem* 2001;39:2206–14.
- [15] Strandman S, Tenhu H. *Polymer* 2007;48:3938–51.
- [16] Mendrek B, Trzebicka B. *Eur Polym J* 2009;45:1979–93.
- [17] Zhao Y, Chen Y, Chen C, Xi F. *Polymer* 2005;46:5808–19.
- [18] Comanita B, Noren B, Roovers J. *Macromolecules* 1999;32:1069–72.
- [19] Sunder A, Krämer M, Hanselmann R, Mühlaupt R, Frey H. *Angew Chem Int Ed* 1999;38:3552–5.
- [20] Chen Y, Shen Z, Barriau E, Kautz H, Frey H. *Biomacromolecules* 2006;7:919–26.
- [21] Claesson H, Malmström E, Johansson M, Hult A. *Polymer* 2002;43:3511–8.
- [22] Kowalczuk A, Vandendriessche A, Trzebicka B, Mendrek B, Szeluga U, Cholewiński G, et al. *J Polym Sci Part A Polym Chem* 2009;47:1120–35.
- [23] Gauthier M, Tichagwa L, Downey J, Gao S. *Macromolecules* 1996;29:519–27.
- [24] Wałach W, Trzebicka B, Justyńska J, Dworak A. *Polymer* 2004;45:1755–62.
- [25] Held D, Müller AHE. *Macromol Symp* 2000;157:225–37.
- [26] Baek KY, Kamigaito M, Sawamoto M. *Macromolecules* 2001;34:215–21.
- [27] Lele BS, Leroux JC. *Polymer* 2002;43:5595–606.
- [28] Whittaker MR, Monteiro MJ. *Langmuir* 2006;22:9746–52.
- [29] Stěpánek M, Uchman M, Procházka K. *Polymer* 2009;50:3638–44.
- [30] Mountrichas G, Mpiri M, Pispas S. *Macromolecules* 2005;38:940–7.
- [31] Taton D, LeBorgne A, Sepulchre M, Spassky N. *Macromol Chem Phys* 1994;195:139–48.
- [32] Tokar R, Kubisa P, Penczek S, Dworak A. *Macromolecules* 1994;27:320–2.
- [33] Dworak A, Wałach W, Trzebicka B. *Macromol Chem Phys* 1995;196:1963–70.
- [34] Wałach W, Kowalczuk A, Trzebicka B, Dworak A. *Macromol Rapid Commun* 2001;22:1272–7.
- [35] Sunder A, Hanselmann R, Frey H, Mühlaupt R. *Macromolecules* 1999;32:4240–6.
- [36] Frey H, Haag R. *Rev Mol Biotechnol* 2002;90:257–67.
- [37] Liu H, Chen Y, Shen Z, Frey H. *Reactive Funct Polym*; 2007:67156–64.
- [38] Dimitrov P, Utrata-Wesołek A, Rangelov S, Wałach W, Trzebicka B, Dworak A. *Polymer* 2006;47:4905–15.
- [39] Dimitrov P, Jamróz-Piegza M, Trzebicka B, Dworak A. *Polymer* 2007;48:1866–74.
- [40] Erberich M, Keul H, Möller M. *Macromolecules* 2007;40:3070–9.
- [41] Backes M, Messenger L, Mourran A, Keul H, Möller M. *Macromolecules* 2010;43:3238–48.
- [42] Fitton AO, Hill J, Jane D, Millar R. *Synthesis*; 1987:1140–2.
- [43] Koppel DE. *J Chem Phys* 1972;57:4814.
- [44] Dworak A, Trzebicka B, Wałach W, Utrata A, Tsvetanov Ch. *Macromol Symp* 2004;210:419–26.
- [45] Oono Y, Kohmoto M. *J Chem Phys* 1983;78:520–8.



## Insight on the periodate oxidation of dextran and its structural vicissitudes

João Maia<sup>a,\*</sup>, Rui A. Carvalho<sup>b,c</sup>, Jorge F.J. Coelho<sup>a</sup>, Pedro N. Simões<sup>a</sup>, M. Helena Gil<sup>a</sup>

<sup>a</sup>Chemical Engineering Department of the Faculty of Sciences and Technology of the University of Coimbra, Coimbra, Portugal

<sup>b</sup>Life Sciences Department of the Faculty of Sciences and Technology of the University of Coimbra, Coimbra, Portugal

<sup>c</sup>Center of Neurosciences and Cell Biology, Coimbra, Portugal

### ARTICLE INFO

#### Article history:

Received 23 June 2010

Received in revised form

30 November 2010

Accepted 30 November 2010

Available online 8 December 2010

#### Keywords:

Oxidized dextran  
Bidimensional NMR  
Thermal analysis

### ABSTRACT

Periodate oxidized dextran has been widely studied in a broad range of biotechnological applications, regardless of this, usually little attention is paid to the oxidation extension consequences on the properties of the final modified dextran. Based on a bidimensional NMR analysis, we suggest that the two aldehydes groups, resulting from the periodate oxidation, are not fully reactive with *N*-nucleophiles, under certain pH conditions. The aldehyde group bonded to C<sub>3</sub> appeared to be the only prone to react. The other aldehyde might be arrested in more stable hemiacetal structures. The hemiacetals are also responsible for oxidized dextran crosslinking, interfering in simple processing steps, such as dissolution and solubility, as well as increasing the viscosity of the solutions. The molecular weight variation on the oxidized samples can be followed by dynamic mechanical thermal analysis in consequence of the variation of glass transition temperature with the molecular weight, which was corroborated by the onset temperature of the thermal degradation.

© 2010 Elsevier Ltd. All rights reserved.

### 1. Introduction

Dextran is a polysaccharide synthesized by a large number of bacteria, when grown on sucrose-containing media [1]. Nowadays, *Leuconostoc mesenteroids* (strain B-512) [2] is responsible for the majority of the commercially available dextrans. They are characterized by having over 95% of  $\alpha$ -1,6 linkages and some low degree of branching. From the late 1940's, dextrans have attracted attention from the biotechnology world. They were accepted as a plasma volume expander, due to its linear structure, high water solubility, and especially owing to its  $\alpha$ -1,6 linkage, more relevant to biological applications, in virtue of the slower hydrolysis by body enzymes, compared to the  $\alpha$ -1,4 linkage (e.g. glycogen) [1,2].

The dextran oxidation by the periodate ion is a catalysis-free aqueous reaction which yields a purified product with a simple dialysis step. The periodate ion attacks vicinal diols promoting bond breaking. Typically, the  $\alpha$ -1,6 residues in dextran are attacked between carbons C<sub>3</sub>–C<sub>4</sub> or C<sub>3</sub>–C<sub>2</sub>, breaking the C–C bond and yielding aldehyde groups, being able to be further reduced on a second and independent oxidation reaction (Scheme 1) [3]. Initially, this method was used in the characterization and elucidation of the polysaccharide structure, through the complete oxidation and

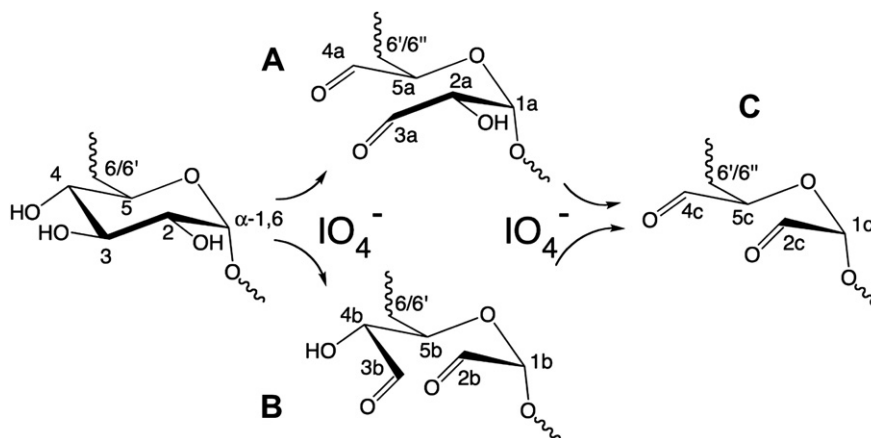
consequent analysis of the degradation products [4]. Nowadays, low and mild periodate oxidations are used to confer the dextran chain with aldehyde functionalities, which have as main characteristic the highly reactive nature towards *N*-nucleophiles, such as amines, hydrazines or carbazates [5].

Concerning the oxidized dextran (dexOx) application on a biomedical perspective, the accurate assessment of the periodate oxidation consequences in mild oxidation conditions is of utmost importance in predicting the extent of drug loading [6] or the final physico-chemical properties of hydrogels [7]. Due to the highly reactive nature of the formed aldehydes, they are easily attacked by neighbouring hydroxyl groups, leading to the formation of hemiacetals [8]. These hemiacetals are the most consensual resulting structures, even taking into account that some studies restrict these structures to a narrow pH window (4.0–5.2) [9]. Other consequences of the dextran oxidation are the decreased average molecular weight and polydispersity increase [10].

Herein we address the consequences of low and mild dextran oxidation and try to further elucidate the structural nature of dexOx through bidimensional NMR, upon reaction with *tert*-butyl carbazate. Our data suggest that only one aldehyde per residue might be involved on this reaction, while the second aldehyde could be arrested to a stable hemiacetal structure. We will explore the oxidation influence on simple manipulation steps, such as aqueous dissolution and the solutions viscosity outcome. Dynamic mechanical thermal analysis (DMTA) data on dexOx are discussed and correlated with the molecular weight trend. The relative thermal

\* Corresponding author. Rua Sílvia Lima, Pólo II, Departamento de Engenharia Química, FCTUC, 3030-790 Coimbra, Portugal. Tel.: +351 239 798 743; fax: +351 239 798 703.

E-mail address: [joaom@eq.uc.pt](mailto:joaom@eq.uc.pt) (J. Maia).



**Scheme 1.** Dextran's  $\alpha$ -1,6 glucose residue possible periodate oxidations. (A) Periodate attack at C<sub>3</sub>–C<sub>4</sub>; (B) C<sub>3</sub>–C<sub>2</sub> and (C) double oxidation.

stability of dexOx samples was evaluated by thermogravimetric (TG) measurements.

## 2. Materials and methods

### 2.1. Materials

Dextran (from *Leuconostoc mesenteroides*;  $M_w$  60 kDa, according to Fluka's specification), sodium periodate, adipic acid dihydrazide (AAD), *tert*-butyl carbazate (tBC), ethyl carbazate (EtC), phosphate buffered saline (PBS; pH 7.4), dialysis membranes (MWCO 12 kDa) and NaOD were purchased from Sigma (Sintra, Portugal) and used as received.

### 2.2. Dextran oxidation

An aqueous solution of dextran (1 g; 12.5% (w/v) ~ pH 5.5) was oxidized with 2 mL of sodium periodate solution with different concentrations (33–264 mg/mL) to yield theoretical oxidations from 5 to 40%, at room temperature (The oxidation degree (OD) of dexOx is defined as the number of oxidized residues per 100 glucose residues). The reaction was stopped after 4 h. The resulting solution was dialyzed for 3 days against water and lyophilized (Snidjers Scientific type 2040, Tillburg, Holland). The scale-up of the reaction was done using the same procedure albeit using 30 g of dextran and a calculated amount of periodate to yield a theoretical oxidation of 5, 10, 25 and 40%, referred hereafter as D5, D10, D25 and D40, respectively.

### 2.3. Nuclear magnetic resonance (NMR)

$^1\text{H}$  spectra were acquired on a Varian 600 NMR spectrometer (Palo Alto, CA) using a 3 mm indirect detection NMR probe with z-gradient.  $^1\text{H}$  NMR spectra were recorded in  $\text{D}_2\text{O}$  (20–25 mg in 0.2 mL; pD of c.a. 4.5 or 10.2 after addition of NaOD) using a  $90^\circ$  pulse and a relaxation delay of 30 s. The water signal, used as reference line, was set at  $\delta$  4.75 ppm and was partially suppressed by irradiation during the relaxation delay. A total of 32 scans were acquired for each  $^1\text{H}$  NMR spectra. Bidimensional spectra were recorded on the same magnet and probe.  $^1\text{H}$ – $^1\text{H}$  correlation spectroscopy (COSY) spectra were collected as a  $2048 \times 1024$  matrix covering a 5 kHz sweep width using 32 scans/increment. Before Fourier transformation, the matrix was zero filled to  $4096 \times 4096$  and standard sine-bell weighting functions were applied in both dimensions.  $^1\text{H}$ – $^{13}\text{C}$  heteronuclear multiple quantum coherence (HMQC) spectra were collected as a  $2048 \times 1024$  matrix covering

sweep widths of 5 and 25 kHz in the first and second dimensions, respectively. Before Fourier transformation, the matrix was zero filled to  $4096 \times 4096$  and standard Gaussian weighting functions were applied in both dimensions. The spectra were analyzed with iNMR software, version 2.6.4 ([www.inmr.net](http://www.inmr.net)). The oxidation degree (OD) refers to the theoretical value unless otherwise stated.

### 2.4. DexOx's solubility and solutions viscosity

The different dexOx and dextran samples were dissolved in PBS (20% w/w). Aliquots of 1 mL were distributed in small glass vials, frozen at  $-20^\circ\text{C}$  and freeze-dried, in order to obtain a similar freeze-drying cake across every sample. The original dextran processed this way will be referred as D0. To each sample, 0.85 mL of milliQ water was added and the dissolution time was recorded at different temperatures ( $n = 3$ ). The reason was to mimic the reconstitution of a pharmaceutical freeze-dried product. The vials were preserved under reduced pressure on a glass desiccator supplied with silica gel. Dextran and dexOx solutions, with concentrations ranging from 10 to 30% w/w, were prepared and tested in a Brookfield Programmable D-II<sup>+</sup> Viscometer with an S18 spindle, assisted by DVLoader v1.0 software. The chamber temperature was controlled by an external bath to  $25^\circ\text{C}$ . Low viscosity solutions were measured by a Labolan V1-R viscometer with an LCP spindle (low viscosity adapter) and controlled temperature to  $25^\circ\text{C}$ .

### 2.5. Size exclusion chromatography

Performed in an HPLC system composed by a degasser and a WellChrom Maxi-Star k-1000 pump (Knauer), coupled to an LS detector (evaporative light scattering PL-EMD 960) and one column (Polymer Laboratories, aquagel-OH Mixed  $8\ \mu\text{m}$ ). The whole system was kept at room temperature and the eluent used was  $\text{KNO}_3$  (0.001 M; pH 3.9) at a flow rate of 0.4 mL/min. Samples and standards were dissolved in the eluent at 4–6 mg/mL (Fluka Chemie AG, dextran standards from 12 to 80 kDa).

### 2.6. Dynamic mechanical thermal analysis

The freeze-drying samples obtained above were subjected to dynamical mechanical thermal analysis (DMTA) on a Triton Tritec 2000 analyzer. About 50 mg of sample were loaded into metal pockets fabricated from a sheet of stainless steel. The pocket was clamped directly into the DMTA using a single cantilever configuration. Temperature scans, from  $-200^\circ\text{C}$  to  $+300^\circ\text{C}$  with a standard heating rate of  $2^\circ\text{C}\ \text{min}^{-1}$  were performed in

a multifrequency mode (1 and 10 Hz) in order to identify the temperature transition peaks.

### 2.7. Thermogravimetric analysis

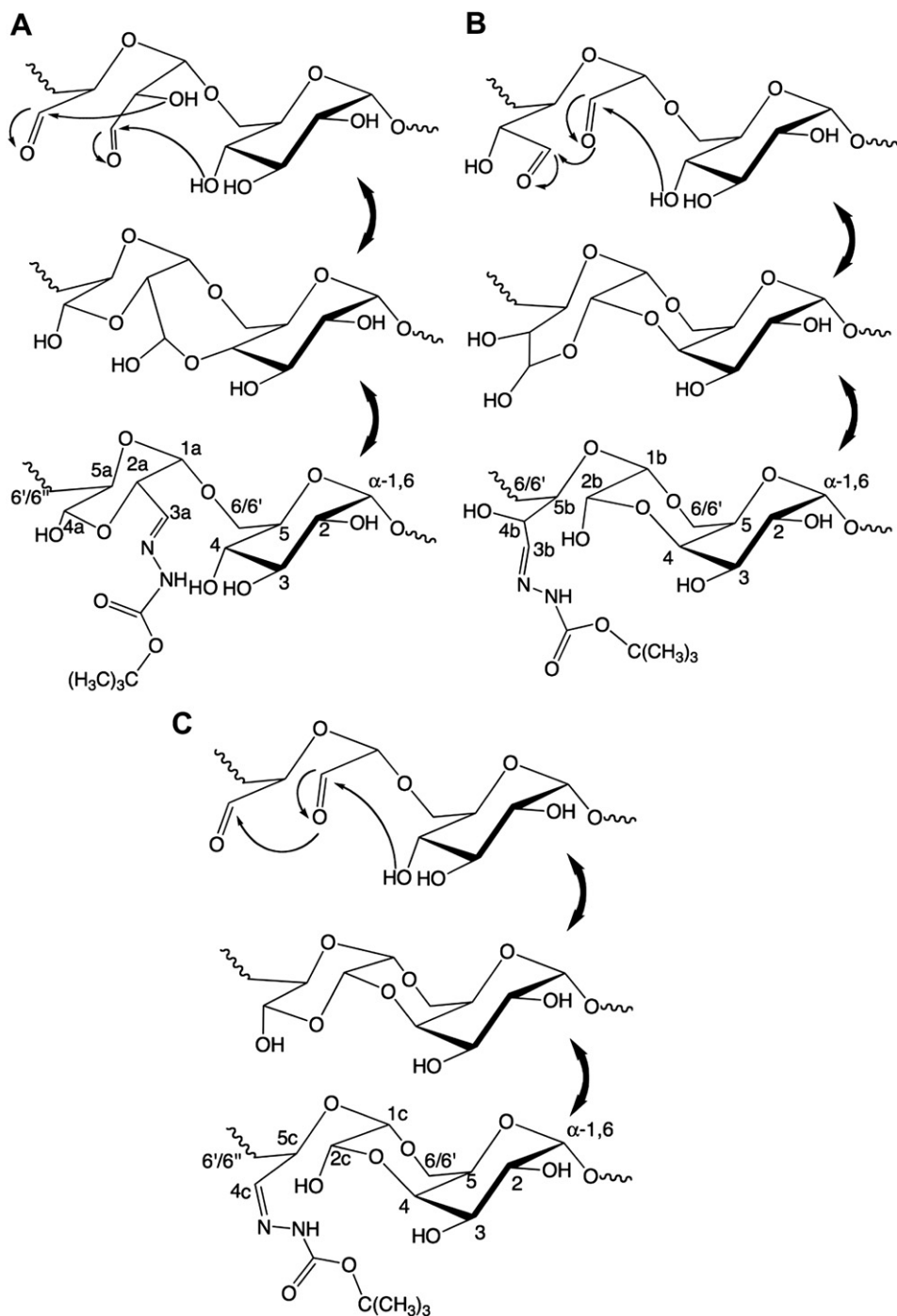
The thermal stability of dextran and dexOx samples was studied in a TA Instruments Q500 thermogravimetric analyzer (thermo-balance sensitivity 0.1  $\mu\text{g}$ ). The temperature calibration was performed in the range 25–1000 °C by measuring the Curie point of nickel standard, using open platinum crucibles, a dry nitrogen purge flow of 100 mL  $\text{min}^{-1}$ , and a heating rate of 10 °C  $\text{min}^{-1}$ , the

later being the conditions applied throughout the thermoanalytical measurements. At least two runs were performed for each sample (sample weights of ca. 8 mg) in order to check the repeatability of measurements.

## 3. Results and discussion

### 3.1. DexOx characterization

Dextran with a molecular weight of 60 kDa, was oxidized with variable amounts of sodium periodate in order to obtain different



**Scheme 2.** (A) Single periodate oxidation outcome after periodate ion attack at C<sub>3</sub>–C<sub>4</sub> and (B) C<sub>3</sub>–C<sub>2</sub> cleavage, followed by possible intra-hemiacetals formation and tBC reaction. (C) Periodate doubly oxidized residue, possible hemiacetals and tBC reactions.

OD. Usually, the aldehyde group is not observed by FTIR spectroscopy, unless in highly oxidized samples ( $1730\text{ cm}^{-1}$ ), nor in the NMR spectrum, except during the first minutes of reaction ( $\sim 9.7\text{ ppm}$ ) [10]. It is widely accepted that the aldehyde groups react with nearby hydroxyl groups, forming hemiacetals or hemiacetals [3,8]. These transitory events could be either intra or inter-residue (Scheme 2) and, in certain situations, interfere with the oxidation evolution. The most important aspect arising from this modification

is the final oxidation degree. It defines the dexOx's reactivity on drug conjugation [6] or gelation rate on hydrogel formulations [7,10]. Concerning the estimation of the oxidation degree, several ways have been used to approach the problem. On extensive oxidations, acid-base titration is useful in assessing the released formic acid and the percentage of doubly oxidized residues [4].

On mild oxidations, colorimetric titrations, such as the hydroxylamine hydrochloride [11] or the TNBS assay [12], have been

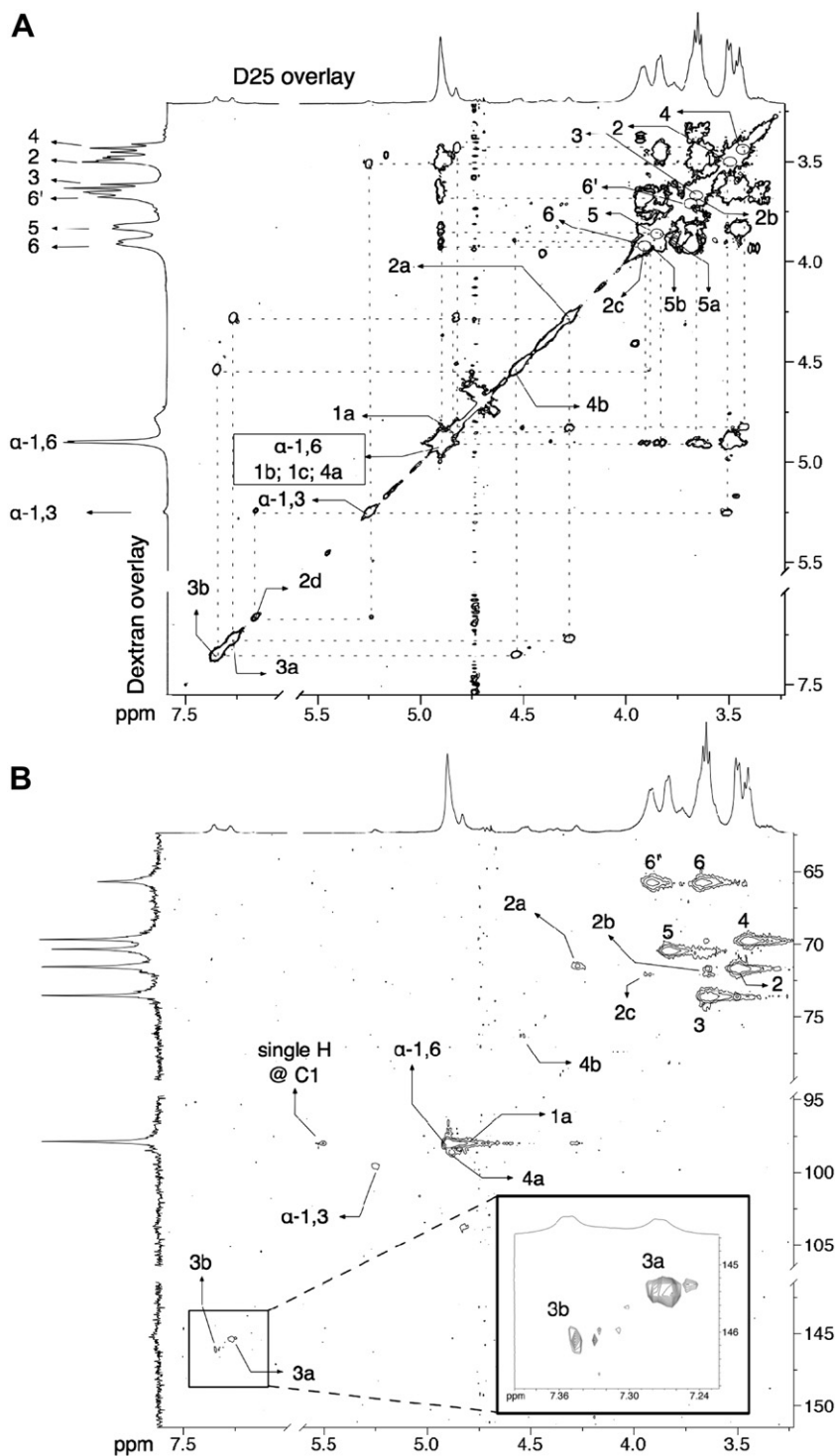


**Fig. 1.** (A) COSY and (B) HMQC spectra of D25. The peaks assigned with plain numbers refer to correlations arising from the intact residue. The correlations arising from the different oxidized residues are represented by: a:  $C_3$ – $C_4$  oxidation; b:  $C_3$ – $C_2$  oxidation; c:  $C_4$ – $C_2$  double oxidation; and d:  $\alpha$ -1,3 branched oxidized residue.



used. However, the calculations are usually performed assuming that both aldehydes react with the carbazates. On an earlier study [10], our two-dimensional NMR results led us to suggest that just one of the aldehydes per residue reacts with the carbazates, in agreement with the single correlation observed on the  $^1\text{H}$ – $^{13}\text{C}$ –HMQC spectrum. Our new results suggest that, under the studied conditions, only one aldehyde per residue is reacting.

### 3.2. Bidimensional NMR

The NMR data was collected in  $\text{D}_2\text{O}$  with a measured pH of  $\sim 4.5$ , which falls inside the consensual pH window for hemiacetal formation. Therefore, our bidimensional NMR analysis will take into account the most likely hemiacetal populations, based on previously proposed structures found in the literature. These structures will serve as a starting ground for the carbazone peak assignment. The  $\text{C}_3$ – $\text{C}_4$  cleavage (Scheme 1A) was described to be 7.5-fold faster than the  $\text{C}_3$ – $\text{C}_2$  cleavage (Scheme 1B) [8]. On a mild oxidation, the double oxidized structure (Scheme 1C) is likely less representative, as most periodate would be rapidly consumed on single oxidations and such scenario is favored by the starting pH ( $\sim 5$ ) [13]. Furthermore, it is thought that the hemiacetal formation could hinder further oxidation, even of neighboring residues [8]. Therefore, the structures arising from the  $\text{C}_3$ – $\text{C}_4$  oxidation will be treated as more representative, followed by the  $\text{C}_3$ – $\text{C}_2$  oxidation and the double oxidation. The titration of dexOx with carbazates yields a carbazone moiety, evidencing the former aldehydic proton, which helps clarifying the bidimensional spectra. The region around 7.3 ppm (proton axis) and 145 ppm (carbon axis) on the  $^1\text{H}$ – $^{13}\text{C}$ –HMQC (Fig. 1B inset) unveiled two main peak populations of carbazone protons. A third carbazone peak exists (7.16 ppm), only seen on the COSY (correlation spectroscopy) spectrum (Fig. 1A) and is apparently correlated with the  $\alpha$ -1,3 anomeric proton (see left axis dextran's proton spectrum overlay for the native peaks). Therefore, it seems to exist two main carbazone peaks, out of four possible different carbazones ( $\text{C}_2$ ,  $\text{C}_4$  and two different  $\text{C}_3$ 's), though each of them could have different environments influencing the chemical shifts. Analyzing the  $\text{C}_3$ – $\text{C}_4$  cleavage (Scheme 2A), an intra-hemiacetal structure is likely to occur, after a hydroxyl ( $\text{C}_2$ ) attack to the  $\text{C}_4$  aldehyde, forming a stable six sides ring [14], despite several different possibilities due to the rotativity of the oxidized residue. The aldehyde on  $\text{C}_3$  could suffer an attack from any hydroxyl group ( $\text{HO}$ – $\text{C}_4$  from the downstream residue suggested in the structure). We propose that this aldehyde would be the more susceptible of attack by tBC, represented by the most shielded of the protons (Fig. 1A 3a;  $\sim 7.28$  ppm) in the 7.3 ppm region. Analyzing this peak correlation on the COSY, one can see a correlation with a proton at  $\sim 4.25$  ppm (2a), correlating itself with a carbon (Fig. 1A) on the same chemical shift as glucose  $\text{C}_2$  ( $\sim 71.6$  ppm). The same proton (2a) further correlates downfield, with a possible anomeric proton/carbon (1a). Considering this structure as the most likely and stable after  $\text{C}_3$ – $\text{C}_4$  cleavage, frames the  $\text{C}_4$  proton in an anomeric-like environment and possibly could be associated with a correlation with  $\text{C}_5$  like those proposed according to the bidimensional spectra (4a and 5a, respectively).

The  $\text{C}_3$ – $\text{C}_2$  cleavage yields an aldehyde on  $\text{C}_2$ , which has been proposed to form a stable and conformationally plausible 1,4-dioxepane ring after reaction with the OH on  $\text{C}_4$  from the downstream residue (Scheme 2B) [8]. Again, the aldehyde on  $\text{C}_3$  (3b) would be more prone to react with tBC. Following the other carbazone proton at  $\sim 7.35$  ppm (Fig. 2B; 3b), it correlates with a proton at  $\sim 4.55$  ppm (4b), which further correlates with a single proton upfield, falling near the glucose residue proton/carbon 5 (5b). There is a strong correlation between an anomeric proton and a proton at  $\sim 3.65$  ppm, which could be an unshielded proton on  $\text{C}_2$  and also

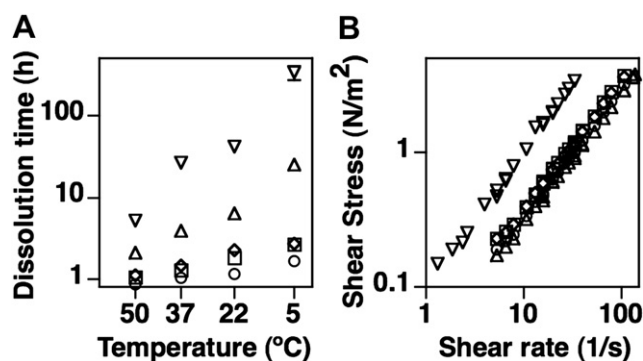


Fig. 2. (A) Dissolution time profiles, at different temperatures and (B) the shear stress vs. shear rate profile at 20% (w/w) concentration and 25 °C for dextran (○), D5 (□), D10 (◇), D25 (△) and D40 (▽).

correlates with a carbon in the same chemical shift as glucose  $\text{C}_2$ . This correlation could likely arise from 1b to 2b, but also 1c and 2c, from the doubly oxidized residue, being the environments very similar. Regarding the doubly oxidized residue, the hemiacetal structure depicted in Scheme 2C was also suggested by Ishak and Painter (1978) [8] to be plausible. Therefore,  $\text{C}_4$  would be more sensitive to a carbazate attack. However, the third major visible correlation in the COSY spectrum, at 7.16 ppm, apparently correlates with the anomeric proton ( $\alpha$ -1,3), which would be an unlikely chemical shift for a proton on  $\text{C}_5$ . It would be more reasonable if this correlation arose from the carbazate attack at  $\text{C}_2$  of the doubly oxidized, but a second correlation would have to be present in the HMQC spectrum (Fig. 1B). It is possible that the correlations from the doubly oxidized residue, as well as other minor populations, are masked within the major peaks. The transient nature of the hemiacetals and the similar environments turn the peak assigning task a hard mission, which could have several interpretations. Anyhow, the two main correlations on the COSY spectrum suggest that not every aldehyde is reacting with a carbazate under these pH conditions.

At alkaline pH (10.2), some new peaks can be seen in the range of 7.5–9.5 ppm for the D25 sample (Supplementary Fig. 1A). These peaks were previously attributed to isomeric enol forms. Such structures are under an aldo–enol equilibrium [15]. Many other peak populations are observed between 4 and 6 ppm, due to the higher resolution (Supplementary Fig. 1A). Though, the addition of EtC, at this pH, did not revert most of the identified new peaks, it presented more correlations on the zone of interest for the carbazone protons ( $\sim 7.3$  ppm; Supplementary Fig. 1B and C). We have observed before, that dexOx crosslinked with AAD hydrogels dissolved quickly at pH 9 [10], suggesting the sensitivity of the hydrazone bond to alkaline pH's, thus, the likelihood of a similar behavior for the carbazone bond also exists. These new correlations, suggest that, every aldehydic carbon is sensitive to a carbazate attack. Under this pH, the aldo–enolic structures are likely more exposed to attack than under the hemiacetal form, establishing a higher number of equilibriums, concomitantly expressed on the COSY spectrum (Supplementary Fig. 1D). The overlay of both COSY spectra shows the appearance of a high number of new correlations after the addition of EtC (Supplementary Fig. 1D, black contour), partially reverting the correlations of D25 (red contour). These results identify pH as a strong modulator of dexOx reactivity, which might be interesting to contemplate under certain pH sensitive applications.

### 3.3. Macroscopic consequences of the oxidation

The extensive and complete dextran oxidation leads to the destruction of the molecule into characteristic degradation by-

products [4]. Low and mild oxidations also degrade dextran, leading to slight molecular weight decrease. The destruction of the glucose residue, yielding aldehydes, could also contribute in altering the dexOx behavior in solution. The periodate oxidation in non-buffered solutions leads to pH decrease, after formic acid release [10], possibly contributing for acid-hydrolysis [16]. This phenomenon can be observed in several ways. The reference technique in the characterization of polymers is the size exclusion chromatography (SEC), which separates the different populations in accordance with the hydrodynamic volume, which can be translated to molecular weight and the polydispersity index (Table 1). The molecular weight is a key property of polymers, defining certain macroscopic characteristics, such as solubility, viscosity and clearance rates in biological systems [17]. Besides  $^1\text{H}$  NMR and SEC, we have gathered results of techniques and empirical evidences, which clearly reflect the molecular weight differences between the several dexOx samples. One direct consequence of the dextran oxidation is the longer dissolution times in aqueous media. This phenomenon is of utmost importance on an off-the-shelf freeze-dried product. The dissolution time periods of the several samples under exactly the same conditions (Fig. 2A) but at different temperatures show that D5 and D10 have very close dissolution profiles to dextran (D0). However, the D25 and D40 dissolution profiles clearly reflect the OD increase. The viscosity of a dextran solution is directly related to the increment of concentration and  $M_w$  [18,19]. The molecular weight decreasing, due to periodate oxidation, should theoretically yield a less viscous solution than the original dextran, for the same concentration conditions. At lower concentrations (5%) the viscosity variation is negligible (Table 1). However, the reactivity of the oxidized dextran, through inter-hemiacetals formation, has great influence on the behavior of the solutions. We observed that the oxidation degree could invert the viscosity trend, depending on the dexOx concentration. Concentrated solutions favor the inter-chain hemiacetals formation, resembling a molecular weight increasing, hence the higher resistance to flow. Within the same concentration range (20% w/w), only D25 viscosity falls below the dextran viscosity. On the other hand, D40 has an extremely high resistance to flow, reflecting the cross-reactivity (Table 1 and Fig. 2B). We suggest that this effect is due to the inter-chain hemiacetals formed, inverting what would be the natural viscosity trend and demonstrating how both parameters (OD and  $M_w$ ) can interfere with the viscosity of a given dexOx solution.

**Table 1**

Macroscopic characteristics of native dextran and the several oxidized samples. OD estimated by  $^1\text{H}$  NMR analysis,  $M_w$  and PDI calculated by SEC, viscosities at different concentrations and time necessary until complete dissolution.

Sample	Oxidation degree		$M_w^c$ kDa	PDI <sup>d</sup>	$\eta^e$ 20% (m Pa s)	$\eta^f$ 5% (m Pa s)	$t_{37^\circ\text{C}}^g$ (hours)
	$\text{IO}_4^-^a$	$\text{EtC}^b$					
Dextran	—	—	60.1	1.47	30.7	2.7	$1.0 \pm 0.04$
D5	5	$3.6 \pm 0.1$	61.2	1.59	35.9	2.9	$1.3 \pm 0.08$
D10	10	$8.6 \pm 0.2$	60.8	1.61	35.1	3.0	$1.5 \pm 0.05$
D25	25	$22.2 \pm 0.7$	60.3	2.03	26.8	2.7	$3.9 \pm 0.65$
D40	40	$33.0 \pm 0.8$	25.4	3.05	102.8	2.7	$26.6 \pm 0.44$

<sup>a</sup> Theoretical OD, calculated as the molar ratio of sodium periodate per initial glucose unit in dextran.

<sup>b</sup> Calculated by  $^1\text{H}$  NMR after titration with ethyl carbazate, taking into account the ratio between the integral of the peak at  $\delta$  7.3 ppm and the integral of the anomeric proton at  $\delta$  4.9 ppm. Five independent integrations.

<sup>c</sup> Weight-average molecular weight estimated by SEC.

<sup>d</sup> Polydispersity index corresponding to  $M_w/M_n$ .

<sup>e</sup> Viscosities of dextran and oxidized dextrans at 20% w/w. Taken from the slope of the curves Shear Stress =  $f$ (Shear Rate) plot. The linear regression was forced to cross the origin as every sample showed a Newtonian behavior.

<sup>f</sup> Viscosities of dextran and oxidized dextrans at 5% w/w, at 200 rpm.

<sup>g</sup> Dissolution time taken, at 37 °C, in PBS, without agitation.

### 3.4. Thermal analysis

We have extended the study on the influence of the oxidation extension by analyzing the thermoanalytical curves of the different oxidized species. DMTA methods is frequently used to evaluate the effects of excipients on polymer's glass transition temperature ( $T_g$ ). In amorphous polymers, a primary relaxation transition may be observed at the characteristic temperature  $T_g$ . In this point, the glass-like state (restricted motion of the polymeric chains) changes to a rubber-like state indicating loss in rigidity (*i.e.* increased relaxation) associated with enhanced polymeric chain mobility. Typically, the glass transition is defined as the temperature(s) at which either a maximum in the mechanical damping parameter ( $\tan \delta$ ) or loss modulus ( $G''$ ) occurs [20]. The presence of moisture can also be assessed by DMTA, being visible in the thermoanalytical curves as characteristic transitions at certain temperatures [21]. In terms of damping, it is possible to identify four main transitions for the original dextran, approximately at  $-80$  °C,  $105$  °C,  $235$  °C and  $305$  °C (Fig. 3A<sup>\*/\*\*</sup>). The peak at  $-80$  °C is a secondary relaxation due to absorbed water, which contributes to the formation of a more diffuse and stronger H-bond network than observed in a dry sample [21]. The peak at  $105$  °C refers to the water evaporation from dextran. These thermal events show that even after the freeze-drying process some residual water is present. These events have different profiles on the oxidized samples (not shown), which will not be addressed since this issue is out of the scope of this work. The next peak at ca.  $235$  °C corresponds to  $T_g$  (\*\*). At this temperature, the storage modulus decreases rapidly and is frequency dependent on the  $\tan \delta$  (Fig. 3A inset). This peak reflects an  $\alpha$ -relaxation from non-frequency dependent events, such as crystallization, melting, curing or thermal degradation [22]. The peak at  $305$  °C reflects an overall degradation stage and will be discussed further ahead.

It has been reported that the molecular weight of dextrans influences the  $T_g$  due to the decrease of the free volume with the  $M_w$  increase [23]. To confirm such influence, the thermoanalytical data of several dextrans ( $M_w$ : 580, 60 and 19.5 kDa; tested as supplied) were analyzed. In fact, the  $T_g$  of the tested dextran samples decrease directly with the  $M_w$ , being the correspondent peak values observed at 237.8, 235.4 and 231.1 °C, respectively (Fig. 3B). These  $T_g$  values are in agreement with the trend described by Icoz et al. [23]. For a comparable  $M_w$  range, despite determined by a different technique. The different oxidized samples were processed in a similar way to avoid any artifacts that could arise from freezing and freeze-drying and there was an effort to minimize the samples moisture.

Interestingly, D0 presented a broader peak and shifted to lower temperature ( $223.6$  °C) when compared with the original dextran (Fig. 3B). The presence of the phosphate salts could interfere with the freezing process of dextran, leading to different dextran chain conformation, which is reflected by the broader  $T_g$  peak and the shift to lower temperatures [24]. By freeze-drying a phosphate buffered aqueous dextran solution, it can impair the crystallization process of the salts [25] as well as the dextran derivative itself. Nevertheless, the  $M_w$  difference, within the dexOx's samples, is clearly visible on the DMTA curves (Fig. 3C and Table 2) corroborating the SEC and NMR data. It is known that crosslinking agents can also increase the  $T_g$  [20]. However, the hemiacetals crosslinking effect, observed on the viscosity studies, apparently is not reflected on the  $T_g$ , suggesting that the real molecular weight is dominant on the  $T_g$  onset.

A first look to the TG curve profiles (Fig. 4A) allows to identify a quite dramatic change in going from native dextran to its processed (freeze-dried PBS solution) counterpart, D0. Apart from a shift in the onset temperature of the main mass loss stage towards lower temperatures (by  $41$  °C), a remarkable difference is observed in the residual mass (at  $600$  °C), which should be ascribed to the

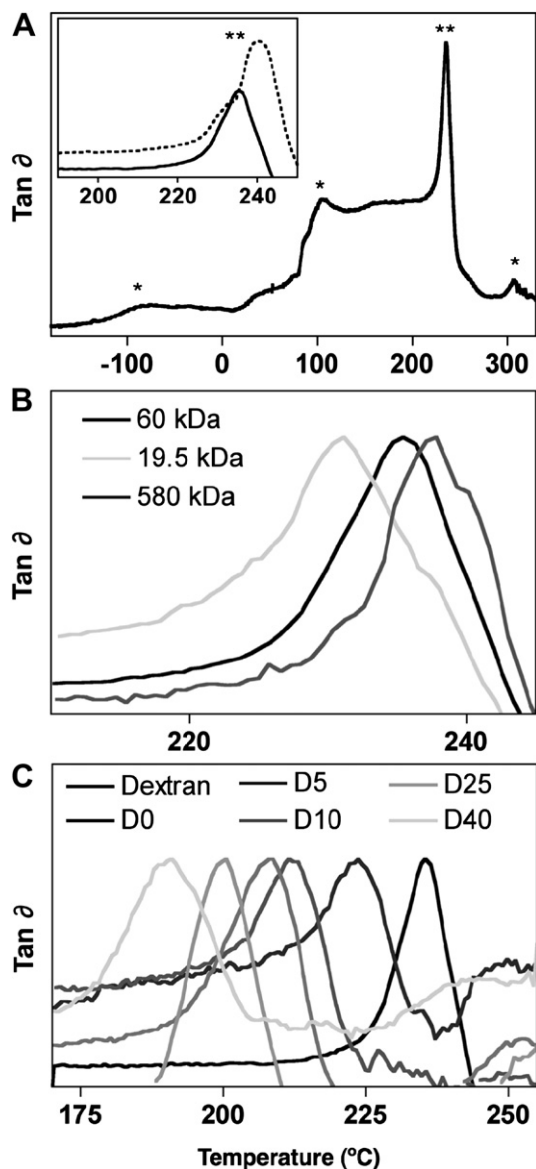


**Fig. 3.** (A) Full thermogram of native dextran marked with the non-frequency dependent transitions (\*) and  $T_g$  identification through frequency dependent transition (\*\*) and inset); (B)  $T_g$  of the different molecular weight dextrans; (C)  $T_g$  of the different oxidized samples. All samples presented with a frequency of 1 Hz, except for dotted line at a frequency of 10 Hz.

salts coming from PBS. The original dextran exhibits a quite familiar behavior [21,26–28], with a first mass loss stage below ca. 120 °C due to the elimination of water, as observed in the DMTA, followed by the overall degradation stage (depolymerization) along the approximate temperature range from 298 to 328 °C, in good correspondence with the fourth transition, identified by the DMTA results (Fig. 3A). However, the thermal decomposition of oxidized dextran samples should be analyzed with reference to thermal decomposition of the sample that reflects the influence of PBS in dextran, D0. In this case, the differences in the thermoanalytical curves appear to be more subtle.

Both D0 and oxidized dextran samples exhibit a first mass loss stage, from the ambient temperature to 150 °C. The correspondent mass loss rate is somewhat variable among the samples, but the residual mass at 150 °C is quite comparable (see Table 2). This first weight change is caused by the loss of adsorbed water, and, probably, of some water of crystallization related with the PBS

**Table 2**

Glass transition temperatures obtained from the DMTA curves and characteristic quantities (mean and standard deviation) obtained from the TG/DTG curves.

Sample	$T_g$ (°C)	$T_{on}^a$ (°C)	$T_p^b$ (°C)	$\Delta m^c$ (%)
Dextran	235.5	298.6 ± 0.4	315.0 ± 0.2	92.8 ± 0.2 8.3 ± 0.4
D0	223.6	257.6 ± 1.4	269.9 ± 1.7	96.3 ± 1.1 29.7 ± 0.2
D5	211.5	195.2 ± 1.4	247.5 ± 0.8	267.1 ± 1.6 94.7 ± 0.2 29.7 ± 0.2
D10	207.9	198.6 ± 0.6	241.5 ± 0.4	279.2 ± 0.2 93.2 ± 0.3 28.8 ± 0.0
D25	200.5	190.8 ± 0.4	234.1 ± 0.3	266.2 ± 0.2 93.1 ± 0.4 30.9 ± 0.3
D40	190.7	179.7 ± 0.2	233.0 ± 0.7	274.4 ± 1.8 94.3 ± 0.3 35.4 ± 0.0

<sup>a</sup>  $T_{on}$ : extrapolated onset temperatures (TG curve).

<sup>b</sup>  $T_p$ : peak temperature, corresponding to the maximum decomposition rate (DTG curve).

<sup>c</sup>  $\Delta m$ : residual mass at the temperatures 150 °C and 600 °C.

components (phosphates). Above 150 °C, the differences in the response of samples under comparison become more apparent. The complexity of the global thermal decomposition, probably involving several kinetically independent processes as suggested by the TG data and, mainly, by the differential thermogravimetric (DTG) curves profiles (Fig. 4B), increases with the degree of the oxidation of the samples. A first change in the mass loss rate within the approximate temperature range 180–220 °C can be observed (Fig. 4B inset), being only incipient in the case of the D5 sample, moderate in the D10 one, and rather evident in the remaining oxidized dextran samples (see also Table 2 for the onset temperatures). This stage is followed by the main decomposition process, whose pattern is also clearly influenced by the oxidation degree, as revealed by the DTG curve profiles. In terms of characteristic quantities, while the onset temperature of the main decomposition stage obeys to a well defined pattern, monotonically decreasing with the increase of the oxidation degree from 247.5 °C (D5) to 233.0 °C (D40), the undefined trend of the peak temperature at the maximum decomposition rate (Table 2) reflects differences in

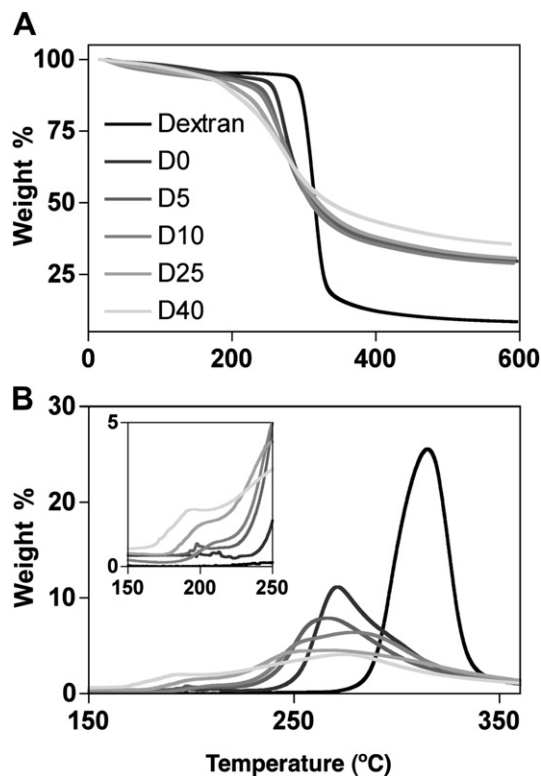


**Fig. 4.** (A) TG and (B) DTG curves of dextran and dexOx samples. ( $\phi = 10$  °C  $\text{min}^{-1}$ ; dry nitrogen at 100 mL  $\text{min}^{-1}$ ).

decomposition pathways. The residual mass at 600 °C for the most oxidized sample (D40) suggests a pronounced different decomposition course when compared to the remaining oxidized samples.

#### 4. Conclusions

Our bidimensional NMR data suggests that only one aldehyde per residue is responding to the carbazate under mildly acidic conditions. We propose that the two main peak populations (~7.3 ppm) arise from carbazates on C<sub>3</sub> from single oxidized residues. There are more downfield shifted peaks, but not more than 5.5 ppm, which indicate the non-existence of more carbazate proton populations. These peaks should arise from protons involved in hemiacetals, which form anomeric-like environments. At alkaline pH, the aldehyde groups appear to be under different structures than hemiacetals. The enol forms appear to be more reactive towards carbazates, though more labile and less stable.

The periodate oxidation of dextran is a harsh reaction which promotes chain degradation, confers high chemical reactivity to a natively neutral molecule and deeply alters its physico-chemical properties. The increasing OD, impairs water solubility, taking longer periods of time to solubilize, and interferes with the resulting viscosity, especially at high polymer concentrations. The solutions viscosity could impair injectability and mixability of certain formulations.

The degree of oxidation is also reflected on the glass transition temperature according to DMTA data. Interestingly, the hemiacetals do not seem to affect the thermal properties of the freeze-dried samples. The glass transition temperatures shift is in direct accordance with the molecular weight decrease, but do not give much insight on the structural consequences of the oxidation. On the other hand, the DTG profiles, for the diverse samples, are quite interesting. An increase in the thermal decomposition complexity with the increase in the oxidation degree was identified, evidencing the deleterious effect of periodate oxidation on dextran's structure. Low oxidative conditions, up to 10%, do not damage extensively dextran's structure, however milder oxidation conditions, result in extensive disruption of the dextran structure. These set of results may rise awareness for the consequences of periodate oxidation on the final structural properties of the modified dextran, helping researchers to better guide the design of dexOx-based formulations.

#### Acknowledgements

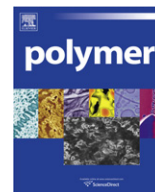
The authors thank Carla Ventura for the support on the viscosity studies. JM acknowledges the financial support of Instituto de Investigação Interdisciplinar (III/BIO/20/2005).

#### Appendix. Supplementary data

Supplementary data related to this article can be found online at doi:10.1016/j.polymer.2010.11.058.

#### References

- [1] Sidebotham RL. *Adv Carbohydr Chem Biochem* 1974;30:371–444.
- [2] Bixler GH, Hines GE, McGhee RM, Shurter RA. *Ind Eng Chem* 1953;45:692–705.
- [3] Guthrie R. *Adv Carbohydr Chem* 1961;16:105.
- [4] Jeanes A, Wilham C. *J Am Chem Soc* 1950;72:2655–7.
- [5] Suvorova OB, Iozep AA, Passet BV. *Rus J App Chem* 2001;74:1016–20.
- [6] Hudson S, Langer R, Fink GR, Kohane DS. *Biomaterials*; 2009.
- [7] Maia J, Ribeiro MP, Ventura C, Carvalho RA, Correia IJ, Gil MH. *Acta Biomat* 2009;5:1948–55.
- [8] Ishak MF, Painter TJ. *Carbohydr Res* 1978;64:189–97.
- [9] Drobchenko SN, Isaevanovna LS, Kleiner AR, Lomakin AV, Kolker AR, Noskin VA. *Carbohydr Res* 1993;241:189–99.
- [10] Maia J, Ferreira LS, Carvalho R, Ramos MA, Gil MH. *Polymer* 2005;46:9604–14.
- [11] Zhao H, Heindel ND. *Pharm Res* 1991;8:400–2.
- [12] Bouhadir KH, Hausman DS, Mooney DJ. *Polymer* 1999;40:3575–84.
- [13] Novikova EV, Tishchenko EV, Iozep AA, Passet BV. *Rus J App Chem* 2002;75:985–8.
- [14] Aalmo KM, Grasdalen H, Painter TJ, Krane J. *Carbohydr Res* 1981;91:1–11.
- [15] Drobchenko SN, Isaevanovna LS, Kleiner AR, Eneyskaya EV. *Carbohydr Res* 1996;280:171–6.
- [16] Basedow AM, Ebert KH, Ederer HJ. *Macromolecules*; 1978.
- [17] Mehvar R. *J Control Rel* 2000;69:1–25.
- [18] Ioan CE, Aberle T, Burchard W. *Macromolecules* 2000;33:5730–9.
- [19] Xu X, Li H, Zhang Z, Qi X. *J App Polym Sci* 2009;111:1523–9.
- [20] Jones DS. *Int J Pharm* 1999;179:167–78.
- [21] Scandola M, Ceccorulli G, Pizzoli M. *Int J Biol Macromol* 1991;13:254–60.
- [22] Coelho JFJ, Carreira M, Goncalves PMOF, Popov AV, Gil MH. *J Vinyl Addit Tech* 2006;12:156–65.
- [23] Icoz DZ, Moraru CI, Kokini JL. *Carbohydr Polym* 2005;62:120–9.
- [24] Izutsu K, Heller MC, Randolph TW, Carpenter JF. *J Chem Soc Far Trans* 1998;94:411–7.
- [25] Randolph TW. *J Pharmaceutical Sci* 1997;86:1198–203.
- [26] Hussain MA, Shahwar D, Tahir MN, Sher M, Hassan MN, Afzal Z. *J Serb Chem Soc* 2010;75:165–73.
- [27] Katsikas L, Jeremic K, Jovanovic S, Velickovic J, Popovic I. *J Therm Anal* 1993;40:511–7.
- [28] Tang M, Dou H, Sun K. *Polymer* 2006;47:728–34.



# Influence of soft segment molecular weight on the mechanical hysteresis and set behavior of silicone-urea copolymers with low hard segment contents

Iskender Yilgor<sup>a,\*</sup>, Tugba Eynur<sup>a</sup>, Sevilay Bilgin<sup>a</sup>, Emel Yilgor<sup>a</sup>, Garth L. Wilkes<sup>b</sup>

<sup>a</sup>Koc University, Chemistry Department, Sariyer 34450, Istanbul, Turkey

<sup>b</sup>Department of Chemical Engineering, Virginia Tech, Blacksburg, VA 24061-0211, USA

## ARTICLE INFO

### Article history:

Received 9 August 2010

Received in revised form

19 October 2010

Accepted 23 November 2010

Available online 1 December 2010

### Keywords:

Silicone-urea

Hysteresis

Elastomer

## ABSTRACT

Effect of polydimethylsiloxane (PDMS) soft segment molecular weight ( $M_n = 3200, 10,800$  and  $31,500$  g/mol) and urea hard segment content (2.0–11.4% by weight) on the hysteresis and permanent set behavior of segmented silicone-urea (TPSU) copolymers were investigated. In spite of very low hard segment contents, all copolymers formed self-supporting films and displayed good mechanical properties. When the mechanical hysteresis and set behavior of the silicone-urea copolymers with similar hard segment contents (around 7.5% by weight) but based on PDMS-3K, PDMS-11K and PDMS-32K were compared, it was very clear that as the PDMS molecular weight increased, hysteresis and instantaneous set values decreased significantly. Copolymers based on the same silicone soft segment (PDMS-11K or PDMS-32K) but with different hard segment contents showed a linear increase in hysteresis and a slight decrease in the instantaneous set as a function of hard segment content. Constant initial stress creep experiments also showed lower creep as the PDMS segment molecular weight increased for copolymers with similar urea contents. Since the critical entanglement molecular weight ( $M_e$ ) of PDMS is stated to be 24,500 g/mol, our results tend to suggest important contribution of chain entanglements on the hysteresis and instantaneous set of these silicone-urea copolymers.

© 2010 Elsevier Ltd. All rights reserved.

## 1. Introduction

Thermoplastic silicone-urea copolymers (TPSU), which combine very nonpolar polydimethylsiloxane (PDMS) soft segments with highly polar urea hard segments display interesting physico-chemical properties. Synthesis and structure–property behavior of silicone-urea copolymers have been extensively investigated since their discovery in the early 1980s [1–10]. The unique combination of properties displayed by TPSU copolymers is due to the very different chemical nature and characteristics of the PDMS and urea segments. These include an extremely low glass transition temperature, good oxidative and thermal stabilities, water repellency, physiological inertness and high gas permeability characteristics gained from the PDMS soft segment. Meanwhile, the high cohesiveness induced by the bidentate hydrogen bonding of the urea based hard segments promote enhanced tensile strength but can still allow melt processability at low urea contents. Due to substantial differences between the solubility parameters of PDMS and urea hard segments, which are 15.6 and 45.6  $(\text{J}/\text{cm}^3)^{1/2}$  respectively [11,12], even at very low hard segment contents,

silicone-urea copolymers display the presence of a microphase morphology. Similar to the soft segment molecular weights in conventional polyether and polyester based TPUs; comparable PDMS soft segments in the preparation of silicone-urea copolymers also have  $\langle M_n \rangle$  values in the range of 1000–5000 g/mol [1–10].

In our earlier publications we reported on the influence of PDMS molecular weight and urea hard segment content on the tensile behavior of silicone-urethane and silicone-urea copolymers [13,14]. Very interestingly and somewhat surprisingly, we found out that at identical hard segment contents, silicone-urea copolymers based on PDMS-32K displayed at least a 40% higher tensile strength as well as a higher elongation at break when compared with copolymers based on PDMS-11K [14]. The critical entanglement molecular weight ( $M_e$ ) of PDMS is reported to be 24,500 g/mol [15,16]. As a result we proposed that the difference in tensile behavior was due to the synergistic influence of the entanglements in PDMS soft segment on the mechanical behavior [14]. In fact, this proposal is in line with the early work of Tong and Jerome [17] who had reached a similar conclusion for classical ABA triblock copolymers such as the SBS type but where the center elastomeric block was kept at nearly the same volume content but was varied in chemistry to, in turn, vary the molecular weight between entanglements of this center block accordingly.

\* Corresponding author. Tel.: +90 212 338 1418; fax: +90 212 338 1559.  
E-mail address: [iyilgor@ku.edu.tr](mailto:iyilgor@ku.edu.tr) (I. Yilgor).

**Table 1**

Average molecular weights of aminopropyl terminated telechelic PDMS obtained from their end group titrations and GPC measurements.

	$\langle M_n \rangle$ titration (g/mol)	$\langle M_w \rangle^a$ (g/mol)	$\langle M_n \rangle$ GPC (g/mol)	$\langle M_w \rangle$ GPC (g/mol)	$\langle M_w \rangle / \langle M_n \rangle$ GPC
PDMS-3K	3200	5000	3700	5750	1.56
PDMS-11K	10,800	17,200	13,300	21,200	1.59
PDMS-32K	31,500	50,400	34,600	55,300	1.60

<sup>a</sup> Obtained by using  $\langle M_n \rangle$  from titration and  $\langle M_w \rangle / \langle M_n \rangle$  from GPC.

In the present study we investigated the influence of average PDMS molecular weight ( $\langle M_n \rangle = 3200, 10,800$  and  $31,500$  g/mol) and urea hard segment content (2.0–14.4% by weight) on the hysteresis, instantaneous set and constant initial stress creep behavior of selected thermoplastic silicone-urea copolymers. Aminopropyl terminated telechelic PDMS soft segments used in this study were obtained by equilibration reactions and therefore exhibit a normal size distribution [18,19]. To our knowledge there are no detailed reports in the open literature where the effect of soft segment entanglements on the hysteresis and set behavior of segmented copolymers was investigated. Cooper[20] discussed the effect of PEO soft segment molecular weight (830–3000 g/mol) on microphase separation and melt rheology of polyurethanes. Gaymans also reported the influence of PPO molecular weight (1000–4000 g/mol) [21] and PTMO molecular weight [22] on the microphase separation and thermal and mechanical properties of segmented polyamides, which also included data on hysteresis and compression set behavior. However, the molecular weights of the PPO and PTMO oligomers used were below  $M_c$ . We believe silicone-urea copolymers are excellent models for the investigation of the effect of soft segment entanglements on the hysteresis behavior. As stated above, that belief extends from the fact that there are no significant intermolecular interactions between the PDMS soft segments and the urea hard segments in these systems which, in turn, promote good microphase separation of the hard and soft segments in these materials [23].

## 2. Experimental

### 2.1. Materials

$\alpha, \omega$ -Aminopropyl terminated polydimethylsiloxanes were kindly supplied by Wacker Chemie, Munich, Germany. Number average molecular weights were determined by end group titration in isopropanol with standard HCl using bromophenol blue indicator. Bis(4-isocyanatocyclohexyl)methane (HMDI) was kindly

supplied by Bayer, Germany, which had a purity better than 99.5% as determined by the dibutylamine back titration. Chain extenders 2-methyl-1,5-diaminopentane (Dytek A, DY) (DuPont) and ethylene diamine (ED) (Aldrich) and reagent grade reaction solvents, isopropyl alcohol (IPA) (Merck) and tetrahydrofuran (THF) (Merck) were all used as received.

### 2.2. Segmented copolymer synthesis

Polymerization reactions were carried out in three-neck, round bottom, Pyrex reaction flasks equipped with an overhead stirrer and an addition funnel. All reactions were carried out in THF/IPA (50/50 by volume) solution, at room temperature using the “pre-polymer” method. A detailed description of the polymerization reactions is provided in earlier publications [8,14].

### 2.3. Characterization methods

Gel permeation chromatography studies were performed on a Shimadzu LC20-A system equipped with a  $8 \times 50$  mm precolumn and 50,  $10^2$ ,  $10^3$ ,  $10^4$ , and  $10^5$  Å SDV columns (from Polymer Standards Service) and a refractive index detector. Measurements were made in a THF solution at 30 °C, with a flow rate of 1.0 mL/min. Polystyrene standards with  $\langle M_n \rangle$  values in 1000–1,000,000 g/mol were used for calibration. Aminopropyl terminated PDMS oligomers were end capped with cyclohexylisocyanate in order to prevent adsorption of amine end groups onto the columns. Table 1 provides the molecular weight data obtained from the end group titration and GPC measurements on PDMS oligomers.

Stress-strain and hysteresis tests were performed on an Instron model 4411 tester, controlled by Series IX software. Polymer films with final thicknesses of 0.3–0.5 mm were cast into Teflon molds from solution (THF/IPA; 50/50 by volume) and kept at room temperature overnight to slowly evaporate the solvent. Then they were transferred into a 50 °C air oven and kept there until the solvent is completely evaporated and the films reached a constant weight. Dog-bone shaped specimens (ASTM D 1708) were cut from these films. Original sample length ( $L_0$ ) was 25.0 mm and samples were stretched and released with a 25.0 mm/min crosshead speed.

The ten-cycle hysteresis behaviors of silicone-urea copolymers were investigated by stretching them to 200 or 300% elongation and immediately releasing (unloading) them with the same crosshead rate of 25.0 mm/min which represents 100% elongation per minute based on the initial undeformed sample length. Consecutive hysteresis cycles were initiated after the crosshead returned to the original starting position. As a result there was an extremely short relaxation time between cycles. Tests were

**Table 2**

Chemical composition and GPC molecular weights of the silicone-urea copolymers.

Polymer Code	PDMS $\langle M_n \rangle$ (g/mol)	Chain Extender (CE)	Molar Ratio <sup>a</sup>	Hard segment (wt%)	$\langle M_n \rangle$ (g/mol) <sup>b</sup>	$\langle M_w \rangle$ (g/mol) <sup>c</sup>
PSU-3-7.6	3200	–	1/1/0	7.57	$4.6 \times 10^4$	$8.2 \times 10^4$
PSU-11-DY-5.1	10,800	DY	1/2/1	5.12	$1.5 \times 10^5$	$2.6 \times 10^5$
PSU-11-ED-7.8	10,800	ED	1/3/2	7.75	$2.0 \times 10^5$	$3.6 \times 10^5$
PSU-11-DY-9.7	10,800	DY	1/3.4/2.4	9.67	$1.2 \times 10^5$	$1.9 \times 10^5$
PSU-11-DY-11.4	10,800	DY	1/4/3	11.4	–	–
PSU-11-DY-14.4	10,800	DY	1/5/4	14.4	–	–
PSU-32-ED-2.8	31,500	ED	1/3/2	2.80	$3.2 \times 10^5$	$5.7 \times 10^5$
PSU-32-ED-3.7	31,500	ED	1/4/3	3.73	$2.1 \times 10^5$	$3.4 \times 10^5$
PSU-32-ED-4.7	31,500	ED	1/5/4	4.70	–	–
PSU-32-DY-2.0	31,500	DY	1/2/1	1.99	$4.1 \times 10^5$	$6.8 \times 10^5$
PSU-32-DY-5.3	31,500	DY	1/5/4	5.34	$3.7 \times 10^5$	$6.1 \times 10^5$
PSU-32-DY-7.4	31,500	DY	1/7/6	7.35	–	–

<sup>a</sup> Molar ratio of [PDMS]/[HMDI]/[CE].

<sup>b</sup> Obtained from reaction stoichiometry.

<sup>c</sup> Obtained from GPC.

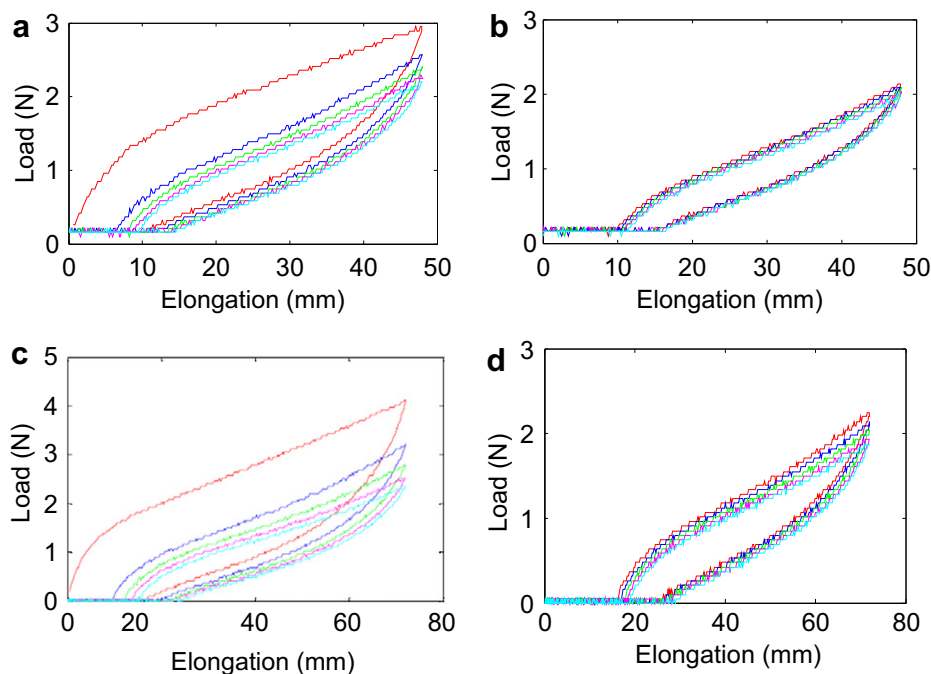


**Fig. 1.** 200% and 300% Hysteresis curves for PSU-3-7.6 (a) 200% hysteresis cycles 1–5, (b) 200% hysteresis cycles 6–10, (c) 300% hysteresis cycles (1–5), (d) 300% hysteresis cycles (6–10).

conducted at room temperature and for each segmented copolymer at least three specimens were tested.

Constant *initial* stress creep tests were performed at room temperature. A dog-bone shaped specimen (ASTM D 1708) was attached to the upper grip of the Instron 4411 tester. A constant weight was applied to the lower end of the hanging dog-bone specimen with a metal grip. Depending on the thickness of the sample different precise loads were applied in order to promote an equivalent stress at the beginning of the test for each sample. The load was applied very quickly but gently. A ruler was attached to the apparatus to measure the extension of the specimen with time for up to 120 h. The initial length of the specimen was 25.0 mm. Two replicates were tested for each initial stress level.

### 3. Results and discussion

As stated in the introduction section, our goals in this study were to investigate the influence of: (i) the PDMS soft segment molecular weight ( $\langle M_n \rangle = 3200, 10,800, 31,500$ ;  $\langle M_w \rangle = 5000, 17,200$  and  $50,400$  g/mol), (ii) the urea hard segment content (2.0–14.4% by weight), and (iii) chain extender structure (ethylene diamine and 2-methyl-1,5-diaminopentane) on the hysteresis and instantaneous set behaviors of selected silicone-urea copolymers.

At this point it is important to note that the critical entanglement molecular weight, which is obtained from conventional melt rheology studies, correlates well with the weight average molecular weight of polymers  $\langle M_w \rangle$ . Functionally terminated PDMS soft segments used in this study were obtained by equilibration reactions and therefore exhibit a normal size distribution [18,19]. As explained in detail in the experimental section and in Table 1, using the molecular weight distribution values ( $\langle M_w \rangle / \langle M_n \rangle$ ) obtained from gel permeation chromatography studies and absolute  $\langle M_n \rangle$  values obtained from the end group analysis,  $\langle M_w \rangle$  values of PDMS-3K, PDMS-11K and PDMS-32K were calculated to be 5000, 17,200 and 50,400 g/mol respectively, which match very well with the GPC data. This means that only PDMS-32K is distinctly above

the critical value of ( $M_e$ ) while PDMS-11K displays a slightly lower  $\langle M_w \rangle$  value than  $M_e$  and PDMS-3K is well below it [15,16].

Table 2 gives the list of silicone-urea copolymers prepared by using aminopropyl terminated PDMS with different molecular weights, HMDI and ED or DY chain extenders and their chemical compositions. The sample abbreviations used to identify the copolymers were as follows: PSU indicates the silicone-urea copolymer; the following number indicates the  $\langle M_n \rangle$  value of PDMS in kg/mole; which is again followed by two letters (ED or DY) which indicate the specific chain extender used. The final numbers indicate the urea hard segment content of the copolymer in weight percent. For example, a PDMS-32K, HMDI and ED based silicone-urea copolymer with 3.73% by weight hard segment content is therefore coded as: PSU-32-ED-3.7. No chain extender was used in PSU-3-7.6.

In spite of their very low hard segment contents, all silicone-urea copolymers listed on Table 2, formed clear, non-tacky, elastomeric films with reasonably good ultimate tensile strengths. A detailed report on the composition dependent thermomechanical (DMA) behavior and tensile properties (excluding hysteresis and set behavior) of these copolymers has already been published [14].

#### 3.1. Influence of the PDMS molecular weight on the hysteresis behavior of silicone-urea copolymers

Prior to providing the hysteresis data it might be stated that the hysteresis behavior of elastomers, whether they are crosslinked or thermoplastic, plays an important role in their commercial applications. Tensile hysteresis results from the energy losses that occur

**Table 3**  
Ten-cycle, 200% hysteresis and instantaneous set behavior of PSU-3-7.6.

Cycles	Percent hysteresis after each cycle									
	1	2	3	4	5	6	7	8	9	10
200% deformation	54	38	36	35	34	33	33	32	32	31
300% deformation	60	47	46	45	45	45	45	44	44	44

in polymers when they are repeatedly stretched and released. Hysteresis depends on the rate, temperature, amount and number of extension cycles applied. During the stretching process the equilibrium structure or morphology of the polymer is often distinctly changed or destroyed thereby causing a major difference in the hysteresis behavior of the first versus the second or any later deformation cycle. Upon removal of the load, which usually is fast following stretching, the polymer chains generally do not

behavior of a silicone-urea copolymer (PSU-3-7.6) based on a PDMS soft segment with  $\langle M_n \rangle = 3200$  g/mol. The 200% hysteresis curves for PSU-3-7.6 are provided on Fig. 1a (cycles 1–5) and Fig. 1b (cycles 6–10), whereas the 300% hysteresis curves are reproduced in Fig. 1c (cycles 1–5) and Fig. 1d (cycles 6–10). The percent hysteresis values, as determined for the respective loading-unloading curves were calculated by using Eq. (1), given below, are provided in Table 3:

$$\% \text{ Hysteresis} = \frac{\text{Area under the loading curve} - \text{Area under the recovery curve}}{\text{Area under the loading curve}} \times 100 \quad (1)$$

completely regain their original configurations. This leads to an energy loss, which is also termed as tensile or mechanical hysteresis. High hysteresis can lead to a large temperature increase in polymers (particularly in cyclic deformation) since the dissipated mechanical energy is converted to heat. Tensile hysteresis of conventional TPUs is fairly high, which leads to heat build-up in the cyclic loading of the materials and can limit their applications. In such segmented copolymers hysteresis partially arises from the disruption of the hard segment organization of the microphase morphology which is often due to the partial destruction of intermolecular hydrogen bonding and hard segment domain disruption. The tensile hysteresis in TPUs is therefore often reported to be a function of the microphase morphology, hard segment type and content, domain ductility, extent of mixing between hard and soft segments and nature of the interfacial region between soft and hard segments [24]. In general, and not surprisingly, chemically crosslinked elastomers typically display lower hysteresis values when compared with thermoplastic elastomers [25]. This is understandable since it is more difficult to alter a chemical network system consisting of covalent crosslinks, when compared to a physical network in a microphase separated thermoplastic elastomer.

In the present study the ten-cycle hysteresis behavior of silicone-urea copolymers were investigated as stated earlier by stretching them ten times to 200% and 300% elongation and unloading at the same crosshead speed for 10 cycles. Since all of the PDMS-10,800 based silicone-urea copolymers failed before reaching 300% elongation [14], their hysteresis and set behaviors (for each loading cycle) were only investigated at 200% elongation and compared with PDMS-3K and PDMS-32K based copolymers.

### 3.1.1. Hysteresis behavior of copolymer based on PDMS-3K at 200% and 300% deformation

As stated in the introduction, segmented thermoplastic polyurethanes and polyureas are typically prepared from soft segments with  $\langle M_n \rangle$  values in the 1000–5000 g/mol range. Therefore, in this study, as a reference/comparison, we investigated the hysteresis

As shown in Fig. 1a,c and Table 3, PSU-3-7.6 displays quite high hysteresis during the first few cycles for both the 200 and 300% deformation and also fairly high hysteresis in the subsequent cycles, as indicated by the relatively large areas associated with each cycle. As can be seen from Table 3, after 200% deformation, the first cycle hysteresis displayed by PSU-3-7.6 is 54%. As expected, in the second cycle hysteresis decreases substantially to 38% and this trend is followed until the tenth cycle, where the hysteresis goes down to 31%. At 300% elongation the hysteresis after the first cycle is 60%, higher than the first cycle hysteresis for 200% elongation which is expected. In the subsequent cycles the hysteresis slowly goes down to 44% after 10 cycles. As expected in each cycle the 300% hysteresis is much higher than the corresponding same cycle hysteresis observed at 200% deformation.

High first cycle hysteresis in PSU-3-7.6 clearly indicates a major reorganization in the microphase morphology of this thermoplastic elastomer upon 200 or 300% stretching. Based on their modulus-temperature behavior it is expected that silicone-urea copolymers even with fairly low hard segment contents display microphase morphologies, where strongly hydrogen bonded urea hard segments are dispersed in a continuous PDMS matrix [14]. The hydrogen bonding between urea groups, as mentioned earlier, is reported to be bidentate in nature [26].

We believe such a high hysteresis in PSU-3-7.6 silicone-urea segmented copolymer is mainly due to the weakening and/or disruption of the bidentate hydrogen bonding in the hard segment domains. This arises due to poorer microphase separation in this system due to low PDMS molecular weight of the soft segments and very short hard segment lengths as well. Furthermore, due to short soft segment lengths, the soft segment extensibility is also limited.

### 3.1.2. 200% hysteresis behavior of copolymers based on PDMS-11K and PDMS-32K with similar hard segment contents

Hysteresis curves for PSU-11-ED-7.8 copolymer are provided in Fig. 2a and b. Similarly, the hysteresis curves for the PDMS-32K based silicone-urea copolymer with hard segment content of 7.4%

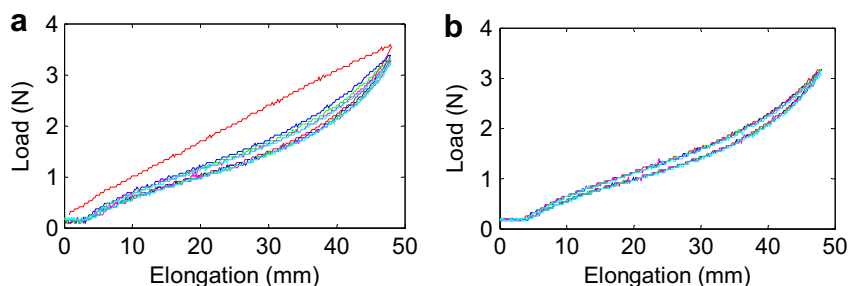


Fig. 2. 200% hysteresis curves for PSU-11-ED-7.8 copolymer. (a) Cycles 1–5 and (b) Cycles 6–10.



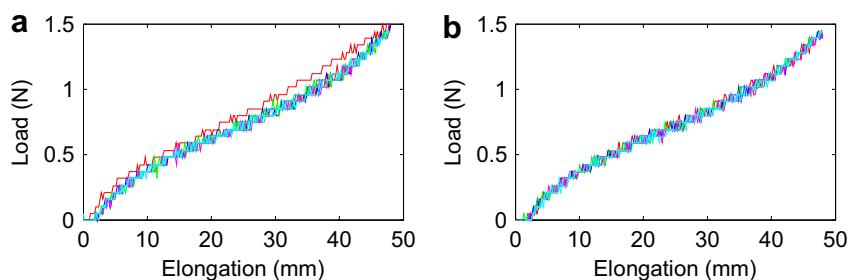


Fig. 3. 200% hysteresis curves for PSU-32-DY-7.4 copolymer. (a) Cycles 1–5 and (b) Cycles 6–10.

(PSU-32-DY-7.4) are reproduced in Fig. 3a and b. The hysteresis values calculated for PSU-11-ED-7.8 and PSU-32-DY-7.4 together with those of PSU-3-7.6 are provided in Table 4 for comparison. Curves provided in Figs. 2 and 3 and the results reported in Table 4 clearly show major differences in the hysteresis behavior of the silicone-urea copolymers with similar hard segment contents but based on different molecular weight PDMS. It is very clear that as the PDMS soft segment molecular weight increases, a dramatic reduction in the hysteresis values of the copolymer is observed. Hysteresis after the first cycle for PDMS-3K, PDMS-11K and PDMS-32K based homologous silicone-urea copolymers are 54, 31 and 11% respectively. Second cycle hysteresis values are significantly lower for PSU-11-ED-7.8 and PSU-32-DY-7.4, which are 13 and 4% respectively. The hysteresis values become smaller after each cycle for both copolymers until the tenth cycle. Fig. 4 graphically shows the dramatic difference between the hysteresis behaviors of silicone-urea copolymers based on PDMS-3K, PDMS-11K and PDMS-32K with similar hard segment contents.

Considering the dramatic downward trend in the hysteresis of silicone-urea copolymers with similar hard segment contents but different PDMS molecular weights, there seems to be a substantial influence of the average PDMS segment molecular weight on hysteresis. It is important to restate that the critical entanglement molecular weight ( $M_e$ ) of PDMS is reported to be 24,500 g/mol [15,16]. Therefore, one may certainly consider that soft segment entanglements in PDMS-32K, which has an  $\langle M_w \rangle$  value of 50,400 g/mol, which distinctly exceeds ( $M_e$ ), may be contributing substantially to lowering the hysteresis in thermoplastic silicone-urea copolymers. As stated earlier, in an earlier publication we demonstrated that there also is a strong contribution from soft segment entanglement on the tensile strengths of silicone-urea copolymers [14].

Another factor that needs to be considered in the hysteresis behavior is the microphase morphologies of the silicone-urea copolymers with similar hard segment contents based on the different PDMS soft segment molecular weights. In this regard Table 5 provides the average molecular weights and average number of repeat units in the urea hard segments in silicone-urea copolymers, calculated from the reaction stoichiometry. In these calculations aminopropyl chain ends of the PDMS oligomers are also considered to be a part of the hard segment. Since PSU-3-7.6 is prepared by a stoichiometric reaction between PDMS-3K and

HMDI, the hard segment only consists of HMDI and aminopropyl end groups of the PDMS, but has no chain extenders.

We have already discussed the morphology of silicone-urea copolymers extensively using SAXS, DMA and DSC data [9]. Due to surface coverage by PDMS caused by their low surface energy, especially when at high PDMS soft segment contents and molecular weights, it is often difficult to obtain morphological features of silicone-urea copolymers by AFM. While we do not yet have direct microscopy evidence showing any differences in the nature of the microphase morphological structure of the PSU-3-7.6 copolymer with those of PSU-11-ED-7.8 or PSU-DY-7.4, all of which have nearly identical hard segment contents, it is clear that there must be a major difference in view of the difference in the mechanical behavior of the latter two from the former material. However, if we tentatively assume that the low molecular weight soft segment system PSU-3-7.6 has a more percolated or interconnected hard segment texture and that the other two much longer soft segment systems possess a more particulate or dispersed hard segment domain texture, the major difference in the hysteresis behavior of these copolymers might well be explainable. We make this argument on the basis of an earlier study [27], where we showed by use of AFM that when very nonpolar and low molecular weight ( $\langle M_n \rangle = 3340$  g/mol) soft segment of poly(ethylene-butylene) was used instead of PDMS, the morphology by AFM led to a considerably interconnected, thread-like hard segment phase. In this copolymer, the hard segment content was also low (7.8% by weight) and the hard segment was based on HDI and DY or ED, which is fairly similar to what has been used in this study. This thread-like textured system displayed considerable instantaneous hysteresis due to the breaking of the hard segment microphase interconnections but, if given enough time, it would recover/heal well. If the

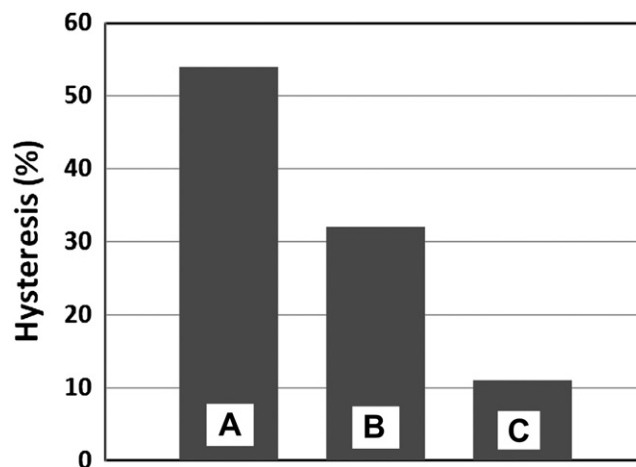


Fig. 4. Effect of PDMS molecular weight on the first cycle, 200% hysteresis behavior of homologous silicone-urea copolymers. (A) PSU-3-7.6, (B) PSU-11-ED-7.8, (C) PSU-32-DY-7.4.

Table 4  
Influence of PDMS molecular weight on 200% hysteresis behavior of homologous silicone-urea copolymers.

Cycles	Percent hysteresis after each cycle									
	1	2	3	4	5	6	7	8	9	10
PSU-3-7.6	54	38	36	35	34	33	33	32	32	31
PSU-11-ED-7.8	32	13	11	10	10	9	9	9	9	9
PSU-32-DY-7.4	11	4	4	4	4	4	4	3	3	3

**Table 5**

Average PDMS soft segment and hard segment molecular weight in the silicone-urea copolymers ( $n$ ) is the average (HMDI-CE) $_n$  repeat unit in urea hard segments (CE, chain extender).

Polymer code	Hard segment (wt %)	Stoichiometry [PDMS]/[HMDI]/[CE]	Hard segment ( $M_n$ ) (g/mol)	Average HS Repeat unit ( $n$ )
PSU-3-7.6	7.57	1/1/0	380	1
PSU-11-ED-7.8	7.75	1/3/2	1023	2
PSU-32-DY-7.4	7.35	1/7/6	2650	6

hard segment texture had initially been of a particulate type, which we hypothesize is the case for the longer soft segment materials but of comparable hard segment contents, we would anticipate less instantaneous hysteresis. We are therefore hoping to verify this in the future using AFM for the PDMS based materials in the present study.

As shown in Table 5, the lengths of the urea hard segments are dramatically different in this series of silicone-urea copolymers. Due to strong microphase separation in silicone-urea copolymers and bidentate hydrogen bonding between urea groups, one would expect the formation of a greater amount of hydrogen bonding in urea hard segments as the hard segment length is increased. It is also expected that much higher energy will be needed to deform or rupture such a strongly hydrogen bonded physical network, which may help to explain the dramatic reduction in the hysteresis in silicone-urea copolymers with high molecular weight PDMS soft segments and longer urea hard segments. However, in our discussions later on in the paper, where we will investigate the effect of hard segment content on the hysteresis behavior of silicone-urea copolymers with identical PDMS soft segment molecular weights, it will become clear that this assumption does not seem to be correct.

### 3.1.3. Effect of hard segment content on 200% hysteresis behavior of copolymers based on PDMS-11K

In order to understand the influence of urea hard segment content on the hysteresis behavior of silicone-urea copolymers, various PDMS-11K based copolymers with different hard segment contents were also investigated. These copolymers are designated PSU-11-ED-7.8, PSU-11-DY-9.7 and PSU-11-DY-11.4 respectively. Hysteresis curves for the former polymer were already provided in Fig. 2. The hysteresis curves (first 5 cycles) for the latter two copolymers are reproduced in Fig. 5. The hysteresis values calculated for these copolymers after various cycles are provided in Table 6, which clearly shows that as the hard segment content of the copolymer increases, the hysteresis also increases *but only very slowly*. This result strongly suggests that the average length of the hard segment is therefore not a very critical factor with respect to the hysteresis behavior – at least in the range we address in this report. Fig. 6 provides the hysteresis after the first cycle as a function

**Table 6**

Influence of hard segment content on hysteresis behavior of thermoplastic silicone-urea copolymers based on PDMS-11K (200%, 10 cycles).

Cycles	Percent hysteresis after each cycle									
	1	2	3	4	5	6	7	8	9	10
PSU-11-ED-7.8	32	13	11	10	10	9	9	9	9	9
PSU-11-DY-9.7	32	14	12	11	11	10	10	10	10	10
PSU-11-DY-11.4	34	14	12	11	11	10	10	10	10	10

of the urea hard segment content for the same copolymers. There seems to be a linear relationship with a positive slope, between the hard segment content and the first cycle hysteresis for these copolymers. (Note: We rounded the hysteresis values to integer numbers. Actual values used in the plot are: 31.6; 32.2; 34.4).

### 3.1.4. Effect of hard segment content on the 300% hysteresis behavior of copolymers based on PDMS-32K

In order to further investigate the effect of hard segment content on the hysteresis behavior, a series of PDMS-32K based silicone-urea copolymers with fairly low hard segment contents were evaluated. In this study 300%, ten-cycle hysteresis behavior of PSU-32-ED-2.8, PSU-32-ED-3.7 and PSU-32-ED-4.7 was investigated. The hysteresis curves obtained are reproduced in Figs. 7 and 8. A summary of the hysteresis results are provided on Table 7. Similar to the results observed for the 200% hysteresis data tabulated on Table 6 for the PDMS-11K based copolymers, the percent hysteresis seems to increase linearly but *only slightly* with the hard segment content (and this average HS length) for PDMS-32K based silicone-urea copolymers (Table 7).

Fig. 9 provides a plot of the percent hysteresis after the first cycle as a function of the hard segment content for PDMS-32K based silicone-urea copolymers. As can clearly be seen in Fig. 9, the hysteresis after the first cycle increases linearly with the hard segment content of the copolymer. These results indicate that during the 300% deformation process (stretching and release cycle) the energy dissipated increases linearly with increasing hard segment content. Or from a different perspective, they also may indicate that upon unloading, the PDMS-32K based silicone-urea copolymers with lower hard segment contents recover more rapidly suggesting their morphological structure is less altered by the prior deformation.

### 3.2. Influence of the chain extender structure on the hysteresis behavior of silicone-urea copolymers

As we have reported earlier [14] structure of the chain extender employed (ethylene diamine (ED) and 2-methyl-1,5-diaminopentane (DY)) do not seem to have any noticeable influence on the tensile properties of silicone-urea copolymers with low hard segment contents. Similarly, the chemical structure of the low

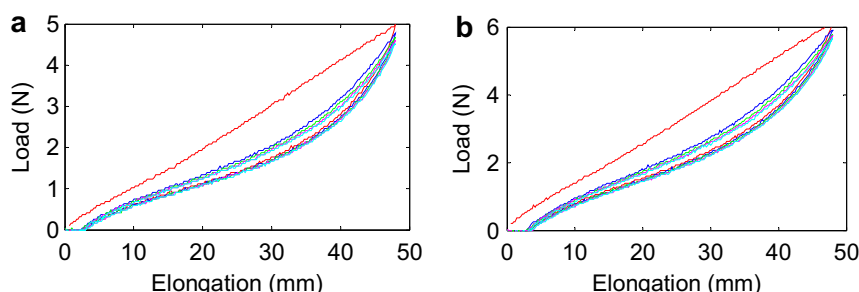


Fig. 5. 200%, 5 cycle hysteresis curves for (a) PSU-11-DY-9.7 and (b) PSU-11-DY-11.4.

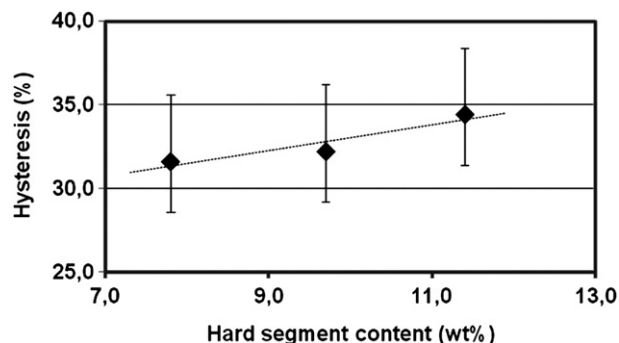


Fig. 6. Influence of hard segment content on 200% hysteresis behavior of PDMS-11K based silicone-urea copolymers after the first cycle.

molecular weight diamine chain extender employed (ED or DY) does not seem to have a significant role on the hysteresis behaviors of silicone-urea copolymers investigated in this study. Hysteresis results provided on Tables 4, 6 and 8, based on different chain extenders seem to follow the same trend. A more detailed study is underway to further investigate the effect of chain extender structure on the hysteresis behaviors of silicone-urea copolymers.

### 3.2.1. Instantaneous set behavior of thermoplastic silicone-urea copolymers

In addition to the tensile strength and hysteresis behavior, other important application parameters for crosslinked rubbers and thermoplastic elastomers are the compression set, instantaneous set and permanent set values. The “set” behavior of a rubber is related to its recovery of the original dimensions after being subjected to a deformation. As is well documented in the literature, and as we have demonstrated for the tensile behavior for the silicone-urea copolymers in this study, when an elastomer is stretched and released it typically does not return to its exact original length. Depending on its structure, after the stretch–release cycle its length is somewhat longer than its original length before stretching. The increase in length of the elastomer sample is usually termed as the

“set”. Set can be divided into two categories, which are the “instantaneous set” and the “permanent set”. Instantaneous set can be defined as the extent (percent) of deformation in length displayed by a sample immediately after deformation and release. If a deformed elastomer sample that has undergone release is left as is, it generally recovers further over time and reaches a constant length at equilibrium, which is often still higher than its original length. “Permanent set” can be defined as the extent (percent) of permanent deformation displayed by the sample at equilibrium, compared to its original length. Similarly “compression set” can be defined as the extent (percent) of deformation experienced by an elastomer subjected to a compressive load for a fixed period of time. It might also be mentioned that the difference between permanent set and instantaneous set is also greatly dependent on the sample’s temperature relative to the  $T_g$  of the elastomeric matrix but we have not addressed this variable in this study for in practical applications of PDMS based elastomers, one is typically well above the  $T_g$  of this segment so that there is considerable soft segment mobility due to the very good microphase separation that occurs in these systems.

Instantaneous set values can be determined by comparing the sample length ( $L$ ) immediately after each reloading cycle with the original length before stretching ( $L_0$ ). Instantaneous set values are calculated by using the Eq. (2), where  $L_0 = 25.0$  mm in our experiments.

$$\text{Instantaneous set} = (L - L_0) \times 100/L_0 \quad (2)$$

Instantaneous set values for the silicone-urea copolymers after 200% and 300% deformation are tabulated in Tables 8 and 9, respectively. These results clearly show that in addition to high hysteresis, PSU-3-7.6 also shows very high instantaneous set values after 200% and 300% deformation, which is calculated to be 42% and 71% respectively after the first cycle. It increases after each subsequent cycle and reaches 70% (for 200% elongation) and 120% (for 300% elongation) after the tenth cycle. The instantaneous set behavior of PSU-3-7.6 is comparable to those of non-chain extended polyether based polyureas [28]. On the other hand PSU-11-ED-7.8, which has a very similar hard segment content as

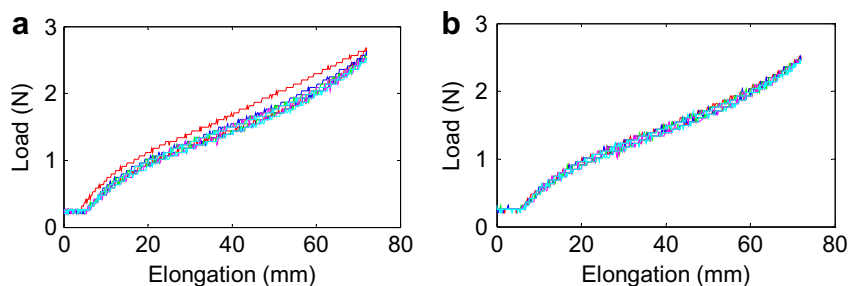


Fig. 7. 300% hysteresis curves for PSU-32-ED-2.8 copolymer (a) Cycles 1–5 and (b) Cycles 6–10.

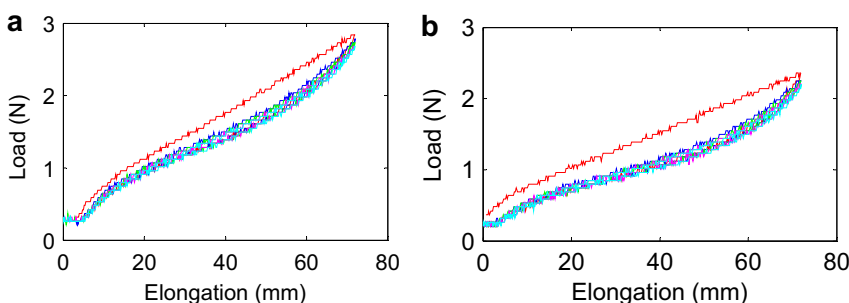


Fig. 8. 300%, 5 cycle hysteresis curves for (a) PSU-32-ED-3.7 and (b) PSU-32-ED-4.7.

**Table 7**

Effect of hard segment content on the hysteresis behaviors of homologous silicone-urea copolymers based on PDMS-32K (300% elongation).

Cycles	Hysteresis after cycles (%)									
	1	2	3	4	5	6	7	8	9	10
PSU-32-ED-2.8	12	6	6	5	5	5	5	5	5	5
PSU-32-ED-3.7	19	8	6	6	6	6	6	6	5	5
PSU-32-ED-4.7	26	8	6	6	6	6	6	5	5	5

that of PSU-3-7.6, but based on PDMS-11K, shows a much smaller instantaneous set value of only 14% after the first cycle at 200% elongation. Compared to the original length, the set values for PSU-11-ED-7.8 increase only fairly slowly after each cycle and reaches 17% after the 10th cycle, which is substantially smaller when compared to 70.0% set for PSU-3-7.6 at 200% elongation.

More interestingly, the homologous silicone-urea copolymer based on PDMS-32K (PSU-32-DY-7.4) strikingly displays a very small instantaneous set value of only 4% after the first cycle and only 7% after the 10th cycle (Table 8). All of these results clearly show the dramatic effect of PDMS soft segment molecular weight on the instantaneous set behavior of these segmented silicone-urea copolymers. Similar to the hysteresis behavior discussed earlier, as the PDMS molecular weight increases, correspondingly instantaneous set values decrease dramatically.

Data provided in Tables 8 and 9 also provide a clear picture on the effect of the urea hard segment content on the instantaneous set behavior of silicone-urea copolymers based on identical PDMS soft segments. Finally, Table 8 provides percent instantaneous set values for PDMS-11K based silicone-urea copolymers with 7.8, 9.7 and 11.4% hard segment contents at 200% elongation. As shown on Table 8, instantaneous set values become smaller with an increase in the hard segment content of the copolymer. Similar behavior is observed for PDMS-32K based silicone-urea copolymers at 300% elongation, as shown on Table 9. Interestingly, this is just the opposite behavior when compared to the hysteresis behaviors of these copolymers, where the hysteresis values displayed a slight increase as a function of the hard segment content, as shown on Figs. 6 and 9. Fig. 10 shows the effect of PDMS molecular weight on the set behavior of silicone-urea copolymers with identical hard segment contents after the first cycle at 200% elongation. As the PDMS molecular weight increases, instantaneous set decreases dramatically from 42% for PSU-3-7.6 to 4% for PSU-32-DY-7.4.

### 3.3. Effect of PDMS molecular weight and urea hard segment content on constant initial stress creep behavior for the silicone-urea copolymers investigated

When a polymeric material is subjected to an initial constant stress, it deforms quickly to a strain roughly predicted by its stress-

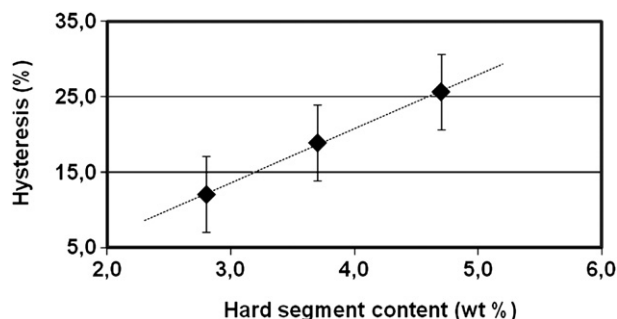


Fig. 9. Tensile hysteresis after the first cycle as a function of the urea hard segment content of silicone-urea copolymers based on PDMS-32K.

**Table 8**

Instantaneous set behaviors of silicone-urea copolymers (200% elongation).

Cycle	Percent instantaneous set after each cycle									
	1	2	3	4	5	6	7	8	9	10
PSU-3-7.6	42	50	56	59	62	63	65	67	68	70
PSU-11-ED-7.8	14	15	15	16	16	16	16	17	17	17
PSU-11-DY-9.7	12	13	13	13	13	14	14	14	14	14
PSU-11-DY-11.4	10	10	11	11	11	11	11	12	12	12
PSU-32-DY-7.4	4	5	5	6	6	6	7	7	7	7

strain modulus and then continues to deform slowly with time. This phenomenon of time dependent deformation now under constant load is denoted as creep [25]. At higher loads and longer times, the polymer may rupture, whereas at a low enough load and time, failure may never occur. It is well recognized that the creep behavior of elastomers (thermoplastic or crosslinked) can play an important role in their applications. The extent of creep depends on several factors, such as; the magnitude of the initial stress applied, loading time, temperature, chemical structure, morphology and topology (i.e., uncross-linked versus crosslinked) of the polymer. In this study the creep behavior of silicone-urea copolymers with similar compositions but based on PDMS segments with quite different molecular weights were investigated – each creep test being initiated at an equivalent initial stress. Time dependent creep curves for PSU-3-7.6, PSU-11-ED-7.8 and PSU-32-DY-7.4 initiated at a constant initial stress ( $\sigma = 1.30$  MPa) are reproduced in Fig. 11. Original lengths of all samples were 25.0 mm.

It is interesting to note in Fig. 11 that after the creep experiment is initiated, the silicone-urea based on PDMS-3K shows the lowest instantaneous deformation and elongates to 31.0 mm (24% elongation) while the sample based on PDMS-11K elongates to 38.5 mm (54% elongation). The copolymer sample based on PDMS-32K, in contrast, displays the highest instantaneous deformation upon application of the initial stress and elongates to 58.0 mm (132% elongation). Very interestingly, following this fairly fast instantaneous elongation, samples based on PDMS-11K and PDMS-32K show only very slow time dependent creep (or elongation) in 24 h, increasing in length to 49.4 mm and 66.5 mm respectively and displaying 28.3% and 14.7% increase in length after the initial deformation. On the other hand, the sample based on PDMS-3K displays a fairly steady deformation and its overall length reaches to 88.0 mm after 24 h indicating 184% increase in length after initial deformation. We believe these results clearly show that for silicone-urea copolymers with similar hard segment contents as the PDMS soft segment molecular weight increases creep decreases substantially.

It is well known that as the crosslink density of an elastomer or hard segment content of a thermoplastic elastomer increases, the magnitude of creep typically decreases for a given initial stress [25]. The constant initial stress (0.60 MPa) creep curves for the PDMS-11K based silicone-urea copolymers with urea contents of 5.1, 7.8 and 14.4% by weight are shown in Fig. 12. As clearly seen in this figure, as the hard segment content of the copolymer increases the creep decreases dramatically.

**Table 9**

Instantaneous set behaviors of silicone-urea copolymers (300% elongation).

Cycle	Percent instantaneous set after each cycle									
	1	2	3	4	5	6	7	8	9	10
PSU-3-7.6	71	79	88	94	100	106	111	115	118	120
PSU-32-ED-2.8	8	9	9	10	10	10	11	11	11	11
PSU-32-ED-3.7	7	8	8	9	10	10	11	11	11	11
PSU-32-ED-4.7	7	7	7	8	8	9	9	9	9	9

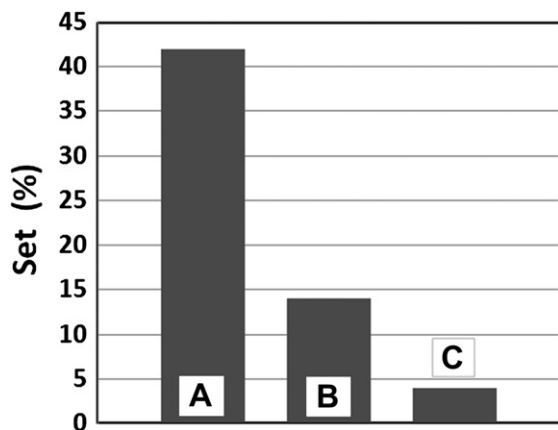


Fig. 10. Effect of PDMS molecular weight on the set behavior of silicone-urea copolymers (after first cycle, 200% elongation). (A) PSU-3-7.6, (B) PSU-11-ED-7.8, (C) PSU-32-DY-7.4.

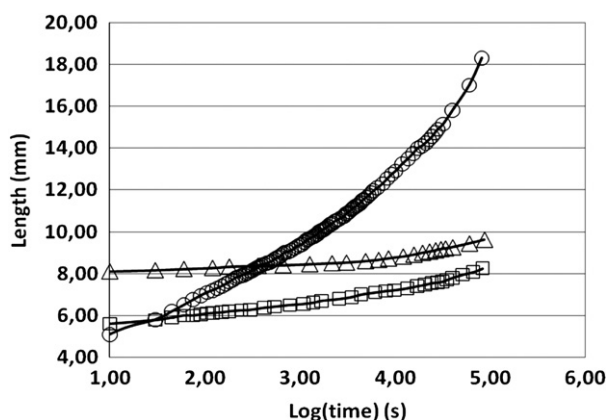


Fig. 11. Comparison of the constant initial stress creep behavior of (O) PSU-3-7.6, (Δ) PSU-32-DY-7.4 and (□) PSU-11-ED-7.8 ( $\sigma = 1.30$  MPa).

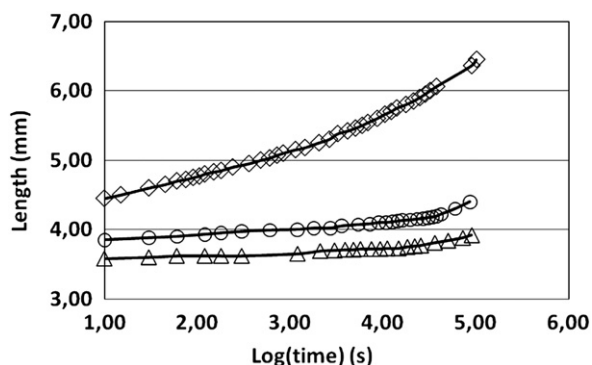


Fig. 12. Effect of the hard segment content on the constant initial stress creep behavior of silicone-urea copolymers based on PDMS-11K ( $\sigma = 0.60$  MPa). (◇) PSU-11-DY-5.1, (O) PSU-11-ED-7.8 and (Δ) PSU-11-DY-14.4.

#### 4. Conclusions

Hysteresis, instantaneous set and creep behaviors of novel thermoplastic silicone-urea copolymers based on PDMS soft segment molecular weights of ( $\langle M_n \rangle = 3200, 10,800, 31,500$  and  $\langle M_w \rangle = 5000, 17,200, 50,400$  g/mol) and fairly low urea hard segment contents of 2–14.4% by weight, were investigated. When the hysteresis and instantaneous set behavior of silicone-urea copolymers with similar hard segment contents (around 7.5% by weight) but based on PDMS-3K, PDMS-11K and PDMS-32K were

compared, it was very clear that as the PDMS molecular weight increased the hysteresis and set values decreased significantly. Copolymers based on the same PDMS soft segment (PDMS-11K or PDMS-32K) but with different hard segment content showed only a small linear increase in the hysteresis and a slight decrease in the instantaneous set as a function of hard segment content. The structure of the chain extender (ED or DY) did not seem to have a major effect on the tensile or hysteresis behavior of silicone-urea copolymers investigated.

Similarly, constant initial stress creep experiments for homologous silicone-urea copolymers indicated a decrease in the amount of creep as the molecular weight of the PDMS increased. When PDMS molecular weight was kept constant the amount of creep decreased as the hard segment content of the copolymer increased.

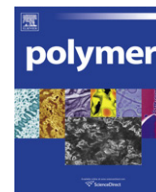
The critical entanglement molecular weight ( $M_e$ ) of PDMS is reported to be 24,500 g/mol [15,16]. ( $M_e$ ) and correlates well with ( $M_w$ ) since it is obtained from melt rheology measurements. Among the three PDMS oligomers utilized, only the  $\langle M_w \rangle$  value of PDMS-32K, which is 50,400 g/mol distinctly exceeded the ( $M_e$ ). We believe one of the most important outcomes of this study is the extremely low hysteresis and instantaneous set values displayed by PDMS-32K based silicone-urea copolymers. This we also believe clearly demonstrates the dramatic effect of soft segment entanglements on lowering the hysteresis and instantaneous set in silicone-urea copolymers.

#### Acknowledgements

We would like to thank Wacker Chemie, Munich Germany, for providing financial support to this research project. We also would like to thank them for their supply of PDMS oligomers.

#### References

- [1] Yilgor I, Riffle JS, Wilkes GL, McGrath JE. *Polym Bull* 1982;8:535–42.
- [2] Tyagi D, Yilgor I, McGrath JE, Wilkes GL. *Polymer* 1984;25(12):1807–16.
- [3] Ho T, Wynne KJ, Nissan RA. *Macromolecules* 1993;26:7029–36.
- [4] Wynne KJ, Ho T, Nissan RA, Chen X, Gardella JA. *Inorg Organomet Chem* 1994;572:64–80.
- [5] Hergenrother RW, Yu XH, Cooper SL. *Biomaterials* 1994;15(8):635–40.
- [6] Kinning DJJ. *Adhesion* 2001;75(1):1–26.
- [7] Adhikari R, Gunatillake PA, Brown MJ. *Appl Polym Sci* 2003;90:1565–73.
- [8] Yilgor E, Atilla GE, Ekin A, Kurt P, Yilgor I. *Polymer* 2003;44(26):7787–93.
- [9] Sheth JP, Aneja A, Wilkes GL, Yilgor E, Atilla GE, Yilgor I, et al. *Polymer* 2004;45(20):6919–32.
- [10] Yilgor I, Yilgor E. *Polym Rev* 2007;47(4):487–510.
- [11] Grulke EA. In: Brandrup J, Immergut EH, editors. *Polymer Handbook*. New York, NY: John Wiley; 1989. p. 519–59.
- [12] Van Krevelen DW. *Properties of polymers*. Ch. 7. Amsterdam, Netherlands: Elsevier; 1990.
- [13] Yilgor E, Yilgor I. *Polymer* 2001;42(19):7953–9.
- [14] Yilgor I, Eynur T, Yilgor E, Wilkes GL. *Polymer* 2009;50(19):4432–7.
- [15] Aharoni SM. *Macromolecules* 1986;19(2):426–34.
- [16] Zang YH, Carreau PJ. *J Appl Polym Sci* 1991;42(7):1965–8.
- [17] Tong JD, Jerome R. *Macromolecules* 2000;33(5):1479–81.
- [18] Yilgor I, McGrath JE, Krukoni VJ. *Polym Bull* 1984;12:499–506.
- [19] Chojnowski J. Ch. 1. In: Clarson SJ, Semlyen JA, editors. *Siloxane polymers*. Englewood Cliffs, NJ: Prentice Hall; 1993. p. 1–71.
- [20] Velankar S, Cooper SL. *Macromolecules* 1998;31:9181–92.
- [21] Van der Schuur M, Gaymans RJ. *J Polym Sci. Part A Polym Chem* 2006;44:4769–81.
- [22] Biemond GJE, Gaymans RJ. *J Mater Sci* 2010;45:158–67.
- [23] Yilgor E, Burgaz E, Yurtsever E, Yilgor I. *Polymer* 2000;41(3):849–57.
- [24] Bonart Macromol RJ. *Sci Phys* 1968;B2:115–38.
- [25] (a) Nielsen LE, Landel RF. *Mechanical properties of polymers and composites*. Ch 3. NY: Marcel Dekker; 1994; (b) Bauman JT. *Fatigue, stress and strain of rubber components*. Munich, Germany: Hanser Publishers; 2008; (c) Gorce JN, Hellgeth JW, Ward TC. *Polym Eng Sci* 1993;33:1170–6.
- [26] Lambila NMK, Woodhouse KA, Cooper SL. *Polyurethanes in Biomedical applications*. Ch. 4. Boca Raton, Florida: CRC Press; 1998.
- [27] Klinedinst DB, Yilgor E, Yilgor I, Beyer FL, Wilkes GL. *Polymer* 2005;46(23):10191–201.
- [28] Das S, Yilgor I, Yilgor E, Inci B, Tezgel O, Beyer FL, et al. *Polymer* 2007;48(1):290–301.



# Living/controlled hex-1-ene polymerization initiated by nickel diimine complexes activated by non-MAO cocatalysts: Kinetic and UV–vis study

Jan Peleška<sup>a</sup>, Zdeněk Hošťálek<sup>b</sup>, Darja Hasalíková<sup>b</sup>, Jan Merna<sup>b,\*</sup>

<sup>a</sup> Institute of Materials Chemistry, Brno University of Technology, Purkyňova 118, 612 00 Brno, Czech Republic

<sup>b</sup> Institute of Chemical Technology, Prague, Department of Polymers, Technická 5, 166 28 Prague 6, Czech Republic

## ARTICLE INFO

### Article history:

Received 4 August 2010

Received in revised form

16 November 2010

Accepted 18 November 2010

Available online 26 November 2010

Dedicated to Prof. Vratislav Ducháček on occasion of his 70<sup>th</sup> anniversary.

### Keywords:

Nickel catalyst

Living/controlled olefin polymerization

Non-MAO cocatalysts

## ABSTRACT

Living/controlled polymerization of hex-1-ene initiated by nickel diimine catalysts of general form  $[\text{ArN}=\text{C}(1,8\text{-naphthalenediyl})\text{C}=\text{NAr}]\text{NiBr}_2$  activated by simple organoaluminium compounds was investigated. Polyhexenes with a very narrow molar mass distribution and molar mass controlled by the monomer/initiator ratio were prepared using diethylaluminiumchloride, ethylaluminiumdichloride and methylaluminiumdichloride as cocatalysts for nickel complexes **1** (Ar = 2,6-*i*Pr<sub>2</sub>C<sub>6</sub>H<sub>3</sub>) and **2** (Ar = 2-*t*BuC<sub>6</sub>H<sub>4</sub>). Nickel complexes with smaller aryl substituents (**3**, Ar = 2,6-Me<sub>2</sub>C<sub>6</sub>H<sub>3</sub>; **4** Ar = 2,4,6-Me<sub>3</sub>C<sub>6</sub>H<sub>2</sub>; **5**, Ar = 2,6-Et<sub>2</sub>C<sub>6</sub>H<sub>3</sub>) undergo transfer reactions significantly. For the most bulky complex **1** activated by ethylaluminiumdichloride living hex-1-ene polymerization was achieved, proved by the reinitiation of polymer growth upon the addition of fresh monomer. The effect of Al/Ni ratio on the activity of the catalytic systems was studied by dilatometry. The catalytic systems were investigated by UV–vis spectrometry and a new interpretation of their absorption spectra was suggested.

© 2010 Elsevier Ltd. All rights reserved.

## 1. Introduction

Polyolefins represent the largest commodity plastics group. It is due to their structural and consequently properties versatility [1]. One of the further developments in a new polyolefin materials preparation is represented by macromolecular engineering [2] and its methods: living/controlled coordination polymerization [3] and chain-shuttling [4]. Despite the lower productivity of living/controlled olefin polymerization (one chain per growing center) in comparison with chain-shuttling, it is the most precise method of macromolecule construction.

One of the interesting post-metallocene catalyst groups allowing living/controlled polymerization of olefins [5] is represented by diimine late metal complexes [6,7]. Especially nickel derivatives are of current interest due to their high polymerization activity toward both ethylene and higher olefins. The lack of the stereospecificity control of these catalysts is balanced by their inconvenient mechanistic feature, so called chain-walking mechanism, allowing the catalytic center to migrate back into the growing polymer chain [6,8]. Chain-walking thus allows one to form branching points in the polymer arising from ethylene homopolymerization or to straighten the incorporated monomer unites in higher olefin polymerization (1, $\omega$ -insertion). In both cases the polyolefin materials ranging from

completely amorphous (rubbery) to semi-crystalline can be prepared [9].

Most of the catalytic systems are bicomponent, formed by the activation of a catalyst precursor (catalyst, initiator) by a cocatalyst (activator). The most common cocatalysts for homogeneous olefin polymerization catalysts are methylalumoxane (MAO), borates, boranes and less often simple organoaluminium compounds ( $\text{AlR}_n\text{X}_{3-n}$ , X = halogen atom) [10]. MAO is the most widely used cocatalyst for nickel diimine catalysts and, in comparison with metallocenes, 10–100 times less of it is sufficient to activate nickel complexes ( $\text{Al/Ni} = 10^1\text{--}10^2$ ) [11]. Compared to other catalytic systems allowing living/controlled olefin polymerization, nickel diimine complexes can be activated directly by commercially available MAO which contains around 30% of trimethylaluminium (TMA) that usually acts as a chain transfer agent and must be removed before contact with a catalyst [12–14]. However, MAO has several drawbacks. Beside the fact that its structure is not perfectly known, MAO is instable and its activation ability decreases during the storage. Safety and economic reasons for its more complicated manufacture in comparison with simple organoaluminium compounds should also be considered.

In contrast to early transition metal based catalysts that are predominantly activated by MAO, nickel diimine catalysts can be activated also by simple organoaluminiums which usually fail in an activator role for the most of metallocene catalysts [15–21]. Moreover, much lower Al/Ni ratios ( $\text{Al/Ni} = 10^0$ ) were shown to be

\* Corresponding author. Tel.: +420 220443194; fax: +420 220443175.

E-mail address: [merna@vscht.cz](mailto:merna@vscht.cz) (J. Merna).

sufficient for activation of nickel diimine complexes in ethylene polymerization when using simple organoaluminium compounds instead of MAO [22,23]. Coates et al. used diethylaluminiumchloride (DEAC) to activate Ni complexes **1** and rac-[ArN=C(1,8-naphthalenediyl)C=NAr]NiBr<sub>2</sub>, Ar=(2-(2,4,6-Me<sub>3</sub>C<sub>6</sub>H<sub>2</sub>)ethyl-4-methyl)C<sub>6</sub>H<sub>3</sub>) to polymerize hex-1-ene, hept-1-ene and oct-1-ene to polymers with very narrow molar mass distribution ( $\bar{D} = 1.06\text{--}1.15$ ) at  $-40\text{ }^{\circ}\text{C}$  to maximize selectivity for  $\omega$ ,2-enchainment [24].

During the investigation of living olefin polymerization Peruch and we found that the activation of nickel complexes by MAO is not quantitative and up to 30% of catalyst is converted into inactive species [11,25]. This behavior was correlated with UV–vis spectra of the catalytic system by Peruch et al. [11]. Species with absorption around 530 nm were ascribed to active species and band at 710 nm was proposed to be caused by inactive species with unknown structure. Interpretation of the spectra was based on the observation that the increase of peak at 710 nm and decrease of peak at 530 nm at room temperature is accompanied with the lost of catalyst livingness. Also the other UV–vis investigations of nickel diimine catalytic systems explained a similar observation by equilibrium between active and inactive (dormant) species [26–28].

Here, we describe several new catalytic systems based on non-MAO cocatalysts and nickel diimine complexes that enable living/controlled olefin polymerization. Kinetics and UV–vis spectral behavior of non-MAO based catalytic systems were investigated and a new interpretation of catalyst absorption spectra was proposed.

## 2. Experimental part

All manipulations with air-sensitive compounds were done using standard Schlenk techniques. Nitrogen (SIAD, 99.999%) was purified by passing through a column packed with Cu-catalyst and molecular sieves to remove traces of oxygen and water. Chlorobenzene (p.a., Penta) was refluxed over CaH<sub>2</sub> and distilled under nitrogen. Hex-1-ene (99%, Aldrich) was dried over sodium/potassium alloy and distilled under nitrogen. MAO (10 wt% solution in toluene, Aldrich), diethylaluminiumchloride (1.8 M in toluene, Aldrich), ethylaluminiumdichloride (EADC, 1.0 M in hexanes, Aldrich), dimethylaluminiumchloride (DMAC, 1.0 M in hexanes, Aldrich), methylaluminiumdichloride (MADC, 1.0 M in hexanes, Aldrich) were used as received. Nickel complexes were synthesized and purified according to reported procedures [7,17].

Polymerizations were carried out under dry nitrogen in magnetically stirred 20 mL glass ampoules. Ampoules with chlorobenzene, hex-1-ene and initiator were placed in a bath kept at a desired temperature and tempered for 15 min. Polymerization was initiated by addition of the cocatalyst solution (MAO, DEAC, EADC, DMAC or MADC). After the desired reaction time the polymerization was quenched by 1 mL of 10% HCl in MeOH, polymer was precipitated in 300 mL of MeOH, washed by MeOH and dried at 50 °C under vacuum until constant weight. Kinetics of hex-1-ene polymerization was followed in 10 mL capillary dilatometer equipped with a PTFE valve. Monomer conversion ( $Y$ ) was calculated according to eq. (1):

$$Y = \frac{L_0 - L_t}{(L_0 - L_{\text{term}}/Y_w)} \quad (1)$$

where  $L_0$  is the level of polymerization mixture at the moment of activation,  $L_t$  is level at time  $t$ ,  $L_{\text{term}}$  is the level at the moment of termination and  $Y_w$  is gravimetrical conversion of monomer calculated from the ratio of mass of the obtained polymer to the mass of monomer. Apparent propagation rate constants and initial propagation rates of the polymerization were calculated from the following expressions (2) and (3):

$$\ln([M_0]/[M]) = \ln(1/(1 - Y)) = k_p^{\text{app}} \times t \quad (2)$$

$$R_p = k_p \times [\text{Ni}]^\alpha [\text{Al}]^\beta [\text{M}]^\gamma = k_p^{\text{app}} \times [\text{M}]^1 \quad (3)$$

where  $[M_0]$  and  $[M]$  are the initial and instantaneous concentration of monomer;  $\alpha$ ,  $\beta$  and  $\gamma$  are the kinetic orders with respect to Ni catalyst, Al cocatalyst and hex-1-ene monomer, respectively. As the first-order time-conversion plots were linear at least up to 50% conversion, initial rates of polymerizations were calculated using  $\gamma = 1$ , assuming first order to monomer kinetics.

UV–vis spectra of catalytic systems were recorded on a Varian Cary 50 spectrometer. A quartz cell (0.5 cm optical length) connected directly to a Schlenk flask was used for measurements.

The microstructure of polyhexenes was determined by <sup>1</sup>H NMR spectroscopy on 500 MHz Bruker Avance DRX 500 spectrometer in CDCl<sub>3</sub> solution at 30 °C.

The total number of branches per 1000 carbon atoms ( $N$ ) was determined by integrating methyl proton signals with respect to signals of all protons in <sup>1</sup>H NMR spectrum and calculated using the formula:

$$N = \frac{2(I_{\text{CH}_3})}{3(I_{\text{CH}+\text{CH}_2+\text{CH}_3})} \times 1000 \quad (4)$$

The degree of polyhexene chain rearrangement ( $x$ ) expressed as the fraction of 1,6-monomer insertions was calculated according to expression (5):

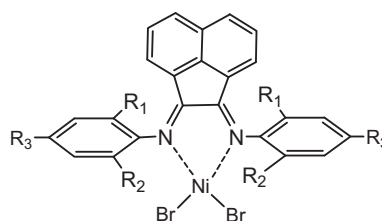
$$x = \left(1 - \frac{N}{167}\right) \times 100(\%) \quad (5)$$

Molar masses were determined using Waters Breeze chromatographic system equipped with RI detector operating at 880 nm and multi-angle laser light scattering (MALLS) miniDawn TREOS from Wyatt operating at 658 nm. Separations were performed with two Polymer Laboratories Mixed C columns at 35 °C in THF at an elution rate of 1 mL min<sup>-1</sup>. The dn/dc value 0.078 ± 0.002 mL g<sup>-1</sup> was used for polyhexene in THF at 35 °C [29].

## 3. Results and discussion

### 3.1. Controlled polymerization

To study the behavior of catalytic systems activated by non-MAO catalysts, five nickel catalysts were used that are known to initiate living/controlled olefin polymerization when activated by MAO (Fig. 1) [29]. First, bulky *t*-butyl substituted catalyst **2** was used in the polymerization of hex-1-ene for screening of four simple organoaluminium compounds: diethylaluminiumchloride (DEAC),



- 1 R<sub>1</sub>=R<sub>2</sub>=iPr, R<sub>3</sub>=H
- 2 R<sub>1</sub>=tBu, R<sub>2</sub>=R<sub>3</sub>=H
- 3 R<sub>1</sub>=R<sub>2</sub>=R<sub>3</sub>=Me
- 4 R<sub>1</sub>=R<sub>2</sub>=Me, R<sub>3</sub>=H
- 5 R<sub>1</sub>=R<sub>2</sub>=Et, R<sub>3</sub>=H

Fig. 1. Structure of nickel diimine complexes used in this work.

**Table 1**

Polymerization of hex-1-ene initiated by complex **2** activated with various cocatalysts.

Run	Cocatalyst	Monomer conversion [%]	$M_n^a$ kg·mol <sup>-1</sup>	$\bar{D}^a$	NPM/N(Ni) <sup>b</sup>	$N^c$
1	MAO	100	84.2	1.3	0.8	93
2	DEAC	100	57.7	1.3	1.2	73
3	EADC	100	74.3	1.4	0.9	67
4	DMAC	85	11.5	2.2	–	64
5	MADC	70	60.5	1.3	0.8	80

[Ni] = 1.0 mM, Al/Ni = 500, [hex-1-ene] = 0.8 M, chlorobenzene, total volume 10 mL,  $T_p$  = 0 °C, time of polymerization 4 h.

<sup>a</sup> Number average molar mass and dispersity determined by SEC with PS standards.

<sup>b</sup> NPM/N(Ni) = polymer mass/(mol<sub>Ni</sub>· $M_n$ ).

<sup>c</sup> Number of branches per 1000 C atoms determined by <sup>1</sup>H NMR spectroscopy.

ethylaluminiumdichloride (EADC), dimethylaluminiumchloride (DMAC) and methylaluminiumdichloride (MADC) in role of cocatalysts (activators) and compared with MAO (Table 1). Compared to methyl aluminium derivatives, ethyl aluminium analogues afforded more active catalytic species, completely transforming monomer into polymer in 4 h at 0 °C. With the exception of DMAC, all catalytic systems produced polyhexene with narrow molar mass distribution, comparable to that of the polyhexene produced by MAO activated catalyst, suggesting controlled polymerization with respect to molar mass. Efficiency of the catalysts was further expressed by number of polymer molecules produced per molecule of initiator [NPM/N(Ni)] calculated from the amount of obtained polymer, amount of Ni catalyst and molar mass of polymer. For all the catalytic systems producing polymers with low dispersity, NPM/N(Ni) is closed to unity showing a good efficiency of simple organoaluminium compounds as the activators of nickel complex **2** and further showing that molar masses of the prepared polymers are appropriate to monomer/initiator ratio, another typical feature of living/controlled polymerizations.

Concerning the microstructure of the polymers we found that the choice of cocatalyst influences also the branching of the polymer chain in agreement with previous studies of ethylene and propylene polymerization [15,17,20]. All polymerizations activated by simple organoaluminium compounds led to polyhexene with lower amount of branches than in MAO activated system, which shows higher degree of chain-walking reactions in comparison to propagation. The highest degree of rearrangement (62%) was observed for DMAC. Comparison with MAO activated catalyst (44% rearrangement) indicates the possibility to efficiently control the polymer microstructure also by choice of the cocatalyst.

Since some chain transfer was evident from slightly broadened molar mass distribution of the polyhexenes prepared at 0 °C, further experiments were carried out at –10 °C to minimize the extent of side reactions. Other four nickel complexes were tested in combination with the most effective cocatalysts DEAC and EADC. Based on the kinetic investigation (see below) and literature data for **2**/MAO [11], which show reaching activity plateau at Al/Ni = 50, we used decreased Al/Ni = 200 ratio for the rest of experiments. As seen from Table 2, all the catalysts activated by MAO gave high yield of polyhexene with a very low dispersity in molar masses in agreement with previously published works [7,29]. Using DEAC or EADC, only bulky catalysts **1** and **2** produced polyhexenes with a narrow molar mass distribution at high yield, indicating a controlled manner of the polymerization. NPM/N(Ni) values within these two nickel complexes are very close to unity using DEAC and EADC as cocatalysts supporting further a controlled character of the polymerization.

In the case of complexes **3** and **4** with methyl ortho-substituents, significantly broadened molar mass distribution was observed and, using EADC, also the catalyst activity dropped substantially.

**Table 2**

Polymerization of hex-1-ene initiated by **1–5** activated by MAO, DEAC and EADC in chlorobenzene.

Run	Catalyst	Cocatalyst	$Y_w^a$ [%]	$M_n^b$ [kg·mol <sup>-1</sup> ]	$\bar{D}^b$	NPM/N(Ni) <sup>c</sup>	$N^d$
1	<b>1</b>	MAO	89	91.6	1.03	0.70	127
2		DEAC	94	59.3	1.07	1.08	113
3		EADC	88	58.3	1.11	1.05	118
4	<b>2</b>	MAO	95	60.8	1.13	1.11	
5		DEAC	84	48.9	1.27	1.11	
6	<b>3</b>	MAO	90	59.1	1.30	1.09	
7		DEAC	94	39.6	1.97	–	
8		EADC	30	89.7	1.67	–	
9	<b>4</b>	MAO	75	60.1	1.13	0.85	
10		DEAC	66	20.2	2.71	–	
11		EADC	4	33.7	2.13	–	
12	<b>5</b>	MAO	90	66.0	1.08	1.09	131
13		DEAC	95	49.7	1.30	1.33	115
14		EADC	50	74.7	1.41	0.46	124

[Ni] = 1.0 mM, Al/Ni = 200, [hex-1-ene] = 0.8 M, polymerization time 5 h,  $T_p$  = –10 °C, total volume 10 mL.

<sup>a</sup> Monomer conversion.

<sup>b</sup> Number average molar mass ( $M_n$ ) and dispersity determined by SEC-MALLS.

<sup>c</sup> NPM/N(Ni) = polymer mass/(mol<sub>Ni</sub>· $M_n$ ).

<sup>d</sup> Number of branches per 1000 C atoms determined by <sup>1</sup>H NMR spectroscopy.

Complex **5** with ethyl substituents was efficiently activated only by DEAC producing polyhexene with fairly low dispersity values. However, when activated by EADC, complex **5** showed only low monomer conversion and, according to NPM/N(Ni) parameter, less than half of the nickel precursor was activated. This is in contrast with our previous experiments in which MAO activated complex **5** controlled hex-1-ene polymerization in a similar or even better manner than the most widely used complex **1** [29]. This stress out the role of MAO as a bulky cocatalyst which helps to protect the Ni center from  $\beta$ -eliminations and ensures the livingness of polymerization even in case of less bulky Ni diimine complexes.

At –10 °C, chain walking is less pronounced [6,30] and polyhexenes with a similar branching degree are obtained with catalysts **1** and **5**. DEAC and EADC again showed higher degree of rearrangement in comparison with MAO leading to less branched polymers in case of both catalysts.

The best control over the polymerization activated by DEAC and EADC was achieved with bulky catalyst **1** demonstrated by a very

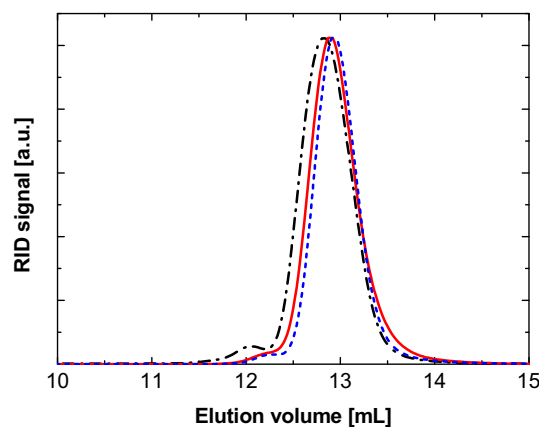


**Fig. 2.** SEC traces of polyhexenes obtained by nickel complex **1** activated by MAO (dash dot), EADC (solid) and DEAC (dash). [Ni] = 1.0 mM, Al/Ni = 200, [hex-1-ene] = 0.8 M, 5 h,  $T_p$  = –10 °C



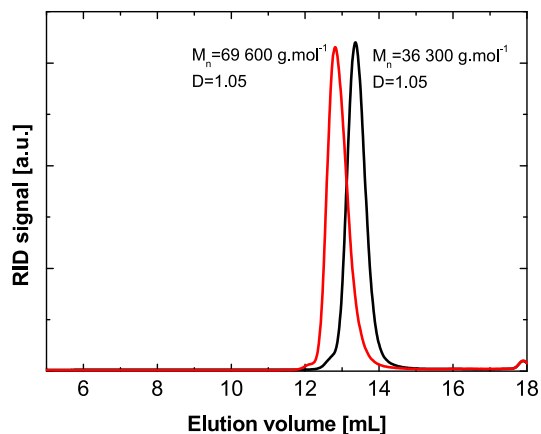


**Fig. 3.** SEC chromatograms of polyhexenes obtained by nickel complex **1** activated by EADC after 5 h of polymerization (right peak) and after reinitiation by addition of second portion of monomer after additional 12 h of polymerization (left peak).  $T_p = -10\text{ }^\circ\text{C}$ ,  $[\text{Ni}] = 1.0\text{ mM}$ ,  $\text{Al/Ni} = 200$ ,  $[\text{hex-1-ene}] = 0.4\text{ M} + 0.4\text{ M}$ . Monomer conversion 96%.

narrow molar mass distribution, similar to that obtained by **1**/MAO (Fig. 2). To investigate the livingness of these catalytic systems we decided to perform a reinitiation experiment consisting of the addition of fresh monomer after the consumption of initial

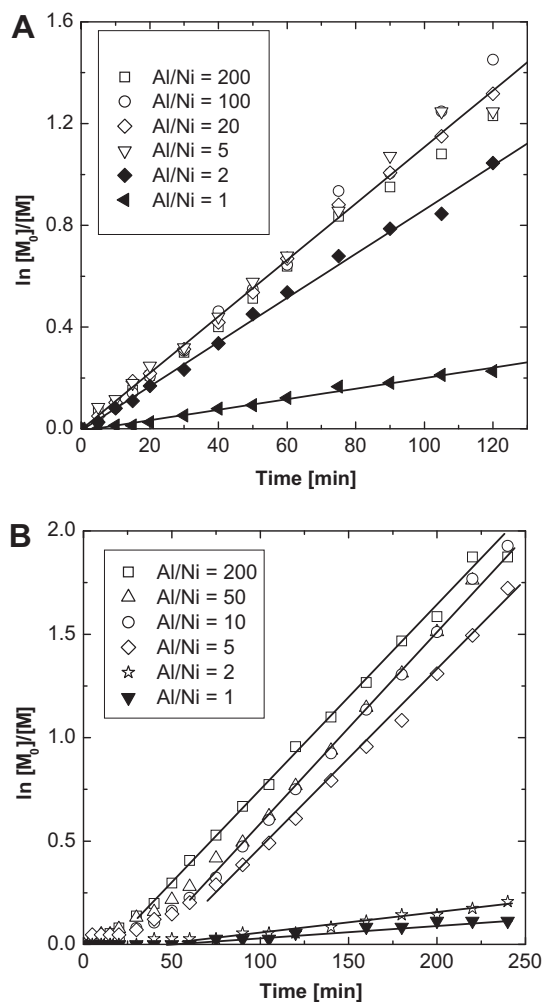


**Fig. 4.** First-order time-conversion plots of hex-1-ene polymerization initiated **2**/DEAC (A) and **2**/EADC (B),  $T_p = -10\text{ }^\circ\text{C}$ ,  $[\text{Ni}] = 1.0\text{ mM}$ ,  $[\text{hex-1-ene}] = 0.8\text{ M}$ ;  $1 < \text{Al/Ni} < 200$ .

**Table 3**

Influence of Al/Ni ratio on hex-1-ene polymerization initiated by **2**/EADC in chlorobenzene.

Run	Al/Ni	$Y_w^a$ %	$M_n^b$ $\text{kg mol}^{-1}$	$\bar{D}^b$	NPM/N(Ni) <sup>c</sup>
1	200	89	52.8	1.14	1.13
2	100	85	53.7	1.23	1.05
3	50	87	59.7	1.22	0.97
4	20	86	72.8	1.07	0.78
5	10	85	62.0	1.15	0.91
6	5	82	67.7	1.07	0.81

$[\text{Ni}] = 1.0\text{ mM}$ ,  $[\text{hex-1-ene}] = 0.8\text{ M}$ , polymerization time 4 h,  $T_p = -10\text{ }^\circ\text{C}$ , total volume 10 mL.

<sup>a</sup> Monomer conversion.

<sup>b</sup> Number average molar mass ( $M_n$ ) and dispersity determined by SEC-MALLS.

<sup>c</sup>  $\text{NPM/N(Ni)} = \text{polymer mass}/(\text{mol}_{\text{Ni}} \cdot M_n)$ .

monomer feed. Although **1**/DEAC produced polyhexene with narrower molar mass distribution than **1**/EADC, DEAC activated system failed in the reinitiation test and, according to SEC traces, significant portion of growing centers was inactive in the second phase of polymerization. On contrary, **1**/EADC system surprisingly displayed very good reinitiation capability, polyhexene molar mass was doubled (and equaled to theoretical value) and its distribution remained very narrow after second monomer addition (Fig. 3). This could be explained by the coordination of activator molecule to Ni center after complete monomer consumption, which is stronger in case of DEAC compared to EADC (vide infra).

### 3.2. Kinetics of polymerization

To investigate the reactivity of catalytic systems toward olefin, kinetic measurements were carried out by means of dilatometry. For this purpose we used nickel complex **2** activated by DEAC and EADC and compared with MAO. All experiments with MAO and DEAC displayed first-order kinetics with respect to hex-1-ene concentration in the initial period of polymerization. Typical first-order kinetic plots for **2**/DEAC system are shown in Fig. 4A. At Al/Ni ratio lower than five, polymerization did not proceed up to high conversion due to the consumption of significant part of cocatalyst by impurities. In the case of **2**/EADC system an induction period, shortening with increase of Al/Ni ratio, was observed caused by

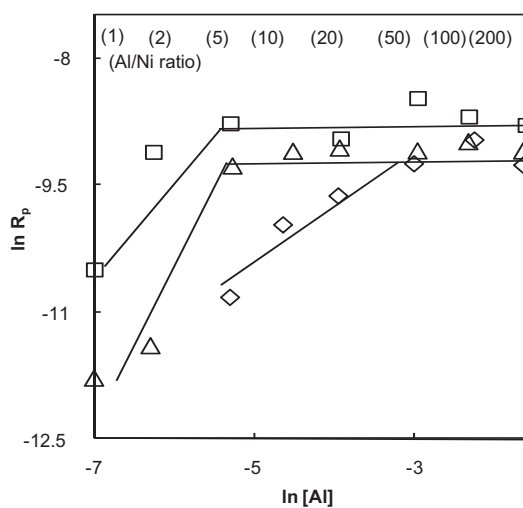


**Fig. 5.** Logarithmic variations of hex-1-ene polymerization rate on activator concentration, in chlorobenzene at  $-10\text{ }^\circ\text{C}$ , complex **2**.  $[\text{Ni}] = 1.0\text{ mM}$ ,  $[\text{hex-1-ene}] = 0.8\text{ M}$ ;  $0.0009 < [\text{Al}] < 0.1966\text{ M}$ ;  $1 < \text{Al/Ni} < 200$ . Cocatalysts: MAO (diamonds), DEAC (squares), EADC (triangles).

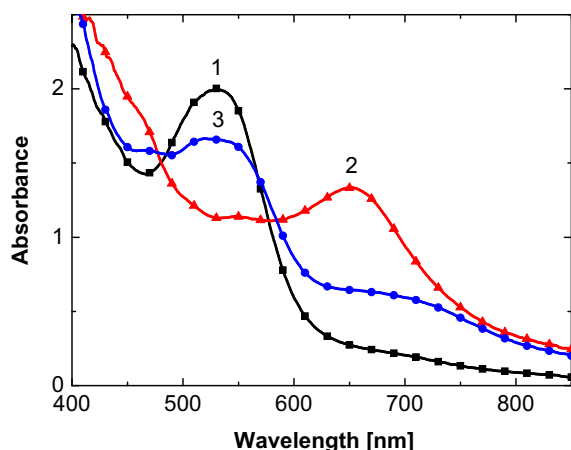


**Fig. 6.** UV–vis spectra of **2**/DEAC catalytic system activated in presence of hex-1-ene: after activation (curve 1), after 8 h of polymerization (curve 2), after addition of second portion of hex-1-ene (curve 3). [hex-1-ene] = 0.4M + 0.4 M, [Ni] = 0.8 mM, Al/Ni = 200,  $T_p = 0^\circ\text{C}$ .

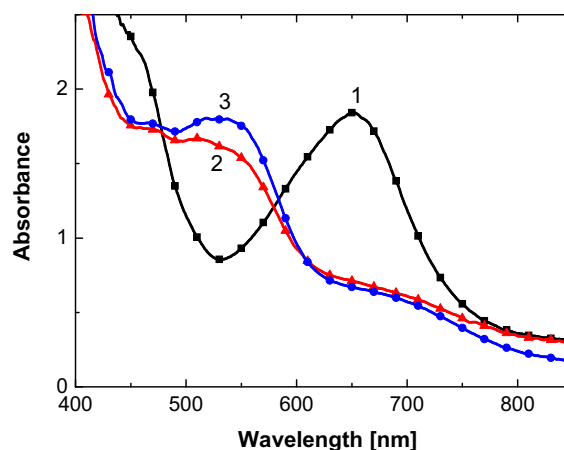


**Fig. 7.** UV–vis spectra of **2**/DEAC catalytic system activated in absence of hex-1-ene (curve 1), in presence of hex-1-ene (curve 2-after monomer addition, curve 3-after 18 h).[hex-1-ene] = 0.4 M, [Ni] = 0.8 mM, Al/Ni = 200,  $T_p = -10^\circ\text{C}$ .

slow activation (Fig. 4B). Once activated all centers propagate at a similar rate and the polymerization follows first-order kinetics to monomer as in the case of DEAC and MAO activation. Propagation constants were therefore calculated from the linear part of  $\ln([M]_0/[M])$  dependence on polymerization time to allow the comparison with the other systems using the same kinetic model. Despite relatively slow activation rate of EADC, polyhexenes with a very low dispersity were prepared even at low Al/Ni ratios as a consequence of rather slower propagation (Table 3). However, the decrease of Al/Ni ratio leads to the detectable decrease of polymerization activity as a consequence of lower initiator efficiency caused by incomplete activation of complex **2** by EADC at Al/Ni ratios below 50, as visible from decrease of NPM/N(Ni) values.

Initial propagation rates of hex-1-ene polymerization were calculated and plotted against Al/Ni ratio (Fig. 5). In case of all the activators, an increase of activity with increase of Al/Ni ratio was observed followed by reaching a plateau. This breakpoint was reached at Al/Ni = 50 for MAO, which is in exact agreement with the previous work of Peruch [11]. For DEAC and EADC the activity plateau was reached at considerably lower Al/Ni ratio equal five. From this point of view, DEAC and EADC seem to be more efficient cocatalysts. According to maximum activity values DEAC forms the most active catalytic system with complex **2** in comparison to EADC and MAO which displayed similar propagation rate.

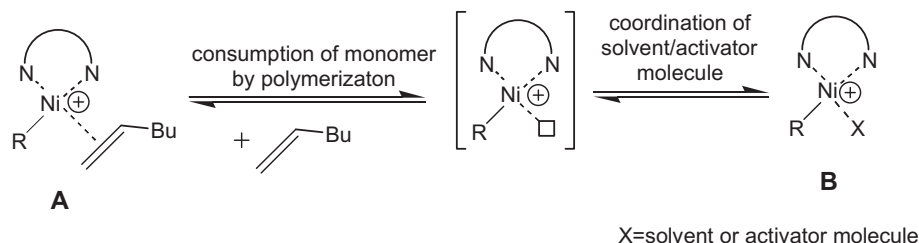
### 3.3. UV–vis spectroscopy of catalytic systems

In previously published literature [11], UV–vis spectroscopy was suggested as a method for investigation of catalytic species obtained by MAO activated catalyst **2**. Two characteristic peaks in **2**/MAO UV–vis spectra were ascribed to two types of species: active,

absorbing at 530 nm, and inactive, absorbing at 700 nm. The stability of the absorption spectra at  $-10^\circ\text{C}$  was correlated with the stability of active centers and therefore with livingness of the catalytic system. At room temperature authors observed the evolution of spectra when peak at 530 nm (active species) decreased while simultaneously peak at 700 nm increased its intensity which was accompanied by the loss of livingness.

In our UV–vis experiments we observed much different behavior of non-MAO activated nickel complexes. In contrast to MAO activated system both DEAC and EADC activated complex **2** displayed only one peak at 530 nm in UV–vis spectra from 400 to 900 nm (Fig. 6, curve 1).

Assuming the active–inactive species hypothesis it would mean that only active species were formed and nickel complexes were quantitatively activated. NPM/N(Ni) values for bulky catalysts **1** and **2** were close to unity (Tables 1 and 2) which would support the idea of complete catalyst activation. However, in the case of **2**/DEAC activated system, we observed the formation of a new peak around 650 nm at prolonged reaction times (after 8 h at  $0^\circ\text{C}$ ), when the conversion of monomer is completed (Fig. 6, curve 2). Simultaneously, the peak at 530 nm disappeared and the mixture color turned from violet to green. At this moment we added fresh hex-1-ene to the mixture. To our surprise, we observed that the apparently inactive catalytic system reacted with the monomer leading to the disappearance of the peak at 650 nm and regeneration of the peak at 530 nm (Fig. 6, curve 3). Simultaneously, the color of the mixture turned to red immediately after monomer addition and increased its intensity returning back to deep violet color in several hours. Such easily observable changes in color mixture could be useful for indication of monomer consumption which could be advantageous e.g. in preparation of block copolymers by sequential monomer addition.



**Scheme 1.** Proposed structures of nickel diimine catalytic species corresponding to observed absorption peaks in UV–vis spectra of **2**/DEAC.

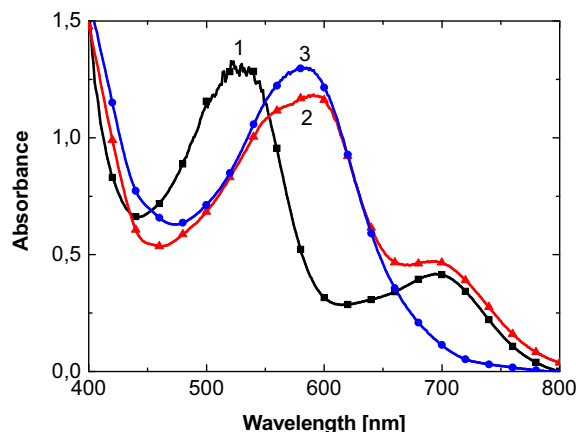


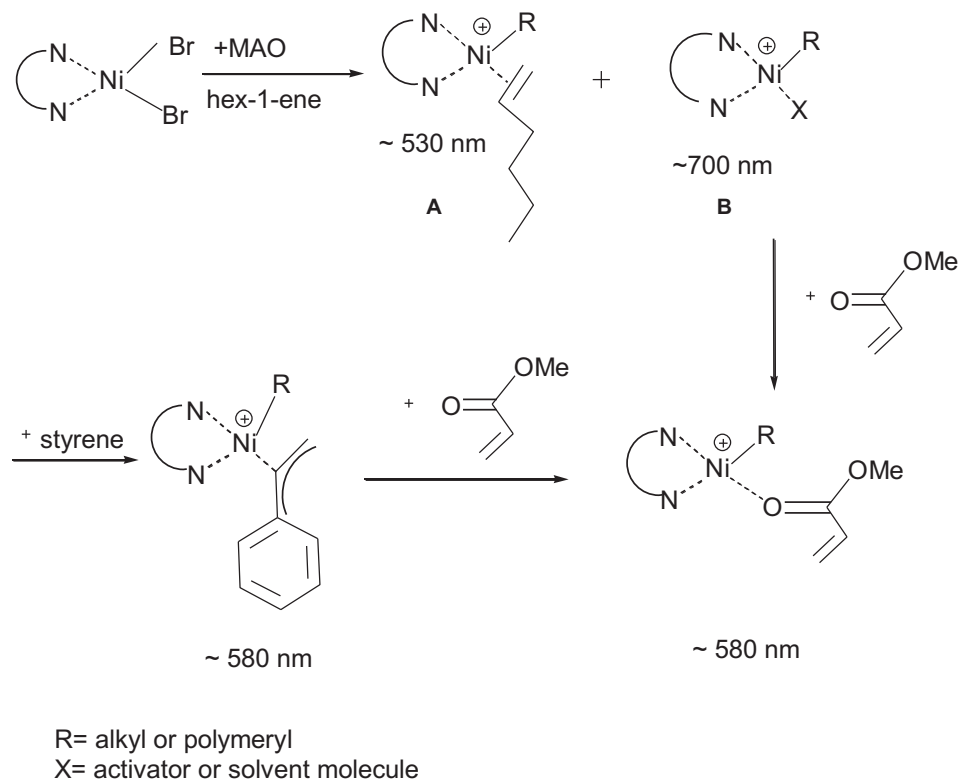
**Fig. 8.** UV–vis spectra of 1/MAO catalytic system activated in presence of hex-1-ene (curve 1), after addition of styrene (curve 2) and after addition of methylacrylate (curve 3). [hex-1-ene] = 0.4 M, [Ni] = 0.8 mM, Al/Ni = 200,  $T_p = -10$  °C, styrene/Ni = 10, methylacrylate/Ni = 10.

However, intensity of the peak at 530 nm did not reach the initial value of freshly activated system indicating some decomposition of the catalytic system in absence of monomer. This instability of nickel diimine catalyst was observed previously for MAO activated system [11]. Despite some catalyst deactivation the most of the monomer from both feeds was converted to polymer (conversion 91%). However, SEC analysis of the sample withdrawn from the polymer mixture before second monomer addition and after it revealed a substantial increase of molar mass dispersity as a consequence of termination of chain growth on deactivated centers.

The above described behavior of the catalytic system led us to a proposal of new explanation of the absorption spectra in which

peak at 530 nm corresponds to alkyl-olefin Ni complex (Scheme 1, structure **A**), known as the resting state (active species) of diimine catalysts [5,9,30], whereas the peak at 650 nm do not belong to inactive centers but corresponds to alkyl-Ni complex with “vacant” coordination position (Scheme 1) which can be converted back to complex **A** by the addition of fresh monomer. It is probable that hypothetical complex with free coordination position would be instable in the reaction mixture and would immediately coordinate either solvent or rather cocatalyst molecule. Therefore, species absorbing at 650 nm could be described more properly as complex **B** (Scheme 1) with coordinated solvent or cocatalyst molecule, which could be replaced by strongly binding olefin molecule to regenerate the active complex **A**. The interaction between Ni center and activator halogen atom ( $\text{Ni}\cdots\text{Cl}\cdots\text{Al}$ ) was already proposed and investigated by several X-ray absorption methods by de Souza et al. [31].

To support our hypothesis, we performed an additional experiment in which complex **2** was activated by DEAC in absence of hex-1-ene. UV–vis spectra (Fig. 7, curve 1) displayed only one peak at 650 nm. Addition of hex-1-ene to the mixture leads to immediate disappearance of the peak at 650 nm and formation of the intensive peak at 530 nm belonging to active species as a consequence of replacement of coordinated activator molecule by hex-1-ene (Fig. 7, curve 2). Complete reaction of hex-1-ene with catalyst took several hours as indicated by slow increase of intensity of the peak at 530 nm (Fig. 7, curve 3). The reaction produced polyhexene with molar mass  $22\,800\text{ g mol}^{-1}$  and dispersity  $\mathcal{D} = 2.66$  after 20 h reaching conversion of only 36% suggesting partial irreversible deactivation of the catalyst centers and competition between monomer and activator coordination to Ni center. Compared to values obtained in experiments when the catalyst was activated in presence of monomer (Table 2, run 5) this observation emphasizes the importance of monomer presence at the stage of nickel catalyst activation.



**Scheme 2.** Proposed mechanism of active and dormant centers origin and their transformation by addition of terminating agents.

A similar behavior was observed also in EADC activated system which afforded a peak at 530 nm after the activation in presence of monomer. In absence of monomer the peak at 700 nm was formed. In comparison with DEAC, no peak at 700 nm is generated even after prolonged reaction times if nickel catalyst is activated by EADC in presence of monomer. That could be explained by the presence of small amount (1% of remaining monomer at 99% conversion is enough to coordinate all Ni centers) of unreacted monomer (or olefin generated by  $\beta$ -H elimination) which is sufficient to form alkyl-olefin complex **A**. The position of peak corresponding to species **B** is thus influenced by cocatalyst and for EADC and MAO have maximum at approximately 700 nm whereas for DEAC at 650 nm. The shift in maximum absorption is probably caused by different interaction of Ni complex cation and counteranion generated from each cocatalyst or by coordination of cocatalyst molecules to vacant position of nickel complex after monomer consumption.

This interaction is important for spectral behavior of the catalytic system, because the addition of hex-1-ene to MAO activated system does not lead to diminution of the peak at 700 nm and even the spectra obtained in presence of monomer at low temperatures, when the system is living, contain the peak at 700 nm [11]. This could be explained by the stabilization of alkyl nickel complex **B** by bulky MAO counteranion (we excluded the coordination of trimethylaluminum present in MAO by using dried MAO in another experiment) which, in absence of monomer, can coordinate to nickel complex and block the coordination of monomer to part of nickel centers. Therefore, we decided to investigate MAO activated catalytic system in more detail to prove the consistency of our mechanistic explanation. For this purpose we reacted MAO activated system with compounds that coordinate to nickel center stronger than hex-1-ene. In Fig. 8, curve 1 represents MAO activated complex **1** in presence of hex-1-ene at  $-10$  °C when the catalyst is considered to be stable. Two main peaks at 530 nm and 700 nm were observed as in previous studies and that we propose to be alkyl-olefin complex **A** and alkyl complex **B** with coordinated activator (Scheme 2). Addition of styrene led to the shift of the peak at 530 nm to 580 nm confirming the replacement of hex-1-ene by strongly coordinating styrene (Fig. 8, curve 2). However, the peak at 700 nm remained unchanged indicating that styrene was not capable to coordinate strong enough to break the interaction between cationic center and MAO. Therefore, we added methylacrylate, which due to its polar group coordinate stronger than non-polar olefins, and we observed immediate disappearance of the peak at 700 nm and increase of intensity of the peak at 580 nm (Fig. 8, curve 3). This shows that the peak at 700 nm represents species that are capable of further coordination and could be represented by alkyl complex **B** in which the vacant position is blocked by MAO.

#### 4. Conclusions

We found that controlled polymerization of olefins can be initiated by bulky nickel diimine complexes **1** and **2** activated by non-MAO cocatalysts resulting in polyolefins with a very narrow molar mass distribution and molar mass tunable by monomer/initiator ratio. EADC activated catalyst **1** displayed truly living behavior enabling reinitiation of chain growth after fresh monomer addition. Kinetics investigation shows that simple organoaluminum compounds are efficient cocatalysts at order of magnitude lower Al/Ni ratios in comparison with MAO while the

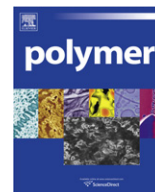
polymerization remains controlled. Despite slower activation, EADC activated catalytic systems afford polyhexenes with a narrow molar mass distribution. We proposed a new interpretation of UV–vis spectra of the catalytic systems based on partially reversible conversion between alkyl-olefin Ni (**A**) and alkyl-Ni complexes with coordinated activator (**B**). The hypothesis was supported by changes of spectra during the polymerization and upon addition of monomer or terminating agents.

#### Acknowledgment

The present research was financially supported by the Grant Agency of the Czech Republic (grant No. 104/07/P264) and Ministry of Education, Youth and Sports (program MSM 6046137302). Dr. Jiri Pinkas (J. Heyrovsky Institute of Physical Chemistry, AS CR) is acknowledged for fruitful discussion. We wish to thank the reviewers for suggestions leading to significant improvements of the paper.

#### References

- [1] Galli P, Vecellio G. *J Polym Sci Part A Polym Chem* 2004;42(3):396–415.
- [2] Mason AF, Coates GW. Coordination polymerization: synthesis of new homo- and copolymer architectures from ethylene and propylene using homogeneous Ziegler–Natta polymerization catalysts. In: Matyjaszewski K, Gnanou Y, Leibler L, editors. *Macromolecular engineering*, vol. 1. Weinheim: Wiley-VCH; 2007. p. 217–49.
- [3] Coates GW, Hustad PD, Reinartz S. *Angew Chem Int Ed* 2002;41:2236–57.
- [4] Arriola DJ, Carnahan EM, Hustad PD, Kuhlman RL, Wenzel TT. *Science* 2006;312(5774):714–9.
- [5] Domski GJ, Rose JM, Coates GW, Bolig AD, Brookhart M. *Prog Polym Sci* 2007;32:30–92.
- [6] Johnson LK, Killian CM, Brookhart M. *J Am Chem Soc* 1995;117(23):6414–5.
- [7] Killian CM, Tempel DJ, Johnson LK, Brookhart M. *J Am Chem Soc* 1996;118(46):11664–5.
- [8] Guan ZB, Cotts PM, McCord EF, McLain SJ. *Science* 1999;283(5410):2059–62.
- [9] Ittel SD, Johnson LK, Brookhart M. *Chem Rev* 2000;100(4):1169–203.
- [10] Chen EYX, Marks TJ. *Chem Rev* 2000;100(4):1391–434.
- [11] Peruch F, Cramail H, Deffieux A. *Macromolecules* 1999;32(24):7977–83.
- [12] Tian J, Hustad PD, Coates GW. *J Am Chem Soc* 2001;123(21):5134–5.
- [13] Mitani M, Furuyama R, Mohri J-I, Saito J, Ishii S, Terao H, et al. *J Am Chem Soc* 2002;124(27):7888–9.
- [14] Azoulay JD, Schneider Y, Galland GB, Bazan GC. *Chem Commun*; 2009:6177–9.
- [15] Simon LC, Mauler RS, De Souza RF. *J Polym Sci Part A Polym Chem* 1999;37(24):4656–63.
- [16] Kumar KR, Sivaram S. *Macromol Chem Phys* 2000;201(13):1513–20.
- [17] Maldanis RJ, Wood JS, Chandrasekaran WA, Rausch MD, Chien JCV. *J Organomet Chem* 2002;645(1–2):158–67.
- [18] Preishuber-Pflugl P, Brookhart M. *Macromolecules* 2002;35(16):6074–6.
- [19] Xue XH, Yang X, Xiao YH, Zhang QX, Wang HH. *Polymer* 2004;45(9):2877–82.
- [20] de Souza CG, de Souza RF, Bernardo-Gusmao K. *Appl Catal A Gen* 2007;325(1):87–90.
- [21] Bahuleyan BK, Son GW, Park YH, Ahn IY, Ha CS, Kim I. *Macromol Res* 2009;17(4):276–9.
- [22] Chien JCV, Fernandes S, Correia SG, Rausch MD, Dickson LC, Marques MM. *Polym Int* 2002;51(8):729–37.
- [23] Pappalardo D, Mazzeo M, Pellicchia C. *Macromol Rapid Commun* 1997;18(12):1017–23.
- [24] Rose JM, Cherian AE, Coates GW. *J Am Chem Soc* 2006;128(13):4186–7.
- [25] Merna J, Cihlar J, Kucera M, Deffieux A, Cramail H. *Eur Polym J* 2005;41(2):303–12.
- [26] Simon LC, Williams CP, Soares JBP, de Souza RF. *J Mol Cat A Chem* 2001;165(1–2):55–66.
- [27] Luo HK, Yang ZH, Mao BQ, Yu DS, Tang RG. *J Mol Cat A Chem* 2002;177(2):195–207.
- [28] Bahuleyan BK, Son GW, Park DW, Ha CS, Kim I. *J Polym Sci Part A Polym Chem* 2008;46(3):1066–82.
- [29] Merna J, Hošťálek Z, Peleška J, Roda J. *Polymer* 2009;50(21):5016–23.
- [30] Gates DP, Svejda SA, Oñate E, Killian CM, Johnson LK, White PS, et al. *Macromolecules* 2000;33:2320–34.
- [31] de Souza RF, Simon LC, Alves MCM. *J Catal* 2003;214(1):165–8.



# Synthesis of emulsion-templated porous polyacrylonitrile and its pyrolysis to porous carbon monoliths

Noa Cohen, Michael S. Silverstein\*

Department of Materials Engineering, Technion - Israel Institute of Technology, Haifa 32000, Israel

## ARTICLE INFO

### Article history:

Received 28 July 2010

Received in revised form

9 November 2010

Accepted 15 November 2010

Available online 23 November 2010

### Keywords:

Porous carbon

High internal phase emulsion

Polyacrylonitrile

## ABSTRACT

PolyHIPEs are emulsion-templated polymers synthesized within high internal phase emulsions (HIPEs). The miscibility of acrylonitrile (AN) with water has made it difficult to synthesize PAN-based polyHIPEs. This paper describes the successful synthesis of PAN-based polyHIPEs by crosslinking through copolymerization with divinylbenzene (DVB), by stabilization with a polyglycerol polyricinoleate surfactant, and by initiation with both oil- and water-soluble initiators. The PAN-based polyHIPEs had porosities of over 86% and porous structures that were different from those of typical polyHIPEs. This paper also describes the production of porous carbon monoliths through the pyrolysis of these PAN-based polyHIPEs. Pyrolysis did not produce significant changes in the porous structures, which were quite similar to those of the original polyHIPEs. The porosities were around 95% and the carbon monoliths were largely macroporous and mesoporous, with some microporosity. These results indicate that PAN-based polyHIPE templates can be used for the *a priori* design of porous carbon monoliths.

© 2010 Elsevier Ltd. All rights reserved.

## 1. Introduction

Porous polymer systems termed polyHIPEs can be produced through an emulsion templating synthesis in which the external phase of a high internal phase emulsion (HIPE) is polymerized and then the internal phase is removed through drying [1–7]. A HIPE is formed when the volume fraction of the internal phase of an emulsion is over 0.74, which is the maximum packing fraction of uniform spheres [4–8]. During polymerization, ruptures can occur at the thinnest point within the film of continuous phase separating droplets of the internal phase [4]. A preponderance of such ruptures leads to the formation of a highly interconnected internal phase. The highly interconnected internal phase can then be removed through drying. PolyHIPEs are usually crosslinked in order to enhance their stability and their resistance to collapse under the capillary stresses generated during drying [4]. The crosslinking is usually achieved through copolymerization with a crosslinking comonomer. A typical porous structure for polyHIPEs consists of empty voids, evacuated internal phase droplets, that are highly interconnected through holes in the polymer walls.

The interest in polyHIPE materials is driven by the large number of applications involving porous polymers (catalyst supports, separation membranes, ion exchange resins, tissue engineering scaffolds,

etc.) and by the ability to adapt the molecular structures and the porous structures of polyHIPEs to particular applications. A wide variety of polyHIPEs and polyHIPE-based materials have been synthesized including copolymers [9,10], interpenetrating polymer networks (IPN) [11], crystallizable side chain polymers [12], hydrogels [13–15], biocompatible polymers [16–18], degradable polymers [19], step-growth polymers [20], bicontinuous polymers [21], functional surfaces [5,22,23], organic-inorganic hybrids [24,25], and composites [26–29]. Porous silica monoliths have been produced through the pyrolysis of porous hybrid polyHIPEs and nanocomposite polyHIPEs [25,30].

Porous carbon is also used for a wide variety of applications including gas separation, water purification, catalyst supports, and electrodes for capacitors and for fuel cells [31]. Porous carbon can be synthesized using various methods. These methods often include the pyrolysis of a polymer that produces a high degree of char either within a porous structure or within a blend containing a polymer that does not produce char [32]. Polyacrylonitrile (PAN) fibers are commonly used as precursors for carbon fibers. PAN undergoes a cyclization reaction at high temperatures producing a ladder polymer and imparting an unusually high thermal stability [33]. It should be possible to design the pore sizes and porous structures of carbon monoliths *a priori* through the synthesis of porous polymer templates [31]. Unfortunately, the miscibility of AN with water makes it difficult to form AN-based HIPEs for the synthesis of PAN polyHIPEs [32].

\* Corresponding author. Tel./fax: +972 4 829 4582.

E-mail address: [michaels@tx.technion.ac.il](mailto:michaels@tx.technion.ac.il) (M.S. Silverstein).

This paper describes the successful synthesis of PAN-based polyHIPEs through a careful choice of crosslinking comonomer, surfactant, and initiator systems. This paper also describes how PAN-based polyHIPEs could be used as templates for the production of porous carbon monoliths through pyrolysis. Ideally, PAN homopolymer would yield the most suitable molecular structure for the formation of carbon. However, crosslinking comonomers are often necessary for the synthesis of stable polyHIPEs. The effects of the synthesis parameters, most importantly, the effects of the crosslinking comonomer content, on the resulting PAN-based polyHIPEs and on pyrolyzed PAN-based polyHIPEs will be described.

## 2. Experimental

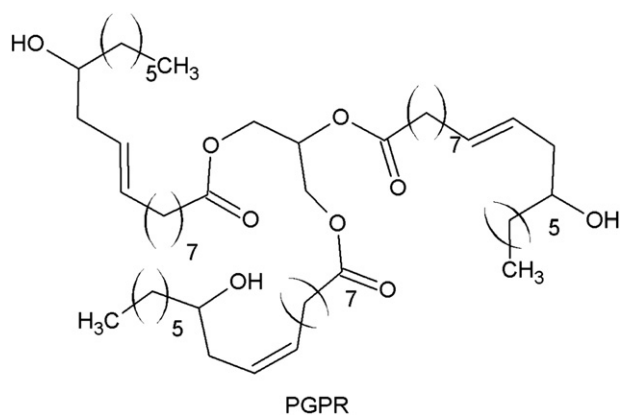
Forming HIPEs containing AN, polymerizing the AN within the HIPEs, and drying the PAN-based polyHIPEs without collapse all posed a great challenge. The procedure described below reflects one of the only systems that consistently produced highly porous PAN-based polyHIPEs.

### 2.1. Materials

The monomer was acrylonitrile (AN, Merck-Schuchardt) and the crosslinking comonomer was divinylbenzene (DVB, which contains 40% ethylstyrene, Riedel-de-Haen). AN was used as received. DVB was washed to remove the inhibitor, three times with a 5 wt % sodium hydroxide (NaOH, Carlo Erba) solution followed by three times with deionized water. The structure of the organic-soluble emulsifier, polyglycerol polyricinoleate (PGPR, C<sub>57</sub>O<sub>9</sub>H<sub>104</sub>, Palsgaard 4125), is illustrated in Scheme 1. The water-soluble initiator was potassium persulfate (KPS, Riedel-de-Haen) and the organic-soluble initiator was benzoyl peroxide (BPO, Fluka). Potassium sulfate (K<sub>2</sub>SO<sub>4</sub>, Frutarom, Israel) was used to stabilize the HIPEs.

### 2.2. Synthesis

The HIPEs were formed in 500 ml polypropylene beakers by adding the internal aqueous phase (water, initiator, and stabilizer) drop-wise to the external organic phase (monomers and emulsifier). The detailed procedure for polyHIPE synthesis was as follows: the external organic phase was placed in the beaker and stirred with a magnetic stirrer. The aqueous phase was added drop-wise with constant stirring and the resulting HIPE was covered with a plastic film. Polymerization took place in a circulating air oven at 65 °C for 24 h. The water was removed from the polyHIPE by drying at room temperature in a vacuum oven for about 3 days, until a constant weight was reached. Soxhlet extraction was used to try



Scheme 1. Schematic illustration of PGPR structure.

and remove salts and emulsifier from the polyHIPE. The polyHIPE was placed in a Soxhlet apparatus using water for 24 h and then methanol for 24 h. The polyHIPE was then dried in a convection oven at 60 °C for 24 h.

The AN content in the AN/DVB mixture,  $w_{AN}$ , was varied from 82.5 to 94.8 wt %. The external phase content was 11.8 wt %. A number of similar AN-based polyHIPEs containing external phase contents of up to 23.1 wt % were also synthesized. The polyHIPE sample names listed in Table 1 reflect the AN content in the AN/DVB mixture with AN83 containing 82.5 wt % AN in the AN/DVB mixture. A typical HIPE recipe (for AN83) is listed in Table 2.

### 2.3. Pyrolysis

The polyHIPEs were pyrolyzed by heating to 250 °C under O<sub>2</sub> at a rate of 10 °C/min and then heating to 960 °C under N<sub>2</sub> at a rate of 10 °C/min.

### 2.4. Characterization

The densities,  $\rho$ , were determined using gravimetric analysis. The porosities,  $p$ , of the polyHIPEs were calculated using Equation (1) by assuming a wall density,  $\rho_w$ , of 1.2 g/cm<sup>3</sup> for the polymer [34]. The porosities of the pyrolyzed polyHIPEs were calculated assuming a wall density of 1.8 g/cm<sup>3</sup> [35]. The densities of some of the pyrolyzed polyHIPEs were difficult to measure accurately due to their high porosities and the associated brittleness. The crystallinity was investigated using X-ray diffraction (XRD, Philips PW 1840 X-ray) with a Ni-filtered Cu K $\alpha$  X-ray beam excited at 40 kV and 40 mA.

$$p = \left(1 - \frac{\rho}{\rho_w}\right) \cdot 100\% \quad (1)$$

The porous structures were investigated through high resolution scanning electron microscopy (HRSEM, Zeiss LEO 982) of cryogenic fracture surfaces. The uncoated polyHIPE samples were viewed using an accelerating voltage of 4 kV. The molecular structure of the polymer was characterized using Fourier transform infrared spectroscopy (FTIR, Equinox 55, Bruker) from 400 to 4000 cm<sup>-1</sup> at a resolution of 4 cm<sup>-1</sup> with a photoacoustic attachment (MTEC Model 300). The FTIR spectra were collected from the polyHIPEs without any sample preparation.

The specific surface areas were determined using the single-point BET (Brunauer–Emmett–Teller) method, with nitrogen adsorption at 77 K (Quantachrome). The pore size distribution for macroporosity was determined using mercury porosimetry from 0 to 400 kPa (Macropore 120, Carlo Erba Instruments) and from 0.1 to 200 MPa (Porosimeter 2000, Carlo Erba Instruments). Mesoporosity, microporosity, and the BJH (Barret–Joyner–Halenda) surface area were determined using nitrogen absorption from 0 to 127 kPa (Micromeritics ASAP 2010).

The composition of the surface was characterized using X-ray photoelectron spectroscopy (XPS, Thermo VG Sigma Probe with Al

Table 1  
Descriptions of the HIPEs, polyHIPEs, pyrolysis, and pyrolyzed polyHIPEs.

Sample	HIPE	PolyHIPE		Pyrolysis		Pyrolyzed PolyHIPE	
	$w_{AN}$ , wt %	$\rho$ , g/cm <sup>3</sup>	$p$ , %	$m_L$ , %	$v_L$ , %	$\rho$ , g/cm <sup>3</sup>	$p$ , %
AN95	94.8	0.17	86	31.7	73.7	0.25	86
AN90	89.7	0.17	86	67.8	54.3	0.12	93
AN85	84.7	0.13	89	61.1	37.6	0.08	96
AN83	82.5	0.12	90	89.3	85.4	0.09	95

**Table 2**  
Typical HIPE recipe (AN83).

	Component	Amount, wt %
Organic phase	AN	8.0
	DVB	1.7
	PGPR	1.9
	BPO	0.2
	Total	11.8
Aqueous phase	Water	87.5
	K <sub>2</sub> SO <sub>4</sub>	0.5
	KPS	0.2
	Total	88.2

K<sub>2</sub> source). Low resolution XPS was used to characterize the atomic composition and high resolution C<sub>1s</sub> XPS was used to characterize the carbon bonds. The high resolution C<sub>1s</sub> XPS data was fit by removing the background and optimizing the sum of two or three peaks, all of which were set to have the same full width at half maximum (FWHM).

### 3. Results and discussion

#### 3.1. Molecular structure

FTIR spectra of three polyHIPEs based on HIPEs with different DVB contents are seen in Fig. 1. The bands at 713, 1452, 2852, and 2930 cm<sup>-1</sup> are associated with the methylene group. The band at 2240 cm<sup>-1</sup> is associated with the nitrile group of AN. The variation of the height of the band at 2240 cm<sup>-1</sup> normalized by the height of the band at 2930 cm<sup>-1</sup> in Fig. 2 represents the variation of the nitrile content in the polyHIPEs. The normalized height of the nitrile band is seen to decrease with increasing DVB content in a linear fashion.

The prominent bands at 3533 and 1734 cm<sup>-1</sup> in Fig. 1 represent hydroxyl groups and carbonyl groups, respectively. These bands are associated with residual PGPR. Previous work on polyHIPEs containing sorbitan monooleate (SMO) as an emulsifier with no PGPR has shown that extraction with water and methanol removes the SMO [36]. This may not be the case with PGPR, which could remain in the polyHIPEs following the extractions.

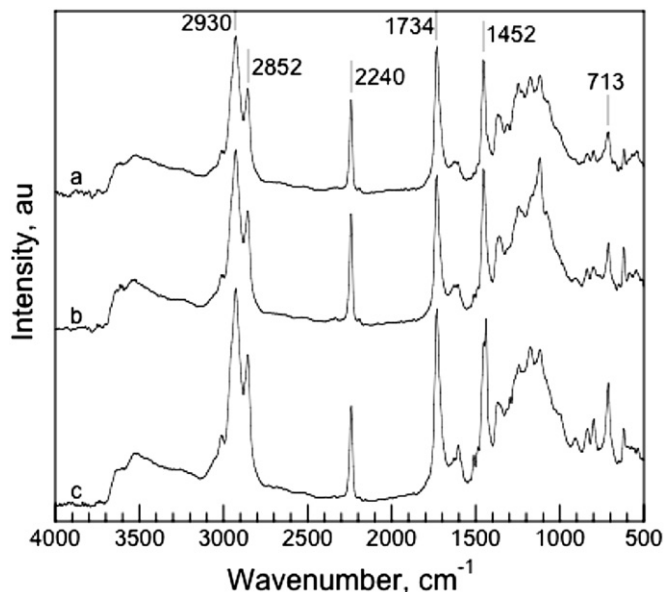


Fig. 1. FTIR spectra of: (a) AN95; (b) AN90; (c) AN85.

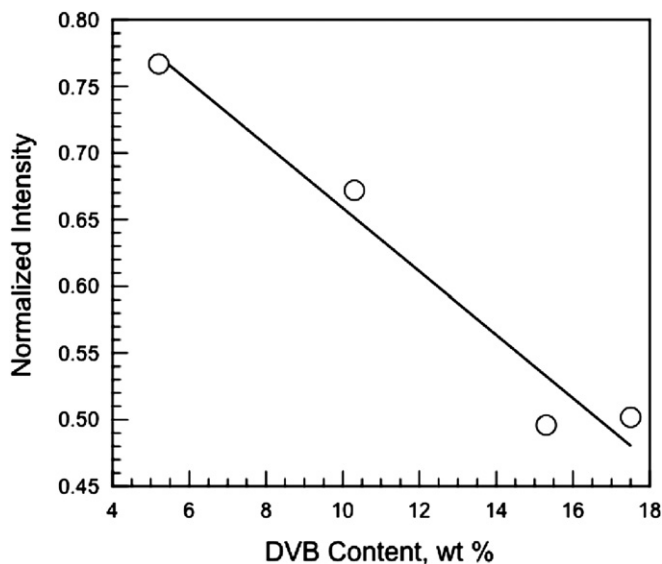


Fig. 2. Variation of normalized nitrile band height with DVB content.

#### 3.2. Porous structure

The polymerizations produced white monoliths with yields of around 90%. Based on the HIPE volume fractions, the densities expected for these polyHIPEs were around 0.1 g/cm<sup>3</sup>. The polyHIPE densities ranged between 0.12 and 0.17 g/cm<sup>3</sup> (Table 1), depending on the DVB content. The polyHIPE density was higher for the lower DVB contents, indicating that the crosslink density and chain stiffness in those polyHIPEs were not high enough to prevent partial collapse from the capillary stresses generated during drying. The polymer network was sufficiently stiff and crosslinked to resist the capillary stresses when there was 15 wt % DVB in the monomer mixture. The corresponding porosities ranged from 90% for the higher DVB contents to 86% for the lower DVB contents (Table 1).

The porous structure of AN83 is seen in the SEM micrographs in Fig. 3. The polyHIPE has an open-cell, highly interconnected porous structure with voids between 5 and 20 μm, however it is quite different from a typical polyHIPE structure [7]. Interestingly, all the AN-based polyHIPEs exhibited this structure, regardless of DVB content. The differences in density that result from the partial collapse at low DVB contents is not reflected in the porous structures seen in the SEM micrographs. Increasing the external phase content produced porous structures that seemed more closed-cell in nature (not shown) reflecting an increase in wall thickness which can limit interconnectivity.

#### 3.3. PolyHIPE surfaces

The atomic composition of the AN83 surface from XPS is listed in Table 3. Based on the monomer feed composition, a nitrogen content of 20.4% was expected from the XPS analysis. The nitrogen content of 10.9 at % was surprisingly low for a polymer based on 82.5 wt % AN in the feed. The FTIR results indicated that residual PGPR was present. The surfactant is preferentially located at the HIPE's water–oil interface [4] and, therefore, the residual surfactant is expected to be preferentially located on the polyHIPE's surface. An analysis of the surface composition from XPS was based upon the following three assumptions: (1) the nitrogen content represents the number of AN units in the polymer; (2) the AN/DVB ratio in the polymer is the same as that in the feed; (3) the oxygen content represents the number of PGPR molecules. The atomic contents calculated on the basis of these three assumptions are also

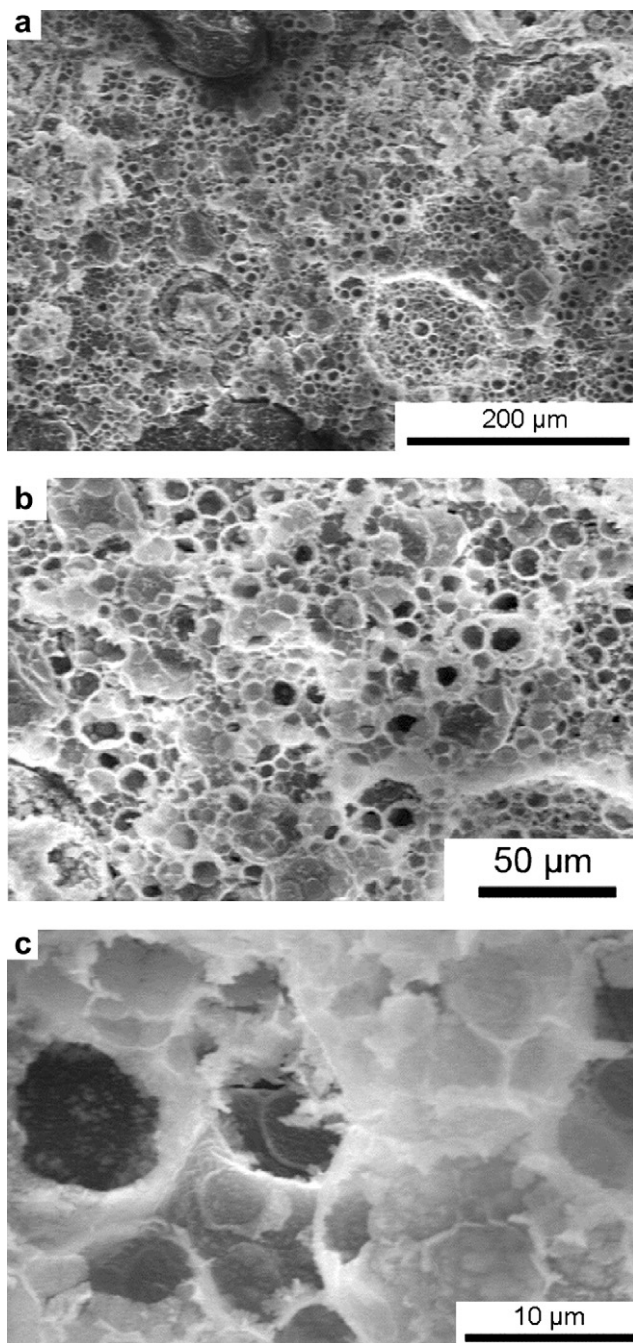


Fig. 3. SEM micrographs of the AN83 cryogenic fracture surface.

listed in Table 3. It is important to emphasize that no assumptions have been made regarding the relative amounts of PGPR and AN. In fact, the relative amounts of PGPR and AN can be calculated using the results of the XPS analysis.

**Table 3**  
XPS atomic compositions of the AN83 and pyrolyzed AN83 surfaces.

	AN83		Pyrolyzed AN83
	XPS, at %	Analysis, at %	XPS, at %
C	82.8	82.7	83.3
N	10.9	11.0	3.8
O	6.3	6.3	8.4
K	0.0	0.0	2.2
S	0.0	0.0	2.3

The negligible differences in the atomic contents between the prediction of the model and the experimental results support the validity of the analysis. According to the recipe in Table 2, the external phase of the HIPE contained 16.1 wt % PGPR. Based on the XPS analysis, the polyHIPE surface consists of 48.2 wt % PGPR, 42.7 wt % AN, and 9.1 wt % DVB. These results confirm that, as expected, the PGPR is preferentially located on the polyHIPE's surface.

The high resolution  $C_{1s}$  XPS spectrum from AN83 and the three peaks used to fit the experimental results are seen in Fig. 4. The positions of the Gaussian peaks used to fit the data are: (1) 285.0 eV (C–C); (2) 286.6 eV (C\*–C≡N, C≡N, C–O); and (3) 289.0 eV (O–C=O). The peak FWHMs were 1.4 eV. The contributions of each peak to the overall spectrum in the optimized fit are listed in Table 4. The contributions of the various groups can also be calculated using the surface composition that was derived from the previous analysis. A comparison of the results from the previous analysis with the results from the curve fit to the  $C_{1s}$  spectrum (Table 4) yields an average error of 18%. The correspondence between the results from the previous analysis and the results from a fit to the  $C_{1s}$  spectrum is quite reasonable and supports the derived surface composition.

### 3.4. Pyrolyzed polyHIPEs

Pyrolysis of the polyHIPEs produced significant mass losses,  $m_L$ , and volume losses,  $v_L$ , in the samples (Table 1). An  $m_L$  of 32.1% is expected from an ideal PAN pyrolysis in which all the hydrogen and nitrogen are removed and all the carbon remains. The  $m_L$  of 31.7% for AN95 is similar to the ideal  $m_L$ . However, increasing the DVB content from 5% to 10% yields a significant increase in  $m_L$  which rises to 67.8%. This increase in  $m_L$  reflects the profound disruption of AN cyclization that hinders the ability to form thermally stable structures. Increasing the DVB content to 17% produces an  $m_L$  of almost 90%. In general, the densities of the pyrolyzed polyHIPEs were lower than those of the original polyHIPEs (Table 1). The one exception is AN95, whose density increased upon pyrolysis. The DVB crosslinking is expected to prevent polyHIPE collapse during pyrolysis as the temperature rises above the PAN glass transition of

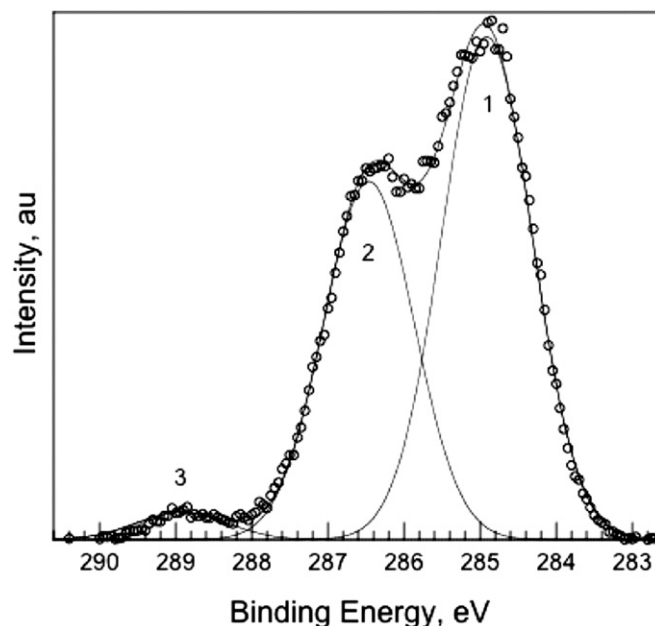


Fig. 4. High resolution XPS curve fit for the AN83 surface.



**Table 4**  
High resolution XPS curve fit parameters for AN83.

Peak	Groups	AN83		Pyrolyzed AN83
		XPS Fit, %	Analysis, %	XPS Fit, %
1	C–C	56.7	65.7	83.2
2	C*–C≡N, C≡N, C–O	40.2	31.7	16.8
3	O–C=O	3.1	2.6	0.0

85 °C. The relatively low degree of crosslinking in AN95 can result in partial collapse during pyrolysis. The reduction in density for the other pyrolyzed polyHIPEs yields an increase in porosity, especially since the density of the carbonaceous wall material following pyrolysis is higher than that of the original PAN-based polymer in the polyHIPE. The porosities in the pyrolyzed polyHIPEs can reach as high as 96% (Table 1).

In spite of the significant reductions in sample mass and volume, the porous structure of the pyrolyzed polyHIPE (Fig. 5) is quite similar to that of the original polyHIPE (Fig. 3). This holds for all the other pyrolyzed polyHIPEs and is similar to the results for pyrolyzed hybrid polyHIPEs and nanocomposite polyHIPEs [25,30]. The lack of crystalline peaks in the X-ray diffractions from the pyrolyzed polyHIPEs (not shown) indicate that they are amorphous materials.

The carbon monoliths have the macroporous structure seen in Fig. 5 as well as mesoporosity and microporosity. The BET surface area of the pyrolyzed AN90 was 26.5 m<sup>2</sup>/g, which is about an order of magnitude lower than that of other macroporous carbonaceous materials [32]. The BJH surface area was 16.4 m<sup>2</sup>/g and the BJH to BET ratio indicates that the mesoporous content was 61.9%. The size distribution of micropores in Fig. 6 exhibits a peak at around

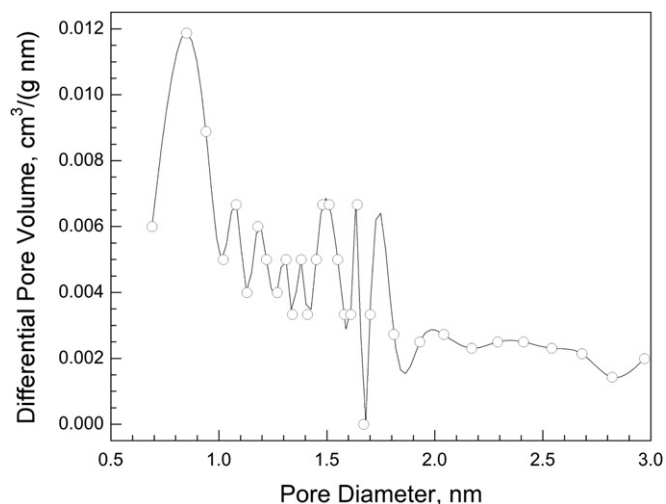


**Fig. 6.** Microporosity from nitrogen adsorption.

0.85 nm and a median pore diameter of 0.91 nm. The total volume of the pores from 1.7 to 300 nm was 0.032 cm<sup>3</sup>/g and the total volume of the macropores was significantly larger, 0.987 cm<sup>3</sup>/g.

Low resolution XPS analysis of the surface of the pyrolyzed AN83 shows that the nitrogen content on the surface is reduced to 3.7 at % by pyrolysis while the oxygen content increases to 8.4 at % (Table 3). The potassium and sulfur in the pyrolyzed polyHIPE originate in residual initiator and stabilizer. The amounts of residual potassium and sulfur are relatively small. These elements are overwhelmed by the amounts of carbon, nitrogen, and oxygen in the original polyHIPE and, therefore, are not detected by low resolution XPS. During pyrolysis there are significant losses of carbon and nitrogen, enhancing the relative potassium and sulfur contents and, thus, their detectability by low resolution XPS [37].

The high resolution C<sub>1s</sub> XPS spectrum from the pyrolyzed AN83 in Fig. 7 is quite different from the spectrum from the original AN83 polyHIPE in Fig. 4 and is quite similar to the spectra from other PAN-based carbonaceous materials [38]. The spectrum in Fig. 7 is best fit

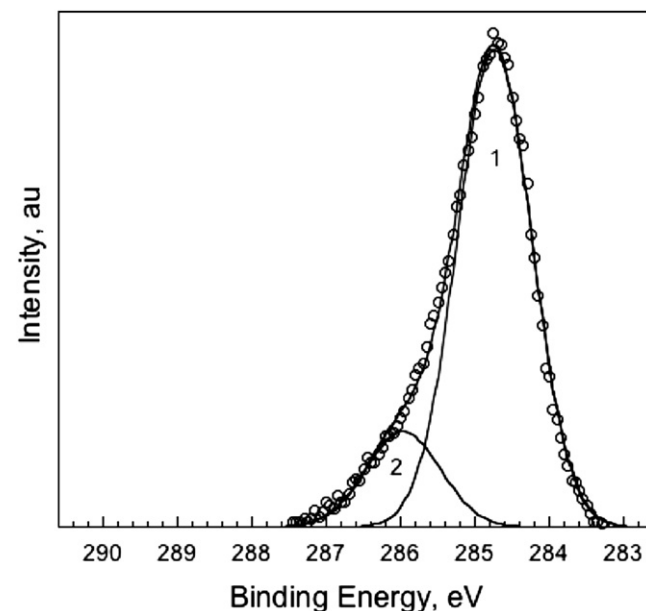


**Fig. 7.** High resolution XPS curve fit for the pyrolyzed AN83 surface.

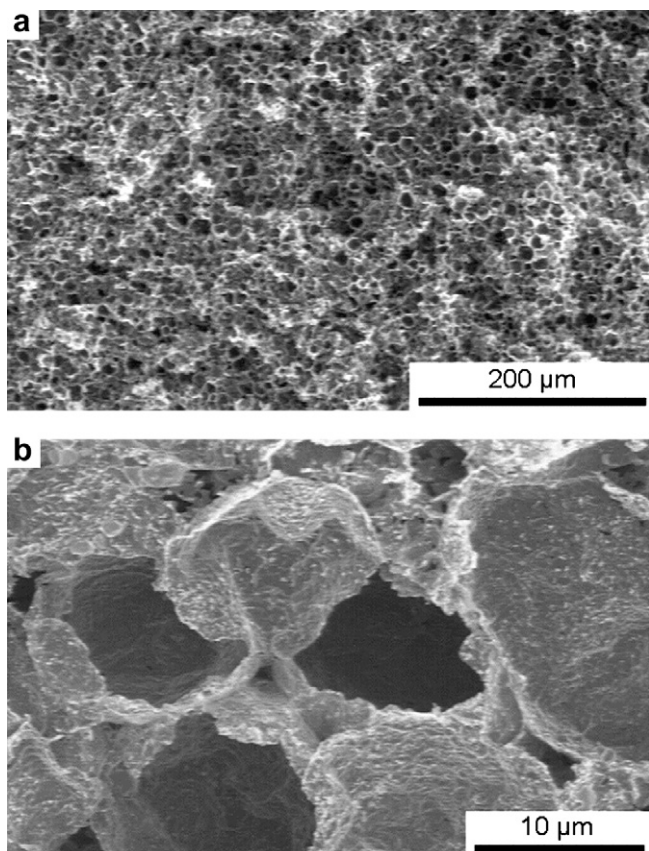


**Fig. 5.** SEM micrographs of the pyrolyzed AN83 fracture surface.

using only two Gaussian peaks with FWHMs of 1.18 eV. The peak at 285.0 eV represents C–C bonds and the peak at 286.2 eV represents C–O and C–N bonds. The contribution of each of these peaks to the total spectrum is listed in Table 4. The nitrogen and oxygen contents listed in Table 3 are reflected in the 16.8% contribution of the C–N and C–O bonds to the spectrum in Fig. 7. These results indicate that the pyrolyzed PAN-based polyHIPEs are highly porous, slightly oxidized, amorphous carbonaceous materials.

#### 4. Conclusions

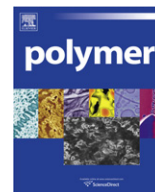
PAN-based polyHIPEs were successfully synthesized by using DVB crosslinking, PGPR stabilization, and both internal phase initiation and external phase initiation. The PAN-based polyHIPEs had porosities of over 86%. The porous structures were not typical polyHIPE structures and the effects of DVB content on the porous structure were negligible. Extraction in water and methanol did not remove the PGPR from the polyHIPE surface. Porous carbon monoliths were successfully produced by pyrolyzing the PAN-based polyHIPEs. Pyrolysis did not produce a significant change in the overall macroporous structure, in spite of the significant reductions in sample mass and volume. The porous structures of the polyHIPEs can act as templates for the production of porous carbon monoliths. The pyrolyzed polyHIPEs, with porosities of around 95%, were largely mesoporous and macroporous with some microporosity.

#### Acknowledgements

The partial support of the Israel Science Foundation and of the Technion VPR Fund is gratefully acknowledged.

#### References

- [1] Barby D., Haq Z. US Pat 4,522,953, 1985.
- [2] Williams JM, Wroblewski DA. *Langmuir* 1988;4:656–62.
- [3] Williams JM, Gray AJ, Wilkerson MH. *Langmuir* 1990;6:437–44.
- [4] Cameron NR, Sherrington DC. *Adv Polym Sci* 1996;126:163–214.
- [5] Cameron NR. *Polymer* 2005;46:1439–49.
- [6] Cameron NR, Krajnc P, Silverstein MS. In: Silverstein MS, Cameron NR, Hillmyer MA, editors. "Porous polymers". Hoboken NJ: Wiley; 2011. Chapter 4.
- [7] Silverstein MS, Cameron NR. "PolyHIPEs - Porous polymers from high internal phase emulsions" in *Encyclopedia of Polymer Science and Technology*. New York: Online, Wiley; 2010. doi:10.1002/0471440264.pst571.
- [8] Chen HH, Rukenstein E. *J Colloid Interface Sci* 1991;145:260–9.
- [9] Sergienko A, Tai H, Narkis M, Silverstein MS. *J Appl Polym Sci* 2004;94:2233–9.
- [10] Leber N, Fay JDB, Cameron NR, Krajnc P. *J Polym Sci A Polym Chem* 2007;45:4043–53.
- [11] Tai H, Sergienko A, Silverstein MS. *Polym Eng Sci* 2001;41:1540–52.
- [12] Livshin S, Silverstein MS. *Macromolecules* 2007;40:6349–54.
- [13] Kulygin O, Silverstein MS. *Soft Matter* 2007;2:1525–9.
- [14] Butler R, Hopkinson I, Cooper AI. *J Am Chem Soc* 2003;125:14473–81.
- [15] Butler R, Hopkinson I, Cooper AI. *Adv Mater* 2001;13:1459–63.
- [16] Busby W, Cameron NR, Jahoda CAB. *Biomacromolecules* 2001;2:154–64.
- [17] Hayman MW, Smith KH, Cameron NR, Pryborski SA. *J Biochem Biophys Methods* 2005;62:231–40.
- [18] Hayman MW, Smith KH, Cameron NR, Pryborski SA. *Biochem Biophys Res Commun* 2004;314:483–8.
- [19] Lumelsky Y, Silverstein MS. *Macromolecules* 2009;42:1627–33.
- [20] David D, Silverstein MS. *J Polym Sci A Polym Chem* 2009;47:5806–14.
- [21] Gitli T, Silverstein MS. *Soft Matter* 2008;4:2475–85.
- [22] Mercier A, Deleuze H, Maillard B, Mondain-Monval O. *Adv Synth Catal* 2002;344:33–6.
- [23] Moine L, Deleuze H, Maillard B. *Tetrahedron Lett* 2003;44:7813–6.
- [24] Tai H, Sergienko A, Silverstein MS. *Polymer* 2001;42:4473–82.
- [25] Silverstein MS, Tai H, Sergienko A, Lumelsky Y, Pavlovsky S. *Polymer* 2005;46:6682–94.
- [26] Menner A, Powell R, Bismarck A. *Soft Matter* 2006;2:337–42.
- [27] Menner A, Haibach K, Powell R, Bismarck A. *Polymer* 2006;47:7628–35.
- [28] Haibach K, Menner A, Powell R, Bismarck A. *Polymer* 2006;47:4513–9.
- [29] Gurevitch I, Silverstein MS. *J Polym Sci A Polym Chem* 2010;48:1516–25.
- [30] Normatov J, Silverstein MS. *Macromolecules* 2007;40:8329–35.
- [31] Lee J, Kim J, Hyeon T. *Adv Mater* 2006;18:2073–94.
- [32] Even W, Gergory D. *MRS Bull* 1994;19(4):29–33.
- [33] Goodhew PJ, Clarke AJ, Bailey JE. *Mater Sci Eng* 1975;17:3–30.
- [34] Fester W. In: Brandrup J, Immergut EH, editors. *Polymer handbook*. 3rd ed. New York: Wiley; 1989. p. V/57.
- [35] Diefendorf RJ. In: Fitzer E, editor. *Carbon fibres and their composites*. Berlin: Springer-Verlag; 1985. p. 54. Chapter 1.
- [36] Sergienko A, Tai H, Narkis M, Silverstein MS. *J Appl Polym Sci* 2002;84:2018–27.
- [37] Normatov J, Silverstein MS. *J Polym Sci A Polym Chem* 2008;46:2357–66.
- [38] Lee WH, Lee JG, Reucroft PJ. *Appl Surf Sci* 2001;171:136–42.



# Molecular dynamics simulations of the interactions and dispersion of carbon nanotubes in polyethylene oxide/water systems

Nasir M. Uddin, Franco M. Capaldi, Bakhtier Farouk\*

Department of Mechanical Engineering and Mechanics, Drexel University, Philadelphia, PA 19104, USA

## ARTICLE INFO

### Article history:

Received 14 July 2010

Received in revised form

24 November 2010

Accepted 27 November 2010

Available online 4 December 2010

### Keywords:

Carbon nanotube

Molecular dynamics simulations

Potential of mean force

## ABSTRACT

Molecular dynamics simulations were carried out to investigate carbon nanotube (CNT) interactions and dispersion in a polyethylene oxide (PEO)/water solution. The potential of mean forces (PMF) which embodies the entropic and enthalpic contributions by the solvent and the polymer molecules were computed. The relative enthalpic and entropic contributions to the PMF were studied in order to understand the CNT interaction mechanisms in solution. An adaptive biasing force (ABF) method was used to speed up the PMF calculations. The simulation results provide detailed atomic arrangements and atomic interactions between the CNTs and surrounding molecules (PEO and water). This molecular level computational study provides insights into the CNT's interactions with PEO polymer/water systems.

© 2010 Elsevier Ltd. All rights reserved.

## 1. Introduction

Single-walled carbon nanotubes (SWNTs) have been vigorously studied in the last two decades because of their outstanding intrinsic properties [1–5]. Incorporating small volume fractions of SWNTs within a polymer matrix may lead to increased stiffness, improved electrical conductivity, and modified permeability of the composite [6–8]. However, experimental studies have shown that aggregation and improper orientation of CNTs in the polymer matrix can degrade the ultimate properties and performance of the composite significantly [9–11]. In order to maximize the improvement in material properties while minimizing the quantity of carbon nanotubes (CNT), one must carefully control the dispersion of CNTs within the polymer matrix. During the initial processing of nanocomposites, CNTs are often dispersed in a liquid [12]. Controlling dispersion of CNTs within the matrix requires a fundamental understanding of how the CNTs interact with the liquid and polymer. Polyethylene oxide (PEO) is a potential candidate to be used for obtaining CNT reinforced nanocomposites specifically for bio-nanofiber based applications due to its water solubility and biocompatibility [13–15].

There are numerous atomistic modeling studies [16–18] conducted for polyethylene oxide (PEO)/water systems investigating

the interactions between PEO [chemical formula:  $\text{CH}_3\text{—O—CH}_2\text{—}(\text{—CH}_2\text{—O—CH}_2\text{—})_{n-1}\text{CH}_2\text{—O—CH}_3$ ] and water. For example, Borodin et al. [16] investigated the influence of the polymer on water dynamics. Simulations were performed on 12-repeat unit  $\text{CH}_3$ -capped PEO chains at 318 K covering a composition range (polymer weight fraction) from 0.17 to 1.0. Pang et al. [19] investigated the dispersion effect of carbon nanotubes (CNTs) in aqueous solutions by a silicon surfactant (ethoxy modified trisiloxane) using experimental method and molecular dynamics simulation. They found that Si—O—Si chain of silicon surfactant was flexible due to long Si—C bond and it could easily wrap around the surface of a CNT through hydrophobic and other intermolecular interactions. From the experimental study, they found that the hydrophilic part of PEO aided in the dispersion of the CNTs in the aqueous solution. They further carried out simulations for CNT/water/Ag-64 systems. Kang et al. [20] revealed that the interaction of poly[*p*-poly[*p*-{2,5-bis(3-propoxysulfonicacidsodiumsalt)}phenylene]ethynylene] (PPES) with SWNTs gives rise to a self-assembled superstructure in which a polymer monolayer helically wraps the nanotube surface. Their experimental structural predictions were confirmed by molecular dynamics simulations. Panhuis et al. [21] elucidated the interaction between single-walled carbon nanotubes and a conjugated polymer by an atomistic molecular dynamics computer simulation. Their calculations indicate an extremely strong non-covalent binding energy between CNT and polymer. The nature of the interaction between a short (10,10)-SWNT and a poly(*m*-phenylenevinylene-2,5-dioctyloxy-*p*-phenylenevinylene) (PmPV) polymer

\* Corresponding author. Tel.: +1 215 895 2287.

E-mail address: [bfarouk@coe.drexel.edu](mailto:bfarouk@coe.drexel.edu) (B. Farouk).

chain of eight repeating units was probed by Lordi and Yao [22]. They found that binding energies and frictional forces play only a minor role in determining the strength of the interface, but helical polymer conformations are essential. Qiao and Ke [23] performed 24 ns atomistic molecular dynamics simulations of the interaction of zwitterionic lysophosphatidylcholine, or LPC (18-carbon chain), with an (18,0) CNT (length 118 Å and diameter 14 Å) in aqueous solution. Their study found that LPC is predominantly aligned along the CNT axis.

This is the first study that determines a potential of mean force (PMF) for the interaction between CNTs in the presence of PEO. Following our previous molecular dynamics study [24] which focused on CNT interactions in water/surfactant systems, we present in this paper the simulation results for CNT/polymer/water systems with PEO polymer and (10,10) single-walled nanotubes (SWNTs) at room temperature and atmospheric pressure. Specifically, we analyze the interactions between SWNTs in PEO/water systems in terms of the potential of mean force (PMF) for two different polymer concentrations. Solvent and PEO induced interactions are also investigated. Entropic and enthalpic contributions to the PMF of CNT interactions in water are reported to understand the CNT/polymer solution interaction mechanisms. The calculated PMF from a molecular perspective characterizes the interactions in the polymer/nanoparticle/water systems in a way which can be used for mesoscale simulation.

## 2. Simulation details

### 2.1. Computational specifications

The present molecular dynamics (MD) study includes a representative volume element (RVE) consisting of two single-walled CNTs surrounded by water molecules and PEO polymer chains. The RVE was equilibrated for 2 ns with a time step of 1 fs in the NPT ensemble (the number of particles  $N$ , the pressure  $P$  and the temperature  $T$ ) using the NAMD software package [25]. The simulation cell dimensions ( $x \times y \times z$ ) are  $(120 \times 60 \times 60) \text{ \AA}^3$ . Periodic boundary conditions with the minimum image convention were applied in all three spatial directions.

The Langevin dynamics method [26], where additional damping and random forces are introduced to maintain an approximately constant temperature across the system, was employed to keep the temperature at 310 K. The pressure was maintained at 1 atm using a Langevin piston.[27] This method was combined with the method of temperature control and Langevin dynamics to simulate the NPT ensemble. The intermolecular three point potential (TIP3P) model was employed [28] to represent water molecules. The empirical ‘Chemistry at HARvard Molecular Mechanics’ (CHARMM) force field [29] was used to describe the inter-atomic interactions. Electrostatic and van der Waals interactions were truncated smoothly by means of a 12 Å spherical cutoff in conjunction with a switching function. To investigate the effect of PEO concentration on CNT interactions in water covering two different PEO compositions (each with 20 chains with  $n$  values of 13 and 21). PEO chains were first distributed randomly in the simulation cell containing two SWNT and then water molecules were inserted randomly to ensure the water density as  $0.99 \text{ gm/cm}^3$ . The MD simulations were carried out to observe the progress of migration and final equilibrium positions of the PEO chains and CNTs in water in NPT ensemble. Once the equilibrium system was obtained, the interactions between the CNTs were determined by calculating the potential of mean force (PMF) between the center of mass of the CNTs. The PMF (denoted by  $W$ ) was computed as a function of separation distance between the CNTs in the NVT (NPT for equilibration and NVT for PMF calculation) ensemble for different systems (CNT/water/polymer).

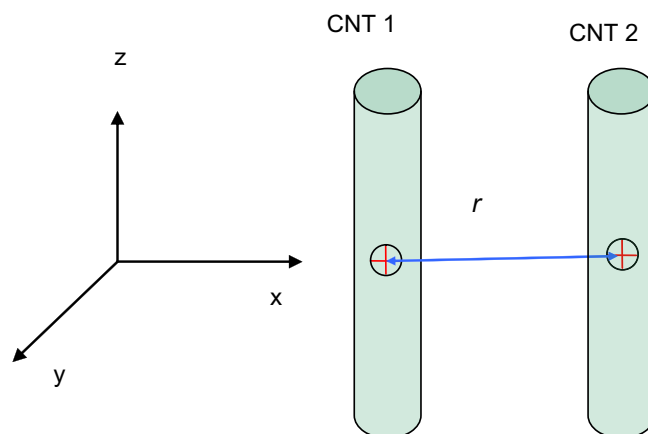


Fig. 1. Schematic of the orientation of two CNTs.

All simulations were carried out using the NAMD software package [25].

### 2.2. Calculation of the potential of mean force, $W$

The PMF between two CNTs can be written as a function of the separation between them,  $W = f(r)$ . The mean force,  $F(r)$  between these two atoms is then defined as:

$$F(r) = -\frac{d}{dr}[W(r)] \quad (1)$$

However, characterizing the interaction between two CNTs (Fig. 1) requires the computation of the PMF:

$$W = f(r) = -kT \ln P(r) + W_0 \quad (2)$$

where  $r$  is the distance between the center of mass of CNT 1 and CNT 2 (see Fig. 1);  $k$  is the Boltzmann constant;  $T$  is the temperature;  $P(r)$  is the probability of finding the system with specified  $r$ ; and  $W_0$  is a constant. In Equation (2),  $W$  is the effective interaction between CNT 1 and CNT 2 averaged over the conformations of all other components in the system.

Using the adaptive biasing method, we use constrained molecular dynamics simulations and a discretization of phase space to obtain the PMF. In each simulation we fix the position of the CNTs in the presence of mobile solvent (water) and PEO and then determine the constraint forces required to hold the molecule in place.

To explore the interactions between CNTs as a function of  $r$ , each system was equilibrated for 2 ns, then the PMF was calculated with the adaptive biasing force (ABF) method from a 10 ns MD simulation. The center of mass of the CNTs,  $r$  was chosen as the reaction coordinate,  $\xi$  for ABF method and simulations were carried

Table 1  
List of cases studied for CNT interactions in water/polymer systems.

No.	Simulation cell composition	Number of PEO repeat units (RU)	Number of PEO chains	Number of water molecules	Temperature (K)
1	CNT/water/polymer	12	20	3174	310
2	CNT/water/polymer	20	20	2782	310
3	CNT/vacuum	–	–	–	310
4	CNT/polymer	12	20	–	310
5	CNT/polymer	20	20	–	310
6	CNT/water	–	–	3762	310
7	CNT/water	–	–	3762	287
8	CNT/water	–	–	3762	333

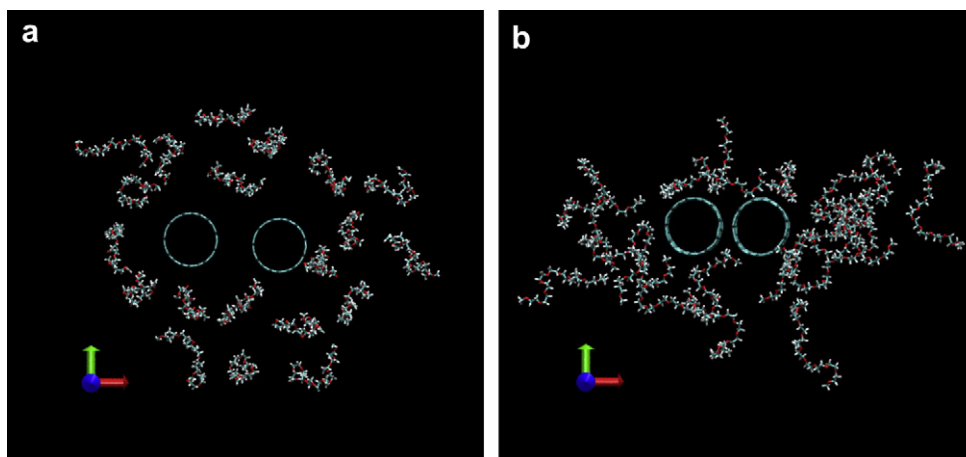


Fig. 2. (a) Initial and (b) Equilibrium system configuration of CNTs with PEO for case 1 (for clarity water molecules are not shown).

out restraining the range of the reaction coordinate to  $d \leq \xi \leq 30 \text{ \AA}$  with a bin size of  $\delta\xi = 0.1 \text{ \AA}$ , where  $d$  represents the diameter of the CNT.

### 3. Results and discussion

In this study, the cases considered are listed in Table 1. Cases 1 and 2 were studied by varying the polymer concentration in water. Case 3 was considered to quantify the solvent and polymer contributions to the governing CNT interaction force, PMF. Cases 4 and 5 were studied to understand the CNT interactions in polymer only cases. Cases 6 to 8 were considered (CNT/water only) in order to calculate the enthalpic and entropic contributions to the CNT interaction energy.

#### 3.1. Description of equilibrium systems

The thermodynamic parameters such as total energy of the system, temperature and pressure were monitored during each simulation case to observe the simulation accuracy. Energy, temperature and water density data were saved after 1000 time steps. The density of water at 310 K fluctuated between 1.02 and 1.03 gm/cm<sup>3</sup>.

The initial configuration was determined by randomly inserting the CNTs, PEO chains, and finally water molecules into the simulation cell. The initial and final (at thermodynamically equilibrium) configurations of the simulation cell of a characteristic CNT/water/polymer (Case 1, Table 1) are presented in Fig. 2. During the simulation the PEO chains were found to migrate towards the CNT surface and wrap around the CNTs in the equilibrium state. The chemical structure of PEO chain,  $\text{CH}_3\text{--O--CH}_2(\text{--CH}_2\text{--O--CH}_2\text{--})_{n-1}\text{CH}_2\text{--O--CH}_3$  contains a large hydrophobic tail. The hydrophobic tail of the PEO chains was attracted to the CNT surface due to van der Waals attraction. This adsorption of PEO chains on the CNT surface creates a layer of polymer between CNTs. However, the surfactant molecules (*not considered in the present paper*) are much more efficient at reducing the attraction between CNTs due to the charged hydrophilic head group on the surfactant molecule. The adsorption of the PEO observed in these simulations matches the experimental investigation of Holland et al. [30] on PEO adsorption onto a graphite substrate. In addition, it is clear that PEO chains form clusters where the chain ends have the tendency to stick to other chain due to hydrophobic tendency of the chain ends. This creates network structures where both ends are tethered or branched structures where only one end is tethered. This

observation agrees with the experimental investigation of Hammouda et al. [31] on clustering of PEO in solutions by using small-angle neutron scattering.

#### 3.2. CNT interactions in CNT/PEO/Water systems (Case 1 in Table 1)

CNT interactions in PEO/water were investigated with two armchair single-walled CNT (10, 10) and 12-repeat unit PEO chains as shown in Fig. 3. Molecular dynamics simulations were carried out for these systems at 310 K temperature in the NPT ensemble. The intermolecular three point potential (TIP3P) model was employed [28] to represent water molecules. The empirical CHARMM force field [29] was used to describe inter-atomic interactions for all other molecules. Periodic boundary conditions with minimum image conventions were applied in all three spatial directions.

The computed PMFs between carbon nanotubes as a function of their separation are shown in Fig. 4 for CNT/water and CNT/water/PEO (case 1 in Table 1). The PMF curves have characteristics

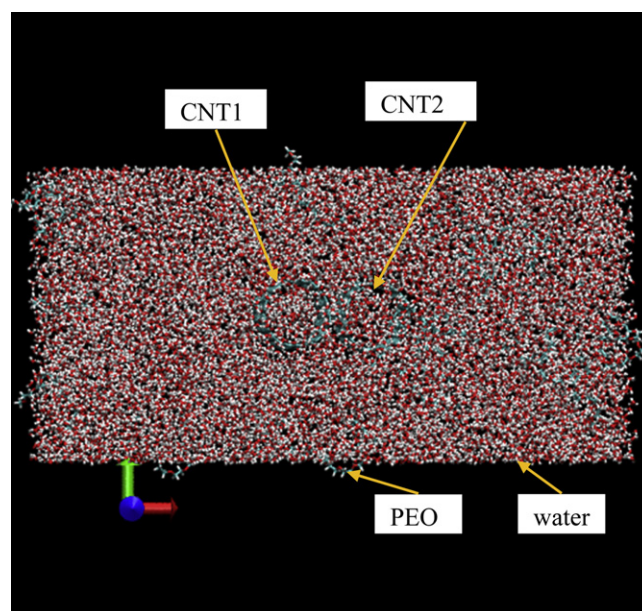
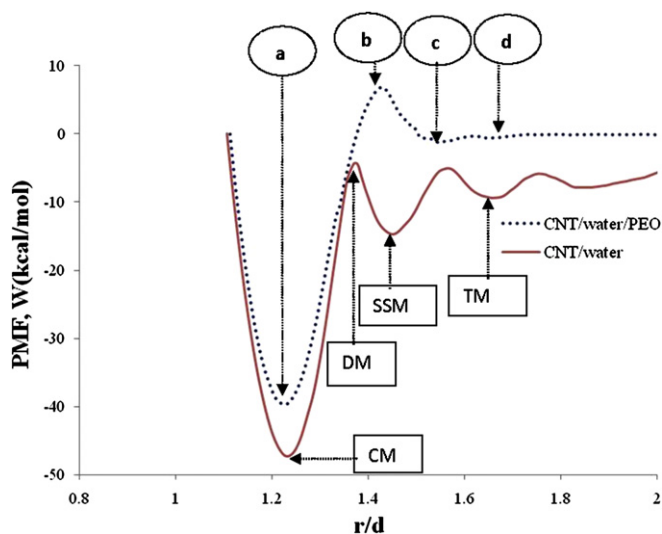


Fig. 3. Image of two CNTs in water/PEO of 12-repeat unit with 20 chains considered in potential of mean force calculations.



**Fig. 4.** Potential of mean force,  $W$  as a function of inter-atomic distance,  $r$  between the center of mass of CNTs for CNT/water (solid line) and CNT/water/PEO (dashed line) systems (Case 1 in Table 1).

shapes with one deep minimum each at about 1.21  $d$  and 1.23  $d$ , corresponding to CNT/water and CNT/water/PEO systems respectively, where  $d \sim 13.6$  Å is the CNT diameter. This minimum is referred to as the contact minimum (CM) [32]. The CM,

configuration (a) for CNT/water/PEO is shifted due to PEO adsorption on hydrophobic CNT surface. The CM for CNT/water is deeper than that of CNT/water/PEO which indicates that free energy between the CNTs in water is more favorable than that in water/PEO. This favorable free energy would enhance CNT interactions and ultimately the tendency of aggregation.

The PMF curves also contain the second minima referred to as 'solvent-separated minima (SSM) at distances about 1.45  $d$  and 1.53  $d$ , corresponding to CNT/water and CNT/water/PEO [configuration (c)] systems respectively. The depth of the SSM minima indicates that the formation of a single layer of water between CNTs is more favorable for CNT/water than that of CNT/water/PEO systems. It can also be noted that the water-separated configurations of hydrophobic CNTs become less favorable relative to the contact configurations with the addition of PEO to the CNT/water system.

The maximum in the PMF curve between the contact and solvent-separated minima is referred to as the desolvation maximum (DM) [32]. The DM is higher (approximately 1.42  $d$ ) for CNT/water/PEO [configuration (b)] than that of CNT/water system (approximately 1.35  $d$ ). As seen from Fig. 4, the heights and the positions of these DMs change significantly due to PEO addition to the CNT/water system. The appearance of a second desolvation barrier and a third minimum (TM) is also clearly observed in case of CNT/water system but not for CNT/water/PEO [configuration (d)]. The four significant corresponding PMF configurations of CNT/water/PEO system are described in Fig. 5.

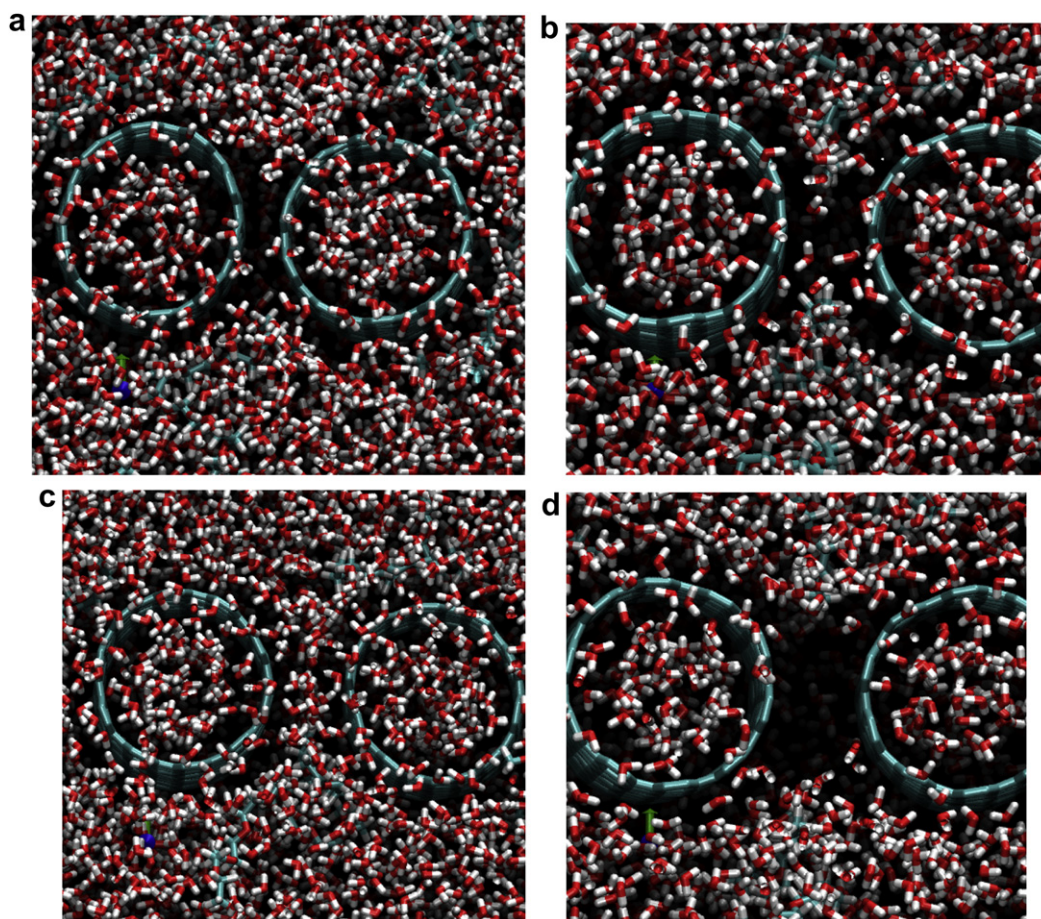


**Fig. 5.** Four different configurations of CNT/water/PEO systems showing the indicated PMF locations in Fig. 4 for (a) contact minimum (CM), (b) desolvation maximum (DM), (c) solvent-separated minimum (SSM), and (d) third minimum (TM). Each configuration is taken from the equilibrated simulations during PMF calculations at 10 000 time steps intervals (Case 1 in Table 1).

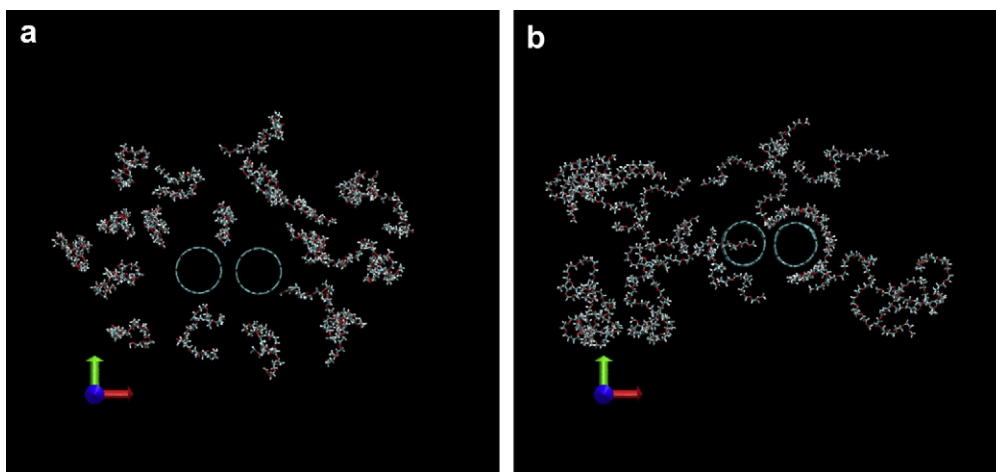


**Fig. 6.** Images (a) initial and (b) equilibrium configurations of two CNTs and PEO of 20 repeat unit with 20 chains considered in potential of mean force calculations (for clarity water molecules are not shown) (Case 1 and 2 of Table 1).

For CNT/water system, the behavior at larger CNT–CNT separations (i.e.,  $>1.3$  d) is considerably different. Both the desolvation barrier and the SSM are relatively weak, and the water-mediated force of interaction is attractive at even larger distances. The fact that PMF has a positive slope that does not approach a value of 0 at larger separations indicates a strong tendency to associate and form aggregates in the system. For CNT/water/PEO, the PMF is significantly different from that of CNT/water system at larger distances. The CM is destabilized by 8.1 kcal/mol; the desolvation barrier moves inward by 0.15 d and increases in height by approximately 10.5 kcal/mol. A significant SSM and a well-developed desolvation barrier appear due to PEO addition. Since the net change in PMF at CM, is very small, the significant changes in the overall nature of the PMF, especially those at larger distances, with the addition of PEO may not be sufficient to destabilize and dissolve the CNT aggregates.

### 3.3. Effects of PEO concentrations (Cases 1 and 2)

The effect of PEO concentration on CNT interactions in water/PEO systems are investigated with two armchair single-walled CNTs (10, 10):

- (a) 12-repeat units as shown in Fig. 2 earlier.
- (b) 20-repeat unit PEO chains as shown in Fig. 6.

MD simulations were carried out for these systems at 310 K temperature in the NPT ensemble. The intermolecular three point potential (TIP3P) model was employed [28] to represent water molecules. The empirical CHARMM force field [29] was used to describe inter-atomic interactions for all other molecules. Periodic boundary conditions with minimum image conventions were applied in all three spatial directions.

The computed PMFs between carbon nanotubes as a function of their separation are shown in Fig. 7 for two different PEO concentrations in water. The PMF clearly depends on the PEO concentration. As compared with the PMF for CNT/water/PEO-12 RU system, we can see that the contact minimum (CM) shifts outward by about 0.03 d and is destabilized by 6.2 kcal/mol; the desolvation barrier moves inward by 0.06 d and decreases in height by approximately 5.5 kcal/mol. A significant solvent-separated minimum (SSM) is more prominent and moves inward by about 0.1 d. Notable changes occur in the SSM configurations: with 12 unit RU, the larger distance between the CM and the SSM indicates a possibility

of CNT-separated configurations in the aggregate near the second minimum (SSM). However, with increasing PEO concentration, the distance between the CM and the SSM shortens indicating dissociated (i.e., water-separated) configurations at the SSM. Appearance of a second barrier and a third minimum is also observed.

All of these four configurations (CM, DM, SSM, and TM) for PEO-20 repeat units (RU) case shown in Fig. 7 are described in Fig. 8. This quantitative potential may be used to evaluate the formation of aggregates during dispersing CNTs in PEO/water. Since the net change in  $W_{CM}$  is small, the significant changes in the overall nature of the PMF, with the increment of PEO concentration, may not be sufficient to destabilize and dissolve the CNT aggregates in PEO solution.

### 3.4. CNT interactions in PEO only (Cases 3–5)

CNT interactions in PEO are investigated with two armchair single-walled CNT (10, 10) and 12-repeat unit (RU) 12-RU PEO and 20-RU PEO chains. The computed PMFs between carbon nanotubes as a function of their separation are shown in Fig. 9 for two different PEO concentrations as well as for two CNTs in vacuum for reference. The PMF changes for CNTs in PEO where there is a little effect of

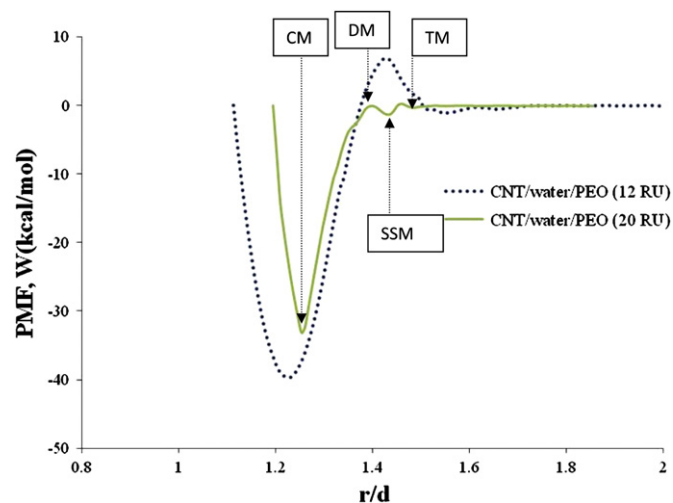


**Fig. 7.** Potential of mean force,  $W$  as a function of inter-atomic distance,  $r$  between the center of mass of CNTs for CNT/water/PEO-12 repeat unit (RU) and CNT/water/PEO-20 repeat unit systems (Cases 1 and 2 in Table 1).

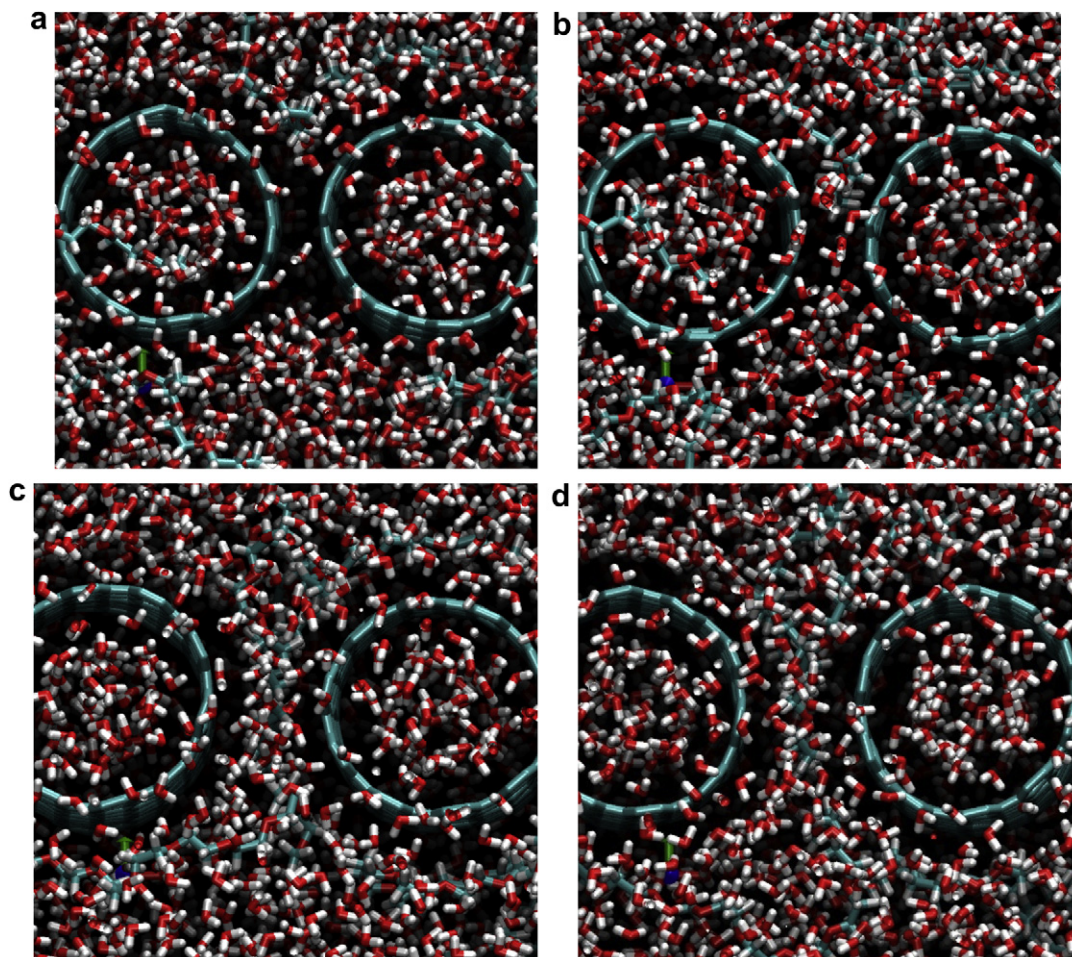


**Fig. 8.** Four different configurations of CNT/water/PEO with 20 repeat units (20 chains) systems showing the indicated PMF locations in Fig. 7 for (a) contact minimum (CM), (b) desolvation maximum, (c) solvent-separated minimum (SSM), and (d) third minimum (TM). Each configuration is taken from the equilibrated simulations during PMF calculations at 10 000 time step intervals (Case 2 Table 1).

PEO concentration on PMF except the contact minima (CM) for PEO-20 RU is deepened by about 8 kcal/mol. As compared with the PMF for CNT/vacuum and CNT/PEO-12 RU, we can see that the CM (configuration 1) is deepened by about 21 kcal/mol indicating

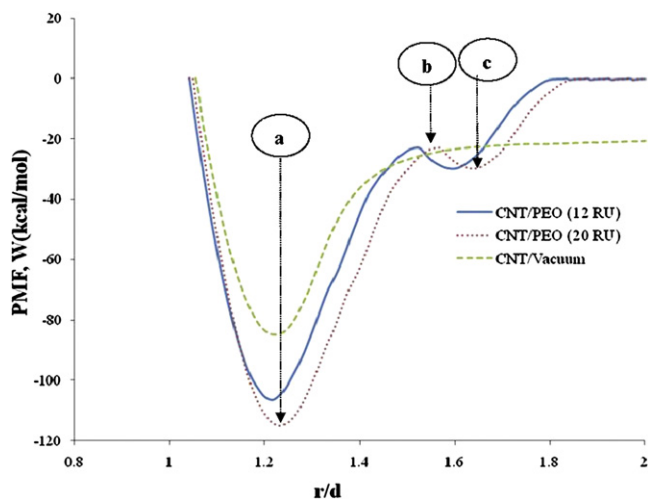


**Fig. 9.** Potential of mean force,  $W$  as a function of inter-atomic distance,  $r$  between the center of mass of CNTs for CNT/PEO-12 repeat unit (RU), CNT/water/PEO-20 RU, and CNT/vacuum (Cases 3–5 in Table 1).

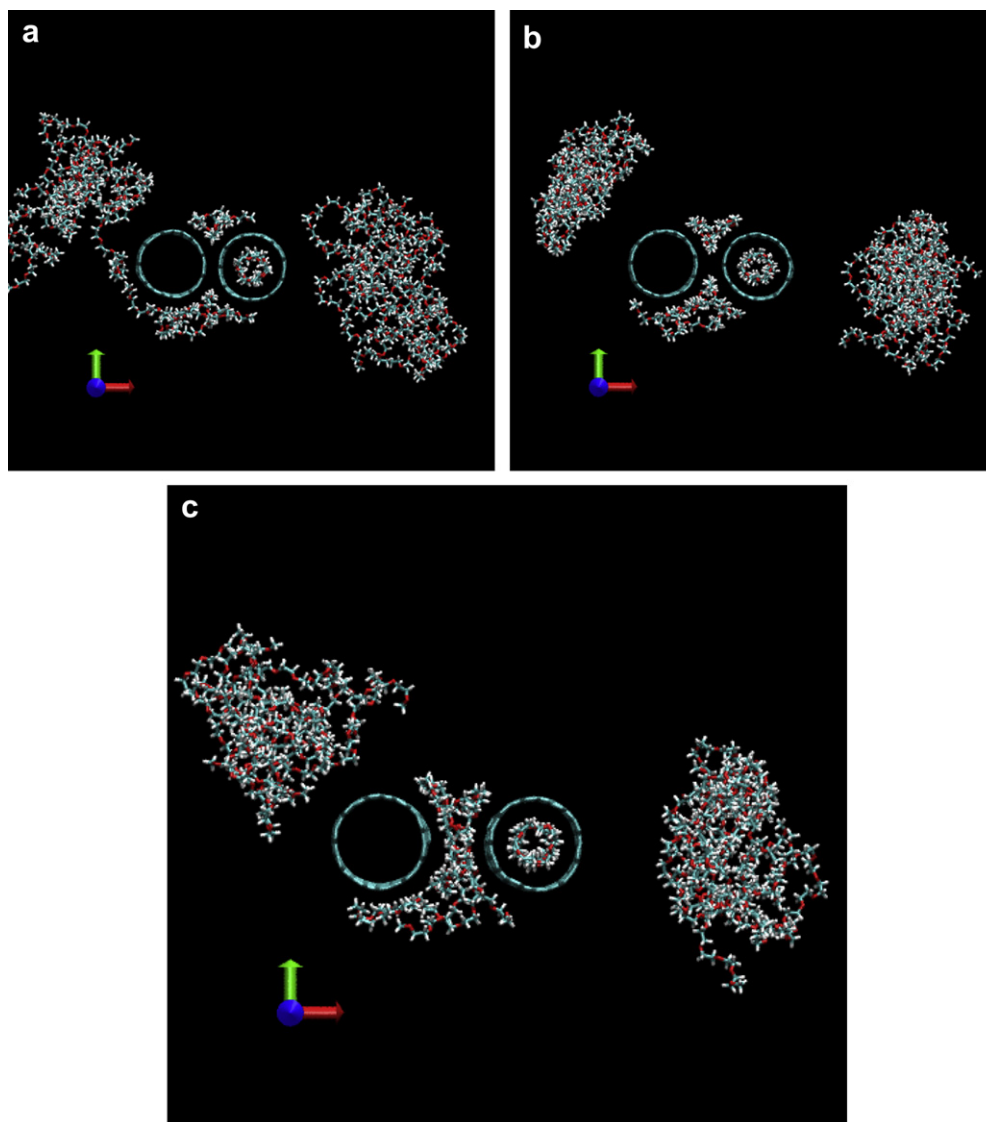
stronger CNT interactions in PEO; a significant PEO-separated minimum (configuration 3) is prominent at about 1.6 d due to PEO chain layer in between the CNTs. The desolvation barriers (configuration 2) for both PEO cases occur at about 1.5 d because of the fact that PEO chains tend to move in between CNTs causing the unfavorable free energy of the system.

At the longer distance, PEO chains become stable in between CNTs and CNT interactions become weaker and weaker as the PMF tends to become zero. The three distinct configurations for the case 5 are described in Fig. 10. Fig. 10 (a) shows the CM for the CNTs where some PEO chains are wrapped around the CNTs and most of the PEO chains are aggregated. Some PEO chains are trying to get in between the CNTs causing the destabilization of the system (DM) as shown in Fig. 10 (b). Fig. 10 (c) shows stable PEO layers in between the CNTs which are similar to SSM.

### 3.5. Solvent and PEO contributions to CNT interactions (Cases 1, 3, and 6)

In order to investigate the solvent and PEO contributions to the CNT interactions in aqueous solutions, molecular dynamics simulations are carried out with the biased method described in Section 2 for two CNTs in vacuum, water, and PEO/water (Cases 1, 3, and 6 in Table 1) at 310 K temperature in the NPT ensemble. The computational specifications are same as the previous sections.

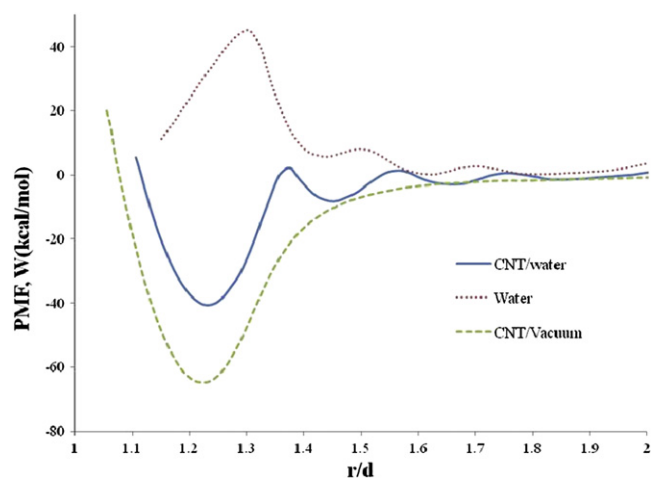




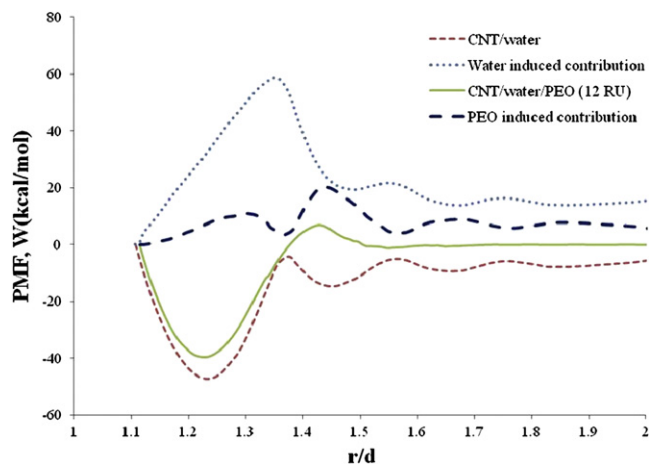
**Fig. 10.** Four different configurations of CNT//PEO-20 RU (20 chains) showing the indicated PMF curve locations in Fig. 9 for (a) contact minimum (CM), (b) desolvation maximum, and (c) PEO-separated minimum. Each configuration is taken from the equilibrated simulations during PMF calculations at 10 000 step intervals (Case 5 Table 1).

Fig. 11 shows the comparison of the computed PMFs between the CNT(10,10)/water and CNT(10,10). It is clear that the interaction between CNTs in vacuum is very strong as the CM is deeper than that in water. Fig. 11 presents also the water contribution to the PMF determined as a difference between the PMFs in water and in vacuum. As seen from Fig. 11, the water contribution to the PMF has one maximum corresponding to the position of the desolvation maximum in the PMF curve for the CNTs in water. It can be seen that the contribution to the PMF by the water solvent is purely a repulsion effect, which agrees very well with several published works such as Li et al.'s works on carbon nanoparticles in water [33], Choudhury and Pettitt's work on graphene in water, [34], and Li et al.'s on C60 fullerenes in water [35] etc.

Fig. 12 shows the PEO induced contributions to PMF determined as a difference between the PMFs in CNT/water/PEO and in CNT/water. It is clear that the PEO contribution to PMF is very weakly repulsive. As seen from Fig. 12, the PEO contribution to the PMF has one maximum corresponding to the position of the desolvation maximum in the PMF curve for CNT/water/PEO and two minima corresponding to the positions of the desolvation



**Fig. 11.** Potential of mean force,  $W$  as a function of inter-atomic distance,  $r$  between the center of mass of CNTs in solvent and in vacuum: CNT (solid line), CNT/water (dashed line), and water (dotted line) (Cases 3 and 6 Table 1).



**Fig. 12.** Potential of mean force,  $W$  as a function of inter-atomic distance,  $r$  between the center of mass of CNTs: CNT/water/PEO (solid line), CNT/water (dashed line), water (dotted line), and PEO (long dashed line) (Cases 1, 3, and 6 Table 1).

maxima in the PMF curve for the CNTs in water. It can be noted that PEO exhibits a weak long-range interactions because PEO chains weakly aggregate in aqueous solution as seen in Fig. 2(b) and 6(b).

### 3.6. Enthalpy–entropy contributions to the CNT interactions (Cases 6–8)

Entropic and enthalpic contributions to the interactions between CNTs, are investigated considering CNT (10,10) in water using molecular dynamics simulations. Simulations are carried out with the biased method described in Section 2 for CNTs immersed in a water system in the NPT ensemble for the equilibration and NVT ensemble for PMF calculations. The intermolecular three point potential (TIP3P) model was employed [28] to represent water molecules. The empirical CHARMM force field [29] was used to describe inter-atomic interactions for all other molecules. The simulation cell dimension ( $x \times y \times z$ ) is  $(120 \times 60 \times 60) \text{ \AA}^3$ . Periodic boundary conditions with minimum image conventions were applied in all three spatial directions.

Entropy is calculated from the finite difference temperature derivative of the PMF,  $W(r)$  at each inter-atomic distance between the COM of CNTs,  $r$ , viz.,

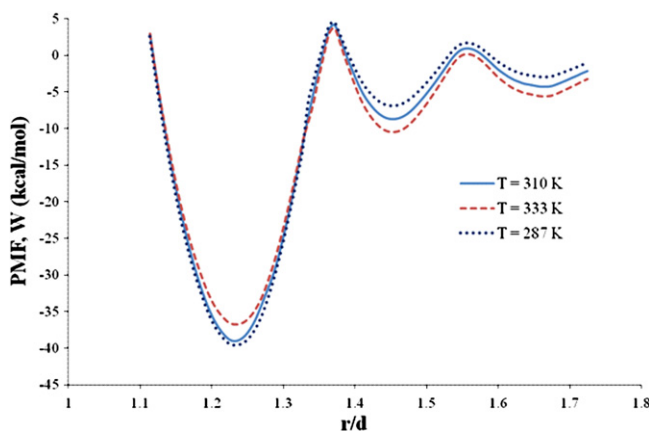


**Fig. 13.** Potential of mean force,  $W$  as a function of inter-atomic distance,  $r$  between the center of mass of CNTs for two CNTs in water at three different temperatures (Cases 6–8).

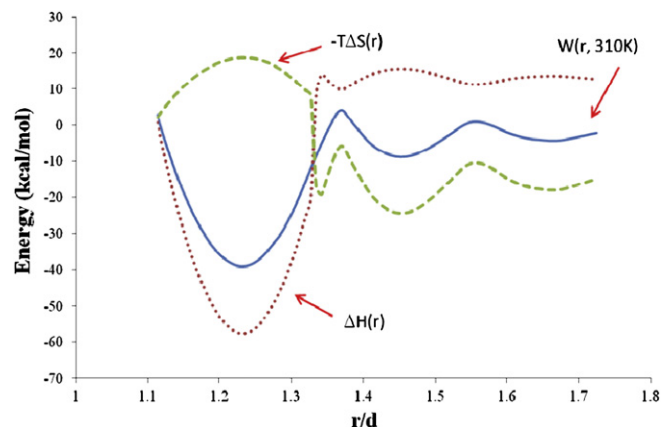


**Fig. 14.** Energy as a function of inter-atomic distance,  $r$  between the center of mass of CNTs for two CNTs in water with enthalpic (dotted line) and entropic (dashed line) contributions to the PMF,  $W(r, 310 \text{ K})$  between CNTs in water calculated based on Fig. 13.

$$-T\Delta S(r) = T \left[ \frac{W(r, T + \Delta T) - W(r, T - \Delta T)}{\Delta T} \right] \quad (3)$$

where,  $\Delta T$  is the temperature difference.

The enthalpy contribution to the free energy,  $H(r)$ , can then be obtained from entropy  $S(r)$  and the PMF,  $W(r)$  at temperature  $T$  as [35],

$$\Delta H(r) = \Delta W(r, T) + T\Delta S(r) \quad (4)$$

In the present calculation for the cases 6, 7, and 8 of Table 1, values of  $T$  and  $\Delta T$  are chosen to be 310 K and 23 K, respectively. Fig. 13 shows the PMF variation at three different temperatures. The corresponding entropic and enthalpic contributions obtained from the data in Fig. 13, to the PMF between the center of mass (COM) of CNTs at 310 K along with the PMF, are shown in Fig. 14. The stabilizing effects of entropic and enthalpic contributions of the PMF act in opposite direction to each other, and the relative proportion of the two contributions depends on the COM of CNTs. The contact minimum state of PMF is entirely stabilized by the favorable enthalpic contribution, entropic contribution being highly unfavorable. The favorable enthalpic contribution is significantly high and it stabilizes the CNT association even after compensating the unfavorable entropic effect.

Beyond the first contact minimum in free energy, there are two other minima which correspond to the second and third SSM states with a CNT-solvent configuration having two/three intervening water layers which is stabilized by enthalpy. The barrier between CM and SSM is determined from a slight imbalance between the stabilizing enthalpic contribution and the destabilizing entropic contribution. Therefore, favorable enthalpic contribution to the CNT interaction is responsible for strong interactions between CNTs and in-turn poor dispersion in water.

## 4. Conclusions

Molecular dynamics simulations aroused to determine the effective interactions between two carbon nanotubes as a function of their separation distance in water/PEO systems. The effect of PEO polymer concentration on CNT interactions as well as water and PEO induced contributions to the PMF were also investigated. In the CNT/water system at larger CNT–CNT separations (i.e.,  $>1.3 \text{ d}$ ), both the desolvation barrier and the solvent-separated minimum are relatively weak, and the water-mediated force of interaction is

attractive distances. For CNT/water/PEO, at larger distances, the PMF is different from that of CNT/water system. A significant SSM and a well-developed desolvation barrier appear due to the addition of PEO. Since the net change in  $W_{CM}$  is very small, the significant changes in the overall nature of the PMF, especially those at larger distances, with the addition of PEO may not be sufficient to destabilize and dissolve the CNT aggregates.

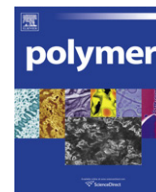
The PMF varied with changes in PEO concentration. As compared with the PMF for CNT/water/PEO-12 RU system, for CNT/water/PEO-20 RU we can see that the contact minimum (CM) is destabilized; the desolvation barrier moves inward and decreases in height. A significant SSM is more prominent and moves inward. Notable changes occur in the SSM configurations which indicate a possibility of CNT-separated configurations in the aggregate near the SSM. However, with increasing PEO concentration, the distance between the CM and the SSM shortens indicating dissociated (i.e., water-separated) configurations at the SSM. Appearance of a second barrier and a third minimum was also observed.

PEO chains were found to be weakly adsorbed at the CNT surface and this adsorption behavior matches well with the experimental investigations reported in the literature on PEO adsorption onto a graphite substrate. In addition, it was clear that PEO chains form cluster where the notable feature is that the chain ends have the tendency to stick to other chain. These chain ends are the dominant factor driving PEO cluster formation because of hydrophobic forces on chain ends. This creates network structures where both ends are tethered or branched structures where only one end is tethered. This finding matches exactly with the experimental investigations.

The contribution to the PMF by the water solvent is purely a repulsion effect, which agrees very well with several published works. The PEO contribution to the PMF is very weakly repulsive and PEO exhibits a weak long-range interaction because PEO chains weakly aggregate in aqueous solution. The entropic and enthalpic contributions to the PMF were calculated from the temperature dependence of the PMF obtained from the MD simulations of CNT/water systems at two different temperatures. This study confirms the theoretical picture of the hydrophobic interactions of CNTs in water. Specifically, it was found that the stabilization of the contact minimum state is mainly due to an increase in entropy arising from the expulsion of the highly structured water layer and the enthalpic effect from the inter-CNT. Understanding these thermodynamic behaviors may help in explaining CNT aggregation phenomena observed in many solvent systems.

## References

- [1] Iijima S. *Nature* 1991;56:56–8.
- [2] Ajayan PM. *Chemical Review* 1999;99:1789–99.
- [3] Thess A. *Science* 1996;273:483–7.
- [4] Salvetat JP. *Applied Physics A-Materials Science & Processing* 1999;69A:255–60.
- [5] Demczyk BG. *Material Science & Engineering A* 2004;A334:173–8.
- [6] Sandler J, Shaffer MSP, Prasse T, Bauhofer W, Schulte K, Windle AH. *Polymer Communication* 1999;40(21):5967–71.
- [7] Rahatekar SS, Rasheed A, Jain R, Zammarano M, Koziol KK, Windle AH, et al. *Polymer* 2009;50(19):4577–83.
- [8] Kharchenko SB, Douglas JF, Obrzut J, Grulke EA, Migler KB. *Nature Materials* 2004;3:564–8.
- [9] Zhuang GS, Sui GX, Sun ZS, Yang R. *Journal of Applied Polymer Science* 2006;102(4).
- [10] Dror Y, Salalha W, Khalfin RL, Cohen Y, Yarin AL, Zussman E. *Langmuir* 2003;19:7012–20.
- [11] Ko F, Gogotsi Y, Ali A, Naguib N, Ye H, Yang G, et al. *Advanced Materials* 2003;15:1161–5.
- [12] Xie X-L, Maia Y-W, Zhou X-P. *Materials Science and Engineering Review* 2005;49:89–112.
- [13] Shin MK, Kim YJ, Kim SI, Kim S-K, Lee H, Spinks GM, et al. *Sensors and Actuators B: Chemical* 2008;134(1):122–6.
- [14] Dror Y, Salalha W, Khalfin RL, Cohen Y, Yarin AL, Zussman E. *Langmuir* 2003;19(17):7012–20.
- [15] Ko F, Kahn S, Rahman A, and Zhou O. Carbon nanotube reinforced nanocomposites by the electrospinning process. ASC 16th Annual Technical Conference. Blacksburg, VA; 2001.
- [16] Borodin O, Smith GD, Bandyopadhyaya R, Redfern P, Curtiss LA. *Modelling and Simulation in Materials Science Engineering* 2004;12:S73–89.
- [17] Ennari J, Neelov I, Sundholm F. *Computational and Theoretical Polymer Science* 2000;10:403–10.
- [18] Borodin O, Trouw F, Bedrov D, Smith GD. *Journal of Physical Chemistry B* 2002;106(20):5184–93.
- [19] Pang J, Xu G, Yuan S, Tan Y, He F. *Colloids and Surfaces A: Physicochemical and Engineering Aspects* 2009;350:101–8.
- [20] Kang YK, Lee O-S, Deria P, Kim SH, Park T-H, Bonne DA, et al. *Nano Letters* 2009;9(4):1414–8.
- [21] Panhuis Mh, Maiti A, Dalton AB, Noort Avd, Coleman JN, McCarthy B, et al. *Journal of Physical Chemistry B* 2003;107(2):478–82.
- [22] Lordi V, Yao N. *Journal of Materials Research* 2000;15(12):2770–9.
- [23] Qiao R, Ke PC. *Journal of American Chemical Society* 2006;128(42):13656–7.
- [24] Uddin NM, Capaldi F, Farouk B. *Journal of Engineering Materials and Technology* 2009;132(2):021012–5.
- [25] NAMD Scalable molecular dynamics. Beckman Institute for Advanced Science and Technology, National Institutes of Health, National Science Foundation, Physics, Computer Science, and Biophysics at UIUC; 2009.
- [26] Wu X, Brooks BR. *Chemical Physics Letters* 2003;381:512–8.
- [27] Feller SE, Zhang Y, Pastor RW. *Journal of Chemical Physics* 1995;103.
- [28] Price DJ, Brooks III CL. *Journal of Chemical Physics* 2004;121:10096–103.
- [29] MacKerell AD, Bashford D, Bellott M, Dunbrack RL, Evanseck JD, Field MJ, et al. *Journal of Physical Chemistry B* 1998;102.
- [30] Holland NB, Xu Z, Vacheethasane K, Marchant RE. *Macromolecules* 2001;34:6424–30.
- [31] Hammouda B, Ho DL, Kline S. *Macromolecules* 2004;37:6932–7.
- [32] Sobolewski E, Makowski M, Czaplowski C, Liwo A, Otdziej S, Scheraga HA. *Journal of Physical Chemistry B* 2007;111:10765–74.
- [33] Li L, Bedrov D, Smith GD. *Journal of Physical Chemistry B* 2006;110:10509–13.
- [34] Choudhury N, Pettitt BM. *Journal of Physical Chemistry B* 2006;110:8459–63.
- [35] Li L, Bedrov D, Smith GD. *Journal of Chemical Physics* 2005;123:204504–7.



# Synthesis of high proton conducting nanoparticles by emulsion polymerization

Emmanuel Pitia<sup>a,\*</sup>, M.T. Shaw<sup>b,1</sup>, R.A. Weiss<sup>a,\*</sup>

<sup>a</sup> University of Akron, Department of Polymer Engineering, Polymer Engineering Academic Center, 250 South Forge Street, Akron, OH 44325-0301, USA

<sup>b</sup> University of Connecticut, Polymer Program and Department of Chemical Engineering, Institute of Materials Science, 97 North Eagleville Road, Storrs, CT 06269-3136, USA

## ARTICLE INFO

### Article history:

Received 27 September 2010

Received in revised form

23 November 2010

Accepted 27 November 2010

Available online 4 December 2010

### Keywords:

Conductivity

Nanoparticles

Styrene sulfonate

## ABSTRACT

High ion-exchange capacity (IEC) sulfonated polystyrene nanoparticles were synthesized by an emulsion copolymerization of styrene, divinyl benzene and sulfonated styrene (SS). The effects of varying the counterion of the sulfonated styrene monomer, the SS concentration, the surfactant and the addition of a crosslinking agent on the ability to stabilize the emulsion nanoparticles to high IEC were studied. Water-insoluble nanoparticles, 20–160 nm in diameter, with IEC as high as 5.2 meq/g were achieved using sulfonated styrene with a quaternary alkyl ammonium cation, a non-ionic surfactant and a crosslinking agent in the emulsion formulation. That IEC corresponds to fully sulfonated crosslinked polystyrene.

© 2010 Elsevier Ltd. All rights reserved.

## 1. Introduction

Ion-exchange resins such as sulfonated crosslinked polystyrene (SXLPS) particles have applications in chromatography [1–3], synthesis of magnetic particles [4–7], catalysis [8,9], polymeric actuators [10,11] and water purification [12]. Recently, it has been considered as a component of a composite proton-exchange membranes (PEM) for fuel cells, because of its high ion-exchange capacity (IEC [=] meq/g) [13–18] and crosslinked structure. The crosslinked structure stabilizes and prevents dissolution of the particles in water. A practical range of the degree of crosslinking is 4–16% [19]. The IEC, degree of crosslinking, and particle size depend on the application.

High IEC, ~4–5 meq/g, micrometer-size particles are commonly obtained via suspension copolymerization of styrene with a crosslinker such as divinyl benzene, followed by sulfonation of the particles [20–23]. In suspension polymerization, the particle size ranges from 10 to 1000  $\mu\text{m}$ . Another method of obtaining XLPS particles is by emulsion polymerization which produces 50–500 nm size particles [14,24]. However, ionic nanoparticles tend to coalesce into  $\mu\text{m}$ -size particles during a post-polymerization sulfonation step. An alternative method for directly producing SXLPS nanoparticles is by an emulsion copolymerization

of sulfonated styrene (SS) with (or without) styrene and a crosslinker such as divinyl benzene (DVB) [15,25–27]. In the aforementioned polymerization methods, the formulation typically consists of monomers, water, surfactant, and initiator. The solubility of the initiator in the water phase differentiates emulsion from suspension polymerization.

Composite PEMs are of interest, because a two-phase system provides the ability to decouple the transport and mechanical properties, which is a problem with single ion membranes such as Nafion<sup>®</sup> and sulfonated homopolymers [28]. For a composite PEM application, one wants SXLPS nanoparticles with high IEC, <100 nm diameter and crosslinked to prevent excessive swelling or dissolution by water. Composite PEMs, containing sulfonated crosslinked polystyrene (SXLPS) dispersed into various polymer matrices have previously been described, though in those cases, usually micrometer-size particles were used [13–18]. The conductivity ( $\sigma$ ) of those composite membranes was as high as 0.3 S/cm [16], which is comparable to that of Nafion<sup>®</sup> 117 ( $\sigma \sim 0.1$  S/cm). High IEC (~3.5–5.2 meq/g) SXLPS microparticles, ~1 to 50  $\mu\text{m}$ , were obtained by either grinding conventional ion-exchange resins [15–18] or post-sulfonation of crosslinked polystyrene particles [13,14]. A disadvantage of micrometer-sized particles is that the particle size is similar to the thickness of the membrane (e.g., Nafion 117 is ~180  $\mu\text{m}$  thick), which produces a poor dispersion of the particles and a relatively small ratio of surface area/volume (S/V) of the conducting phase.

In summary, previous work [13–18], has demonstrated that crosslinked sulfonated polystyrene micro- and nanoparticles can be

\* Corresponding authors. Tel.: +1 330 972 2581; fax: +1 330 258 2339

E-mail addresses: [esp9@ziips.uakron.edu](mailto:esp9@ziips.uakron.edu) (E. Pitia), [montgomery.shaw@uconn.edu](mailto:montgomery.shaw@uconn.edu) (M.T. Shaw), [rweiss@uakron.edu](mailto:rweiss@uakron.edu) (R.A. Weiss).

<sup>1</sup> Tel.: +1 860 486 3980.

used to prepare composite PEMs and that alignment [18,29,30] of the particles improved the proton conductivity. However, that work was limited to either high IEC microparticles or low IEC nanoparticles. The hypothesis driving the research reported herein is that one might expect better dispersion, higher proton conductivity, and improved mechanical properties of a composite membrane if the dispersed particles were nm-sized and had high IEC.

Weiss and coworkers [25–27] previously described the synthesis of the sodium salt of poly(styrene-co-sulfonated styrene) (PSSS-Na) using an emulsion copolymerization, but they were concerned with the development of ionomers with low IEC. Brijmohan et al. [31] extended that work to prepare the sodium salt of crosslinked poly(styrene-co-sulfonated styrene) (XLPSSS-Na) nanoparticles (~50 nm) using an emulsion copolymerization of styrene, sodium styrene sulfonate (Na-SS) and divinyl benzene (DVB). The highest IEC achieved in that work, however, was 2.2 meq/g, which is lower than the theoretical limit for fully sulfonated polystyrene, 5.4 meq/g. The IEC was limited by the stability of the emulsion and the solubility of the Na-SS in the polymerizing particles. In the emulsion copolymerization used, the styrene and DVB monomers were in the dispersed oil phase and the Na-SS was in the continuous aqueous phase. Weiss and coworkers [25–27] concluded that the locus of the polymerizing species was the interface between the two phases.

Kim et al. [32] studied the synthesis of emulsifier-free copolymerization of Na-SS and styrene where the targeted IEC was ~0.50 meq/g. They proposed that homogenous nucleation was the primary source of particles at low concentration of Na-SS. When the Na-SS concentration increased, they proposed a dual particle nucleation mechanism where particles were formed by homogeneous and micelle nucleation. They suggested that micelles formed from aggregation of either the Na-SS or a water-soluble polyelectrolyte rich in Na-SS. They concluded that synthesis of high IEC particles was not possible due to formation of high IEC water-soluble polymer. More recently, Arunbabu et al. [33] reported the formation of water-soluble polymer due to homopolymerization of Na-SS in the water phase. Hence, in order to eliminate the production of water-soluble polymer and achieve high IEC nanoparticles, the solubility of sulfonated styrene needs to be altered so that it is soluble in the oil phase. That, together with the addition of a crosslinker, should improve its incorporation into the nanoparticles.

This paper reports on the synthesis and characterization of high IEC (~5.2 meq/g) crosslinked poly(styrene-co-sulfonated styrene) (XLPSSS) nanoparticles prepared by emulsion copolymerization of a quaternary alkyl ammonium (QAA) neutralized-sulfonated styrene, styrene, and divinyl benzene. The effects of varying the counterion of the sulfonated styrene (SS) monomer (alkali metal and QAA cations), SS concentration, and the addition of a crosslinking agent (divinyl benzene) on the ability to stabilize the nanoparticles to higher IECs were assessed. The QAA salts were chosen specifically to shield the polar character of the sulfonate group in SS and alter its partition between the water and the oil phase in the emulsion polymerization. In addition, the QAA cations were expected to be beneficial in membrane fabrication by suppressing agglomeration of the nanoparticles and improving dispersion in a hydrophobic matrix.

## 2. Experimental details

### 2.1. Materials

Sodium styrene sulfonate, NaSS; tetrabutyl ammonium hydroxide (TBAH) 30-hydrate; a 40 wt% aqueous solution of tetrabutyl ammonium hydroxide (TBAH); a 25 wt% aqueous solution

of tetramethyl ammonium hydroxide (TMAH); tetrahexyl ammonium bromide (99% THAB); tetraoctyl ammonium bromide (98% TOAB); potassium persulfate (99.99% KPS); sodium dodecyl sulfate (98% SDS); poly(oxyethylene-4-lauryl ether), (Brij 30; FW 362.6; HLB 9.7); poly(oxyethylene-20-lauryl ether), (Brij 99; FW 1149.5; HLB 15); lithium acetate dihydrate; hydroxide-exchange resin (Amberlite IRN-78, 1.1 meq/mL); and a proton-exchange resin (Amberlite IRN-77, 1.8 meq/mL) were obtained from Aldrich Chemical Co. and used as received. A water-soluble non-ionic initiator, 2,2'2'-azobis[2-(2-imidazolin-2-yl)propane] dihydrochloride (VA-044) was obtained from Wako Chemicals, and used as received. Styrene (>99%) and divinyl benzene (~80% mixture of isomers, DVB) from Aldrich Chemical Co. were washed three times with an aqueous solution consisting of 5 wt% NaOH and 25 wt% NaCl, and then twice with de-ionized water to remove the inhibitors. De-ionized water (18 MΩ cm @ 25 °C) was used in all the polymerizations.

### 2.2. Synthesis of PSSS-Na nanoparticles

Although crosslinked nanoparticles are needed for a PEM application to prevent dissolution in an aqueous medium, most of the synthetic work reported in this paper was carried out on uncrosslinked systems, i.e., DVB was not incorporated into the formulation. However, some preliminary result using DVB in the formulations are also reported.

The Na-SS was converted to the free acid form (H-SS) by passing an aqueous solution through a bed of proton-exchange resin. The extent of ion exchange was 95–98%, as determined by titration with 0.01 N NaOH. The H-SS was neutralized to the QAA salt (QAA-SS) by adding an aqueous solution of a QAA hydroxide to the aqueous H-SS solution and agitating at 25 °C for 0.5 h, see Fig. 1. In a separate investigation, the neutralization reaction of H-SS with QAA salt was determined to go to completion. This was done by neutralizing a given amount of QAA hydroxide with excess H-SS. The amounts of unreacted and reacted H-SS were determined by titration using 0.01 N NaOH. Equal amounts of QAA hydroxide and reacted H-SS indicated complete reaction.

Tetrahexyl and tetraoctyl ammonium hydroxides (THA-OH and TOA-OH) were prepared by passing a solution of TOAB or THAB (20 g/L) in a mixed solvent of water and methanol (30/70 g/g) through a packed column of a hydroxide-exchange resin. Methanol was used because TOAB and THAB are not soluble in water. The addition of a small amount of water increased the ion-exchange. The extent of ion exchange was 90–95%, as determined by titration with 0.01 N HCl. Similarly, the Li-SS monomer was prepared by passing an aqueous solution of Na-SS (20 g/L) through a packed column of a Li<sup>+</sup>-ion-exchange resin, which was prepared by

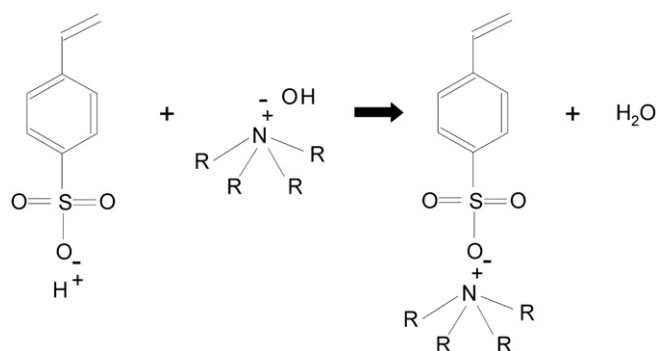


Fig. 1. Schematic of the preparation of QAA salt of styrene sulfonate. R = C<sub>x</sub>H<sub>2x+1</sub>, where x = 1, 4, 6, 8.

regenerating the proton-exchange resin using an aqueous solution of lithium acetate dihydrate. For some of the experiments, the sodium dodecyl sulfate (SDS) surfactant, was converted to tetrahexyl ammonium-dodecyl sulfate (THA-DS) by first converting SDS to the sulfonic acid derivative using a proton-exchange resin and then neutralizing the sulfonic acid to THA-DS with THA-OH.

The nanoparticle synthesis was carried out in a 250-mL three-necked jacketed reactor at 70 °C under a continuous nitrogen feed. The reactor was equipped with a condenser, natural rubber septa, magnetic stirrer, and a nitrogen blanket. The reactor was first purged with nitrogen for 5 min and then charged with de-ionized water, surfactant (Brij 30, SDS, Brij 99, or a mixture of the two surfactants) and M-SS, where M denotes the cation. After slightly agitating the mixture, styrene and DVB (for the crosslinked nanoparticles) were added and the solution was agitated more vigorously. The initiator (KPS or VA-044) was added 5 min later. A typical reaction time was ~6 h, at which time a 3-mL aliquot of 10% hydroquinone solution was used to terminate the reaction.

The product solution was dialyzed using cellulose dialysis tubing (12,000 MWCO) placed in a de-ionized water bath. The solid product was isolated by vacuum drying at 60 °C overnight. In some reactions, the product was isolated without dialysis to determine the mass fraction of water-soluble/polymer and insoluble nanoparticles. This was achieved by first isolating the solid product by drying the reaction solution. The resulting solid product was washed and filtered several times using hot water (~60 °C) and dried at 60 °C. The water-soluble polymer was isolated by evaporating the wash water. The nomenclature used for the poly(styrene-co-sulfonated styrene) nanoparticles is *xyPSSS-M* where *xy* is the concentration of M-SS in the product expressed as ion-exchange capacity (meq/g) and M denotes the cation. Crosslinked nanoparticles are denoted as *xyXLPSSS-M*. The materials that were produced in this research are summarized in Tables 1 and 2. Note that all of these formulations produced nanoparticles, except the samples indicated as bold faced. The conversion data are provided only for the experiments where the nanoparticles were isolated

**Table 1**  
Polymerization experiments: dialyzed samples.

Sample	Feed (mol% M-SS) <sup>a</sup>	Feed (mol% styrene/DVB)	Product IEC (meq/g) <sup>b</sup>
1.9 PSSS-Li	10	90/0	1.9
3.1 PSSS-Li	20	80/0	3.1
3.3 PSSS-Li	50	50/0	3.3
4.4 PSSS-Li	32	68/0	4.4
<b>4.8 PSSS-Li</b>	80	20/0	4.8
1.2 PSSS-Na	15	85/0	1.2
1.5 PSSS-Na	20	80/0	1.5
2.5 PSSS-Na	31	69/0	2.5
3.5 PSSS-Na	50	50/0	3.5
3.9 PSSS-Na <sup>c</sup>	53	47/0	3.9
<b>5.0 PSSS-Na</b>	75	25/0	5
1.1 PSSS-TMA	15	85/0	1.1
1.5 PSSS-TMA	20	80/0	1.5
2.1 PSSS-TMA	30	70/0	2.1
3.5 PSSS-TMA	50	50/0	3.5
<b>5.5 PSSS-TMA</b>	80	20/0	5.5
1.1 PSSS-TBA	11	89/0	1.1
2.4 PSSS-TBA	28	72/0	2.4
3.7 PSSS-TBA	20	80/0	3.7
3.9 PSSS-TBA	50	50/0	3.9
4.0 PSSS-TBA	50	50/0	4
<b>5.2 PSSS-TBA</b>	75	25/0	5.2

Bold face: Samples where the product was only water-soluble polymer, i.e., no particles.

<sup>a</sup> mol% M-SS was based on the total monomer feed (styrene, DVB, and M-SS).

<sup>b</sup> The product IEC was measured by elemental analysis.

<sup>c</sup> SDS was used as the surfactant in this batch.

and dried. For the other experiments, the emulsions were dialyzed, but the particles were not precipitated. Unless otherwise stated, in all formulations, the surfactant used was Brij 30–0.02–0.05 pph in water and the initiator was KPS ~1–3 pph based on the total monomer feed.

### 2.3. Characterization of PSSS-M

#### 2.3.1. Composition

A Nicolet™ 380 Fourier transform infrared (FTIR) spectrometer in reflection mode was used to confirm the conversion of Na-SS to QAA-SS or Li-SS, and also to confirm the incorporation of the sulfonated monomer into the copolymer. The IR samples for the Na-SS, Li-SS, QAA-SS monomers, and polymers were compression molded thin films. Spectra covered a frequency range of 400–4000 cm<sup>-1</sup> using 32 scans, which provided a resolution of ~2 cm<sup>-1</sup>. Prior to analysis each sample was dried in an oven at ~95 °C overnight and then placed in a desiccator to cool to room temperature.

#### 2.3.2. Ion-exchange capacity (IEC)

As described above, some of the samples in Table 1 were dialyzed and others were not. All samples were vacuumed dried at 60 °C and elemental analysis (C, H, N, S) was carried out by combustion with an Elementar Vario Micro Cube. The S content was used to calculate the IEC (based on the mass of the acid form of the ionomer) using Eq. (1). The standard error of the mean determined from analyses of multiple samples was ~±0.01 meq/g.

$$\text{IEC}(\text{meq/g}) = \frac{\%S}{32(\text{g/eq})} \times 10 \quad (1)$$

#### 2.3.3. Morphology

Samples obtained from the emulsion solution were dialyzed and diluted with water. A 3-μL drop was then placed onto a carbon-coated grid and the water was allowed to evaporate at room temperature for at least 20 min. The particle sizes were measured from images of unstained samples obtained with a Philips 420 or a FEI Tecnai G<sup>2</sup> BioTwin transmission electron microscope (TEM) operating at 80 kV.

## 3. Results and discussion

### 3.1. Conversion of Na-SS to M-SS

The exchange of the Na<sup>+</sup> cation of Na-SS with QAA<sup>+</sup> or Li<sup>+</sup> was confirmed by FTIR. Fig. 2 shows the FTIR spectral region from 850 to 1650 cm<sup>-1</sup> for the five M-SS monomers that were studied. This spectral region includes the SO<sub>3</sub><sup>-</sup> stretching vibrations. The sulfonate absorptions for the different monomers are summarized in Table 3. The interaction between the cation and the sulfonate anion (SO<sub>3</sub><sup>-</sup>) affected the position of the symmetric and anti-symmetric stretching vibrations of the sulfonate anion, which show up at ~1040 cm<sup>-1</sup> and ~1200 cm<sup>-1</sup>, respectively, for a solvated anion. However, the interaction had no effect on the S–O bending band at ~905 cm<sup>-1</sup>. The bands at ~950 cm<sup>-1</sup> and ~865–905 cm<sup>-1</sup> for TMA-SS and TBA-SS respectively arise from vinyl C–H out of plane bending.

The Coulombic field strength of the ion pair, i.e., the cation and the sulfonate anion, is  $F = kq_cq_a/a^2$ , where  $q_c$  and  $q_a$  are the charges on the cation and anion respectively,  $k$  is Coulomb's constant ( $8.99 \times 10^9 \text{ N m}^2 \text{ C}^{-2}$ ), and  $a$  is the ionic radius of the cation. In general, as the Coulombic field strength between ion pair increases, the symmetric stretching vibration moved to higher frequency and

**Table 2**  
Polymerization experiments: fractionated product.

Sample	Feed (mol% M-SS) <sup>a</sup>	Feed (mol% styrene/DVB)	Conversion (%)	Product IEC (meq/g) <sup>b</sup>	Water-soluble fraction (wt%)	IEC of water-soluble fraction (meq/g)	IEC of nanoparticles (meq/g)
2.4 PSSS-Li	31	69/0	75	2.2	42	4.5	0.9
<b>4.6 PSSS-Li</b>	65	35/0	79	4.6	100	4.6	–
1.7 PSSS-Na	17	83/0	45	1.7	35	4.4	0.3
2.0 PSSS-Na	30	70/0	99	2	31	4.7	0.8
<b>4.7 PSSS-Na</b>	55	45/0	58	4.7	100	4.7	–
<b>5.1 PSSS-Na</b>	95	5/0	80	5.1	100	5.1	–
1.1 PSSS-TMA	12	88/0	97	1.1	1	5.8	1.1
2.1 PSSS-TMA	27	73/0	98	2.1	22	5.4	1.2
<b>4.9 PSSS-TMA</b>	95	5/0	77	4.9	100	4.9	–
1.5 PSSS-TBA	14	86/0	81	1.5	28	3.8	0.6
2.4 PSSS-TBA	27	73/0	87	2.4	55	3.4	1.1
2.6 PSSS-TBA	30	70/0	87	2.6	63	3.4	1.2
4.0 PSSS-TBA	49	51/0	78	4	84	4.4	2.4
<b>4.6 PSSS-TBA</b>	95	5/0	90	4.6	100	4.6	–
3.8 XLPSSS-THA	62	0/38	–	3.8 <sup>c</sup>	0	–	4.5
4.1 XLPSSS-THA	68	0/32	91	4.1 <sup>c</sup>	0	–	4.9
4.4 XLPSSS-THA	74	0/26	90	4.4 <sup>d</sup>	0	–	5.4
1.3 XLPSSS-Na	11	76/12	96	1.3	8	5.5	1
1.7 XLPSSS-Na	21	67/12	99	1.7	15	4.3	1.3
2.4 XLPSSS-Na	29	59/12	95	2.4	29	3.8	1.8
3.4 XLPSSS-Na	51	38/11	93	3.4	43	5	2.2
<b>4.8 XLPSSS-Na</b>	76	13/11	99	4.8	100	4.8	–
<b>4.5 XLPSSS-Na</b>	80	9/11	96	4.5	100	4.5	–

Bold face: Samples where the product was only water-soluble polymer, i.e., no particles.

<sup>a</sup> mol% M-SS was based on the total monomer feed (styrene, DVB, and M-SS).

<sup>b</sup> The product IEC was calculated by  $IEC = x \cdot IEC(\text{soluble}) + (1 - x) \cdot IEC(\text{nanoparticles})$ , where  $x$  is the mass fraction of the water-soluble polymer. The IEC of water-soluble polymer and nanoparticles were measured by elemental analysis.

<sup>c</sup> VA-044 was used as initiator. A mixture of surfactants was used, Brij 30 and Brij 99 with mass proportions of 1:1.4. The product was ~70 wt% stable emulsion and ~30% coagulated polymer. The product IEC was calculated assuming that the concentration of M-SS in the product was the same as in the feed.

<sup>d</sup> VA-044 was used as initiator. Brij 99 was used as a surfactant. The product was 84 wt% stable emulsion and 16 wt% coagulated polymer. The product IEC was calculated assuming that the concentration of M-SS in the product was the same as in the feed.

the splitting of the two asymmetric stretching bands, which constitute a doublet centered around  $1200\text{ cm}^{-1}$ , also increases as was expected for sulfonated polystyrenes [34]. The in plane skeleton vibration of M-SS at  $\sim 1140\text{ cm}^{-1}$  also followed a similar trend as the symmetric stretching. The symmetric stretching frequency increased, but the splitting of the asymmetric stretching doublet decreased as the cation was changed from  $\text{Na}^+$  to  $\text{Li}^+$ . The increase

in frequency is expected, because for alkali metal cations the Coulombic force decreases with increasing size of the cation [34]. However, the splitting of the asymmetric stretching doublet is also expected to increase. The deviation in that behavior observed here can probably be attributed to difficulty in removing water from the Li-SS. The stronger Coulombic field strength allows  $\text{Li}^+$  to hold onto water more strongly, and the hydrogen bonding of water with  $\text{Li}^+$  weakens the interaction between  $\text{Li}^+$  and sulfonate anion ( $\text{SO}_3^-$ ) [34]. For the TMA-SS, TBA-SS, THA-SS, and TOA-SS monomers, the symmetric stretching frequency decreased and the splitting of the asymmetric stretch doublet also decreased, see Table 3, which is due to the weaker Coulombic force of the ion-pair. The splittings of the asymmetric stretching doublet of the anion for THA-SS and TOA-SS were slightly higher than for TMA-SS and TBA-SS, which may be due to residual hydrogen-bonded water in the latter two monomers, which are more hydrophilic than the former.

The solubility of M-SS in water and styrene were determined by adding excess M-SS to the solvent, extracting a known volume of sample from the clear phase and measuring the monomer concentration gravimetrically. The solubility behavior is described in Table 4. The TMA-SS, TBA-SS and Li-SS monomers formed clear, viscous solutions in water with relatively high concentration ( $>37\text{ g}/100\text{ g}$  water), which may have been a consequence of the formation of micelles. Similar to the metal salts of the SS monomer, TMA-SS was insoluble in styrene; however, TBA-SS was slightly soluble in styrene. As the alkyl chain length of the QAA-SS increased, the monomer became less soluble in water and more soluble in the styrene phase. It was thought that this would be beneficial with regard to incorporation of the SS monomer into the emulsified styrene phase and, consequently into the nanoparticles during the emulsion polymerization. Neat TOA-SS and THA-SS were viscous oils that were insoluble in water. Thus, they can be used

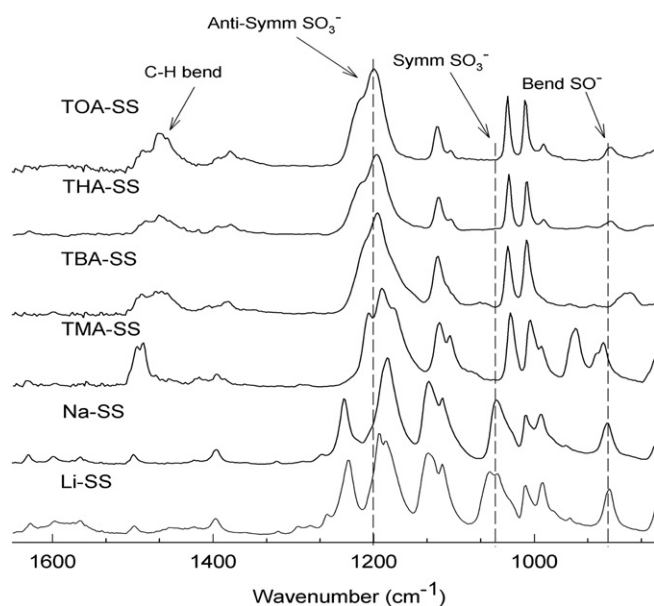


**Fig. 2.** FTIR absorption spectra of M-SS monomers. The dashed lines represent anti-symmetric, symmetric  $\text{SO}_3^-$  stretching, and the bending of  $\text{SO}^-$ .

**Table 3**  
IR assignments for M-SS monomers.

Group	Wavenumber (cm <sup>-1</sup> )					
	Li-SS	Na-SS	TMA-SS	TBA-SS	THA-SS	TOA-SS
SO <sup>-</sup> bending	905	905	–	–	904	904
SO <sub>3</sub> symmetric stretching	1051	1046	1030	1032	1032	1032
In-plane skeleton vibration of substituted styrene	1130	1130	1120	1120	1120	1120
Asymmetric stretching doublet of sulfonate	1232	1235	1206	1206	1217	1216
	1188	1182	1191	1193	1198	1199
Splitting of doublet	44	53	15	13	19	17
Methylene/methyl C–H sym./asym. bending	–	–	1465–1510	1430–1510	1410–1510	1410–1510

directly as the oil phase in an emulsion polymerization without including styrene.

### 3.2. Polymerization of PSSS-M nanoparticles

The emulsion polymerization produced two different products: 1) dispersed nanoparticles and 2) water-soluble polymer. The IECs of the total PSSS-M products from the emulsion polymerizations are summarized in Table 1 and plotted as a function of the feed composition in Fig. 3. The IEC calculated from the elemental sulfur analysis (see Eq. (1)) was based on the free acid derivative. The solid line in Fig. 3 represents stoichiometric conversion of M-SS in the product. Data from Refs. [31] and [27] are included in Fig. 3. Only the experimental data from the present study for the polymers that were dialyzed, see Table 1, were used in this graph. The polymers from Ref. [31] were also dialyzed, but the products from Ref. [27] were not.

In general, the polymerization reaction produced a near stoichiometric incorporation of the sulfonated monomer into the product, regardless of what monomer was used. Where the data deviated significantly from stoichiometry (data above the line in Fig. 3), a higher concentration of the sulfonated monomer was incorporated into the product as a result of a loss of styrene monomer during the reaction, primarily because of absorption by the rubber septa. That problem was resolved by using glass stoppers. Nonetheless, some styrene was still carried away by nitrogen gas stream. The results from Weiss et al. [27] were generally lower than the stoichiometric line, which may be due to the presence of buffer, reducing agent and/or chain transfer agent residues, as a consequence of not dialyzing the product.

The water-soluble polymer was separated from the nanoparticles by first forming a film from the entire polymer product on a glass substrate, drying it and then washing the film with 60 °C water several times to remove the water-soluble fraction. The water-soluble polymer was isolated by filtering the wash solutions with a cotton-filled syringe that served to remove any water-insoluble material transferred from the glass surface during the washing steps. Fig. 5 plots the mass fraction of the water-soluble polymer and water-insoluble nanoparticles produced by the

**Table 4**  
Solubility of M-SS in water and styrene at room temperature.

Monomer	Water (g/100 g)	Styrene (g/100 g)
Li-SS	Clear, viscous solution (gelled at concentration >68% > 44)	0
Na-SS	18	0
TMA-SS	Clear, viscous solution (gelled at concentration >68%)	0
TBA-SS	Clear, viscous solution (gelled at concentration >37%)	4.0
THA-SS	0	Miscible (viscous solution)
TOA-SS	0	Miscible (viscous solution)

emulsion polymerizations as a function of the sulfonate monomer concentration in the feed. The feed compositions were corrected for loss of styrene due to absorption by the rubber septa. The solubility of styrene in the rubber septa was determined separately by exposing the septa to styrene vapor. The water-soluble fraction of the PSSS-TBA samples included some water-insoluble nanoparticles due to insufficient separation. As a result, the IEC of the water-soluble fractions were slightly lower compared to the other cations for the feed composition range of ~1.5–2.5 meq/g; see Fig. 6.

Fig. 4 shows that as the sulfonate monomer concentration in the feed increased, the fraction of nanoparticles produced decreased and the amount of water-soluble polymer increased. Above a feed composition of about 50 mol% M-SS, essentially only water-soluble polymer was produced. The relative amounts of water-soluble polymer and nanoparticles produced by the emulsion polymerization appeared to be insensitive to the sulfonate salt used and to the use of divinyl benzene as a crosslinking agent. However, the incorporation of divinyl benzene significantly lowered the relative amount of water-soluble polymer produced, due to stabilization of the high IEC nanoparticles by crosslinking.

As might be expected, the water-soluble polymer was rich in the sulfonated monomer. The IECs for the water-soluble fraction ranged between 3.0 and 5.4 meq/g. The water-insoluble nanoparticles had much lower IEC than the water-soluble polymer, see Fig. 5. For most of the M-SS monomers used, the nanoparticles had an IEC ~ 1 meq/g. The one notable exception was a single experiment with TBA-SS, where an IEC >2 meq/g was achieved. Also noteworthy is that the IECs for the nanoparticles from the QAA-SS

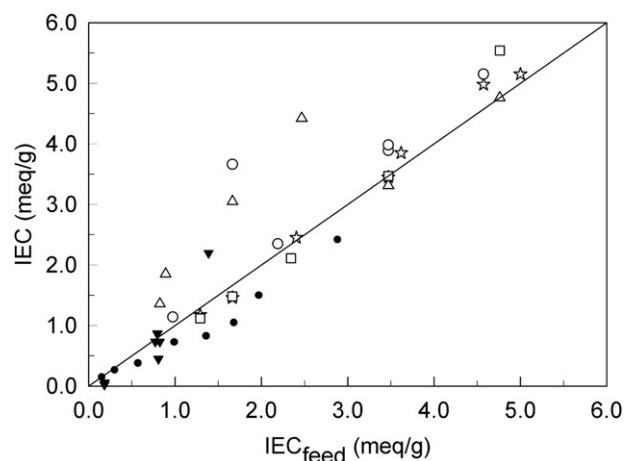


**Fig. 3.** IEC (meq/g) of emulsion products (based on the acid form of the ionomer) versus the IEC of the M-SS in the feed. The IEC of the product was calculated by elemental analysis, except for the data from Ref. [8], where the IEC was calculated by titration. The solid line represents stoichiometric conversion of the M-SS in the product. The products are: (Δ) PSSS-Li, (∗) PSSS-Na, (□) PSSS-TMA, (○) PSSS-TBA, (▼) XLPSSS-Na from Ref. [31], and (●) PSSS-Na from Ref. [27].



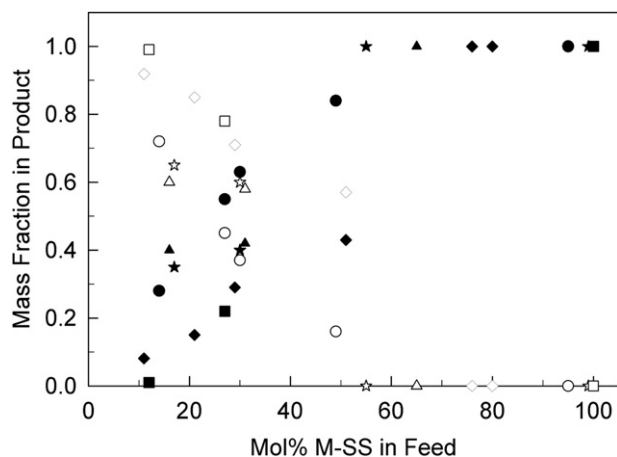


**Fig. 4.** Mass fraction of water-soluble polymer and water-insoluble nanoparticles in the emulsion polymerization product versus concentration of M-SS in the feed. The filled symbols represent the water-soluble fraction and the open symbols are the nanoparticle fraction: ( $\Delta$ ,  $\blacktriangle$ ) Li-SS ( $\star$ ,  $\blackstar$ ) Na-SS, ( $\square$ ,  $\blacksquare$ ) TMA-SS, ( $\circ$ ,  $\bullet$ ) TBA-SS, and ( $\diamond$ ,  $\blacklozenge$ ) XLPSS-Na.

polymerizations had a mean value of  $1.3 \pm 0.2$  meq/g, while for the metal salts, the mean value was  $0.54 \pm 0.03$  meq/g. The values after the  $\pm$  sign are the 95% confidence interval from the mean. These two observations are consistent with the earlier hypothesis that the QAA-SS monomer is more soluble in the oil-phase micelles and thus should be more efficient at incorporation into the nanoparticles than the more water-soluble monomers, see Table 4.

Brijmohan et al. [31] reported the synthesis of an XLPSS-Na emulsion where the isolated polymer had an IEC  $\sim 2.2$  meq/g for 16 mol% NaSS in the feed. In that work, however, no attempt was made to isolate a water-soluble fraction, so the IEC of the nanoparticles per se was not known. Fig. 5 shows that by crosslinking the nanoparticles as they are produced, higher IEC nanoparticles were stabilized, since the particles were no longer water soluble. Crosslinked nanoparticles had IEC  $\sim 1$ – $2$  meq/g, which was similar to that obtained by using TBA-SS as the sulfonate monomer, though a higher concentration of nanoparticles was obtained using the crosslinker.

Figs. 4 and 5 show, however, that crosslinking alone was not sufficient for producing nanoparticles with IEC  $>2$  meq/g. That may

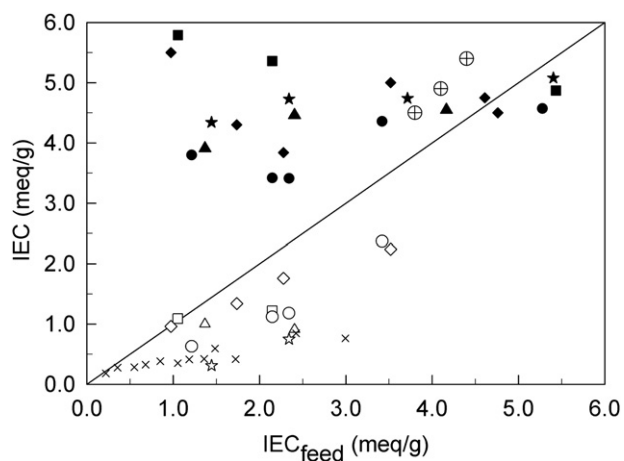


**Fig. 5.** IEC of the water-soluble and nanoparticle fractions of the emulsion polymerization product versus the concentration of M-SS in the feed. The filled symbols are for the water-soluble polymer and the open symbols are for the insoluble nanoparticles: ( $\Delta$ ,  $\blacktriangle$ ) Li-SS ( $\star$ ,  $\blackstar$ ) Na-SS, ( $\square$ ,  $\blacksquare$ ) TMA-SS, ( $\circ$ ,  $\bullet$ ) TBA-SS, ( $\times$ ) from Ref. [25], ( $\diamond$ ,  $\blacklozenge$ ) XLPSS-Na, and ( $\oplus$ ) XLPSS-THA.

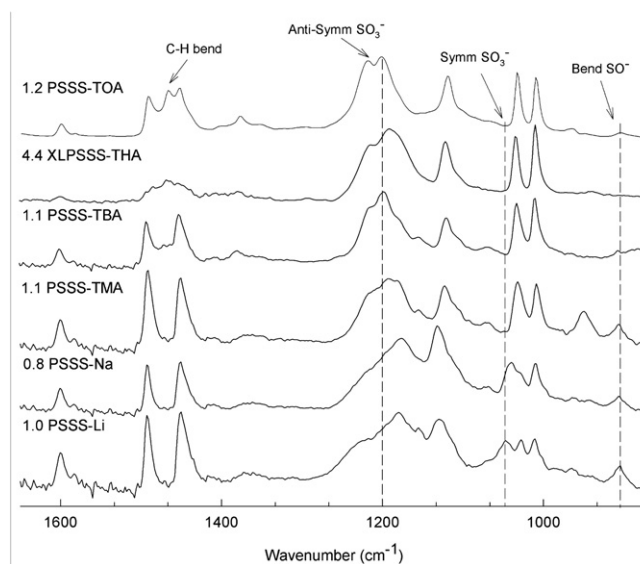


**Fig. 6.** FTIR absorption spectra of PSSS-M nanoparticles. The dashed lines the anti-symmetric stretching doublet of the  $\text{SO}_3^-$ , the symmetric stretching of the  $\text{SO}_3^-$  and S–O bending $^-$ .

require using the crosslinker in combination with a completely oil-soluble QAA-SS monomer to maximize the concentration of sulfonated monomer in the oil domains. THA-SS was chosen to test that hypothesis, because it was observed to be soluble in styrene and it produced a lower-viscosity mixture with styrene than did the higher molecular weight TOA-SS. A higher viscosity within the emulsified nanoparticle domains presented two problems: 1) poorer dispersion of the two monomers (styrene and the QAA-SS) and 2) increased difficulty of exchanging the QAA cation with an acid once the polymer was produced.

With a combination of the THA-SS monomer and the addition of divinyl benzene, very high IEC nanoparticles, ranging from 4.5 to 5.4 meq/g, were obtained, see Fig. 5. The data deviated from stoichiometry (i.e., the point is above the line in Fig. 5), which suggests some monomer was lost either due to evaporation into the nitrogen purge stream or by less than complete conversion. The amount of monomer (DVB) lost by evaporation was estimated to be  $>50$  wt% of its initial amount, assuming the amount lost is the only cause for IEC to deviate from stoichiometry. Note that the crosslink density of the crosslinked nanoparticles particles produced is not known. This is not a trivial characterization for nanoparticles and was considered beyond the scope of this project.

In the synthesis of XLPSS-THA, a non-ionic initiator (VA-044) was used, because of concern that the THA-SS would be converted to M-SS and become water soluble in the presence of ionic initiator or surfactants containing metal cations. Attempts to produce stable nanoparticles were unsuccessful, except when the non-ionic surfactant, Brij 99, was used. Nanoparticles are stabilized electrostatically when similar charges are located at the surface of adjacent particles, i.e., in the electrical double layer. This electrostatic repulsion is greatly reduced when a non-ionic surfactant and the bulky tetraalkylammonium cation are present, as in the case of the XLPSS-THA nanoparticles. The QAA may actually behave as an organic electrolyte, which is known as a latex coagulant [35,36]. The strong attraction between water molecules, due to hydrogen bonding, forces the QAA out of the aqueous phase, resulting in neutral particles which can coagulate the nanoparticles because of their weak repulsive interactions.

In sterically stabilized emulsions, a non-ionic surfactant is used to increase the separation of adjacent particles, which prevents



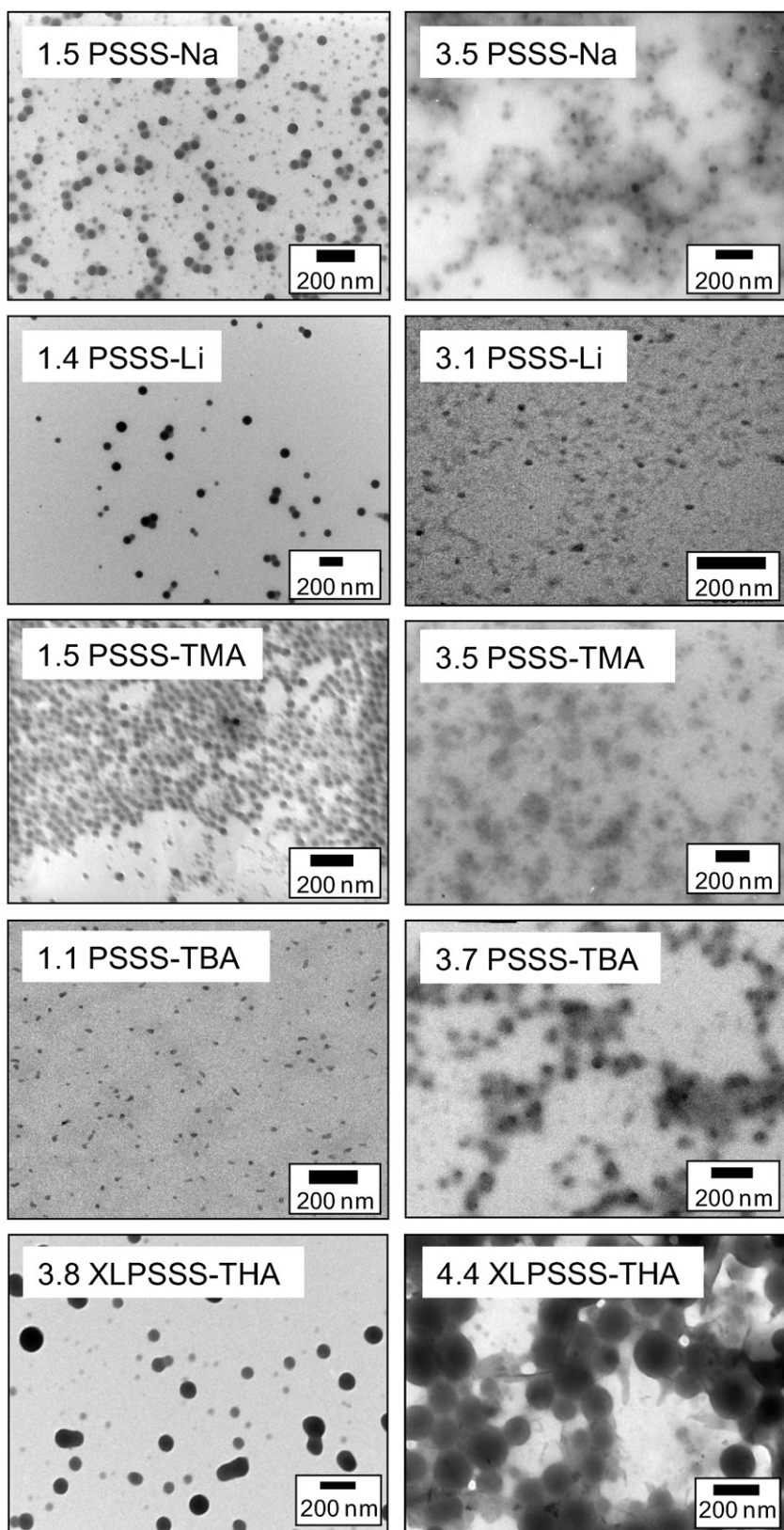


Fig. 8. TEM images of xyPSSS-M nanoparticles.

**Table 6**  
Average nanoparticle size for PSSS-M and XLPSSS-M copolymers.

Samples	Number of particles counted	Diameter (std dev) (nm)	$a$ (nm)	$q/a$ (nm <sup>-1</sup> )
1.5 PSSS-Na	104	42 (17)	0.097 [41]	10.3
3.5 PSSS-Na	67	34 (7)	0.097	10.3
5.2 PSSS-Na	None	–	0.097	10.3
1.4 PSSS-Li	58	73 (19)	0.068 [42]	14.7
3.1 PSSS-Li	45	18 (3)	0.068	14.7
1.5 PSSS-TMA	53	42 (4)	0.347 [42,43]	2.88
3.5 PSSS-TMA	None	–	0.347	2.88
1.1 PSSS-TBA	70	19 (3)	0.494 [44]	2.02
3.7 PSSS-TBA	87	61 (17)	0.494	2.02
3.8 XLPSSS-THA	91	83 (22)	0.560 [45]	1.78
4.4 XLPSSS-THA	74	156 (27)	0.560	1.78

particles form by homogenous nucleation. Nonetheless, the particle size distribution usually has a relatively low polydispersity.

For the copolymerization of styrene and Na-SS, monomer-swollen micelles were not the only source of particle formation. Particles also form simultaneously by homogenous nucleation in the aqueous phase [32]. Water-soluble Na-SS oligomeric radicals grow to a critical length by capturing styrene prior to precipitating and forming aggregates that absorb styrene and behave as styrene-swollen micelles. Homogenous nucleation of particles occurs throughout the reaction; and, as a result, particles grow at different rates which leads to a broader particle size distribution compared to polymerization of styrene, see Table 6.

The diameter data are plotted against the quantity  $cq/a$  in Fig. 9 as a log–log plot, where  $c$  is the sulfonate ion concentration of the emulsion product,  $a$  is the ionic radius of the cation and  $q$  is the charge of the cation. Values for  $a$  are listed in Table 6. The Coulombic energy of the ion-pair is  $E_c = kq_cq_a/a$ , where  $q_c$  and  $q_a$  are the charges on the cation and anion, respectively, and  $k$  is Coulomb's constant ( $8.99 \times 10^9 \text{ N m}^2 \text{ C}^{-2}$ ). For a fixed anion, in this case the sulfonate anion,  $q_a$  is a constant and the Coulombic energy is proportional to  $q/a$ , where  $q = q_c$ . For ionomers, many properties scale with the product of the Coulombic energy and the ion concentration ( $cq/a$ ) [47–51]. The data in Fig. 9 were fitted using a continuous kink function [46]. The kink function consists of two straight lines connected with a small curve of certain width. The equation used for the continuous kink function is:

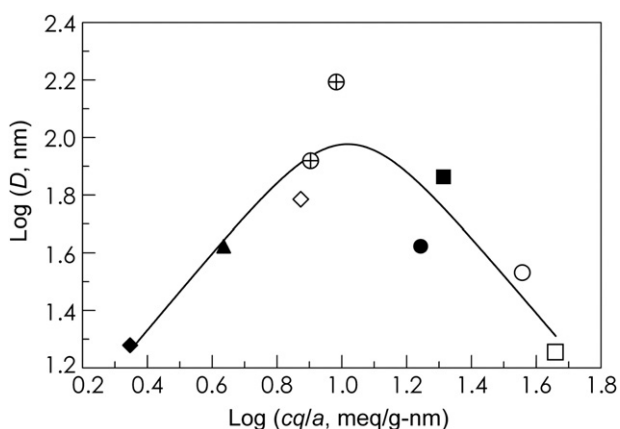


**Fig. 9.** Nanoparticles size versus the product of Coulombic energy and sulfonate concentration for PSSS-M and XLPSSS-M;  $a$  is the ionic radius of the cation,  $q$  is the charge, and  $c$  is the concentration of sulfonate ion of the emulsion product expressed as ion-exchange capacity: (□) M = Li; (○) Na; (Δ) TMA; (◇) TBA; (⊕) THA. Filled symbols are polymers with IEC between 1.1 and 1.5 meq/g and open symbols represent polymers with IEC between 3.1 and 5.4 meq/g. The curve is a kink function [46] with  $s \sim 0.1$ , Eq. (3).

**Table 7**  
Kink function parameters.

Parameter <sup>a</sup>	Value	95% confidence interval	$p$ values <sup>b</sup>
$b$	1.3	$\pm 1.2$	0.017
$d$	-1.3	$\pm 1.4$	0.028
$x_0$	1.0	$\pm 0.4$	<0.001
$y_0$	2.2	$\pm 0.3$	<0.001
$s$	0.1 (fixed)	–	–

<sup>a</sup> See Eq. (3) for definition of parameter symbols

<sup>b</sup> Probability of Type I error by rejecting zero value hypothesis using one-tail  $t$  test; see text for explanation.

$$y - y_0 = b(x - x_0) + s(d - b) \ln \left\{ 1 + \exp \left[ \frac{x - x_0}{s} \right] \right\} \quad (3)$$

where  $b$  and  $d$  are the slopes of the straight lines,  $x_0$  and  $y_0$  are the intercepts and  $s$  is known as the “sharpness” parameter. The statistics obtained from fitting the data with the kink function are listed in Table 7. We hypothesize the kink in the curve is due to distinct differences in the mechanism of particle formation and stabilization of QAA and metal neutralized particles. The positive and negative slope regions of the curve illustrate the behavior of QAA and metal neutralized particles, respectively. For QAA neutralized particles, the particle size increased with increasing  $cq/a$ , or since  $q/a$  was relatively constant for those data, with increasing sulfonate ion concentration,  $c$ . On the other hand, for the metal neutralized particles, the particle size decreased with increasing  $cq/a$ .

The difference in the number of particles formed during the reaction may be responsible for these two opposite effects of  $cq/a$  on particle size, at low sulfonate concentration. Na-SS is reported to aggregate in aqueous solution at concentrations  $>0.1$  M, due to its amphiphilic nature, i.e., a hydrophobic phenyl ring and a hydrophilic sulfonate group [32]. The lower hydrophilic-lipophilic balance (HLB) of the QAA-SS salt is expected to lower the critical micelle concentration (CMC) of M-SS and also increase the number of micelles formed in the order of  $\text{THA}^+ \geq \text{TBA}^+ \geq \text{TMA}^+ \geq \text{Na}^+ \geq \text{Li}^+$ . Higher micelle concentration produces more primary particles. More primary particles reduces the average particle size. At high concentration of sulfonated monomer, the effect of the cation on the particle size reverses as a consequence due to poor electrostatic stabilization of the emulsion by the QAA cations, reducing the effect of the electrical double layer.

#### 4. Conclusions

Water-insoluble sulfonated polystyrene nanoparticles with IEC up to  $\sim 5.4$  meq/g, can be synthesized by an emulsion copolymerization of styrene, divinyl benzene and a salt of *p*-styrene sulfonic acid (M-SS). The choice of the sulfonate cation affects the polymerization reaction; the most significant effect occurs for bulky quaternary alkyl ammonium (QAA) salts, such as tetrahexyl ammonium. Changing the cation from an alkali metal to a quaternary alkyl ammonium makes the M-SS monomer less water soluble and more soluble in the oil phase of the emulsion. The IEC of the nanoparticles increased with increasing solubility of the M-SS monomer in the oil phase, but increasing the hydrophobic nature of the sulfonated polymer is not by itself sufficient to achieve nanoparticles with IEC  $>2.4$  meq/g.

The addition of crosslinking agent, such as divinyl benzene, stabilizes the nanoparticles to higher IEC by preventing their dissolution into the water phase. But, if the sulfonate monomer is water soluble, adding a crosslinker has limited effectiveness for achieving nanoparticles with IEC  $>2.4$  meq/g. An emulsion polymerization using a combination of a water-insoluble sulfonated styrene monomer (e.g., using the tetrahexyl ammonium salt) and

a crosslinking agent can achieve water-insoluble sulfonated polystyrene nanoparticles with IEC up to ~5.4 meq/g.

When a water-soluble M-SS monomer is used, nanoparticles with sizes ranging from 20 to 70 nm are produced when the feed concentration of M-SS is <50 mol%. At higher M-SS concentration in the feed, the water-soluble M-SS oligomeric radicals do not precipitate into particles, because of the low concentration of styrene: and, as a result, only water-soluble, highly sulfonated polymer is formed, even when a crosslinker is added. For oil-soluble M-SS, monomers, high IEC nanoparticles with sizes of 80–160 nm are produced at feed concentrations of M-SS >50 mol%. The choice of the surfactant is also important in achieving high IEC nanoparticles. Non-ionic surfactants with a high hydrophilic/lipophilic balance (HLB) are the most effective at stabilizing the nanoparticle emulsion to high IEC.

However, in the case of oil-soluble, THA-SS, high IEC nanoparticles with sizes ~80–160 nm were formed at high THA-SS concentration in the feed. Compared to Brij 99, the mixture of Brij 30 and Brij 99 stabilized smaller particles (~80 nm). The formation of smaller particles can be attributed to the ability of Brij 30 to produce more micelles. The critical micelle concentration for Brij 30 and Brij 99 are 0.004 and 0.265 mM, respectively.

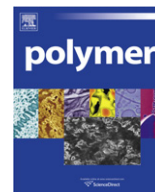
Future work will include preparing larger quantities of the high IEC crosslinked nanoparticles prepared from tetrahexyl ammonium (THA) neutralized styrene sulfonate monomer, and these will be used to prepare composite proton-exchange membranes with a relatively hydrophobic polymer matrix. The use of the QAA counterions of sulfonated styrene is expected to improve the dispersion of the nanoparticles in a relatively hydrophobic polymer matrix.

#### Acknowledgment

This work was supported by the Civil, Mechanical and Manufacturing Innovation Program (Directorate of Engineering) of the National Science Foundation, Grant CMMI 0727545.

#### References

- [1] Mariaulle P, Sinapi F, Lamberts L, Walcarius A. *Electrochimica Acta* 2001;46: 3543–53.
- [2] Himmelhoch SR. *Meth Enzymol* 1971;22:273–86.
- [3] Peterson EA, Sober HA. *J Am Chem Soc* 1956;78:751–5.
- [4] Baharvand H. *J Appl Polym Sci* 2008;109:1823–8.
- [5] Ma Z, Guan Y, Li H. *J Polym Sci A1* 2005;43:3433–9.
- [6] Utkan G, Sayar F, Batat P, Ide S, Kriechbaum M, Piskin E. *J Colloid Interf Sci* 2011;353:372–9.
- [7] Brijmohan SB, Shaw MT. *J Memb Sci* 2007;303:64–71.
- [8] Wena H, Yao E, Zhang Y, Zhou Z, Kirschning A. *Catal Commun* 2009;10: 1207–11.
- [9] Coutinho FMB, Rezende SM, Soares BG. *J Appl Polym Sci* 2006;102:3616–27.
- [10] Salehpoor K, Shahinpoor M, Mojarrad M. In: *Proceedings of the SPIE Smart Material Structure*, San Diego; 1997, vol. 3040: p. 192–198.
- [11] Tamagawa H, Nogata F. *J Memb Sci* 2004;243:229–34.
- [12] Geise GM, Lee H, Miller DJ, Freeman BD, McGrath JE, Paul DR. *J Polym Sci Pol Phys* 2010;48:1685–718.
- [13] Hong L, Chen N. *Polym Sci* 2000;38:1530–8.
- [14] Chen N, Hong L. *Solid State Ionics* 2002;146:377–85.
- [15] Gasa J, Brijmohan SB, Weiss RA, Shaw MT. *J Memb Sci* 2006;269:177–86.
- [16] Chen SL, Krishnan L, Rinivasan SS, Benziger J, Bocarsly AB. *J Memb Sci* 2004;243:327–33.
- [17] Brijmohan SB, Shaw MT. *Polymer* 2006;47:2856–64.
- [18] Oren Y, Freger V, Linder C. *J Memb Sci* 2004;239:17–26.
- [19] Dechow FJ. *Separation and purification techniques in biotechnology*. Park Ridge, NJ: Noyes Publications; 1989 [chapter 3].
- [20] Barar DG, Staller KP, Peppas NA. *Ind Eng. Chem Prod R&D* 1983;22:161.
- [21] Peppas NA, Staller KP. *Polym Bull* 1982;8:233–7.
- [22] Kaghan WS, Shreve RN. *Ind Eng Chem* 1953;45:292–7.
- [23] Lucchesi C, Pascual S, Jouanneaux A, Dujardin G, Fontaine L. *J Polym Sci A* 2007;45:3677–86.
- [24] Ottewill RH. In: Lovell PA, El-Aasser MS, editors. *Emulsion polymerization and emulsion polymers*. New York: John Wiley; 1997.
- [25] Weiss RA, Turner SR, Lundberg RD. *J Polym Sci Polym Chem Ed* 1985;23:525–33.
- [26] Turner SR, Weiss RA, Lundberg RD. *J Polym Sci Polym Chem Ed* 1985;23:535–48.
- [27] Weiss RA, Lundberg RD, Turner SR. *J Polym Sci Polym Chem Ed* 1985;23: 549–68.
- [28] Smitha B, Sridhar S, Khan AA. *J Memb Sci* 2005;259:10–26.
- [29] Brijmohan SB. Field-structured proton exchange membranes for fuel cells. Paper AAI3252571. Dissertations Collection for University of Connecticut; January 1, 2007.
- [30] Shapiro V, Freger V, Linder C, Oren Y. *J Phys Chem B* 2008;112:9389–99.
- [31] Brijmohan SB, Swier B, Weiss RA, Shaw MT. *Ind Eng Chem Res* 2005;44: 8039–45.
- [32] Kim JH, Chainey M, El-Aasser MS, Vanderhoff JW. *J Polym Sci Part A Polym Chem* 2003;30:171–83.
- [33] Arunbabu D, Sanga Z, Seenimeera KM, Jana T. *Polym Int* 2009;58:88–96.
- [34] Zundel G. *Hydration and intermolecular interaction: infrared investigations of polyelectrolyte membranes*. New York: Academic Press; 1969.
- [35] Parfitt GD, Rochester CH. *Adsorption from solution at the solid-liquid interface*. London: Academic Press; 1983.
- [36] Ingram BT, Ottewill RH. In: Rubingh DN, Holland PM, editors. *Cationic surfactants*, vol. 37. New York: Marcel Dekker; 1991. p. 130–5.
- [37] Harkins WD. *J Am Chem Soc* 1947;69:1428–44.
- [38] Smith WV. *J Am Chem Soc* 1948;70:3695–702.
- [39] Smith WV, Ewart RW. *J Chem Phys* 1948;16:592–601.
- [40] Ewart RH, Carr CI. *J Phys Chem* 1954;58:640–4.
- [41] Lide DR, editor. *CRC handbook of chemistry and physics*. 85th ed. Boca Raton, FL: CRC Press; 2004. p. 14.
- [42] Robinson RA, Stokes RH. *The limiting Mobilities of ions in electrolyte solutions*. London: Butterworths Scientific Publications; 1955. p. 113–127.
- [43] Gill DS. *Electrochim Acta* 1979;24:701–3.
- [44] Barthel J, Gores HJ, Schmeer G, Wachter R. *Top Curr Chem* 1983;111:33–144.
- [45] Barthel JMG, Krienke H, Kunz W. In: Baugärtel H, Franck EU, Grünbein W, editors. *Physical chemistry of electrolytes solutions: modern aspects*. New York: Steinkopff; Darmstadt, Springer; 1998. p. 39.
- [46] Shaw MT. *J Rheol* 2007;51(6):1303–18.
- [47] Sullivan MJ, Weiss RA. *SPE ANTEC Tech. Pap.* 1991; 37: p. 964.
- [48] Lu X, Weiss RA. *Polym Mater Sci Eng* 1991;64:163–4.
- [49] Lu X, Weiss RA. *Macromolecules* 1991;24:4381–5.
- [50] Lu X, Weiss RA. In: Roe RJ, O'Reilly JM, editors. *Symposium proceedings of the fall meeting of the MRS, Pittsburgh: Materials Research Society*; 1991. p. 29.
- [51] Molnar A, Eisenberg A. *Polym Commun* 1991;32:1001.



# Poly(benzoxazine-co-urethane)s: A new concept for phenolic/urethane copolymers via one-pot method

Mohamed Baqar<sup>a,1</sup>, Tarek Agag<sup>b,\*</sup>, Hatsuo Ishida<sup>b</sup>, Syed Qutubuddin<sup>a,b</sup>

<sup>a</sup> Department of Chemical Engineering, Case Western Reserve University, Cleveland, OH 44106-7202, USA

<sup>b</sup> Department of Macromolecular Science and Engineering, Case Western Reserve University, Cleveland, OH 44106-7202, USA

## ARTICLE INFO

### Article history:

Received 13 September 2010

Received in revised form

24 November 2010

Accepted 27 November 2010

Available online 4 December 2010

### Keywords:

Hydroxymethyl-benzoxazine

Polyurethane

Copolymers

## ABSTRACT

Historically, applications for traditional phenolic resin/polyurethane materials are limited due to the inherently weak thermal stability of urethane-phenolic linkage and slow reaction rate. A novel concept has been developed to produce phenolic resin/polyurethane copolymers via benzoxazine chemistry. Through one-pot synthesis, a series of linear poly(benzoxazine-co-urethane) materials has been synthesized via the reaction of a newly developed dimethylol functional benzoxazine monomer with 4,4'-methylene diphenyl diisocyanate and poly(1,4-butylene adipate). The structure of the copolymers has been characterized by Fourier transform infrared spectroscopy (FT-IR) and nuclear magnetic resonance spectroscopy (NMR). The copolymers in the film forms have been further thermally treated for crosslinking to produce crosslinked poly(benzoxazine-co-urethane) via the ring opening polymerization of cyclic benzoxazine moieties in the main-chain. The tensile properties of the films have been studied and compared with those of traditional high performance materials. The thermal properties of the crosslinked copolymers have also been studied by dynamic mechanical analysis, and thermogravimetric analysis (TGA).

© 2010 Elsevier Ltd. All rights reserved.

## 1. Introduction

Polyurethanes (PUs) represent one of the most versatile classes of polymers due to their advantages, which include excellent low temperature flexibility, superb oil and abrasion resistance, and extraordinary easy processability [1–3]. PUs are segmented polymers that consist of soft segments derived from polyols and hard segments derived from isocyanate and chain extenders. The hard segments offer stiffness to the resulting materials, whereas the soft segments act as flexible connectors between the hard segments. PUs also have a wide variety of properties, ranging from elastic to plastic behavior, which make them suitable for a broad number of applications, such as coatings and paints, flexible foams, insulations, adhesives, and sealants. Nonetheless, the use of PUs is associated with some disadvantages, including high water up-take, poor resistance to polar solvents, and poor thermal stability. They also undergo dissociation of urethane linkages at elevated temperatures [4]. As a result, tremendous research efforts have been reported to improve the thermal stability of PUs. Most of the

reported approaches are based on copolymerization or blending with other polymers of high thermal stability such as polyimides [5–8], polyurea [9,10], polyamide [11,12], epoxy [13], and polydiacetylene [14].

Polybenzoxazines, as a newly developed class of high performance polymers, have attracted much interest of academia and industries. They are characterized by many useful properties, such as low moisture absorption, excellent mechanical properties, self-extinguishing properties, and excellent dimensional stability [15–18]. They also offer a remarkable flexibility in molecular design of monomers and, consequently, a versatile performance as polymers [19–21]. Benzoxazine monomers are polymerized by the thermally activated cationic ring opening polymerization of benzoxazine without any added initiators, catalysts, or by-product formation [22–26]. The potential application areas of polybenzoxazines include coatings, electronic packaging materials, printed circuit boards, frictional materials, catalysis, and matrices for composite materials.

Due to the excellent thermal and mechanical properties of polybenzoxazines, they have been incorporated into PUs aiming at improving their thermal and mechanical properties. The flow chart shown in Fig. 1 represents all reported routes for preparing polybenzoxazine/PU materials. The concept adapted in all the previous studies is based on blending of either preformed

\* Corresponding author. Tel.: +1 20 40 3326357; fax: +1 20 40 3350804.

E-mail address: [taa16@cwru.edu](mailto:taa16@cwru.edu) (T. Agag).

<sup>1</sup> On leave from Nasser International University-Libya

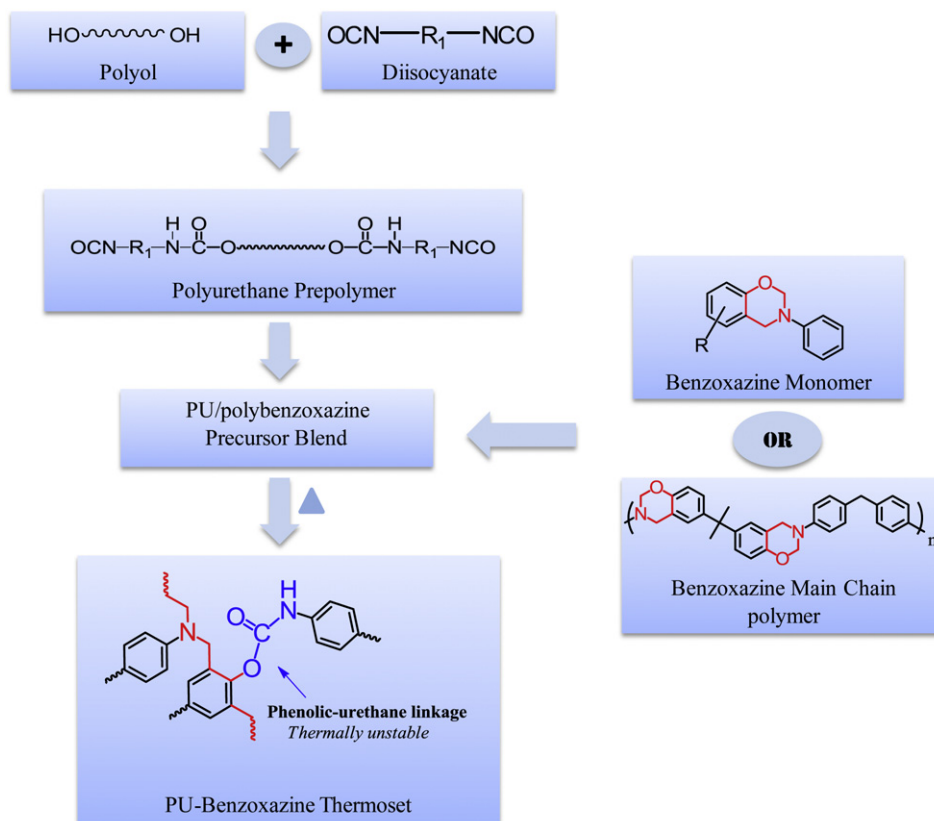


Fig. 1. Previous approaches of polybenzoxazine/PU materials.

benzoxazine monomers or main-chain benzoxazine polymers as polybenzoxazine precursors, with NCO-terminated PUs followed by thermal treatment. As a result, the phenolic groups produced upon ring opening polymerization of benzoxazine react with the NCO groups of PU prepolymer, leading to the formation of phenolic-urethane linkage.

The first study of polybenzoxazine/PU systems was reported by Takeichi et al. [27,28]. They blended bisphenol A/aniline-type benzoxazine monomer (BA-a) and phenol/aniline-type monomer (P-a) with NCO-terminated PU prepolymer. The results of thermal and mechanical properties indicated that polybenzoxazine/PU materials with elastomeric properties can be obtained by adding ca. 10–15% of polybenzoxazine, whereas films with greater plasticity can be produced by increasing the polybenzoxazine content. They also further improved the tensile modulus by adding organoclay to produce polybenzoxazine/PU nanocomposites [29]. Wang et al. [30] prepared interpenetrating polymer networks (IPNs) of polybenzoxazine/PU system. Their morphological studies indicated that the copolymer networks exhibit only physical bonding with slight phase separation behavior. Rimdusit et al. investigated various aspects of polybenzoxazine/PU systems. They found that a system with 10 wt.% PU content exhibited improved flexural strength without deterioration of the thermal degradation temperature [31]. The char yield was slightly increased by using a polyol of higher molecular weight [32]. They also studied the effect of various isocyanates on the properties of a polybenzoxazine/PU system and the reinforcement of the system by carbon fiber [33]. Yeganeh et al. studied various polybenzoxazine/PU systems for electrical insulation applications by blending BA-a monomer and main-chain benzoxazine polymer (BA-ddm) with epoxy-terminated PU prepolymer [34,35]. They have also recently prepared phenolic-

terminated PU prepolymer by end-capping of NCO-terminated PU prepolymer with bisphenol A, which was then mixed with BA-a to form polybenzoxazine/PU materials [36].

Despite the known slow kinetics of isocyanate reacting with phenolic compounds and the poor thermal stability of the urethane linkages produced, most of the aforementioned methods of synthesizing polybenzoxazine/PU materials used similar concept of reacting NCO-terminated PU prepolymers with the phenolic groups of polybenzoxazine [27–36]. It is known that the nature of the group attached to a urethane linkage controls its thermal stability. In general, the thermal stability increases in the presence of electron donating groups and decreases in the presence of electron withdrawing groups in the following order; aryl-NHCOO-aryl < alkyl-NHCOO-aryl < aryl-NHCOO-alkyl < alkyl-NHCOO-alkyl [4,37,38]. Thus, urethane-phenolic linkage produced through the previous approaches is considered to have lowest thermal stability. As a result of these disadvantages, phenolic/PU materials have historically limited applications.

Thus, it is believed that the use of an aliphatic hydroxyl-functional benzoxazine for urethane linkage formation instead of a phenolic hydroxyl group will lead to polybenzoxazine/PU materials of fundamentally different structure and properties than the previously reported approaches. This new approach preserves the oxazine ring upon main-chain polymer formation, which can then be used to further crosslink the copolymer to produce polybenzoxazine/PU network that contains free phenolic moieties. Preservation of the phenolic moieties will maintain the well-known advantages of polybenzoxazines by allowing the formation of intramolecular 6-membered ring hydrogen bonding that offers polybenzoxazines the unique characteristics [22,23]. In the current study, a newly developed hydroxymethyl functional benzoxazine

monomer has been used to produce poly(benzoxazine-co-urethane)s as a main-chain type benzoxazine polymers. The reaction of aliphatic hydroxymethyl functionalities with isocyanate groups is expected to produce thermally stable urethane linkages. Applying this concept of one-pot method will also lead to avoid the drawbacks associated with the use of NCO-terminated PU prepolymer, such as poor shelf life due to their high sensitivity towards moisture and susceptibility to undesirable side reactions. Furthermore, the unique advantage of the recently developed concept of thermo-plastic-thermosetting crossover of main-chain type benzoxazine polymers [39,40] will be highly beneficial in designing varieties of poly(benzoxazine-co-urethane)s with unique characteristics in terms of processability and performance. The preparation, characterization, crosslinking and properties of this new class of copolymers are discussed in the current study.

## 2. Experimental

### 2.1. Materials

4,4'-Methylenediphenyldiisocyanate (**MDI**) (>99%), 4,4'-diaminodiphenylmethane (**DDM**) (98%), and paraformaldehyde (96%) were obtained from Acros Organics USA and used as received. 4-Hydroxybenzyl alcohol (**4HBA**) (98%) was purchased from Sigma Aldrich. Poly(1,4-butylene adipate) (**PBA**) with molecular weight of 1000 was purchased from Sigma Aldrich and dried at 80 °C for 10 h under vacuum just before use. *N,N*-dimethylformamide (**DMF**) was purchased from Fisher and dried over molecular sieves prior to use.

### 2.2. Synthesis of methylol-functional benzoxazine monomer (4HBA-ddm)

In a 500 mL flask, **4HBA** (19 g, 150 mmol), **DDM** (15.02 g, 75 mmol), and paraformaldehyde (9.01 g, 300 mmol) were mixed together and heated at 140 °C in xylenes (175 mL) for 5 h. The reaction was allowed to cool to room temperature followed by washing with hexane to afford a yellow product. The product was then recrystallized in chloroform, (Yield: 80–85%).

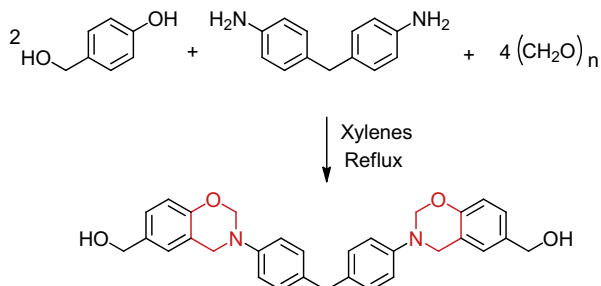
IR spectra (KBr,  $\text{cm}^{-1}$ ): 1228 (asymmetric stretching of Ar–O–C), 1076 (asymmetric stretching of C–O–C), 952 (out-of-plane vibration, benzene ring to which oxazine is attached).

$^1\text{H}$  NMR spectra (DMSO- $d_6$ , frequency: 600 MHz, ppm:  $\delta$ ) 4.36 (d,  $-\text{CH}_2-\text{O}$ ), 4.57 (s, C– $\text{CH}_2-\text{N}$ ), 4.99 (t,  $-\text{OH}$ ), 5.36 (s, N– $\text{CH}_2-\text{O}$ –).

$^{13}\text{C}$  NMR spectra (DMSO- $d_6$ , ppm,  $\delta$ ): 49.23 (C– $\text{CH}_2-\text{N}$ –), 62.61 (s,  $-\text{CH}_2-\text{OH}$ ), 78.87 (N– $\text{CH}_2-\text{O}$ –).

### 2.3. Synthesis of model compound

The model compound has been synthesized by dissolving **4HBA-ddm** (0.5 g, 1 mmol) and phenyl isocyanate (0.238 g,



**Scheme 1.** Preparation of dimethylol benzoxazine monomer (4HBA-ddm).

2 mmol) in a 50 mL dry three neck flask in extra dry DMF (<50 ppm, 20 mL) containing dibutyltindilaurate (0.02 g) under nitrogen atmosphere. The mixture was heated at 70 °C for 30 min to afford a yellow solution. The solution was then cooled and precipitated in cold water, washed by ethanol, and dried in a vacuum oven at room temperature for 24 h to afford a white powder, (Yield: 84%).

IR spectra (KBr,  $\text{cm}^{-1}$ ): 1224 (asymmetric stretching of Ar–O–C), 1037 (asymmetric stretching of C–O–C), 950 (out-of-plane vibration, benzene ring to which oxazine is attached).

$^1\text{H}$  NMR spectra (DMSO- $d_6$ , ppm:  $\delta$ , frequency: 600 MHz): 4.59 (s, C– $\text{CH}_2-\text{N}$ –), 4.98 (s,  $-\text{CH}_2-\text{O}$ ), 5.38 (s, N– $\text{CH}_2-\text{O}$ –), 9.67 (s,  $-\text{NH}$ ).

$^{13}\text{C}$  NMR spectra (DMSO- $d_6$ , ppm,  $\delta$ ): 49.15 (C– $\text{CH}_2-\text{N}$ –), 65.62 (s,  $-\text{CH}_2-\text{OH}$ ), 79.03 (N– $\text{CH}_2-\text{O}$ –).

### 2.4. Synthesis of poly(benzoxazine-co-urethane)s

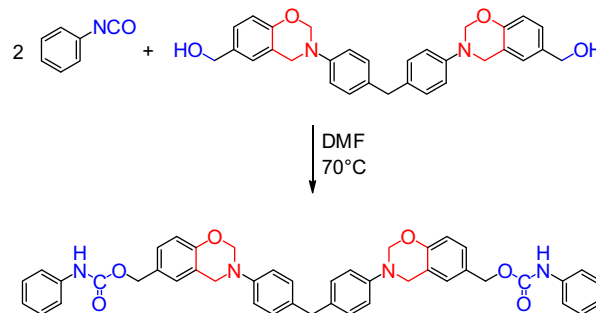
The following is an example of the synthesis of poly(benzoxazine-co-urethane)s with a 1:0.8:0.2 M ratio of MDI:4HBA-ddm:PBA respectively. Into a 50 mL dried three neck flask was dissolved **4HBA-ddm** (0.594 g, 1.2 mmol), and **PBA** (0.3 g, 0.3 mmol) in an extra dry DMF (<50 ppm, 35 mL) solvent containing dibutyltindilaurate (0.02 g), under dry nitrogen atmosphere. The mixture was stirred until clear solution was obtained, followed by adding **MDI** (0.376 g, 1.5 mmol). The mixture was then continually stirred at 70 °C for 30 min. The resulting solution was precipitated in water to afford a slightly yellowish powder, which was dried under vacuum at room temperature for 24 h.

IR spectra (KBr,  $\text{cm}^{-1}$ ): 1733 (the C=O stretching of non-hydrogen bonded carbonyl group of urethane and ester groups), 1540 (the C–N stretching, combined with N–H out-of-plane bending), 1414 (the stretching of C–NH), 1228 (the asymmetric stretching of Ar–O–C), 1076 (the asymmetric stretching of C–O–C), 955 (the out-of-plane vibration of benzene ring to which oxazine is attached).

$^1\text{H}$  NMR spectra (DMSO- $d_6$ , ppm:  $\delta$ , frequency: 600 MHz): 4.58 (s, C– $\text{CH}_2-\text{N}$ –), 4.99 (s,  $-\text{CH}_2-\text{O}$ ), 5.38 (s, N– $\text{CH}_2-\text{O}$ –).

### 2.5. Crosslinking of poly(benzoxazine-co-urethane)s

Solutions of the copolymers in DMF were cast onto glass plates that were pretreated by methylmethoxysilane and dried in an air-circulating oven at 70 °C for 24 h. The produced films were then crosslinked at various temperatures in the air-circulating oven. The temperature profile used to crosslink the samples was as follows: 90 °C/2 h, 120 °C/2 h, 150 °C/2 h, and 180 °C/3 h. The color of the film changed from yellow to red during the crosslinking process.



**Scheme 2.** Preparation of model compound.



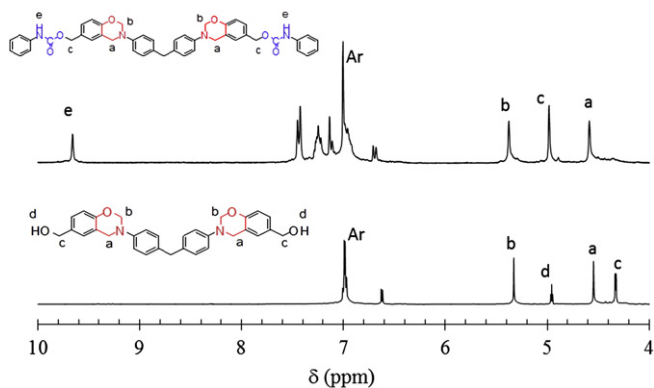


Fig. 2.  $^1\text{H}$  NMR spectrum of model compound and benzoxazine monomer.

## 2.6. Measurements

Both proton ( $^1\text{H}$ ) and carbon ( $^{13}\text{C}$ ) NMR spectra were obtained by Varian Oxford AS600 spectrometer, operating at a proton frequency of 600 MHz and a corresponding carbon frequency of 150.9 MHz. Deuterated dimethylsulfoxide (DMSO- $d_6$ ) was used as a solvent.

Fourier transform infrared spectra (FTIR) were obtained using a Bomem Michelson MB-100 FT-IR spectrometer, which was equipped with a deuterated triglycine sulfate (DTGS) detector. Thirty two scans were recorded at a resolution of  $4\text{ cm}^{-1}$  after purging with dry air. The spectrum was taken by casting a film from polymer solution onto a KBr crystal.

Thermal analysis was performed with differential scanning calorimetry (DSC) using TA Instruments DSC model 2920 to study the curing behavior and thermal stability. The temperature was ramped at  $10\text{ }^\circ\text{C}/\text{min}$  and a nitrogen flow rate of  $65\text{ mL}/\text{min}$  was used for all tests. All samples were crimped in hermetic aluminum pans with lids.

The thermal stability was studied by thermogravimetric analysis (TGA) with a TA Instruments High Resolution 2950 thermogravimetric analyzer using nitrogen as a purging gas. A heating rate of  $10\text{ }^\circ\text{C}/\text{min}$  and nitrogen flow rate of  $60\text{ mL}$  was used for all tests.

Dynamic mechanical behavior (DMA) was performed on a TA Instruments Q800 DMA applying controlled strain tension mode with amplitude of  $10\text{ }\mu\text{m}$  and a temperature ramp rate of  $3\text{ }^\circ\text{C}/\text{min}$ .

Atomic force microscopy (AFM) experiments were performed by tapping mode at ambient temperature in air. Phase and height images of the cross sections were recorded simultaneously using the Nanoscope IIIa instrument Multi-Mode scanning probe (Digital Instruments, Santa Barbara, CA). A tip made of silicon ( $110\text{--}140\text{ }\mu\text{m}$  in length with ca.  $327\text{--}383\text{ kHz}$  resonant frequency and at  $20\text{--}80\text{ N}/\text{m}$  of force) was used. In these images, the height of any spot in the phase image together with the corresponded height of the same spot in the topography image was used to study the morphology of any specific system under study.

Table 1

Compositions of poly(benzoxazine-co-urethane)s.

Copolymer code	MDI (g, mmol)	4HBA-ddm (g, mmol)	PBA (g, mmol)	4HBA-ddm (mol%, wt.%)
I-0	0.25, 1	0.495, 1	0, 0	50, 66.4
I-10	0.25, 1	0.396, 0.8	0.2, 0.2	40, 46.8
I-20	0.25, 1	0.297, 0.6	0.4, 0.4	30, 31.4
I-30	0.25, 1	0.198, 0.4	0.6, 0.6	20, 18.9
I-40	0.25, 1	0.099, 0.2	0.8, 0.8	10, 8.6

Mechanical properties of crosslinked films were evaluated in uniaxial tension on an Instron 5565 universal tester. Dog bone shaped specimens were punched from the films using an ASTM D638 punch tool. An average of four to five specimens were cut and tested at ambient temperature using  $1\text{ mm}/\text{min}$  as a strain rate. The reported modulus values were calculated from the initial slope of the stress-strain curve at 1% strain.

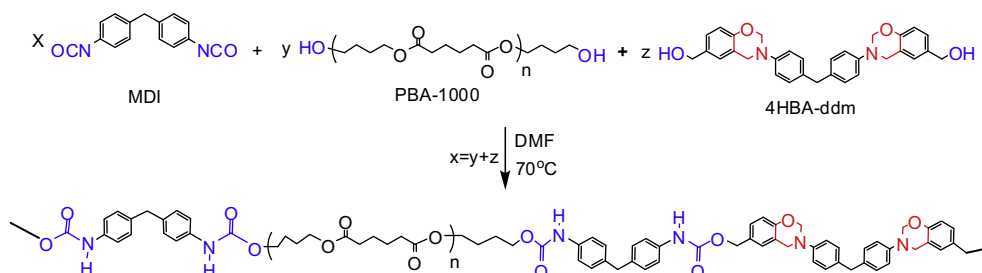
## 3. Results and discussion

### 3.1. Synthesis of dimethylol-functional benzoxazine monomer (4HBA-ddm)

4HBA-ddm as a novel benzoxazine monomer has been synthesized following the newly developed method in our laboratory for the synthesis of difficult benzoxazine monomers [41]. Scheme 1 shows the preparation of 4HBA-ddm. The structure of the monomer has been confirmed by  $^1\text{H}$  NMR,  $^{13}\text{C}$  NMR, and FT-IR spectra. In the  $^1\text{H}$  NMR spectrum, the characteristic resonances attributed to cyclic benzoxazine structure are observed at 4.57 ppm (s,  $\text{C}-\text{CH}_2-\text{N}$ ) and 5.36 ppm (s,  $\text{N}-\text{CH}_2-\text{O}-$ ), whereas the resonances of methylol group are observed at 4.36 ppm (d,  $-\text{CH}_2-\text{O}$ ) and 4.99 ppm (t,  $-\text{OH}$ ).  $^{13}\text{C}$  NMR spectra showed the typical resonances for benzoxazine structure at 49.23 ppm ( $\text{C}-\text{CH}_2-\text{N}-$ ) and 78.87 ppm ( $\text{N}-\text{CH}_2-\text{O}$ ) that further support the formation of benzoxazine monomer. The FT-IR spectra further show the characteristic absorption bands of benzoxazine structure at  $1228\text{ cm}^{-1}$  due to the stretching of  $\text{C}-\text{O}-\text{C}$  and at  $952\text{ cm}^{-1}$  due to the out-of-plane bending vibration of the benzene ring attached to the oxazine ring [42,43].

### 3.2. Synthesis of model compound

A model compound has been synthesized from the reaction of 4HBA-ddm and phenyl isocyanate. The reaction was carried out in dry DMF under nitrogen atmosphere as illustrated in Scheme 2. This model compound helps to understand the reaction condition at which the methylol groups ( $-\text{CH}_2\text{OH}$ ) of the benzoxazine monomer react with the isocyanate group ( $-\text{NCO}$ ) to form urethane linkages and to confirm the stability of cyclic benzoxazine structure under the reaction condition. The structure of the model



Scheme 3. Preparation of main-chain poly(benzoxazine-co-urethane)s.

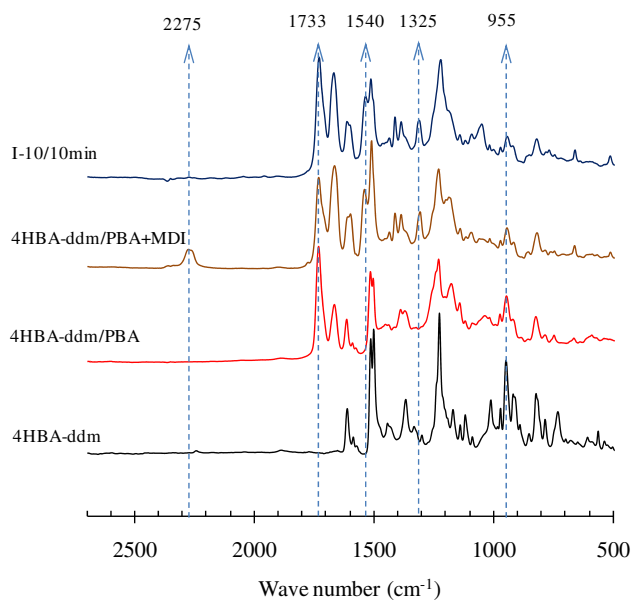


Fig. 3. FT-IR spectra of I-10 and related compounds.

compound has been confirmed by  $^1\text{H}$  NMR,  $^{13}\text{C}$  NMR, and FT-IR spectra.  $^1\text{H}$  NMR spectrum depicted in Fig. 2 shows the characteristic resonances at 4.59 ppm (s,  $\text{C}-\text{CH}_2-\text{N}$ ) and 5.38 ppm (s,  $\text{N}-\text{CH}_2-\text{O}-$ ) due to benzoxazine structure, indicating its stability at this reaction condition. A new resonance was observed at 9.67 ppm attributed to the  $-\text{NH}$  of urethane linkage. In the FT-IR spectra, benzoxazine structure was confirmed by the characteristic absorption bands at  $1224\text{ cm}^{-1}$  due to the stretching of  $\text{C}-\text{O}-\text{C}$  and the band at  $950\text{ cm}^{-1}$  due to the out-of-plane bending vibration of the benzene ring that is attached to the oxazine ring. This confirms the high reactivity of the methylol group in a benzoxazine

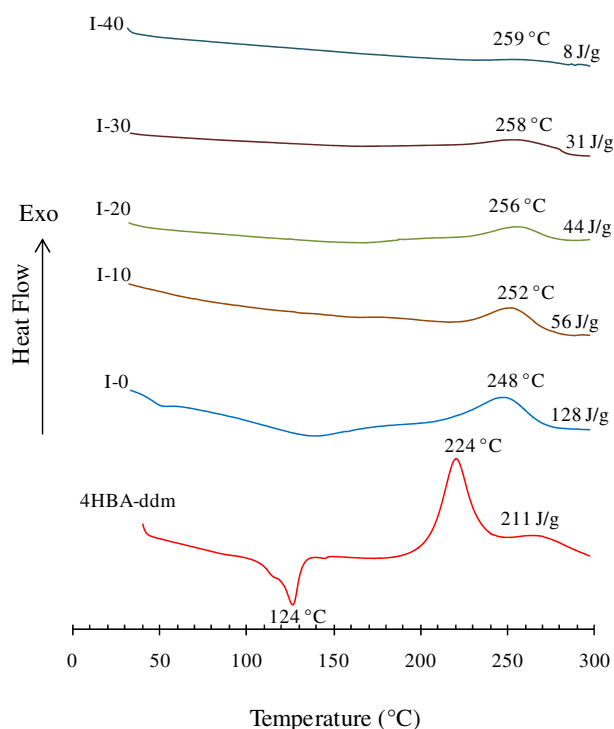


Fig. 4. DSC thermograms of uncrosslinked films at different benzoxazine molar ratio.

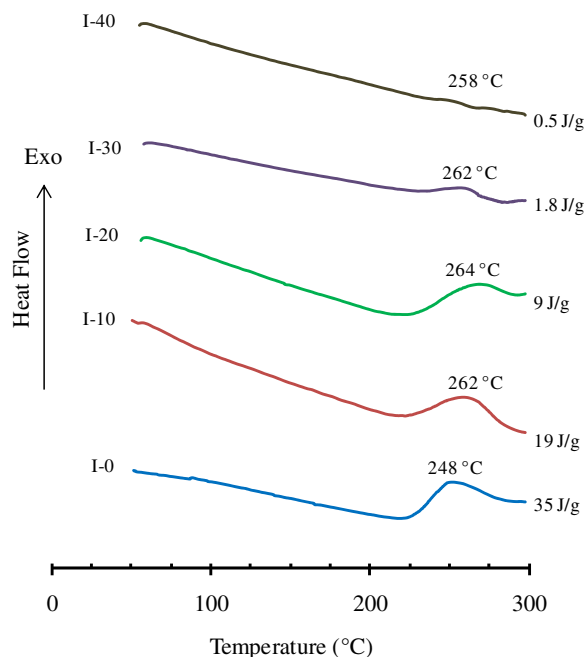


Fig. 5. DSC thermograms of crosslinked films at different benzoxazine molar ratio.

monomer towards the isocyanate group to form urethane linkage in a short time at relatively low reaction temperature.

### 3.3. Synthesis of main-chain type poly(benzoxazine-co-urethane)s

Main-chain type poly(benzoxazine-co-urethane)s have been prepared by the reaction of MDI, PBA and different molar ratio of 4HBA-ddm. The proposed structure is depicted in Scheme 3. This structure does not represent the exact structures of the copolymers, but rather idealized structure is shown. The compositions of the synthesized copolymers and their nomenclature are illustrated in Table 1. The uncrosslinked copolymers will be abbreviated as I# and the crosslinked forms will be poly(I#). The number (#) is used to indicate the molar percent of polyol in copolymer.

The consumption of the NCO groups of MDI due to the reaction with the OH groups of both 4HBA-ddm and PBA to produce urethane linkages has been followed by FT-IR. Fig. 3 illustrates the FT-IR spectra of I-10, as an example. FT-IR spectra indicate that the typical absorption at  $2275\text{ cm}^{-1}$  due to  $-\text{NCO}$  group disappeared

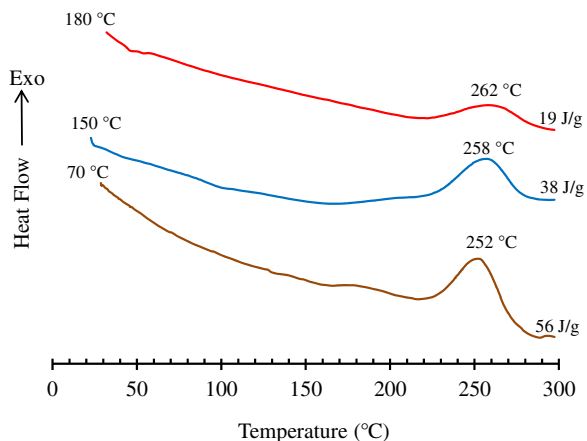


Fig. 6. DSC thermograms for I-10 at various polymerization temperatures.

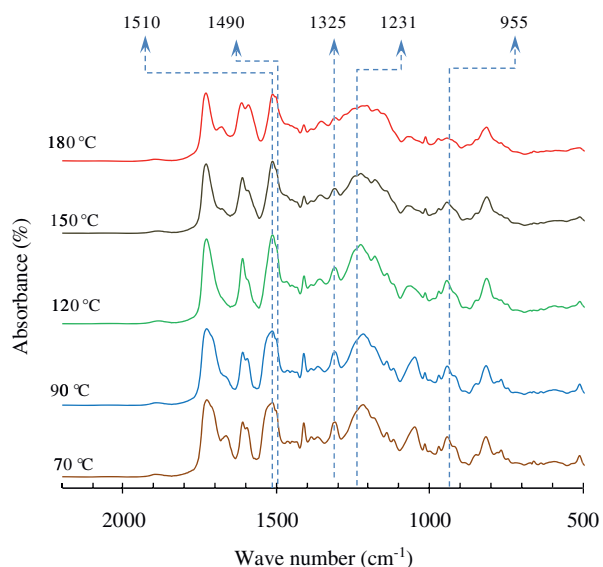


Fig. 7. FT-IR spectra of I-10 film after polymerizing at different temperature.

quickly within 10 min. It was also observed that the C=O stretching of non-hydrogen bonded carbonyl group of urethane and ester groups at  $1733\text{ cm}^{-1}$  and the C–N stretching combined with N–H out-of-plane bending at  $1540\text{ cm}^{-1}$  attributed to the formation of urethane linkage increased. Also, the band at  $955\text{ cm}^{-1}$  due to the out-of-plane bending vibration of the benzene ring attached to oxazine ring is maintained intact, confirming the presence of benzoxazine structure in the resulting polymer [27,34,38,42,43].

#### 3.4. Polymerization behavior of poly(benzoxazine-co-urethane)s

Differential scanning calorimetry (DSC) has been used to monitor the crosslinking behavior of the main-chain type poly(benzoxazine-co-urethane). Fig. 4 shows the DSC thermograms of copolymers containing different content of cyclic benzoxazine in the main-chain after drying at  $70\text{ }^\circ\text{C}$ . The DSC thermograms indicate that as the content of benzoxazine in copolymers increases, the amount of the exothermic heat increases. The heat of polymerization of benzoxazine for crosslinking are 128, 46, 41, 31, and  $8\text{ J/g}$  for I-0, I-10, I-20, I-30 and I-40, respectively. This exothermic heat is attributed to the crosslinking reaction of poly(benzoxazine-co-urethane)s via ring opening polymerization of benzoxazine structure.

DSC thermograms have been used to monitor the residual benzoxazine in the main-chain of the crosslinked copolymers after

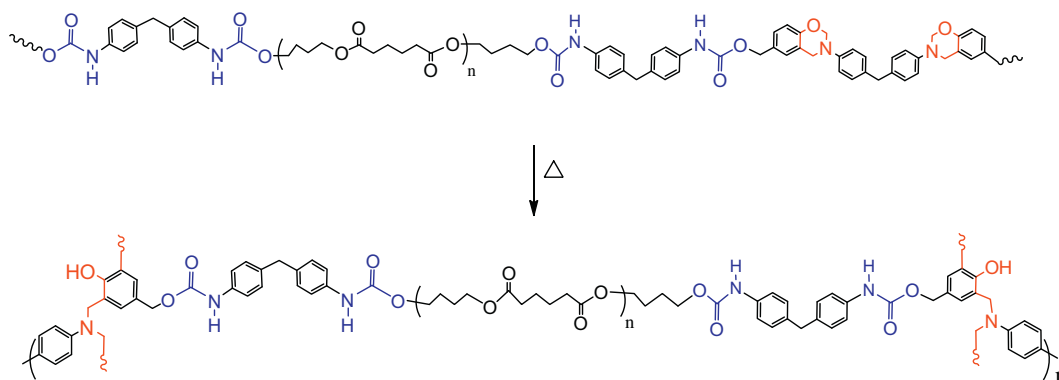
thermal treatment up to  $180\text{ }^\circ\text{C}$  as depicted in Fig. 5. The residual exothermic peaks represent the remaining unpolymerized benzoxazine in the copolymers. Since the amount of benzoxazine is varied in the main-chain copolymer, there is a gradual decrease in the remaining exothermic peaks with decreasing the benzoxazine content in the copolymers. By comparison of the amount of exotherm before and after the crosslinking (Figs. 4 and 5), we can conclude that the copolymers with low benzoxazine content such as poly(I-40) and poly(I-30) showed the completion of polymerization of more than 93%, whereas copolymers with higher benzoxazine content such as poly(I-20), poly(I-10) and poly(I-0) showed the completion of polymerization of  $\sim 66\text{--}80\%$ .

The crosslinking of I-10 as an example has been studied by DSC and FT-IR after each thermal treatment cycle. Fig. 6 shows the DSC thermograms of the films at various thermal treatments. The DSC thermograms show that the heat of polymerization decreases from  $56\text{ J/g}$  to  $19\text{ J/g}$  as the temperature increases from  $70$  to  $180\text{ }^\circ\text{C}$ , indicating the presence of residual benzoxazine structure. Further thermal curing has been avoided to eliminate the possibility of partial degradation of aliphatic segment of PUs copolymer [1,4,27,28].

To further confirm the crosslinking of the copolymers, FT-IR spectra of the copolymers have been studied. Fig. 7 shows the FT-IR spectra of I-10 after various thermal treatments. A gradual decrease of the characteristic absorption bands of benzoxazines with thermal treatment was observed at  $1510\text{ cm}^{-1}$  of trisubstituted benzene,  $1325\text{ cm}^{-1}$  of  $\text{CH}_2$  of benzoxazine ring, and  $1231\text{ cm}^{-1}$  of ether linkage. Meanwhile, a new band appeared at  $1490\text{ cm}^{-1}$  of tetrasubstituted benzene rings, indicating the formation of polybenzoxazine and hence the crosslinking of the copolymer [18,25]. However, a residual absorption band at  $955\text{ cm}^{-1}$  due to the out-of-plane bending vibration of benzene ring is still observed. Nonetheless, thermal treatment up to  $180\text{ }^\circ\text{C}$  has been fixed as last polymerization cycle to avoid any partial degradation of the aliphatic component of PU [1,4]. Scheme 4 shows the proposed structure of the crosslinked copolymer network structure. As a result of the thermally activated ring opening polymerization of cyclic benzoxazine in the main-chain, crosslinking is achieved through the formation of polybenzoxazine as crosslinkers between copolymer chains.

#### 3.5. Morphology studies

The surface morphologies of main-chain poly(benzoxazine-co-urethane) films were monitored by AFM in tapping mode and are displayed in Fig. 8. It was obvious, by comparing the images (a)–(e), that the higher benzoxazine ratio creates more wrinkled surface



Scheme 4. Proposed idealized, crosslinked structure of the main-chain poly(benzoxazine-co-urethane).

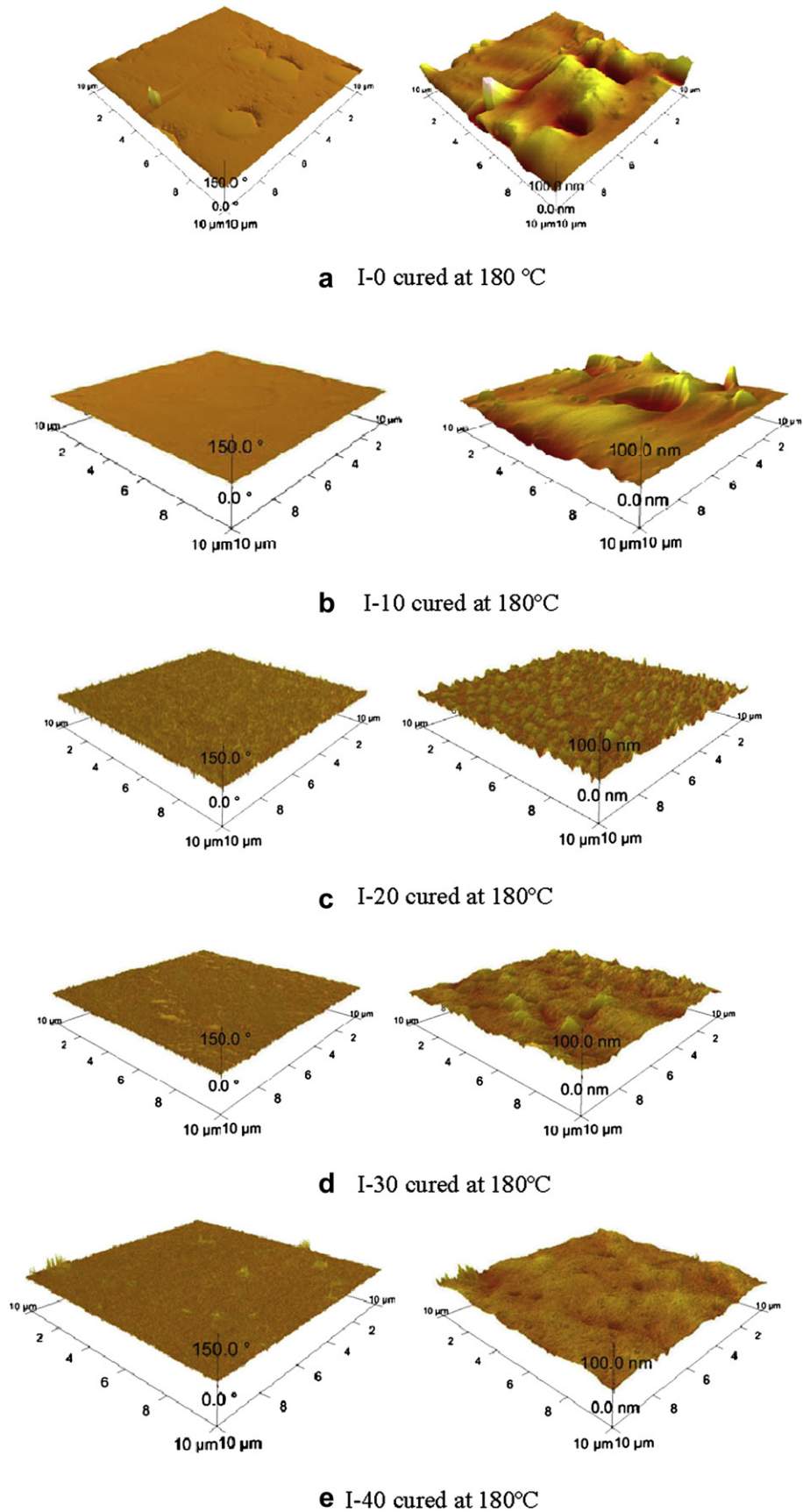


**Fig. 8.** AFM morphology of crosslinked films at 180 °C for 3 h: a) poly(I-0), b) poly(I-10), c) poly(I-20), d) poly(I-30), and e) poly(I-40). Left: phase images and right: topographic images.

than the system with lower benzoxazine ratio. This phenomenon was attributed to the increase in the hard segment content which is represented by aromatic structure in MDI and 4HBA-ddm in comparison to the PBA that is responsible for the soft segments in the moiety. The AFM images exhibit difference in height and phase in micro-regions around 100 nm, which indicates the presence of specific microphase-separated morphologies. These regions consist of hard segment-rich and soft segment-rich domains as in poly(I-40) and poly(I-30) samples. Besides the small phase micro-regions, many rougher domains appear in the poly(I-20) and poly(I-10) samples with the dimension of around 200 nm and more. In the case of poly(I-0) film as a control, it shows a rough surface due to the presence of hard segment-rich domains which is attributed to the high aromatics content in the molecular structure.

### 3.6. Tensile properties

The tensile properties of the crosslinked poly(benzoxazine-co-urethane) films have been evaluated. The effect of varying the thermal treatments of the main-chain poly(benzoxazine-co-urethane) films on the tensile properties has been studied in details for the I-20 sample. Fig. 9 shows stress-strain curves of the I-20 films after various thermal treatment cycles for crosslinking. The tensile properties data of I-20 including tensile modulus, tensile strength, and elongation at break are tabulated in Table 2. It is obvious that, as the thermal treatment temperature increases, both tensile modulus and tensile strength increase whereas the elongation at break decreases. This behavior is attributed to the increase of crosslinking density coupled with the increase of the thermal treatment temperature, which leads to further ring opening polymerization of benzoxazine structures in the main-chain to take place and the formation of a more rigid three dimensional network structure. As a result, both tensile modulus and tensile strength increased whereas elongation at break decreases.

The effect of benzoxazine content as a crosslinking agent on the tensile properties of poly(benzoxazine-co-urethane) films has also been studied. Fig. 10 shows the stress-strain curves of copolymers after thermally treated up to 180 °C. Table 3 summarizes the results of the tensile properties. Both the tensile modulus and tensile strength increase with an increase in the benzoxazine content in copolymers as depicted in Fig. 11. For example, the tensile modulus values are 2360, 737, 517, 54 and 18 MPa whereas the tensile strengths are 78, 40, 32, 13 and 3 MPa for samples poly(I-0), poly(I-10), poly(I-20), poly(I-30), and poly(I-40) respectively. On the other hand, the elongation at break increased with decreasing the benzoxazine content to be 4, 12, 16, 73 and 109% for samples poly(I-0), poly(I-10), poly(I-20), poly(I-30), and poly(I-40) respectively.

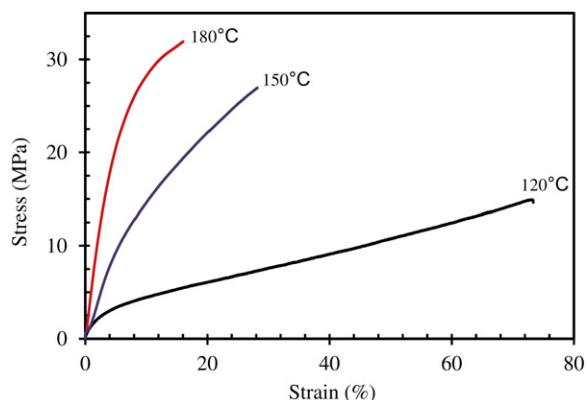


Fig. 9. Stress-strain curves of I-20 treated at different temperatures.

**Table 2**  
Tensile properties of I-20 films after different thermal treatment.

Polymerization temp.(°C)	Modulus (MPa)	Tensile strength (MPa)	Elongation at break (%)
120 °C	90	15	73
150 °C	197	27	28
180 °C	533	32	16

This behavior is attributed mainly to the decrease of crosslinking density as the content of benzoxazine decreases. Thus, the more benzoxazine content in the copolymer, the greater the crosslinking density, leading to a more rigid structure. The trends in mechanical behavior are in agreement with reported studies [27,31–36]. Nonetheless, the values of tensile modulus and tensile strength of crosslinked poly(benzoxazine-co-urethane)s produced through the concept adapted in this study are higher than that of the reported polybenzoxazine/PU materials. For example, poly(I-30) with ca. 18 wt.% of polybenzoxazine content showed tensile strength and tensile modulus of 13.0 and 73.0 MPa. These values are significantly higher than the reported values for polybenzoxazine/PU materials containing the same content of polybenzoxazine which showed tensile strength and tensile modulus of <5 and < 20 MPa, respectively [27,34,35]. For polybenzoxazine/PU materials reported by Takeichi et al. [27], the films cured at 180 °C had higher elongation at break than the current concept and all the reported approaches for

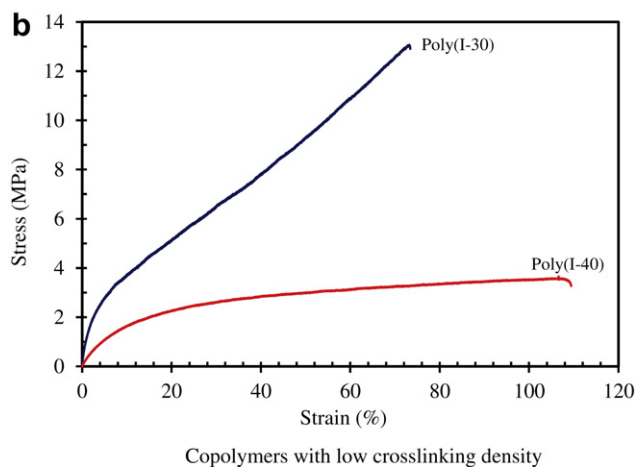
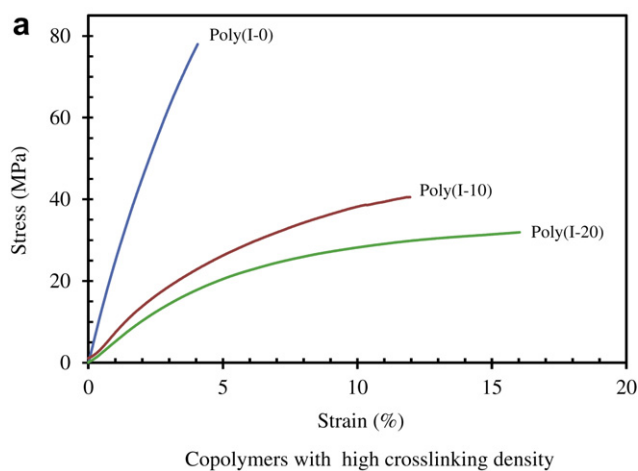


Fig. 10. Stress-strain curves of crosslinked copolymer films at different benzoxazine molar ratio.

**Table 3**

Tensile properties of copolymer films of different benzoxazine content after thermal treatment at 180 °C.

Sample code	Modulus (MPa)	Tensile strength (MPa)	Elongation at break (%)
Poly(I-0)	2358	78	4
Poly(I-10)	737	40	12
Poly(I-20)	517	32	16
Poly(I-30)	54	13	73
Poly(I-40)	18	3	109

polybenzoxazine/PU materials. This high value of the elongation at break is attributed to the use of benzoxazine monomer that leads to lower crosslinking density than the current concept through the main-chain type benzoxazine polymers. In addition, the lower elongation at break in this method for polybenzoxazine/PU materials is presumably due to the role of the inter- and intra-molecular hydrogen bonding of free phenolic groups of polybenzoxazine that acts as additional physical crosslinks between the chains of the copolymer [22,44]. Moreover, most of the previously reported approaches for polybenzoxazine/PU materials used toluene diisocyanate (TDI) and 1,6-hexamethylene diisocyanate (HDI) to prepare PU prepolymer. However, in this study methylene diphenyl diisocyanate (MDI) of more rigid aromatic content has been used that adds more rigidity in the molecular structure [1,44]. Also, in comparison to well-known high performance poly(urethane-imide), the crosslinked poly(benzoxazine-co-urethane) copolymers showed comparable values for samples containing similar PU content. For example poly(I-20) exhibited higher tensile strength but lower elongation at break than poly(urethane-imide) of the same urethane content [5,8].

### 3.7. Thermal properties of crosslinked poly(benzoxazine-co-urethane)s

Dynamic mechanical analysis (DMA) of crosslinked copolymer films has been performed and the results are shown in Fig. 12. The DMA results indicate that the initial storage moduli ( $E'$ ) of the copolymer films increased with increasing the content of benzoxazine in the main-chain. It was also observed that the storage modulus maintained at higher value by increasing the benzoxazine

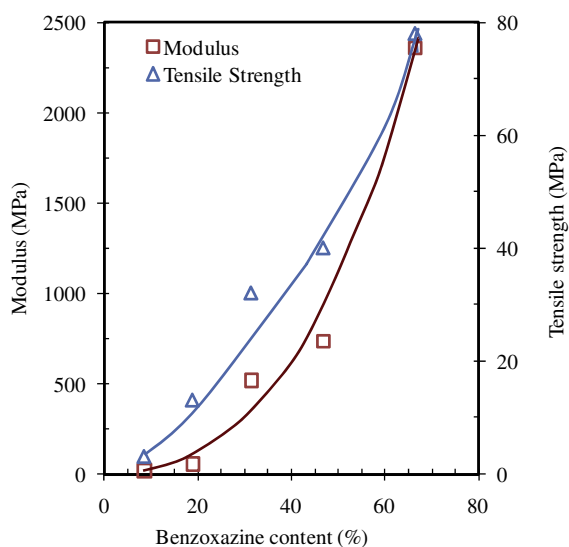
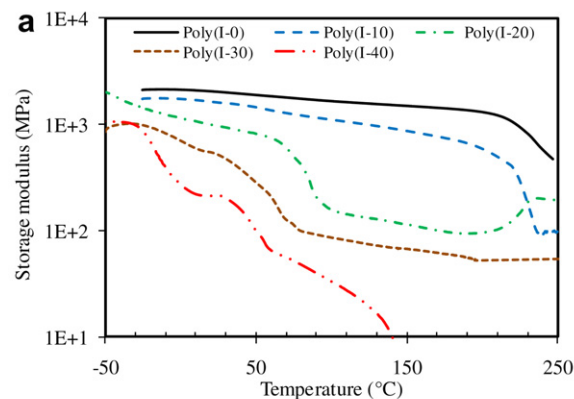
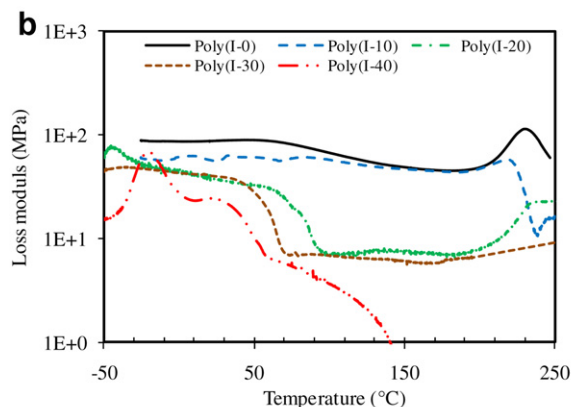


Fig. 11. The effect of benzoxazine content on the modulus and tensile strength.



Storage modulus temperature relationship of polymerized films at 180 °C



Loss modulus temperature relationship of polymerized films at 180 °C

Fig. 12. DMA analysis for poly(benzoxazine-co-urethane) films polymerized at 180 °C.

content, indicating the increase in the stiffness of the copolymers. In addition, the  $T_g$  of crosslinked poly(benzoxazine-co-urethane)s shifted to lower temperature with increasing the content of PBA as a soft segment and decreasing the crosslinking density. For example,  $T_g$  decreased from 230 to 219 °C by increasing the polyols content in the main-chain from 0 to 10 mol% for samples poly(I-0)

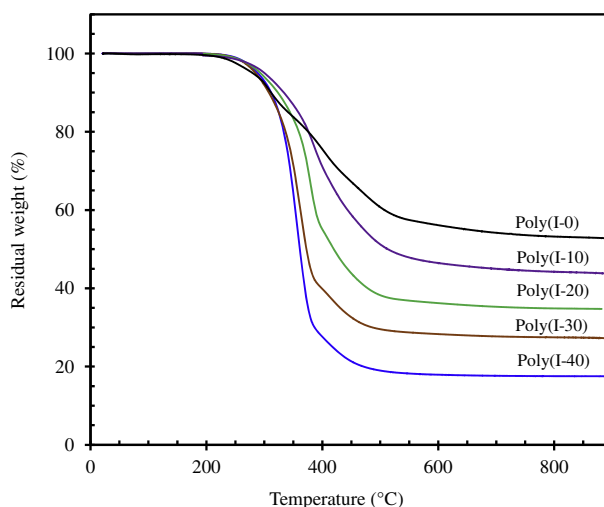


Fig. 13. TGA analysis of cured poly(benzoxazine-co-urethane)s films.

**Table 4**  
TGA data of poly(benzoxazine-co-urethane) films cured up to 180 °C.

Sample	Td <sub>5</sub> (°C)	Td <sub>10</sub> (°C)	Char yield (%)
Poly(I-0)	280	311	53.0
Poly(I-10)	300	333	44.3
Poly(I-20)	293	323	35.0
Poly(I-30)	287	310	27.5
Poly(I-40)	285	309	17.5

and poly(I-10), respectively. This behavior is attributed to the increased chain mobility of the copolymer as a result of decreasing the crosslinking density that leads to decreased T<sub>g</sub>.

Thermogravimetric analysis (TGA) has been used to investigate the thermal stability of the crosslinked poly(benzoxazine-co-urethane) films. Fig. 13 shows the TGA profiles of copolymer films after 180 °C treatment. The results of TGA are summarized in Table 4. The thermal stability of poly(I-0), which can be used as a control, shows an early weight loss from 280 °C. 4HBA-ddm monomer which has been used in this study is a methylol functional end-capped benzoxazine which, by thermal treatment, will condensate to produce water at about 200 °C, similar to traditional resole. Since the copolymer poly(I-0) contains the highest content of 4HBA-ddm and the thermal treatment did not exceed 180 °C, the early weight lost is attributed to the condensation reaction of methylol end groups in the copolymer which will be discussed in details elsewhere [41]. For the rest of the crosslinked copolymers, a higher benzoxazine content led to an improvement in the onset of the degradation as can be seen from the 5 and 10% weight loss temperatures, Td<sub>5</sub> and Td<sub>10</sub>. For example, Td<sub>5</sub>s are 300, 293, 287, and 285 °C whereas Td<sub>10</sub>s are 333, 323, 310, and 309 °C for samples poly(I-10), poly(I-20), poly(I-30), and poly(I-40), respectively. The onset of degradation is higher than the control due to the absence of methylol groups that are consumed for urethane linkage formation. Although depolymerization of urethane bonds occurred at about 240 °C [8], the incorporation of benzoxazine in the poly (benzoxazine-co-urethane) copolymer shifted the decomposition temperature to ~285–300 °C, depending on the benzoxazine content. The onset of the degradation did not improve significantly, since the increase of the benzoxazine content will shift the initial weight to low temperature due to methylol condensation. On the other hand, the increase of polyol content as aliphatic component will contribute to the shift of initial weight loss to lower temperature. Despite the aforementioned reasons of the initial weight loss of the copolymers, the thermal stability of this new system is still comparable with the reported similar polybenzoxazine/PUs. For example, Td<sub>5</sub> changed from 285 °C for poly(I-40) copolymer of 8.6 wt.% benzoxazine weight percent to 300 °C for poly(I-10) copolymer of 46.8 wt.%, respectively. The char yield also showed significant increase upon increasing the benzoxazine content in the main-chain. For example samples poly(I-0), poly(I-10), poly(I-20), poly(I-30) and poly(I-40) have char yield of ca. 53.0, 44.3, 35.0, 28.0 and 18.0%, respectively. Thus, this new concept of crosslinked poly (benzoxazine-co-urethane) copolymer is shown to be effective for producing polybenzoxazine/PU materials of significant higher thermal stability than the previously reported approaches. For example, sample poly(I-20) of ca. 70 wt.% of PU has char yield of 35.0%, whereas the previously reported polybenzoxazine/PU materials of similar PU content showed a char yield in the range of 22–25% [27,28,36] and not more than 30% for systems of ca. 30 wt.% of PU [32,33]. This enhancement in thermal stability is attributed to the presence of polybenzoxazine as a part of the copolymer main-chain and the thermal stability of urethane linkage that result in better thermal properties than the reported polybenzoxazine/PU materials.

## 4. Conclusions

A new concept to produce polybenzoxazine/PU copolymers has been developed by incorporating oxazine and urethane groups in one molecule through main-chain type poly(benzoxazine-co-urethane)s. These copolymers have been synthesized via copolymerization of diisocyanate monomer with a dimethylol-functional benzoxazine monomer and polyol to afford a linear main-chain type polymer. The produced copolymers were further crosslinked through thermally activated ring opening polymerization of benzoxazine to produce network structure. Films were subjected to mechanical and thermal tests and the results were associated with the chemical structure of corresponding films according to the content of benzoxazine in the moiety. This novel class of polybenzoxazine/PU materials is characterized by the following:

- One-pot synthesis of phenolic-urethane materials that avoids the drawbacks associated with the use of preformed NCO-terminated PU prepolymers.
- Superior thermal stability compared to previous approaches.
- Excellent mechanical integrity as can be seen from high tensile modulus and tensile strength due to the presence of polybenzoxazine as part of the main-chain.
- These copolymers showed thermal and mechanical properties that are comparable to the well-known high performance poly (urethane-imide).

## Acknowledgement

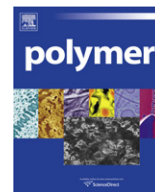
We thank the Ministry of Education of Libya for the financial support of M. Baqar. We also thank Mr. Saeed Alhassan, Case Western Reserve University, for his kind help in taking AFM images.

## References

- [1] Król P. Linear polyurethanes synthesis methods, chemical structures, properties and applications. Boston: VSP; 2008.
- [2] Kumar MNS, Manjula KS, Siddaramaiah A. *J Appl Polym Sci* 2007;105:3153–61.
- [3] Benes H, Rosner J, Holler P, Synkova H, Kotek J, Horak Z. *Polym Adv Technol* 2007;18:149–56.
- [4] Oertel G, editor. *Polyurethane handbook*. Munich: Hanser; 1985.
- [5] Takeichi T, Ujjiie K, Inoue K. *Polymer* 2005;46:11225–31.
- [6] Zuo M, Takeichi T. *J Polym Sci Part A Polym Chem* 1997;35:3745–53.
- [7] Zuo M, Xiang Q, Takeichi T. *Polymer* 1998;39:6883–9.
- [8] Yeganeh H, Mehdipour-Ataei S, Ghaffari M. *High Perform Polym* 2008;20:126–45.
- [9] Jaisankar SN, Nelson DJ, Brammer CN. *Polymer* 2009;50:4775–80.
- [10] Harjunalanen T, Lahtinen M. *Eur Polym J* 2003;39:817–24.
- [11] Petrini P, Tanzi MC, Moran CR, Graham NB. *J Mater Sci Mater Med* 1999;10:635–9.
- [12] Ashraf SM, Ahmad S, Riaz U. *Polym Int* 2007;56:1173–81.
- [13] Ho TH, Wang CS. *Polymer* 1996;37:2733–42.
- [14] Rubner MF. *Macromolecules* 1986;19:2119–28.
- [15] Yagci Y, Kiskan B, Ghosh NN. *J Polym Sci Part A Polym Chem* 2009;47:5565–76.
- [16] Ghosh N, Kiskan B, Yagci Y. *Prog Polym Sci* 2007;32:1344–91.
- [17] Liu X, Gu Y. *J Appl Polym Sci* 2002;84:1107–13.
- [18] Agag T, Arza CR, Maurer FHJ, Ishida H. *Macromolecules* 2010;43:2748–58.
- [19] Ishida H, Low HY. *Macromolecules* 1997;30:1099–106.
- [20] Wang CF, Su YC, Kuo SW, Huang CF, Sheen YC, Chang FC. *Angew Chem Int Ed* 2006;45:2248–51.
- [21] Agag T, Takeichi T. *High Perform Polym* 2002;14:115–32.
- [22] Sudo A, Kudoh R, Nakayama H, Arima K, Endo T. *Macromolecules* 2008;41:9030–4.
- [23] Kim HD, Ishida H. *Macromolecules* 2003;36:8320–9.
- [24] Andreu R, Reina JA, Ronda JC. *J Polym Sci Part A Polym Chem* 2008;46:3353–66.
- [25] Agag T, Takeichi T. *Macromolecules* 2001;34:7257–63.
- [26] Dunkers J, Ishida H. *J Polym Sci Part A Polym Chem* 1999;37:1913–21.
- [27] Takeichi T, Guo Y, Agag T. *J Polym Sci Part A Polym Chem* 2000;38:4165–76.
- [28] Takeichi T, Guo Y. *J Appl Polym Sci* 2003;90:4075–83.
- [29] Takeichi T, Guo Y. *Polym J* 2001;33:437–43.
- [30] Cui Y, Chen Y, Wang X, Tian G, Tang X. *Polym Int* 2003;52:1246–8.
- [31] Rimdusit S, Pirstpindvong S, Tanthapanichakoon W, Damrongsakkul S. *Polym Eng Sci* 2005;45:288–96.

- [32] Rimdusit S, Mongkhonsi T, Kamonchaivanich P, Sujirote K, Thiptipakorn S. *Polym Eng Sci* 2008;48:2238–46.
- [33] Rimdusit S, Liengvachiranon C, Tiptipakorn S, Jubsilp C. *J Appl Polym Sci* 2009;113:3823–30.
- [34] Yeganeh H, Razavi-Nouri M, Ghaffari M. *Polym Adv Technol* 2008;19:1024–32.
- [35] Yeganeh H, Razavi-Nouri M, Ghaffari M. *Polym Eng Sci* 2008;48:1329–38.
- [36] Yeganeh H, Jamshidi S, Mehdipour-Ataei S. *Polym Adv Technol*; 2010. doi:10.1002/pat.1634.
- [37] Kordomenos PI, Kresta JE. *Macromolecules* 1981;14:1434–7.
- [38] Takeichi T, Suefuji K, Inoue K. *J Polym Sci Part A Polym Chem* 2002;40:3497–503.
- [39] Takeichi T, Kano T, Agag T. *Polymer* 2005;46:12172–80.
- [40] Chernykh A, Agag T, Ishida H. *Polymer* 2009;50:382–90.
- [41] Agag T, Baqar M, Ishida H, Qutubuddin S, in preparation.
- [42] Dunkers J, Ishida H. *Spectrochim Acta* 1995;51A:855–67.
- [43] Luo N, Wang DN, Ying SK. *Macromolecules* 1997;30:4405–9.
- [44] Huang SL, Lai JY. *Eur Polym J* 1997;33:1563–7.





# Bridge length effect of new dinuclear constrained geometry catalysts on controlling the polymerization behaviors of ethylene/styrene copolymerization

Thi Dieu Huyen Nguyen<sup>a</sup>, Thi Le Thanh Nguyen<sup>a</sup>, Seok Kyun Noh<sup>a,\*</sup>, Won Seok Lyoo<sup>b</sup>

<sup>a</sup>School of Display and Chemical Engineering, Yeungnam University, 214-1 Daedong, Gyeongsan, Gyeongbuk 712-749, Republic of Korea

<sup>b</sup>School of Textiles, Yeungnam University, 214-1 Daedong, Gyeongsan, Gyeongbuk 712-749, Republic of Korea

## ARTICLE INFO

### Article history:

Received 29 September 2010

Received in revised form

24 November 2010

Accepted 29 November 2010

Available online 4 December 2010

### Keywords:

Bridge length effect

Dinuclear constrained geometry catalyst

Ethylene copolymerization

## ABSTRACT

According to the observable evidence from <sup>1</sup>H and <sup>13</sup>C nuclear magnetic resonance and mass spectrometry, new dinuclear constrained geometry catalysts (DCGCs) with a structure of  $[\{\text{Ti}(\eta^5\text{-C}_9\text{H}_5)\text{Si}(\text{CH}_3)_2\text{N}^t\text{Bu}\text{Cl}_2(\text{CH}_2)_n\}_2(\text{C}_6\text{H}_4)]$  [ $n = 0$  (**10**),  $n = 1$  (**11**),  $n = 2$  (**12**)] were synthesized successfully. Copolymerization of ethylene and styrene were tested by using three new DCGCs and Dow CGC. The catalyst activity, the molecular weight (MW) and styrene content of the copolymers were sharply improved as the bridge structure was transformed from *para*-phenyl (**10**) to *para*-xylyl (**11**) and *para*-diethylenephenyl (**12**). The activity of **11** and **12** was about four to five times greater than that of **10** regardless of the polymerization conditions. In addition, the capability to form high MW polymers increased in the order of Dow CGC  $\approx$  **10** < **11** < **12**. The styrene contents in copolymers generated by **11** and **12** were higher than those of **10**.

© 2010 Elsevier Ltd. All rights reserved.

## 1. Introduction

Since applying metallocene catalyst in olefin polymerization became more usual, a variety of dinuclear metallocene compounds [1–15], which contain two mechanically linked metallocene units, have been prepared and tested their polymerization properties. These systems may provide a new possibility to improve the catalytic properties of metallocene ascribed by the cooperative electronic and chemical interaction between two active sites [11–23]. Beside of the properties of well-defined mononuclear metallocenes, the natures of the bridging unit such as the length, the flexibility or the rigidity were the key effective features to lead to the unique catalytic behaviors of the dinuclear metallocenes references. Mülhaupt first studied the propylene polymerization using phenylene-bridged dinuclear zirconocene in 1993, and showed that the molecular weights of polypropylenes obtained with these catalysts were smaller than those made by the mononuclear one because of the electronic and cooperative interaction of the two adjacent zirconium center [3]. In 1996, Green demonstrated that the activities and molecular weights of polymers were varied according to the various dimethylsilyl-bridged dinuclear metallocenes used [4]. In 2002, Mark's group reported that the copolymers of ethylene and  $\alpha$ -olefin obtained by ethylene bridged dinuclear zirconium CGC had the higher monomer incorporation

than those obtained by mononuclear CGC presumably due to the nuclearity effects caused by the close spatial proximity between two active sites of dinuclear CGC [13,14]. Our previous studies also demonstrated that the presence of a long and flexible polymethylene bridge between two active sites facilitated both the polymerization activity and the comonomer response of DCGC [15,16]. Recently, it was found that the presence of a phenyl ring in dinuclear metallocene catalyst was even more effective in improving the polymerization activity. This result was able to be interpreted that the bridge unit contributed not only to limit the free movement of the active species but also to reduce the frequency of the intramolecular deactivation [17–23]. Sun's group showed that the catalytic activities of 4,4'-bis(methylene)biphenylene-bridged dinuclear metallocene were more than three times and twice higher than that of the phenyldimethylene bridged dinuclear metallocene and the corresponding mononuclear, respectively, in ethylene polymerization [19]. In addition, dinuclear compound produced polyethylene with broad molecular weight distribution. Consequently, both the electronic and steric effects of the active site induced by the bridge unit of the dinuclear metallocene can be considered as the major element to be responsible for the final polymerization behaviors of the catalyst.

Although many studies have investigated the effect of the bridge structure on dinuclear metallocenes, few have reported specifically on the effect of bridge length on the DCGC characteristics free from the steric issue. Herein, we therefore describe the polymerization properties of three DCGCs having a distinguished bridge length of

\* Corresponding author. Tel.: +82 53 810 2526; fax: +82 53 810 4651.  
E-mail address: [sknoh@ynu.ac.kr](mailto:sknoh@ynu.ac.kr) (S.K. Noh).

*para*-phenyl (**10**), *para*-xylyl (**11**) and *para*-diethylenephenyl (**12**), in order to examine the role of the bridge length of dinuclear metal-locene (Scheme 1).

## 2. Experimental

### 2.1. Materials

Toluene and tetrahydrofuran (THF) were distilled from sodium-benzophenone ketyl prior to use. Diethyl ether and hexane were purified by using MBRAUN MB-SPS-800 series. 1,4-dichlorobenzene,  $\alpha,\alpha'$ -dichloro-*p*-xylene, titanium chloride (Aldrich Co. USA), 1,4-bis(2-chloroethyl)benzene (TCI Tokyo Chemical Industry), *n*-BuLi (2.5 M solution in hexane, Aldrich Co. USA), and indene (Aldrich Co. USA) were used without further purification.  $[\text{TiCl}_3(\text{THF})_3]$  was prepared by literature methods [24]. Dichlorodimethyl silane and *tert*-butyl amine purchased from Aldrich Co. USA were used after distilling from calcium hydride. Ethylene (polymer grade) was purified by passage through a column of molecular sieve (4 Å) and Drierite (8mesh). MMAO (type 4, 6.4 wt.% Al, Akzo, USA) was used without further purification.

### 2.2. Methods

#### 2.2.1. General considerations

All reactions were carried out under a dry, oxygen-free atmosphere using standard Schlenk techniques with a double manifold

vacuum line. Nitrogen gas was purified by passage through a column of molecular sieve (4 Å) and Drierite (8mesh).

### 2.3. Measurements

$^1\text{H}$  NMR and  $^{13}\text{C}$  NMR spectra were recorded on a VNS-300 NMR spectrometer at >300 MHz, using  $\text{CDCl}_3$  as a solvent at 25 °C. Mass spectra were measured on an Autospec-Ultima E with high-resolution condition using  $\text{CHCl}_3$  as a solvent for liquid samples. The styrene contents were calculated based on the  $^1\text{H}$  NMR assays of the polymer which were conducted in 1,1,2,2-tetrachloroethane- $d_2$  at 110 °C [25,26]. Differential scanning calorimetry (DSC) was carried out with a Pyris Diamond DSC under nitrogen atmosphere [conditions: heating from 20 °C to 300 °C (10 °C/min), cooling from 300 °C to 20 °C (10 °C/min)]. The second heating cycle was used for collecting the DSC thermogram data at a ramping rate of 10 °C/min. The viscosity averaged MW (Mv) of the polymer was measured in decahydronaphthalene at 135 °C by a modified Ubbelohde-type viscometer according to ASTM-4020. MW and MW distribution were measured by GPC (PLGPC220) at 170 °C using 1,2,4-trichlorobenzene. The MW was calculated by a standard procedure based on the calibration with standard polystyrene samples.

### 2.4. Synthesis

#### 2.4.1. Preparation of $[(\text{C}_9\text{H}_6)_2(\text{C}_6\text{H}_4)]$ (**1**)

A solution of Indene lithium (IndLi) salt (1.72 g, 14.21 mmol)/THF (40 ml) was cooled to -78 °C. 1,4-Dichlorobenzene (0.84 g, 5.68 mmol)/THF (20 ml) was dropped into solution of IndLi salt. The reactor was warmed to room temperature, then heated up 60 °C in 48 h. THF was volatilized in vacuo at least 4 h. Product was separated by filter through celite with ether. The light yellow solution was removed solvent to get light yellow powder. (1.69 g, 98.25%).  $^1\text{H}$  NMR (300 MHz,  $\text{CDCl}_3$ , 25 °C,  $\delta$ , ppm): 7.45 (d, 2H,  $\text{C}_9\text{H}_7$ ), 7.40 (d, 2H,  $\text{C}_9\text{H}_7$ ), 7.28 (t, 2H,  $\text{C}_9\text{H}_7$ ), 7.17 (t, 2H,  $\text{C}_9\text{H}_7$ ), 6.86 (s, 4H,  $\text{C}_6\text{H}_4$ ), 6.55 (s, 2H,  $\text{C}_9\text{H}_7$ ), 3.38 (s, 4H,  $\text{C}_9\text{H}_7$ ).

#### 2.4.2. Preparation of $[(\text{C}_9\text{H}_6)(\text{CH}_2)_2(\text{C}_6\text{H}_4)]$ (**2**)

The compound was synthesized from  $\alpha,\alpha'$ -dichloro-*p*-xylene (3.27 g, 18.68 mmol) using the same reaction conditions and procedures as for **1**. A light yellow compound was obtained (5.81 g, 93%).  $^1\text{H}$  NMR (300 MHz,  $\text{CDCl}_3$ , 25 °C,  $\delta$ , ppm): 7.49 (d, 2H,  $\text{C}_9\text{H}_7$ ), 7.32 (d, 2H,  $\text{C}_9\text{H}_7$ ), 7.30 (t, 2H,  $\text{C}_9\text{H}_7$ ), 7.29 (t, 2H,  $\text{C}_9\text{H}_7$ ), 7.21 (s, 4H,  $\text{C}_6\text{H}_4$ ), 6.16 (s, 2H,  $\text{C}_9\text{H}_7$ ), 3.91 (s, 4H,  $\text{CH}_2$ ), 3.38 (s, 4H,  $\text{C}_9\text{H}_7$ ).

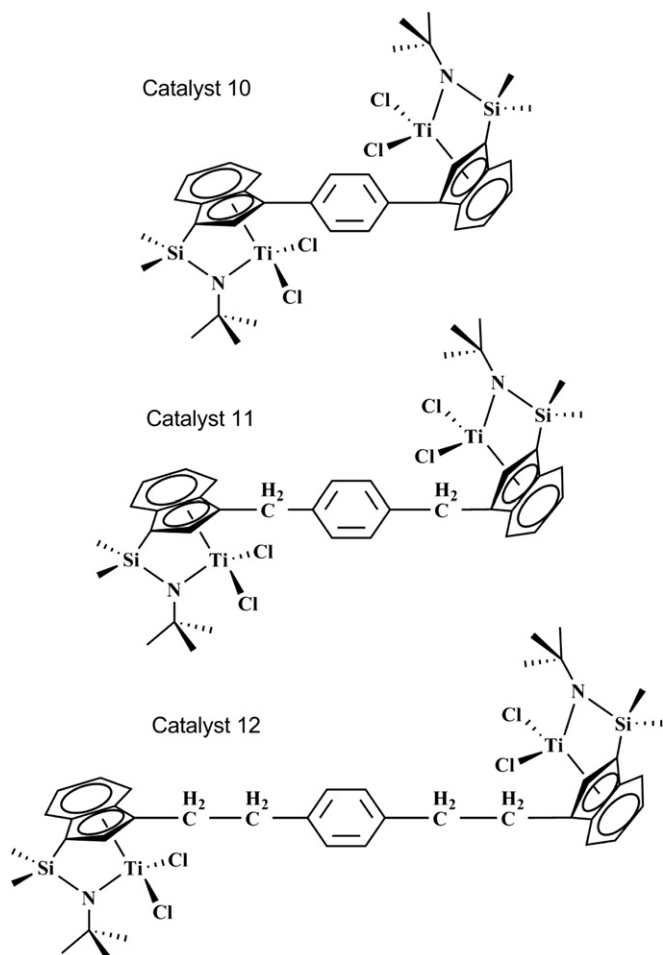
#### 2.4.3. Preparation of $[(\text{C}_9\text{H}_6)(\text{CH}_2)_2]_2(\text{C}_6\text{H}_4)]$ (**3**)

The compound was synthesized from 1,4-bis(2-chloroethyl)benzene (1.29 g, 6.35 mmol) using the same reaction conditions and procedures as for **1**. A light yellow compound was obtained (2.15 g, 93.4%).  $^1\text{H}$  NMR (300 MHz,  $\text{CDCl}_3$ , 25 °C,  $\delta$ , ppm): 7.46 (d, 2H,  $\text{C}_9\text{H}_7$ ), 7.38 (d, 2H,  $\text{C}_9\text{H}_7$ ), 7.32 (t, 2H,  $\text{C}_9\text{H}_7$ ), 7.26 (t, 2H,  $\text{C}_9\text{H}_7$ ), 7.13 (s, 4H,  $\text{C}_6\text{H}_4$ ), 6.22 (s, 2H,  $\text{C}_9\text{H}_7$ ), 3.32 (s, 4H,  $\text{C}_9\text{H}_7$ ), 2.86 (s, 4H,  $\text{CH}_2$ ), 2.81 (s, 4H,  $\text{CH}_2$ ).

#### 2.4.4. Preparation of $[(\text{CH}_3)_2\text{SiCl}(\text{C}_9\text{H}_6)]_2(\text{C}_6\text{H}_4)]$ (**4**)

The solution of *n*-BuLi 2.5 M (5.55 ml, 13.88 mmol) was dropped directly in solution of  $[(\text{C}_9\text{H}_7)_2(\text{C}_6\text{H}_4)]$  (1.69 g, 5.55 mmol)/THF (60 ml) at -78 °C. The solution was stirred at room temperature in 1 h and heated up 60 °C for 12 h, then cooled to room temperature before removed THF. The salt was purified by filtering with hexane and drying under vacuum pressure (1.55 g, 88%).

A solution of  $\text{Me}_2\text{SiCl}_2$  (1.48 ml, 12.25 mmol) in ether (40 ml) was cooled to -78 °C and treated dropwise over 15–20 min with a solution of  $[\text{Li}(\text{C}_9\text{H}_6)]_2(\text{C}_6\text{H}_4)]$  (1.55 g, 4.9 mmol) in ether (25 ml). The mixture was quickly warmed at room temperature (RT) and



Scheme 1. Structure of DCGC **10**, **11** and **12**.

a yellow suspension solution appeared. The reaction was then stirred at RT for 6 h. The yellow compound was extracted with ether to afford a yellow sticky product (1.83 g, 76.47%).  $^1\text{H}$  NMR (300 MHz,  $\text{CDCl}_3$ , 25 °C,  $\delta$ , ppm): 7.58 (d, 2H,  $\text{C}_9\text{H}_6$ ), 7.48 (d, 2H,  $\text{C}_9\text{H}_6$ ), 7.28 (t, 2H,  $\text{C}_9\text{H}_6$ ), 7.21 (t, 2H,  $\text{C}_9\text{H}_6$ ), 7.00 (s, 4H,  $\text{C}_6\text{H}_4$ ), 6.66 (s, 2H,  $\text{C}_9\text{H}_6$ ), 3.74 (s, 2H,  $\text{C}_9\text{H}_6$ ), 0.24 (s, 6H, Si– $\text{CH}_3$ ), 0.18 (s, 6H, Si– $\text{CH}_3$ ).

#### 2.4.5. Preparation of $\{[(\text{CH}_3)_2\text{SiCl}(\text{C}_9\text{H}_6)(\text{CH}_2)_2(\text{C}_6\text{H}_4)]\}_2(\text{C}_6\text{H}_4)$ (**2**)

The compound was synthesized from  $\{[(\text{C}_9\text{H}_6)(\text{CH}_2)_2(\text{C}_6\text{H}_4)]\}_2(\text{C}_6\text{H}_4)$ , (**2**) using the same reaction conditions and procedures as for **4**. A light yellow compound was obtained (79.27%).  $^1\text{H}$  NMR (300 MHz,  $\text{CDCl}_3$ , 25 °C,  $\delta$ , ppm): 7.54 (d, 2H,  $\text{C}_9\text{H}_6$ ), 7.34 (d, 2H,  $\text{C}_9\text{H}_6$ ), 7.23 (t, 2H,  $\text{C}_9\text{H}_6$ ), 7.21 (t, 2H,  $\text{C}_9\text{H}_6$ ), 7.18 (s, 4H,  $\text{C}_6\text{H}_4$ ), 6.23 (s, 2H,  $\text{C}_9\text{H}_6$ ), 3.91 (s, 4H,  $\text{CH}_2$ ), 3.62 (s, 2H,  $\text{C}_9\text{H}_6$ ), 0.17 (s, 12H, Si– $\text{CH}_3$ ).

#### 2.4.6. Preparation of $\{[(\text{CH}_3)_2\text{SiCl}(\text{C}_9\text{H}_6)(\text{CH}_2)_2(\text{C}_6\text{H}_4)]\}_2(\text{C}_6\text{H}_4)$ (**6**)

The compound was synthesized from  $\{[(\text{C}_9\text{H}_6)(\text{CH}_2)_2(\text{C}_6\text{H}_4)]\}_2(\text{C}_6\text{H}_4)$ , (**3**) using the same reaction conditions and procedures as for **4**. The yellow sticky product was obtained (79.96%).  $^1\text{H}$  NMR (300 MHz,  $\text{CDCl}_3$ , 25 °C,  $\delta$ , ppm): 7.59 (d, 2H,  $\text{C}_9\text{H}_6$ ), 7.50 (d, 2H,  $\text{C}_9\text{H}_6$ ), 7.36 (t, 2H,  $\text{C}_9\text{H}_6$ ), 7.28 (t, 2H,  $\text{C}_9\text{H}_6$ ), 7.16 (s, 4H,  $\text{C}_6\text{H}_4$ ), 6.37 (s, 2H,  $\text{C}_9\text{H}_6$ ), 3.73 (s, 2H,  $\text{C}_9\text{H}_6$ ), 3.01 (m, 4H,  $\text{CH}_2$ ), 2.99 (m, 4H,  $\text{CH}_2$ ), 0.20 (s, 12H, Si– $\text{CH}_3$ ).

#### 2.4.7. Preparation of $\{[(\text{NHtBu})(\text{CH}_3)_2\text{Si}(\text{C}_9\text{H}_6)]_2(\text{C}_6\text{H}_4)\}$ (**7**)

A solution of **4** (1.83 g, 3.74 mmol) in THF (60 ml) was treated with *tert*-butylamine (1.97 ml, 18.69 mmol) via a syringe slowly at below 0 °C. As the reactor was warmed to RT, more suspension was formed. The mixture was then heated to 60 °C and stirred overnight. After THF was removed in vacuo for 4 h, hexane was added to extract the product. Volatiles were removed in vacuo for 4 h to afford an orange-yellow sticky product. (1.54 g, 73.08%).  $^1\text{H}$  NMR (300 MHz,  $\text{CDCl}_3$ , 25 °C,  $\delta$ , ppm): 7.57 (d, 2H,  $\text{C}_9\text{H}_6$ ), 7.48 (d, 2H,  $\text{C}_9\text{H}_6$ ), 7.28 (t, 2H,  $\text{C}_9\text{H}_6$ ), 7.22 (t, 2H,  $\text{C}_9\text{H}_6$ ), 7.14 (s, 4H,  $\text{C}_6\text{H}_4$ ), 6.66 (s, 2H,  $\text{C}_9\text{H}_6$ ), 3.57 (s, 2H,  $\text{C}_9\text{H}_6$ ), 1.17 (s, 18H, *t*-Bu), 0.68 (s, 2H, NH), –0.09 (d, 6H, Si– $\text{CH}_3$ ), –0.14 (d, 6H, Si– $\text{CH}_3$ ).

#### 2.4.8. Preparation of $\{[(\text{NHtBu})(\text{CH}_3)_2\text{Si}(\text{C}_9\text{H}_6)(\text{CH}_2)_2(\text{C}_6\text{H}_4)]\}_2(\text{C}_6\text{H}_4)$ (**8**)

The compound was synthesized from **5** (6.34 g, 12.2 mmol) using the same reaction conditions and procedures as for **7**. An orange-yellow sticky product was obtained (6.2 g, 85.7%).  $^1\text{H}$  NMR (300 MHz,  $\text{CDCl}_3$ , 25 °C,  $\delta$ , ppm): 7.33 (d, 2H,  $\text{C}_9\text{H}_6$ ), 7.26 (t, 2H,  $\text{C}_9\text{H}_6$ ), 7.21 (t, 2H,  $\text{C}_9\text{H}_6$ ), 7.14 (s, 4H,  $\text{C}_6\text{H}_4$ ), 6.27 (s, 2H,  $\text{C}_9\text{H}_6$ ), 3.92 (s, 4H,  $\text{CH}_2$ ), 3.47 (s, 2H,  $\text{C}_9\text{H}_6$ ), 1.14 (s, 18H, *t*-Bu), 0.86 (s, 2H, NH), –0.06 (d, 6H, Si– $\text{CH}_3$ ), –0.15 (d, 6H, Si– $\text{CH}_3$ ).

#### 2.4.9. Preparation of $\{[(\text{NHtBu})(\text{CH}_3)_2\text{Si}(\text{C}_9\text{H}_6)(\text{CH}_2)_2(\text{C}_6\text{H}_4)]\}_2(\text{C}_6\text{H}_4)$ (**9**)

The compound was synthesized from **6** using the same reaction conditions and procedures as for **7**. The orange-yellow sticky product was obtained (95.47%).  $^1\text{H}$  NMR (300 MHz,  $\text{CDCl}_3$ , 25 °C,  $\delta$ , ppm): 7.59 (d, 2H,  $\text{C}_9\text{H}_6$ ), 7.55 (d, 2H,  $\text{C}_9\text{H}_6$ ), 7.36 (t, 2H,  $\text{C}_9\text{H}_6$ ), 7.28 (t, 2H,  $\text{C}_9\text{H}_6$ ), 7.16 (s, 4H,  $\text{C}_6\text{H}_4$ ), 6.37 (s, 2H,  $\text{C}_9\text{H}_6$ ), 3.68 (s, 2H,  $\text{C}_9\text{H}_6$ ), 3.01 (m, 4H,  $\text{CH}_2$ ), 2.98 (m, 4H,  $\text{CH}_2$ ), 1.14 (s, 18H, *t*-Bu), 0.63 (s, 2H, NH), –0.06 (d, 6H, Si– $\text{CH}_3$ ), –0.12 (d, 6H, Si– $\text{CH}_3$ ).

#### 2.4.10. Preparation of $\{[\text{Ti}(\eta^5\text{-C}_9\text{H}_5\text{Si}(\text{CH}_3)_2\text{NtBu})\text{Cl}_2(\text{CH}_2)_2(\text{C}_6\text{H}_4)]\}_2(\text{C}_6\text{H}_4)$ (**10**)

In this 2-stage step, tetralithium salt was created in the first stage. A solution of **7** (1.54 g, 2.74 mmol) in hexane (40 ml) was treated with five equivalents of *n*-BuLi (2.5 M hexane solution, 5.47 ml, 13.68 mmol) at –78 °C drop by drop, and then slowly warmed to RT and heated to 60 °C. After stirring for at least 12 h, the solution of tetralithium salt was cooled down to RT, the salt was washed with hexane and the volatiles were removed at reduced pressure overnight to afford an orange salt (1.49 g, 93%). The complex **10** was created in the second stage.  $\text{TiCl}_3(\text{THF})_3$  (1.38 g,

3.75 mmol)/THF (25 ml) was cooled to –78 °C and cannula transfer was used to dropwise the solution of tetralithium salt (1 g, 1.7 mmol) to  $\text{TiCl}_3(\text{THF})_3$ . After the reaction was warmed to RT, the color of the solution changed very quickly from dark brown to black and the reaction was continued for 3 h more. Then, AgCl (0.54 g, 3.75 mmol) was added and the silver mirror precipitated immediately. After stirring for 1 h at RT, THF was removed in vacuo for 4 h. Toluene was added to the residue and stirred for a while. After being filtered and having the toluene removed, the residue was recrystallized with mix of toluene and hexane, washed with hexane. Recrystallization of the resulting solution gave the product as a dark brown-yellow solid (0.41 g, 30.1%).  $^1\text{H}$  NMR (300 MHz,  $\text{CDCl}_3$ , 25 °C,  $\delta$ , ppm): 7.72 (t, 2H,  $\text{C}_9\text{H}_5$ ), 7.40 (t, 2H,  $\text{C}_9\text{H}_5$ ), 7.28 (d, 2H,  $\text{C}_9\text{H}_5$ ), 7.22 (d, 2H,  $\text{C}_9\text{H}_5$ ), 7.14 (s, 4H,  $\text{C}_6\text{H}_4$ ), 6.57 (s, 2H,  $\text{C}_9\text{H}_5$ ), 1.17 (s, 18H, *t*-Bu), 0.92 (d, 6H, Si– $\text{CH}_3$ ), 0.70 (d, 6H, Si– $\text{CH}_3$ ).  $^{13}\text{C}$  NMR (75.46 MHz,  $\text{CDCl}_3$ , 25 °C,  $\delta$ , ppm): 138.00 ( $\text{C}_6\text{H}_4$ ), 136.07 ( $\text{C}_9\text{H}_5$ ), 134.87 ( $\text{C}_9\text{H}_5$ ), 129.23 ( $\text{C}_9\text{H}_5$ ), 128.36 ( $\text{C}_9\text{H}_5$ ), 127.53 ( $\text{C}_9\text{H}_5$ ), 125.42 ( $\text{C}_9\text{H}_5$ ), 120.06 ( $\text{C}_6\text{H}_4$ ), 98.52 ( $\text{C}_9\text{H}_5$ ), 63.44 (C, *t*-Bu), 32.41 ( $\text{CH}_3$ , *t*-Bu), 3.56 (Si– $\text{CH}_3$ ), 1.13 (Si– $\text{CH}_3$ ). High-resolution mass spectrum:  $[\text{P}^+]$   $\text{C}_{36}\text{H}_{44}\text{N}_2\text{Ti}_2\text{Cl}_4\text{Si}_2$ ,  $m/z = 800$  ( $\text{M}^+$ ), 763 ( $\text{M}^+ - \text{Cl}$ ), 728 ( $\text{M}^+ - \text{Cl}_2$ ), 689 ( $\text{M}^+ - \text{Cl}_3$ ).

#### 2.4.11. Preparation of $\{[\text{Ti}(\eta^5\text{-C}_9\text{H}_5\text{Si}(\text{CH}_3)_2\text{NtBu})\text{Cl}_2(\text{CH}_2)_2(\text{C}_6\text{H}_4)]\}_2(\text{C}_6\text{H}_4)$ (**11**)

The compound was synthesized from **8** using the same reaction conditions and procedures as for **10**. Recrystallization of the resulting solution gave the product as a dark brown-yellow solid (31.5%).  $^1\text{H}$  NMR (300 MHz,  $\text{CDCl}_3$ , 25 °C,  $\delta$ , ppm): 7.71 (d, 2H,  $\text{C}_9\text{H}_5$ ), 7.58 (d, 2H,  $\text{C}_9\text{H}_5$ ), 7.38 (t, 2H,  $\text{C}_9\text{H}_5$ ), 7.28 (t, 2H,  $\text{C}_9\text{H}_5$ ), 7.10 (s, 4H,  $\text{C}_6\text{H}_4$ ), 6.35 (s, 2H,  $\text{C}_9\text{H}_5$ ), 4.35 (q, 4H,  $\text{CH}_2$ ), 1.35 (s, 18H, *t*-Bu), 0.86 (d, 6H, Si– $\text{CH}_3$ ), 0.63 (d, 6H, Si– $\text{CH}_3$ ).  $^{13}\text{C}$  NMR (75.46 MHz,  $\text{CDCl}_3$ , 25 °C,  $\delta$ , ppm): 138.01 ( $\text{C}_6\text{H}_4$ ), 136.38 ( $\text{C}_9\text{H}_5$ ), 135.18 ( $\text{C}_9\text{H}_5$ ), 129.19 ( $\text{C}_9\text{H}_5$ ), 128.90 ( $\text{C}_9\text{H}_5$ ), 128.38 ( $\text{C}_9\text{H}_5$ ), 128.08 ( $\text{C}_9\text{H}_5$ ), 124.75 ( $\text{C}_6\text{H}_4$ ), 97.43 ( $\text{C}_9\text{H}_5$ ), 63.48 (C, *t*-Bu), 34.80 ( $\text{CH}_2$ ), 32.54 ( $\text{CH}_3$ , *t*-Bu), 3.52 (Si– $\text{CH}_3$ ), 1.22 (Si– $\text{CH}_3$ ). High-resolution mass spectrum:  $[\text{P}^+]$   $\text{C}_{38}\text{H}_{48}\text{N}_2\text{Ti}_2\text{Cl}_4\text{Si}_2$ ,  $m/z = 828$  ( $\text{M}^+$ ), 790 ( $\text{M}^+ - \text{Cl}$ ), 758 ( $\text{M}^+ - \text{Cl}_2$ ), 720 ( $\text{M}^+ - \text{Cl}_3$ ).

#### 2.4.12. Preparation of $\{[\text{Ti}(\eta^5\text{-C}_9\text{H}_5\text{Si}(\text{CH}_3)_2\text{NtBu})\text{Cl}_2(\text{CH}_2)_2(\text{C}_6\text{H}_4)]\}_2(\text{C}_6\text{H}_4)$ (**12**)

The compound was synthesized from **9** using the same reaction conditions and procedures as for **10**. The dark brown-yellow solid was obtained (35.1%).  $^1\text{H}$  NMR (300 MHz,  $\text{CDCl}_3$ , 25 °C,  $\delta$ , ppm): 7.71 (d, 2H,  $\text{C}_9\text{H}_5$ ), 7.55 (d, 2H,  $\text{C}_9\text{H}_5$ ), 7.41 (t, 2H,  $\text{C}_9\text{H}_5$ ), 7.28 (t, 2H,  $\text{C}_9\text{H}_5$ ), 7.16 (s, 4H,  $\text{C}_6\text{H}_4$ ), 6.30 (s, 2H,  $\text{C}_9\text{H}_5$ ), 3.33 (m, 4H,  $\text{CH}_2\text{-C}_6\text{H}_4$ ), 3.03 (m, 4H,  $\text{CH}_2\text{-C}_9\text{H}_5$ ), 1.36 (s, 18H, *t*-Bu), 0.92 (d, 6H, Si– $\text{CH}_3$ ), 0.66 (d, 6H, Si– $\text{CH}_3$ ).  $^{13}\text{C}$  NMR (75.46 MHz,  $\text{CDCl}_3$ , 25 °C,  $\delta$ , ppm): 138.92 ( $\text{C}_6\text{H}_4$ ), 135.77 ( $\text{C}_9\text{H}_5$ ), 135.00 ( $\text{C}_9\text{H}_5$ ), 129.06 ( $\text{C}_9\text{H}_5$ ), 128.42 ( $\text{C}_9\text{H}_5$ ), 127.91 ( $\text{C}_9\text{H}_5$ ), 127.42 ( $\text{C}_9\text{H}_5$ ), 124.43 ( $\text{C}_6\text{H}_4$ ), 96.83 ( $\text{C}_9\text{H}_5$ ), 63.11 (C, *t*-Bu), 35.67 ( $\text{CH}_2$ ), 32.23 ( $\text{CH}_3$ , *t*-Bu), 31.37 ( $\text{CH}_2$ ), 3.42 (Si– $\text{CH}_3$ ), 1.11 (Si– $\text{CH}_3$ ). High-resolution mass spectrum:  $[\text{P}^+]$   $\text{C}_{40}\text{H}_{52}\text{N}_2\text{Ti}_2\text{Cl}_4\text{Si}_2$ ,  $m/z = 852$  ( $\text{M}^+$ ), 815 ( $\text{M}^+ - \text{Cl}$ ), 786 ( $\text{M}^+ - \text{Cl}_2$ ), 711 ( $\text{M}^+ - \text{Cl}_3$ ).

## 2.5. Polymerization

Ethylene/styrene copolymerizations were carried out in a dry 300-ml glass reactor, sealed with a rubber septum and cycled two times between vacuum and nitrogen to remove the oxygen. After nitrogen evacuation, the reactor was saturated with a continuous flow of ethylene at atmospheric pressure (1.0 atm) and reaction temperature. Then, proper amounts of toluene, MMAO and styrene monomer were injected into the flask. The polymerization was initiated by injection of the prepared catalyst solution in toluene. After a measured time interval, the polymerization was quenched by the addition of acidified methanol containing 10% HCl. The

polymer was collected by filtration, washed with excess methanol, and dried under vacuum overnight to a constant weight.

### 3. Results and discussion

#### 3.1. Synthesis and characterization

The three DGCs, distinguished by their bridge structure of *para*-phenyl, *para*-xylyl, and *para*-diethylenephenyl were prepared by the procedure shown in Scheme 2. The complexes **10**, **11**, and **12** were prepared by the reaction of  $\text{TiCl}_3(\text{THF})_3$  with the corresponding tetralithium salt of ligand in THF at  $-78^\circ\text{C}$  followed by oxidation with  $\text{AgCl}$  [27–29]. These catalysts can be separated as a reddish brown solid via recrystallization in a mixed solvent of toluene and hexane with a moderate yield ( $\sim 35\%$ ). All the produced catalysts were easily contaminated through decomposition by moisture or air exposure.

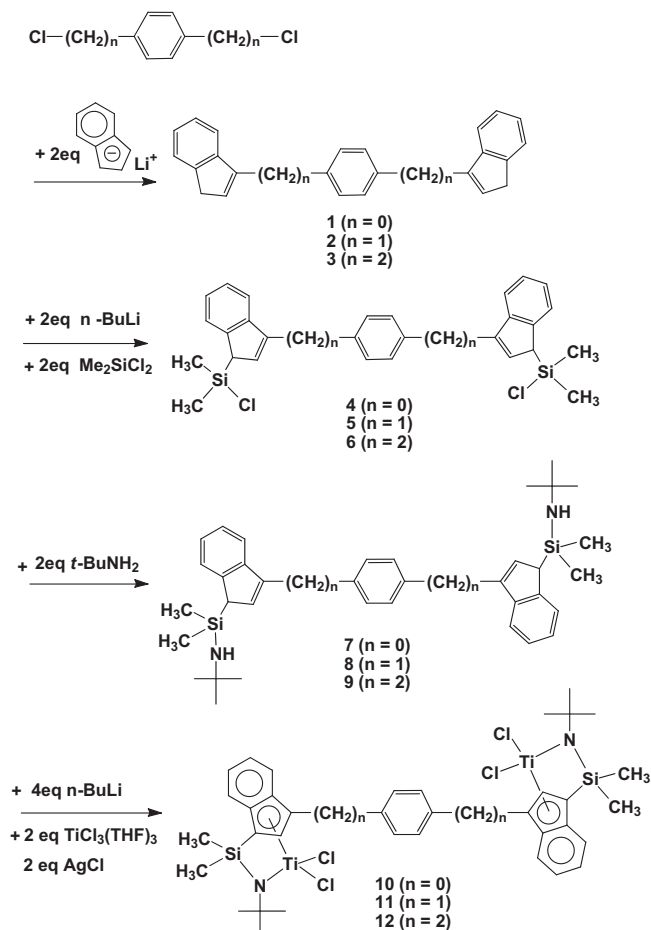
The dinuclear metallocenes catalysts **10**, **11**, and **12** were characterized by  $^1\text{H}$  and  $^{13}\text{C}$  nuclear magnetic resonance (NMR) and mass spectrometry. The  $^1\text{H}$  NMR spectra of the complexes **10**, **11**, and **12** were conveniently used to identify the assigned DGC structure. All of these outcomes were in accord with the reported results of DGC with polymethylene bridges [15,16]. The remaining assignments are summarized in the Experimental section. In the proton NMR spectra of these compounds, the four resonances exhibited between 7.2 and 7.6 ppm were assigned as the four protons of the six-member ring in the indenyl fragment. The single peak at 7.1 ppm indicated the four protons of phenyl bridge. The

peak located at about 6.3 ppm as a singlet was due to one proton of the five-member ringside at the indenyl group (Fig. 1). In the  $^1\text{H}$  NMR catalyst spectra, two positions of chemical shift changed at 0.92 ppm and 0.66 ppm comparing to amine ligand spectra (instead of  $-0.14$  ppm and  $-0.09$  ppm). It indicated that the existence of the metallated dinuclear complexes as these chemical shifts of two methyl groups at silicon moved to the high field. In addition, the chemical shifts of the two protons of the methylene ( $\text{CH}_2$ ) in DGC **11** between the indenyl and phenyl groups presented as two strongly coupling doublets at 4.35 ppm because these two protons became chemical shift inequivalent due to titanium coordination to the indenyl ring. For DGC **12**, the resonances of the two methylene groups between the indenyl and phenyl groups appeared as two multiplets at 3.03 and 3.33 ppm. The  $^{13}\text{C}$  NMR spectra of the complexes also exhibited these features well. Chemical shifts from 120 ppm to 140 ppm indicated the aromatic carbons of the phenyl and indenyl groups. The peak at 32 ppm was assigned to 3 methyl carbons at the *t*-butyl group and the peaks near 1 and 3 ppm indicated 2 methyl carbons connected at the silicon atom. The resonance signals at 63 ppm which are attributed to the quaternary carbon of the *tert*-butyl group connected at the coordinated nitrogen demonstrated the right structure of catalyst. In contrast, the chemical shift of the carbon bridgehead of the indenyl ring moved toward the high field to present at around 98 ppm due to the metal coordination.

Because these catalysts were extremely sensitive to moisture and air exposure, successful elemental analysis could not be obtained. Therefore, mass spectrometry was used to confirm their formulation. The mass spectra of these compounds exhibited not only molecular ions of catalysts **10** (800), **11** (828) and **12** (855), but also the fragment masses of  $(\text{M}^+ - 35)$  and  $(\text{M}^+ - 70)$  generated from the exclusion of one and two chlorines, respectively.

#### 3.2. Copolymerization

Since CGC proved to be powerful catalyst when activated with methylaluminoxane (MAO) for the copolymerization of ethylene and  $\alpha$ -olefin [30–32], the dinuclear complexes **10**, **11** and **12** were used, along with Dow CGC as the typical mononuclear CGC for comparison, for the copolymerization of ethylene and styrene to



Scheme 2. Preparation route of the catalysts **10**, **11**, and **12**.

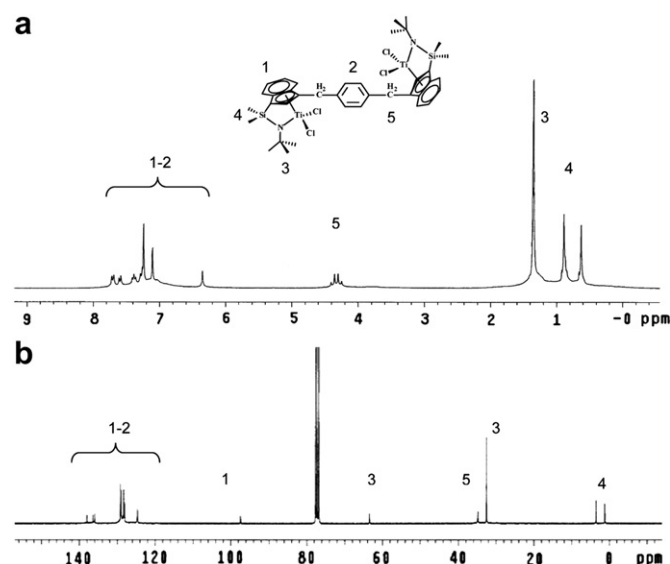


Fig. 1.  $^1\text{H}$  NMR (a) and  $^{13}\text{C}$  NMR (b) spectrum catalyst **11**.

identify the catalytic characteristics. The results are summarized in Table 1 and Table 2.

### 3.3. Polymerization activity

From the standpoint of the catalyst activity, several important points should be noted for characterizing DCGC in terms of the nature of the bridge. Firstly, the catalytic activity increased dramatically with lengthening of the bridging ligand. At a styrene concentration of 1.3 mol/l at 70 °C, the catalyst activity increased in the order of **10** (168.7 kg of polymer/mol of Ti.h.atm) < Dow CGC (290.5 kg of polymer/mol of Ti.h.atm) < **11** (739.9 kg of polymer/mol of Ti.h.atm) < **12** (791.0 kg of polymer/mol of Ti.h.atm), which illustrated that DCGCs **11** and **12** with *para*-xylene and *para*-diethylenephenyl bridges, respectively, showed four to five times greater activity than DCGC **10** with *para*-phenyl bridge and about three times higher activity than Dow CGC. This basic tendency was observed consistently even in a variety of changing reaction condition such as styrene concentration and polymerization temperature, as shown in Fig. 2. This result supports the critical role played by the length of the linkage unit between two active sites in enhancing the DCGC activity.

To compare the approximated length of the bridge between two indenyl groups, the well-known software ChemBio 3D Ultra 11.0 was applied because of its simplicity. The separation distance of approximately 5.4 Å (*para*-phenyl) between the two indenyl fragments of the catalyst **10** may not have permitted a satisfactory room for monomer coordination that lead to the low activity. In contrast, the equivalent distances of 7.3 Å and 9.8 Å for the catalysts **11** and **12**, respectively, should provide sufficient space for copolymerization to enhance the activity. The length of the styrene monomer of about 6.6 Å implies that the DCGC bridge length should be at least 6.6 Å in order to provide an appropriate active site volume for styrene for moving in and out and thus increase the activity. A minimum of five methylene molecules is required for polymethylene-bridged dinuclear zirconocene to exhibit greater activity than that of mononuclear zirconocene [33]. The activities of the dinuclear zirconocenes with three methylenes were lower than those of the mononuclear one. Interestingly, the stretched lengths of five and three methylenes, at 7.3 Å and 4.9 Å, respectively, are similar to the lengths of *para*-xylyl (7.3 Å) and *para*-phenyl (5.4 Å), which further supports the mechanism presented above.

Regarding the activity gap between the three DCGCs, the average activity of DCGC **11** was about four-fold greater than that of **10**, while that of DCGC **12** was only 20–30% greater than that of DCGC **11**, even though the 2.5 Å length difference between *para*-diethylenephenyl and *para*-xylyl is actually more than that (of 1.9 Å) between *para*-phenyl and *para*-xylyl. This outcome suggests

**Table 1**  
Results of ethylene/styrene copolymerization<sup>a</sup> at styrene concentration [S] = 1.3 M.

Tp <sup>b</sup>	Catalyst	Activity <sup>c</sup>	S <sup>d</sup>	Mw (×10 <sup>-3</sup> ) <sup>e</sup>	MWD <sup>e</sup>
40	Dow CGC	253.7	19.9	75.0	2.40
	<b>10</b>	101.7	20.0	62.8	2.42
	<b>11</b>	481.0	22.4	135.5	2.82
	<b>12</b>	594.6	22.3	213.0	2.56
70	Dow CGC	290.5	25.2	38.3	1.72
	<b>10</b>	168.7	26.0	28.4	2.25
	<b>11</b>	739.9	32.5	56.0	3.37
	<b>12</b>	791.0	32.5	105.0	4.01

<sup>a</sup> Conditions: [cat] = 20 μmol/l, [MMAO]/[cat] = 2000, styrene concentration [S] = 1.3(mol/l), 100 ml toluene, ethylene 1atm, 2 h.

<sup>b</sup> Polymerization temperature (°C).

<sup>c</sup> Activity (kg-polymer mol<sup>-1</sup> h<sup>-1</sup>).

<sup>d</sup> Styrene content in copolymer calculated by <sup>1</sup>H NMR spectra of E/S copolymer (%).

<sup>e</sup> GPC data in 1,2,4-trichlorobenzene(TCB) vs polystyrene standards at 170 °C.

**Table 2**  
Results of ethylene/styrene copolymerization<sup>a</sup> at styrene concentration [S] = 0.4 M.

Tp <sup>b</sup>	Catalyst	Activity <sup>c</sup>	S <sup>d</sup>	Mv (×10 <sup>-3</sup> ) <sup>e</sup>
40	Dow CGC	190.6	9.5	44.6
	<b>10</b>	92.3	11.3	87.0
	<b>11</b>	293.1	14.2	342.0
	<b>12</b>	394.8	16.5	461.0
70	Dow CGC	240.5	10.4	42.6
	<b>10</b>	102.8	11.3	47.7
	<b>11</b>	385.5	16.0	121.0
	<b>12</b>	473.9	16.5	135.0

<sup>a</sup> Conditions: [cat] = 20 μmol/l, [MMAO]/[cat] = 2000, styrene concentration [S] = 0.4(mol/l), 100 ml toluene ethylene 1 atm, 2 h.

<sup>b</sup> Polymerization temperature (°C).

<sup>c</sup> Activity (kg-polymer mol<sup>-1</sup> h<sup>-1</sup>).

<sup>d</sup> Styrene content in copolymer calculated by <sup>1</sup>H NMR spectra of E/S copolymer (%).

<sup>e</sup> The viscosity averaged molecular weight (g/mol).

the existence of a critical bridge length in dinuclear metallocenes that determines the catalyst performance, which is actually an obvious merit of dinuclear metallocene compared to the normal mononuclear metallocene system. These experimental results provided further confirmation that the critical DCGC bridge length is around 6.6 Å, which is the length of the styrene monomer. It is likely that the effect of the bridge length gradually diminishes to reach a plateau as the length exceeds the critical length.

The second point to be considered regarding the activity difference between DCGCs **11** and **12** is the potential difference in the electronic effect between the *para*-xylyl and *para*-diethylenephenyl groups. The active site with greater electron density generally exhibits more pronounced activity because a greater electron density is able to stabilize the electron-deficient active site more effectively. Accordingly, the *para*-diethylenephenyl bridge of DCGC **12** was assumed to deliver greater electron density to the electron-deficient titanium cationic species than the *para*-xylyl bridge of DCGC **11**. Considering the distance from the methylene to the active site, the contribution of the increased electron density induced by the single methylene unit to the catalytic activity may have been a secondary factor compared to that of the bridge length effect.

An important feature of the DCGC activity is that the composition of the monomer feed was the primary influence on the catalytic activity. Irrespective of the catalyst type or the polymerization temperature, the activities with styrene concentration ([S]) [S] = 1.3 mol/l were significantly higher than those with [S] = 0.4 mol/l. With DCGC **12**, the activities with the condition of [S] = 1.3 mol/l at 70 °C and at 40 °C were 1.7 and 1.5 times, respectively, larger than those with the condition of

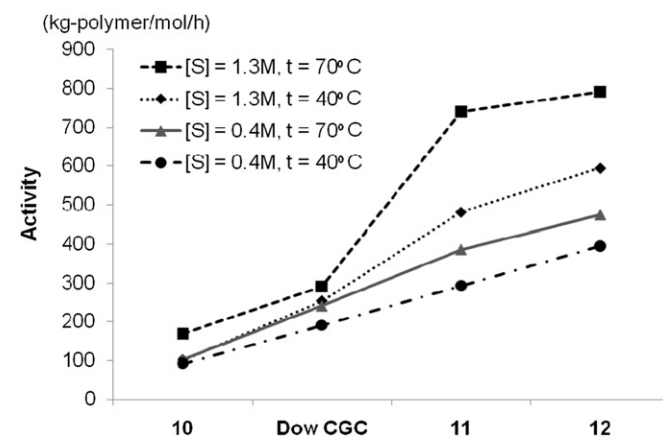


**Fig. 2.** The correlation between activity and the catalysts.

[S] = 0.4 mol/l at the same temperatures. However, the decrease in polymerization temperature from 70 °C to 40 °C at the same styrene concentration enhanced the activity by 20–30%. The high styrene concentration eased the reversible deactivation of the active site to a dormant species by additional coordination of the phenyl ring's  $\pi$ -electron system [28–30]. However, in this study the correlation of the activity of DCGC and styrene concentration was considered unlikely to comply with this tendency.

### 3.4. Molecular weight (MW)

The variations of molecular weight (MW) with the type of catalyst are plotted in Fig. 3 at constant temperature and styrene concentration. Because GPC was not able to be used to measure MWs of some copolymer samples formed at [S] = 0.4 M, the viscosity average molecular weights (Mv) were measured to obtain MWs of those polymers instead. Among the noticeable trends, the DCGC structure primarily affected the MW of the copolymer. The capability to form a high MW polymer increased in the order of Dow CGC  $\approx$  **10** < **11** < **12** either [S] = 1.3 M or [S] = 0.4 M. Mw as well as Mv values of copolymers made by DCGCs **11** and **12** were greater at least 2 and 3 times, respectively, than those made by either DCGC **10** or Dow CGC. Beside the difference of MWs, the molecular weight distribution (MWD) of copolymers obtained by DCGC **11** and **12** became broader than those obtained by DCGC **10** or Dow CGC. It is a general feature that the polymers made by the dinuclear metallocenes exhibit broader distribution of MW [19]. This large difference in the MWs and MWDs of the polymers may have been caused by the bridge length difference in the dinuclear metallocene. Some previous studies showed that MW variation was not sensitive to the catalyst structure, and that polymerization

conditions such as temperature and concentration were more important factors in determining the MW of the polymer [15–18]. However, the present study results clearly demonstrated the predictive power of the DCGC structure, as determined by the bridge length, in characterizing the polymer properties.

In another surprising result, DCGC **12**, with the longest *para*-diethylenephanyl linkage, generated copolymers with the highest MW, followed by DCGC **11** with the second longest *para*-xylyl one. In cases of polymethylene-bridged dinuclear metallocenes, the catalyst with a longer bridge formed a lower MW polymer [15,16]. Accordingly, the influence of the bridge length with the rigid property of the phenyl-containing bridge group on MW was actually opposite to that with the flexible property of the polymethylene bridge. We considered that the more facile interaction of the two active sites through the short flexible linkage was responsible for the formation of a long polymer chain due to the disturbed termination via  $\beta$ -H elimination. The *para*-diethylenephanyl bridge may have been long enough to permit sufficient and untouchable room between the two active sites. Similarly, the 7.3 Å long bridge of *para*-xylyl, which is slightly longer than 6.6 Å, may have experienced some steric hindrance that may have been a minor factor in increasing the polymer MW. Consequently, the effect of the steric interference of the two active sites of DCGCs **11** and **12** in reducing the  $\beta$ -H elimination frequency should not be considered the principal factor to explain the formation of a high MW polymer.

This introduces the question of what is the secondary cause of this result. Exclusion of the steric issue surely leaves the electronic factor behind. In terms of the electronic effect of DCGC, the bridge of *para*-diethylenephanyl of DCGC **12** was anticipated to generate the most stable active site among the three DCGCs due to the greater electron supply arising from the existence of two methylene units at the active site. This explanation is in good agreement with action of DCGC **12**, followed by DCGC **11**, in forming a longer polymer since the more stable active site affords a higher MW polymer in metal-catalyzed polymerization systems. Another reason may have been the combined effect of the rate of coordination and the  $\beta$ -H elimination because the degree of polymerization is determined by the relation between the rate of propagation and that of termination. This suggested that catalyst **12** may have not only a faster rate of coordination but also easier  $\beta$ -H elimination compared with catalysts **10** and **11**. The final degree of polymerization derived from the relation of the two factors of DCGC **12** was actually greater than those of DCGCs **10** and **11**. As a final point, DCGC **10** could be used to fabricate copolymers with similar

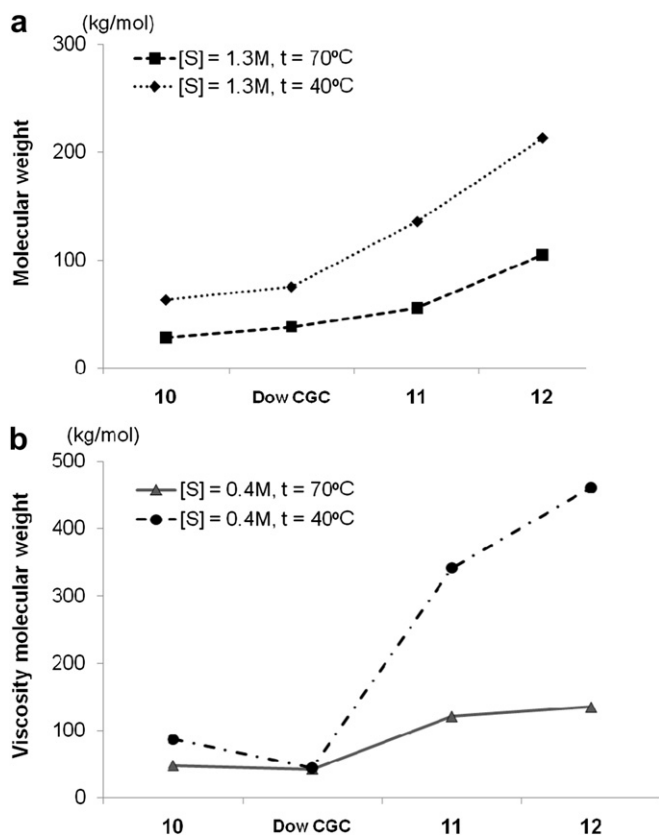


Fig. 3. The correlation of molecular weight of Ethylene/Styrene copolymer with the catalysts: (a) styrene concentration [S] = 1.3 M; (b) styrene concentration [S] = 0.4 M.

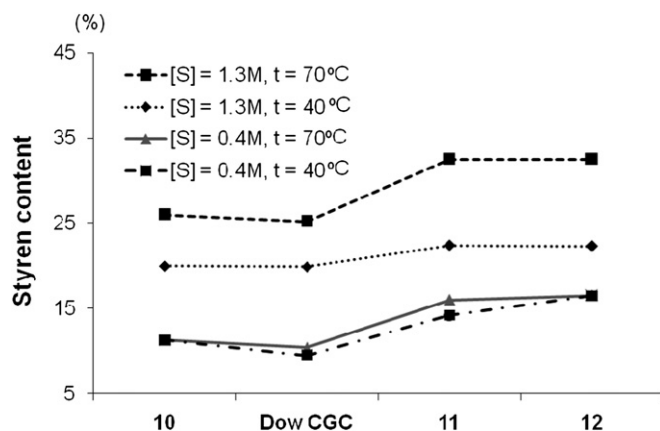


Fig. 4. The correlation between styrene content of Ethylene/Styrene copolymer and the catalysts.

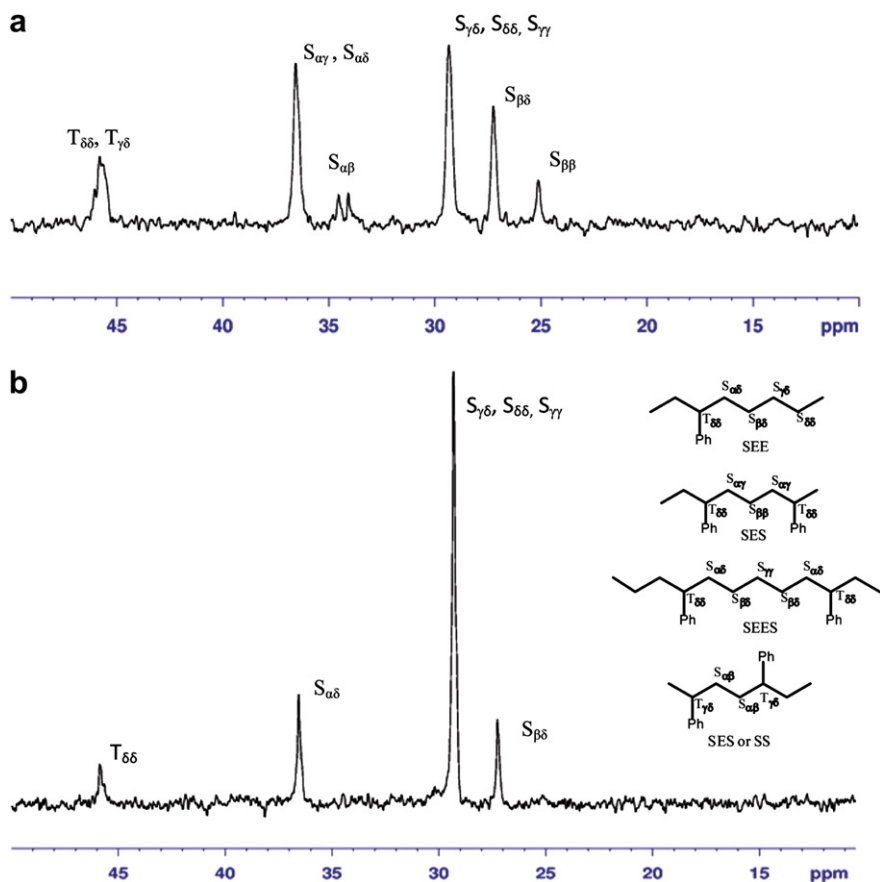


Fig. 5.  $^{13}\text{C}$  NMR spectra of poly(ethylene-co-styrene) prepared by catalyst 11 at  $70^\circ\text{C}$ , (a)  $[\text{S}] = 1.3\text{ M}$ , styrene content 32.5%; (b)  $[\text{S}] = 0.4\text{ M}$ , styrene content 16.0%.

MW to those achieved with Dow CGC. The close proximity of the two active sites may have delayed the  $\beta$ -H elimination process and thereby offered an opportunity for chain lengthening.

### 3.5. Styrene contents in copolymer

The study results revealed the efficiency of DCGC for incorporating styrene into the polyethylene backbone. Among the three catalysts **10**, **11** and **12**, the styrene contents in the generated copolymers increased in order of catalyst Dow CGC  $< \mathbf{10} < \mathbf{11} < \mathbf{12}$  at the same styrene concentration (Fig. 4). Remarkably, DCGC **10** exhibited a higher styrene reactivity than the mononuclear Dow CGC, considering that the  $5.4\text{ \AA}$  long *para*-phenyl bridge is actually shorter than the styrene length of  $6.6\text{ \AA}$  in DCGC **10**. This may reflect that the nucleating effect of DCGC with short ethylene bridge proposed by Marks [13,19] is likely to be active in dinuclear metallocene possessing short phenyl-based rigid bridges. Despite the strong ability of DCGC **10** to incorporate styrene on the polyethylene backbone, a comparison between the styrene reactivity of DCGCs **11** and **12** supports the inferior styrene reactivity of DCGC **10**. The styrene contents in the copolymers generated by DCGCs **11** and **12** were almost same, regardless of the polymerization conditions. However, the styrene incorporation capability differed between DCGCs **10** and **11**. This result was attributed to the critical effect of the DCGC bridge length in determining the reactivity of the comonomer. In an outstanding result, DCGC **12**, with the longest *para*-diethylenephenyl bridge, was used to prepare copolymers with not only the greatest MW but also the highest styrene contents.

Fig. 5 shows  $^{13}\text{C}$  NMR spectra (methylene and methane region) of the copolymers prepared by catalyst **11** at  $70^\circ\text{C}$ . From the styrene

concentration  $0.4\text{ M}$ – $1.3\text{ M}$ , the reducing resonance intensities of strong signals at  $29.7\text{ ppm}$  of the polyethylene sequences, the increasing of resonance intensities at  $27.5$ ,  $36.9$ , and  $46.2\text{ ppm}$  ( $S_{\beta\beta}$ ,  $S_{\alpha\delta}$ , and  $T_{\delta\delta}$ , respectively) of sequences of EESEE and in addition of peak at  $25.3\text{ ppm}$  ( $S_{\beta\beta}$ ) which represents the SES sequence indicated that produced polymers had a substantially alternating structure. The absence of a signal for  $T_{\beta\beta}$  at  $41.3\text{ ppm}$  and for  $S_{\alpha\alpha}$  at  $43.6\text{ ppm}$  shows that there is no styrene–styrene sequence in the copolymers. This demonstrated that the dinuclear CGC in this experiment might be advantageous over the reported catalysts to obtain more randomly distributed poly(ethylene-co-styrene)s.

Beside that the copolymerization products are rubber-like in appearance. The melting points ( $T_m$ ) of the obtained copolymers could not be detected by DSC measurements, no matter how high the comonomer incorporation in the copolymers is. The melting point ( $T_m$ ) is attributed to a unique blocky microstructure which offers enough consecutive sequences of comonomer units in the polymer backbone to form a crystalline phase. Therefore, all ethylene/styrene copolymer produced by our catalyst were amorphous.

### 4. Conclusion

A series of new DCGCs with the structure of  $[\{\text{Ti}(\eta^5\text{-C}_9\text{H}_5)\text{Si}(\text{CH}_3)_2\text{N}^t\text{Bu}\text{Cl}_2(\text{CH}_2)_n\}_2(\text{C}_6\text{H}_4)]$  [ $n = 0$  (**10**),  $n = 1$  (**11**),  $n = 2$  (**12**)] were synthesized and characterized successfully. In the presence of modified MAO as cocatalyst, ethylene and styrene were copolymerized to examine specifically the effect of bridge length on the polymerization behaviors of DCGCs, with Dow CGC being used for comparison. Not only the catalyst activity but also the MWs and styrene contents of the copolymers were promoted as the bridge

structure was extended from *para*-phenyl (**10**) to *para*-xylyl (**11**) and then to *para*-diethylenephanyl (**12**), which demonstrated that the overall DCGC performance could be controlled by the addition of a long and rigid unit as the bridge ligand of DCGC. The activity of the catalysts increased in the order of **10** < **Dow** < **11** < **12**. The important feature of the DCGC activity is that the composition of the monomer feed was the principal factor affecting the catalytic activity. Irrespective of the catalyst type or the polymerization temperature, the activities with  $[S] = 1.3$  mol/l were significantly higher than those with  $[S] = 0.4$  mol/l. The capability to form high MW polymer increased in the order of **Dow** < **10** < **11** < **12**, which indicated that the DCGC structure, as distinguished by the bridge length, could be used as a decisive tool to characterize the polymer length. This result provided further support for the existence of a critical bridge length in dinuclear metallocenes to control the MW of the produced polymer. In addition, the electron donating effect of the longer bridge may be regarded as the secondary factor promoting the polymerization properties of DCGC. The styrene contents in the copolymers increased in order of catalyst **Dow** < **10** < **11** < **12** at the same styrene concentration. Remarkably, DCGC **12**, with the longest *para*-diethylenephanyl bridge, exhibited the highest activity while being used to prepare copolymers with not only the greatest MW but also the highest styrene contents.

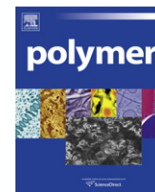
#### Acknowledgements

The authors are grateful for the Korea Ministry of Knowledge and Economy (Grant RT 104-01-04, Regional Technology Innovation Program).

#### References

- [1] Reddy KP, Petersen JL. *Organometallics* 1989;8(9):2107–13.
- [2] Ciruelos S, Cuenca T, Flores JC, Gomez R, Gomez-Sal P, Royo P. *Organometallics* 1993;12(3):944–8.
- [3] Juengling S, Muelhaupt R, Plenio H. *J Organomet Chem* 1993;460(2):191–5.
- [4] Ushioda T, Green MLH, Haggitt J, Yan XF. *J Organomet Chem* 1996;518(2):155–66.
- [5] Ban HT, Uozumi T, Soga K. *J Polym Sci Part A Polym Chem* 1998;36(13):2269–74.
- [6] Deppner M, Burger R, Alt HG. *J Organomet Chem* 2004;689(7):1194–211.
- [7] Guo N, Stern CL, Marks TJ. *J Am Chem Soc* 2008;130:2246–61.
- [8] Braunschweig H, Breiting FM. *Coord Chem Rev* 2006;250:2691–720.
- [9] Horáček M, Gyepes R, Merna J, Kubišta J, Mach K, Pinkas J. *J Organomet Chem* 2010;695:1425–33.
- [10] Li H, Stern CL, Marks TJ. *Macromolecules* 2005;38:9015–27.
- [11] Li X, Zhao X, Zhu B, Lin F, Sun J. *Catal Commun* 2007;8:2025–31.
- [12] Noh SK, Lee J, Lee DH. *J Organomet Chem* 2003;667:53–60.
- [13] Li L, Metz MV, Li H, Chen MC, Marks TJ, Liable SL, et al. *J Am Chem Soc* 2002;124:12725–41.
- [14] Guo N, Li L, Marks TJ. *J Am Chem Soc* 2004;126:6542–3.
- [15] Noh SK, Yang Y, Lyoo WS. *J Appl Polym Sci* 2003;90:2469–74.
- [16] Noh SK, Lee M, Kum DH, Kim K, Lyoo SW, Lee DH. *J Polym Sci Part A Polym Chem* 2004;42:1712–23.
- [17] Xiao XH, Zhu BC, Zhao XT, Wang YA, Sun JQ. *Inorg Chim Acta* 2007;360:2432–8.
- [18] Xiao XH, Sun JQ, Lia X, Li HF, Wang YG. *J Mol Catal A Chem* 2007;267:86–91.
- [19] Sun JQ, Zhang H, Liu X, Xiao A, Lin F. *Eur Polym J* 2006;42:1259–65.
- [20] Antonio P, Francesca G, Carmine C. *Eur Polym J* 2009;45:2138–41.
- [21] Noh SK, Jung W, Oh H, Lee YR, Lyoo WS. *J Organomet Chem* 2006;691:5000–6.
- [22] Thanh NTL, Noh SK, Lyoo WS, Lee DH. *Chin J Polym Sci* 2008;26(5):611–20.
- [23] Linh NTB, Noh SK. *J Organomet Chem* 2009;694:3438–43.
- [24] Fackler JP, editor. *Inorganic Syntheses*, vol. XXI. New York: A Wiley-Interscience Publication; 1982. p. 137–8.
- [25] Son K, Jöge F, Waymouth RM. *Macromolecules* 2008;41:9663–8.
- [26] Lobón PM, Barcina JO, Martínez AG, Expósito MT, Vega JF, Martínez SJ, et al. *Macromolecules* 2006;39:7479–82.
- [27] McKnight AL, Waymouth RM. *Chem Rev* 1998;98:2587–98.
- [28] Stevens JC, Timmers FJ, Wilson DR, Schmidt GF, Nickias PN, Rosen RK, et al. *Eur Pat Appl*; 1991:0416815A2.
- [29] Stevens JC, Neithamer DR. *Eur Pat Appl*; 1991:0418044A2.
- [30] Sernetz FG, Mülhaupt R, Amor F, Eberle T, Okuda J. *J Polym Sci Part A Polym Chem* 1997;35:1571–8.
- [31] Arai T, Ohtsu T, Suzuki S. *Macromol Rapid Commun* 1998;19:327–31.
- [32] Xu G. *Macromolecules* 1998;31:2395–402.
- [33] Noh SK, Kim J, Jung J, Ra CS, Lee DH, Lee HB, et al. *J Organomet Chem* 1999;580:90–7.





## Bulky side-chain density effect on the photophysical, electrochemical and photovoltaic properties of polythiophene derivatives

Hsing-Ju Wang<sup>a</sup>, Li-Hsin Chan<sup>b,\*</sup>, Chih-Ping Chen<sup>c</sup>, Shin-Lei Lin<sup>c</sup>, Rong-Ho Lee<sup>a</sup>, Ru-Jong Jeng<sup>a,\*\*</sup>

<sup>a</sup>Department of Chemical Engineering, National Chung Hsing University, Taichung, Taiwan

<sup>b</sup>Department of Applied Materials and Optoelectronic Engineering, National Chi Nan University, Puli, Taiwan

<sup>c</sup>Material and Chemical Laboratories, Industrial Technology Research Institute, Hsinchu, Taiwan

### ARTICLE INFO

#### Article history:

Received 7 September 2010

Received in revised form

19 November 2010

Accepted 21 November 2010

Available online 27 November 2010

#### Keywords:

Polymer solar cell

Polythiophenes

Side-chain density

### ABSTRACT

Low band-gap polythiophene (PT) derivatives, with bulky conjugated side-chains composed of the triphenylamine, thiophene, and vinylene groups (TPATH), are synthesized. The copolymers, synthesized by Grignard metathesis and Stille coupling with different copolymer configurations and side-chain densities, are regioregular-TPATH-PT (*rr*-TPATH-PT) and random-TPATH-PT (*r*-TPATH-PT), respectively. The incorporation of bulky conjugated moiety curtails the effective conjugation length in the main chain; thus, low HOMO levels are obtained for the copolymers. Moreover, *r*-TPATH-PT with less bulky side-chain content exhibits a better conjugation along the polymer backbone than *rr*-TPATH-PT. Higher absorption intensity in the vision region is observed for *r*-TPATH-PT in comparison with *rr*-TPATH-PT. In addition, polymer solar cells (PSCs) are fabricated based on an interpenetrating network of PT derivatives as the electron donor and the fullerene derivatives (PC<sub>61</sub>BM and PC<sub>71</sub>BM) as the electron acceptors. Better compatibility is observed for the *r*-TPATH-PT/PC<sub>61</sub>BM-blend film as compared to the *rr*-TPATH-PT/PC<sub>61</sub>BM-blend film. Higher photovoltaic (PV) performances of the *r*-TPATH-PT/PC<sub>61</sub>BM-based PSCs are observed in comparison with the *rr*-TPATH-PT/PC<sub>61</sub>BM-based PSCs. The power conversion efficiency (PCE) of the PSC based on the blend of *r*-TPATH-PT and PC<sub>61</sub>BM (*w/w* = 1:1) reaches 0.94% under an illumination of AM 1.5G, 100 mW cm<sup>-2</sup>, which is almost twice that of the cell based on *rr*-TPATH-PT. Further improvement of PV performance is achieved for the PSC fabricated from the blend of *r*-TPATH-PT and fullerene derivative PC<sub>71</sub>BM (*w/w* = 1:3), with a short-circuit current of 6.83 mA cm<sup>-2</sup>, an open-circuit voltage of 0.71 V and a PCE of 1.75%.

© 2010 Elsevier Ltd. All rights reserved.

### 1. Introduction

During the past decade, polymer solar cells (PSCs) have been attracting considerable attention. PSCs are considered the most promising fossil fuel alternative due to their being potentially low-cost, lightweight, suitable for a large area manufacture, and their flexibility [1,2]. For PSCs, significant progress in solar energy conversion efficiency has been accomplished by replacing the double-layer cell with a bulk heterojunction (BHJ) blend for the photo-active layer [2]. The photo-active layer of a PSC is based on a blend of an electron-donor polymer and an electron-acceptor fullerene derivative, [6,6]-phenyl C<sub>61</sub> butyric acid methyl ester (PC<sub>61</sub>BM), for most BHJ cells. Polythiophenes (PT)s are one of the most important classifications of conjugated polymers utilized in

a wide variety of applications, such as conducting polymers [3–5], light-emitting diodes [6], field-effect transistors [7] and PSCs, due to their excellent optical and electrical properties. In particular, regioregular poly(3-hexylthiophene) (*rr*-P3HT) has been widely studied as the donor material in the photo-active layer of PSCs. The power conversion efficiency (PCE) of an *rr*-P3HT-based PSC has reached 4.37% [8]. Although PTs are considered to be the most promising conjugated polymers for PSC applications [9,10], some issues have yet to be resolved.

The mismatched and narrow absorption bands of PTs have hindered further improvement of the photovoltaic (PV) properties of PSCs. Therefore, many research groups have designed novel PTs with a broader absorption bands to produce photocurrent density more effectively [11–13]. Several strategies have been demonstrated to enhance the related properties of PTs, such as introducing a conjugated side-chain moiety to the 3-position of the thiophene ring in the PT backbone. By introducing the conjugated side-chain to the thiophene ring, the resulting polymer possesses two absorption bands in the UV and visible regions. The absorption band in the UV

\* Corresponding author. Tel.: +886 49 2910960 4908; fax: +886 49 2912238.

\*\* Corresponding author. Tel.: +886 4 22852581; fax: +886 4 22854734.

E-mail addresses: [lhchan@ncnu.edu.tw](mailto:lhchan@ncnu.edu.tw) (L.-H. Chan), [rjeng@nchu.edu.tw](mailto:rjeng@nchu.edu.tw) (R.-J. Jeng).

region is ascribed to the absorption of the thiophene units with the conjugated side-chains, and that in the visible region corresponds to the absorption of the PT main chains [11–15]. Therefore, PT absorption behavior is expected to be accurately modulated by introducing conjugated moiety as pendants with various densities. Generally, an open-circuit voltage ( $V_{oc}$ ) value of the PT-based PSCs is about 0.4–0.6 V [16,17]. Moreover, the  $V_{oc}$  of a BHJ cell is proportional to the difference between the highest occupied molecular orbital (HOMO) level of the electron-donor polymer and the lowest unoccupied molecular orbital (LUMO) level of the electron-acceptor fullerene derivatives. The lower HOMO levels of the polymers will provide a higher  $V_{oc}$  value according to the theoretical prediction [18]. With the introduction of bulky side-chains onto the polymer backbone, the effective conjugation length can be curtailed via twisting the conjugated  $\pi$ -system out of planarity and, thus, the HOMO level can be decreased [15,19]. As a result, a high  $V_{oc}$  value of a PSC can be obtained by using a conjugated polymer with bulky side-chains. On the other hand, the PV performance of polymer/fullerene derivative-blend film-based PSCs is also heavily influenced by the interpenetrating nanostructure formed by the two semiconductors. The literature has reported that polymer chains with sufficient free volume are helpful for the intercalation of fullerene molecules into polymer chains, which is favorable for the improvement of PV performance [20,21]. Moreover, the packing density and morphology in polymer thin film are strongly dependent on the spaces between the polymer side-chains [22,23]. Hence, the appropriate side-chain spacing of conjugated polymer is also an important parameter to be considered for designing a new electron-donor polymer for PSC applications.

In this study, we synthesized novel PT derivatives with bulky conjugated side-chains, which comprised triphenylamine, thiophene, and vinylene groups (TPATH). The TPATH group was known to exhibit a good electron-donating capacity and high hole-mobility [24,25]. The copolymers regioregular-TPATH-PT (*rr*-TPATH-PT) and random-TPATH-PT (*r*-TPATH-PT) with different copolymer configurations and side-chain densities were synthesized by Grignard metathesis (GRIM) and Stille coupling, respectively. A lower side-chain density of *r*-TPATH-PT was designed and synthesized as compared to that of *rr*-TPATH-PT. The influence of configuration and side-chain density of these copolymers on the photophysical and electrochemical properties were investigated in detail. Moreover, the morphological and PV characteristics of the copolymer/fullerene derivative-blend films were also discussed.

## 2. Experimental details

### 2.1. Chemical materials

The starting material triphenylamine, 5-Bromothiophene-2-carbaldehyde (**3**), reagents and chemicals were purchased from Aldrich, Alfa, TCI Chemical Co. and used as received without any further purification. All the solvents, such as dichloromethane (DCM), tetrahydrofuran (THF) and dimethylformamide (DMF), and toluene were freshly distilled over appropriate drying agents prior to use and were purged with nitrogen. 4-Bromotriphenylamine (**1**) [26], *N,N*-diphenyl-4-(4,4,5,5-tetramethyl-1,3,2-dioxaborolan-2-yl)aniline (**2**) [27], diethyl (2,5-dibromothiophen-3-yl) methylphosphonate (**5**) [15], 2,5-dibromo-3-hexylthiophene (**7**) [28] and 2,5-bis(trimethylstannyl)-thiophene (**8**) [29], as shown in Scheme 1, were synthesized according to the literature.

#### 2.1.1. 5-(4-(diphenylamino)phenyl)thiophene-2-carbaldehyde (**4**)

A mixture of compound **2** (3.0 g, 8.08 mmol), 5-Bromothiophene-2-carbaldehyde (**3**) (0.88 g, 8.08 mmol), and Pd(PPh<sub>3</sub>)<sub>4</sub> (467 mg, 5 mol %) was added in a mixture solution of degassed

toluene (40 mL) and 10 mL of degassed aqueous K<sub>2</sub>CO<sub>3</sub> (2 M). The reaction mixture was vigorously stirred at 90–95 °C for 8 h under a nitrogen atmosphere. After cooling, the reaction solution was extracted with dichloromethane and water. The organic layer was collected and dried over magnesium sulfate. Further purification was performed using silica gel chromatography (EA/hexanes, 1:10) to generate a yellow solid (2.13 g, yield = 74%). <sup>1</sup>H NMR (d-CDCl<sub>3</sub>, 300 MHz,  $\delta$ /ppm): 9.87 (s, 1H), 7.72 (d, 1H,  $J$  = 3.5 Hz), 7.52 (d, 2H,  $J$  = 8 Hz), 7.22 (m, 7H), 6.99 (m, 6H). <sup>13</sup>C NMR (d-CDCl<sub>3</sub>, 150 MHz,  $\delta$ /ppm): 182.62, 154.59, 149.13, 146.95, 141.28, 137.75, 129.47, 127.23, 126.10, 125.16, 123.86, 122.84, 122.34. MS( $m/z$ ): 355.2[M<sup>+</sup>]. Anal. Calcd for C<sub>23</sub>H<sub>17</sub>NOS: C, 77.72; H, 4.82; N, 3.94. Found: C, 77.79; H, 4.59; N, 3.40.

#### 2.1.2. (E)-4-(5-(2-(2,5-dibromothiophen-3-yl)vinyl)thiophen-2-yl)-*N,N*-diphenylaniline (**6**)

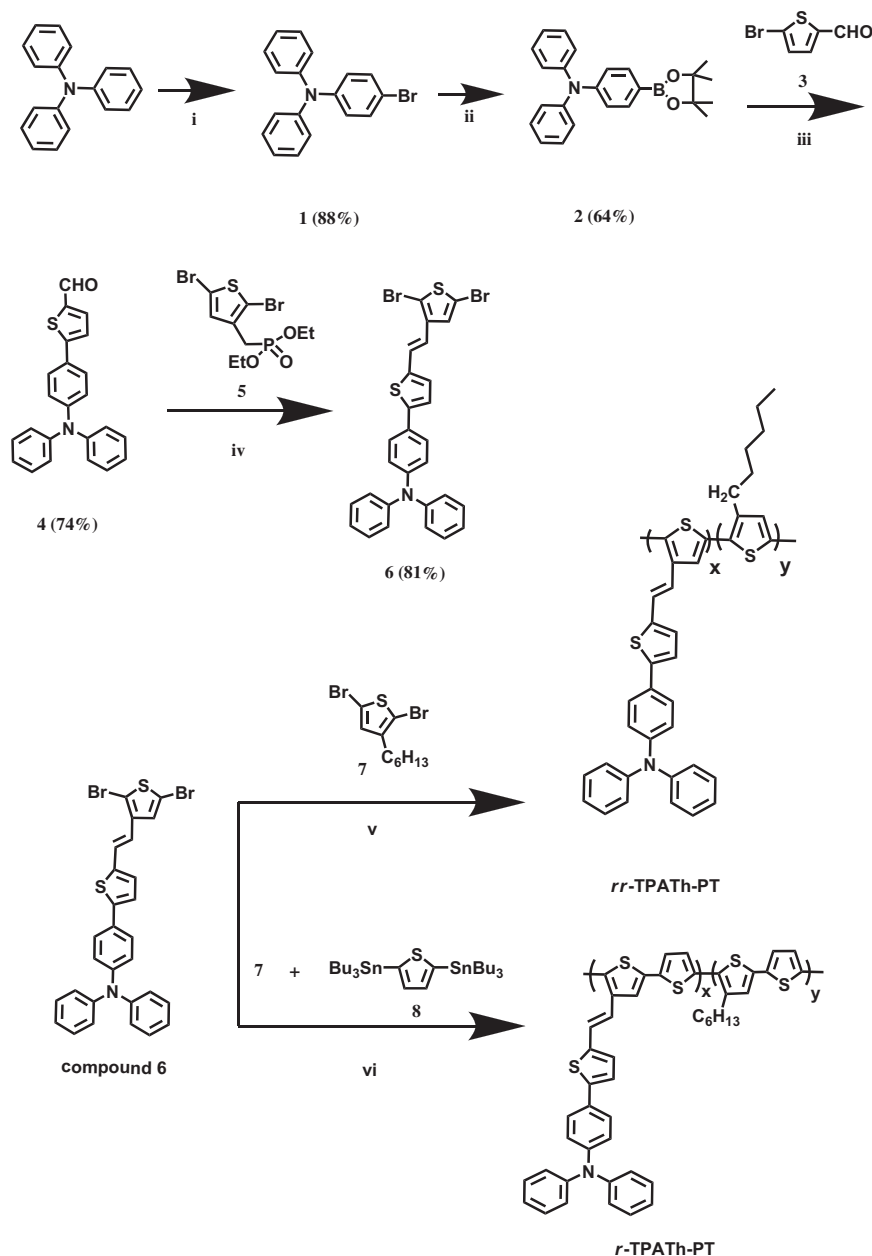
A mixture of compound **5** (2 g, 5.10 mmol) and CH<sub>3</sub>ONa (0.75 g, 13.89 mmol) in 10 mL DMF was stirred under an ice water bath for several minutes. Compound **4** (1.64 g, 4.62 mmol) was then added to the solution. After 2 h, the reaction was quenched with ice water and the yellow powder was precipitated. The precipitate was filtered and washed with water several times. Further purification was performed using silica gel chromatography (hexane as eluent) to give a yellow solid (2.22 g, yield = 81%). The product was filtered and dried under vacuum. The yellow solid product obtained had an 81% yield (2.22 g). <sup>1</sup>H NMR (d-CDCl<sub>3</sub>, 300 MHz,  $\delta$ /ppm): 7.47 (d, 2H,  $J$  = 8.7 Hz), 7.27 (m, 4H), 7.14 (m, 6H), 7.05 (m, 5H), 6.99 (d, 1H,  $J$  = 15.6 Hz), 6.77 (d, 1H,  $J$  = 15.9 Hz). <sup>13</sup>C NMR (CDCl<sub>3</sub>, 150 MHz,  $\delta$ /ppm): 147.53, 147.35, 144.00, 140.37, 138.86, 129.33, 128.33, 127.89, 127.16, 126.45, 124.62, 124.48, 123.40, 123.23, 122.69, 118.89, 111.88, 109.57. MS( $m/z$ ): 593.0[M<sup>+</sup>]. Anal. Calcd for C<sub>28</sub>H<sub>19</sub>Br<sub>2</sub>NS<sub>2</sub>: C, 56.67; H, 3.23; N, 2.36. Found: C, 56.51; H, 3.86; N, 2.57.

#### 2.1.3. *rr*-TPATH-PT

As shown in Scheme 1, *rr*-TPATH-PT was synthesized via condensation polymerization using the GRIM method initially reported by McCullough and coworkers [30,31]. Compound **6** (0.59 g, 1 mmol) and compound **7** (0.33 g, 1 mmol) were dissolved in 10 mL of dry THF under an N<sub>2</sub> atmosphere. Methylmagnesium bromide (2 mL, 1.0 M solution in THF) was then added to the stirred mixture. The mixture solution was refluxed for 2 h. Then, Ni(dppp)Cl<sub>2</sub> (10 mg, 1 mol%) was added to the reaction mixture and the reactions were continued for a further 8 h. The whole mixture was then poured into methanol (100 mL) and the precipitated material was filtered into a Soxhlet thimble. Soxhlet extractions were performed with methanol, hexane, acetone and chloroform. The polymer was recovered from the chloroform fraction by rotary evaporation. The solid was dried under vacuum for 24 h. After drying, *rr*-TPATH-PT was obtained as a red solid with isolated yields of 36%. Gel permeation chromatography (GPC) (THF):  $M_w$  = 13.3 kg/mol and PDI = 1.7. <sup>1</sup>H NMR (d-DCM, 600 MHz,  $\delta$ /ppm): 6.9–7.3 (br, 21H, vinylic and aromatic hydrogens), 2.75–2.85 (t, 4H,  $\alpha$ CH<sub>2</sub> alkyl chain), 1.25–1.7 (m, 16H, CH<sub>2</sub>), 0.92 (br, 6H, CH<sub>3</sub>).

#### 2.1.4. *r*-TPATH-PT

The synthesis of *r*-TPATH-PT via the Stille coupling route is shown in Scheme 1. Compound **6** (0.30 g, 0.5 mmol), compound **7** (0.17 g, 0.5 mmol), and compound **8** (0.41 g, 1 mmol) were dissolved in 10 mL of dry toluene. The reaction mixture was purged with N<sub>2</sub> and subjected to three freeze-pump thaw cycles to remove O<sub>2</sub>. Pd(PPh<sub>3</sub>)<sub>4</sub> (11.5 mg, 1 mol %) was added to the mixture solution. Then, the mixture was stirred and refluxed for 24 h. The whole mixture was then poured into methanol (100 mL) and the precipitated material was filtered into a Soxhlet thimble. Soxhlet extractions were performed with methanol, hexane, acetone and chloroform.



**Scheme 1.** Synthesis of the compound 6, and copolymers *rr*-TPATH-PT and *r*-TPATH-PT. i) NBS, THF, 0 °C, 1h; ii) *n*-BuLi 1h, afterward 2-Isopropoxy-4,4,5,5-tetramethyl-1,3,2-dioxaborolane 5h, -78 °C → 0 °C, THF; iii) Pd(PPh<sub>3</sub>)<sub>4</sub>, 2M K<sub>2</sub>CO<sub>3</sub>(aq), toluene, reflux, 8h; iv) CH<sub>3</sub>ONa, DMF, overnight, 90%; v) CH<sub>3</sub>MgBr, THF, reflux 2h, afterward Ni(dppp)Cl<sub>2</sub>, 8h; vi) Pd(PPh<sub>3</sub>)<sub>4</sub>, toluene, reflux, 24h.

The polymer was recovered from the chloroform fraction by rotary evaporation. The purified solid product was dried under vacuum for 24 h. After drying, the *r*-TPATH-PT was obtained as a black-red solid with isolated yields of 41%. GPC (THF):  $M_w = 11.7$  kg/mol and PDI = 2.3, <sup>1</sup>H NMR (d-DCM, 600 MHz,  $\delta$ /ppm): 6.9–7.3 (br, 24H, vinylic and aromatic hydrogens), 2.75–2.85 (b, 2H,  $\alpha$ CH<sub>2</sub> alkyl chain), 1.25–1.7 (m, 8H, CH<sub>2</sub>), 0.88 (br, 3H, CH<sub>3</sub>).

## 2.2. Characterization of copolymers

<sup>1</sup>H NMR (300 MHz) and <sup>13</sup>C NMR (150 MHz) spectra were recorded on a Varian Unity Inova Spectrometer. The average molecular weights of the polymers were measured by the GPC method. GPC was carried out on a Waters chromatography (Waters, 717 plus Autosampler), using two Waters Styragel linear columns,

with polystyrene as the standard and tetrahydrofuran (THF) as the eluent. The glass transition temperatures ( $T_g$ ) and thermal decomposition temperatures ( $T_d$ ) of the copolymers were determined by differential scanning calorimetry (DSC) and thermogravimetric analysis (TGA) using the Seiko DSC 6220, SII Extra 6000 and Thermo Cahn Versa Thermo analyzer systems, respectively. Both thermal analyses were performed in a nitrogen atmosphere at a scanning (both heating and cooling) rate of 10 °C/min. The temperatures at the intercept of the curves on the thermogram (endothermic, exothermic, or weight loss) and the leading baseline were taken as the estimates for the onset  $T_g$  and  $T_d$ . Absorption spectra were measured using a HITACHI U3010 UV-vis spectrometer. Fluorescence spectra were measured using a Varian Cary Eclipse luminescence spectrometer. Redox potentials of the polymers were determined by cyclic voltammetry (CV) using an



P-VP Al4083) was passed through a 0.45- $\mu\text{m}$  filter prior to being deposited on the ITO-coated glass by the spin-coating method (3000 rpm). The sample was then dried at 150 °C for 30 min in a glove box. A mixture solution of fullerene derivatives (both PC<sub>61</sub>BM and PC<sub>71</sub>BM were used) and the copolymer [with various weight ratios (w/w), 15 mg/mL in *o*-dichlorobenzene (*o*-DCB)] was stirred overnight and then filtered through a 0.2- $\mu\text{m}$  poly(tetrafluoroethylene) (PTFE) filter. The copolymer/fullerene-derivatives composite films-based photo-active layer was formed above the PEDOT:PSS layer by the spin-coating (1000 rpm, 30 s) of the mixture solution. By using AFM, film thicknesses of the photo-active layer in PSCs are shown as follows: *rr*-TPATH-PT/PC<sub>61</sub>BM (1:1, w/w), 124 nm; *r*-TPATH-PT/PC<sub>61</sub>BM (1:1, w/w), 77 nm; *r*-TPATH-PT/PC<sub>61</sub>BM (1:3, w/w), 119 nm; *r*-TPATH-PT/PC<sub>71</sub>BM (1:3, w/w), 98 nm. The Ca-based (30 nm)/Al (100 nm) cathode was thermally deposited onto the photo-active thin film in a high-vacuum chamber. The active area of the PSC was 4 mm<sup>2</sup>. After the Al electrode deposition, the PSC was encapsulated using UV-curing glue (Nagase, Japan). Current density–voltage (*I*–*V*) curves of the PSCs were measured on a programmable electrometer with current and voltage sources (Keithley 2400) under the illumination of a 100 mW cm<sup>-2</sup> solar light from an AM 1.5G solar simulator (Peccell solar simulator). The illumination intensity was calibrated using a standard Si photodiode detector equipped with a KG-5 filter. The output photocurrent was adjusted to match the photocurrent of the Si reference cell to obtain a power density of 100 mW cm<sup>-2</sup>.

### 3. Results and discussion

#### 3.1. Characterization of polymers

The chemical structures of the conjugated polymers were characterized by <sup>1</sup>H NMR spectroscopy, and the <sup>1</sup>H NMR spectra of the copolymers *rr*-TPATH-PT and *r*-TPATH-PT are shown in Fig. 1. Chemical shifts, in the range of 6.8–7.6 ppm, were attributed to the signal of protons (e–j) in the vinylene, phenyl and thiophene groups. Moreover, the signals of protons (a–d) in the hexyl chains were observed at chemical shifts ranged from 0.8 to 2.8 ppm. The regioregularity of the thiophene-based copolymer could be determined from the chemical shifts of  $\alpha$ -methylene protons in the hexyl chains [32]. In Fig. 1(a), the chemical shift of  $\alpha$ -methylene protons d was observed at  $\delta = 2.5$ –2.9 ppm, which indicates that the protons were in the same chemical environment for *rr*-TPATH-PT. This result demonstrates that the regioregular head-to-tail (HT) linkage in the thiophene-based polymer backbone was larger than 98.5% [32]. Thus, the copolymerization of *rr*-TPATH-PT using the GRIM method led to a high regioregularity of the polymer backbone. The integral values of protons d and e–j were about 9.01 and 44.2, respectively. This demonstrates that the repeat unit ratio (*x*/*y*) of co-monomers TPATH (compound 6) and thiophene (compound 7) was about 1:2.04. The molar percentage of TPATH in *rr*-TPATH-PT was about 33%. Apart from that, two absorption bands of proton d were observed in the range of 2.4–2.8 ppm for the *r*-TPATH-PT (Fig. 1(b)). This implies that the  $\alpha$ -methylene proton d was present in two different chemical environments. In other words, the polymer backbone exhibited HT and head-to-head (HH) regioisomeric structures. The integral values of two absorption bands imply that the ratio of HT and HH linkages in *r*-TPATH-PT was about 0.49. For *r*-TPATH-PT, the integral values of protons d and e–j were about 5.42 and 62.18, respectively. This demonstrates that the molar ratio (*x*/*y*) of repeat units TPATH–thiophene and hexyl-substituted thiophene–thiophene was about 1:1.05. The molar percentage of TPATH-containing repeat unit in *r*-TPATH-PT was about 49%. On the other hand, the weight-average molecular weights (*M*<sub>w</sub>) and polydispersity indexes (PDIs, *M*<sub>w</sub>/*M*<sub>n</sub>) were characterized by GPC,

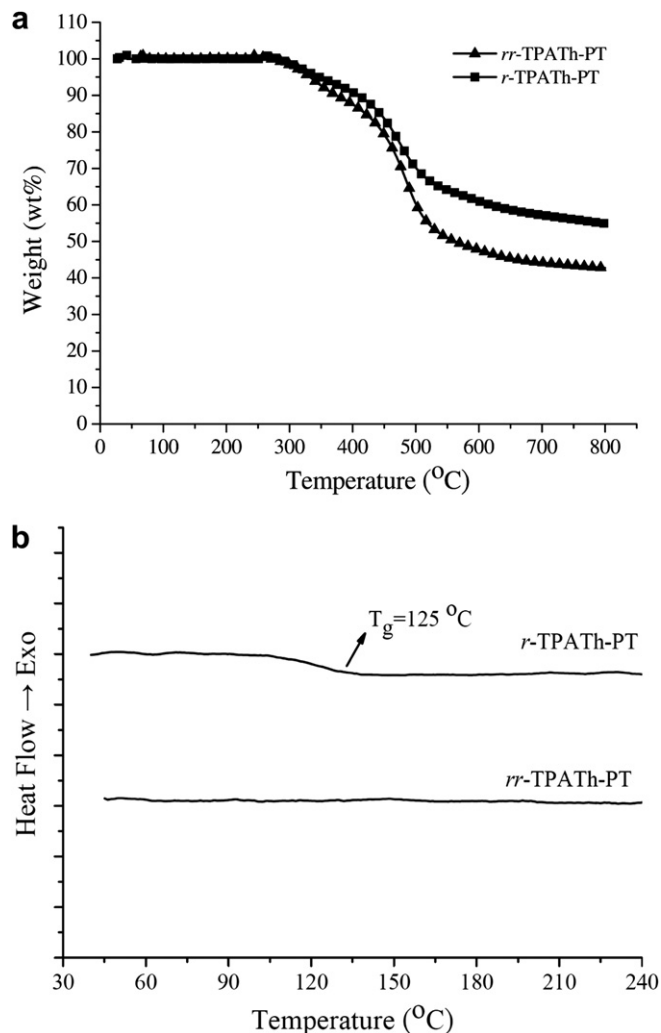


Fig. 2. TGA and DSC thermograms of *rr*-TPATH-PT and *r*-TPATH-PT.

with THF as the eluent and polystyrenes as the internal standards. The copolymers were readily soluble in THF. *M*<sub>w</sub> and PDI were about  $1.33 \times 10^4$  g/mol and 1.77 for the *rr*-TPATH-PT. For the *r*-TPATH-PT, *M*<sub>w</sub> and PDI were about  $1.17 \times 10^4$  g/mol and 2.34, respectively.

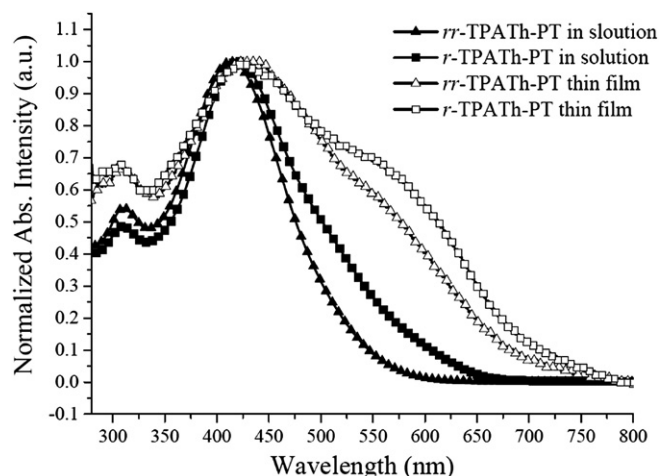


Fig. 3. Normalized UV-vis absorption spectra of copolymers.

**Table 1**  
Optical and electrochemical properties of copolymers.

Copolymers	In solution (nm)		In Film <sup>b</sup> (nm)			$E_g^{\text{opt}}$ (eV) <sup>c</sup>	$E_{\text{on}}^{\text{ox}}$ (V)	HOMO/LUMO <sup>d</sup>
	$\lambda_{\text{max}}^{\text{abs}}$	$\lambda_{\text{max}}^{\text{em}}$	$\lambda_{\text{max}}^{\text{abs}}$ <sup>a</sup>	$\lambda_{\text{max}}^{\text{em}}$	$\lambda_{\text{onset}}$			
<i>rr</i> -TPATH-PT	413	594	421/532	662	652	1.90	0.67	−5.38/−3.48
<i>r</i> -TPATH-PT	421	596	434/556	667	681	1.82	0.64	−5.35/−3.35

<sup>a</sup> UV-vis absorption wavelength of two maximum absorbencies.

<sup>b</sup> Films cast on quartz substrates, excitation wavelength was 400 nm.

<sup>c</sup> Measurements performed on films from the onset absorption ( $\lambda_{\text{onset}}$ ):  $E_g^{\text{opt}} = 1240/\lambda_{\text{onset}}$ .

<sup>d</sup> The energy levels were calculated according to: (HOMO =  $-e(E_{\text{on}}^{\text{ox}} - E_{\text{on,ferrocene}}^{\text{ox}} + 4.8)$ (eV), LUMO = (HOMO -  $E_g^{\text{opt}}$ )(eV)).

The operational stability of an optoelectronic device is directly related to the thermal stability of the conjugated polymers. Thus, high  $T_g$  and high  $T_d$  are desirable for the application of a conjugated polymer in PSCs. DSC and TGA thermograms of *rr*-TPATH-PT and *r*-TPATH-PT are shown in Fig. 2. The  $T_{d5}$  (at which a 5% weight loss occurred) of *rr*-TPATH-PT and *r*-TPATH-PT were observed at 332 °C and 347 °C under a nitrogen atmosphere, respectively. It was apparent that the two copolymers exhibited good thermal stability. As to DSC experiments, *r*-TPATH-PT exhibited a broad glass transition centered at 125 °C, whereas *rr*-TPATH-PT showed no clear thermal transitions in a temperature range of 40–300 °C. No significant order phase transition signal was observed under the DSC trace, which implied that the bulky pendant suppressed the crystal formation for the copolymers.

### 3.2. Optical properties of the conjugated copolymers

The normalized UV-visible absorption spectra of *rr*-TPATH-PT and *r*-TPATH-PT in CHCl<sub>3</sub> solution and as solid films are shown in Fig. 3. The photophysical properties of the copolymers are summarized in Table 1. Two absorption bands were observed for the copolymers: one located at 275–350 nm, which was attributed to the electronic transition absorption of the bulky pendant group; and the other, at 350–650 nm, was due to the  $\pi$ - $\pi^*$  transition of the thiophene-based conjugated main chains [12]. With increased conjugated bulky pendant group content in the copolymer, increased absorption intensity in the UV region (275–350 nm) could be observed [15]; yet the absorbance in the visible region (350–650 nm) might be decreased. Moreover, the maximal absorption wavelengths were observed at around 413 nm and 421 nm for the copolymers *rr*-TPATH-PT and *r*-TPATH-PT, respectively. A red shifting of the absorption band was observed for *r*-TPATH-PT as compared to *rr*-TPATH-PT. This indicated that *r*-TPATH-PT with less bulky side-chain content exhibited a longer conjugation length

and a better  $\pi$ -electron delocalization along the main chains than *rr*-TPATH-PT. The presence of the three-dimensional non-coplanarity configuration of TPA moiety resulted in the twist of the molecular structure [33,34]. The effective conjugation length of the polymer backbone was therefore reduced with increases in the bulky TPA side-chain density. As a result, the maximal absorption wavelength of *r*-TPATH-PT with less TPA moiety content was larger than that of *rr*-TPATH-PT. In addition, a red shift and a full-width at half-maximum enhancement of the absorption bands were observed for the copolymers as solid film, as compared to those in solution. These results were attributed to the interaction and  $\pi$ - $\pi$  stacking between the polymer chains. In particular, higher thiophene-based segment content resulted in the higher absorption intensity in the range of 500–700 nm for *r*-TPATH-PT as compared with *rr*-TPATH-PT. The quantification absorption spectra of *rr*-TPATH-PT and *r*-TPATH-PT as thin films were also investigated. Thin film of *r*-TPATH-PT ( $100158 \text{ cm}^{-1}$  at  $\lambda_{\text{max}} = \text{ca. } 434 \text{ nm}$ ) displayed higher absorption coefficients than that of *rr*-TPATH-PT film ( $86856 \text{ cm}^{-1}$  at  $\lambda_{\text{max}} = \text{ca. } 421 \text{ nm}$ ) in the UV–vis region. In general, conjugated polymer with relatively high absorption intensity was favorable for the light harvesting of solar light. This strong absorption characteristic was expected to improve the absorption efficiency of the photo-active layer and, thus, induce a larger photocurrent generation of PSC.

Normalized UV-vis absorption spectra of *r*-TPATH-PT/PC<sub>61</sub>BM- and *rr*-TPATH-PT/PC<sub>61</sub>BM-blend films are also shown in Fig. 4. The absorption band of the conjugated polymer ranged from 350 to 700 nm, while the absorption band of PC<sub>61</sub>BM ranged from 300 to 375 nm. The maximal absorption wavelengths of *rr*-TPATH-PT, *r*-TPATH-PT and PC<sub>61</sub>BM were observed at around 421 nm, 434 nm, and 325 nm, respectively. Moreover, the absorption intensity of the conjugated polymer was reduced as the PCBM content increased for the conjugated polymer/PC<sub>61</sub>BM-based blend films. From a photon-absorption viewpoint, employing less PCBM in the photo-active layer was preferred. However, the typical stoichiometry of

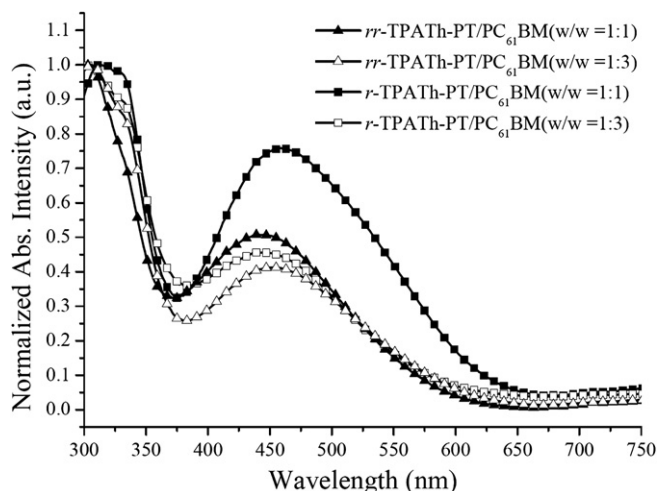


Fig. 4. Normalized UV-vis absorption spectra of copolymer/PC<sub>61</sub>BM-blend films.

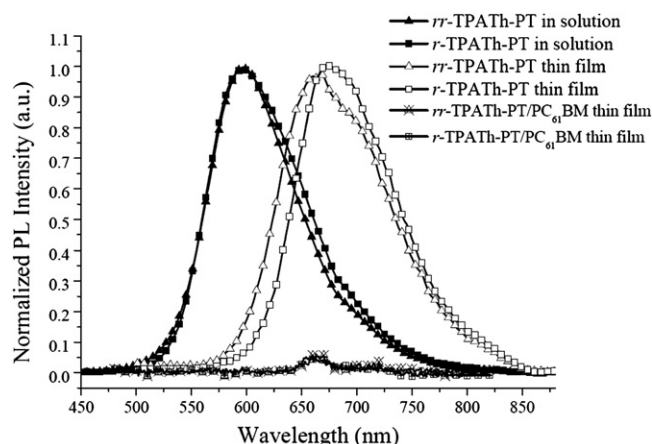


Fig. 5. Normalized PL spectra of copolymers and copolymer/PC<sub>61</sub>BM-blend films.

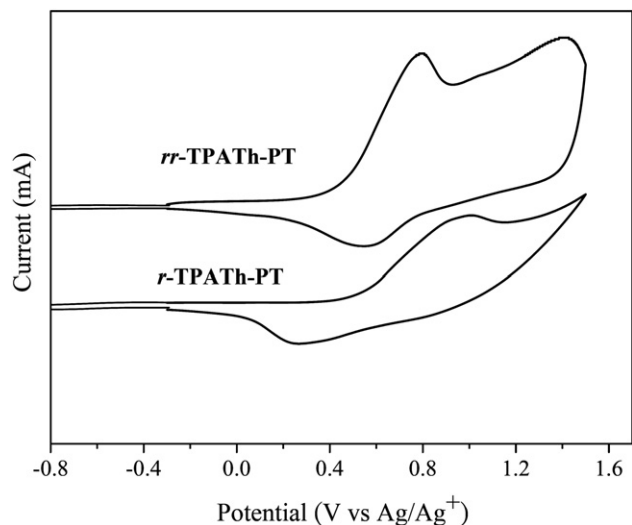


Fig. 6. Cyclic voltammograms of copolymer films on platinum plates in acetonitrile solution of  $0.1 \text{ mol L}^{-1}$  of  $\text{Bu}_4\text{NClO}_4$ .

a polymer/PCBM blend is 1:4 by weight, which has been found to be optimal for devices in several PSC systems [35]. A high proportion of PCBM limits optical absorption in the composite layer because the PCBM absorption is quite inefficient in the visible region [36,37]. In addition, the maximal absorption wavelengths of the conjugated polymer/PC<sub>61</sub>BM-blend films were varied with PC<sub>61</sub>BM content. For the *rr*-TPATH-PT/PC<sub>61</sub>BM-blend films, the maximal absorption wavelengths of the conjugated polymer had a slight red shift with increases in the PC<sub>61</sub>BM content. This implied that the dilution of the small molecules PC<sub>61</sub>BM resulted in the decrease of the main chains aggregation of *rr*-TPATH-PT. As a result, the effective conjugation length of *rr*-TPATH-PT was enhanced by the blending of PC<sub>61</sub>BM. In particular, the dilution effect of PC<sub>61</sub>BM was more pronounced for the *r*-TPATH-PT/PC<sub>61</sub>BM-blend films. The maximal absorption wavelength of the conjugated polymer had a significant red shift for the *r*-TPATH-PT/PC<sub>61</sub>BM-blend ( $w/w = 1:1$ ) film. Noticeably, the maximal absorption wavelength showed a blue shift as the blending content of PC<sub>61</sub>BM was further enhanced. A blue shift of the maximal absorption wavelength was observed for the *r*-TPATH-PT/PC<sub>61</sub>BM-blend ( $w/w = 1:3$ ) film as compared to the *r*-TPATH-PT/PC<sub>61</sub>BM-blend ( $w/w = 1:1$ ) film. This was attributed to the excellent compatibility between *r*-TPATH-PT and PC<sub>61</sub>BM. The intercalating of PC<sub>61</sub>BM into the polymer chains led to the twist of the polymer backbone. Hence, the maximal absorption wavelength of *r*-TPATH-PT showed a blue shift for the *r*-TPATH-PT/PC<sub>61</sub>BM-blend ( $w/w = 1:3$ ) film.

PL spectra of the copolymers *rr*-TPATH-PT and *r*-TPATH-PT and the copolymer/PCBM-based composite films are shown in Fig. 5. PL emission maximums of *rr*-TPATH-PT and *r*-TPATH-PT in solution were observed at 594 and 596 nm, respectively. PL emission bands of *rr*-TPATH-PT and *r*-TPATH-PT as solid films were near the red-emission region with maximum emission at wavelengths of 662 and 667 nm, respectively. A red shift and a broadening of the emission peaks were observed for the copolymers as solid film, as compared to in solution, due to the inter-chain aggregation formation in the polymer film. Moreover, *r*-TPATH-PT with less bulky side-chain content exhibited a longer conjugation length and a better  $\pi$ -electron delocalization along the main chains than *rr*-TPATH-PT. For that reason, a red-shift of the emission band was observed for *r*-TPATH-PT as compared to that of *rr*-TPATH-PT. However, PL emissions were almost completely quenched upon the addition of PC<sub>61</sub>BM ( $w/w = 1:1$ ) for copolymers, as shown in

Fig. 5. The same quenched PL emissions were observed for the polymer-blend film with higher PC<sub>61</sub>BM content ( $w/w = 1:3$ ). High efficient PL quenching phenomena suggested that the excitons generated by the absorbed photons completely dissociated to free charge carriers (electrons and holes). Moreover, an effective charge transfer from the copolymer to PC<sub>61</sub>BM was achieved, which was a basic requirement for preparing a PSC with excellent PV performance [38].

### 3.3. Electrochemical properties of conjugated copolymers

Cyclic voltammetry (CV) was employed to investigate electrochemical behavior and to estimate the HOMO and LUMO energy levels of the conjugated polymers. The reversible oxidation behaviors in the CV curves of the copolymers are shown in Fig. 6. The electrochemical properties of the copolymers are summarized in Table 1. The oxidation potentials of *rr*-TPATH-PT and *r*-TPATH-PT were 0.67 V and 0.64 V, respectively. From those values, the HOMO levels of the copolymers were calculated according to the follow equation:

$$\text{HOMO} = -e(E_{\text{on}}^{\text{ox}} - E_{\text{on,ferrocene}}^{\text{ox}} + 4.8) (\text{eV})$$

The 4.80 eV was the energy level of ferrocene below the vacuum level and the  $E_{\text{on}}^{\text{ox}}$  of Ferrocene/Ferrocene<sup>+</sup> was 0.09 V in the evaluation 0.1 M  $\text{Bu}_4\text{NClO}_4/\text{MeCN}$  solution. Hence the corresponding HOMO levels were  $-5.38 \text{ eV}$  for *rr*-CzPh-PT and  $-5.35 \text{ eV}$  for *r*-TPATH-PT. Because no reversible n-doping process was observed in the CV spectrum, the LUMO levels were estimated from the HOMO levels and UV-vis absorption  $E_{\text{g}}^{\text{opt}}$  using the equation:

$$\text{LUMO} = (\text{HOMO} + E_{\text{g}}^{\text{opt}}) (\text{eV})$$

As shown in Fig. 3, the onset of absorption in the thin films of *rr*-TPATH-PT and *r*-TPATH-PT were observed at 652 nm and 681 nm, respectively. From the onset of absorption, the energy band-gap ( $E_{\text{g}}^{\text{opt}}$ ) values of *rr*-TPATH-PT and *r*-TPATH-PT were 1.90 eV and 1.82 eV, respectively. As a result, the LUMO levels were  $-3.48 \text{ eV}$  for *rr*-CzPh-PT and  $-3.35 \text{ eV}$  for *r*-TPATH-PT. A relatively lower  $E_{\text{g}}^{\text{opt}}$  for *r*-TPATH-PT would improve the light harvesting of the photo-active layer and, therefore, enhance the photocurrent generation of PSC. In addition, the HOMO levels of PTs were approximately  $-4.7 \sim -4.9 \text{ eV}$  [11,39]. The HOMO levels of the copolymers *rr*-TPATH-PT and *r*-TPATH-PT were about  $-5.35$  and  $-5.38 \text{ eV}$ , respectively, which were approximately 0.4 eV lower than the PTs. The effective conjugation length of the copolymers with bulky conjugated side-chains was curtailed due to the twist of the main chain out of the  $\pi$ -system conjugation planar. Consequently, the HOMO energy level was lowered by grafting the bulky pendant groups in PT [15,19]. In general, the HOMO level of the p-type conjugated polymer was an important parameter in BHJ cells. High  $V_{\text{oc}}$  values were obtained for PSCs fabricated from *r*-TPATH-PT and *rr*-TPATH-PT with low HOMO levels.

### 3.4. Morphology investigation of copolymer/fullerene derivatives blend films

PSC performance was strongly dependant on the morphology of the conjugated polymer/fullerene-derivative composite film [40]. To avoid the recombination of exciton, the P/N heterojunction phase was controlled under nano-scale distribution, as the diffusion range of the charge carrier was about 3–10 nm [2,41]. It has been shown earlier that PC<sub>61</sub>BM was capable of organizing crystalline order in pristine PC<sub>61</sub>BM films at elevated temperatures [42]. The existence of micro-meter clusters indicated that the large-scale

phase separation of P/N heterojunction led to a recombination of electrons and holes. Moreover, the charge mobility decreased due to the aggregation of PC<sub>61</sub>BM [22]. Therefore, it was important to study the crystalline morphology of PC<sub>61</sub>BM in polymer-blend films. The POM images of pristine copolymer films and copolymer/PC<sub>61</sub>BM-blend films are shown in Fig. 7. No crystals were observed in Fig. 7(a–b), which presents the amorphous morphology of *rr*-TPATH-PT and *r*-TPATH-PT pristine films. As shown in Fig. 7(c–d), several crystalline domains were observed for both the *rr*-TPATH-PT/PC<sub>61</sub>BM- and *r*-TPATH-PT/PC<sub>61</sub>BM-blend ( $w/w = 1:1$ ) films. For copolymer film with a higher weight ratio of PC<sub>61</sub>BM ( $w/w = 1:3$ ) (Fig. 7(e–f)), the amount and size of PC<sub>61</sub>BM-based crystalline domains were larger apparently in *rr*-TPATH-PT-blend film than in *r*-TPATH-PT-blend film. The acute micro-phase separation and poor miscibility was verified for the *rr*-TPATH-PT-blend film with a higher PC<sub>61</sub>BM ratio ( $w/w = 1:3$ ). In contrast, only a small portion of PC<sub>61</sub>BM-based crystalline domain was observed for *r*-TPATH-PT/

PC<sub>61</sub>BM-blend film. Poor miscibility between PC<sub>61</sub>BM and *rr*-TPATH-PT was attributed to less intercalating of PC<sub>61</sub>BM into the polymer chains [20]. In other words, *r*-TPATH-PT with less bulky conjugated side-chains was favorable for the intercalating of PC<sub>61</sub>BM into the polymer chains. As a result, better compatibility was observed for the *r*-TPATH-PT/PC<sub>61</sub>BM-blend film as compared to the *rr*-TPATH-PT/PC<sub>61</sub>BM-blend film. The phase separation of polymer/PCBM-blend film reduced the hole-mobility in the photo-active layer [22]. Consequently, a better PCE of *r*-TPATH-PT/PC<sub>61</sub>BM-based PSC was expected in comparison with the *rr*-TPATH-PT/PC<sub>61</sub>BM-based PSC.

Recently, it has been reported that the PV properties of PSCs can be improved by manipulating the morphology within the photo-active polymer-blend [36]. The compatibility and morphology of the conjugated copolymer/PCBM composite films were investigated using AFM microscopy. The topography (a–d) and phase (e–h) nano-scale images of the *rr*-TPATH-PT/PC<sub>61</sub>BM and *r*-TPATH-PT/PC<sub>61</sub>BM-blend films are shown in Fig. 8. As shown in Fig. 8(a–b, e–f),

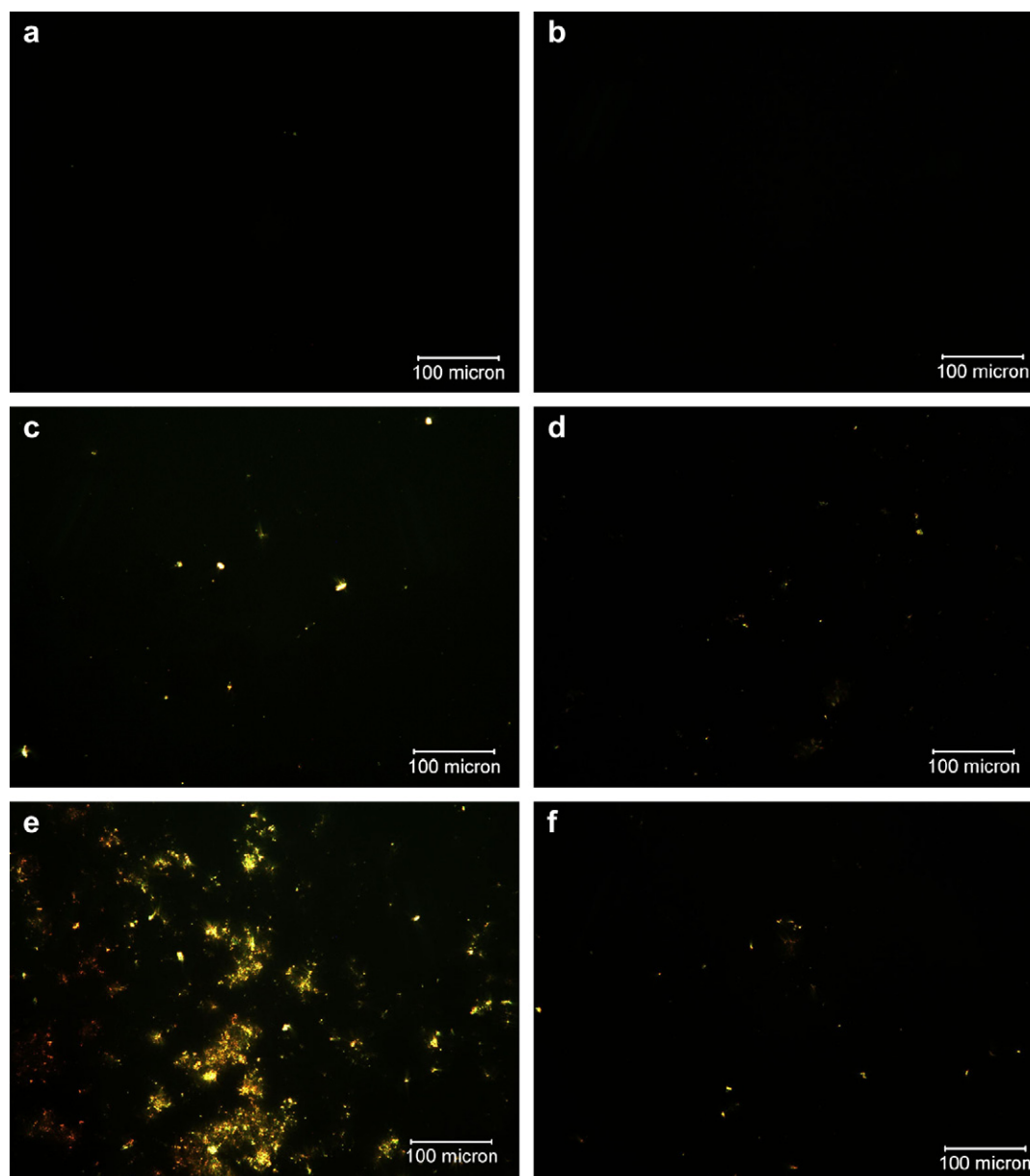


**Fig. 7.** POM images of (a) *rr*-TPATH-PT, (b) *r*-TPATH-PT, (c) *rr*-TPATH-PT/PC<sub>61</sub>BM ( $w/w = 1:1$ ), (d) *r*-TPATH-PT/PC<sub>61</sub>BM ( $w/w = 1:1$ ), (e) *rr*-TPATH-PT/PC<sub>61</sub>BM ( $w/w = 1:3$ ), and (f) *r*-TPATH-PT/PC<sub>61</sub>BM ( $w/w = 1:3$ ) films.



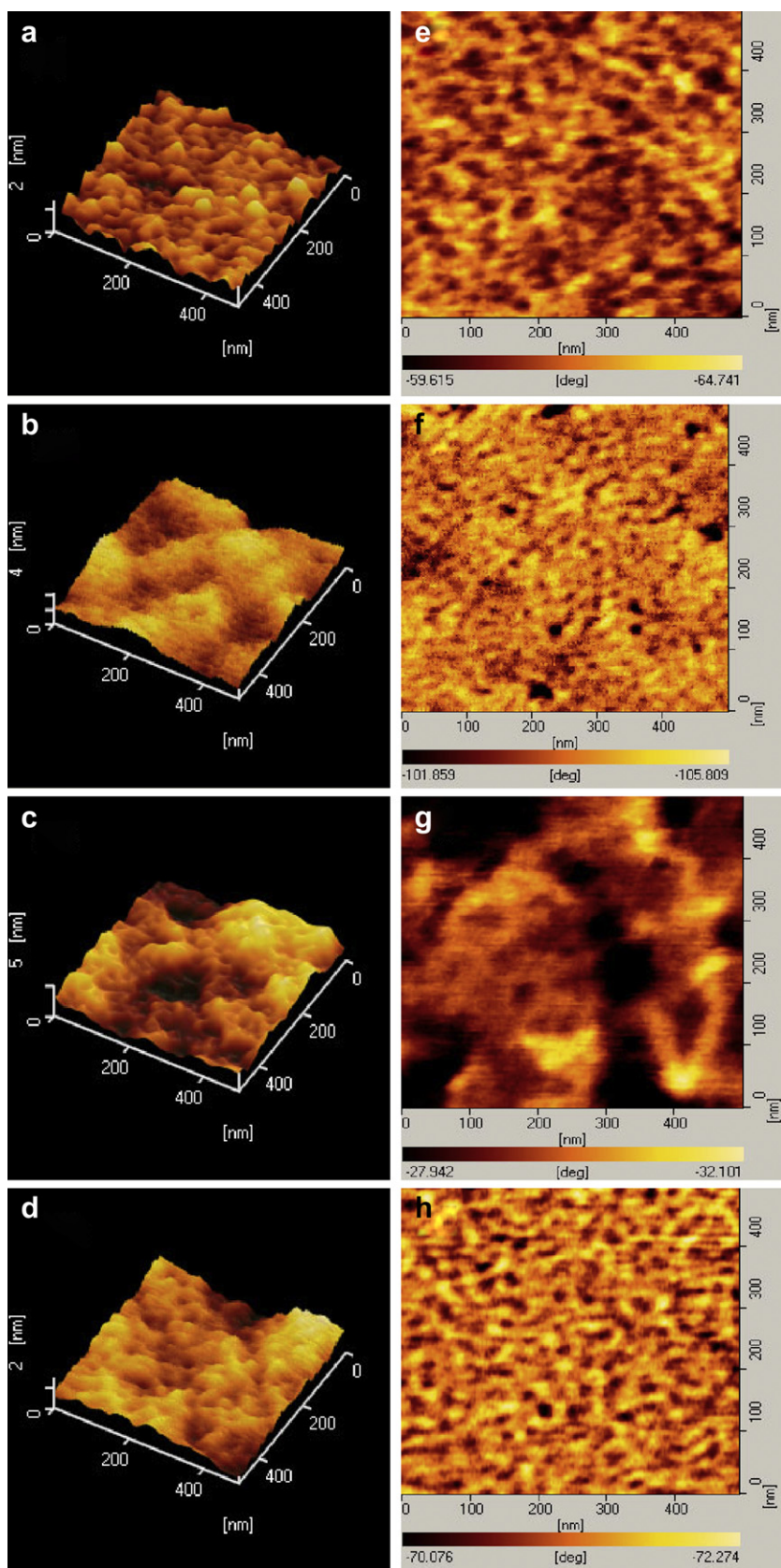


**Fig. 8.** Tapping mode topographic (a–d) and phase (e–h) images of *rr*-TPATH-PT/PC<sub>61</sub>BM (*w/w* = 1:1) (a, e), *r*-TPATH-PT/PC<sub>61</sub>BM (*w/w* = 1:1) (b, f), *rr*-TPATH-PT/PC<sub>61</sub>BM (*w/w* = 1:3) (c, g), and *r*-TPATH-PT/PC<sub>61</sub>BM (*w/w* = 1:3) (d, h). The area was 500 nm × 500 nm.

the copolymers/PC<sub>61</sub>BM ( $w/w = 1:1$ ) films displayed low levels of root-mean-square (RMS) (0.34 nm for *rr*-TPATH-PT and 0.53 nm for *r*-TPATH-PT), which presented a satisfactory miscibility of films. The introduction of electron-donating side-chains reduced the phase separation due to the intermolecular steric hindrance of the bulky side-chains to the conjugated main chain [16]. The presence of the bulky side-chains reduced the packing density of the polymer main chains and, subsequently, enhanced the miscibility of the copolymer and PC<sub>61</sub>BM. In addition, with a higher PC<sub>61</sub>BM content of *rr*-TPATH-PT/fullerene derivatives-blend film (Fig. 8 (c, g)), the higher surface roughness (0.91 nm) and apparent phase separation in nano-scales were observed. However, the *r*-TPATH-PT-blend film with higher a PC<sub>61</sub>BM content (Fig. 8(d, h)) retained a lower surface roughness (0.41 nm) and smoother surface. *r*-TPATH-PT with a low bulky side-chain density provided more free volume between the side-chains to accommodate the higher amount of fullerene molecules, thus improving the compatibility between the polymer and fullerene molecules for the *r*-TPATH-PT/fullerene derivative-blend films.

In order to further characterize the distribution of fullerene derivatives in polymer/fullerene derivative-blend film, TEM investigation was carried out [43]. Bright field (BF)-TEM images of *rr*-TPATH-PT/PC<sub>61</sub>BM and *r*-TPATH-PT/PC<sub>61</sub>BM-blend films are shown in Fig. 9. The dark areas of the BF-TEM images were attributed to the PC<sub>61</sub>BM domains. This is because the electron scattering density of PC<sub>61</sub>BM is greater than that of the conjugated polymer [44]. As shown in Fig. 9(a), the phase separation and aggregation of PC<sub>61</sub>BM were formed in the *rr*-TPATH-PT/PC<sub>61</sub>BM ( $w/w = 1:1$ ) blend film. The PC<sub>61</sub>BM clusters could be observed more obviously in the magnified TEM image (Fig. 9(b)). In contrast, a relatively homogeneous morphology was present in the *r*-TPATH-PT/PC<sub>61</sub>BM ( $w/w = 1:1$ ) blend film (Fig. 9(c)). Indeed, the TEM images indicate that the *r*-TPATH-PT/PC<sub>61</sub>BM-blend film exhibited better compatibility than the *rr*-TPATH-PT/PC<sub>61</sub>BM-blend film. This is also confirmed by POM and AFM investigations.

Based on the results of POM, AFM, and TEM, the side-chain density effect on the compatibility of the polymer and fullerene derivatives is further illustrated in Fig. 10. The distribution of the fullerene molecules is sketched out in the polymer chains of the *rr*-TPATH-PT/PC<sub>61</sub>BM- and *r*-TPATH-PT/PC<sub>61</sub>BM-blend films. As illustrated in Fig. 10 (a), the PC<sub>61</sub>BM clusters (the shadow area) were formed between the polymer chains in the *rr*-TPATH-PT/PCBM-blend film. There was insufficient space between the side-chains of *rr*-TPATH-PT for intercalation to occur. On the other hand, excitons in nonintercalated blends split only at the interface between two different phases, a polymer phase and a fullerene phase [22]. Even though the PC<sub>61</sub>BM-based electron-transporting channel was formed between the polymer backbones. In contrast, the free volume is sufficient for the fullerene molecules to accommodate between the side-chains of *r*-TPATH-PT (Fig. 10(b)). Sufficient room for PC<sub>61</sub>BM intercalation was evidenced by the good compatibility between *r*-TPATH-PT and PC<sub>61</sub>BM. The intercalation of PC<sub>61</sub>BM was favorable for the electron-transfer from polymer backbone to PC<sub>61</sub>BM. It was concluded that *r*-TPATH-PT with less bulky side-chains possessed sufficient free volume for PC<sub>61</sub>BM to intercalate into the polymer chains, which was a crucial factor for the morphology of the polymer/fullerene derivative-based blend film.

### 3.5. Current density versus electrical field of the polymer/PC<sub>61</sub>BM-based hole-only and electron-only devices

In order to investigate the charge-transporting properties in polymer/PC<sub>61</sub>BM-blend films, hole-only devices (ITO/PEDOT:PSS/polymer:PC<sub>61</sub>BM/Au) and electron-only devices (ITO/Ca/polymer:PC<sub>61</sub>BM/Ca/Al) were fabricated in this study [45–47]. Current density was plotted as a function of electrical field of the polymer/

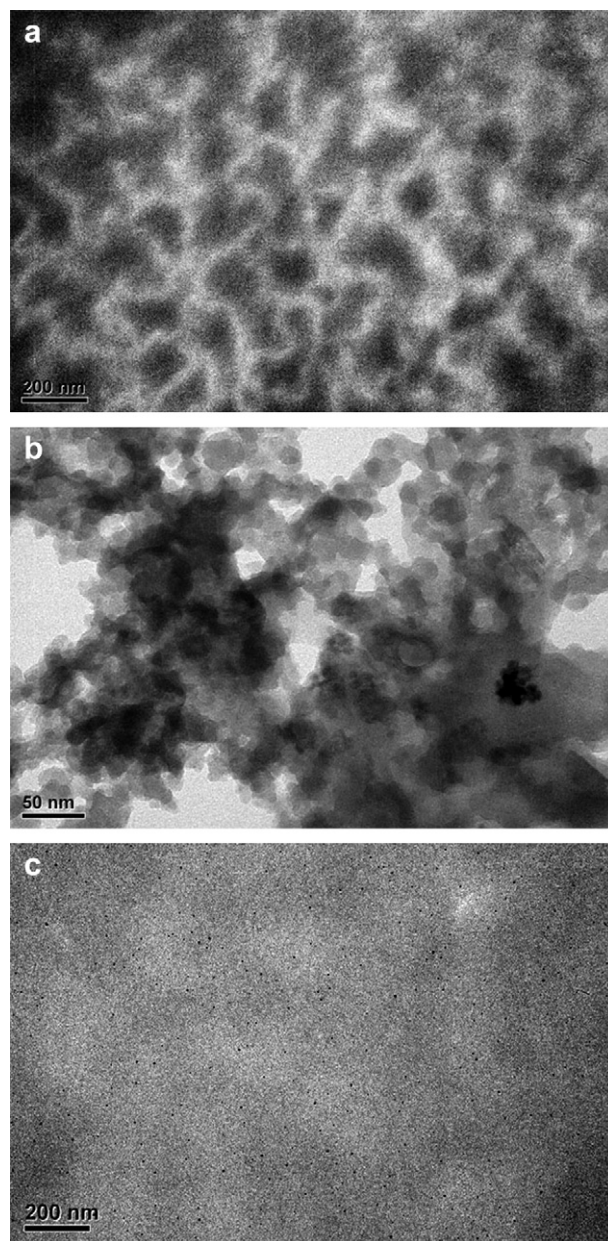


Fig. 9. BF-TEM images of (a, b) *rr*-TPATH-PT/PC<sub>61</sub>BM ( $w/w = 1:1$ ) and (c) *r*-TPATH-PT/PC<sub>61</sub>BM ( $w/w = 1:1$ ).

PC<sub>61</sub>BM-based hole-only (Fig. 11(a)) and electron-only (Fig. 11(a)) devices, respectively. Based on current density versus electrical field plots, the hole-current density of *r*-TPATH-PT/PC<sub>61</sub>BM-based device was much higher than that of the *rr*-TPATH-PT/PC<sub>61</sub>BM-based device. Higher hole-current density was attributed to the longer conjugation in polymer backbone of *r*-TPATH-PT. This is due to the fact that holes in photo-active layer were transported through the p-type polythiophene derivative to the electrode. The results indicate that the hole-transporting property was strongly dependent on the side-chain density of polythiophene derivatives. In addition, the electron-current density of *r*-TPATH-PT/PC<sub>61</sub>BM-based device was slightly higher than that of the *rr*-TPATH-PT/PC<sub>61</sub>BM-based device. The side-chain density effect on the electron-transporting property was not as significant as that on hole-transporting property. This is because the electrons were mainly

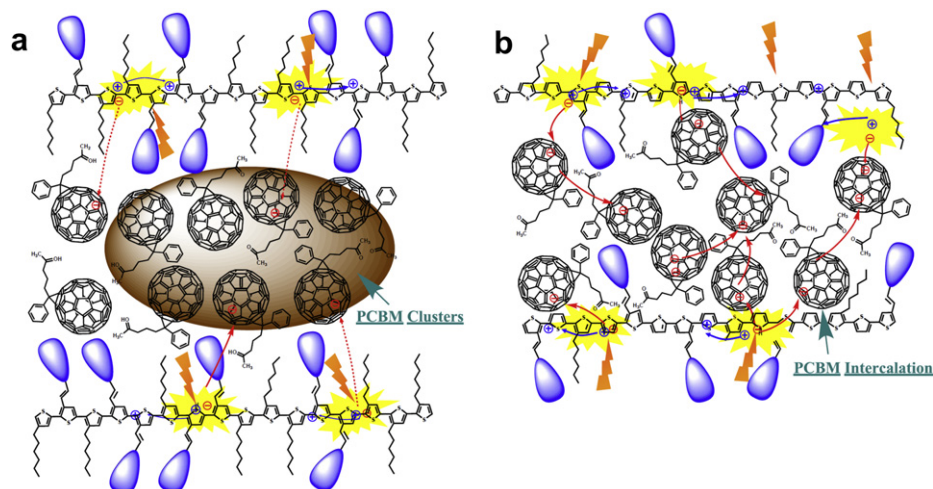


Fig. 10. Possible distribution of fullerene molecules in the copolymer chains of (a) *rr*-TPATH-PT, and (b) *r*-TPATH-PT.

transported through the PC<sub>61</sub>BM phase to the electrode. It is concluded that higher electron- and hole-transporting capacities were observed for the *r*-TPATH-PT/PC<sub>61</sub>BM-based device as compared to the *rr*-TPATH-PT/PC<sub>61</sub>BM-based device.

### 3.6. Photovoltaic properties of PSCs

The PSCs were fabricated from copolymer/PC<sub>61</sub>BM- and copolymer/PC<sub>71</sub>BM-blend films in various weight ratios via the spin-coating method. The optimal PCE performance of the PSCs was observed when the photo-active layer was spin-coated (1000 rpm) from the *o*-DCB solution. The photocurrent density versus voltage (*I*–*V*) characteristics of PSCs prepared from copolymer/PC<sub>61</sub>BM and copolymer/PC<sub>71</sub>BM with various weight ratios are shown in Fig. 12. PV properties of these PSCs, including *V*<sub>oc</sub>, short-circuit current density (*J*<sub>sc</sub>), fill factor (FF), and PCE are summarized in Table 2. The *r*-TPATH-PT/PC<sub>61</sub>BM-based (*w/w* = 1:1) PSC showed an *V*<sub>oc</sub> of 0.74 V, *J*<sub>sc</sub> of 3.43 mA/cm<sup>2</sup>, FF value of 0.37, and a PCE of 0.94%; while the *rr*-TPATH-PT/PC<sub>61</sub>BM-based (*w/w* = 1:1) PSC presented a equal FF, but lower *V*<sub>oc</sub> (0.66 V) and *J*<sub>sc</sub> (2.21 mA/cm<sup>2</sup>) values, resulting in a lower PCE of 0.49%. Basically, the *V*<sub>oc</sub> is mainly determined by the energy difference between the LUMO of the electron-acceptor PC<sub>61</sub>BM and the HOMO of the electron-donor (conjugated polymer). The *V*<sub>oc</sub> value of *rr*-TPATH-PT was smaller than those of *r*-TPATH-PT, despite the fact that the HOMO level of *rr*-TPATH-PT was lower than that of *r*-TPATH-PT. This was attributed to the aggregation of PC<sub>61</sub>BM in blend film. The formation of PC<sub>61</sub>BM cluster in *rr*-TPATH-PT/PC<sub>61</sub>BM-blend film would reduce the effective LUMO level of PCBM [48]. Consequently, the *V*<sub>oc</sub> value of *rr*-TPATH-PT/PCBM-based PSC was smaller than the *r*-TPATH-PT/PCBM-based PSC. Furthermore, the larger *V*<sub>oc</sub> and higher *J*<sub>sc</sub> values led to a superior PCE value, which was supposed to a satisfactory HOMO level and high light harvest ability in the visible region of *r*-TPATH-PT. Nevertheless, the regioregularity of *rr*-TPATH-PT promoted organization of the polymer backbone and facilitated the enhancement of the charge mobility and photocurrent density [49,50]. In addition, low molecular weights of the polymers results in poor film quality, leading to the current leakage in the PSC [51,52]. As a result of that, moderate FF values were observed for the *r*-TPATH-PT/PC<sub>61</sub>BM-based and *rr*-TPATH-PT/PC<sub>61</sub>BM-based PSCs as compared to those reported in previous literature [15,34].

To further improve the PV performance of *r*-TPATH-PT-based PSC, the PSC was prepared based on the blend film of *r*-TPATH-PT/PC<sub>61</sub>BM with a higher PC<sub>61</sub>BM content (*w/w* = 1:3). Moreover, PC<sub>71</sub>BM was introduced instead of PC<sub>61</sub>BM as the electron-acceptor in the photo-active layer of the PSC. The PV properties of the *r*-TPATH-PT/PC<sub>71</sub>BM-blend (*w/w* = 1:3) film-based PSC were also investigated. Both *r*-TPATH-PT/PC<sub>61</sub>BM- and *r*-TPATH-PT/PC<sub>71</sub>BM-blend film-based photo-active layers were thermal annealed above

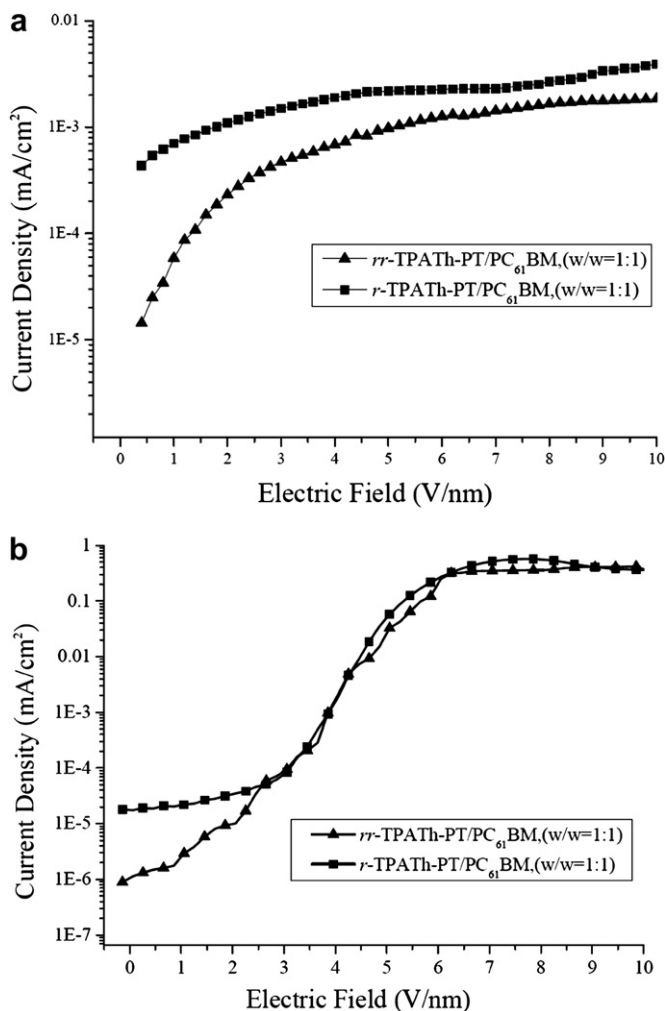


Fig. 11. Current-density versus electrical field of the polymer/PC<sub>61</sub>BM-based (a) hole-only and (b) electron-only devices.

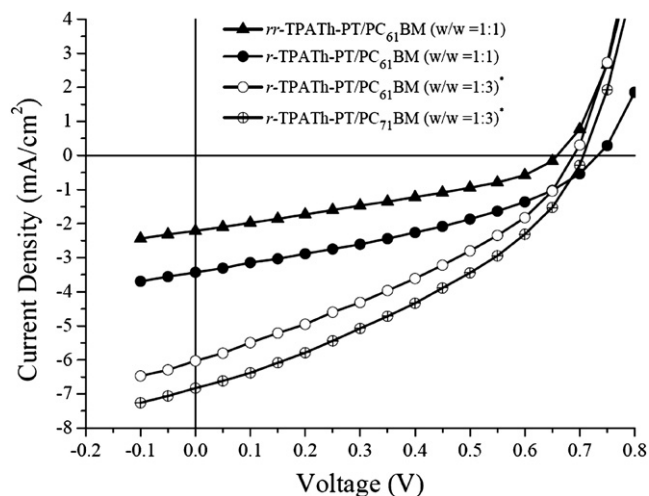


Fig. 12. Current density-potential characteristics of illuminated (AM 1.5G, 100 mW/cm<sup>2</sup>) copolymer/PCBM-based solar cells (\* with annealing).

Table 2  
Photovoltaic performances of copolymer/PCBM based solar cells.

Active layer(w/w ratio)	$V_{oc}$ (V)	$J_{sc}$ (mA/cm <sup>2</sup> )	FF	$\eta$ (%)
<i>rr</i> -TPATH-PT: PC <sub>61</sub> BM (1:1)	0.66	2.21	0.37	0.49
<i>r</i> -TPATH-PT: PC <sub>61</sub> BM (1:1)	0.74	3.43	0.37	0.94
<i>r</i> -TPATH-PT: PC <sub>61</sub> BM (1:3) <sup>a</sup>	0.69	6.03	0.35	1.45
<i>r</i> -TPATH-PT: PC <sub>71</sub> BM (1:3) <sup>a</sup>	0.71	6.83	0.36	1.75

<sup>a</sup> The photo-active layer was annealed under 140 °C for 20 min.

the  $T_g$  of the copolymer (140 °C for 20 min) [53,54]. The  $J_{sc}$  value of the *r*-TPATH-PT/PC<sub>61</sub>BM-based ( $w/w = 1:3$ ) PSC was 6.03 mA/cm<sup>2</sup>, a value which was two times of magnitude higher than the  $J_{sc}$  value (2.21 mA/cm<sup>2</sup>) of the *rr*-TPATH-PT/PC<sub>61</sub>BM-based ( $w/w = 1:1$ ) PSC. In addition to the thermal annealing effect on PV performance, the PV properties of PSCs were also determined from the electro-acceptor content in the photo-active layer. The enhancement of photocurrent for the PSC fabricated from the PC<sub>61</sub>BM-rich blend film might have been attributed to the formation of an adequate electron and hole percolation path in the photo-active layer. An efficient dissociation of the exciton and higher charge collection to the electrode were therefore achieved. Moreover, the enhancement of the photocurrent might have been attributed to the intercalation of PC<sub>61</sub>BM in the polymer chains for the *r*-TPATH-PT/PC<sub>61</sub>BM-blend ( $w/w = 1:3$ ) film-based PSC [20,22]. In addition, PSC fabricated from the *r*-TPATH-PT/PC<sub>71</sub>BM-blend ( $w/w = 1:3$ ) film showed a  $V_{oc}$  of 0.71 V,  $J_{sc}$  of 6.83 mA/cm<sup>2</sup>, FF of 0.36, and a PCE of 1.75%. Better PV performance was observed for the *r*-TPATH-PT/PC<sub>71</sub>BM-based ( $w/w = 1:3$ ) PSC as compared to the *r*-TPATH-PT/PC<sub>61</sub>BM-based ( $w/w = 1:3$ ) PSC. This was because of the enhanced light absorption in the visible region of PC<sub>71</sub>BM [55,56].

#### 4. Conclusion

The regioregular and random polythiophene derivatives (*rr*-TPATH-PT and *r*-TPATH-PT) with conjugated side-chains were synthesized and developed for PSC application. *r*-TPATH-PT with less bulky side-chain content exhibited a longer conjugation length and a better  $\pi$ -electron delocalization along the main chains than *rr*-TPATH-PT. Higher thiophene-based segment content resulted in the higher absorption intensity in the vision region for *r*-TPATH-PT in comparison with *rr*-TPATH-PT. Moreover, *r*-TPATH-PT with less side-chain content provided sufficient free volume between the side-chains for the intercalation of fullerene molecules into the polymer

main chains. Better compatibility was observed for the *r*-TPATH-PT/PC<sub>61</sub>BM-blend film as compared to the *rr*-TPATH-PT/PC<sub>61</sub>BM-blend film. Therefore, the *r*-TPATH-PT/PC<sub>61</sub>BM-based PSCs showed higher PV performances than the *rr*-TPATH-PT/PC<sub>61</sub>BM-based PSCs. In addition, the incorporation of bulky conjugated moiety also curtailed the effective conjugation length in the main chain; thus, a low HOMO level and a satisfactory  $V_{oc}$  value of the copolymers were obtained. The optimum PSC performance in our study was demonstrated by the *r*-TPATH-PT/PC<sub>71</sub>BM ratio of 1:3 ( $w/w$ ), when the PCE was 1.75% under AM 1.5G simulated solar light. The suitable bulky conjugated side-chain density had a crucial influence on the photophysical, electrochemical, morphological and PV properties of the PT derivatives.

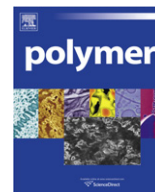
#### Acknowledgements

Financial support from the National Science Council (NSC) and Ministry of Education, Taiwan under ATU plan is gratefully acknowledged.

#### References

- [1] Gunes S, Neugebauer H, Sariciftci NS. Chem Rev 2007;107(4):1324–38.
- [2] Mayer AC, Scully SR, Hardin BE, Rowell MW, McGehee MD. Mater Today 2007;10(11):28–33.
- [3] Rudge A, Raistrick I, Gottesfeld S, Ferraris JP. Electrochim Acta 1994;39(2):273–87.
- [4] Li XG, Li J, Huang MR. Chem-Eur J 2009;15(26):6446–55.
- [5] Li XG, Li J, Meng QK, Huang MR. J Phys Chem B 2009;113(29):9718–27.
- [6] Perepichka IF, Perepichka DF, Meng M, Wudl F. Adv Mater 2005;17(19):2281–305.
- [7] Kozuka H, Tsumura A, Ando T. Synth Met 1987;18(1):699–704.
- [8] Li G, Shrotriya V, Huang J, Yao Y, Moriarty T, Emery K, et al. Nat Mater 2005;4(11):864–8.
- [9] Zhang S, He C, Liu Y, Zhan X. J Chem Polym 2009;50(15):3595–9.
- [10] Cheng YJ, Yang SH, Hsu CS. Chem Rev 2009;109(11):5868–923.
- [11] Hou JH, Tan ZA, Yan Y, He YJ, Yang CH, Li YF. J Am Chem Soc 2006;128(14):4911–6.
- [12] Yu CY, Ko BT, Ting C, Chen CP. Sol Energy Mater Sol Cells 2009;93(5):613–20.
- [13] Li YF, Zou YP. Adv Mater 2008;20(15):2952–8.
- [14] Chang YT, Hsu SL, Chen GY, Su MH, Singh TA, Diau EWG, et al. Adv Funct Mater 2008;18(16):2356–65.
- [15] Li YW, Xue LL, Xia JH, Xu B, Wen SP, Tian WJ. J Polym Sci Pol Chem 2008;46(12):3970–84.
- [16] Li WW, Han Y, Chen YL, Li CH, Li BS, Bo ZS. Macromol Chem Phys 2010;211(8):948–55.
- [17] Wu PT, Xin H, Kim FS, Ren G, Jenekhe SA. Macromolecules 2009;42(22):8817–26.
- [18] Scharber M, Mühlbacher D, Koppe M, Denk P, Waldauf C, Heeger A, et al. Adv Mater 2006;18(6):789–94.
- [19] Sun YM. Polymer 2001;42(23):9495–504.
- [20] Mayer AC, Toney MF, Scully SR, Rivnay J, Brabec C, Scharber M, et al. Adv Funct Mater 2009;19(8):1173–9.
- [21] Chung DS, Kong H, Yun WM, Cha H, Shim KH, Kim YH, et al. Org Electron 2010;11(5):899–904.
- [22] Cates NC, Gysel R, Dahl JEP, Sellinger A, McGehee MD. Chem Mater 2010;22(11):3543–8.
- [23] Kline RJ, DeLongchamp DM, Fischer DA, Lin EK, Richter LJ, Chabinyc ML, et al. Macromolecules 2007;40(22):7960–5.
- [24] Cravino A, Roquet S, Aleveque O, Leriche P, Frere P, Roncali J. Chem Mater 2006;18(10):2584–90.
- [25] Shirota Y, Kageyama H. Chem Rev 2007;107(4):953–1010.
- [26] Pudzich R, Salbeck J. Synth Met 2003;138(1):21–31.
- [27] Medina A, Claessens CG, Rahman GMA, Lamsabhi AM, Mo O, Yanez M, et al. Chem Commun; 2008:1759–61.
- [28] Tamao K, Kodama S, Nakajima I, Kumada M, Minato A, Suzuki K. Tetrahedron 1982;38(22):3347–54.
- [29] Tsui B, Reddinger JL, Sotzing GA, Soloduchko J, Katritzky AR, Reynolds JR. J Mater Chem 1999;9:2189–200.
- [30] Iovu MC, Sheina EE, Gil RR, McCullough RD. Macromolecules 2005;38(21):8649–56.
- [31] Loewe RS, Khersonsky SM, McCullough RD. Adv Mater 1999;11(3):250–3.
- [32] Chen TA, Wu X, Rieke RD. J Am Chem Soc 1995;117(1):233–44.
- [33] Roquet S, Cravino A, Leriche P, Aleveque O, Frere P, Roncali J. J Am Chem Soc 2006;128(10):3459–66.
- [34] Sang GY, Zhou EJ, Huang Y, Zou YP, Zhao GG, Li YF. J Phys Chem C 2009;113(14):5879–85.
- [35] Shaheen SE, Brabec CJ, Sariciftci NS, Padinger F, Fromherz T, Hummelen JC. Appl Phys Lett 2001;78(6):841–3.

- [36] Lee RH, Liu LW. *Dyes Pigment* 2010;84(2):190–202.
- [37] Lee RH, Syu JY, Huang JL. *Polym Adv Technol*, in press, doi: 10.1002/pat.1730.
- [38] Maher AI, Klaus RH, Uladzimir ZH, Gerhard G, Steffi SF. *Sol Energy Mater Sol Cells* 2005;85(1):13–20.
- [39] Chang YT, Hsu SL, Su MH, Wei KH. *Adv Mater* 2009;21(20):2093–7.
- [40] Hoppe H, Sariciftci NS. *J Mater Chem* 2006;16(1):45–61.
- [41] Scully SR, McGehee MD. *J Appl Phys* 2006;100(3):034907–0034911.
- [42] Müller C, Ferenczi TAM, Mariano CQ, Frost JM, Bradley DDC, Smith P, et al. *Adv Mater* 2008;20(18):3510–5.
- [43] Svetlana SB, Maik B, Gijssbertus W, Harald H, Joachim L. *Adv Funct Mater* 2010;20(9):1458–63.
- [44] Yang KN, Jeroen KJ, Janssen RA, Michels AJM, Loos JC. *Macromolecules* 2004;37(6):2151–8.
- [45] Liao CH, Lee MT, Tsai CH, Chen CH. *Appl Phys Lett* 2005;86(20):203507.
- [46] Koster LJA, Strien WJ, Beek WJE, Blom PWM. *Adv Funct Mater* 2007;17(8):1297–302.
- [47] Lee RH, Lai HH. *Eur Polym J* 2007;43(3):715–24.
- [48] Vandewal K, Gadisa A, Oosterbaan WD, Bertho S, Banishoeib F, Severen IV, et al. *Adv Funct Mater* 2008;18(14):2064–70.
- [49] Kim YK, Cook S, Tuladhar SM, Choulis SA, Nelson J, Durrant JR, et al. *Nat Mater* 2006;5(3):197–203.
- [50] Chang YT, Hsu SL, Su MH, Wei KH. *Adv Funct Mater* 2007;17(16):3326–31.
- [51] Christoph W, Sariciftci NS. *J Mater Chem* 2004;14(7):1077–86.
- [52] Winder C, Matt G, Hummelen JC, Janssen RAJ, Sariciftci NS, Brabec CJ. *Thin Solid Films* 2002;403–404:373–9.
- [53] Kim Y, Choulis SA, Nelson J, Bradley DDC, Cook S, Durrant JR. *Appl Phys Lett* 2005;86(6):063502–4.
- [54] Sivula K, Ball ZT, Watanabe N, Fréchet JM. *Adv Mater* 2006;18(2):206–10.
- [55] Wienk MM, Kroon JM, Verhees WJH, Knol J, Hummelen JC, Paul AVH, et al. *Angew Chem Int Ed* 2003;42(29):3371–5.
- [56] Chen MH, Hou J, Hong Z, Yang G, Sista S, Chen LM, et al. *Adv Mater* 2009;21(42):4238–42.



## PAMAM dendrimer with a 1,2-diaminoethane surface facilitates endosomal escape for enhanced pDNA delivery

Geun-woo Jin<sup>a</sup>, Heebeom Koo<sup>b</sup>, Kihoon Nam<sup>a</sup>, Heejin Kim<sup>a</sup>, Seonju Lee<sup>a</sup>, Jong-Sang Park<sup>a,\*</sup>, Yan Lee<sup>a,\*</sup>

<sup>a</sup> Department of Chemistry, Seoul National University, 599 Gwanak-ro, Gwanak-gu, Seoul 151-747, Republic of Korea

<sup>b</sup> Biomedical Research Center, Korea Institute of Science and Technology, 39-1 Hawolgok-dong, Seongbuk-gu, Seoul 136-791, Republic of Korea

### ARTICLE INFO

#### Article history:

Received 3 August 2010

Received in revised form

4 October 2010

Accepted 10 October 2010

Available online 24 November 2010

#### Keywords:

Dendrimer

1,2-Diaminoethane moiety

Endosomal escape

### ABSTRACT

We synthesized a polyamidoamine (PAMAM) dendrimer with a 1,2-diaminoethane surface by an amidation reaction of PAMAM (G3.5) with diethylenetriamine (DET; PAM-DET). By titration and a lactate dehydrogenase (LDH) assay, we showed that PAM-DET has excellent buffering capacity and pH-dependent membrane destabilizing activity during the acidification process from pH 7.4 to pH 5.5. Further, through transfection experiments with various PAMAM derivatives that have different surface amines, we showed that the high transfection efficiency of PAM-DET was due to the introduction of a 1,2-diaminoethane moiety. Even though the intracellular uptake of PAM-DET was not significantly different from that of PAMAM, its transfection efficiency was highly dependent upon the presence of nigericin—an inhibitor of endosomal acidification—which verified that the increased transfection efficiency by PAM-DET originated from the facilitation of endosomal escape during endosome acidification. DNA-delivery efficiency can be greatly enhanced by this simple modification and small change to the surface amine structure.

© 2010 Elsevier Ltd. All rights reserved.

### 1. Introduction

Polyamidoamine (PAMAM) dendrimers are nanoscale biomaterials with highly controlled branched structures and monodispersed array ( $M_w/M_n < 1.01$ ); they are recognized as a unique class of synthetic macromolecules replacing traditional synthetic polymers such as linear, cross-linked, and branched polymers with relatively broad molecular weight distributions [1,2]. PAMAM dendrimers are often referred to as “artificial proteins” since their structures are similar to those of globular proteins. From earlier to higher generation, PAMAM dendrimers closely match the sizes and shapes of natural proteins. For example, PAMAM G3.0, G4.0, and G5.0 have approximately the same size and shape as insulin ( $\sim 30$  Å), cytochrome C ( $\sim 40$  Å), and haemoglobin ( $\sim 55$  Å), respectively [3]. In addition, PAMAM dendrimers have high potential in gene delivery because the structure resembles that of the histone protein core around which the DNA in chromatin is wrapped [4].

The globular structure of PAMAM dendrimers can be divided into two parts: the surface that has primary amine groups and the interior that contains tertiary amine groups, which are closely

related with the capability of the complex formation with DNA and efficient delivery into the cytosol or nucleus. Due to their relatively high  $pK_a$  value ( $pK_a$  9.2), the primary amine groups undergo protonation at neutral pH so that there is a high density of positive charges on the surface of PAMAM dendrimers, which enables the formation of a nano-sized complex with negatively charged DNA (a polyplex) through electrostatic interactions [5,6]. Since excess amounts of dendrimers are usually used for polyplex formation, the DNA-dendrimer polyplex exhibits a net positive charge, which facilitates interactions with negatively charged glycoproteins and phospholipids on the surface of cells to promote entry into the cell by endocytosis [7,8].

Due to their low  $pK_a$  ( $pK_a$  6.7), tertiary amine groups in the PAMAM interior are protonated only at acidic pH environments, such as that in the endosome [9]. Previous studies revealed that the escape from the early endosome is one of the most important steps for successful transfection [10,11]. According to the proton sponge hypothesis suggested by Behr et al., the buffering effect of the low  $pK_a$  moieties in polycations, which are protonated at acidic endosomal pH, induces the excessive uptake and accumulation of protons and its counterions in the endosome causing disruption of the endosomal membrane possibly by mechanical or osmotic swelling [12]. Although the detailed role of the PAMAM dendrimer as a DNA-delivery carrier leading to gene expression is not fully

\* Corresponding authors. Tel.: +82 2 880 4344; fax: +82 2 871 2496.  
E-mail address: [gacn@snu.ac.kr](mailto:gacn@snu.ac.kr) (Y. Lee).

understood and is being investigated, it has been suggested that the high buffering capacity of the dendrimer at endosomal pH values facilitates endosomal escape. However, the transfection efficiency of PAMAM dendrimers is still not sufficiently satisfactory for clinical use; further investigation is needed to increase its transfection efficiency [13,14].

Recently, it has been reported that introduction of a 1,2-diaminoethane moiety into cationic polymers can be a good strategy to enhance transfection efficiency. The 1,2-diaminoethane moiety undergoes a distinctive two-step protonation process from the mono-protonated state (*gauche* form) at neutral pH to di-protonated state (*anti* form) at weakly acidic pH, thereby exhibiting an effective buffering function in the early endosome (Fig. 1). Furthermore, the di-protonated state of the 1,2-diaminoethane moiety shows strong membrane destabilizing activity, although the mono-protonated state causes minimal membrane destabilization. Some of the recently developed gene-delivery carriers have exceptional transfection efficiency due to the endosomal destabilizing activity of 1,2-diaminoethane moieties [15,16].

In this paper, we combine the structural uniqueness of PAMAM dendrimers with the strong endosomal destabilizing activity of 1,2-diaminoethane moieties. Assuming that the transfection efficiency limit of PAMAM dendrimers is due to inefficient endosomal escape, enhancement of transfection efficiency is expected due to the endosomal destabilizing activity of the 1,2-diaminoethane moiety. In addition, the mechanism of transfection efficiency enhancement will provide important information for the further development of an ideal polymer-based gene-delivery carrier.

## 2. Experimental section

### 2.1. Materials

PAMAM (G3.0, 4.0, 5.0), PAM-OH, PEI 25 kDa, methyl acrylate (MA), diethylenetriamine (DET), dipropylenetriamine (DPT), 1,5-pentanediamine (PD), nigericin, chloroquine, 3-[4,5-dimethylthiazol-2-yl]-2,5-diphenyltetrazolium bromide (MTT), methanol (MeOH), and deuterium oxide (D<sub>2</sub>O) were purchased from Sigma–Aldrich (St. Louis, MO). Methanol-d<sub>4</sub> (MeOD) was purchased from Cambridge Isotope Laboratories Inc., (Andover, MA, USA). The lactate dehydrogenase (LDH) Cytotoxicity Detection kit was purchased from Clontech Laboratories, Inc. (Mountain View, CA, USA). Luciferase 1000 Assay System and Reporter Lysis Buffer were purchased from Promega (Madison, WI). Dulbecco's Modified Eagle's Medium (DMEM), trypsin-ethylenediaminetetraacetic acid (EDTA), antibiotic-antimycotic and fetal bovine serum (FBS) were purchased from GIBCO (Gaithersburg, MD). Phosphate-buffered saline (PBS) was purchased from Cambrex Bio Science (Walkersville, MD). Label ITR<sup>®</sup> CX-Rhodamine Nucleic acid labeling kit was purchased from Mirus Bio (Japan). Micro BCA<sup>™</sup> Protein Assay Kit was purchased from Pierce (Rockford, IL). All chemicals were used without further purification. The firefly luciferase expression plasmid pCN-Luci was constructed by subcloning *Photinus pyralis* luciferase cDNA with the 21 amino acid nuclear localization signal of the Simian vacuolating virus 40 (SV40) large T antigen into pCN.

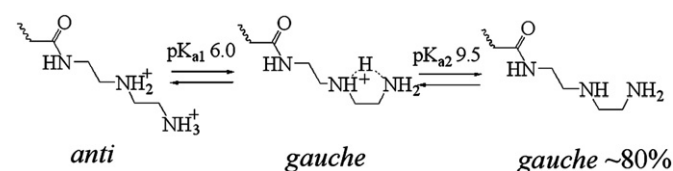


Fig. 1. Two-step protonation of the 1,2-diaminoethane moiety with a distinctive *gauch-anti* conformational change.

### 2.2. Synthesis of PAMAM derivatives

A mixture of PAMAM (G3.0) and 100 equivalents of MA per surface primary amine group of the PAMAM dendrimer in MeOH were stirred at 37 °C (Fig. 2). After 1 d, MeOH and excess MA were evaporated under reduced pressure. For introduction of DET (DPT, PD), the resulting PAMAM (G3.5) was reacted with 100 equivalents of DET (DPT, PD) per surface methyl ester group of the PAMAM (G3.5) for 3 d at 50 °C. The resulting mixture was dialyzed against distilled water and lyophilized. Products were analyzed using <sup>1</sup>H NMR (Fig. S1). (<sup>1</sup>H NMR (300 MHz, MeOD,  $\delta$  ppm) of PAMAM (G3.5):  $\delta$  2.40–2.42 (t, –NHCH<sub>2</sub>CH<sub>2</sub>CONH–),  $\delta$  2.42–2.50 (t, –NHCH<sub>2</sub>CH<sub>2</sub>COO–),  $\delta$  2.53–2.65 (m, –CH<sub>2</sub>CH<sub>2</sub>NHCH<sub>2</sub>– and –NHCH<sub>2</sub>CH<sub>2</sub>NHCH<sub>2</sub>–),  $\delta$  2.73–2.90 (m, –NHCH<sub>2</sub>CH<sub>2</sub>CONH– and –NHCH<sub>2</sub>CH<sub>2</sub>COO–),  $\delta$  3.22–3.36 (t, –CONHCH<sub>2</sub>CH<sub>2</sub>NH–),  $\delta$  3.65–3.72 (s, –COOCH<sub>3</sub>)).

### 2.3. Acid–base titration

An acid–base titration was performed for the comparison of the buffering capacity of PAM-DET with that of PAM-OH (G4.0) and PAMAM (G4.0). In this assay, each dendrimer was dissolved in 10 mL of water at a concentration of 10  $\mu$ M, and then 100  $\mu$ L of 1 N NaOH was added to each solution to adjust the pH into the alkaline range. HCl (0.01 N) was used as the titrant to lower the pH to acidic conditions.

### 2.4. LDH assay

The membrane destabilization activity according to pH change was examined by measuring the activity of cytosolic LDH released from cells into the media. HeLa (human cervical cancer cell) cells were seeded on 96-well plates and incubated overnight in 100  $\mu$ L of DMEM containing 10% FBS. The cell culture medium was changed to 100  $\mu$ L of the PAMAM (G4.0) and PAM-DET solutions with various concentrations in 20 mM HEPES buffered saline (pH 7.4) or 20 mM MES buffered saline (pH 5.5). After incubation at 37 °C for 1 h, samples were centrifuged at 180 $\times$  g. Aliquots of each sample (100  $\mu$ L) were collected for the LDH assay. The LDH activity was determined using a commercial kit according to the manufacturer's protocol, which determines the LDH activity from the amount of diformazan that is produced through the two-step reduction of nicotinamide adenine dinucleotide (NAD) and nitrobluetetrazolium in the presence of LDH and diaphorase. The amount of the diformazan was measured from the absorbance at 570 nm using a microplate reader (Molecular Devices Co., Menlo Park, CA).

### 2.5. Zeta potential and size determination

The zeta potential and size distribution of the dendrimer/plasmid DNA (pDNA) complexes were analyzed using a Malvern Zetasizer Nano ZS (Malvern Instruments Ltd., Worcestershire, U.K.) at 37 °C. PAMAM (G4.0) and PAM-DET polyplex solutions with varying charge ratios were prepared with a pDNA concentration of 10  $\mu$ g/mL in 10 mM Tris–HCl (pH 7.4) buffer.

### 2.6. Cell lines and culture

Human cervical cancer HeLa cells and mouse myoblast C2C12 cells were grown in DMEM with 10% FBS. HeLa and C2C12 cells were incubated in plastic tissue culture dishes (Falcon) in a 5% CO<sub>2</sub> humidified incubator.

### 2.7. In vitro transfection

HeLa and C2C12 cells were seeded at 30,000 cells/well in 24-well plates in 600  $\mu$ L of DMEM containing 10% FBS and incubated at

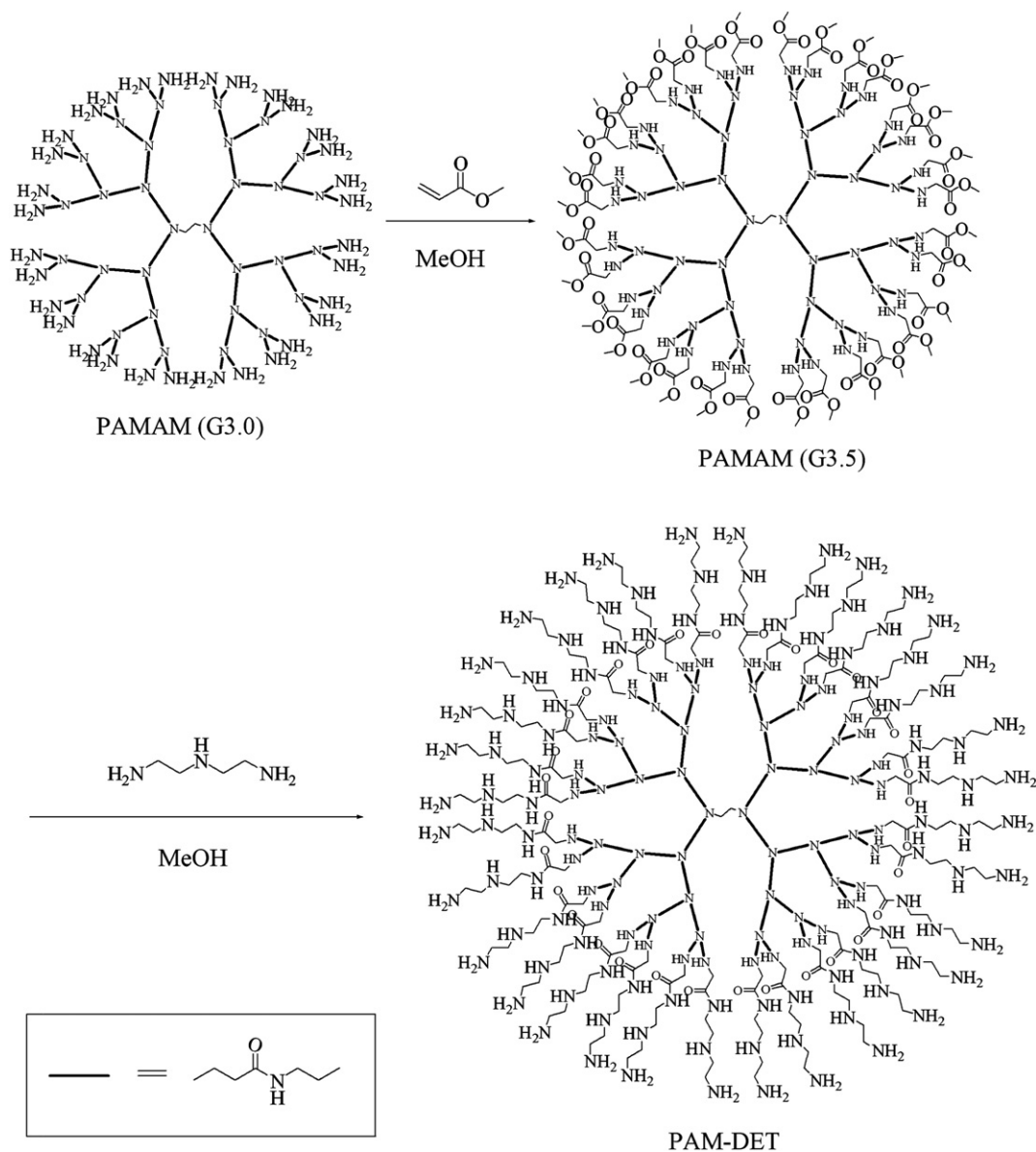


Fig. 2. The synthetic scheme of PAM-DET.

37 °C for 1 d before transfection. Polyplexes were prepared with 1  $\mu\text{g}$  of pDNA at different charge ratios in 120  $\mu\text{L}$  of FBS-free medium, and the mixtures were incubated for 30 min at room temperature. After adding the polyplex, the cells were further incubated for 48 h. For the assay, growth medium was removed and the cells were washed with PBS and lysed for 30 min at room temperature with 120  $\mu\text{L}$  of reporter lysis buffer (Promega, Madison, WI). Luciferase activity in the transfected cells was measured using an LB 9507 luminometer (Berthold, Germany) with 10  $\mu\text{L}$  of the lysate dispensed into a luminometer tube and 50  $\mu\text{L}$  of Luciferase Assay Reagent injected automatically. All experiments were performed in triplicate.

#### 2.8. MTT cytotoxicity assay

To measure the cytotoxicity of the polyplex, MTT assays were performed. HeLa and C2C12 cells were seeded at 6000 cells/well in 96-well plates in 120  $\mu\text{L}$  of DMEM containing 10% FBS and incubated at 37 °C for 1 d prior to polyplex addition. Polyplexes were

prepared with 0.2  $\mu\text{g}$  of pDNA at different charge ratios in 24  $\mu\text{L}$  of FBS-free medium. After adding the polyplex, the cells were further incubated for 48 h. The cells were then washed with PBS, followed by the addition of 26  $\mu\text{L}$  of filtered MTT solution (2 mg/mL in PBS). After incubation at 37 °C for 4 h, the medium was removed from the well and 150  $\mu\text{L}$  of DMSO was added to dissolve the insoluble formazan crystals. The absorbance was measured at 570 nm using a microplate reader (Molecular Devices Co., Menlo Park, CA) and the cell viability was calculated as a percentage relative to untreated control cells.

#### 2.9. Labeling of pDNA

Labeling of pDNA was performed using a Label IT<sup>®</sup> CX-Rhodamine Nucleic Acid Labeling Kit. Nuclease-free water (35  $\mu\text{L}$ ), 5  $\mu\text{L}$  of 10 $\times$  Labeling buffer A and 5  $\mu\text{L}$  of plasmid DNA sample (1 mg/mL) were mixed together. After the addition of 5  $\mu\text{L}$  of Label IT<sup>®</sup> Reagent, the mixture was incubated at 37 °C for 1 h. The labeled pDNA was purified by ethanol precipitation.



## 2.10. FACS analysis

HeLa cells were seeded at a density of 30,000 cells/well in a 24-well plate in DMEM medium containing 10% FBS and incubated at 37 °C for 1 d prior to transfection. Before transfection, the medium of each well was exchanged with fresh medium containing 10% FBS. The cells were incubated with polyplex solutions (2 µg of rhodamine-labeled pDNA) for 8 h at 37 °C. The medium was then aspirated from the wells and cells were washed 3 times with PBS. Cells were incubated with trypsin–EDTA for 5 min and detached from the well by washing with PBS. The trypsinized cells were collected by centrifugation at 1000 rpm and suspended in 1 mL PBS containing 1% FBS. The cellular uptake of rhodamine-labeled pDNA in 10,000 cells was examined using the FACS Canto II with an excitation wavelength of 488 nm (Becton Dickinson, Mountain View, CA).

## 2.11. Transfection in the presence of nigericin and chloroquine

Transfection experiments were performed with or without nigericin and chloroquine to investigate the mechanism of transfection enhancement in the PAM-DET polyplex system. HeLa cells were seeded at 30,000 cells/well in 24-well plates in 600 µL of DMEM containing 10% FBS and incubated at 37 °C for 1 d. Then, 2.5 µM nigericin or 100 µM chloroquine was added to the cells before transfection. After incubation for 4 h, cells were washed with PBS and maintained in DMEM containing 10% FBS at 37 °C for 2 d. Cell lysis and luciferase assays were performed using the same protocol described above. To compare the RLU values of PAMAM (G4.0) and PAM-DET in the presence or absence of nigericin or chloroquine, parametrical analysis using the Student's *t*-test was performed.

## 3. Results and discussion

### 3.1. Synthesis and characterization of PAMAM derivatives

For the introduction of a 1,2-diaminoethane moiety into the PAMAM dendrimer, ester-surface PAMAM (G3.5) was synthesized from PAMAM (G 3.0), as described by Tomalia et al. [17]. PAM-DET was synthesized by the aminolysis of PAMAM (G3.5) with excess DET (Fig. 2). Comparison of the integration ratio of the proton peaks (c and e–g) reveals that 89% of dendrimer surface was substituted by DET moiety (Fig. S1). The imperfect introduction of DET moiety, contrasting to the nearly perfect introduction of ethylenediamine to dendrimer surface during the synthesis of PAMAM dendrimer, may be related with the longer chain length and higher steric hindrance of DET than ethylenediamine. Similarly, other PAMAM derivatives which will be discussed below (PAM-PD and PAM-DPT) showed similar conjugation efficiencies of about 90%. Based on the <sup>1</sup>H NMR analysis, we calculated the molecular weights of PAMAM derivatives and the number of amines and size of the PAMAM derivatives. The 1,2-diaminoethane moiety was in a mostly mono-protonated state (*gauche* form) at pH 7.4; hence, one 1,2-diaminoethane moiety in PAM-DET was considered as one positive charge [14]. We calculated the size of PAM-DET on the basis of the average length of newly added carbon–carbon (C–C) and carbon–nitrogen (C–N) bonds and the molecular diameter of the PAMAM (G4.0) dendrimer [18]. In this calculation, we also considered the angle between 3 atoms (109.5° for C–C–C bond and 120° for C–N–C bond) and between adjacent branch points in dendrimers (45°) as described below [19]. All these characteristics of PAMAM derivatives are summarized in Table 1.

**Table 1**  
Properties of PAMAM derivatives.

	PAMAM (G4.0)	PAM-PD	PAM-DET	PAM-DPT	PAMAM (G5.0)
Molecular weight	14214 <sup>a</sup>	16398 <sup>b</sup>	16428 <sup>b</sup>	17967 <sup>b</sup>	28825 <sup>a</sup>
No of protonatable amines	128	122	178	178	256
Dendrimer diameter (Å)	40	44 <sup>c</sup>	45 <sup>c</sup>	48 <sup>c</sup>	54

<sup>a</sup> Molecular weight provided by the manufacturers.

<sup>b</sup> Molecular weight determined by <sup>1</sup>H NMR analysis of each polymer.

<sup>c</sup> Dendrimer diameter calculated from the average bond lengths between carbon–carbon and carbon–nitrogen atoms.

### Diameter of PAMAM derivative

$$\begin{aligned}
 &= \text{Diameter of PAMAM (G4.0)} \\
 &+ 2 \left[ \left( \text{number of C–C} \times \text{bond length of C–C} \times \sin \frac{109.5^\circ}{2} \right) \right. \\
 &+ \left. \left( \text{number of C–N} \times \text{bond length of C–N} \times \sin \frac{120^\circ}{2} \right) \right] \\
 &\times \cos 45^\circ
 \end{aligned}$$

### 3.2. Buffering capacity and pH-dependent membrane destabilizing ability of the dendrimers

Previous studies revealed that an essential factor for high transfection efficiency is efficient endosomal escape of DNA cargos, which can often be accomplished by the endosomal disruption of polycations [20–22]. Endosomal disruption can be facilitated by protonation of polymers in endosomal acidic compartments (the proton sponge effect). Hence, the development of polycations with high buffering capacity between neutral pH and early endosomal pH (pH 7.4 and pH 5.5, respectively) is recommended for successful transfection [23]. In this regard, the buffering capacity of PAMAM (G4.0) and PAM-DET was compared by titration over the pH range of 2–11 (Fig. 3a). Considering the ionization degree ( $\alpha$ ) and total number of amines in each dendrimer, the number of protonated amines was calculated and plotted against pH, as shown in Fig. 3b [24]. Fig. 3a shows that PAMAM (G4.0) exhibits two distinct protonation steps. Compared with the titration curve of PAM-OH (G4.0), which has only internal tertiary amine groups without any primary amine on the surface, the primary amine groups in PAMAM (G4.0) were protonated in the first step from pH 10 to pH 7, while the tertiary amine groups were protonated in the second step from pH 7 to pH 3.

Protonation of PAM-DET shows even more dramatic features. As shown in Fig. 3b, PAM-DET has about 2-times higher buffering capacity than PAMAM (G4.0) during acidification from pH 7.4 to pH 5.5, which is likely due to the 57 more protonatable secondary amine groups (in addition to 64 internal tertiary amine groups) on PAM-DET. As mentioned above, the 1,2-diaminoethane moiety maintains a mainly mono-protonated state at pH 7.4; the di-protonated state is generated during the acidification procedure.

Furthermore, the potential to destabilize the early endosomal membrane was examined. Since the endosomal membrane initially originates from the plasma membrane, the destabilizing activity of the plasma membrane at the endosomal pH can be a reasonable estimate of the activity of the actual endosomal membrane destabilization. For the estimation, we measured the enzymatic activity of cytosolic LDH liberated from cells into media [25]. Fig. 4 shows that the activity of LDH liberated from HeLa cells incubated with PAMAM (G4.0) was low regardless of the pH value. The activity of LDH from the cells incubated with PAM-DET at pH 7.4 was the same as that of PAMAM (G4.0), while the activity of LDH at pH 5.5 was

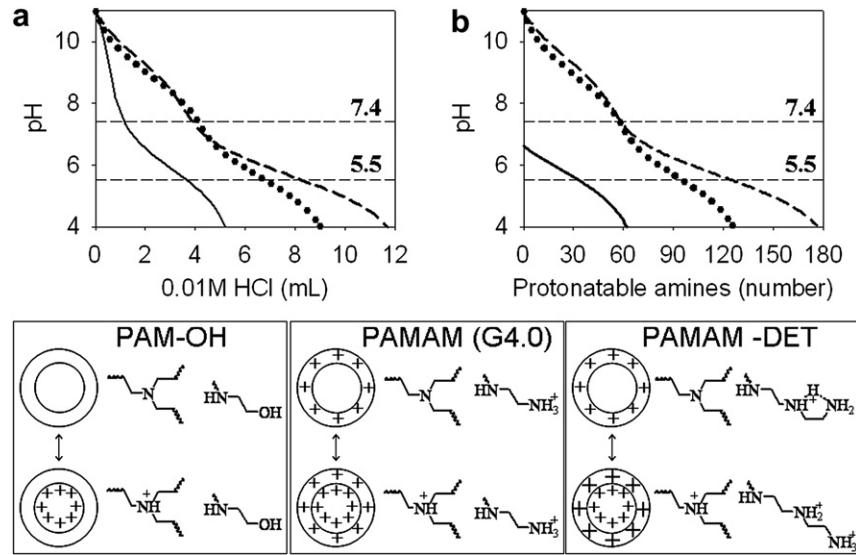


**Fig. 3.** Comparison of buffering capacity of PAM-OH (G4.0), PAMAM (G4.0), and PAM-DET. (a) acid-base titration profile (b) change in pH against the protonated numbers of amines in PAM-OH (solid line), PAMAM (dotted line), and PAM-DET (dashed line).

surprisingly increased. In other words, PAM-DET can destabilize the biomembrane only at the early endosomal pH due to the di-protonated state of the 1,2-diaminoethane moiety. Based on the high buffering capacity and pH-dependent membrane destabilization activity of PAM-DET, it is likely that PAM-DET facilitates effective endosomal escape.

### 3.3. Analysis and characterization of the polyplex formation

As described above, protonated primary amine groups in PAMAM (G4.0) and mono-protonated 1,2-diaminoethane moieties of PAM-DET provide positive charges on the surface of each dendrimer at neutral pH. The positively charged dendrimers can form polyplexes with negatively charged pDNA through electrostatic interactions. To measure the stoichiometry of polyplex formation, charge ratios between the positive charges of dendrimers and negative charges of pDNA were used. The number of positive charges was calculated from the number of primary amine groups of PAMAM (G4.0) or the number of mono-protonated 1,2-diaminoethane moieties of PAM-DET because protonation of internal tertiary amines of both dendrimers and the di-protonation of 1,2-diaminoethane moieties in PAM-DET can only be accomplished at

an acidic pH (Table 1). The number of negative charges was also calculated based on the fact that pDNA has one phosphate group per 330 Da of molar mass [26].

At various charge ratios, the hydrodynamic diameter and zeta-potential of the polyplex from PAMAM (G4.0) and PAM-DET were measured by the light scattering method. As shown in Fig. 5a, each

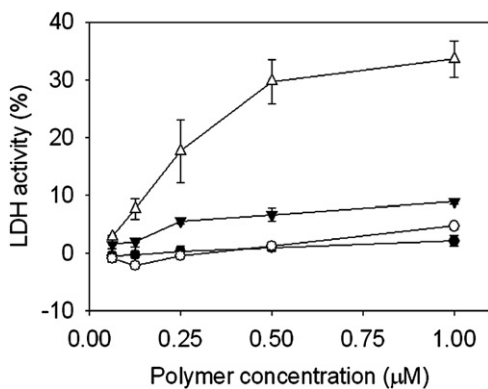


**Fig. 4.** pH-dependent membrane destabilizing activity of PAMAM (G4.0) at pH 7.4 (●) and 5.5 (▼) and PAM-DET at pH 7.4 (○) and 5.5 (△). X axis means the concentration of protonated amine groups of PAMAM (G4.0) and PAM-DET at pH 7.4. Error bars indicate standard deviation.

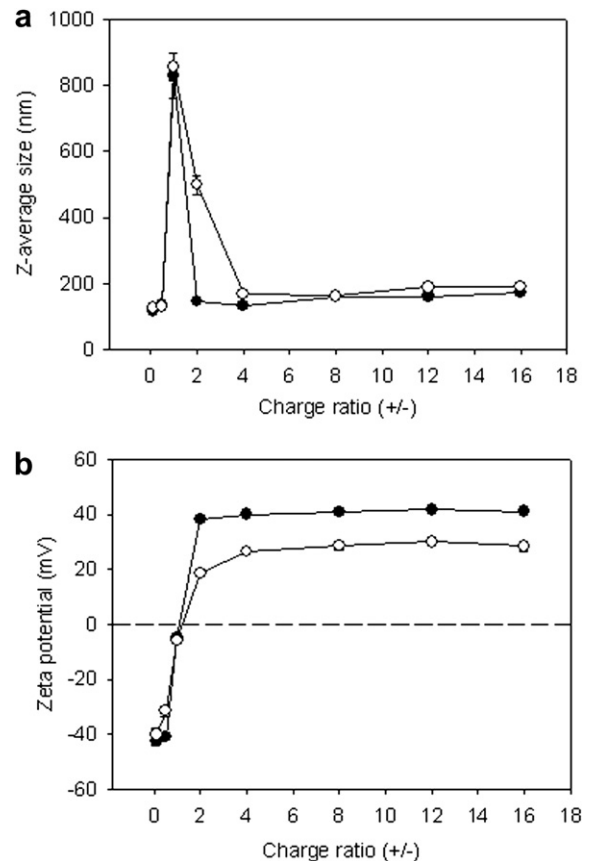


**Fig. 5.** Change in the size and zeta-potential of PAMAM (G4.0) and PAM-DET polyplexes according to charge-ratio variation. (a) Hydrodynamic diameter and (b) zeta-potential: (●) PAMAM, (○) PAM-DET. Error bars indicate standard deviations.

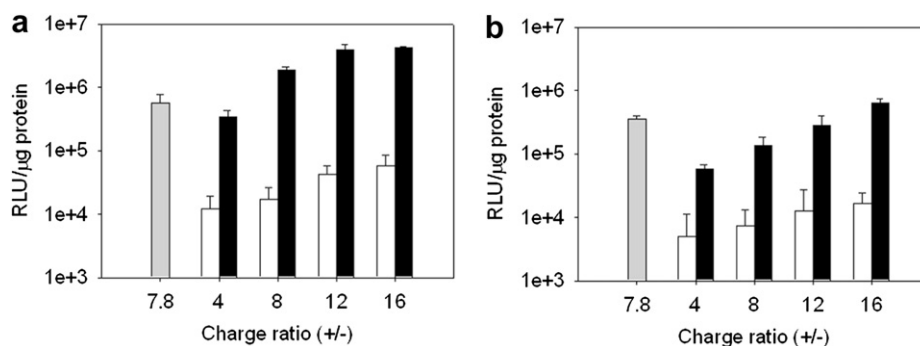


**Fig. 6.** In vitro transfection efficiency in (a) HeLa and (b) C2C12 cells with PAMAM (G4.0) (white bars), PAM-DET (black bars) and PEI 25 kDa (gray bars) polyplexes at varying charge ratios, which was determined by luciferase assays. Error bars indicate standard deviations.

polyplex had the critical charge ratio of 1 with a large size of about 800–900 nm. Considering that the zeta-potential of each polyplex was close to zero at this charge ratio (Fig. 5b), the large-sized particles were supposed to be the aggregation between polyplexes due to the neutralization of the charges and insufficient electrostatic repulsive stabilization [27]. By addition of the cationic dendrimers over the critical charge ratio, the size of both polyplexes can be maintained below 200 nm with a unimodal size distribution (Fig. S2). Both polyplexes in this size range exhibited almost constant positive zeta-potentials: +40 mV for the PAMAM (G4.0) polyplex and +30 mV for the PAM-DET polyplex. It is supposed that the relatively low positive zeta-potential of PAM-DET polyplex comparing to PAMAM polyplex is due to the imperfect conjugation efficiency of DET moiety on the surface of dendrimer as mentioned in Section 3.1, resulting to the loss of positive charge of dendrimer at pH 7.4.

#### 3.4. In vitro transfection efficiency and cytotoxicity

The transfection efficiencies of the luciferase gene against two cancer cell lines (HeLa and C2C12) were compared between the PAMAM (G4.0), PAM-DET and PEI (25 kDa), which is a well-known polymeric transfection reagent [28,29]. The transfection efficiency data are shown in Fig. 6. In both cell lines, the PAM-DET polyplexes exhibit high transfection efficiency, which was almost 10–20 times greater than that of PAMAM (G4.0) polyplexes and 2–7 times greater than that of PEI 25 kDa. The luciferase gene expression of PAM-DET in HeLa cells was nearly one order of magnitude higher than in C2C12 cells, so PAM-DET was able to transfect HeLa cells more efficiently than C2C12 cells. Furthermore, the higher the charge ratio, the higher the overall transfection efficiency of both polyplexes.

The cytotoxicity of the polyplex was evaluated by the MTT cell viability assay [30]. Neither polyplex was cytotoxic at any charge ratios used in this study (Fig. S3).

#### 3.5. Structure-transfection efficiency relationship

To elucidate how structural factors are related to the significant enhancement of transfection efficiency of PAM-DET comparing to PAMAM (G4.0), we synthesized other PAMAM derivatives with variations in the surface moiety. It was previously reported that the transfection efficiency of PAMAM dendrimers was related to the size of the dendrimers; larger dendrimers generally had higher transfection efficiency than smaller dendrimers [31]. Therefore, PAMAM derivatives with different sizes were prepared and the molecular diameter was estimated by the calculation in Section 3.1. PAM-PD and PAM-DPT were synthesized by the aminolysis of PAMAM (G3.5) with pentaethylenediamine (PD) and dipropylene-triamine (DPT), respectively. By comparing the integration ratio of the proton peaks (c and e–h) in Fig. S1, the introduction of 90% PD and 89% DPT on the surface of the PAMAM dendrimer was confirmed. The calculated physicochemical characteristics of all the PAMAM derivatives are summarized in Table 1.

The PD moiety has the same chain length as the 1,2-diaminoethane moiety but has a central methylene group instead of the secondary amine that is in 1,2-diaminoethane [32]. Therefore, PAM-PD might be a useful control to elucidate the effect of the central secondary amine groups of PAM-DET. Although the 1,3-diaminopropane moiety of PAM-DPT has a secondary amine in the middle of the chain, it does not undergo the characteristic *gauche-anti* type of protonation process with distinct  $pK_a$  values as clearly shown in the protonation of the 1,2-diaminoethane moiety. Therefore, PAM-DPT can be used as a control to examine the influence of pH-dependent protonation on transfection efficiency [33].

Fig. 7 compares the transfection efficiency of the dendrimer derivatives in HeLa cells. There is no strong correlation between dendrimer size and transfection efficiency. Although PAMAM (G5.0) (54 Å) showed somewhat higher transfection efficiency than PAMAM (G4.0) (40 Å), two middle-sized dendrimers, PAM-DET (45 Å) and PAM-DPT (48 Å) showed even higher transfection efficiency than the larger

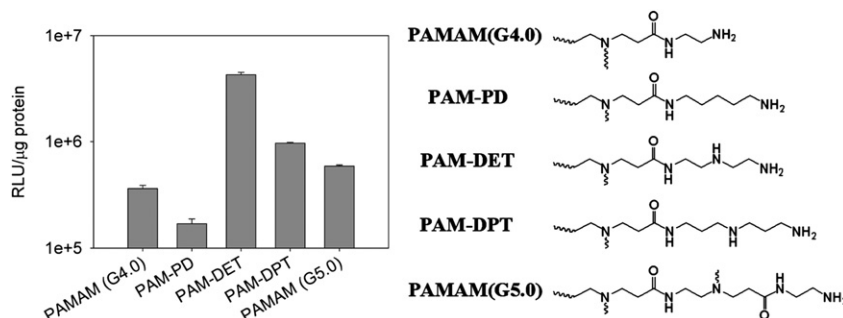


**Fig. 7.** Comparison of the transfection efficiency in HeLa cells with various PAMAM derivative polyplexes (Charge ratio = 1:8). Error bars indicate standard deviations.

PAMAM (G5.0). Also, PAM-PD, which has a larger size (44 Å) than PAMAM (G4.0), showed significantly lower transfection efficiency than PAMAM (G4.0). The importance of the secondary amines can be demonstrated by comparison of the transfection efficiency between PAM-PD, PAM-DET and PAM-DPT. However, the high transfection efficiency of PAM-DET over other PAMAM derivatives, especially PAM-DPT, can not be explained by the existence of secondary amine group and the size effect but by the buffering capacity and endosome destabilization effect. As shown in Fig. S4, the order of the buffering capacity of PAMAM derivatives coincided with the order of transfection efficiency shown in Fig. 7 (PAM-DET > PAM-DPT > PAMAM (G5.0) > PAMAM (G4.0) > PAM-PD). Furthermore, remarkable pH-dependent membrane destabilization ability of PAM-DET comparing with all other PAMAM derivatives (Fig. S5) strongly supported that the high transfection efficiency of PAM-DET was closely related to the endosome disrupting activity of 1,2-diaminoethane moiety. Based on these results, we can verify that the introduction of the 1,2-diaminoethane moiety onto the surface of dendrimers is the key-factor in the enhancement of transfection efficiency.

### 3.6. Cellular uptake

Flow cytometry analysis was performed to examine the influence of the 1,2-diaminoethane on the internalization of the

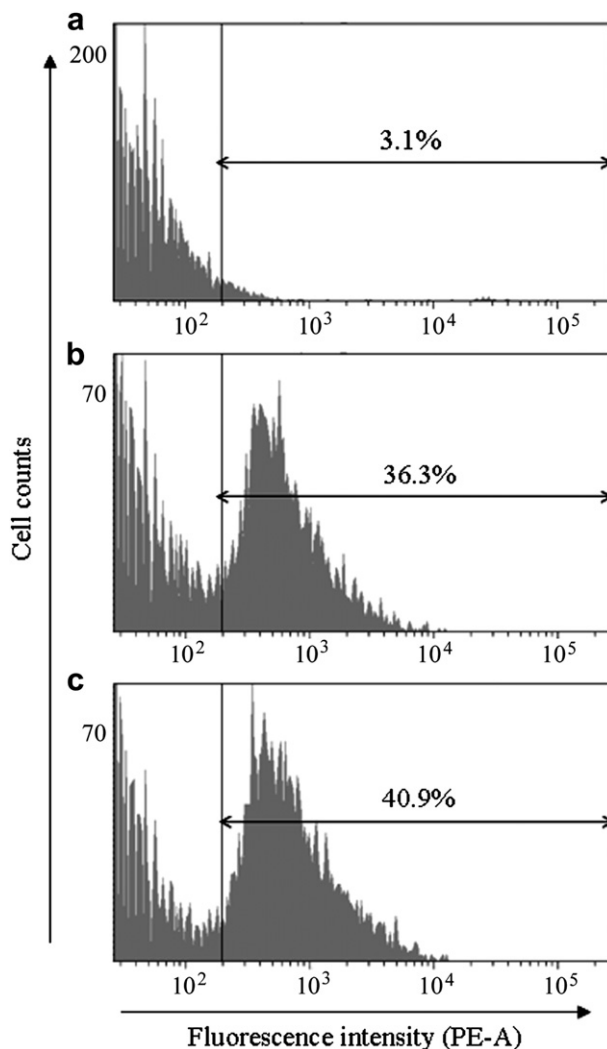


**Fig. 8.** Cellular uptake of rhodamine-labeled pDNA in HeLa cells (a) cells only, (b) PAMAM (G4.0) polyplex, (c) PAM-DET polyplex.

polyplexes. The intracellular fluorescence of HeLa cells that had been transfected with rhodamine-labeled pDNA/dendrimer polyplexes was compared (Fig. 8). There was no significant difference of fluorescence distributions between PAMAM (G4.0) and PAM-DET polyplexes. Therefore, it was concluded that the higher transfection efficiency of PAM-DET is not derived from an enhancement in cellular uptake of the polyplexes [34,35].

### 3.7. Endosomal disruption

Finally, transfection experiments were performed in the presence of nigericin or chloroquine to determine if the enhanced transfection efficiency of PAM-DET is due to efficient endosomal escape (Fig. 9). Chloroquine is a well-known transfection helper reagent with an endosome buffering capacity [34,36]. Chloroquine facilitates release of polyplexes from the endosome even if the polyplexes do not have endosome disrupting activity. In other words, the transfection efficiency of the gene delivery carriers that have low endosome disrupting activity would be increased by the addition of chloroquine, but the gene delivery carriers that have enough endosome disrupting activity would show little changes in transfection efficiency. In fact, the transfection efficiency of PAMAM (G4.0) was significantly ( $P < 0.01$ ) enhanced by chloroquine treatment. In contrast, the transfection efficiency of PAM-DET was slightly decreased in the presence of chloroquine. We hypothesized that PAM-DET, unlike PAMAM (G 4.0), already possesses enough endosomal destabilization activity so that no further enhancement could be obtained by treatment with chloroquine.

Nigericin is an inhibitor of endosomal acidification. Nigericin is an inhibitor of endosomal acidification [37,38]. By the co-treatment of nigericin, the endosomal escape of gene delivery carriers was significantly inhibited. Therefore, nigericin can suppress the transfection of the gene delivery carriers with high endosomal escape activity the most effectively. Even though PAMAM (G4.0) showed some increase of transfection, PAM-DET exhibited only 20% of its transfection efficiency when co-incubated with nigericin. This result strongly supports that transfection of PAM-DET proceeds mainly through an endosomal acidification-dependent pathway.

The dependence of transfection efficiency on transfection time was also investigated (Fig. S6). When HeLa cells were transfected with PAMAM (G4.0), gene expression gradually increased after 4 h of transfection, and expression continued to increase with an unsatisfactory efficiency up to 24 h after transfection. While

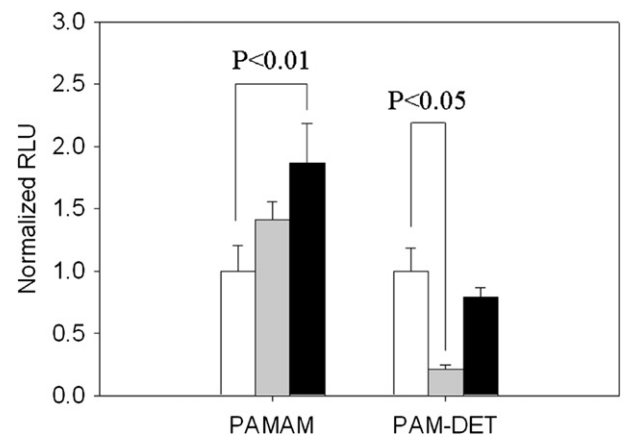


**Fig. 9.** Effect of nigericin or chloroquine treatment on the transfection efficiency of PAMAM (G4.0) and PAM-DET polyplexes at a charge ratio = 1:8. RLU values in the presence of nigericin (gray bars) or chloroquine (black bars) were normalized as the relative values comparing to RLU values without nigericin and chloroquine (white bars). Error bars indicate standard deviations.

expression in cells that had been transfected with PAM-DET increased at 2 h after transfection, there was a sharp increase from 4 h to 12 h, which reached a maximum plateau 12 h after transfection. The rapid induction of gene expression in cells transfected with PAM-DET versus PAMAM (G4.0) provides strong supporting evidence of the efficient and fast endosomal escape of PAM-DET polyplexes [39].

#### 4. Conclusion

We can greatly enhance the transfection efficiency of PAMAM dendrimers by the introduction of the 1,2-diaminoethane moiety on the surface of PAMAM. Detailed comparative analysis with various PAMAM derivatives revealed that the 1,2-diaminoethane moiety on the surface of PAM-DET is essential for enhancement of transfection efficiency. The 1,2-diaminoethane moiety does not significantly influence the intracellular uptake of polyplexes, but facilitates endosomal escape by the high buffering capacity and membrane destabilizing activity during endosomal acidification. The augmentation of transfection efficiency provides an important starting point for future development of synthetic gene delivery vehicles. The surface modification of 1,2-diaminoethane moieties can be a simple and effective method to construct an efficient carrier system for the successful intracellular delivery of biomacromolecules.

#### Acknowledgements

This work was supported by the Research Settlement Fund for new faculty of Seoul National University (SNU), Basic Science Research Program (2010-0007118) through the National Research Foundation of Korea (NRF), and a grant from the Gene Therapy Project (M10534030004-09N3403-00410) of the Ministry of Education, Science and Technology. This research was supported by the Converging Research Center Program through the National Research Foundation of Korea(NRF) funded by the Ministry of Education, Science and Technology (2009-0093632)

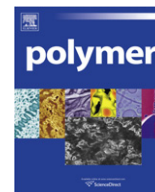
#### Appendix. Supplementary material

The supplementary data associated with this article can be found in online version at doi:10.1016/j.polymer.2010.10.066.

#### References

[1] Tomalia DA, Fréchet JM. *J Polym Sci A Polym Chem* 2002;40:2719–28.

- [2] Malik N, Wiwattanapatapee R, Klopsch R, Lorenz K, Frey H, Weener JW, et al. *J Control Release* 2000;65:133–48.
- [3] Esfand R, Tomalia DA. *Drug Discov Today* 2001;6:427–36.
- [4] Hudde T, Rayner SA, Comer RM, Weber M, Isaacs JD, Waldmann H, et al. *Gene Ther* 1999;6:939–43.
- [5] Mitra A, Imae T. *Biomacromolecules* 2003;5:69–73.
- [6] Choi YS, Cho T-S, Kim JM, Han SW, Kim SK. *Biophys Chem* 2006;121(2):142–9.
- [7] Lai JC, Yuan C, Thomas JL. *Ann Biomed Eng* 2002;30:409–16.
- [8] Kukowska-Latallo JF, Bielinska AU, Johnson J, Spindler R, Tomalia DA, Baker JR. *Proc Nat Acad Sci U S A* May 14, 1996;93:4897–902.
- [9] Leisner D, Imae T. *J Phys Chem B* 2003;107:13158–67.
- [10] Moore NM, Sheppard CL, Barbour TR, Sakiyama-Elbert SE. *J Gene Med* 2008;10:1134–49.
- [11] Caracciolo G, Caminiti R, Digman MA, Gratton E, Sanchez S. *J Phys Chem B* 2009;113:4995–7.
- [12] Boussif O, Lezoualc'h F, Zanta MA, Mergny MD, Scherman D, Demeneix B, et al. *Proc Nat Acad Sci U S A* 1995;92:7297–301.
- [13] Pouton CW, Seymour LW. *Adv Drug Deliver Rev* 2001;46:187–203.
- [14] Schmidt-Wolf GD, Schmidt-Wolf IG. *Trends Mol Med* 2003;9:67–72.
- [15] Kanayama N, Fukushima F, Nishiyama N, Itaka K, Jang W-D, Miyata K, et al. *Chem Med Chem* 2006;1:439–44.
- [16] Lee Y, Miyata K, Oba M, Ishii T, Fukushima S, Han M, et al. *Angew Chem Int Ed* 2008;47:5163–6.
- [17] Tomalia DA, Baker H, Dewald J, Hall M, Kallos G, Martin S, et al. *Polym J* 1985;17:117–32.
- [18] Hornback JM. *Organic chemistry*. 2nd ed. California: Brooks/Cole; 1998. 33–34.
- [19] Maiti PK, Çağın T, Wang G, Goddard WA. *Macromolecules* 2004;37:6236–54.
- [20] Beyerle A, Merkel O, Stoeger T, Kissel T. *Toxicol Appl Pharmacol* 2009;242:146–54.
- [21] Boeckle S, Fahrmeir J, Roedel W, Ogris M, Wagner E. *J Control Release* 2006;112:240–8.
- [22] Oishi M, Kataoka K, Nagasaki Y. *Bioconjug Chem* 2006;17:677–88.
- [23] Sakae M, Ito T, Yoshihara C, Iida-Tanaka N, Yanagie H, Eriguchi M, et al. *Biomed. Pharmacother.* 2008;62:448–53.
- [24] Wang QZ, Chen XG, Liu N, Wang SX, Liu CS, Meng XH, et al. *Carbohydr Polym* 2006;65:194–201.
- [25] Thomas TP, Majoros I, Kotlyar A, Mullen D, Banaszak Holl MM, Baker JR. *Biomacromolecules* 2009;10:3207–14.
- [26] Fabio K, Gaucheron J, Di Giorgio C, Vierling P. *Bioconjug Chem* 2003;14:358–67.
- [27] Gebhart CL, Kabanov AV. *J Control Release* 2001;73:401–16.
- [28] Arote R, Kim T-H, Kim Y-K, Hwang S-K, Jiang H-L, Song H-H, et al. *Biomaterials* 2007;28:735–44.
- [29] Ou M, Xu R, Kim SH, Bull DA, Kim SW. *Biomaterials* 2009;30:5804–14.
- [30] Kean T, Roth S, Thanou M. *J Control Release* 2005;103:643–53.
- [31] Haensler J, Szoka FC. *Bioconjug Chem* 1993;4:372–9.
- [32] Berna M, Dalzoppo D, Pasut G, Manunta M, Izzo L, Jones AT, et al. *Biomacromolecules* 2005;7:146–53.
- [33] Miyata K, Oba M, Nakanishi M, Fukushima S, Yamasaki Y, Koyama H, et al. *J Am Chem Soc* 2008;130:16287–94.
- [34] Kim T-I, Ou M, Lee M, Kim SW. *Biomaterials* 2009;30:658–64.
- [35] Luedtke NW, Carmichael P, Tor Y. *J Am Chem Soc* 2003;125:12374–5.
- [36] Min S-H, Kim DM, Kim MN, Ge J, Lee DC, Park IY, et al. *Biomaterials* 2010;31:1858–64.
- [37] Lim Y-B, Kim S-M, Suh H, Park J-S. *Bioconjug Chem* 2002;13:952–7.
- [38] Sugiyama M, Matsuura M, Takeuchi Y, Kosaka J, Nango M, Oku N. *Biochim Biophys Acta Biomembr* 2004;1660:24–30.
- [39] Takae S, Miyata K, Oba M, Ishii T, Nishiyama N, Itaka K, et al. *J Am Chem Soc* 2008;130:6001–9.



# Novel polyrotaxanes comprising $\gamma$ -cyclodextrins and Pluronic F127 end-capped with poly(*N*-isopropylacrylamide) showing solvent-responsive crystal structures

Jin Wang, Peng Gao, Pei-jing Wang, Lin Ye, Ai-ying Zhang, Zeng-guo Feng\*

School of Materials Science and Engineering, Beijing Institute of Technology, Beijing 100081, People's Republic of China

## ARTICLE INFO

### Article history:

Received 13 July 2010

Received in revised form

10 November 2010

Accepted 6 December 2010

Available online 15 December 2010

### Keywords:

Atom transfer radical polymerization

Poly(*N*-isopropylacrylamide)

Polyrotaxanes

## ABSTRACT

Herein novel polyrotaxanes (PRs) comprising  $\gamma$ -CDs and Pluronic F127 end-capped using poly(*N*-isopropylacrylamide) blocks were prepared via the atom transfer radical polymerization in aqueous medium at room temperature. The structure was characterized in detail by  $^1\text{H}$  NMR, 2D NOESY NMR, FTIR, GPC, WAXRD and DSC analyses. Solvent treatments were conducted on the resulting PRs via incubation in water and DMF, respectively. Interestingly the treatments resulted in two crystal structures: the DMF-incubated PRs appeared to give a novel crystal structure, while the water treated samples yielded a typical channel-type crystal structure. The entrapped  $\gamma$ -CDs were found to be aggregated mainly around the central PPO segment in the DMF-incubated PRs while some of  $\gamma$ -CDs were randomly dispersed on the PEO segments in the water treated samples. The two crystal structures exhibited a strong solvent dependence and were convertible through solvent incubation. The solubility and flexibility were greatly changed with the crystal structure conversion. Hence this provides an opportunity to alter the physical properties of PRs without any chemical modification of entrapped CD. The aggregated/dispersed state of  $\gamma$ -CDs along the Pluronic F127 chain as a result of response to solvent treatment renders the PRs great potential to be used as smart materials.

© 2010 Elsevier Ltd. All rights reserved.

## 1. Introduction

Polyrotaxanes (PRs) are one of the most vigorously investigated types of supramolecular polymers with many cyclic molecules threaded onto a linear polymer axis and end-capped with two bulky moieties on both terminals of the linear polymer axis [1–6]. Cyclodextrins (CDs) are 1–4  $\alpha$ -linked cyclic oligomers of anhydroglucopyranose with six ( $\alpha$ -), seven ( $\beta$ -), or eight ( $\gamma$ -) glucose units. These CDs assume a toroidal shape with the primary hydroxyl groups at the narrow side and the secondary hydroxyl groups at the wide side [3,4]. Since the first discovery of PRs made from  $\alpha$ -CDs with poly(ethylene glycol) (PEG) reported by Harada and colleagues [7], tremendous effort has been devoted to designing and preparing various advanced architectural CD-based PRs, such as main and side chain PRs [4,7–12], insulated molecular wires [13–16], slide-ring gels [17–20], and other amazing PR derivatives [4,21–25], because CDs can be selectively self-assembled with a number of polymers and readily functionalized by a variety of synthetic strategies [3–5,8].

Recently, the atom transfer radical polymerization (ATRP) was successfully introduced as an end-capping technique in preparing PRs at almost the same time by three independent groups in China [26–28]. Since then, a variety of novel PR-based triblock copolymers have been prepared, including dual thermo-responsive PRs [29], amphiphilic PRs as carrier for the controlled drug release [30], and H-type polymers [31]. Regarding the coupling reactions typically used in the preparation of PRs, the ATRP technique exhibits several superiorities, such as it can be carried out in aqueous solution at room temperature to depress the dethreading of entrapped CDs, which is substantial at higher temperatures in *N,N*-dimethylformamide (DMF) or *N,N*-dimethylacetamide (DMAc), and the end-capping groups with a controlled architecture and tunable block length greatly improve the PR solubility in water, tetrahydrofuran, chloroform and so on. Additionally these PR-based triblock copolymers can be further modified from the two flanked blocks while the native CDs remain unchanged [23,28–31].

Since a great deal of effort is drawn to the end-capping techniques and the intriguing characteristics of free sliding and rotation of the threaded CDs around the polymer chains, little attention has been ever paid to the CD residence states on the guest polymers due to an accepted viewpoint that the unique steric fittings exist between CDs and polymers so that single PEO is included by  $\alpha$ -CDs and poly(propylene oxide) (PPO) by either  $\beta$ -CDs or  $\gamma$ -CDs, while

\* Corresponding author. Tel.: +86 01 68912650; fax: +86 01 68944630.  
E-mail address: [sainfeng@bit.edu.cn](mailto:sainfeng@bit.edu.cn) (Z.-g. Feng).

two PEO chains are fitted into the cavity of  $\gamma$ -CDs to give a characteristic channel-type crystal structure [1–6]. Recently a kind of  $\beta$ -CD dispersed state rather than typical channel-type or aggregated state structure PRs was prepared in our group [29]. Furthermore, Yui et al. also reported  $\gamma$ -CD-based loose-fit PRs in which only one PEO molecule is fitted in the  $\gamma$ -CD cavity, and this leaves room to accommodate another PEO chain or other small molecules [32].

In this paper, a kind of novel PRs was prepared via the *in situ* ATRP of *N*-isopropylacrylamide (NIPAAm) initiated with self-assemblies of a distal 2-bromopropionyl end-capped Pluronic F127 (PEO<sub>100</sub>-b-PPO<sub>65</sub>-b-PEO<sub>100</sub>) with a varying amount of  $\gamma$ -CDs in aqueous solution at ambient temperature (Scheme 1). Similar to  $\beta$ -CD-based PPRs or inclusion complexes (ICs) [33,34],  $\gamma$ -CDs may preferably select the PPO segment to encircle [35], and as a result these PRs would also exhibit a solvent-responsive feature with a  $\gamma$ -CD dispersed or aggregated solid state structure along the Pluronic F127 chain. Moreover, the movement of  $\gamma$ -CDs toward the PEO segments was expected to form a loose-fit structure. In fact the resulting PRs gave rise to a  $\gamma$ -CD aggregated state mainly on the PPO segment having a novel crystal structure after DMF treatment with anhydrous ether while they yielded a  $\gamma$ -CD aggregated state holding a typical channel-type crystal structure after water incubation. Their physical properties were markedly changed as a function of solvent treatments. These findings not only contribute to the theoretical understanding of the CD residual state along the PR axle, but also provide an opportunity to improve the physical properties of PRs without any chemical modification of the entrapped CDs.

## 2. Experimental section

### 2.1. Materials

$\gamma$ -Cyclodextrin ( $\gamma$ -CD) (WAKO, Japan) was used as received. *N*-isopropylacrylamide (NIPAAm) (Acros, Belgium) was purified by recrystallization from *n*-hexane. Pluronic F127 ( $M_n = 127$  kDa,  $M_n/M_w = 1.07$ ), and *N,N,N',N',N''*-pentamethyldiethylenetriamine (PMDETA) were both purchased from Sigma, USA. 2-Bromopropionyl bromide and 4-dimethylaminopyridine (DMAP) were available from Alfa Aesar, USA. Triethylamine (TEA) (VAS Chemical Reagents Company, Tianjin, China) was refluxed with *p*-toluenesulfonylchloride and distilled under vacuum. The resultant free TEA was stored over CaH<sub>2</sub>. Copper(I) chloride (Cu(I)Cl) was prepared from CuCl<sub>2</sub>, purified by stirring in acetic acid, washed with methanol and finally dried under vacuum prior to use. DMF was stirred with CaH<sub>2</sub> and distilled under reduced pressure. All other solvents and reagents were of analytical grade.

### 2.2. Synthesis of a distal 2-bromopropionyl end-capped Pluronic F127 (BrP-F127-PBr)

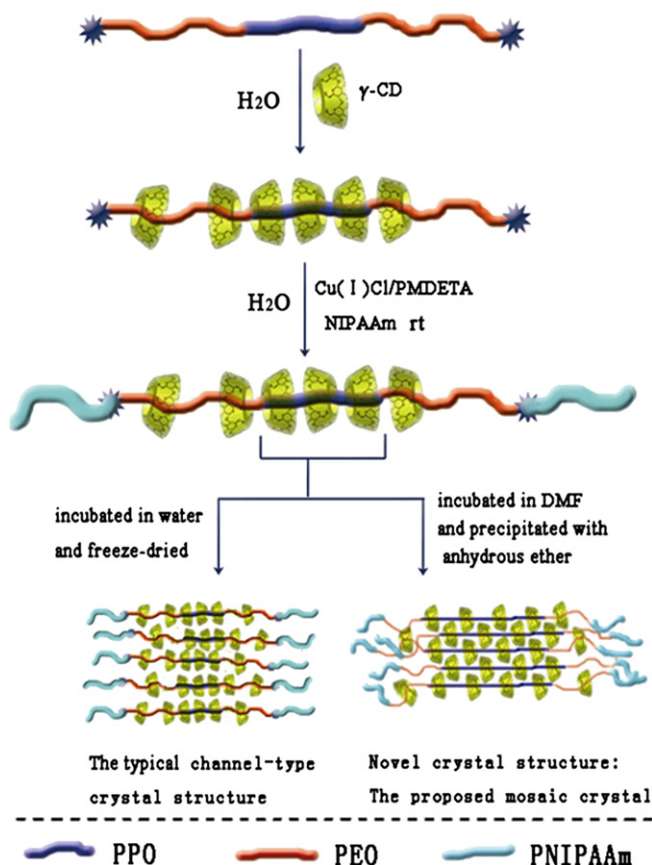
Pluronic F127 was converted to the corresponding ATRP macroinitiator by the end-capping reaction with a fourfold molar excess of 2-bromopropionyl bromide in CH<sub>2</sub>Cl<sub>2</sub> using a method similar to one described previously [28]. <sup>1</sup>H NMR analysis was used to determine the degree of esterification (>98%). <sup>1</sup>H NMR (DMSO-*d*<sub>6</sub>):  $\delta$  4.23–4.24 (s, 4H, –CH<sub>2</sub>–O–C(=O)–), 1.02–1.04 (d, 210H, –O–CCH<sub>3</sub>–C–O–), 1.71–1.73 (d, 3H, CH<sub>3</sub>–C–Br) ppm.

### 2.3. Synthesis of PR-based triblock copolymers

A typical protocol for the synthesis of PR-based triblock copolymer via the ATRP of NIPAAm was similar to the method described previously [29]. In a sealable Pyrex reactor, a saturated aqueous solution containing a predetermined amount of  $\gamma$ -CD was added to 1 ml aqueous solution of BrP–F127–PBr (0.13 g,  $1.0 \times 10^{-5}$  mol), followed by vigorous stirring at room temperature for 24 h to produce PPR. NIPAAm (0.113 g, 1.0 mmol) and PMDETA (4.3 mg, 0.024 mmol) were then added to the resulting suspension of PPR. After quenching in the liquid nitrogen, Cu(I)Cl (2.0 mg, 0.02 mmol) was added, followed by three degassings using a nitrogen purge. The reactor was sealed under vacuum and the reaction started and maintained at 25 °C for 8.0 h. The polymerization stopped after breaking the Pyrex reactor. The product was purified through dialysis using a cellulose membrane (MWCO 3500) for 4 days with water changing every 12 h. All the contents were freeze-dried. <sup>1</sup>H NMR (DMSO-*d*<sub>6</sub>):  $\delta$  1.02–1.04 (d, 210H + 6m H, –O–CCH<sub>3</sub>–CO– and –C(CH<sub>3</sub>)–CH<sub>3</sub>), 1.44–1.57 (d, 2m H, –CH<sub>2</sub>–C(C=O)–C–), 1.97 (s, 1m H, –C–CH(C=O)–C–), 3.85 (s, 1m H, –N–HC(C)–C), 7.21–7.33 (d, 1m H, –C(=O)–NH–C–), 4.50 (s, 7n H, –O(6)H), 4.88 (s, 7n H, H(1)), 5.71 (s, 7n H, –O(3)H), 5.74–5.75 (d, 7n H, –O(2)H) ppm.

As a control, a pentablock copolymer PNIPAAm-b-F127-b-PNIPAAm was prepared with the same protocol as described above but in the absence of  $\gamma$ -CDs. <sup>1</sup>H NMR (DMSO-*d*<sub>6</sub>):  $\delta$  1.02–1.04 (d, 210H + 6m H, –O–CCH<sub>3</sub>–CO– and –C(CH<sub>3</sub>)–CH<sub>3</sub>), 1.44–1.57 (d, 2m H, –CH<sub>2</sub>–C(C=O)–C–), 1.97 (s, 1m H, –C–CH(C=O)–C–), 3.85 (s, 1m H, –N–HC(C)–C), 7.21–7.33 (d, 1m H, –C(=O)–NH–C–) ppm.

For the convenience of expression, the obtained PR-based triblock copolymers were designated as F<sub>n</sub>, where F means Pluronic F127 used as axle chain molecule and n stands for the feed molar ratio of  $\gamma$ -CD to BrP-F127-PBr. The feed molar ratio of NIPAAm to BrP-F127-PBr kept constant at 100, and the number (m) in the <sup>1</sup>H NMR shift captions means the found NIPAAm repeat units. When the products were subjected to post-treatment with water (incubated in



**Scheme 1.** Schematic description of PR-based triblock copolymers and their solvent-responsive structures.

water and then freeze-dried) or DMF (incubated in DMF and then precipitated with anhydrous ether), W or D was added ahead of Fn.

#### 2.4. Solvent treatment of as-prepared PRs

The solvent-responsive behavior means the variation of the  $\gamma$ -CD dispersed or aggregated state or the crystal structure in the resulting PRs in response to solvent treatment [29]. Herein DMF and water treatments were conducted toward the PR samples in order to gain insight into their structure and physical property changes. A protocol for DMF treatment was as follows: a predetermined amount of the purified PRs was dissolved in 6 ml DMF and vigorously stirred for 5 min at room temperature. Then 100 ml anhydrous ether was added to the solution under stirring, and the precipitate was collected by centrifugation and dried under vacuum at 30 °C for 48 h. The procedure for water treatment was slightly different from that of DMF: a predetermined amount of the purified PR-based triblock copolymer was added into 12 ml distilled water, vigorously stirred at room temperature until it was fully swollen to form a suspension, and then freeze-dried.

#### 2.5. Measurements

$^1\text{H}$  NMR (400 MHz) spectra were recorded on a Bruker ARX 400 spectrometer at room temperature using DMSO- $d_6$  as solvent and tetramethylsilane (TMS) as internal standard. 2D NOSEY experiment was carried out at 400 MHz with DMSO- $d_6$  as the solvent at 25 °C on a Bruker ARX 400. FTIR spectra were measured using Shimadzu IR Prestige-21 FTIR spectrometer at room temperature in the range between 4500 and 500  $\text{cm}^{-1}$ , with a resolution of 2  $\text{cm}^{-1}$  and 20 scans. Powder samples were prepared by dispersing the samples in KBr and compressing the mixtures to form disks. Gel permeation chromatographic (GPC) measurements were carried out at 40 °C on a Waters 2410 instrument using DMF as eluent at a flow rate of 1.0 ml/min. All the GPC data were calibrated by using polystyrene (PS) standards. The wide-angle X-ray diffraction (WAXRD) measurements were carried out with powder samples using Philips X'Pert Pro diffractometer with an X'celerator detector in a reflection mode. The radiation source used was Ni-filtered, Cu  $K\alpha$  radiation with a wavelength of 0.154 nm. The voltage was set at 40 kV and the current 20 mA. Samples were mounted on a sample holder and scanned from 4.5° to 60° in  $2\theta$  at a speed of 5°/min. The differential scanning calorimetry (DSC) analysis was conducted on a NETZSCH DSC 204 differential scanning calorimeter with a scanning temperature range from –50 to 150 °C at a scanning rate of 10 °C/min. A typical DSC sample size was about 4 mg. The samples were encapsulated in hermetically sealed aluminum pans, and the pan weights were kept constant. The following protocol was used for each sample: heating from –50 °C to 150 °C at 10 °C/min, holding at 150 °C for 5 min, then cooling from 150 °C to –50 °C at 10 °C/min, and finally reheating from –50 °C to 150 °C at 10 °C/min. Data were collected during the second heating run. The morphologies of the PRs (F0, WF30, DF30) were visualized by field-emission scanning electron microscopy (FE-SEM) on a Hitachi S-4800 scanning electron microscopy at room temperature. The FE-SEM samples were prepared by drop a PR solution (50 mg/ml) on an aluminum foil and dried at 50 °C in an oven for 5 days, and were coated with a thin conductive Au layer prior to observation.

### 3. Results and discussion

#### 3.1. Preparation and characterization of $\gamma$ -CD-based PRs

As reported previously, a series of PRs consisting of  $\beta$ -CD and Pluronic F127 end-capped with PNIPAAm were prepared via the *in*

*situ* ATRP of NIPAAm in aqueous solution at room temperature [29]. Although  $\gamma$ -CD is well known to self-assemble with a variety of polymers, few  $\gamma$ -CD-based PRs have been reported due to the larger cavity of  $\gamma$ -CDs that only a few bulky stopper groups can effectively hinder the dethreading of  $\gamma$ -CDs [32,35]. To combine the  $\gamma$ -CD-Pluronic F127 PPR with PNIPAAm would create multiple stimuli-responsive PRs, as the middle PPR block shows both thermo and solvent-responsive in the manner of sliding and rotation of  $\gamma$ -CD along the Pluronic F127 chain [29,33,34], as well as the two flanking PNIPAAm blocks display a clear lower critical solution temperature (LCST) around 32 °C in aqueous solution [34]. Therefore, a kind of novel  $\gamma$ -CD-based PRs end-capped by two PNIPAAm blocks was synthesized via the *in situ* ATRP at room temperature using self-assemblies of a varying amounts of  $\gamma$ -CD with a distal 2-bromopropionyl terminated Pluronic F127 as macroinitiator (Scheme 1). Their compositions and GPC analytical results are summarized in Table 1.

As illustrated in Table 1, the yield of the resulting  $\gamma$ -CD-based PRs in a range of 76.2–91.9% was greatly improved as compared to  $\beta$ -CD-based ones having yields generally around 40% [29]. The number of entrapped  $\gamma$ -CDs as determined by  $^1\text{H}$  NMR analysis was in accordance with the feed molar ratio unless it went beyond a saturated inclusion complex value of 34 (on the assumption that one CD molecule can accommodate two repeating units of PPO) [1]. As a result ca. 32  $\gamma$ -CDs were entrapped in F40 even though the molar feed ratio of  $\gamma$ -CDs to BrP-F127-PBr was 40. Herein the relatively controlled number of entrapped CDs was probably arisen from the *in situ* ATRP process at 25 °C, which effectively depressed the dethreading of  $\gamma$ -CD. Notably the polydispersity index was kept around 1.30. It suggested that the *in situ* ATRP of NIPAAm initiated with PPRs made from a varying amount of  $\gamma$ -CDs with 2-bromopropionyl end-capped Pluronic F127 was successful and the resulting PRs exhibited a narrow molecular weight distribution and relative high yields.

The PR products were characterized using  $^1\text{H}$  NMR analysis with DMSO- $d_6$  as solvent. Fig. 1 shows the  $^1\text{H}$  NMR spectra of pure  $\gamma$ -CD (A), F0 (B) and F20 (C), respectively. As can be seen, all the proton peaks of  $\gamma$ -CDs, Pluronic F127, and PNIPAAm were discernable in F20. However, the resonance peaks of O(2)H, O(3)H and O(6)H of  $\gamma$ -CD in F20 are sharp without any broadening and chemical shifts. According to literature [28,36], the corresponding resonance peaks of O(2)H, O(3)H and O(6)H of  $\alpha$ - and  $\beta$ -CD would be broadened with slightly changed chemical shifts due to the decrease in the conformational flexibility upon forming a PR. In fact as the inner cavity of  $\gamma$ -CD is larger than that of  $\alpha$ - and  $\beta$ -CD, and the included PPO chain is still slim with regard to the cavity of  $\gamma$ -CD, the conformation flexibility of the  $\gamma$ -CD is so high that no broadening and shift of the resonance peaks of O(2)H, O(3)H and O(6)H were observed here. This phenomenon was also seen in the following 2D NOESY NMR spectrum of the F30 PR sample. In order to calculate

**Table 1**  
Compositions and GPC analytical results of PR-based triblock copolymers.

Entry	Molar composition (BrP-F127-PBr:CD:NIPAAm)		Molecular weight and polydispersity index			Yield (%) <sup>c</sup>
	Feed ratio	Found ratio <sup>a</sup>	$M_n(10^{-3})^a$	$M_n(10^{-3})^b$	$M_w/M_n^b$	
F0	1:0:100	1:0:119.9	26.5	38.8	1.54	86.8
F10	1:10:100	1:8.6:176.5	44.1	45.9	1.29	76.2
F20	1:20:100	1:25.1:163.3	64.0	53.8	1.28	91.9
F30	1:30:100	1:27.1:135.5	63.5	52.3	1.31	82.7
F40	1:40:100	1:31.9:114.1	67.3	54.4	1.25	79.1

<sup>a</sup> Determined by  $^1\text{H}$  NMR analysis in DMSO- $d_6$ .

<sup>b</sup> Determined by GPC in DMF at 1.0 ml/min using PS standards.

<sup>c</sup> Yields are calculated based on the weight of product divided by that of all raw materials.



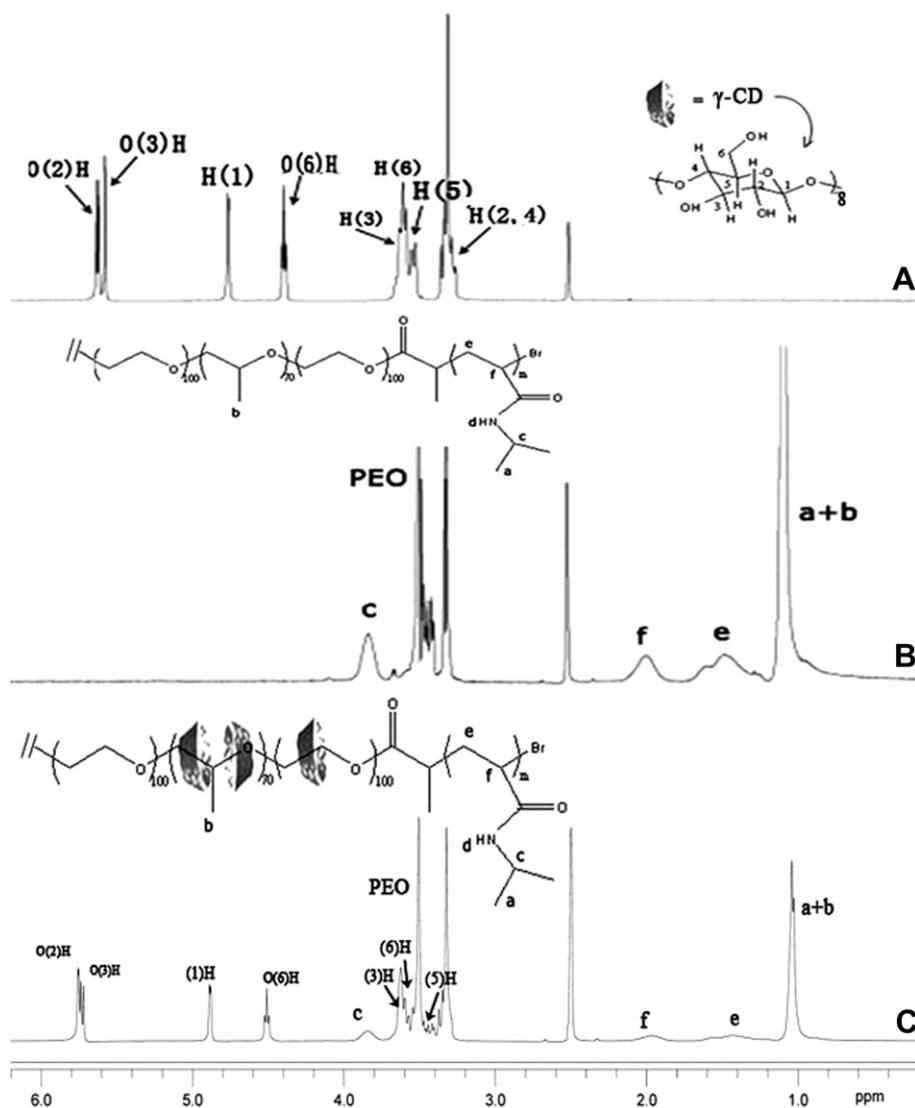


Fig. 1.  $^1\text{H}$  NMR spectra of  $\gamma$ -CD (A), F0 (B) and F20 (C) in  $\text{DMSO-d}_6$ .

the number of incorporated NIPAAm monomers and that of entrapped  $\gamma$ -CDs on the Pluronic F127 chain, the integration area of methylene proton peak of the side group of PNIPAAm (c) and that of (1)H proton resonance peak of  $\gamma$ -CD should be employed. As the methyl proton peaks of Pluronic F127 were superposed with that of the end methyl of NIPAAm (a + b), it should be subtracted 6 times the integration area of peak c from the integration area of methyl proton peaks.

The 2D NOESY NMR spectrum of F30 is depicted in Fig. 2. According to a previous report [37], the signals of (3)H and (5)H protons of  $\alpha$ -CD which are directed toward the cavity are correlated with the resonance of the  $\text{CH}_2$  of PEO upon forming a PR. However, in the  $\gamma$ -CD-based PRs, no such correlation was noticed between the resonance of (3)H of  $\gamma$ -CD and that of the methyl proton of Pluronic F127 as indicated at a and a' in Fig. 2. However, the signal of (5)H of  $\gamma$ -CD was found to correlate with the resonance of  $-\text{CH}_3$  of Pluronic F127 (b and b' in Fig. 2), indicating that the Pluronic F127 chain is preferably included into the  $\gamma$ -CD cavity even in a polar DMSO solvent. It is most likely due to the fact that the cavity of  $\gamma$ -CD is larger with regard to the slim PEO segment. Therefore, the (3)H proton located at the wider side of  $\gamma$ -CD cannot correlate

with the  $-\text{CH}_3$  protons, while the (5)H proton located at the narrow side of  $\gamma$ -CD is correlated with the  $-\text{CH}_3$  protons.

The FTIR spectra of powder samples of pure  $\gamma$ -CDs (a), macro-initiator (b), F0 (c), F10 (d) and F30 (e) are outlined in Fig. 3. The vibration absorption peaks for the amide bond of PNIPAAm appear at 1643 and 1547  $\text{cm}^{-1}$ , clearly indicating that the NIPAAm monomers were polymerized and attached to two ends of PPRs because of a significant increase in the intensity of the amide bond stretching vibration of Fn compared to BrP-F127-PBr. In addition, the N–H symmetric and asymmetric stretching vibration modes of the amide bond in F0 are located at 3562, 3259 and 3073  $\text{cm}^{-1}$ , while for the traces d, and e, the peaks at 3562 and 3259  $\text{cm}^{-1}$  disappear because they are superposed with the peak of O–H bonds from  $\gamma$ -CDs. However, the peak at 3073  $\text{cm}^{-1}$  was still clearly observed. The characteristic peaks of  $\gamma$ -CD at 1029 and 1159  $\text{cm}^{-1}$  were also seen in the spectra of F10, and F30. This provided direct evidence confirming that the PR-based triblock copolymers were successfully synthesized via the *in situ* ATRP of NIPAAm in aqueous solution at room temperature.

The WXR patterns of pure  $\gamma$ -CD, F0, PPO- $\gamma$ -CD PPR and PRs are presented in Fig. 4. The major diffraction peaks of pure  $\gamma$ -CD of the

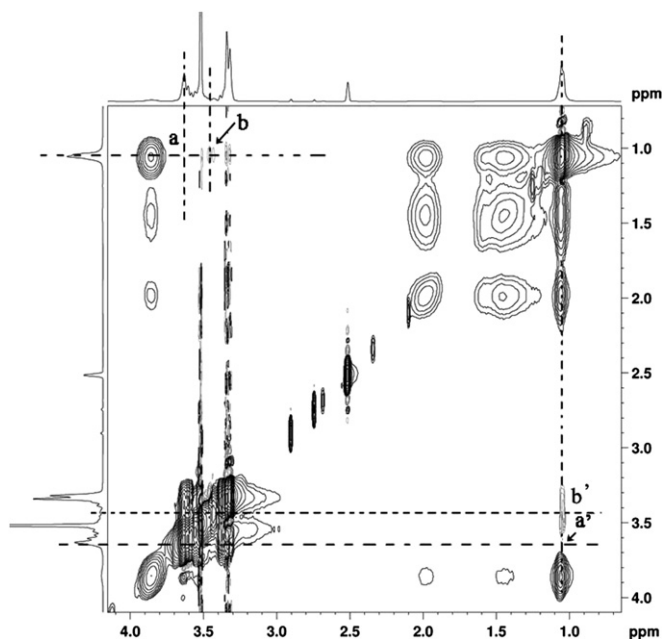


Fig. 2. 2D NOESY NMR spectrum of the F30 PR in DMSO- $d_6$ .

cage-type crystalline appear at  $2\theta = 5.13^\circ, 6.22^\circ, 12.34^\circ, 16.45^\circ, 18.77^\circ,$  and  $21.69^\circ$ , respectively. And the pentablock copolymer F0 shows two strong peaks at  $19.02^\circ$  and  $23.29^\circ$  arising from the crystal structure of PEO blocks [28,29]. Both the  $\gamma$ -CD-PPO PPR and the water treated PRs were found to adopt a head-to-head channel-type crystal structure in which  $\gamma$ -CD molecules are stacked along a PPO axis to form a cylinder [38]. This clearly indicated that the  $\gamma$ -CDs accommodate the Pluronic F127 chain. However, it should be noted that  $\gamma$ -CDs cannot only self-assemble with a single PPO chain but also include double PEO chains in their cavity [1,6,31]. Thereafter when Pluronic F127 is accommodated with  $\gamma$ -CDs, both the cases may exist. According to the previous report [35], the WXR D results in Fig. 4 as well as the DSC results in Fig. 5, the  $\gamma$ -CDs seemed to preferably include the middle PPO block rather than the flanking PEO blocks in Pluronic F127. As can be seen, all the water treated

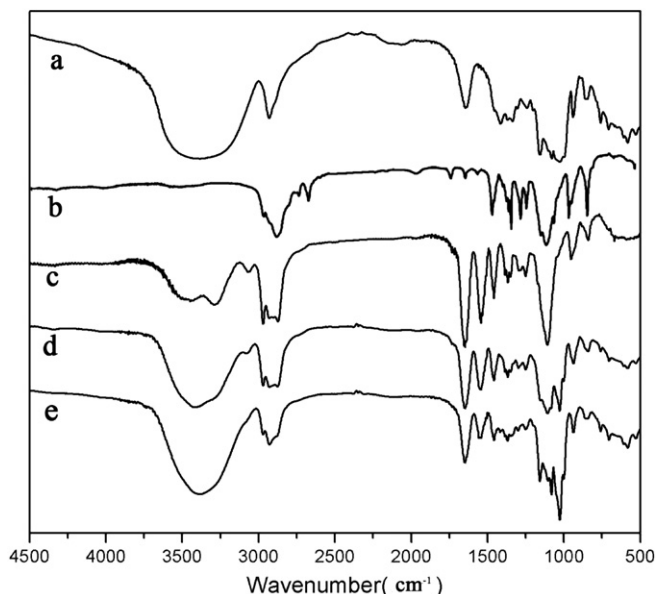


Fig. 3. FTIR spectra of pure  $\gamma$ -CD (a), BrP-F127-PBr (b), F0 (c), F10 (d) and F30 (e).

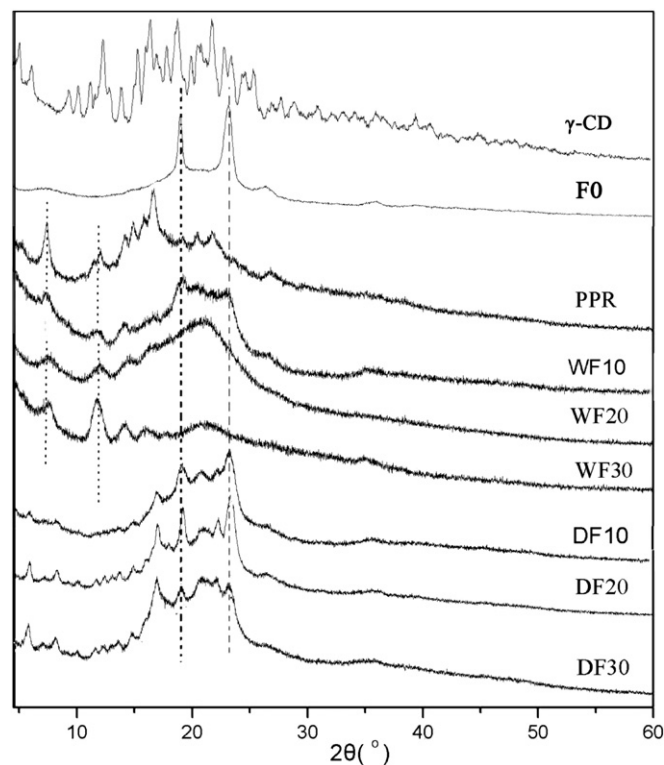


Fig. 4. WXR D patterns of pure  $\gamma$ -CDs, F0, PPO- $\gamma$ -CD PPR and PRs after water and DMF treatments.

PRs (WF10, WF20, WF30) present two peaks at  $7.54^\circ$  and  $12.01^\circ$ , respectively, which are ascribed to the channel-type crystal structure formed from  $\gamma$ -CDs and the PPO block as in the case of  $\gamma$ -CD-PPO PPR. With decreasing the number of entrapped  $\gamma$ -CDs, the PEO crystal diffraction peaks located at  $19.02^\circ$  and  $23.29^\circ$  gradually appeared, suggesting that the  $\gamma$ -CDs are mainly resided on the PPO block unless an excess of  $\gamma$ -CDs is added so that part of  $\gamma$ -CDs are extruded to the PEO blocks to restrict the crystallization of PEO. This is well coherent with the DSC results as illustrated in Fig. 5, where there is a PEO crystal melting peak in WF10 while no such melting peak occurs in WF30. At the same time, if  $\gamma$ -CDs can form double chain stranded ICs with the PEO block, the ICs of  $\gamma$ -CDs with central PPO block cannot be formed because PPO was flanked by two PEO segments. If this is true, the different WXR D and DSC results of the PRs would be observed.

Interestingly the aforementioned channel-type crystal structure of all the PRs was destroyed after DMF treatment with anhydrous ether, while a novel crystal structure emerged with five characteristic diffraction peaks appeared at  $2\theta$  of  $5.89^\circ, 8.27^\circ, 10.15^\circ, 16.99^\circ,$  and  $22.21^\circ$ , respectively. From their WXR D patterns, it can be sure that this novel crystal structure is different from either the pure  $\gamma$ -CD cage-type crystal structure or the typical channel-type crystal structure as previously reported in nearly all the literature except for the recently reported loose-fit  $\gamma$ -CDs-based PRs [32].

Fig. 5 depicts the heating and cooling DSC curves of pure  $\gamma$ -CDs, F0, and water and DMF treated PRs (F10, F20, F30, and F40), respectively. The pentablock copolymer F0 exhibits an endothermic peak at  $48.7^\circ\text{C}$ , and it corresponds to the melting temperature ( $T_m$ ) of crystallized PEO segments [29]. Upon forming a PR, this crystalline melting peak disappears in WF30 and WF40 due to part of threaded  $\gamma$ -CDs being randomly dispersed on the PEG segments to restrict their crystallization. However, all the water and DMF treated F10 and F20 show a PEO melting peak, indicating that the entrapped  $\gamma$ -CDs preferably reside on the PPO segment under such

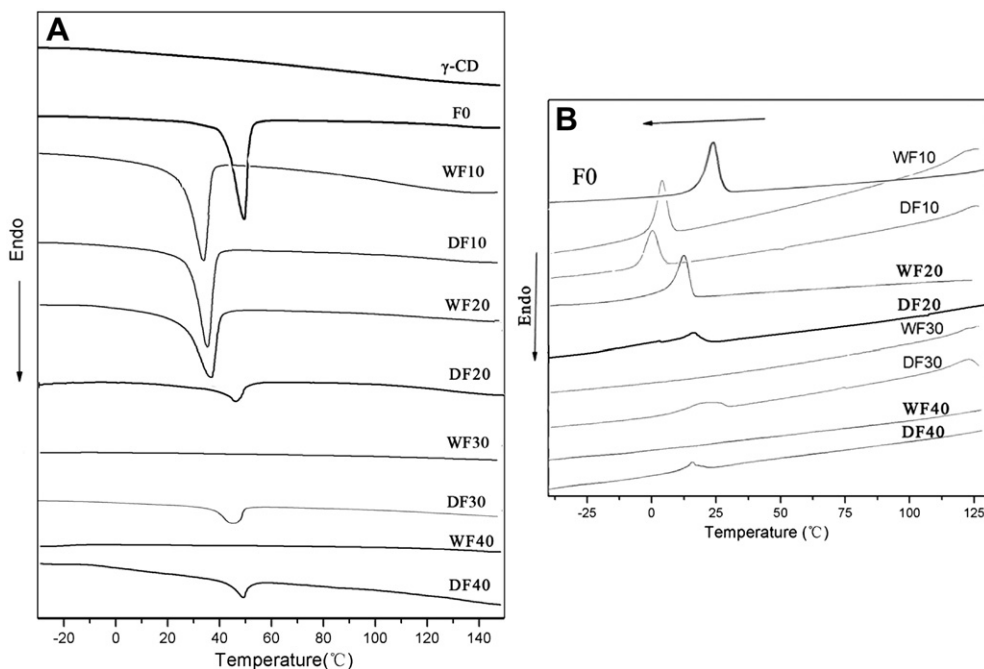


Fig. 5. DSC curves of pure  $\gamma$ -CD, F0 and PRs after water and DMF treatments: the heating run (A) and the cooling curves (B).

circumstances. Otherwise, if PEO is double chain stranded in the  $\gamma$ -CD cavity, there appears no PEO melting peak [31]. This also provided direct evidence that  $\gamma$ -CDs cannot form double chain stranded ICs with Pluronic F127. Similar to our previously report [29], the  $T_m$  of PEO crystalline in F10 and F20 is lower than that of F0, possibly due to the fact that some  $\gamma$ -CD molecules are dispersed on the PEO segments to give imperfect PEO crystalline domains, as well as the existence of  $\gamma$ -CDs on the Pluronic chain reduces the chain flexibility to lower crystalline ability for PEO as illustrated in Fig. 5B of the cooling run. As for WF30 and WF40, the DSC curves and the WXRd results (Fig. 4, WF30) indeed display no PEO crystalline phase existence because more entrapped CDs get randomly dispersed on the PEO segments as compared to F10 and F20, and those  $\gamma$ -CD molecules resided on the PEO segments hinder their crystallization. However, a broad PEO crystalline melting peak around 46.7 °C was observed in DF30 and DF40 after DMF treatment with anhydrous ether, which is well coherent with the WXRd data of DF30 and DF40 (Fig. 4 for DF30 and Fig. 7A for DF40), respectively. Consequently, quite different from our previous report [29], these  $\gamma$ -CD-based PRs obtained from DMF treatment with anhydrous ether showed a novel crystal structure with  $\gamma$ -CD mainly being aggregated around the central PPO segment, while those from water treatment exhibited a typical channel-like crystal structure with some  $\gamma$ -CDs being randomly dispersed on the PEO segments. A proposed mosaic structure of this novel crystal structure will be described below.

As mentioned above, the PR structure formed from  $\gamma$ -CDs with Pluronic F127 was confirmed by 2D NOESY NMR, WXRd, and DSC analyses. However, whether or not the end-capping PNIPAAm blocks effectively hinder the dethreading of  $\gamma$ -CDs is not fully elucidated. Hence GPC measurements were conducted and the curves of pure  $\gamma$ -CD, F0 and F20 are illustrated in Fig. 6. Meanwhile, the GPC curves of F10, F30 and F40 are displayed in Figure S3. As can be seen, the molecular weight of PRs is increased and the elution time becomes shorter with the number of  $\gamma$ -CDs increasing. All PR samples exhibit a nearly symmetrical and unimodal main peak with a relatively low polydispersity index range from 1.25 to 1.28. However, very small peaks at relatively shorter elution time of 10–15 min were also

observable, maybe arisen from self-aggregation of the resulting PRs in the DMF eluent solvent. This aggregation behavior of PRs in GPC analysis was also noticed in previously reports [28,29]. As for F0, a relatively broad molecular weight distribution was possibly ascribed to the uncontrolled ATRP nature of NIPAAm in aqueous solution. As no  $\gamma$ -CD peak appeared in all PR samples, it suggested that the PNIPAAm blocks can impede the dethreading of  $\gamma$ -CDs and the  $\gamma$ -CD-based PR supramolecular polymers were successfully prepared via the *in situ* ATRP of NIPAAm in aqueous solution at room temperature.

### 3.2. Proposed model of the novel crystal structure

Since the first report on PRs made from  $\alpha$ -CDs with PEO, [7] a large variety of PRs comprising  $\alpha$ -,  $\beta$ - or  $\gamma$ -CDs with various polymers have been prepared. As for their crystal structure, one particular characteristic is always mentioned, that is the channel-type

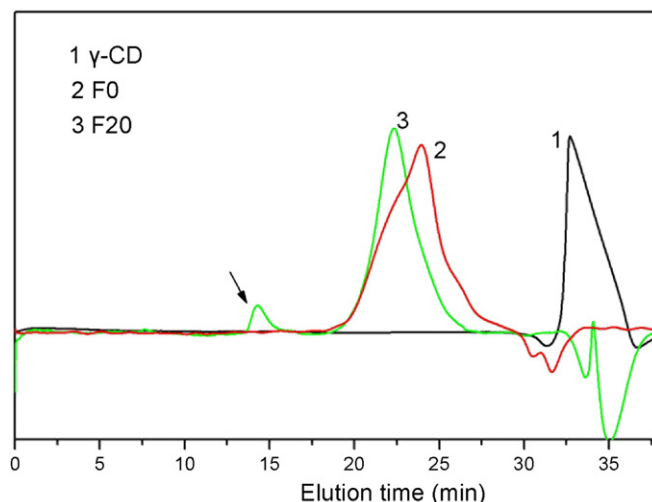
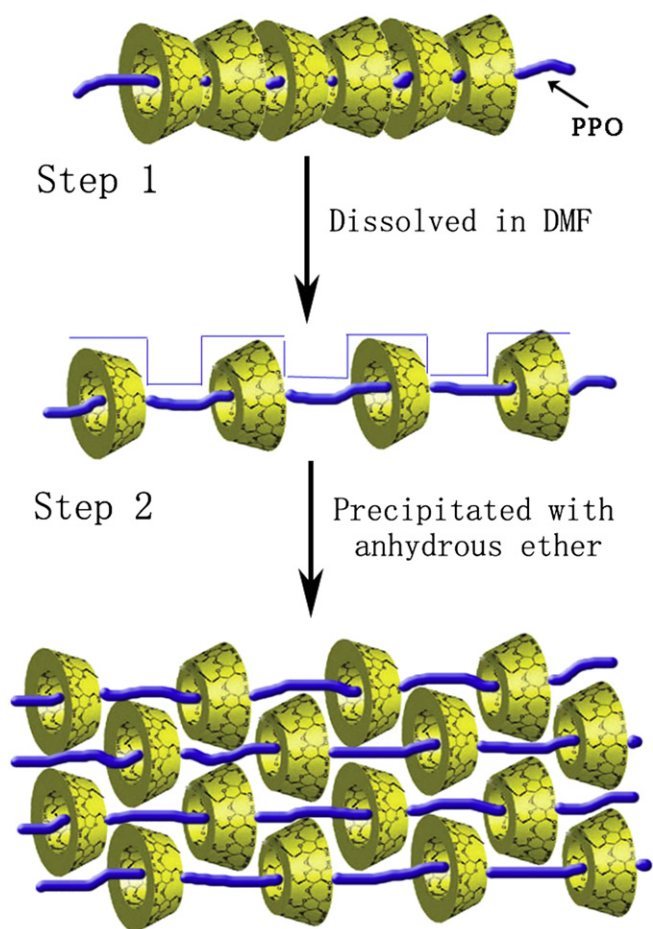


Fig. 6. GPC traces of pure  $\gamma$ -CD (1), F0 (2) and F20 (3) using DMF as eluent at 40 °C.

crystal structure. As a result WXR D analysis becomes an essential technique to distinguish the PRs [2,6]. Recently Kawaguchi et al. [39] and Hirayama et al. [40] described hexagonal and tetragonal columnar crystal structures formed from  $\alpha$ - and  $\gamma$ -CD ICs, while the building blocks for these columnar crystals are still the channel-type crystal structure ICs. This situation was kept until the loose-fit PRs [32] and dispersed state PRs [29] were reported, both of which are featured by no channel-type crystal structure. Notably the resulting PRs after DMF treatment with anhydrous ether in this study gave a novel crystal structure as evidenced by the WXR D results in Fig. 4. This crystal structure is different from the channel-type crystal structure yielded after water treatment with  $\gamma$ -CD being aggregated mainly around the central PPO segment.

According to our previous report [29], a mosaic crystal structure model was proposed to gain insight into the WXR D data as shown in Fig. 4, in which the most  $\gamma$ -CDs are aggregated around the PPO segment forming a concave-convex structure and several PR molecules are embedded in each other resulting in a mosaic crystal structure as illustrated in Scheme 2 and Fig. 7B. As proposed in Scheme 2, the hydrogen bonds between neighboring  $\gamma$ -CDs are broken after dissolution in DMF and the  $\gamma$ -CDs get dispersed along the PPO block to form a concavo-convex morphology in step 1, where a concave space forms between two adjacent  $\gamma$ -CDs and the round wall of  $\gamma$ -CD gives a convex part. In step 2, with addition of anhydrous ether, a non-solvent for both  $\gamma$ -CD and Pluronic F127, the concavo-convex state PRs inset into each other to yield a novel mosaic crystal structure.



**Scheme 2.** Proposed process of  $\gamma$ -CD-based PRs forming a mosaic crystal structure by DMF treatment.

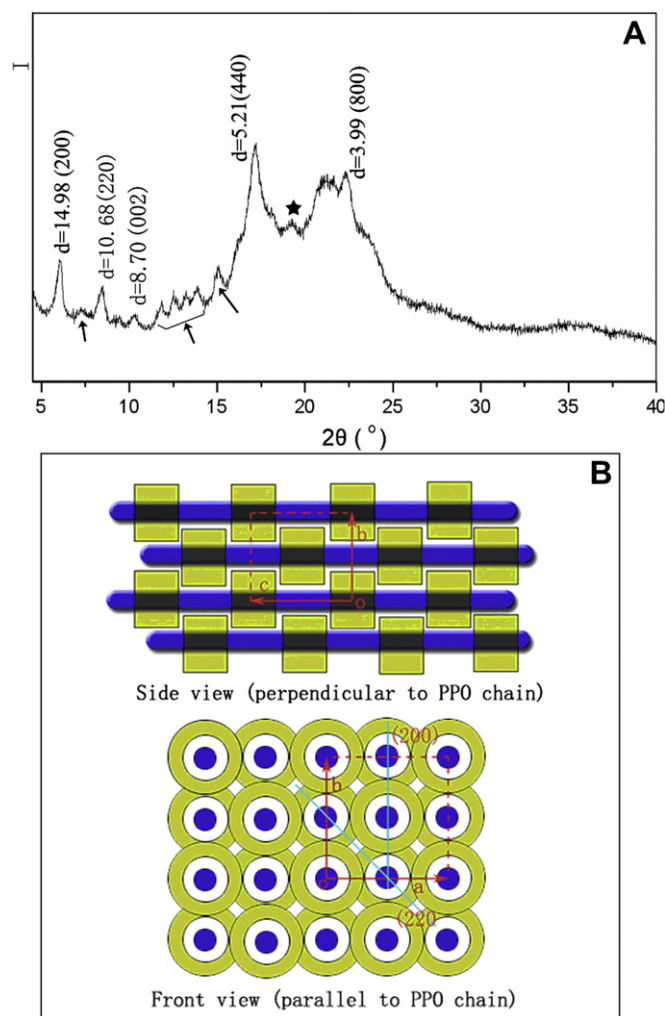


**Fig. 7.** The d-spacing values and Miller indices of DF40 (A) and different direction views of the mosaic crystal structure model (B).

According to the proposed mosaic crystal structure as presented in Scheme 2, a tetragonal column would be formed as illustrated in Fig. 7B. Different from the tetragonal columnar channel structure obtained from double chain stranded PEO and  $\gamma$ -CDs [39], the existence of the PPO block between two PR molecules results in a relatively larger unit cell, and the building block of the tetragonal column appears to be a mosaic structure rather than a channel-type structure. The value  $a$  of the unit cell should be in a range between 16.9 Å (average diameter of  $\gamma$ -CD molecule) and 33.8 Å (two times of the diameter of  $\gamma$ -CD). The observed d-spacing values and the corresponding Miller indices are presented in Fig. 7A. Table 2 summarizes the observed and calculated d values of the mosaic crystal structure. As can be seen, the proposed tetragonal columnar mosaic crystal has a cell dimension of  $a = b \approx 30$  Å, and  $c = 17.4$  Å ( $>2$  times of the depth of  $\gamma$ -CD). Based on this result, the observed d spacing is well fitted to the calculated result, and the slight differences (for instance,  $d_{\text{obs}}$  of (220) is 10.68 Å while  $d_{\text{calc}}$  of (220) is 10.61 Å) may arise from defects in the crystal structure as it was yielded via precipitation from DMF with anhydrous ether. However, as reported previously [29], the  $\beta$ -CD-based PRs using Pluronic F127 as guest end-capped with PNIPAAm held a dispersed state rather than a mosaic structure after DMF treatment. The reason for this difference maybe the fact that the diameter of  $\beta$ -CD molecule (15.3 Å) is shorter than that of  $\gamma$ -CD molecules (16.9 Å) [41]. This meant that even though the  $\beta$ -CDs can be distributed around the

**Table 2**  
Crystallographic characteristics of DMF treated  $\gamma$ -CD-based PRs.

$2\theta$ ( $^\circ$ )	hkl	$d_{\text{obs}}$ ( $\text{\AA}$ )	$d_{\text{calc}}$ ( $\text{\AA}$ ) <sup>a</sup>
5.89	200	14.98	15.00
8.27	220	10.68	10.61
10.15	002	8.70	— <sup>b</sup>
16.99	440	5.21	5.30
22.21	800	3.99	3.75

<sup>a</sup> Calculated assuming a tetragonal unit cell with  $a = b \approx 30.00$   $\text{\AA}$ .

<sup>b</sup> The observed results indicated that the unit cell with  $c = 17.4$   $\text{\AA}$ , a little bigger than 2 times of the depth of two CDs (ca. 16  $\text{\AA}$ ), as they are loosely packed.

PPO segment to form a concavo-convex morphology, the concaves maybe not deep enough to form a stable mosaic structure due to the shorter diameter of  $\beta$ -CD. As a result, they form a dispersed state structure with  $\beta$ -CDs being randomly dispersed along the whole Pluronic F127 chain. Herein the DMF-incubated PRs can give rise to the novel mosaic crystal structure with  $\gamma$ -CDs being aggregated mainly around the central PPO block while those water treated ones only yield the channel-type crystal structure with part of  $\gamma$ -CDs being dispersed onto the PEG segments. To our knowledge, this is the first time to observe this novel crystal structure beyond the typical channel-type crystal structure in the native CD-based PRs. It may contribute to a better understanding of the crystal structure of ICs and/or PRs made from CDs and polymers. However, as indicated by arrows in Fig. 7A, a tiny part of channel-type crystal structure was still observed which is similar to our previous observation [29]. Because there are 25–32 CD molecules entrapped on PPO block, some of them would be packed head-to-head even after DMF treatment. Moreover, as indicated by a star sign, the diffraction peak of PEO crystalline was also seen here, which is correlated with the melting peak in its DSC curves (Fig. 5).

The micro-topography of the DMF treated PRs was also visualized by FE-SEM. As shown in Fig. 8C, the DMF treated F30 (DF30) sample gives ordered tetragonal blocks, suggesting that it is build up with numerable tetragonal unit cells. At the same time, the images of F0 and WF30 are also shown in Fig. 8A and B, respectively. As can be seen, neither F0 nor WF30 exhibits tetragonal topographies. Although WF30 holds a channel-type crystal structure as evidenced by WXR, no tetragonal or channel-type topography exists in its SEM image. This is most likely due to the fact that the sample was made by evaporation of water, and consequently the hydrophilic PNIPAAm segments may spread on the surface of the channel-type crystal after drying. This may also explain why the images of F0 and WF30 are similar to each other. It is noteworthy that the sample preparation for FE-SEM characterization was slightly different from the standard solvent treatment as described in the experimental section. However, the WXR results presented in Figure S1 demonstrated that the crystal structures are identical whether a PR was dried directly from DMF or precipitated from DMF with anhydrous ether. The only difference is the former to form a more perfect mosaic structure crystal, showing sharper characteristic diffraction peaks than the latter using the standard treatment

method. This maybe due to the fact that the precipitation was a rapid process, while air drying was a relatively prolonged one.

### 3.3. Observation of solvent responsiveness and impacts of solvent treatment on physical properties

Similar to our previous report [29], the solid state structure of these  $\gamma$ -CD-based PRs is also solvent-responsive. It means that the aggregated/dispersed state of  $\gamma$ -CDs along the Pluronic F127 chain and the crystal structure are a function of solvent treatment. As can be seen in Fig. 4, all the water treated samples (WF10, WF20, WF30) exhibit two channel-type crystal diffraction peaks at  $7.54^\circ$  and  $12.01^\circ$ , respectively. After DMF treatment, their crystal structure is transformed into a novel crystal structure as demonstrated by the appearance of five new diffraction peaks at  $5.89^\circ$ ,  $8.27^\circ$ ,  $10.15^\circ$ ,  $16.99^\circ$ , and  $22.21^\circ$ . The difference between DSC curves of WF30 and DF30 also implied their different structures, respectively. The FE-SEM images of WF30 and DF30 presented in Fig. 8 also confirmed that the different structures exist between WF30 and DF30. Although the  $\gamma$ -CD-based PRs exhibit a solvent response similar to our previous report [29], the WXR and FE-SEM results suggested that they form a novel mosaic crystal structure having the  $\gamma$ -CD aggregated state on the PPO chain in response to DMF treatment.

The impact of the solvent treatments on the physical properties, such as solubility and film flexibility was also briefly investigated. As illustrated in Table S1, the water treated PRs were almost insoluble in water, while the solubility of DMF treated samples in water was greatly enhanced (ca. 93.7 mg/10 ml for DF10 and 63.5 mg/10 ml for DF40, respectively). As discussed above, these DMF treated PRs give rise to a mosaic crystal structure, in which most PEO segments are left uncomplexed leading to water solubility. Furthermore, the mosaic crystal structure is looser than the channel-type crystal structure in the water treated samples, probably allowing water molecules easily to enter the mosaic crystal to dissolve the product.

Figure S2 shows the images of water and DMF treated PR samples. Here the water treated samples can form thin slices except for WF30, while for WF0 and WF10 slices less than 0.3 mm in thickness, they exhibit a bit of flexibility and can be rolled up. However, for the DMF treated PR samples, they are too brittle to form slices or films. Furthermore, with the increase of entrapped  $\gamma$ -CDs, all the samples become more and more brittle. For example, WF30 cannot form films, while WF10 can give rise to a film but with some cracks as indicated by arrows in Figure S2C. The F0 samples without any  $\gamma$ -CDs can be cast into slices in both water and DMF treatments. The FE-SEM results revealed that the DMF treated PRs are crystallized with a tetragonal topography while the water treated ones are similar to the F0 samples. So it was reasonable that the DMF treated samples are more brittle than the water treated ones. It was a pity that the mechanical properties (maximum tensile strength, elongation at break and so forth) cannot be tested because even though F0 and WF10 can form slices, they are too

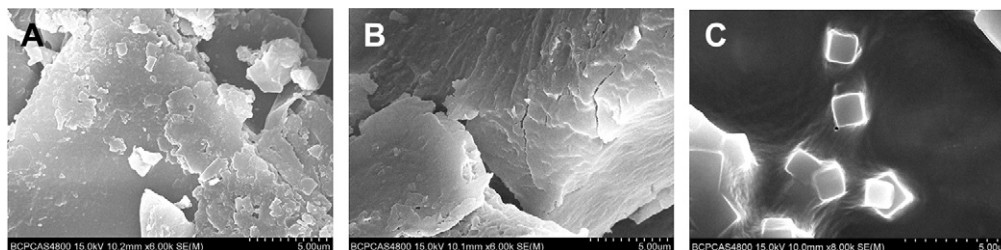


**Fig. 8.** FE-SEM images of F0, WF30 and DF30.

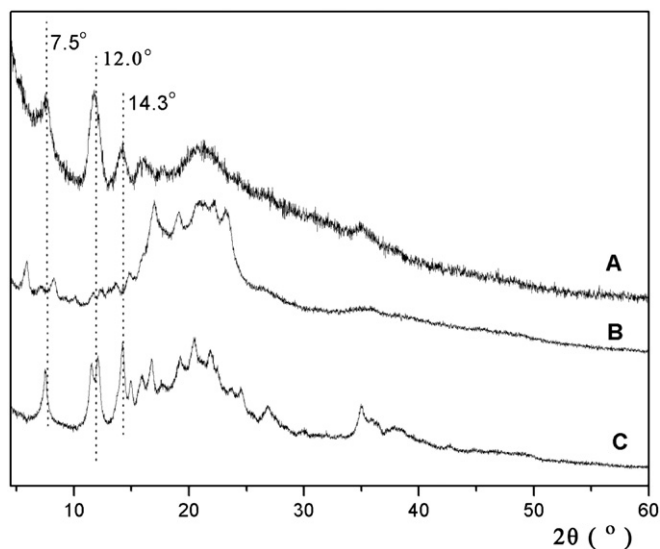


**Fig. 9.** WAXRD patterns of WF30 (A), sample A after DMF treatment (B) and sample B after water treatment (C).

brittle to go through the mechanical testing, possibly due to their relatively low molecular weights.

As the solvent response of the resulting PRs is a physical process, the structure transformation must be a reversible process. Fig. 9 presents the WAXRD patterns of F30 subjected to successive solvent treatments. The water treated WF30 shows the channel-type crystal diffractions peaks at  $7.54^\circ$  and  $12.01^\circ$ , respectively (Fig. 9A). After DMF treatment, it was transformed into the novel mosaic crystal structure (Fig. 9B). If it was treated with water again, the typical channel-type crystal structure was recovered with the reappearance of the diffraction peaks at  $7.54^\circ$  and  $12.01^\circ$ , (Fig. 9C), respectively. These results demonstrated that the crystal structures of these as-prepared  $\gamma$ -CD-based PRs are not only solvent-responsive but also convertible by the corresponding solvent treatments.

Evidently an introduction of two flanking PNIPAAm segments produced a kind of novel PR-based triblock copolymers. Their thermo-responsive behaviors in aqueous solution and solid state due to the introduction of PNIPAAm segments are our ongoing studies.

#### 4. Conclusions

A series of novel PR-based triblock copolymers comprising  $\gamma$ -CD-Pluronic F127-PPR as a middle block and two PNIPAAm as flanking blocks were prepared via the ATRP of NIPAAm in aqueous medium at room temperature. Interestingly the resulting PRs gave a  $\gamma$ -CD aggregated state around the PPO segment showing a novel crystal structure after DMF treatment, while they yielded a  $\gamma$ -CD aggregated state onto the PPO segments exhibiting a typical channel-type crystal structure after water incubation. The two crystal structures were found to be not only a function of solvent incubations, but also convertible by the solvent treatments. The solubility and flexibility of the PRs were greatly changed after solvent treatments. These findings provide an opportunity to alter the physical properties of PRs without any chemical modifications of entrapped CDs. Furthermore, the changes of aggregated and

dispersed states of  $\gamma$ -CDs along the polymer chain as a function of solvent stimuli render these PRs potential to be used as smart materials.

#### Acknowledgment

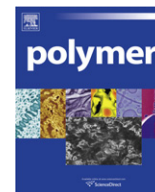
The authors acknowledge the support from the Natural Science Foundation of China (No. 20974015) and the Doctoral Program Foundation of Ministry of Education of China (No. 20091101110029).

#### Appendix. Supplementary material

Supplementary material related to this article can be found online at doi:10.1016/j.polymer.2010.12.014.

#### References

- [1] Harada A, Okada M, Kawaguchi Y, Kamachi M. *Polym Adv Technol* 1999;10:3–12.
- [2] Huang F, Gibson HW. *Prog Polym Sci* 2005;30:982–1018.
- [3] Wenz G, Han BH, Muller A. *Chem Rev* 2006;106:782–817.
- [4] Araki J, Ito K. *Soft Matter* 2007;3:1456–73.
- [5] Li J, Loh XJ. *Adv Drug Deliv Rev* 2008;60:1000–17.
- [6] Harada A, Takashima Y, Yamaguchi H. *Chem Soc Rev* 2009;38:875–82.
- [7] Harada A, Kamachi M. *Macromolecules* 1990;23:2821–3.
- [8] Harada A. *Coord Chem Rev* 1996;148:115–33.
- [9] Ritter H. *Angew Makromol Chem* 1994;223:165–75.
- [10] Born M, Koch T, Ritter H. *Acta Polym* 1994;45:68–72.
- [11] Born M, Ritter H. *Angew Chem Int Ed Engl* 1995;34:309–11.
- [12] Sarvothaman MK, Ritter H. *Macromol Rapid Commun* 2004;25:1948–52.
- [13] Anderson S, Aplin RT, Claridge TDW, Goodson III T, Maciel AC, Rumbles G. *J Chem Soc Perkin Trans 1* 1998;998:2383–98.
- [14] Taylor PN, O'Connell MJ, McNeill LA, Hall MJ, Aplin RT, Anderson HL. *Angew Chem Int Ed Engl* 2000;39:3456–60.
- [15] Michels JJ, O'Connell MJ, Taylor PN, Wilson JS, Cacialli F, Anderson HL. *Chem Eur J* 2003;9:6167–76.
- [16] Frampton MJ, Anderson HL. *Angew Chem Int Ed Engl* 2007;46:1028–64.
- [17] Ito K. *Polym J* 2007;39:489–99.
- [18] Karino T, Shibayama M, Ito K. *Physica B* 2006;385–386:692–6.
- [19] Fleury G, Schlatter G, Brochon C, Hadziioannou G. *Polymer* 2005;46:8494–501.
- [20] Okumura Y, Ito K. *Adv Mater* 2001;13:485–7.
- [21] Araki J, Ito K. *J Polym Sci A Polym Chem* 2006;44:532–8.
- [22] Araki J, Ito K. *J Polym Sci A Polym Chem* 2006;44:6312–23.
- [23] Tong XM, Zhang XW, Ye L, Zhang AY, Feng ZG. *Soft Matter* 2009;5:1848–55.
- [24] Xie ZG, Hou DD, Ye L, Zhang AY, Feng ZG. *Front Mater Sci China* 2007;1:395–400.
- [25] Hou DD, Geng X, Ye L, Zhang AY, Feng ZG. *Front Mater Sci China* 2010;4:70–7.
- [26] Dai X, Dong C, Yan D. *J Phys Chem B* 2008;112:3644–52.
- [27] Ren LX, Chen YM, Ke FY, Liang DH, Huang J. *Macromolecules* 2008;41:5295–300.
- [28] Zhang XW, Zhu XQ, Tong XM, Ye L, Zhang AY, Feng ZG. *J Polym Sci A Polym Chem* 2008;46:5283–93.
- [29] Wang J, Gao P, Ye L, Zhang AY, Feng ZG. *J Phys Chem B* 2010;114:5342–9.
- [30] Zhang XW, Zhu XQ, Ke FY, Ye L, Chen EQ, Zhang AY. *Polymer* 2009;50:4343–51.
- [31] Tong XM, Gao P, Zhang XW, Ye L, Zhang ZY, Feng ZG. *Polym Int* 2010;59:917–22.
- [32] Takahashi A, Katoono R, Yui N. *Macromolecules* 2009;42:8587–9.
- [33] Fujita H, Ooya T, Yui N. *Macromolecules* 1999;32:2534–41.
- [34] Fujita H, Ooya T, Yui N. *Macromol Chem Phys* 1999;200:706–13.
- [35] Yang C, Yang J, Ni X, Li J. *Macromolecules* 2009;42:3856–9.
- [36] Tong XM, Zhang XW, Ye L, Zhang AY, Feng ZG. *Polymer* 2008;49:4489–93.
- [37] Harada A, Li J, Kamachi M. *J Am Chem Soc* 1994;116:3192–6.
- [38] Okumura H, Kawaguchi Y, Harada A. *Macromolecules* 2001;34:6338–43.
- [39] Kawasaki J, Satou D, Takagaki T, Nemoto T, Kawaguchi A. *Polymer* 2007;48:1127–38.
- [40] Higashi T, Hirayama F, Yamashita S, Misumi S, Arima H, Uekama K. *Int J Pharm* 2009;374:26–32.
- [41] Loethen S, Kim J, Thompson D. *Polym Rev* 2007;47:383–418.



## Synthesis and self-assembly of miktoarm star copolymers of (polyethylene)<sub>2</sub>–(polystyrene)<sub>2</sub>

Ran Liu<sup>a</sup>, Zhiyun Li<sup>a</sup>, Dan Yuan<sup>a</sup>, Chunfeng Meng<sup>a</sup>, Qing Wu<sup>a,b</sup>, Fangming Zhu<sup>a,b,\*</sup>

<sup>a</sup>Institute of Polymer Science, School of Chemistry and Chemical Engineering, Sun Yat-Sen University, Guangzhou 510275, China

<sup>b</sup>Laboratory of Synthesis Design and Application of Polymer Materials, School of Chemistry and Chemical Engineering, Sun Yat-Sen University, Guangzhou 510275, China

### ARTICLE INFO

#### Article history:

Received 24 June 2010

Received in revised form

16 September 2010

Accepted 6 December 2010

Available online 14 December 2010

#### Keywords:

Miktoarm star copolymer

Click chemistry

Atom transfer radical polymerization (ATRP)

### ABSTRACT

We report on the synthesis and self-assembly of a novel well-defined miktoarm star copolymer of (polyethylene)<sub>2</sub>–(polystyrene)<sub>2</sub>, (PE)<sub>2</sub>–(PS)<sub>2</sub>, with two linear crystalline PE segments and two PS segments as the building blocks based on chain shuttling ethylene polymerization (CSEP), click reaction and atom transfer radical polymerization (ATRP). Initially, alkynyl-terminated PE (PE–≡) was synthesized via the esterification of pentynoic acid with hydroxyl-terminated PE (PE–OH), which was prepared using CSEP with 2,6-bis[1-(2,6-dimethylphenyl) imino ethyl] pyridine iron (II) dichloride/methylaluminumoxane/diethyl zinc and subsequent *in situ* oxidation with oxygen. (PE)<sub>2</sub>–(OH)<sub>2</sub> was then obtained by the click reaction of PE–≡ with diazido and dihydroxyl containing coupling agent. The two hydroxyl groups in (PE)<sub>2</sub>–(OH)<sub>2</sub> were then converted into bromoisobutyrate by esterification. At last, the (PE)<sub>2</sub>–(PS)<sub>2</sub> miktoarm star copolymers were synthesized by ATRP of styrene initiated from (PE)<sub>2</sub>–Br<sub>2</sub> macroinitiator. All the intermediates and final products were characterized by <sup>1</sup>H NMR and gel permeation chromatography (GPC). The self-assembly behavior was studied by dynamic light scattering (DLS) and atomic force microscopy (AFM). The crystallization of the (PE)<sub>2</sub>–(PS)<sub>2</sub> miktoarm star copolymers was studied by differential scanning calorimetry (DSC).

© 2010 Elsevier Ltd. All rights reserved.

### 1. Introduction

The synthesis of functionalized polyethylene has attracted a great deal of interest due to its improved properties in adhesion, compatibility with other polymer materials [1,2]. The use of functionalized polyethylene can widen its application in polymer blends, thermoplastic elastomers and polymer alloy [3]. However, the synthesis difficulty is due to the fact that polar functional groups can hardly be incorporated into polyethylene chains when produced by catalytic ethylene polymerization [4–6]. Fortunately, the advancements in chain transfer technologies permit the synthesis of functionalized polyethylene with desired structure successfully. The introduction of chain shuttling ethylene polymerization (CSEP) seems to shed a light for the highly efficient preparation of end-functionalized polyethylene with narrow molecular weight distribution [7–9]. Chain transfers to silicon [10], boron [11], zinc [12], aluminum [13] and magnesium [14] are most

commonly used to achieve the end-functionalized polyethylene and many polyethylene-based block copolymers have been synthesized by combination of chain transfer reaction and chain extension reaction, including coupling reaction and living polymerization initiated from macroinitiator, such as living ring-opening polymerization (ROP) [15], atom transfer radical polymerization (ATRP) [3,16–18] and reversible addition-fragmentation chain transfer (RAFT) polymerization [19,20].

Compared to their linear block copolymers, miktoarm star copolymers consisting of chemically different chains emanating from a central junction point, have received ever-increasing attention due to their unique properties in bulk and solution [21,22]. The synthesis routine can be generally categorized into two strategies, namely the “core-first” and “arm-first” approaches. In the core-first approach, a multifunctional initiator or macroinitiator which is usually prepared by living polymerization and post-functionalized reaction is employed to grow arms via various controlled/living polymerizations including living anionic polymerization [23], ROP [24,25] and controlled/living radical polymerization, such as nitroxide-mediated polymerization (NMP) [26], ATRP [27,28], RAFT [29,30] and single-electron-transfer living radical polymerization (SET-LRP) [31]. The second approach relies on the preparation of terminally functionalized linear polymer chains followed by linking

\* Corresponding author. Institute of Polymer Science, School of Chemistry and Chemical Engineering, Sun Yat-Sen University, Guangzhou 510275, China. Tel.: +86 20 84113250; fax: +86 20 84114033.

E-mail address: [ceszfm@mail.sysu.edu.cn](mailto:ceszfm@mail.sysu.edu.cn) (F. Zhu).

to the multifunctional cores. Especially in recent years, click coupling reaction has been applied to the synthesis of polymers with complex topologies. Miktoarm star copolymers can also be synthesized by the click coupling reaction between end-clickable-functionalized polymer chains [32–34]. Two AB block copolymer chains were linked together to form  $A_2B_2$  type miktoarm star copolymers, the chemical connection in the junction point can play an important role in bulk and solution properties. Originally, the  $A_2B_2$  miktoarm star copolymers were synthesized by living anionic polymerization. Hadjichristidis reported the synthesis of  $(PS)_2-(PB)_2$  and  $(PI)_2-(PB)_2$  [35]. Up to date, the living/controlled polymerizations, such as ROP, ATRP and RAFT, have provided versatile routines to synthesize  $A_2B_2$  miktoarm star copolymers. Hadjichristidis has prepared  $(PCL)_2-(PS)_2$  by combination of ROP of caprolactone and ATRP of styrene [36]. Likewise, Tunca also has reported  $(PS)_2-(PMMA)_2$  by two steps including NMP of styrene and ATRP of methyl methacrylate [37]. Zhu has reported  $(PAA)_2-(PVAc)_2$  by combination of ATRP and RAFT [30]. Recently, click chemistry has been proved to be a powerful tool to synthesize polymers with complex architecture. Accordingly, one can prepare the  $A_2-B_2$  miktoarm star copolymers by click coupling reactions between end-functionalized polymer chains [38].

To the best of our knowledge, the synthesis of  $A_2-B_2$  miktoarm star copolymers with linear crystalline polyethylene (PE) and polystyrene (PS) as building blocks has not been reported. In this work, we reported a convenient route for the preparation of novel  $A_2-B_2$  miktoarm star copolymer,  $(PE)_2-(PS)_2$ . At first, alkynyl end-terminated PE (PE $\equiv$ ) was synthesized via the esterification of pentynoic acid with monohydroxyl-terminated PE (PE-OH), which was prepared using CSEP with 2,6-bis[1-(2,6-dimethylphenyl) imino ethyl] pyridine iron(II) dichloride (complex **1**)/methylaluminumoxane (MAO)/diethyl zinc ( $ZnEt_2$ ) and subsequent in situ oxidation with oxygen. Then two PE $\equiv$  chains were linked together by click reaction with 2,2-bis(azidomethyl)-1,3-propanediol as the coupling agent. Then the two hydroxyl groups at the junction point were converted to the ATRP initiators by esterification with 2-bromo-2-methylpropionyl bromide. In the end, the polyethylene macroinitiator was used to grow polystyrene arms via ATRP to yield the  $(PE)_2-(PS)_2$  miktoarm star copolymer. All the intermediates and final products were characterized by  $^1H$  NMR and gel permeation chromatography (GPC). The thermal behavior of the PE and PS blocks was investigated by differential scanning calorimetry (DSC). The resultant miktoarm star copolymers can self-assemble into spherical micelles in cyclohexane through the study of dynamic light scattering (DLS) and atomic force microscopy (AFM).

## 2. Experimental section

### 2.1. Materials

Styrene was purified twice by passing through a basic alumina to remove the inhibitor.  $ZnEt_2$  was purchased from Alfa Aesar as a 1.0 mol/L solution in hexane. Toluene was refluxed over sodium/benzophenone. Chlorobenzene was dried over  $CaH_2$  and distilled under reduced pressure.  $N,N'$ -dimethylformamide (DMF) was dried and distilled over  $CaH_2$  under vacuum. Dichloromethane ( $CH_2Cl_2$ ) was distilled from  $P_2O_5$ . pentynoic acid, sodium azide ( $NaN_3$ ),  $N,N,N',N''$ -pentamethyldiethylenetriamine (PMDETA) and 2-bromo-2-methyl-propionyl bromide were purchased from Aldrich and used as received. Copper(I)bromide (Acros 99.5%) was stirred in glacial acetic acid overnight, washed with ethanol and ether, dried under vacuum overnight. 2,2-bis(bromomethyl)-1,3-propanediol (TGI 98%) was recrystallized from hot water. Other

reagents if not specified were purchased from Sinopharm Chemical Reagent Co. Ltd. and used as received.

2,6-bis[1-(2,6-dimethylphenyl) imino ethyl] pyridine iron(II) dichloride (complex **1**) was synthesized according to the literature [39]. MAO was prepared by partial hydrolysis of trimethylaluminum in toluene at 0–60 °C with  $Al_2(SO_4)_3 \cdot 18H_2O$  as the water source. The initial  $[H_2O]/[Al]$  in molar ratio was 1.3.

#### 2.1.1. Synthesis of PE-OH

To a 300 mL steel reactor equipped with a mechanical stirrer and a temperature probe were introduced 100 mL toluene, MAO (0.23 g,  $[Al] = 3.75$  mmol),  $ZnEt_2$  (2.5 mL, 2.5 mmol) and saturated with ethylene. 2,6-bis[1-(2,6-dimethylphenyl) imino ethyl] pyridine iron(II) dichloride (3.0 mg, 5.0  $\mu$ mol) in 10 mL toluene was then added to start the polymerization. The pressure of ethylene was kept at 2.5 Mpa. After 30 min, the mixture was warmed to 100 °C and dry oxygen was bubbled for 2 h. Followed the oxidation reaction, the mixture was poured into acidic methanol to precipitate the product. After filtration, washed with methanol and dried under vacuum at 60 °C overnight, a white powder was obtained. Yield 2.3 g  $^1H$  NMR (300 MHz,  $CDCl_3$ , ppm):  $\delta = 0.87-0.90$  (t,  $-CH_3$ ), 1.20–1.30 (m,  $-CH_2CH_2-$ ), 3.62 (t,  $-CH_2OH$ ).

#### 2.1.2. Synthesis of PE- $CH_2OCOCH_2CH_2C\equiv CH$ (PE $\equiv$ )

To a 150 mL round bottom flask were added 80 mL anhydrous toluene, PE-OH (1.4 g,  $[OH] = 1.5$  mmol), pentynoic acid (1.5 g, 15 mmol) and a small amount of  $HfCl_4 \cdot 2THF$  under nitrogen atmosphere. The reaction mixture was refluxed for 24 h with a water separator to remove water. After reaction, the mixture was cooled, poured into methanol to precipitate the product. The white powder was dried under vacuum at 60 °C overnight. Yield 1.3 g, 91%.  $^1H$  NMR (300 MHz,  $CDCl_3$ , ppm):  $\delta = 0.87-0.90$  (t,  $-CH_3$ ), 1.20–1.40 (m,  $-CH_2CH_2-$ ), 1.97–2.01 (t,  $-CH_2C\equiv CH$ ), 2.46–2.51 (m,  $-COCH_2CH_2$ ), 4.03–4.05 (t,  $-CH_2OCOCH_2$ ).

#### 2.1.3. Synthesis of 2,2-Bis(azidomethyl)-1,3-propanediol

To a 50 mL round bottom flask were added 2-bis(azidomethyl)-1,3-propanediol (5 g, 19.2 mmol), sodium azide (3 g, 46.8 mmol) and 20 mL DMSO. The mixture was heated to 100 °C for 36 h. After the reaction, the mixture was poured into 40 mL water and extracted for five times with dichloromethane, the organic layer was then washed three times with water and dried under reduced pressure to yield a light yellow oil. Yield 3.4 g, 78%.  $^1H$  NMR (300 MHz,  $CDCl_3$ , ppm):  $\delta = 3.60-3.64$  (s,  $-CH_2OH$ ), 3.42–3.46 (s,  $-CH_2N_3$ ), 2.32–2.41 (b,  $CH_2OH$ ).

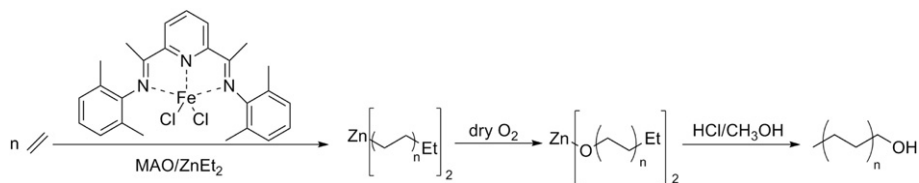
#### 2.1.4. Coupling reaction between PE $\equiv$ and 2,2-Bis(azidomethyl)-1,3-propanediol

To a 25 mL round bottom flask were added 2-bis(azidomethyl)-1,3-propanediol (0.03 g, 0.17 mmol), PE $\equiv$  (0.40 g, 0.38 mmol) and 10 mL DMF. The mixture was heated to 120 °C until PE $\equiv$  melt. Then  $CuSO_4$  (0.01 g, 0.06 mmol) and sodium ascorbate (0.025 g, 0.12 mmol) were added. Rapidly, the color turned from yellow to brown. After 3 h, the mixture was cooled, poured into 100 mL methanol. The solid was filtrated, washed with EDTA solution (0.01 mol/L), methanol and dried under vacuum at 60 °C for 2 h. The resultant brown solid was then extracted with boiling THF for 2 h. The insoluble fraction was collected, dissolved in 10 mL toluene at 100 °C, poured into 200 mL methanol. The obtained pale yellow powder was filtrated, dried under vacuum at 60 °C overnight.

#### 2.1.5. Synthesis of polyethylene macroinitiator for ATRP $[(PE)_2-(PS)_2]$

In the typical procedure,  $(PE)_2-(OH)_2$  (0.5 g, 0.27 mmol), triethylamine (0.17 mL, 2.1 mmol), 2-bromo-2-methyl-propionyl bromide (0.22 mL, 1.7 mmol) and 20 mL toluene were introduced





**Scheme 1.** Synthetic Route Employed for the Synthesis of PE–OH.

into a 100 mL flask under nitrogen. The flask was then sealed with a rubber septum and heated to 90 °C for 12 h. After reaction, the mixture was poured into 200 mL acidic methanol (containing 20 mL HCl). The resulting polymer was filtrated, washed with methanol, dried at 60 °C overnight to yield a light brown solid.

#### 2.1.6. Synthesis of (PE)<sub>2</sub>–(PS)<sub>2</sub> miktoarm star copolymers

In the typical polymerization, polyethylene macroinitiator ((PE)<sub>2</sub>–(Br)<sub>2</sub>, 0.3 g, 0.32 mmol–Br) was added to a 10 mL Schlenk tube. This tube was then deoxygenated by degassing and backfilling nitrogen for 4 times, then 2.0 mL styrene, PMDETA (0.14 mL, 0.64 mmol) and 6 mL chlorobenzene were added via syringe. Then nitrogen was bubbled for 30 min to remove the residual oxygen. CuBr (0.048 g, 0.32 mmol) was then added to the tube under nitrogen atmosphere. The Schenk tube was sealed under nitrogen and stirred at room temperature for 30 min. At last the tube was immersed into 100 °C oil bath for a certain time. After the polymerization, the solution was cooled, poured into 100 mL methanol. The resulting blue solid was washed with EDTA solution (0.01 mol/L), methanol and dried under vacuum at 60 °C overnight to yield an off-white solid.

#### 2.1.7. Self-assembly of (PE)<sub>2</sub>–(PS)<sub>2</sub> mikroarm star copolymer in cyclohexane

Typically, 10 mg of copolymer was placed in a 50 mL flask and 20 mL cyclohexane was then added. The resultant mixture was stirred at 50 °C for 24 h, then the transparent solution was slowly cooled down and passed through a 0.45 μm PTFE filter. All the micelle solutions were stood for 48 h before analysis.

**2.1.7.1. Measurements.** <sup>1</sup>H NMR (300 MHz) spectra were recorded in CDCl<sub>3</sub> or in 1,2-dichlorobenzene-*d*<sub>4</sub> at 80 °C. Molecular weight and molecular weight distribution (*M<sub>w</sub>*/*M<sub>n</sub>*) were determined by gel permeation chromatography (GPC) against narrow molecular weight distribution polystyrene standards on a Waters 2414 refractive index detector at ambient temperature with THF as solvent or a Water 150C at 135 °C with 1,2,4-trichlorobenzene as solvent.

DSC experiments were carried out on a Perkin–Elmer Pyris 1. The calibration was performed with indium and tin, and all tests were run employing ultra pure nitrogen as purge gas. DSC heating scans were performed at 10 °C/min over a temperature range of –20 to + 150 °C.

DLS measurements were conducted at 25 °C on a Brookhaven BI-200SM apparatus with a BI-9000AT digital correlator and a He–Ne laser at 532 nm. The angle was fixed to be 90°. The samples were placed in an index-matching decaline bath with temperature control within ±0.2 °C. Each solution was clarified by passing through a 0.45 μm PTFE filter to remove dust. The stock aqueous solution (0.5 mg/mL) was first prepared and then diluted to a proper concentration for the DLS measurement. The data were analyzed by CONTIN algorithm, while the hydrodynamic radius (*R<sub>h</sub>*) and size polydispersity of the particles (individual chains or micelles) were obtained by a cumulant analysis of the experimental correlation function. In DLS, the Laplace inversion of each measured

intensity time-correlated function in a dilute solution can result in a characteristic line width distribution *G*(Γ). For a purely diffusive relaxation, *G*(Γ) can be converted to a hydrodynamic radius (*R<sub>h</sub>*) distribution by using the Stokes–Einstein equation.

The morphological observation of the micelle was performed on SPA300HV Probe station (Japan) in tapping mode. The samples were prepared by drying the micelle solution on freshly cleaved mica at room temperature.

### 3. Results and discussion

#### 3.1. Synthesis and characterization of (PE)<sub>2</sub>–(PS)<sub>2</sub> miktoarm star copolymers

As shown in Scheme 1, chain shuttling ethylene polymerization was conducted with complex 1/MAO as catalyst and ZnEt<sub>2</sub> as chain shuttling agent to produce linear PE–OH according to our previous report and literature [16,40]. In this case, at a ratio of Fe:Al:Zn = 1:750:500, a white product was obtained. <sup>1</sup>H NMR of PE–OH was shown in Fig. 1a. By comparing the integration areas of *c* and *a* peaks (0.89 and 3.62 ppm), the efficiency of hydroxyl termination could be estimated to be about 80%. On the basis of the 80% functionality, the molecular weight of PE–OH in terms of the proportion of integration areas of *c* and *b* peaks (0.89 and 1.25 ppm) was 800. GPC analysis (Fig. 2a) of the PE–OH also revealed a monomodal and symmetric elution peak, *M<sub>n</sub>* = 1100 and *M<sub>w</sub>*/*M<sub>n</sub>* = 1.12.

PE–CH<sub>2</sub>OCOCH<sub>2</sub>CH<sub>2</sub>C≡CH (PE–≡) was easily obtained by esterification of PE–OH with pentynoic acid using HfCl<sub>4</sub>·2THF as catalyst. The <sup>1</sup>H NMR of PE–CH<sub>2</sub>OCOCH<sub>2</sub>CH<sub>2</sub>C≡CH was shown in Fig. 1b. The signal of the methylene protons adjacent to the hydroxyl group at 3.62 ppm completely disappeared. Alternatively, the new signal of methylene protons adjacent to the ester group was observed at 4.05 ppm. Furthermore, the signal assignable to the hydrogen on the alkynyl appeared at 1.95 ppm. These results indicated the efficiency of the esterification was almost 100%. So, 80% of the PE chains were capped with alkynyl group.

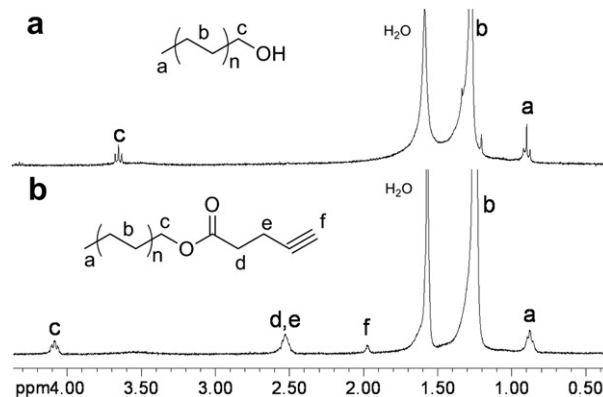


**Fig. 1.** <sup>1</sup>H NMR spectra for PE–OH (a) and PE–COCH<sub>2</sub>CH<sub>2</sub>C≡CH (b).

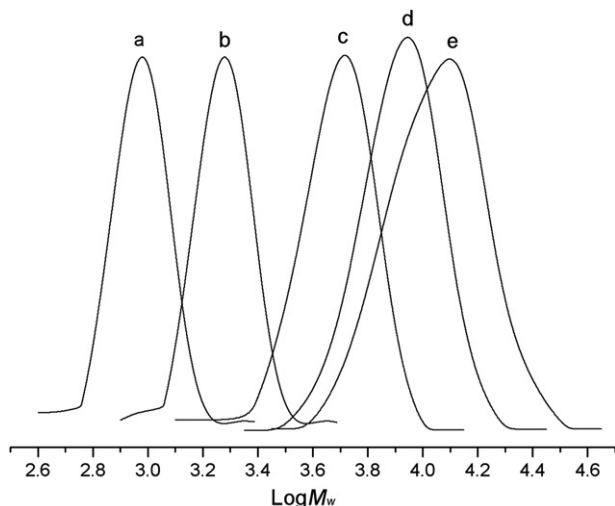


**Fig. 2.** GPC curves of PE–OH (a),  $(PE)_2$ –(OH) $_2$  (b),  $(PE)_2$ –(PS) $_2$ –2 h (c),  $(PE)_2$ –(PS) $_2$ –4 h (d) and  $(PE)_2$ –(PS) $_2$ –6 h (e).

Click chemistry is widely used in the polymer coupling reactions to prepare linear and star copolymers due to its high efficiency [41–43]. In this work, 2,2-bis(azidomethyl)-1,3-propanediol was used as the coupling agent to combine two polyethylene chains together.  $CuSO_4$ /Sodium ascorbate were used as the catalyst system to produce Cu(I) in situ according to the literature [13]. To make sure the complete consumption of the azido containing coupling agent, a slight excess of PE–≡ was used. After reaction, the residual copper salt could be easily removed by washing with EDTA solution. Then the crude product was extracted with boiling THF to remove PE homopolymers, the insoluble fraction was collected and dried under vacuum [40]. The resultant polymer was studied by GPC. Fig. 2b showed the GPC curves of coupling product. The elution peak was monomodal and quite symmetric with narrow molecular weight distribution ( $M_w/M_n = 1.15$ ). Compared to PE–≡ (Fig. 2a), the elution peak clearly shifted toward higher molecular

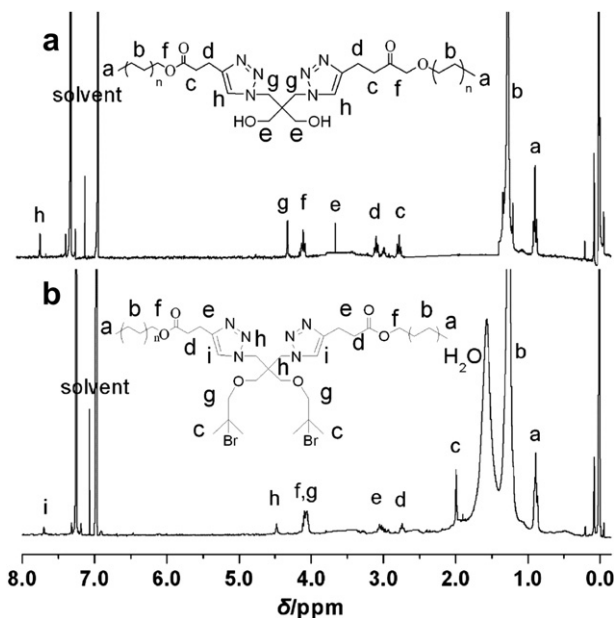
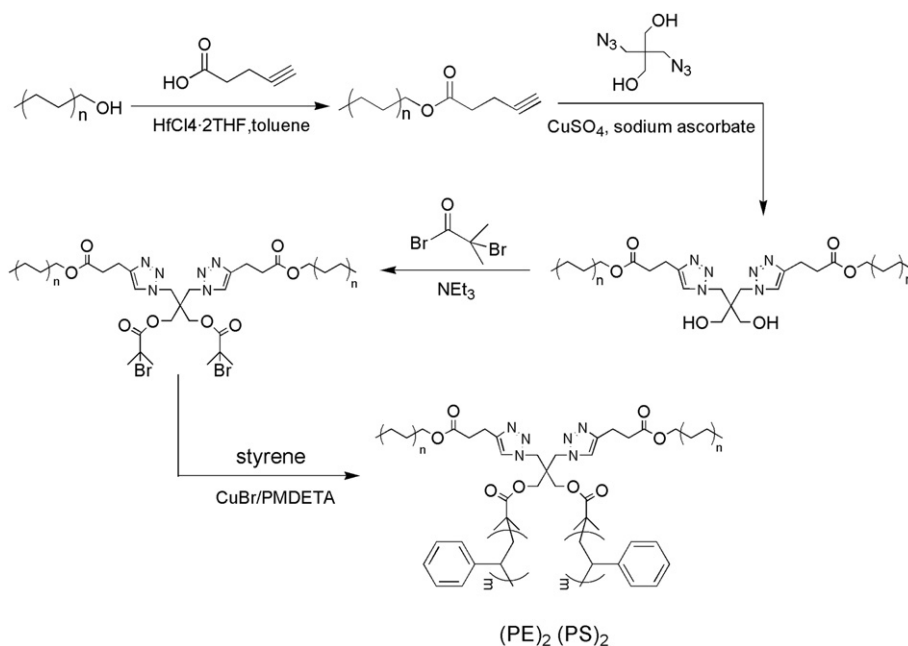


**Fig. 3.**  $^1H$  NMR spectra for  $(PE)_2$ –(OH) $_2$  (a) and  $(PE)_2$ –(Br) $_2$  (b).

weight region. The product was also characterized by  $^1H$  NMR. Fig. 3a revealed the  $^1H$  NMR spectra of the coupling product. The signal of hydrogen on the alkyne at 1.95 ppm completely disappeared and the new signal of methine proton in the triazole ring was observed at 7.68 ppm. Furthermore, the signals assigned to the methylene protons in the neighborhood of the triazole ring and hydroxyl group appeared at 4.27 ppm and 3.62 ppm respectively. We also confirmed all the azido groups which were consumed in terms of the complete disappearance of the methylene protons next to azido group at 3.42 ppm. So based on the above results, we demonstrated that well-defined coupled PE with two hydroxyl group at the junction point was prepared by combination of CSEP and click reaction.



**Scheme 2.** Synthetic Route Employed for the Synthesis of  $(PE)_2$ –(PS) $_2$  Miktoarm Star Copolymer.

**Table 1**  
GPC results of the  $(PE)_2-(PS)_2$  miktoarm star copolymers.

Polymers	$M_n^a$ (kg/mol)	$M_n^b$ (kg/mol)	$M_w/M_n^a$	PS wt%
PE	1.1	0.8	1.12	/
$(PE)_2-(OH)_2$	1.8	1.7	1.15	/
$(PE)_2-(PS)_2-2\text{ h}$	4.7	5.6	1.15	62.7
$(PE)_2-(PS)_2-4\text{ h}$	7.5	8.7	1.16	76.2
$(PE)_2-(PS)_2-6\text{ h}$	10.1	12.4	1.21	82.2

<sup>a</sup> Determined by GPC

<sup>b</sup> Determined by  $^1\text{H}$  NMR.

The hydroxyl groups in  $(PE)_2-(OH)_2$  can be easily converted to bromo groups by esterification with 2-bromo-2-methylpropionyl bromide in the presence of  $\text{NET}_3$  [16,17]. To make sure the complete conversion of hydroxyl into bromoisobutyrate, a large excess of 2-bromo-2-methylpropionyl bromide was used. Fig. 3b showed the  $^1\text{H}$  NMR spectra of the  $(PE)_2-(Br)_2$  macroinitiator. The signal of  $-\text{CH}_2\text{OH}$  at 3.62 ppm disappeared completely and the methylene group next to the ester group  $-(\text{CH}_2)_2\text{Br}$  could also be observed at 1.98 ppm. These results indicated that the esterification of hydroxyl group proceeded quantitatively.

Finally, the  $(PE)_2-(Br)_2$  macroinitiator was used to grow polystyrene arms via ATRP to yield  $(PE)_2-(PS)_2$  miktoarm star copolymer. ATRP of styrene was conducted with  $\text{CuBr}/\text{PMDETA}$  as catalyst system and chlorobenzene as solvent to dissolve the  $(PE)_2-(Br)_2$  macroinitiator efficiently [16,17]. The synthesis routine was illustrated in Scheme 2. The polymerization time varied from 2 h to 6 h to control the length of PS blocks. After polymerization, the solution was poured into methanol to precipitate the product and the copper salt could also be removed by EDTA solution. The final product was analyzed by GPC. Fig. 2c–e showed GPC curves of miktoarm star copolymers and the results were summarized in Table 1. All the resultant miktoarm star copolymers showed monomodal peaks with narrow molecular weight distribution, although with polymerization time increasing, the molecular weight distribution broadened slightly. Compared to their precursors, the elution peaks clearly shifted toward higher molecular weight region. These results indicated the successful ATRP of styrene from  $(PE)_2-(Br)_2$  macroinitiator. The product was also characterized by  $^1\text{H}$  NMR. Fig. 4 revealed the  $^1\text{H}$  NMR spectrum of the typical miktoarm star copolymer  $(PE)_2-(PS)_2-6\text{ h}$ . The resonance signals of the corresponding protons of both blocks were found in  $^1\text{H}$  NMR spectra. The characteristic

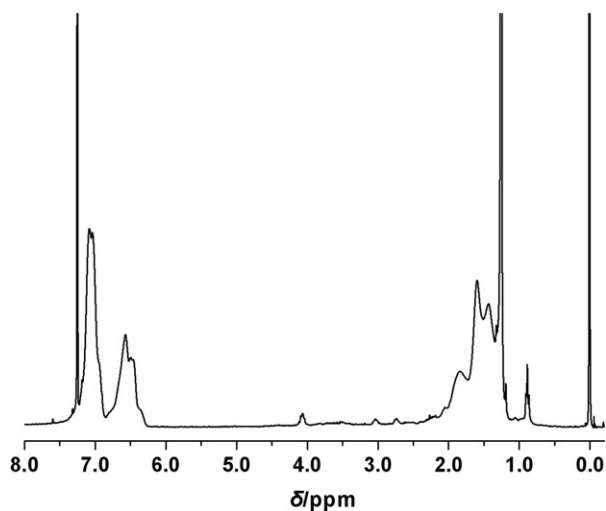


Fig. 4.  $^1\text{H}$  NMR spectrum for  $(PE)_2-(PS)_2$  miktoarm star copolymer.

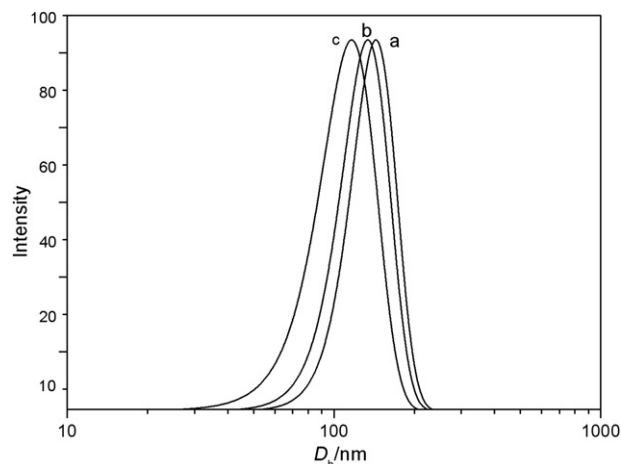


Fig. 5. Hydrodynamic diameters ( $D_h$ ) of the micelles of  $(PE)_2-(PS)_2-2\text{ h}$  (a),  $(PE)_2-(PS)_2-4\text{ h}$  (b) and  $(PE)_2-(PS)_2-6\text{ h}$  (c) self-assembled in cyclohexane at  $25\text{ }^\circ\text{C}$ .

resonance peak of  $-\text{CH}_2\text{CH}_2-$  repeating unit in PE block appeared at 1.25 ppm. Two new broad peaks for the hydrogen of phenyl ring ( $-\text{Ph}$ , 6.52–7.28 ppm) and the alkyl chain proton linked to the phenyl ( $-\text{CH}_2-\text{CH}-\text{Ph}$ , 1.90–2.46 ppm) could be also observed. So based on the above results, we demonstrated that well-defined  $(PE)_2-(PS)_2$

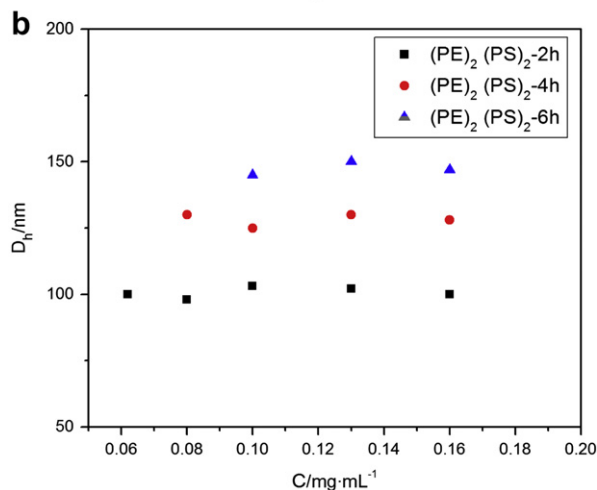
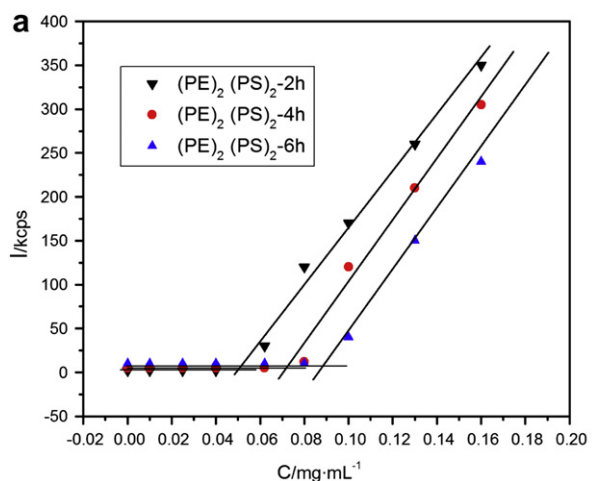


Fig. 6. Scattering intensity  $I$  (a) and micelle diameter  $D_h$  (b) versus polymer concentration.

miktoarm star copolymers with different content of PS segments were obtained by combination of CSEP, click chemistry and ATRP.

### 3.2. Self-assembly of $(PE)_2-(PS)_2$ miktoarm star copolymers in cyclohexane

Note that the self-assembly of linear polymethylene-*b*-polystyrene in THF has just been reported recently, spherical micelles with a diameter of 150 nm were formed [44]. Here linear polyethylene could not be dissolved in cyclohexane, but polystyrene can be easily dissolved. So micelles may be formed when  $(PE)_2-(PS)_2$  miktoarm star copolymers were dissolved in cyclohexane as selective solvent. The  $(PE)_2-(PS)_2$  miktoarm star copolymers were directly dissolved in cyclohexane at 50 °C for 24 h for sufficient dissolution and micellization, then the solution was filtrated through a 0.45  $\mu\text{m}$  filter to yield a transparent solution. First, the self-assembly behavior was carefully studied by DLS. Fig. 5 showed the hydrodynamic diameters ( $D_h$ ) determined by DLS at 25 °C and  $C = 0.20$  mg/mL for all the  $(PE)_2-(PS)_2$  miktoarm star copolymers. The results showed a clear aggregation of the polymer chains, as the average  $D_h$  was between 100 and 150 nm, much larger than the individual chains. The critical micelle concentration (CMC) was also studied to determine whether the polymer forms aggregates or exists as a unimer by DLS. Fig. 6a showed the relationship between light scattering intensity and polymer concentration. The CMC values were determined from the crossover point which were in the range of 0.05 mg/mL to 0.1 mg/mL. Also the micelle size showed

a rather small dependence on the polymer concentration above CMC within the studied ranges as shown in Fig. 6b. These results further indicated that stable micelles were formed in cyclohexane. Finally, the morphology of the micelles was studied by AFM. Fig. 7 showed the typical AFM images of the micelles formed from  $(PE)_2-(PS)_2$ -2 h and  $(PE)_2-(PS)_2$ -6 h. Spherical micelles were formed, the lateral dimensions were in the range of 100–180 nm and the heights of the micelles were in the range of 30–50 nm, which were significantly smaller than the diameters, these results indicated that the micelles may lay flat due to the adsorption of the PS corona on the silicon wafer [45,46].

### 3.3. Crystallization of $(PE)_2-(PS)_2$ miktoarm star copolymers

The crystallization of the  $(PE)_2-(PS)_2$  miktoarm star copolymers was studied by DSC. The cooling scans from melt and the subsequent heating scans were presented in Fig. 8. In the cooling scans, PE block in the miktoarm star copolymers exhibited a crystallization exotherm signal around 80 °C (first crystallization) and a small second crystallization around 60 °C. For the crystalline-amorphous block copolymers with chemically distinct blocks, the crystallization of the crystalline block is chemically restricted by the neighborhood amorphous block. Meanwhile the crystalline surroundings have a profound influence on the crystallization [47]. In this article, neat linear PE with  $M_w$  about 1000 and  $M_w/M_n = 1.12$  showed a broad crystallization temperature ( $T_c$ ) from 60 °C to 90 °C due to its low  $M_w$ , the glass transition temperature ( $T_g$ ) of PS block with  $M_w$  5000 located around 60 °C [48]. Upon cooling from melt,

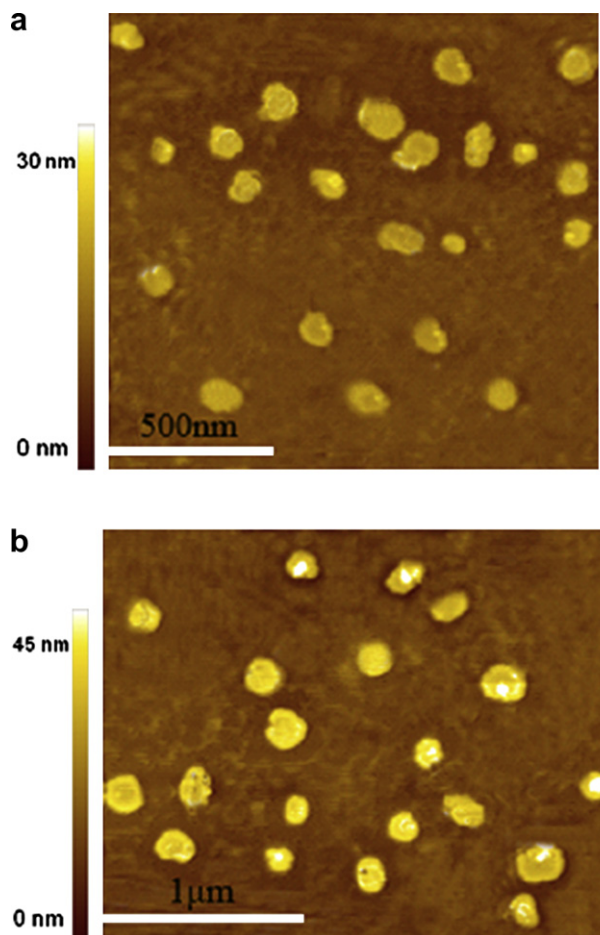


Fig. 7. AFM images of the micelles of  $(PE)_2-(PS)_2$ -6 h (a) and  $(PE)_2-(PS)_2$ -2 h (b) self-assembled in cyclohexane at 25 °C.

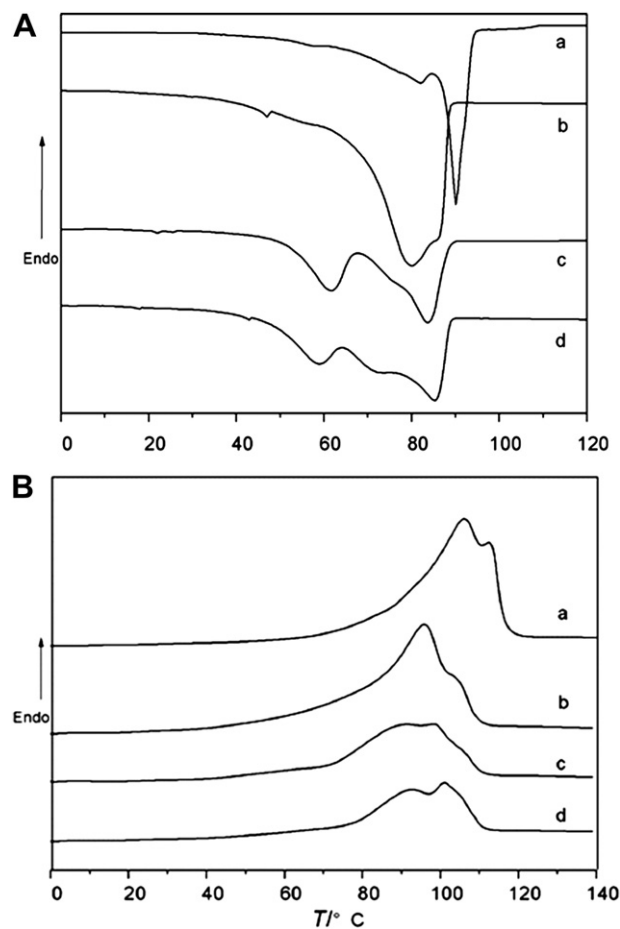


Fig. 8. DSC cooling curves (A) and heating curves (B) of PE (a),  $(PE)_2-(PS)_2$ -2 h (b),  $(PE)_2-(PS)_2$ -4 h (c) and  $(PE)_2-(PS)_2$ -6 h (d).

when temperature was above the  $T_g$  of PS block, PS domains were rubbery and PS chains were easy to move, the crystallization of PE was confined by chemically connected PS block [49,50], this chemical confinement led to a lower  $T_c$  than neat PE at 80 °C [36,51,52]. As temperature dropped below  $T_g$  of PS, PS block became glassy and the mobility of PS block was frozen, the crystallization of PE developed between the glassy PS boundaries. Compared to the rubbery PS chains, the rigid PS blocks provided stronger confinements on PE crystallization, thus a small second crystallization appeared around 60 °C much lower than neat PE [50,52]. For the heating scans, PE blocks in miktoarm star copolymers showed lower  $T_m$  than the corresponding polyethylene homopolymers. These results further indicated the confinements from PS blocks in the  $(PE)_2-(PS)_2$  miktoarm star copolymers during the crystallization of PE blocks [36,52,53].

#### 4. Conclusions

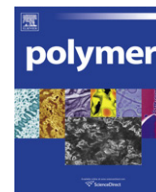
$(PE)_2-(PS)_2$  miktoarm star copolymers were prepared via a combination of CSEP, click chemistry and ATRP. First, PE—≡ with narrow molecular weight distribution was highly effectively synthesized by CSEP and post-functionalization. Then, the  $(PE)_2-(Br)_2$  macroinitiator was obtained from the esterification of 2-bromo-2-methylpropionyl bromide with  $(PE)_2-(OH)_2$ , which was synthesized by click coupling reaction between PE—≡ and 2,2-bis(azidomethyl)-1,3-propanediol. The resultant miktoarm star copolymers were yielded by ATRP of styrene initiated from  $(PE)_2-Br_2$  macroinitiator. The obtained  $(PE)_2-(PS)_2$  miktoarm star copolymers could self-assemble to form spherical micelles in cyclohexane with crystallized PE core and swollen PS shell. The crystallization of  $(PE)_2-(PS)_2$  miktoarm star copolymers was investigated by DSC.  $T_m$  of PE blocks was lower than the corresponding polyethylene homopolymer resultant from the confinement from PS blocks during the crystallization of PE blocks.

#### Acknowledgment

The financial supports of the National Natural Science Foundation of China (contract grant number: 20974123, 20774109 and 20734004) and the Guangdong Natural Science Foundation (contract grant number: 8151027501000103) are gratefully acknowledged.

#### References

- [1] Baffa LS, Novak BM. *Chem Rev* 2000;100:1479–94.
- [2] Singh RP. *Prog Polym Sci* 1992;17:251–81.
- [3] Kaneyoshi H, Matyjaszewski K. *J Polym Sci Part A Polym Chem* 2004;42:496–504.
- [4] Lu YY, Hu YL, Wang ZM, Manias E, Chung TC. *J Polym Sci Part A Polym Chem* 2002;40:3416–25.
- [5] Dong JY, Hu YL. *Coord Chem Rev* 2006;250:47–65.
- [6] Berkefeld A, Mecking S. *Angew Chem Int Ed Engl* 2008;47:2538–42.
- [7] Gibson VC. *Science* 2006;312:703–4.
- [8] Arriola DJ, Carnahan EM, Hustad PD, Kuhlman RL, Wenzel TT. *Science* 2006;312:714–9.
- [9] Kempe R. *Chem Eur J* 2007;13:2764–73.
- [10] Amin SB, Marks TJ. *J Am Chem Soc* 2007;129:2938–53.
- [11] Chung TC, Xu G, Lu YY, Hu YL. *Macromolecules* 2001;34:8040–50.
- [12] Britovsek G, Cohen SA, Gibson VC, Maddox PJ, Vanmeurs M. *Angew Chem Int Ed* 2002;41:489–91.
- [13] Kashiwa N, Matsugi T, Kojoh SI, Kaneko H, Kawahara N, Matsuo S, et al. *J Polym Sci Part A Polym Chem* 2003;41:3657–66.
- [14] Briquel R, Mazzolini J, Le Bris T, Boyron O, Boisson F, Delolme F, et al. *Angew Chem Int Ed* 2008;47:9311–3.
- [15] Han CJ, Lee MS, Byun DJ, Kim SY. *Macromolecules* 2002;35:8923–5.
- [16] Kaneyoshi H, Inoue Y, Matyjaszewski K. *Macromolecules* 2005;38:5425–35.
- [17] Chen JZ, Cun K, Zhang SY, Xie P, Zhao QL, Huang J, et al. *Macromol Rapid Commun* 2009;30:532–8.
- [18] Terao H, Ishii SI, Saito J, Matsuura S, Mitani M, Nagai N, et al. *Macromolecules* 2006;39:8384–93.
- [19] Lopez GR, Boisson C, Agosto FD, Spitz R, Boisson F, Gimes D, et al. *J Polym Sci Part A Polym Chem* 2007;45:2705–18.
- [20] Lopez GR, Boisson C, Agosto FD, Spitz R, Boisson F, Gimes D, et al. *Macromol Rapid Commun* 2006;27:173–81.
- [21] Riess G. *Prog Polym Sci* 2003;28:1107–70.
- [22] Hadjichristidis N, Iatrou H, Pitsikalis M, Mays J. *Prog Polym Sci* 2006;31:1068–132.
- [23] Pispas S, Hadjichristidis N. *Macromolecules* 2000;33:1741–6.
- [24] Liu H, Xu J, Jiang L, Yin R, Narain Y, Cai YL, et al. *J Polym Sci Part A Polym Chem* 2007;45:1446–62.
- [25] Li QB, Li FX, Jia L, Li Y, Liu YC, Yu JY, et al. *Biomacromolecules* 2006;7:2377–87.
- [26] Hawker CJ, Bosman AW, Harth E. *Chem Rev* 2001;101:3664–88.
- [27] Babin J, Taton D, Brinkmann M, Lecommandoux S. *Macromolecules* 2008;41:1384–92.
- [28] Cai YL, Armes SP. *Macromolecules* 2005;38:271–9.
- [29] Barner L, Davis TP, Stenzel MH, Kowolik CB. *Macromol Rapid Commun* 2008;29:539–59.
- [30] Zhang WD, Zhang W, Zhu J, Zhang ZB, Zhu XL. *J Polym Sci Part A Polym Chem* 2009;47:6908–18.
- [31] Tang XD, Liang XC, Yang Q, Fang XC, Shen ZH, Zhou QF. *J Polym Sci Part A Polym Chem* 2009;47:4420–7.
- [32] Gao HF, Matyjaszewski K. *Macromolecules* 2006;9:3154–60.
- [33] Wu ZM, Liang H, Lu J, Deng WL. *J Polym Sci Part A Polym Chem* 2010;48:3223–30.
- [34] Zhang YF, Li CH, Liu SY. *J Polym Sci Part A Polym Chem* 2009;47:3066–77.
- [35] Allgaier J, Young RN, Efstratiadis V, Hadjichristidis N. *Macromolecules* 1996;29:1794–7.
- [36] Lorenzo AT, Muller AJ, Pifftis D, Pitsikalis M, Hadjichristidis N. *J Polym Sci Part A Polym Chem* 2007;45:5387–97.
- [37] Gouger E, Hizal G, Tunca U. *J Polym Sci Part A Polym Chem* 2008;46:6703–11.
- [38] Gou PF, Zhu WP, Xu N, Shen ZQ. *J Polym Sci Part A Polym Chem* 2009;47:6962–76.
- [39] Britovsek G, Cohen SA, Gibson VC, Meurs MV. *J Am Chem Soc* 2004;126:10701–12.
- [40] Li T, Wang WJ, Liu R, Liang WH, Zhao GF, Li ZY, et al. *Macromolecules* 2009;42:3804–10.
- [41] Agut W, Taton D, Lecommandoux S. *Macromolecules* 2007;40:5653–61.
- [42] He WD, Han SC, Sun XL, Ying LL, Zhang BY. *J Polym Sci Part A Polym Chem* 2008;46:786–96.
- [43] Gao HF, Matyjaszewski K. *J Am Chem Soc* 2007;129:6633–9.
- [44] Chen JZ, Zhao QL, Lu HC, Huang J, Cao SH, Ma Z. *J Polym Sci Part A Polym Chem* 2010;48:1894–900.
- [45] Shamalz H, Schmelz J, Drechsler M, Yuan JY, Walther A, Schweimeimer K, et al. *Macromolecules* 2008;41:3235–42.
- [46] Kaditi E, Pispas S. *J Polym Sci Part A Polym Chem* 2010;48:24–33.
- [47] Li YL, Register RA, Rygn AJ. *Macromolecules* 2002;35:2365–74.
- [48] Zhu L, Mimnaugh BR, Ge Q, Qurik RP, Cheng SZD, Thomas EL, et al. *Polymer* 2001;42:9121–31.
- [49] Yu PQ, Xie XM, Wang Z, Li HS, Bates FS. *Polymer* 2006;47:1460–4.
- [50] Zhu L, Cheng ZSD, Calhoun BH, Ge Q, Qurik RP, Thomas EL, et al. *J Am Chem Soc* 2000;122:5957–67.
- [51] Fu J, Luan B, Yu X, Cong Y, Li J, Pan CY, et al. *Macromolecules* 2004;37:976–86.
- [52] Castillo RV, Arnal ML, Muller AJ, Hamley LW, Castelletto V, Schmalz H, et al. *Macromolecules* 2008;41:879–89.
- [53] Opitz R, Lambrea DM, Jeu WH. *Macromolecules* 2002;35:6930–6.



# A fluorescence sensor based on chiral polymer for highly enantioselective recognition of phenylalaninol

Jie Meng<sup>a</sup>, Guo Wei<sup>a</sup>, Xiaobo Huang<sup>a,c</sup>, Yu Dong<sup>a</sup>, Yixiang Cheng<sup>a,\*</sup>, Chengjian Zhu<sup>b,\*\*</sup>

<sup>a</sup>Key Lab of Mesoscopic Chemistry of MOE, School of Chemistry and Chemical Engineering, Nanjing University, Nanjing 210093, China

<sup>b</sup>State Key Laboratory of Coordination Chemistry, School of Chemistry and Chemical Engineering, Nanjing University, Nanjing 210093, China

<sup>c</sup>College of Chemistry and Materials Engineering, Wenzhou University, Wenzhou 325027, China

## ARTICLE INFO

### Article history:

Received 12 October 2010

Received in revised form

2 December 2010

Accepted 7 December 2010

Available online 15 December 2010

### Keywords:

Chiral polymer

Fluorescence sensor

Molecular recognition

## ABSTRACT

The chiral polymer **P-1** incorporating (*S*)-2,2'-binaphthol (BINOL) and (*S*)-2,2'-binaphthyldiamine (BINAM) moieties in the main chain of the polymer backbone was synthesized by the polymerization of (*S*)-6,6'-dibutyl-3,3'-diformyl-2,2'-binaphthol (*S*-**M-1**) with (*S*)-2,2'-binaphthyldiamine (*S*-**M-2**) via nucleophilic addition–elimination reaction, and the chiral polymer **P-2** could be obtained by the reduction reaction of **P-1** with NaBH<sub>4</sub>. The fluorescence intensity of the chiral polymer **P-1** exhibits gradual enhancement upon addition of (*D*)- or (*L*)-phenylalaninol and keeps nearly a linear correlation with the concentration molar ratios of (*D*)- or (*L*)-phenylalaninol. The value of enantiomeric fluorescence difference ratio (*e*<sub>f</sub>) is 6.85 for the chiral polymer on (*D*)-phenylalaninol. On the contrary, the chiral polymer **P-2** shows no obvious fluorescence response toward either (*D*)- or (*L*)-phenylalaninol.

© 2010 Elsevier Ltd. All rights reserved.

## 1. Introduction

Molecular recognition, especially chiral recognition, is one of the most fundamental and crucial properties of various natural systems. It is of particular significance for understanding the interactions of biological molecules and for the designing of asymmetric catalysis systems [1–5]. More and more attentions have been paid on fluorescence-based enantioselective sensors due to their high selectivity and potential application in analytical, biological, clinical and biochemical environments. They can also effectively provide a real-time analytical tool for chiral compound assay [4,6–9]. Using chiral fluorescence-based sensors can not only greatly facilitate rapid determination of enantiomeric composition of chiral compounds, but also allow a rapid screening of high-throughput catalysts for their asymmetric synthesis [10–13]. So far, reports of successful enantiodiscriminating sensors are mainly focused on a variety of chiral macrocycles (fluorophore-modified calixarenes, cyclodextrins, and crown ethers), dendrimers, and oligomers [4,14–17].

Chiral amino alcohols are very useful as intermediates for making a variety of biologically active molecules or as ligands for stereoselective catalysts. Due to their great application in medical

and biological fields, there have been some reports on developing sensors for amino alcohols, especially the enantioselective recognition of chiral amino alcohols [18,19]. Although great progress has been made for the asymmetric synthesis of chiral amino alcohol compounds, the search for highly enantioselective as well as practical catalysts still keeps great interest. Therefore, the design of fluorescent sensors for the highly enantioselective recognition of chiral molecules and the rapid determination of their enantiomeric composition is highly desirable [5,20–24].

The chirality of 2,2'-binaphthol, 2,2'-binaphthyldiamine and their derivatives is derived from the restricted rotation of the two naphthalene rings. The rigid structure and C<sub>2</sub> symmetry of the chiral binaphthyl molecules can play an important role in inherently chiral induction [25–33]. The skeletal structure of BINOL at the 3,3'-, 5,5'- or 6,6'-positions of binaphthyl can be selectively functionalized at well-defined molecular level and lead to a variety of polybinaphthyls which can exhibit efficient and stable chiral configuration as well as high chiral induction and chiral discrimination in fluorescence chemosensor and asymmetric catalysis [34–41]. Pu's group reported that the bisbinaphthyl macrocycles containing chiral diamine were useful for the enantioselective fluorescence recognition for amino acid derivatives and  $\alpha$ -hydroxycarboxylic acids [15,42–44]. Hou and his coworkers also reported that the enantioselective fluorescent sensors based on multiple chiral center could exhibit highly enantioselectivity for the recognition of diverse  $\alpha$ -hydroxycarboxylic acids [45,46].

\* Corresponding author. Tel.: +86 25 83685199; fax: +86 25 83317761.

\*\* Corresponding author.

E-mail addresses: [yxcheng@nju.edu.cn](mailto:yxcheng@nju.edu.cn) (Y. Cheng), [cjzhu@nju.edu.cn](mailto:cjzhu@nju.edu.cn) (C. Zhu).

Many chiral fluorescence host compounds for enantioselective recognition of chiral guest compounds have been reported, but most of them are based on chiral small molecules, and fluorescent polymer-based sensors are very few [47–54]. Recently, we have initiated a project to focus on the chiral polymer used as fluorescence sensors for enantioselective recognition of chiral molecules [50]. Chiral polymers used as fluorescence-based sensors for chiral molecule enantioselective recognition offer several advantages over small molecule sensors, such as fluorescence efficiency enhancement and possible cooperative effects of multiple chiral units [55–61]. Moreover, these fluorescent chiral polymers can be systematically modified by the introduction of the functional groups based on steric and electronic property and represent a new generation of materials used as chemosensors in chiral molecule recognition.

In this paper, we report the synthesis of chiral polymers **P-1** and **P-2**. The chiral (*S*)-BINOL and (*S*)-BINAM moieties can orient a well-defined spatial arrangement in the main chain of the polymer backbone. This kind fluorescence polymer **P-1** can exhibit the most pronounced chiral discrimination of *D*-phenylalaninol. The results also indicated that **P-1** can be used as a fluorescence sensor for enantiomer composition determination of phenylalaninol. However, the chiral polymer **P-2** obtained by the reduction reaction of **P-1** with NaBH<sub>4</sub> shows no obvious fluorescence response toward phenylalaninol.

## 2. Experimental part

### 2.1. Materials

All solvents and reagents were commercially available and analytical-reagent-grade. (*S*)-2,2'-binaphthol and (*S*)-2,2'-binaphthylidiamine were purchased from Aldrich directly used without purification. THF and toluene were purified by distillation from sodium in the presence of benzophenone. CH<sub>3</sub>CN was distilled from P<sub>2</sub>O<sub>5</sub>.

### 2.2. Measurements

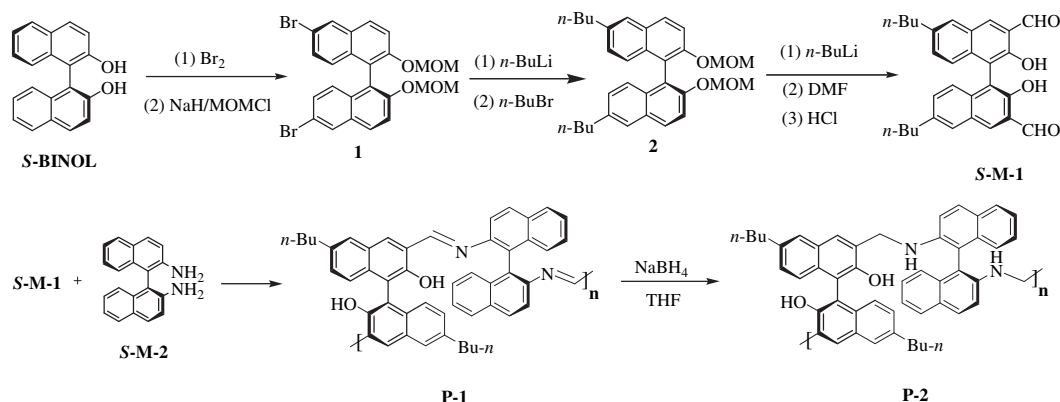
NMR spectra were obtained using a 300-Bruker spectrometer 300 MHz for <sup>1</sup>H NMR and 75 MHz for <sup>13</sup>C NMR and reported as parts per million (ppm) from the internal standard TMS. FT-IR spectra were taken on a Bruker VERTEX70 FT-IR spectrometer. Fluorescence spectra were obtained from an RF-5301PC spectrometer. Specific rotation was determined with a Ruololph Research Analytical Autopol III. MS was determined on a Micromass GCT. C, H, N of elemental analyses were performed on an Elemental Vario MICRO analyzer. GPC measurements were carried out on a BI-200SM using polystyrene as a standard and HPLC grade THF as eluent.

### 2.3. Preparation of (*S*)-6,6'-dibutyl-2,2'-bis(methoxymethoxy)-1,1'-binaphthyl (**2**) (Scheme 1) [62]

(*S*)-6,6'-Dibromo-2,2'-bis(methoxymethoxy)-1,1'-binaphthyl (**1**) [63] (5.9 g, 11.1 mmol) was dissolved in anhydrous THF (50 mL), *n*-BuLi (15.0 mL, 2.5 mol/L in hexanes, 37.5 mmol) was added by syringe injection at –78 °C under N<sub>2</sub> atmosphere. After the reaction mixture was stirred for 10 min, *n*-C<sub>4</sub>H<sub>9</sub>Br (5.3 g, 38.7 mmol) was added to the above solution at –78 °C under N<sub>2</sub> atmosphere. The reaction mixture was gradually warmed to room temperature and stirred overnight. The mixture was extracted with ethyl acetate (2 × 100 mL). The combined organic layers were washed with water and brine, and then dried over anhydrous Na<sub>2</sub>SO<sub>4</sub>. After removal of solvent under reduced pressure, the crude product was purified by column chromatography (petroleum ether/ethyl acetate) (30:1, v/v) to afford a colorless viscous product (*S*)-6,6'-Dibutyl-2,2'-bis(methoxymethoxy)-1,1'-binaphthyl (**2**) in 70.4% yield (3.8 g). [ $\alpha$ ]<sub>D</sub><sup>25</sup> = –38.0 (c 0.5, CH<sub>2</sub>Cl<sub>2</sub>). Mp: 150–152 °C. <sup>1</sup>H NMR (300 MHz, CDCl<sub>3</sub>):  $\delta$  7.93 (d, 2H, *J* = 9.0 Hz), 7.71 (s, 2H), 7.6 (d, 2H, *J* = 9.0 Hz), 7.19 (s, 4H), 5.12 (d, 2H, *J* = 6.6 Hz), 5.01 (d, 2H, *J* = 6.6 Hz), 3.21 (s, 6H), 2.79 (t, 4H, *J* = 7.2 Hz), 1.75–1.67 (m, 4H), 1.48–1.41 (m, 4H), 0.98 (t, 6H, *J* = 7.2 Hz). <sup>13</sup>C NMR (75 MHz, CDCl<sub>3</sub>):  $\delta$  152.6, 138.5, 132.9, 130.4, 129.0, 128.1, 126.6, 125.9, 121.7, 117.5, 95.3, 55.7, 35.9, 33.8, 22.8, 14.3. FT-IR (KBr, cm<sup>-1</sup>): 2956, 2929, 2857, 1596, 1500, 1480, 1241, 1151, 1028. MS (EI, *m/z*): 486 (M<sup>+</sup>, 7%), 410 (100%), 382 (48%), 339 (34%).

### 2.4. Preparation of (*S*)-6,6'-dibutyl-3,3'-diformyl-2,2'-binaphthol (**S-M-1**) (Scheme 1) [62]

Compound **2** (3.36 g, 6.6 mmol) was dissolved in anhydrous THF (80 mL), *n*-BuLi (9.4 mL, 2.5 mol/L in hexanes, 23.5 mmol) was added by syringe injection at room temperature under a N<sub>2</sub> atmosphere. The mixture was first stirred for 2 h, and then cooled to 0 °C. 1.9 mL of DMF (24.8 mmol) was added to the above solution. The reaction mixture was gradually warmed to room temperature and continued to stir for 4 h. After 60 mL of HCl (12 mol/L) was added to the solution, the solution was stirred at room temperature overnight. After the removal of the solvent under reduced pressure, the residue was extracted with CH<sub>2</sub>Cl<sub>2</sub> (3 × 50 mL). The combined extract was washed with 100 mL of saturated NaHCO<sub>3</sub> solution and brine twice and then dried over anhydrous Na<sub>2</sub>SO<sub>4</sub>. After removal of solvent under reduced pressure, the crude product was purified by column chromatography (petroleum ether/ethyl acetate) (10:1, v/v) to afford (*S*)-6,6'-dibutyl-3,3'-diformyl-2,2'-binaphthol (**S-M-1**) as yellow solids in 38.4% yield (1.2 g). [ $\alpha$ ]<sub>D</sub><sup>25</sup> = –216.0 (c 0.5, CH<sub>2</sub>Cl<sub>2</sub>). Mp: 150–152 °C. <sup>1</sup>H NMR (300 MHz, CDCl<sub>3</sub>):  $\delta$  10.55 (s, 2H),



**Scheme 1.** Synthesis procedures of two chiral polymers **P-1** and **P-2**.

10.19(s, 2H), 8.28(s, 2H), 7.77(s, 2H), 7.30(dd, 2H,  $J = 8.7, 1.8$  Hz), 7.15(d, 2H,  $J = 8.7$  Hz), 2.75(t, 4H,  $J = 7.8$  Hz), 1.73–1.67(m, 4H), 1.47–1.35(m, 4H), 0.96(t, 6H,  $J = 7.2$  Hz).  $^{13}\text{C}$  NMR (75 MHz,  $\text{CDCl}_3$ ):  $\delta$  196.9, 153.1, 139.0, 137.9, 136.0, 132.5, 128.2, 127.9, 124.8, 122.1, 116.6, 35.3, 33.2, 22.4, 14.0. FT-IR (KBr,  $\text{cm}^{-1}$ ): 3426, 2955, 2928, 2856, 1658, 1506, 1377, 1294. MS (EI,  $m/z$ ): 454 ( $\text{M}^+$ , 100%), 436 (11%), 411 (21%), 393 (15%). Anal. Calcd for  $\text{C}_{30}\text{H}_{30}\text{O}_4$ : C, 79.27; H, 6.65. Found: C, 79.21; H, 6.67.

### 2.5. Preparation of **P-1** (Scheme 1)

A mixture of Compound **S-M-1** (0.1 g, 0.22 mmol) and **S-BINAM** (**S-M-2**) (62.5 mg, 0.22 mmol) was dissolved in 10 mL of toluene. The obtained solution was stirred at 80 °C for 48 h. 20 mL of Methanol was added to precipitate the yellow polymer. The resulting polymer was filtrated and washed with methanol several times and dried in the yield of 75% (0.12 g). GPC results:  $M_w = 10800$ ,  $M_n = 6230$ , PDI = 1.73;  $[\alpha]_D^{25} = +83.4$  ( $c$  0.28, THF);  $^1\text{H}$  NMR (300 Hz,  $\text{CDCl}_3$ ):  $\delta = 0.87$ – $2.77$  (m, 21H), 6.88– $8.64$  (m, 20H), 10.04– $10.54$  (m, 0.04H), 11.90 (s, 0.54H). FT-IR (KBr,  $\text{cm}^{-1}$ ): 3467, 2957, 2927, 1625, 1610, 1588, 1506, 1260. Anal. Calcd for  $\text{C}_{50}\text{H}_{42}\text{N}_2\text{O}_2$ : C, 85.44; H, 6.02; N, 3.99. Found: C, 79.07; H, 6.00; N, 4.04.

### 2.6. Preparation of **P-2** (Scheme 1)

0.15 g polymer **P-1** was dissolved in the mixed solvents of 10 mL THF and 10 mL MeOH, and then  $\text{NaBH}_4$  was added in batches to the above solution. The reaction mixture was stirred at room temperature until the yellow color disappeared. The colorless solution was stirred for another 30 min, and 10 mL water was added to stop the reduction reaction. The mixture was extracted with  $\text{CH}_2\text{Cl}_2$  ( $3 \times 20$  mL). The combined organic layers were dried with anhydrous  $\text{Na}_2\text{SO}_4$  and evaporated under reduced pressure to afford salan-based polymer **P-2** as a white solid (0.11 g, 73% yield).  $[\alpha]_D^{25} = +71.9$  ( $c$  0.17, THF);  $^1\text{H}$  NMR (300 Hz,  $\text{CDCl}_3$ ):  $\delta = 0.91$ – $2.68$  (m, 25H), 6.55– $8.45$  (m, 20H), 10.19 (s, 0.10H), 10.52 (s, 0.04H). FT-IR (KBr,  $\text{cm}^{-1}$ ): 3528, 3412, 2963, 2927, 1619, 1598, 1511, 1262. Anal. Calcd for  $\text{C}_{50}\text{H}_{46}\text{N}_2\text{O}_2$ : C, 84.95; H, 6.56; N, 3.96. Found: C, 84.78; H, 6.64; N, 4.01.

### 2.7. General procedure for the enantioselective molecular recognition of host compounds to guest compounds

$1.0 \times 10^{-5}$  mol/L solution of host compounds in toluene and 0.1 mol/L solution of guest compounds in THF were freshly prepared. To give the mixed solutions of host and guest compound with the mole ratio 1:1, 1:5, 1:10, 1:20, 1:50, 1:80 and 1:100, 3.00 mL host compound solution and a certain volume of guest compound solution were added in each micro-test tube, respectively. The resulting solution was allowed to stand at room temperature for 12 h before the fluorescence measurement. Fluorescence intensity of alone host compound solution and above solution of host-guest compound solution were obtained on the RF-5301PC Spectrometer under respective optimal exciting wavelength with 3 nm exciting slit width and 3 nm emission wavelength in fast scan speed.

## 3. Results and discussion

### 3.1. Syntheses and feature of the polymers

The synthesis procedures of the monomer **S-M-1** and chiral polymer sensors are shown on Scheme 1. (*S*)-6,6'-dibutyl-2,2'-bis(methoxymethoxy)-1,1'-binaphthyl (**2**) was synthesized from (*S*)-

6,6'-dibromo-2,2'-bis(methoxymethoxy)-1,1'-binaphthyl (**1**) according to reported literatures [63]. Compound **2** was first lithiated with *n*-BuLi, and then followed by carbonylation to afford the MOM-protected intermediate, which was hydrolysed in HCl solution to afford the crude product (*S*)-6,6'-dibutyl-3,3'-diformyl-2,2'-binaphthol (**S-M-1**). The purification of **S-M-1** could be carried out by column chromatography on silica gel to afford a yellow solid product in 38.4% yield [62]. The chiral polymer **P-1** incorporating (*S*)-2,2'-binaphthol and (*S*)-2,2'-binaphthyldiamine moieties could be obtained by Schiff-base formation via nucleophilic addition–elimination reaction between **S-M-1** and **S-M-2** in 75% yield. And polymer **P-2** could be obtained by the reduction of **P-1** with  $\text{NaBH}_4$  in 81% yield. This two chiral polymers are air stable solid and show good solubility in common solvents, such as toluene, THF,  $\text{CHCl}_3$ , and  $\text{CH}_2\text{Cl}_2$ , which can be attributed to the nonplanarity of the twisted polymer chain backbone and the flexible *n*-butyl substituents. TGA result of **P-1** shows the chiral polymer has high thermal stability without loss weight before 420 °C and tends to completely decompose at 750 °C. (See Supporting information Fig. S1) Therefore, polymer **P-1** can provide a desirable thermal property for practical application as a fluorescence sensor.

### 3.2. Fluorescence recognition of (*D*)- or (*L*)-phenylalaninol

The fluorescence response behavior of the two chiral polymers on (*D*)- or (*L*)-phenylalaninol has been investigated by fluorescence spectra. Fig. 1(a) shows the fluorescence spectra of **P-1** ( $1.0 \times 10^{-5}$  mol/L corresponding to (*S*)-BINOL unit in toluene solution) upon addition of (*D*)- or (*L*)-phenylalaninol (0.1 mol/L in THF) at 1:100 M ratio on excitation at 360 nm. Remarkable differences in fluorescence enhancement were observed as demonstrated in Fig. 1(a), (*L*)-phenylalaninol has little effect on the fluorescence of the polymer, on the contrary, (*D*)-phenylalaninol causes a large increase in the fluorescence intensity of the polymer under the same determination condition. It also can be found that the fluorescent emission wavelengths do not show an obvious difference between the guest-free polymer and guest–polymer complexes. The selective recognition effect on the guest of the chiral molecular isomers is related to the enantiomeric fluorescence difference ratio,  $ef$  [ $ef = (I_D - I_0)/(I_L - I_0)$ ]. Herein,  $I_0$  represents the fluorescence emission intensity in the absence of the chiral substrate,  $I_D$  and  $I_L$  are the fluorescence intensities in the presence of (*D*)-substrate and (*L*)-substrate, respectively [50,64]. The value of  $ef$  is 6.85 for this polymer, which indicates that this polymer can exhibit highly enantioselective response toward (*D*)-phenylalaninol. The reason may be attributed to an inherent chiral recognition property based on the steric repulsion of the chiral polymer sensor for (*D*)-phenylalaninol. The building block of (*S,S*)-receptor containing imine and hydroxyl groups can well fit for the formation of a more stable complex of *S,S-D* complex as compared to the *S,S-L* diastereomeric complex. On the contrary, chiral polymer **P-2** shows no obvious enantioselective response toward (*D*)- or (*L*)-phenylalaninol (Fig. 1(b)). In a set of comparable experiments, we also studied the fluorescence response behavior of polymer **P-1** on other guest molecules. As shown in Fig. 1(c), polymer **P-1** can exhibit obvious enantioselective response toward *D*-alaninol, and the value of  $ef$  is 1.86 at 1:100 M ratio. While using (*D*)-/(*L*)-mandelic acid, (*R*)-/(*S*)-phenylethylamine, or (*D*)-/(*L*)-phenylglycinol as guest molecules, no obvious fluorescence response on the enantioselectivity of these guest molecule enantiomers was observed although the fluorescence intensities can appear great enhancement (See Supporting information Figs. S2–S4).

In addition, the interaction of the chiral polymer **P-1** with phenylalaninol was investigated at a much broader concentration range of the substrate. In regard to the fluorescence signal changes of this



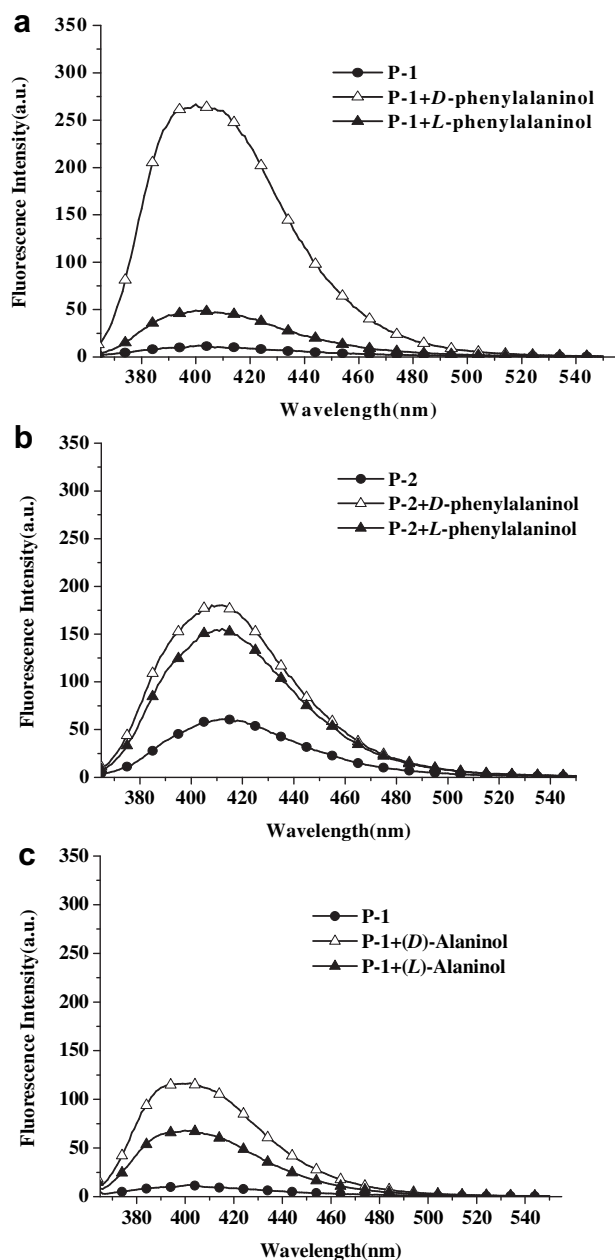


**Fig. 1.** Fluorescence spectra of **P-1** ( $1.0 \times 10^{-5}$  mol/L in toluene) with and without (D)- and (L)-phenylalaninol ( $\lambda_{\text{ex}} = 360$  nm,  $\lambda_{\text{em}} = 404$  nm) (a), **P-2** ( $1.0 \times 10^{-5}$  mol/L in toluene) with and without (D)- and (L)-phenylalaninol ( $\lambda_{\text{ex}} = 360$  nm,  $\lambda_{\text{em}} = 414$  nm) (b), and **P-1** with and without (D)- and (L)-alaninol (c) at 1:100 M ratio ( $\lambda_{\text{ex}} = 360$  nm,  $\lambda_{\text{em}} = 404$  nm).

chiral polymer sensor on (L)- or (D)-phenylalaninol, the fluorescence intensities appear gradual enhancement upon addition of (D)- or (L)-phenylalaninol in the range from 1:0 to 1:100 M ratios (Fig. 2). Meanwhile, it can also be found that the addition curve keeps a nearly linear correlation with the molar ratio of (L)- or (D)-phenylalaninol (Fig. 3). The obvious fluorescence enhancement can be attributed to suppressed **PET** (photoinduced-electron-transfer) quenching [65–68] when the protons of phenylalaninol interact with the nitrogen atoms of imine moieties in the chiral polymer main chain through the intramolecular hydrogen bonding. On complexation, the lone pair of electrons on the nitrogen atom is no longer available for **PET**, leading to the fluorescence enhancement.

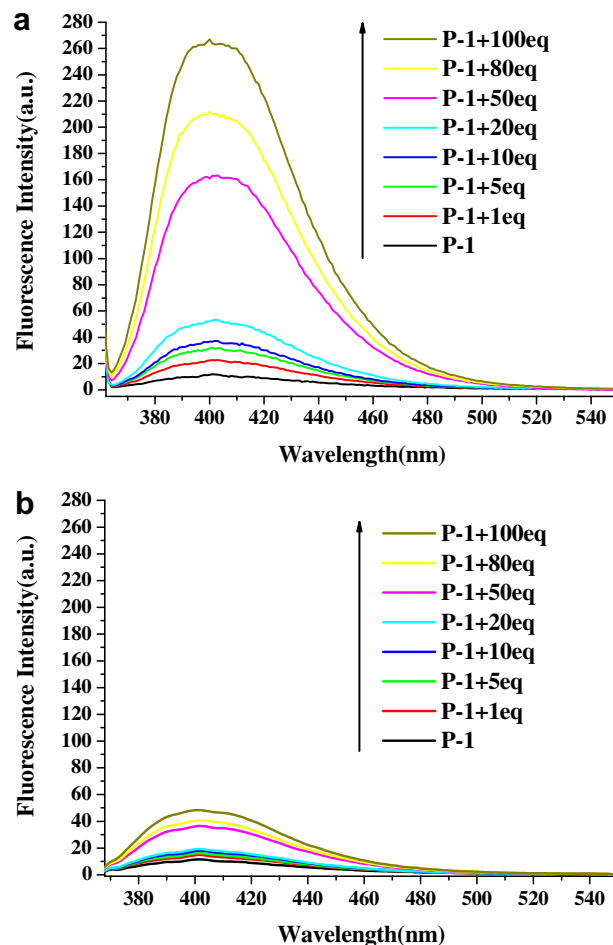


**Fig. 2.** Fluorescence spectra of **P-1** with and without (D)-phenylalaninol (a), (L)-phenylalaninol (b) at different molar ratios.

We further investigated the fluorescence response of polymer **P-1** on different enantiomeric compositions of phenylalaninol. The fluorescence intensities based on various molar ratios of (L)- or (D)-phenylalaninol revealed a fair linear relationship between  $I/I_0$  and the percent of the (D)-phenylalaninol component (Fig. 4). The result indicates that the enantioselective fluorescence sensor can be effectively applied for enantiomer composition determination of phenylalaninol.

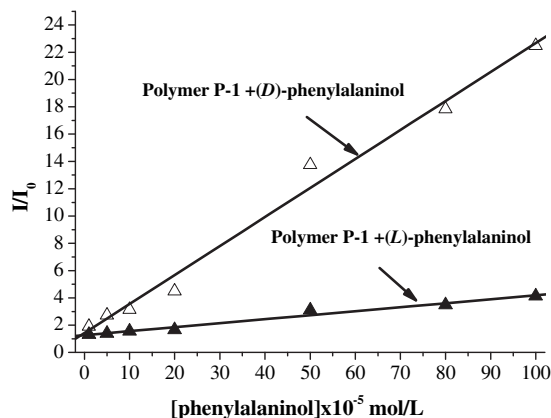


**Fig. 3.** Fluorescence enhancement of the chiral polymer **P-1** ( $1.0 \times 10^{-5}$  mol/L in toluene) vs molar ratios of (D)- and (L)-phenylalaninol from 1:1 to 1:100.

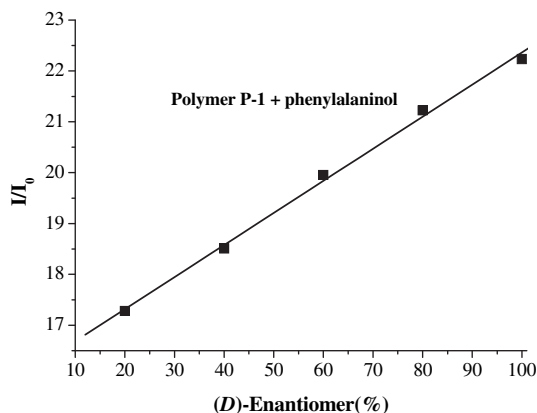


**Fig. 4.** Fluorescence enhancement of the chiral polymer **P-1** ( $1.0 \times 10^{-5}$  mol/L in toluene) vs the enantiomeric composition of phenylalaninol ( $1.0 \times 10^{-3}$  mol/L in THF).

In summary, a novel fluorescence-based polymer **P-1** incorporating (*S*)-BINOL and (*S*)-BINAM moieties in the main chain backbone can exhibit an excellent fluorescence sensor for enantioselective recognition of (*D*)-phenylalaninol, and can also be used in ascertaining the enantiomeric composition of (*D*)- or (*L*)-phenylalaninol. The value of enantiomeric fluorescence difference ratio (*ef*) is 6.85 for the chiral polymer on (*D*)-phenylalaninol.

#### Acknowledgment

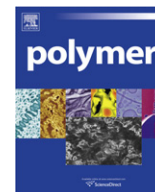
This work was supported by the National Natural Science Foundation of China (No. 20774042, 20832001, 21074054), National Basic Research Program of China (2010CB923303) and the Bureau of Science and Technology of Wenzhou (No. S20100007).

#### Appendix. Supporting information

Supporting information associated with this article can be found online at doi:10.1016/j.polymer.2010.12.011.

#### References

- Zhang XX, Bradshaw JS, Izatt RM. *Chem Rev* 1997;97:3313–62.
- Finn MG. *Chirality* 2002;14:534–40.
- Kočovsky P, Vyskočil Š, Smrčina M. *Chem Rev* 2003;103:3213–46.
- Li ZB, Lin J, Qin YC, Pu L. *J Org Lett* 2005;7:3441–4.
- Hembury GA, Borovkov VV, Inoue Y. *Chem Rev* 2008;108:1–73.
- Mei X, Wolf C. *Chem Comm* 2004;18:2078–9.
- Pu L. *Chem Rev* 2004;104:1687–716.
- Al Rabaa AR, Tfibel F, Mérola F, Pernot P, Fontaine-Aupart MPJ. *Chem Soc Perkin Trans* 1999;2:341–51.
- Xu Y, McCarroll ME. *J Phys Chem B* 2005;109:8144–52.
- Ding K, Ishii A, Mikami K. *Angew Chem Int Ed* 1999;38:497–501.
- Matsushita M, Yoshida K, Yamamoto N, Wirsching P, Lerner RA, Janda KD. *Angew Chem Int Ed* 2003;42:5984–7.
- Korbel GA, Lalic G, Shair MD. *J Am Chem Soc* 2001;123:361–2.
- Gokel GW, Leevy WM, Weber ME. *Chem Rev* 2004;104:2723–50.
- Corradini R, Paganuzzi C, Marchelli R, Pagliari S, Sforza S, Dossena A, et al. *Mater Chem* 2005;15:2741–6.
- Li ZB, Lin J, Sabat M, Hyacinth M, Pu L. *J Org Chem* 2007;72:4905–16.
- Shirakawa S, Moriyama A, Shimizu S. *Org Lett* 2007;9:3117–9.
- Upadhyay SP, Pissurlenkar RRS, Coutinho EC, Karnik AV. *J Org Chem* 2007;72:5709–14.
- Qing G, Sun T, He Y, Wang F, Chen Z. *Tetrahedron Asymmetry* 2009;20:575–83.
- Kim KM, Park H, Kim HJ, Chin J, Nam W. *Org Lett* 2005;7:3525–7.
- Yoon J, Kim SK, Singh NJ, Kim KS. *Chem Soc Rev* 2006;35:355–60.
- Gale PA. *Acc Chem Res* 2006;39:465–75.
- Beer PD, Gale PA. *Angew Chem Int Ed* 2001;40:486–516.
- Schmidtchen FP, Berger M. *Chem Rev* 1997;97:1609–46.
- O'Neil EJ, Smith BD. *Coord Chem Rev* 2006;250:3068–80.
- Shi M, Wang CJ. *Tetrahedron Asymmetry* 2002;13:2161–6.
- Liu Y, Zhang SW, Miao Q, Zheng LF, Zong LL, Cheng YX. *Macromolecules* 2007;40:4839–47.
- Liu Y, Zong LL, Zheng LF, Wu LL, Cheng YX. *Polymer* 2007;48:6799–807.
- Pu L. *Chem Rev* 1998;98:2405–94.
- Pu L, Yu HB. *Chem Rev* 2001;101:757–824.
- Fan QH, Li YM, Chan ASC. *Chem Rev* 2002;102:3385–466.
- Brunel JM. *Chem Rev* 2005;105:857–98.
- Huang XB, Xu Y, Zheng LF, Meng J, Cheng YX. *Polymer* 2009;50:5996–6000.
- Chen Y, Yekta S, Yudin AK. *Chem Rev* 2003;103:3155–212.
- Huang H, Miao Q, Kang YX, Huang XB, Xu JQ, Cheng YX. *Bull Chem Soc Jpn* 2008;81:1116–24.
- Liu Y, Miao Q, Zhang SW, Huang XB, Zheng LF, Cheng YX. *Macromol Chem Phys* 2008;209:685–94.
- Deussen HJ, Hendrickx E, Boutton C, Krog D, Clays K, Bechgaard K, et al. *J Am Chem Soc* 1996;118:6841–52.
- Koeckelberghs G, Verbiest T, Vangheluwe M, DeGroof L, Asselberghs I, Picard I, et al. *Chem Mater* 2005;17:118–21.
- Wu LL, Zheng LF, Zong LL, Xu JQ, Cheng YX. *Tetrahedron* 2008;64:2651–7.
- Zhang SW, Liu Y, Huang H, Zheng LF, Wu LL, Cheng YX. *Synlett* 2008;6:853–7.
- Huang XB, Wu LL, Xu JQ, Zong LL, Hu HW, Cheng YX. *Tetrahedron Lett* 2008;49:6823–6.
- Cheng YX, Zou XW, Zhu D, Zhu TS, Liu Y, Zhang SW, et al. *J Polym Sci A Polym Chem* 2007;45:650–60.
- Li ZB, Lin J, Zhang HC, Sabat M, Hyacinth M, Pu L. *J Org Chem* 2004;69:6284–93.
- Gao G, Wang Q, Yu XQ, Xie RG, Pu L. *Angew Chem Int Ed* 2006;45:122–5.
- Li ZB, Liu TD, Pu L. *J Org Chem* 2007;72:4340–3.
- Liu HL, Peng Q, Wu YD, Chen D, Hou XL, Sabat M, et al. *Angew Chem Int Ed* 2010;122:612–6.
- Liu HL, Hou XL, Pu L. *Angew Chem Int Ed* 2009;48:382–5.
- Cozzi PG. *Chem Soc Rev* 2004;33:410–21.
- Canali L, Sherrington DC. *Chem Soc Rev* 1999;28:85–93.
- Ma L, White PS, Lin W. *J Org Chem* 2002;67:7577–86.
- Xu Y, Zheng LF, Huang XB, Cheng YX, Zhu CJ. *Polymer* 2010;51:994–7.
- Xi XJ, Lou LP, Jiang LM, Sun WL, Shen ZQ. *Polymer* 2008;49:2065–70.
- Zhang HC, Pu L. *Macromolecules* 2004;37:2695–702.
- Huang X, He Y, Hu C, Chen ZJ. *Fluorescence* 2009;19:97–104.
- Qing GY, Sun TL, He YB, Wang F, Chen ZH. *Tetrahedron Asymmetry* 2009;20:575–83.
- McQuade DT, Pullen AE, Swager TM. *Chem Rev* 2000;100:2537–74.
- Thomas SW, Joly GD, Swager TM. *Chem Rev* 2007;107:1339–86.
- Kim IB, Dunkhorst A, Gilbert J, Bunz UHF. *Macromolecules* 2005;38:4560–2.
- Fan LJ, Jones WE. *J Am Chem Soc* 2006;128:6784–5.
- Miao Q, Huang H, Huang XB, Xu Y, Zong Y, Cheng YX. *Polym Int* 2010;5:712–8.
- Huang XB, Meng J, Dong Y, Cheng YX. *J Polym Sci A Polym Chem* 2010;48:997–1006.
- Zheng LF, Huang XB, Shen YG, Cheng YX. *Synlett* 2010;3:453–6.
- Huang XB, Xu Y, Miao Q, Zong LL, Hu HW, Cheng YX. *Polymer* 2009;50:2793–805.
- Ishitani H, Ueno M, Kobayashi S. *J Am Chem Soc* 2000;122:8180–6.
- Lin J, Hu QS, Xu MH, Pu L. *J Am Chem Soc* 2002;124:2088–9.
- Bojinov VB, Georgiev NI, Bosch PJ. *Fluoresc* 2009;19:127–39.
- Bissell RA, de Silva AP, Gunaratne HQN, Lynch PLM, Maguire GEM, McCoy CP, et al. *Top Curr Chem* 1993;168:223–64.
- Bissell RA, de Silva AP, Gunaratne HQN, Lynch PLM, Maguire GEM, Sandanayake KRAS. *Chem Soc Rev* 1992;21:187–95.
- Czarnik AW. *Acc Chem Res* 1994;27:302–8.



# Well-defined multi-stimuli responsive fluorinated graft poly(ether amine)s (fgPEAs)

Rui Wang<sup>a</sup>, Xuesong Jiang<sup>a,\*</sup>, Guilin Yin<sup>b</sup>, Jie Yin<sup>a,\*</sup>

<sup>a</sup>School of Chemistry & Chemical Technology, State Key Laboratory for Metal Matrix Composite Materials, Shanghai Jiao Tong University, Shanghai, China

<sup>b</sup>National Engineering Research Center for Nanotechnology, Shanghai 200240, People's Republic of China

## ARTICLE INFO

### Article history:

Received 11 May 2010

Received in revised form

29 September 2010

Accepted 29 November 2010

Available online 4 December 2010

### Keywords:

Multi-stimuli responsive

Fluorinated

Graft poly(ether amine)

## ABSTRACT

Well-defined multi-stimuli responsive fluorinated graft poly(ether amine)s (fgPEAs) were synthesized through nucleophilic substitution/ring-opening reaction of commercial poly(propylene glycol) diglycidyl ether and Jeffamine L100, followed by functionalization of hydroxyl groups in backbone by fluorinated alkyl carboxylic acid. fgPEAs are comprised of hydrophilic short poly(ethylene oxide) (PEO) and hydrophobic fluorinated alkyl chains, which are grafted on poly(propylene oxide) (PPO) backbone alternately to form well-defined structure. In aqueous solution, fgPEA11 and fgPEA12 self-assembled into multi-dispersed micelles, while fgPEA13 formed the uniform-sized micro-micelles with diameter of about 200 nm. These obtained micelles from fgPEAs were multi-responsive to temperature, pH and ionic strength with tunable cloud point (CP). It's notable that CP of fgPEAs aqueous solution increased with the increasing amount of graft fluorinated alkyl chains.

© 2010 Elsevier Ltd. All rights reserved.

## 1. Introduction

Due to their potential applications in waste-water treatment, oil recovery, nanotechnology and drug delivery, stimuli-responsive polymers have been extensively investigated [1–4]. Among them, amphiphilic block copolymers with stimuli-responsive properties are of particular interests. They can self-assemble into various supramolecular structures which can solubilize lipophilic guest molecules such as drug molecules while the release of guest molecules can be triggered by external stimuli such as light [5–7], temperature [8–10], pH [11–15], redox potential [16,17] and polarity [18,19]. Quite a few stimuli-sensitive polymeric micellar systems have been reported so far, but most of them focus on response to single stimuli. However, the environmental change of nature is not a single factor but complex ones. Therefore, much attention should be paid on amphiphilic polymer responsive to multi-stimuli [6,7,20,21].

Because of their interest in academic and technological field, fluorinated amphiphilic polymers have attracted much attention. Fluorinated groups can improve surface active properties, molecular aggregation and self-assembling morphology, which can not be achieved by other amphiphilic polymers [22,23]. As fluorine confers extreme hydrophobicity and water insolubility to polymers,

fluorinated polymers have been widely applied in many fields, such as blood substitutes, drug delivery and fire-fighting foams [24–26]. In addition, their excellent inertness to oil and moisture adsorption as well as their good thermal stability and evidently low surface energy make them advantageous [27–33]. Herein, we introduced fluorinated alkyl side chains to the responsive graft poly(ether amine) (PEA). Perfluorinated alkyl chains are considerably more hydrophobic than hydrocarbon chains, and their introduction greatly intensified the amphiphilic character, resulting in strong tendencies to self-associate into supermolecular assemblies.

Recently, we reported a series of novel responsive poly(ether amine)s (PEAs), which exhibited sharp response to temperature, pH and ionic strength [34–37]. PEA can be obtained through nucleophilic substitution/ring-opening reaction of commercial di-epoxy and di-amine monomer, which possesses characteristics of “click-chemistry” [38]. This one-step synthesis of PEA is facile and “green”. Moreover, hydroxyl groups generated in reaction between epoxy and amine groups can be used for the further functionalization. As a continuous work in this text, a series of fluorinated graft PEAs (fgPEAs) were synthesized through functionalization of hydroxyl groups in backbone of PEA, which was expected to endow micelles with enhanced stability and lower surface energy. These obtained fgPEAs exhibit multi-response to temperature, pH and ionic strength with controlled cloud point (CP), and can self-assemble into responsive micelles, which could be revealed by DLS and TEM.

\* Corresponding authors. Tel.: +86 21 54743268; fax: +86 21 54747445.

E-mail addresses: [ponygle@sjtu.edu.cn](mailto:ponygle@sjtu.edu.cn) (X. Jiang), [jjin@sjtu.edu.cn](mailto:jjin@sjtu.edu.cn) (J. Yin).

**Table 1**  
Component and molecular weight data of fgPEAs.

Polymer <sup>a</sup>	Molar ratio in raw materials			Molar ratio in products		$M_n(\times 10^4)^c$	$M_w/M_n^c$	CMC (g/L) <sup>d</sup>
	gPEA	NDFDA	F(%) <sup>b</sup>	C <sub>9</sub> F <sub>19</sub> Chain/L100	F(%) <sup>b</sup>			
fgPEA11	1	1	14.6	0.9	1.3	1.46	0.23	
fgPEA12	1	2	19.7	1.3	1.2	1.43	0.18	
fgPEA13	1	3	24.6	1.8	1.1	1.44	0.16	

<sup>a</sup> fgPEA<sub>x</sub>y, x,y represent the molar ratio of the raw gPEA and NDFDA, respectively.

<sup>b</sup> The content of fluorine in fgPEAs were determined by element analysis.

<sup>c</sup> Molecular weight and molecular weight polydispersity were measured by GPC.

<sup>d</sup> CMC of fgPEAs were measured by using Nile Red as the fluorescent probe at pH 7.4.

## 2. Experimental

### 2.1. Materials

Poly(propylene glycol) diglycidyl ether (PPO-DE, Aldrich,  $M_n = 640$  g/mol), Jeffamine L100 (Hunstman,  $M_n = 1000$  g/mol), Nonadecafluorodecanoic acid (NDFDA, ABCR Chemical Reagent), Dicyclohexylcarbodiimide (DCC, Alfa Aesar), 4-Dimethylamino-pyridine (DMAP, Alfa Aesar) were used as received.

### 2.2. Synthesis of gPEA

gPEA was synthesized according to previous report [35]. The reaction was conducted in a 50-mL two-neck flask equipped with a nitrogen inlet tube and a reflux condenser. PPO-DE and Jeffamine L100 were added to the flask with molar ratio of 1:1. Then ethanol was added to dissolve these monomers. The total monomer concentration was kept at 0.5 g/mL. The reaction was carried out

by refluxing for 12 h. Then the reaction was poured into n-hexane. After removing the supernatant, the product was collected and dried. Then the product was dialyzed against water (Cellulose ester dialysis membrane MWCO3500).

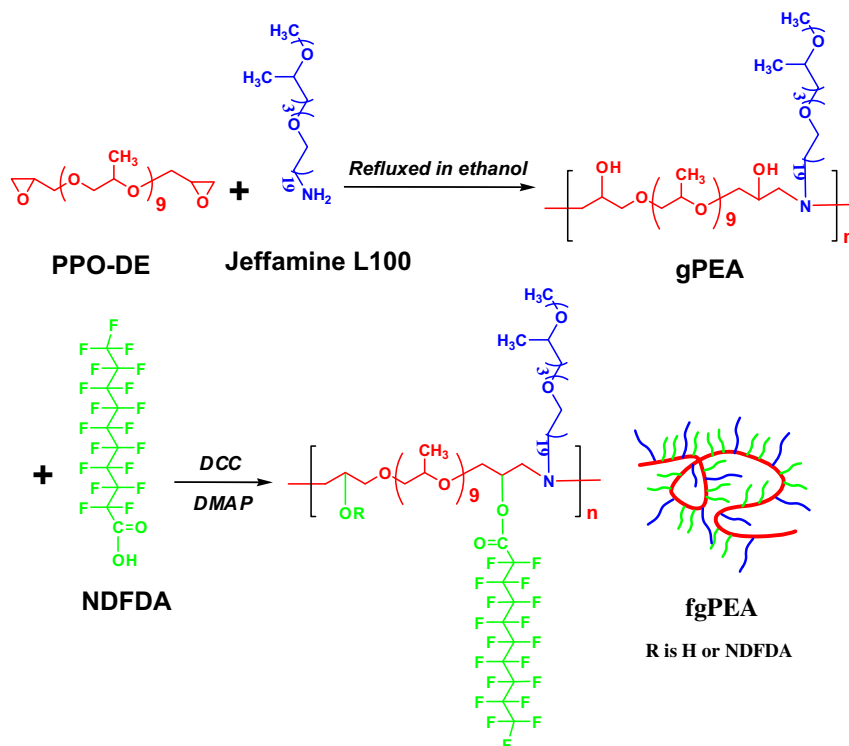
### 2.3. Synthesis of fgPEAs

To the solution of dichloromethane in a 50-mL two-neck flask equipped with a nitrogen inlet tube, gPEA and NDFDA were added in proportion (shown in Table 1). Then DCC and DMAP were added to the solution. The reaction was carried out at room temperature for 18 h. After filtration of unreacted NDFDA and DCU and removing the solvent by rotary evaporation, water was added. The suspension was centrifugated to get the clear solution, which was concentrated and dried to obtain the product. Then the product was dialyzed against water (Cellulose ester dialysis membrane MWCO3500).

## 3. Characterization

FT-IR spectra of products were recorded on a Perkin–Elmer Paragon 1000 FT-IR spectrometer. <sup>1</sup>H NMR & <sup>19</sup>F NMR measurements were carried out on a Varian Mercury Plus spectrometer, operating at 400 MHz by using CDCl<sub>3</sub> as solvent and TMS as an internal standard. The ratios of fluorine in products were determined by vario EL III of Elementar Company. Molecular weights ( $M_n$ ) and molecular weight distributions ( $M_w/M_n$ ) were determined by a Series 200 gel permeation chromatography (GPC). N,N-dimethylformamide (DMF) was used as the eluent at a flow rate of 1.0 mL/min and polystyrene as the calibration standard.

The optical transmittance of the polymer solutions were measured at 500 nm with a UV-2550 spectrophotometer (Shimadzu, Japan) equipped with circulating water bath. The temperature at 90% light transmittance of the polymer solution was defined as the CP.  $\Delta T$  was defined as the difference in temperature



**Scheme 1.** The synthesis process of fgPEAs.

measured between 90% and 10% transmittance of the overall heating process. The copolymer aqueous solutions were prepared from 0.1 M citrate buffered aqueous solutions with 1 wt.% copolymer concentration.

The Critical Micelle Concentration (CMC) of fgPEAs were determined at pH 7.4 by using Nile Red as the fluorescent probe. Solutions of fgPEAs with concentrations ranging from  $1 \times 10^{-4}$  to 1 g/L were prepared. Excess amount of Nile Red was put into the solution and fully oscillated. Nile Red was then encapsulated into the hydrophobic micellar interior (Fig. 3a). The emission spectra were recorded under LS-50B luminescence spectrometer (Perkin–Elmer Co.). The emission wavelength was set at 559 nm. The fluorescence emission spectra were recorded between 580 nm and 700 nm at room temperature.

Dynamic Light Scattering (DLS) was performed in the 1 mg/mL copolymer solution with pH 7.0 using a Malvern Instruments Zeta sizer Nano S instrument (Malvern Instruments) equipped with a 4 mW He–Ne laser ( $\lambda = 633$  nm) at an angle of  $173^\circ$ , an avalanche photodiode detector with high quantum efficiency, and an ALV/LSE-5003 multiple  $\tau$  digital correlator electronics system. The CONTIN analysis method was used. Transmission Electron Microscopy (TEM) images were recorded using a JEOLZ 100F microscope, operating at 200 kV. Before measurement, a drop of 1 mg/mL fgPEAs solution was placed onto a copper grid and the excess solution was removed by a filter paper.

## 4. Results and discussion

### 4.1. Synthesis and characterization of fgPEAs

fgPEAs were synthesized through nucleophilic substitution/ring-opening reaction of commercial available poly(propylene glycol) diglycidyl ether and Jeffamine L100, followed by esterification of hydroxyl groups in backbone by fluorinated alkyl carboxylic acid (NDFDA) of different amount. The whole process for synthesis of fgPEAs is illustrated in Scheme 1. Because two hydroxyl groups are generated in reaction between one PPO-DE and L100, the ratio between hydrophilic chain L100 and fluorinated alkyl chain  $C_9F_{19}$  will keep 1/2 if all hydroxyl groups are esterified. By controlling the esterification degree of hydroxyl groups in gPEA, we synthesized three fgPEAs containing different amount of  $C_9F_{19}$  as side-chain, which were named by fgPEA11, fgPEA12 and fgPEA13. Their component and molecular weight ( $M_n$ ) are summarized in Table 1.

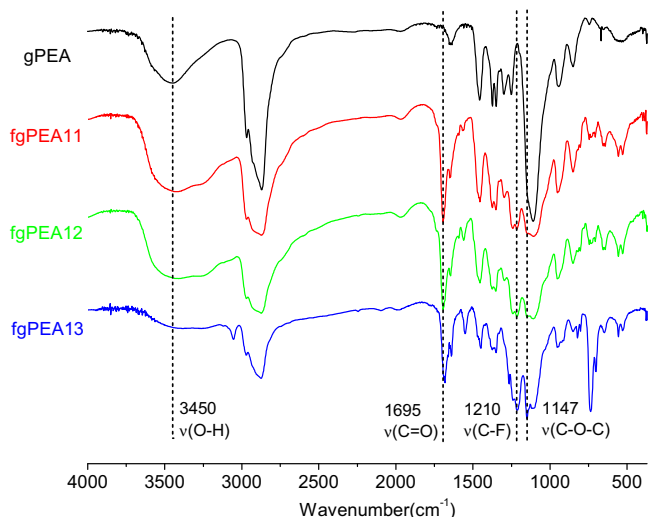


Fig. 1. FT-IR spectra of gPEA and fgPEAs.

The synthesis of fgPEAs was confirmed by FT-IR, NMR, elemental analysis and GPC.

As shown in the FT-IR spectra (Fig. 1), the peaks at 3400, 1695 and  $1210\text{ cm}^{-1}$  are attributed to stretching vibration of O–H in gPEA, C=O and C–F in fgPEA, respectively. The appearance of peaks at 1695 and  $1210\text{ cm}^{-1}$  indicated that fluorinated alkyl chain  $C_9F_{19}$  has been introduced into the backbone of gPEA. From fgPEA11 to fgPEA13, the peak at  $3400\text{ cm}^{-1}$ , attributed to O–H group decreased obviously, indicating the gradual increase of the amount of  $C_9F_{19}$ . As a result of the almost full esterification of O–H group in fgPEA13, the peak at  $3400\text{ cm}^{-1}$  almost disappeared in FT-IR spectrum of fgPEA13, which is in agreement with the elemental analysis. The preparation of fgPEAs is further supported by NMR spectra. As shown in Fig. 2a, the peak assigned to Ha ( $\delta = 4.3$  ppm) appeared and became more and more obvious with the increase of the amount of  $C_9F_{19}$  from fgPEA11 to fgPEA13, resulted from esterification of hydroxyl groups in gPEA. In Fig. 2b, every peak in  $^{19}\text{F}$  NMR spectrum of fgPEA13 could be well assigned to each fluorine atom in  $C_9F_{19}$  fluorinated alkyl chain, which also indicates presence of fluorinated alkyl chain in the structure of fgPEA13.

The graft amounts of  $C_9F_{19}$  were determined by element analysis, and are summarized in Table 1. The molar ratio of grafted  $C_9F_{19}$  and L100 chain increases with the increasing amount of NDFDA from fgPEA11 to fgPEA13. In the structure of fgPEA13,  $C_9F_{19}/L100$  is about 1.8, indicating that 90% hydroxyl groups have been esterified. The molecular weight ( $M_n$ ) of fgPEAs was determined by GPC, and the results are shown in Table 1. It is interesting that  $M_n$  of fgPEAs

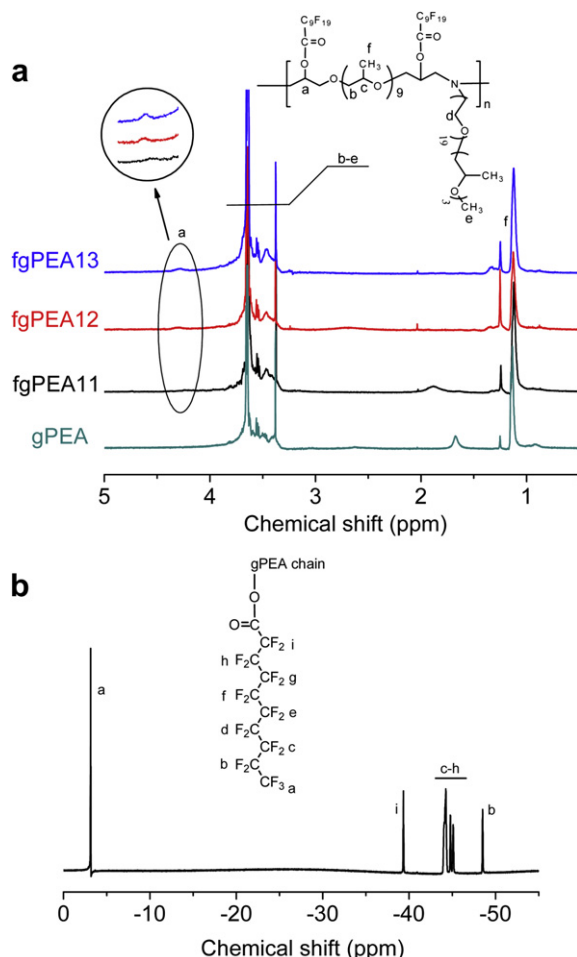
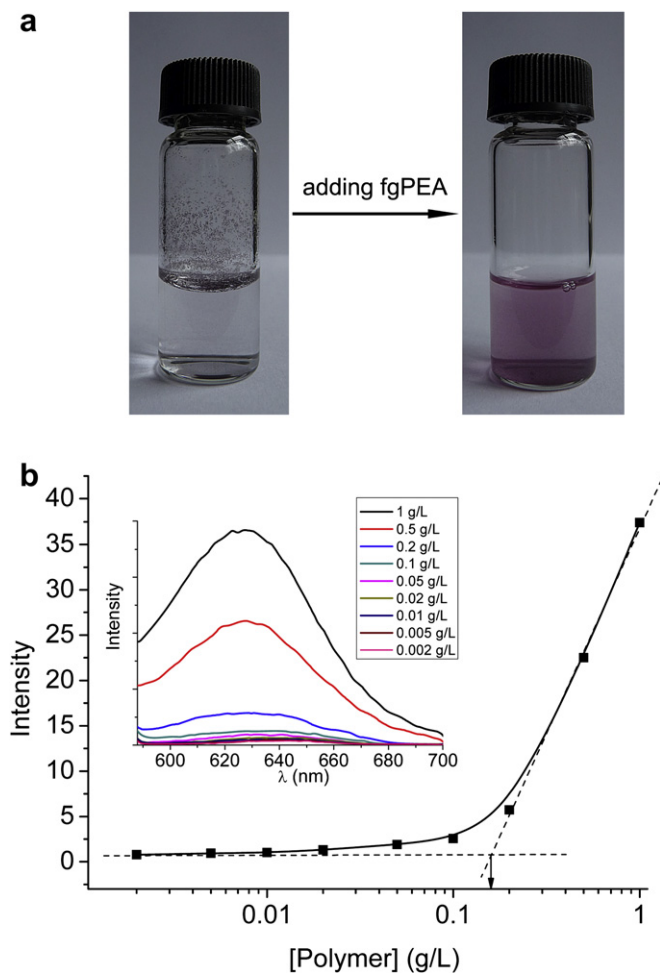


Fig. 2. (a)  $^1\text{H}$  NMR spectra of fgPEAs; (b)  $^{19}\text{F}$  NMR Spectrum of fgPEA13 in  $\text{CDCl}_3$ .

decreases with the increasing amount of C<sub>9</sub>F<sub>19</sub> chain from fgPEA11 to fgPEA13. This might be ascribed to the special hydrophobic and hydrophilic effect of C<sub>9</sub>F<sub>19</sub> fluorinated alkyl chain. Due to the poor solubility of C<sub>9</sub>F<sub>19</sub> fluorinated alkyl chain in DMF (eluent in GPC measurement), the hydrodynamic volume of fgPEAs decreases with the increasing amount of C<sub>9</sub>F<sub>19</sub> chain, resulting in the decrease of M<sub>n</sub> from fgPEA11 to fgPEA13.

#### 4.2. Micelle formation behavior of fgPEAs

With hydrophilic L100 and hydrophobic C<sub>9</sub>F<sub>19</sub> fluorinated alkyl chain, fgPEAs could self-assemble into micelles in aqueous solution above critical micelle concentration (CMC), which is similar to other amphiphilic polymers [39–42]. As a strong evidence for self-assembly of amphiphilic polymer into micelle, CMC value for fgPEAs was determined by a fluorescence spectroscopy using Nile Red as a fluorescence probe. In the presence of fgPEAs, the hydrophobic dye Nile Red can be dispersed in water, indicating that Nile Red was encapsulated into the hydrophobic micellar interior (Fig. 3a). The fluorescence emission spectra of Nile Red in fgPEA13 solution with different concentration are recorded in Fig. 3b. An increasing intensity of the Nile Red band was observed with the increasing fgPEA13 concentration shown in the inset of Fig. 3b, resulted from the micellar solubilization of Nile Red. The intensity increases significantly beyond a certain concentration, indicating



**Fig. 3.** (a) Photograph of the aqueous solution of Nile Red; (left) before and (right) after adding fgPEA13. (b) Intensity of Nile Red plotted versus fgPEA13 concentration. Inset: fluorescence emission spectra of Nile Red solution with different fgPEA13 concentration, pH = 7.4.

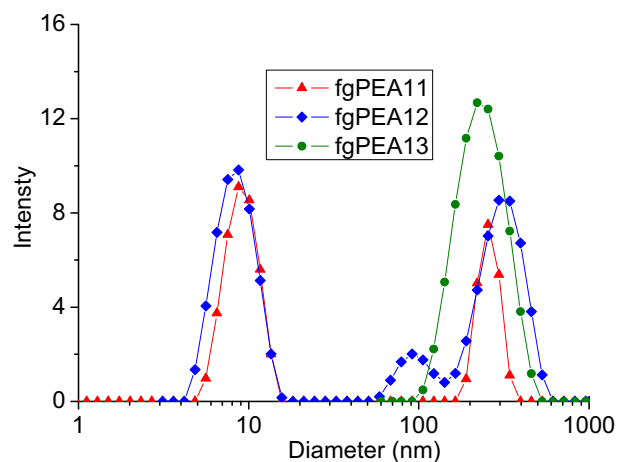


**Fig. 4.** Micelle size distribution of fgPEAs obtained by DLS at room temperature, pH = 7.0.

the formation of the micelles. A plot of the intensity against the logarithm of the polymer concentration exhibits an inflection point at the critical micelle concentration (CMC) [20]. The CMC of fgPEA13 is about 0.16 g/L. The CMC of fgPEA11 and fgPEA12 was also determined through this method, and summarized in Table 1. The CMC of fgPEAs decreases with the increasing amount of C<sub>9</sub>F<sub>19</sub> chain in fgPEAs. Besides the increasing emission intensity with the increasing fgPEA13 concentration, it's also observed that the emission wavelength maximum of Nile Red is systematically blue-shifted from 638 nm to 627 nm, also indicating that Nile Red was encapsulated into the hydrophobic micellar interior.

The formation of micelle from fgPEAs was further verified by DLS experiments, which were carried out in aqueous solutions at 25 °C with concentration of 1 mg/mL (Fig. 4). fgPEAs can be well dispersed in aqueous solution to form transparent solution at room temperature, indicating that fgPEAs are dispersed as micelle in water. fgPEA displayed relative uniform-sized nano-micelles of ~30 nm in diameter [35]. The nano-micelles might be comprised of hydrophobic PPO as the core and hydrophilic L100 as the corona, which make nano-micelles stable in aqueous solution. While in aqueous solution at pH 7.0, fgPEA11 presents most nano-micelles of ~10 nm in diameter, and some bigger micelles of ~200 nm are formed. Compared with gPEA, fgPEA11 contains the hydrophobic fluorinated alkyl graft chains, which enlarge the hydrophobic core

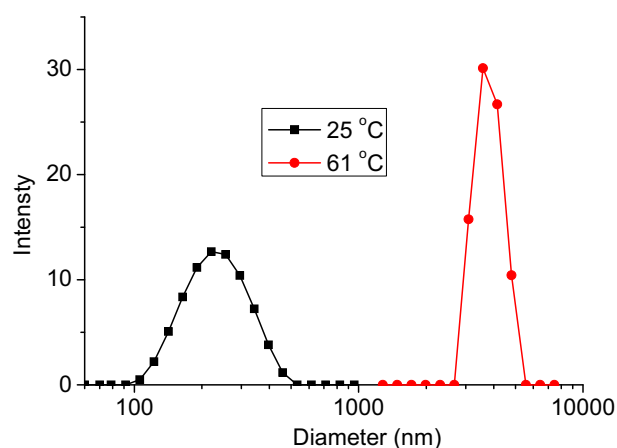


**Fig. 5.** Micelle size distribution of fgPEA13 obtained by DLS at different temperature, pH = 7.0.

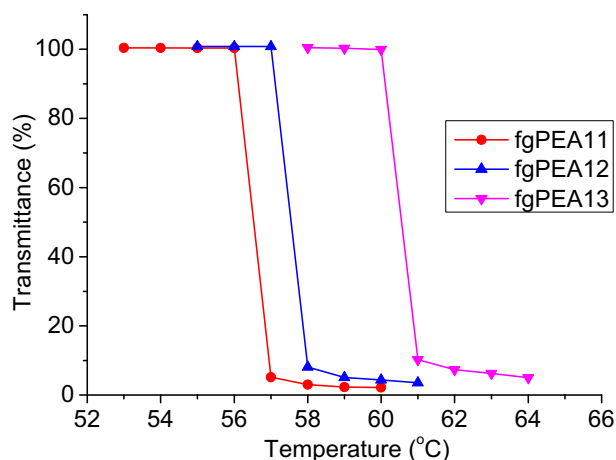


Fig. 6. Temperature dependence of optical transmittance at 500 nm for 10 mg/mL fgPEAs aqueous solution, pH = 7.0.

of the micelles. A fluorocarbon chain is stiffer than a hydrocarbon one because of the bulky fluorine atoms. Hence, the aggregates of fluorinated amphiphiles have a tendency to form a structure with less surface curvature, which can explain the larger molecular volume of the aggregates [43,44]. With the increasing fluorine contents from fgPEA11 to fgPEA13, more large micelles are formed. For fgPEA13, the relative uniform-sized micelles of ~200 nm in diameter are formed. However, its aqueous solution was still transparent, which indicates the good optical property due to its low refractive indexes [45,46].

#### 4.3. Responsive aggregation behaviors of micelles.

The aggregation behaviors of micelles formed by fgPEAs under different conditions were investigated. Due to the formation and cleavage of hydrogen bond between water molecules and hydrophilic L100 chain, amphiphilic polymers containing L100 chain exhibit the thermo-sensitive behaviors [35]. Micelles formed by fgPEAs are comprised of hydrophobic fluorinated alkyl chain as core and hydrophilic L100 chain as outer shell, which optimizes the surface contacting with water and prevent the micelles to aggregate further. If this hydrophilic outer shell become less hydrophilic with the increase of temperature, the micelles will aggregate, then resulting in turbidity of solution. To test the possibility of response to temperature, the size distribution of micelle formed by fgPEA13 at low and high temperature was checked by DLS, and shown in Fig. 5. It was observed that fgPEA13 can converted into large particles with a diameter of several micrometers at high temperature. To study systematically the responsive aggregation behavior of micelles under different conditions, temperature dependent transmittance measurements were carried out using a UV-vis spectrometer. In all cases, the concentration of three obtained fgPEAs was 10 mg/mL, which was much higher than CMC to ensure the formation of micelle. The corresponding temperature dependence of transmittance for three aqueous solutions of fgPEAs

Table 2  
CP of fgPEAs aqueous solution at different pH.

Copolymer	CP of fgPEAs aqueous solution at different pH (°C)			
	pH = 5.0	pH = 6.0	pH = 7.0	pH = 8.0
fgPEA11	62.0	59.1	56.3	55.8
fgPEA12	62.4	59.3	57.1	56.0
fgPEA13	67.2	64.1	60.1	58.0

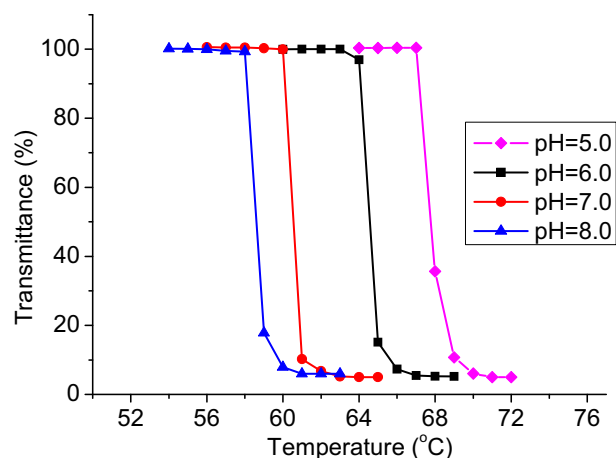


Fig. 7. pH dependence of optical transmittance at 500 nm for 10 mg/mL fgPEA13 aqueous solution at room temperature.

at pH 7.0 is shown in Fig. 6, from which cloud point (CP) can be obtained. These solutions exhibit sharp transition from transparency to turbidity with increase of temperature. It should be noted that CP for fgPEAs increased with the increasing amount of hydrophobic C<sub>9</sub>F<sub>19</sub> chain from fgPEA11 to fgPEA13. Generally, CP for responsive amphiphilic polymer decreases with the increasing

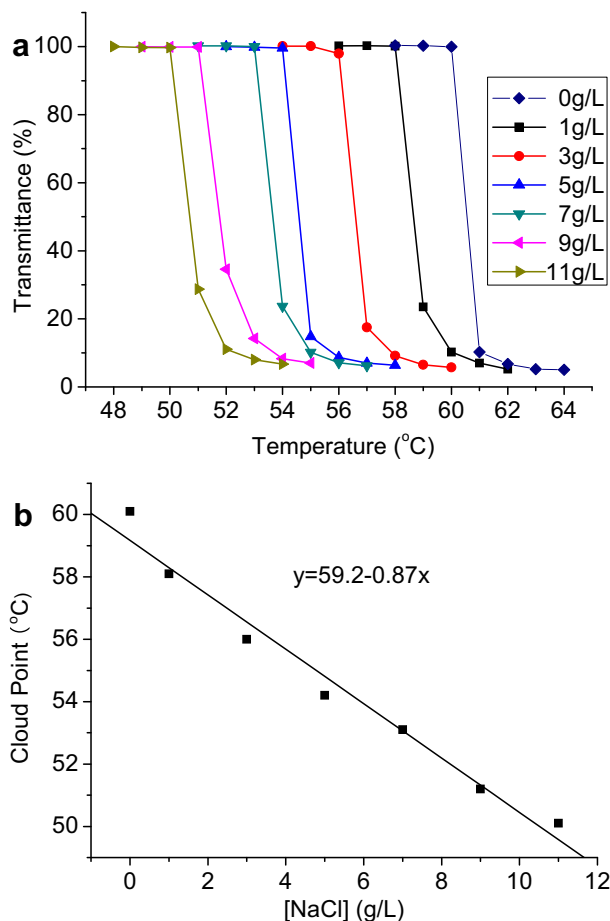
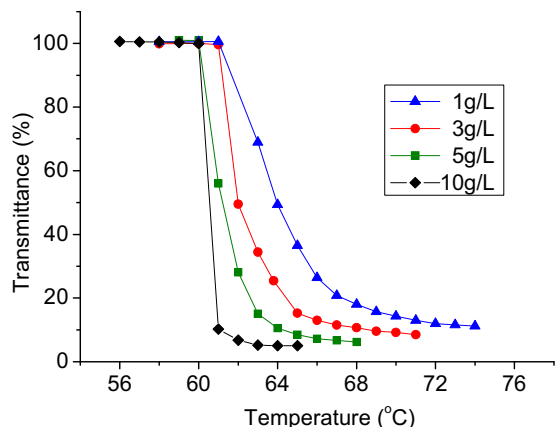


Fig. 8. Ionic strength-response of fgPEA13 in aqueous solution (a) temperature dependence of transmittance for fgPEA13 aqueous solutions at different NaCl concentration by UV-Vis spectra, (b) Dependence of the CP of fgPEA13 on NaCl concentration. Polymer concentration is 10 mg/mL, pH = 7.0.



**Fig. 9.** The phase transition behavior of fgPEA13 aqueous solution with different concentration, pH = 7.0.

amount of hydrophobic parts. The interesting phenomenon of fgPEAs' CP which is completely different out previous report of other PEAs [35,36], was not fully understood yet, and might be attributed to different size of the formed micelle. The micellar size

increased with the increase of the amount of C<sub>9</sub>F<sub>19</sub> chain, thus might resulting in the increase of CP from fgPEA11 to fgPEA13. That means CP of fgPEAs aqueous solution is determined not only by the macromolecular structure but also by the size of the formed micelles.

The backbone of fgPEAs is comprised of ternary amino moieties, which can be protonated or deprotonated at different pH, resulting in fgPEAs' response to pH. To test this possibility of pH effect on aggregation of micelles, temperature dependence of transmittance for fgPEAs aqueous solutions at different pH were measured (Fig. 7). From Fig. 7, the effect of pH on transition temperature of fgPEA13 solution is significant, suggesting that transition temperature can be controlled by pH: i.e. by increasing pH value, the transition temperature became lower accordingly. With decreasing pH value from 8.0 to 5.0, CP of fgPEA13 increases from 58.0 °C to 67.2 °C. CP of all fgPEAs at different pH value is summarized in Table 2. For all fgPEAs, the decreasing pH value leads to the increase of CP.

Because of its outer shell comprising of L100 chain, the aggregation of micelle formed by fgPEAs is also expected to be sensitive to ionic strength, which is one of the dominating parameter in various aqueous system. Fig. 8a shows transmittance versus temperature curves of fgPEA13 with different NaCl concentration. fgPEA13 exhibits very sharp phase transition in wide range of

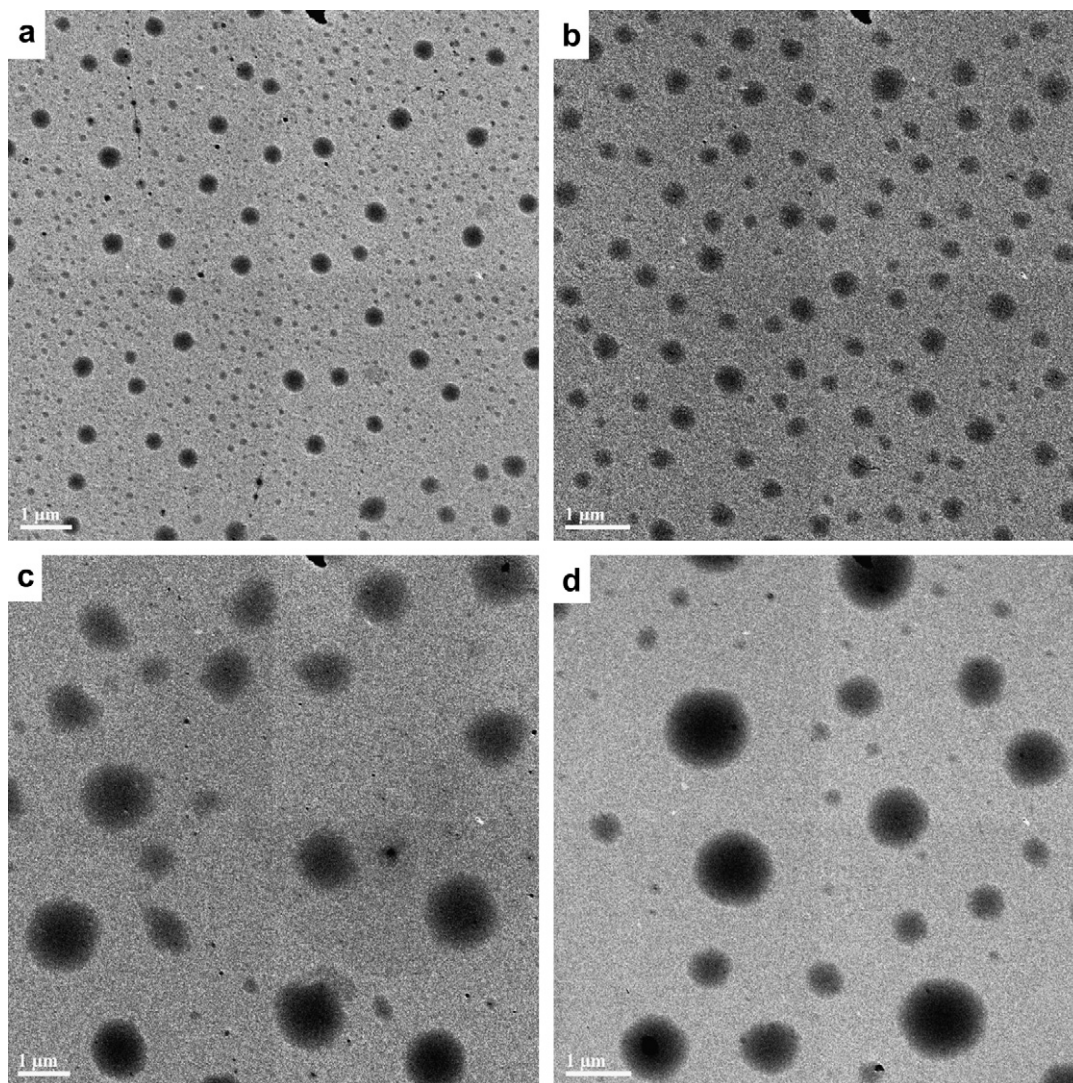
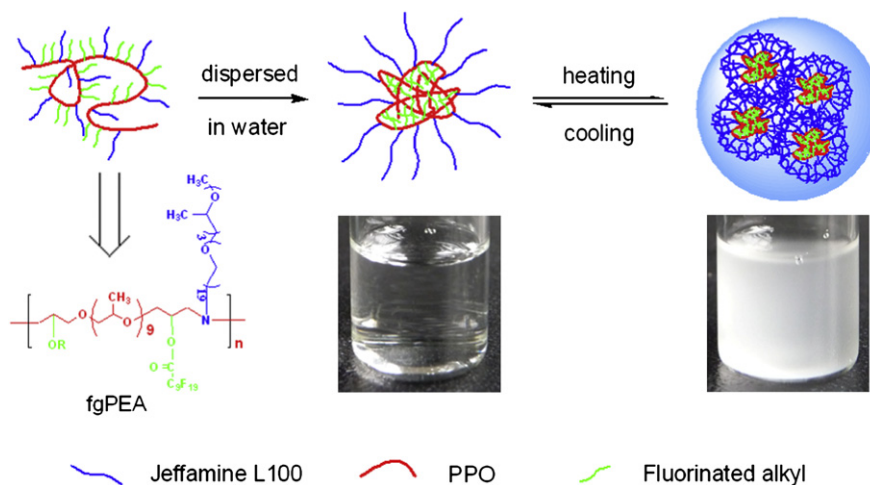


**Fig. 10.** TEM images of (a) fgPEA12 and (b) fgPEA13 at room temperature; (c) fgPEA12 and (d) fgPEA13 at temperature higher than their CP. The concentration of sample solutions is 1 mg/mL, pH = 7.0.





**Scheme 2.** Micelle formation & proposed mechanism of phase transition of fgPEAs aqueous solution.

NaCl concentration when heated. CP decreases obviously with the increasing NaCl concentration because of partial dehydration of polymer chain. These results can be explained by salt-out effect, and also indicates that the aggregation behaviors of micelles formed by fgPEAs can be controlled by ionic strength. It is notable that CP of fgPEA13 aqueous solution exhibited a linear relationship to NaCl concentration (Fig. 8b).

The phase transition of fgPEA13 aqueous solution with different concentration, ranging from 1 to 10 mg/mL, was further investigated (Fig. 9). CP of fgPEA13 aqueous solution showed no obvious dependence on the polymer concentration. Meanwhile, when the polymer concentration decreased,  $\Delta T$  increased from one to several degrees.

#### 4.4. Morphology of micelles formed by fgPEAs

The morphology of fgPEAs in aqueous solution was revealed by TEM. Fig. 10 shows the representative TEM images of the micelles formed by fgPEA12 and fgPEA13 at room temperature, indicating that fgPEAs were dispersed as micelles in water. The size of fgPEA12 micelle is not uniform, while fgPEA13 can form uniform-sized micelle in water. These results are in good agreement with the results obtained by DLS. When temperature is higher than their CP, fgPEAs aggregates were observed with diameter more than 1  $\mu\text{m}$  by TEM results.

The proposed transition process of fgPEAs aqueous solution is presented in Scheme 2. The transition of gPEA has already been investigated by our group. Similar to gPEA, fgPEAs form micelles with hydrophobic core of fluorinated alkyl graft chains and PPO backbones and hydrophilic corona of L100 when dispersed in aqueous solution at room temperature. Raising temperature higher than their CP, the L100 graft chains becomes less hydrophilic, resulting in aggregation of micelles.

## 5. Conclusions

We have synthesized a series of multi-stimuli responsive graft fluorinated poly(ether amine)s (fgPEAs) with varied fluorine contents. The amphiphilic fgPEAs exhibit very sharp response to temperature, pH and ionic strength. In aqueous solution, fgPEAs can self-assemble into stable micro & nano-micelles and are capable of encapsulating hydrophobic guest molecules, such as Nile Red. CP of fgPEAs aqueous solution increases with the increasing

amount of graft fluorinated alkyl chains or the decreasing ionic strength and pH value.

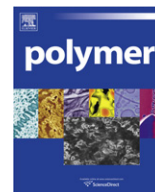
## Acknowledgements

We thank the National Nature Science Foundation of China (No: 50803036) and Science & Technology Commission of Shanghai Municipal Government (No: 08520704700) for their financial support.

## References

- [1] Kasgoz H, Orbay M. *Polymer* 2003;44:1785–93.
- [2] Jeong B, Gutowska A. *Trends Biotechnol* 2002;20:305–11.
- [3] Haag R. *Angew Chem Int Ed* 2004;43:278–82.
- [4] Lutz JF. *Polym Int* 2006;55:979–93.
- [5] Goodwin AP, Mynar JL, Ma Y, Fleming GR, Frechet MJM. *J Am Chem Soc* 2005;127:9952–3.
- [6] Jiang XG, Jin S, Zhong QX, Dadmun MD, Zhao B. *Macromolecules* 2009;42:8468–76.
- [7] Jochum FD, Theato P. *Polymer* 2009;50:3079–85.
- [8] Sundararaman A, Stephan T, Grubbs RB. *J Am Chem Soc* 2008;130:12264–5.
- [9] Quan CY, Wu DQ, Chang C, Zhang GB, Cheng SX, Zhang XZ, et al. *J Phys Chem C* 2009;113:11262–7.
- [10] Keerl M, Pedersen JS, Richtering W. *J Am Chem Soc* 2009;131:3093–7.
- [11] Li Y, Du W, Sun G, Wooley KL. *Macromolecules* 2008;41:6605–7.
- [12] Kale AA, Torchilin VP. *J Drug Target* 2007;15:538–45.
- [13] Shome A, Debnath S, Das PK. *Langmuir* 2008;24:4280–8.
- [14] Saboktakin MR, Maharramov A, Ramazanov MA. *Carbohydr Polym* 2009;77:634–8.
- [15] Chen W, Meng FH, Cheng R, Zhong ZY. *J Control Release* 2010;142:40–6.
- [16] Ghosh S, Irvin K, Thayumanavan S. *Langmuir* 2007;23:7916–9.
- [17] Takae S, Miyata K, Oba M, Ishii T, Nishiyama N, Itaka K, et al. *J Am Chem Soc* 2008;130:6001–9.
- [18] Signore G, Nifos R, Albertazzi L, Storti B, Bizzarri R. *J Am Chem Soc* 2010;132:1276–88.
- [19] Rijcken CJF, Soga O, Hennink WE, Nostrum CF. *J Controlled Release* 2007;120:131–48.
- [20] Klaiherd A, Nagamani C, Thayumanavan S. *J Am Chem Soc* 2009;131:4830–8.
- [21] Ganta S, Devalapally H, Shahiwala A, Amiji M. *J Controlled Release* 2008;126:187–204.
- [22] Szczubiatka K, Moczek Ł, Goliszek A, Nowakowska M, Kotzev A, Laschewsky A. *J Fluor Chem* 2005;126:1409–18.
- [23] Riess JG. *Curr Opin Colloid Interface Sci* 2009;14:294–304.
- [24] Riess JG. *J Fluorine Chem* 2002;114:119–26.
- [25] Krafft MP. *Adv Drug Deliv Rev* 2001;47:209–28.
- [26] Moody CA, Field JA. *Environ Sci Technol* 2000;34:3864–70.
- [27] Kharitonov AP, Taege R, Ferrier G, Teplyakov VV, Syrtsova DA, Koops GH. *J Fluor Chem* 2005;126:251–63.
- [28] Nazarov VG, Kondratov AP, Stolyarov VP, Evlampieva LA, Baranov VA, Gagarin MV. *Polym Sci Ser A* 2006;48:1164–70.
- [29] Graham P, Stone M, Thorpe A, Nevell TG, Tsibouklis J. *J Fluor Chem* 2000;104:29–36.
- [30] Wu WL, Zhu QZ, Qing FL, Han CC. *Langmuir* 2009;25:17–20.

- [31] Creutz S, Stam JV, Schryver FCD, Jerome R. *Macromolecules* 1998;31:681–9.
- [32] Jankova K, Hvilsted S. *J Fluorine Chem* 2005;126:241–50.
- [33] Tan H, Xie XY, Li JH, Zhong YP, Fu Q. *Polymer* 2004;45:1495–502.
- [34] Ren YR, Jiang XS, Yin J. *J Polym Sci Part A Polym Chem* 2009;47:1292–7.
- [35] Ren YR, Jiang XS, Liu R, Yin J. *J Polym Sci Part A Polym Chem* 2009;47:6353–61.
- [36] Ren YR, Jiang XS, Yin GL, Yin J. *J Polym Sci Part A Polym Chem* 2010;48:327–35.
- [37] Jiang XS, Wang R, Ren YR, Yin J. *Langmuir* 2009;25:9629–32.
- [38] Nandivada H, Jiang XW, Lahann J. *Adv Mater* 2007;19:2197–208.
- [39] Lin SL, Numasawa N, Nose T, Lin JP. *Macromolecules* 2007;40:1684–92.
- [40] Lin SL, Lin JP, Nose T, Iyoda T. *J Polym Sci Part B Polym Phys* 2007;45:1333–43.
- [41] Tonelli C, Meo AD, Fontana S, Russo A. *J Fluor Chem* 2002;118:107–21.
- [42] Skrabania K, Berlepsch HV, Bottcher C, Laschewsky A. *Macromolecules* 2010;43:271–81.
- [43] Wang K, Karlsson G, Almgren M, Asakawa T. *J Phys Chem B* 1999;103:9237–46.
- [44] Matsuoka K. *Langmuir* 2007;23:10990–4.
- [45] Matsuoka K, Moroi Y. *Curr Opin Colloid Interface Sci* 2003;8:227–35.
- [46] Koenderink GH, Sacanna S, Pathmamanoharan C, Rasa M, Philipse AP. *Langmuir* 2001;17:6086–93.



# Hyperbranched poly(methyl methacrylate)s prepared by miniemulsion polymerization and their (non)-Newtonian flow behaviors

Chaolong Li, Hao Jiang, Yu Wang, Yuechuan Wang\*

State Key Laboratory of Polymer Materials Engineering, College of Polymer Science and Engineering, Sichuan University, Chengdu 610065, PR China

## ARTICLE INFO

### Article history:

Received 5 September 2010  
Received in revised form  
2 November 2010  
Accepted 29 November 2010  
Available online 4 December 2010

### Keywords:

Branched polymer  
Shear thickening  
Miniemulsion

## ABSTRACT

Miniemulsion polymerization is most suitable for the targeted synthesis of vinyl copolymers than the conventional emulsion polymerization, because in miniemulsion polymerization each monomer nanodroplet is a nanoreactor, and the monomers in each droplet are in situ converted to the corresponding polymers. Soluble and hyperbranched poly(methyl methacrylate)s (PMMA) were prepared with quantitative monomer conversion and without gelation by the miniemulsion copolymerization with di- and tri-acrylate and mediated with 1-dodecyl thiol (DDT). DDT acted both as a gelation prohibitor and as a reactive cosurfactant. The PMMAs with varied “X” or “Ж” shaped branches, depending on the di- and tri-functional acrylate used as the branching agent, are characterized and interpreted in terms of the repeating units per part, parts and branches per macromolecule, average molecular weight, latex particle size and size distribution. Effects of topology changes of the branched PMMAs on the rheological behaviors are observed for the first time: from Newtonian flow for the densely branched PMMAs to the non-Newtonian flow with pronounced shear thickening for the PMMA samples with high-molecular-weight and longer parts.

© 2010 Elsevier Ltd. All rights reserved.

## 1. Introduction

Compared with the step-growth polymerization, the chain polymerization of vinyl monomer is simpler, cost-effective and can be performed in aqueous medium. Inspired by the dendritic polymers from step-growth polymerization, branched vinyl polymers have attracted great attentions in research and development, especially for applications where viscosity and reactivity are more emphasized than mechanical properties, such as the case of reactive molding, sealing or coating [1]. Due to the lack of chain entanglements, the hyperbranched vinyl polymers resembled the compact globular structure, and possess Newtonian flow behavior, i.e., no shear thinning or thickening, observed in dendritic polymers produced by step-growth polymerization of AB<sub>x</sub> monomers [2]. However, the effects of chain topology on the rheological properties are found very evident [2,3]. The number of branch points, the length and number of the arms are essential to define the rheological behavior. It is of fundamental importance and practical interest to develop a synthetic methodology capable of finely

controlling the chemical and topological structures, and to further reveal the rheological properties of these polymers.

Several approaches to the synthesis of branched vinyl polymers have been proposed [4–11]. Originally, the self-condensing vinyl polymerization (SCVP) was first reported by Fréchet [7]. Group transfer polymerization [8] and controlled radical polymerization with multivinyl monomers as the branching units were later exploited. For example, Wang [9] et al. prepared hyperbranched vinyl polymers by deactivation enhanced atom transfer radical polymerization (ATRP) of multivinyl monomers, and Armes et al. [10,11] prepared branched vinyl polymers by reversible addition fragmentation chain transfer (RAFT) polymerization and by atom transfer radical polymerization (ATRP). These controlled polymerizations provided a handle for preparing macromolecules with tailorable molecular weight and branching structures, but the overall monomer conversion had to be kept below 60% in order to prevent cross-linking or microgel formation [9]. A facile method for the preparation of branched poly(meth)acrylates was recently developed [12–14] by conventional free radical polymerization under the presence of both multifunctional acrylates and a thiol compound. The multifunctional monomer leads to chain branching, and the thiol compound prevents gelation. When applying this method to emulsion polymerization, however, the limited solubility of thiol compounds in water retards its transportation from

\* Corresponding author. Fax: +86 028 85405243.  
E-mail address: [wangyc@scu.edu.cn](mailto:wangyc@scu.edu.cn) (Y. Wang).

monomer droplets through water to the polymerization loci. To ensure enough thiols existed in the droplets, either smaller thiol molecules (thus with relatively higher solubility in water), such as benzylthiol, or a phase transfer agent to help the transportation of thiols through water was used [15,16]. As the odour of thiol compounds is tightly molecular size dependent, the use of smaller thiol molecules for emulsion polymerization is not convenient. For the latter method, phase transfer agent will remain in the final latex, and impurity problem results.

Miniemulsion polymerization is a unique and useful technique for preparing vinyl copolymers. Unlike the conventional emulsion polymerization, for an ideal miniemulsion polymerization polymer particles are formed primarily by the radical entering into monomer droplets, in other words, polymer particle nucleation takes place at the monomer droplets, not at the swollen monomer micelles as the case of conventional emulsion polymerization. This feature has been supported by the fact that polymer particle size was found the same as the size of monomer droplets [17–19]. Because most of the polymer latex particles are in situ converted from the monomer droplets, there is no mass transportation during polymerization, and thus no need to take account of the water solubility when using thiol compounds. Furthermore the polymers have the same composition as the monomers in each droplet. As the branched vinyl polymers are usually prepared by the copolymerization of monomers, rather than by the homopolymerization of a single monomer, from the point of view of practical application, miniemulsion polymerization is the best way for this targeted synthesis than conventional emulsion polymerization. Thus it is worthy to develop the thiol mediated miniemulsion polymerization, and it is surprising that there is scarcely a study on this important issue.

In this paper we report the synthesis and the unique rheological behaviors of branched PMMAs prepared by thiol mediated miniemulsion copolymerizations of methyl methacrylate (MMA) with 1,6-hexanediol diacrylate (HDDA) and with trimethylolpropane triacrylate (TMPTA). Soluble and highly branched PMMAs with varied degrees of branching were prepared with narrow distribution of latex particle sizes and with quantitative monomer conversion without gelation. The dramatic changes of Newtonian flow to shear thickening (non-Newtonian flow) of PMMA melts resulted from changes of chain topology from dense to medium branches are first observed.

## 2. Experimental section

### 2.1. Materials

MMA (99%, analytical grade from Shanghai Chemical Company, China) was purified by passing through activated basic alumina prior to use. 4,4'-Azobis(4-cyanovaleric acid) (ACVA, 95%), sodium hydrogen carbonate (NaHCO<sub>3</sub>, 95%), 1-dodecyl thiol (DDT, 98%), sodium dodecyl sulfate (SDS, 98%), tetrahydrofuran (THF) and *n*-hexane were used as supplied by Kelong Chemical Co., Chengdu,

China. 1,6-Hexanediol diacrylate (HDDA, 92%) and trimethylolpropane triacrylate (TMPTA, 90%) (Cytec Industries Inc. USA, in Shanghai China), were industrial grade and used without further purification. The impurities in the multifunctional monomers include the non-completely esterified acrylates and trace of higher degree oligomers.

### 2.2. Miniemulsion polymerization

In a typical polymerization, (as sample PMMA3, Table 1), the organic phase composed of 10 g of MMA, 1.1 g of HDDA, 2.02 g of DDT, were mixed with 0.24 g of SDS and 42 g of deionized water. After vigorously stirring by magnetic stirrer for 30 min, the dispersion was ultrasonicated on ice bath for 7 min with a Vibra-Cell Ultrasonic Processor (BILON 98, Shanghai). The miniemulsion was deaerated using a stream of nitrogen, and then 0.2 g of ACVA and 0.1 g of NaHCO<sub>3</sub> in 8 g of water were introduced. The polymerization was carried out at 70 °C for 5 h under mechanical stirring at 200 rpm and the protection of nitrogen atmosphere. Crude polymer was recovered by freezing and thawing the synthesized polymer latex. Samples for characterization were purified by precipitation of the THF solution of the crude product from *n*-hexane. The purification was repeated for three times, and then the polymer samples were dried under reduced pressure at 60 °C.

## 3. Characterizations

### 3.1. Latex characterization

The volume weighted average diameters ( $D_v$ ) of monomer droplets and polymer particles, as well as their dispersities, were measured with a granulometer (Malvern Mastersizer Hydro MS2000) at 25 °C. Particle sizes were determined by transmission electron microscopy (TEM) with a JEOL 1200 microscope. The number of droplets  $N_d$  or latex particles  $N_p$  were calculated by  $N = 6\tau/\pi(D_v)^3\rho$ , here  $\tau$  stands for concentration (g/mL<sub>Latex</sub>), and  $\rho$  for the density of monomers or the polymer. The density of monomer mixture was calculated by:  $\sum w_i\rho_i/\sum w_i$ , here  $w_i$  and  $\rho_i$  are the mass fraction and the density of each monomer, respectively. The density of the branched PMMA was assumed as that of linear PMMA. Solid content of latex and monomer conversion were determined gravimetrically at the end of polymerization. The obtained data are listed in Table 1.

### 3.2. Molecular weight evaluation

The apparent molecular weights ( $M_{wGPC}$ ) and the polydispersities ( $M_w/M_n$ ) were determined by gel permeation chromatography (GPC) (Agilent 1100 series) with a 30 cm PLgel Mixed-C column and a refractive index detector, calibrated with linear polystyrene standards (Polymer Laboratories), using THF (1.0 mL/min) as the eluent at 30 °C. The weight averaged molecular weights ( $M_{wMALLS}$ ) were determined by GPC (515 HPLC PUMP,

**Table 1**  
The miniemulsion copolymerization of MMA with di- or tri-functional acrylate.

Latex samples	Feed mole ratio	Mole ratio <sup>a</sup>	Conv (%)	$D_d$ (nm)	$N_d$ ( $\times 10^{-14}$ ) (g <sub>Latex</sub> <sup>-1</sup> )	$D_p$ (nm)	$N_p$ ( $\times 10^{-14}$ ) (g <sub>Latex</sub> <sup>-1</sup> )	$N_p/N_d$	
PMMA1	MMA/HDDA/DDT	100/2/4	100/2.6/5	99.2	105	3.65	103	2.85	0.783
PMMA2	MMA/HDDA/DDT	100/2/6	100/2.7/6	98.8	118	2.77	105	2.88	1.039
PMMA3	MMA/HDDA/DDT	100/5/10	100/8/16	98.7	116	3.18	103	3.06	0.963
PMMA4	MMA/HDDA/DDT	100/10/20	100/13.7/27	99.1	122	2.82	106	3.33	1.18
PMMA5	MMA/TMPTA/DDT	100/1/4	100/0.8/4.2	99.4	117	2.36	104	2.65	1.123
PMMA6	MMA/TMPTA/DDT	100/3/12	100/2.4/15	99.6	121	2.51	112	2.38	0.949
PMMA7	MMA/TMPTA/DDT	100/5/20	100/4/19.7	98.2	129	2.43	107	2.58	1.065

$D_d$  and  $D_p$ : the droplet size and latex particle size respectively.  $N_d$  and  $N_p$ : the number of droplets and latex particles per gram of latex respectively.

<sup>a</sup> Determined by <sup>1</sup>H NMR.

Waters Corp.) on a Waters 2690 separation module fitted with a DAWN EOS multiangle laser light scattering (MALLS) detector from Wyatt Technology Corp. with 18 detectors placed at different angles (laser wavelength = 690 nm) and a RI detector (Wyatt Technology). THF was used as the mobile phase at a flow rate of 1.0 mL/min at 40 °C. The data were processed using software ASTRA 4.90.07 (Wyatt Technology).

### 3.3. Copolymer chemical composition

$^1\text{H}$  NMR spectra were recorded using a Bruker 400 spectrometer. The copolymer composition was determined by comparing the integral at about 4.10 ppm from  $-\text{OCH}_2$  groups of HDDA or TMPTA with that at 3.6 ppm from  $-\text{OCH}_3$  group on MMA. The incorporation of DDT residues in polymer was determined from the  $^1\text{H}$  NMR spectra with the integral at 2.5 ppm (from  $-\text{CH}_2-\text{S}-$ ).

### 3.4. Glass transition temperature, $T_g$

$T_g$  was recorded with a Perkin–Elmer Pyris-1 series differential scanning calorimeter (DSC) under a flowing nitrogen atmosphere with about 10 mg sample at 10 °C/min heating rate. Samples were heated to about 110 °C and then rapidly cooled.  $T_g$  was recorded from the second run.

### 3.5. Rheology measurements

All rheological characterizations of the polymer melts were conducted on a stress controlled rheometer (AR2000ex, TA) in a 25 mm parallel plate mode with a gap of 1.0 mm. The experiments were performed at 130 °C, with the exception for PMMA4 and PMMA7 that were performed at 80 °C. The polymer samples were subject to steady-shear and small-amplitude oscillatory shear. In the steady-shear mode, at least 3 orders of magnitude of shear rates were covered. In the small-amplitude dynamic oscillation mode, the frequency was varied from 0.01 to 50 Hz.

## 4. Results and discussion

### 4.1. Miniemulsification

Miniemulsion is not thermodynamically stable, but can be stabilized by the combined help of surfactant and cosurfactant. It was found that cosurfactant is a key component for miniemulsification, and the predominant requirement for it is the extremely low water solubility. DDT was reported as a suitable cosurfactant for the miniemulsion polymerization of styrene and methyl methacrylate [20,21]. SDS and DDT were used as surfactant and cosurfactant for the miniemulsion in this work.

The miniemulsion was prepared by vigorously stirring the aqueous dispersion of the monomers, DDT and SDS for 30 min, and immediately followed with ultrasonication. The effect of ultrasonication time on the structure of miniemulsion was studied, and is illustrated in Fig. 1(a). When the dispersion was ultrasonicated for only 1 min, the distribution of droplet sizes was quite broad. Even after 4.5 min of ultrasonication the swollen micelles (droplets size below 50 nm) still existed. After ultrasonication for 7 min the droplet size was decreased to about  $D_v = 118$  nm, and size distribution became narrowed with no free micelles. Further ultrasonication did not reduce the size and narrow the size distribution of droplets.

In miniemulsion polymerization there exists an interval (typically about 10 min) for particle nucleation [22]. To ensure well controlling over the polymer particle size and size distribution, the metastable miniemulsion must be stable during the interval without the help of ultrasonication. The stability of the metastable miniemulsion was studied by analyzing the changes of the droplet size and its distribution respect to the delay time after finishing ultrasonication, and the results are showed in Fig. 1(b) for the miniemulsion sample PMMA2. With the increasing of delay time, the droplet sizes and size distribution gradually increased. The droplet sizes ( $D_v$ ) were about 118, 121, 137, 139, 246 nm for delay time of 2, 50, 90, 120, 270 min, respectively, and after 270 min, the swollen micelles emerged. The droplet size and the size distribution were kept almost constant within 50 min after ultrasonication. The stabilities of other miniemulsion samples with higher level of DDT were better. Ostwald ripening in these miniemulsions is sufficiently retarded to allow nucleation and polymerization taken place before significant diffusional degradation of monomer droplets.

### 4.2. Miniemulsion polymerization

For the miniemulsion polymerization as listed in Table 1, all the miniemulsions were used immediately after the preparation, and no monomer micelles were detectable. The droplet sizes were in the range of 50–230 nm, within the typical range for miniemulsions (50–500 nm). The amount of DDT in these samples was varied from 7.2 to 24.8 wt% (relative to all monomer weight), corresponding to the ratio of DDT/SDS was about 3.0–15.3. The average size of polymer latex particle,  $D_p$ , was found slightly smaller than that of monomer droplets,  $D_d$ , owing to volume shrinkage by polymerization. This is expected and indicates that the mechanism of latex particle nucleation is primarily radical entry into the monomer droplets. When every nucleated droplet results in the formation of polymer particle, the ratio of latex particle number,  $N_p$ , to monomer droplet number,  $N_d$ , ( $N_p/N_d$ ), is around one. It can be seen that when the ratio of DDT/SDS was above 4.6 (samples PMMA2 to PMMA7), the ratio  $N_p/N_d$  was roughly around one, and  $D_d$  and  $D_p$  data do support a mechanism of droplet nucleation, see Fig. 2(a) and Table 1. At lower ratio,

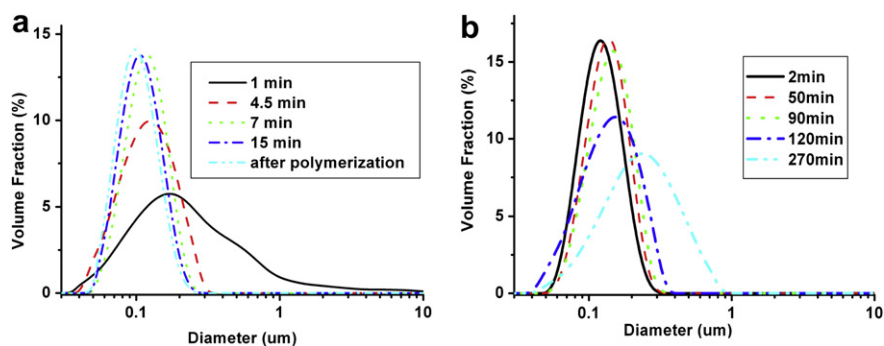


Fig. 1. The distribution of droplet size of a miniemulsion (for sample PMMA2), (a) by varied ultrasonication time; (b) after delay time.

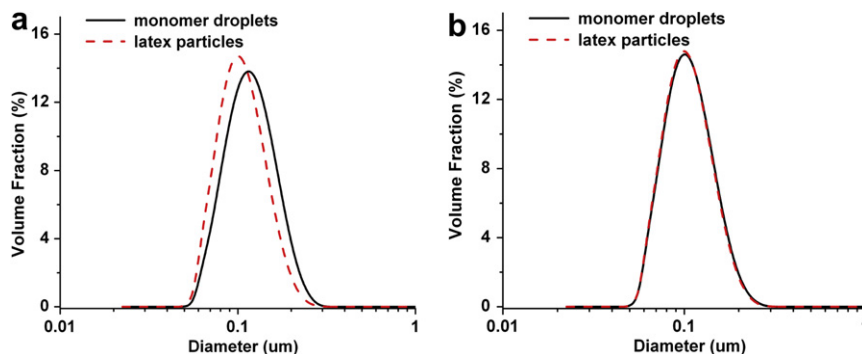


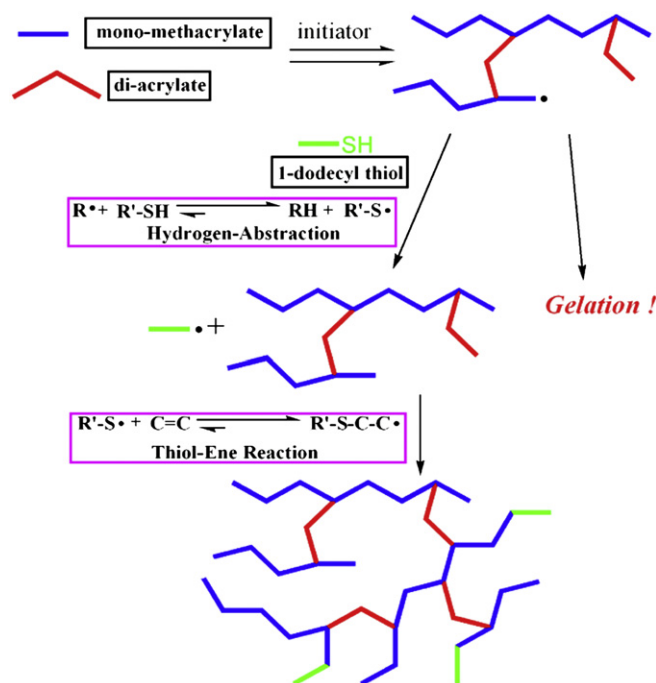
Fig. 2. The size distributions of monomer droplets and latex particles of PMMA2 (a) and PMMA1 (b).

however, such as the case of PMMA1, the  $N_p/N_d$  is less than one, and the curves of particle size distribution were almost overlapped with that of monomer droplets, as showed in Fig. 2(b), indicating that the polymerization did not follow a true miniemulsion process. Thus when the ratio DDT/SDS is below 3.0 (as the case of PMMA1), coalescence of monomer droplets or Ostwald ripening may accompany with the droplet nucleation during miniemulsion polymerization. TEM micrographs of PMMA2 and PMMA5 latexes are shown in Fig. 3. It can be seen that the distribution of particle sizes is nearly monodisperse.

#### 4.3. Synthesis of branched PMMAs

Besides the action as an effective cosurfactant, DDT also prevents gel formation through the mechanism as showed in Scheme 1. The propagating carbon radical species abstract hydrogen from the thiol, and further growing stops. The thus generated thiyl radical subsequently adds to the C=C bonds of monomers or of the appended acrylate groups on the macromolecular chains to initiate another growth of polymer chain. Thus gelation is prohibited by changing the site of chain growth, and branching structure results.

Topologically, each multifunctional acrylate (MFA) monomer with  $f$  functionalities will introduce additional  $2(f-1)$  chain parts into the macromolecular backbone. Thus the homopolymerization of the multifunctional monomer with  $f$  functionalities requires at least  $(f-1)$  moles of thiols to inhibit the cross-linking reaction. Similarly chain growth will be stopped with  $2(f-1)$  moles of thiols. For the copolymerization of multifunctional monomer with a monomer, more thiol molecules than the least  $(f-1)$  moles are required for preventing gelation, because the monomer will also consume the thiols. The copolymerizations of MMA with HDDA with three ratios of DDT/HDDA: 1.5, 1.6, 1.8, were investigated to study the effects of thiol amount on the polymerization. It was found that when the ratio DDT/HDDA was above 1.8, no gelation occurred in the



Scheme 1. The schematic illustration of polymerization and formation of branches by thiol mediated copolymerization of vinyl monomer with a difunctional monomer.

miniemulsion polymerization, and if the ratio was less than 1.6, the polymerization became gelled at high monomer conversion.

It is worth to note that in the copolymerization of an acrylate ( $M_1$ ) with a methacrylate ( $M_2$ ), the reactivity ratios are typically  $r_1 \sim 0.5$  and  $r_2 \sim 2.0$  [23], or acrylate prefers to react with methacrylate, rather than with itself, whilst methacrylate prefers to react

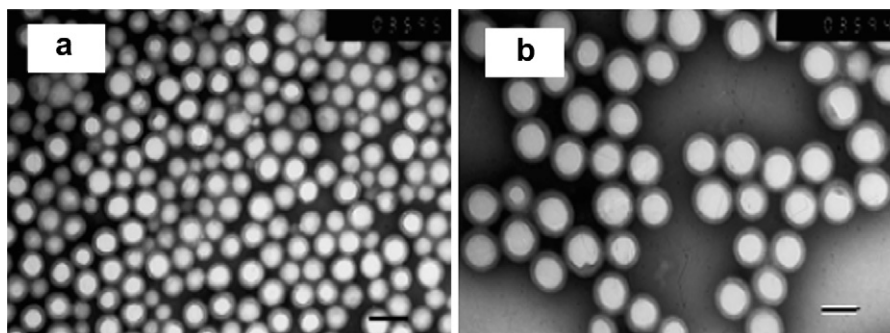


Fig. 3. The transmission electron microscopy images of the branched polymer latex particles: (a) PMMA2, scale bar 200 nm, (b) PMMA5, scale bar 100 nm.

with itself. As a result, at the reaction stage with lower monomer conversion, the immediate copolymer composition is methacrylate rich, and most part of the acrylate groups are consumed at the later stage of polymerization. Therefore, gelation will occur at reaction stage of high monomer conversion. On the other side, as the chain transfer constant of thiol toward acrylic and methacrylic free radical  $C_s$ , is  $\sim 1.7$  and  $\sim 0.6$  [24], respectively, thiols might exist within the monomer/polymer particle till the last stage of polymerization reaction. Otherwise, more thiol is required to prevent gelation. When the trifunctional acrylate monomer (TMPTA) is used as the branching unit, more DDT is required and the gelation was completely inhibited with the ratio DDT/TMPTA was about 4.

Branching control was realized by adjusting the feed ratio of MMA/MFA, while gel formation was prevented by the appropriate amount of DDT. Branched polymer using HDDA and TMPTA as the branching agents, with several ration of MFA/MMA from 1 to 10 mol%, were synthesized and carefully characterized. The results are listed in Table 2. It is well known that linear polymer possess much larger hydrodynamic volume than the branched analogue with the same molecular weight. Comparing the molecular weight ( $M_{wMALLS}$ ) obtained by MALLS-GPC and that ( $M_w$ ) by conventional GPC with single detector, for all these samples,  $M_{wMALLS}$  is much larger than the apparent  $M_w$ . The difference for sample PMMA4 was even about 10 times. It seems the difference became even greater when trifunctional monomer was used as the branching units. The difference of molecular weight is an indication of the branched structure of these polymers.

Topologically, when a difunctional acrylate monomer is copolymerized with monomer, such as MMA, “X” shaped or branched macromolecule with four chain parts results, and “Ж” shaped or branched macromolecule with six chain parts results when a trifunctional acrylate monomer is used as the branching unit. The mole fractions of MFA, MMA and DDT in the polymer chains are calculated by the ratio of the integrals at 4.1 ppm–3.8 ppm, 3.47–3.80 ppm and 2.6–2.40 ppm in the  $^1\text{H}$  NMR spectra (Fig. 4). With the MMA/MFA ratios and the number average molecular weight ( $M_{nMALLS}$ ) obtained by MALLS-GPC, the average number of MMA units and branching units per macromolecule, denoted as  $N_{MMA}$  and  $N_{MFA}$ , respectively, is calculated. With these data, the average number of MMA units per part ( $n_{MMA}$ ) is also calculated. Thus, an MFA with functionalities  $f$  will divide the polymer chain into  $\Phi$  parts by:

$$\Phi = N_{MFA} \times (2f - 1) + 1 \quad (1)$$

The average number of MMA units per part ( $n_{MMA}$ ) is obtained by:

$$n_{MMA} = N_{MMA} / \Phi \quad (2)$$

The average number of chain-end groups per macromolecule ( $N_{end}$ ) is given by the equation:

$$N_{end} = 2[1 + (f - 1) \times N_{MFA}] \quad (3)$$

These characteristic structure parameters of these branched PMMAs are calculated and summarized in Table 2, together with the  $T_g$  values. From Table 2 and Table 1, it can be seen that with the increase of MFA and DDT, the molecular weight of the branched polymer reduced, and the average length of parts decreased, indicating higher the degree of branching. For the four samples using HDDA as the branching agent,  $n_{MMA}$  decreased from 12.4 to only about 2.3 as the feed ratio of HDDA/MMA increasing from 2 mol% to 10 mol%. For sample PMMA7, prepared with TMPTA as the branching agent, the average repeating units per parts are also only about 4.9. It can be seen that  $T_g$  of these samples decreases from 80.5 to 6.3 °C with the increase of branching. The decrease of  $T_g$  could be a result of the free volume of branches and the free chain-ends. The low  $T_g$  values also indicate a highly branched architecture without cross-linking. Nevertheless, the opposite trend was observed that  $T_g$  increased gradually with branching in the polyesters prepared by the copolymerization of  $AB_2$  and  $AB$  monomers [25]. For this branched polyester, H-bonding interactions were confirmed by FTIR measurements [26], and were found increasing with the degree of branching and the number of chain-end groups (–OH).

However, it is not directly comparable for the samples prepared with di- and tri-functional acrylate as branching agent. For instance, sample PMMA4 and PMMA7 have the same  $T_g$ , but the part length of the latter is longer than of former. Anyway, the changes of  $T_g$  with the structure parameters are quite complex, and need further study.

#### 4.4. Melt properties

The rheological properties of these branched PMMA melts toward shearing were studied by the small-amplitude oscillatory shear and by the steady-shear methods. For samples PMMA4 and PMMA7, the shear experiments were carried out at 80 °C, and for all other PMMA samples the experiments were carried out 130 °C. Oscillatory shear deformation is an effective way to probe the complex fluids and can provide rich information on structural changes of viscoelastic materials. Fig. 5 shows the dependences of complex viscosity on oscillation frequency for the PMMAs with different degree of branching. For comparison, the shear behavior of a linear PMMA melt ( $M_w = 24000$ ,  $M_w/M_n = 1.9$ ) is also showed in Fig. 5. The complex viscosity at low frequency of linear PMMA is much higher (over several magnitudes), even though its molecular weight is much less than that of branched PMMAs. Increasing oscillation frequency decreased the complex viscosity of linear PMMA about two magnitudes, a typical shear thinning behavior of linear polymers, owing to disentanglement of the polymer chains, whilst the samples PMMA2, PMMA3 and PMMA5 only showed a slightly shear thinning, and the PMMA4 and

**Table 2**  
Characteristics of the branched PMMAs by miniemulsion polymerization.

Samples	$M_w(\text{kg mol}^{-1})^a$	$M_w/M_n^a$	$M_w(\text{kg mol}^{-1})^b$	$M_w/M_n^b$	$T_g$ (°C)	$N_{MMA}$	$N_{MFA}$	$\Phi$	$n_{MMA}$	$N_{end}$	$N_{DDT}$
PMMA1	299.6	6.17	73.3	53.07	80.5	419	10.9	33.7	12.4	23.8	26
PMMA2	113.5	3.82	47	2.81	68.8	243	6.8	21.5	11.3	15.6	15
PMMA3	35.4	4.74	15.9	6.98	32.6	50	4.0	13	3.8	10	8
PMMA4	39.7	5.75	16.4	5.81	6.3	37	5.1	16.2	2.3	12.2	10
PMMA5	690	3.77	218	5.56	90.5	165	1.3	7.6	21.7	7.2	6.9
PMMA6	2830	2.12	217	196	31	1834	44.0	221	8.3	178	275
PMMA7	37.7	1.36	7.0	4.43	7.3	183	7.3	37.5	4.9	31.2	36

$N_{MMA}$ : average number of MMA units per macromolecule (polymer chain);  $N_{MFA}$ : average number of branching units per macromolecule polymer chain;  $\Phi$ : parts per macromolecule;  $n_{MMA}$ : average number of MMA units per part;  $N_{end}$ : average number of chain-end groups per macromolecule;  $N_{DDT}$ : average number of DDT units per macromolecule.

<sup>a</sup> Obtained by GPC-MALLS.

<sup>b</sup> Obtained by GPC with single refractive index detector.

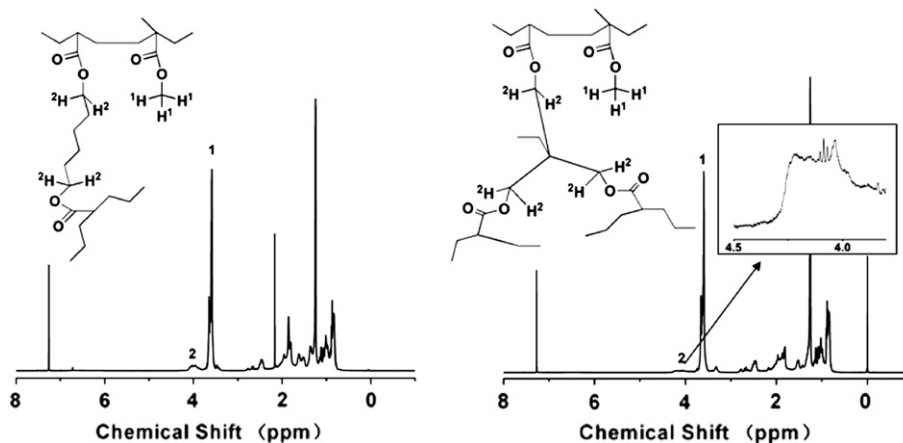


Fig. 4.  $^1\text{H}$  NMR spectra (in  $\text{CDCl}_3$ ) of PMMA2 (left) and PMMA5 (right) using hexanediol diacrylate and trimethylolpropane triacrylate as the branching agent, respectively.

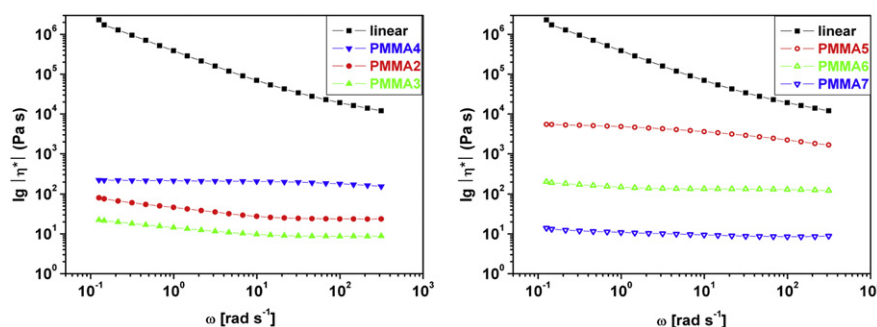


Fig. 5. Complex viscosity as a function frequency for the branched PMMAs (at 80 °C for PMMA4 and PMMA7, and at 130 °C for all the other samples).

PMMA7 samples showed Newtonian flow behavior, i.e., no shear thinning. It is also worthy to note the melt difference between PMMA6 and PMMA5, both were prepared with the trifunctional TMPTA as the branching agent. The number averaged repeating units per macromolecule,  $N_{\text{MMA}}$ , of PMMA6 are over 10 times greater than that of PMMA5, but its complex viscosity is lower. This could be attributed to the difference of  $n_{\text{MMA}}$ , i.e., the number averaged repeating units per part, or the length of each branched part.  $n_{\text{MMA}}$  of PMMA6 is much smaller than that of PMMA5, meaning PMMA6 is more densely branched with more compact globular conformations than PMMA5. Thus interpenetration between neighboring molecules is greatly reduced in the PMMA6 melt, and viscosity is decreased.

In the steady-shear experiments, interesting phenomena of shear thickening were observed for the first time: except for PMMA4 and PMMA7 samples that exhibit a Newtonian flow

behavior of highly branched polymers, the melt viscosity of PMMAs melts increased with the increasing of shear rate, after the initial shear thinning (decrease of viscosity), (Fig. 6). The shear thickening behaviors for “Ж” shape branched PMMAs were more pronounced than “X” shape branched PMMAs. For more clearly showing the shear thickening, the viscosities at the initial ( $\eta_i$ ), the minima ( $\eta_m$ ) and at the end ( $\eta_e$ ) of shear experiments are summarized in Table 3. The relative increments of viscosity,  $(\eta_e - \eta_m)/\eta_m$ , at the end of experiment were about 35–42% from the minima, for samples PMMA2, PMMA5 and PMMA6. The initial shear thinning is a result of disentanglement of the branched chains, and the shear thickening indicates the rebuilding up of fluid structure, or the increasing of frictions among the parts on the branched macromolecules. A detailed expression of the shear thickening mechanism needs more experiments, but we would briefly outline it, as illustrated in Scheme 2. At lower shear rate, shearing results in

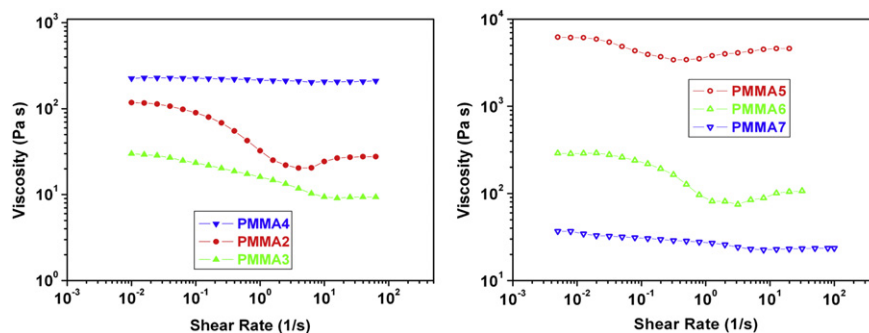


Fig. 6. Steady-shear viscosity as a function of shear rate for the branched PMMAs (at 80 °C for PMMA4 and PMMA7, and at 130 °C for all the other samples).

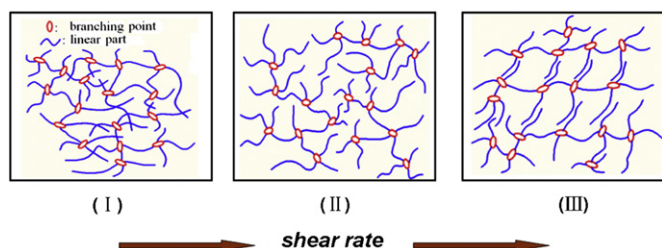


**Table 3**

The viscosities of the branched PMMAs by miniemulsion polymerization under steady shearing.

Samples	$\eta_i$ (Pa s)	$\eta_m$ (Pa s)	$\eta_e$ (Pa s)	$\eta_e/\eta_m$ (%)	$(\eta_e - \eta_m)/(\eta_i - \eta_m)$ (%)
PMMA2	118	20.4	27.7	1.36	7.5
PMMA3	30	9.1	9.4	1.03	1.4
PMMA4	229	213	213	1.00	0
PMMA5	6215	3411	4600	1.35	42.4
PMMA6	289.5	75	107	1.42	14.9
PMMA7	36.8	22.2	23.5	1.05	8.9

$\eta_i$ : The viscosity at the initial of shear experiment,  $\eta_m$ : the minima viscosity during the shear experiment,  $\eta_e$ : the viscosity at the end of shear experiment.



**Scheme 2.** Schematic illustration for the mechanism of shear thickening of the branched polymer melts from the entangled state (I) through disentanglement (II) and finally leading to extended conformation by steady shearing with increased inner frictions among the interpenetrated parts on the periphery of the branched macromolecules (III).

disentanglement and an extended conformation of macromolecules in melt, and the viscosity decreased (Scheme 2II). Because the motion of the parts is limited by the branched molecular skeleton, further increasing shear rate leads to the increase of inner frictions among molecules through the interpenetrated parts on the periphery of the branched macromolecules, and thus the melt exhibits shear thickening (Scheme 2III). The ratio of  $\eta_e/\eta_m$  indicates the increment of viscosity, and the ratio of  $(\eta_e - \eta_m)/(\eta_i - \eta_m)$  is a measurement of relative importance of shear thickening to chain disentanglement. The high-molecular-weight samples PMMA2 and PMMA6 exhibited the higher  $\eta_e/\eta_m$ , and the PMMA5 sample showed both high  $\eta_e/\eta_m$  and the highest  $(\eta_e - \eta_m)/(\eta_i - \eta_m)$ . Thus the branched macromolecules with higher molecular weight and longer parts, i.e., greater  $N_{MMA}$  and  $n_{MMA}$ , will exhibit greater shear thickening,  $\eta_e/\eta_m$ ; the branched macromolecules with dense and compact branching structures, i.e., with smaller  $n_{MMA}$ , will show less or even no shear thickening, as the case of PMMA4 ( $n_{MMA} = 2.3$ ) and PMMA7 ( $n_{MMA} = 4.9$ ) that only exhibited the typical Newtonian flow behavior.

## 5. Summary

We synthesized branched PMMA with varied degree of branching by aqueous miniemulsion polymerization using di- and trifunctional

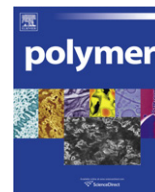
acrylates as the branching agents, and 1-dodecyl thiol both as a reactive cosurfactant to suppress Ostwald ripening and as a chain transfer agent to prevent gelation. Soluble and high-molecular-weight polymers with varied branching densities, as indicated by the repeating units per part between the branching points, are prepared with narrow distribution of latex particle sizes and with quantitative monomer conversion without gelation. Using 1-dodecyl thiol as the reactive cosurfactant ensures no residue in the final latex. The rheological properties for the branched PMMAs are also examined. We observed for the first time that the melts of branched PMMAs with high-molecular-weight and with certain length of part ( $\sim 8$  repeating units per part) show shear thickening in steady-shear experiments. More experimental data, however, are still needed to better understand the branching structure and properties.

## Acknowledgment

This work is partly supported by “grand science and technology special project, Guangdong Province” (Project No. 2008A090300014).

## References

- [1] Voit BI, Lederer A. *Chem Rev* 2009;109:5924–73.
- [2] Ye ZB, Zhu SH. *Macromolecules* 2003;36:2194–7.
- [3] Larson RG. *Macromolecules* 2001;34(13):4556–71.
- [4] Matyjaszewski K, Pyun J, Gaynor SG. *Macromol Rapid Commun* 1998;19:665–70.
- [5] Ishizu K, Mori A. *Macromol Rapid Commun* 2000;21:665–8.
- [6] Zhang K, Wang J, Subramanian R, Ye Z, Lu J, Yu Q. *Macromol Rapid Commun* 2007;28:2185–91.
- [7] Frechet MJM, Henmi M, Gitsov I, Aoshima S, Leduc MR, Grubbs RB. *Science* 1995;269:1080–3.
- [8] Simon PFW, Radke W, Muller AHE. *Macromol Rapid Commun* 1997;18:865–73.
- [9] Wang W, Zheng Y, Roberts E, Duxbury CJ, Ding L, Irvine DJ, et al. *Macromolecules* 2007;40:7184–94.
- [10] Bannister I, Armes SP, Rannard SP, Findlay P. *Macromolecules* 2006;39:7483–92.
- [11] Vo CD, Armes SP, Billingham NC. *Macromolecules* 2007;40:7119–25.
- [12] Baudry R, Sherrington DC. *Macromolecules* 2006;39:1455–60.
- [13] Isaure F, Cormack PAG, Sherrington DC. *J Mater Chem* 2003;13:2701–10.
- [14] Isaure F, Cormack PAG, Sherrington DC. *Macromolecules* 2004;37:2096–105.
- [15] Liu Y, Schroeder WF, Haley JC, Lau W, Winnik MA. *Macromolecules* 2008;41:9104–11.
- [16] Liu Y, Deng K, Haley JC, Lau W, Winnik MA. *Macromolecules* 2008;41:4220–5.
- [17] Miller CM, Blythe PJ, Sudol ED, Silebi CA, El-Aasser MS. *J Polym Sci A Polym Chem* 1994;32:2365–76.
- [18] Delgado J, El-Aasser MS, Silebi CA, Vanderhoff JW. *J Polym Sci A Polym Chem* 1990;28:777–94.
- [19] Antonietti M, Landfester K. *Prog Polym Sci* 2002;27:689–757.
- [20] Mouran D, Reimers J, Joseph Schork F. *J Polym Sci A Polym Chem* 1996;34:1073–81.
- [21] Wang ST, Poehlein GW, Schork FJ. *J Polym Sci A Polym Chem* 1997;35:595–603.
- [22] Bechthold N, Landfester K. *Macromolecules* 2000;33:4682–9.
- [23] Greenly RZ. In: Brandrup E, Immergut EH, editors. *Polymer handbook*. New York: John Wiley & Sons; 1989.
- [24] Berger KC, Brandrup G. In: Brandrup E, Immergut EH, editors. *Polymer handbook*. New York: John Wiley & Sons; 1989.
- [25] Schallausky F, Erber M, Komber H, Lederer A. *Macromol Chem Phys* 2008;209:2331–8.
- [26] Mikhaylova Y, Adam G, Häussler L, Eichhorn K-J, Voit B. *J Mol Struct* 2006;788:80–8.



# Water-soluble conjugated polyelectrolyte with pendant glycocluster: Synthesis and its interaction with heparin

Qi Chen<sup>a</sup>, Yi Cui<sup>a,b</sup>, Jie Cao<sup>c</sup>, Bao-Hang Han<sup>a,\*</sup>

<sup>a</sup>National Center for Nanoscience and Technology, Beijing 100190, China

<sup>b</sup>Graduate University of Chinese Academy of Sciences, Beijing 100049, China

<sup>c</sup>Department of Chemistry, Beijing Institute of Technology, Beijing 100081, China

## ARTICLE INFO

### Article history:

Received 16 August 2010

Received in revised form

4 October 2010

Accepted 29 November 2010

Available online 4 December 2010

### Keywords:

Conjugated polymers

Fluorescence

Glucosamine hydrochloride

## ABSTRACT

A novel fluorescent conjugated polyelectrolyte with pendant glucosamine hydrochloride clusters was prepared through Cu(I)-catalyzed azide/alkyne “click” ligation and Suzuki coupling polymerization. Compared with monosugar-functionalized conjugated polymer, the water-solubility and fluorescence quantum yield of the glycocluster-containing polymer (**P-3**) were significantly improved. As a glucosamine-containing cationic fluorescent polyelectrolyte, the water-soluble fluorescent polymer can interact with heparin through electrostatic bindings, which induce great fluorescence quenching of **P-3** due to the polymer aggregation. Furthermore, upon treatment of the **P-3**–heparin ensemble with protamine, the fluorescence emission of **P-3** recovered since the protamine possesses a competitively strong binding affinity to the heparin and thus results in the release of the fluorescent glycopolymer **P-3** from the **P-3**–heparin ensemble.

© 2010 Elsevier Ltd. All rights reserved.

## 1. Introduction

With intrinsic optoelectronic properties of  $\pi$ -conjugated polymers and good water-solubility of polyelectrolytes, water-soluble fluorescent conjugated polymers with pendant charged groups have gained much attention during the past decade in exploiting novel electro-optical devices [1], chemo- and bio-sensors [2]. Most of water-soluble conjugated polymers possess pendant charged groups such as carboxylate groups [3], sulfonate groups [4], phosphonate groups [2,5], and ammonium groups [6]. In the presence of oppositely charged acceptors, these polymers exhibit exceptional fluorescence quenching or energy transfer efficiency, resulting in amplification of optical signals for the transduction of biological recognizing events [2b,c]. However, water-soluble conjugated polymers have a strong tendency to aggregate in aqueous media due to the  $\pi$ -conjugated polymer backbone, resulting in their fluorescence self-quenching to some extent and the decrease in their photoluminescence quantum efficiency [7]. Therefore, sensitivities of the chem- and bio-sensors will decrease owing to the aggregations. To overcome this drawback, dendrimers or cluster functional groups were introduced into the branch of polymers to form envelopes that

can effectively prevent the conjugated polymer backbone from aggregating and cross-talking due to the “site isolation” effect [8].

Heparin is a linear, unbranched, highly anionic polysaccharide with alternating disaccharide units consisting of 1→4-linked glucosamine and uronic acid residues. The uronic acid residues can either be an L-iduronic acid (90%) or a D-glucuronic (10%), and the glucosamine may either be N-acetylated or N-sulfonated [9]. As to most complex glycosaminoglycans, heparin plays diverse roles in a number of physiological and pathological processes including coagulation, angiogenesis, immune response, and viral infection [10]. Especially, it has been widely used as clinical anticoagulant drug for decades during surgery and kidney dialysis [11]. It is noted that heparin overdose can either induce thrombocytopenia or lead to bleeding problems in patients during surgery [12]. Therefore, it is critical to detect the heparin accurately and quickly. In recent years, fluorescent assays for heparin based on chem-sensing or bio-sensing have been reported [2j,13], in which water-soluble conjugated polymers containing pendant ammonium groups have been successfully applied in multicolor detection assay for trace heparin in aqueous solution based on the electrostatic interaction.

Sugar-carrying fluorescent conjugated polymers, most of which are neutral and water-soluble, also provide a unique platform for studies of carbohydrate-mediated biological interactions and biosensor applications due to their distinctive optical properties, specific selectivities, and high sensitivities to minor stimuli [14]. Our group has explored the facile prepolymerization and

\* Corresponding author. Fax: +86 10 82545576.

E-mail address: [hanbh@nanoctr.cn](mailto:hanbh@nanoctr.cn) (B.-H. Han).

postpolymerization functionalization approaches to prepare well-defined fluorescent conjugated glycopolymers through Cu(I)-catalyzed azide/alkyne “click” ligation [15]. Using those methods, various conjugated polymers containing neutral sugars were prepared for studies of specific carbohydrate-mediated biological interactions [16]. Furthermore, the first cationic water-soluble conjugated glycopolymer, polyfluorene with pendant glucosamine hydrochloride, was also synthesized to investigate its interaction with single-stranded DNA [17].

Owing to high efficiencies in both photoluminescence and electroluminescence, conjugated backbones containing fluorene or carbazole have gained much attention during the past decade as versatile active materials in optoelectronic devices and fluorescent sensory materials [18,19]. To extend the potential applications of the fluorescent conjugated glycopolymers in biomacromolecule detections, we prepared a water-soluble conjugated polymer with pendant glucosamine hydrochloride cluster (**P-3**) through the prepolymerization functionalization approach based on Cu(I)-catalyzed azide/alkyne “click” ligation (Schemes 1 and 2). Conjugated poly(fluorene-*alt*-carbazole) is chosen as the polymer backbone, considering its intrinsic optoelectronic properties and facile modification with other functional moieties. As compared with the monoglucosamine-functionalized polymer [17], grafting glucosamine hydrochloride cluster residues to the side chains of the conjugated polymers can not only improve the water-solubility of the resulted polymers, but also provide high density of positively charged ammonium binding sites for conjugated polymers towards

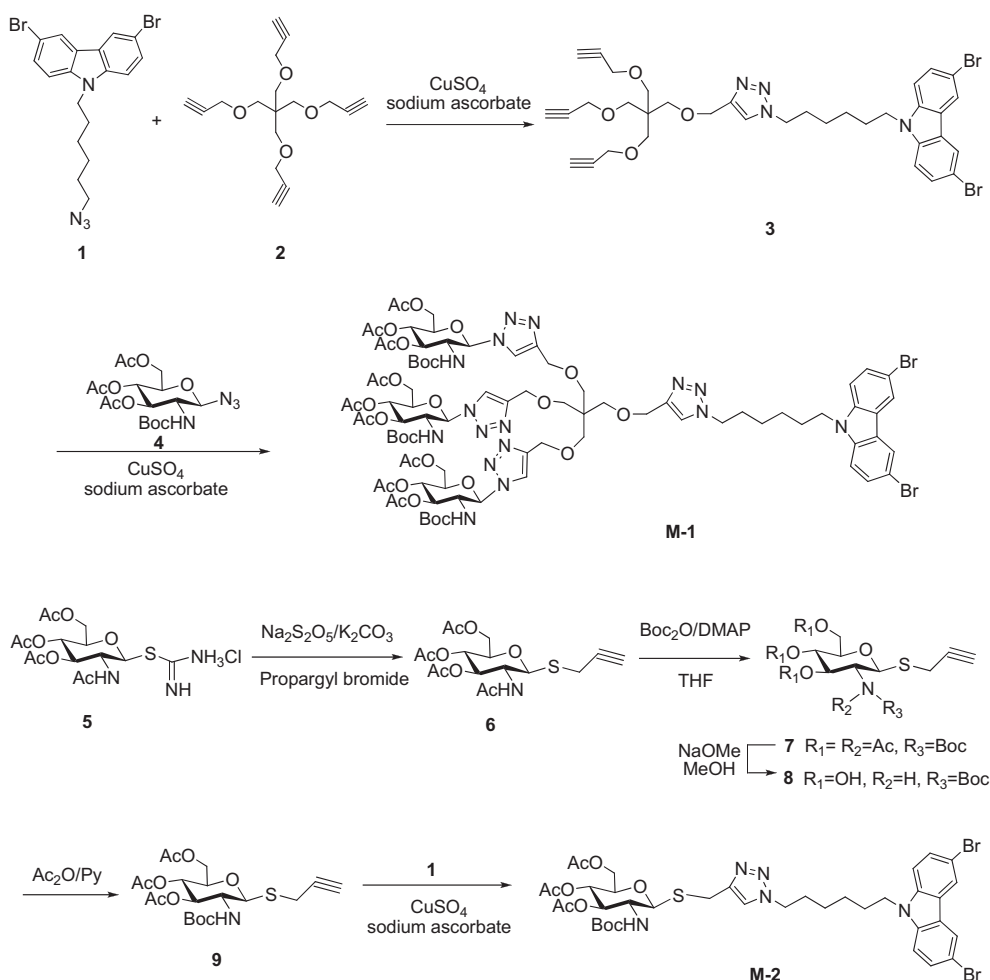
artificial or natural polyanions. The preliminary studies of **P-3**–heparin interaction were performed by a series of spectrofluorometric titration. In addition, protamine, a positively charged peptide in nature with high binding affinity to heparin, was used to investigation of the relative binding ability of synthetic polymer **P-3** with heparin.

## 2. Experimental

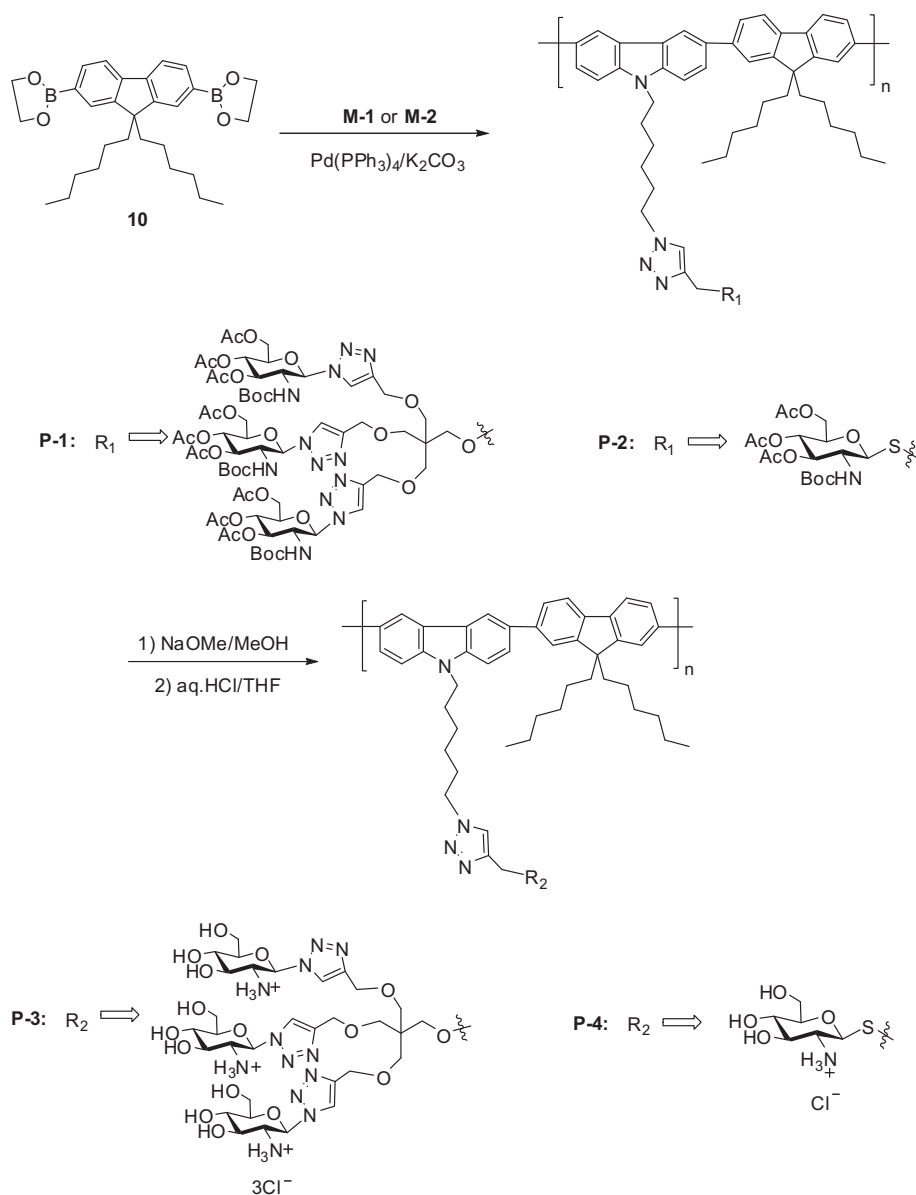
### 2.1. Materials and measurements

All chemical reagents were commercially available and used as received unless otherwise stated. Heparin was provided by Biodee, China and protamine was purchased from Sigma Company for direct use. Carbazole derivative **1** [15], tetrakis(2-propynyloxy)methane **2** [20], and sugar intermediates **4** [17] and **5** [21] (Scheme 1) were prepared according to reported procedures.

The  $^1\text{H}$  NMR and  $^{13}\text{C}$  NMR spectra were recorded on a Bruker DMX300 NMR spectrometer. The optical rotations were measured with a JASCO DIP-1000 digital polarimeter. Mass spectra were recorded with a VG PLATFORM mass spectrometer using the ESI technique. The molecular weights of the polymers were determined by an Agilent 1100 GPC system in THF. The number-average and weight-average molecular weights ( $M_n$  and  $M_w$ ) were estimated using a calibration curve of polystyrene standard. IR spectra were recorded using a Perkin–Elmer Spectrum One FTIR spectrometer. Ultraviolet–visible (UV–vis) spectra were measured



Scheme 1. Synthetic routes to monomers.



using a Perkin–Elmer Lambda 950 UV–vis–NIR spectrophotometer and quartz cells with 1 cm path length. The fluorescence spectra were measured in a conventional cell with 1 cm path length using a Perkin–Elmer LS55 luminescence spectrometer.

## 2.2. Synthesis of monomers and polymers

### 2.2.1. Carbazole intermediate **3**

To a mixture of **1** (450 mg, 1.0 mmol) and **2** (2.88 g, 10 mmol) in H<sub>2</sub>O–THF (1:1, 20 mL) were added freshly prepared aqueous 1.0 M sodium ascorbate (150 μL, 0.15 mmol) and CuSO<sub>4</sub> (12 mg, 0.075 mmol). The heterogeneous mixture was stirred vigorously in dark place at room temperature for 12 h. After removal of THF under reduced pressure, water (20 mL) was added and the product was extracted with ethyl acetate (3 × 50 mL). The combined organic layer was dried over anhydrous Na<sub>2</sub>SO<sub>4</sub> and evaporated *in vacuo*. The crude product was subjected to column chromatography (ethyl acetate–petroleum ether, 1:2) to give **3** as a foamy solid (368 mg, 50%). <sup>1</sup>H NMR (300 MHz, CDCl<sub>3</sub>): δ 8.12 (d, *J* = 1.5 Hz, 2H), 7.54 (dd, *J* = 8.7, 1.8 Hz,

2H), 7.48 (s, 1H), 7.22 (d, *J* = 8.7 Hz, 2H), 4.63 (s, 2H), 4.27 (t, *J* = 7.2 Hz, 2H), 4.22 (t, *J* = 7.8 Hz, 2H), 4.09 (d, *J* = 2.4 Hz, 6H), 3.50 (s, 6H), 3.49 (s, 2H), 2.37 (s, 3H), 1.88–1.75 (m, 4H), 1.35–1.28 (m, 4H). <sup>13</sup>C NMR (75 MHz, CDCl<sub>3</sub>): δ 144.8, 138.2, 128.1, 122.5, 122.3, 120.9, 111.1, 109.3, 79.1, 73.1, 68.2, 68.0, 64.3, 57.7, 49.0, 43.9, 42.1, 29.1, 27.7, 25.6, 25.3. ESI (+)-MS: calcd for C<sub>35</sub>H<sub>38</sub>Br<sub>2</sub>N<sub>4</sub>O<sub>4</sub>: 738.5 [M]. Found: 761.8 [M + Na]<sup>+</sup>.

### 2.2.2. Monomer **M-1**

To a mixture of **3** (739 mg, 1.0 mmol) and **4** (1.72 g, 4.0 mmol) in H<sub>2</sub>O–THF (1:1, 30 mL) were added freshly prepared aqueous 1.0 M sodium ascorbate (300 μL, 0.30 mmol) and CuSO<sub>4</sub> (24 mg, 0.15 mmol). The heterogeneous mixture was stirred vigorously in dark room at 50–60 °C until the complete consumption of the reactants based on TLC analyses. After removal of THF under reduced pressure, water (30 mL) was added and the product was extracted with ethyl acetate (3 × 50 mL). The combined organic layer was dried over anhydrous Na<sub>2</sub>SO<sub>4</sub> and evaporated *in vacuo*. The crude product was subjected to column chromatography (ethyl acetate–petroleum ether, 3:1) to give **M-1** as a foamy solid (1.74 g,

86%).  $[\alpha]_D^{25} -76^\circ$  (c 1, CHCl<sub>3</sub>); <sup>1</sup>H NMR (300 MHz, CDCl<sub>3</sub>):  $\delta$  8.07 (s, 2H), 7.87 (br, 3H), 7.49–7.43 (m, 3H), 7.22–7.17 (m, 2H), 6.01 (d,  $J = 9.0$  Hz, 3H), 5.50–5.40 (m, 6H), 5.24–5.22 (m, 3H), 4.48 (s, 8H), 4.36–4.12 (m, 7H), 4.11–4.00 (m, 6H), 3.99–3.88 (m, 3H), 3.50–3.30 (m, 8H), 2.05–1.95 (m, 27H), 1.85–1.75 (m, 4H), 1.35–1.27 (m, 4H), 1.19 (s, 27H). <sup>13</sup>C NMR (75 MHz, CDCl<sub>3</sub>):  $\delta$  170.7, 170.3, 169.5, 155.0, 145.2, 139.2, 129.1, 123.4, 123.3, 122.0, 112.0, 110.4, 85.9, 80.3, 74.8, 72.4, 70.8, 69.0, 68.3, 64.6, 61.9, 60.4, 54.6, 50.0, 45.3, 43.1, 30.0, 28.6, 28.0, 26.6, 26.2, 21.0, 20.9, 20.6, 20.5. ESI(+)-MS: calcd for C<sub>86</sub>H<sub>116</sub>Br<sub>2</sub>N<sub>16</sub>O<sub>31</sub>: 2029.7 [M]. Found: 2052.9 [M + Na]<sup>+</sup>.

### 2.2.3. 2-Propynyl 3,4,6-tri-O-acetyl-2-acetamido-2-deoxy- $\beta$ -D-thioglucopyranoside **6**

To a cooled (0 °C) stirred solution of K<sub>2</sub>CO<sub>3</sub> (93.7 mg, 0.68 mmol) and Na<sub>2</sub>S<sub>2</sub>O<sub>5</sub> (104.0 mg, 0.55 mmol) in H<sub>2</sub>O (5 mL) was added **5** (300 mg, 0.68 mmol) in acetone (5 mL). And then propargyl bromide (84 mg, 0.7 mmol) was added to the stirred solution. The reaction mixture was stirred for 1.5 h at room temperature, and then poured into ice-water. The product was extracted with ethyl acetate (3 × 20 mL), and the organic layer was washed with 0.5 M KHSO<sub>4</sub>, water, and brine. The combined organic layer was dried over Na<sub>2</sub>SO<sub>4</sub> and evaporated *in vacuo*. The residue was purified by silica gel column chromatography (ethyl acetate–petroleum ether, 1.5:1) to afford **6** as a white solid (240 mg, 88%).  $[\alpha]_D^{25} -45^\circ$  (c 1, CHCl<sub>3</sub>); <sup>1</sup>H NMR (300 MHz, CDCl<sub>3</sub>):  $\delta$  5.56 (d,  $J = 9.3$  Hz, 1H), 5.21–5.18 (m, 2H), 4.80 (d,  $J = 10.5$  Hz, 1H), 4.27–4.12 (m, 3H), 3.73–3.54 (m, 1H), 3.57 (dd,  $J = 2.7, 16.5$  Hz, 1H), 3.28 (dd,  $J = 2.7, 16.5$  Hz, 1H), 2.26 (t,  $J = 2.7$  Hz, 1H), 2.08 (s, 3H), 2.04 (s, 3H), 2.03 (s, 3H), 1.96 (s, 3H). <sup>13</sup>C NMR (75 MHz, CDCl<sub>3</sub>):  $\delta$  170.2, 169.7, 169.1, 168.2, 82.1, 78.2, 72.8, 70.6, 67.3, 61.1, 52.0, 22.2, 19.7, 19.6, 19.5, 16.4. ESI(+)-MS: calcd for C<sub>17</sub>H<sub>23</sub>NO<sub>8</sub>S: 401.4 [M]. Found: 402.3 [M + H]<sup>+</sup>.

### 2.2.4. 2-Propynyl 3,4,6-tri-O-acetyl-2-deoxy-2-tert-butoxycarbonylamino- $\beta$ -D-thioglucopyranoside **9**

To a stirred mixture of compound **6** (2.0 g, 5 mmol) and dimethylaminopyridine (DMAP, 0.61 g, 0.5 mmol) in THF (30 mL) was added Boc<sub>2</sub>O (5.5 g, 25.0 mmol). Stirring was continued at 60 °C for 3 h. Then, the reaction mixture was concentrated *in vacuo* to give crude **7**. Without further purification, crude **7** was dissolved in a solution of dry CH<sub>2</sub>Cl<sub>2</sub> (20 mL) and MeOH (20 mL) under a nitrogen atmosphere and followed by 1.0 M CH<sub>3</sub>ONa/CH<sub>3</sub>OH solution (2.0 mL). The reaction mixture was stirred at room temperature overnight. After removal of the solvent under reduced pressure, acetic anhydride (8 mL) and pyridine (15 mL) were added to the residue. The resulting solution was stirred at room temperature overnight and concentrated *in vacuo*. The residue was purified with silica gel column chromatography (ethyl acetate–petroleum ether, 1:1) to give the desired product **9** (1.95 g, 85%).  $[\alpha]_D^{25} -47^\circ$  (c 1, CHCl<sub>3</sub>); <sup>1</sup>H NMR (300 MHz, CDCl<sub>3</sub>):  $\delta$  5.16–5.10 (m, 1H), 5.00 (t,  $J = 9.6$  Hz, 1H), 4.92 (d,  $J = 6.0$  Hz, 1H), 4.74 (d,  $J = 10.2$  Hz, 1H), 4.66 (d,  $J = 8.4$  Hz, 1H), 4.20–4.15 (m, 1H), 4.10–4.02 (m, 1H), 3.75–3.72 (m, 1H), 3.50 (dd,  $J = 2.7, 16.5$  Hz, 1H), 3.22 (dd,  $J = 2.7, 16.5$  Hz, 1H), 2.20 (t,  $J = 2.7$  Hz, 1H), 2.01 (s, 3H), 1.98 (s, 3H), 1.96 (s, 3H), 1.36 (s, 9H). <sup>13</sup>C NMR (75 MHz, CDCl<sub>3</sub>):  $\delta$  170.6, 169.5, 168.5, 154.8, 84.6, 80.2, 79.3, 73.7, 72.8, 71.4, 68.5, 62.1, 54.3, 28.2, 20.6, 20.5, 20.3. ESI(+)-MS: calcd for C<sub>20</sub>H<sub>29</sub>NO<sub>9</sub>S: 459.5 [M]. Found: 482.3 [M + Na]<sup>+</sup>.

### 2.2.5. Monomer **M-2**

To a mixture of **1** (450 mg, 1.0 mmol) and **9** (551 mg, 1.2 mmol) in H<sub>2</sub>O–THF (1:1, 15 mL) were added freshly prepared aqueous 1.0 M sodium ascorbate (150  $\mu$ L, 0.15 mmol) and CuSO<sub>4</sub> (12 mg, 0.075 mmol). The heterogeneous mixture was stirred vigorously in dark room at 50–60 °C until the complete consumption of the reactants based on TLC analyses. After removal of THF under reduced pressure, water (20 mL) was added and the product was extracted

with ethyl acetate (3 × 25 mL). The combined organic layer was dried over anhydrous Na<sub>2</sub>SO<sub>4</sub> and evaporated *in vacuo*. The crude product was subjected to column chromatography (ethyl acetate–petroleum ether, 1.5:1) to give **M-2** as a foamy solid (891 mg, 98%).  $[\alpha]_D^{25} -63^\circ$  (c 1, CHCl<sub>3</sub>); <sup>1</sup>H NMR (300 MHz, CDCl<sub>3</sub>):  $\delta$  8.00 (d,  $J = 1.8$  Hz, 2H), 7.43 (dd,  $J = 1.8, 6.9$  Hz, 2H), 7.38 (s, 1H), 7.12 (d,  $J = 8.7$  Hz, 2H), 5.12 (t,  $J = 9.9$  Hz, 1H), 5.01 (t,  $J = 9.6$  Hz, 1H), 4.94 (d,  $J = 9.6$  Hz, 1H), 4.68 (d,  $J = 10.5$  Hz, 1H), 4.19–4.15 (m, 3H), 4.11–3.98 (m, 4H), 3.82 (d,  $J = 10.5$  Hz, 1H), 3.72–3.61 (m, 2H), 1.99 (s, 3H), 1.97 (s, 3H), 1.95 (s, 3H), 1.70–1.65 (m, 4H), 1.34 (s, 9H), 1.23–1.19 (m, 4H). <sup>13</sup>C NMR (75 MHz, CDCl<sub>3</sub>):  $\delta$  170.6, 170.5, 169.4, 155.0, 145.2, 139.1, 129.0, 123.3, 123.2, 122.1, 111.9, 110.4, 84.0, 79.9, 75.7, 73.7, 68.7, 62.2, 60.3, 50.1, 42.3, 29.9, 28.6, 28.2, 26.5, 26.2, 20.7, 20.6, 20.5. ESI(+)-MS: calcd for C<sub>38</sub>H<sub>47</sub>Br<sub>2</sub>N<sub>5</sub>O<sub>9</sub>S: 909.7 [M]. Found: 910.5 [M + H]<sup>+</sup>.

### 2.2.6. Polymer **P-1**

Under a nitrogen atmosphere, sugar-carrying monomer **M-1** (448 mg, 0.31 mmol), fluorene diborate **10** (60 mg, 0.36 mmol), Pd (PPh<sub>3</sub>)<sub>4</sub> (30 mg), and potassium carbonate (0.5 g, 3.62 mmol) were placed in a 50 mL round-bottom flask, and then THF (20 mL) was added. The mixture was stirred at 70 °C for 36 h under a nitrogen atmosphere. The resulting polymer was purified by precipitation in methanol and washed with methanol–acetone in a Soxhlet apparatus for 48 h. **P-1** was obtained as a gray powder (328 mg, 78%). <sup>1</sup>H NMR (300 MHz, CDCl<sub>3</sub>):  $\delta$  7.94 (br, 2H), 7.83 (br, 2H), 7.70–7.50 (m, 6H), 7.45–7.30 (m, 2H), 7.25–7.10 (m, 4H), 6.04 (br, 3H), 5.47–5.30 (m, 6H), 5.25–5.10 (m, 3H), 4.46 (br, 8H), 4.35–4.15 (m, 7H), 4.13–4.02 (m, 6H), 3.99–3.90 (m, 3H), 3.52–3.32 (m, 8H), 2.15–1.70 (m, 35H), 1.35–1.18 (m, 31H), 1.15–1.10 (m, 12H), 0.98–0.78 (m, 10H). <sup>13</sup>C NMR (75 MHz, CDCl<sub>3</sub>):  $\delta$  170.5, 170.3, 169.5, 155.1, 149.8, 145.3, 143.3, 141.0, 132.7, 130.2, 129.2, 124.2, 122.8, 119.5, 113.4, 111.5, 110.4, 107.2, 85.9, 82.2, 81.8, 80.9, 74.8, 72.1, 70.8, 69.2, 68.3, 64.2, 61.9, 60.5, 54.1, 50.4, 44.5, 31.2, 30.4, 29.1, 28.9, 27.2, 27.0, 26.8, 26.3, 23.5, 21.1, 14.2. GPC (THF, polystyrene standard):  $M_n = 33400$  g/mol; polydispersity = 1.85.

### 2.2.7. Polymer **P-2**

Polymer **P-2** was prepared from monomer **M-2** (320 mg) using the same procedure for preparation of polymer **P-1** as a gray powder (270 mg, 81%). <sup>1</sup>H NMR (300 MHz, CDCl<sub>3</sub>):  $\delta$  7.78 (br, 2H), 7.76–7.52 (m, 4H), 7.50–7.20 (m, 5H), 7.17–6.98 (m, 3H), 5.09–4.95 (m, 2H), 4.67 (br, 1H), 4.29–4.12 (m, 5H), 4.03–3.96 (m, 2H), 3.81–3.76 (m, 1H), 3.66–3.61 (m, 2H), 2.15–1.90 (m, 17H), 1.70–1.65 (m, 4H), 1.31 (s, 9H), 1.25–1.15 (m, 4H), 1.10–0.95 (m, 12H), 0.89–0.78 (m, 10H). <sup>13</sup>C NMR (75 MHz, CDCl<sub>3</sub>):  $\delta$  170.3, 169.4, 155.0, 149.6, 145.3, 143.5, 132.6, 129.8, 129.2, 124.4, 122.8, 120.1, 113.4, 111.7, 107.2, 83.9, 79.9, 75.8, 73.7, 68.9, 62.2, 60.3, 50.7, 44.5, 31.5, 30.4, 29.3, 28.9, 27.2, 26.9, 26.7, 26.3, 23.5, 20.9, 14.0. GPC (THF, polystyrene standard):  $M_n = 21700$  g/mol; polydispersity = 1.95.

### 2.2.8. Polymer **P-3**

Protected polymer **P-1** (200 mg) was added to a solution of dry CH<sub>2</sub>Cl<sub>2</sub> (5 mL) and MeOH (10 mL) under a nitrogen atmosphere and followed by 1.0 M CH<sub>3</sub>ONa/CH<sub>3</sub>OH solution (0.25 mL). The reaction mixture was stirred at room temperature overnight. After removal of the solvent under reduced pressure, the residue was dissolved in 5 mL THF and aqueous HCl solution (6 M, 10 mL), and then stirred for 24 h at room temperature. The solvent was removed and 10 mL of acetonitrile was added to precipitate the product as a brown solid (137 mg, 95%). <sup>1</sup>H NMR (300 MHz, DMSO-*d*<sub>6</sub>):  $\delta$  8.56 (br, 6H), 8.43 (s, 3H), 8.08 (br, 1H), 7.80–7.60 (m, 8H), 7.45–7.40 (m, 4H), 6.05 (br, 3H), 5.45–4.95 (br, 12H), 4.53 (br, 8H), 4.25–4.23 (m, 2H), 3.83–3.61 (m, 6H), 3.55–3.14 (m, 17H), 2.05–1.99 (m, 4H), 1.85–1.70 (m, 4H), 1.40–1.19 (m, 4H), 1.10–0.95 (m, 12H), 0.79–0.58 (m, 10H). <sup>13</sup>C NMR (75 MHz, DMSO-*d*<sub>6</sub>):  $\delta$  156.9, 143.2, 139.2, 139.0,

138.4, 137.8, 137.0, 136.2, 132.1, 131.5, 129.0, 128.9, 127.2, 126.5, 126.2, 125.0, 114.0, 83.5, 80.0, 72.7, 69.2, 60.1, 55.9, 54.3, 50.4, 44.5, 31.2, 30.4, 29.1, 28.9, 27.2, 27.0, 26.8, 26.3, 23.5, 21.1, 14.2.

### 2.2.9. Polymer P-4

Polymer **P-4** was prepared from polymer **P-2** (150 mg) using the same procedure for preparation of polymer **P-3** as a gray powder (114 mg, 93%).  $^1\text{H}$  NMR (300 MHz,  $\text{DMSO}-d_6$ ):  $\delta$  8.38 (br, 3H), 8.13 (s, 1H), 8.08 (br, 1H), 7.80–7.60 (m, 6H), 7.59–7.40 (m, 6H), 6.80 (br, 1H), 4.80–4.60 (m, 4H), 4.53–4.23 (m, 2H), 4.03 (br, 2H), 3.72–3.51 (m, 6H), 3.20 (br, 2H), 2.05–1.99 (m, 4H), 1.87–1.70 (m, 4H), 1.40–1.15 (m, 4H), 1.10–0.95 (m, 12H), 0.80–0.60 (m, 10H).  $^{13}\text{C}$  NMR (75 MHz,  $\text{DMSO}-d_6$ ):  $\delta$  157.0, 143.5, 139.4, 139.0, 138.4, 137.6, 136.8, 136.5, 132.0, 131.5, 128.8, 127.2, 126.5, 126.3, 125.3, 114.0, 83.5, 79.9, 72.5, 69.0, 61.1, 54.4, 46.5, 32.2, 31.4, 29.4, 28.9, 27.4, 27.1, 26.8, 26.3, 23.5, 21.4, 14.3.

### 2.3. Preliminary studies of the interaction between polymer P-3 and heparin

A solution of polymer **P-3** was prepared in HEPES buffer solution (5.0 mM, pH = 7.4). Aliquots of the heparin in the same buffer were

added to the solution. The final concentration of polymer **P-3** is  $1.5 \times 10^{-5}$  M, corresponding to the repeating unit. After each addition, the sample was allowed to equilibrate for 30 min prior to recording a spectrum. The concentration of heparin ranges from 0 to  $1.0 \times 10^{-6}$  M. The excitation wavelength was 380 nm and the emission scan ranged from 380 to 650 nm.

### 2.4. Studies of the interaction between heparin and protamine

For the study of interaction between heparin and protamine, a buffer solution of **P-3** [ $1.5 \times 10^{-5}$  M in HEPES buffer solution (5.0 mM, pH = 7.4)] was pre-saturated with heparin ( $3.0 \times 10^{-6}$  M), followed by the addition of aliquots of protamine stock solution. The solution was carefully mixed for fluorescence spectral measurements. The excitation wavelength was 380 nm and the emission scan ranged from 380 to 650 nm.

## 3. Results and discussion

The synthetic routes to the monomers are outlined in Scheme 1. Cu(I)-catalyzed “click” ligation between carbazole derivative **1** and

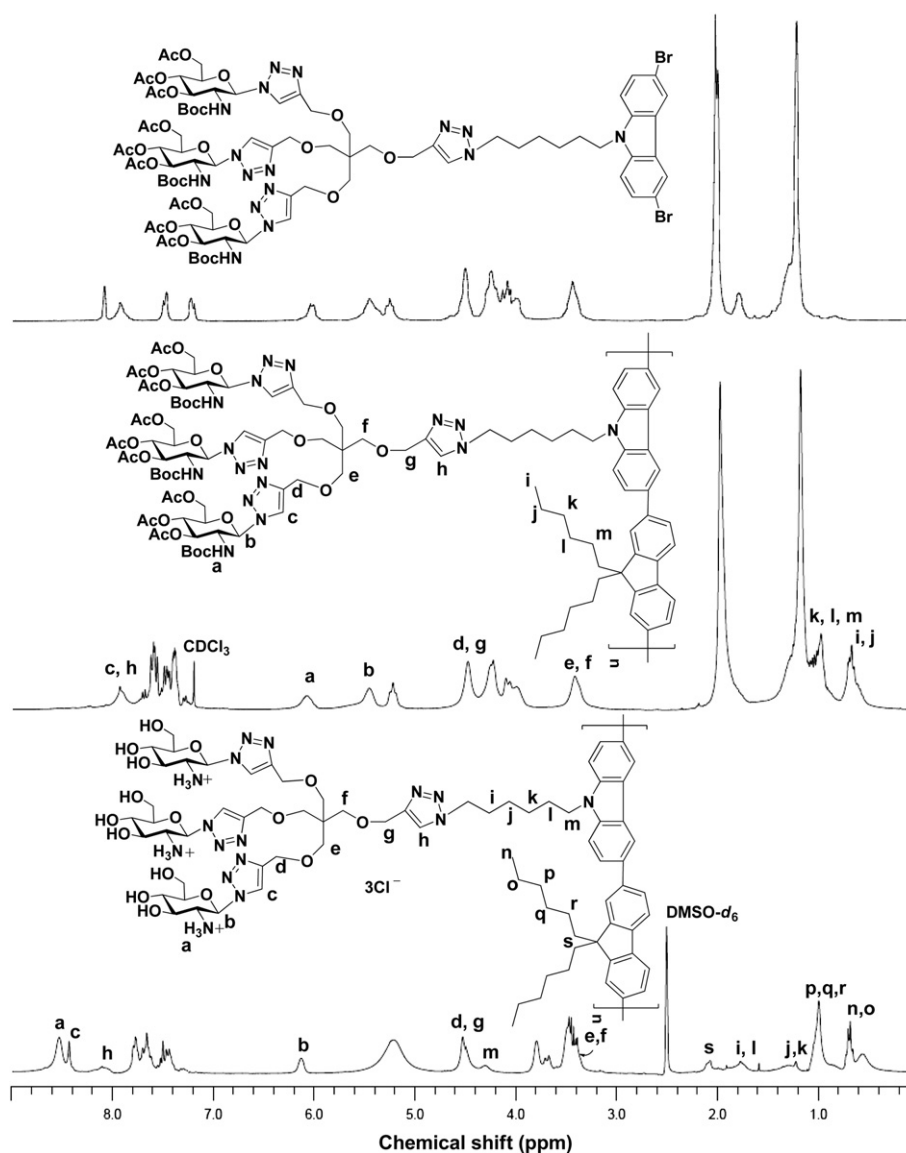


Fig. 1.  $^1\text{H}$  NMR spectra of monomer **M-1** and polymers **P-1** and **P-3**.

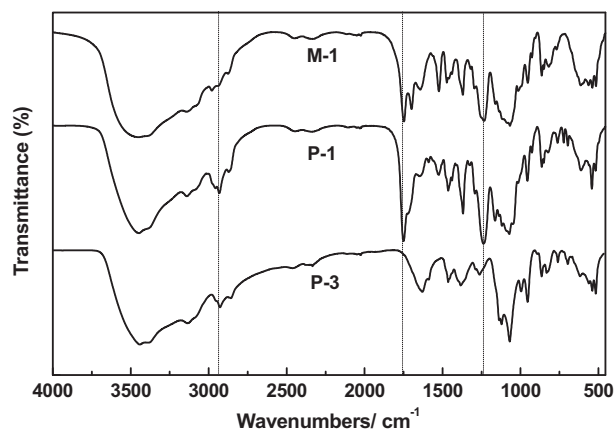


Fig. 2. FTIR spectra of monomer **M-1** and polymers **P-1** and **P-3**.

an excess of tetrakis(2-propynyloxymethyl)methane **2** furnished tripropargyl-attached carbazole intermediate **3**, which is suitable for azide/alkyne click conjugation with azido group-functionalized glucosamine **4** to afford the glycocluster-containing carbazole monomer **M-1** in a high yield. Formation of triazole ring is confirmed by chemical shift at 7.96 ppm (single peak) on  $^1\text{H}$  NMR spectrum and two peaks at 121.2 and 143.2 ppm on  $^{13}\text{C}$  NMR spectrum. For control study, monosugar-carrying monomer counterpart **M-2** was also prepared by the same method from **1** and propargyl-bearing thioglycoside **9**, which is obtained through four steps using the known *N*-acetyl glucosamine isothiourea derivative **5** as the starting material. One-pot *S*-alkylation of **5** gave *N*-acetyl glucosamine thioglycoside **6**, which was treated with  $\text{Boc}_2\text{O}/\text{DMAP}$  to afford **7** as *N*-diastereomeric mixture. Without further purification, all the acetyl groups in **7** were removed under Zemplén condition to furnish **8**. After acetylation of all the hydroxyl groups in **8**, the glucosamine intermediate **9** mentioned above was finally obtained with 89% overall yield from **6** in three steps.

With monomers **M-1** and **M-2** in hand, palladium-catalyzed Suzuki coupling polymerization between the monomers and fluorene diborate **10** gave well-defined copolymers **P-1** and **P-2**, that is, poly(fluorene-*alt*-carbazole) derivatives containing pendant triglucosamine and monoglucosamine, respectively (Scheme 2). After removing all the acetyl groups with  $\text{CH}_3\text{ONa}/\text{CH}_3\text{OH}$  and deprotecting *N*-Boc groups in aqueous  $\text{HCl}$ -THF solution (6 M), the desired water-soluble glycopolymer **P-3** and the polymer **P-4** used for control studies were obtained in an excellent yield (95% in two steps). Fig. 1 shows  $^1\text{H}$  NMR spectra of polymers **P-1** and polymer **P-3**. We can find that the peak intensities of Boc ( $\delta = 1.20$  ppm), Ac

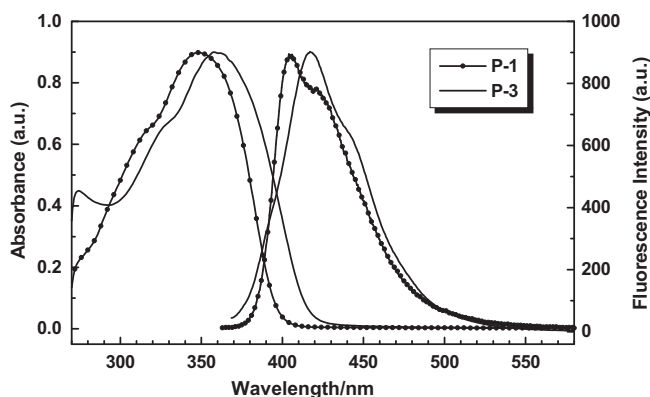


Fig. 3. UV-vis absorption and fluorescence spectra of polymers **P-1** and **P-3**.

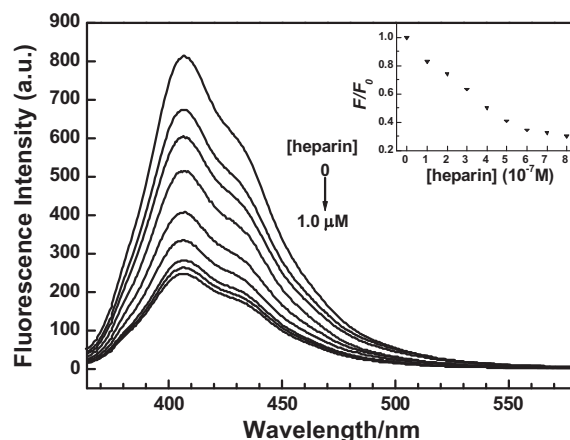


Fig. 4. Fluorescence spectra of polymer **P-3** in the absence and presence of different concentrations of heparin in HEPES buffer solution (5.0 mM, pH = 7.4) and normalized fluorescence intensity of polymer **P-3** ( $1.5 \times 10^{-5}$  M) as a function of heparin concentration (from 0 to  $1.0 \times 10^{-6}$  M) (inset).

( $\delta = 2.04$  ppm), and  $\text{NH-Boc}$  ( $\delta_{\text{N-H}} = 6.04$  ppm) groups in **P-1** disappeared after final efficient global deprotections and the peak intensity of  $\text{NH}_3^+$  group ( $\delta = 8.56$  ppm) in **P-3** appeared clearly. The successful polymerization and deprotection are also confirmed by FTIR spectra of the monomers and glycopolymers as shown in Fig. 2. Compared with monomer **M-1**, the absorption bands at 2850–2950  $\text{cm}^{-1}$  on the FTIR spectra of polymers **P-1** and **P-3** indicate the C–H stretching of alkyl chains derived from the fluorene monomer **10**. When the protecting groups Ac and Boc were removed, the corresponding absorption bands at 1750  $\text{cm}^{-1}$  (C=O) and 1200  $\text{cm}^{-1}$  (C–O stretching in ester) of **P-1** disappeared for FTIR spectra of the **P-3**. All these data apparently indicate that polymerization of sugar-bearing monomers is a good approach to prepare well-defined fluorescent conjugated glycopolymers.

Gel-permeation chromatography (GPC) analysis with polystyrene standards shows number-averaged molecular masses ( $M_n$ ) of 33400 g/mol for **P-1** and 21700 g/mol for **P-2**, with polydispersities of 1.85 and 1.95, respectively. Both **P-1** and **P-2** are readily soluble in common solvents such as methylene chloride, chloroform, and THF, but insoluble in methanol, ethanol, acetone, and water. However, the solubility of the deprotected polymer **P-3** is distinctly different from its precursor **P-1**. **P-3** is soluble in aqueous media and easily dissolves in DMF and DMSO. As for **P-4**, it

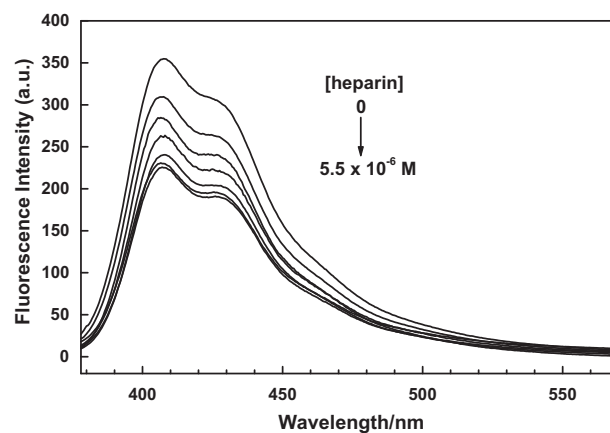
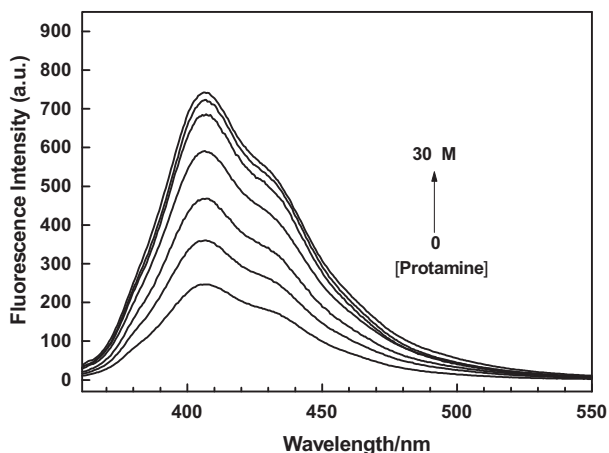


Fig. 5. Fluorescence spectra of polymer **P-4** in the absence and presence of different concentrations of heparin in HEPES buffer/DMF (8/2, V/V) solution: heparin concentrations ( $\mu\text{M}$ ) from the top downwards are 0, 1.0, 2.0, 3.0, 4.0, 5.0, and 5.5.



**Fig. 6.** Fluorescence spectra of the ensemble of **P-3** [20  $\mu\text{M}$  in HEPES buffer solution (5.0 mM), pH = 7.4] and heparin (1.5  $\mu\text{M}$ ) in the absence and presence of different concentrations of protamine. Protamine concentrations ( $\mu\text{M}$ ) from the bottom upwards are 0, 5, 10, 15, 20, 25, and 30.

is hardly dissolved in water due to low density of glucosamine hydrochloride moieties in the side chains of the polymer. The same phenomenon has been observed in differently dendronized polyfluorenes containing charged amino groups [22].

The precursor polymer **P-1** exhibits an absorption maximum peak at 348 nm and an emission maximum peak at 407 nm with a vibronic shoulder peak at 421 nm in THF solution, which are assigned to the  $\pi-\pi^*$  transition of the conjugated polymer backbone (see Fig. 3). As for the resulting polymer **P-3**, it displays an absorption maximum peak at 361 nm and an emission maximum peak at 418 nm with a vibronic shoulder peak at 441 nm in water (see Fig. 3). The obvious bathochromic/red shift in both absorption and emission spectra for the same polymer backbone in different solvents could be attributed to the solvatochromism of the conjugated poly(flourene-*alt*-carbazole) in the solvent with increased polarity (water). When conjugated molecule is excited from the ground state to the excited state, polarity of the excited molecule is higher than that at the ground state. Solvent with higher polarity can produce better stabilizing effect on the excited molecule, and then the energy for electron excitation become lower [23]. Therefore, the obvious bathochromic/red shift in both absorption and PL spectra of **P-3** in high polarity solvent were observed. Fluorescence quantum yields of the polymer were measured in dilute DMSO, and calculated by using quinine sulfate in 0.1 M sulfuric acid as the reference absolute quantum efficiency (55%) [24]. The fluorescence quantum yields for **P-3** and **P-4** are 61% and 22% in DMSO solution,

respectively. Apparently, polymer **P-3** possesses a much higher fluorescence quantum yield than the monoglucosamine-containing **P-4**. Furthermore, both the water-solubility (4.5 mg/mL) and fluorescence quantum yield in water of **P-3** (47%) are higher than glucosamine hydrochloride functionalized water-soluble conjugated polyfluorene we prepared before [17]. These data indicated that the introduction of glucosamine hydrochloride cluster onto the poly(flourene-*alt*-carbazole) backbone significantly enhance the photoluminescence quantum yields of the polymer, which is consistent with the similar reported results related to differently dendronized polyfluorenes containing charged amino groups [22].

Chitosan is a natural cationic polysaccharide comprising  $\beta(1\rightarrow4)$ -linked *D*-glucosamines, which shows great potential to condense anionic biomacromolecules such as DNA, heparin, and hyaluronic acid into compact complexes through electrostatic interactions [25]. As an artificial glucosamine-containing fluorescent polyelectrolyte, the water-soluble cationic conjugated polymer **P-3** is expected to show potential applications in biomacromolecule detections. The preliminary study of the interaction between **P-3** and heparin was performed by monitoring the changes of fluorescence intensity of **P-3** when titrated with the heparin. As shown in Fig. 4, a substantial fluorescence quenching of **P-3** ( $1.5 \times 10^{-5}$  M) was observed upon gradual addition of the heparin ( $0-1.0 \times 10^{-6}$  M) in HEPES buffer solution (5.0 mM, pH = 7.4). The emission quenching is observed at a concentration as low as 0.1  $\mu\text{M}$ , which is more sensitive than reported result [2j]. A possible mechanism for the fluorescence quenching of **P-3** is attributed to its aggregation derived from **P-3**–heparin electrostatic bindings, resulting in a significant self-quenching. We have observed the apparent increase in particle size accompanying the decrease in the fluorescence emission due to the aggregation for another system [16b]. As a control study, a solution of **P-4** in HEPES buffer/DMF (8/2, V/V) at the same concentration was also exposed to heparin, and a less efficient concentration-dependent fluorescence quenching occurring at relatively higher concentrations of the heparin was observed. When concentration of the heparin is up to 5.5  $\mu\text{M}$ , the fluorescence intensity of **P-4** is only quenched by 30% (see Fig. 5). The less sensitivity for **P-4** to heparin could be ascribed to its lower PL quantum efficiency and weaker binding affinity to heparin due to the low density of glucosamine moieties.

As a positively charged peptide possessing a strong binding affinity to heparin, protamine can combine with heparin as an ion pair to form a stable complex devoid of anticoagulant activity and prevents heparin from enhancing the anticoagulant effect of antithrombin III [26]. When treated with protamine(0–30  $\mu\text{M}$ ), the fluorescence intensity of the **P-3**–heparin ensemble in HEPES buffer solution (5.0 mM, pH = 7.4) at 480 nm started to increase (see Fig. 6) and finally was recovered almost up to the initial value of the free

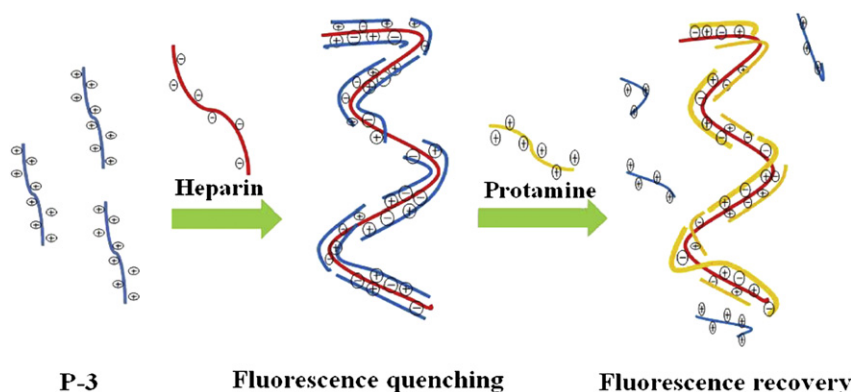


**Fig. 7.** Schematic representation for studies of heparin–protamine interactions using polymer **P-3** as a fluorescent probe.



state polymer without heparin, which means that the fluorescent glycopolymer **P-3** is gradually released from the **P-3**–heparin aggregation complex. It could be inferred that protamine possesses a competitively strong binding affinity to heparin, therefore, protamine can replace glycopolymer **P-3** from the **P-3**–heparin ensemble resulting in the disassembly of the aggregated complex. This confirms the formation of the **P-3**–heparin aggregate. On the other hand, the glycopolymer **P-3** can be employed as fluorescent probe for the heparin–protamine interaction. A schematic representation of the whole processes of fluorescence quenching and recovery was shown in Fig. 7. These results revealed that water-soluble conjugated glycopolymer **P-3**, possessing fluorescent backbone and multiple charged branches, was expected to have potential applications as the fluorescent probe in detecting biomacromolecules or gene delivery.

#### 4. Conclusions

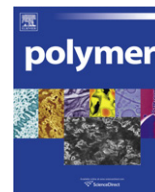
Water-soluble cationic conjugated polymer with pendant glyco-clusters was prepared through Cu(I)-catalyzed azide/alkyne “click” ligation and Suzuki coupling polymerization. The introduction of glucosamine hydrochloride cluster, as expected, should not only provide the conjugated polymers with good solubility in water due to the glucosamine moieties, but also reduce the aggregation of polymers through the “site isolation” effect. The glycocluster branch of polymer can form envelopes that will effectively prevent the conjugated backbone from self-aggregation in aqueous solution, resulting in the increase of its PL quantum efficiency. Fluorescent assays for heparin based on **P-3**–heparin electrostatic bindings have been successfully achieved. Moreover, the studies to evaluation of the relative binding affinity of glycopolymer **P-3** with heparin were also performed by a series of spectrofluorometric titration using protamine as a reference. Treatment of the **P-3**–heparin ensemble with protamine in HEPES buffer solution can release the fluorescent glycopolymer **P-3** from the aggregated complex and then lead to fluorescence recovery, which might be ascribed to the competitively strong binding affinity and the better bio-compatibility for protamine in the interaction with heparin. As an artificial water-soluble fluorescent conjugated glycopolymer, its interactions with various artificial or natural polyanions are still under exploration.

#### Acknowledgment

The financial supports of the Ministry of Science and Technology of China (National Basic Research Program, grant no. 2007CB808000) and National Science Foundation of China (grants no. 20972035 and 21002107) are acknowledged.

#### References

- [1] (a) Huang F, Hou LT, Wu HB, Wang XH, Shen HL, Cao W, et al. *J Am Chem Soc* 2004;126:9845–53; (b) Jiang H, Zhao X, Shelton AH, Lee SH, Reynolds JR, Schanze KS. *ACS Appl Mater Interfaces* 2009;1:381–7; (c) Yang R, Xu Y, Dang XD, Nguyen TQ, Cao Y, Bazan GC. *J Am Chem Soc* 2008;130:3282–3; (d) Garcia A, Brzezinski JZ, Nguyen TQ. *J Phys Chem C* 2009;113:2950–4; (e) Jain V, Sahoo R, Mishra SP, Sinha J, Montazami R, Yochum HM, et al. *Macromolecules* 2009;42:135–40; (f) Wilson JS, Frampton MJ, Michels JJ, Sardone L, Marletta G, Friend RH, et al. *Adv Mater* 2005;17:2659–63.
- [2] (a) Ho HA, Najari A, Leclerc M. *Acc Chem Res* 2008;41:168–78; (b) Thomas SW, Joly GD, Swager TM. *Chem Rev* 2007;107:1339–86; (c) Feng F, He F, An L, Wang S, Li Y, Zhu D. *Adv Mater* 2008;20:2959–64; (d) Wosnick JH, Mello CM, Swager TM. *J Am Chem Soc* 2005;127:3400–5; (e) Rininsland F, Xia WS, Wittenburg S, Shi XB, Stankewicz C, Achyuthan K, et al. *Proc Natl Acad Sci USA* 2004;101:15295–300; (f) Liu B, Bazan GC. *J Am Chem Soc* 2004;126:1942–3; (g) Feng F, Wang H, Han L, Wang S. *J Am Chem Soc* 2008;130:11338–43; (h) Liu Y, Ogawa K, Schanze KS. *Anal Chem* 2008;80:150–8; (i) Li H, Yang R, Bazan GC. *Macromolecules* 2008;41:1531–6; (j) Pu KY, Liu B. *Macromolecules* 2008;41:6636–40; (k) Fang Z, Pu KY, Liu B. *Macromolecules* 2008;41:8380–7; (l) Qin C, Cheng Y, Wang L, Jing X, Wang F. *Macromolecules* 2008;41:7798–804; (m) Li J, Meng J, Huang XB, Cheng YX, Zhu CJ. *Polymer* 2010;51:3425–30.
- [3] (a) Pinto MR, Schanze KS. *Proc Natl Acad Sci USA* 2004;101:7505–10; (b) Kim IB, Dunkhorst A, Gilbert J, Bunz UHF. *Macromolecules* 2005;38:4560–2.
- [4] (a) Kim S, Jackiw J, Robinson E, Schanze KS, Reynolds JR. *Macromolecules* 1998;31:964–74; (b) Child AD, Reynolds JR. *Macromolecules* 1994;27:1975–7.
- [5] (a) Pinto MR, Kristal BM, Schanze KS. *Langmuir* 2003;19:6523–33; (b) Stokes K, Heuze K, McCullough R. *Macromolecules* 2003;36:7114–8.
- [6] (a) Gaylord BS, Heeger AJ, Bazan GC. *J Am Chem Soc* 2003;125:896–900. (b) Huang F, Wu H, Wang D, Yang W, Cao Y. *Chem Mater* 2004;16:708–16.
- [7] (a) Tan C, Pinto MR, Schanze KS. *Chem Commun* 2002:446–7; (b) Fan QL, Lu S, Lai YH, Hou XY, Huang W. *Macromolecules* 2003;36:6976–84; (c) Goto H, Okamoto Y, Yashima E. *Macromolecules* 2002;35:4590–601; (d) Wang S, Bazan GC. *Chem Commun* 2004:2508–9.
- [8] (a) Marsitzky D, Vestberg R, Blainey P, Tang BT, Hawker CJ, Carter KR. *J Am Chem Soc* 2001;123:6965–72; (b) Setayesh S, Grimsdale AC, Weil T, Enkelmann V, Müllen K, Meghdadi F, et al. *J Am Chem Soc* 2001;123:946–53; (c) Chou CH, Shu CF. *Macromolecules* 2002;35:9673–7; (d) Fu YQ, Li Y, Li J, Yan SK, Bo ZS. *Macromolecules* 2004;37:6395–400.
- [9] Noti C, Seeberger PH. *Chem Biol* 2005;12:731–56.
- [10] (a) Linhardt RJ, Toida T. *Acc Chem Res* 2004;37:431–8; (b) Raghuraman A, Mosier PD, Desai UR. *J Med Chem* 2006;49:3553–62.
- [11] (a) Linhardt RJ, Gunay NS. *Semin Thromb Hemost* 1999;25:5–16; (b) Fareed J, Hoppensteadt DA, Bick RL. *Semin Thromb Hemost* 2000;26:5–21.
- [12] (a) Freedman MD. *J Clin Pharmacol* 1992;32:584–96; (b) Wallis DE, Lewis BE, Messmore H, Wehrmacher WH. *Clin Appl Thromb Hemost* 1998;4:160–3; (c) Walenga JM, Bick RL. *Med Clin North Am* 1998;82:635–48.
- [13] (a) Zhong Z, Anslin EV. *J Am Chem Soc* 2002;124:9014–5; (b) Wright AT, Zhong Z, Anslin EV. *Angew Chem Int Ed* 2005;44:5679–82; (c) Sun W, Bandmann H, Schrader T. *Chem Eur J* 2007;13:7701–7; (d) Saucedo JC, Duke RM, Nitz M. *ChemBioChem* 2007;8:391–4.
- [14] (a) Takasu A, Iso K, Dohmae T, Hirabayashi T. *Biomacromolecules* 2006;7:411–4; (b) Xue C, Luo FT, Liu H. *Macromolecules* 2007;40:6863–70; (c) Disney MD, Zheng J, Swager TM, Seeberger PH. *J Am Chem Soc* 2004;126:13343–6; (d) Phillips RL, Kim IB, Carson BE, Tidbeck B, Bai Y, Lowary TL, et al. *Macromolecules* 2008;41:7316–20; (e) Xue C, Velayudham S, Johnson S, Sha R, Smith A, Brewer W, et al. *Chem Eur J* 2009;15:2289–95; (f) Shi JB, Cai LP, Pu KY, Liu B. *Chem Asian J* 2010;5:301–8.
- [15] Chen Q, Han BH. *J Polym Sci A Polym Chem* 2009;47:2948–57.
- [16] (a) Chen Q, Xu Y, Du Y, Han BH. *Polymer* 2009;50:2830–5. (b) Chen Q, Cui Y, Zhang TL, Cao J, Han BH. *Biomacromolecules* 2010;11:13–9.
- [17] Chen Q, Cheng QY, Zhao YC, Han BH. *Macromol Rapid Commun* 2009;30:1651–5.
- [18] (a) Pu KY, Liu B. *Adv Funct Mater* 2009;19:277–84; (b) Li HP, Bazan GC. *Adv Mater* 2009;21:964–7; (c) Lu HY, Tang YL, Xu W, Zhang DQ, Wang S, Zhu DB. *Macromol Rapid Commun* 2008;29:1467–71.
- [19] (a) Liaw DJ, Wang KL, Kang NT, Pujari SP, Chen MH, Huang YC, et al. *J Polym Sci A Polym Chem* 2009;47:991–1002; (b) Aly SM, Ho CL, Wong WY, Fortin D, Harvey PD. *Macromolecules* 2009;42:6902–16; (c) Sasano T, Sogawa H, Tamura K, Shiotsuki M, Masuda T, Sanda F. *J Polym Sci A Polym Chem* 2010;48:1815–21.
- [20] Touaibia M, Shiao TC, Papadopoulos A, Vaucher J, Wang Q, Benhamioud K, et al. *Chem Commun* 2007:380–2.
- [21] Ohnishi Y, Ichikawa M, Ichikawa Y. *Bioorg Med Chem Lett* 2000;10:1289–91.
- [22] (a) Zhu B, Han Y, Sun M, Bo ZS. *Macromolecules* 2007;40:4494–500; (b) Yu M, Liu L, Wang S. *J Polym Sci A Polym Chem* 2008;46:7462–72.
- [23] Lakowicz JR. *Principles of fluorescence spectroscopy*. 3rd ed. New York: Springer; 2006.
- [24] Demasa JN, Crosby GA. *J Phys Chem* 1971;75:991–1024.
- [25] Dang JM, Leong KW. *Adv Drug Deliv Rev* 2006;58:487–99.
- [26] Caplia I, Linhardt RJ. *Angew Chem Int Ed* 2002;41:390–412.



## Thermosets with core–shell nanodomain by incorporation of core crosslinked star polymer into epoxy resin

Yuan Meng, Xing-Hong Zhang\*, Bin-Yang Du, Bo-Xuan Zhou, Xin Zhou, Guo-Rong Qi

Key Laboratory of Macromolecular Synthesis and Functionalization of the Ministry of Education, Department of Polymer Science and Engineering, Zhejiang University, Hangzhou 310027, China

### ARTICLE INFO

#### Article history:

Received 20 July 2010

Received in revised form

13 October 2010

Accepted 26 November 2010

Available online 2 December 2010

#### Keywords:

Core cross-linked star polymer

Epoxy resin

Reaction-induced microphase separation

### ABSTRACT

Core crosslinked star (CCS) polymers, which have crosslinked poly (divinyl benzene-co-styrene) [P(DVB-St)] core and multiple arms of polystyrene-*b*-poly(ethylene oxide) diblock copolymer (PEO-*b*-PS) [denoted as PEO-*b*-PS/P(DVB-St) CCS], were synthesized via atom transfer radical polymerization (ATRP). PEO-*b*-PS/P(DVB-St) CCS polymer was spherical with average diameters of scores of nanometers from transmission electron microscopy (TEM) and dynamic light scattering (DLS), and blended with diglycidyl ether of bisphenol (DGEBA) and 4,4'-diamino diphenyl methane (DDM) in tetrahydrofuran (THF). With 5 or 10 wt% PEO-*b*-PS/P(DVB-St) CCS polymer, spherical core–shell nanodomains with average diameters of 29 or 32 nm were observed from atomic force microscopy (AFM), which were randomly distributed in the resultant thermosets. Considering the difference in miscibility of the epoxy with P(DVB-St) and PEO-*b*-PS after and before curing reaction, a reaction-induced microphase separation (RIMPS) mechanism was proposed to account for the formation of the core–shell nanodomains in the thermosets. During curing, the RIMPS of PS subchain occurred but was confined by P(DVB-St) core, resulting in formation of thermoplastic PS shell around the crosslinked core. Such core–shell nanodomain could be easily etched away by THF, whereas the control thermosets containing PEO/P(DVB-St) CCS polymer could not be etched by THF. The glass transition temperatures ( $T_g$ s) of the epoxy thermosets containing PEO-*b*-PS/P(DVB-St) CCS polymer were significantly improved compared with pure epoxy thermosets.

© 2010 Elsevier Ltd. All rights reserved.

### 1. Introduction

Epoxy resin is a kind of densely studied thermosetting material with excellent thermal and mechanical properties, and widely used as electrical/electric materials [1–6]. To construct nanostructures in epoxy matrix is a useful pathway for obtaining epoxy thermosets with improved overall properties [7–14]. It is an efficient approach to achieve nanostructured thermosets by incorporating amphiphilic block copolymers into thermoset, which has attracted more and more attentions in recent years [13–19]. To date, the strategies of constructing nanostructure in a thermoset can be generally categorized into two classes. One ingenious approach is pre self-assembly/curing method, which was initially reported by Bates et al [13,14]. In this protocol, driving force for the formation of nanostructure in thermoset is self-assembly of block copolymers when the precursors of thermosets act as the selective solvents of block copolymers. The subsequent curing process only serves to fix the formed nanophase in the matrix. It is a facile method to construct

nanostructured thermoset, and the structure of the nanophases can be adjusted via the modification of the block copolymers and the concentration of block copolymers. However, in many circumstances, this method does not work when all the subchains of block copolymers are miscible with the precursor, as was pointed out by Zheng et al. [15].

Another successful strategy involves reaction-induced microphase separation (RIMPS). The driving force of RIMPS method is the combined action of curing reaction kinetics and phase separation kinetics. In such case, the blend is initially homogeneous. A part of subchains of block copolymers demixes and forms the microphases, while another part of subchains is still miscible with the matrix during curing. Thus, the phase separation of the immiscible subchains can generally take place in a nanometer scale due to the restraint of the miscible subchain in the thermosetting matrix. Some typical nanostructured epoxy thermosets were developed via RIMPS method by Zheng and coworkers [15–20].

By applying the aforementioned methods solely or simultaneously, ordered and/or disordered nanostructures and various nanodomains in the thermosets can be formed after the curing process via blending of the block polymers with precursors of the

\* Corresponding author. Tel./fax: +86 571 87953732.

E-mail address: [xhzhang@zju.edu.cn](mailto:xhzhang@zju.edu.cn) (X.-H. Zhang).

thermosets. However, few works were reported for constructing core–shell nanodomains in a matrix although such structure was useful to improve the toughness of the resultant thermosets [19]. Zheng and coworkers reported the preparation of a thermoset with PDMS-core/PS-shell nanodomains in the matrix via RIMPS of PDMS-*b*-PCL-*b*-PS [19]. However, the thermal properties (e.g. glass transition temperature,  $T_g$ ) of the resultant thermosets were clearly weakened. To date, the reported copolymers applied for constructing nanostructured epoxy thermosets were mostly linear diblock or triblock polymers [13–19], which generally led to some loss of the thermal properties of the resultant thermoset due to incorporation of relatively more thermal unstable subchains (e.g.: PEO, PCL [17,19]) of the copolymers into the matrix. Furthermore, there is not any report concerning the construction of a crosslinked core/thermoplastic shell nanostructure in epoxy thermoset, which may possibly improve the thermal properties of the resultant thermoset.

In the present work, we report for the first time the fabrication of epoxy thermosets with nanostructured core–shell nanodomains via the solution blending of the epoxy resin and core crosslinked star (CCS) polymers [21,22]. In this protocol, the CCS polymers, which contain PEO-*b*-PS arms and P(DVB-St) cores (denoted as PEO-*b*-PS/P(DVB-St) CCS polymer) and are of spherical shape with scores of nanometers, were synthesized via “arm-first” method [21,22] and then mixed with diglycidyl ether of bisphenol (DGEBA) and 4,4'-diamino diphenyl methane (DDM) in THF solution. The crosslinked P(DVB-St) cores were immiscible with epoxy resin, whereas the PEO subchains of PEO-*b*-PS arms were miscible with epoxy throughout the curing reaction [16]. Noting that the PS subchains were covalently linked to P(DVB-St) cores, the PEO-*b*-PS underwent reaction-induced microphase separation process around the core due to the confinement of the nanoscale P(DVB-St) core. Therefore, in this model, the curing reaction not only fixed the pre-made P(DVB-St) core, but also induced the phase separation of PS subchains in a confined environment. Novel thermosets with core–shell nanodomains of crosslinked core/thermoplastic shell were obtained. These core–shell nanodomains largely improved the  $T_g$ s of the resultant epoxy thermoset.

## 2. Experimental section

### 2.1. Materials

Poly (ethylene glycol) methyl ether with  $M_w$  of 5000 (MPEG 5000, Aldrich) was distilled azeotropically with toluene to remove trace water. 2-bromoisobutyl bromide (2-BiB) and N,N,N',N'-pentamethyl diethylene triamine (PMDETA) were purchased from Aldrich and used as received. Diglycidyl ether of bisphenol (DGEBA) with epoxide equivalent weight of 184–190 g/mL was supplied by Jiadida chemical co., Ltd. 4,4'-diamino diphenyl methane (DDM) was purchased from SSS reagent Co., Shanghai and used as the hardener. Triethyl amine ( $Et_3N$ ), styrene (St) and divinyl benzene (DVB, Aladdin) were distilled according to the standard method. Cuprous chloride (CuCl) was repeatedly washed with acetic acid until the CuCl appeared pale gray. Ethanol was then used to remove the remaining acetic acid in the treated CuCl. Dichloro methane, tetrahydrofuran (THF), anisole, hexane and acetone were used without further purification.

### 2.2. Synthesis of PEO-Br macroinitiator

MPEG 5000 (25 g, 5 mmol) and  $Et_3N$  (2.1 mL, 15 mmol, here served as an acid acceptor) were dissolved in THF (dried over with Na chips, 130 mL). 2-BiB (1.85 mL, 15 mmol)/THF (dried over with Na chips, 50 mL) mixed solution was then dripped into the system

under 10 °C, followed by stirring at room temperature for 24 h. The reaction product was collected by filtration, the filtrate was concentrated, and the obtained solid was dissolved into deionized water (85 mL). This aqueous solution was extracted by  $CH_2Cl_2$  (300 mL), and the obtained  $CH_2Cl_2$  solution was dehydrated in the presence of  $CaCl_2$ . The dried solution was then concentrated using a rotary evaporator and precipitated into hexane (800 mL). The precipitates were collected by filtration and dried under vacuum.  $^1H$  NMR ( $CDCl_3$ , ppm): 4.30–4.32 ( $CH_2$ , 2H), 3.43–3.82 ( $OCH_2CH_2O$ , 4H), 3.36 ( $OCH_3$ , 3H), 1.93 ( $CH_3$ , 6H).

### 2.3. Synthesis of PEO-*b*-PS-Br macroinitiator

A 50 mL round-bottom flask was charged with a mixture of PEO-Br macroinitiator (5.5 g, 1.1 mmol), CuCl (0.1111 g, 1.1 mmol), PMDETA (0.460 mL, 2.2 mmol) and St (6.0 mL, 52 mmol). The mixture was degassed by three freeze–pump–thaw cycles. The flask was then backfilled with nitrogen and immersed in an oil bath at 110 °C. The reaction was stopped after 4 h via exposure to air and then diluted with THF. The residual copper catalysts were removed by passing the THF solution through a column of basic alumina. The purified solution was concentrated using a rotary evaporator and then precipitated into hexane. The precipitates were collected by filtration and dried under vacuum.  $^1H$  NMR ( $CDCl_3$ , ppm): 6.30–7.20 (Ph, 5H), 3.64 ( $OCH_2CH_2O$ , 4H), 1.20–2.10 ( $-CH_2CH\equiv$ , 3H).

### 2.4. Synthesis of PEO-*b*-PS/P(DVB-St) CCS polymer

The PEO-*b*-PS/P(DVB-St) CCS polymer was prepared by using the atomic transfer radical polymerization (ATRP) technique. A mixture of PEO-*b*-PS-Br macroinitiator (0.42 g, 0.04 mmol), CuCl (0.0040 g, 0.04 mmol), PMDETA (0.016 mL, 0.08 mmol), DVB (0.15 mL, 0.80 mmol), St (0.093 mL, 0.80 mmol) and anisole (1.2 mL) were added into a 50 mL flask and degassed by three freeze–pump–thaw cycles. The flask was then backfilled with nitrogen and immersed in an oil bath thermostated at 110 °C. After 15 h, the reaction was stopped via exposure to air. The mixture was diluted with THF, which was then passed through a column of basic alumina to remove the copper complex. The purified solution was first concentrated and then precipitated into large amount of n-hexane. The precipitates were collected and dried under vacuum.

### 2.5. Synthesis of PEO/P(DVB-St) CCS polymer

Similarly, the PEO/P(DVB-St) CCS polymer was also prepared by using ATRP technique. PEO-Br macroinitiator (0.30 g, 0.06 mmol) along with a mixture of CuCl (5.9 mg, 0.06 mmol), PMDETA (0.024 mL, 0.12 mmol), DVB (0.16 mL, 0.90 mmol), St (0.10 mL, 0.90 mmol) and anisole (1.2 mL) were charged into a dried round-bottom flask. The flask was connected to a Schlenk line. The reactive mixture was degassed via three freeze–pump–thaw cycles and then backfilled with nitrogen and immersed in an oil bath at 110 °C for 10h. The crude product was dissolved in THF and the copper complex was removed by passing the THF solution through a column of basic alumina. The purified THF solution was then precipitated into hexane. The precipitates were collected and dried under vacuum.

### 2.6. Preparation of the nanostructured epoxy thermoset

CCS polymers (0.062 and 0.125 g) were dissolved in THF. The CCS THF solution was then mixed with DGEBA (1.00 g) at room temperature under stirring. DDM, which was equimolar with the epoxy resin (0.25 g), was then added into the mixture of epoxy resin and CCS polymer under stirring. A homogeneous and

transparent mixed solution was obtained. The mixed solution was heated to 50 °C with vigorous stirring for 10 min to evaporate the majority of THF until the mixture became viscous. The viscous mixture was then poured into a mold and cured at 80 °C for 2 h and at 160 °C for another 2 h to give the epoxy thermosets with nanostructures.

### 3. Measurement and characterization

The molecular weights and molecular weight distributions of the CCS polymers were measured by Gel Permeation Chromatography (GPC) using a PL-GPC 220 instrument at 35 °C with THF as the eluent and monodispersed polystyrene as the calibration standard. <sup>1</sup>H NMR data were obtained on an Avance DMX 500 NMR spectrometer at 35 °C using CDCl<sub>3</sub> as the solvent and tetramethylsilane as the internal standard. Elemental analysis was performed on a Flash EA1112 CHN-O-Rapid elemental analyzer using acetanilide as the standard. Infrared spectra were recorded by using a Vector 22 FTIR spectrophotometer (400–4000 cm<sup>-1</sup>, KBr pellet).

The average particle size of the CCS polymer was determined by dynamic light scattering (DLS) on a Brookhaven 90 Plus DLS instrument at 25 °C. The CCS polymers were dissolved into THF to give a clear solution and then filtered through 0.45 μm Millipore PVDF filters before DLS measurements. Each sample was parallelly measured for 5 times. The morphology of the CCS polymers was observed by transmission electron microscopy (TEM) on a JEOL JEM-1230 high-resolution TEM at an acceleration voltage of 80 kV. CCS polymer was firstly dissolved into THF to give a concentration of 0.1 mg/mL. A droplet of the solution was cast on the copper grid and dried at room temperature. The samples were negatively stained with phosphotungstic acid before TEM measurement.

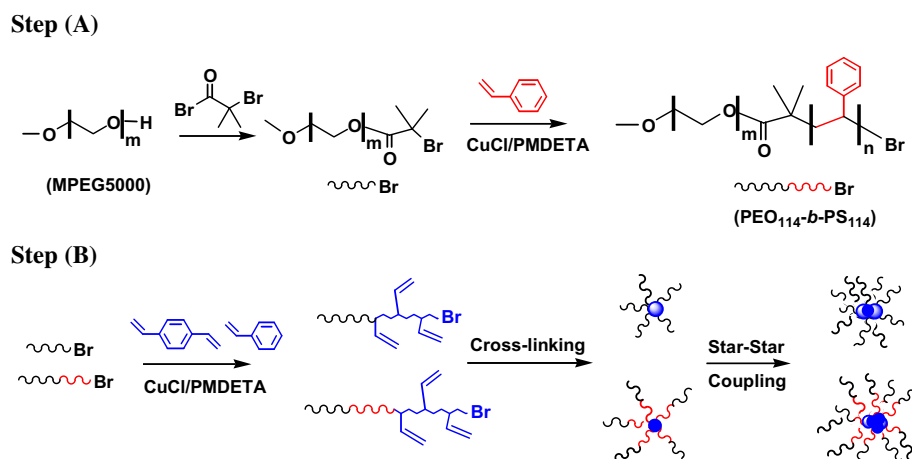
The surface morphology and inner structure of the cured epoxy thermosets with CCS polymers were investigated by using atomic force microscopy (AFM) and scanning electron microscopy (SEM). The AFM experiments were performed with a SEIKO SPI 3800N scanning probe microscope operated under tapping mode. A thin film of epoxy thermoset with ca. 90 nm thick was trimmed from the bulk epoxy thermoset by a microtome machine. The thermoset thin film was placed in 200 mesh copper grids for AFM observation. The silicon tips (Olympus) with a resonant frequency of ca. 300 KHz were used. The SEM observation was carried out on a Hitachi S4800 SEM. The epoxy thermoset was first fractured and then etched by THF. Before SEM observation, the etched thermoset samples were coated with gold vapor for 20s.

To evaluate the thermal property of the epoxy thermosets with CCS polymers, the glass transition temperatures (*T*<sub>g</sub>s) of the epoxy thermosets were determined by differential scanning chromatography (DSC). The epoxy thermosets of 3.0–5.0 mg were placed in aluminum pan and measured on a Q200 (TA) thermal analyzer at a heating rate of 10 °C/min under N<sub>2</sub>. The *T*<sub>g</sub>s of the epoxy thermosets were obtained from the second run of heating curves.

### 4. Results and discussion

#### 4.1. Preparation of PEO-*b*-PS/P(DVB-St) and PEO/P(DVB-St) CCS polymers

Core crosslinked star (CCS) polymers have attracted more and more attention because of their unique core–shell structure with highly branched arms [21–25]. Two approaches have been reported to synthesize CCS polymers [22,26]. One is the “core-first” method, which employs a multifunctional initiator to initiate the polymerization of vinylic monomers to form the arms of the star polymer [27,28]. The other is the “arm-first” method, with which linear macroinitiators were used as arms to initiate the polymerization of difunctional vinylic monomers to form a crosslinked core with branched arms [29–35]. In present work, “arm-first” method was used to synthesize CCS polymers with P(DVB-St) cores and PEO-*b*-PS arms (or PEO arms, as control sample) via ATRP technique. The synthetic route of the CCS polymers is shown in Scheme 1. In step (A), PEO-Br was synthesized via the reaction of monomethoxyl PEO5000 and 2-bromoisobutyryl bromide [36]. The obtained PEO-Br was then used as the macroinitiator for synthesizing PEO-*b*-PS-Br via ATRP. The GPC curves of PEO-Br and PEO-*b*-PS-Br are shown in Fig. 1. The number-average molecular weight (*M*<sub>n</sub>) of PEO-*b*-PS-Br was ca. *M*<sub>n,GPC</sub> = 1.83 × 10<sup>4</sup> with a narrow polydispersity of *M*<sub>w</sub>/*M*<sub>n</sub> = 1.13. *M*<sub>n</sub> of PEO-*b*-PS-Br was also determined to be ca. 1.68 × 10<sup>4</sup> by <sup>1</sup>H NMR, which indicated that the PS block contained 114 St units and the molar ratio of PEO/PS was close to 1. In step (B), PEO-*b*-PS-Br or PEO-Br was used as macroinitiator to initiate the ATRP of DVB and St. The multifunctional monomer DVB behaved as cross-linker, leading to the formation of crosslinked P(DVB-St) core. The optimal molar ratio of macroinitiator/DVB/St was 1:15:15 for the successful preparation of both CCS polymers, and optimal reaction time was found to be 15 h for the formation of PEO-*b*-PS/P(DVB-St) CCS polymer and 10 h for PEO/P(DVB-St) CCS polymer, respectively. No NMR signals could be captured with normal <sup>1</sup>H NMR method for both CCS polymers with crosslinked structures because of the loss of intramolecular mobility of the P(DVB-St) cores



Scheme 1. Synthetic route of PEO/P(DVB-St) and PEO-*b*-PS/P(DVB-St) CCS polymers via ATRP.

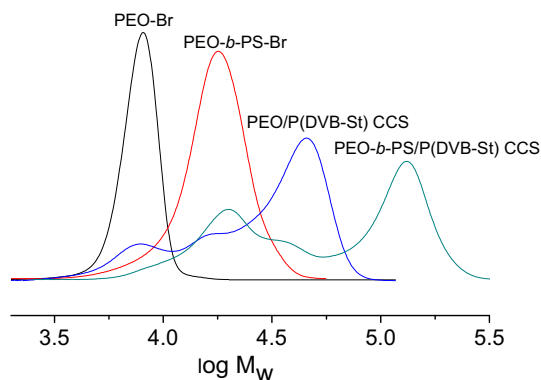


**Fig. 1.** GPC curves of PEO-Br, PEO-*b*-PS-Br ( $1.83 \times 10^4$ ), PEO/P(DVB-St) CCS polymer ( $M_n = 4.38 \times 10^4$  for main peak) and PEO-*b*-PS/P(DVB-St) CCS polymer ( $12.64 \times 10^4$  for main peak).

[29]. GPC curves (Fig. 1) of the obtained PEO-*b*-PS/P(DVB-St) and PEO/P(DVB-St) CCS polymers show that a majority of macro-initiators were consumed in both systems. For the synthesis of PEO-*b*-PS/P(DVB-St) CCS polymer, small amounts of linear copolymers with the segments containing divinyl groups (see step B in Scheme 1) could not be introduced to crosslinked cores due to steric effect of long chains of PEO-*b*-PS during copolymerization. This is consistent to the reported work concerning of the synthesis of CCS polymers with long arms [22].

The average particle size and size distribution of the PEO/P(DVB-St) and PEO-*b*-PS/P(DVB-St) CCS polymers were characterized by dynamic light scattering (DLS) measurements. Fig. 2 shows the particle size and size distribution of the PEO/P(DVB-St) and PEO-*b*-PS/P(DVB-St) CCS polymers in THF. A bimodal distribution of particle size can be observed for both CCS polymers. This was in good agreement with the corresponding GPC curves of which three elution peaks were observed (the peak with low molecular weight is linear and has no signal in DLS). PEO/P(DVB-St) CCS polymer contained small particles with peak size of ca. 20 nm and large particles with peak size of ca. 69 nm. Similarly, PEO-*b*-PS/P(DVB-St) CCS polymer contained small particles with peak size of ca. 33 nm and large particles with peak size of ca. 112 nm. Furthermore, both small and large particles had relatively narrow size distribution. Fig. 2 also indicates that CCS polymers obtained here were free of gels or large size aggregates. TEM measurements were employed to directly image the morphology of the CCS polymers. Fig. 3 shows that the CCS polymers indeed exhibited spherical shape. The size distributions of the CCS polymers obtained from TEM images were in good agreement with those from DLS. The sizes of PEO/P(DVB-St) and PEO-*b*-PS/P(DVB-St) CCS polymers were in the range of

18.6–34.4 nm and 25.0–54.6 nm, respectively, which were smaller than those measured by DLS. It is reasonable that the CCS polymers would swell in solvent (THF) and hence present larger hydrodynamic diameter in solvent as measured by DLS.

Considering the CCS polymers were composed of carbon, hydrogen and oxygen, the structural constitution (i.e.: PEO, PS subchains and P(DVB-St) core) of the CCS polymer can be obtained if the weight percentage of carbon, hydrogen and oxygen were known. The CCS polymers were thus subjected to the elemental analysis and the structural constitution of the CCS polymers was deduced, as shown in Table 1. It can be seen that the weight percentage of PEO arms in the PEO-*b*-PS/P(DVB-St) CCS polymer was only 18.5 wt% and smaller than that of PEO/P(DVB-St) CCS polymer (68.5 wt%). Hence the epoxy thermosets containing PEO-*b*-PS/P(DVB-St) CCS polymer with small amounts of thermal unstable PEO chain will present relatively high thermal stability.

#### 4.2. Nanostructured epoxy thermosets containing CCS polymers

The CCS polymers were then applied to prepare epoxy thermosets with possible nanostructures and improved thermal properties, as described in the experimental section. The amount of CCS polymers was controlled to be 5 or 10 wt% of the total weight of the epoxy thermosets. The resultant epoxy thermosets were transparent, suggesting that no macroscopic phase separation occurred in the thermoset during the curing reaction.

Fig. 4 shows the AFM images of the epoxy thermosets containing 5 and 10 wt% PEO-*b*-PS/P(DVB-St) CCS polymer. Note that a thin film of the epoxy thermoset with ca. 90 nm thick was microtomed from the bulk thermoset and then subjected to AFM measurements. Randomly distributed spherical nanodomains can be observed from the topology image of the epoxy thermoset (Fig. 4, left images). Such spherical nanodomains appeared as dark region in the phase image (Fig. 4, right images). According to the volume fraction of the PEO-*b*-PS/P(DVB-St) CCS polymer and the difference of viscoelastic properties between epoxy matrix and the CCS polymer, these dispersed nanodomains were attributed to the PEO-*b*-PS/P(DVB-St) CCS polymer. The mean sizes of the spherical nanodomains in the thermoset with 5wt% and 10 wt% PEO-*b*-PS/P(DVB-St) CCS polymers were ca. 29 nm and 32 nm, respectively. Some spherical nanodomains also interconnected together, to form the slightly bigger nanodomains. The size of the nanodomains was clearly smaller than that of the original PEO-*b*-PS/p(DVB-St) CCS polymer from DLS and TEM. It was understandable because the PS blocks shrank due to the phase separation and the PEO blocks were mixed into the matrix of epoxy thermoset. Hence, the observed nanodomains were mainly composed of the PS blocks and P(DVB-St) cores.

Fig. 5 shows the AFM images of the control epoxy thermosets containing 5 and 10 wt% PEO/P(DVB-St) CCS polymer. Similarly,

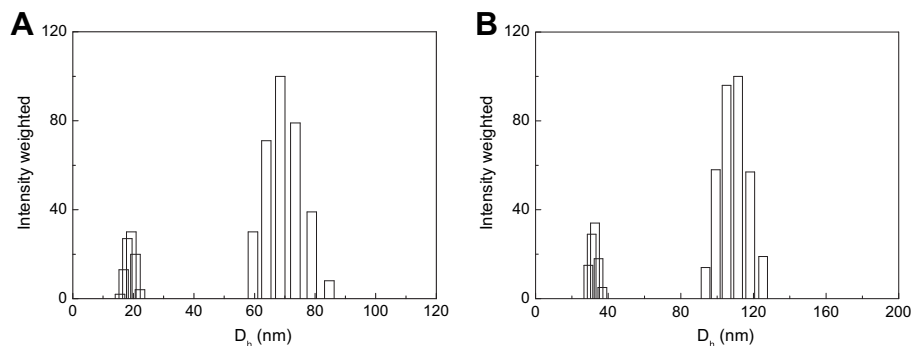


**Fig. 2.** DLS size distribution of (A) PEO/P(DVB-St) CCS polymer and (B) PEO-*b*-PS/P(DVB-St) CCS polymer.

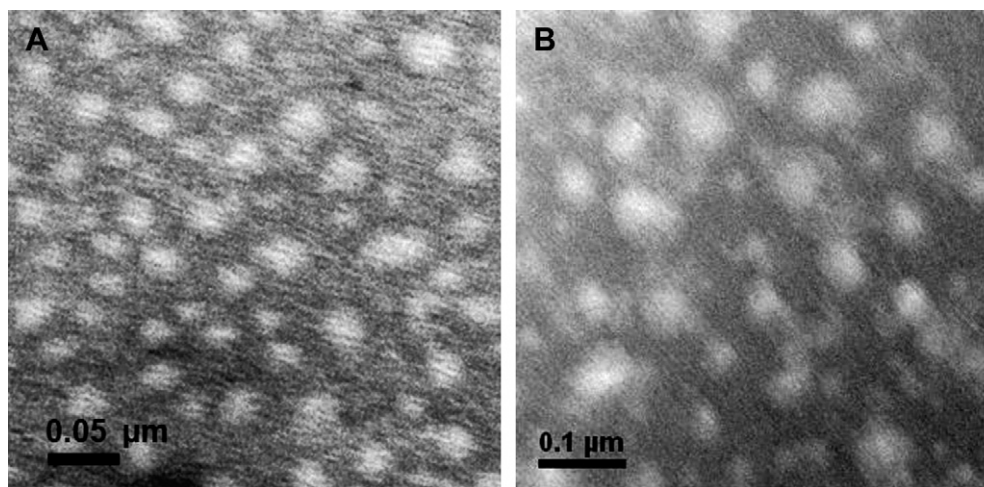


Fig. 3. TEM images of (A) PEO/P(DVB-St) CCS polymer, and (B) PEO-*b*-PS/P(DVB-St) CCS polymer.

nanodomains with average sizes of ca. 23 and 26 nm were observed for the epoxy thermosets with 5 and 10 wt% PEO/P(DVB-St) CCS polymer, respectively. In these cases, the nanodomains were mainly the P(DVB-St) cores because the PEO arms were miscible with the epoxy matrix. Again, the average sizes of nanodomains were smaller than those of original PEO/P(DVB-St) CCS polymer as measured by TEM and DLS.

The PEO subchains of the PEO-*b*-PS/P(DVB-St) CCS polymer were proved to be fully miscible with the epoxy thermoset by FTIR spectra (Fig. 6). It can be clearly seen that the free hydroxyl groups in the epoxy networks at  $3570\text{ cm}^{-1}$  became indistinctive with increasing the amounts of PEO-*b*-PS/P(DVB-St) CCS polymer to the system, which indicates the formation of the intermolecular hydrogen-bonding interactions between epoxy networks and PEO subchains. The intermolecular hydrogen-bonding interactions became stronger with increasing the CCS content. These results were in good agreement with those reported in literature that PEO (with various blocks, PCL, PS, etc.) was very well miscible with epoxy resin [16,37–39]. In other word, the PEO segments of CCS polymer were miscible with the epoxy thermoset. Moreover, the crosslinked P(DVB-St) cores couldn't dissolve into the precursors and were hence immiscible with epoxy thermoset before and after curing reaction. Whereas, the PS subchain was immiscible with the cured epoxy resin after the reaction [16]. Based on the miscibility of PEO, PEO-*b*-PS arms and P(DVB-St) cores with the epoxy matrix before and after curing reaction, the formation of nanodomain in the resultant epoxy thermosets containing the PEO/P(DVB-St) and PEO-*b*-PS/P(DVB-St) CCS polymer can be rationalized as following: (i) the nanosized crosslinked P(DVB-St) cores were randomly dispersed into the epoxy matrix, which guaranteed the formation of the spherical nanodomains; (ii) the diblock PEO-*b*-PS arms, which were fixed covalently by the P(DVB-St) core, followed the mechanism of reaction-induced microphase separation (RIMPS)

[10]; (iii) the PEO subchains were mixed with the epoxy matrix after curing.

For the epoxy thermoset with PEO-*b*-PS/P(DVB-St) CCS polymer, the microphase separation of PEO-*b*-PS arms occurred and was confined on the surface of the P(DVB-St) cores due to the connection of covalent bonds, leading to the formation of core-shell nanostructures with thin PS shells and P(DVB-St) cores. This process may be somewhat similar to the epoxy thermoset containing PDMS-*b*-PCL-*b*-PS triblock copolymer [18]. However, in the present systems, the size of spherical core-shell nanodomain can be well controlled by the crosslinked P(DVB-St) cores of the CCS polymers. Therefore, the final structures of the epoxy thermoset containing CCS polymers were less affected by the curing conditions, which may have influences on the self-assembly and RIMPS process of the linear block copolymers.

Fig. 7 shows the possible mechanism of the formation of core-shell nanodomains in the epoxy thermosets containing PEO-*b*-PS/P(DVB-St) CCS polymer. Before the curing reaction, both of PEO and PS blocks were miscible with the precursors of epoxy, while the crosslinked P(DVB-St) cores were immiscible but swelled with the precursors. Note that the copolymerization of St and DVB were designed to modulate the crosslink density of the P(DVB-St) cores, leaving spaces for the filling of epoxy precursors into the cores. In such way, nanoscale interpenetrating networks may be possibly generated after the curing reaction. During the curing reaction, microphase separation of the PEO-*b*-PS arms occurred and a thin PS shell was formed onto the surface of the P(DVB-St) core. The precursors inside the P(DVB-St) cores may be repelled out from the cores. The miscible PEO blocks remained in the cured epoxy matrix after curing. However, the immiscible PS shells may keep the crosslinked P(DVB-St) cores isolated from the epoxy matrix. Isolated nanodomains with a crosslinked P(DVB-St) core and

**Table 1**  
Weight percentage of PEO, PS subchain and P(DVB-St) core in two CCS polymers.<sup>a</sup>

CCS polymer	Elemental analysis		Composition of CCS polymer (wt %)		
	C	H	PEO subchain	PS subchain	P(DVB-St) core
PEO/P(DVB-St) <sup>b</sup>	66.28	8.78	68.5	0	31.5
PEO- <i>b</i> -PS/P(DVB-St) <sup>c</sup>	85.26	8.03	18.5	43.7	37.8

<sup>a</sup> Determined by CHN elemental analysis,  $O_{wt\%} = 1 - C_{wt\%} - H_{wt\%}$ .

<sup>b</sup>  $PEO_{wt\%} = O_{wt\%} \times (M_{CH_2CH_2O}/M_O) = 44O_{wt\%}/16$ ,  $p(DVB-St)_{wt\%} = 1 - 44O_{wt\%}/16$ .

<sup>c</sup>  $PEO_{wt\%} = 44 O_{wt\%}/16$ ,  $PS_{wt\%} = PEO_{wt\%} \times (M_{PS}/M_{PEO})$ ,  $p(DVB-St)_{wt\%} = 1 - PEO_{wt\%} - PS_{wt\%}$ ,  $M_{PS}$  and  $M_{PEO}$  are the molecular weight of PS segment and PEO segment in the PEO-*b*-PS block polymer.

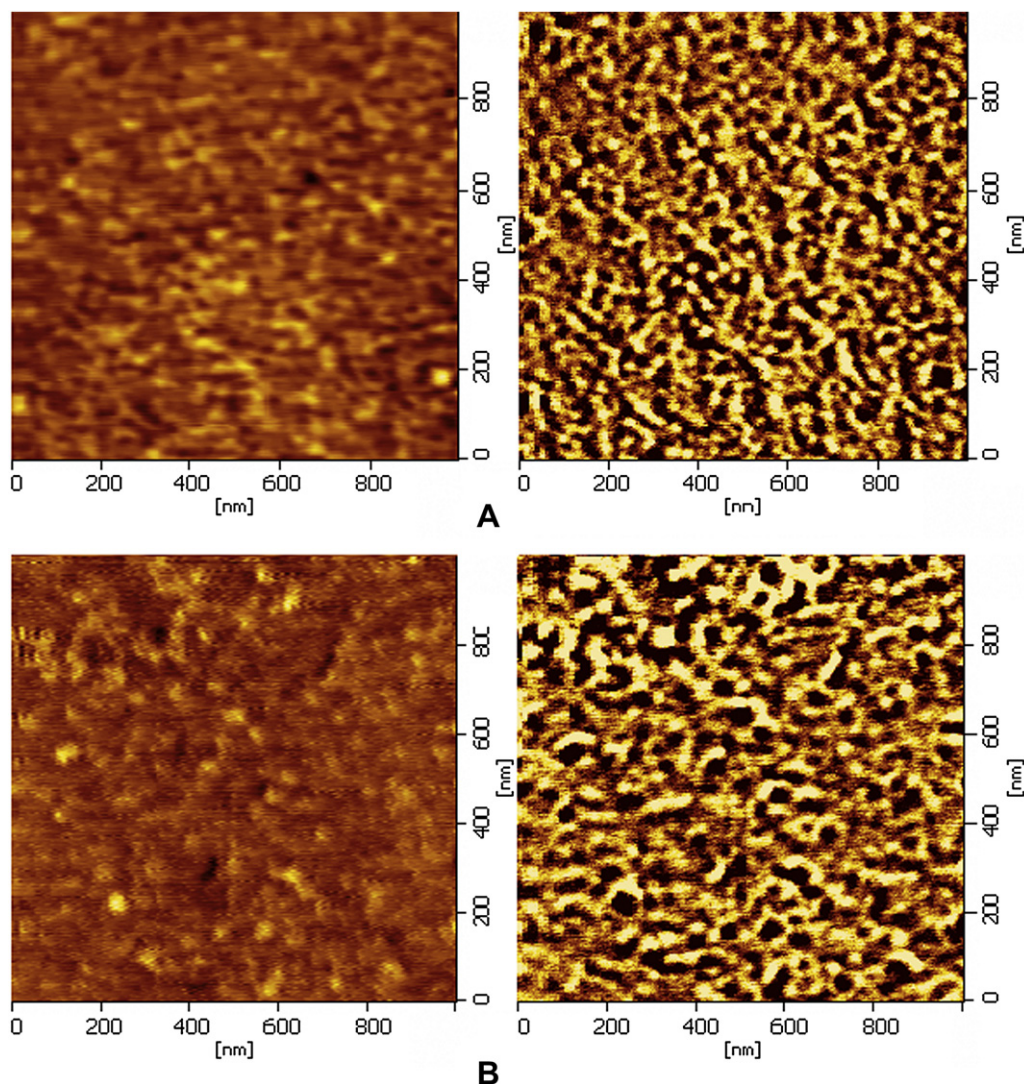


**Fig. 4.** AFM images of epoxy thermostets containing (A) 5wt% PEO-*b*-PS/P(DVB-St) CCS polymer and (B) 10 wt% PEO-*b*-PS/P(DVB-St) CCS polymer. Left: height image; right: phase image.

a thermoplastic PS shell were formed. If so, these nanodomains isolated from the epoxy matrix may be etched away by a good solvent.

However, for the epoxy thermostets containing PEO/P(DVB-St) CCS polymer, due to the miscibility of PEO arms with the precursors of the epoxy, the precursors swelled in the P(DVB-St) cores took part in the curing reaction, leading to the formation of interpenetration network of epoxy and P(DVB-St) cores. As a result, the nanodomains shown in Fig. 5 were interpenetrating network of epoxy and P(DVB-St) cores, which cannot be etched away by good solvent.

To confirm the above supposed mechanism, the epoxy thermostets containing 5 wt% PEO-*b*-PS/P(DVB-St) and PEO/P(DVB-St) CCS polymers were fractured and etched with THF for 1 h. Fig. 8 shows the SEM images of the fracture surface of the epoxy thermostets after etching in THF. Randomly distributed nanoholes with size of 14.0–74.5 nm were clearly observed for the epoxy thermostet containing PEO-*b*-PS/P(DVB-St) CCS polymer. While, the surface was rather smooth for epoxy thermostet containing PEO/P(DVB-St) CCS polymer. These results strongly support the above explanation of the formation of nanostructure epoxy thermostet containing PEO-*b*-PS/P(DVB-St) and PEO/P(DVB-St) CCS polymers.

Generally, the formation of nanostructures in thermostets via incorporation of linear block copolymer will lead to the depression of glass transition temperature ( $T_g$ ) compared with pristine epoxy resin [13,18]. Interestingly, a major increase in  $T_g$  was observed in the present epoxy thermostets containing PEO-*b*-PS/P(DVB-St) CCS polymer. Fig. 9 shows the DSC curves of the CCS polymers, the pristine epoxy thermostet, and the epoxy thermostets containing CCS polymers. A sharp melting transition peak at 50.8 °C was observed for the PEO/P(DVB-St) CCS polymer (curve 1), which was attributed to the crystalline PEO chains. However, no clear melting peak of crystalline PEO was found for the PEO-*b*-PS/P(DVB-St) CCS polymer (curve 2). A  $T_g$  at 72.7 °C was also observed for the PEO-*b*-PS/P(DVB-St) CCS polymer, which can be attributed to the PS blocks. Furthermore, for all of the thermostets containing CCS polymers, no melting transition of PEO chains was observed (curves 3–7), suggesting that the miscible PEO arms were stretched and mixed into the epoxy matrix very well [16].  $T_g$ s of epoxy thermostets containing 5 wt% and 10 wt% PEO-*b*-PS/P(DVB-St) CCS polymers were 146.9 and 147.9 °C (curves 4 and 5), respectively, which were significantly higher than that of the pristine epoxy thermostet (138.1 °C, curve 3). The widths of the glass transition regions of both thermostets were similar with that of the pristine epoxy thermostets, indicating that

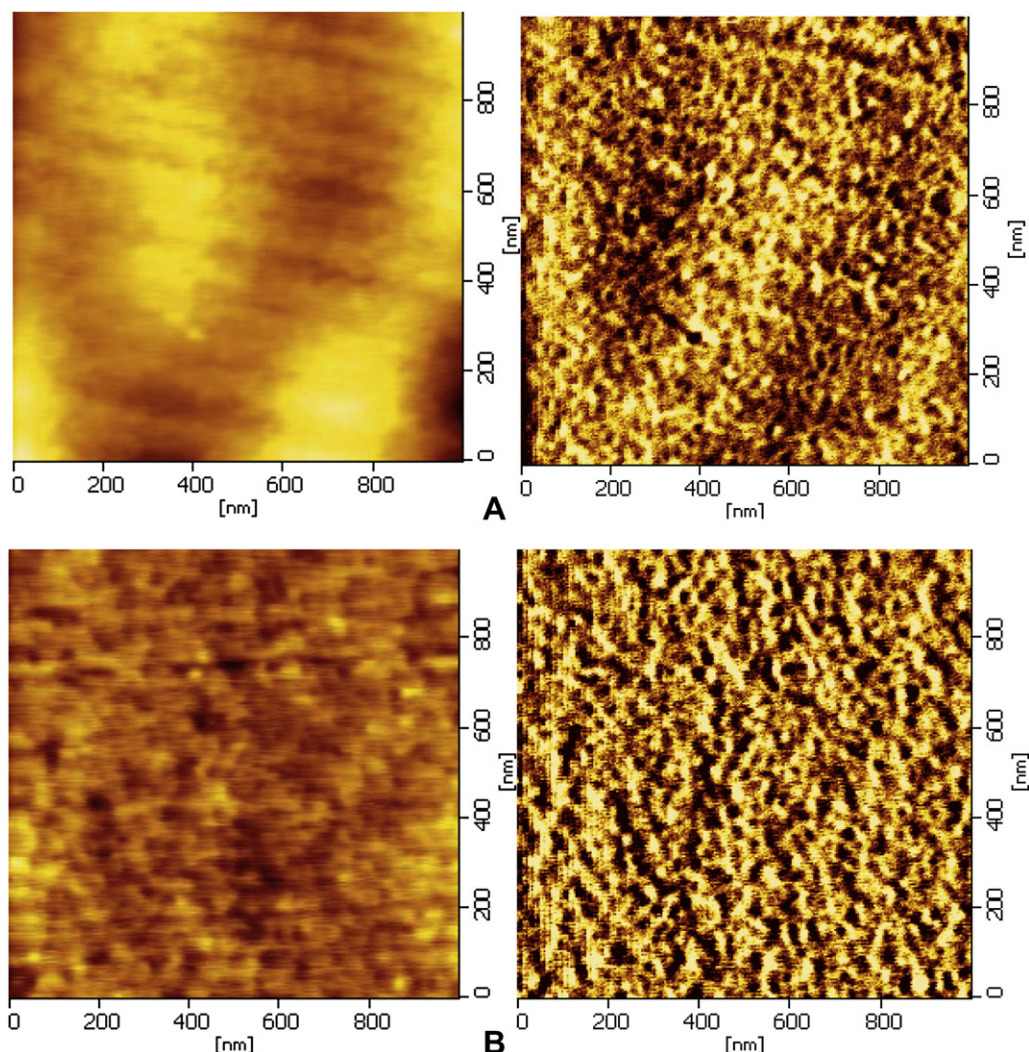


Fig. 5. AFM images of epoxy thermostets containing (A) 5wt% PEO/P(DVB-St) CCS polymer; (B) 10 wt% PEO/P(DVB-St) CCS polymer. Left: height image; right: phase image.

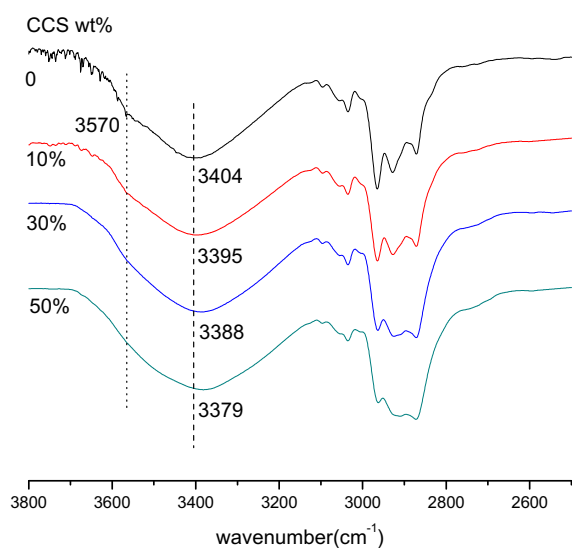


Fig. 6. FTIR spectra of epoxy thermostets containing 0, 10, 30 and 50wt% PEO/P(DVB-St) CCS polymer.

the plasticization of PEO chains could be indistinctive. For the control epoxy thermostets containing with 5 wt% and 10 wt% PEO/P(DVB-St) CCS polymer (curves 6 and 7),  $T_g$ s were slightly lower than that of the pristine epoxy thermostet (curve 3).

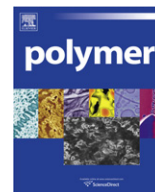
There were four possible factors accounting for the  $T_g$  of the final thermostets containing PEO-*b*-PS/P(DVB-St) CCS polymers. They were (1) PEO behaved a plasticizer and hence can decrease the  $T_g$  of the resultant thermostet; (2) P(DVB-St) CCS polymers with a cross-linked core may be possibly response to the increase of  $T_g$  of the resultant thermostet because no  $T_g$  transition were found below 200 °C (curves 1 and 2, Fig. 9); (3) PS segments had lower  $T_g$  than that of the epoxy matrix, which may decrease  $T_g$  of the resultant thermostet; (4) The cured epoxy resin was the main component (90% and 95%) in the final thermostet. The bigger the crosslinked density of the epoxy matrix was, the higher the  $T_g$  was observed.

For the thermostets with 5 and 10% PEO/P(DVB-St) CCS polymers (contain larger amounts of PEO chains), the plasticization of PEO on epoxy matrix was predominant, leading to the decrease of  $T_g$  and the broadened glass transition. However, the factors (1) to (3) will lead to the decrease of  $T_g$  of the epoxy thermostets. Because the cured epoxy resin was the main component (90% and 95%) in the final thermostet, it was then accepted that the increase of  $T_g$  of both thermostets studied here was mainly resulted from the increase of the crosslinked density of the epoxy matrix. Generally,





- [3] Morell M, Ramis X, Ferrando F, Yu Y, Serra A. *Polymer* 2009;50:5374–83.
- [4] Ragosta G, Musto P, Abbate M, Scarinzi G. *Polymer* 2009;50:5518–32.
- [5] Chen Z, Yang J, Ni Q, Fu S, Huang Y. *Polymer* 2009;50:4753–9.
- [6] Chen Z, Yang G, Yang J, Fu S, Ye L, Huang Y. *Polymer* 2009;50:1316–23.
- [7] Ritzenthaler S, Court F, David L, Girard-Reydet E, Leibler L, Pascault JP. *Macromolecules* 2002;35:6245–54.
- [8] Ruiz-Perez L, Royston GJ, Fairclough JPA, Ryan AJ. *Polymer* 2008;49(21):4475–88.
- [9] Maiez-Tribut S, Pascault JP, Soule ER, Borrajo J, Williams RJJ. *Macromolecules* 2007;40:1268–73.
- [10] Rebizant V, Abetz V, Tournilhac F, Court F, Leibler L. *Macromolecules* 2003;36:9889–96.
- [11] Grubbs RB, Dean JM, Broz ME, Bates FS. *Macromolecules* 2000;33:9522–34.
- [12] Mijovic J, Shen M, Sy JW. *Macromolecules* 2000;33:5235–44.
- [13] Hillmyer MA, Lipic PM, Hajduk DA, Almdal K, Bates FS. *J Am Chem Soc* 1997;119:2749–50.
- [14] Lipic PM, Bates FS, Hillmyer MA. *J Am Chem Soc* 1998;120:8963–70.
- [15] Meng F, Zheng S, Zhang W, Li H, Liang Q. *Macromolecules* 2006;39:711–9.
- [16] Meng F, Zheng S, Li H, Liang Q, Liu T. *Macromolecules* 2006;39:5072–80.
- [17] Xu Z, Zheng S. *Macromolecules* 2007;40:2548–58.
- [18] Meng F, Xu Z, Zheng S. *Macromolecules* 2008;41:1411–20.
- [19] Fan W, Wang L, Zheng S. *Macromolecules* 2009;42:327–36.
- [20] Fan W, Zheng S. *Polymer* 2008;49:3157–67.
- [21] Du JZ, Chen YM. *J Polym Sci Part A Polym Chem* 2004;42:2263–75.
- [22] Blencowe A, Tan JF, Goh TK, Qiao GG. *Polymer* 2009;50:5–32.
- [23] Gurr PA, Qiao GG, Solomon DH, Harton SE, Spontak RJ. *Macromolecules* 2003;36:5650–4.
- [24] Kharchenko SB, Kannan RM. *Macromolecules* 2003;36:407–15.
- [25] Furukawa T, Ishizu K. *Macromolecules* 2003;36:434–9.
- [26] Ho AK, Gurr PA, Mills MF, Qiao GG. *Polymer* 2005;46:6727–35.
- [27] Ueda J, Kamigaito M, Sawamoto M. *Macromolecules* 1998;31:6762–8.
- [28] Ueda J, Matsuyama M, Kamigaito M, Sawamoto M. *Macromolecules* 1998;31:557–62.
- [29] Zhang X, Xia JH, Matyjaszewski K. *Macromolecules* 2000;33:2340–5.
- [30] Xia JH, Zhang X, Matyjaszewski K. *Macromolecules* 1999;32:4482–4.
- [31] Baek K, Kamigaito M, Sawamoto M. *Macromolecules* 2001;34:215–21.
- [32] Baek K, Kamigaito M, Sawamoto M. *Macromolecules* 2001;34:7629–35.
- [33] Baek K, Kamigaito M, Sawamoto M. *Macromolecules* 2002;35:1493–8.
- [34] Bosman AW, Heumann A, Klaerner G, Benoit D, Fre'chet JMJ, Hawker CJ. *J Am Chem Soc* 2001;123:6461–2.
- [35] Bosman AW, Vestberg R, Heumann A, Fre'chet JMJ, Hawker CJ. *J Am Chem Soc* 2003;125:715–28.
- [36] Ishizu K, Makino M, Uchida S. *Macromol Rapid Commun* 2007;28:882–7.
- [37] Zheng S, Zhang N, Lou X, Ma D. *Polymer* 1995;36:3609–13.
- [38] Yin M, Zheng S. *Macromol Chem Phys* 2005;206:929–37.
- [39] Guo Q, Harrats C, Groeninckx G, Koch MHJ. *Polymer* 2001;42:4127–40.



# Synthesis and characterization of side chain polymer with helical PLLA segments containing mesogenic end group

Hongru Chen, Qingbin Xue\*, Zhuohua Li, Lingmin Sun, Quanxuan Zhang

Key lab of Colloid and Interface Chemistry, Ministry of Education, Chemistry and Chemical Engineering College, Shandong University, Shanda South Road No. 27, Jinan 250100, China

## ARTICLE INFO

### Article history:

Received 7 June 2010

Received in revised form

18 October 2010

Accepted 23 November 2010

Available online 1 December 2010

### Keywords:

Poly-L-Lactide

Side chain liquid crystals

Ring-opening polymerization

## ABSTRACT

Series of mesogenic biphenol derivatives HO6OPPO $n$  ( $n = 4,6,8$ ) were prepared by asymmetric reaction and purified. Then HOLAxO6OPPO $n$  were prepared with controlled molecular weights by adjusting the feed ratios of HO6OPPO $n$ , SnO $_2$  catalyst and LLA by Ring-Opening Polymerization. **P-AOLAxO6OPPO $n$**  materials were obtained in high yields by the free radical polymerization of polymerizable macromonomers of **AOLAxO6OPPO $n$**  synthesized by esterization of HOLAxO6OPPO $n$  with acrylic acid in the presence of DCC/DMAP. Their molecular weights were characterized by  $^1\text{H}$  NMR and GPC. Differential Scanning Calorimeter method and Polarized Optical Microscopy method were used to study their thermal behaviors. Both **AOLAxO6OPPO $n$**  and **P-AOLAxO6OPPO $n$**  materials are found to form LCs with increased  $T_g$ ,  $T_m$  and  $T_i$  with longer O-LLA segment length. Polymerization of **AOLAxO6OPPO $n$**  also resulted in the increase of  $T_g$ ,  $T_m$  and  $T_i$ . X-ray diffraction measurements revealed the presence of smectic phase in these materials. The O-LLA segments are in helical structure from CD spectra and this makes the resulting polymer materials good candidate of optical materials for huge optical rotation power.

© 2010 Elsevier Ltd. All rights reserved.

## 1. Introduction

PolyLactide (PLA) is one of the most important bioactive polymers used as biodegradable and biocompatible materials [1–10]. It is also noticeable that L, L-Lactide or D, D-Lactide, as important two enantiomers of Lactide, can form interesting helical chiral polymers, Poly-L-Lactide (PLLA) or PDLA. Compared to those well studied racemic PLAs used as biomaterials, PLLA and PDLA as optical pure chiral helical polymers are still not well studied [11–16].

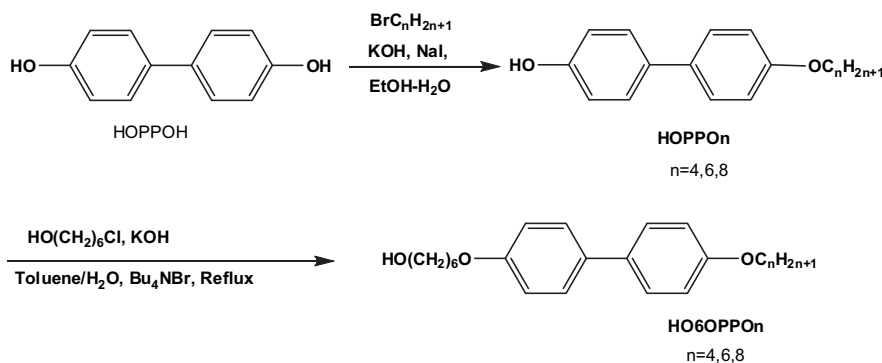
Until now many papers have focused on the research of helical polymers [17–27], but extensive study on PLLA helical polymer as optically active polymers is still rare [28–31]. Helical PLLA polymers were expected to exhibit optical rotation power in solid state due to the asymmetric arrangement of atoms in helical main chain structure. Kobayashi [32] has processed and measured the huge intrinsic optical rotation power of PLLA in the fiber axis direction of uniaxial crystal,  $\rho$ , as large as 7200°/mm, 300 times larger than that of  $\alpha$ -quartz. Also the measured response change in the amplitude of transmitted light was up to 10 MHz for fast light modulation [33]. This devotes PLLA as potential materials for optical elements and devices.

Kimura et al. [34] has prepared series of oligo(L-lactic acid) with an isopropoxyl end group. The ellipticity of oligo(L-lactic acid) (O-LLA) by Circular Dichroism (CD) increased with the increase of degree of polymerization and reached a maximal value at  $n = 8$ , indicating the completely built up of the helical structure in O-LLA. The ellipticity was kept almost constant for O-LLA with more repeating numbers but the ellipticity is a little lower than the maximal value. The better processability of O-LLAs than PLLAs is an advantage for large area flexible thin film optical devices.

Samuel I. Stupp et al. [35,36] has reported for the first observation of Liquid Crystal (LC) behavior of O-LLA with Cholesteryl groups attached at the end and studied the self-assembling property of Chol-(L-Lactic Acid)xOH as building blocks for self-assembling materials. Attachment of LC groups to form LC-LLA materials can be also a very good way of combining the self-organization property of LC group and the optical rotation power of helical O-LLA to get self-organized materials with huge optical rotation power. Considering that these self-assembling materials could be very good candidates as biomaterials and also good optical materials, the study of LC-OLLA materials is one of the very interesting areas of future.

This report presents the preparation, thermal and phase behaviors of series of side chain polymers with O-LLA as important helical chain segments, involving the preparation of molecular weight-controlled LC-OLLA materials HOLAxOmOPPO $n$ , **AOLAxOmOPPO $n$**  and **P-AOLAxOmOPPO $n$**  (Scheme 2 and Scheme 3).

\* Corresponding author. Tel.: +86 531 88366096; fax: +86 531 88564464.  
E-mail address: [qbxue@sdu.edu.cn](mailto:qbxue@sdu.edu.cn) (Q. Xue).



Scheme 1. Synthesis routine of the initiators.

## 2. Experimental sections

### 2.1. Materials

L-Lactide (LLA) was purified by recrystallization three times from toluene dried as following method. The polymerization of LLA was performed under Argon atmosphere. Toluene used for the ring-opening polymerization of L-Lactide as best solvent was dried on Sodium/potassium alloy Na/K (Benzophenone) and distilled off just before use and transferred with syringes.

Acrylic acid was distilled just before use. Azodiisobutyronitrile (AIBN) was recrystallized from ethanol and stored in refrigerator at 0 °C. Stannous octoate, SnOct<sub>2</sub>, was redistilled three times first as reported in reference [37] and used by quantitatively transferring with syringe as toluene (Na/K dried) solution of known concentration. N, N'-Dicyclohexylcarbodiimide (DCC), 4-N, N'-dimethylamino- pyridine (DMAP) was vacuum dried before use. CH<sub>2</sub>Cl<sub>2</sub> was dried over P<sub>2</sub>O<sub>5</sub>, when necessary. All the other materials are commercial available and used as received unless noted elsewhere.

### 2.2. Synthesis

#### 2.2.1. Synthesis of mono-substituted biphenol compounds

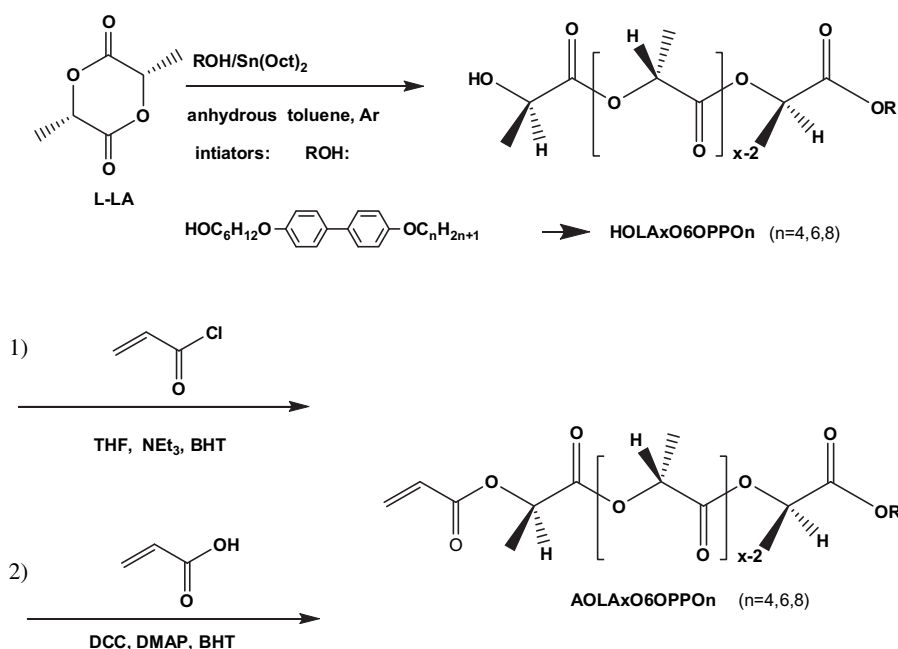
The synthesis procedure of the initiators was presented as Scheme 1.

The general operations were as following [38]: After biphenol (30 g, 0.16 mol) and KOH (40 g, 0.71 mol) forming a clear solution in 192 mL Ethanol/H<sub>2</sub>O (v/v 2:1) solution at reflux by magnetic stirring, equimolar BrC<sub>n</sub>H<sub>2n+1</sub> (n = 4,6,8) in ethanol were added dropwisely under stirring and reflux for 12 h by Thin Layer Chromatography (TLC) monitor. The filtrates after filtering off nOPPOn solid were diluted with large amount of diluted sodium hydroxide water to recover the resultants by filtration as noted HOPPOn (n = 4,6,8) and recrystallized twice from ethanol.

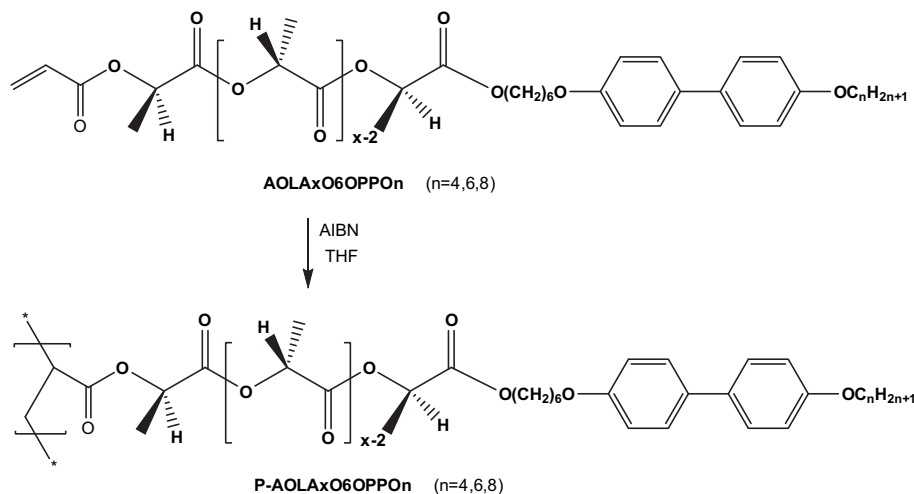
HOPPO4 yield 32.8%,  $R_f = 0.46$  (CHCl<sub>3</sub>:C<sub>2</sub>H<sub>5</sub>OH = 15:1)

HOPPO6 yield 23.3%,  $R_f = 0.44$  (CHCl<sub>3</sub>:C<sub>2</sub>H<sub>5</sub>OH = 15:1)

HOPPO8 yield 32.0%,  $R_f = 0.46$  (CHCl<sub>3</sub>:C<sub>2</sub>H<sub>5</sub>OH = 15:1)



Scheme 2. Ring-opening polymerization of LLA and the synthesis of the acrylic esters of the PLLA macromonomers.



**Scheme 3.** Radical polymerization of the acrylic ester macromonomers of O-LLAs.

### 2.2.2. Initiators HO6OPPO<sub>n</sub> (n = 4,6,8)

HO6OPPO<sub>n</sub> were reacted with NaOH, NaI, and Cl(CH<sub>2</sub>)<sub>6</sub>OH in proper amount of solvent for 48 h with refluxing or by phase-transfer reaction in toluene with catalytic amount of Bu<sub>4</sub>NBr for 8 h, monitoring by TLC. HO6OPPO<sub>n</sub> were recovered by Rotary Evaporator and recrystallization from ethanol yielding white solid. HO6OPPO<sub>n</sub> were then recrystallized in toluene and dried for ROP reaction.

HO6OPPO<sub>4</sub>, yield 83.1%,  $R_f = 0.35$  (CH<sub>2</sub>Cl<sub>2</sub>:C<sub>2</sub>H<sub>5</sub>O  
C<sub>2</sub>H<sub>5</sub>:CH<sub>3</sub>(CH<sub>2</sub>)<sub>4</sub>CH<sub>3</sub> = 2:1:1)

HO6OPPO<sub>6</sub>, yield 60.6%,  $R_f = 0.40$   
(CH<sub>2</sub>Cl<sub>2</sub>:C<sub>2</sub>H<sub>5</sub>OC<sub>2</sub>H<sub>5</sub>:CH<sub>3</sub>(CH<sub>2</sub>)<sub>4</sub>CH<sub>3</sub> = 2:1:1)

HO6OPPO<sub>8</sub>, yield 73.1%,  $R_f = 0.35$  (CHCl<sub>3</sub>:C<sub>2</sub>H<sub>5</sub>OH = 15:1)

### 2.2.3. Ring-opening polymerization of L-LA

A general procedure for the Ring-Opening Polymerization (ROP) of L-LA was shown in Scheme 2. The feed ratios of L-LA to HO6OPPO<sub>n</sub> and SnOct<sub>2</sub> were adjusted in order to get oligomers/polymers of different molecular weight. The procedure was briefly as following:

Proper amount of L-LA, HO6OPPO<sub>n</sub> were vacuum dried at near 50 °C for 3 h and then mixed with SnOct<sub>2</sub> (tridistilled) solution in toluene with typical ratio (x:1:1, x = 5,10,15,20) and toluene. After stirring for 10 h at 100 °C the viscous mixture was cooled and evaporated to dryness. Then the residual was dissolved with CH<sub>2</sub>Cl<sub>2</sub> and washed with 1 M HCl aqueous and water, concentrated. The concentrated solution was then poured into ethanol or petroleum ether to precipitate. The final targeted polymer compounds were collected as white solid by filtration and dried (The H atoms marked for <sup>1</sup>H NMR measurement were shown as in Fig. 1).

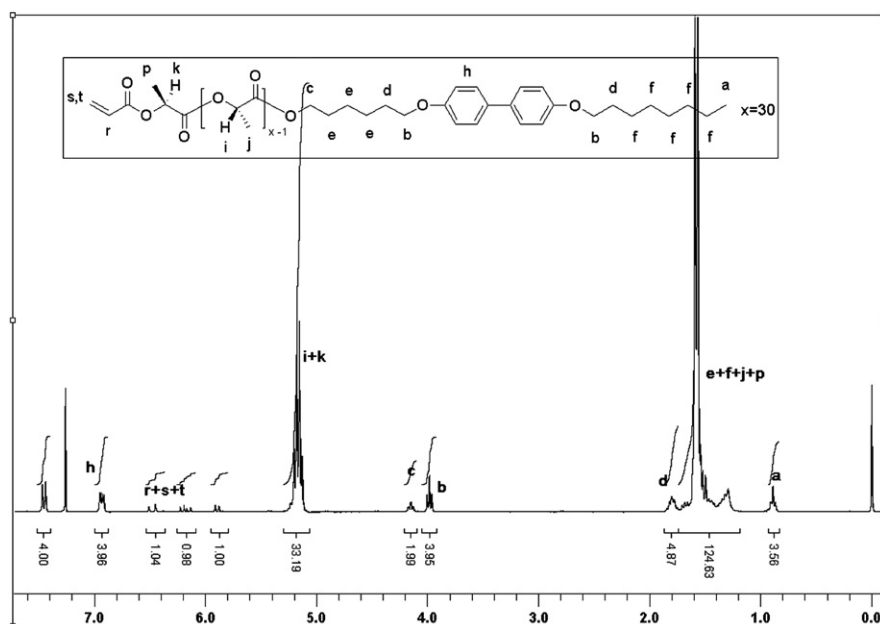


**Fig. 1.** A representative <sup>1</sup>H NMR spectral of AOLA<sub>x</sub>O6OPPO<sub>n</sub>.

**Table 1**Molecular weight and degree of polymerization and Degree of Polydispersity Index (DPI) of HOLA<sub>x</sub>O6OPPO<sub>n</sub> obtained by <sup>1</sup>H NMR and GPC methods.

	Theo.		<sup>1</sup> H NMR		GPC		
	n	Mn	n	Mn	Mn	Mw	Mw/Mn
HOLA <sub>10</sub> O6OPPO <sub>4</sub>	10	1063	10.8	1119	1944	2425	1.25
HOLA <sub>20</sub> O6OPPO <sub>4</sub>	20	1783	19.9	1777	2880	3952	1.37
HOLA <sub>30</sub> O6OPPO <sub>4</sub>	30	2504	29.1	2436	3633	5018	1.38
HOLA <sub>40</sub> O6OPPO <sub>4</sub>	40	3225	39.6	3196	4328	6213	1.44
HOLA <sub>10</sub> O6OPPO <sub>8</sub>	10	1119	9.9	1110	1924	2390	1.24
HOLA <sub>20</sub> O6OPPO <sub>8</sub>	20	1839	19.5	1802	2827	3917	1.39
HOLA <sub>30</sub> O6OPPO <sub>8</sub>	30	2560	29.1	2497	3681	5100	1.39
HOLA <sub>40</sub> O6OPPO <sub>8</sub>	40	3281	37.6	3111	4932	6352	1.29

**HOLA<sub>x</sub>O6OPPO<sub>4</sub>** <sup>1</sup>H NMR (300 MHz, CDCl<sub>3</sub>): δ(ppm) = 0.986 (t, 3H, a); 1.406–1.706 (m, 3x + 8, e + f + j + p); 1.739–1.831 (m, 4H, d); 2.700 (b, 1H, q); 3.986 (t, 4H, b); 4.155 (t, 2H, c); 4.319–4.389 (m, 1H, k); 5.116–5.230 (m, n – 1, i); 6.913–7.469 (m, 8H, h).

**HOLA<sub>x</sub>O6OPPO<sub>6</sub>** <sup>1</sup>H NMR (300 MHz, CDCl<sub>3</sub>): δ(ppm) = 0.941 (t, 3H, a); 1.255–1.703 (m, 3x + 12, e + f + j + p); 1.749–1.842 (m, 4H, d); 2.700 (b, 1H, q); 3.984 (t, 4H, b); 4.156 (t, 2H, c); 4.323–4.392 (m, 1H, k); 5.094–5.235 (m, n – 1, i); 6.914–7.470 (m, 8H, h).

**HOLA<sub>x</sub>O6OPPO<sub>8</sub>** <sup>1</sup>H NMR (300 MHz, CDCl<sub>3</sub>): δ(ppm) = 0.941 (t, 3H, a); 1.255–1.703 (m, 3x + 16, e + f + j + p); 1.749–1.842 (m, 4H, d); 2.700 (b, 1H, q); 3.984 (t, 4H, b); 4.156 (t, 2H, c); 4.323–4.392 (m, 1H, k); 5.094–5.235 (m, n – 1, i); 6.914–7.470 (m, 8H, h).

#### 2.2.4. Preparation of macromonomers

The preparation of the macromonomers was performed by the reactions either with excess amount of acryloyl chloride/triethylamine or acrylic acid/DCC/DMAP using 2,6-Di-tert-butyl-4-methylphenol (BHT) as inhibitor. Generally, the mixture of LC-OLLA-OH corresponding to macromonomer with BHT, DCC/DMAP, dissolved in CaH<sub>2</sub>-dried CH<sub>2</sub>Cl<sub>2</sub>, was kept magnetic stirring for 60 h at room temperature and stopped with small amount of Ethanol/Acetic acid mixture. After filtration and concentration the residual was poured into cooled ethanol (–18 °C) and kept hours in refrigerator. White powder was collected by the filtration of the cooled ethanol solution and vacuum dried to get the polymerizable macromonomers in good yield.

**AOLA<sub>x</sub>O6OPPO<sub>4</sub>** <sup>1</sup>H NMR (300 MHz, CDCl<sub>3</sub>): δ(ppm) = 0.986 (t, 3H, a); 1.496–1.706 (m, 3x + 8, e + f + j + p); 1.739–1.827 (m, 4H, d); 3.962–4.016 (m, 4H, b); 4.113–4.170 (m, 2H, c); 5.129–5.200 (m, nH, i + k); 5.878–5.913 6.135–6.227 6.451–6.507 (m, 1H + 1H + 1H, r + s + t); 6.913–7.468 (m, 8H, h).

**Table 2**Molecular weight and degree of polymerization and Degree of Polydispersity Index (DPI) of AOLA<sub>x</sub>O6OPPO<sub>n</sub> and P-AOLA<sub>x</sub>O6OPPO<sub>n</sub> obtained by <sup>1</sup>H NMR and GPC method.

Samples	M.W. of AOLA <sub>x</sub> O6OPPO <sub>n</sub> <sup>a</sup>			M.W. of P-AOLA <sub>x</sub> O6OPPO <sub>n</sub> By GPC			
	x	Mn	<sup>1</sup> H NMR <sup>a</sup>	Mn × 10 <sup>–3</sup>	Mw × 10 <sup>–3</sup>	Mw/Mn	DP of PA <sup>b</sup>
			O-LLA x/Mn				
P-AOLA <sub>10</sub> O6OPPO <sub>4</sub>	10	1117	12/1261	21.2	23.2	1.09	17
P-AOLA <sub>20</sub> O6OPPO <sub>4</sub>	20	1837	25/2137	24.5	26.7	1.09	11
P-AOLA <sub>30</sub> O6OPPO <sub>4</sub>	30	2558	33/2774	28.7	31.7	1.11	10
P-AOLA <sub>40</sub> O6OPPO <sub>4</sub>	40	3279	44/3567	38.5	47.7	1.24	11
P-AOLA <sub>10</sub> O6OPPO <sub>6</sub>	10	1144	9/1072	11.6	14.6	1.26	11
P-AOLA <sub>20</sub> O6OPPO <sub>6</sub>	20	1864	23/2070	12.5	15.2	1.22	7
P-AOLA <sub>30</sub> O6OPPO <sub>6</sub>	30	2588	31/2660	20.3	30.7	1.51	8
P-AOLA <sub>40</sub> O6OPPO <sub>6</sub>	40	3303	43/3519	21.9	28.1	1.28	6
P-AOLA <sub>10</sub> O6OPPO <sub>8</sub>	10	1171	15/1531	15.9	17.5	1.1	10
P-AOLA <sub>20</sub> O6OPPO <sub>8</sub>	20	1893	24/2181	23.3	27.3	1.17	11
P-AOLA <sub>30</sub> O6OPPO <sub>8</sub>	30	2614	33/2830	33.1	37.2	1.13	12
P-AOLA <sub>40</sub> O6OPPO <sub>8</sub>	40	3335	42/3479	33.6	39.5	1.18	10

<sup>a</sup> The theoretical molecular weight and degree of polymerization of macromonomers AOLA<sub>x</sub>O6OPPO<sub>n</sub>;

<sup>b</sup> The degree of polymerization of P-AOLLA determined based on the Mn of P-AOLLAs by GPC and Mw of macromonomers as repeat units as side chains.

**Table 3**Phase transition temperatures (°C) of macromonomers AOLA<sub>x</sub>O6OPPO<sub>n</sub>.

Samples	T <sub>g</sub>	T <sub>m</sub>	T <sub>i</sub>
AOLA <sub>10</sub> O6OPPO <sub>4</sub>	22.8	53.0	89.0
AOLA <sub>20</sub> O6OPPO <sub>4</sub>	26.4	102.2	118.0
AOLA <sub>30</sub> O6OPPO <sub>4</sub>	30.0	119.6	125.2
AOLA <sub>40</sub> O6OPPO <sub>4</sub>	35.2	117.2	137.2
AOLA <sub>10</sub> O6OPPO <sub>6</sub>	17.0	62.0	107.9
AOLA <sub>20</sub> O6OPPO <sub>6</sub>	–	56.8	125.2
AOLA <sub>30</sub> O6OPPO <sub>6</sub>	28.2	28.2	129.6
AOLA <sub>40</sub> O6OPPO <sub>6</sub>	32.4	75.6	139.1
AOLA <sub>10</sub> O6OPPO <sub>8</sub>	–	39.4	107.9
AOLA <sub>20</sub> O6OPPO <sub>8</sub>	17.8	51.8	126.9
AOLA <sub>30</sub> O6OPPO <sub>8</sub>	21.7	87.3	130.4
AOLA <sub>40</sub> O6OPPO <sub>8</sub>	30.4	90.6	136.8

**AOLA<sub>x</sub>O6OPPO<sub>6</sub>** <sup>1</sup>H NMR (300 MHz, CDCl<sub>3</sub>): δ(ppm) = 0.913 (t, 3H, a); 1.24–1.70 (m, 3x + 12H, j + p + e + f); 1.76–1.85 (m, 4H, d); 3.988 (t, 4H, b); 4.154 (m, 2H, c); 4.350 (m, 1H, k); 5.129–5.200 (m, nH, i + k); 5.892 (d, 1H, s); 6.180 (t, 1H, t); 6.44 (d, 1H, r); 6.913–7.468 (m, 8H, h).

**AOLA<sub>x</sub>O6OPPO<sub>8</sub>** <sup>1</sup>H NMR (300 MHz, CDCl<sub>3</sub>): δ(ppm) = 0.890 (t, 3H, a); 1.294–1.707 (m, 3x + 16H, e + f + j + p); 1.754–1.844 (m, 4H, d); 3.962–4.005 (m, 4H, b); 4.125–4.177 (m, 2H, c); 5.129–5.200 (m, nH, i + k); 5.815–5.913 6.134–6.227 6.385–6.509 (m, 1H + 1H + 1H, r + s + t); 6.914–7.470 (m, 8H, h).

#### 2.2.5. Polymerization of macromonomers

Side chain grafted comb-like polymers with biphenyl group and O-LLA segments were prepared by the radical polymerization of the macromonomers, **AOLA<sub>x</sub>O6OPPO<sub>n</sub>**, prepared above. General routine was as follows (**AOLA<sub>10</sub>O6OPPO<sub>4</sub>** as an example): **AOLA<sub>10</sub>O6OPPO<sub>4</sub>** (0.1069 g, 95.7 μmol) was placed in a 10 mL flask, and purged with dry Argon gas to remove oxygen before THF 3 mL and AIBN (46 μL AIBN/THF solution, 0.96 μmol) were added. The resulting mixture was kept for 10 h at 70 °C under magnetic stirring under Argon atmosphere. The targeted polymers were collected in good yield by filtration as white solid after poured the reaction mixture into petroleum ether to precipitate and then vacuum dry overnight for further characterization.

#### 2.3. Measurements and characterization

<sup>1</sup>H NMR was recorded on a AVANCE 300M/400M spectrometer (Bruker) in CDCl<sub>3</sub> or DMSO-D<sub>6</sub> at room temperature. By <sup>1</sup>H NMR,

**Table 4**  
Phase transition temperatures (°C) and degree of crystallinity of P-AOLAxO6OPPOn.

Samples	$T_g^a$	$T_g$	$T_m$	$T_i$	$\Delta H_m$ (J/g)	$\chi_c$ (%) <sup>b</sup>
P-AOLA <sub>10</sub> O6OPPO4	-3.1	24.8	43.1	—	—	—
P-AOLA <sub>20</sub> O6OPPO4	-3.8	39.8	106.4	120.5	14.32	15.28
P-AOLA <sub>30</sub> O6OPPO4	-5.5	31.6	106.9	120.6	23.72	25.31
P-AOLA <sub>40</sub> O6OPPO4	-5.1	41.1	106.9	127.9	33.08	35.30
P-AOLA <sub>10</sub> O6OPPO6	-4.4	30.1	61.0	—	—	—
P-AOLA <sub>20</sub> O6OPPO6	-4.7	24.5	107.9	131.9	22.17	24.36
P-AOLA <sub>30</sub> O6OPPO6	-4.3	45.1	105.7	127.3	10.39	11.42
P-AOLA <sub>40</sub> O6OPPO6	-4.5	20.1	107.2	132.3	12.65	13.90
P-AOLA <sub>10</sub> O6OPPO8	-4.2	25.3	68.9	106.0	—	—
P-AOLA <sub>20</sub> O6OPPO8	-4.2	44.2	106.0	137.6	31.70	33.80
P-AOLA <sub>30</sub> O6OPPO8	-5.4	36.8	106.4	139.2	36.70	39.20
P-AOLA <sub>40</sub> O6OPPO8	-5.5	41.4	106.8	130.3	40.10	42.80

<sup>a</sup> The  $T_g$ 's are the glass transition temperatures of the polyacrylate ester main chain parts;

<sup>b</sup> the  $\Delta H_m$  of complete crystal of PLLA is 93.7 J/g.

the DPs of O-LLAs,  $DP = a + 1$ , where the values of  $a$  were evaluated by comparing the proton peak areas of triple peak  $\alpha$ -CH<sub>2</sub>- of active -O-R at  $\delta$ (ppm) = 4.15 with those of chiral -\*CH- of PLLA at  $\delta$ (ppm) = 5.17 (Fig. 1, where the  $H$  peaks were noted).

GPC measurements were performed on an HPLC equipped with 515HPLC pump, Waters 2414 Refractive Index Detector and Ultravis detector and HR3/HR4/HR6 columns at 1.00 mL/min using THF as eluent under 40.0 °C with Polystyrene standard (Shodex Standard SL-105, Japan). The samples were prepared by passing the THF solution through a short neutral Al<sub>2</sub>O<sub>3</sub> to remove any metal cations and then pass 0.22  $\mu$ m microfilter film.

UV and the Circular Dichroism (CD) spectra were recorded on J-810-150L Spectropolarimeter (Jasco, Japan) from 190 nm to 550 nm at scan rate 0.1 nm using acetonitrile solvent under inert N<sub>2</sub> at 20 L/min, cell length 0.5 mm, pure acetonitrile as blank. The  $[\theta]$  value was only contributed LA part and thus calculated based on the O-LLA segments.

Differential Scanning Calorimeter (DSC) measurements were performed on a DSC-SP (Rheometric Scientific Inc., New Jersey, USA) from -50–200 °C under inert N<sub>2</sub> atmosphere with a scanning rate of 10 °C/min. Glass transition temperatures ( $T_g$ ) were determined by the mid point of baseline shift. Polarized Optical Microscope observation was performed on a Olympus BX51p with a Linkam THMSE600 cold-hot stage (-196–600 °C) and photographed by a Q-imaging Micropublisher 5.0RTV (CCD). The thermal transition temperatures were determined combining the DSC measurement and POM observation.

The X-ray diffraction measurements were performed on a Rigaku D/Max-rB X-ray diffractometer equipment (Japan) with Cu-K ( $\lambda = 1.54056 \text{ \AA}$ ), 40 KV\* 100 mA and scanned from 0.5° to 5° at a scan rate of 2°/min and 3°–50° at 4°/min. The samples were spin-coated or melt-pressed into pellets and annealed at 80 °C for 12 h.

### 3. Results and discussions

#### 3.1. Preparation of initiators

The preparation of mono-substituted derivatives, HOPPOn, is the most important step, while the resulting mixtures always contain three possible compounds HOPPOH, HOPPOn and nOPPOn because of the o-alkylation's selectivity of homo- and bis- substitutions biphenol, HOPPOH. Recrystallization only is not enough to separate. The pure HOPPOn were obtained by a two-step operation according to the different solubility in different solutions: HOPPOH is completely removed first by dissolving in alkaline solution and then nOPPOn can be removed as solid by filtration of the hot Ethanol/water alkaline solution. The HOPPOn could be recovered by neutralization of the resulting filtrate. Further twice recrystallization is enough to get pure HOPPOn free of HOPPOH and nOPPOn. Best for initiators could be achieved by phase-transfer reaction of HOPPOn with corresponding  $\omega$ -HO-alkane bromide or chloride for ROP of L-LA.

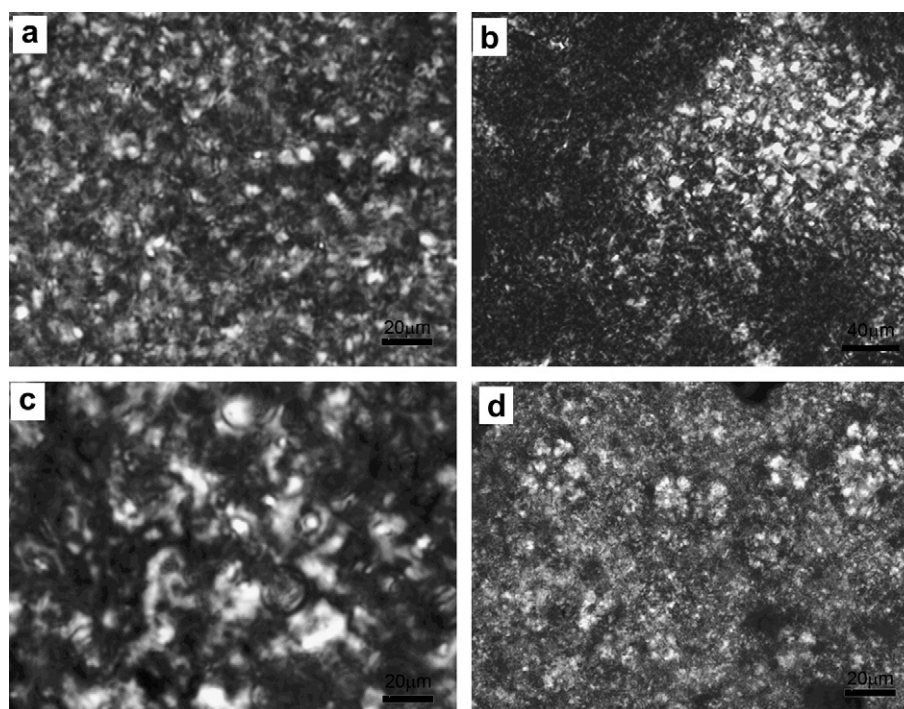


**Fig. 2.** POM textures of P-AOLAxO6OPPOn. a, P-AOLA<sub>30</sub>O6OPPO4 at heating the original sample to 84 °C; b, P-AOLA<sub>40</sub>O6OPPO6 heated to 104 °C; c, P-AOLA<sub>20</sub>O6OPPO8 cooled to 111 °C; d, P-AOLA<sub>40</sub>O6OPPO8 heated to 113 °C.

### 3.2. Preparation and characterization of AO-LAxO6OPPOn

#### 3.2.1. ROP of L-LA

The HO-group of HO6OPPOn was sufficient active for the ROP of L-Lactide if SnOct<sub>2</sub> was used as catalyst but, for best results; need to be recrystallized with dry toluene just before use to remove any HO-containing molecules. Better control of the molecular weights of the resulting O-LLAs can be achieved when SnOct<sub>2</sub> was distilled under vacuum for three times or more just before use. It is also important that the L-LA solid were recrystallized with toluene (Na/K dry) three times or more and used just before use. Among the solvents used to recrystallize the L-LA, toluene is easy to purify and dry for the best results.

The ROP reaction was almost complete around 12 h at 80 °C in toluene but best results were achieved for 10 h at 100 °C.

The SnOct<sub>2</sub> was removed by washing with cold HCl (0.5 M) aqueous solution and water. Generally, the O-LLA samples with lower feed ratios often have much lower yields due to the more apparent weight loss caused by water-dissolve of low molecular weight O-LLAs when washing with water.

#### 3.2.2. Molecular weight of O-LLA segments

The molecular weights of O-LLAs were determined by <sup>1</sup>H NMR, GPC and listed in Table 1. The measured molecular weights of O-LLAs were in good agreement with the theoretical results and found to be well controlled by the feed molar ratios of the SnOct<sub>2</sub> catalyst, L-LA to HO6OPPOn ( $n = 4, 8$ ) providing enough SnOct<sub>2</sub> was used.

#### 3.2.3. Preparation of macromonomers AOLAxO6OPPOn (AOLLA)

To form the polymerizable macromonomers, the acrylate esters of O-LLA segments, acrylic group was attached by reacting with HO-group of O-LLA. Considering that the HO-group percentages were very low in each HOLLAxO6OPPOn's, acrylic acid was used in excess amount and used in its activated state. The procedure involving the acrylic chloride, a highly active species, and triethylamine, proton absorbent, was fast but the products color are slight yellow and difficult to be avoided and removed. It changed much more when acrylic acid/DCC/DMAP was used instead. White powder samples were thus obtained from the later. However more acrylic acid was necessary to achieve better conversion of HOLLAxO6OPPOn to AOLAxO6OPPOn. For example, here 10 times excess of acrylic acid was used in this paper. The appearance of the peaks of CH<sub>2</sub> = CH– around 5.8 to 6.3 in <sup>1</sup>H NMR spectra and the proper amount of protons indicated the successful complete attachment of the acrylic group to the end of the O-LLA segments (as may have noted in Fig. 1, for example). Also a slightly increase of the average DP or the molecular weights of AOLAxO6OPPOn were observed from <sup>1</sup>H NMR, indicating the weight loss of AO-LLA molecules with lower DPs in the precipitation process due to their higher solubility in the cold ethanol solution. The weight loss of lower DPs also lead to the lower yields of AOLAxO6OPPOn, around 60% for  $x = 10$  and above 90% for  $x = 40$ . The molecular weights of the resulting products AOLAxO6OPPOn were then determined by <sup>1</sup>H NMR and GPC measurements and listed in Table 1.

### 3.3. Preparation and characterization of Poly-AOLAxO6OPPOn

The macromonomers, as acrylate esters, can polymerize to form comb-like polymers with polyacrylate as main chain and O-LLA segments with mesogenic end group at the free end as side chains. As the DP of AO-LLA may be controlled by changing the initiator feed ratios, the resulting P-AOLLA will be formed with a distinct side chain length. The molecular weights of the polymers P-AOLLA characterized by GPC were listed in Table 2, together with the <sup>1</sup>H NMR results listed for the calculation of the DP of AO-LLA segments

and the DP of P-AOLLA. The disappearance of the peaks in <sup>1</sup>H NMR spectra between 5.8 and 6.3, the acrylate part, is also distinct. The polymerization of AO-LLA can be again confirmed by the appearance of peaks at higher molecular weight region and the disappearance of the peak corresponding to a lower molecular weight of AO-LLA by GPC. The only single peak thus detected from each GPC was corresponding to the Mw/Mn of P-AOLAxO6OPPOn as listed in Table 2.

### 3.4. Thermal behavior of macromonomers AOLAxO6OPPOn and Poly-AOLAxO6OPPOn

The thermal behavior was evaluated by DSC measurements and transition temperatures were confirmed again with POM observations. One or two heat scans were performed for macromonomers (Table 3) and polymers (Table 4).

By POM observation on a hot stage with crossed polarizer all these materials showed distinct birefringent texture, characteristic

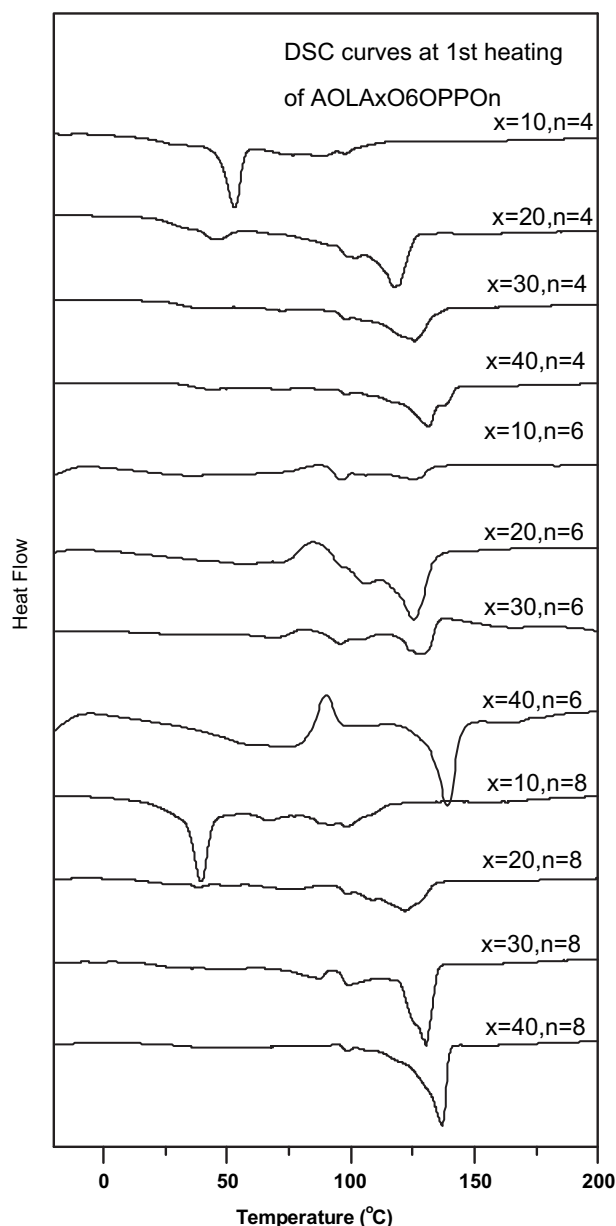


Fig. 3. DSC curves of AOLAxO6OPPOn.



of layered smectic mesophase, Fig. 2, until  $T_i$  was reached. Similar to what had been reported by Samuel I. Stupp, not only the  $T_m$  and  $T_i$  of both the **AOLAxO6OPPOn** and **P-AOLAxO6OPPOn** samples moved to higher temperature end, but also the LC phase ranges of higher regime liquid crystal phases were decreased with longer O-LLA segments length. Again, the  $T_m$  and  $T_i$  of the **AOLAxO6OPPOn** became higher after polymerized to **P-AOLAxO6OPPOn**. POM observations also give evidence that between  $T_g$  and  $T_m$ , POM textures also existed if only treated by proper cut or press to confirm, however the viscosity was relatively high compared to samples at higher temperatures. This means that LC phases may exist at these temperature ranges, as reported by Samuel I. Stupp.

From DSC curves, each macromonomer **AOLAxO6OPPOn** (Fig. 3) showed a distinct  $T_g$  around 30 °C and the  $T_g$  increased with the increase of the degree of polymerization,  $x$ , of O-LLA segments from  $x = 10$  to 40. The fact that  $T_g$ s of **AOLAxO6OPPOn** and **P-AOLAxO6OPPOn** with  $x = 10$ , presented as distinct relative apparent endothermic peaks, not baseline shifts only as those samples with

higher  $x$  values as shown in Fig. 4, indicates the melting behavior of PLLA segments but not a simple glass transition behavior.

For the **P-AOLAxO6OPPOn**s, compared with those corresponding macromonomers, **AOLAxO6OPPOn**s,  $T_g$ s moved to higher temperature ranges and another  $T_g'$  appeared distinctly at lower temperature range, around  $-4 \sim -5$  °C, denoted to those of the polyacrylate ester main chains, and generally were more apparent at second scans. However they are still not distinguished more apparent at the second scans than those of  $T_g$ . The  $T_g'$ s baseline-shifted not large enough compared with the  $T_g$ s of O-LLA segment parts. This is apparently corresponding to the relative higher percentage of O-LLA segments and the lower percentage of acrylate parts in **P-AOLAxO6OPPOn**. The almost constant  $T_g'$ s are also the indication of the similarity DPs of **P-AOLAxO6OPPOn**s, which were listed in Table 2, while those always increase of  $T_g$ s changed much from 20 to 40 °C for **P-AOLAxO6OPPOn**s with the apparent increase of  $x$ , from  $x = 10$  to  $x = 40$ . Anyway these values are still lower than 57 °C, the normal Tg of those of high molecular weight PLLA [39].

Low  $T_g$ s are good help for the movement of the O-LLA segments to form layered smectic phase which existed in both **AOLAxO6OPPOn** and **P-AOLAxO6OPPOn** samples. Generally, both types of compounds have more than one peak on DSC curves indicating the formation of mesophase at higher temperatures above  $T_g$ . Also listed in Table 4 are the degrees of crystallinity,  $\chi_c$ , of the **P-AOLAxO6OPPOn** materials. Apparently the  $\chi_c$  [40] values increased with the increase of LLA chain length, indicating a stronger crystallization tendency for higher molecular weight

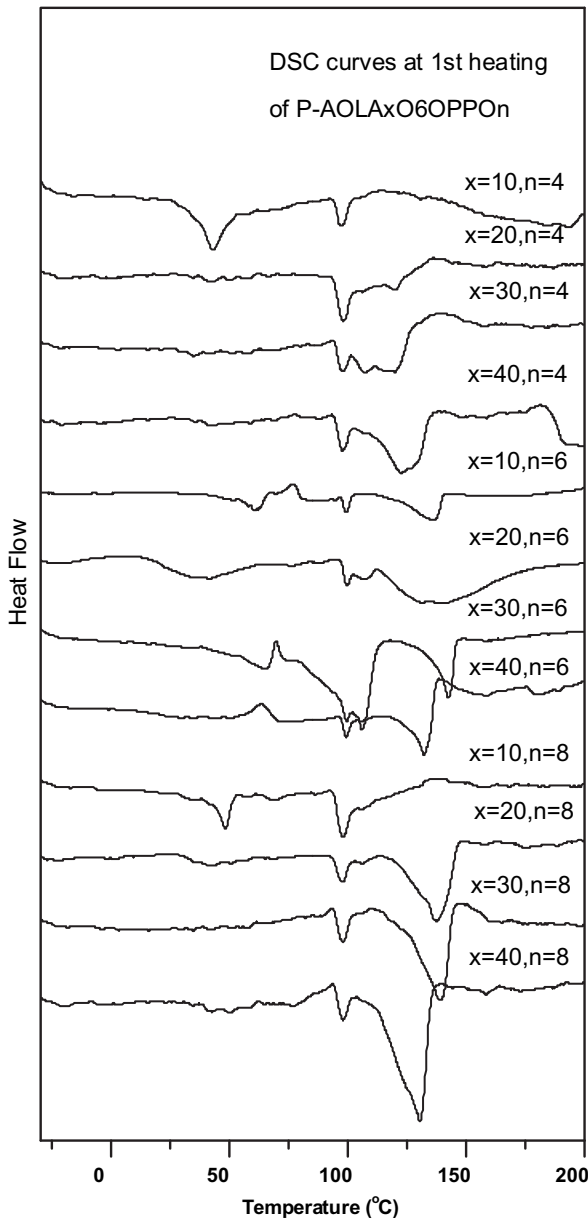


Fig. 4. DSC scans of **P-AOLAxO6OPPOn**.

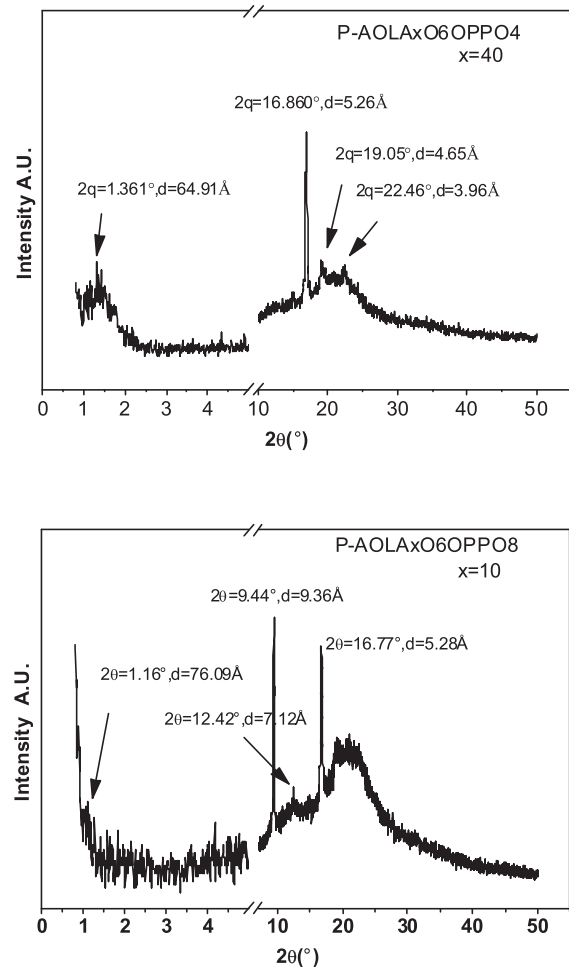


Fig. 5. XRD scans of **P-AOLAxO6OPPO4** at 80 °C and **P-AOLAxO6OPPO8** at 80 °C.

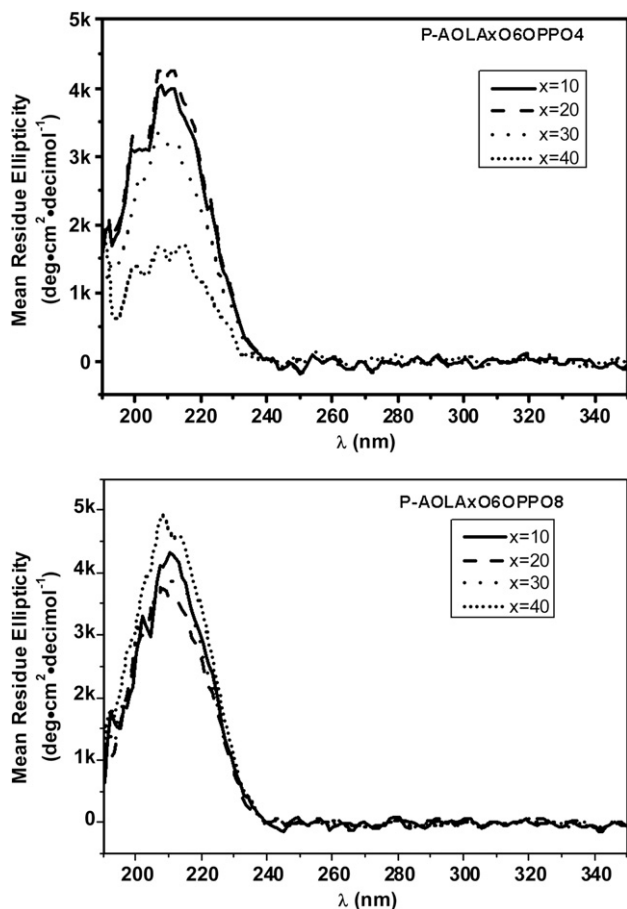


Fig. 6. Typical CD spectra of P-AOLAxO6OPPO4 and P-AOLAxO6OPPO8.

PLLA. The  $\chi_c$  values are important for the preparation of layered phase, because the crystals of PLLA are often spherulites.

### 3.5. Phase behaviors of P-AOLAxO6OPPOn

X-Ray diffraction characterizations were performed to confirm the LC phase structure which may exist in P-AOLAxO6OPPOn and several were listed in Fig. 5. Peaks in the wide angle region, strong one at  $2\theta = 16.86^\circ$  and those weak peaks at  $2\theta = 19.05^\circ, 22.46^\circ$  (corresponding to  $d = 5.26 \text{ \AA}, 4.65 \text{ \AA}, 3.96 \text{ \AA}$ ), were found to be the (110), (100), (203), (205) diffractions of  $\alpha$ -form crystal of PLLA as have been reported by Miyata [41,42]. This is rational result for PLLA materials which formed  $\alpha$ -crystal from solution and bulk. This implies that the LC phase of P-AOLAxO6OPPOn was apparently formed from the melting of PLLA  $\alpha$ -crystals. Unfortunately, no obvious peaks of layered structure were found by temperature variable X-ray diffraction measurements without or with only short time annealing, while samples after overnight annealing have peaks appeared in small angle region. Because of the high molecular weight, the chemical bonding attachment at both ends of PLLA segments and the higher viscosity of P-AOLAxO6OPPOns, the ordering of the PLLA segments to form mesophases was much slower than those of common side chain Liquid Crystal Polymers and also chol-LAxOH samples. Thus reasonable frozen mesophases should exist after annealing overnight long and quenching to ice-cold metal plate and be observed by X-Ray Diffraction measurements. The weak peaks found at  $d = 6.49 \text{ nm}$  for P-AOLA<sub>40</sub>O6OPPO4 annealing at  $80^\circ\text{C}$  overnight and that at  $d = 7.61 \text{ nm}$  for P-AOLA<sub>10</sub>O6OPPO8 annealing at  $80^\circ\text{C}$  overnight indicating the

presence of the layered structures for P-AOLAxO6OPPOn polymers (Fig. 5). This is in good agreement with cholesterol initiated O-LLA materials, which form layered phase reported by Samuel I. Stupp.

### 3.6. CD spectra of P-AOLAxO6OPPOn

All the CD spectra of P-AOLAxO6OPPOn materials showed typical positive cotton effect, a peak can be observed for each polymer around 210 nm, the absorption of C=O groups of O-LLA segments, with  $[\theta] = 4000\text{--}5000 \text{ deg}\cdot\text{cm}^2 \text{ decimol}^{-1}$  (Fig. 6). This indicated that stable helical structure has formed for these polymers because the  $[\theta]$  value is comparative with any high Mw PLLA materials with good helical structure. The CD spectra give clear evidence that the P-AOLAxO6OPPOn materials may show strong optical rotation power if they are proper treated to form ordered films. Considering that LC materials can self-organized easily to form ordered materials, the study of P-AOLAxO6OPPOn may be used as optical materials in the future.

## 4. Conclusions

Series of mesogenic biphenol derivatives with active HO-group have been used as initiators successively to form Oligomeric L-LA materials with controlled molecular weight by adjusting the feed ratios by Ring-Opening Polymerization of LLA with SnOct<sub>2</sub> catalyst. Main Chain polymers P-AOLAxO6OPPOn were finally prepared by free radical polymerization of these polymerizable macromonomers esters that obtained by attaching acrylic group to these Oligomeric L-LA materials correspondingly. These macromolecules can be prepared with a controlled LLA length confirmed by <sup>1</sup>H NMR and GPC. All these materials can form good LC smectic phase from  $\alpha$ -crystal. The O-LLA segments are in helical structure and this makes the resulting polymer materials good candidate of optical materials.

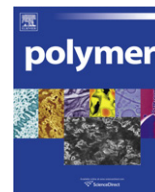
## Acknowledgements

This work was financially supported by the National Natural Foundation of China (No. 20304006) and Key Technologies R&D Program of Shandong Province, China (No. 200810002017). The authors also thank much for the kind help of Prof. Zaijun Lu of Shandong University for GPC measurements and kind discussions. The authors thank the Prof. Minghua Liu, Dr. Penglei Chen (Institute of Chemistry, Chinese Academy of Sciences (CAS)).

## References

- [1] Zhao YL, Shuai XT, Chen CF, Xi F. Chem Mater 2003;15:2836–43.
- [2] Goddard H, Kenneth KM, Sosely OS. Eur Pat Appl 1988;830866(A2):25.
- [3] Bhardwaj R, Blanchard J. Int J Pharm 1998;170:109.
- [4] Winet H, Bao JY. J Biomed Mater Res 1998;40:567.
- [5] Hedrick JL, Trollsas M, Hawker CJ, Atthoff B, Claesson H, Heise A, et al. Macromolecules 1998;31:8691.
- [6] Breitenbath A, Kissel T. Polymer 1998;39:3261.
- [7] Fujiwara T, Miyamoto M, Kimura Y, Sakurai S. Polymer 2001;42:1515.
- [8] Lee D, Teraoka I, Fujiwara T, Kimura Y. Macromolecules 2001;34:4949.
- [9] D'Angelo S, Galletti P, Maglio G, Malinconico M, Morelli P, Palumbo R, et al. Polymer 2001;42:3383.
- [10] Nijenhuis J, Grijpma DW, Pennings AJ. Macromolecules 1992;25:6419.
- [11] Kister G, Cassanas G, Vert M. Polymer 1998;39:267.
- [12] Degee P, Dubois P, Jerome R. Macromol Symp 1997;123:67.
- [13] Leengslag JW, Pennings AJ. Makromol Chem 1987;188:1809.
- [14] Spassky N, Wisniewski M, Pluta C, LeBorgne A. Macromol Chem Phys 1996;197:2627.
- [15] Okihara T, Tsuji M, Kawaguchi A, Katayama K, Tsuji H, Hyon SH, et al. J Macromol Sci Phys 1991;B30:119.
- [16] Miyata T, Masuko T. Polymer 1997;38:4003.
- [17] Green MM, Park JW, Sato T, Teramoto A, Lifson S, Selinger RLB, et al. Angew Chem Int Ed 1999;38:3138–54.
- [18] Rowan AE, Nolte RJM. Angew Chem Int Ed 1998;37:63–8.
- [19] Nakano T, Okamoto Y. Chem Rev 2001;101:4013–38.

- [20] Tang HZ, Lu YJ, Tian GL, Capracotta MD, Novak BM. *J Am Chem Soc* 2004; 126:3722–3.
- [21] Yashima E, Maeda K, Furusho Y. *Acc Chem Res* 2008;41:1166–80.
- [22] Tang BZ, Kotera N. *Macromolecules* 1989;22:4388–90.
- [23] Okamoto Y, Suzuk K, Yuki HJ. *Am Chem Soc* 1979;101:4763–5.
- [24] Okamoto Y, Yashima E. *Prog Polym Sci* 1990;15(2):263–98.
- [25] Yu ZN, Wan XH, Zhang HL, Chen XF, Zhou QF. *Chem Commun*; 2003:974–5.
- [26] Cui JX, Liu AH, Zhi JG, Zhu ZG, Guan Y, Wan XH, et al. *Macromolecules* 2008;41:5245–54.
- [27] Zhi JG, Zhu ZG, Liu AH, Cui JX, Wan XH, Zhou QF. *Macromolecules* 2008;41:1594–7.
- [28] Shibashima K, Seide SW, Novak BM. *Macromolecules* 1997;30:3159.
- [29] Xue QB, Kimura T, Fukuda T, Shimada S, Matsuda H. *Liquid Crystals* 2004;31 (2):137–43.
- [30] Sato T, Sato Y, Umemura Y, Teramoto A, Nagamura Y, Wagner J, et al. *Macromolecules* 1993;26:4551.
- [31] Green MM, Peterson NC, Sato T, Teramoto A, Cook R, Lifson S. *Science* 1995; 268:1860.
- [32] Kobayashi J, Asahi T, Ichiki M, Suzuki H, Watanabe T, Fukuda E, et al. *J Appl Phys* 1995;77:2957–73.
- [33] Tajitsu Y, Hosoya R, Maruyama T, Aoki M, Shikinami Y, Date M, et al. *J Mater Sci Lett* 1999;18:1785–7.
- [34] Kimura T, Fukuda T, Shimada S, Matsuda H. *Chem Lett* 2004;33:608–9.
- [35] Hwang JJ, Iyer SN, Li LS, Claussen R, Harrington DA, Stupp SI. *PNAS* 2002;99:9662–7.
- [36] Klok H, Hwang J, Iyer S, Stupp SI. *Macromolecules* 2002;35:746–59.
- [37] Kowalski A, Duda A, Penczek S. *Macromol Rapid Comm* 1998;19:567–72.
- [38] Zhang QX. Master thesis, Shandong University (China) 2007.
- [39] Jamshidi K, Hyon SH, Ikada Y. *Polymer* 1988;29:2229–34.
- [40] Fischer EW, Sterzel HJ, Wegner G. *Colloid Polym Sci* 1973;251:980–90.
- [41] Yoshito I, Khosrow J, Hideto T, Suong HH. *Macromolecules* 1987;20(4):904–6.
- [42] Tadakazu M, Toru M. *Polymer* 1997;38:4003–9.



# Controlling the morphology of micrometre-size polystyrene/polyaniline composite particles by Swelling–Diffusion–Interfacial-Polymerization Method

Yunxing Li<sup>a</sup>, Zhaoqun Wang<sup>a,\*</sup>, Chunjian Wang<sup>a</sup>, Zhen Zhao<sup>a</sup>, Gi Xue<sup>a,b</sup>

<sup>a</sup> Department of Polymer Science and Engineering, School of Chemistry and Chemical Engineering, Nanjing University, Nanjing 210093, China

<sup>b</sup> State Key Laboratory of Coordination Chemistry, Nanjing National Laboratory of Microstructures, Nanjing University, Nanjing 210093, China

## ARTICLE INFO

### Article history:

Received 5 September 2010

Received in revised form

19 October 2010

Accepted 13 November 2010

Available online 23 November 2010

### Keywords:

Conducting polymer

Core-shell composite particle

Diffusion control

## ABSTRACT

By means of the “Swelling–Diffusion–Interfacial-Polymerization Method” (SDIPM), we successfully coated polyaniline (PANi) onto micrometre-size, uncharged polystyrene (PS) particles, which were synthesized by dispersion polymerization. After initially forming aniline-swollen PS particles, diffusion of the aniline toward the aqueous phase was controlled through a slow addition of hydrochloric acid, eventually leading to its polymerization on the substrate particle surface. The resultant PS/PANi composite particles have been extensively characterized using scanning electron microscope (SEM), transmission electron microscope (TEM), Fourier transform infrared (FTIR) and Raman spectroscopy, X-ray photoelectron spectroscopy (XPS), and C, H, and N elemental microanalysis. At very low aniline/PS weight ratio, the thin, uniform, but intact PANi overlayer was obtained owing to its unique “inside-out” formation mechanism and considerably high efficiency of aniline to transform into the resultant composites. As increasing the initial amount of addition of aniline, the uniform size and well-defined morphology of the PS/PANi core-shell composite particles could still be maintained with a relatively high PANi mass loading yield.

© 2010 Elsevier Ltd. All rights reserved.

## 1. Introduction

Synthesis of conducting composites has been focused on intense researches over the last 15 years for alleviating the poor processability of intrinsically conducting polymers [1–9]. Such hybrid materials have the advantages of unique properties owing to the core constituted by inorganic particle or vinyl-polymer endows the system with mechanical properties while a conducting polymer as the shell provides its conductivity [10–12]. Hence, as potential materials they are promising for application in versatile fields such as optoelectronic devices, chemical sensors, fuel cell, lightweight batteries and space science [13–17].

Amongst conducting polymers, polyaniline (PANi) is the most attractive one because of its electronic and optical properties, coupled with excellent environmental stability [18–24]. Up to now, the deposition of PANi onto various colloidal particle substrates has been extensively investigated, especially when polystyrene (PS) is used for the core, giving its spherical shape as well as mono-dispersity. Hence, PANi-coated PS latex is one of the most promising candidates for conducting polymer composites. Despite

a massive amount of work on the synthesis and characterization of PS/PANi composite particles, total control over the structure and morphology, which has a significant effect on the ultimate properties of the composite particles, is not yet achieved and remains a scientific challenge.

In general, all the synthetic methods for preparing conducting composite particles can be divided into deposition method and in situ polymerization method based on the locus of polymerization of aniline monomer. Deposition method means the monomer is first dissolved in medium in the presence of the seed particles, and then polymerization is initiated by the addition of an aqueous solution of the oxidant. The suspended seed particles were coated with conducting polymer by in situ and induced deposition from the aqueous medium. Armes's group initiated the polymerization of aniline monomer in a strongly acidic solution in the presence of the PS seed latex stabilized by poly(N-vinylpyrrolidone) (PVP) and explored various surface modification strategies to improve the coating of PANi [25]. Reynaud and co-workers reported a relatively high coverage of PANi based on crosslinked PS particles stabilized by a surfactant bearing an amide group, which allows the formation of hydrogen bond with the PANi backbone [26]. In contrast to the simple deposition or induced deposition of the formed PANi by deposition method, in situ polymerization method means that one or more of the reactants is enriched or immobilized on the substrate surface inducing

\* Corresponding author. Tel.: +86 25 8161 5138; fax: +86 25 8331 7761.

E-mail address: [zqwang@nju.edu.cn](mailto:zqwang@nju.edu.cn) (Z. Wang).

polymerization of aniline monomer in a given area. Zhou and co-workers assembled polyelectrolyte (PE) multilayers onto melamine formaldehyde particles via the layer-by-layer (LbL) self-assembly technique [27]. Subsequently, aniline monomer was absorbed into PE multilayers and oxidized in situ. The amount of PANi mass loading and thickness of PANi shells were adjusted with the change of the initial PE layer numbers. Liu et al. immobilized oxidant on the surface of PS particles by electrostatic interaction, and then initiated polymerization of aniline monomer on the surface of PS particles [28]. Besides, in order to increase the thickness of the PANi shell, the seeded growth method was applied repeatedly. Obviously, time-consuming surface pretreatment of the work mentioned above complicates the synthetic procedure, even though it could generally optimize the deposition architecture of the PANi overlayer.

Recently, we reported a distinctly novel strategy, so-called “Swelling–Diffusion–Interfacial-Polymerization Method” (SDIPM), which could be classified into interfacial polymerization method [29]. It can fabricate sub-micrometre core-shell PS/PANi composite particles with well-defined shape regardless of the surface electrical property of the PS seed particles. In comparison with the widely used conventional methods containing in situ polymerization or induced deposition, SDIPM presents a unique “inside-out” mechanism to afford much more effective controlling over the structure and morphology of the resultant PS/PANi composite particles by simply changing the aniline/PS weight ratio or the rate of addition of the doping acid.

In this work, PS particles, synthesized by dispersion polymerization using azoisobutyronitrile (AIBN) as initiator, were chosen as the seed particles, and thus these particles bear no chemically bound ionic groups. By means of SDIPM, we explored the success of coating PANi onto the substrate particles almost without surface charge and furthermore, independent of any other assistance, to fabricate micrometre-sized PS/PANi core-shell conductive composites with uniform size and well-defined morphology. Additionally, the influences of PVP, presenting to the PS surface derived from the dispersion polymerization, on the morphology of PS/PANi composite particles were investigated.

## 2. Experimental section

### 2.1. Materials

Styrene and aniline (AR, Shanghai Chemical Reagent Co.) were purified by distillation under reduced pressure. Azoisobutyronitrile (AIBN) of chemical reagent grade (Shanghai Chemical Reagent Co.) was purified by recrystallization in 95% ethanol. Ammonium persulfate (APS) of analytical reagent grade (Shanghai Chemical Reagent Co.) was purified by recrystallization in water. All the other chemicals were analytical reagent grade and used as received. Poly(vinylpyrrolidone) (PVP) with an average molar mass of 58 kg/mol (PVP K-30) was purchased from Acros Organics. Absolute ethanol, 95% ethanol, isopropanol and hydrochloric acid were purchased from Nanjing Chemical Reagent Co. Distilled water was applied for all of the polymerizations and treatment processes.

### 2.2. Synthesis of polystyrene seed particles

Polystyrene (PS) particles were prepared by dispersion polymerization. The PVP stabilizer (2.8 g) were dissolved in isopropanol (160 mL) and heated up to 70 °C in a four-necked round-bottom flask. It was purged with nitrogen to eliminate the inhibiting effect of oxygen. A solution of AIBN initiator (0.2 g) predissolved in styrene monomer (20 g) was added to the reaction vessel, with vigorous mechanical stirring. The polymerization was allowed to proceed for 24 h before cooling to room temperature. Subsequently,

the PS particles were purified by repeated centrifugation and redispersion cycle, washing three times with ethanol and then three times with water. Finally, the PS latex was diluted with water to solid content of 10 wt % before use.

### 2.3. Preparation of polystyrene/polyaniline composite particles

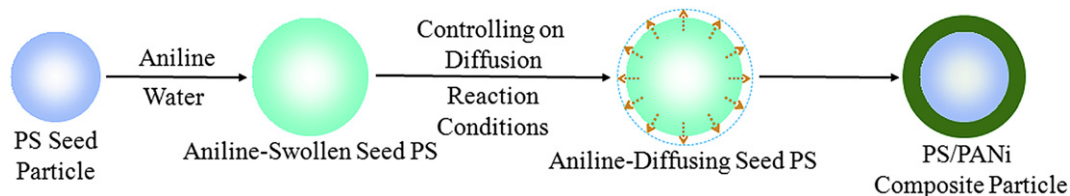
First, aniline was added to water at 0 °C and under ultrasonic treatment for 15 min followed by the addition of the PS seed particles. The mixture was stirred with ultrasonic assistance for 30 min at 0 °C to allow sufficient swell of aniline into PS seed particles, which was confirmed by the gradual disappearance of aniline droplets appearing initially after mixing the PS latex and aniline under optical microscope observation. The dispersion of aniline-swollen PS particles was transferred to a three-necked round-bottom flask in an ice bath. The aqueous solution of APS was added to the dispersion in one batch and the initial oxidant/monomer molar ration was fixed at 1:1. This was followed by the addition of hydrochloric acid (1 mol/L), also in an equimolar amount relative to aniline, dropwise via syringe. The temperature was maintained at 0 °C for the first 5 h of the polymerization, after which the polymerization was carried out for 18 h at room temperature. The solid content of the PS latexes was kept constant at 4 wt %, and the weight ration of aniline monomer to the seed latex was varied from 1:40 to 1:2. If the aniline/PS weight ratio was further increased, the system became colloiddally unstable, and finally, macroscopic precipitation and its amorphous suspensions, derived from the dissolving of PS in aniline and thus the disintegration of the microspheres, were observed. The resulting green PS/PANi composite particles were washed repeatedly by centrifugation until the supernatant became colorless. Finally, the product was dried in a vacuum oven for 48 h at 40 °C.

### 2.4. Characterization

The morphology of the PS seed particles and the resultant PS/PANi composite particles were observed both by scanning electron microscope (SEM) using an S-4800 instrument (Hitachi Co., Japan) operated at an accelerating voltage of 10 kV and transmission electron microscope (TEM) using a JEM-100 CX (JEOL Co., Japan) microscope. The samples were not sputter-coated with a metal overlayer for SEM study. X-ray photoelectron spectroscopy analysis was carried out on a VG ESCALAB MKII-X-ray photoelectron spectrometer. Fourier transform infrared (FTIR) analysis was performed with a Bruker VECTORTM 22 FTIR spectrometer (Bruker Co., Germany). Raman spectrum was measured by use of the MultiRam spectrometer (Bruker Co., Germany). A continuous wave Nd:YAG laser working at 1064 nm was employed for Raman excitation. A total of 200 scans were averaged in each spectrum obtained with laser power 10 mW. C, H, N elemental microanalyses of both PANi bulk power prepared in the absence of latex particles and PS/PANi composite particles were carried out on a CHN-O-Rapid instrument (Heraeus Co., Germany).

## 3. Results and discussion

The schematic process for “Swelling–Diffusion–Interfacial-Polymerization Method” (SDIPM) is displayed in Scheme 1. In the initial stage, upon mixing the monomer (i.e., aniline) with the original seed latex, the former would be enriched inside the seed particles after a certain period according to their good affinity, eventually forming monomer-swollen seed particles [30]. That is, the monomer is distributed mainly in the solid seed particles while the other reactants participating in the chemical reaction exists in the continuous phase, and hence the polymerization is almost restrained at this stage. Following the change on factors of



**Scheme 1.** Schematic representation of the proposed “Swelling–Diffusion–Interfacial-Polymerization Method” (SDIPM).

controlling the diffusion of the monomer from the seed particles toward the aqueous phase, the original thermodynamic equilibrium of the reactants between the two phases will be broken. During diffusing toward the aqueous phase, the monomer could encounter the other reactants existing in the water, such as oxidant APS in present system, to initiate interfacial reaction, i.e., chemical oxidation polymerization of the aniline at the external surface of the seed particles. Thus, it would yield readily coats on the seed particles simultaneously. As the formation proceeds, the swollen seed particles act as reservoirs that constantly release monomer under control to the external surface to keep the processes of diffusion and

interface reaction going. In brief, the incorporation of second component, i.e., PANi, with the seed particles can be carried out with a unique “inside-out” way, in contrast to the prevalent thinking toward random deposition or induced deposition. In the process, the outer surface of the seed particles is the necessary path where the diffusing monomer passes through. As a result, an overlayer of the PANi can be formed more efficiently and well controllable, moreover, with a homogeneous distribution independent of the surface modifications or functionalizations of the seed latex.

On the basis of the strategic considerations for SDIPM, systems have to meet following requirements: first, at least one of reactants

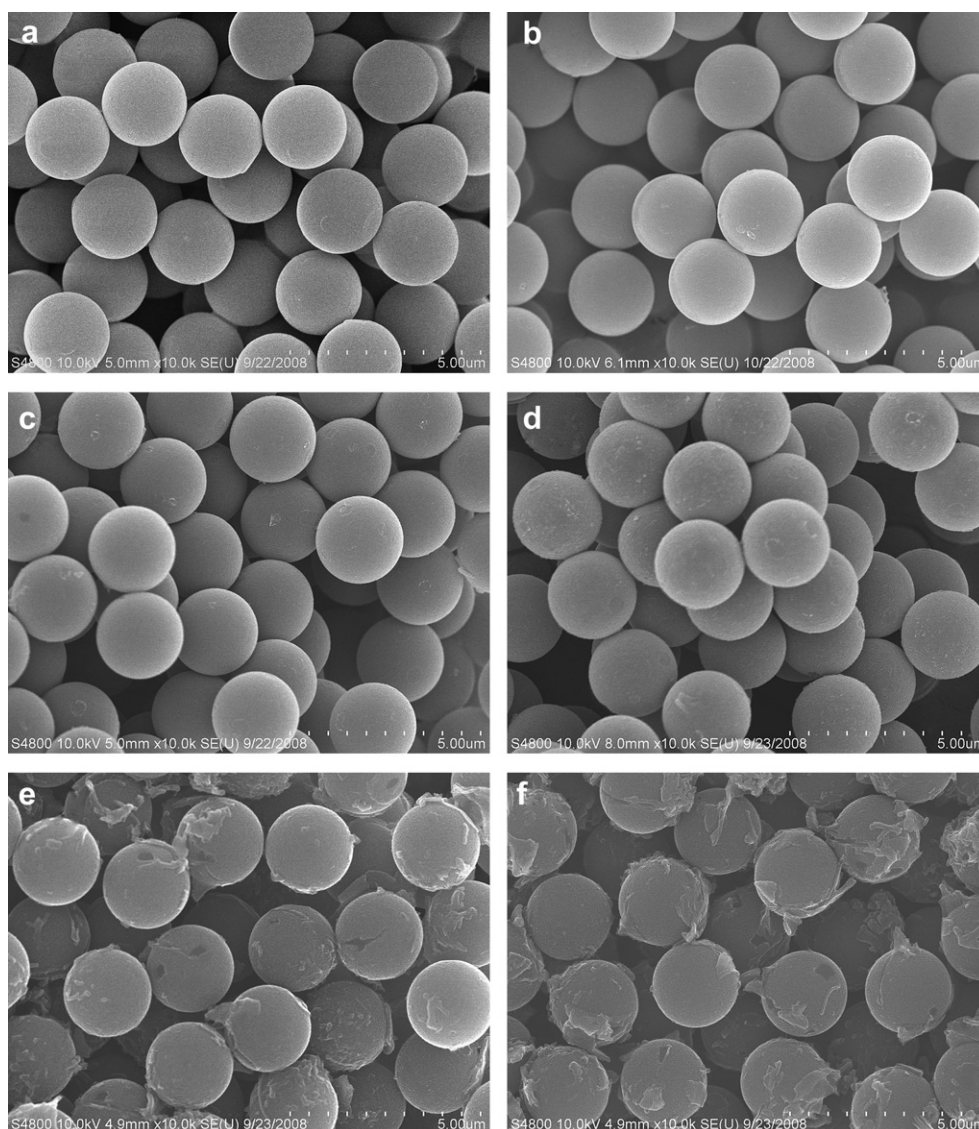


**Fig. 1.** SEM images of PS seed particles (a), and PS/PANi composite particles prepared by using different aniline/PS weight ratio: (b) 1:20, (c) 1:12, (d) 1:6, (e) 1:3, (f) 1:2.

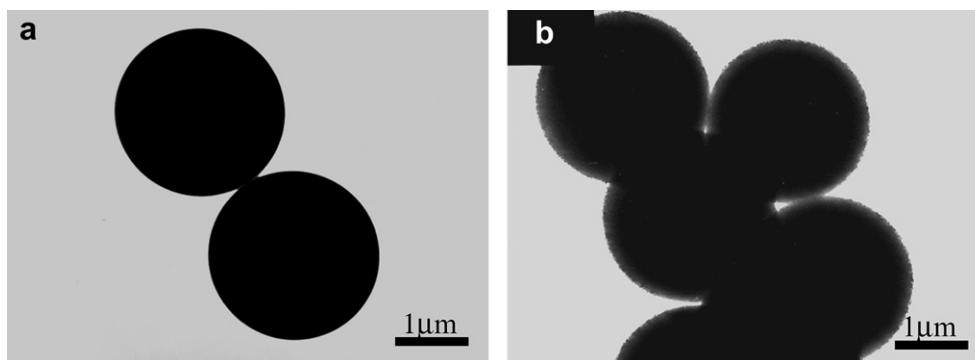


Fig. 2. TEM images of PS seed particles (a), and PS/PANi composite particles prepared by using aniline/PS weight ratio of 1:6 (b).

participating in the chemical reaction, preferably of the monomer, can be swelled into the selected seed beads whereas another involving initiator, catalyst etc. must exist in continuous phase. Second, effective manners of governing the absorbate diffusion from the seed beads toward the continuous phase can be found. In this system, the hydrochloric acid, acting as doping agent of conductive polymer, was used to control the diffusion since hydrophobic aniline should be transformed into hydrophilic aniline hydrochloride as adding HCl into the system.

Fig. 1 illustrates the scanning electron microscope (SEM) images of the PS seed particles, which were synthesized by dispersion polymerization, and PS/PANi hybrid particles prepared with different aniline/PS weight ratio from 1:20 to 1:2. When the aniline/PS weight ratio is lower than 1:3, the resultant composite particles show almost the same smooth surface as the original PS seed particles (Fig. 1b, c and d). Together with the elemental analysis, indicating that the weight percent of conducting polymer inside these composite particles was up to 12 wt %, these results suggested that the PS seed particles were uniformly and smoothly coated with PANi overlayers. It is no exaggeration to say that the morphology of the PS/PANi composite particles is so excellent that no direct evidence for the deposition of PANi overlayer is detected, especially at a relative high mass loading of PANi (12 wt %). The core-shell structure of the resultant composite particles can be visually displayed in TEM image. As shown in Fig. 2, a uniform thin ring around the PS core was clearly observed (Fig. 2b), different from the original PS particles (Fig. 2a). These results obviously exceed the previously reported ones that the PS/PANi composite particles with patchy and coarse morphology were obtained by the conventional methods at similar reaction condition [25]. This relatively perfect morphology can be comparable with the

micrometre-sized polystyrene/polypyrrole (PS/PPy) composite particles, whose easy control on morphology was acknowledged [31]. Only at higher concentration of aniline, a few of precipitate is observed on the surface of composite particles (Fig. 1e and f), which should be due to the predominance of aniline diffusing over its interfacial polymerization. With an increase in the initial amount of aniline, a large amount of aniline would diffuse outward, polymerize in medium and ultimately, the formed anomalous PANi fragments randomly deposit onto the composite particles surface. In addition, the precipitate was also partially arisen from the aniline originally dissolved in water based on the thermodynamic balanced distribution between the PS particles and water.

Fig. 3 displays X-ray photoelectron spectroscopy (XPS) of the PS/PANi composite particles with the lowest aniline/PS weight ratio (i.e. 1:20). The N (1s) core spectrum (Fig. 3a) can be fitted with three components at 399.2, 400.8 and 401.8 eV. The lowest binding energy (399.2 eV) is attributed to the neutral amine nitrogen, whereas the components at 400.8 and 401.8 eV are due to two cationic nitrogens. Moreover, two distinct peaks at 284.5 and 286.0 eV appeared in C (1s) core spectrum are also in conformity with the characteristics of HCl doped PANi, and they are attributed to C atoms linked to C or H atoms (284.5 eV) and N atom (286.0 eV), respectively. XPS is known to be powerful for investigating the surface compositions of colloidal particles. Armes et al. detailedly examined the surface of micrometre-sized PPy-coated PS and PANi-coated PS composite particles by XPS [32]. They affirmed that if the surface of PS particles was successfully coated by PPy or PANi overlayer, the corresponding N (1s) characteristic peaks would appear. Therefore, even at very low aniline/PS weight ratio, the PANi was successfully coated onto the surface of PS seed particles by the SDIPM.

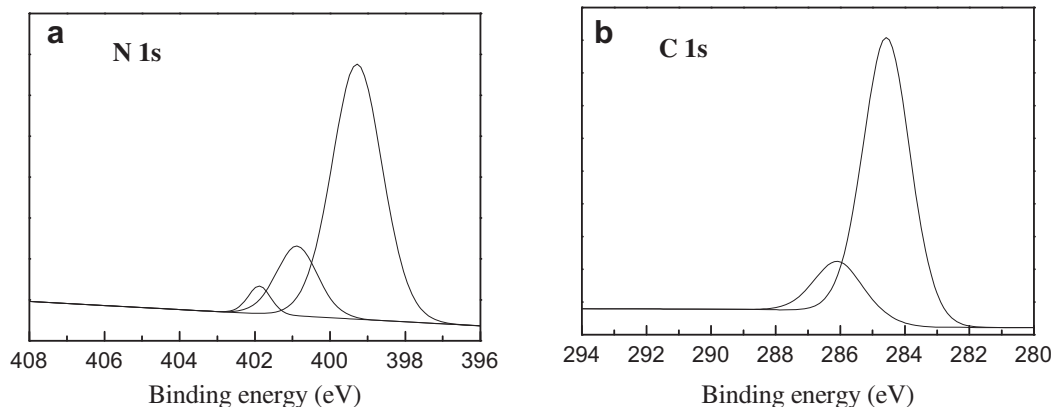
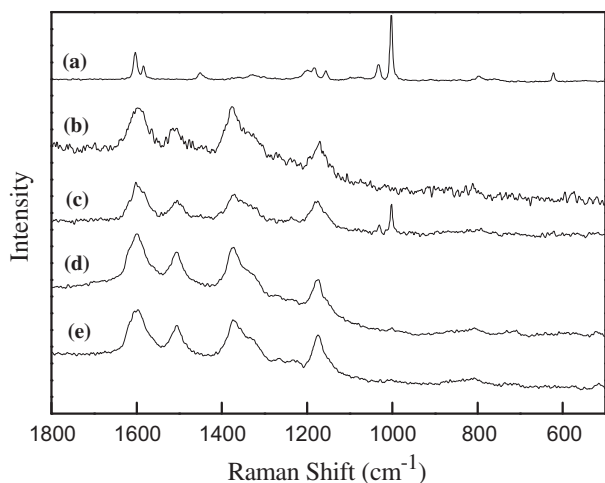
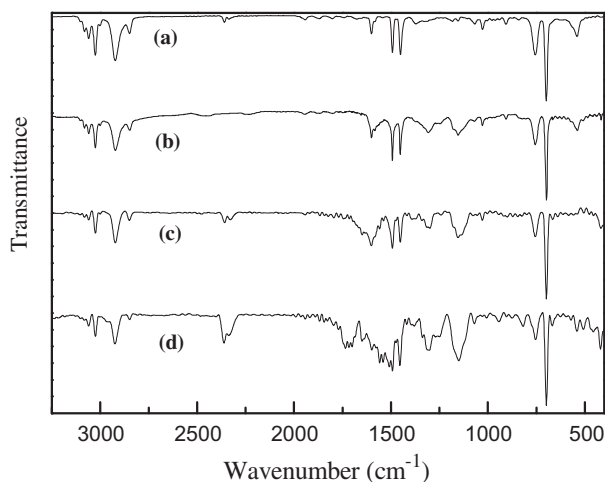


Fig. 3. XPS spectra (a) N (1s) and (b) C (1s) of PS/PANi composite particles with aniline/PS weight ratio of 1:20.



**Fig. 4.** Raman spectra of a dried PS latex (a), a dried PANi bulk powder (b), a heterogeneous admixture of 10 wt % PANi with 90 wt % PS (c), PS/PANi composite particle with aniline/PS weight ratio of 1:40 (d) and 1:20 (e).

The Raman spectra of a series of samples, involving PS particles, PANi bulk powder, a heterogeneous admixture of 90 wt% PS particles with 10 wt% PANi bulk powder, and the PS/PANi composite particles prepared with different aniline/PS weight ratio, are depicted in Fig. 4. In curve a for the PS, there is a very strong signal at about  $1002\text{ cm}^{-1}$ , which can be assigned to  $\nu_1$  ring-breathing mode of the PS component according to the Raman spectra of PS reported by previous workers [31b]. For the heterogeneous admixture (curve c), the signal at the same wave number is readily observed with a relatively high strength. It means that the PANi cannot obscure the signals of PS even though it has much higher content. However, in sharp contrast to the admixture, this characteristic signal completely disappears in the Raman spectrum (curve e) of the resulting composite particles prepared at a very low initial weight ratio of aniline/PS, i.e. 1:20. More importantly, when a much lower aniline/PS weight ratio of 1:40 was adopted, the strong signal of PS can also be well obscured by a newly formed overlayer, as shown in the curve d. Together with the all results mentioned above, therefore, we could come to the conclusion that not only the uniform and smooth, but also intact and perfect PANi overlayer was formed on the surface of “naked” PS particles without any surface functionalizations and modifications by the



**Fig. 5.** FTIR spectra of PS seed particles (a), PS/PANi composite particles with different aniline/PS weight ratio: (b) 1:12, (c) 1:6, (d) 1:4.

proposed SDIPM, even though adopting a very small initial amount of addition of aniline.

FTIR spectra of the PS seed particles and the PS/PANi composite particles prepared with different aniline/PS weight ratio (i.e. 1:12, 1:6 and 1:4) are represented in Fig. 5. For the PS latex, the main absorption bands are typical at  $1500, 1465, 750$  and  $698\text{ cm}^{-1}$ . In the spectra of PS/PANi composite particles, additional absorption bands attributed to the PANi component are notably observed at  $1300$  and  $1150\text{ cm}^{-1}$  [33]. These strong characteristic peaks of the PANi component could be regarded as other supporting evidence for the core-shell structure of the composite particles. Furthermore, the intensity of these peaks enhances proportionally in accordance with an increasing initial amount of addition of monomer, suggesting that the PANi mass loading is increased. In other words, increasing the thickness of PANi overlayer can be conveniently achieved by changing the weight ratio of aniline/PS based on the SDIPM.

Measurement of the PANi loading yield quantitatively reveals the efficiency for the monomer to transform into the resultant composite particles, and it was determined by comparing the nitrogen content of the PS/PANi composite particles relative to the theoretical value using C, H, and N elemental microanalyses. Fig. 6 depicts PANi loading yields of PS/PANi composite particles prepared by using different aniline/PS weight ratio. When the aniline/PS weight ratio was lower (e.g., 1:12, 1:9), there was the great efficiency above 90%. Therefore, almost entire transform of aniline at its low added amount, as an outstanding advantage of the SDIPM compared to the widely used conventional synthetic protocols, can still be achieved by using the PS seed particles without surface charge and further pretreatments. This is also the reason of successfully obtaining the smooth, intact PANi overlayers at very low concentration of aniline. With increasing aniline/PS weight ratio, the values of loading yield decline, but a plateau value is soon reached and maintains a relatively high value above 80%. In addition, the PS/PANi composite particles are still provided with the smooth surface when the aniline/PS weight ratio is high to 0.17 (i.e. 1:6) as shown in Fig. 1d.

PS seed particles used in our system were specially prepared. Almost all of the PVP adsorbed on the surface of the seed particle were washed off [34]. Direct evidence could be found in the FTIR spectra (Fig. 5a), in which the characteristic absorption band at  $1660\text{ cm}^{-1}$  attributed to PVP is hardly be detected. In order to investigate the influence of the existence of PVP on morphology of PANi overlayer prepared by SDIPM, PS/PANi composite particles were fabricated by using PVP-stabilized and “naked” PS seed particles, respectively, at constant aniline/PS weight ratio of 1:6.

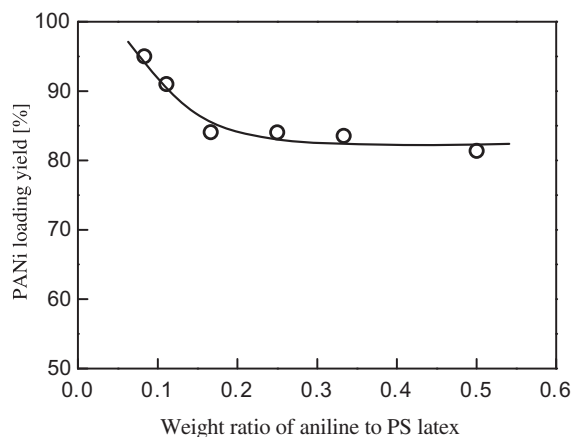


**Fig. 6.** PANi loading yields according to the swelling–diffusion–interfacial-polymerization method.



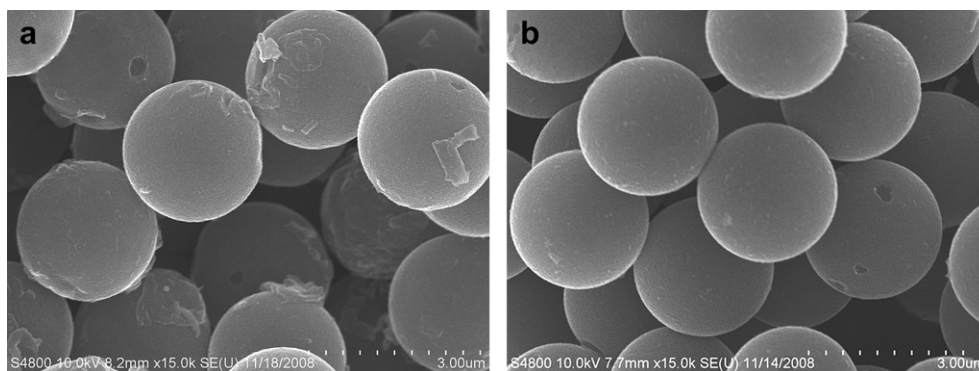


Fig. 7. SEM images of PS/PANi composite particles prepared by using different PS seed particles with constant aniline/PS weight ratio (1:6), a) PVP-stabilized PS, b) "naked" PS.

SEM images of the resultant composite particles are shown in Fig. 7. It is easy to find the distinct difference that the PS/PANi composite particles prepared by "naked" seed particles have uniform surface. On the other hand, the referenced composite particles fabricated by PVP-stabilized PS particles have uneven shells and some PANi fragments deposit on their surface. In the colloidal system, the existence of PVP will affect the thermodynamic balance of aniline between the polymeric phase and aqueous phase. In other words, there would exist much more aniline in the aqueous medium. Hence, the aniline distributed in the aqueous phase was oxidized, polymerized and deposited onto the surface of the seed particles. In fact, this phenomenon is essentially consistent with the fact that the rough PANi overlayer formed at higher aniline/PS weight ratio as shown in Fig. 1e and f. As discussing above, the two conditions, at higher aniline/PS weight ratio and with addition of PVP, would all bring polymerization of more aniline in aqueous phase, and finally result in the rougher surface of composite particles and simultaneously, decreasing PANi loading yield.

#### 4. Conclusions

In summary, monodisperse micrometre-sized polystyrene/polyaniline (PS/PANi) core-shell composite particles were controllably fabricated using micrometre-sized, "naked" PS seed particles without surface charge and further pretreatments according to the proposed SDIPM. By means of this unique approach, the thin, uniform but intact PANi overlayers were formed even on the common, "naked" PS substrate particles, which profited from its unique "inside-out" forming process and considerably high efficiency of aniline to transform into the resultant composites. At larger amounts of addition of aniline, the uniform size and well-defined morphology of the PS/PANi core-shell composite particles could be still maintained with a relatively high PANi mass loading yield. To be brief, the SDIPM should be applied validly for such common, uncharged PS particles as substrate and moreover, can give powerful control over the structure and morphology of the core-shell PS/PANi conducting composite particles.

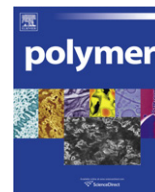
#### Acknowledgements

This work was supported by the National Basic Research Program of China (No. 2007CB925101) and National Natural Science Foundation of China (No. 20973092).

#### References

[1] Gangopadhyay R, De A. *Chem Mater* 2000;12:608–22.

- [2] Gomez-Romero P. *Adv Mater* 2001;13:163–74.
- [3] Roux S, Soler-Illia Galo JAA. *Adv Mater* 2003;15:217–21.
- [4] Percy MJ, Michailidou V, Armes SP. *Langmuir* 2003;19:2072–9.
- [5] Li W, McCarth PA, Liu D, Huang J, Yang S, Wang H. *Macromolecules* 2002;35:9975–82.
- [6] Nogales A, Broza G, Roslanied Z, Schulte K, Sics I, Hsiao BS, et al. *Macromolecules* 2004;37:7669–72.
- [7] Thiyagarajan M, Samuelson LA, Kumar J, Cholli AL. *J Am Chem Soc* 2003;125:11502–3.
- [8] Somboonsub B, Srisuwan S, Invernale MA, Thongyai S, Praserttham P, Scola DA, et al. *Polymer* 2010;51:4472–6.
- [9] Somboonsub B, Invernale MA, Thongyai S, Praserttham P, Scola DA, Sotzing GA. *Polymer* 2010;51:1231–6.
- [10] Han MG, Armes SP. *Langmuir* 2003;19:4523–6.
- [11] Cairns DB, Armes SP, Bremer LGB. *Langmuir* 1999;15:8052–8.
- [12] Pojanavaraphan T, Magaraphan R. *Polymer* 2010;51:1111–23.
- [13] (a) Rummyantsev BM, Berendyaev VI, Tsegelskaya AY, Zhuravleva TS, Klimenko IV. *Synth Met* 2005;152:85–8; (b) Li ZF, Swihart MT, Ruckenstein E. *Langmuir* 2004;20:1963–71.
- [14] Bossi A, Piletsky SA, Piletska EV, Righetti PG, Turner APF. *Anal Chem* 2000;72:4296–300.
- [15] Narayanan SR, Yen S, Liu L, Greenbaum SG. *J Phys Chem B* 2006;110:3942–8.
- [16] Tsutsumi H, Yamashita S, Oishi T. *J Appl Electrochem* 1997;27:477–81.
- [17] (a) Khan MA, Armes SP. *Adv Mater* 2000;12:671–3; (b) Goldsworthy BJ, Burchell MJ, Cole MJ, Armes SP, Khan MA, Lascelles SF, et al. *Astron Astrophys* 2003;409:1151–67.
- [18] Huang J, Virji S, Weiller BH, Kaner RB. *J Am Chem Soc* 2003;125:314–5.
- [19] MacDiarmid AG. *Synth Met* 1997;84:27–34.
- [20] MacDiarmid AG. *Angew Chem Int Ed* 2001;40:2581–90.
- [21] Long Y, Luo J, Xu J, Chen Z, Zhang L, Li J, et al. *J Phys Condens Matter* 2004;16:1123–30.
- [22] Virji S, Kaner RB, Weiller BH. *J Phys Chem B* 2006;110:22266–70.
- [23] Kahol PK, Ho JC, Chen YY, Wang CR, Neeleshwar S, Tsai CB, et al. *Synth Met* 2005;151:65–72.
- [24] Tan S, Zhai J, Xue B, Wan M, Meng Q, Jiang YL, et al. *Langmuir* 2004;20:2934–7.
- [25] Barthet C, Armes SP, Lascelles SF, Luk SY, Stanley HME. *Langmuir* 1998;14:2032–41.
- [26] Kohut-Svelko N, Reynaud S, Dedryvere R, Martinez H, Gonbeau D, Francois J. *Langmuir* 2005;21:1575–83.
- [27] Shi XY, Briseno AL, Sanedrin RJ, Zhou FM. *Macromolecules* 2003;36:4093–8.
- [28] Ding KL, Miao ZJ, Liu ZM, An GM, Xie Y, Tao RT, et al. *J Mater Chem* 2008;18:5406–11.
- [29] (a) Wu Q, Wang ZQ, Xue G. *Adv Funct Mater* 2007;17:1784–9; (b) Li YX, Wang ZQ, Wang Q, Wang CJ, Xue G. *Macromolecules* 2010;43:4468–71.
- [30] (a) Stejskal J, Hlavatá D, Sikora A, Koňák Č, Pleštil J, Kratochvíl P. *Polymer* 1992;33:3675–85; (b) Hilfiker R, Wu DQ, Chu B. *J Colloid Interface Sci* 1990;135:573–9; (c) Sapurina I, Stejskal J, Tuzar Z. *Colloids Surf A* 2001;180:193–8.
- [31] (a) Lascelles SF, Armes SP. *J Mater Chem* 1997;7:1339–47; (b) Lascelles SF, Armes SP, Zhdan PA, Greaves SJ, Brown AM, Watts JF, et al. *J Mater Chem* 1997;7:1349–55.
- [32] (a) Perruchot C, Chehimi MM, Delamar M, Lascelles SF, Armes SP. *Langmuir* 1996;12:3245–51; (b) Barthet C, Armes SP, Chehimi MM, Bilem C, Omastova M. *Langmuir* 1998;14:5032–8.
- [33] (a) Chen SA, Lee HT. *Macromolecules* 1995;28:2858–66; (b) Park MK, Onishi K, Locklin J, Caruso F, Advincula RC. *Langmuir* 2003;19:8550–4.
- [34] Wu Q, Wang ZQ, Kong XF, Gu XD, Xue G. *Langmuir* 2008;24:7778–84.



# Low bandgap polymers with benzo [1,2-b:4,5-b'] dithiophene and bithiophene-dioxopyrrolothiophene units for photovoltaic applications

Guobing Zhang<sup>a</sup>, Yingying Fu<sup>b</sup>, Zhiyuan Xie<sup>b,\*</sup>, Qing Zhang<sup>a,\*</sup>

<sup>a</sup> Department of Polymer Science and Engineering, School of Chemistry and Chemical Engineering, Shanghai Jiao Tong University, Shanghai 200240, China

<sup>b</sup> State Key Laboratory of Polymer Physics and Chemistry, Changchun Institute of Applied Chemistry, Chinese Academy of Science, Changchun 130022, China

## ARTICLE INFO

### Article history:

Received 9 April 2010

Received in revised form

5 October 2010

Accepted 13 November 2010

Available online 22 November 2010

### Keywords:

Conjugated polymer

Polymer solar cells

Benzo [1,2-b:4,5-b'] dithiophene

## ABSTRACT

New donor/acceptor polymers **PBDTTPT1** and **PBDTTPT2** with alternating benzodithiophene (BDT) and bithiophene-dioxopyrrolothiophene (TPT) units were synthesized by Stille coupling reaction. The polymers had optical bandgaps of 1.78 and 1.82 eV, and HOMO energy levels of  $-5.30$  and  $-5.35$  eV for **PBDTTPT1** and **PBDTTPT2**, respectively. Polymeric solar cell devices based on these copolymers as donors and PC<sub>71</sub>BM as acceptor showed the highest open circuit voltage of 0.95 V and power conversion efficiency of 2.68% under the illumination of AM 1.5, 100 mW/cm<sup>2</sup>.

© 2010 Elsevier Ltd. All rights reserved.

## 1. Introduction

Research on polymeric solar cells (PSCs) has been intensified in recent years because PSCs have a potential to generate electricity from sunlight at low cost [1–8]. Bulk heterojunction (BHJ) structure based on blending of electron-donating conjugated polymers and high-electron-affinity fullerene derivatives such as PCBM has become the most successful device structure for organic photovoltaics (OPVs) [9,10]. So far, the power conversion efficiency (PCE) of PSCs is still low in comparison with the silicon based solar cells. Four steps are involved in the organic photovoltaic phenomena. They are photon absorption and generation of exciton, exciton diffusion, exciton separation and separated charge carriers migrate to electrodes. Short circuit current ( $J_{sc}$ ), open circuit voltage ( $V_{oc}$ ) and fill factor (FF) are three main parameters that determine the PCE of the PSC devices. Many examples of low bandgap polymers, absorbing in the red and near-IR regions of the solar spectrum, have been developed for maximizing solar photon harvest, thereby increasing  $J_{sc}$  and PCE [11–14]. Systematic studies on matching the energy levels of donor polymers with those of PCBM have been carried out [15,16]. Low bandgap polymers with deep HOMO energy level will result high  $J_{sc}$  and  $V_{oc}$  simultaneously, thereby maximizing power conversion efficiency.

Recently, low bandgap polymers with deep HOMO energy level have been studied for achieving high  $V_{oc}$  in PSC devices [17–20]. Polymers containing dioxopyrrolothiophene (**DPT**) unit have achieved the  $V_{oc}$  of about 0.9 V and PCE around 4–7% [21–25]. In our previous work, two polymers (**PBDTDPTs**) based on benzo [1,2-b:4,5-b'] dithiophene (**BDT**) and **DPT** units were synthesized and were shown relatively high performance in solar cell devices [25]. However, **PBDTDPT** polymer films have absorption spectra edged around 675 nm. Design and synthesis of new polymers with substantial absorption in longer wavelength will have lower bandgap and may result better solar photon harvest. Recently, there are reports on further reduction of polymer bandgaps by incorporation of additional electron-rich thiophene moieties into existing donor/acceptor polymers [26–28]. Herein, we report the synthesis and structure/property relationship on two new low bandgap polymers based on **BDT** and **DPT** units with additional alkyl-substituted thiophene moieties.

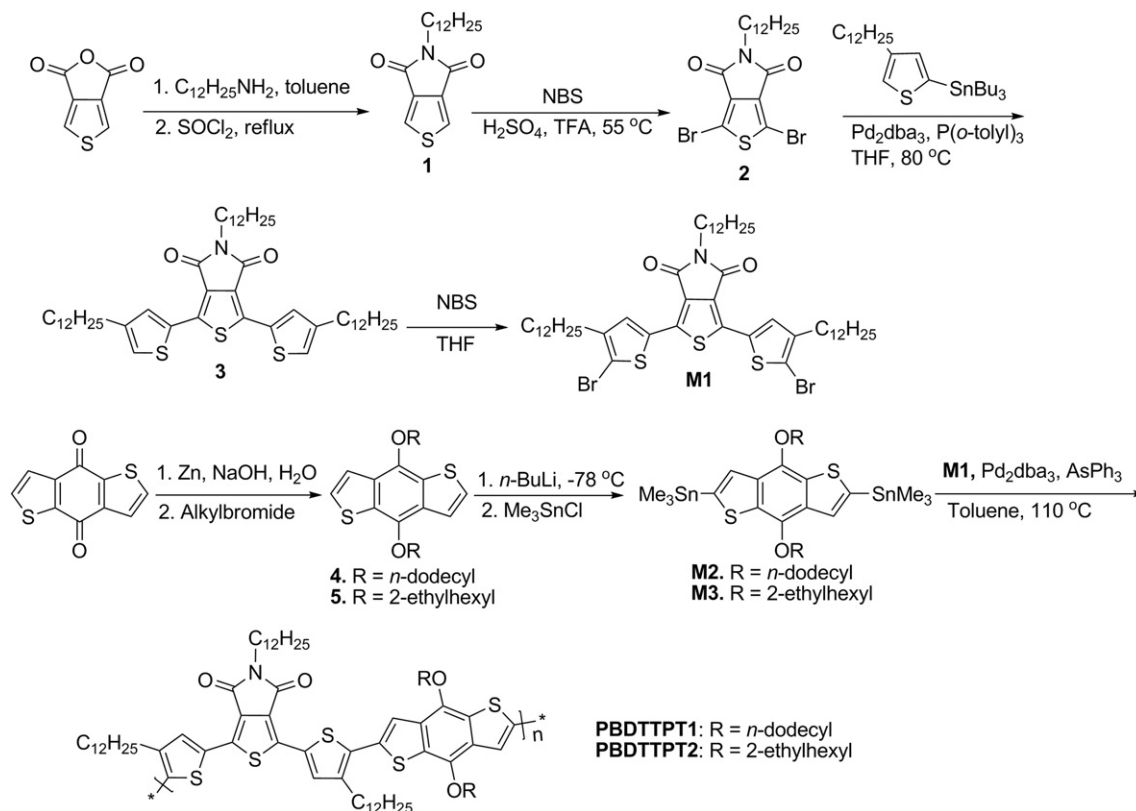
## 2. Experimental section

### 2.1. Materials

*n*-Butyllithium, trimethyltin chloride and triphenylarsine were obtained from Alfa Aesar Chemical Company. Tris (dibenzylideneacetone) dipalladium (Pd<sub>2</sub>dba<sub>3</sub>) and *tri-o*-tolylphosphine were purchased from Sigma–Aldrich Chemical Company. All materials were used as

\* Corresponding authors.

E-mail addresses: [xiezy\\_n@ciac.jl.cn](mailto:xiezy_n@ciac.jl.cn) (Z. Xie), [qz14@sjtu.edu.cn](mailto:qz14@sjtu.edu.cn) (Q. Zhang).



Scheme 1. Synthesis of monomers and polymer **PBDTTPT1** and **BDTTPT2**.

received without further purification. Tetrahydrofuran (THF) and toluene were freshly distilled over Na wire under nitrogen prior to use.

## 2.2. Measurements and characterization

Nuclear Magnetic Resonance spectra were recorded on a Mercury plus 400 MHz machine. Gel permeation chromatography (GPC) analyses were performed on a Perkin Elmer Series 200 gel coupled with UV–vis detector using tetrahydrofuran as eluent with polystyrene as standards. Thermogravimetric analysis (TGA) analyses were conducted with a TA instrument Q5000IR at a heating rate of  $20\text{ }^\circ\text{C min}^{-1}$  under nitrogen gas flow. Differential scanning calorimetry (DSC) analysis was performed on a TA instrumentation Q2000 in a nitrogen atmosphere. All the samples (about 10.0 mg in weight) were first heated up to  $300\text{ }^\circ\text{C}$  and held for 2 min to remove thermal history, followed by the cooling rate of  $20\text{ }^\circ\text{C/min}$  to  $20\text{ }^\circ\text{C}$  and then heating rate of  $20\text{ }^\circ\text{C/min}$  to  $300\text{ }^\circ\text{C}$  in all cases. UV–vis absorption spectra were recorded on a Perkin Elmer model  $\lambda$  20 UV–vis spectrophotometer. Electrochemical measurements were conducted with a CHI 600 electrochemical analyzer under nitrogen in a deoxygenated anhydrous acetonitrile solution of tetra-*n*-butylammonium hexafluorophosphate (0.1 M). A platinum electrode was used as a working electrode, a platinum-wire was used as an auxiliary electrode, and an  $Ag/Ag^+$  electrode was used as a reference electrode. Polymer thin films were coated on platinum electrode and ferrocene was added as reference. A potential scan rate of  $100\text{ mV/s}$  was used for all experiments.

## 2.3. Device fabrication and characterization of solar cells

Polymer solar cells (PSCs) with the device structures of ITO/PEDOT: PSS/polymer:  $PC_{70}BM$  (1:2, w/w)/LiF/Al were fabricated as

follows: a ca. 40-nm-thick PEDOT: PSS (Baytron P AI 4083) was spin-coated from an aqueous solution onto the pre-cleaned ITO substrates, and dried at  $120\text{ }^\circ\text{C}$  for 30 min in air. Then the substrates were transferred into a nitrogen filled glove box. The prepared solution of **PBDTTPT**:  $PC_{70}BM$  (5 mg/mL: 10 mg/mL) in chloroform with or without diiodooctane (2 vol%) was spin-coated on top of the PEDOT/PSS layer. Finally the samples were transferred into an evaporator and LiF (1 nm) and Al (100 nm) with area of  $0.12\text{ cm}^2$  were thermally deposited under a vacuum of  $10^{-6}$  Torr. The devices were encapsulated in a glove box and measured in air. Current–voltage characteristics were measured using a computer controlled Keithley 236 source meter. The photocurrent was measured under AM 1.5G illumination at  $100\text{ mW/cm}^2$  from a solar simulator (Oriel, 91160A-1000). The external quantum efficiency (EQE) was measured at a chopping frequency of 280 Hz with a lock-in amplifier (Stanford, SR830) during illumination with the monochromatic light from a Xenon lamp.

## 2.4. Synthetic procedures

4,8-Dihydrobenzoldithiophene-4,8-dione [29], thiophene-3,4-dicarboxylic anhydride [30] and 5-tri-*n*-butylstannyl-3-dodecylthiophene [31] were synthesized according to the literature. The synthesis of monomer **M1**, **M2**, **M3** and the polymers are showed in Scheme 1.

### 2.4.1. 5-Dodecylthieno [3,4] pyrrole-4,6-dione (1)

A solution of thiophene-3,4-dicarboxylic anhydride (3.09 g, 20.05 mmol) and *n*-dodecylamine (4.09 g, 22.06 mmol) in toluene (250 mL) was refluxed for 24 h in a flask. After cooled to room temperature, the reaction mixture was filtrated and was dried under vacuum to afford a brown solid. Thionyl chloride (200 mL)

was added and the mixture was refluxed for 5 h. The volatile was removed under vacuum. The residue was recrystallization from hexane to afford the titled compound as white crystals (3.25 g, 50.5%).  $^1\text{H}$  NMR (400 MHz,  $\text{CDCl}_3$ ),  $\delta$  (ppm): 7.82 (s, 2H), 3.60 (t,  $J = 4.0$  Hz, 2H), 1.63 (m, 2H), 1.25 (m, 18H), 0.87 (t,  $J = 6.8$  Hz, 3H).

#### 2.4.2. 1,3-Dibromo-5-dodecylthieno [3,4] pyrrol-4,6-dione (2)

*N*-Bromosuccinimide (NBS) (6.65 g, 37.33 mmol) was added to the solution of compound **1** (3.0 g, 9.33 mmol), concentrated sulfuric acid (12.0 mL) and trifluoroacetic acid (40 mL). The reaction mixture was stirred at 55 °C for 24 h. The brown solution was poured into ice water (500 mL) and was extracted with dichloromethane. The organic layer was collected and was dried with anhydrous sodium sulfate. Solvent was removed under reduced pressure and residue was purified by flash chromatography on silica gel with diethyl ether/dichloromethane/petroleum ether (1: 1: 15) as eluent to give the titled compound (2.79 g, 62.5%).  $^1\text{H}$  NMR (400 MHz,  $\text{CDCl}_3$ ),  $\delta$  (ppm) 3.58 (t,  $J = 7.2$ , 2H), 1.62 (m, 2H), 1.25 (m, 18H), 0.87 (t,  $J = 6.8$  Hz, 3H).  $^{13}\text{C}$  (100 MHz,  $\text{CDCl}_3$ ),  $\delta$  (ppm): 160.58, 135.00, 113.13, 39.05, 32.14, 29.86, 29.80, 29.67, 29.57 (2C), 29.38, 28.48, 27.02, 22.92, 14.37.

#### 2.4.3. 1,3-Bis(4-*n*-dodecylthiophene)-5-dodecylthieno [3,4] pyrrol-4,6-dione (3)

5-Tri-*n*-butylstannyl-3-dodecylthiophene (5.64 g, 10.43 mmol) and compound **2** (2.0 g, 4.17 mmol) were dissolved in tetrahydrofuran (20 mL) in a pressure tube. The solution was degassed by a nitrogen flow for 30 min. Then  $\text{Pd}_2\text{dba}_3$  (0.076 g, 0.0834 mmol) and tri-*o*-tolylphosphine (0.051 g, 0.167 mmol) were added into the solution. The tube was capped and heated to 80 °C for 36 h. After cooled to room temperature, the mixture was poured into an aqueous solution of potassium fluoride (100 mL, 1.0 M) and stirred for 30 min. The mixture was extracted with dichloromethane (3x). The combined organic layer was dried over anhydrous sodium sulfate. After removing solvent, the residue was purified by column chromatography on silica gel using petroleum ether/dichloromethane (30: 1) as eluent. A yellow solid was obtained after removal of the solvent (2.2 g, 64.3%).  $^1\text{H}$  NMR (400 MHz,  $\text{CDCl}_3$ ),  $\delta$  (ppm): 7.87 (s, 2H), 7.02 (s, 2H), 3.65 (t,  $J = 7.6$  Hz, 2H), 2.62 (t,  $J = 7.6$  Hz, 4H), 1.65 (m, 6H), 1.23–1.35 (m, 54H), 0.88 (t,  $J = 6$  Hz, 9H).  $^{13}\text{C}$  (100 MHz,  $\text{CDCl}_3$ ),  $\delta$  (ppm): 162.88, 145.14, 136.97, 132.35, 131.28, 128.23, 123.72, 38.80, 32.16, 30.68, 30.64, 29.92, 29.90, 29.85, 29.82, 29.60, 29.58, 29.54, 29.50, 28.78, 27.24, 22.93, 14.37.

#### 2.4.4. 1,3-Bis(4-*n*-dodecyl-5-bromo-thiophene)-5-dodecylthieno [3,4] pyrrol-4,6-dione (M1)

Compound **3** (1.66 g, 2.02 mmol) and tetrahydrofuran (80 mL) were added into a flask (250 mL) wrapped with aluminum foil. The solution was stirred and degassed for 30 min. *N*-Bromosuccinimide (NBS) (0.79 g, 4.45 mmol) was added in portions over a period of 30 min. The mixture was stirred at room temperature for 2 h, and then the solution was poured into water (100 mL) and was extracted with diethyl ether. The combined organic layer was dried with anhydrous sodium sulfate. Solvent was removed under reduced pressure and the residue was purified by column chromatography on silica gel with petroleum ether/dichloromethane (30: 1) as eluent. After removing solvent, a yellow solid (1.28 g, 65.3%) was obtained.  $^1\text{H}$  NMR (400 MHz,  $\text{CDCl}_3$ ),  $\delta$  (ppm): 7.63 (s, 2H), 3.64 (t,  $J = 7.6$  Hz, 2H), 2.57 (t,  $J = 7.6$  Hz, 4H), 1.62 (m, 6H), 1.20–1.35 (m, 54H), 0.87 (t,  $J = 6.4$  Hz, 9H).  $^{13}\text{C}$  (100 MHz,  $\text{CDCl}_3$ ),  $\delta$  (ppm): 162.64, 143.94, 135.66, 132.05, 130.45, 128.47, 113.76, 38.90, 32.18, 32.16, 29.92, 29.89, 29.82, 29.75, 29.74, 29.62, 29.48, 29.61, 28.74, 27.22, 22.95, 14.38.

#### 2.4.5. 4,8-Didodecyloxybenzo [1,2-*b*:4,5-*b'*] dithiophene (4)

Water (40 mL) was added to benzo [1,2-*b*:4,5-*b'*] dithiophene-4,8-dione (2.20 g, 10.0 mmol), zinc powder (1.96 g, 30.0 mmol) and sodium hydroxide (8.00 g, 200.0 mmol) in a round bottom flask (150 mL). After refluxing for 1 h, a catalytic amount of tetra-*n*-butylammonium bromide (0.032 g, 0.1 mmol) was added. 1-Bromododecane (7.50 g, 30 mmol) was added drop-wise to the flask. The reaction was refluxed overnight. After cooled to room temperature, it was poured into water (200 mL). The mixture was extracted with diethyl ether for three times. The combined organic layer was dried with anhydrous sodium sulfate. Solvent was removed under reduced pressure and residue was purified by flash chromatography on silica gel with dichloromethane/hexane (1: 15) as eluent to give the titled compound as white solid (3.61 g, 64.7%).  $^1\text{H}$  NMR (400 MHz,  $\text{CDCl}_3$ ),  $\delta$  (ppm): 7.48 (d,  $J = 5.2$  Hz, 2H), 7.36 (d,  $J = 5.2$  Hz, 2H), 4.27 (t,  $J = 6.4$  Hz, 4H), 1.86–1.92 (m, 4H), 1.54 (m, 4H), 1.23–1.37 (m, 32H), 0.88 (t,  $J = 6.4$  Hz, 6H).

#### 2.4.6. 4,8-Di(2-ethylhexyloxy)benzo [1,2-*b*:4,5-*b'*] dithiophene (5)

Same procedure was used as for compound **4**. Compound used were benzo [1,2-*b*:4,5-*b'*] dithiophene-4,8-dione (2.20 g, 10.0 mmol), zinc powder (1.96 g, 30.0 mmol), sodium hydroxide (8.00 g, 200.0 mmol), 1-bromo-2-ethylhexane (5.79 g, 30.0 mmol) and a catalytic amount of tetra-*n*-butylammonium bromide (0.032 g, 0.1 mmol). A light yellow oil was obtained (2.61 g, 58.2%).  $^1\text{H}$  NMR (400 MHz,  $\text{CDCl}_3$ ),  $\delta$  (ppm): 7.49 (d,  $J = 5.2$  Hz, 2H), 7.37 (d,  $J = 5.2$  Hz, 2H), 4.19 (d,  $J = 5.6$  Hz, 4H), 1.78–1.86 (m, 1H), 1.66–1.74 (m, 1H), 1.56–1.64 (m, 2H), 1.46–1.56 (m, 2H), 1.25–1.45 (m, 12H), 1.03 (t,  $J = 7.2$  Hz, 6H), 0.95 (t,  $J = 7.2$  Hz, 6H).

#### 2.4.7. 2,6-Bis(trimethyltin)-4,8-didodecyloxybenzo [1,2-*b*:4,5-*b'*] dithiophene (M2)

A solution of *n*-butyllithium (7.7 mL, 19.25 mmol, 2.5 M in hexane) was added slowly to compound **4** (4.88 g, 8.75 mmol) in tetrahydrofuran (120 mL) at  $-78$  °C. After addition, the mixture was stirred for 1 h at  $-78$  °C. Trimethyltin chloride solution (20.4 mL, 20.4 mmol, 1.0 M in hexane) was added to the mixture. The mixture was warmed to room temperature and was stirred overnight. The reaction was quenched with addition of water (150 mL) and the mixture was extracted with diethyl ether for three times. The combined organic layer was dried with anhydrous sodium sulfate. Solvent was removed under reduced pressure and residue was purified by recrystallization in isopropanol to afford a white solid (6.37 g, 82.2%).  $^1\text{H}$  NMR (400 MHz,  $\text{CDCl}_3$ ),  $\delta$  (ppm): 7.51 (s, 2H), 4.29 (t,  $J = 6.5$  Hz, 4H), 1.86 (m, 4H), 1.57 (m, 4H), 1.23–1.37 (m, 32H), 0.88 (t,  $J = 6.8$  Hz, 6H), 0.45 (s, 18H).  $^{13}\text{C}$  (100 MHz,  $\text{CDCl}_3$ ),  $\delta$  (ppm): 143.32, 140.68, 134.27, 133.20, 128.27, 73.87, 32.20, 30.77, 29.96, 29.92, 29.76, 29.63, 26.36, 22.99, 14.43,  $-8.00$ .

#### 2.4.8. 2,6-Bis(trimethyltin)-4,8-di(2-ethylhexyloxy)benzo [1,2-*b*:4,5-*b'*] dithiophene (M3)

Same procedure was used as for compound **M2**. Compound used were *n*-butyllithium (10.56 mL, 26.4 mmol, 2.5 M in hexane), compound **5** (5.35 g, 12 mmol), trimethyltin chloride solution (27.96 mL, 27.96 mmol, 1M in hexane). After workup, product was obtained as pale needle (7.07 g, 76.3%).  $^1\text{H}$  NMR (400 MHz,  $\text{CDCl}_3$ ),  $\delta$  (ppm): 7.51 (s, 2H), 4.18 (d, 5.2 Hz, 4H), 1.78–1.86 (m, 1H), 1.66–1.74 (m, 1H), 1.56–1.64 (m, 2H), 1.46–1.56 (m, 2H), 1.28–1.45 (m, 12H), 1.02 (t,  $J = 7.2$ , 6H), 0.92 (t,  $J = 7.2$ , 6H), 0.45 (s, 18H).  $^{13}\text{C}$  (100 MHz,  $\text{CDCl}_3$ ),  $\delta$  (ppm): 143.46, 140.81, 134.10, 133.10, 128.19, 75.84, 40.88, 30.75, 29.47, 24.12, 23.42, 14.45, 11.60,  $-8.11$ .

### 2.4.9. Polymer **PBDTTPT1**

Tris(dibenzylideneacetone)dipalladium (0.015 g, 0.016 mmol) and triphenylarsine (0.0098 g, 0.032 mmol) were added to a solution of **M1** (0.78 g, 0.80 mmol) and **M2** (0.71, 0.80 mmol) in toluene (20 mL) under nitrogen. The solution was subjected to three cycles of evacuation and admission of nitrogen. The mixture was heated to 110 °C for 72 h. After cooled to room temperature, the mixture was poured into methanol (100 mL) and stirred for 2 h. A purple precipitate was collected by filtration. The product was purified by washing with methanol and hexane in a Soxhlet extractor for 24 h each. The residue was extracted with hot chloroform in an extractor for 24 h. After removing solvent, a purple solid was collected (0.98 g, 89.5%).  $M_n = 16.8$  kDa; PDI = 1.59.  $^1\text{H NMR}$  (400 MHz,  $\text{CDCl}_3$ ),  $\delta$  (ppm): 7.98 (br, 2H), 7.27 (br, 2H), 4.25 (br, 4H), 3.71 (br, 2H), 2.5–2.7 (br, 4H), 1.02–2.02 (br, 100H), 0.7–0.95 (br, 15H).

### 2.4.10. Polymer **PBDTTPT2**

**PBDTTPT2** are synthesized according to the same procedure as for **PBDTTPT1**. Compound used were  $\text{Pd}_2\text{dba}_3$  (0.015 g, 0.016 mmol), triphenylarsine (0.098 g, 0.032 mmol), **M1** (0.78 g, 0.80 mmol) and **M3** (0.62 g, 0.80 mmol). After workup, a purple solid was obtained (0.87 g, 86.3%).  $M_n = 21.5$  kDa; PDI = 1.84.  $^1\text{H NMR}$  (400 MHz,  $\text{CDCl}_3$ ),  $\delta$  (ppm): 7.95 (br, 2H), 7.28 (br, 2H), 4.15 (br, 4H), 3.65 (br, 2H), 2.50–2.90 (br, 4H), 0.98–2.05 (br, 78), 0.70–0.95 (br, 21H).

## 3. Results and discussion

### 3.1. Synthesis of polymers

The synthetic routes for the monomers **M1**, **M2**, **M3** and polymers were illustrated in Scheme 1. The *N*-alkylated imide (**1**) was reacted with an excess amount of *N*-bromosuccinimide (NBS) to give the dibrominated imide (**2**) as a pale solid. The dibrominated imide (**2**) was reacted with 5-tri-*n*-butylstannyl-3-dodecylthiophene to give **3** by Stille coupling reaction. The compound **3** was halogenated by NBS in tetrahydrofuran to afford **M1** in 65.3% yield. The synthesis of benzo-dithiophenes were also outlined in Scheme 1. The tin containing monomers **M2** and **M3** were synthesized from compound **5** and **6** by lithiation with *n*-butyllithium and quenching with trimethyltin chloride. The alternating polymer **PBDTTPT1** and **PBDTTPT2** were prepared by Stille coupling reaction with 1:1 monomer ratio in the presence of  $\text{Pd}_2\text{dba}_3$  as catalyst and triphenylarsine as ligand to give **PBDTTPT1** (yield 89.5%) and **PBDTTPT2** (yield 86.3%). The crude copolymers were purified by precipitating in methanol and by washing with methanol and hexane in a Soxhlet. The number average molecular weights ( $M_n$ ) of the copolymers were 16.8 kDa and 21.5 kDa with a polydispersity of 1.59 and 1.84 for **PBDTTPT1** and **PBDTTPT2**, respectively. Both copolymers showed good solubility in common organic solvents, such as tetrahydrofuran, dichloromethane and toluene.

### 3.2. Thermal stability

The thermal stabilities of copolymers were investigated by thermogravimetric analysis (TGA). The TGA plots of **PBDTTPT1**, and **PBDTTPT2** were showed in Fig. 1. The point of five percent weight loss was selected as the onset decomposition point. The thermal decomposition temperatures for **PBDTTPT1** and **PBDTTPT2** were determined around 352 °C under  $\text{N}_2$  atmosphere. This indicates that the two copolymers have adequate thermal stability for application in polymer solar cells and other optoelectronic devices. Neither polymers displayed noticeable glass transition in differential scanning calorimetry (DSC) analysis.

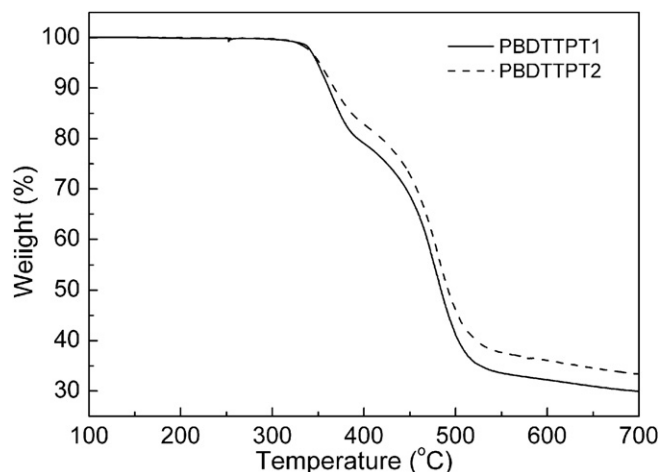


Fig. 1. TGA curves of the polymer **PBDTTPT1** and **PBDTTPT2**.

### 3.3. Optical property

The UV–vis absorption spectra of the copolymers in chloroform solution and as thin film were shown in Fig. 2. The optical absorption properties of the copolymers were listed in Table 1. The

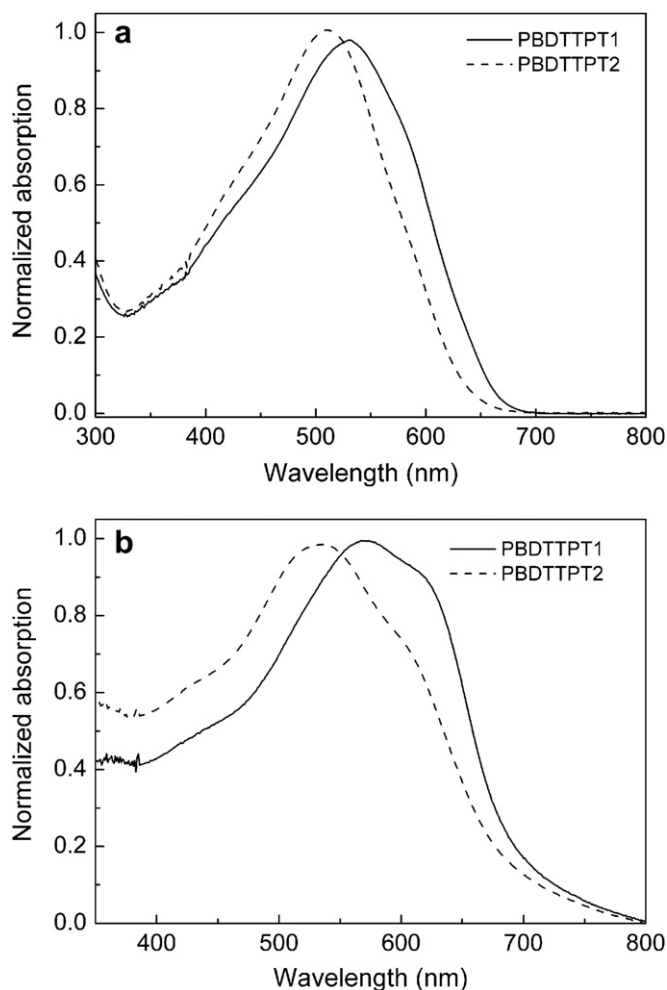


Fig. 2. Normalized UV–vis spectra of **PBDTTPT1** and **PBDTTPT2** (a) in chloroform solution and (b) as thin film.

**Table 1**  
Optical and redox properties of **PBDTTPT1** and **PBDTTPT2**.

Polymer	Solution		Film		Film			
	$\lambda_{\max}^{\text{abs}}$ (nm)	$\lambda_{\max}^{\text{abs}}$ (nm)	$\lambda_{\text{onset}}^{\text{abs}}$ (nm)	$E_g^{\text{opt}}$ (eV)	$E_{\text{onset}}^{\text{ox}}$ (V)	HOMO (eV) <sup>a</sup>	$E_{\text{onset}}^{\text{red}}$ (V) <sup>b</sup>	LUMO (eV) <sup>c</sup>
<b>PBDTTPT1</b>	531	576	695	1.78	0.59	−5.30	−1.19	−3.52
<b>PBDTTPT2</b>	511	535	680	1.82	0.64	−5.35	−1.18	−3.53

$$^a \text{HOMO} = -(4.71 + E_{\text{onset}}^{\text{ox}}).$$

$$^b E_{\text{onset}}^{\text{red}} = E_{\text{onset}}^{\text{ox}} - E_g^{\text{opt}}.$$

$$^c \text{LUMO} = -(4.71 + E_{\text{onset}}^{\text{red}}).$$

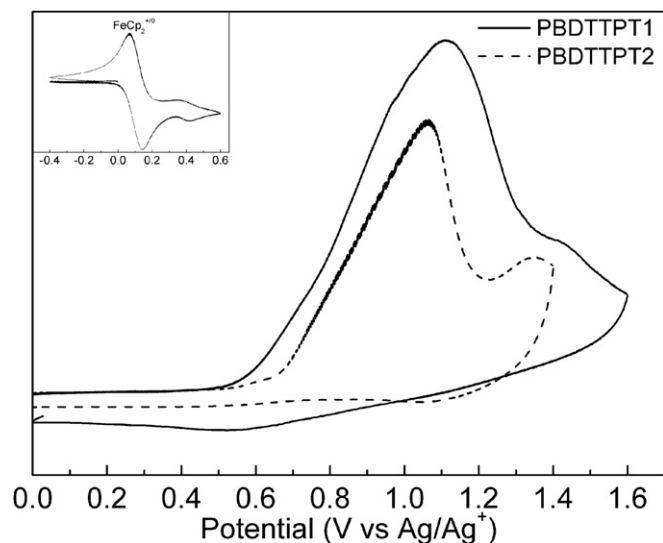


**Fig. 3.** Cyclic voltammograms of polymers thin film on a platinum electrode in  $\text{Bu}_4\text{NPF}_6/\text{MeCN}$  (0.1 M) at a scan rate of 100 mV/s.

maximal absorption of **PBDTTPT1** and **PBDTTPT2** were at 531 and 511 nm in solution, respectively. The two copolymers exhibited broad absorption between 350 and 700 nm, which resulted from intramolecular charge transfer (ICT) between the donor and acceptor units. The film absorption spectra of copolymers were depicted in Fig. 2b, the absorption maximums of **PBDTTPT1** and **PBDTTPT2** solid films were at 576 and 535 nm, respectively. The thin film absorption spectra of **PBDTTPT1** and **PBDTTPT2** were broadened. The absorption maximums were red-shifted about 35 and 24 nm in thin film comparing with those of the solution spectra. These indicated that the strong intermolecular interaction and aggregation occurred in solid-state of those polymers. The absorption spectra of **PBDTTPT1** (with all straight side chains) were red-shifted both in solution and as thin film compared with those of **PBDTTPT2** (with two ethylhexyl side chains). The branch alkyl chains of **PBDTTPT2** might prevent effective conjugation of the polymer. The optical bandgap ( $E_g^{\text{opt}}$ ) was calculated from the absorption edge of solid-state film. The optical bandgap was 1.78 eV (absorption edge at 695 nm) for **PBDTTPT1** and 1.82 eV (absorption edge at 680 nm) for **PBDTTPT2**. Only a slight decrease in bandgap was observed compared with our previous reported polymer

**Table 2**  
Devices performance of polymers solar cells.

Weight ratio	<b>PBDTTPT1</b> : PC <sub>71</sub> BM				<b>PBDTTPT2</b> : PC <sub>71</sub> BM			
	1:1	1:2	1:3	2:1	1:1	1:2	1:3	2:1
$J_{\text{sc}}$ (mA/cm <sup>2</sup> )	3.04	2.06	1.73	2.18	3.93	3.12	2.20	2.49
$V_{\text{oc}}$ (V)	0.89	0.88	0.88	0.92	0.92	0.93	0.93	0.95
FF	0.62	0.60	0.58	0.53	0.57	0.56	0.56	0.50
PCE (%)	1.68	1.09	0.89	1.08	2.05	1.62	1.14	1.18

**PBDTDP1** and **PBDTDP2** (both of 1.84 eV) [25]. Unlike other reported system [26,27], incorporation of additional thiophene moieties into **BDT** and **DPT** system did not show significant change on the bandgaps of polymers. The steric hindrance of the alkyl side chains on thiophenes may introduce additional distortion on the main chain of polymers and disrupt conjugation.

### 3.4. Electrochemical property

The electrochemical properties of the copolymers were investigated by cyclic voltammetry (CV). The onset oxidations (HOMO energy level) were determined by CV. The CV curves of two copolymers film in acetonitrile containing tetra-*n*-butylammonium hexafluorophosphate (0.1 M) at a potential scan rate of 100 mV/s were shown in Fig. 3. The potentials were referenced to the ferrocene/ferrocenium redox couple (Fc/Fc<sup>+</sup>). It was assumed that the redox potential of Fc/Fc<sup>+</sup> had an absolute energy level of −4.8 eV to vacuum [32]. The potential of Fc/Fc<sup>+</sup> was measured under the same conditions and located at 0.09 V related to the Ag/Ag<sup>+</sup> electrode. The CV data were summarized in Table 1. The onset oxidation potential of **PBDTTPT1** and **PBDTTPT2** were located at 0.59 and 0.64 eV, respectively. The HOMO energy levels of copolymer **PBDTTPT1** and **PBDTTPT2** were calculated to be −5.30 and −5.35 eV. The HOMO energy levels of **PBDTTPT1** and **PBDTTPT2** are slightly higher than polymer **PBDTDP1**s (−5.42 and 5.44 eV) [25]. The small increasing of HOMO energy levels was resulted from the addition of electron rich alkyl-substituted thiophene units. The similar results were reported before [27,33]. The relatively low HOMO energy level of two copolymers are desirable for achieving higher open-circuit voltage when they are used as donors blended with PCBM in PSCs. The relative lower HOMO energy levels in these new polymers can be attributed to electron deficient imide group

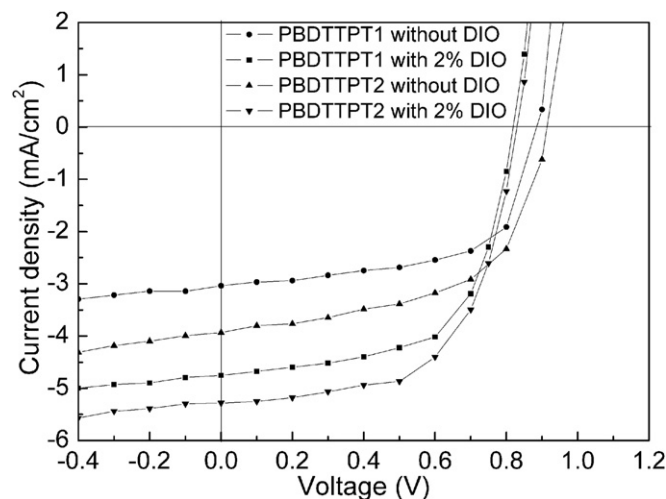


**Fig. 4.** Current-voltage characteristics of polymers/PC<sub>71</sub>BM solar cells under illumination of AM 1.5G, 100 mW/cm<sup>2</sup>.

**Table 3**  
Devices performance of polymers solar cells with and without processing additive.

	<b>PBDTTPT1:</b> PC <sub>71</sub> BM = 1: 1		<b>PBDTTPT2:</b> PC <sub>71</sub> BM = 1: 1	
	No DIO	2% DIO	No DIO	2% DIO
J <sub>sc</sub> (mA/cm <sup>2</sup> )	3.04	4.75	3.93	5.28
V <sub>oc</sub> (V)	0.89	0.82	0.92	0.83
FF	0.62	0.62	0.57	0.61
PCE (%)	1.68	2.43	2.05	2.68

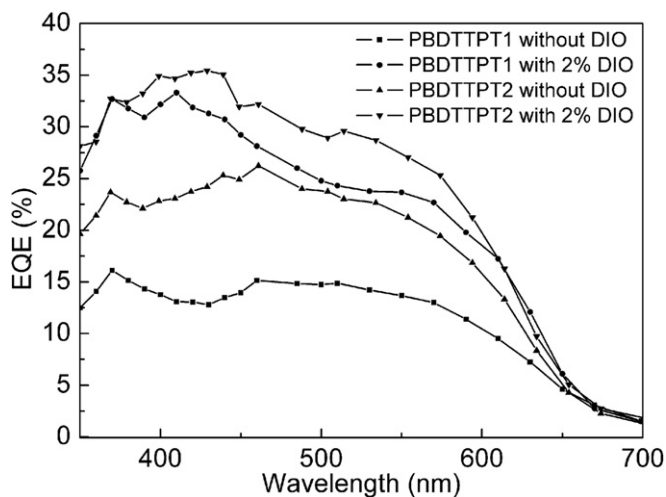


**Fig. 5.** External quantum efficiency of polymer/PC<sub>71</sub>BM blends.

on **TPT** unit. The LUMO energy levels of **PBDTTPT1** and **PBDTTPT2** were  $-3.52$  and  $-3.53$  eV which were calculated from the optical bandgap and HOMO energy levels of the polymers.

### 3.5. Photovoltaic property

The photovoltaic properties of polymer **PBDTTPT1** and **PBDTTPT2** were evaluated in BHJ solar cell devices. The copolymers were used as donors and PC<sub>71</sub>BM was used as electron acceptor. The device structures were ITO/PEDOT: PSS/ Polymer:PCBM/LiF/Al. Solar cells were characterized under AM 1.5G illumination at 100 mW/cm<sup>2</sup> from a solar simulator. The photovoltaic performance of the devices based on the blend of copolymers and PC<sub>71</sub>BM at deference weight ratio were summarized in Table 2. The short-circuit current densities (J<sub>sc</sub>) of devices were varied at different weight ratio of donor polymer to PC<sub>71</sub>BM. The weight ratios were optimized for device performance. The changing the weight ratio of donor polymer to PC<sub>71</sub>BM had little influence on open circuit voltage (V<sub>oc</sub>). The highest V<sub>oc</sub> of 0.95 V was achieved with blend of **PBDTTPT2**: PC<sub>71</sub>BM (wt. ratio of 2: 1). The optimized devices had J<sub>sc</sub> of 3.04 and 3.93 mA/cm<sup>2</sup>, V<sub>oc</sub> of 0.89 and 0.92 V, which yield PCE of 1.68% and 2.05% for **PBDTTPT1** and **PBDTTPT2**, respectively. Adding a small amount of diiodooctane (DIO) to the blend of copolymer and PCBM before spin-coating significantly improved the efficiency of the cells. The current density-voltage (J-V) curves of the devices based on the polymers: PC<sub>71</sub>BM blend with additive (DIO, 2% by volume) were presented in Fig. 4 and the data were summarized in Table 3. The enhanced J<sub>sc</sub> and PCE value were observed in both **PBDTTPT1** and **PBDTTPT2** based devices, the devices with DIO had the J<sub>sc</sub> of 4.75 and 5.28 mA/cm<sup>2</sup>, the PCE of 2.43% and 2.68% for **PBDTTPT1** and **PBDTTPT2**, respectively. This increasing of performance was attributed to the improvement of charge separation in BHJ [34]. The external quantum efficiency (EQE) of the optimized devices with and without DIO were shown in Fig. 5. The

EQE of devices processed with DIO and without DIO were very different in the region of 350–700 nm. The EQE values of devices with DIO processing additives are much higher in this region and result the higher J<sub>sc</sub>.

## 4. Conclusions

We have successfully synthesized two new low bandgap copolymers by incorporation of additional alkylthiophene moieties into the **BDT** and **DPT** system. The new polymers show good solubility in common organic solvent, high thermal stability and broad absorption in the region from 350 to 700 nm. The effect of incorporation of additional alkylthiophene units on the optical, electrochemical and photovoltaic properties of polymers were studied. Only a slight decreasing in bandgap was observed in new polymers compared with our previous reported copolymer **PBDTDPTs**. The devices based on the blends of new copolymers and PC<sub>71</sub>BM exhibited V<sub>oc</sub> of 0.82–0.95 V. The PCEs of devices with the copolymer: PC<sub>71</sub>BM (wt. ratio of 1: 1) achieved 2.43% for **PBDTTPT1** and 2.68% for **PBDTTPT2** under the illumination of AM 1.5G, 100 mW/cm<sup>2</sup>. The results indicate that these new copolymers with high V<sub>oc</sub> might become useful materials for organic solar cells applications.

## Acknowledgement

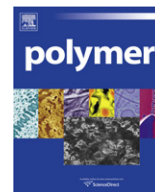
This work was supported by National Nature Science Foundation of China (NSFC Grant no. 20674049 and Grant no. 20834005), and Shanghai municipal government (Grant no. B202 and Grant no. 10ZZ15).

## References

- Peet J, Kim JY, Coates NE, Ma WL, Moses D, Heeger AJ, et al. Nat Mater 2007;6: 497–500.
- Kim JY, Lee K, Coates NE, Moses D, Nguyen TQ, Dante M, et al. Science 2007;317:222–5.
- Invernale MA, Bokria JG, Ombaba M, Lee K-R, Mamangun DMD. Polymer 2010;51:378–82.
- Brabec CJ, Sariciftci NS, Hummelen JC. Adv Funct Mater 2001;11:15–26.
- Yildirim M, Kaya I. Polymer 2009;50:5653–60.
- Hou J, Chen H-Y, Zhang S, Li G, Yang Y. J Am Chem Soc 2008;130:16144–5.
- Liu Y, Chen X, Qin J, Yu G, Liu Y. Polymer 2010;51:3730–5.
- Kumar AK, Jang S-Y, Padilla J, Otero TF, Sotzing GA. Polymer 2008;49: 3686–92.
- Yu G, Gao J, Hummelen JC, Wudl FA, Heeger AJ. Science 1995;270:1789–91.
- Coakley K, McGehee MD. Chem Mater 2004;16:4533–42.
- Xin H, Guo XG, Kim FS, Ren G, Waston MK, Jenekhe SA. J Mater Chem 2009;19:5303–10.
- Blouin N, Michaud A, Leclerc M. Adv Mater 2007;19:2295–300.
- Chen JW, Cao Y. Acc Chem Res 2009;42:1709–18.
- Qin RP, Li WW, Li CH, Du C, Veit C, Schleiermacher H-F, et al. J Am Chem Soc 2009;131:14612–3.
- Scharber MC, Muhlbacher D, Koppe M, Denk P, Waldauf C, Heeger AJ, et al. Adv Mater 2006;18:789–94.
- Bredas J-L, Beljonne D, Coropceanu V, Cornil J. Chem Rev 2004;104: 4971–5004.
- Park SH, Roy AJ, Beaupre S, Cho S, Coates N, Moon JS, et al. Nat Photon 2009;3:297–303.
- Wang E, Wang L, Lan L, Luo C, Zhuang W, Peng J, et al. Appl Phys Lett 2008;92: 033307.
- Huang F, Chen K-S, Yip H-L, Hau SK, Acton O, Zhang Y, et al. J Am Chem Soc 2009;131:13886–7.
- He Y, Chen H-Y, Hou J, Li YF. J Am Chem Soc 2010;132:1377–82.
- Yuan M-C, Chiu M-Y, Liu S-P, Chen C-M, Wei K-H. Macromolecules 2010;43:6936–8.
- Zou Y, Najari A, Berrouard P, Beaupre S, Aich BR, Tao Y, et al. J Am Chem Soc 2010;132:5330–1.
- Piliago C, Holcombe TW, Douglas JD, Woo CH, Beaujuge PM, Frecher JM. J Am Chem Soc 2010;132:7595–7.
- Zhang Y, Hau SK, Yip H-L, Sun Y, Acton O, Jen AK-Y. Chem Mater 2010;22: 2696–8.
- Zhang G, Fu Y, Xie Z, Zhang Q. Chem Commun 2010;46:4997–9.
- Bundgaard E, Krebs FC. Macromolecules 2006;39:2823–31.
- Yue W, Zhao Y, Tian H, Song D, Xie Z, Yan D, et al. Macromolecules 2009;42: 6510–8.

- [28] Biniek L, Chochois CL, Hadziioannou G, Leclerc N, Leveque P, Heiser T. *Macromol Rapid Commun* 2010;31:651–6.
- [29] Hou J, Park MH, Zhang S, Yao Y, Chen LM, Li JH, et al. *Macromolecules* 2008;41:6102–8.
- [30] Nielsen CB, Bjornholm T. *Org Lett* 2004;6:3381–4.
- [31] Zoombelt AP, Gilot J, Wienk MM, Janssen RAJ. *Chem Mater* 2009;21:1663–9.
- [32] Li YF, Cao Y, Gao J, Wang D, Yu G, Heeger AJ. *Syn Met* 1999;99:243–8.
- [33] Price SC, Stuart AC, You W. *Macromolecules* 2010;43:4609–12.
- [34] Lee JK, Ma LW, Brabec CJ, Yuen J, Moon JS, Kim JY, et al. *J Am Chem Soc* 2008;130:3619–23.





## Nanoporous materials from stable and metastable structures of 1,2-PB-*b*-PDMS block copolymers

Lars Schulte<sup>a</sup>, Anne Grydgaard<sup>b</sup>, Mathilde R. Jakobsen<sup>b</sup>, Piotr P. Szewczykowski<sup>a,b</sup>, Fengxiao Guo<sup>a,b</sup>, Martin E. Vigild<sup>b</sup>, Rolf H. Berg<sup>a</sup>, Sokol Ndoni<sup>a,\*</sup>

<sup>a</sup> Department of Micro and Nanotechnology, Technical University of Denmark, Frederiksborgvej 399, Build 124, DK-4000 Roskilde, Denmark

<sup>b</sup> Danish Polymer Centre, Department of Chemical and Biochemical Engineering, Technical University of Denmark, DK-2800 Kgs. Lyngby, Denmark

### ARTICLE INFO

#### Article history:

Received 28 September 2010

Received in revised form

19 November 2010

Accepted 22 November 2010

Available online 28 November 2010

#### Keywords:

Nanoporous  
1,2-Polybutadiene  
Block copolymer

### ABSTRACT

Experimental procedures used at the preparation and characterization stages of nanoporous materials (NPM) from 1,2-polybutadiene-*b*-polydimethylsiloxane (1,2-PB-*b*-PDMS) block copolymers are presented. The NPM were obtained from self-assembled block copolymers after firstly cross-linking 1,2-PB (the matrix component) and secondly degrading PDMS (the expendable component). Depending on the temperature of the cross-linking reaction different morphologies can be 'frozen' from the same block copolymer. Starting with a block copolymer precursor of lamellar morphology at room temperature, the gyroid structure or a metastable structure showing hexagonal symmetry (probably HPL) were permanently captured by cross-linking the precursor at 140 °C or at 85 °C, respectively. PDMS was degraded by reaction with tetrabutylammonium fluoride; considerations on the mechanism of cleaving reaction are presented. The characterization of the materials at different stages of preparation includes gravimetry, infrared spectroscopy, small angle x-ray scattering, electron microscopy and isothermal nitrogen adsorption experiments.

© 2010 Elsevier Ltd. All rights reserved.

### 1. Introduction

A diblock copolymer macromolecule consists of two chemically distinct parts (blocks) linked by a covalent bond. Depending on the relative block composition, the total degree of polymerization, temperature and pressure, the interplay between block immiscibility and connectivity can generate a variety of morphologies in the mesoscopic range of length-scales [1]. This self-organization in block copolymers is relevant in relation to bottom-up active material nanostructuring [2,3]. The targeted removal of part of the block copolymer molecule in the self-assembled state is an appealing strategy for the preparation of nanoporous polymers and a number of cleaving schemes have been reported [2–8a,b]. Among the possible applications of NPM are templates for electronics, special dielectric materials, and substrates for catalysis, nano-reactors, micro-filtration membranes and use in medical diagnostics.

A necessary condition for the stability of NPM is mechanical stability of the matrix after the removal of the expendable part. Polymers that are glassy at room temperature, like polystyrene (PS), are expected to be stable as matrix component in the dry state or in

the presence of non-solvents. However, contact with solvents or heating close to or above the glass transition temperature ( $T_g$ ) can irreversibly erase polymer's nanoporosity. The introduction of covalent cross-links in the matrix [7,9,10] can warrant 'memory' of the nanoporous morphology even at such conditions.

Few years ago we reported the preparation of nanoporous polystyrene from block copolymers with polydimethylsiloxane (PS-*b*-PDMS) after the targeted degradation of the PDMS block [8a]. Two groups reported shortly afterwards the preparation of nanoporous cross-linked polyisoprene from PI-*b*-PDMS precursors [9,10]. See Ref. [10] for a review of the subject. Highly uniform PS-*b*-PDMS and polydiene-*b*-PDMS block copolymers are readily synthesized by living anionic polymerization [12]; the block copolymer precursors can be aligned in a shear field [11,13] or an electrical field [14]. Most polydienes show  $T_g$  below 0 °C and therefore are unstable as NPM at room temperature. Cross-linking of the polydiene block before the removal of PDMS is necessary and feasible [9,10,13] in a controlled way.

This contribution presents the procedures for the preparation and characterization of 1,2-Polybutadiene-*b*-PDMS (1,2-PB-*b*-PDMS) diblock copolymer precursors and of the resulting nanoporous cross-linked 1,2-PB. Compared to nanoporous polyisoprene [9], the amount of cross-linker needed to prepare nanoporous 1,2-PB

\* Corresponding author. Tel.: +45 4677 4784; fax: +45 4677 4791.

E-mail address: [sokol.ndoni@nanotech.dtu.dk](mailto:sokol.ndoni@nanotech.dtu.dk) (S. Ndoni).

samples with similar mechanical properties is reduced by factors in the range 30–100. This difference is related to the different cross-linking reaction mechanisms in the two cases, as shown in the [Electronic Supplementary Information \(SEI\)](#). A discussion of the PDMS etching reaction mechanism by tetrabutylammonium fluoride is presented. Thermal cross-linking performed at specific temperatures 'freezes' sample's morphology at the cross-linking temperature. This can be utilized as an additional control parameter for the morphology of nanoporous polymers. Even thermodynamically metastable block copolymer micro-phases can be stabilized by this strategy, as shown in the following.

## 2. Experimental

### 2.1. Materials

#### 2.1.1. Block copolymer synthesis

The 1,2-PB-*b*-PDMS block copolymers were prepared by sequential 'living' anionic polymerization under Argon [12]. *Sec*-butyllithium was used as initiator for all the polymerizations. 1,2-PB-*b*-PDMS was polymerized in tetrahydrofuran (THF). The temperature of polymerization was either  $-40 \pm 5$  °C or  $-20 \pm 3$  °C, with polymerization times of 13 h and 3 h, respectively. The building unit of PDMS, hexamethylcyclotrisiloxane ( $D_3$ ), was added as a THF solution into the reactor containing the living polybutadienyllithium (pale green–yellow) at the respective temperature mentioned above. The temperature then was gradually increased to 0 °C and  $D_3$  was left to polymerize for up to 3 days at  $0 \pm 1$  °C. The complete crossover from the hydrocarbon to the siloxy lithium was associated with colour disappearance within few minutes from the addition of  $D_3$ . At that stage of synthesis 3–5 ml samples were taken out of the polymerization reactor. These samples were used for the characterization of the molar mass and molar mass distribution of the hydrocarbon blocks in the block copolymers. After the formation of the PDMS block, all the samples were terminated with a three times molar excess of trimethylchlorosilane. The finished polymers were isolated from the polymerization solutions by first precipitating and washing in excess of methanol and then by drying under vacuum overnight.

#### 2.1.2. Cross-linking

Dicumyl peroxide (bis( $\alpha,\alpha$ -dimethylbenzyl) peroxide) (DCP) and dilauryl peroxide (DLP) (both from Merck) were used as received for the cross-linking of 1,2-PB. A controlled quantity of 1% mole cross-linker per mole double bonds were co-dissolved in THF with the polymer prior to solution casting into flat bottom Petri dishes; the solvent was then left overnight to evaporate under a gentle flow of Ar. Smooth polymer films containing cross-linker were thus obtained. The Petri dish with the film was enclosed into a home-made steel cylinder and the air inside the cylinder quantitatively replaced with Argon. The gas tight closed cylinder was placed into a preheated thermostated oven for the cross-linking reaction to happen. DCP alone was used as cross-linking agent for all but one sample and in these cases the reaction temperature was 140 °C and the reaction time 2 h. For one single sample an equimolar mixture of DLP and DCP was used to carry the cross-linking reaction in two steps: the sample was first kept at 85 °C for 72 h then at 140 °C for 2 h. Structurally aligned samples of a 1,2-PB-PDMS block copolymer showing hexagonal morphology were prepared by first solvent casting a co-solution of polymer and 1% DCP (see above). Portions of the dry polymer-DCP mixture were then squeezed between two microscope glasses with 0.5 mm Teflon spacers in between and shear-aligned by hand: the glasses were moved back and forth relative to each other realizing shear amplitudes between 400 and 500%. The shear-aligned samples were cross-linked for 2 h at 140 °C.

#### 2.1.3. Etching of PDMS

Tetrabutylammonium fluoride (TBAF) (Aldrich) was used as cleaving reactant for PDMS. Cross-linked samples were reacted for 36 h with 1 M TBAF in THF at 2–5 times molar excess relative to the concentration of PDMS' repeating unit. After etching each sample was taken out of the solution and rinsed in fresh THF followed by a 24 h methanol bath before gradual solvent evaporation under a stream of Argon.

### 2.2. Characterization techniques

#### 2.2.1. Chromatography

The molar mass and molar mass distribution of the 1,2-PB block and the final block copolymer samples were characterized by SEC in stabilized THF. Two mixed-D columns (Polymer Laboratories) and a triple detector setup (Viscotek) (right angle light scattering, viscometer and differential refractometer) were used.

#### 2.2.2. Spectroscopy

The average composition of the di-block copolymers was determined by proton magnetic resonance spectroscopy,  $^1\text{H}$  NMR in a 250 MHz Avance DPX 250 Bruker instrument with *d*-chloroform as solvent. An independent estimate of the number average molar mass of the 1,2-PB block was obtained by  $^1\text{H}$  NMR, as well. The number of double bonds surviving cross-linking and etching of the 1,2-PB-PDMS samples was monitored by Raman (Renishaw system 3000) and Fourier transform infrared FT-IR (PerkinElmer Spectrum) spectroscopies.

#### 2.2.3. Rheology

The viscoelastic properties which reflect the diblock copolymer morphology were investigated by isothermal and temperature-gradient dynamic mechanical measurements on a Rheometrics RS 800 using parallel plate geometry. The data included in this paper refer to temperature gradients of 2.5 °C/min.

#### 2.2.4. Small angle X-ray scattering

Small angle X-ray scattering (SAXS) was measured either at Risø-DTU or at beam line I711 at MAX-lab in Lund, Sweden. At Risø the source was a rotating anode, with X-rays of wavelength  $\lambda = 1.54$  Å. The scattered radiation was collected with a 2-D position-sensitive wire detector at a distance of 1435 mm or 4656 mm from the sample. At Lund the distance from sample to detector was 1632.5 mm, the wavelength 1.10 Å and the scattering recorded on a MAR Research 165 CCD detector with 2048·2048 pixels. The scattering accumulation time for each measurement was 5 min or 2.5 min, after 5 min of waiting for sample equilibration at the set temperature. The heating gradient from one set point to the next was 12 °C/min in the interval 22–80 °C, 2 °C/min between 80 and 100 °C, and 1 °C/min above 100 °C. The data in this paper are raw data, shown as obtained from the detector after sensitivity and distortion corrections.

#### 2.2.5. Electron microscopy

A typical sample for *Scanning Electron Microscopy (SEM)* was prepared by first freeze fracturing or microtoming a piece of nanoporous polymer film in liquid nitrogen; the pieces were then mounted onto an aluminum specimen mount using Ted Pella double coated carbon conductive tabs and CCC Carbon Adhesive (Electron Microscopy Science). Each sample was sputter-coated with a 2–3 nm gold layer in a Polaron SC7640 and kept under vacuum in the microscopy chamber for 14–16 h before scanning. SEM imaging were collected either from a FIB-SEM Zeiss 1540 EsB Gemini at a 2 kV or a FEI Quanta 200 FEG MKII at 3 kV accelerating voltage. *Transmission electron microscopy (TEM)* was performed either in a Jeol

**Table 1**

Summary of molecular mass (MW) and composition data on 2 block copolymers. The transition order-to-order and order-to-disorder temperatures,  $T_{OOT}$  and  $T_{ODT}$ , respectively were determined by rheology (see Fig. 1).

Sample	$\langle M_n \rangle_1$ (g mol <sup>-1</sup> ) <sup>a</sup>	$\langle M_n \rangle_{total}$ (g mol <sup>-1</sup> ) <sup>b</sup>	PDI <sub>total</sub> <sup>c</sup>	$w_{PDMS}$ <sup>d</sup>	$f_{PDMS}$ <sup>e</sup>	Morphology	$T_{OOT}$ and $T_{ODT}$ (°C)
BD4	10 400	15 030	1.22	0.308	0.294	HEX DIS	255 (ODT)
BD14	8400	14 200	1.04	0.408	0.392	LAM 'HPL' GYR DIS	64 (OOT) 100 (OOT) 205 (ODT)

<sup>a</sup> Number average MW of the 1,2-PB block as obtained by SEC.

<sup>b</sup> Number average MW obtained by SEC and <sup>1</sup>H NMR.

<sup>c</sup> Polydispersity index  $PDI = \langle M_w \rangle / \langle M_n \rangle$  ( $\langle M_w \rangle$  is the weight average MW) obtained by SEC.

<sup>d</sup> Mass fraction of PDMS determined by <sup>1</sup>H NMR.

<sup>e</sup> Volume fraction of PDMS at 20 °C; density values:  $\rho_{1,2-PB} = 0.902$  g/cm<sup>3</sup> and  $\rho_{PDMS} = 0.966$  g/cm<sup>3</sup> [15,16].

3000F operated at 300 kV at Risø-DTU, or in a FEI TECNAI T20 operated at 200 kV, at DTU-CEN. Nanoporous films were sectioned into 90 nm slices on a Leica ultramicrotome with a cryo 35 diamond knife (DIATOME) at room temperature. For some experiments TEM samples were prepared by pulverizing 50 mg portions of NPM under liquid nitrogen in an agate mortar. The produced powder was suspended in 2 ml toluene (Fluka 99.8% grade) in a glass beaker. The suspension was ultrasonicated in a Branson 1510 bath for 40–60 min and few drops of it were applied onto a copper/carbon grid (Agar Scientific, 04-hole) before toluene evaporation. The dry grids were kept in a grid holder in order to avoid contamination.

### 2.2.6. Nitrogen adsorption

No particular sample preparation is needed for the nitrogen adsorption experiments. The amount of sample used for the measurements was in the range 100–200 mg. The measurements were performed on a Micromeritics ASAP 2020 Surface Area and Porosity Analyzer. The isothermal physisorption (adsorbed mass against pressure) was analyzed by the method of Langmuir and Brunauer–Emmett–Teller (BET), while the calculation of the pore size and distribution followed the scheme of Barrett–Joyner–Halenda (BJH).

To make nanoporous material the mother polymer was taken via several intermediate steps that are reflected in the sample

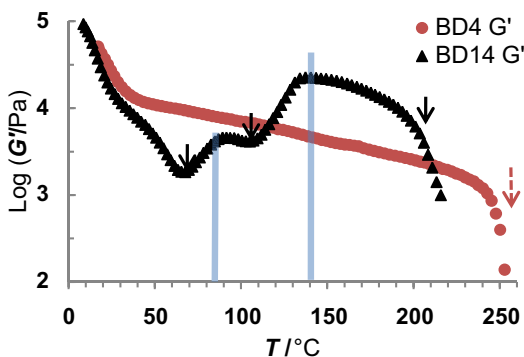


**Fig. 1.** Rheology traces of storage moduli  $G'$  at 1 rad/s and 2.5 °C/min as a function of temperature for the two block copolymer precursors, BD4 (circles) and BD14 (triangles). The dashed (solid) arrows point to the temperatures taken as micro-phase transition temperatures for the samples BD4 (BD14). The vertical bars at 85 and 140 °C show the cross-linking temperatures, the first applied to a sample of BD14 in order to stabilize the 'HPL' structure, and the second applied to samples from both BD4 and BD14, in order to stabilize the HEX and GYR morphologies, respectively, before PDMS etching.

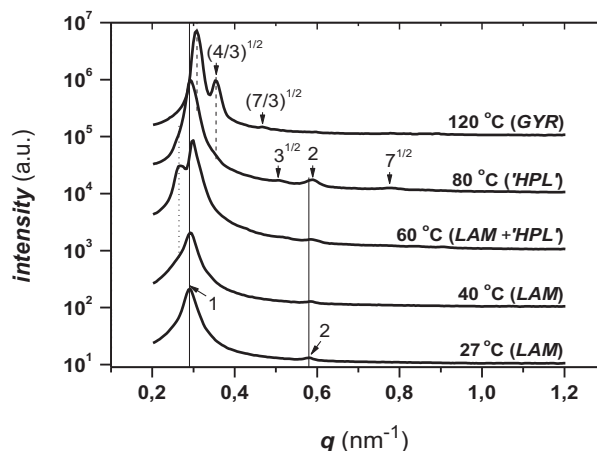


**Fig. 2.** Azimuthally integrated SAXS profiles for the sample BD14 recorded at five temperatures, as shown. The profiles were vertically translated by factors of 10, 10<sup>2</sup>, 10<sup>3</sup>, 10<sup>4</sup> and 10<sup>5</sup> for clarity. The vertical solid lines show the position of the two LAM peaks at 27 °C, the dotted line shows the position of the 'fluctuation' peak and the dashed lines show the position of the first two characteristic peaks from the GYR morphology. Arrows show expected scattering peak positions for lamellar at  $q^*$ ,  $2q^*$  (27 °C); hexagonal at  $3^{1/2}q^*$ ,  $2q^*$ ,  $7^{1/2}q^*$  (80 °C) and gyroid at  $(4/3)^{1/2}q^*$ ,  $(7/3)^{1/2}q^*$  (120 °C).  $q^*$  is the length of the scattering vector for the major scattering peak.

name. For example, BD14-x(85 °C)-E designates a sample cross-linked (x) at 85 °C and etched (E). The sample was derived from a 1,2-PB-*b*-PDMS diblock copolymer (BD) precursor prepared by synthesis batch 14. If no cross-linking temperature is shown then the sample has been cross-linked at the default temperature of 140 °C. Table 1 summarizes properties of two block copolymer precursors prepared by sequential anionic polymerization. The data in the first five columns were obtained by combining SEC and <sup>1</sup>H NMR. <sup>1</sup>H NMR analyses provided also information on the microstructure of the polybutadiene block: 89.5 ± 1.5% of the repeating units were 1,2-units and the rest were *trans*-1,4-units. The morphology was determined by SAXS.

## 3. Results and discussion

### 3.1. Block copolymer precursors

Different diblock copolymer structures exhibit distinctive viscoelastic properties [17]. Five morphologies were observed for the two samples in Table 1: lamellar (LAM), 'HPL', *la3d* gyroid (GYR), hexagonally packed cylinders (HEX) and disordered. The 'HPL'

**Table 2**

Data on cross-linking and etching of three samples. The temperature of cross-linking reaction was 140 °C for the first two samples. The last sample was first cross-linked at 85 °C for 72 h and then at 140 °C for 2 h.

Sample	$n_{DLP}/n_{=,0}$ <sup>a</sup>	$n_{DCP}/n_{=,0}$ <sup>a</sup>	$t/h$ <sup>b</sup>	$n_{=,x}/n_{=,0}$ <sup>c</sup>	$\Delta m_E/\Delta m_0$ <sup>d</sup>	$\Delta m_E/\Delta m_{E,max}$ <sup>e</sup>
BD4-x-E	0	0.01	2	0.36	0.30	0.97
BD14-x (140 °C)-E	0	0.01	2	0.34	0.40	0.99
BD14-x (85 °C)-E	0.01	0.01	72 (85 °C) 2 (140 °C)	0.30	0.39	0.98

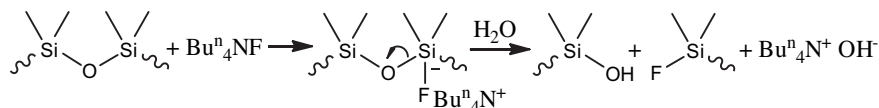
<sup>a</sup> Molar ratio between cross-linker (DCP or DLP) and polydiene double bonds in the block copolymer precursor.

<sup>b</sup> Cross-linking reaction time in hours.

<sup>c</sup> Fraction of double bonds measured by FT-IR in the cross-linked sample relative to the double bonds in the block copolymer precursor (uncertainty ± 5%).

<sup>d</sup> Fractional mass loss due to etching of PDMS.

<sup>e</sup> Fractional mass loss relative to maximal expectation.



**Scheme 1.** Proposed PDMS cleaving reaction mechanism by TBAF through the  $S_N2$ -Si pathway, which involves a pentacoordinate silicon intermediate anion. The wavy lines depict the polymer chain.

structure between *LAM* and *GYR* was observed for sample BD14 by both rheology and SAXS. It will be shown further on in this paper that the nanoporous samples prepared from samples cross-linked within the observation temperature region of this morphology show a structure with hexagonal symmetry. The structure is reminiscent of the metastable phase of hexagonally perforated lamellae [18a,b], therefore the designation ‘*HPL*’. The fact that cross-linking takes place at 140 °C (and in one case at 85 °C) and effectively freezes the morphology at that temperature, introduces the possibility to gain evidence for the morphology at elevated temperatures by performing room temperature SAXS measurements on samples cross-linked at the respective elevated temperature.

Fig. 1 shows the storage shear modulus  $G'$  (1 rad/s) traces from rheology of samples BD4 and BD14 recorded at a temperature gradient of 2.5 °C/min. The initial fall in  $G'$  for both samples up to roughly 30 °C is interpreted as due to the very end of the 1,2-PB block's glass transition ( $T_g \approx -16^\circ\text{C}$ ). The observed rheology trace for the sample BD4 is consistent with only one ordered phase up to the ODT at 255 °C marked with the dashed arrow in Fig. 1. As will be shown below SAXS and electron microscopy data are consistent with a *HEX* morphology. The sample BD14 showed a more complex behaviour. At least three micro-phase transitions were discerned by rheology, as marked by the three solid arrows at 64, 100 and 205 °C in Fig. 1. The sample was disordered above 205 °C. In order to elucidate the structures between the microphase transitions we performed SAXS at five different temperatures, 27, 40, 60, 80 and 120 °C, as shown in Fig. 2. The scattering trace at 27 °C is consistent with a *LAM* morphology, where two peaks at  $q$ -ratio 1:2 are visible (see also Fig. 7); the calculated lamella period is 21.6 nm. The two vertical solid lines in Fig. 2 show simply the position of the two *LAM* peaks at 27 °C; they are shown as a visual reference for the scattering peaks' position at higher temperatures. The trace at 40 °C is also consistent with *LAM* morphology (period 21.5 nm); however a broadening of the principal peak at the low  $q$  slope is visible. The broadening is probably due to the development of an additional peak, which becomes evident at  $q \approx 0.27 \text{ nm}^{-1}$  in the scattering profile recorded at 60 °C. The position of this additional, rather broad peak is approximately  $0.90 \cdot q^*$ , where  $q^*$  is the position of the main scattering peak at 60 °C. It could be due to the development of lamellae fluctuations that characterize the transition to or the metastable state itself of perforated lamellae [19]. Such a state is probably captured by the scattering profile at 80 °C, which shows a structure with similar length-scale as the *LAM*, but with additional peaks at  $3^{1/2} \cdot q^*$  and  $7^{1/2} \cdot q^*$ , which are characteristic for the hexagonal symmetry. The main scattering peak at 80 °C is at a  $q$  position only 0.7% higher than that for the *LAM* morphology at 27 °C, which is 7–12 times less than reported from other researchers [20]. The ‘fluctuation’ peak is visible also here as a shoulder on the low  $q$  slope of the main scattering peak. The dotted vertical line shows the  $q$ -position of the ‘fluctuation’ peak. It's worth mentioning here that the intensity of the ‘fluctuation’ peak was not reproducible in our experiments, as shown in the Supplementary Information. The scattering profile at 80 °C clearly shows two other shoulders at the high  $q$  side of the main peak, which in our opinion is related to the stable gyroid morphology, fully developed at 120 °C. The dashed

vertical lines mark the position of the two characteristic peaks for the *GYR* morphology, showing a  $q$  ratio of  $(6/8)^{1/2}$ .

From the above observations we conclude that BD14 shows *LAM* up to 64 °C and *GYR* from 100 °C up to some temperature below or equal to ODT. The morphology between 64 and 100 °C, which we again designate by ‘*HPL*’, appears where other researchers have observed the metastable microphase of hexagonally perforated lamellae (*HPL*) [18]. The coincidence of the observed scattering peaks with the predicted ones for each morphology is better than 0.2%. Note the coincidence of the scattering peak positions for the *LAM* and two of the peaks from the ‘*HPL*’ structures, which hints to the interpretation of structure ‘*HPL*’ as a lamellae morphology with superimposed hexagonal features (see also Figs. 7 and 8). The observation that the scattering profile between 60 and 100 °C was not reproducible (see ESI) is well in line with the alleged unstable/metastable nature of this state, which most probably comprises different non equilibrium microstructures developing in the transition from *LAM* to *GYR*. For the features of the morphology captured by cross-linking the sample at 85 °C and the resulting nanoporous polymer see Figs. 7 and 8 and related discussion in the ‘Nanoporosity’ section.

### 3.2. Cross-linking of 1,2-polybutadiene and etching of PDMS

The cross-linking reaction of 1,2-PB by peroxides is quite different from the cross-linking of polyisoprene (PI) [9,21,22]. At the same cross-linking conditions as for PI, just one single addition of 1 M% of DCP relative to the double bonds was sufficient to generate a wide range of cross-linking degrees simply by changing the reaction time. E.g., at 140 °C, 1 M% DCP suffices to generate networks which range from rubbery to glassy matrices, simply by changing the reaction time in the interval 0.5–4 h. This is a clear indication that the cross-linking reaction in this case is a chain reaction, where one peroxide molecule can generate more than one cross-link, in neat contrast to the  $\sim 1:1$  proportion in the case of PI. This can only happen by direct involvement of double bonds as shown in Scheme S1 of ESI.

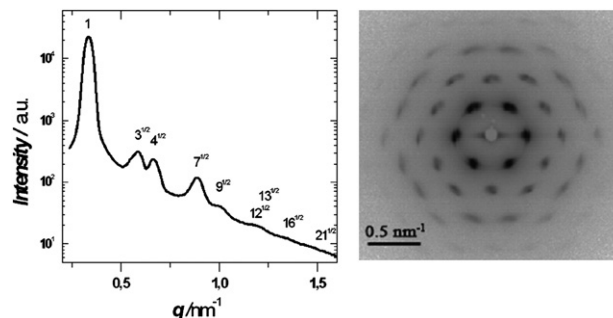


**Fig. 3.** 2-D and 1-D SAXS profiles for shear-aligned BD4-x-E with x-ray beam parallel to the shear direction. The scattering profiles show characteristic peaks for *HEX* morphology; the profiles are consistent with a high degree of shear-alignment. Characteristic length-scales of the structure were calculated from the scattering profile as shown in Table 3.

**Table 3**  
Characteristics of nanoporous materials obtained from SAXS, electron microscopy and nitrogen adsorption data. Uncertainties were estimated from at least three measurements.

Sample	$d^*_{\text{SAXS}}/\text{nm}^a$	$d^*_{\text{EM}}/\text{nm}^b$	$r_{\text{calc}}/\text{nm}^c$	$r_{\text{EM}}/\text{nm}^d$	$r_{\text{BJH}}/\text{nm}^e$	$A_{\text{calc}}/(\text{m}^2\text{g}^{-1})$	$A_{\text{BET}}/(\text{m}^2\text{g}^{-1})^f$
BD4-x-E	19.3 (HEX)	$18.3 \pm 3.4$	6.30	$6 \pm 1$	$6.1 \pm 1.0$	130 <sup>g</sup>	$75 \pm 20$
BD14-x(140 °C)-E	19.4 (GYR)	$19.3 \pm 2.5$	n.m/c <sup>h</sup>	$5 \pm 2$	$7.1 \pm 0.5$	230 <sup>i</sup>	$278 \pm 40$
BD14-x(85 °C)-E	21.0 (HPL)	$21 \pm 3^j$	n.m/c	$(4 \pm 2) \times (7 \pm 4)^k$	n.m/c	n.m/c	n.m/c

<sup>a</sup> Characteristic length-scales corresponding to the first structural peak from SAXS.

<sup>b</sup> Distance between principal Bragg planes from SEM/TEM.

<sup>c</sup> Cylindrical pore radius calculated from SAXS and porosity<sup>13</sup> (volume fraction 0.29).

<sup>d</sup> Pore radius from SEM/TEM.

<sup>e</sup> Pore radius from N<sub>2</sub> isothermal adsorption.

<sup>f</sup> Specific surface area from N<sub>2</sub> isothermal adsorption.

<sup>g</sup> Specific surface area calculated from pore radius  $r_{\text{calc}}$  above and the average density (0.71 g/cm<sup>3</sup>) of the NPM.

<sup>h</sup> Not measured/not calculated.

<sup>i</sup> Calculated as explained in Ref. [30].

<sup>j</sup> From Fig. 8(b).

<sup>k</sup> Elongated pores (see Fig. 8a).

The cross-linking conditions for BD4-x and BD14-x are summarized in Table 2. The first to third data columns in Table 2 include data on cross-linker amount and cross-linking time. These data confer in a nutshell the significant difference between the mechanisms of cross-linking reactions of 1,2-PB contra PI – as described in the previous paragraph and in ESI. As an illustration, in order to obtain BD4-x-E with similar mechanical properties as a corresponding nanoporous PI, 35 times less DCP was used in just 1/7-th of cross-linking time. The fourth column contains data on the fraction of double bonds surviving cross-linking relative to the double bonds in the diblock copolymer precursor, as measured by FT-IR. The dependence of consumed double bonds on the cross-linking degree and on the degree of collapse of the resulting materials after the removal of PDMS is discussed in a separate publication [13].

The reaction of TBAF with PDMS in THF (containing approx. 5% w/w H<sub>2</sub>O) is much gentler than the reaction with anhydrous HF [8,23]. While anhydrous HF is a strong protonating acid with acidity function ( $H_0$ ) of about –11 [24], TBAF is perhaps a base in polar aprotic solvents such as THF. It's reasonable to expect that cleavage with HF operate by an S<sub>N</sub>1-type process, via silicon–oxygen cleavage to give water and silico-cations, which react with fluoride anions. In contrast, cleavage with TBAF probably proceeds via the so-called S<sub>N</sub>2-Si pathway (Scheme 1) known from the rapid cleavage of silyl ethers to alcohols by treatment with 2–3 eq. TBAF in THF at 25 °C [25a,b].

Data on the fabrication of three samples (BD4-x-E, BD14-x(85 °C)-E and BD14-x(140 °C)-E) are summarized in the last two columns of Table 2. The data in the two last columns of the table reflect the nearly quantitative removal of PDMS after the reaction with TBAF.

### 3.3. Nanoporosity

The nanoporosity of the samples fabricated from the block copolymer precursors was analyzed by combining data obtained by FT-IR (see SEI), SAXS, electron microscopy and isothermal Nitrogen adsorption measurements.

Fig. 3 shows 2-D raw data in the direction of shear (right panel) and the 1-D reduced data (left panel) for the nanoporous sample BD4-x-E. This sample was subjected to reciprocal shearing before cross-linking and etching. The SAXS instrument measures the scattering from a sample volume of approximately one cubic millimetre. The extraordinarily well-resolved 2-D scattering indicates that the sample is aligned to such a degree that the order can be compared to a single crystal-like hexagonal arrangement of the cylindrical cavities. The shear planes were parallel to the (10) crystallographic plane of the morphology. The etched sample BD4-x-E shows a 9% smaller characteristic distance between primary Bragg planes compared to the diblock copolymer precursor (not shown), 19.3 nm against 21.1 nm, as listed in the first data column of

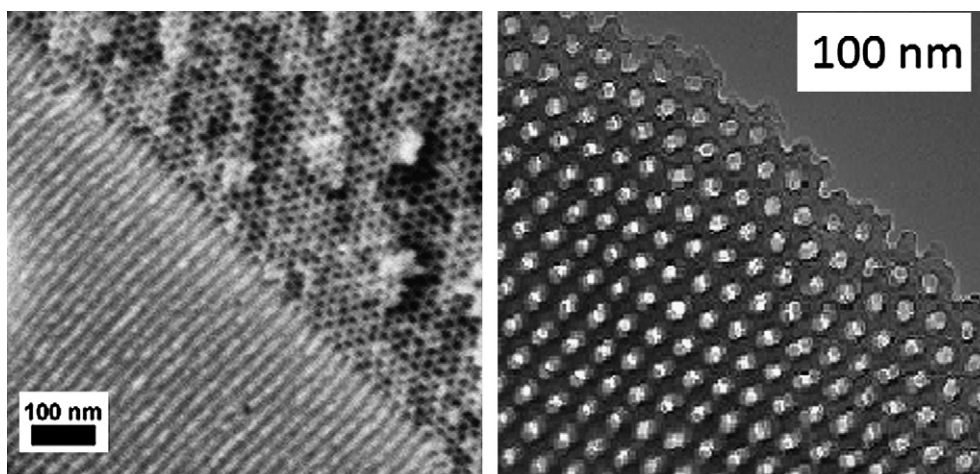


**Fig. 4.** SEM and TEM micrographs of the shear-aligned BD4-x-E. Characteristic length-scales of the structure were calculated from the pictures as shown in Table 3.

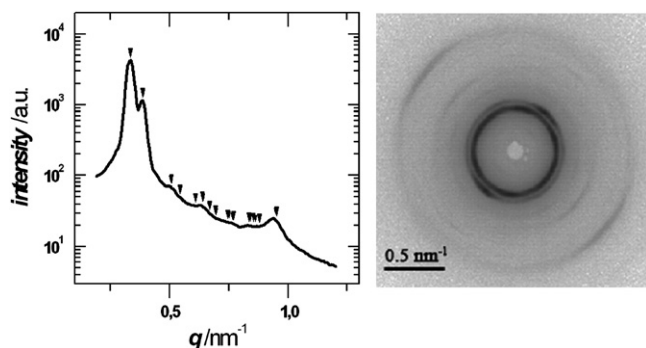


**Fig. 5.** 1-D and 2-D SAXS profiles of a nanoporous sample BD14-x(140 °C)-E. The [211], [220] and other characteristic peaks for the gyroid morphology are marked in the 1-D profile (the marked positions, expected for scattering from gyroid have the following  $q$  ratios:  $6^{1/2}$ ,  $8^{1/2}$ ,  $14^{1/2}$ ,  $16^{1/2}$ ,  $20^{1/2}$ ,  $22^{1/2}$ ,  $24^{1/2}$ ,  $26^{1/2}$ ,  $30^{1/2}$ ,  $32^{1/2}$ ,  $38^{1/2}$ ,  $40^{1/2}$ ,  $42^{1/2}$ ,  $50^{1/2}$ ).

**Table 3.** This shrinkage is mainly due to increased density of the 1,2-PB phase in the process of cross-linking.

**Fig. 4** shows SEM and TEM micrographs of the same sample BD4-x-E. The single crystal-like order of the cavities is clearly evident in the two pictures. The SEM micrograph shows the area around the diagonally running edge of two (fracture) surfaces that are tilted with respect to one another. The upper right-hand part of the picture displays an “end view” of the cavities, which gives a perfectly uniform hexagonal pattern. The lower left-hand part of the picture displays a “side view” of the structure, where the cylindrical cavities are exposed along their length, which clearly exceeds the frame of the SEM picture. Both micrographs yield information on the characteristic length scales of the NPM (2<sup>nd</sup>, 4<sup>th</sup> data columns in Table 3).

The 1-D and 2-D SAXS profiles of the nanoporous sample BD14-x-E are shown in Fig. 5. The 1-D scattering curve is indexed to match the reflections of the gyroid morphology. We have previously demonstrated a gyroid NPM in a PS matrix [8a]. The lattice constant of the cubic lattice calculated from the position of the first allowed SAXS diffraction peak in Fig. 5 is 47.5 nm. The 2-D profile shows anisotropy due to sample alignment. The sample was simply prepared by solvent casting, with no application of alignment field prior to cross-linking. We speculate that the observed anisotropy might have been induced from some partial orientation of the original lamellar structure during sample preparation, due to the ease of alignment of such morphology for relatively short polymer blocks above their glass transition temperatures. Scanning and transmission electron microscopy pictures of BD14-x-E are shown

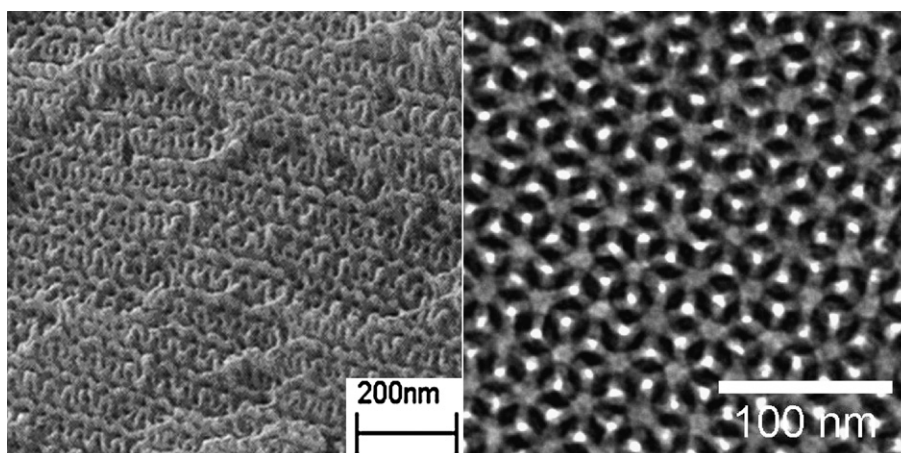


**Fig. 6.** SEM (left) and TEM (right) images of BD14-x(140 °C)-E clearly showing gyroid morphology.

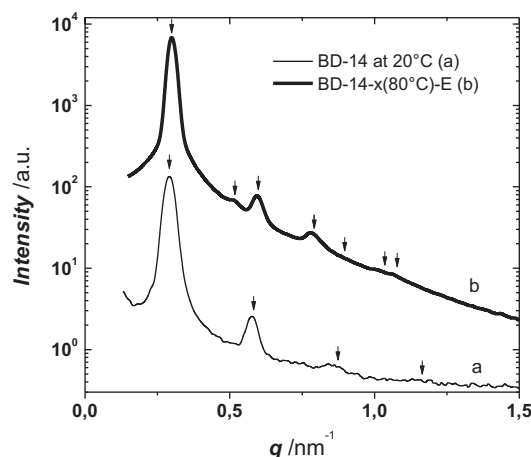


**Fig. 7.** Azimuthally integrated SAXS profiles for the precursor BD14 (a) and the nanoporous BD14-x(85 °C)-E (b), both recorded at room temperature. The arrows show expected scattering peak positions for lamellar at  $q^*$ ,  $2q^*$ ,  $3q^*$  (a); hexagonal at  $q^*$ ,  $3^{1/2}q^*$ ,  $2q^*$ ,  $7^{1/2}q^*$ ,  $3q^*$ ,  $12^{1/2}q^*$ ,  $13^{1/2}q^*$  (b).

in Fig. 6. The SEM micrograph shows the (211) projection known also as ‘knitting pattern’, while the (111) or the ‘wagon wheel’ projection is visible in the TEM micrograph. The crystallographic cell size estimated from the TEM micrograph was  $47 \pm 2$  nm, in good agreement with the one calculated from SAXS. A pore radius of  $5 \pm 1$  nm and a strut length of  $18 \pm 2$  nm was estimated from the TEM image.

**Fig. 7** shows SAXS profiles of the BD14 precursor and the nanoporous BD14-x(85 °C)-E sample, both recorded at 20 °C. The scattering profile of BD14 reproduces the length scales already seen in Fig. 2 for the BD14 melt at 27 °C; at least the three first scattering peaks are visible in Fig. 7 with scattering lengths at ratios 1:2:3, consistent with LAM morphology. The nanoporous polymer with the structure earlier labelled by ‘HPL’ was prepared by cross-linking sample BD14 for 72 h at 85 °C, then for additional 2 h at 140 °C, and finally by selectively degrading PDMS. The reason for the two-step cross-linking is related to the slow kinetics of the first step. A rubbery material of rather low degree of cross-linking was obtained after the first step. The second step provided sufficient mechanical stability to the sample to prevent pore collapse after the removal of PDMS by TBAF. However, the cross-linking at the first step is expected to suppress the mobility of the chains at length scales above some fraction of the radius of gyration of the original chains, therefore effectively freezing the morphology at that of 85 °C. The primary peak of the etched sample is shifted by 2.0% (from 0.293 to

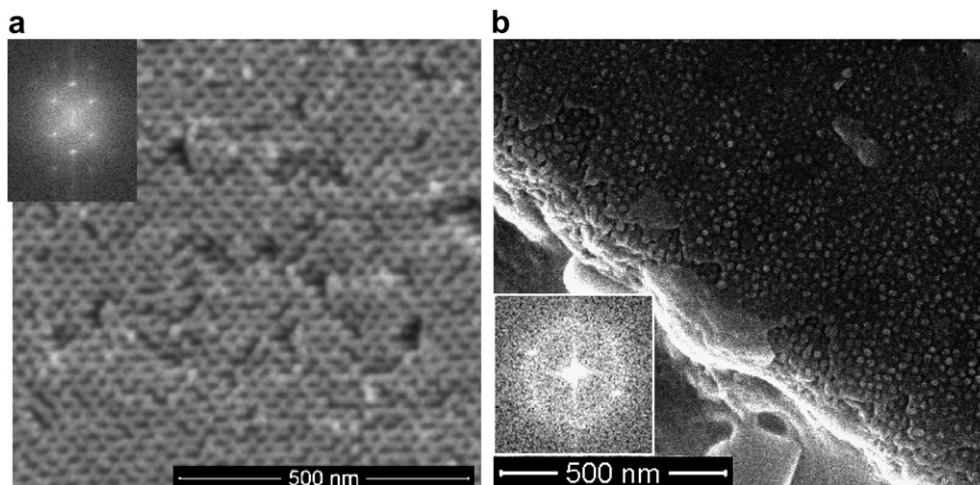


**Fig. 8.** (a) SEM image of a sample with 'HPL' morphology, similar to BD14-x(85 °C)-E; top-left insert is FFT of the image. (b) Morphology close to the surface of a sample cross-linked at 140 °C [26] showing lamellae interconnected by loosely hexagonally packed cylindrical protrusions. Bottom-left insert is an FFT of an image square section within the area of protrusions.

$0.299 \text{ nm}^{-1}$ ) relative to the primary peak of the polymer melt at 80 °C, shown in Fig. 2. This might be due to sample contraction as a result of cross-linking and etching. We do not observe here the 'shoulders' around the primary peak mentioned in relation to the polymer melt at 80 °C in Fig. 2. The scattering intensity at the primary peak position is two orders of magnitude higher than that of the melt, due to the increased electron density contrast in the nanoporous sample. Fig. 8(a) is a SEM image of a sample similar to BD14-x(85 °C)-E. The SEM image and its Fast Fourier Transform (FFT) in the top-left insert are very similar to reported observations on HPL [18]. At present we don't have reliable images of other projections from the same sample that could conclusively determine the morphology, therefore the quotation marks in 'HPL'. Fig. 8 (b) shows the morphology close to the surface of another sample, cross-linked at 140 °C [26]. At this temperature the GYR morphology was shown to be stable in the bulk. However, close to the polymer–argon interface (during cross-linking) the morphology is different, LAM at the very surface and HPL right beneath. The discussion of the role of the surface energy in stabilizing morphologies different from the bulk morphology will be presented elsewhere [26]. The image shows a pattern of protrusions (nanopillars) with some hexagonal packing order as demonstrated by the FFT pattern shown in the insert. A layered structure is visible at different locations between the up-left diagonal and the bright sample edge. The pattern in Fig. 8(b) is consistent with the structure expected for the majority microphase of perforated lamellae morphology with some degree of hexagonal packing (HPL). The diameter of the protrusions can be estimated to  $14 \pm 3 \text{ nm}$  and the characteristic distance between the principal Bragg planes to  $21 \pm 3 \text{ nm}$ . To the best of our knowledge stabilization of a metastable micro-phase by cross-linking and the further preparation of the corresponding nanoporous polymer have not been previously reported.

Finally Fig. 9 shows the results from isothermal adsorption of Nitrogen into the nanoporous sample BD14-x(140 °C)-E and the resulting pore size and pore size distribution as calculated from the Barrett–Joyner–Halenda (BJH) scheme [27]. The adsorption isotherm is of type IV with a hysteresis loop of type H1, characteristic of mesoporous materials with a narrow pore size distribution [28]. The plot of pore radius as calculated from the desorption branch ( $4.8 \pm 0.5 \text{ nm}$ ) is shown by the narrow peak in Fig. 9. The corresponding radius calculated from the adsorption branch peaks at 7.1 nm. This last is the value conventionally reported in the literature from BJH analysis of gas sorption data. Table 3

summarizes the characteristic geometrical scales obtained by different techniques for the NPM samples of the present study.

The pore sizes calculated by the isothermal adsorption for both the hexagonal and the gyroid nanoporous samples are shown in the sixth column of Table 3. The sizes listed in Table 3 as measured/calculated by different methods are reasonably consistent. The specific surface area of the HEX and the GYR samples shown in the last column of Table 3 were derived from Nitrogen sorption measurements analyzed by the BET scheme. The calculation of surface area for the NPM BD4-x-E was straightforward; it's shown in the next to last column of Table 3 ( $139 \text{ m}^2/\text{g}$ ). It is significantly higher than  $A_{\text{BET}}$  ( $75 \pm 20 \text{ m}^2/\text{g}$ ), hinting to the possibility that part of the cylindrical pores were not accessible to Nitrogen, probably due to hindered percolation from the outer surface. The  $A_{\text{BET}}$  for the sample BD14-x-E with gyroid structure was  $278 \pm 40 \text{ m}^2/\text{g}$ . The specific surface area for the same sample was also estimated from a mathematical model of the 'double gyroid' [29]. The model represents gyroid surfaces (or interfaces) by minimal surfaces or surfaces of constant mean curvature (cmc) and the surfaces are measured by triangulation. The surface area of a cmc enclosing same volume fraction and scaled to same crystallographic cell size as our gyroid sample was calculated to  $230 \text{ m}^2/\text{g}$  [30]. This value is

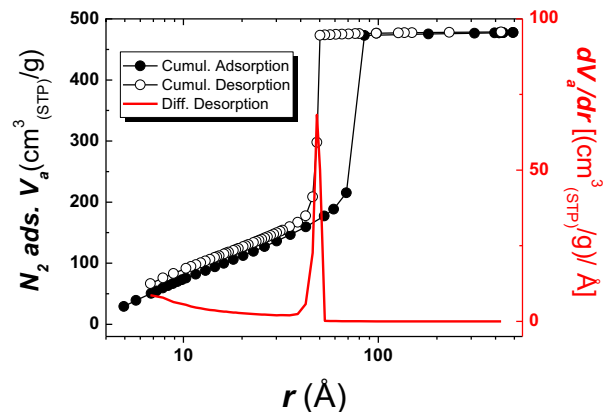


**Fig. 9.** BET nitrogen adsorption data. Cumulative (black) and differential (red) distribution of adsorbed Nitrogen per unit mass of nanoporous polymer as a function of pore size as calculated from the BJH scheme. (For interpretation of the reference to colour in this figure legend, the reader is referred to the web version of this article).

somewhat smaller than  $A_{\text{BET}}$  ( $278 \pm 40 \text{ m}^2/\text{g}$ ); at the moment we have no precise clue on the reason for this discrepancy.

#### 4. Conclusions

The preparation procedure of nanoporous materials from 1,2-polybutadiene-*b*-PDMS diblock copolymers was presented. The 1,2-PB matrix was stabilized by cross-linking before the production of nanoporosity. Free radical cross-linking of the polydiene block was initiated by thermally scissioned peroxides, DCP and DLP. A possible reaction scheme for the cross-linking of 1,2-PB is presented as [Supplementary Information](#). TBAF in THF was used to quantitatively degrade PDMS from the cross-linked samples. A short discussion of the degradation reaction mechanism was presented. The morphology of the remaining polymer matrix was largely conserved after PDMS cleaving as ascertained by SAXS. Images in direct space realized by scanning and transmission electron microscopy were shown as a direct proof of the morphology and alignment and were in quantitative agreement with the SAXS data. Controlling the temperature of cross-linking reaction of same block copolymer precursor allowed capturing different accessible morphologies from the microphase diagram, thermodynamically stable (*GYR*) or metastable (*HPL*). Pore size, size distribution and specific surface area were measured by isothermal Nitrogen adsorption. This is the first report describing the preparation of nanoporous cross-linked polydiene with stabilized metastable morphology.

#### Acknowledgments

We thank the Danish Agency for Research, Technology and Innovation (FTP) for supporting the project. We thank Thomas W. Hansen from DTU-CEN for TEM imaging. Marina Kustova and Søren K. Klitgaard (Centre of Sustainable and Green Chemistry, DTU) supported with the nitrogen adsorption characterization.

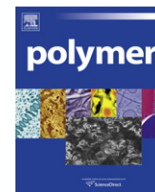
#### Appendix. Supplementary data

Supplementary data related to this article can be found online at [doi:10.1016/j.polymer.2010.11.038](https://doi.org/10.1016/j.polymer.2010.11.038).

#### References

- [1] For an early summary of the subject, see e.g., In: Aggarwal SL, editor. Block copolymers. New York: Plenum Press; 1970.
- [2] Lee J-S, Hirao A, Nakahama S. *Macromolecules* 1988;21:274–6.
- [3] Hashimoto T, Tsutsumi K, Funaki Y. *Langmuir* 1997;13:6869–72.
- [4] Park M, Harrison C, Chaikin PM, Register RA, Adamson DH. *Science* 1997; 276:1401–4.
- [5] Thurn-Albrecht T, Schotter J, Kastle GA, Emlay N, Shibauchi T, Krusin-Elbaum L, et al. *Science* 2000;290:2126–9.
- [6] Zalusky AS, Olayo-Valles R, Wolf JH, Hillmyer MA. *J Am Chem Soc* 2002; 124:12761–73.
- [7] Liu G, Ding J, Guo A, Herfort M, Bazzett-Jones D. *Macromolecules* 1997;30: 1851–3.
- [8] (a) Ndoni S, Vigild ME, Berg RH. *J Am Chem Soc* 2003;125:13366–7; (b) Guo F, Jankova K, Schulte L, Vigild ME, Ndoni S. *Macromolecules* 2007;41:1486–93.
- [9] Hansen MS, Vigild ME, Berg RH, Ndoni S. *Polymer Bulletin* 2004;51:403–409; Hansen MS. *Polysisoprene Glass with Nanopores* Jan 2003. Diplom K Thesis, Dept of Chemical Engineering, Technical University of Denmark.
- [10] Cavicchi KA, Zalusky AS, Hillmyer MA, Lodge TP. *Macromol Rapid Commun* 2004;25:704–9.
- [11] Hillmyer MA. *Adv Polym Sci* 2005;190:137–81.
- [12] Ndoni S, Papadakis CM, Almdal K, Bates FS. *Rev Sci Instrum* 1995;66: 1090–5.
- [13] Guo F, Andreasen JW, Vigild ME, Ndoni S. *Macromolecules* 2007;40:3669–75.
- [14] Hentschel T. *Electrical field alignment of nanoporous polymers obtained by a 1,2-PB-PDMS block copolymer* 2006, BSc thesis Polymer Dept., Risø National Laboratory and Danish Polymer Centre, Dept. Chem. Eng., Technical University of Denmark.
- [15] Mark JE, editor. *Polymer data handbook*. Oxford University Press; 1999.
- [16] Brandrup J, Immergut EH. *Polymer handbook*. 3<sup>rd</sup> ed. New York: John Wiley & Sons; 1989.
- [17] Frederickson GH, Bates FS. *Dynamics of block copolymers: theory and experiment*. *Annu Rev Mater Sci* 1996;26:501–50.
- [18] (a) Hamley IW, Koppi KA, Rosedale JH, Bates FS, Almdal K, Mortensen K. *Macromolecules* 1993;26:5959; (b) Khandpur AK, Förster S, Bates FS, Hamley IW, Ryan AJ, Bras W, et al. *Macromolecules* 1995;28:8796.
- [19] Qi S, Wang Z-G. *Macromolecules* 1997;30:4491.
- [20] (a) Hajduk DA, Ho R-M, Hillmyer MA, Bates FS, Almdal K. *J Phys Chem B* 1998;102:1356; (b) Loo Y-L, Register RA, Adamson DH, Ryan AJ. *Macromolecules* 2005;38: 4947.
- [21] Van Krevelen DW, editor. *Properties of polymers*. Amsterdam, Oxford, New York, Tokyo: Elsevier; 1990.
- [22] *Encyclopedia of polymer science and engineering*. 2<sup>nd</sup> ed., vol. 14. New York: John Wiley & Sons; 1985–1989.
- [23] Booth HS, Freedman ML. *J Am Chem Soc* 1950;72:2847–50.
- [24] Hyman HH, Garber RA. *J Am Chem Soc* 1959;81:1847–9.
- [25] (a) Corey EJ, Venkateswarlu A. *J Am Chem Soc* 1972;94:6190–1; (b) Corey EJ, Snider BB. *J Am Chem Soc* 1972;94:2549–50.
- [26] Li L, Jonsson G, Clausen LD, Hansen KM, Ndoni S. Unpublished results. Manuscript in preparation.
- [27] Barrett EP, Joyner LG, Halenda PP. *J Am Chem Soc* 1951;73:373–80.
- [28] IUPAC. *Pure Appl Chem* 1985;57:603–19.
- [29] Grosse-Brauckmann KJ. *Coll Interface Sci* 1997;187:418–28.
- [30] Table 8 in Ref. [29] gives an area per volume of  $\sigma = 2.50$  (by interpolation at 44% volume fraction of minority component) with a scaling to 1 of the first allowed reflection. The specific volume of BD14-x-E is  $V_{\text{sp}} = 1.79 \cdot 10^{-6} \text{ m}^3/\text{g}$  and the first allowed reflection from SAXS corresponds to  $2\pi/q^* = 19.47 \text{ nm}$ . Therefore the scale length factor [29]  $\lambda$  is  $19.47 \cdot 10^{-9} \text{ m}$ . The specific area for BD14-x-E can be calculated as:  $A_{\text{sp}} = \sigma \cdot V_{\text{sp}} / \lambda = [2.50 \cdot 1.79 \cdot 10^{-6} (\text{m}^3/\text{g})] / [19.47 \cdot 10^{-9} (\text{m})] = 230 \text{ m}^2/\text{g}$ .





# Influence of molar mass and temperature on the dynamics of network formation in polycarbonate/carbon nanotubes composites in oscillatory shear flows

R. Zeiler<sup>a,b</sup>, U.A. Handge<sup>b,\*</sup>, D.J. Dijkstra<sup>a</sup>, H. Meyer<sup>c</sup>, V. Altstädt<sup>b</sup>

<sup>a</sup> Bayer MaterialScience AG, CAS-INN-Physics, 51368 Leverkusen, Germany

<sup>b</sup> Department of Polymer Engineering, Faculty of Engineering Science, University of Bayreuth, Universitätsstrasse 30, 95447 Bayreuth, Germany

<sup>c</sup> Bayer MaterialScience AG, CAS-INN-CNT, 51368 Leverkusen, Germany

## ARTICLE INFO

### Article history:

Received 25 August 2010

Received in revised form

12 November 2010

Accepted 22 November 2010

Available online 29 November 2010

### Keywords:

Polycarbonate/carbon nanotubes composites

Electrical conductivity

Shear rheology

## ABSTRACT

The influence of molar mass and temperature on the formation of networks of multiwalled carbon nanotubes (MWCNT) in oscillatory shear flows was investigated. Combined rheological and electrical investigations were performed using composites with 0.5–5.0 wt% MWCNT in a low- and a high-viscosity polycarbonate (PC) at 190 °C and 250 °C. The objective of this work was to study the dynamics of the simultaneous formation of electrical and rheological networks by taking into account the superposition of (i) network breakup by the applied shear field and (ii) the diffusion-controlled clustering of carbon nanotubes. The formation (i.e. the buildup) of electrical and rheological networks proceeds more rapidly for a lower-viscosity matrix and at higher temperatures, whereas breakup of the electrical network is more pronounced at lower temperatures because of a larger stress-transfer between polymer matrix and MWCNT network. Sinusoidal shear deformation results in an oscillatory electrical conductivity with decreasing average value at large shear amplitudes, indicating that the electrical nanotubes network consists of weakly bonded carbon nanotube clusters which can be easily released and reformed. These data also show that MWCNT–MWCNT bonds can be reversibly deformed up to a maximum deformation. The latter experimental result precises the current understanding of electrical carbon nanotubes networks.

© 2010 Elsevier Ltd. All rights reserved.

## 1. Introduction

Carbon nanotubes have created a considerable interest in research and industry due to the expectation of engineering polymer composites with greatly enhanced electrical, thermal and structural properties [1–10]. Especially in the field of conductive polymer composites, carbon nanotubes are ideal candidates for use as filler materials [10–13]. Due to their high length-to-diameter ratio in the 100–1000 range [14,15] they can form percolated structures at extremely low contents [2,16–18]. Electrical measurements can reveal the existence of a percolated network of conductive fillers in an isolating matrix [19–26]. Since oscillatory melt rheology is a sensitive tool to probe the structure of polymer melts [27–32], simultaneous rheological and electrical investigations of polymer composites with multiwalled carbon nanotubes (MWCNT) have recently been the focus of several studies.

Investigations of the electrical resistivity of polycarbonate filled with MWCNT at ambient temperature indicated that electrical

percolation is attained between 1 and 1.5 wt% [33]. Dielectric spectroscopy revealed that the influence of the MWCNT on the complex permittivity and alternating current conductivity is frequency-dependent and that the percolation composition becomes clearly evident in the conductivity spectra through increased and constant values in the real part  $\sigma'$  of the complex conductivity  $\sigma^*$  at low frequencies [31]. The percolation threshold and the electrical conductivity in general strongly depend on the measurement temperature, the interaction potential between the nanotubes and the interfacial stabilizers used [31,34–38].

Rheometer plates acting as capacitors for dielectric spectroscopy enable the simultaneous observation of electrical conductivity, dielectric permittivity and rheological values [19,20,39]. Investigations of the transient recovery of the direct current (DC) conductivity after a shear deformation by Alig et al. showed an increase for several orders of magnitude [19]. The nanotubes network was primarily destroyed by shear, followed by the reorganization of the MWCNT via agglomeration [19]. Furthermore, single and double shear deformations were applied [20]. Shearing caused a severe drop in the electrical conductivity and a strong decrease of the storage modulus. The conductivity and storage modulus regained their initial values in the subsequent idle period. The recovery

\* Corresponding author. Tel.: +49 921 557476; fax: +49 921 557473.  
E-mail address: [ulrich.handge@uni-bayreuth.de](mailto:ulrich.handge@uni-bayreuth.de) (U.A. Handge).

proceeded faster after applying a single deformation than after a double shear. Alig et al. concluded that loosely packed nanotubes form agglomerates (“conductive beads”), which are destroyed during deformation and reform in the polymer melt [19–21].

Skipa et al. observed a transition from an insulator to a conductor for PC/MWCNT-melts with well dispersed nanotubes under steady shear [39]. The decrease in dynamic moduli during shearing originates in the agglomeration of dispersed nanotubes, leading to a reduction of mechanical reinforcement. A substantial difference in the nature of “electrical” and “mechanical” networks is presumed and it was pointed out that the experimental findings demonstrate the constructive and destructive effects of steady shear. Richter et al. focused on nonlinear rheological experiments and also performed an X-ray scattering analysis [40]. In shear, breakage of MWCNT clusters dominates whereas orientation of MWCNT is only observed at high shear rates. Agglomeration of carbon nanotubes manifested itself in an increase of the storage modulus [40].

Investigations of the orientational behaviour of MWCNT in PC showed that although an overshoot in transient shear viscosity is measured at shear rates as low as  $0.1 \text{ s}^{-1}$ , the nanotube network is disturbed only at considerably higher shear rates [25]. Furthermore, MWCNT in thermoplastic composites will only be oriented at high shear rates [25,41,42]. It was assumed that the viscosity of the composite depends strongly on the MWCNT network density, whereas the proximity of the tubes at the network points seems to determine the electrical properties of the MWCNT composite. In melt elongation single isolated MWCNT and clusters of MWCNT are oriented and the elongational viscosity is determined by the flow of MWCNT clusters in the matrix of polycarbonate [43].

The experimental results were summarized in models for carbon nanotube filled polymer melts. These models illustrate the difference in rheological and electrical percolation thresholds [44], highlight the different network types which are associated with polymer and nanotube interactions [31] and demonstrate the development of electrical conductivity by agglomeration of nanotubes [19,20]. In the melt, agglomeration of single nanotubes in clusters and agglomeration of nanotubes clusters can lead via percolation to an electrically conductive network, depending on the filler concentration [20,21]. This process can be modelled by combining agglomeration kinetics and percolation theory [19].

Although molecular weight of the polymer matrix and temperature are obviously coupled via the viscosity to the diffusion coefficient, the differences of the dynamics of formation of electrical and rheological networks are only partially explored, in particular the interplay of time-dependent buildup and shear dependent breakup of the electrical and rheological networks. The superposition of these phenomena is highly relevant for polymer processing where time-dependent and instationary phenomena generally dominate. In contrast to measurements in the transient mode, shear oscillations allow one to distinguish between the elastic and the viscous contributions. Since polymer–nanotube interactions play an essential role for a profound understanding of the network formation in these nanocomposites, the objective of this study is to depict the differences in the rheological and electrical properties in the context of the formation of networks of MWCNT in polycarbonate matrices, to elucidate the role of matrix viscosity and to focus on the processes determining the transition

zone between linear and nonlinear behaviour. The influence of the temperature and molar mass of the polycarbonate matrix is studied in detail in the oscillatory mode. Simultaneous measurements of the electrical and rheological properties in oscillatory shear at temperatures of 190 °C and 250 °C of composites of MWCNT and polycarbonate of different molecular weights allow conclusions regarding the phenomena participating in the simultaneous, time-dependent formation and the destruction of both electrical and rheological nanotube networks.

## 2. Experimental

### 2.1. Materials

Two different batches of neat polycarbonate (PC) with different molecular weight distributions (Makrolon® M2200 and Makrolon® M2800) and composites containing 0.5, 1.0, 1.5, 2.0, 3.0 and 5.0 wt% Baytubes® (MWCNT) were supplied in granular form from Bayer MaterialScience AG. The composites were compounded using a Werner & Pfleiderer ZSK26 extruder operated at 280 °C bulk temperature by dilution of a 15 wt% masterbatch MWCNT with commercially available PC M2200 and M2800, respectively. The masterbatch did not contain any dispersing agent which could influence the formation of a nanotubes network. The MWCNT were produced by catalytic chemical vapour deposition and had a mean outer diameter of 13 nm. The mean inner diameter amounted to 4 nm and the length was greater than 1  $\mu\text{m}$  and 0.1–0.2  $\mu\text{m}$  before and after dispersion, respectively [45]. The glass transition temperature  $T_g$ , as determined (i) by the derivative heat flow of the second heating using the inflection point method, and (ii) by the maximum of the loss modulus  $G''$  measured in dynamic mechanical experiments, the number and weight average of the molecular weight  $M_n$  and  $M_w$  and the steady-state viscosity  $\eta$  at 190 °C and 250 °C as determined by start-up experiments in shear ( $\dot{\gamma}_0 = 0.3 \text{ s}^{-1}$ ) are listed in Table 1. The average values of  $M_n$  and  $M_w$  of the composites are reduced due to degradation during compounding, e.g., for PC M2200 containing 3.0 wt% MWCNT values in  $M_n$  and  $M_w$  amount to 8580 g/mol and 18,330 g/mol, respectively. By choosing two different molecular weights and two different measurement temperatures (190 °C and 250 °C) four clearly different values of the steady-state viscosity were obtained, see Table 1.

Granules of PC and the PC/MWCNT composites were dried at 80 °C in a vacuum for 12 h. Then samples for shear experiments were prepared by compression moulding of the dried pellets in a vacuum at 220 °C for 8 min. The diameter of the cylindrical samples for shear experiments was 24.0 mm, and the thickness was 2.1 mm. For simultaneous electrical and rheological measurements the granules were compression moulded into circular plates with a diameter of 29 mm and a thickness of 2.1 mm. The samples were dried again in a vacuum at 80 °C before the experiments were started.

### 2.2. Electrical and rheological measurements

The rheological and the simultaneous rheological and electrical measurements were performed using an Advanced Rheometric Expansion System (ARES) rheometer manufactured by Rheometrics Inc. (Piscataway, USA). A plate–plate geometry was used with a plate diameter of 25 mm for solely rheological measurements.

**Table 1**

Glass transition temperature  $T_g$ , number and weight average of the molecular weight  $M_n$  and  $M_w$  and steady-state viscosity  $\eta$  at 190 °C and 250 °C of PC M2200 and PC M2800.

	$T_g$ (°C) DSC	$T_g$ (°C) DMA	$M_n$ (g/mol)	$M_w$ (g/mol)	$M_w/M_n$	$\eta$ (Pa s) at 190 °C	$\eta$ (Pa s) at 250 °C
PC M2200	143	144	9300	20,300	2.18	96,000	680
PC M2800	146	147	12,800	27,800	2.17	210,000	2500

The gap between the two plates was set to 2.0 mm. For simultaneous rheological and electrical measurements a plate–plate geometry with electrically isolated tools with a plate diameter of 30 mm was chosen [19,46]. A similar setup was used in Refs. [20,39]. A schematic view of the ring-shaped electrodes is given in Fig. 1. A Keithley electrometer model 6517A was utilized to measure the high volume resistivities above 200 k $\Omega$ . The device applies a fixed voltage of 40 V and measures the current in order to calculate the resistivity. For the range of 0.1  $\Omega$  and 100 M $\Omega$  a four-point test fixture combined with a Keithley digital multimeter model 2100 was used. The applied test current ranged between 1 mA and 10  $\mu$ A. The electrical conductivity  $\sigma$  was calculated using

$$\sigma = 4 \cdot h / \left[ \pi \cdot R \cdot (d_o^2 - d_i^2) \right], \quad (1)$$

where  $h$  is the thickness of the specimen,  $R$  is the measured resistance and  $d_o$  and  $d_i$  are the outer and the inner diameters of the ring-shaped measuring electrode, respectively. Shear deformation may lead to an anisotropic conductivity which is discussed, e.g., in the work of Semeriyarov et al. [47]. However, only the conductivity perpendicular to the flow direction can be measured with the current setup.

Before starting every experiment an equilibration time of 7.5 min in the measurement chamber at the chosen temperature was allowed in order to attain sample melting, temperature stability and a good electrical contact between the rheometer tools and the sample. Because of relevance for processing, measurements were performed directly after this thermal equilibration time in order to avoid degradation of the polymer matrix.

The linear viscoelastic properties of the materials under investigation were examined in time sweeps (cf. Section 3.3) at an angular frequency of  $\omega = 0.1$  rad/s and frequency sweeps (cf. Section 3.4) in the interval between  $\omega = 500$  rad/s and 0.01 rad/s at temperatures of 190  $^{\circ}$ C and 250  $^{\circ}$ C with a strain amplitude of  $\gamma_0 = 3\%$ . The nonlinear behaviour was investigated by performing strain sweeps (cf. Section 3.5) in the range of  $\gamma_0 = 0.4$  and 300% at an angular frequency of  $\omega = 0.1$  rad/s and at temperatures of 190  $^{\circ}$ C and 250  $^{\circ}$ C. Start-up experiments were also carried out for 50 s at a shear rate of  $\dot{\gamma}_0 = 0.3$  s $^{-1}$ . Dynamic mechanical analysis in the melt (cf. Section 3.6) was performed at a frequency of  $f = 1$  Hz and a deformation amplitude of 5% at 280  $^{\circ}$ C and decreasing amplitudes at lower temperatures. Cylindrical samples as described above were tested in the temperature range between 280  $^{\circ}$ C and 140  $^{\circ}$ C.

The cooling rate was 2 K/min. In all experiments the prehistory of the samples (i.e. drying, compression moulding, time for thermal equilibration in the rheometer before the test) was identical. Furthermore, our experimental data (e.g., no discontinuous stress signal) and the strong adhesion of the samples to the rheometer plates indicate the absence of wall slip in our range of shear rates.

### 2.3. Morphological and thermal investigations

The morphology was investigated by transmission electron microscopy (TEM). Compression-moulded samples were cut using a Reichert-Jung Ultracut microtome. The ultramicrotome was equipped with a diamond knife with a cut angle of 6 $^{\circ}$  and a knife angle of 35 $^{\circ}$  and used at room temperature. The thickness of the thin sections was approximately 50 nm. The TEM used was a Carl Zeiss CEM 902. The acceleration voltage was 80 keV.

DSC measurements were conducted with a Mettler Toledo DSC/SDTA 821e at a scan rate of 10 K/min under a nitrogen atmosphere in the temperature range from 25  $^{\circ}$ C to 270  $^{\circ}$ C. The sample mass was about 8 mg. The glass transition temperature of PC and composites was determined from the derivative heat flow of the second heating using the inflection point method.

## 3. Results and discussion

### 3.1. Dispersion and morphology of composites

Generally, MWCNT prepared by chemical vapour deposition are not completely straight, but partially bent. Depending on the degree of dispersion, they are arranged in clusters of entangled nanotubes (agglomerates) and single nanotubes [48]. Fig. 2 presents transmission electron micrographs of the composites. The gray lines correspond to different thicknesses of the ultrathin slices which cannot be completely avoided during ultramicrotoming. After compression moulding no preferential orientation of the nanotubes is visible (Fig. 2). Small residues of catalyst are recognizable in the electron micrographs at high resolution. The MWCNT were well dispersed by the extrusion process and compression moulding at 220  $^{\circ}$ C only moderately influences the dispersion state. The electrical conductivity of the compression-moulded samples in the solid state is listed in Table 2. Only the samples with a MWCNT loading of 3 wt% and more were moderately electrically conductive.

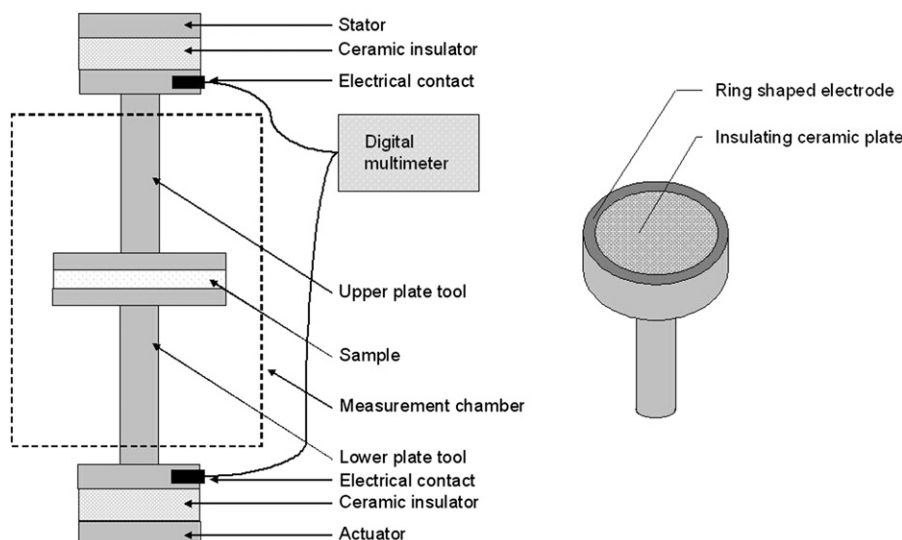


Fig. 1. Experimental setup for simultaneous measurements of the rheological and electrical properties of polymer melts.

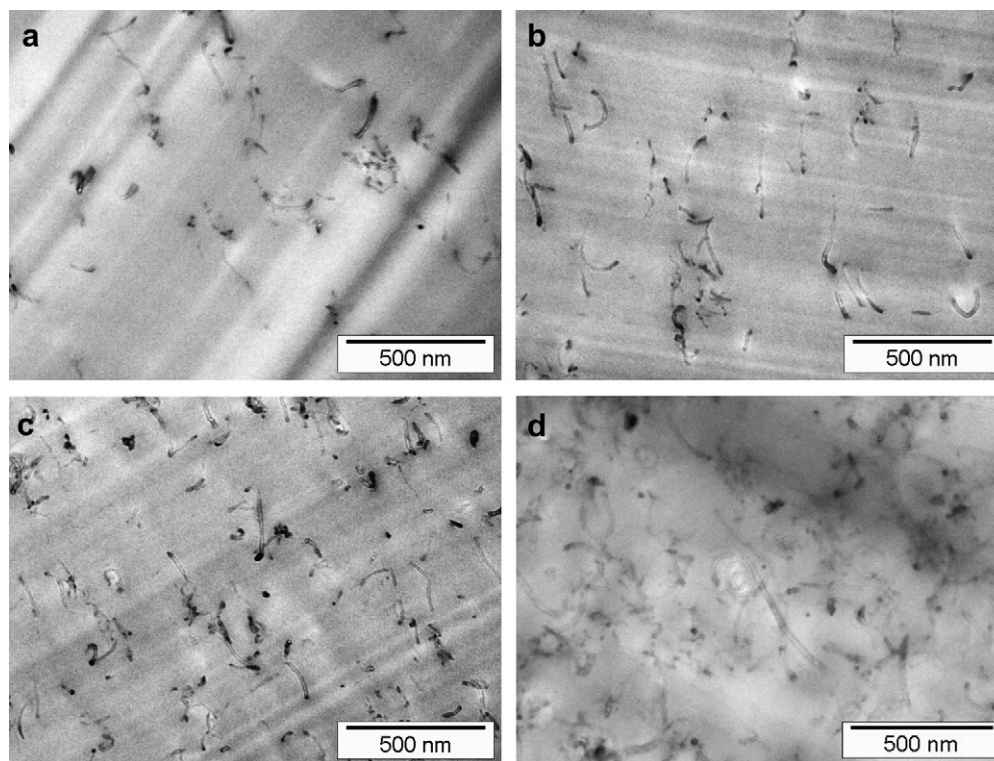


Fig. 2. Transmission electron micrographs of composites of PC M2200 and (a) 0.5 wt%, (b) 1.0 wt%, (c) 2.0 wt% and (d) 5.0 wt% multiwalled carbon nanotubes.

In suspensions of rod-like particles (with diameter  $d$  and length  $L$ ) in a polymer matrix, different concentration regimes can be distinguished which are characterized by the number  $\nu$  of nanotubes per volume element [49]. In the dilute regime ( $\nu < 1/L^3$ ), the carbon nanotube concentration is low and interactions between the nanotubes can be neglected. In the semi-dilute regime we have  $1/L^3 < \nu < 1/(dL^2)$  where the interactions between the nanotubes are highly relevant [50,51]. In the concentrated regime ( $1/(dL^2) < \nu$ ), a dense network of nanotubes exists [52].

Assuming a density of  $1.75 \text{ g/cm}^3$  for the carbon nanotubes [1] and  $1.1 \text{ g/cm}^3$  for the PC melt [53] the volume concentration  $\Phi$  of the MWCNT for the composites of this study ranges in the interval between approximately 0.3 vol% and 3.2 vol%. The number  $\nu$  of carbon nanotubes per volume element can be calculated using  $\nu = 4\Phi/(\pi dL^2)$ . In the semi-dilute regime the number of carbon nanotubes ranges between  $\sim 16 \mu\text{m}^{-3}$  and  $\sim 481 \mu\text{m}^{-3}$ , assuming a cylindrical shape with a diameter  $d$  of 13 nm [45] and a length  $L$  of 400 nm [54]. Therefore our composites containing 0.5 wt% ( $\nu \sim 59 \mu\text{m}^{-3}$ ) to 3.0 wt% ( $\nu \sim 359 \mu\text{m}^{-3}$ ) belong to the semi-dilute regime and the 5.0 wt% ( $\nu \sim 603 \mu\text{m}^{-3}$ ) samples are situated in the concentrated regime. Since the nanotubes of this study are partially bent, the true distance between single, isolated MWCNT is slightly larger than the theoretical one.

### 3.2. Time–temperature superposition of matrix polymers

The time–temperature superposition was applied in order to obtain master curves for the complex modulus  $G^*$  of PC M2200 and

PC M2800, see Fig. 3. The data measured at temperatures between  $150 \text{ }^\circ\text{C}$  and  $250 \text{ }^\circ\text{C}$  were shifted to a master curve using the ARES software at a reference temperature of  $T_{\text{ref}} = 190 \text{ }^\circ\text{C}$  (upper abscissa) and  $T_{\text{ref}} = 250 \text{ }^\circ\text{C}$  (bottom abscissa), respectively. Both grades of polycarbonate show the three typical distinct regions of homopolymer melts. At low frequencies (liquid-like behaviour) the dynamic moduli attain power-laws. The power-law exponents slightly differ from the prediction of a Maxwell element ( $G' \sim \omega^2$ ;  $G'' \sim \omega$ ) which indicates the presence of long relaxation times. With increasing frequency the crossover to the rubbery plateau is notable, where  $G'$  exceeds  $G''$ . The plateau is followed by the glass transition (maximum in  $G''$ ) and a solid-like (glassy) behaviour at larger frequencies.

### 3.3. Temporal stability under oscillatory shear

The results of linear viscoelastic shear oscillations at an angular frequency of  $0.1 \text{ rad/s}$  and a strain amplitude of 3% at  $190 \text{ }^\circ\text{C}$  and  $250 \text{ }^\circ\text{C}$  during 5 h are shown in Fig. 4. The storage modulus  $G'$  of neat PC M2200 is approximately 300 Pa and is constant with time. Values in the same order of magnitude are attained by the nanocomposites containing 1.0 wt% and 2.0 wt% MWCNT at the beginning of the time sweep tests. The value of  $G'$  increases by about five orders of magnitude up to above  $10^6 \text{ Pa}$  over a period of 5 h. The increase proceeds more rapidly for the composite containing the larger filler content (2.0 wt% MWCNT), whereas the plateau value does not depend on the MWCNT fraction. The same increase occurs if the sample is simply annealed at  $190 \text{ }^\circ\text{C}$  and only sheared for

Table 2

Electrical conductivity  $\sigma$  (in units of S/m) of compression-moulded plates of polycarbonate M2200, M2800 and its composites with MWCNT in the solid state ( $T = 25 \text{ }^\circ\text{C}$ ).

Concentration of MWCNT (wt%)	0.0	0.5	1.0	1.5	2.0	3.0	5.0
Matrix PC M2200 $\sigma$ (S/m)	$<10^{-13}$	$<10^{-13}$	$<10^{-13}$	$<10^{-13}$	$2.7 \times 10^{-9}$	$2.9 \times 10^{-5}$	$6.5 \times 10^{-4}$
Matrix PC M2800 $\sigma$ (S/m)	$<10^{-13}$	$<10^{-13}$	$<10^{-13}$	$<10^{-13}$	$<10^{-13}$	$8.1 \times 10^{-6}$	$3.0 \times 10^{-3}$

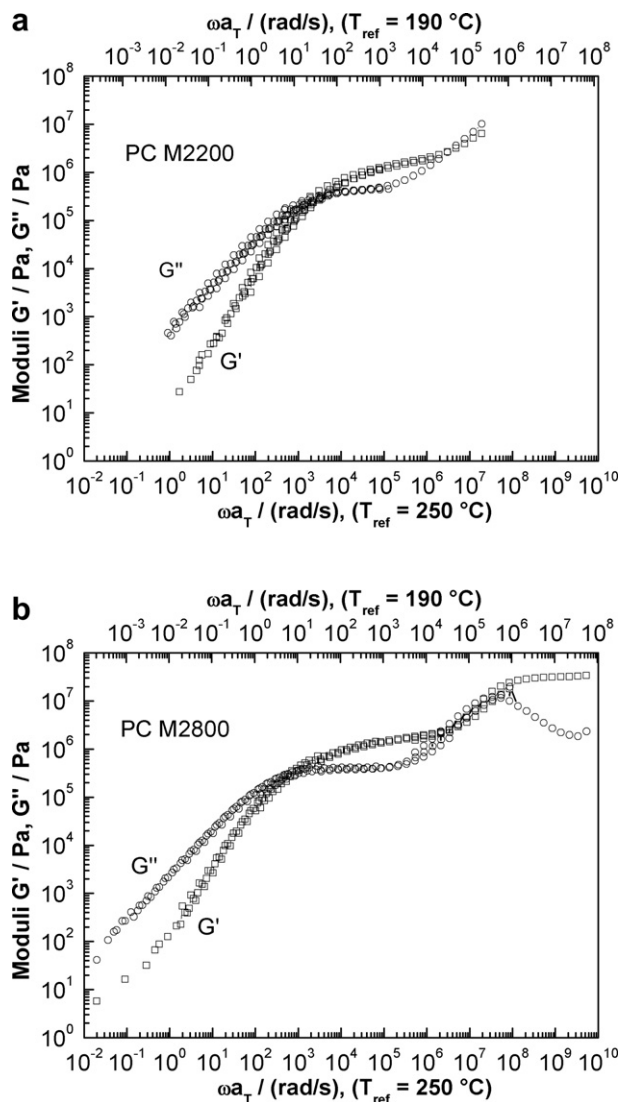


Fig. 3. Master curves for the storage and loss moduli  $G'$  and  $G''$  of PC M2200 and PC M2800 at reference temperatures of 190 °C and 250 °C.

5 min every half an hour (discontinuous measurement). These results indicate that the increase of the storage modulus seems to be driven by diffusion and is caused by MWCNT–MWCNT interaction. Furthermore, the data reveal that the electric field itself does not influence the measurements by, e.g., orientation of nanotubes. This result was also checked by discontinuous electrical measurements, where the electrical field was only applied for 30 s every half an hour (data not shown). The increase in storage modulus of about four orders of magnitude during the time sweeps at 190 °C arises from the formation of stable agglomerates of MWCNT that are tightly embedded in a relatively high viscous PC matrix. The diffusion-controlled process of agglomeration of carbon nanotubes [19,20] due to MWCNT–MWCNT interactions [55–57] leads to a framework of entangled nanotubes.

The electrical conductivity  $\sigma$  of the PC M2200 sample with 1.0% MWCNT is in the range of  $10^{-10}$  S/m and hence below the percolation threshold. A rapid increase in  $\sigma$  at the very beginning of the test is followed by a flat decrease for less than one order of magnitude over 5 h. The sample containing 2.0 wt% MWCNT reveals an electrical conductivity between  $10^{-7}$  and  $10^{-5}$  S/m. Continuous and discontinuous measurements again differ only

marginally. Fig. 4(a, b) clearly shows that at 190 °C the timescale of increase in moduli differs from the timescale of increase in electrical conductivity. This result indicates that different mechanisms, i.e. increase of entanglements of MWCNT and agglomeration of neighbored MWCNT, respectively, are responsible for the increase in storage modulus and the formation of electrical networks. The increase in storage modulus of the PC M2200 composite containing 1.0 wt% MWCNT while its electrical conductivity  $\sigma$  remains around  $10^{-10}$  S/m shows that the rheological and electrical quantities do not always correlate. The slight decrease of  $\sigma$  with time confirms the assumption that MWCNT progressively agglomerate, leading to a larger number of isolated agglomerates at this filler concentration. The relatively marked increase in  $\sigma$  of the 2.0 wt% sample during the first hour of the experiment clarifies the slow network formation at low temperatures. The formation of agglomerates leads to an increase in  $\sigma$  since the agglomerates are percolated because of sufficient filler content, and progressive agglomeration improves the electrical conductivity along percolated pathways of clustered agglomerates.

Fig. 4(c, d) presents the temporal stability for composites of PC M2200 and PC M2800 containing 1.5% and 2.0% MWCNT at 250 °C. The increase in storage moduli for all composites is only moderate compared to measurements at 190 °C. Surprisingly, the  $G'$  values for lower-viscosity PC M2200 containing 2.0% MWCNT are larger than for PC M2800 containing the same amount of filler. Thus it seems that the specific configuration of the MWCNT network strongly influences the rheological properties. Additionally the increase in  $G'$  is faster for PC M2200 composites. The rise in storage modulus with time at 250 °C is less pronounced than at 190 °C because the stress in the matrix decreases with temperature and the matrix contributes less stress-transfer towards the nanotube network. At higher temperatures, the MWCNT network is deformed to a lesser extent.

Electrical conductivity for composites of 2.0 wt% MWCNT and for the PC M2200 composite with 1.5 wt% MWCNT exceeds  $10^{-1}$  S/m at the end of the test. On the contrary the composite of PC M2800 and 1.5 wt% MWCNT shows a slower increase in  $\sigma$  with time and its conductivity  $\sigma$  attains a value of  $\sim 10^{-2}$  S/m at the end of the time sweep. Generally, the electrical conductivity of the composites increases with temperature because of a more rapid agglomeration of clusters of carbon nanotubes. The electrical conductivity at large times is nearly constant since the network structure only marginally changes at large times. The time sweeps at 250 °C compared with measurements at 190 °C reveal that the formation of electrically conductive networks is enhanced by increasing temperature. A similar effect was observed in recovery experiments [20,21].

### 3.4. Frequency-dependent behaviour

The frequency-dependent rheological properties of polycarbonate containing different concentrations of MWCNT were extensively studied in the past [see e.g., [27,31–33,35,38,58–60]]. Here we comment on simultaneous rheological and electrical measurements at  $T = 250$  °C, see Fig. 5.

The plateau value in  $G'$  for low frequencies amounts to 2000–3000 Pa for the 3.0 wt% composites of both PC grades, revealing a similar network arrangement for these two composites. The electrical conductivity ranges between 0.1 and 1 S/m, increasing slightly as the experiment proceeds. For the 2.0 wt% composites the influence of matrix polymer is visible: while the low-molecular-weight PC (M2200) composite exhibits a plateau value in  $G'$  of  $\sim 1000$  Pa for frequencies below  $\sim 1$  rad/s, the high-molecular-weight PC (M2800) composite shows a plateau in the storage modulus at angular frequencies below  $\sim 0.1$  rad/s of less than 200 Pa. This result reveals that the specific network of nanotubes determines the value of  $G'$  at low  $\omega$ . The evolution of electrical

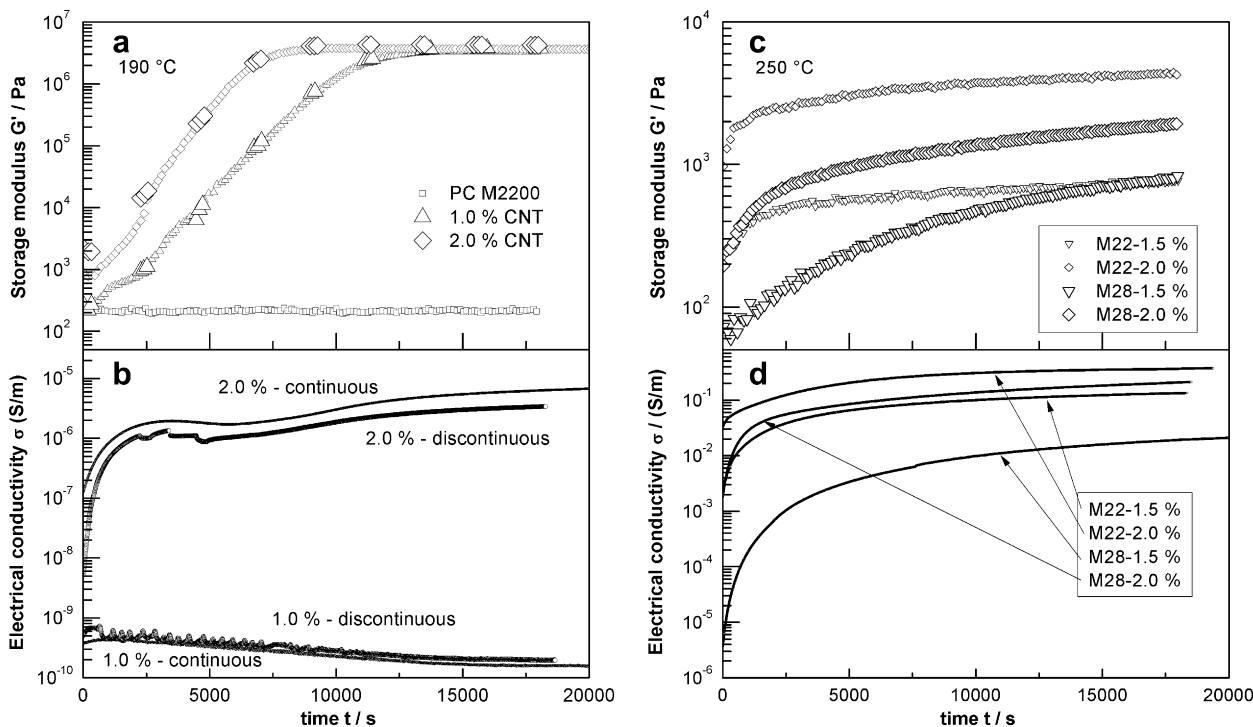


Fig. 4. Temporal stability under oscillatory shear of (a, b) PC M2200 and composites containing 1.0 wt% and 2.0 wt% MWCNT at 190 °C and (c, d) composites of PC M2200 and PC M2800 containing 1.5% and 2.0% MWCNT at 250 °C.

conductivity over time mirrors the slower formation of (electrically conductive) nanotube networks at lower frequencies for the high-molecular-weight PC composite. The PC M2200 composite with 2.0 wt% MWCNT exhibits an electrical conductivity in the range of 0.01 and 0.1 S/m, which is about one order of magnitude less than  $\sigma$  of

the 3.0 wt% samples, and a similar increase in  $\sigma$  during the test. The PC M2800 composite containing 2.0 wt% MWCNT shows an electrical conductivity of approximately  $10^{-3}$  S/m at the beginning of the frequency sweep and increases for about two orders of magnitude, attaining the same value as the PC M2200 2.0 wt%

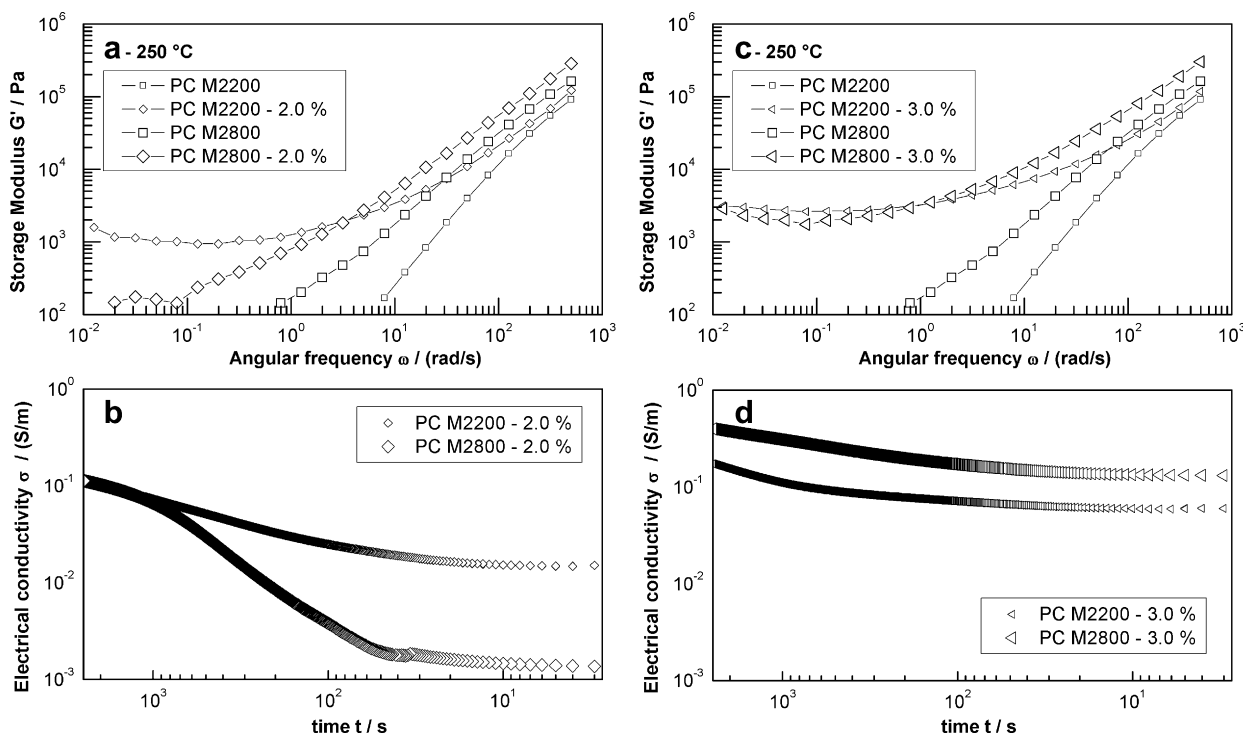


Fig. 5. Storage modulus and electrical conductivity of neat PC M2200 and PC M2800 and composites containing 2.0 wt% MWCNT (a, b) and 3.0 wt% MWCNT (c, d), respectively. The strain amplitude applied was 3% at a temperature of 250 °C and the angular frequency ranged from 500 to 0.01 rad/s. The time axis division of (b) and (d) is constituted so that time-dependent data of electrical conductivity correspond to vertically aligned frequency-dependent data in  $G'$ .

composite of 0.1 S/m at the end of the test. The increase of conductivity can be described by the approach based on percolation theory and agglomeration kinetics, see Ref. [20] for details. The data in Fig. 5 reveal, like Fig. 4, that the electrical conductivity does not necessarily correlate with the values of the moduli as also stated in Refs. [31,44].

### 3.5. Strain-amplitude-dependent behaviour

In order to probe the nonlinear behaviour of the composites, strain sweeps with increasing shear amplitude were conducted at temperatures of 190 °C and 250 °C. Fig. 6 shows the behaviour of neat PC M2200 and composites containing 1.0–5.0 wt% of MWCNT at strain amplitudes between 0.4 and 300% at a frequency of  $\omega = 0.1$  rad/s and a temperature of  $T = 190$  °C. Fig. 6(a)–(c) shows data for experiments acquired by measuring five points per decade, leading to a test duration of about half an hour, while Fig. 6(d)–(f) shows data acquired by measuring 10 points per decade, leading to a test duration of about an hour.

The neat matrix polymer behaves in a linearly viscoelastic manner for strain amplitudes below 100%. The dynamic moduli  $G'$

and  $G''$  increase with MWCNT concentration, while the value of  $\tan \delta$  (not shown) decreases with filler concentration at low strain amplitudes indicating the increase of elasticity by the addition of MWCNT. In the range of small strain amplitudes composites show an increase in  $G'$  and  $G''$  with strain amplitude and time respectively (cf. temporal stability, Fig. 4 (a)). This increase is more pronounced in the slower run (10 points per decade). With increasing filler content the maxima become more pronounced and are located towards smaller amplitudes. The decreases in  $G'$  and  $G''$  at high strain amplitudes are larger for the higher amounts of MWCNT. In particular the 5.0 wt% sample presents a dramatic decrease in  $G'$  (similar to “brittle fracture” [40,61]), whereas the drop in  $G''$  is not as well marked. TEM micrographs of the composite after the amplitude sweeps did not allow one to quantify the fine morphological changes, i.e. the change of number of entanglements of MWCNT.

Samples containing 1.0 wt% MWCNT or less show no indication of a percolated nanotube network. Although the values for electrical conductivity for the 2.0 wt% sample are relatively low (below  $10^{-6}$  S/m) the behaviour is very similar to that of the samples containing 3.0 and 5.0 wt% MWCNT: an increase for more than one

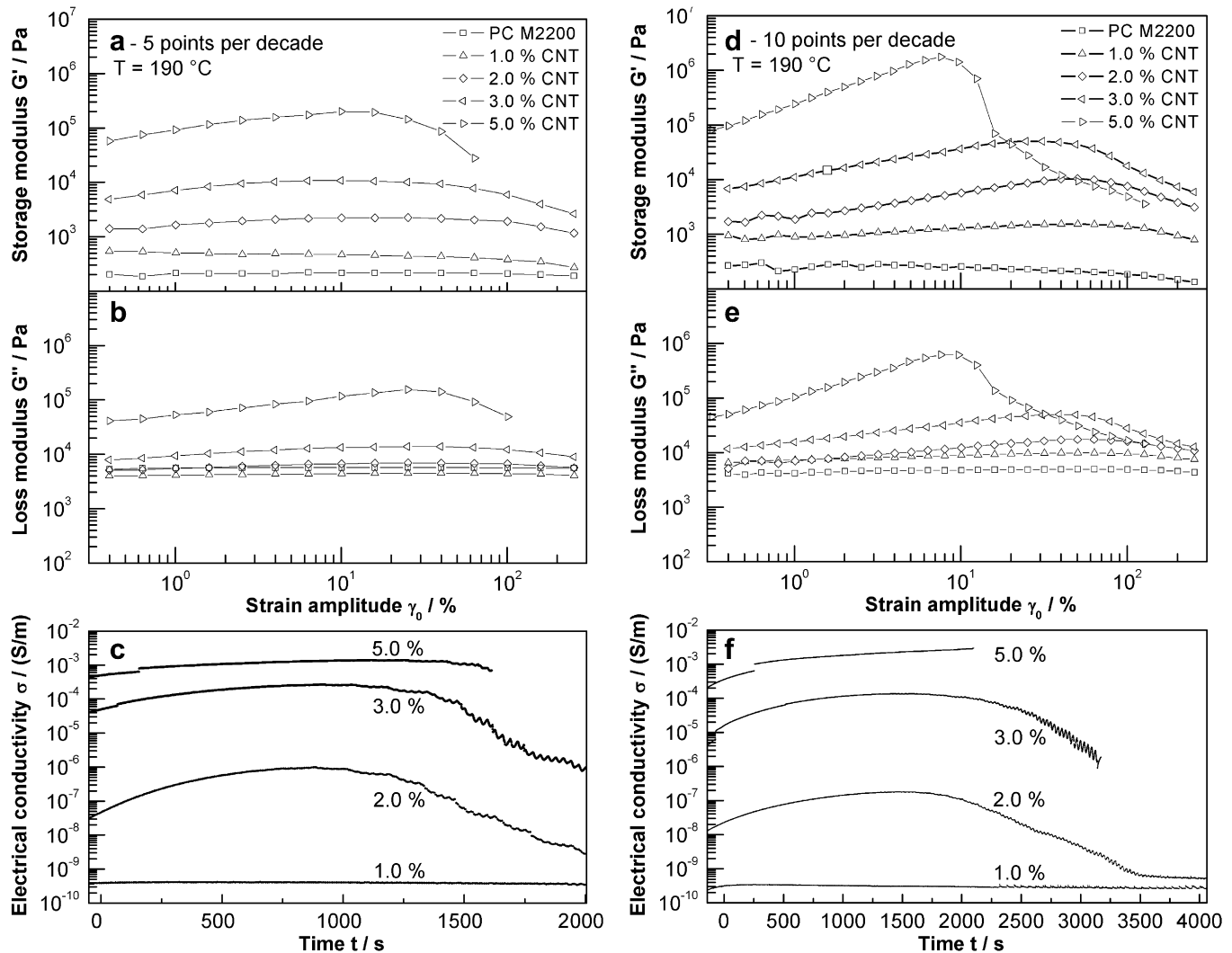


**Fig. 6.** Results of strain sweeps of neat PC M2200 and its composites containing 1.0–5.0 wt% MWCNT. The shear amplitude was  $\gamma_0 = 0.4$ –300% at a frequency of  $\omega = 0.1$  rad/s and a temperature of  $T = 190$  °C. The time axis division of (c) and (f) is constituted so that time-dependent data of electrical conductivity correspond to vertically aligned strain-amplitude-dependent data in  $G'$  and  $G''$ . The left-hand charts (a–c) display data acquired by measuring five points per decade (leading to a shorter test duration) and right hand charts (d–f) show experiments conducted by measuring 10 points per decade (yielding a longer test duration), cf. time axis division.

decade during the initial part of the strain amplitude experiment occurs and, at least for the 2.0 wt% and 3.0 wt% sample, is followed by a decrease below initial data. Since simultaneous rheological and electrical experiments with 3.0 wt% and 5.0 wt% samples could not be performed for high strain amplitudes due to torque overload of the rheometer transducer, electrical conductivity data for high strain amplitudes are only partially available. The maxima in electrical conductivity for 2.0 wt% and 3.0 wt% composites occur after approximately 1500 s (800 s for the short test duration), corresponding 4–5% strain amplitude. Assuming a similar behaviour for the 5.0 wt% sample, the maxima of electrical conductivity emerge while samples are exposed to the same amplitudes; hence electrical conductivity of as tested percolated samples of PC M2200 containing 5.0 wt% MWCNT or less is strain-amplitude-dependent. In addition to the decrease in  $\sigma$  at large strain amplitudes, oscillations in electrical conductivity are visible (vide infra).

Strain-amplitude-dependent behaviour of PC M2200 and PC M2800 composites containing 1.0–5.0 wt% and 1.5–5.0 wt% MWCNT respectively is shown in Fig. 7 for the larger test temperature of 250 °C. The amplitude of shear ranges between 0.4 and 300% at an angular frequency of  $\omega = 0.1$  rad/s.

In contrast to strain sweeps at 190 °C (cf. Fig. 6) where the modulus increases with measurement time, the composites containing 1.5–5.0 wt% MWCNT display an approximately linear viscoelastic behaviour at 250 °C at small amplitudes. The values of  $G'$  and  $G''$  increase with rising content of MWCNT, while the value of  $\tan \delta$  (not shown) decreases with filler concentration. Only weakly marked maxima in  $G'$  and  $G''$  are visible for all the composites shown, although a conspicuous shift of the maxima towards smaller strain amplitudes with increasing filler content is evident. Since network buildup proceeds much more rapidly during experiments conducted at 250 °C and a percolated, electrically conductive network already exists at the very beginning of the strain sweeps (cf. Fig. 7), no pronounced maxima in  $G'$  emerge and linear behaviour is exhibited for small amplitudes.

The comparison of  $G'$  in composites of different matrix polymers containing equal amount of filler gives a good impression of the strength/level of developed MWCNT networks and the influence of the molar mass of the matrix polymer. Samples of PC M2200 containing 1.5–5.0 wt% MWCNT and samples of PC M2800 containing 2.0–5.0 wt% MWCNT are present in a percolated state, since they display good electrical conductivities. The two 5.0 wt% composites

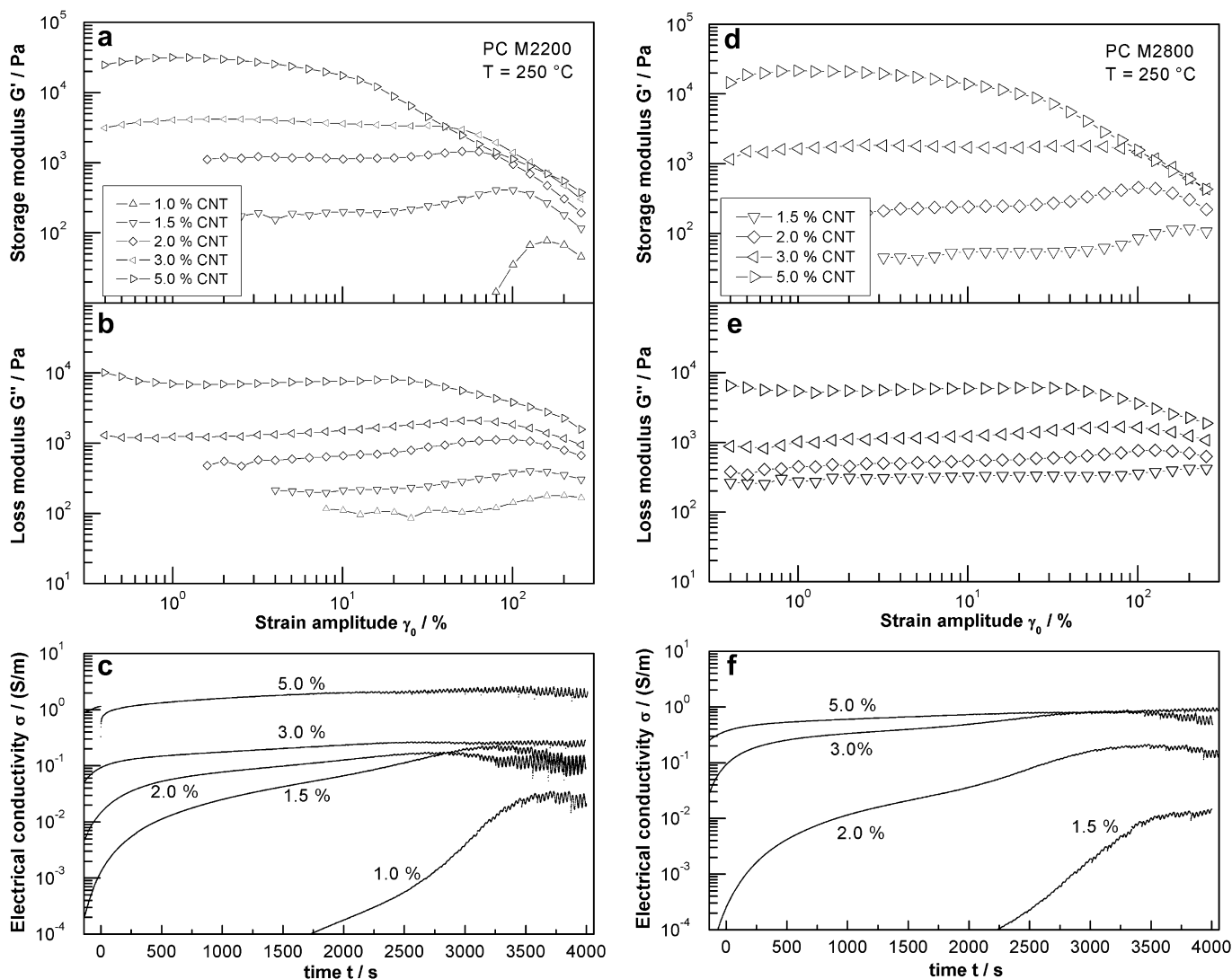


Fig. 7. Results of strain sweeps of PC M2200 (a–c) and PC M2800 (d–f) composites containing 1.0–5.0 wt% MWCNT. The angular frequency was  $\omega = 0.1$  rad/s and the temperature was  $T = 250$  °C. The time axis division of (c) and (f) is constituted so that time-dependent data of electrical conductivity correspond to vertically aligned strain-amplitude-dependent data in  $G'$  and  $G''$ .



show very similar behaviour in  $G'$  as well as in  $G''$  and feature nearly equal electrical conductivities. This behaviour emphasizes the dominance of the MWCNT network in the concentrated regime and the negligible influence of the matrix polymer. The samples of PC M2200 containing 1.5–3.0 wt% MWCNT and the 2.0 and 3.0 wt% PC M2800 samples feature percolated nanotube networks. Since the 1.5, 2.0 and 3.0 wt% samples of PC M2200 reveal higher values in  $G'$  for small strain amplitudes than the PC M2800 counterparts with equal filler concentrations, the lower molar mass polymer matrix enables a larger number of bonds and entanglements between MWCNT. Although the maxima in  $G'$  for PC M2800 composites are located at higher strain amplitudes compared with PC M2200 composites (see above), a comparison of the absolute values leads to the picture just described. The occurrence of maxima in  $G'$  at smaller amplitudes and the higher values in  $G'$  at equal amplitudes for the low molecular weight PC M2200 composites lead to the conclusion that more entangled networks of MWCNT are more sensitive regarding high strain amplitudes.

The enhanced MWCNT network formation in PC M2200 is also visible in electrical conductivity. While good electrical conductivity arises for the 1.0 wt% sample of PC M2200 during the experiment, the same is evident for the 1.5 wt% sample of PC M2800. Furthermore a very similar course of  $\sigma$  during the experiment is apparent for the 1.5 wt% sample of PC M2200 and the 2.0 wt% sample of PC M2800. The percolation threshold is situated between 1.0 and 1.5 wt% for the PC M2200 composites and between 1.5 and 2.0 wt% for the PC M2800 samples. For amounts of filler well above the percolation threshold no significant differences in  $\sigma$  are apparent. The electrical conductivity of the composites does not decrease significantly at high shear amplitudes because network formation proceeds rapidly and compensates for the network breakup. These comparisons of composites of PC with different molar masses and at distinct temperatures clearly reveal that the formation of percolated networks is favoured by lower molecular weight polymer matrices and higher temperatures. A similar effect was observed in the absence of flow in recovery experiments in Ref. [21]. Depending on the matrix viscosity and the applied shear forces, i.e. the transferred forces via the polymer matrix onto the nanotube network, the influence of network buildup or breakup predominates. Whereas at high shear strain amplitudes at 190 °C network breakup leads to a decrease in moduli and electrical conductivity of the composite samples because of high stresses, at a temperature of 250 °C formation of the electrical network partially compensates for the rupture of nanotube clusters resulting

in steady  $\sigma$  values. The decrease in moduli is thought to be due to the breakup of relatively weak bonds between clusters of agglomerates of MWCNT. The competition between buildup and breakup leads to these pronounced maxima which are influenced by the specific network configuration which are more pronounced than in related works [39,55,56].

Our simultaneous electrical and rheological measurements allow us to elucidate the influence of the viscosity and the polymer–nanotube interactions on the dynamics of network formation. In the works of Alig et al. percolation theory and agglomeration kinetics were applied to model electrical conductivity and storage modulus in carbon nanotubes filled systems [19,20]. In this work we discuss the reinforcement factor of the storage modulus  $G'$  as a function of shear amplitude for the composites with 2 wt% and 5 wt% MWCNT at the two different temperatures, see Fig. 8. Here we define the reinforcement factor  $\nu$  by

$$\nu = G'(\gamma_0)/G'(\gamma_0 = 1\%), \quad (2)$$

i.e. with respect to a shear amplitude of 1%. We emphasize that in this presentation shear amplitude and time are two dependent quantities. This empirical approach allows one to discuss the influence of matrix viscosity on the storage modulus. A more detailed discussion has to take into account the evolution of cluster size distribution with time and (oscillating) shear strain and is beyond the scope of this experimental paper. In Fig. 8, one can distinguish between a breakup and a buildup regime. Buildup of the MWCNT network (i.e. the slope of  $\log G'$  versus  $\log \gamma_0$  for increasing  $G'$  values) is more pronounced at lower temperatures because of a slower formation of the network and in the experiments conducted with a larger number of data points per decade because of a longer duration of the experiment. The breakup rate of the rheological network (i.e. the slope of  $\log G'$  versus  $\log \gamma_0$  for decreasing  $G'$ ) does not show a clear trend with temperature in the double logarithmic presentation. At large strain amplitude the storage modulus drastically decreases. It seems that the destruction of entangled carbon nanotubes only moderately depends on temperature. On the contrary, breakup of the electrical network (with a large number of contributions of neighbored, but unentangled carbon nanotubes) is more pronounced at lower temperatures, cf. Figs. 6 and 7.

Fig. 9 displays the electrical conductivity of samples of PC M2200 and PC M2800 containing 2.0 wt% MWCNT at high strain amplitudes. This extract of Fig. 7 illustrates the oscillations in  $\sigma$  arising while shearing with high strain amplitudes. In the depicted

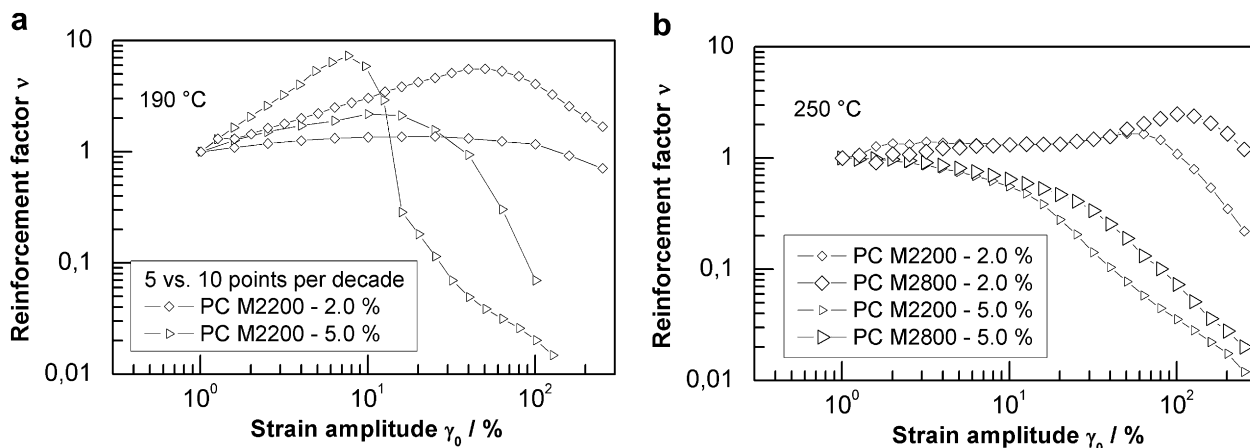


Fig. 8. Reinforcement factor (Eq. (2)) for the PC/MWCNT composites with 2 wt% and 5 wt% MWCNT, respectively. The molar mass of the polycarbonate matrix and the temperature are indicated.

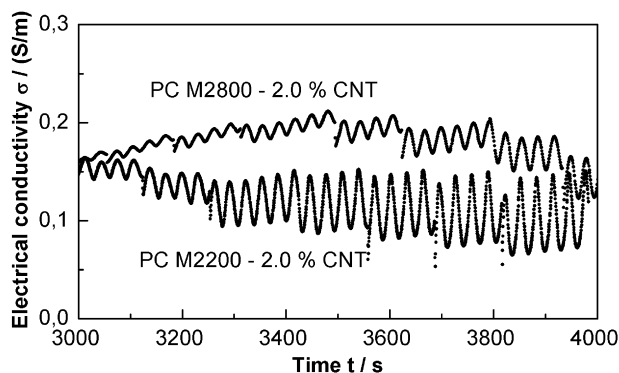


Fig. 9. Oscillations of electrical conductivity  $\sigma$  for PC M2200 and PC M2800 composites with 2.0 wt% MWCNT. The figure depicts the data of the strain sweeps of Fig. 7(c) and (f), respectively.

excerpt the time axis from 3000 s to 4000 s corresponds to seven different strain amplitudes of between 63 and 253%.

The oscillations in  $\sigma$  are interpreted as deformation of agglomerates and MWCNT–MWCNT bonds during oscillatory shear and are independent of the direction of applied shear. The periodic time of  $\sigma$  amounts to  $T_{\sigma} = 31.5$  s. The angular frequency of conducted amplitude strain experiments was set to  $\omega = 0.1$  rad/s, corresponding to a cycle duration of  $T_{\text{strain}} = 62.83$  s and yielding that  $T_{\sigma} = T_{\text{strain}}/2$  respectively  $\omega_{\sigma} = 2 \cdot \omega_{\text{strain}}$ . This relation pertains to strain amplitude experiments conducted at 190 °C and 250 °C. The twice as fast oscillation in  $\sigma$  as in strain signifies a deformation of the electrical conductive network of MWCNT, as also explained in Ref. [25].

Fig. 9 clearly reveals an oscillatory deformation of the electrical network. While amplitudes in  $\sigma$  are relatively small for small strain amplitudes (Fig. 9 left) the largest amplitudes in  $\sigma$  occur for high strain amplitudes. The toggling towards higher applied strain amplitudes leads to an increase in amplitude of electrical conductivity in the observed interval. However, the average value of the oscillating conductivity continuously decreases at large shear amplitude, see Fig. 6(c) and (f). In addition to the data of Ref. [25], the strain amplitude was varied in this work which shows that the absolute value of the deformation of the MWCNT–MWCNT bonds strongly influences the electrical conductivity.

Steady-state viscosity  $\eta$  versus content of MWCNT as revealed by start-up experiments is shown in Fig. 10 on a linear scale. An increase in  $\eta$  for composites of both PC grades with increasing nanotube content is visible. Up to a filler loading of 1.0 wt% MWCNT this increase is very weak and the viscosity is dominated by the matrix properties. In transient shear flow, the viscosity of the

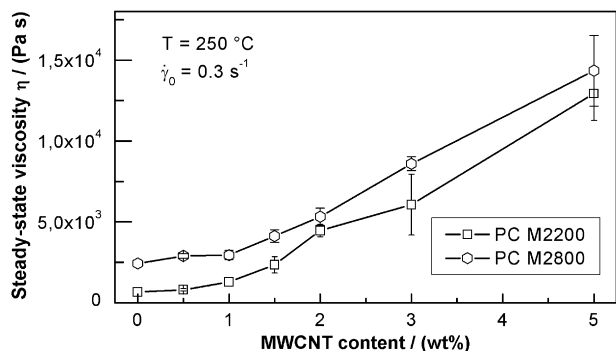


Fig. 10. Steady-state viscosity  $\eta$  of PC M2200 and PC M2800 containing 0–5 wt% MWCNT as determined by transient shear experiments conducted at a temperature of  $T = 250$  °C and a shear rate of  $\dot{\gamma} = 0.3$  s<sup>-1</sup>.

matrix polymer strongly influences the steady-state viscosity, whereas at low frequencies of linear viscoelastic shear oscillations (low stress regime) the specific configuration of the MWCNT network strongly influences the values of the moduli. At higher filler contents the influence of the nanotubes increases and the steady-state viscosity  $\eta$  grows linearly with MWCNT content, which is comparable to the behaviour of spherical particles. This is in contrast to other fibre reinforced thermoplastics, where the increase in  $\eta$  is not linear [62]. The reason for the more pronounced increase of steady-state viscosity with fibre content is the larger number of fibre–fibre interactions (e.g., collisions). In contrast, in polymer/MWCNT composites, the entangled clusters themselves are not broken up. This effect was observed in shear as well as in melt elongation of a PC/MWCNT composite [40,43]. Thus we assume that the steady-state viscosity is determined by the flow of MWCNT clusters in a polymer matrix. The absolute difference in steady-state viscosity between the different PC composites is equal over the whole range of nanotube loading. During shearing with constant shear rate, friction and collisions between the nanotubes/agglomerates contribute to the rise in steady-state viscosity while the matrix polymer controls the degree of transferred stress onto the embedded nanotube network.

### 3.6. Dynamic mechanical analysis

The results of dynamic mechanical analysis in the melt and simultaneous electrical measurements are shown in Fig. 11. The time axis divisions of Fig. 11(c) and (f) are constituted so that time-dependent data of electrical conductivity correspond to vertically aligned temperature-dependent data in  $G'$  and  $G''$ , respectively.

Starting the temperature scan at 280 °C, the so-called terminal region is achieved where the effect of  $M_w$  of the polymer matrix is visible. Higher molecular weight PC reveals higher moduli at the same temperature. A decrease in temperature results in an increase of the moduli. In addition, the slope in  $G'$  and  $G''$  of PC M2200 is slightly steeper than the slope of PC M2800. Rubbery behaviour appears between 152 °C and 163 °C for PC M2200 and between 156 °C and 171 °C for PC M2800. As the free volume continues to decrease (decreasing temperature), glass transition takes place and the movement of large chain segments is hindered.

The addition of MWCNT of up to 5.0 wt% leads to an increase in  $G'$  and  $G''$  for temperatures above  $T_g$  and in particular for higher temperatures (terminal zone). The rise in  $G'$  is more pronounced than that in  $G''$ . The networks formed by 5.0 wt% samples are very dense and nearly constant values in  $G'$  (solid-like behaviour) are exhibited in the temperature range above ~200 °C for the PC M2200 composite and above ~210 °C for the PC M2800 composite. The electrical conductivity of these samples is above 10<sup>-1</sup> S/m and is nearly constant over the whole temperature range. With a decreasing filler content the temperature range for solid-like behaviour moves towards higher temperatures and a slight increase in  $G'$  with decreasing temperature is exhibited by composites containing less than 5.0 wt% MWCNT in the temperature scan experiments. We emphasize that the formation of MWCNT networks is a time-dependent process resulting in minor deviations between the behaviour revealed in dynamic mechanical analysis (performed from high to low temperatures) compared with frequency sweeps (conducted from high to small frequencies, corresponding low to high temperatures, cf. Fig. 5). In the latter case composites of PC M2200 containing 2.0 wt% MWCNT or more and composites of PC M2800 containing at least 3.0 wt% MWCNT display a pronounced plateau for small frequencies.

The percolation threshold is situated between 0.5 wt% and 1.0 wt% for the PC M2200 composites and between 1.0 wt% and 1.5 wt% for the PC M2800 composites. According to frequency

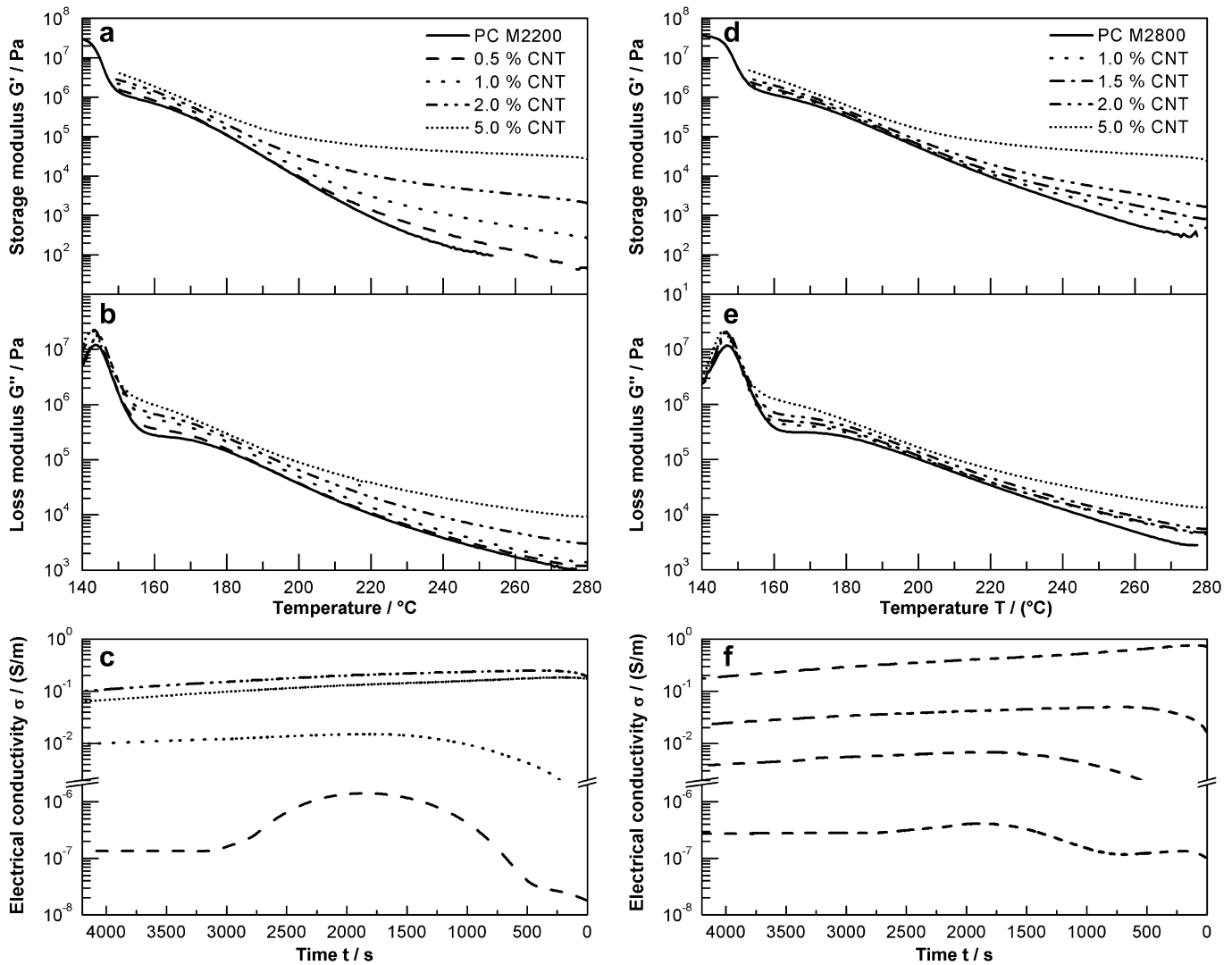


**Fig. 11.** Results of dynamic mechanical analysis of PC M2200 and PC M2800 composites. The frequency was 1 Hz and the (initial) strain amplitude was 5% at 280 °C, decreasing at lower temperatures. The cooling rate was 2 K/min.

sweep and strain amplitude sweep experiments, a lower matrix viscosity yields a lower percolation threshold for electrical conductivity. The electrically conductive networks persist below the glass transition temperature and thereby maintain in the glassy state of the PC composites. The pathway of electrical conductivity over temperature elucidates the process of network formation and preservation. The formation of electrical conductivity is a degressive process facilitated by high temperature and low matrix viscosity and proceeds faster with higher filler content. Cooling leads to a larger stress in the PC matrix, causing larger deformations of the electrical network and thus a marginal decrease in electrical conductivity. This effect exceeds the process of network formation with decreasing temperature, since network formation is constrained with lower temperature and higher stresses in the matrix polymer. The superposition of agglomeration and breakup is strongly pronounced for the PC M2200 composite with 0.5% MWCNT and results in a pronounced maximum of the electrical conductivity, since the filler concentration is close to the percolation threshold.

The results of the combined rheological and electrical investigations show that network deformation which is caused by the applied shear flow and the diffusion-controlled clustering of carbon

nanotubes are two superposing processes which are strongly influenced by the temperature. The data of the dynamic mechanical analysis reveal that depending on time and temperature either buildup or breakup dominates. Recovery experiments of rheological and electrical properties have already demonstrated that breakup and buildup of nanotube networks are reversible processes [20,39]. In this work, this effect was clearly shown in oscillatory shear. The timescale of network buildup is not influenced by the oscillatory shear flow (see Fig. 4).

Based on our experimental data, the model of Alig et al. and Pötschke et al. [19,20,26,31], can be extended in order to illustrate the development of electrical conductivity by the incorporation of MWCNT into PC, see Fig. 12. The model consists of partially bent nanotubes (black) forming agglomerates (gray circles) through entanglements and bonds. These clusters are embedded in the polymer matrix. The clustering of agglomerates, leading to electrical conductivity [20], is highlighted by the contacting circles. Our experimental data clearly indicate that the bonds between neighbouring MWCNT can easily be released and reformed and are the cause of the oscillations in electrical conductivity. This model explains our observations in terms of electrical conductivity that are interpreted as the superposition of three contributing



**Fig. 12.** Schematic of the microstructure of polycarbonate/carbon nanotube composites: agglomerates of entangled nanotubes (indicated by circles) that cluster and constitute electrical conductive pathways are embedded in the polymer matrix.

phenomena: (i) Formation and reformation of percolated electrically conductive networks by agglomeration and clustering of nanotubes, (ii) destruction/interruption of pathways of clusters leading to decreasing electrical conductivity at high shear amplitudes and (iii) deformation of clusters/MWCNT–MWCNT bonds emerging in oscillations in  $\sigma$ . Electrical conductivity can be achieved if infinite pathways of clustered agglomerates are formed, whereas a large storage modulus is already attained if a large number of entangled MWCNT exists.

#### 4. Conclusions

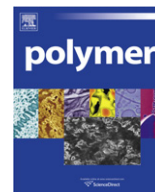
Our simultaneous rheological (i.e. shear oscillations) and electrical measurements of composites of a low- and high-molecular-weight polycarbonate with a MWCNT loading between 0.5 wt% and 5.0 wt% at different temperatures revealed that the formation of nanotube networks is favoured by high temperatures and a low molecular weight of the matrix polymer. Lower temperatures generally lead to a larger stress in the matrix and thus to a more pronounced breakup of the electrical network of carbon nanotubes as revealed by strain sweeps at large shear amplitudes and DMA experiments at low temperatures. The influence of carbon nanotubes dominates in the low stress regime (e.g., in linear viscoelastic shear oscillations at low frequencies and low shear amplitudes), whereas the matrix polymer has a strong influence on the rheological properties after breakup of a large number of nanotubes clusters (e.g., in the steady-state regime of transient shear flow). Breakup of nanotubes clusters caused by an applied shear field and diffusion-controlled clustering of nanotubes are two opposite processes which superimpose. Time sweeps revealed that oscillatory shear flow does not influence the timescale of diffusion-controlled clustering of carbon nanotubes. Our experimental results confirm the assumptions of the model of Alig and Pötschke, i.e. that the formation of nanotube networks is diffusion-controlled and that agglomeration of entangled nanotubes cluster can lead to electrically conductive pathways. The electrical measurements during shear oscillations show that the carbon nanotube network is continuously broken up at large shear deformations, but can be rapidly formed again. The periodically varying electrical conductivity in shear oscillations reveals that a large number of deformable nanotube–nanotube bonds persist. Hence, our experimental data indicate that the carbon nanotube network is composed of weakly bonded clusters which breakup and reaggregate and

deformable, reversible bonds between neighbored carbon nanotubes. The deformation of the MWCNT–MWCNT bonds strongly influences the electrical conductivity of the composite as revealed by the oscillatory experiments in shear.

#### References

- [1] Shaffer MSP, Windle AH. *Adv Mater* 1999;11(11):937–41.
- [2] Andrews R, Jacques D, Minot M, Rantell T. *Macromol Mater Eng* 2002;287(6):395–403.
- [3] Du F, Fischer JE, Winey KI. *J Polym Sci B Polym Phys* 2003;41(24):3333–8.
- [4] Coleman J, Cadek M, Blake R, Nicolosi V, Ryan K, Belton C, et al. *Adv Funct Mater* 2004;14(8):791–8.
- [5] Coleman JN, Khan U, Blau WJ, Gun'ko YK. *Carbon* 2006;44(9):1624–52.
- [6] Alig I, Lellinger D, Dudkin SM, Pötschke P. *Polymer* 2007;48(4):1020–9.
- [7] Ahir S, Huang Y, Terentjev E. *Polymer* 2008;49(18):3841–54.
- [8] Choi HJ, Jhon MS. *Soft Matter* 2009;5(8):1562–7.
- [9] Chou TW, Gao L, Thostenson ET, Zhang Z, Byun JH. *Compos Sci Technol* 2010;70(1):1–19.
- [10] Spitalsky Z, Tasis D, Papagelis K, Galiotis C. *Prog Polym Sci* 2010;35(3):357–401.
- [11] Ling QD, Liaw DJ, Zhu C, Chan DSH, Kang ET, Neoh KG. *Prog Polym Sci* 2008;33(10):917–78.
- [12] Sharma P, Ahuja P. *Mater Res Bull* 2008;43(10):2517–26.
- [13] Rajesh, Ahuja T, Kumar D. *Sens Actuators B Chem* 2009;136(1):275–86.
- [14] Treacy MMJ, Ebbesen TW, Gibson JM. *Nature* 1996;381(6584):678–80.
- [15] Ferguson DW, Bryant EWS, Fowler HC. *SPE ANTEC*; 1998. p. 1219.
- [16] Sandler JKW, Kirk JE, Kinloch IA, Shaffer MSP, Windle AH. *Polymer* 2003;44(19):5893–9.
- [17] Jiang X, Bin Y, Matsuo M. *Polymer* 2005;46:7418–24.
- [18] Balberg I. *Philos Mag B* 1987;56(6):991–1003.
- [19] Alig I, Skipa T, Engel M, Lellinger D, Pegel S, Pötschke P. *Phys Status Solidi B* 2007;244(11):4223–6.
- [20] Alig I, Skipa T, Lellinger D, Pötschke P. *Polymer* 2008;49(16):3524–32.
- [21] Alig I, Lellinger D, Engel M, Skipa T, Pötschke P. *Polymer* 2008;49(7):1902–9.
- [22] Kyrlyuk AV, Schoot P. *PNAS* 2008;105(24):8221–6.
- [23] Triebel C, Kaschta J, Katsikis N, Münstedt H, Funck A, Kaminsky W. *AIP Conf Proc* 2008;1027(1):66–8.
- [24] Deng H, Skipa T, Zhang R, Lellinger D, Bilotti E, Alig I, et al. *Polymer* 2009;50(15):3747–54.
- [25] Dijkstra DJ, Cirstea M, Nakamura N. *Rheol Acta* 2010;49(7):769–80.
- [26] Pötschke P, Abdel-Goad M, Pegel S, Jehnichen D, Mark JE, Zhou D, et al. *J Macromol Sci A* 2010;47(1):12–9.
- [27] Pötschke P, Fornes TD, Paul DR. *Polymer* 2002;43(11):3247–55.
- [28] Utracki LA. *Polym Compos* 1986;7(5):274–82.
- [29] Utracki LA. Rheology and processing of multiphase systems. In: Ottenbrite RM, Utracki LA, Inoue S, editors. *Current topics in polymer science, Rheology and polymer processing/multiphase systems*, vol. II. Munich: Carl Hanser; 1987. p. 7–59.
- [30] Shenoy AV. *Rheology of filled polymer systems*. Dordrecht: Kluwer Academic Publishers; 1999.
- [31] Pötschke P, Abdel-Goad M, Alig I, Dudkin S, Lellinger D. *Polymer* 2004;45(26):8863–70.
- [32] Bangarusampath D, Ruckdäschel H, Altstädt V, Sandler JK, Garray D, Shaffer MS. *Polymer* 2009;50(24):5803–11.
- [33] Pötschke P, Bhattacharyya AR, Janke A, Goering H. *Compos Interface* 2003;10(4–5):389–404.
- [34] Wei B, Spolenak R, Kohler-Redlich P, Ruhle M, Arzt E. *Appl Phys Lett* 1999;74(21):3149–51.
- [35] Abdel-Goad M, Pötschke P. *J Nonnewton Fluid Mech* 2005;128(1):2–6.
- [36] Vigolo B, Coulon C, Maugey M, Zakri C, Poulin P. *Science* 2005;309(5736):920–3.
- [37] Hobbie EK, Obrzut J, Kharchenko SB. *J Chem Phys* 2006;125(4):044712.
- [38] Bangarusampath D, Ruckdäschel H, Altstädt V, Sandler JK, Garray D, Shaffer MS. *Chem Phys Lett* 2009;482(1–3):105–9.
- [39] Skipa T, Lellinger D, Böhm W, Saphiannikova M, Alig I. *Polymer* 2010;51(1):201–10.
- [40] Richter S, Saphiannikova M, Jehnichen D, Biederl M, Heinrich G. *Express Polym Lett* 2009;3(12):753–68.
- [41] Hobbie EK, Wang H, Kim H, Lin-Gibson S, Grulke EA. *Phys Fluids* 2003;15(5):1196–202.
- [42] Hobbie EK, Wang H, Kim H, Han CC, Grulke EA, Obrzut J. *Rev Sci Instrum* 2003;74(3):1244–50.
- [43] Handge UA, Pötschke P. *Rheol Acta* 2007;46(6):889–98.
- [44] Du F, Scogna RC, Zhou W, Brand S, Fischer JE, Winey KI. *Macromolecules* 2004;37(24):9038.
- [45] Baytubes® C 150 P. Agglomerate of multi-wall carbon nanotubes product information. 2008-03-10 ed. Leverkusen: Bayer MaterialScience AG.
- [46] Hepperle J, Rainer T, Dijkstra DJ, Cueper T. 2009. *Leitfähigkeitsmessvorrichtung, Gebrauchsmusterschrift DE 20 2007 018 634 U1*.
- [47] Semeriyonov F, Saphiannikova M, Heinrich G. *J Phys A: Math Theor* 2009;42. 465001-1–465001-17.

- [48] Kasaliwal GR, Pegel S, Gödel A, Pötschke P, Heinrich G. *Polymer* 2010;51(12):2708–20.
- [49] Larson RG. *The structure and rheology of complex fluids*. New York: Oxford University Press; 1999.
- [50] Schmid CF, Switzer LH, Klingenberg DJ. *J Rheol* 2000;44(4):781–809.
- [51] Switzer III LH, Klingenberg DJ. *J Rheol* 2003;47(3):759–78.
- [52] Doi M, Edwards SF. *The theory of polymer dynamics*. New York: Clarendon, Oxford University Press; 1986.
- [53] CAMPUSplastics. *CAMPUSplastics datasheet Makrolon® 2200*. 2009-04-15 ed. Leverkusen: Bayer MaterialScience AG.
- [54] Lin B, Sundararaj U, Pötschke P. *Macromol Mater Eng* 2006;291(3):227–38.
- [55] Kharchenko SB, Douglas JF, Obrzut J, Grulke EA, Migler KB. *Nat Mater* 2004;3(8):564–8.
- [56] Hough LA, Islam MF, Janmey PA, Yodh AG. *Phys Rev Lett* 2004;93(16):168102.
- [57] Hobbie EK, Fry DJ. *Phys Rev Lett* 2006;97(2):036101.
- [58] Mitchell CA, Bahr JL, Arepalli S, Tour JM, Krishnamoorti R. *Macromolecules* 2002;35(23):8825–30.
- [59] Sung YT, Han MS, Song KH, Jung JW, Lee HS, Kum CK, et al. *Polymer* 2006;47(12):4434–9.
- [60] Abbasi S, Carreau PF, Derdouri A, Moan M. *Rheol Acta* 2009;48(9):943–59.
- [61] Satapathy BK, Weidisch R, Pötschke P, Janke A. *Compos Sci Technol* 2007;67(5):867–79.
- [62] Chauche M, Koch DL. *J Rheol* 2001;45(2):369–82.



## Water-assisted extrusion of polypropylene/clay nanocomposites: A comprehensive study

Dimitri D.J. Rousseaux, Naïma Sallem-Idrissi, Anne-Christine Baudouin, Jacques Devaux, Pierre Godard, Jacqueline Marchand-Brynaert<sup>\*\*</sup>, Michel Sclavons<sup>\*</sup>

*Institute of Condensed Matter and Nanosciences (IMCN), Université Catholique de Louvain, Place Louis Pasteur 1, Bâtiment Lavoisier, B-1348 Louvain-la-Neuve, Belgium*

### ARTICLE INFO

#### Article history:

Received 18 August 2010  
Received in revised form  
8 November 2010  
Accepted 12 November 2010  
Available online 23 November 2010

#### Keywords:

Polypropylene  
Polymer clay nanocomposites  
Water-assisted extrusion

### ABSTRACT

Water-assisted extrusion process has been used to successfully prepare polypropylene (PP)/clay nanocomposites with high degree of clay delamination and markedly improved rheological, thermal and mechanical properties. PP-graft-maleic anhydride (PP-g-MA)-based nanocomposites and masterbatches were synthesized from untreated clay and organoclay, respectively, and fully characterized. The effects of using high-shear rates and water injection during the melt-compounding were examined. A mechanism explaining the formation of such nanocomposites is then proposed. The best clay dispersion and properties improvements of PP-g-MA/organoclay nanocomposites and masterbatches were obtained using high-shear rates and water injection (synergy effect). PP-based nanocomposites were then synthesized by dilution of PP-g-MA-based masterbatches into neat PP. For comparison, nanocomposites were also prepared by a one-pot process where PP, PP-g-MA and organoclay are directly melt-blended with or without water injection. The nanocomposites prepared by dilution into PP of a masterbatch prepared through water-assisted extrusion showed the highest clay dispersion and consequently the best thermal, mechanical and rheological properties.

© 2010 Elsevier Ltd. All rights reserved.

### 1. Introduction

In recent years, polymer/clay nanocomposites received a considerable scientific and technological interest. The main reason is the enhancement of the polymer matrix properties that could be obtained with only a few percents of filler. In comparison to neat polymer matrix, polymer/clay nanocomposites usually exhibit higher mechanical and barrier properties and flame retardant behavior [1–5]. A few weight percents of layered silicate clays allow reaching similar properties than much higher amounts (20–40%) of conventional filler (talca, glass fibers, calcium carbonate) [6–9].

Montmorillonite (MMT) is the most employed clay for the preparation of polymer/clay nanocomposites. MMT is a layered aluminosilicate mineral with sodium counterions present between the clay layers. MMT silicate layers present a high aspect ratio (length/thickness ratio) with their one nanometer thickness and hundreds nanometers length. They offer thus a large surface area for polymer/filler interactions. Naturally stacked into aggregates of

several microns, MMT layers need to be separated and dispersed into the polymer matrix to obtain a nanocomposite.

The most usual way to produce polymer/clay nanocomposites is by melt-blending in an extruder because it is inexpensive, environment-friendly and straightforward [10,5,11]. Nanocomposites prepared by melt-blending are synthesized almost exclusively from organoclay to solve the lack of compatibility between the polymer and the clays [12,1,2,10]. Organoclays are MMT in which the interlayer sodium counterions have been replaced by organic cationic surfactants, mostly alkylammoniums [12]. The introduction of surfactants increases the interlayer spacing and lowers the clay surface energy, thus facilitating the separation and dispersion of the clay layers into the polymer matrix.

Polypropylene (PP) is one of the most used matrix in polymer/clay nanocomposites due to its very large commercial importance [6]. PP/clay nanocomposites are usually prepared by melt-blending, with compatibilizer such as PP-graft-maleic anhydride (PP-g-MA) and organoclays [13–15]. Compatibilizers are required due to the huge polarity difference between the polyolefin matrix and the clay. PP-g-MA allows wetting of the clay surface by hydrogen-bond interactions between the anhydride functions (acid functions when hydrolyzed) and the oxygen atoms at the surface of the silicate layers [16,17]. Even when using organoclay and compatibilizers, PP/

<sup>\*</sup> Corresponding author. Tel.: +32 0 10474015; fax: +32 0 10451593.

<sup>\*\*</sup> Corresponding author. Tel.: +32 0 10472746; fax: +32 0 10474168.

E-mail addresses: [jacqueline.marchand@uclouvain.be](mailto:jacqueline.marchand@uclouvain.be) (J. Marchand-Brynaert), [michel.sclavons@uclouvain.be](mailto:michel.sclavons@uclouvain.be) (M. Sclavons).

clay nanocomposites usually exhibit poor clay dispersion and, consequently, limited properties improvements are obtained. The main reason is the poor thermal stability of the alkylammonium-surfactants, which often decompose at extrusion temperatures leading to a collapse of the silicate layers [18–21].

Water-assisted extrusion was firstly described in 1999 in a patent of DSM [22]. The invention focuses on the preparation of polyamide (PA) nanocomposites by mixing in the melt phase a PA, a high aspect ratio particle (like a clay) and a liquid (preferably water). The mixing was carried out in a twin-screw extruder equipped with a water injection system and a degassing zone. The recommended amount of injected water varies from 5 to 50 wt% and more preferably from 10 to 40 wt%. Exfoliated PA/MMT nanocomposites were obtained using water injection without requiring the expensive clay organomodification. The patent claims the applicability of the technique to all polymers containing the polar CONH function between repeating aliphatic units.

Since this pioneering work, different research groups reported the aid of water for the elaboration of nanocomposites based mainly on polar (PA), but also on non polar (PP, poly(styrene-co -acrylonitrile)) matrices, using untreated MMT or organomodified clays [23–31] (see Supporting information for complete descriptions).

With the aim of improving the PP/clay nanocomposite properties, we have performed a detailed, in-depth study of the effect of water injection on the classical extrusion process.

The present paper discusses the water-assisted preparation of PP/clay nanocomposites and the study of their structural, thermal, rheological and mechanical properties. PP-g-MA/clay nanocomposites and masterbatches from untreated clay (CNa) and organoclay (C30B) with or without (for comparison) water injection and at low- or high-shear rates, have been synthesized and characterized. The first part of this work is a comprehensive study on the possible interactions occurring between the untreated MMT or the organoclay and the PP-g-MA with and without the aid of water. In the second part of this work, PP/clay nanocomposites are produced by dilution of PP-g-MA/clay masterbatches into PP (masterbatch process), and compared with nanocomposites prepared by water-assisted direct melt-compounding of PP, PP-g-MA and clay (called the one-pot process).

The influence of shear rate and water-assisted extrusion process is studied at different stages of the PP/clay nanocomposites preparation and a mechanism explaining the formation of PP/MMT nanocomposites through water-assisted extrusion is proposed.

## 2. Experimental

### 2.1. Materials

PP Moplen HF500N was purchased from Basell and PP-g-MA Polybond 3200 (labeled Plb) from Chemtura. Untreated sodium-Montmorillonite (Cloisite Na, labeled CNa) and sodium-Montmorillonite modified with methyl-tallow-bis(2-hydroxyethyl) ammonium chloride (Cloisite 30B, labeled C30B) were purchased from Southern Clay Product.

### 2.2. Sample preparation

All references and composites were prepared in a co-rotating twin-screw extruder Krupp WP ZSK25. The extruder screw length is 1000 mm with a L/D ratio of 40. The barrel temperature ( $T$ ) is fixed at 180 °C for PP-g-MA-based samples and 200 °C for PP-based ones. Water, when used, was pumped into the extruder in the high compression zone. The special design of the screw allows the pressure to increase up to 125 bars in this zone which maintains the water liquid [28]. The water is degassed in the transport zone and

fully removed using a vacuum pump. The throughput (TP), the screw speed (SP) and the water injection rate (W) were adapted to the experience. PP-g-MA-based references, nanocomposites and masterbatches were processed at a screw speed of 200 or 1000 RPM and a throughput of 7 or 21 kg/h. The water injection rate was adapted to the screw speed to ensure a constant amount of water (5.7 wt%) for the different experiments. PP-based references and nanocomposites were extruded at a screw speed of 200 RPM and a throughput of 7 kg/h. The extruded samples were immediately quenched into cold water and pelletized.

PP-g-MA-based references (R), nanocomposites (NC) and masterbatches (MB) (Table 1) contain 0, 5 and 15 wt% of clay (CNa or C30B) in inorganic content, respectively. PP-based references and nanocomposites contain 0 and 3 wt% of C30B clay in inorganic content, respectively (Table 2). PP-g-MA-based references are labeled R, nanocomposites NC-A (from CNa) or NC-B (from C30B) and masterbatches MB-B (from C30B). PP-based references are labeled PP-Plb. Nanocomposites made by dilution of PP-g-MA-based masterbatches into PP are labeled NC-MB-B and nanocomposites made by the one-pot process are labeled NC-OP-B. The description of the PP-based nanocomposites is more deeply introduced in the paragraph 3.2 dealing with the masterbatch process.

After extrusion, all samples were injection-molded using a Krauss-Maffei type KM 80-160E injection-molding machine into standard dog-bone specimens (ASTM 527). The barrel temperatures ranged within 170–200 °C and the mold temperature was kept at 25 °C. Before injection-molding, pelletized samples were dried for 24 h at 70 °C under vacuum.

### 2.3. Characterizations

All characterizations were performed onto injection-molded dog-bone specimens. Raw Plb and PP were also injection-molded into dog-bone specimens for analysis.

#### 2.3.1. Structural characterizations

2.3.1.1. *X-ray diffraction (XRD)*. The interlayer spacing of the nanocomposites was measured by XRD on a Bruker D8 Advance diffractometer using  $\text{CuK}\alpha$  radiation ( $\lambda = 1.5418 \text{ \AA}$ ) at 40 kV and 30 mA.

2.3.1.2. *Transmission electron microscopy (TEM)*. Clay dispersion of nanocomposite samples was examined on TEM micrographs. Samples were ultra-microtomed at ambient temperature with

**Table 1**

Composition of the PP-g-MA-based references, nanocomposites and masterbatches samples. Legend: Inorganic Content (IC), Screw Speed (SS), Throughput (TP), Water injection rate (W).

Samples	Clay	Plb (wt%)	Clay (wt%)	IC (wt%)	SS (RPM)	TP (kg/h)	W (ml/min)
R1	/	100	0	0	200	7	0
R2	/	100	0	0	200	7	7
R3	/	100	0	0	1000	21	0
R4	/	100	0	0	1000	21	21
NC-A1	CNa	94.5	5.5	5	200	7	0
NC-A2	CNa	94.5	5.5	5	200	7	7
NC-A3	CNa	94.5	5.5	5	1000	7	0
NC-A4	CNa	94.5	5.5	5	1000	7	21
NC-B1	C30B	92.9	7.1	5	200	7	0
NC-B2	C30B	92.9	7.1	5	200	7	7
NC-B3	C30B	92.9	7.1	5	1000	21	0
NC-B4	C30B	92.9	7.1	5	1000	21	21
MB-B1	C30B	79	21	15	200	7	0
MB-B2	C30B	79	21	15	200	7	7
MB-B3	C30B	79	21	15	1000	21	0
MB-B4	C30B	79	21	15	1000	21	21

**Table 2**

Composition of the PP-based references and nanocomposites samples. Legend: Masterbatch (MB), Inorganic Content (IC), Water injection rate (W).

Samples	PP (wt%)	P1b (wt%)	C30B (wt%)	MB (wt%)	IC (wt%)	W (ml/min)
PP-P1b1	85	15	0	0	0	0
PP-P1b2	85	15	0	0	0	7
NC-OP-B1	81	15	4	0	3	0
NC-OP-B2	81	15	4	0	3	7
NC-MB-B3	80	0	0	20	3	0
NC-MB-B4	80	0	0	20	3	0

a Reichert Microtome and collected on a 300-mesh copper grid. TEM micrographs were recorded with a LEO 922 microscope operating at 200 kV.

**2.3.1.3. Fourier Transform Infrared (FTIR) spectroscopy.** FTIR spectra were recorded on a Nicolet Nexus 870 FTIR spectrometer on compression-molded films in transmission mode by collecting 16 scans at a resolution of  $4\text{ cm}^{-1}$  over a spectral range from  $4000\text{ cm}^{-1}$  to  $400\text{ cm}^{-1}$ . Films were obtained by compression-molding of one head of the injection-molded dog-bone specimens. The spectra were normalized by setting the peak height of the  $2723\text{ cm}^{-1}$  absorption band (characteristic C-H stretching of PP) to an absorbance of 1.

### 2.3.2. Rheological, thermal and mechanical characterizations

**2.3.2.1. Rheology.** Rheological measurements were carried out in an oscillatory mode on a Bohlin Gemini II rheometer equipped with a parallel plate geometry using 25 mm diameter plates. Frequency sweep tests were performed on compression-molded samples of about 1.0 mm in thickness at a strain rate of 10% for references and nanocomposites and 5% for masterbatches. Testing temperature was  $180\text{ }^{\circ}\text{C}$  for PP-g-MA/clay nanocomposites and  $200\text{ }^{\circ}\text{C}$  for PP/clay nanocomposites. Experimental conditions were preliminary adjusted to work in the linear viscoelastic range.

**2.3.2.2. Thermogravimetric analysis (TGA).** The thermal stability of the references and composites was studied by TGA. The analyses were performed on a Mettler Toledo TGA/SDTA 851e using a heating rate of  $20\text{ }^{\circ}\text{C}/\text{min}$  under air or nitrogen atmosphere ( $100\text{ ml}/\text{min}$ ) from  $25$  to  $1000\text{ }^{\circ}\text{C}$ . TGA results are presented as temperatures at 5% (T-5), 10% (T-10) and 50% (T-50) weight loss under air atmosphere and each value is the average of three experiments. T-5, T-10 and T-50 are usually considered as the initial decomposition temperature, the onset and the midpoint of the degradation, respectively [32].

**2.3.2.3. Mechanical testing.** Tensile tests were performed on a Zwick tensile machine using a 50 kN force sensor and an extensometer for strain measurement. Tests were conducted at a cross-head speed of  $5\text{ mm}/\text{min}$  for Young's modulus measurement and at  $50\text{ mm}/\text{min}$  for elongation measurement. Presented results are averaged on three experiments.

## 3. Results and discussion

### 3.1. PP-g-MA-based references, nanocomposites and masterbatches

Understanding the possible interactions occurring between PP-g-MA and the CNa untreated MMT or the C30B organoclay with and without the help of higher shear rates and/or water injection has been first investigated. The morphology of these PP-g-MA-based references and nanocomposites is examined by XRD and TEM and the interactions between the clay and PP-g-MA are investigated by FTIR. The PP-g-MA-based references and nanocomposites are also characterized using TGA, rheology and mechanical testing, in order

to understand the observed structural changes onto the materials properties.

#### 3.1.1. Structural characterizations

The nanocomposites are characterized by XRD to follow the evolution of the clay basal spacing. Fig. 1a and b show the X-ray diffraction patterns of the PP-g-MA-based nanocomposites from CNa and C30B, respectively. The native CNa exhibits only a (001) basal spacing centered at  $1.24\text{ nm}$  ( $7.1\text{ }^{\circ}2\theta$ ) corresponding to the presence of one layer of water in the clay interlayer [33, 34]. All PP-g-MA/CNa microcomposites (NC-A1 to NC-A4) present the same clay basal spacing as CNa, indicating that no intercalation of CNa by P1b occurs whatever the extrusion conditions. The native C30B exhibits only a (001) basal spacing centered at  $1.88\text{ nm}$  ( $4.7\text{ }^{\circ}2\theta$ ). In PP-g-MA/C30B nanocomposites (NC-B1 to NC-B4), the basal spacing of C30B disappears, a new reflexion appears at  $1.42\text{ nm}$  ( $6.2\text{ }^{\circ}2\theta$ ) and a shoulder can be seen around  $3\text{--}3.5\text{ nm}$  ( $2.5\text{--}3\text{ }^{\circ}2\theta$ ). Moreover, for NC-B2 and NC-B4 a gradual increase in the diffraction intensity toward low angles is observed. The new peak at  $1.42\text{ nm}$  indicates that part of the C30B silicate layers has collapsed. The collapse results from surfactant degradation in C30B and has already been observed by other authors [35,36]. The shoulder around  $3\text{--}3.5\text{ nm}$  means that another part of the C30B silicate layers has been intercalated. The increase in the diffraction intensity toward low angles is commonly attributed to completely dispersed clay layers [13,37]. It indicates that NC-B2 and NC-B4 exhibit a mixed distribution of completely dispersed clay layers with intercalated and collapsed clay stacks while NC-B1 and NC-B3 exhibit only intercalated and collapsed clay stacks.

TEM analyses are performed to examine the clay layers dispersion in the nanocomposites. TEM micrographs of PP-g-MA/CNa

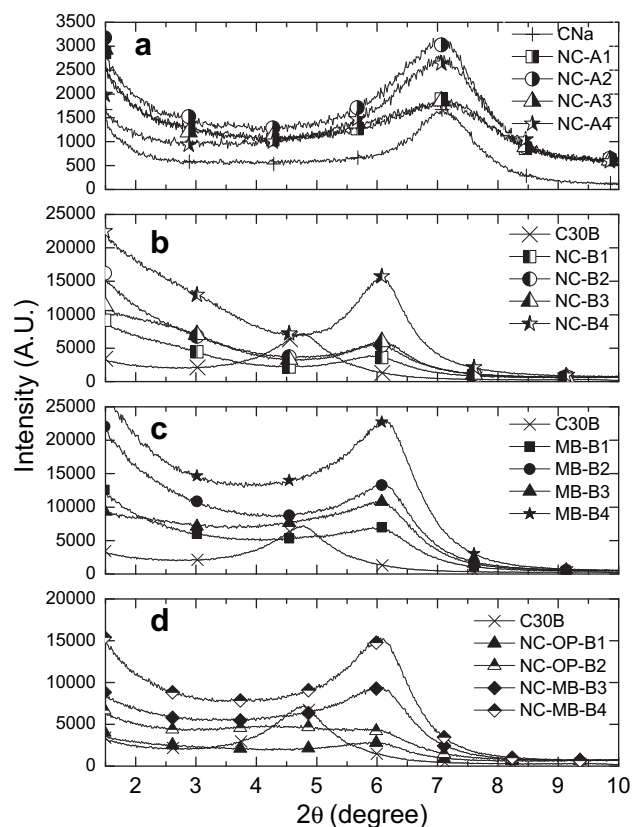


**Fig. 1.** XRD patterns of PP-g-MA-based nanocomposites from CNa (a) and C30B (b), of PP-g-MA/C30B masterbatches (c) and of PP/C30B nanocomposites (d).



samples (not shown) only present large clay aggregates of several microns. Accordingly, PP-g-MA/CNa samples are called microcomposites instead of nanocomposites. For these microcomposites, neither the high-shear extrusion nor the water injection can help to increase the clay dispersion into the polymer matrix.

Fig. 2 presents TEM micrographs of PP-g-MA/C30B nanocomposites. NC-B1 (Fig. 2a) shows a highly heterogeneous morphology, composed of huge clay stacks and few individual clay platelets. NC-B3 (Fig. 2c) shows better clay dispersion than NC-B1. The use of high-shear rates mainly breaks the large clay aggregates and generates homogeneously distributed small clay stacks. NC-B2 (Fig. 2b) still exhibits micron-sized clay stacks, but homogeneously distributed individualized clay layers are mainly observed. The use of water injection markedly improves the C30B dispersion (see also Section 3.1.2). The best clay dispersion is observed when combining high-shear rates with water injection in NC-B4 (Fig. 2d) where the clay platelets are almost all individualized with few small clay stacks. In the case of PP-g-MA/CNa microcomposites, during the water degassing, the high difference of polarity between CNa (unmodified clay) and PP-g-MA (or PP, see Section 3.2) makes that the clay re-aggregates. XRD measurements and TEM micrographs are in good agreement since only NC-B2 and NC-B4 exhibit completely dispersed clay layers (see Supporting information for further discussion on Fig. 1).

### 3.1.2. Mechanistic considerations

The interaction between the clay and the PP-g-MA matrix has been further investigated by FTIR. Fig. 3 shows infrared spectra enlargement of the respective carbonyl regions for R1, NC-A1, and NC-B1 to NC-B4 samples. R2 to R4 and NC-A2 to NC-A4 spectra are

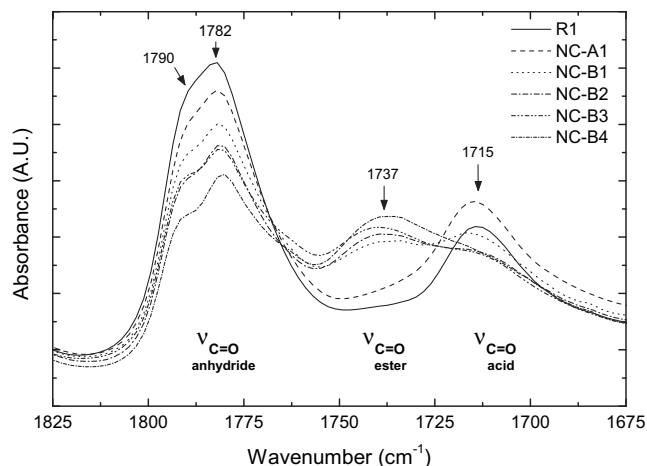


Fig. 3. FTIR spectra of R1, NC-A1, and NC-B1 to NC-B4 samples (see experimental section for normalization).

not shown since they are similar to R1 and NC-A1, respectively. Two main absorption bands can be observed in the 1675–1825  $\text{cm}^{-1}$  carbonyl region for R1 and NC-A1: the maleic anhydride band (carbonyl symmetric stretching) around 1780–1790  $\text{cm}^{-1}$  and the carboxylic acid band (carbonyl stretching) around 1715  $\text{cm}^{-1}$ . The presence of a carboxylic acid band is explained by the hydrophilicity of the PP-g-MA anhydride moieties, which absorb ambient moisture and form carboxylic diacid functions [38]. No band shift is observed

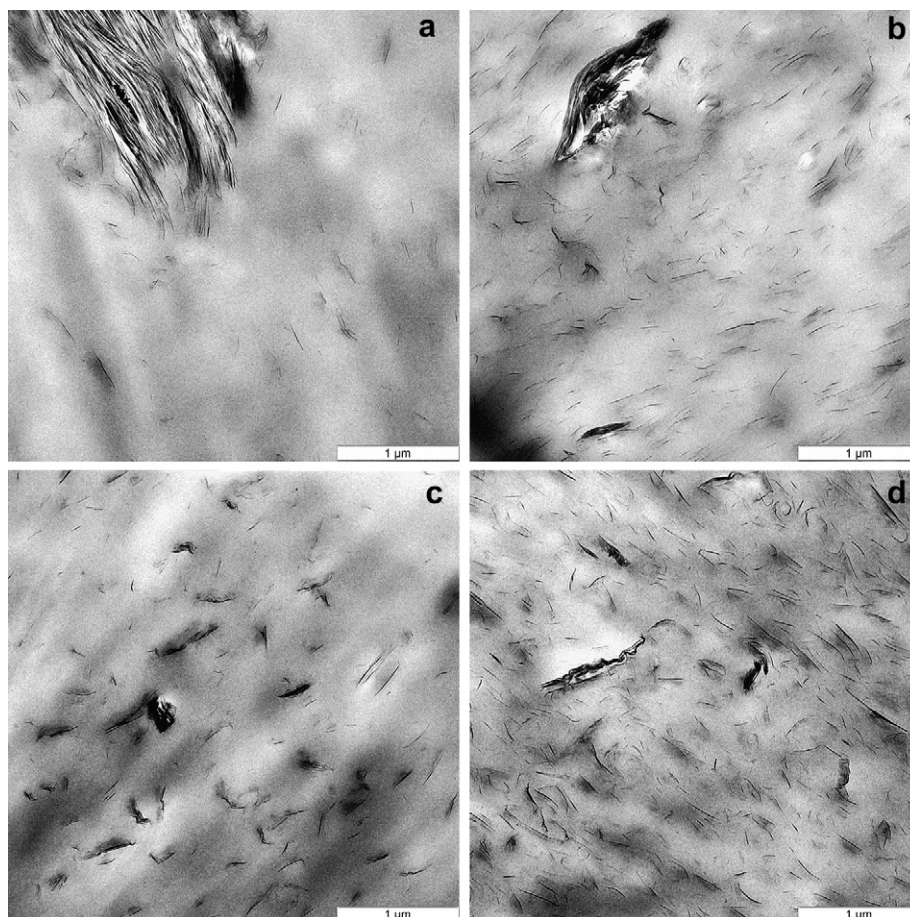


Fig. 2. PP-g-MA-based TEM micrographs of a) NC-B1, b) NC-B2, c) NC-B3 and d) NC-B4 at a magnification of 5,000.

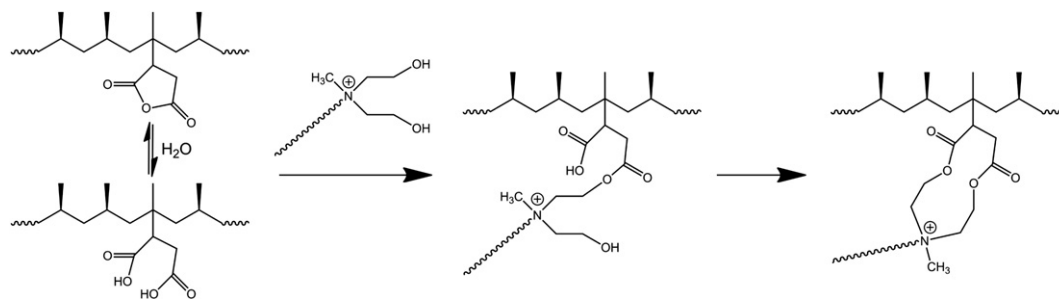


Fig. 4. Esterification reaction between  $\text{--COOH}$  of PP-g-MA and  $\text{--OH}$  of C30B's surfactant.

for NC-A1 in comparison with the R1 spectrum. For all PP-g-MA/C30B nanocomposites, a new band appears around  $1735\text{--}1740\text{ cm}^{-1}$  assigned to an ester function (carbonyl stretching). The appearance of an ester band and the related intensity decrease of the anhydride band result from a Fisher esterification reaction occurring between hydroxyl functions of C30B and carboxylic acid functions of PP-g-MA (Fig. 4). As a matter of fact, for all PP-g-MA/C30B nanocomposites, there is also a reduction of the acid band intensity. The two carboxylic acid functions of PP-g-MA may react with the two hydroxyl functions of C30B, the second esterification being an entropically favored intramolecular reaction. Indeed, if only one esterification reaction occurs, an increase of the acid band should be observed. Ranking NC-B samples on their ester band intensity and anhydride and acid bands decrease gives  $\text{NC-B1} < \text{NC-B2} \approx \text{NC-B3} < \text{NC-B4}$ . In PP-g-MA/C30B nanocomposites, the best clay dispersion is observed for NC-B4 which displays the most intense ester band.

On that experimental basis, a hypothesis on the role of the water injection can be developed. Water injected into the extruder where PP-g-MA and C30B are melt-blended, remains liquid and creates an aqueous suspension of C30B which is strongly melt-mixed with PP-g-MA. Moreover, considering that the C30B surfactant contains hydroxyl groups and that high temperature and high pressure occur inside the extruder, a partial delamination of the C30B clay layers can be obtained. Thus after water degassing, a more homogeneous distribution of the C30B platelets into molten PP-g-MA can be reached. Furthermore, injected water hydrolyzes anhydride functions of PP-g-MA into carboxylic diacid functions. Since the Fisher esterification is acid-catalyzed, more esterification reactions can take place between PP-g-MA and C30B surfactant. The role of water is then double: it directly increases C30B layers distribution during the melt-blending and it indirectly favors bonding between PP-g-MA and C30B through acid-catalyzed esterification.

### 3.1.3. Rheological, thermal and mechanical characterizations

Rheological characterization is used to evaluate the dispersion state of the filler. Indeed, the melt flow behavior is quite sensitive to the structure, particle size and shape and surface properties of a dispersed phase [39, 40]. When adding fillers to a polymer matrix, that create favorable filler-matrix interactions, an increase of the elastic modulus ( $G'$ ) and of the complex viscosity ( $\eta^*$ ) at low frequencies is observed. If a percolating mesoscopic filler network is formed, an elastic modulus plateau most often appears and the complex viscosity continuously raises at low frequencies.

Fig. 5a, b and c show the elastic modulus and complex viscosity curves of PP-g-MA-based references, PP-g-MA/CNa microcomposites and PP-g-MA/C30B nanocomposites, respectively. There is no significant difference in  $G'$  or  $\eta^*$  curves for PP-g-MA-based references which all show typical liquid-like behavior (at low frequencies,  $G'$  has a slope close to 2 and  $\eta^*$  reaches a Newtonian plateau). The  $G'$  or  $\eta^*$  curves of PP-g-MA/CNa microcomposites are

slightly increased compared to PP-g-MA references. However, as PP-g-MA references, they all exhibit a typical liquid-like behavior. No significant difference is observed between them (their  $G'$  slopes at low frequencies are around 1.8–1.9). This slight increase of rheological properties of PP-g-MA/CNa microcomposites is in agreement with the poor dispersion of CNa which consequently brings weak matrix reinforcement. On the contrary, PP-g-MA/C30B nanocomposites show higher  $G'$  and  $\eta^*$  curves than PP-g-MA references (and PP-g-MA/CNa microcomposites). Moreover their  $G'$  curves show a decrease of the frequency dependence at low frequencies. This is the consequence of the better clay dispersion obtained using C30B, instead of CNa, which induces higher matrix reinforcement. Even if NC-B3 exhibits a better clay dispersion than NC-B1 according to the TEM characterization, the rheological behavior of both samples is similar.

Rheological characterizations thus confirm the previous structural observations showing that high-shear rates mainly break clay stacks into more homogeneously distributed smaller ones without

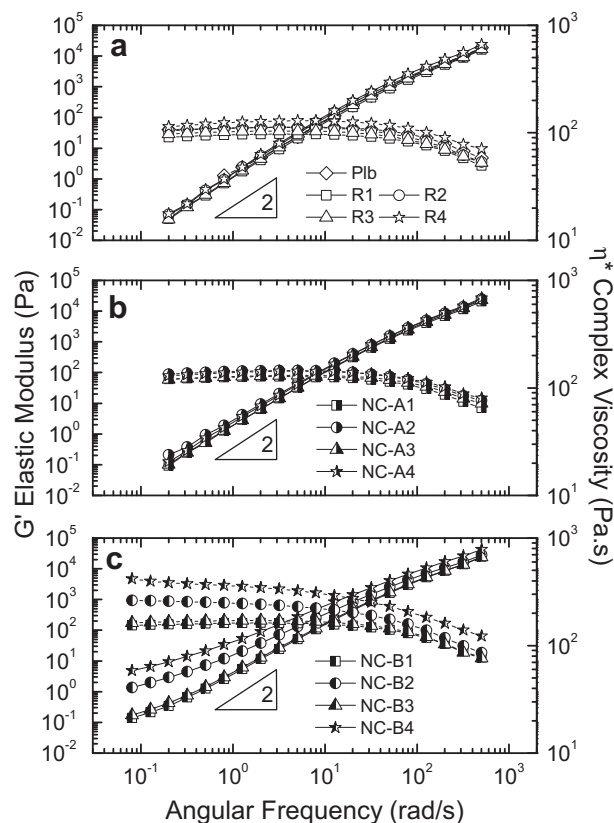


Fig. 5. Elastic modulus and complex viscosity at  $180\text{ }^\circ\text{C}$  as a function of the frequency of PP-g-MA-based references and nanocomposites.

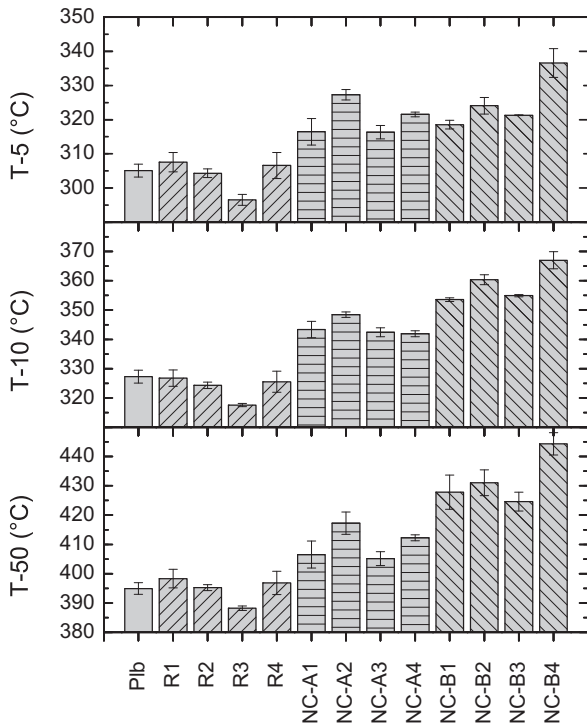


Fig. 6. Temperatures at 5% ( $T-5$ ), 10% ( $T-10$ ) and 50% ( $T-50$ ) weight loss under air atmosphere for PP-g-MA-based references and nanocomposites.

increasing the extent of completely dispersed clay layers. Therefore, almost no difference is observed in their rheological behavior. NC-B2 and NC-B4, show higher  $G'$  and  $\eta^*$  curves than their respective PP-g-MA/C30B nanocomposites prepared without water. The  $G'$  slopes at low frequencies are 0.86 for NC-B2 and 0.78 for NC-B4. Thus, the use of water injection when producing PP-g-MA/C30B nanocomposites markedly lead to the rheological properties improvement, in agreement with their good clay layers dispersion. The combination of high-shear rates and water injection highly enhances the rheological properties of PP-g-MA/C30B nanocomposites.

Higher thermal stability is commonly observed when clay platelets are well dispersed into the polymer matrix, as a result of hindered out-diffusion of the volatile decomposition products and also of char formation that acts as a physical barrier between the polymer and the oxidative medium [1]. Fig. 6 presents the TGA

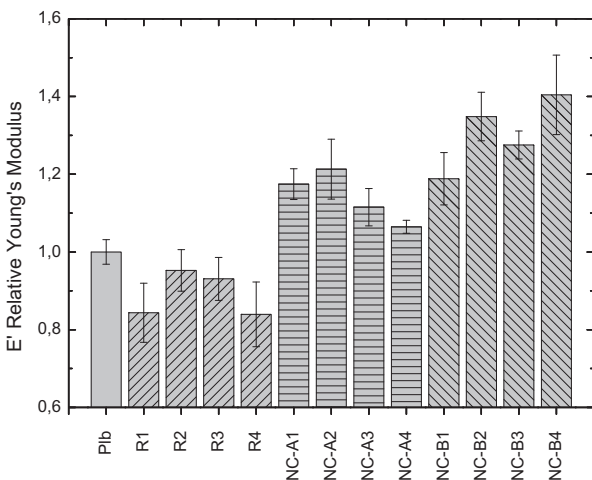


Fig. 7. Relative Young's modulus of PP-g-MA-based references and nanocomposites.

results for PP-g-MA-based references and nanocomposites. Except for R3, the thermal stability of PP-g-MA-based references is not significantly different from as-received Plb. The lower thermal stability of R3 can be explained by the high-shear rates applied, which raise the melt temperature and could consequently increase the thermo-mechanical degradation. Compared to Plb, PP-g-MA/CNa samples exhibit a slight but significant increase of their thermal stability despite the poor CNa dispersion into Plb. These thermal stability improvements are comparable with those observed by Villaluenga et al. for PP filled with CNa [41]. In opposition to the water injection, higher shear rates do not increase the thermal stability of PP-g-MA/CNa microcomposites.

PP-g-MA/C30B samples show superior thermal stability than PP-g-MA/CNa samples. This is consistent with the better clay dispersion obtained in PP-g-MA/C30B nanocomposites than in PP-g-MA/CNa microcomposites. As for PP-g-MA/CNa, in the absence of water, high-shear rates do not change the thermal stability of PP-g-MA/C30B nanocomposites. The higher clay dispersion reached in PP-g-MA/C30B nanocomposites using water injection, hinders more efficiently the out-diffusion of the volatile decomposition products. NC-B4 exhibits thus the greatest thermal stability. Contrary to PP-g-MA/CNa microcomposites, a synergy effect by using high-shear rates and water injection for PP-g-MA/C30B nanocomposites is marked. This result is in good agreement with the rheological measurements.

Mechanical reinforcement is expected when clay platelets are well dispersed into the polymer matrix. Especially, Young's modulus commonly increases and depends on the filler dispersion and the interfacial interactions. Indeed, enlarging the interface between the matrix and the filler increases the volume of polymer chains influenced by the rigid clay platelets.

Fig. 7 shows the relative Young's modulus ( $E'$ ) from tensile tests of PP-g-MA-based references and nanocomposites. All PP-g-MA-based references have lower  $E'$  values than as-received Plb and all PP-g-MA/CNa microcomposites exhibit higher  $E'$  than starting PP-g-MA. Despite their poor clay dispersion, their  $E'$  is increased from 6 to 21% in comparison with starting Plb. Rheological, thermal and mechanical properties, all agree that NC-A2 shows the better properties improvement in PP-g-MA/CNa microcomposites. These modulus improvements are comparable with those obtained for thermoplastic polyolefins filled with talc [8]. This is in good agreement with TEM micrographs of PP-g-MA/CNa microcomposites (not shown) where only large micron-sized clay aggregates are observed.

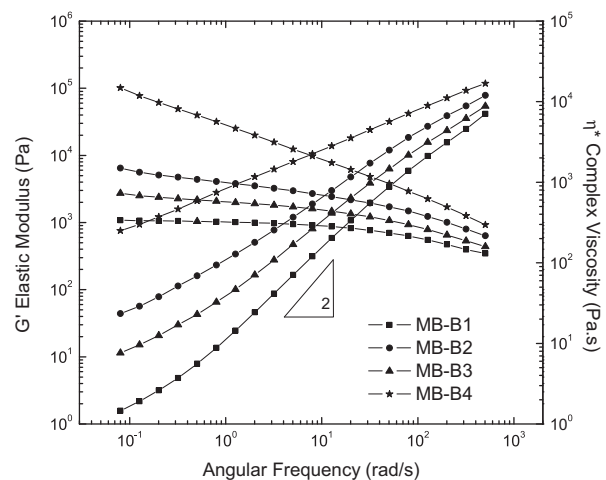
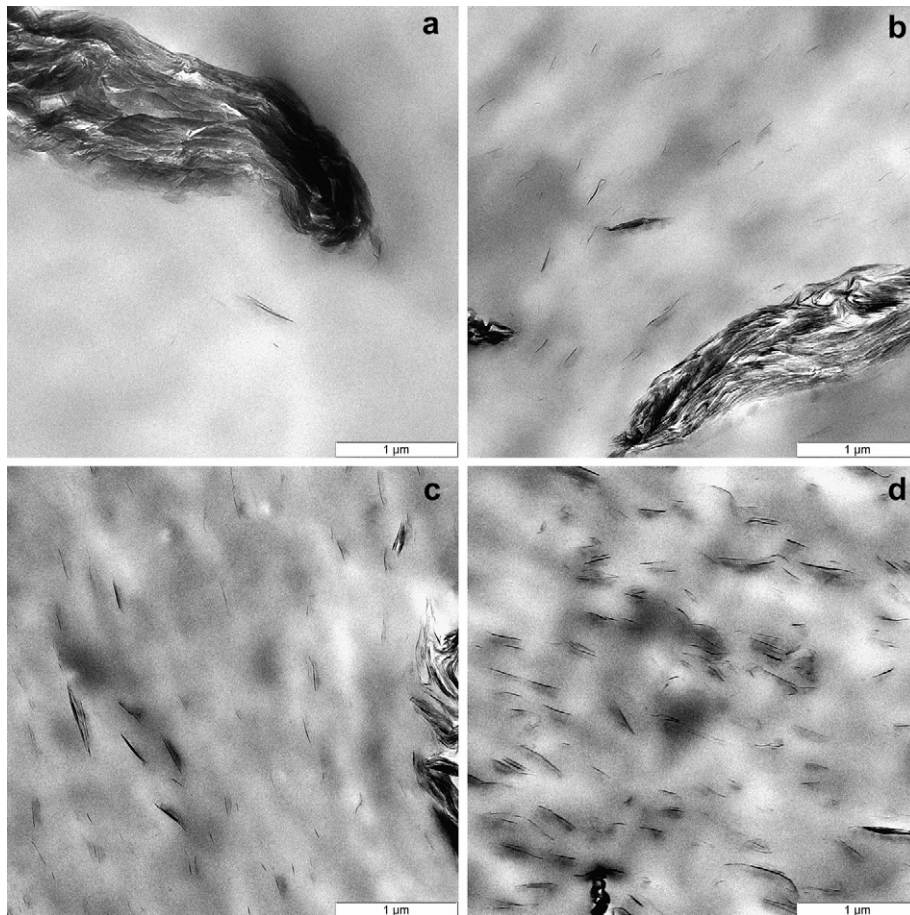


Fig. 8. Elastic modulus and complex viscosity at 180 °C as a function of the frequency for PP-g-MA-based masterbatches.



**Fig. 9.** PP-based TEM micrographs of a) NC-OP-B1, b) NC-OP-B2, c) NC-MB-B3 and d) NC-MB-B4 at a magnification of 5,000.

In absence of water and with low shear rates, the same mechanical reinforcement is basically obtained with CNa (NC-A1) or C30B (NC-B1). Indeed, except that NC-B1 exhibits a few completely dispersed clay layers, the clay dispersion in NC-A1 and NC-B1 is mainly composed of very large clay stacks. In opposition to the rheological results, the Young's modulus of NC-B3 is significantly higher than the one of NC-B1. High-shear rates thus increase

the mechanical reinforcement of the matrix in PP-g-MA/C30B nanocomposites. This can be explained by the presence of smaller clay stacks which offer more clay surface available for interaction with the PP-g-MA matrix. The use of water injection for producing PP-g-MA/C30B nanocomposites again leads to further mechanical reinforcement since NC-B2 and NC-B4 show higher  $E'$  values than NC-B1 and NC-B3, respectively. As for the rheological properties, a synergy effect by using high-shear rates and water injection is observed on the mechanical properties of PP-g-MA/C30B nanocomposites.

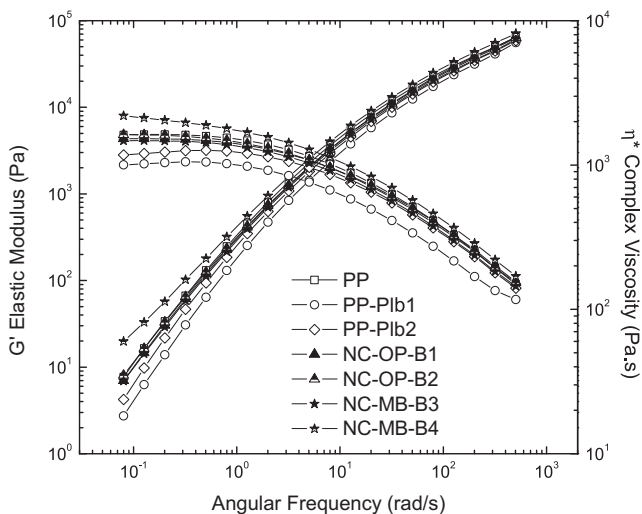


**Fig. 10.** Elastic modulus and complex viscosity at 200 °C as a function of the frequency for PP-based references and nanocomposites.

### 3.1.4. PP-g-MA-based masterbatches

Since PP-g-MA/CNa microcomposites exhibit poor clay dispersion and weak properties improvement, masterbatches are only considered by using C30B. Four PP-g-MA/C30B masterbatches have been extruded similarly to the four PP-g-MA/C30B nanocomposites (Table 1) and characterized by XRD and rheology.

Fig. 1 c shows the X-ray diffraction patterns of the PP-g-MA/C30B masterbatches. All samples show only one reflexion at 1.42 nm ( $6.2^\circ 2\theta$ ) indicating that C30B silicate layers have collapsed due to the surfactant decomposition. A gradual increase in the diffraction intensity toward low angles is observed for MB-B1, MB-B2 and MB-B4 indicating a mixed distribution of collapsed clay stacks and completely dispersed clay layers.

Fig. 8 shows  $G'$  and  $\eta^*$  curves of PP-g-MA/C30B masterbatches. Despite the high clay amount, MB-B1 still exhibits a Newtonian plateau (on its  $\eta^*$  curve) and a  $G'$  slope of 0.93 at low frequencies. Using high-shear rates increase  $G'$  and  $\eta^*$  curves of MB-B3. However, this increase is higher with water injection (MB-B2). Even

if both MB-B2 and MB-B3 have a  $G'$  slope of 0.76 in the terminal zone, the effect of water injection appears more important than high-shear rates. A further raise of  $G'$  and  $\eta^*$  curves is obtained when combining water injection and high-shear rates. MB-B4 presents an important reduction of the frequency dependence on its  $G'$  curve with a  $G'$  slope of 0.58, while its  $\eta^*$  curve continuously increases at low frequencies, indicating that the percolation threshold is reached. As for PP-g-MA/C30B nanocomposites, the best improvement is obtained when combining high-shear rates and water injection.

Based on the properties improvement of PP-g-MA/C30B nanocomposites and masterbatches, the MB-B4 sample has been selected for dilution into PP matrix in the next step of the work. The further results will be compared to MB-B3 considered as a reference to evaluate the influence of water.

### 3.2. PP-based references and nanocomposites

This second part of the work is focused on the production and characterization of PP-based nanocomposites by dilution of PP-g-MA-based masterbatches into neat PP. The selected masterbatch, MB-B4, is diluted into PP and the resulting PP-based nanocomposite is labeled NC-MB-B4. Similarly, MB-B3 diluted into PP is named NC-MB-B3 and used as the control without water. The relevance of the masterbatch dilution process will be confronted to the one-pot process in which PP, PP-g-MA and clay are directly melt-compounded together in one step to furnish the PP-based nanocomposite labeled NC-OP-B1. Moreover, another sample is considered, made by direct melt-compounding of PP, PP-g-MA and clay with water injection (NC-OP-B2) to study the effect of water injection when the main matrix is PP (see Supporting information for complete description of Figs. 9–12).

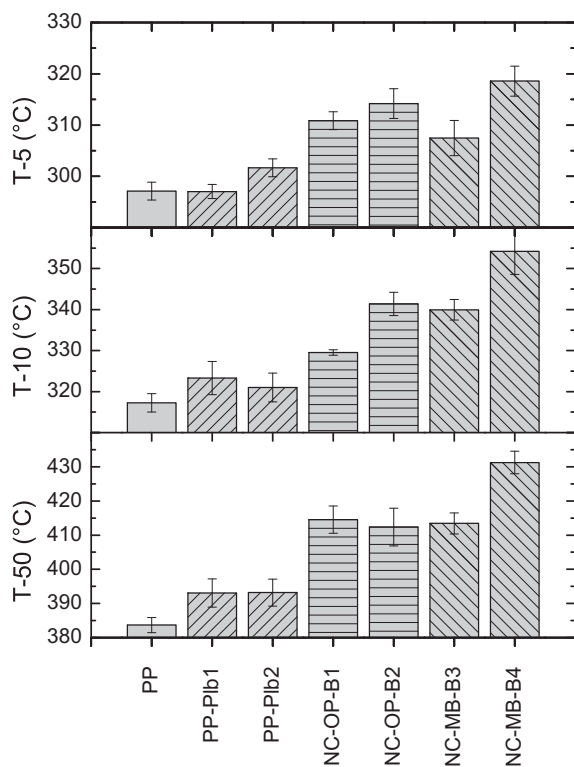


Fig. 11. Temperatures at 5% (T-5), 10% (T-10) and 50% (T-50) weight loss under air atmosphere for PP-based references and nanocomposites.

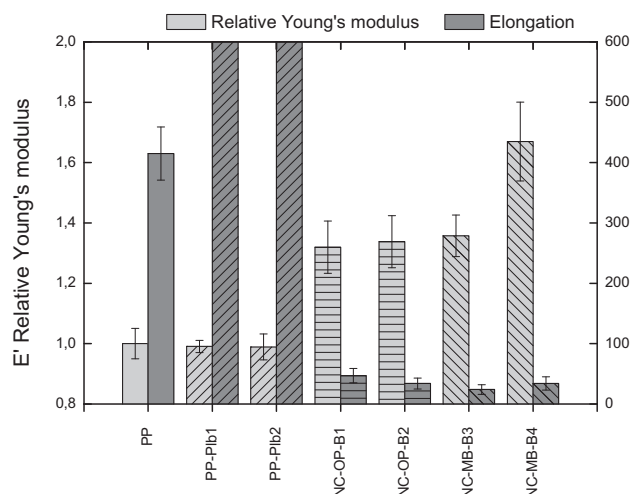


Fig. 12. Relative Young's modulus and elongation for PP-based references and nanocomposites.

#### 3.2.1. Structural characterizations

XRD patterns and TEM micrographs of PP/C30B nanocomposites are shown in Figs. 1d and 9, respectively. The best clay dispersion in PP-based nanocomposites is obtained for NC-MB-B4 where well distributed, completely dispersed clay layers and small stacks are exclusively observed. Considering both XRD and TEM results, it can be noticed that the effect of water injection on the clay dispersion is much less important in PP/C30B nanocomposites prepared by the one-pot process than in PP-g-MA/C30B nanocomposites.

#### 3.2.2. Rheological, thermal and mechanical characterizations

Elastic modulus and complex viscosity curves of PP-based references and nanocomposites are presented in Fig. 10. Only NC-MB-B4 shows a significant increase of the  $G'$  and  $\eta^*$  curves in comparison with the other samples. The  $G'$  curve displays a decrease of the frequency dependence at low frequencies with a slope of 1.19.

Fig. 11 presents the TGA results for PP-based references and nanocomposites. NC-MB-B4 shows the best thermal stability indicating an increase of the hindered out-diffusion of the volatile decomposition products due to a better clay dispersion.

Fig. 12 shows the relative Young's modulus ( $E'$ ) and the elongation from tensile tests of PP-based references and nanocomposites. NC-MB-B4 shows the best increase of  $E'$ , of approximately 65–70%.

## 4. Conclusions

PP-based nanocomposites with a high level of clay delamination and very significant properties improvement have been successfully prepared through dilution into neat PP of PP-g-MA-based masterbatches synthesized with Cloisite 30B organoclay, by a water-assisted extrusion process using high-shear rates; a remarkable synergy effect has been shown. This masterbatch process is preferred over the so-called "one-pot process". The accurate FTIR study revealed an esterification reaction occurring between the hydroxyl functions of Cloisite 30B organoclay surfactant and the carboxyl functions of the PP-g-MA compatibilizer, hydrolyzed in situ. The success of our process results from the double role played by water on the clay dispersion: (i) water increases the clay dispersion during the melt-blending step by creating an aqueous suspension of Cloisite 30B organoclay which strongly improves the melt-mixing; (ii) water favors the bonding between PP-g-MA and the organoclay surfactant

through MA hydrolysis and then acid-catalyzed esterification reactions.

This work paves the route toward the development of water-assisted extrusion process for other apolar matrix-based nanocomposites.

### Acknowledgments

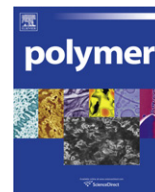
The authors thank La Région Wallonne and FRIA (Fonds pour la formation à la Recherche dans l'Industrie et dans l'Agriculture) for financial support. J. Marchand-Brynaert is Senior Research Associate of the FRS-FNRS (Fonds National de la Recherche Scientifique, Belgium).

### Appendix. Supplementary data

Supplementary data related to this article can be found online at doi:10.1016/j.polymer.2010.11.027.

### References

- Alexandre M, Dubois P. Polymer-layered silicate nanocomposites: preparation, properties and uses of a new class of materials. *Mater Sci Eng, R* 2000;28:1–63.
- Ray SS, Okamoto M. Polymer/layered silicate nanocomposites: a review from preparation to processing. *Prog Polym Sci* 2003;28:1539–641.
- Utracki LA. Clay-containing polymeric nanocomposites, Vol. 1 and 2. Shawbury, England: RAPRA Technology Ltd; 2004.
- Krishnamoorti R, Vaia RA. Polymer nanocomposites. *J Polym Sci, Part B: Polym Phys* 2007;45(24):3252–6.
- Paul DR, Robeson LM. Polymer nanotechnology: nanocomposites. *Polymer* 2008;49(15):3187–204.
- Manias E, Touny A, Wu L, Strawhecker K, Lu B, Chung T. Polypropylene/montmorillonite nanocomposites. review of the synthetic routes and materials properties. *Chem Mater* 2001;13:3516–23.
- Vaia RA, Wagner HD. Framework for nanocomposites. *Mater Today* 2004;7(11):32–7.
- Lee H-S, Fasulo PD, Rodgers WR, Paul DR. Tpo based nanocomposites. part 1. morphology and mechanical properties. *Polymer* 2005;46(25):11673–89.
- Harrats C, Groeninckx G. Features, questions and future challenges in layered silicates clay nanocomposites with semicrystalline polymer matrices. *Macromol Rapid Commun* 2008;29(1):14–26.
- Pavlidou S, Papaspyrides CD. A review on polymer-layered silicate nanocomposites. *Prog Polym Sci* 2008;33:1119–98.
- Kumar AP, Depan D, Tomer NS, Singh RP. Nanoscale particles for polymer degradation and stabilization—trends and future perspectives. *Prog Polym Sci* 2009;34(6):479–515.
- Vaia RA, Teukolsky RK, Giannelis EP. Interlayer structure and molecular environment of alkylammonium layered silicates. *Chem Mater* 1994;6(7):1017–22.
- Kawasumi M, Hasegawa N, Kato M, Usuki A, Okada A. Preparation and mechanical properties of polypropylene-clay hybrids. *Macromolecules* 1997;30:6333–8.
- Hasegawa N, Kawasumi M, Kato M, Usuki A, Okada A. Preparation and mechanical properties of polypropylene-clay hybrids using a maleic anhydride-modified polypropylene oligomer. *J Appl Polym Sci* 1998;67(1):87–92.
- Liu X, Wu Q. PP/clay nanocomposites prepared by grafting-melt intercalation. *Polymer* 2001;42(25):10013–9.
- Pucciariello R, Villani V, Guadagno L, Vittoria V. Nanocomposites of syndiotactic polypropylene: phase behavior and morphology. *Polym Eng Sci* 2006;46(10):1433–42.
- Park JH, Lee HM, Chin I-J, Choi HJ, Kim HK, Kang WG. Intercalated polypropylene/clay nanocomposite and its physical characteristics. *J Phys Chem Solids* 2008;69(5-6):1375–8.
- Xie W, Gao Z, Pan WP, Hunter D, Singh A, Vaia R. Thermal degradation chemistry of alkyl quaternary ammonium montmorillonite. *Chem Mater* 2001;13(9):2979–90.
- Shah RK, Paul DR. Organoclay degradation in melt processed polyethylene nanocomposites. *Polymer* 2006;47(11):4075–84.
- Cervantes-Uc JM, Cauch-Rodríguez JV, Vázquez-Torres H, Garfias-Mesías LF, Paul DR. Thermal degradation of commercially available organoclays studied by TGA-FTIR. *Thermochim Acta* 2007;457(1-2):92–102.
- Hedley CB, Yuan G, Theng BKG. Thermal analysis of montmorillonites modified with quaternary phosphonium and ammonium surfactants. *Appl Clay Sci* 2007;35(3-4):180–8.
- Korbee RA, Van Geneen AA. Process for the preparation of a polyamide nanocomposite composition. WO 1999/9929767.
- Hasegawa N, Okamoto H, Kato M, Usuki A, Sato N. Nylon 6/na-montmorillonite nanocomposites prepared by compounding nylon 6 with na-montmorillonite slurry. *Polymer* 2003;44(10):2933–7.
- Kato M, Matsushita M, Fukumori K. Development of a new production method for a polypropylene-clay nanocomposite. *Polym Eng Sci* 2004;44(7):1205–11.
- Yu Z-Z, Hu G-H, Varlet J, Dasari A, Mai Y-W. Water-assisted melt compounding of nylon-6/pristine montmorillonite nanocomposites. *J Polym Sci, Part B: Polym Phys* 2005;43(9):1100–12.
- Dasari A, Yu Z-Z, Mai Y-W, Hu G-H, Varlet J. Clay exfoliation and organic modification on wear of nylon 6 nanocomposites processed by different routes. *Comp Sci Technol* 2005;65(15-16):2314–28.
- Fedullo N, Sclavons M, Bailly C, Lefebvre J-M, Devaux J. Nanocomposites from untreated clay: a myth? *Macromol Symp* 2006;233(1):235–45.
- Fedullo N, Sorlier E, Sclavons M, Bailly C, Lefebvre J-M, Devaux J. Polymer-based nanocomposites: overview, applications and perspectives. *Prog Org Coat* 2007;58(2-3):87–95.
- Wevers MGM, Pijpers TJJ, Mathot VBF. The way to measure quantitatively full dissolution and crystallization of polyamides in water up to 200 °C and above by dsc. *Thermochim Acta* 2007;453(1):67–71.
- Aloui M, Soulestin J, Lacrampe MF, Krawczak P, Rousseaux D, Marchand-Brynaert J, et al. A new elaboration concept of polypropylene/unmodified montmorillonite nanocomposites by reactive extrusion based on direct injection of polypropylene aqueous suspensions. *Polym Eng Sci* 2009;49(11):2276–85.
- Mainil M, Urbanczyk L, Calberg C, Germain A, Jerome C, Bourbigot S, et al. Morphology and properties of san-clay nanocomposites prepared principally by water-assisted extrusion. *Polym Eng Sci* 2010;50(1):10–21.
- Wang D, Jiang DD, Pabst J, Han Z, Wang J, Wilkie CA. Polystyrene magadiite nanocomposites. *Polym Eng Sci* 2004;44(6):1122–31.
- Norrish K. The swelling of montmorillonite. *Discuss Faraday Soc* 1954;18:120–34.
- Karaborni S, Smit B, Heidug W, Urai J, van Oort E. The swelling of clays: molecular simulations of the hydration of montmorillonite. *Science* 1996;271(5252):1102–4.
- Ton-That M-T, Perrin-Sarazin F, Cole KC, Bureau MN, Denault J. Polyolefin nanocomposites: formulation and development. *Polym Eng Sci* 2004;44(7):1212–9.
- Rohlmann CO, Horst MF, Quinzani LM, Failla MD. Comparative analysis of nanocomposites based on polypropylene and different montmorillonites. *Eur Polym J* 2008;44(9):2749–60.
- Wang Y, Chen F-B, Li Y-C, Wu K-C. Melt processing of polypropylene/clay nanocomposites modified with maleated polypropylene compatibilizers. *Composites Part B* 2004;35(2):111–24.
- Rousseaux DDJ, Sclavons M, Godard P, Marchand-Brynaert J. Carboxylate clays: a model study for polypropylene/clay nanocomposites. *Polym Degrad Stab* 2010;95(7):1194–204.
- Rohlmann CO, Failla MD, Quinzani LM. Linear viscoelasticity and structure of polypropylene-montmorillonite nanocomposites. *Polymer* 2006;47(22):7795–804.
- Wang K, Liang S, Deng J, Yang H, Zhang Q, Fu Q, et al. The role of clay network on macromolecular chain mobility and relaxation in isotactic polypropylene/organoclay nanocomposites. *Polymer* 2006;47(20):7131–44.
- Villaluenga JPG, Khayet M, Lopez-Manchado MA, Valentin JL, Seoane B, Mengual JL. Gas transport properties of polypropylene/clay composite membranes. *Eur Polym J* 2007;43(4):1132–43.



# An experimental study of interaction between surfactant and particle hydrogels

Yongfu Wu<sup>a</sup>, Tingji Tang<sup>a</sup>, Baojun Bai<sup>a,\*</sup>, Xiaofen Tang<sup>b</sup>, Jialu Wang<sup>b</sup>, Yuzhang Liu<sup>b</sup>

<sup>a</sup> Department of Geological Science and Engineering, Missouri University of Science and Technology, 129 McNutt Hall, 1400N Bishop Avenue, Rolla, MO 65409, USA

<sup>b</sup> Research Institute of Petroleum Exploration and Development, PetroChina, 20 Xueyuan Road, Beijing 100083, China

## ARTICLE INFO

### Article history:

Received 15 September 2010

Received in revised form

29 November 2010

Accepted 1 December 2010

Available online 9 December 2010

### Keywords:

Hydrogel

Surfactant

Dynamic modulus

## ABSTRACT

Polyacrylamide gel was synthesized to study interaction between surfactant and particle hydrogel. Surfactants used in this study include cationic surfactants, *n*-dodecylpyridinium chloride, (1-hexadecyl) pyridinium bromide; anionic surfactants, sodium salt of dodecylbenzene sulfonic acid, sodium 4-*n*-octyl benzene sulfonate and sodium branched alcohol propoxylate sulfate; and nonionic surfactants, Igepal<sup>®</sup> CO-530, Tergito<sup>®</sup> NP-10 and Neodol<sup>®</sup> 25-12. It has been found that, after swelling of the dry particles, surfactant concentration shows a substantial increase. Meanwhile, dynamic modulus ( $G'$  and  $G''$ ) of the gels shows a significant decrease in the surfactant solutions. Based on the experimental results, a mechanism has been proposed to elucidate the reduction of the gel dynamic modulus. Furthermore, this mechanism was discussed through surfactant critical packing parameters ( $CPP$ ) at the interface of the hydrogel particle and surfactant aqueous solution, and confirmed by recovery of the gel dynamic modulus after removal of the surfactant from the hydrogels.

© 2010 Elsevier Ltd. All rights reserved.

## 1. Introduction

Interaction between surfactant and polymer hydrogel has been a subject of considerable theoretical and practical interest, and has been extensively studied [1–9]. Philippova and co-workers studied interaction of gels with ionic surfactants *n*-cetylpyridinium chloride and sodium dodecylbenzenesulfonate. They reported that adsorption of anionic surfactant is governed primarily by hydrophobic interactions. Due to conditions of electro-neutrality, anionic surfactant penetrates the gel together with corresponding co-ions. Therefore, the uptake of cationic surfactant ions results in gel shrinkage, while the uptake of anionic surfactant induces gel swelling. In the anionic gel/anionic surfactant system, a significant interaction is observed only for the most hydrophobic gels when hydrophobic interactions overcome the electrostatic repulsion between similarly charged groups [10]. Ashbaugh and co-workers studied interactions of mixed dodecyl trimethylammonium bromide ( $C_{12}TAB$ ) and octaethylene glycol monododecyl ether ( $C_{12}E_8$ ) micelles with a lightly cross-linked Na polyacrylate gel. They found that gel preferentially absorbs  $C_{12}TA^+$  under most conditions owing to electrostatic attraction to the oppositely charged gel. For low initial  $C_{12}E_8$  surfactant fractions and moderate  $C_{12}TA^+$  concentrations, however, the situation is reversed and the nonionic surfactant is preferentially absorbed [11]. Nichifor and co-workers studied interaction of hydrophobically modified cationic

dextran hydrogels with biological surfactants. They found that an increase in the length of the alkyl substituent of the hydrogel strongly increases the binding constants  $K_0$  and  $K$ , but decreases the cooperativity parameter  $\mu$ . This was explained by the formation of mixed micelles between pendant groups of the gel and surfactant molecules [12].

It is well recognized that surfactants play a critical roles in tribology [13]. One of the results caused by addition of surfactants to hydrogel particles is the influence on the frictional behavior of gels. Friction of hydrogels on solid surface or on gels has been extensively studied during the last decade, especially in Gong's group, and considerable number of papers have been published [14–24]. It has been found that the frictional behaviors of the hydrogels do not conform to Amonton's law  $F = \mu W$ , which well describes the friction of solids [15]. Based on the complex friction behavior of polymer gels, Gong and co-workers proposed a repulsion–adsorption mechanism to describe the friction of hydrogels on a smooth substrate. If the interfacial interaction between hydrogel and solid surface is repulsive, then friction is due to lubrication of the hydrated water layer of the polymer network at the interface. In this case, friction is proportional to sliding velocity. If the interaction is attractive, then friction is from two contributions: (1) elastic deformation of the adsorbed polymer chain; (2) lubrication of the hydrated layer of the polymer network [16]. They reported that the friction behavior of hydrogels sliding on smooth substrates strongly depends on the adhesive strength and hydrophobicity of the substrate [17]. Du and co-workers studied friction behaviors of PVA gel sliding against a glass surface in dilute poly

\* Corresponding author. Tel.: +1 573 341 4016; fax: +1 573 341 6935.

E-mail address: [baib@mst.edu](mailto:baib@mst.edu) (B. Bai).

**Table 1**  
Surfactant Molecular Structure and Gel Swelling Ratio in Surfactant Solutions.

Surfactant	Molecular structure	Swelling ratio
<i>n</i> -Dodecylpyridinium chloride	$\text{H}_3\text{C}-(\text{CH}_2)_{10}-\text{CH}_2-\text{N}^+(\text{C}_5\text{H}_5) \text{Cl}^-$	22.2–23.2
(1-Hexadecyl)pyridinium bromide	$\text{H}_3\text{C}-(\text{CH}_2)_{14}-\text{CH}_2-\text{N}^+(\text{C}_5\text{H}_5) \text{Br}^-$	22.3–23.3
Benzalkonium chloride	$\text{C}_6\text{H}_5-\text{CH}_2-\text{N}^+(\text{CH}_3)_2-\text{C}_n\text{H}_{2n+1} \text{Cl}^-$ ( $n=8 \sim 18$ )	22.1–23.1
Alfoterra® 23 Sodium branched alcohol propoxylate sulfate	$\text{H}_3\text{C}-(\text{CH}_2)_{8-10}-\text{CH}_2-\text{CH}(\text{CH}_3)-\text{CH}_2-\text{O}-(\text{CH}_2-\text{CH}(\text{CH}_3)-\text{O})_3-\text{S}(=\text{O})_2\text{O}^- \text{Na}^+$	22.3–23.3
Sodium 4- <i>n</i> -octyl benzene sulfonate	$\text{H}_3\text{C}-(\text{CH}_2)_6-\text{CH}_2-\text{C}_6\text{H}_4-\text{S}(=\text{O})_2\text{O}^- \text{Na}^+$	22.8–23.8
Sodium salt, dodecylbenzene sulfonic acid	$\text{H}_3\text{C}-(\text{CH}_2)_{10}-\text{CH}_2-\text{C}_6\text{H}_4-\text{S}(=\text{O})_2\text{O}^- \text{Na}^+$	22.6–23.6
Igepal® CO-530 Nonylphenoxy poly(ethyleneoxy) alcohol	$\text{H}_3\text{C}-\text{C}(\text{CH}_3)_2-\text{CH}_2-\text{C}(\text{CH}_3)_2-\text{CH}_2-\text{C}_6\text{H}_4-(\text{OCH}_2\text{CH}_2)_6-\text{OH}$	22.1–23.1
Tergitol® NP-10 Nonylphenol ethoxylated alcohol	$\text{H}_3\text{C}-\text{C}(\text{CH}_3)_2-\text{CH}_2-\text{C}(\text{CH}_3)_2-\text{CH}_2-\text{C}_6\text{H}_4-(\text{OCH}_2\text{CH}_2)_{10}-\text{OH}$	22.0–23.0
Neodol® 25–12 Linear primary alcohol ethoxylate	$\text{H}_3\text{C}-(\text{CH}_2)_{12}-\text{CH}_2-(\text{OCH}_2\text{CH}_2)_{12}-\text{OH}$	22.6–23.6
In distilled water		22.8–23.8
In 1.00 wt.% NaCl brine		22.4–23.4

(ethylene oxide) (PEO) aqueous solution, and they found that PEO concentration has a significant influence on the friction of a water-swollen PVA gel on glass surface [20]. Osada and co-workers studied kinetics of surfactant binding into polymer gel and effect of hydrophobic side chain on poly(carboxyl acid) dissociation. They reported that the driving force of surfactant diffusion into the gel is the concentration gradient of the surfactant. The binding of surfactant with the polymer network sustains a high concentration gradient that facilitates the subsequent surfactant diffusion [21]. They also analyzed the structure of poly(ADA-co-AA) polymer and surfactant-poly(ADA-co-AA) complexes by SAXD and WAXD and found that the complexes change their structures from micelle-like to lamellar-like with an increase of mole fraction of acryloyl dodecanoic acid (ADA) in the complexes [24].

To date, interaction between surfactant and particle hydrogel has not been studied systematically. In this paper, we study the

influence of surfactant in aqueous solution on dynamic modulus of water-swollen gel in 1.0 wt% NaCl. Surfactants used in this study include nonionic, anionic and cationic surfactants. Gel frictions were measured in terms of storage modulus  $G'$  and loss modulus  $G''$  under the same conditions of stress, gap, oscillation frequency and temperature for all surfactants. Gel used in this study was synthesized from acrylamide monomer with ethylene-bis-acrylamide cross-linker.

## 2. Experimental

### 2.1. Materials

Monomer acrylamide (98.5%) and cross-linker methylene-bis-acrylamide (97+%) were purchased from Alfa Aesar Company (Ward Hill, MA) and used without further purification. Ammonium



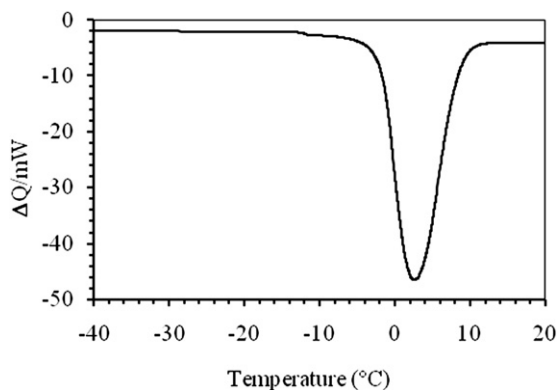


Fig. 1. DSC curve of the swollen PPGs in the distilled water.

persulfate was used as initiator for polymer gel synthesis. Cationic surfactants, *n*-dodecylpyridinium chloride (98%), (1-hexadecyl)pyridinium bromide monohydrate (98%), benzalkonium chloride and anionic surfactant, sodium 4-*n*-octyl benzene sulfonate were also purchased from Alfa Aesar (Ward Hill, MA) and used without further purification. Sodium dodecylbenzene sulfonic acid was purchased from Sigma–Aldrich (St. Louis, MO) and used without further purification. Other commercial surfactants were requested from their manufacturers, Igepal® CO-530 from Rhodia, Inc. (Bristol, PA), Tergitol® NP-10 from Dow Chemical (Midland, MI), Alfoterra® 23 from Sasol North America Inc. (Houston, TX), Neodol® 25-12 from Shell Chemical Company (Houston, TX), and used without further purification. NaCl (99.8%) was purchased from Fisher Scientific Inc. Water used in all experiments was distilled water produced in this lab. Molecular structures of the surfactants are listed in Table 1.

## 2.2. Synthesis and fabrication of preformed particle gels (PPGs)

150 g of acrylamide were added to 498.7 g of distilled water. The solution was purged with nitrogen gas for 60 min and stirred at 270 RPM until all the solid dissolved. 0.650 g of methylene-*bis*-acrylamide was added to the solution and stirred until completely dissolved. 0.650 g of (NH<sub>4</sub>)<sub>2</sub>S<sub>2</sub>O<sub>8</sub> was then added with stirring to the solution prepared above. The mixture solution was placed in an oven at 60 °C for 14 h. A strong bulk gel was formed and it was cut into small pieces. The formed hydrogel was then purified by soaking in large amount of distilled water for one week and followed by drying at 60 °C for 4 days to yield 168.390 g of a slightly yellow gel. The yellow color may be due to oxidation of acrylamide. The dried gel solids were crushed into small particle powder in a blender machine (Black & Decker). PPGs with the particle size between 100 and 120 mesh (150 μm–120 μm) were selected through the standard testing sieves (Fisher Scientific Company).

## 2.3. Measurement of swelling ratio and pore size of PPGs

0.30 g of PPGs (120–150 μm size) was swollen in 14.70 g of distilled water contained in a clean test tube. After the resulting suspension was left overnight to reach the equilibrium, the test tube was centrifuged at 5 000 rpm for 15 min to separate the particle gel and distilled water. Volume of the swollen PPG was calculated by measuring the height of the PPG in the tube and diameter of the tube. The same procedures were used for the swelling ratio measurement in 200 ppm surfactant solutions prepared in 1.00 wt.% NaCl solution. The swelling ratio is calculated by the total volume of the swollen particle gel measured in the test tube over the volume of 0.300 g of the dry particles and the results are listed in Table 1. Pore size of the synthesized hydrogel was measured by a TA Instrument DSC 2920 equipped with low temperature cooling accessory (–60 °C). Swollen hydrogel sample (10–20 mg) was sealed in an aluminum DSC pan with an added excess of bulk water (1–2 mg). During experiment, the temperature was first decreased to –40 °C, and then held for 15 min for freezing, after which the sample was heated to 15 °C at a rate of 1 °C min<sup>–1</sup> using an empty pan as reference. The DSC spectrum is shown in Fig. 1. The pore size is related to the temperature shift (Δ*T*) of the two peaks originated from bulk and confined water, respectively and it can be calculated based on the following equation, where Δ*T* is a negative value and quantified as the difference between the temperature at the confined water peak and the onset of the bulk water peak [25].

$$D_p = -\frac{39.604}{\Delta T(K) + 0.1207} + 2.24 \quad (1)$$

where, Δ*T* is temperature shift in *K*; *D<sub>p</sub>* is pore size of the swollen hydrogel particle in nm.

## 2.4. Measurement of the NaCl concentration change upon gel swelling

All the tested surfactant solutions were made in 1.0 wt % NaCl solution which is dependent on the salinity of the reservoir formation water and concentration change of the NaCl solution after complete swelling was measured by the anion metathesis of NaCl with AgNO<sub>3</sub>. By measuring the weight of precipitation of AgCl, the concentration NaCl can be calculated. The data and results are listed in Table 2.

## 2.5. Measurement of the concentration change of surfactants after gel swelling

Initial concentration for all surfactants was prepared at relatively low concentration of 200.00 ppm for higher accuracy from the UV–Vis spectroscopy measurement. Dry PPGs at 2.00 wt% were swollen in different surfactant solutions. This equilibrium solution over the top of the swollen gels contains NaCl, surfactant and un-

Table 2  
Analysis Results of NaCl Concentration after Particle Gel Swelling.

Parallel Tests	For 1.00 wt.% NaCl solution (g)	For Equilibrium NaCl solution after swelling (g)
Empty Test Tube	13.9754	13.9021
NaCl Solution	5.0100	5.0081
NaCl Contained	0.0501	To be measured
Total weight after drying	14.0986	14.0259
Mass of AgCl (MW: 143.5)	0.1232	0.1238
Mass of NaCl (MW: 58.5)	0.0502	0.0505
Test Results	Equili. NaCl concentration after gel swelling is 1.01 wt.%, which is almost the same as the initial NaCl concentration.	

**Table 3**  
Measurement of Concentration Change of Surfactant after Gel Swelling.

Surfactant Initial Concentration: 200 ppm		At Equilibrium of Swelling			
Surfactant	$\lambda_{\max}$ (nm)	Initial ABS	Net ABS	$C_{\text{eq}}$ (ppm)	Conc. Change
<i>n</i> -Dodecylpyridinium chloride	257	2.451	2.326	190	–5.0%
(1-Hexadecyl)pyridinium bromide	259	2.106	2.432	231	15.5%
Benzalkonium chloride	261	0.179	0.187	209	4.5%
Sodium 4- <i>n</i> -octyl benzene sulfonate	260	0.232	0.247	213	6.5%
Sodium salt, dodecylbenzene sulfonic acid	260	0.227	0.262	231	15.5%
Igepal® CO-530	276	0.806	1.137	282	41.0%
Tergitol® NP-10	275	0.429	0.608	283	41.5%

crosslinked polymer dissolved from the particle gel and the absorbance of this solution was used to calculate the equilibrium surfactant concentration after swelling. The background absorbance of the excess solution from the PPGs in 1.00 wt% NaCl solution is measured as the background absorbance, which will be deducted from the above measured total UV absorbance. For each surfactant solution, the UV–Vis spectrum was scanned from 1100 nm to 190 nm to identify the absorption peak position ( $\lambda_{\max}$ ). The equilibrium concentrations for each surfactant were calculated through its absorbance at  $\lambda_{\max}$  by use of a UV–Vis spectrophotometer (UVmini-1240V, Shimadzu). Concentration changes for the surfactants investigated are listed in Table 3.

### 2.6. Measurement of particle gel dynamic modulus

To investigate influence of surfactant on the particle gel strength, a rheometer, HAAKE RheoScope 1 (Thermo Scientific) was employed to measure storage modulus  $G'$  and loss modulus  $G''$  for the swollen gels. Measurement was set oscillation mode with frequency  $f = 1.000$  Hz, controlled stress (CS) and the stress applied to the gel was set  $\tau = 1.0$  Pa to ensure that the gel's strain and stress have a linear relationship during the measurement. The sensor used for measurement is PP35 Ti Po LO2 016 with a gap of 0.200 mm; Temperature: 25.0 °C. For each sample, measurements of  $G'$  and  $G''$  were taken every 30 s for 5 min. The results are shown in Table 4 and Fig. 2.

## 3. Results and discussion

### 3.1. Particle gel swelling ratio

The swelling ratios in different surfactant solutions at 200.00 ppm concentration as well as in 1% NaCl brine and distilled water are listed in Table 1. It can be clearly seen from Table 1 that the swelling ratios in surfactant solutions, distilled water and 1.0 wt.% NaCl are between 22 and 24. The difference in the swelling ratios is in the range of experimental error and thus the swelling ratio is independent on the swelling media. This implies the neutral charge balance of the synthesized polyacrylamide gels. Therefore, the pore size and distributions of the synthesized polyacrylamide gels do not change when the surfactants and NaCl were added. Also,

DSC was used to measure the pore size of the swollen PPGs as shown in Fig. 1. Based on the Eq. (1), it can be derived that the average pore size of the PPGs is around 4.1 nm, which is much less than the size of micelles formed from our tested surfactants [26].

### 3.2. Concentration change of NaCl after equilibrium of swelling

Accuracy of the experimental results was evaluated by analysis results of a standard NaCl aqueous solution. The expected NaCl for the analyzed solution is 0.0501 g. The mass of NaCl calculated through the precipitation of AgCl after anion metathesis is 0.0502 g, leading to a relative experimental error of 0.2%. When PPGs were swollen in the brine solution, the equilibrium concentration of NaCl was found to be at 1.01 wt % changing from 1.00 wt %. The difference of 0.01 wt.% is attributed to the experimental error. The analysis results are listed in Table 2, from which it can be concluded that the NaCl concentration in the excess brine is the same as the initial concentrations. After swelling equilibrium, particle gel doesn't change the concentration of NaCl in the excess solution since the sizes of sodium and chloride ions are much smaller than the pore sizes of the swollen PPGs.

### 3.3. Concentration change of surfactants after equilibrium swelling of PPGs

The initial concentration for all surfactants used in this experiment is 200.00 ppm. After PPGs were completely swollen, equilibrium concentration of surfactant in the excess solution was measured by the UV absorbance. The equilibrium concentrations for different surfactant solutions at PPG swelling equilibrium are listed in Table 3.

In Table 3, it was found that the concentration of the most of the surfactant solutions increased after the swelling equilibrium of PPGs. For cationic surfactant, (1-hexadecyl) pyridinium bromide, the concentration was changed to 231 ppm from 200 ppm corresponding to an increase of 15.5% from its initial concentration. However, for another cationic surfactant of *n*-dodecylpyridinium chloride and non-surfactant chemical of benzalkonium chloride, their concentrations were changed as –5% and 4.5%, respectively, which were considered in the experimental error of  $\pm 5\%$  originated from the UV absorbance measurement and thus the surfactant

**Table 4**  
Results of Storage Modulus  $G'$  and Loss Modulus  $G''$  for Gel Particles in Surfactant Solution (1000 ppm) and in 1.0 wt.% NaCl Brine.

Surfactant	Conc. in 1.0% NaCl	$G'$ (Pa)	Change	$G''$ (Pa)	Change
In 1.0 wt.% NaCl	brine	2582	0%	112	0%
Alfoterra® 23	$1.93 \times 10^{-3}$ M	689	–73%	45	–59%
Sodium salt, dodecylbenzene sulfonic acid	$2.87 \times 10^{-3}$ M	1042	–60%	64	–43%
<i>n</i> -Dodecylpyridinium chloride	$3.52 \times 10^{-3}$ M	1133	–56%	66	–41%
(1-Hexadecyl)pyridinium bromide	$2.45 \times 10^{-3}$ M	1739	–33%	87	–22%
Igepal® CO-530 (HLB = 10.8)	$2.16 \times 10^{-3}$ M	824	–68%	51	–54%
Neodol® 25–12 (HLB = 14.4)	$1.35 \times 10^{-3}$ M	946	–63%	56	–50%

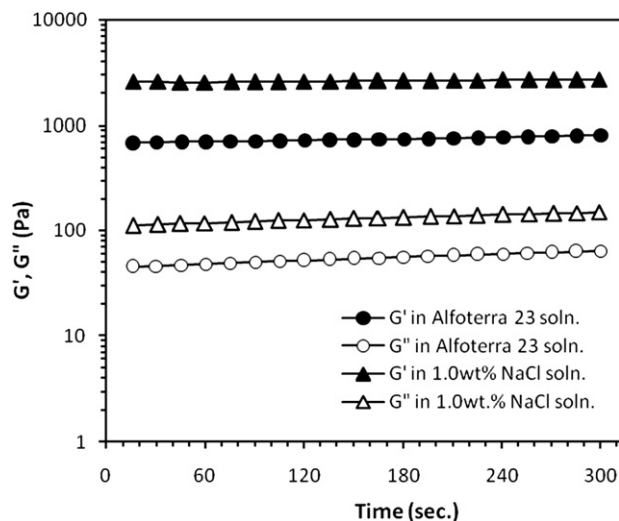


Fig. 2. Results of  $G'$  and  $G''$  for particle gel in surfactant Alfoterra 23 solution (1000 ppm) prepared with 1.0wt.% NaCl brine and in 1.0wt.% NaCl brine only (blank test).

molecules (not forming micelles, see Table 5) can migrate freely through the swollen PPG porous structure. For the two anionic surfactants tested, sodium 4-*n*-octyl benzene sulfonate and sodium dodecylbenzene sulfonic acid, the latter shows an obvious increase of its equilibrium concentration after gel swelling, but sodium 4-*n*-octyl benzene sulfonate shows little change in the final equilibrium concentration due to its higher CMC than 200 ppm (see Table 5). For the commercial nonionic surfactants of Igepal<sup>®</sup> CO-530 and Tergitol<sup>®</sup> NP-10, their equilibrium concentrations increased to 282 and 283 ppm, respectively, from the initial concentration of 200 ppm, corresponding to the change of 41% and 41.5%.

The reason that contributes to the dramatic increase of surfactant concentration after gel particle swelling is the formation of surfactant micelles in the solution, which has a much larger size than that of opening of the gel network. Average area per surfactant molecule adsorbed at the air/liquid interface is  $60 \text{ \AA}^2$  [26], therefore, one surfactant molecule has a dimension of 9 Å in diameter of hydrophilic head and about 20 Å in length of a hydrophobic tail. This size is much smaller than the average pore size of the hydrogel, 4.1 nm or 41 Å. On the other hand, approximate size for a rod-like surfactant micelle is about 54 Å in the rod diameter and 140 Å in the rod length [27], which is much larger than the average pore size of the hydrogel. When the dry PPGs contact with the aqueous surfactant solution, the particles absorb water first, other molecules and ions will diffuse into the network structure because of the concentration gradient and their much smaller size. However, surfactant micelles cannot go through the network due to their much larger size. Only unassociated single surfactant molecules can go through the opening and diffuse into the network of the swollen gel, which forms the dynamic equilibrium with the formed micelles

absorbed outside the swollen gel network. After the swelling reaches equilibrium, more water has been absorbed by the gel and less surfactant molecules can get into gel network. As a result, the concentration of surfactants remained in the excess solution increases. Therefore, it is expected that the lower the surfactant critical micelle concentration (CMC) is, the greater the increase of concentration in the excess solution will be after swelling since the initial concentration of surfactants was all set at 200 ppm. For a surfactant, if its CMC is high or its initial concentration is about or lower than CMC, the concentration will change little after the gel swelling reaches equilibrium such as *n*-dodecylpyridinium chloride and sodium 4-*n*-octyl benzene sulfonate from Table 5.

From Table 5, it can be found that the change of surfactant concentration is related to the ratio of the initial concentration ( $C_{\text{init}}$ ) to surfactant CMC. If the ratio is less than 1.0, that means the surfactant initial concentration is lower than its CMC, the concentration change is little and in the range of experimental error. If the ratio is greater than 1.0, the equilibrium concentration increased dramatically. For example, this ratio for nonionic surfactants, Igepal<sup>®</sup> CO-530 and Tergitol<sup>®</sup> NP-10, is greater than 10, their equilibrium concentration increased from their initial concentration by 41.0% and 41.5%, respectively. This suggests that most of their molecules exist in the solution in the form of micelles for these nonionic surfactants with very low CMC. The micelles cannot go through network of the swollen particle gel due to their bigger size than the average pore size of the PPGs, resulting in the dramatic increase of their equilibrium concentration since PPGs absorbs a large amount of water during the swelling.

### 3.4. Influence of surfactant on friction of the particle gel surface

To study influence of surfactant on the particle gel viscoelasticity, the dry PPGs at 2 wt.% were mixed with 1000 ppm surfactant solutions prepared with 1.0 wt.% NaCl brine in a centrifuge tube, and the PPGs and surfactant solution mixture was shaken well to ensure the particles get completely swollen. The reason to prepare surfactant solution at 1000 ppm that is much higher than that in previous study is to ensure all surfactants investigated in this study get aggregated in the solution. The gel viscoelasticity was measured by the HAAKE RheoScope as described before. During the process of measurement, both  $G'$  and  $G''$  show a slow and steady increase because of the evaporation of water contained in gel sample, data taken at the very beginning of measurement are used as  $G'$  and  $G''$  results. A blank test of the gel strength in 1.0 wt.% NaCl brine without surfactant was also conducted for comparison. Measurement results for the particle gel strength (both  $G'$  and  $G''$ ) in 1000 ppm and 1.0 wt % NaCl brine solution are listed in Table 4. A typical measurement of the gel strength as a function of scan time was illustrated in Fig. 2 for PPGs in 1.0 wt% NaCl and 1.0 wt % NaCl/1000 ppm Alfoterra<sup>®</sup> 23, respectively. It can be clearly seen from Table 4 and Fig. 2 that the introduction of Alfoterra<sup>®</sup> 23 into the swelling media significantly decreased the swollen gel strength. For

Table 5  
Surfactant CMC, ratio of  $C_{\text{init}}/\text{CMC}$  and Concentration Change after Gel Swelling.

Surfactant	M.W.	CMC* in 1.0% NaCl	$C_{\text{init}}(200 \text{ ppm})$	$C_{\text{init}}/\text{CMC}$	Conc. Change
<i>n</i> -Dodecylpyridinium chloride	284	$2.8 \times 10^{-3} \text{ M}$	$7.0 \times 10^{-4} \text{ M}$	0.3	−5.0%
(1-Hexadecyl)pyridinium bromide	402	$4.5 \times 10^{-4} \text{ M}$	$5.0 \times 10^{-4} \text{ M}$	1.1	15.5%
Benzalkonium chloride	~410	Not a surfactant	$4.9 \times 10^{-4} \text{ M}$	n/a	4.5%
Sodium 4- <i>n</i> -octyl benzene sulfonate	292	$1.3 \times 10^{-3} \text{ M}$	$6.8 \times 10^{-4} \text{ M}$	0.5	6.5%
Sodium salt, dodecylbenzene sulfonic acid	348	$4.6 \times 10^{-4} \text{ M}$	$5.7 \times 10^{-4} \text{ M}$	1.2	15.5%
Igepal <sup>®</sup> CO-530	464	$4.1 \times 10^{-5} \text{ M}$	$4.3 \times 10^{-4} \text{ M}$	10.5	41.0%
Tergitol <sup>®</sup> NP-10	660	$2.8 \times 10^{-5} \text{ M}$	$3.0 \times 10^{-4} \text{ M}$	10.7	41.5%

\* Rosen, M. J.: "Surfactants and Interfacial Phenomena", Wiley-Interscience, 3rd Ed., 2004, 185–188.

example, in the blank test,  $G'$  and  $G''$  for the particle gel are 2582 Pa and 112 Pa, respectively. However, when Alfoterra® 23 was used in the swelling solution,  $G'$  and  $G''$  dramatically decrease to 689 Pa and 45 Pa, corresponding to the significant reduction of 73% and 59%, respectively. From the data listed in Table 4, it can also be observed that all the tested surfactants have strong influence on viscoelasticity of the particle gel. Addition of surfactant to NaCl brine used for gel swelling can substantially reduce the gel dynamic modulus  $G'$  and  $G''$ . Another anionic surfactant of sodium dodecylbenzene sulfonic acid reduced the gel's storage modulus  $G'$  by 60%, along with the reduction of the loss modulus  $G''$  by 43%. For the cationic surfactants such as *n*-dodecylpyridinium chloride and (1-hexadecyl) pyridinium bromide, they can decrease the gel's storage modulus by 56% and 33%, respectively, and loss modulus by 41% and 22%, respectively. For nonionic surfactants such as Igepal® CO-530 and Neodol® 25-12, their presence in the swelling solution reduced the gel's storage modulus by 68% and 63%, respectively, along with the loss modulus decrease by 54% and 50%, respectively.

In order to further elucidate the reason of the dramatic decrease of the dynamic modulus ( $G'$  and  $G''$ ) of the particle gel by the introduced surfactant in the solution, one has to understand that the measurement of the dynamic modulus ( $G'$  and  $G''$ ) by a plate rheometer is accomplished by measuring the torque exerted on the tested and swollen PPGs. The swollen particle gel sample is placed on the horizontal glass plate and another metal sensor plate is placed on top of the gel samples. Typically the top sensor plate is rotated and the torque exerted on it is measured. However, the movement of this plate is resisted by the frictional force, which is proportional to the frictional coefficient and the stress applied on it. Equations (2), (3) and (4) below describe quantitatively the relationship for torque ( $T$ ), stress ( $N$ ) and frictional coefficient ( $\mu$ ).

$$T = r \times F \quad (2)$$

$$F = \mu \cdot N \quad (3)$$

$$T = r \times F = r \times (\mu \cdot N) \quad (4)$$

where,  $T$  is the torque exerted on the sample;  $r$  is typically the length of the lever arm and here it is related to geometry of the rheometer sensor. For a given sensor, it is the same for all gel samples measured;  $F$  is the frictional force, it is the product of frictional coefficient ( $\mu$ ) between two surfaces and the force applied on the surfaces ( $N$ ). In this experiment, a model of controlled stress is employed for the measurement. Therefore, the torque exerted on the sample is directly proportional to the frictional force between the particle gel and the surfaces of the plates. Furthermore, for a given gap of 0.200 mm between the plate and sensor, measurement results of the dynamic modulus ( $G'$  and  $G''$ ) are directly

**Table 6**  
Critical Packing Parameters (CPP) of the Surfactants Investigated.

Surfactant	$v$ (nm) <sup>3</sup>	$l$ (nm)	$a_0$ (nm) <sup>2</sup>	CPP	Micelle structure
Alfoterra® 23	0.538	2.690	0.600	0.333	Spherical
Sodium salt, dodecylbenzene sulfonic acid	0.486	2.245	0.600	0.361	Rod-like
<i>n</i> -Dodecylpyridinium chloride	0.324	1.505	0.584	0.369	Rod-like
(1-Hexadecyl)pyridinium bromide	0.532	2.155	0.584	0.423	Rod-like
Igepal® CO-530	0.405	1.420	0.829	0.344	Rod-like
Neodol® 25-12	0.378	1.801	0.595	0.353	Rod-like

proportional to the frictional force coefficient between the particle gel and the plate surfaces.

Surface friction of polymer bulk gels on solid surfaces has been intensively investigated through the use of commercial tribometer or rheometer. It has been reported by Gong and co-worker that the friction behaviors of the bulk hydrogels on glass or other solid surfaces do not conform to Amonton's law as shown in Eq. (3) which describes the friction of solid materials [16]. However, to our best knowledge, the friction investigation between the PPGs and surfactants has not been reported. Therefore, we proposed a simple mechanism, shown in Fig. 3, as a qualitative discussion of friction reduction by surfactant between the surfaces of particle gels, stainless steel sensor plate and glass plate. As shown in Fig. 3 (a) without addition of surfactant to NaCl brine for the particle gel swelling, the stainless steel sensor plate presses the particle gel and rotates on it at a constant stress mode when the dynamic modulus is measured. The original dried particle size ranges between 0.125 and 0.150 mm. Based on the volume swelling ratio of 23, the swollen particle size is between 0.355 and 0.427 mm in diameter. The gap between the sensor plate and bottom glass plate for  $G'$  and  $G''$  measurement is at 0.200 mm, which is only about half of the particle size. Therefore, the swollen gel particles experienced a remarkable deformation during the measurement along with the friction between the surfaces of particle gels, the sensor plate and the glass plate which is dominated by the sliding or translational motion, very similar to the case of bulk hydrogel on the solid surfaces. In Fig. 3(b), however, with the addition of surfactant, most of surfactant molecules aggregate to form the micelles, which have a much larger size than that of the opening of the gel network and are adsorbed onto the swollen particle gel surface as discussed in the previous section of this paper. These micelles may act as many small and flexible balls between the surfaces of particle gels, the sensor plate and the glass plate in the similar way of a lubricant. In this manner, the friction behaviors between these surfaces may be dominated by the rolling motion of the micelles. Hence, this will dramatically reduce the frictional coefficient between the surfaces of particle gel, the sensor plate and the glass plate. Consequently,

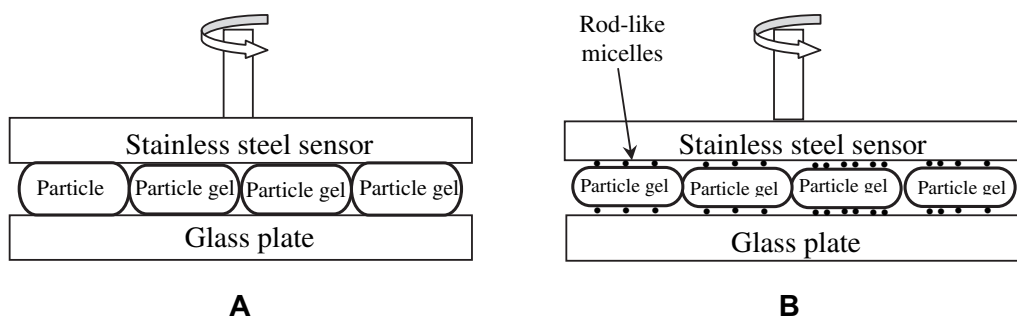


**Fig. 3.** Schematic illustration of the mechanism for friction reduction between the surfaces of particle gels, stainless steel sensor and glass plate. (A) Without addition of surfactant; (B) With addition of surfactant to NaCl brine for the particle gel swelling.

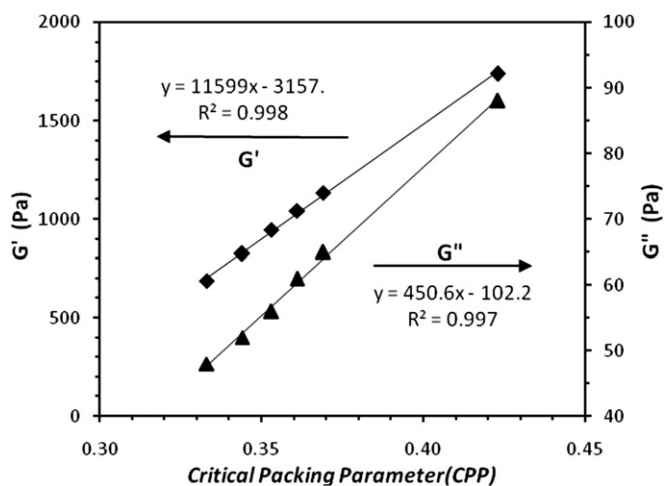


Fig. 4. Plots of  $G' \sim CPP$  and  $G'' \sim CPP$  for the surfactants investigated at 1000 ppm.

motion resistance of the sensor and the torque exerted on the instrument during the measurement will be dramatically decreased as well. As a result, the dynamic modulus of  $G'$  and  $G''$  are decreased comparing with those measured without surfactant added.

Based on this above mentioned mechanism, the ability of surfactants to reduce hydrogels dynamic modulus may be related to geometry of the surfactant micelles such as shape and size. For each surfactant, it has a critical packing parameter in different medium. Israelachvili and co-workers [28] have defined this packing parameter,  $CPP$ , which is related to the shape of a surfactant molecule.

$$CPP = \frac{v}{l \cdot a_0} \quad (5)$$

where,  $v$  is the volume of surfactant hydrocarbon core in  $(\text{nm})^3$ ;  $l$  is the length of surfactant hydrocarbon chain in  $\text{nm}$ ;  $a_0$  is effective area of surfactant hydrophilic group in  $(\text{nm})^2$ .  $v$ ,  $l$  and  $a_0$  can be calculated using the following equations [29]:

$$v = 0.027(n_c + n_{\text{methyl}}) \quad (6)$$

$$l = 0.15 + 0.127n_c \quad (7)$$

$$a_0 = 0.016m + 0.333 \quad (8)$$

where,  $n_c$  is the number of carbon atoms of hydrocarbon chain without methyl groups;  $n_{\text{methyl}}$  is the number of methyl groups in the hydrocarbon chain;  $m$  is the number of ethylene oxide groups.

The critical packing parameters for the surfactants investigated in this study have been calculated using Eqs. (5)–(8). The results are listed in Table 6. From the table, it can be found that the packing parameters for all the surfactants investigated are between 0.333 and 0.423. It was known that geometry of surfactant micelle depends upon the value of  $CPP$ . If  $CPP$  is less than  $1/3$ , the surfactant will form spherical micelles in solution; if  $CPP$  is between  $1/3$  and  $1/2$ , it will form rod-like micelles; if  $CPP$  is close to 1, it will form the lamellar structure; if  $CPP$  is greater than 1, it will form bi-continuous phase; if  $CPP$  is much greater than 1, it will form the reversed micelles or reversed rod-like micelles in solution. It is expected that surfactants with a  $CPP$  less than 0.333 will be the most efficient agent to reduce the particle hydrogels dynamic modulus because they form spherical micelles in solution. For surfactants with the  $CPP$  between 0.333 and 0.500, the smaller the  $CPP$  is, the more

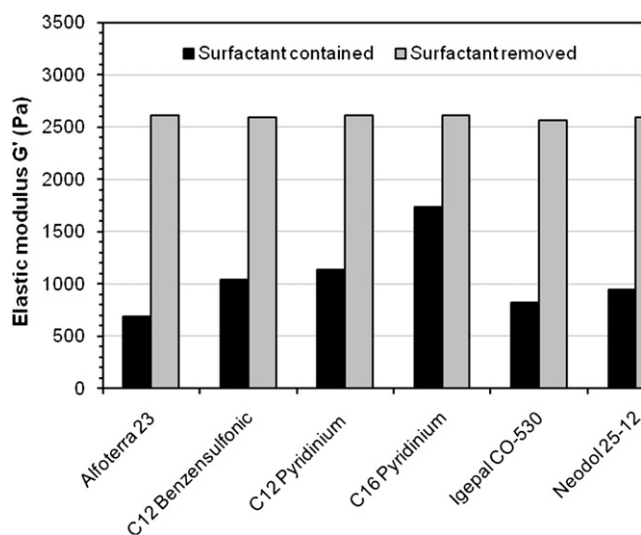


Fig. 5. Storage modulus  $G'$  of particle gels with and without surfactant. After surfactant molecules have been washed off, the modulus  $G'$  increases to the value of the particle gel swollen in 1.0 wt.% NaCl.

effective on reduction it will be. The gel strength in terms of  $G'$  and  $G''$  in different surfactant solutions are plotted against  $CPP$  and shown in Fig. 4. In the figure, it can be found that the particle gel strength decreases with decrease of the surfactant  $CPP$  and there is a linear relationship for  $G' \sim CPP$  and  $G'' \sim CPP$ . The linear correlation coefficients for the two plots are 0.9989 and 0.9974, respectively. This indicates that surfactant micelles absorbed on the particle gel surface play a key role to reduce friction of the gel on the surface and the measured dynamic modulus  $G'$  and  $G''$ . The surfactant forming spherical micelles like Alforterra® 23 is the most effective agent to reduce the gel friction. The other surfactants with  $CPP$  between 0.333 and 0.500 should have rod-like micelles in the solution and listed in Table 6. For rod-like micelles, it is expected that both rod diameter and rod length should have effect on the hydrogel  $G'$  and  $G''$ , and the micelles with greater rod diameter and less rod length should be more effective on reducing the  $G'$  and  $G''$ . But this assumption of relation between micelle size and performance needs more work to get confirmed.

In order to confirm our proposed mechanism discussed above, some parallel tests were also conducted for all the surfactants listed in Table 6. In the parallel test, the dry gel particle samples were mixed with surfactant solutions following the exact procedures described previously. After the particles were completely swollen, the swollen PPGs were washed by 1.0 wt% NaCl brine solution to remove all the surfactants with the aid of centrifuge. For the samples prepared in 1.0 wt% NaCl solution, it was also conducted at the similar procedure in order to maintain all the particle gel samples treated under the same conditions of shearing and agitation which is believed to have significant impact on the rheological properties of the gels. The gel strength after removing the surfactants is shown in Fig. 5. Surprisingly, it has been found that the values of  $G'$  for all the particle gels after removing surfactants increase significantly back to the values of the particle gel mixed with 1.0 wt. NaCl solution, which indicates that the friction behaviors between the surfaces of the particle gel, the sensor plate and the glass plate has been switched from rolling motion back to the sliding or translational motion because the surfactant micelles have been removed from the gel particle surface, leading to the recovery of  $G'$  and  $G''$ .

To provide further support of the proposed possible mechanism responsible for the dynamic modulus reduction of the particle

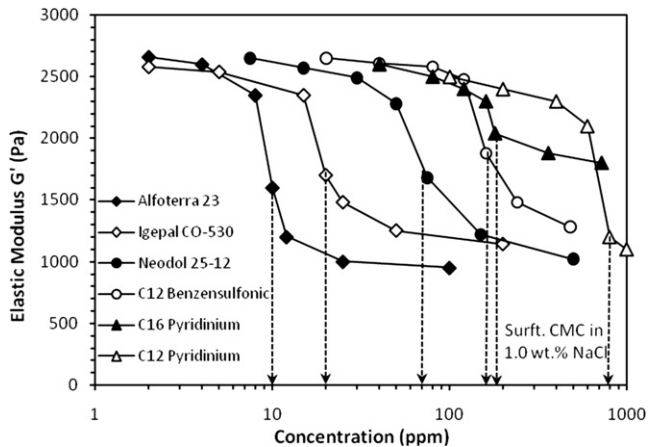


Fig. 6. Storage modulus  $G'$  of particle gels measured with various surfactants at different concentrations shows a substantial decrease at the concentration of their critical micelle concentration (CMC).

hydrogel by surfactant, the elastic modulus  $G'$  of the synthesized particle hydrogel swollen in the surfactant solution prepared with 1.0 wt.% NaCl at the concentrations below and above their critical micelle concentration (CMC) has been systematically measured. The results are shown in Fig. 6. In the figure, one can see that for the six surfactants used in this study, the  $G'$  shows a substantial decrease at their CMC for each surfactant. Alfoterra<sup>®</sup> 23 with a CMC of 10 ppm,  $G'$  decreases from 2660 Pa to 1600 Pa around the CMC; Igepal<sup>®</sup> CO-530 with a CMC of 20 ppm,  $G'$  decreases from 2580 Pa to 1700 Pa around the CMC; Neodol<sup>®</sup> 25-12 with a CMC of 70 ppm,  $G'$  decreases from 2650 Pa to 1680 Pa around the CMC; Sodium salt of dodecylbenzene sulfonic acid (C12 Benzenesulfonic) with a CMC of 160 ppm,  $G'$  decreases from 2650 Pa to 1880 Pa around the CMC; (1-Hexadecyl)pyridinium bromide (C16 Pyridinium) with a CMC of 181 ppm,  $G'$  decreases from 2600 Pa to 2040 Pa around the CMC; *n*-Dodecylpyridinium chloride (C12 Pyridinium) with a CMC of 795 ppm,  $G'$  decreases from 2500 Pa to 1200 Pa around the CMC. The very slow decrease of  $G'$  for all surfactants at the concentrations below CMC may be due to the experimental errors. However, the noticeable decrease of  $G'$  at the concentrations above CMC is due to the increase of micelle concentration for the all surfactants investigated. Because as a surfactant solution is continuously increased to a concentration above its CMC, the monomer concentration in the solution will no longer increase while the micelle concentration in the solution will continue increasing with increase of the surfactant concentration. This results in a continuous decrease in the dynamic modulus ( $G'$ ) of the hydrogel. Furthermore, it can also be found that among these surfactants investigated, Alfoterra<sup>®</sup> 23 has the lowest CMC. At 10 ppm, it can effectively reduce elastic modulus because it is the only one that can form spherical aggregates in the solution and most effective on reducing gel surface friction.

#### 4. Potential applications

Gel treatment has been proved to be an effective method to reduce water production in oil industry. A new trend in gel treatments is application of preformed particle gels (PPG) that are formed at surface facilities before injection. In order to improve the gel treatment efficacy, gel particles are placed in the surfactant brine solution. When the particle gel and surfactant solution are injected into the underground reservoir, the filtrated solution can be squeezed into the matrix during the injection. As a result, the gel

particles enter and stay in the fracture and large size porous media while the surfactant solutions enter into the small pores in the formation where most hydrocarbon oil is trapped by the capillary force. In this way, the surfactant solution will reduce interfacial tension at oil/brine interface and change wettability of rock surface in the formation. Based on our results of interaction between the particle gel and surfactant, it has been found that surfactants have strong influence on particle gel friction. Therefore, injectivity of the particle gels can be greatly improved by the proper screening of surfactant. In other words, the gel resistance can be modified by the selected surfactants for the best applications.

It is also worth mentioning that the results of this investigation of the interaction between the surfactant and particle gels demonstrate a new idea of forced imbibitions through combination of particle gel injection and surfactant imbibition. Development of forced imbibition technology will enable oil producers to increase oil recovery while reduce water production. This study benefits the oil industry with development of a new technology combining gel treatment and surfactant flooding to improve oil/gas recovery while reduce water production.

#### 5. Conclusions

- Equilibrium concentration of NaCl in excess brine remains the same after the swelling of particle gel. It is also expected that concentration of water-soluble salts, e.g. KCl, MgCl<sub>2</sub>, CaCl<sub>2</sub>, Na<sub>2</sub>CO<sub>3</sub>, Na<sub>2</sub>SO<sub>4</sub>, will not change as well after the swelling of particle gels. This means that gel swelling will not increase the salinity of the underground formation water.
- Equilibrium surfactant concentration in excess brine increases after swelling of gel particles, which is due to formation of surfactant micelles in the brine. Comparing with the open pore size (4.1 nm) of the synthesized gels, the larger size of the formed micelles could not diffuse into the network of particle gel. Surfactants with larger size of molecules and lower critical micelle concentration (CMC) show greater increase in equilibrium. It is expected that nonionic surfactants will show greater increase.
- Gel friction in terms of dynamic modulus  $G'$  and  $G''$  can be reduced dramatically which might be due to the fact that the surfactant micelles adsorbed on the surface of particle gel change the friction between the surfaces of particle gel and solid from sliding/translational motion to the rolling motion. The latter has a much smaller friction coefficient. However, the gel resistance can be recovered after the surfactants have been removed indicating the physical absorption of the formed micelles over the surfaces of the swollen PPGs.
- Injectivity of particle gels can be significantly improved by use of proper surfactants. Moreover, a new technology of forced surfactant imbibition can be developed by combination of the PPGs and surfactant. The new technology will greatly benefit to oil industry by the way to improve oil recovery while reduce water production.

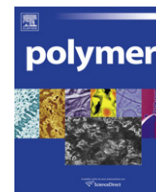
#### Acknowledgements

The authors are grateful for financial support from Research Partnership to Secure Energy for America (RPSEA) and PetroChina Research Institute of Petroleum Exploration & Development (RIPED). Funding for this project provided by RPSEA is through the "Ultra-Deepwater and Unconventional Natural Gas and Other Petroleum Resources" program authorized by the U.S. Energy Policy Act of 2005. RPSEA ([www.rpsea.org](http://www.rpsea.org)) is a nonprofit corporation whose mission is to provide a stewardship role in ensuring the focused research, development and deployment of safe and

environmentally responsible technology that can effectively deliver hydrocarbons from domestic resources to the citizens of the United States. RPSEA, operating as a consortium of premier U.S. energy research universities, industry, and independent research organizations, manages the program under a contract with the U.S. Department of Energy's National Energy Technology Laboratory.

## References

- [1] Kokufuta E, Suzuki H, Yoshida R, Yamada K, Hirata M, Kaneko F. *Langmuir* 1998;14(4):788.
- [2] Starodoubtsev SG, Churochkina NA, Khokhlov AR. *Langmuir* 2000;16(4):1529.
- [3] Shinde VS, Badiger MV, Lele AK, Mashelkar RA. *Langmuir* 2001;17(9):2585.
- [4] Lynch I, Sjoström J, Piculell L. *J Phys Chem B* 2005;109(9):4258.
- [5] Caykara T, Demiray M, Gueven O. *Colloid Polym Sci* 2005;284(3):258.
- [6] Chen L, Yu X, Li Q. *J App Polym Sci* 2006;102(4):3791.
- [7] Mohan YM, Joseph DK, Geckeler KE. *J App Polym Sci* 2007;103(5):3423.
- [8] Mangiapia G, Ricciardi R, Auriemma F, De Rosa C, Lo Celso F, Triolo R, et al. *J Phys Chem B* 2007;111(9):2166.
- [9] Yamazaki Y, Matsunaga T, Ichinokawa A, Fujishiro Y, Saito E, Sato T. *J App Polym Sci* 2009;114(5):2764.
- [10] Philippova OE, Hourdet D, Audebert R, Khokhlov AR. *Macromolecules* 1996;29(8):2822.
- [11] Ashbaugh HS, Piculell L, Lindman B. *Langmuir* 2000;16(6):2529.
- [12] Nichifor M, Zhu XX, Cristea D, Carpov A. *J Phys Chem B* 2001;105(12):2314.
- [13] Barreiro-Iglesias R, Alvarez-Lorenzo C, Concheiro A. *J Controlled Release* 2001;77:59.
- [14] Osada Y, Gong J-P. *Adv Mater* 1998;10:827.
- [15] Gong J-P, Osada Y. *Prog Polym Sci* 2002;27:3.
- [16] Du M, Gong JP. In: Biresaw G, Mittal KL, editors. *Surface friction and lubrication of polymer gels*. Boca Raton, Florida: CRC Press; May 2008. p. 223–46. ch. 11.
- [17] Tominaga T, Takedomi N, Biederman H, Furukawa H, Osada Y, Gong J-P. *Soft Matter* 2008;4:1033.
- [18] Oogaki S, Kagata G, Kurokawa T, Kuroda S, Osada Y, Gong J-P. *Soft Matter* 2009;5:1879.
- [19] Tominaga T, Takayuki T, Furukawa H, Osada Y, Gong J-P. *Soft Matter* 2008;4:1645.
- [20] Du M, Maki Y, Tominaga T, Furukawa H, Gong J-P, Osada Y, et al. *Macromolecules* 2007;40:4313.
- [21] Narita T, Gong JP, Osada Y. *J Phys Chem B* 1998;102:4566.
- [22] Kagata G, Gong JP, Osada Y. *J Phys Chem B* 2003;107:10221.
- [23] Kagata G, Gong JP, Osada Y. *J Phys Chem B* 2002;106:4596.
- [24] Chen YM, Matsumoto S, Gong JP, Osada Y. *Macromolecules* 2003;36:8830.
- [25] Wang J, Gonzalez AD, Ugaz VM. *Adv Mater* 2008;20:4482.
- [26] Rosen MJ. *Surfactants and interfacial phenomena*. 3rd ed. Wiley-Interscience; 2004.
- [27] Robson RJ, Dennis EA. *J Phys Chem* 1997;81(11):1075.
- [28] Israelachvili J, Mitchell DJ, Ninham BW. *J Chem Soc. Faraday Trans* 1976;72:1525.
- [29] Chevalier Y, Zemb T. *Rep Prog Phys* 1990;53:279.



# Intermolecular interactions and crystallization behaviors of biodegradable polymer blends between poly(3-hydroxybutyrate) and cellulose acetate butyrate studied by DSC, FT-IR, and WAXD

Nattaporn Suttiwijitpukdee<sup>a</sup>, Harumi Sato<sup>a,\*</sup>, Jianming Zhang<sup>b</sup>, Takeji Hashimoto<sup>a,c</sup>, Yukihiro Ozaki<sup>a,\*</sup>

<sup>a</sup> Department of Chemistry, School of Science and Technology and Research Center for Environment Friendly Polymers, Kwansei-Gakuin University, Sanda 669-1337, Japan

<sup>b</sup> Key Laboratory of Rubber-plastics, Ministry of Education, Qingdao University of Science and Technology, Qingdao City 266042, People's Republic of China

<sup>c</sup> Professor Emeritus, Kyoto University, Kyoto 606-8501, Japan

## ARTICLE INFO

### Article history:

Received 18 May 2010

Received in revised form

10 November 2010

Accepted 12 November 2010

Available online 19 November 2010

### Keywords:

Cellulose acetate butyrate (CAB)

Poly(3-hydroxybutyrate)(PHB)

Biodegradable polymers

## ABSTRACT

Relationships between composition- and temperature-dependent intermolecular interactions and cold crystallization behaviors of poly(3-hydroxybutyrate) (PHB)/ cellulose acetate butyrate (CAB) blends have been investigated mainly by infrared (IR) spectroscopy, together with differential scanning calorimetry, and wide-angle X-ray diffraction (WAXD). Weak intermolecular hydrogen bondings between OH groups in CAB and C=O groups in amorphous part of PHB define as *inter* were detected in OH stretching bands of the blends. These interactions occur in the blends with high CAB content ( $w_{\text{CAB}}$ ) and highly depend on temperature. For all the blends having  $0.2 \leq w_{\text{CAB}} \leq 0.7$ , when temperature is raised (e.g., above 90 °C for the blend with  $w_{\text{CAB}} = 0.5$ ) the cold crystallization of PHB was discerned, as evidenced by an increase of the absorbance of the band due to C=O stretching in the crystal field. The crystallization was found to involve the dissociation of *inter* and transformation of *inter* into intramolecular hydrogen bondings within PHB and within CAB as summarized in Table 2 in this text, which promotes the crystallization and enhances stabilization of the crystals. Consequently, the crystallization of the PHB is influenced by exchanges of the hydrogen bondings as described above with raising temperatures. X-ray diffraction from PHB crystals in the blends show a remarkable decrease of crystallinity with  $w_{\text{CAB}}$  and eventually disappear when  $w_{\text{CAB}} \geq 0.8$ .

© 2010 Elsevier Ltd. All rights reserved.

## 1. Introduction

Recently, the vast wastes of plastic products have become a serious environmental problem, because the majority of them are made from synthetic polymers that cannot be degraded in environments. Biodegradable polymers are one of the most promising alternative substances for solving this serious problem, because of their superior biodegradable properties compared to those of synthetic polymers [1–3]. Besides being degradable, they can be produced also as renewable sources that are environment friendly. As a biosynthesized aliphatic polyester and biodegradable thermoplastic, poly(3-hydroxybutyrate) (PHB) (Fig. 1(a)) has been attracting a considerable practical attention for the biodegradability, biocompatibility, and possibility of the synthesis from glycerol [4]. For these advantages, their crystal structure and thermal or crystallization behaviors have been extensively studied by using various techniques from the academic viewpoint as well as from the viewpoint of practical applications.

However, as a biologically produced stereo-regular macromolecule, PHB is highly crystalline and, hence, rigid and brittle [5], which also acts as a kind of defect for some practical applications. It has a high melting temperature relative to its thermally stable temperature range, which also acts as a defect for its melt processability. From the industrial viewpoint, these defects are really serious for the wide-scale practical applications. Thus, PHB copolymers were synthesized such as Poly(hydroxybutyrate-*ran*-hydroxyvalerate) (PHB-*co*-PHV) [6–8] and graft copolymer of atactic PHB/Poly(methyl methacrylate) (PHB-*g*-PMMA) [9]. In addition, several polymers such as poly(ethylene glycol) (PEG) [10], poly(ethylene oxide) (PEO) [11], poly(vinyl acetate) (PVAc) [12,13], poly(4-vinylphenol) (PVPh) [14,15], poly(vinyl alcohol) (PVA) [16], polylactide (PLLA) [17], and cellulose esters (CE) [2,18–22] have been selected to be blended for lowering the melting temperature and enhancing the processability.

In view of actual applications, blending between PHB and CE, especially for amorphous cellulose acetate butyrate (CAB) hold very promising features such as the elongation at break and toughness [2]. Miscibility analysis of PHB/CAB blends was investigated by Scandola et al. using dynamic-mechanical thermal analysis (DMTA)

\* Corresponding authors.

E-mail address: [ozaki@kwansei.ac.jp](mailto:ozaki@kwansei.ac.jp) (Y. Ozaki).



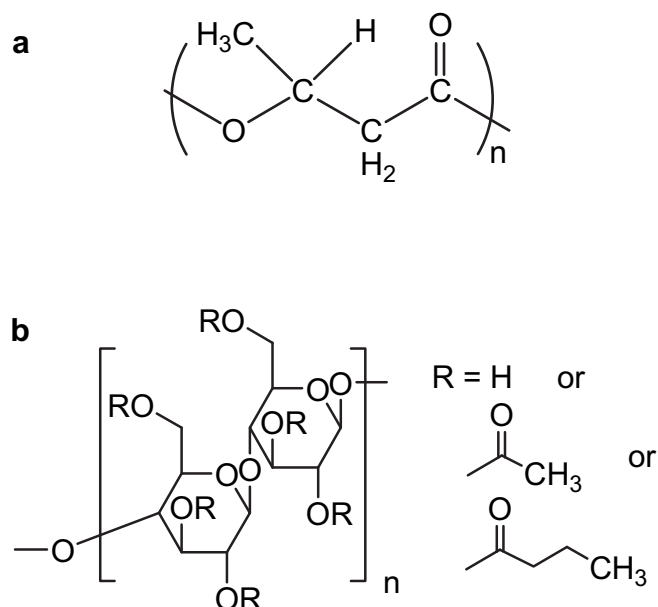


Fig. 1. Chemical structures of (a) poly(3-hydroxybutyrate) (PHB) and (b) cellulose acetate butyrate (CAB).

measurements [18]. They reported that the blends of PHB/CAB are miscible in the amorphous state. The result was in agreement with that by Ceccorulli et al. who further investigated effects of low molecular weight plasticizer on the miscibility of PHB/CAB blends [19]. Pizzole et al. [20], who explored miscibility between PHB and two kinds of CAB in the melt, reported that no interspherulitic segregation was observed, when the blends were crystallized under the given crystallization conditions. Recently, El-Shafee et al. [21] confirmed the miscible blend in melts, showing the effect of the equilibrium melting point depression of PHB crystals upon the addition of CAB. Moreover, it was found that, after crystallization of the PHB component in the blends, CAB exists in the interlamellar amorphous regions and becomes a major component there, as detected by small-angle X-ray scattering (SAXS) [21]. In the drawing process of blend, Park et al. indicated that the orientation behavior of PHB crystals in the blends changes from *c*-axis orientation to *a*-axis orientation with an increase in the CAB content [22]. However, in all of the previous studies described above, intermolecular interactions and their effects on crystallization in PHB/CAB blends have not been fully explored yet.

The purpose of the present study is to investigate the intermolecular interactions and their effects on crystallization behaviors of PHB/CAB blends, primarily with infrared (IR) spectroscopy, together with differential scanning calorimetry (DSC) and wide-angle X-ray diffraction (WAXD) as supporting experimental methods, as a function of the blend composition and temperature. The IR results obtained suggest the existence of weak intermolecular interactions between the C=O groups of PHB and the O–H groups of CAB (designated hereafter as *inter*). Moreover, the estimated crystallinity from WAXD patterns of the blends suggests that the crystallinity of PHB in the blends is influenced by the intermolecular interactions.

## 2. Experimental section

### 2.1. Materials and sample preparation

The bacterial PHB (number-average molecular weight,  $M_n$ , is  $2.9 \times 10^5$ ) and CAB (number-average molecular weight,  $M_n$ , is  $6.5 \times 10^4$ ) were purchased from Aldrich Chemical Co., Ltd., and

Table 1  
Thermal properties of the PHB/CAB blend in the second heating process.

PHB/CAB (%wt./wt.)	$T_g$ (°C)	$T_{cc}$ (°C)	$T_m$ (°C)	$\Delta H_m$ (J g <sup>-1</sup> )	$X_c$
100/0	-1.72	–	166.65	93.56	0.64
80/20	-4.86	43.01	166.47	70.71	0.48
60/40	-7.21	43.21	161.95	52.19	0.36
50/50	-7.05	46.25	160.34	40.81	0.28
40/60	-8.13	49.29	156.19	28.67	0.20
30/70	-7.71	50.99	154.83	8.42	0.06
20/80	-2.02	n.d.	n.d.	–	–
10/90	117.94	n.d.	n.d.	–	–
5/95	127.52	n.d.	n.d.	–	–
0/100	145.08	n.d.	n.d.	–	–

n.d.: Not detected.

were used as received. Chemical structures of both samples are given in Fig. 1. As shown in Fig. 1(b), the CAB polymer consists of hydroxyl groups, acetyl groups, and butyryl groups. The weight fraction of each group with respect to the total weight of CAB is 0.0089, 0.293, and 0.18, respectively. Thus, the number of each group per single CAB chain is  $6.5 \times 10^4 \times 0.89 \times 10^{-2} / 17.0 = 34.0$  for hydroxyl groups,  $6.5 \times 10^4 \times 0.293 / 43.04 = 442$  for acetyl groups, and  $6.5 \times 10^4 \times 0.18 / 71.1 = 165$  for butyryl groups.

Samples of PHB/CAB blends were prepared by mixing the prescribed amount of powders and then dissolving them in chloroform. The as-prepared solutions were cast into films of about 5 mg in weight in an aluminum pan for DSC measurements. For WAXD analysis, the solutions were cast on copper plates to form thin films with the thickness of around 200 μm. For IR spectral measurements, thin film specimens of the thickness of around 10 μm were prepared by casting the solutions on CaF<sub>2</sub> substrates. All the prepared films were allowed to evaporate solvent at room temperature for forming thin films. Then, the films were put in a vacuum oven at 60 °C for 16 h to completely remove the residual solvent and then naturally cooled down to room temperature for the measurements. The films thus prepared are designated hereafter as “as-prepared films” and used for DSC, WAXD, and IR measurements.

### 2.2. DSC

Thermal analyses of the blends were performed with a Perkin–Elmer Pyris 6 by sealing the as-prepared films in an aluminum pan, and a pure indium was used as a standard material for temperature calibration of the calorimeter. For a standard thermal characterization of the blends with DSC, the blends were firstly melted at 190 °C for 1 min to erase the previous thermal history. Then, the DSC thermograms were obtained in the first cooling run from 190 °C to –40 °C at a rate of 20 °C/min and in the second heating run from –40 °C to 190 °C at a rate of 20 °C/min. The thermal properties of blends such as the glass transition temperature ( $T_g$ ), cold crystallization temperature ( $T_{cc}$ ), melting temperature ( $T_m$ ), and enthalpy of fusion ( $\Delta H_m$ ) were determined from the thermograms of the second heating run (see Table 1). Moreover, the net crystallinity ( $X_c$ ) of each blend as a whole, including amorphous CAB, was also determined using the following equation (see also Table 1):

$$X_c = \frac{\Delta H_m}{\Delta H_{PHB}^0} \quad (1)$$

where  $\Delta H_{PHB}^0$  is the enthalpy of melting of pure PHB crystals, i.e., neat PHB having 100% crystallinity, (146 J/g) [23,24];  $\Delta H_m$  is the measured enthalpy of fusion in each blend.

We tried directly to compare the cold crystallization behavior of the blends as observed by IR spectroscopy with that as observed by

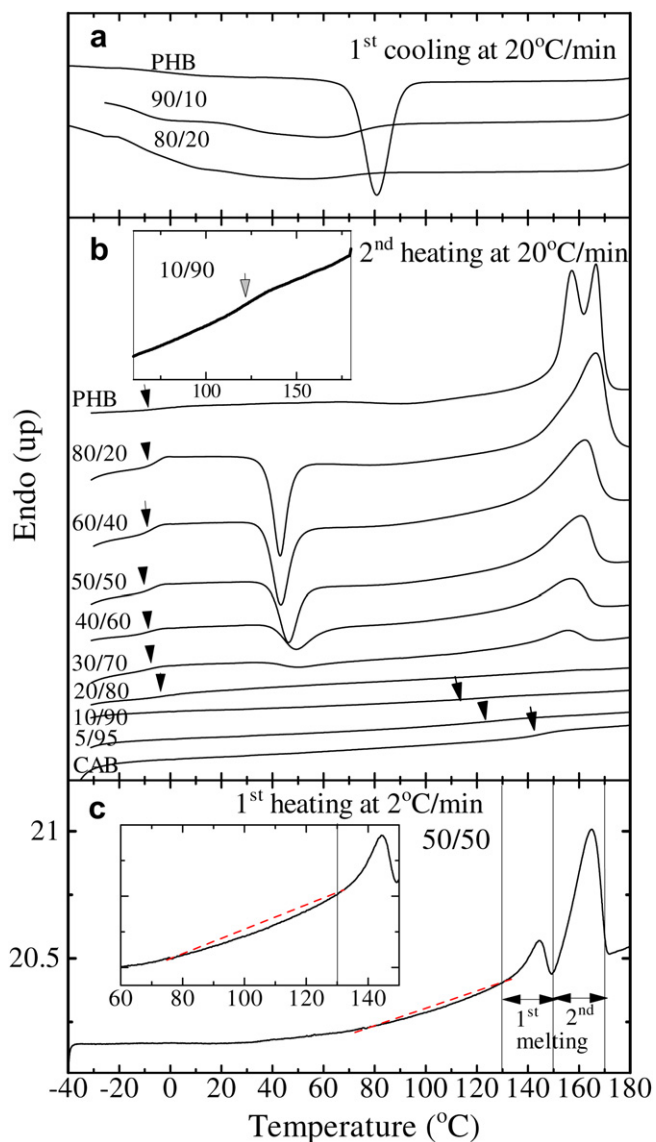


**Fig. 2.** DSC thermograms of the as-prepared PHB/CAB blends with various compositions in the first cooling runs (a) and the second heating runs (b), both at a rate of 20 °C/min, and the first heating run of the as-prepared sample at a rate of 2 °C/min (c).

DSC. For this purpose, the DSC analyses also were deliberately conducted in the first heating run of the as-prepared samples at a slow heating rate of 2 °C/min, which is close enough to the average heating rate used for the IR spectroscopy on the as-prepared sample, as will be detailed in the next section.

### 2.3. Measurements of Fourier-transform infrared (FT-IR) spectroscopy

FT-IR spectra of the blends in the region of 4000–800  $\text{cm}^{-1}$  were collected with a Thermo Nicolet Magna 870 spectrometer equipped with a mercury cadmium telluride (MCT) detector. The normal transmission mode was applied to the spectral measurements. To obtain an acceptable S/N, the spectra were accumulated over 256 scans with a 2  $\text{cm}^{-1}$  resolution. The as-prepared specimens were stepwisely heated from 30 to 80 °C with an increment of 10 °C, and from 80 to 190 °C with an increment of 5 °C at heating rate of 10 °C/min in between the two closest temperatures by using an Instec thermoelectric control unit (HCS302, INSTEC Inc., USA)

with an accuracy of  $\pm 0.1$  °C. During the stepwise heating process, the cell was maintained at each temperature for 3 min after reaching the preset temperature to equilibrate the specimen at that temperature before the FT-IR measurement and the measurement was conducted for 3 min at that temperature. After the measurement the specimen was heated to the next higher temperature, and this process was repeated. An average overall heating rate is approximately 0.9 °C/min.

### 2.4. WAXD measurements

WAXD patterns of the as-prepared blend films were measured with a Rigaku RINT2100 X-ray diffractometer equipped with a scintillation detector (Rigaku PT30). The diffraction patterns were recorded at room temperature from  $2\theta = 11.5$  to 35° at a scanning rate of 0.2°/min. The X-ray beam of Cu-K $\alpha$  radiation was generated at 40 kV and 50 mA and passed through a Ni filter (wavelength: 0.154 nm).

## 3. Results and discussion

### 3.1. DSC studies

DSC thermograms of the blends with various compositions measured in the first cooling run and the second heating run are shown in part (a) and (b) in Fig. 2, respectively. Hereafter the blend composition will be denoted by weight fraction of CAB,  $w_{\text{CAB}}$ , too. The pure PHB sample was rapidly crystallized in the first cooling process, while the crystallization in the blends was suppressed as typically shown for PHB/CAB = 90/10 and 80/20 ( $w_{\text{CAB}} = 0.1$  and 0.2) (see Fig. 2 (a)). The cold crystallization temperature ( $T_{\text{cc}}$ ) of the blends, which is clearly observed as an endothermic peak, in the second heating process was slightly shifted to a higher temperature with increasing  $w_{\text{CAB}}$ , as obviously seen for the blends with  $0.2 \leq w_{\text{CAB}} \leq 0.7$  in Fig. 2 (b). On the contrary, the endotherm for the cold crystallization was not clearly discernible for pure PHB. This may be because the first cooling process involves enough crystallization, which in turn suppresses the cold crystallization in the second heating run. On the other hand, the blends did not undergo enough crystallization in the first cooling process so that they underwent the remarkable cold crystallization in the second heating process.

The DSC thermogram of pure PHB in the second heating run shows double melting-endothermic peaks. The melting temperature ( $T_{\text{m}}$ ) of the blends shifts to a lower temperature with  $w_{\text{CAB}}$  (Table 1). The melting endotherm cannot be observed for the blends with  $w_{\text{CAB}} \geq 0.8$ , so that the blends are amorphous, which will be due to formation of physically crosslinked network in the blends via *inter* between PHB and CAB as well as intramolecular hydrogen bondings within CAB, as will be discussed later in Section 3.5. The enthalpy of melting also decreases with  $w_{\text{CAB}}$  (see Table 1).

On the basis of the report by Gunartne et al. [25], the double melting thermogram can be explained by the effect of thermal history, i.e., the crystallization condition of PHB. In the neat PHB, the first endothermic peak is due to the melting of the crystals crystallized in the first cooling process, while the second peak is due to the recrystallization and melting of the crystals. The melting temperature of the blend decreases with  $w_{\text{CAB}}$ , partly (i) because of an increased entropy of melting upon mixing PHB and CAB and partly (ii) because of a greater suppression of mobility of PHB component for the cold crystallization with increasing  $w_{\text{CAB}}$ , that creates less perfect crystallites with enhanced distortions of the intramolecular hydrogen bondings within PHB crystals, as will be detailed later. We think the latter effect (ii) dominates the former effect (i) on the melting point depression with  $w_{\text{CAB}}$ , because the entropy of melting of the blends associated with mixing PHB and

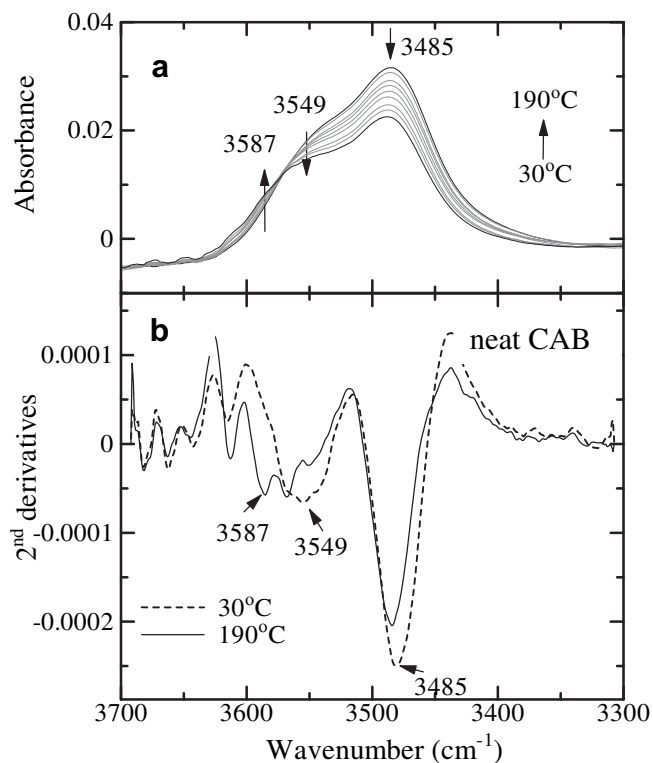


**Fig. 3.** IR spectra (a) and their second derivatives (b) in the O–H stretching region of pure CAB measured in the heating process from 30 to 190 °C. Since the intensity of the band at 3587  $\text{cm}^{-1}$  increases monotonously and that of the bands at 3549 and 3485  $\text{cm}^{-1}$  decrease monotonously with increasing the temperature from 30 to 190 °C, these trends are indicated by the upward and downward arrows, respectively.

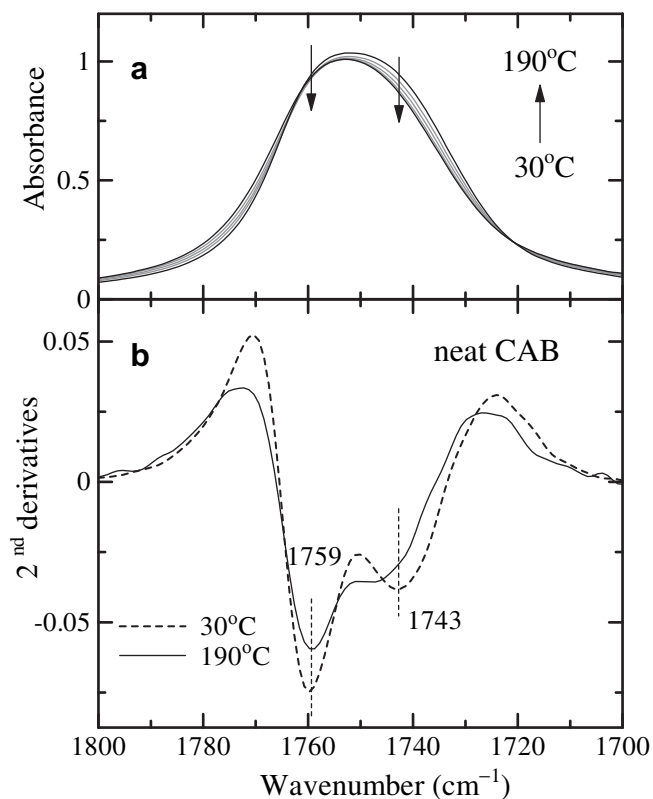


**Fig. 4.** IR spectra (a) and their second derivatives (b) in the C=O stretching region of pure CAB measured in the heating process from 30 to 190 °C. The arrows attached to 1759 and 1743  $\text{cm}^{-1}$  have the same meaning as those in Fig. 3.

**Table 2**  
Band assignments for FT-IR spectra of PHB/CAB blends.

Peak No.	Wavenumber ( $\text{cm}^{-1}$ )	Assignment
1	3587	free O–H
2	3549	intra CAB–CAB { –OH...O–(ether), CAB–CAB –OH...O=C, CAB–CAB
3	3485	inter OH, O–H...O=C, CAB–CAB
4	3465	1st overtone, free C=O, PHB (amorphous)
5	3460	inter O–H, O–H...O=C, CAB–PHB
6	3435	1st overtone, intra C=O, PHB (crystal)
7	1759 and ~1743	free C=O, CAB
8	1747	free C=O, PHB (amorphous)
9	1723	intra C=O, PHB (crystal)

inter: Intermolecular, intra: Intramolecular.

CAB chains is expected to be small for the blends with high molecular weights.

Although these blends have been reported to be entirely miscible [19–22], the relationship of  $T_g$  vs.  $w_{\text{CAB}}$  is far from that expected to the Fox law [26]. The  $T_g$ 's of blends observed slightly shift to a lower temperature than pure PHB with  $w_{\text{CAB}}$  up to  $w_{\text{CAB}} \sim 0.6$ , followed by a slight increase of the  $T_g$  with further increase of  $w_{\text{CAB}}$  from 0.6 to 0.7. When  $w_{\text{CAB}} > 0.7$ , this low  $T_g$  is obscured and the  $T_g$  shifts steeply to a higher temperature with  $w_{\text{CAB}}$  at  $w_{\text{CAB}} > 0.8$ . For the blend with  $w_{\text{CAB}} = 0.9$ , the thermogram around  $T_g$  (shown by the arrow) was highlighted in the inset to Fig. 2(b). The characteristic parameters for the thermal properties of these blends are summarized in Table 1. Even though all the blends apparently exhibited single  $T_g$ , the  $T_g$  vs.  $w_{\text{CAB}}$  behavior may infer existence of the two  $T_g$ 's due to the local heterogeneities of the blend composition mediated by a difference in the “self-concentration” of the stiff (CAB) and flexible components (PHB) in the blends [27,28]. Probably the higher  $T_g$  for the blends

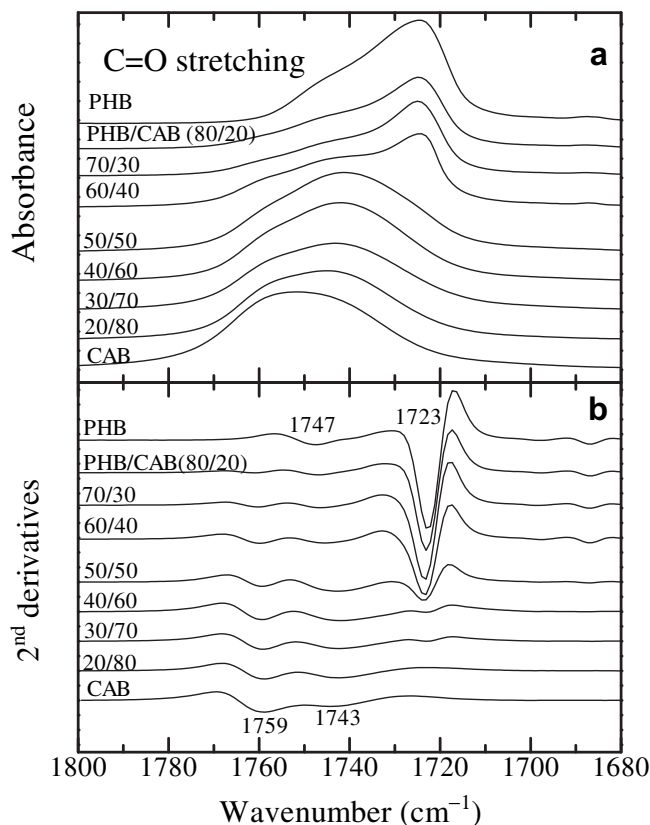


**Fig. 5.** IR spectra in the C=O stretching region of PHB and their blends with various blending ratios measured at 30 °C (a) and their second derivatives of the spectra (b).

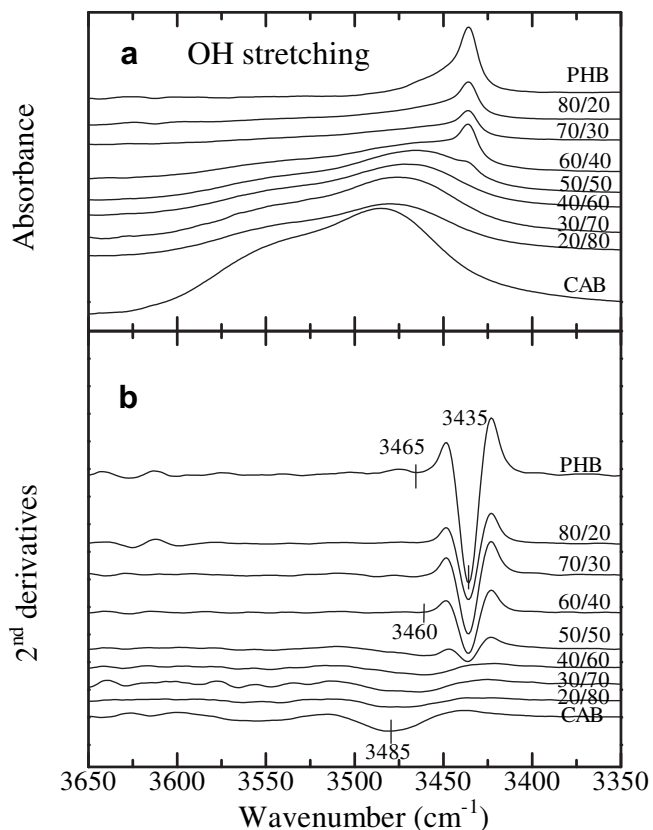


Fig. 6. IR spectra in the O–H stretching region of PHB and their blends with various blending ratios measured at 30 °C (a) and their second derivatives of the spectra (b).

with  $w_{\text{CAB}} \leq 0.7$ , if it existed, is obscured by the cold crystallization of PHB.

Fig. 2(c) and its inset present a typical DSC thermogram taken in the first heating process of the as-prepared blend sample with  $w_{\text{CAB}} = 0.5$  at a slow heating rate of 2 °C/min. The experimental conditions chosen here are almost the same as those chosen for the FT-IR studies to be discussed in the Sections 3.2 and 3.5 for a fair comparison of the thermal analyses of DSC and FT-IR. It is noted that the cold crystallization of the as-prepared blend sample at the slow heating rate is not so obvious as that found for the same blend sample in the second heating run shown in Fig. 2(b). We interpret the disparity described above is due to the fact that the crystallization occurred sufficiently during the preparation process of the as-prepared sample, hence suppressing the cold crystallization in the as-prepared sample in the first heating process. As will be shown later in conjunction with Figs. 8 and 9, the FT-IR clearly indicated the cold crystallization in the temperature range between 80 and ~130 °C. Based on the FT-IR result, we attempted to draw an expected DSC thermogram by dotted line in the case where the cold crystallization did not occur. The downward deviation of the real thermogram from that shown by the dotted line is very roughly assigned to be an endotherm due to the cold crystallization and partial melting of the crystals formed. Fig. 2(c) also exhibits the double melting thermogram. The first endothermic peak may be due to the melting of the crystals formed in the preparation process of the as-prepared sample and those formed in the cold crystallization process in the first heating process, while the second endothermic peak may be due to the recrystallization of molten crystals in the first endotherm and melting process of the recrystallized crystals.

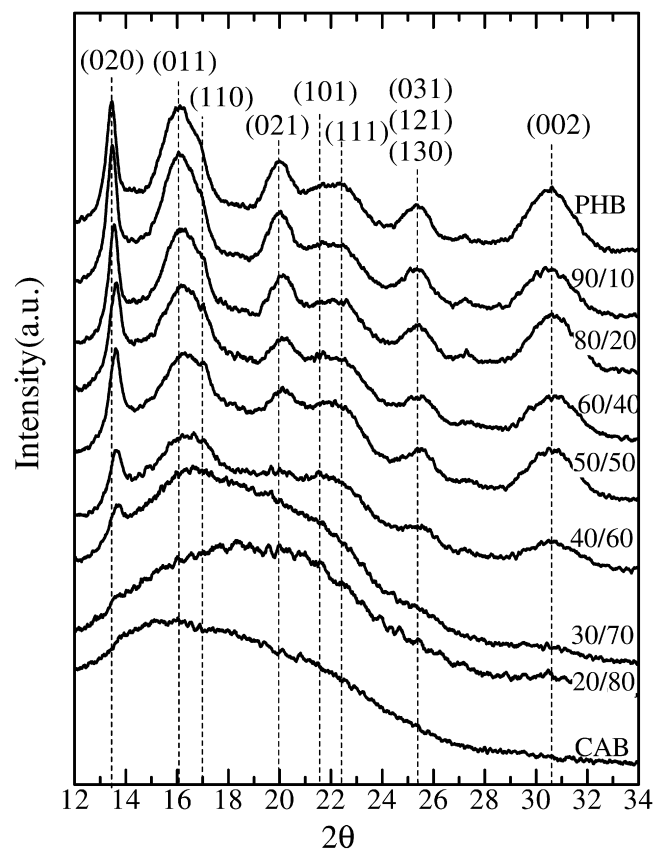
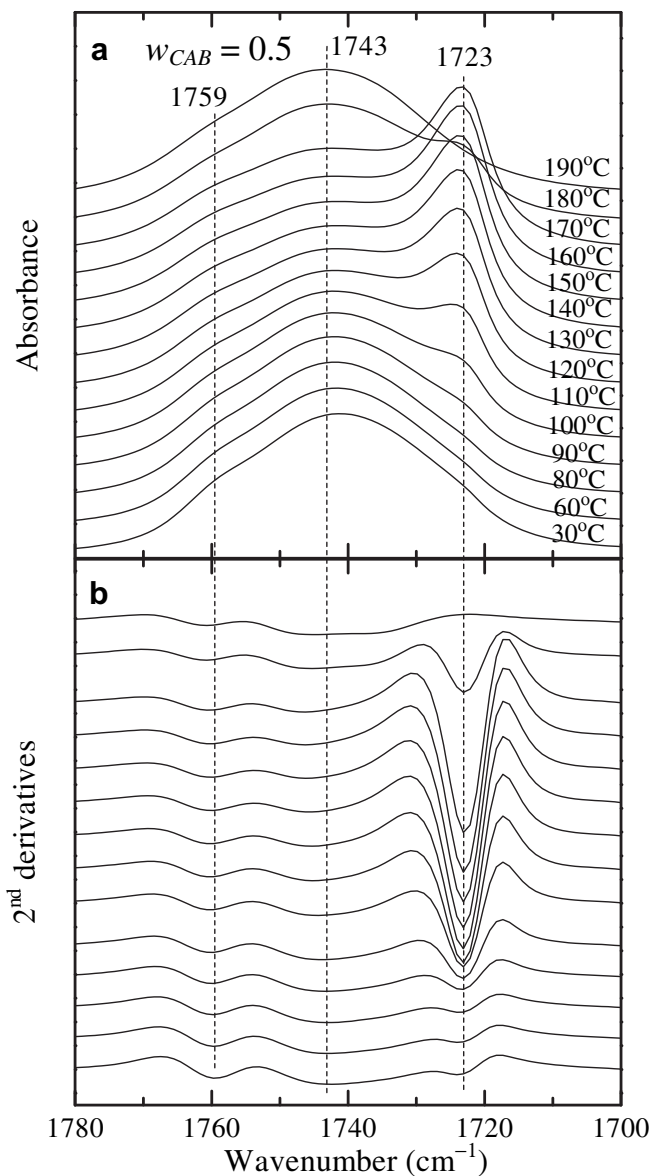


Fig. 7. WAXD patterns of the blends with various blending ratios measured at room temperature.

### 3.2. Temperature-dependent IR spectral variations of pure CAB

To explore molecular interactions, specifically hydrogen bondings, of the blends, temperature-dependent IR spectra of neat CAB were first investigated.

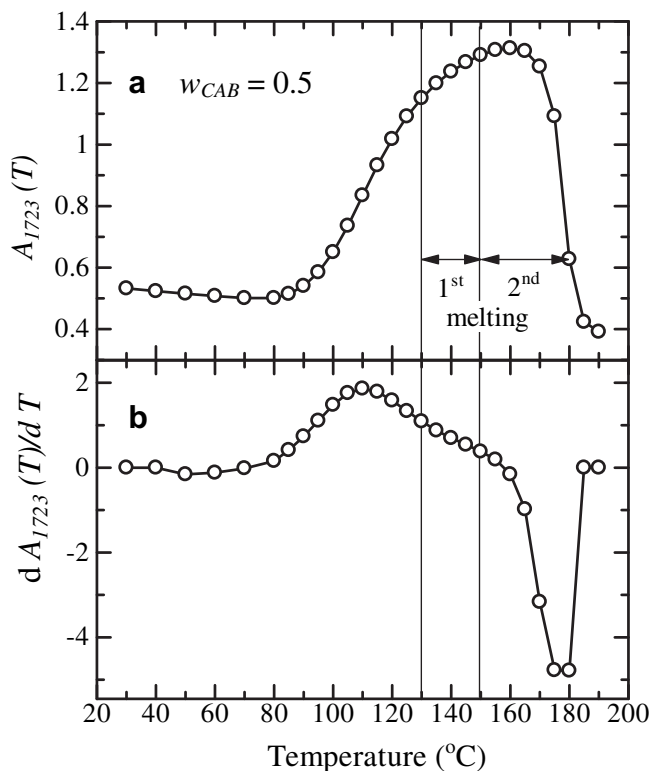
Fig. 3(a) presents IR spectra in the OH stretching region of 3700–3300  $\text{cm}^{-1}$  of pure CAB measured in the heating process of the as-prepared sample from 30 to 190 °C. It is important to note the fact that the OH stretching bands can clarify or focus on the intermolecular and intramolecular interactions of OH groups within CAB, no matter how small is a number fraction of OH groups per single CAB chain [ $34.0/(34.0 + 442 + 165) = 0.053$  mol%] compared with other groups, acetyl and butyryl groups. The selected second derivative spectra at 30 and 190 °C are given in part (b). One can easily recognize one broad band at 3485  $\text{cm}^{-1}$  and two weak shoulders at 3587 and 3549  $\text{cm}^{-1}$ . It is noted that the intensity of the 3485  $\text{cm}^{-1}$  band decreases significantly, as indicated by the downward arrow, and shifts toward a higher wavenumber of ~3489  $\text{cm}^{-1}$  with temperature. The intensity of the 3549  $\text{cm}^{-1}$  band also decreases, as indicated also by the downward arrow, and shifts toward a higher wavenumber. On the other hand, the intensity at 3587  $\text{cm}^{-1}$  certainly increases as shown by the upward arrow. The present results together with the previous ones on cellulose and CAB [22,29] lead us to assign the band at 3485  $\text{cm}^{-1}$  to the OH stretching mode of inter-chain hydrogen bondings (C=O...H–O) (defined as *inter* CAB–CAB) [22], while the band at 3549  $\text{cm}^{-1}$  may be ascribed to intramolecular hydrogen bondings of OH...O– (ether) and O–H...O=C in CAB (defined as *intra* CAB–CAB). This is because the absorbance of these bands (3549 and 3485  $\text{cm}^{-1}$ ) decreases with temperature, as typically observed



**Fig. 8.** Temperature-dependent (a) IR spectra and (b) their second derivatives in the C=O stretching vibration region of the blend with  $w_{CAB} = 0.5$  in a temperature range of 30–190 °C.

for bands associated with hydrogen bondings, and because of the relative peak positions of the two bands relative to that at  $3587\text{ cm}^{-1}$  [29]. We should note here that CAB contains much more C=O groups than cellulose and its derivatives contain. The third peak at  $3587\text{ cm}^{-1}$  arises from free O–H groups, because it appears at the highest wavenumber and increases with temperature as shown by the upward arrow in Fig. 3(a) [29–31]. The results in Fig. 3 reveal that most of the OH groups of CAB are involved in the hydrogen bondings, although the fractions of OH groups themselves are small among all the substituent groups.

The gradual intensity decreases in the bands at  $3485$  and  $3549\text{ cm}^{-1}$  together with the higher wavenumber shift with temperature suggest that both *inter* CAB–CAB and *intra* CAB–CAB become weak and some of them undergo dissociations with temperature. The intensity increase in the free OH stretching band is not so large, qualitatively indicating that a rather small fraction of the hydrogen bondings are dissociated into the free OH groups, although they become weak significantly with temperature.



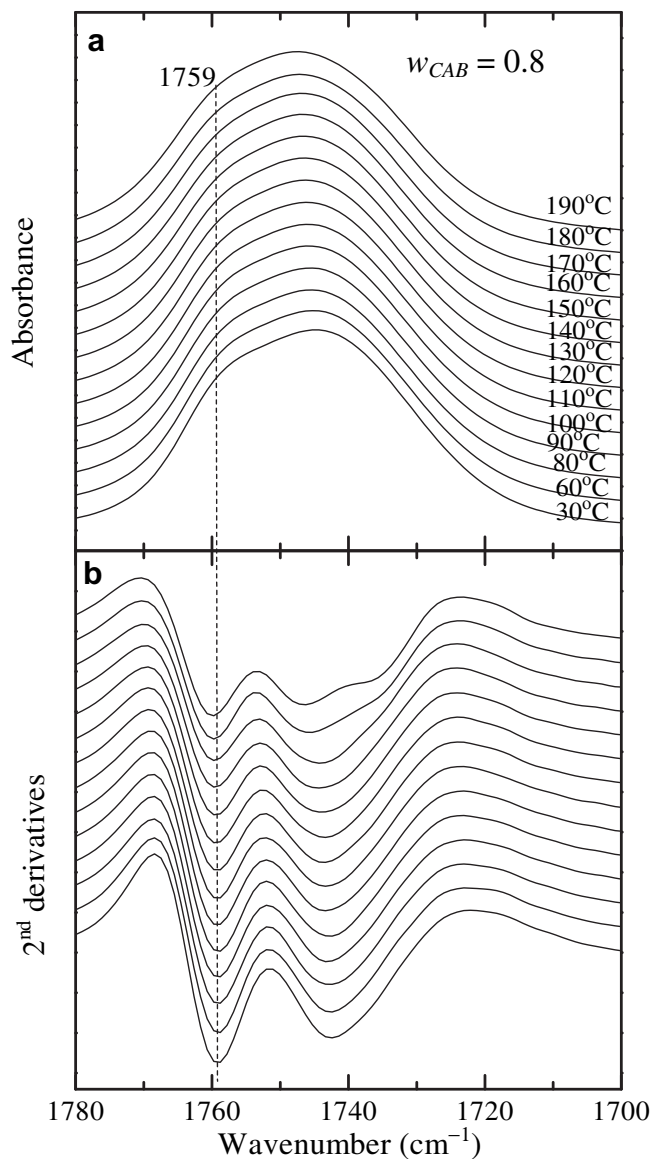
**Fig. 9.** Plot of absorbance at  $1723\text{ cm}^{-1}$  in the C=O stretching band (a) and its first derivatives with respect to  $T$  (b) versus  $T$  for the blend with  $w_{CAB} = 0.5$ .

Fig. 4(a) shows IR spectra in the C=O stretching band region of the as-prepared pure CAB sample measured in the heating process from 30 to 190 °C. The second derivative spectra presented in Fig. 4 (b) reveal that at least two kinds of C=O stretching bands appear at  $1759$  and  $\sim 1743\text{ cm}^{-1}$  at 30 °C. Firstly, we should note the fact that (1) most of the C=O groups of CAB exist as free C=O, because 94.7 mol% of the substitutes are acetyl and butyryl groups, and only 5.3 mol% are OH groups; only one out of 18 C=O groups can encounter OH groups, because the number ratio of C=O groups to OH groups is  $\sim 18$  to 1. From this viewpoint, it is not easy to identify the C=O stretching band due to *inter* CAB–CAB and/or *intra* CAB–CAB C=O  $\cdots$  H–O– in the spectra shown in Fig. 4. Nevertheless, we should note also the fact that (2) there are certainly the C=O  $\cdots$  H–O hydrogen bonds, as already evidenced by the OH stretching band region shown in Fig. 3. From these facts (1) and (2) described above, we can conclude that there are two stretching bands due to the free C=O groups which exist in slightly different environments.

Detailed band assignments for the neat CAB are summarized in Table 2, together with those of PHB and PHB/CAB which will be discussed later.

### 3.3. Composition-dependent IR spectra

Fig. 5 shows composition-dependent IR spectra in the C=O stretching band region at room temperature (a) and their second derivatives (b) for the blends. Based on the detail IR studies of neat PHB in the C=O and C–H stretching band regions [32–36], together with X-ray crystallographic studies [37,38], we have proposed that there are a chain of intramolecular hydrogen bondings (designated hereafter as *intra* C=O) C–H  $\cdots$  O=C between one of C–H groups in the  $\text{CH}_3$  of one helical chain and the C=O groups of another helical chain in the PHB lamellar



**Fig. 10.** Temperature-dependent (a) IR spectra and (b) their second derivatives in the C=O stretching vibration region of the blend with  $w_{CAB} = 0.8$  in a temperature range of 30–190 °C.

crystals along *a*-axis [32–36,39]. According to our previous investigations [32–36], the bands at 1747 and 1723  $\text{cm}^{-1}$  of pure PHB are assigned to C=O stretching modes of free C=O groups in amorphous regions (designated hereafter *free* C=O) and *intra* C=O, respectively.

Of note in Fig. 5(a) is that there is a marked difference between the spectrum of the 50/50 blend and that of the 60/40 blend. Upon going from the 60/40 blend to the 50/50 blend, the *intra* C=O at 1723  $\text{cm}^{-1}$  almost disappears and the *free* C=O band at 1747  $\text{cm}^{-1}$  increases. Thus, it is very likely that the crystallinity of PHB sharply decreases upon going from the 60/40 blend to the 50/50 blend. New bands appear at 1759 and 1743  $\text{cm}^{-1}$  with the increase in  $w_{CAB}$ . These are assigned to the stretching modes of free C=O groups of CAB (cf. Fig. 4)

The corresponding spectra in the O–H stretching band region of 3700–3300  $\text{cm}^{-1}$  and their second derivatives are presented in Fig. 6. In the original spectra (a), pure PHB shows a strong band at 3435  $\text{cm}^{-1}$ , assigned to the first overtone of the *intra* C=O, and a weak shoulder near 3465  $\text{cm}^{-1}$ , attributed to the first overtone of

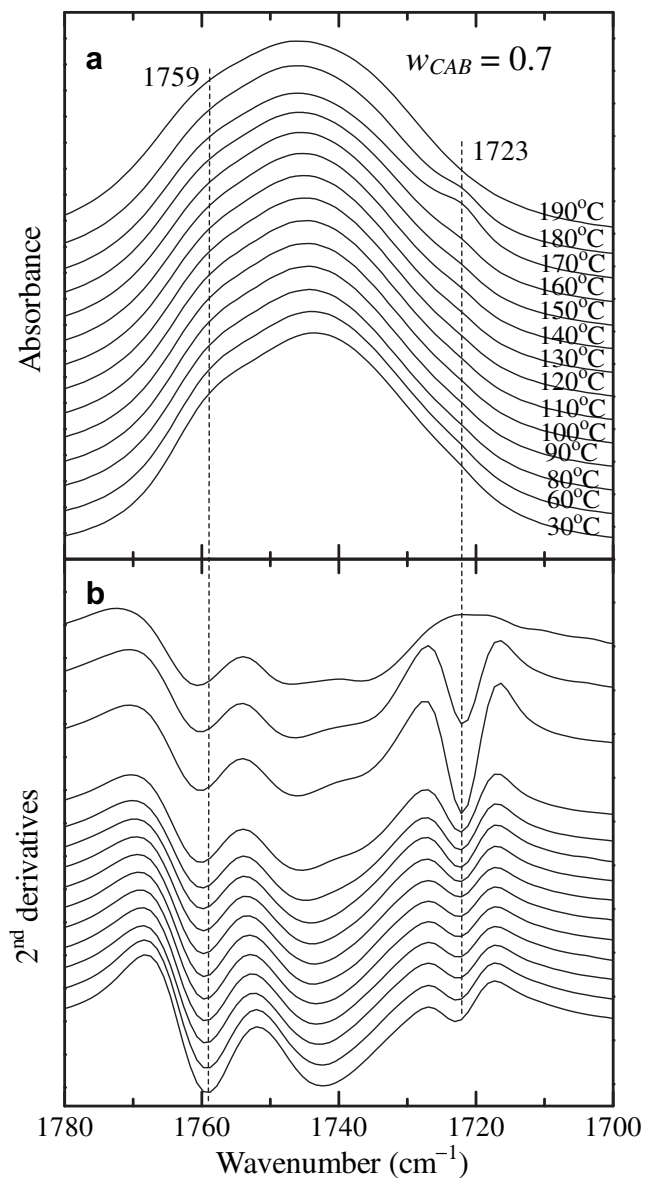


**Fig. 11.** Temperature-dependent (a) IR spectra and (b) their second derivatives in the C=O stretching vibration region of the blend with  $w_{CAB} = 0.7$  in a temperature range of 30–190 °C.

the *free* C=O [34–36]. These two characteristic bands can be clearly observed in the corresponding second derivative spectra in Fig. 6 (b). With the increase in  $w_{CAB}$ , the intensity of the 3435  $\text{cm}^{-1}$  band decreases markedly, while a new band appears at 3460  $\text{cm}^{-1}$  in the 50/50 blend. Again, there is a large variation between the spectrum of the 60/40 blend and that of the 50/50 blend as shown in Fig. 6(a). The band at 3460  $\text{cm}^{-1}$  may be assigned to the OH stretching mode in OH groups hydrogen-bonded with C=O groups of PHB, (CAB)–O–H...O=C–(PHB) (designated hereafter *inter* OH, CAB–PHB). It seems that there is weak intermolecular interactions between the OH groups in CAB and the C=O groups in amorphous part of PHB. The band at 3460  $\text{cm}^{-1}$  gradually becomes weak with increasing  $w_{CAB}$  from 0.5 to 1, while the band at 3485  $\text{cm}^{-1}$  becomes strong. This indicates an exchange of hydrogen bondings between *inter* C=O...HO, PHB–CAB and *inter* C=O...H–O, CAB–CAB with  $w_{CAB}$ , through dissociations of the former, followed by association of the latter via reassociation of the dissociated OH groups of CAB with free C=O groups in CAB (see Table 2).

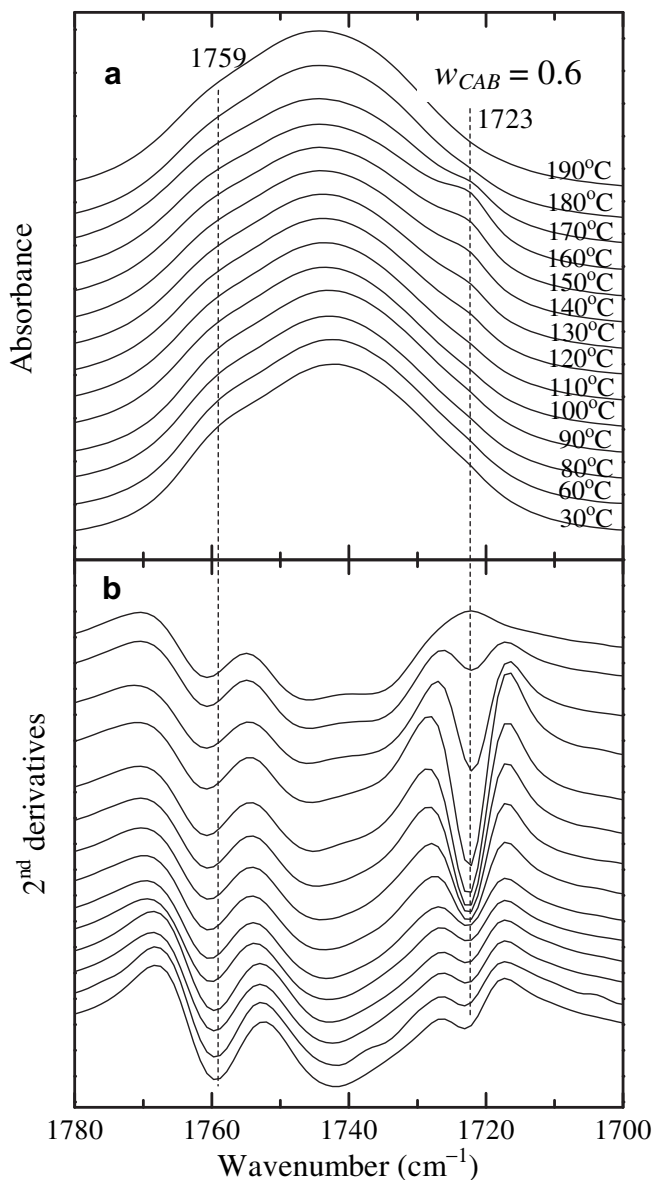


Fig. 12. Temperature-dependent (a) IR spectra and (b) their second derivatives in the C=O stretching vibration region of the blend with  $w_{CAB} = 0.6$  in a temperature range of 30–190 °C.

#### 3.4. Crystal structure and crystallinity of PHB in the blends

The wide-angle X-ray diffraction (WAXD) method was employed to explore the local spatial arrangements of atoms in the crystal and amorphous regions in the blends as a function of  $w_{CAB}$ . The measured X-ray diffraction patterns for the blends are shown in Fig. 7. For the neat PHB, the crystal structure has been determined as the orthorhombic structure with lattice parameters ( $\alpha = \beta = \gamma = 90^\circ$ ,  $a = 5.76$ ,  $b = 13.20$ , and  $c = 5.96$  Å) using the X-ray diffraction technique [37]. Therefore, the several sharp peaks from the blends located at  $13.4^\circ$ ,  $16.1^\circ$ ,  $16.7^\circ$ ,  $19.9^\circ$ ,  $21.7^\circ$ ,  $22.5^\circ$ , and  $30.3^\circ$  can be assigned to the diffraction peaks from the (020), (011), (110), (021), (101), (111), and (002) lattice planes from the PHB crystal in the blends, respectively.

Comparing these diffraction peaks in the blends with those in the neat one, we can conclude that the crystal structure of PHB in the blends is almost the same as that of the neat PHB. Nevertheless, the diffraction peaks from crystals gradually decrease with  $w_{CAB}$  and eventually disappear in the blends with  $w_{CAB} \geq 0.8$ , indicating that the

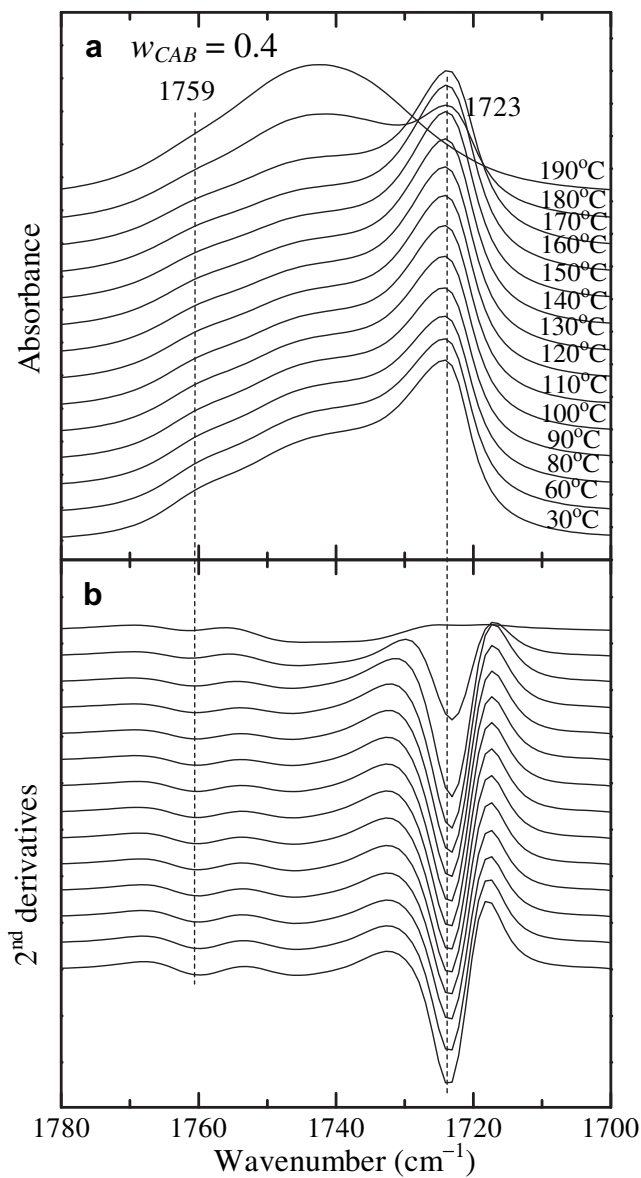


Fig. 13. Temperature-dependent (a) IR spectra and (b) their second derivatives in the C=O stretching vibration region of the blend with  $w_{CAB} = 0.4$  in a temperature range of 30–190 °C.

crystallinity of blends decreases with  $w_{CAB}$ . These results are in good agreement with the IR spectral results observed around  $1723\text{ cm}^{-1}$  (Fig. 5) and  $3435\text{ cm}^{-1}$  (Fig. 6), though the IR peak disappears at a slightly small  $w_{CAB}$ ,  $w_{CAB} \geq 0.5$ . This disparity in the value of  $w_{CAB}$ , above which the crystallinity as observed by IR and WAXD disappears, may infer that with increasing  $w_{CAB}$ , the *intra* C=O in the PHB crystal breaks prior to distortions of the regular positional orders of atoms registered in the crystals as observed by WAXD, and that the break of the *intra* C=O triggers the distortions of the positional order of atoms in the crystal, giving rise to less stable crystals, smaller net crystallinity, as observed by WAXD, and eventually to the transformation into an amorphous state at  $w_{CAB} \geq 0.8$ . Thus, formation of a perfect crystal structure of PHB is obstructed with increasing  $w_{CAB}$ , which may be driven through the increasing amount of *inter* between CAB and PHB.

#### 3.5. Temperature-induced IR spectral variations of the blends

For clarifying relationships among the crystallization behavior of PHB in the blends, the intermolecular interactions between CAB

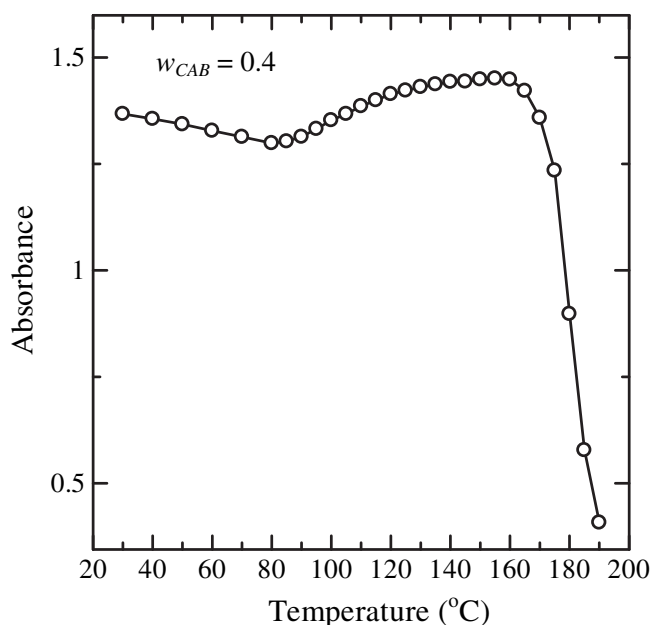


Fig. 14. Plot of the absorbance at  $1723\text{ cm}^{-1}$  in C=O stretching band versus temperature for the blend with  $w_{\text{CAB}} = 0.4$ .

and PHB, and intramolecular interactions within CAB and within PHB, IR spectra of the blends were measured in the heating process. Fig. 8(a) and (b) display the temperature-dependent IR spectra in the C=O stretching region and their second derivatives of the blend with  $w_{\text{CAB}} = 0.5$  measured over a temperature range from 30 to  $190\text{ }^{\circ}\text{C}$ , respectively. One can observe three bands at  $1759$ ,  $1743$ , and  $1723\text{ cm}^{-1}$  in the spectrum at  $30\text{ }^{\circ}\text{C}$  (see, the second derivatives). The  $1759$  and  $1723\text{ cm}^{-1}$  bands are already ascribed to the stretching modes of free C=O groups of CAB and *intra* C=O of PHB, respectively (see Fig. 5). The broad peak around  $1743\text{ cm}^{-1}$  contains contributions from both CAB (free C=O) and PHB (*free* C=O) (see

also Fig. 5). Of note is that the intensity of the  $1723\text{ cm}^{-1}$  band increases markedly above  $90\text{ }^{\circ}\text{C}$ .

Fig. 9 plots  $A_{1723}(T)$ , the absorbance at  $1723\text{ cm}^{-1}$  (a) and  $dA_{1723}(T)/dT$ , the first derivative of the absorbance at  $1723\text{ cm}^{-1}$  with  $T$ , for the blend with  $w_{\text{CAB}} = 0.5$  versus temperature (b). It can be seen from Fig. 9 that the intensity of the  $1723\text{ cm}^{-1}$  band increases from  $80$  to  $160\text{ }^{\circ}\text{C}$ . Above  $165\text{ }^{\circ}\text{C}$ , it decreases rapidly. The intensity variation suggests that *intra* C=O is formed within the PHB component in the blend from  $90$  to  $160\text{ }^{\circ}\text{C}$  and that they are broken above  $165\text{ }^{\circ}\text{C}$  [45]. These changes suggest that the cold crystallization of PHB in the blends and melting of PHB crystals take place in the temperature range between  $80$  and  $\sim 180\text{ }^{\circ}\text{C}$ .

Since  $A_{1723}(T)$  is proportional to  $X_c(T)$ , the crystallinity at a given  $T$ ,  $dA_{1723}(T)/dT$  is proportional to  $dX_c(T)/dT$ , the amount of crystals formed between  $T$  and  $T + dT$ . Thus the derivatives are related to heat evolved in the cold crystallization at  $T$ , and hence is related to the DSC thermogram shown in Fig. 2(c). Fig. 9(b) qualitatively suggests that the cold crystallization and a partial melting of the crystals (the crystals newly formed via the cold crystallization and the crystals existed in the as-prepared blends) and recrystallization of the molten crystals from  $\sim 80$  to  $\sim 150\text{ }^{\circ}\text{C}$  and the melting of the recrystallized crystals above  $\sim 150\text{ }^{\circ}\text{C}$ . Here it is noted that the onset temperature of the cold crystallization and the temperature of completion of the melting are subjected to some errors due to a serious overlap of band having peak at  $1743\text{ cm}^{-1}$  to the band at  $1723\text{ cm}^{-1}$ , because the intensity of the band at  $1723\text{ cm}^{-1}$  is small around these temperatures.

We may be able to envision that the cold crystallization process involves exchanges of hydrogen bondings from *inter* between PHB and CAB to *intra* within PHB via dissociation of *inter* and association of free C=O, formed as a consequence of the dissociation and its transformation into *intra* within PHB and that formation of *intra* improves perfection and stabilization of the PHB crystals. Here it is important to note that the average of OH groups per single CAB chain (34) is substantially large, although the fraction of OH groups among all the substituent groups is very small (only  $5.3\text{ mol}\%$ ). Consequently *inter* affects considerably the cold crystallization process and the crystallization from the melts as well. This is because the small fraction of OH groups in the CAB gives a sufficiently large number of OH groups per single CAB chain to form physically crosslinked networks between PHB and CAB in the blends via *inter* as the crosslinking points which are stable in the temperature range where crystallization occurs. Hence *inter* suppresses the crystallization rate and net crystallinity too attained under given crystallization conditions.

Figs. 10–13 display temperature-dependent variations of IR spectra (a) and their second derivatives (b) in the  $1780$ – $1700\text{ cm}^{-1}$  region of the blends with  $w_{\text{CAB}} = 0.8, 0.7, 0.6$ , and  $0.4$ , respectively. In the case of the blend with  $w_{\text{CAB}} = 0.8$ , the spectra did not exhibit the peak at  $1723\text{ cm}^{-1}$ , indicating that *intra* is not formed in the blend. Consequently, the cold crystallization of PHB does not occur even at high temperatures due to the incorporation of the large fraction of CAB in the blends. The  $1723\text{ cm}^{-1}$  band was clearly observed in the blends with  $w_{\text{CAB}} = 0.7, 0.6$ , and  $0.4$ . The intensity of the  $1723\text{ cm}^{-1}$  band of the blends with  $w_{\text{CAB}} = 0.7$  and  $0.6$  increases significantly with increasing temperature from  $\sim 120$  to  $180\text{ }^{\circ}\text{C}$ , indicating that the cold crystallization occurs remarkably in the blends with  $w_{\text{CAB}} = 0.7$  and  $0.6$ .

The intensity of the  $1723\text{ cm}^{-1}$  band of the blend with  $w_{\text{CAB}} = 0.4$  versus temperature is plotted in Fig. 14. As can be found that the  $1723\text{ cm}^{-1}$  band is intense even at room temperature, reflecting that the as-prepared blend sample with  $w_{\text{CAB}} = 0.4$  itself has a relatively large crystallinity in the initial state.

Fig. 15 shows the IR spectra from  $3650$  to  $3390\text{ cm}^{-1}$  region (part a) and their corresponding second derivatives (part b) in the whole

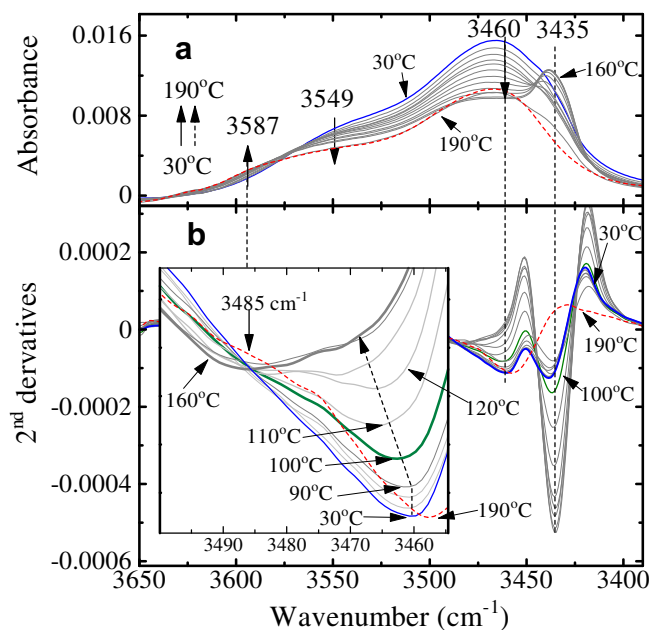


Fig. 15. IR spectra with  $w_{\text{CAB}} = 0.5$  (a) in the  $3650$ – $3390\text{ cm}^{-1}$  region and their second derivatives (b) of the blend ratio at 50/50 measured in the heating process in a temperature range of  $30$ – $190\text{ }^{\circ}\text{C}$ .



heating process. As can be seen from the second derivative spectra in the inset of part (b), the peak at  $3460\text{ cm}^{-1}$  shows a gradual shift toward the higher wavenumber with increasing temperature above  $90\text{ }^{\circ}\text{C}$ . Therefore, we can ascribe the band at  $3460\text{ cm}^{-1}$  to the stretching mode of OH groups which involves the intermolecular hydrogen bondings between OH groups of CAB and C=O groups of PHB. We can ascribe the shift of the bands to a weakening of the hydrogen bonding. Moreover as shown in the inset of part (b), the gradual shift of the peak at  $3460\text{ cm}^{-1}$  start to display another peak  $\sim 3485\text{ cm}^{-1}$ , when the temperature is raised to  $120\text{ }^{\circ}\text{C}$ . Upon further increasing the temperature up to  $160\text{ }^{\circ}\text{C}$ , the new peak at  $\sim 3485\text{ cm}^{-1}$  dominates. This indubitable result seems to support our idea that the intermolecular hydrogen bonding between CAB and PHB is dissociated in the heating process from  $90$  to  $160\text{ }^{\circ}\text{C}$  and is transformed into *inter*  $\text{OH}\cdots\text{O}=\text{C}$ , CAB–CAB as listed in Table 2. The dissociation involves the association of *intra* at  $1723\text{ cm}^{-1}$  within PHB also. The transformation of the hydrogen bonding from *inter* between PHB and CAB into *intra* within PHB and *inter* CAB–CAB is driven by the cold crystallization. The transformation is also confirmed by the decrease of the intensity at  $3460\text{ cm}^{-1}$  in the original spectra in part (a) with increasing  $T$  to  $160\text{ }^{\circ}\text{C}$ , as indicated by the downward arrow. The melting process of PHB crystal involves the reverse exchange and transformation of the hydrogen bondings, as evidenced by the change of the original and second derivative spectra from  $160$  to  $190\text{ }^{\circ}\text{C}$ .

#### 4. Conclusions

The molecular interactions, specifically hydrogen bonding interactions, of the PHB/CAB blends with various blending compositions have been investigated by means of IR spectroscopy, DSC, and WAXD. From the DSC analysis, it has been shown that the cold crystallization temperature of the blends in the second heating process increases with  $w_{\text{CAB}}$  and that the melting temperature of the blends decreases with  $w_{\text{CAB}}$  primarily due to the suppressed mobility of PHB component in the blends with  $w_{\text{CAB}}$ . In addition, their glass transition temperatures ( $T_g$ ) are not strongly composition-dependent in the entire composition range except for the range of CAB between 80 and 90 wt%. We proposed that the difference in the self-concentrations of CAB and PHB plays an important role.

In the IR analysis of neat CAB, the bands due to the C=O and OH stretching modes of CAB have been assigned as follows (Table 2). The bands due to free C=O groups in slightly different environments appear at  $\sim 1743$  and  $1759\text{ cm}^{-1}$  (peak#7 in Table 2). The bands at  $3587$ ,  $3549$ , and  $3485\text{ cm}^{-1}$  have been assigned to the OH stretching modes of free OH groups (peak#1 in Table 2), intramolecularly hydrogen-bonded OH groups ( $-\text{OH}\cdots\text{O}-$ (ether) and  $-\text{OH}\cdots\text{O}=\text{C}$ ) (peak#2 in Table 2), and intermolecularly hydrogen-bonded OH groups ( $-\text{OH}\cdots\text{O}=\text{C}$ ) (peak#3 in Table 2), respectively.

For the PHB/CAB blends, the weak intermolecular hydrogen bondings of  $\text{OH}\cdots\text{O}=\text{C}$  between the OH groups in CAB and the C=O groups in amorphous part of PHB (*inter*) are observed by monitoring the apparent wavenumber shift of the characteristic IR bands in the  $3485$ – $3460\text{ cm}^{-1}$  region (Figs. 6 and 15) and  $3460$ – $3465\text{ cm}^{-1}$  region (Fig. 6) (peak#5 in Table 2). However, these interactions highly depend on the blend composition (Fig. 6) and temperature (Fig. 15) as a consequence of the competitive interactions between CAB and CAB and between PHB and PHB. With increasing temperature, it dissociates and is transformed into the intramolecular hydrogen bondings of  $\text{C}-\text{H}\cdots\text{O}=\text{C}$  within PHB (*intra*, peak#6 and peak#9) and within CAB (*intra* and *inter*, peaks#2 and #3 in Table 2, respectively), which is closely related to the cold crystallization. The reverse transformation occurs in the melting process of PHB crystals.

The X-ray crystallinity was found to decrease with increasing  $w_{\text{CAB}}$  and to disappear at  $w_{\text{CAB}} \geq 0.8$ , which imply the suppression of crystallization of PHB component via the intermolecular and intramolecular interactions which act as physical crosslinks of PHB and CAB chains in the blends as detailed in the text.

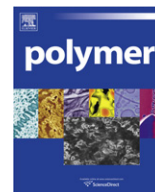
#### Acknowledgements

This work was supported by Grant-in-Aid for Scientific Research (C) from MEXT (No. 20550026, No. 20550197), Grant-in-Aid for Scientific Research on Innovative Areas from MEXT (No. 21106521), and Shiseido Female Researcher Science Grant 2009. This work was supported also by Kwansai-Gakuin University "Special Research" project 2009–2014.

#### References

- [1] Miyasaki SS, Yep AR, Kolton F, Hermida B, Povofo F, Fernandes E, et al. Bio-based and synthetic biodegradable polymers. In: Chiellini E, Solaro R, editors. Recent advances in biodegradable polymer and plastics. Wiley-VCH; 2003. p. 57–64.
- [2] Yu L, Dean K, Li L. Prog Polym Sci 2006;31:576–602.
- [3] Dorgan JR. Poly(lactic acid) properties and prospects of an environmentally benign plastic. Washington, DC: American Chemical Society; 1999. p. 145–149.
- [4] Mothes G, Schnorpfel C, Ackermann J-U. Eng Life Sci 2007;7:475–9.
- [5] Furukawa T, Sato H, Murakami R, Zhang J, Noda I, Ochiai S, Ozaki Y. Polymer 2007;48:1749–55.
- [6] Doi Y, Kunioka M, Nakamura Y, Soga K. Macromolecules 1986;19:2860–4.
- [7] Rhee YH, Jang JH, Rogers PL. Biotechnol Lett 1993;15(4):377–82.
- [8] Majid MIA, Akmal DH, Few LL, Agustien A, Toh MS, Samian MR, et al. Int J Biol Macromol 1999;25:95–104.
- [9] Jedlinski Z, Kowalczyk M, Adamus G, Sikorska W, Rydz J. Int J Biol Macromol 1999;25:247–53.
- [10] Rodrigues JAFR, Parra DF, Lugao AB. J Therm Anal Cal 2005;79:379–81.
- [11] Avella M, Martuscelli E, Greco P. Polymer 1991;32(9):1647–53.
- [12] Chiu HJ, Chen HL, Lin TL, Lin JS. Macromolecules 1999;32(15):4969–74.
- [13] Chiu HJ. J Appl Polym Sci 2006;100:980–8.
- [14] Iriondo P, Iruin JJ, Fernandez-Berridi MJ. Macromolecules 1996;29(17):5605–10.
- [15] Xing P, Dong L, An Y, Feng Z, Avella M, Martuscelli E. Macromolecules 1997;30:2726–33.
- [16] Huang H, Yun H, Zhang J, Sato H, Zhang H, Noda I, Ozaki Y. J Phys Chem B 2005;109(41):19175–83.
- [17] Zhang J, Sato H, Furukawa T, Tsuji H, Noda I, Ozaki Y. J Phys Chem B 2006;110(48):24463–71.
- [18] Scandola M, Ceccorulli G, Pizzoli M. Macromolecules 1992;25(24):6441–6.
- [19] Ceccorulli G, Pizzoli M, Scandola M. Macromolecules 1993;26(25):6722–6.
- [20] Pizzoli M, Scandola M, Ceccorulli G. Macromolecules 1994;27(17):4755–61.
- [21] El-Shafee E, Saad GR, Fahmy SM. Eur Polym J 2001;37:2091–104.
- [22] Park JW, Tanaka T, Doi Y, Iwata T. Macromol Biosci 2005;5:840–52.
- [23] Barham PJ, Keller A, Otun EL, Holms PA. J Mater Sci 1984;19:2781–94.
- [24] Barham PJ. J Mater Sci 1984;19:3826–34.
- [25] Gunaratne LMWK, Shanks RA, Amarasinghe G. Thermochim Acta 2004;423:127–35.
- [26] Fox TG. Bull Am Phys Soc 1953;1:123.
- [27] Lodge TP, Mcleish TCB. Macromolecules 2000;33:5278–84.
- [28] Zhao J, Ediger MD, Sun Y, Yu L. Macromolecules 2009;42:6777–83.
- [29] Kokot S, Czarnik-Matuszewicz B, Ozaki Y. Biopolym (Biospectrosc) 2002;67:456–69.
- [30] Watanabe A, Morita S, Kokot S, Matsubara M, Fukai K, Ozaki Y. J Mol Struct 2006;799:102–10.
- [31] Kondo T. Cellulose 1997;4:281–92.
- [32] Sato H, Mori K, Murakami R, Ando Y, Takahashi I, Zhang J, et al. Macromolecules 2006;39(4):1525–31.
- [33] Sato H, Murakami R, Padermshoke A, Hirose H, Senda K, Noda I, Ozaki Y. Macromolecules 2004;37(19):7203–13.
- [34] Murakami R, Sato H, Dybal J, Iwata T, Ozaki Y. Polymer 2007;48:2672–80.
- [35] Sato H, Nakamura M, Padermshoke A, Yamaguchi H, Terauchi H, Sanong E, et al. Macromolecules 2004;37:3763–9.
- [36] Sato H, Ando Y, Dybal J, Iwata T, Noda I, Ozaki Y. Macromolecules 2008;41:4305–12.
- [37] Yokouchi M, Chatani Y, Tadakoro H, Teranishi K, Tani H. Polymer 1973;14:267.
- [38] Marchessault RH, Kawada J. Macromolecules 2004;37:7418–20.
- [39] We would like to point out that there are a variety of weak hydrogen bondings, including  $\text{C}-\text{H}\cdots\text{O}=\text{C}$ , have been reported and accepted since early 1990s: One can find a huge number of reviews, books, and papers [40–44].

- [40] Scheiner S. Hydrogen bonding: a theoretical perspective. New York: Oxford University Press; 1997.
- [41] Jeffrey GA. An introduction of hydrogen bonding. New York: Oxford University Press; 1997.
- [42] Desiraju GR, Steiner T. The weak of hydrogen bond: in structure chemistry and biology. New York: Oxford University Press; 1999.
- [43] Harada T, Yoshida H, Ohno K, Matsuura H. Chem Phys Lett 2002;362:453–60.
- [44] Matsuura H, Yoshida H, Hieda M, Yamanaka S, Harada T, Shin-ya K, et al. J Am Chem Soc 2003;125:13910–1.
- [45] The concentration of intra C=O...H–O within PHB, [intra C=O], relative to the concentration of free C=O in PHB, [free C=O], is given by  $[\text{intra C=O}]/[\text{free C=O}] \sim \exp(\Delta E_{\text{intra}}/k_{\text{B}}T)$  in the context of the Boltzmann statistics, where  $\Delta E_{\text{intra}} = E_{\text{free}} - E_{\text{intra}}$  with  $E_{\text{free}}$  and  $E_{\text{intra}}$  being energy of free C=O and intra C=O. Since *intra* is a weak hydrogen bond, the relative concentration [intra C=O]/[free C=O] depends on temperature not only through  $k_{\text{B}}T$  but also through temperature dependence of  $\Delta E_{\text{intra}}$ . If *intra* were a strong hydrogen bond,  $\Delta E_{\text{intra}}$  should be almost independent of  $T$ .



# High-crystallization polyoxymethylene modification on carbon nanotubes with assistance of supercritical carbon dioxide: Molecular interactions and their thermal stability

Ning Yu, Linghao He, Yuanyuan Ren, Qun Xu\*

College of Materials Science and Engineering, Zhengzhou University, Zhengzhou 450052, People's Republic of China

## ARTICLE INFO

### Article history:

Received 10 August 2010

Received in revised form

24 October 2010

Accepted 26 November 2010

Available online 7 December 2010

### Keywords:

Polyoxymethylene

Supercritical carbon dioxide

Carbon nanotube

## ABSTRACT

As a typical engineering plastic and high-crystallization polymer, polyoxymethylene (POM) has been successfully wrapped on single-walled carbon nanotubes (SWCNTs) using a simple supercritical carbon dioxide (SC CO<sub>2</sub>) antisolvent-induced polymer epitaxy method. The characterization results of scanning electron microscopy (SEM) and transmission electron microscopy (TEM) reveal that the SWCNTs are coated by laminar POM with the thicknesses of a few nanometers. The polymer adsorption on CNTs via multiple weak molecular interactions of CH groups with CNTs has been identified with FTIR and Raman spectroscopy. The experimental results indicate that the decorating degree of POM on the surface of CNTs increases significantly with the increase of SC CO<sub>2</sub> pressure, and accordingly the dispersion of SWCNT modified by POM at higher pressure are more excellent than that of obtained at lower pressure. Further the processing stability of POM/CNTs composites are investigated by differential scanning calorimetry and thermogravimetric analysis. The experimental results obtained show that their thermal stability behavior is closely related to surface properties of CNTs. Apparently, the composites with POM-decorating SWCNTs as the filler shows higher melting points compared to the POM composites with pristine SWCNTs as the filler. Therefore, we anticipate this work may lead to a controllable method making use of peculiar properties of SC CO<sub>2</sub> to help to fabricate the functional CNTs-based nanocomposites containing highly crystalline thermoplastic materials such as POM.

© 2010 Elsevier Ltd. All rights reserved.

## 1. Introduction

Carbon nanotubes (CNTs) have been intensively studied because of their remarkable electronic, mechanical properties and unique one-dimensional (1D) structures [1–3]. In addition, due to their nanometer size, high aspect ratios, and more importantly, extraordinary mechanical strength and thermal conductivity, carbon nanotubes (CNTs) have been considered as ideal candidates to substitute for the conventional nanofillers in multifunctional polymer nanocomposites [4–8]. However, a major remaining challenge is how to achieve homogenous dispersion of CNTs within polymeric matrix because the as-prepared CNTs usually aggregate into bundles and/or entangle together. There are some methods to solve this problem, including chemical functionalization techniques and noncovalent wrapping methods [9]. Comparing to the covalent method which is the attachment of chemical groups through

chemical reactions onto the  $\pi$ -conjugated skeleton of SWCNTs, the noncovalent wrapping methods can not destroy the original structure of CNTs, therefore the electronic network of the tubes can be maintained.

Supercritical fluids (SCFs) have been widely used in the synthesis and processing of materials due to their unusual properties such as low viscosity, high diffusivity, near-zero surface tension, and tenability [10]. Among SCFs, supercritical CO<sub>2</sub> (SC CO<sub>2</sub>) is the most popular one because it is nonflammable, nontoxic, inexpensive, and naturally abundant and has consequently been promoted as a sustainable solvent [11–14]. In addition, the solubility of SC CO<sub>2</sub> in many organic solvents is very high, but it is very poor for many polymers [15,16]. So SC CO<sub>2</sub> can act as an antisolvent to enhance the precipitation or absorption of polymers on the surface of CNTs [17–22]. In our previous study, we have successfully achieved the modification of CNTs with polyethylene (PE), poly(ethylene glycol) (PEG), poly(vinyl alcohol) (PVA) and poly(vinylidene fluoride) (PVDF) using a simple SC CO<sub>2</sub> antisolvent-induced polymer epitaxy method (SAIPE method) [19–22]. These results motivated us to go on investigating other typical polymers

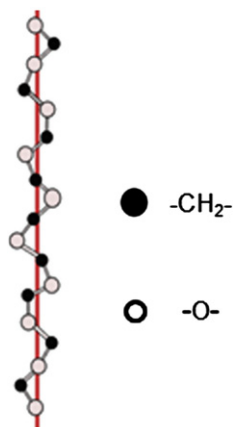
\* Corresponding author. Tel./fax: +86 371 67767827.

E-mail address: [qunxu@zzu.edu.cn](mailto:qunxu@zzu.edu.cn) (Q. Xu).

and study their modification on CNTs with assistance of SC CO<sub>2</sub>. We are very interesting to go on investigating new polymer and fabricate functional CNTs-based nanocomposites, especially which is hard to synthesis or fabricate using traditional methods.

Polyoxymethylene (POM) is an engineering plastic with excellent properties, such as high mechanical strength, good abrasion resistance, exceptional dimensional stability, and has a wide range of applications in industries [23,24]. Because of the flexibility of its significant main chain  $[-CH_2-O-]$  (Scheme 1), POM has a high-degree of crystallization, and such a high-crystallization makes it difficult to obtain the POM/CNTs nanocomposites. In addition, considering the properties of POM/CNTs nanocomposites can be influenced by the varying crystal structure and morphology [25,26], the design and construction of functional CNTs-based composites are very necessary from academia and to industry. However, there is little information on the POM/CNTs nanocomposites because of the very poor compatibility of POM with other materials, comparing with other polymers such as polyethylene (PE), nylon66, polyethylene-b-poly (ethyleneoxide) (PE-b-PEO) [27–29]. Recently, Zeng et al. have used the conventional melt-mixing technique to fabricate POM/CNTs composites. They have found that when CNTs were added into the molten POM, a drastic degradation of POM occurred and toxic formaldehyde gas was emitted [30]. Another group has studied the thermal conductivity, mechanical properties and the structure of POM/CNTs nanocomposites. Zhao et al. have prepared POM/MWCNTs (multiwalled carbon nanotubes) nanocomposites by a simple solution-evaporation method. In their work, MWCNTs were chemically functionalized for purpose of the dispersion in POM matrix, and the interfacial bonding of them was enhanced [31]. Although the two groups have investigated the properties of POM/CNTs nanocomposites, there is still little information on the interaction between POM and CNTs. Another one point needs to note is that it is hard to overcome the shortcoming that the continuous deformaldehyde reaction may occur due to the rupture of methyl oxide bonds under heat and oxygen [32]. Therefore, exploring a novel and green fabrication method is necessary.

Thus, in this study, first, we aim to realize the modification of CNTs with POM via the environmental benign SC CO<sub>2</sub> – assisted method. Second, we try to explore the effect of different experimental conditions on CNTs' decoration, in order to achieve the controllable morphology and properties of the composite of POM/CNTs. Third, the processing stabilities of POM/CNTs composites are investigated. The ultimate purpose is to help realize the functional design for these tailored nanohybrid architecture of CNTs-based nanocomposites containing highly crystalline thermoplastic of POM.



**Scheme 1.** The molecular helix conformation of POM (H9<sub>5</sub>).

## 2. Experimental

### 2.1. Raw materials

The single-walled carbon nanotubes (SWCNTs) were supplied by Carbon Nano Materials R&D Center, Chengdu Desran Technology Co., Ltd. (China), with a purity of 90 wt.%. Polyoxymethylene (POM) was the experimental grade granule purchased (CAS NO: 30525-89-4) from Sinopharm Chemical Reagent Co., Ltd (China). Acetic acid glacial (HAc) was purchased from Tianli Chemical Reagent Co., Ltd (China), with a purity of 99.5%. CO<sub>2</sub> with purity of 99.9% was provided by Zhengzhou Gas Company.

### 2.2. Experimental procedure

In a typical experiment, there were three basic steps to fabricate the POM/SWCNTs nanocomposites. First, POM (0.5 mg) solution was dissolved in HAc (3 g) at the suitable temperature (80 °C, 90 °C) close to the crystallization temperature of POM. SWCNTs (0.5 mg) were unbundled in HAc (2 g) and the mixture was ultrasonicated for 1 h at 45 °C before being added to the prepared POM solution. Second, the hybrid solution was transferred into the SC CO<sub>2</sub> apparatus as quickly as possible, to reach the determined conditions of temperature and pressure. Third, it was the crystallization process and the crystallization time was controlled for 3 h. At last, CO<sub>2</sub> was slowly released to atmospheric pressure and the sample obtained was collected and labelled.

The processing stabilities of POM/CNTs composites are investigated by differential scanning calorimetry and thermogravimetric analysis. The POM/CNTs composites are prepared as the following. The SWCNTs decorated (15 wt.%) is put into the POM solution and the mixture was ultrasonicated at 45 °C for 1 h. Then the mixture evaporated in a vacuum oven at the room temperature for 2 days. As a control test, we put the pristine SWCNTs (15 wt.%) into the POM solution with the same process and the obtained composite is used for the comparison.

### 2.3. Characterization methods

Field emission scanning electron microscopy (SEM JEOL JSM-6700F) and transmission electron microscopy (TEM FEI Tecnai G<sup>2</sup> 20) were used to observe the morphologies and microstructures of the decorated CNTs. Structural parameters of SWCNTs were characterized by IR spectra and Raman spectroscopy, respectively. IR spectra were acquired using a TENSOR 27 FTIR spectrometer (Bruker) in the absorption mode with 32 scans at a resolution of 2 cm<sup>-1</sup> intervals. Raman spectra were collected on a Renishaw Microscope System RM 2000 at room temperature at 514.5 nm laser excitation. Spectra were collected at various locations for each sample studied to determine reproducibility. Differential Scanning Calorimetry (DSC) was carried out using TA-Q100 at a heating and cooling rate of 10 °C/min under a nitrogen atmosphere. Samples of ~2 mg each were encapsulated in aluminum pans and sealed. A consecutive heating sequence was followed at a rate of 10 K/min from 40 °C to 180 °C. For thermogravimetric analysis (TG/TDA 300), a sample weighing about 5 mg was measured in the dynamic mode at a heating rate of 10 K/min from 25 °C to 300 °C.

## 3. Results and discussion

### 3.1. Microstructures of POM/SWCNTs nanocomposites

In our previous study, we developed a facile and efficient method for decorating CNTs using the supercritical CO<sub>2</sub> antisolvent-induced polymer epitaxy (SAIPE) method. In this study, the SAIPE method is

used to help to build a nanohybrid structure of POM wrapping on SWCNTs. The SWCNTs that are considered as the role of catalyst are added into the POM solution, it can decrease the potential energy for nucleation due to the external surface of SWCNTs to encourage the polymer to crystallize on it [33]. The compatibility of SC CO<sub>2</sub> and HAC is much better than that of SC CO<sub>2</sub> and POM system. Therefore, SC CO<sub>2</sub> is considered as the antisolvent for POM in the POM/HAC/SC CO<sub>2</sub> system. This process can be described as follows. When CO<sub>2</sub> is injected into the POM/SWCNTs/HAC system, the phenomenon of phase separation can be observed because of the degree of reduced viscosity and surface tension of the HAC-rich phase becoming higher and the liquid phase is expanded gradually, which can lead to POM molecules separated out of the supersaturated solution successively. Further POM molecules can be adsorbed on the surface of SWCNTs.

The presence of POM coating on CNT is evident from the SEM images of the composites (Fig. 1). For supercritical fluid, experimental pressure has an important effect on the solvent power, and the variation of experimental pressure can be regarded as a typical outside effect [18]. Therefore, we are very interesting to investigate the effect of SC CO<sub>2</sub> on the induced POM crystallization and decoration on SWNTs. We changed the experimental pressure of SC CO<sub>2</sub> from 11 MPa to 13 MPa and 15 MPa with the fixed concentration of POM at 0.01 wt.% and CNTs concentration at 0.01 wt.%. When the experimental temperature is 80 °C, the obtained results with TEM characterization are shown in Fig. 2. As marked by the arrows in Figure a<sub>2</sub>, b<sub>2</sub> and c<sub>2</sub>, the surface of CNTs or CNT bundles are coated

by POM lamellae. With the increase of SC CO<sub>2</sub> pressure to 15 MPa, SC CO<sub>2</sub> enhances the diffusivity of the polymers and facilitates the growth of POM chains near the entanglement area, and the wrapping walls can be found thicker at 15 MPa compared to that at 11 MPa. In addition, when the pressure increases to 15 MPa, we even can observe the polymer nanocrystals as we observed in our previous study [21]. At the same experimental temperature, the volume of the liquid phase at 15 MPa is more expanded due to the dissolution of more CO<sub>2</sub>, and the density and the solvent power of HAC-rich phase decrease more. The polymer chains may prefer to undergo transition from a loose coil to a dense globule so as to minimize polymer–solvent interactions in the poorer solvent [33].

We also find a tendency that the modified effect becomes better from 11 MPa to 15 MPa at 90 °C (Fig. 3). Apparently at 11 MPa, the CNTs cannot be wrapped perfectly and totally, when the CO<sub>2</sub> pressure increases to 15 MPa, a more complete wrapping on CNT bundles is observed, and also the POM nanocrystals can be observed. Since from the microstructure, we can observe the better decoration of CNTs with POM at higher CO<sub>2</sub> pressure, we are very interesting if these CNTs obtained at higher CO<sub>2</sub> pressure have more excellent dispersion? Our experimental results shown in Figs. 4 and 5 confirm it is. We can see that the pristine CNTs subsided at the bottom of the bottle (Figs. 4 and 5a), however, the modified SWCNTs are dispersed in the solvent. No matter at 80 °C or 90 °C, the CNTs decorated at 15 MPa indeed has the better dispersion. This indicates that the perfect modification on CNTs can help the excellent dispersion of CNTs in the solution.

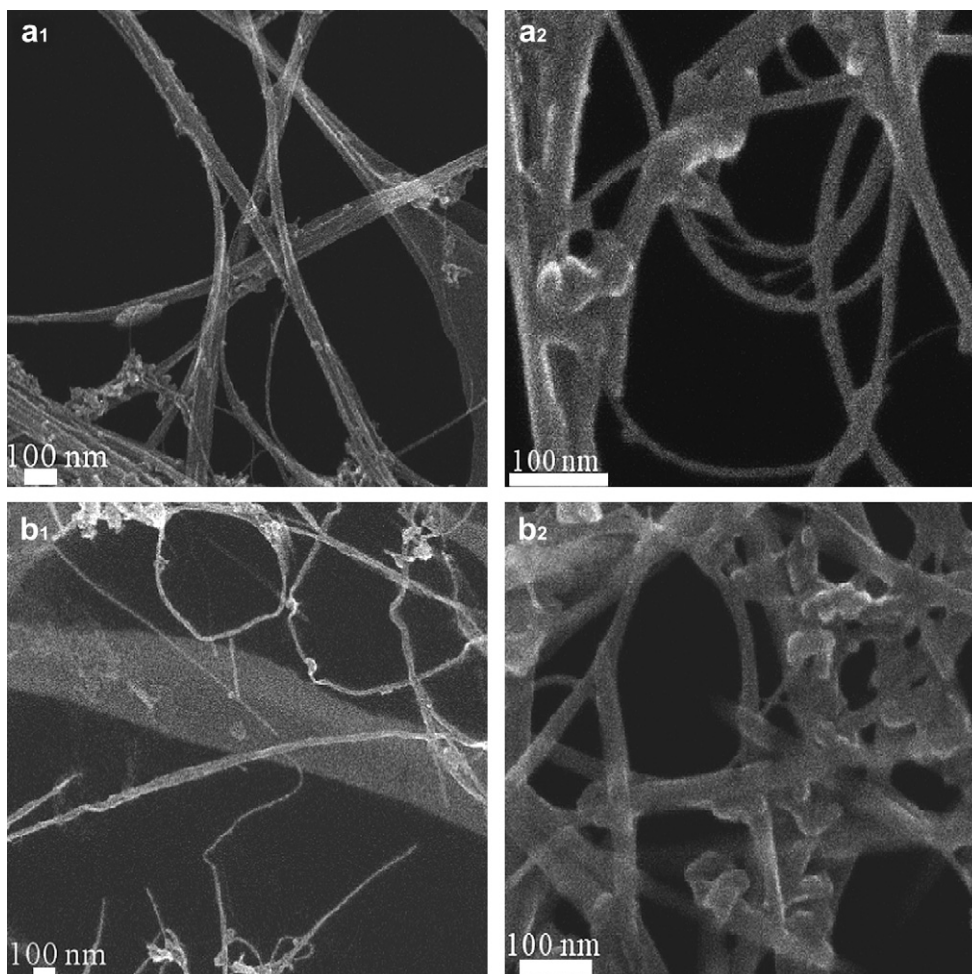
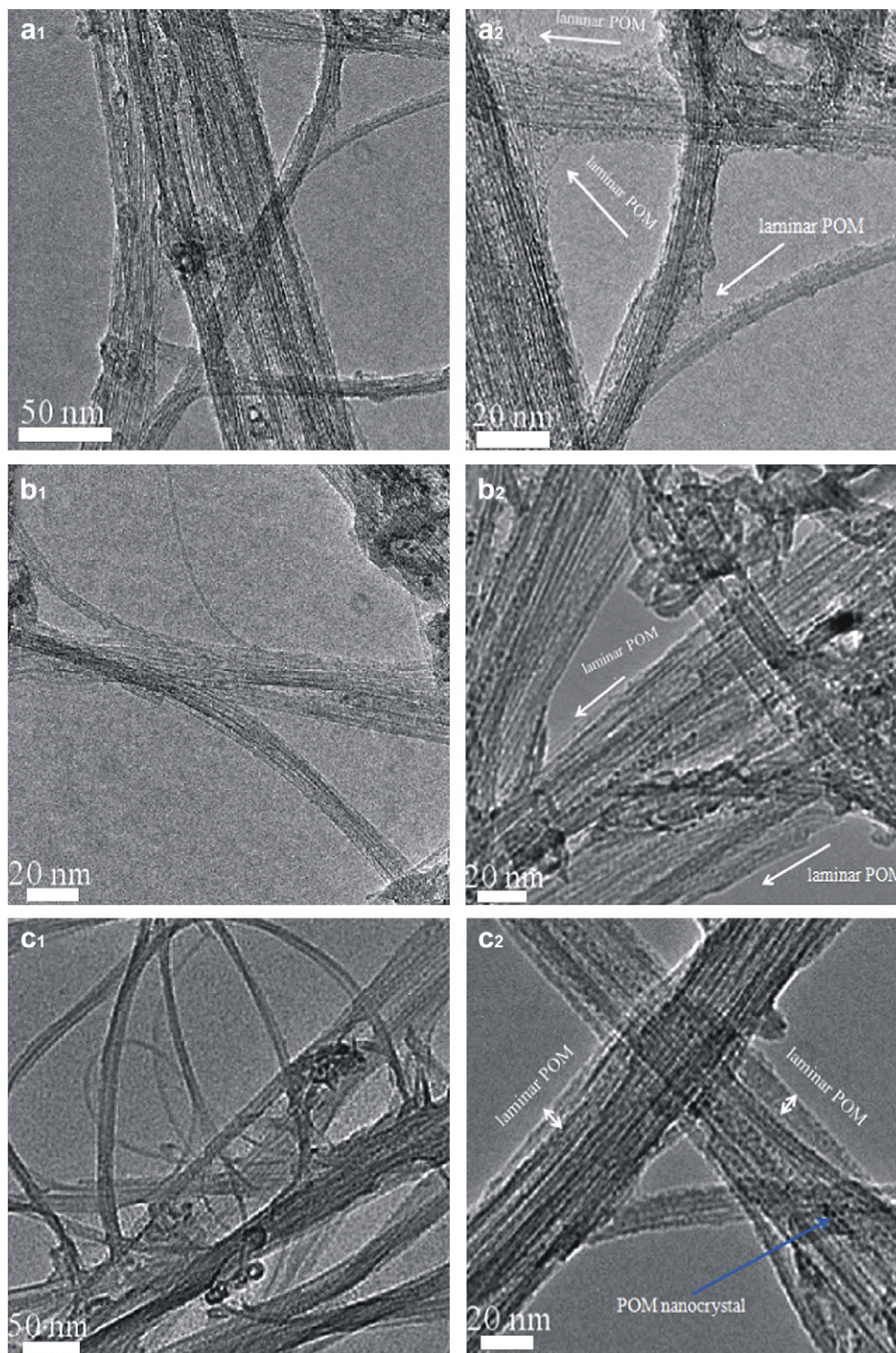


Fig. 1. SEM images of the SWCNTs decorated with POM at 80 °C for 3 h, with different CO<sub>2</sub> pressure: (a) 13 MPa and (b) 15 MPa.



**Fig. 2.** TEM images of the SWCNTs decorated with POM at 80 °C for 3 h, but with different experimental pressures: (a) 11 MPa, (b) 13 MPa and (c) 15 MPa.

### 3.2. Interaction analysis between CNTs and POM

Adsorption could occur from molecular interactions between carbon–hydrogen groups (CH groups) and  $\pi$  systems and the existence of CH– $\pi$  interactions has been known for several years [34]. Klopman has classified the CH– $\pi$  interactions as a soft acid/soft base interaction using orbital energy data [35]. Although the strength of CH– $\pi$  interactions have been considered as only one-tenth of the hydrogen bond, their cooperative multiple interactions

significantly could influence many chemical and biochemical phenomena [36]. Furthermore, Baskaran et al. have used the FTIR and Raman spectra of the composites to show the evidence for the presence of CH group interactions with MWCNTs. Although the intermolecular CH– $\pi$  interaction was weak, its effect on the dissolution of CNTs in organic solvent was very apparent [34].

In an attempt to confirm what kind of interaction between POM and SWCNT bundles, the composite mixtures are subjected to FTIR analysis and the results are presented in Fig. 6. For the pristine POM

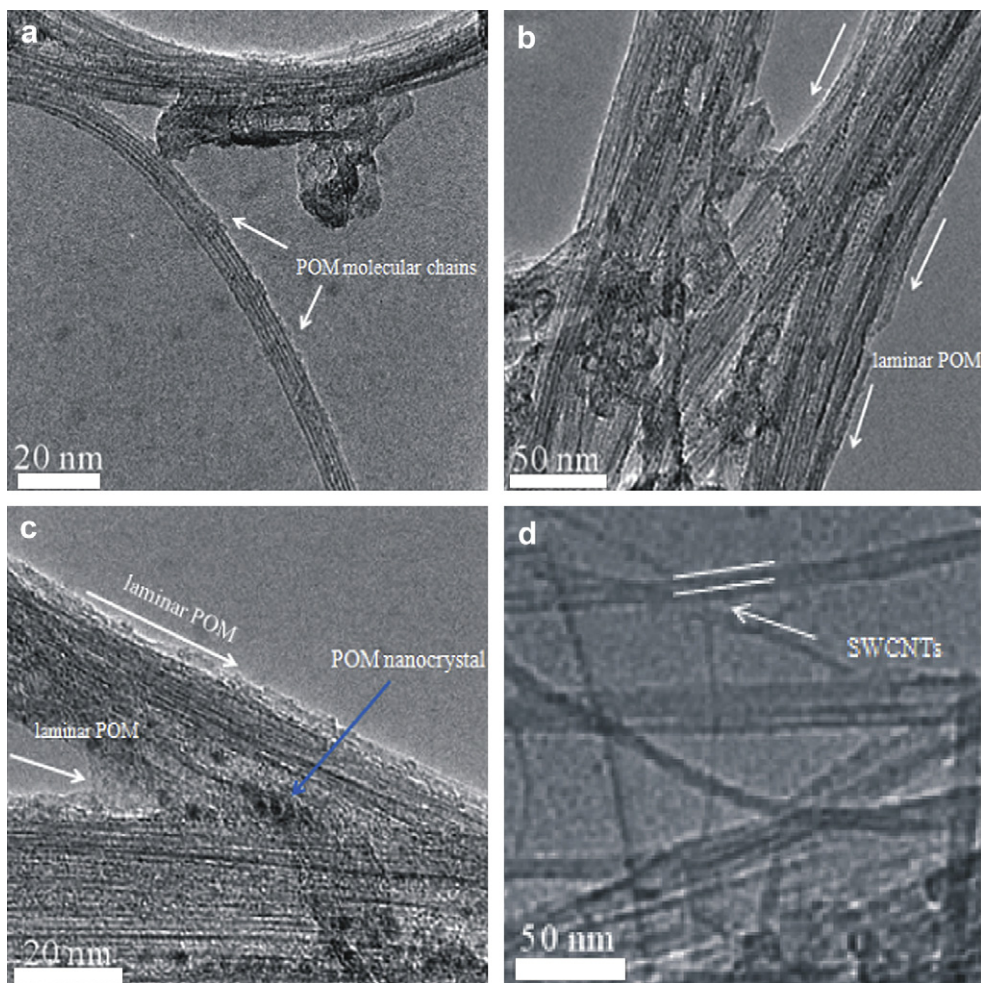


**Fig. 3.** TEM images of the SWCNTs decorated with POM at 90 °C for 3 h, but with different experimental pressures: (a) 11 MPa, (b) 13 MPa and (c) 15 MPa and (d) the pristine SWCNTs.

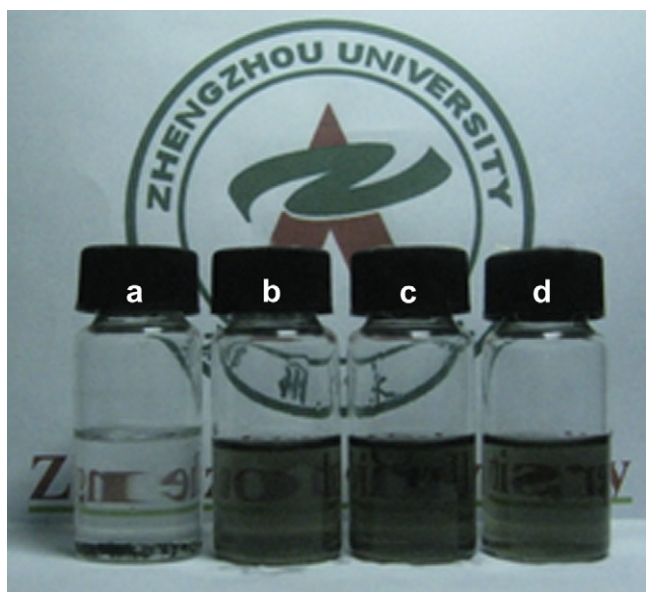


**Fig. 4.** Photographs of four different samples: (a) SWCNTs/HAc mixture after sonification; SWCNTs decorated with POM in HAc at different SC CO<sub>2</sub> pressures: (b) 11 MPa, (c) 13 MPa and (d) 15 MPa at 80 °C for 3 h.

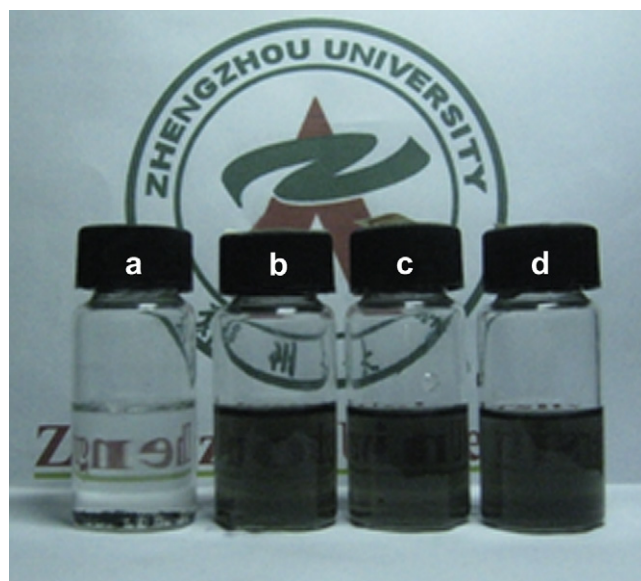


**Fig. 5.** Photographs of four different samples: (a) SWCNTs/HAc mixture after sonification; SWCNTs decorated with POM in HAc at different SC CO<sub>2</sub> pressures: (b) 11 MPa, (c) 13 MPa and (d) 15 MPa at 90 °C for 3 h.

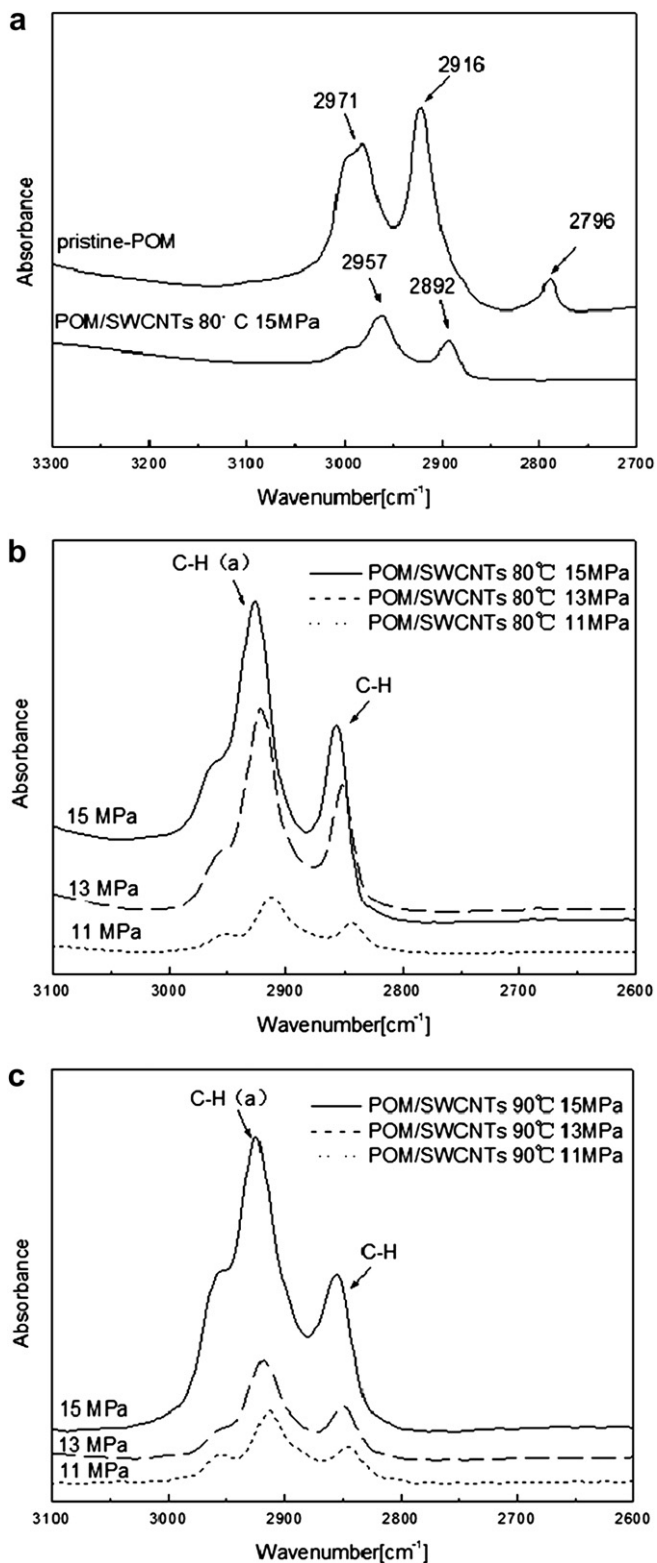


**Fig. 6.** FTIR spectra of pristine POM and pristine SWCNTs (a) and POM-decorating SWCNTs using HAC as solvent at different SC CO<sub>2</sub> pressures of 11 MPa, 13 MPa and 15 MPa at 80 °C (b) and 90 °C (c) for 3 h.

(Fig. 6a), the peak at 2971 cm<sup>-1</sup> is due to the antisymmetric stretching vibration band of C–H, and the peak at 2916 cm<sup>-1</sup> and 2796 cm<sup>-1</sup> are owing to the symmetric stretching vibration band of C–H. Obviously there are two differences between pristine POM and

POM/SWCNTs nanocomposites. On the one hand, a very significant shift to lower wavenumber from pristine POM to POM/SWCNTs nanocomposites can be observed. On the other hand, the intensity of C–H antisymmetric stretching vibration band of pristine POM is smaller than the symmetric stretching vibration band of C–H, however, the intensity of C–H antisymmetric stretching vibration band of POM/SWCNTs nanocomposites is higher than the symmetric stretching vibration band of C–H. So it is suggested that the relative intensity of them can reflect the presence of interactions of C–H groups in the POM/SWCNTs nanocomposites. Baskaran et al. think the presence of interactions of C–H groups in the POM/SWCNTs nanocomposites can shift the frequency of the C–H stretching vibration of the POM to the low wavenumber [34]. Fig. 6b shows the FTIR spectra of POM/SWCNTs nanocomposites prepared under different SC CO<sub>2</sub> pressure, but at the same temperature of 80 °C. When the pressure is as low as 11 MPa, the absorption intensity of C–H antisymmetric stretching vibration and symmetric stretching vibration bands of POM/SWCNTs nanocomposites are very weak due to only a few of POM molecules decorating on SWCNTs. With the increase of pressure, the C–H antisymmetric stretching vibration and symmetric stretching vibration bands ascribed to POM are higher, confirming that more POM molecules are decorated on the surface of SWCNTs and the stronger non-covalent interactions between POM molecules and SWCNTs under the higher SC CO<sub>2</sub> pressure. We also can find the same inclination at the Fig. 6c, which are the FTIR spectra of POM/SWCNTs nanocomposites prepared under different SC CO<sub>2</sub> pressure at 90 °C.

Raman spectroscopy (RS) is convenient for both the qualitative and quantitative analysis of multi-component mixtures without degradation of the samples. RS has the advantage of using a selected monochromatic laser beam which may be focused precisely and selectively over any part of a solid sample, which may consist of different components [37]. A common feature of CNTs when dispersed or embedded in polymers is often the arrangement in various directions [38–40]. Fig. 7 shows the Raman spectra of pristine SWCNTs and the POM-decorated SWCNTs in SC CO<sub>2</sub>, at the temperature of 80 °C for 3 h, the results are recorded on a confocal Raman spectrometer using the laser excitation at 514.5 nm. All carbon forms contribute to the Raman spectra in the range from 1000 cm<sup>-1</sup> to 1700 cm<sup>-1</sup>. The observation of the characteristic peak features around 1580 cm<sup>-1</sup> provides a signature of CNTs [37], typically giving rise to a two-band feature with two peaks named the D-band around 1345.2 cm<sup>-1</sup> and G-band around 1586.1 cm<sup>-1</sup> in

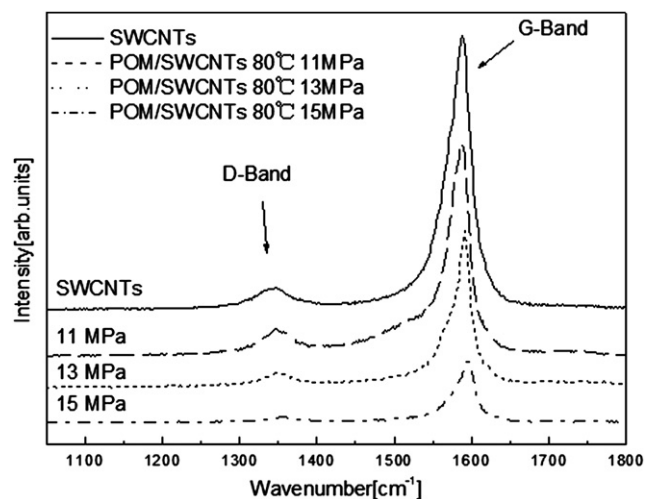


**Fig. 7.** Raman spectra of pristine SWCNTs and POM-decorated SWCNTs using HAC as solvent at 80 °C for 3 h, with different SC CO<sub>2</sub> pressures: 11 MPa, 13 MPa and 15 MPa.



**Table 1**

D- and G- bands shifts and Raman  $I_D/I_G$  intensity ratios of pristine SWCNTs and POM-decorating SWCNTs using HAC as solvent at 80 °C, with different SC CO<sub>2</sub> pressure of 11 MPa, 13 MPa and 15 MPa.

	D-Band(cm <sup>-1</sup> )	G-Band(cm <sup>-1</sup> )	$I_D/I_G$
SWCNTs	1345.2	1586.1	0.0425
POM/SWCNTs 80 °C 11 MPa	1346.3	1586.8	0.0624
POM/SWCNTs 80 °C 13 MPa	1349.3	1589.7	0.0651
POM/SWCNTs 80 °C 15 MPa	1351.7	1591.2	0.0687

the first-order Raman spectra of SWCNTs. The D-band is activated in the first-order scattering process of sp<sup>2</sup> carbons by the presence of in-plane substitutional hetero-atoms, vacancies, grain boundaries or other defects and by finite size effects, all of which lower the crystalline symmetry of the quasi-infinite lattice [41]. The G-band is attributed to sp<sup>2</sup>-hybridized carbon (C=C) [42]. Athalin et al. have investigated the two most intense G peaks of SWCNTs, G<sup>+</sup> at 1592 cm<sup>-1</sup> assigned to semiconducting and 1587 cm<sup>-1</sup> assigned to metallic, for atomic displacements along the tube axis. The G peak at 1570 cm<sup>-1</sup> was assigned to semiconducting and at 1550 cm<sup>-1</sup> assigned to metallic, for modes with atomic displacement along the circumferential direction [37].

The intensity of the G and D bands of SWCNTs in the POM-decorating SWCNTs composites has a tendency to diminish with the increasing pressure of SC CO<sub>2</sub> (Fig. 7). There are some shifts in G-band and D-bands peaks to higher wavenumber with the increasing pressure of SC CO<sub>2</sub> from 11 MPa to 13 and 15 MPa at 80 °C. We could also find this tendency in Table 1 that provides the details. Both the G and D bands of SWCNTs in the POM-decorating SWCNTs composites prepared at SC CO<sub>2</sub> pressure of 15 MPa are broad and shift of ~3.6 and ~6.5 cm<sup>-1</sup>, respectively, compared to the pristine SWCNTs. With the increase of CO<sub>2</sub> pressure, more POM molecules can be separated out of the organic solvent, due to the antisolvent effect of the SC CO<sub>2</sub>. The higher concentration of POM in the composites increases the probability of polymer coverage on SWCNTs' surface, which affects the vibration movements of C–C bands on the SWCNTs due to CH–π interactions [34]. The extent of vibration frequency shifting in these composites should depend on the proportions of different types of C–H interactions between polymer molecules and the SWCNTs. In the composites, the molecular interactions associated with different vibration modes (C–H antisymmetric stretching vibration and symmetric stretching

**Table 2**

D- and G- bands shifts and Raman  $I_D/I_G$  intensity ratios of pristine SWCNTs and POM-decorating SWCNTs using HAC as solvent at 90 °C, with different SC CO<sub>2</sub> pressure of 11 MPa, 13 MPa and 15 MPa.

	D-Band(cm <sup>-1</sup> )	G-Band(cm <sup>-1</sup> )	$I_D/I_G$
SWCNTs	1345.2	1586.1	0.0425
POM/SWCNTs 90 °C 11 MPa	1347.8	1586.3	0.0604
POM/SWCNTs 90 °C 13 MPa	1349.3	1586.9	0.0613
POM/SWCNTs 90 °C 15 MPa	1352.2	1591.2	0.0652

vibration bands) are heterogeneous in nature and hence overall average frequency changes are attributed to the total effect of CH–π interactions.

In addition, the  $I_D/I_G$  ratio is defined as the intensity ratio of the D-band to G-band of CNTs and directly indicates the structure changes of CNTs [43]. As listed in Table 1, the  $I_D/I_G$  ratio of pristine SWCNTs is 0.0425, furthermore, the  $I_D/I_G$  ratio of the POM-decorating SWCNTs tends to be higher with the increasing pressure of SC CO<sub>2</sub>. The tendency is in accord with the results reported by Athalin [37] and Yang [43]. Athalin et al. have demonstrated that the  $I_D/I_G$  value increased with increasing disorder and with decreasing crystallite size for each CNT component. Yang et al. have thought that the enhancement of the  $I_D/I_G$  ratio was attributed to the increase in sp<sup>3</sup>-hybridized sidewall carbons by the functionalization. We can also find the similar trend in Fig. 8 and Table 2, which are the Raman spectra of POM/SWCNTs nanocomposites prepared under different SC CO<sub>2</sub> pressure at 90 °C.

### 3.3. Thermal stability of POM-decorating SWCNTs in POM matrix

It is well-known that POM has a strong tendency to crystallize. The size of the spherulites of POM may be reduced by following the principle of mixing the POM with some nucleating agents [44]. Some inorganic fillers such as glass fibers, clay, carbon black, etc., which are incorporated into polymer matrix, usually act as nucleation agents to accelerate crystallization. Compared to conventional carbon fibers or glass fibers, carbon nanotubes filled polymer composites are easily processed due to their small diameters. Among the most versatile polymers, CNTs provide the great opportunities for designing new multifunctional materials with broad industry applications [32]. We are very interesting to investigate the thermal

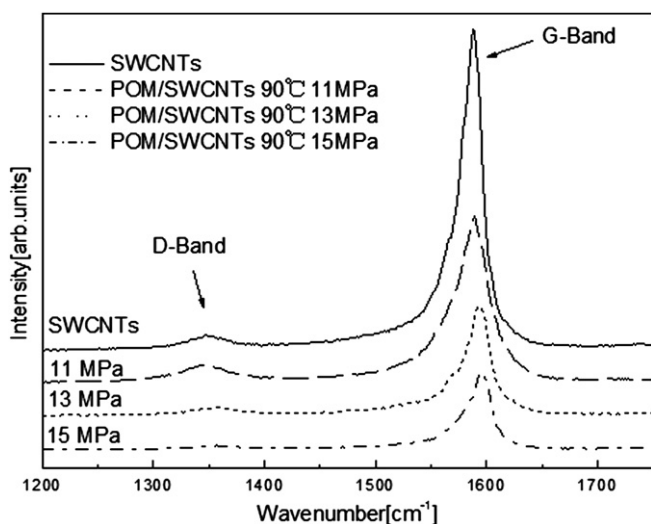


Fig. 8. Raman spectra of pristine SWCNTs and POM-decorating SWCNTs using HAC as solvent at 90 °C for 3 h, with different SC CO<sub>2</sub> pressures: 11 MPa, 13 MPa and 15 MPa.

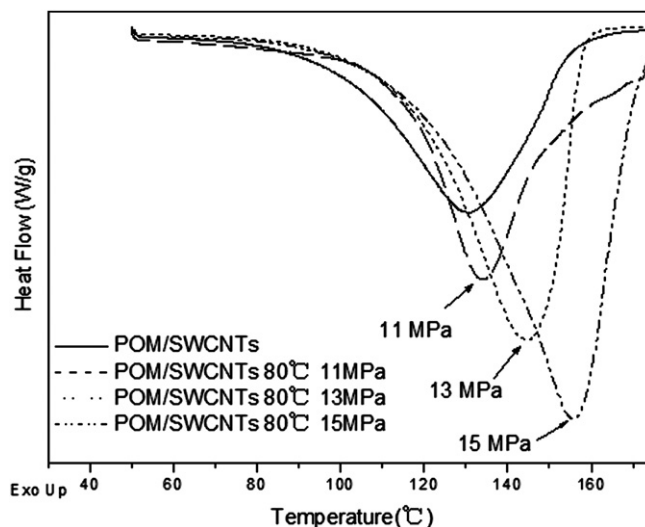
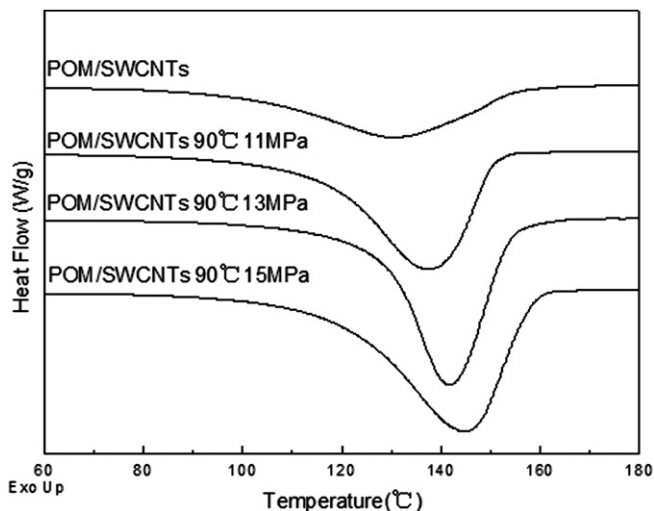


Fig. 9. DSC heating scans for POM samples with pristine SWCNTs and POM-decorating SWCNTs obtained at 80 °C for 3 h, with different SC CO<sub>2</sub> pressures: 11 MPa, 13 MPa and 15 MPa.



**Fig. 10.** DSC heating scans for POM samples with pristine SWCNTs and POM-decorated SWCNTs at 90 °C for 3 h, with different SC CO<sub>2</sub> pressures: 11 MPa, 13 MPa and 15 MPa.

stability of the nanocomposites, which depends on the interfaces between the CNTs and the surrounding polymer matrix. Especially considering the problem is more acute for CNTs, because their interfacial area is very huge due to their tiny size.

DSC analysis is generally one of the most convenient methods for analyzing crystallization and melting of crystalline polymers [45], which are the reflection of the thermal stability of composites. Two kinds of nanocomposites (pristine SWCNTs and SWCNTs decorated with POM) samples with varying preparation conditions were subjected to DSC analysis under non-isothermal conditions. An exciting phenomenon shown in Figs. 9–11 can be observed. Apparent  $T_m$  of the nanocomposite increases with the decorated SWCNTs as the filler compared with pristine SWCNTs used as the filler. And the  $T_m$  of samples with the decorated SWCNTs is progressively increased as the pressure of SC CO<sub>2</sub> increases in their preparation processes (Table 3). Fig. 11 shows the TGA thermograms of POM samples with pristine SWCNTs and POM-decorating SWCNTs as the fillers, respectively. The thermal degradation temperature of POM samples with the decorated SWCNTs is higher than that with pristine SWCNTs as the filler. Combining the experimental results (Figs. 2–5) and the discussion about the relation of modification of CNTs and

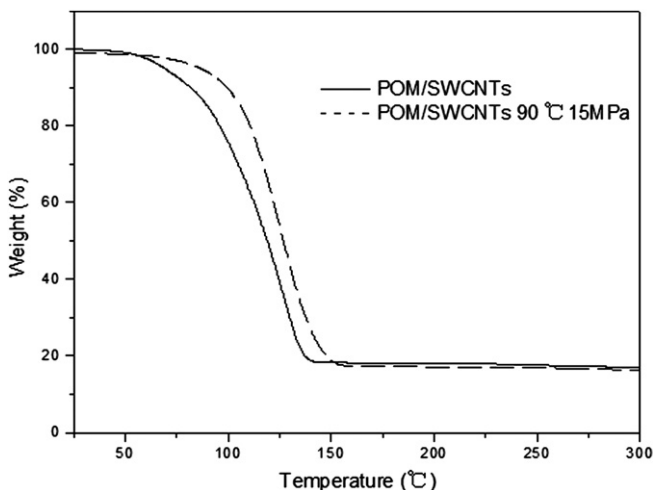


**Fig. 11.** TGA thermograms of POM samples with pristine SWCNTs and POM-decorating SWCNT at SC CO<sub>2</sub> pressures: 15 MPa and 90 °C for 3 h.

**Table 3**

The melting temperatures of POM samples with pristine SWCNTs and POM-decorating SWCNTs from Fig. 8.

	POM/SWCNTs	POM/SWCNTs 11 MPa	POM/SWCNTs 13 MPa	POM/SWCNTs 15 MPa
$T_m$ (°C)	130	134	144	155
$\Delta T_m$ (°C)	0	4	14	25

their dispersion, it is suggested that the perfect modification of CNTs can bring the excellent dispersion of CNTs, further can ensure the good mixing of CNTs and form a comparable homogenous dispersion throughout the matrix of POM, which is decisive for the improved stability of nanocomposites.

#### 4. Conclusions

In this study, we have further developed the supercritical CO<sub>2</sub> antisolvent method to help a highly crystalline linear thermoplastic – POM, to precipitate and decorate on SWCNTs and further fabricate the functional nanocomposites of the POM/SWCNTs. It is found that the SWCNTs are covered by laminar POM with the thicknesses of a few nanometers. FTIR and Raman spectra indicate the presence of CH group interactions with CNTs and the excellent POM-decorating on CNTs are due to the CH– $\pi$  interactions. There is a tendency for the melting points of POM samples to rise; the higher the pressure of SC CO<sub>2</sub>, the better the modification of POM-decorating on CNTs. Moreover, the thermodynamic stability of POM samples with the decorated CNTs as the fillers are apparently higher than that with pristine CNTs as the fillers. Therefore, this work not only provides the possibilities of fabricating POM/SWCNTs nanocomposites with the assistance of SC CO<sub>2</sub>, but also illustrates the vital effect of surface modification of CNTs on the processability during the fabrication of CNTs-filled polymer composites. So combining the properties of SC CO<sub>2</sub> and POM into one system is a novel field and it may lead to the development of new multifunctional materials, for instance, preparation of conducting nanocomposites at low CNTs loading.

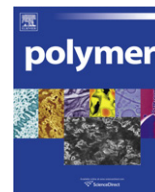
#### Acknowledgements

We are grateful for the National Natural Science Foundation of China (No. 20974102, 50955010), the financial support from the Program for New Century Excellent Talents in Universities (NCET) and from the Ministry of Personnel of China.

#### References

- [1] Baughman RH, Zakhidov AA, Heer WA. *Science* 2002;297:787–92.
- [2] Vigolo B, Coulon C, Maugey M, Zakri C, Poulin P. *Science* 2005;309:920–3.
- [3] Gao C. *Macromol Rapid Commun* 2006;27:841–7.
- [4] Iijima S. *Nature* 1991;354:56–8.
- [5] Moniruzzaman M, Winey KI. *Macromolecules* 2006;39:5194–250.
- [6] Kim JA, Seong DG, Kang TJ, Youn JR. *Carbon* 2006;44:1898–905.
- [7] Kuila BK, Malik S, Batabyal SK, Nandi AK. *Macromolecules* 2007;40:278–87.
- [8] Urugami T, Katayama T, Miyata T, Tamura H, Shiraiwa T, Higuchi A. *Bio-macromolecules* 2004;5:1567–74.
- [9] Tasis D, Tagmatarchis N, Bianco A, Prato M. *Chem Rev* 2006;106:1105–36.
- [10] Liu ZM, Han BX. *Adv Mater* 2009;21:825–9.
- [11] Khlobystov AN, Britz DA, Wang J, O’Neil AS, Poliakov M, Briggs GA D. *J Mater Chem* 2004;14:2852–7.
- [12] Desimone JM. *Science* 2002;297:799–803.
- [13] Kendall JL, Canelas DA, Young JL, DeSimone JM. *Chem Rev* 1999;99:543–63.
- [14] Johnston KP, Shah PS. *Science* 2004;303:482–3.
- [15] Eckert CA, Knutson BL, Debenedetti PG. *Nature (London)* 1996;383:313–8.
- [16] Dai XH, Liu ZM, Han BX, Sun ZY, Wang Y, Xu J, et al. *Chem Commun* 2004; 19:2190–1.
- [17] Tomasko DL, Li H, Liu D, Han X, Wingert MJ, James Lee L, et al. *Ind Eng Chem Res* 2003;42:6431–56.
- [18] Li ZP, Guan HT, Yu N, Xu Q, Imae I, Wei JY. *J Phys Chem C* 2010;114:10119–25.
- [19] Yue J, Xu Q, Zhang ZW, Chen ZM. *Macromolecules* 2007;40:8821–6.

- [20] Zhang ZW, Xu Q, Chen ZM, Yue J. *Macromolecules* 2008;41:2868–73.
- [21] Zhang F, Zhang H, Zhang ZW, Chen ZM, Xu Q. *Macromolecules* 2008;41:4519–23.
- [22] He LH, Zheng XL, Xu Q. *J Phys Chem B* 2010;114:5257–62.
- [23] Goossens S, Groeninckx G. *Macromolecules* 2006;39:8049–59.
- [24] Girard-Reydet E, Sautereau H, Pascault JP, Keates P, Navard P, Thollet G, et al. *Polymer* 1998;39:2269–80.
- [25] Hasegawa S, Takeshita H, Yoshii F, Nishimoto S. *Polymer* 2000;41:111–20.
- [26] Hisakatsu H, Kohji T. *Polymer* 2003;44:3107–16.
- [27] Li LY, Li CY, Ni CY. *J Am Chem Soc* 2006;128:1692–9.
- [28] Li LY, Li CY, Ni CY, Rong LX, Hsiao B. *Polymer* 2007;48:3452–60.
- [29] Li B, Li LY, Wang BB, Li CY. *Nat Nanotechnology* 2009;4:358–62.
- [30] Zeng Y, Ying Z, Du JH, Cheng HM. *J Phys Chem C* 2007;111:13945–50.
- [31] Zhao XW, Ye L. *J Polym Science Part B Polym Phys* 2010;48:905–12.
- [32] Sun TJ, Lai Y, Ye L, Zhao XW. *Polym Adv Technol* 2008;19:1286–95.
- [33] Zhang F, Xu Q, Zhang H, Zhang ZW. *J Phys Chem C* 2009;113:18531–5.
- [34] Baskaran D, Mays JW, Bratcher MS. *Chem Mater* 2005;17:3389–97.
- [35] Klopman G. *Am J Chem Soc* 1968;90:223–34.
- [36] Hirota M, Sakaibara K, Suezawa H, Yuzuri T, Ankai E, Nishio M. *J Phys Org Chem* 2000;13:620–3.
- [37] Athalin H, Lefrant S. *J Raman Spectrosc* 2005;36:400–8.
- [38] Jin ZX, Sun X, Xu GQ, Goh SH, Ji W. *Chem Phys Lett* 2000;318:505–10.
- [39] Kumar S, Doshi H, Srinivasarao M, Park JO, Schiraldi DA. *Polymer* 2002;43:1701–3.
- [40] Shaffer MSP, Windle AH. *Adv Mater* 1999;11:937–41.
- [41] Brown SDM, Jorio A, Dresselhaus MS, Dresselhaus G. *Phys Rev B* 2001;64:073403–6.
- [42] Price BK, Hudson JL, Tour JM. *J Am Chem Soc* 2005;127:14867–70.
- [43] Yang Q, Pan XJ, Huang F, Li KC. *J Phys Chem C* 2010;114:3811–6.
- [44] Xu W, Ge M, He P. *J Appl Polym Sci* 2001;82:2281–9.
- [45] Pracella M, Chionna D, Fina A, Tabuani D, Frache A, Camino G. *Macromol Symp* 2006;234:59–67.



## Solubility of neutral and charged polymers in ionic liquids studied by laser light scattering

Ye Chen<sup>a,b</sup>, Yumei Zhang<sup>a</sup>, Fuyou Ke<sup>b</sup>, Jihan Zhou<sup>b</sup>, Huaping Wang<sup>a,\*\*</sup>, Dehai Liang<sup>b,\*</sup>

<sup>a</sup> State Key Laboratory for Modification of Fiber Materials, College of Material Science and Engineering, Donghua University, Shanghai 201620, China

<sup>b</sup> Beijing National Laboratory for Molecular Sciences and the Key Laboratory of Polymer Chemistry and Physics of Ministry of Education, College of Chemistry and Molecular Engineering, Peking University, Beijing 100871, China

### ARTICLE INFO

#### Article history:

Received 19 August 2010

Received in revised form

28 October 2010

Accepted 20 November 2010

Available online 26 November 2010

#### Keywords:

Ionic liquids

Neutral polymers

Charged polymers

### ABSTRACT

The solubility and chain conformation of different types of homopolymers in low viscosity ionic liquids (ILs), 1-allyl-3-methylimidazolium chloride ([AMIM][Cl]) at 50 °C and 1-butyl-3-methylimidazolium formate ([BMIM][COOH]) at 25 °C, were studied by laser light scattering (LLS). For neutral polymers, such as polyvinyl alcohol and polysulfonamide, aggregation occurred in all the cases except for polyvinyl alcohol in [BMIM][COOH]. For negative polyelectrolytes, such as DNA and polystyrene sulfonate, single chain conformation was observed. However, the hydrodynamic radius of both polymers was much smaller than that in good solvents, suggesting that the chains were condensed. Cellulose was soluble in [AMIM][Cl], and non-diffusive mode was observed by dynamic light scattering. Zeta potential analysis indicated that cellulose exhibited the feature of polyelectrolyte. The solubility of homopolymers could be qualitatively explained by treating polymer/IL as a ternary system: polymer, cation, and anion. It was the mutual interactions determined the solubility and conformation of polymers in ILs.

© 2010 Elsevier Ltd. All rights reserved.

### 1. Introduction

Ionic liquids (ILs) are usually composed of large organic cations and either inorganic or organic anions [1]. Compared with the traditional inorganic salts, most ILs are liquid under ambient conditions [2]. When used as solvents, ILs have many distinct advantages [3], such as extremely low volatility and toxicity, excellent thermal and chemical stability, high ionic conductivity and ease of recycling. ILs have found many practical applications in the fields of synthesis and catalysis [4,5], extraction and separation [6,7], crystallization [8], electrochemistry [9], and are considered as the potential “green solvents” for chemistry [10,11].

In the past decade, ILs also attract a great deal of attention in polymer science. On one hand, ILs are used as the media for several types of polymerization processes, [12,13] such as living radical polymerization, group transfer polymerization, and polycondensation. On the other hand, ILs are served as the solvents into which the polymer transformation or material processing to be carried out. It has been reported that ILs show good solubility to natural polymers and biopolymers, such as cellulose [14], chitin

[15], various polysaccharides [16], Bombyx mori silk [17], and wool keratin [18], most of which are insoluble in water or in conventional organic solvents. As for synthetic polymers, some of them, such as poly(ethylene oxide) (PEO) [19], poly(methyl methacrylate) [20], polyacrylonitrile [21], poly(m-phenylene isophthalamide) [22], and polyarylsulfone [23] are soluble in ILs. But most synthetic polymers, such as polyethylene, polyester, polyurethane, and nylon, have not found suitable ILs for dissolution.

ILs are different from water and conventional organic solvent to certain extent. Ueki and Watanabe [24] reported that poly(*N*-isopropylacrylamide) in 1-ethyl-3-methylimidazolium bis(trifluoromethane sulfone) imide [EMIM][NTf<sub>2</sub>] exhibited an upper critical solution temperature (UCST) behavior, in contrast to its typical lower critical solution temperature (LCST) behavior in aqueous solutions. He et al. [25] reported the micellization behavior of poly((1,2-butadiene)-block-ethylene oxide) (PB-PEO) in 1-butyl-3-methylimidazolium hexafluorophosphate ([BMIM][PF<sub>6</sub>]), as well as the temperature-induced transportation of PB-PEO between ILs and water [26]. Susan et al. proposed that the compatible IL and polymer binary systems form ion gels, in which the ion transport is decoupled from the segmental motion of the polymer [27].

Understanding the forces governing the solubility and solvation of polymers in ILs are still at early stage of development. Compared with molecular solvents, ILs combine strong Coulomb interactions

\* Corresponding author. Tel./fax: +86 10 62756170.

\*\* Corresponding author. Tel./fax: +86 21 67792958.

E-mail addresses: [wanghp@dhu.edu.cn](mailto:wanghp@dhu.edu.cn) (H. Wang), [dliang@pku.edu.cn](mailto:dliang@pku.edu.cn) (D. Liang).

and many other weak interactions, including hydrogen bonding, cation- $\pi$  interaction, van der Waals interactions and so on. The general principle of “like dissolves like” is not applied to polymer/IL systems [28]. The slow kinetics of dissolution, as well as the occurrence of phase separation [29] and gel formation [30], made the situation even more complicated. It is not an easy task to predict the factors responsible for polymer solubility in ILs [31].

Laser light scattering (LLS) is a powerful technique to study the solubility of polymers in ILs at low concentrations. However, LLS study on polymer/IL system is limited. On one hand, the viscosities of ILs are generally two or more orders higher than those of molecular solvents under similar conditions. The diffusion of polymer chains in IL is extremely slow. Sometimes it will take unrealistic long time to measure the time-averaged intensity–intensity correlation functions. On the other hand, it is difficult to remove all the impurities, including water, from ILs [1]. The amount of impurity is in the order of ~1% or more, higher than the polymer concentrations used in LLS. Moreover, the water content varies with time because of the hygroscopicity of ILs. It is difficult to determine the  $dn/dC$  values of polymers in ILs by conventional differential refractometer. Without  $dn/dC$  value, the weight-averaged molecular weight ( $M_w$ ) cannot be accurately determined by LLS.

In this work, we attempt to elucidate the solubility of different kinds of homopolymers in ILs by LLS. To bypass the above mentioned difficulties, we chose two ILs with relatively low viscosity, 1-allyl-3-methylimidazolium chloride ([AMIM][Cl]) and 1-butyl-3-methylimidazolium formate ([BMIM][COOH]). Their formulae are shown in Scheme 1. The chosen homopolymers form clear solutions in either or both ILs, and they are divided into three categories: (1) neutral polymers, including hydrophilic polyvinyl alcohol (PVA) and hydrophobic polysulfonamide (PSA); (2) polyelectrolytes, mainly including anionic polymers of DNA and sodium polystyrene sulfonate (PSS); and (3) cellulose. The polymer samples dissolved in [AMIM][Cl] are studied at 50 °C to alleviate the effect of high viscosity, while those samples in [BMIM][COOH] are studied at 25 °C. Our study focuses on the chain conformation of different polymers in ILs. The calculated  $dn/dC$  value is applied when the determination of  $M_w$  is necessary. Our study indicates that the solubility of polymers in ILs is quite different from that in water or organic solvents.

## 2. Experimental

### 2.1. Materials

PVA (98–99% hydrolyzed,  $M_w = 1.5\text{--}1.9 \times 10^5$ ), salmon testes DNA (~2000 bps), and PSS ( $M_w: 1.0 \times 10^6$ ) were purchased from Sigma–Aldrich (USA). PSA ( $4.0 \times 10^5$  determined by GPC) was provided by Shanghai Tanlon Fiber Co. (China). Scheme 1 shows the structure of PSA. All these polymers were used as received. The cotton cellulose with degree of polymerization (DP) about 2400

was received from Shandong Helon Co., Ltd (China) as a gift. It was vacuum-dried at 60 °C for 24 h to remove the moisture before use. [AMIM][Cl] was synthesized and purified by following a known procedure [32]. The purity of >97 wt% was determined by NMR spectroscopy. [BMIM][COOH] (98 wt%) was purchased from Shanghai Cheng Jie Chemicals Co.(China). Both ILs were dried in vacuum oven at 60 °C for 24 h before use. The physicochemical parameters of the ILs are listed in Table 1.

### 2.2. Laser light scattering

A commercial spectrometer from Brookhaven Instruments Corporation (BI-200SM Goniometer, Holtsville, NY) was used to perform both static light scattering (SLS) and dynamic light scattering (DLS) over a scattering angular range of 20–120°. A solid-state laser polarized at the vertical direction (CNI Changchun GXC-III, 532 nm, 100 Mw) was used as the light source, and a BI-TurboCorr Digital Correlator was used to collect and process data. In SLS measurements, the time-averaged excess scattered intensity at an angle  $\theta$ , also known as the Rayleigh ratio  $R_{vv}(q)$ , is related with the  $M_w$ , the Z-averaged root mean square radius  $R_g$ , the second virial coefficient  $A_2$ , and the scattering vector  $q$  as

$$\frac{HC}{R_{vv}(q)} \approx \frac{1}{M_w} \left( 1 + \frac{1}{3} R_g^2 q^2 \right) + 2A_2 C \quad (1)$$

where  $H = 4\pi^2 n^2 (dn/dc)^2 / (N_A \lambda_0^4)$  and  $q = (4\pi n / \lambda) \sin(\theta/2)$ , with  $N_A$ ,  $n$ ,  $(dn/dc)$  and  $\lambda_0$  being the Avagadro constant, the refractive index of the solvent, the specific refractive index increment of the solution, and the wavelength of light in vacuum, respectively. The  $dn/dC$  value is calculated according to  $dn/dC = (n - n_0) / \rho$  [33], with  $n_0$ ,  $n$  and  $\rho$  being the refractive index of ionic liquid, the refractive index of polymer, and the density of polymer, respectively. Other physicochemical parameters used in this work are listed in Table S1.

In DLS, the intensity–intensity time autocorrelation function  $G^{(2)}(t, \theta)$  was measured in the self-beating mode. It is related with the normalized first order electric field time correlation function  $g^{(1)}(t, \theta)$  as  $G^{(2)}(t, \theta) = A [1 + \beta |g^{(1)}(t, \theta)|^2]$ , where  $A$  is the measured base line,  $\beta$  is a spatial coherence factor,  $t$  is the delay time, and  $\theta$  is the scattering angle.  $G^{(1)}(t, \theta)$  is further related to the line width distribution  $G(\Gamma)$ . By using a Laplace inversion program, CONTIN [34], the normalized distribution function  $G(\Gamma)$  of the characteristic line width is obtained. The line width  $\Gamma$  is a function of both concentration  $C$  and scattering vector  $q$ , which can be expressed as

$$\Gamma/q^2 = D_0(1 + k_d C) [1 + f(R_g q)^2] \quad (2)$$

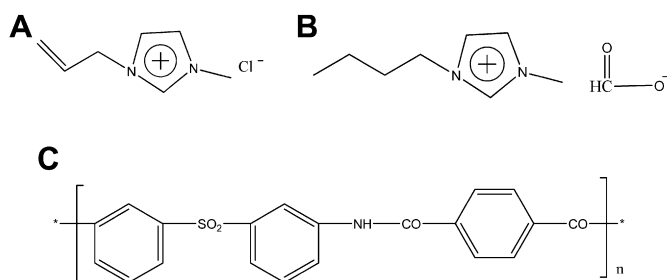
with  $D_0$ ,  $k_d$ ,  $f$  being the translational diffusive coefficient, the diffusion second virial coefficient, and a dimensionless constant, respectively.  $D_0$  can be further converted into the hydrodynamic radius  $R_h$  by using the Stokes–Einstein equation

$$D_0 = \frac{k_B T}{6\pi\eta R_h} \quad (3)$$

where  $k_B$ ,  $T$ ,  $\eta$  are the Boltzmann constant, the absolute temperature, and the viscosity of the solvent, respectively. The viscosities of the ILs at corresponding temperature were measured by a stress-

**Table 1**  
physicochemical parameters of ILs.

ILs	Viscosity/cP	Refractive index	Conductivity/(mS.cm <sup>-1</sup> )
[AMIM][Cl] at 50 °C	120	1.540	1.35
[BMIM][COOH] at 25 °C	38	1.478	14.6



**Scheme 1.** Chemical structures of (A) [AMIM][Cl], (B) [BMIM][COOH], and (C) PSA.

controlled rheometer (physica MCR301, Anton Paar Company, Austria). The values are listed in Table 1.

The concentration of the polymer solution is ranged from 0.2 mg/mL to 5.0 mg/mL. Each polymer with known amount was dissolved in IL and stored in vacuum oven at 25 °C until the solution become homogeneous. To facilitate the dissolution of polymers in [AMIM][Cl], the oven temperature was initially set at 80 °C. Once the solution became clear, the temperature decreased to 25 °C. Only those samples without phase separation in at least two weeks after temperature drop were studied by LLS. If the solution became cloudy, we considered the polymer was not soluble in [AMIM][Cl]. The dust in solution was removed by filtration through a 0.45  $\mu\text{m}$  Millex filter (Nylon membrane, Millipore, USA).

### 2.3. Zeta potential analysis

The charge carried by polymers in ILs was determined by the Zeta PALS  $\zeta$ -potential Analyzer (Brookhaven Instruments Corporation, USA). Three single runs of three cycles were taken. The data was analyzed by BIC PALS zeta potential analyzer software palsw32 (ver.3.43).

## 3. Results and discussion

To clarify the solubility of polymers in ILs, we firstly study the behavior of ILs themselves by LLS, and then conduct a detailed study on each of the polymers following the order of neutral polymer, charged polymer and cellulose. On the basis of the obtained results, we propose a qualitative dissolution mechanism in the end.

### 3.1. Behavior of ILs

The scattered intensity of molecular solvents, such as toluene, exhibits no angular dependence due to its small size. As shown in Fig. 1, the standard deviation of the scattered intensity of toluene at the range of 20–120° is less than 2%. [AMIM][Cl] shows similar behavior at 50 °C, but with 3.5% deviation. However, a strong angular dependence of the scattered intensity is observed in [BMIM][COOH]. As indicated in Fig. 1, the intensity of [BMIM][COOH] at 20° is 43 kcps, much larger than that (28 kcps) at 120°, indicating the occurrence of large-scale density fluctuations in [BMIM][COOH]. Computer simulations [35–37] at atomic level have revealed the existence of spatial heterogeneity in ILs. The heterogeneity is caused by the aggregation or domain segregation

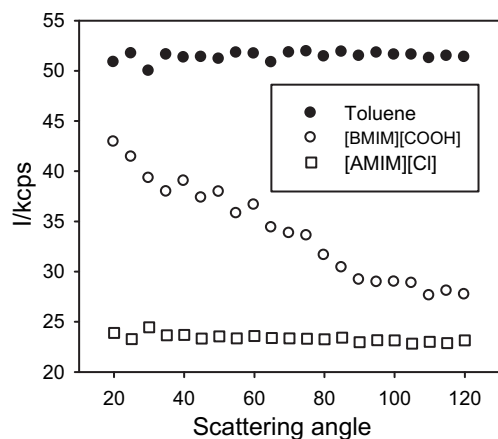


Fig. 1. Angular dependence of the scattered intensity from toluene at 25 °C, [BMIM][COOH] at 25 °C, and [AMIM][Cl] at 50 °C.

of alkyl chains in ILs, with longer or more hydrophobic neutral groups leading to aggregates with larger size. The curves in Fig. 1 suggest that [BMIM][COOH] at 25 °C has a stronger tendency to form spatial heterogeneity than [AMIM][Cl] at 50 °C.

### 3.2. Neutral polymers in ILs

We chose PVA and PSA to study the solubility of neutral polymers in ILs. PVA is hydrophilic. LLS study indicates that its  $M_w$  in water is  $2.0 \times 10^5$ , and  $R_h$  is 15 nm (Fig. S1). The size is similar to that measured by Budhlall et al. [38] PSA is hydrophobic and soluble in DMF. Its  $M_w$  and  $R_h$  are determined to be  $2.4 \times 10^5$  and 14 nm, respectively (Fig. S2). Fig. 2 shows the size distributions of PVA and PSA in [AMIM][Cl]. Similar results are observed at other concentrations and other scattering angles. As shown in Fig. 2A, PVA shows only one distribution with strong concentration dependent. The  $R_{h,app}$  at zero angle is 97 nm at 0.8 mg/mL and 116 nm at 2.0 mg/mL. These size values are much larger than that (15 nm) of single PVA chain in good solvent, suggesting that PVA forms aggregates in [AMIM][Cl]. PSA also formed aggregates or associates in [AMIM][Cl]. As shown in Fig. 2B, a bimodal distribution is observed at 0.5 mg/mL PSA in [AMIM][Cl]. The fast mode with  $R_h$  of about 5 nm is attributed to the condensed single PSA chains, and the slow mode with the  $R_h$  of 40 nm is attributed to the associates formed by PSA.

Fig. 3 compares the behavior of PVA and PSA in [BMIM][COOH]. In spite of the spatial heterogeneity in [BMIM][COOH], PVA and PSA are readily soluble in [BMIM][COOH]. As shown in Fig. 3A, the angular dependence of the scattered intensity of [BMIM][COOH] is alleviated after adding 3.0 mg/mL PVA, but it is stronger after adding 3.3 mg/mL PSA. Moreover, the scattered intensity after adding PVA is only slightly higher than that of [BMIM][COOH] itself, while the intensity is increased by 20–40 times after adding PSA at similar concentration. Fig. 3B compares the correlation functions of [BMIM][COOH] with and without polymers. The corresponding CONTIN results are also shown in the same figure. For [BMIM]

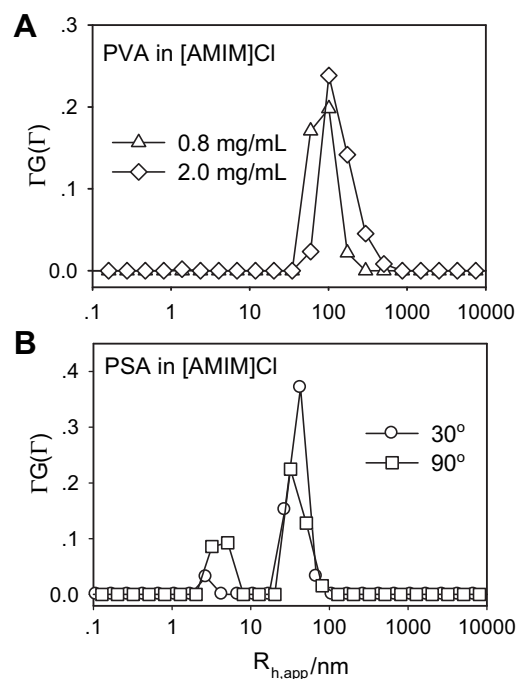
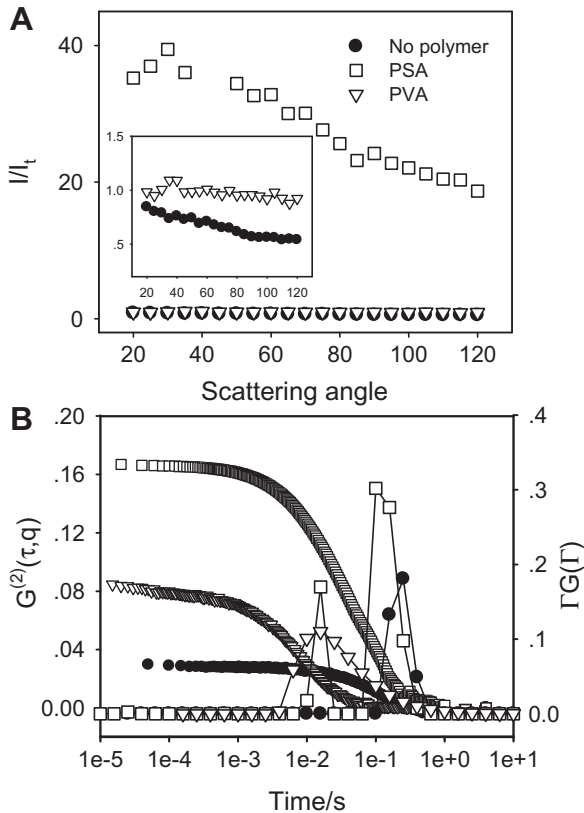


Fig. 2. Size distribution of (A) PVA in [AMIM][Cl] at 90°, and (B) PSA in [AMIM][Cl] at 0.5 mg/mL. Temperature: 50 °C.



**Fig. 3.** PSA and PVA in [BMIM][COOH]. (A): angular dependence of the scattered intensity, the inset magnifies the data on PVA and solvent, (B): correlation functions and the corresponding relaxation modes at  $30^\circ$  obtained by CONTIN. The concentrations of PSA and PVA are 3.3 mg/mL and 3.0 mg/mL, respectively.

[COOH] itself, the special heterogeneity (or aggregates) exhibits one relaxation mode with the characteristic relaxation time  $\tau$  about 0.2 s. After adding 3.0 mg/mL PVA, the relaxation becomes faster and broad, whose  $\tau$  is about 0.015 s. While in 3.3 mg/mL PSA, two relaxation modes with  $\tau_1 = 0.016$  s and  $\tau_2 = 0.12$  s are obtained.

Fig. 4 shows the size distribution of PVA and PSA in [BMIM][COOH]. The modes with  $R_h$  about 8 nm are attributed to the diffusion of single PVA or PSA chains. However, it is difficult to attribute the slow mode with  $R_h$  about 70 nm in 3.3 mg/mL PSA. As shown in Fig. 3B, the slow mode after adding PSA overlaps with the relaxation mode observed in [BMIM][COOH], and the scattered intensity also sharply increases (Fig. 3A). Therefore, the slow mode

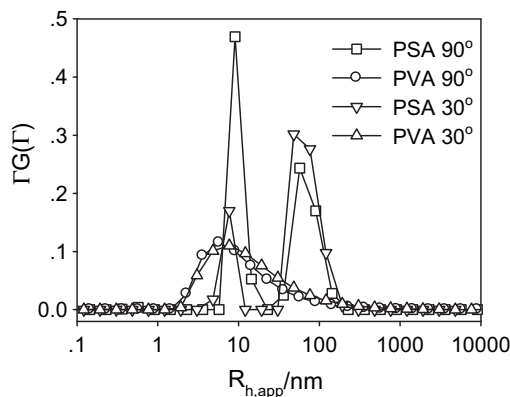


**Fig. 4.** Size distribution of PSA and PVA in [BMIM][COOH]. The concentrations of PSA and PVA are 3.3 and 3.0 mg/mL, respectively. Temperature:  $25^\circ\text{C}$ .

could be caused by the aggregate formed by PSA, by the enhanced spatial heterogeneity of [BMIM][COOH], or by both. On the contrary, the addition of 3.0 mg/mL PVA destroys the spatial heterogeneity in [BMIM][COOH], as demonstrated by the single mode with faster relaxation time (Fig. 4) and the weak angular dependence of the scattered intensity (Fig. 3A). The disappearance of the slow mode after the addition of PVA suggests that the large-scale density fluctuation in [BMIM][COOH] is mainly caused by the hydrophobic alkyl groups[39] instead of impurities.

For neutral polymers in ILs, aggregation is observed in all the cases, except that PVA in [BMIM][COOH] achieves solubility at molecule level. Since ILs contain both polar groups (cations or anions) and non-polar groups (alkyl chains), the hydrophilic PVA chains show strong affinity to the polar groups, which will alleviate the aggregation of the alkyl chains, and facilitate the dissolution. While the hydrophobic PSA chains have the tendency to stay in the domains rich of non-polar groups, which will enhance the attractive forces and result in strong aggregation. Such phenomenon is similar to the solubilize-enhanced micellization of block copolymers [40]. For general ILs with weak interactions between polar groups and neutral polymer, aggregation could be commonly observed. In other words, ILs dissolve hydrophilic polymers better than hydrophobic polymers. This is probably the reason that non-polar polymers, such as polyethylene, are not soluble in most of the ILs.

### 3.3. Charged polymer in ILs

Polyelectrolytes carrying negative charges, such as DNA and PSS, are soluble in [AMIM][Cl] and [BMIM][COOH]. As for positive polyelectrolyte, such as poly(4-vinylpyridinium tribromide) (P4VP), the solubility is extremely low. Fig. 5 shows the DLS data on DNA in [AMIM][Cl] at  $50^\circ\text{C}$ . Only one narrow distribution is observed at the studied concentrations. The  $R_h$  is determined to be 54 nm, smaller than that (103 nm) of DNA in aqueous solution (Fig. S3A). The  $\Gamma$  vs  $q^2$

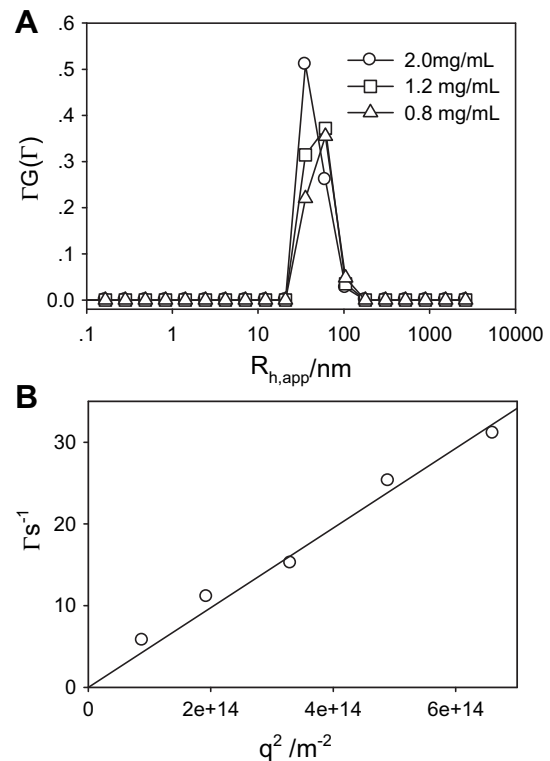


**Fig. 5.** DLS results of DNA in [AMIM][Cl] at  $50^\circ\text{C}$ . (A) size distribution at  $30^\circ$ ; (B) plot of  $\Gamma$  vs.  $q^2$  at 2.0 mg/mL.

plot (Fig. 3B) is linear and passes through the origin, indicating that the relaxation mode of DNA in [AMIM][Cl] is diffusive. Fig. 6 shows the Zimm plot of DNA in [AMIM][Cl] at 50 °C. The  $R_g$  is 89 nm, also smaller than that (about 195 nm) in aqueous solution (Fig. S3B). With the calculated  $dn/dc = -0.023 \text{ cm}^3/\text{g}$ , the  $M_w$  of DNA in [AMIM][Cl] is determined to be  $2.9 \times 10^6 \text{ g/mol}$ , smaller than that ( $4.8 \times 10^6 \text{ g/mol}$ ) in aqueous solution (Fig. S3B). The difference is probably caused by the inaccuracy of the calculated  $dn/dc$  value. The second virial coefficient, obtained from the Zimm plot in Fig. 6, is  $1.6 \times 10^{-4} \text{ mol mL/g}^2$ . Treating ILs similarly as molecular solvents, the interaction parameter can be calculated according to  $\chi = (1/2 - A_2\rho^2V)$  [60], where  $\rho$  and  $V$  are the density of the polymer and molar volume of solvent, respectively. With the known values of  $\rho$  ( $1.71 \text{ g/cm}^3$ ) and  $V$  ( $139.1 \text{ cm}^3/\text{mol}$ ),  $\chi$  value is determined to be 0.434, slightly smaller than 0.5, indicating that [AMIM][Cl] is a good solvent for DNA. The conformation of DNA could be estimated from the  $R_g/R_h$  ratio [41]. On the basis of the obtained values from Figs. 5 and 6, the  $R_g/R_h$  ratio of DNA in [AMIM][Cl] is 1.6, suggesting that DNA chain is in random coil conformation.

Fig. 7A shows the SLS results of PSS in [BMIM][COOH] at 25 °C. Compared with that of [BMIM][COOH] itself, the scattered intensity sharply increases after adding 2.6 mg/mL PSS. CONTIN analysis (Fig. 7B) indicates that the spatial heterogeneity in [BMIM][COOH] is disappeared, only a narrow distribution with  $R_h$  about 23 nm is observed. The small size accounts for the weak angular dependence of the scattered intensity shown in Fig. 7A. For PSS in aqueous solution, the  $R_h$  of single chain is highly dependent on the salt concentration. Without salt, the diffusion of single chain is coupled with that of the counterion, and the real  $R_h$  cannot be determined by DLS. [42] The addition of enough salt screens the electrostatic interaction and thus breaks down the coupling, which also causes PSS chain to collapse because of the hydrophobicity of PSS backbone. It is reported that the  $R_h$  of PSS with  $M_w$  about  $1.2 \times 10^6$  is about 20 nm ( $D = 1.2 \times 10^{-11} \text{ m}^2/\text{s}$ ) in aqueous solution after adding enough salt. [42] The size of PSS in collapsed state is close to that of PSS in [BMIM][COOH].

The behavior of DNA in [BMIM][COOH] is similar to that of PSS. The spatial heterogeneity is disappeared, and only one narrow size distribution is observed at the studied concentrations (Fig. S4). The  $R_h$  of DNA in [BMIM][COOH] is determined to be 14 nm, four times smaller than that in [AMIM][Cl], and seven times smaller than that in aqueous solution. Since the size distribution of DNA in aqueous solution is quite broad (Fig. S3), the sharp reduction in size and size distribution implies that DNA is denatured and condensed in [BMIM][COOH]. Unfortunately, SLS measurement does not yield valuable information on  $M_w$  and  $R_g$  because of the existence of heterogeneity in [BMIM][COOH].

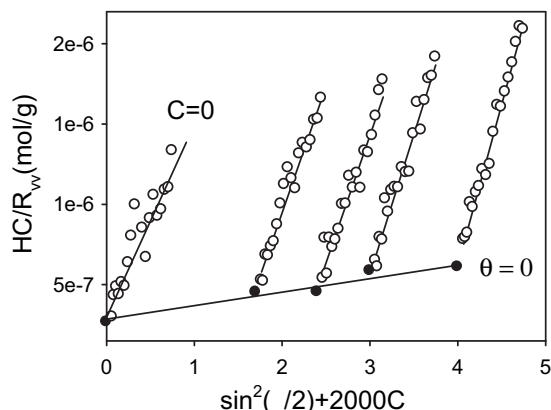


Fig. 6. Zimm plot of DNA in [AMIM][Cl] at 50 °C.

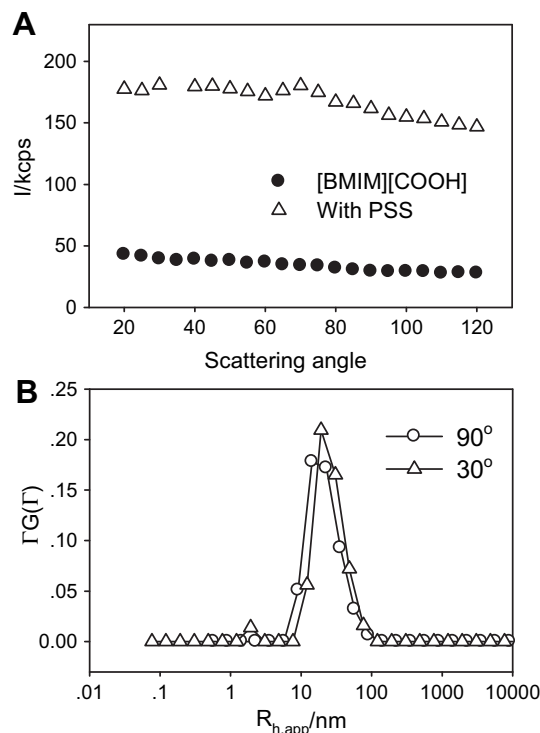


Fig. 7. LLS results of PSS in [BMIM][COOH] at 25 °C (A) angular dependence of 2.6 mg/mL PSS in [BMIM][COOH]; (B) size distribution at 30° and 90°.

Zeta potential analysis indicates that neither DNA nor PSS is effectively charged in ILs, suggesting that the ion disassociation is suppressed. IL is composed of cations and anions. Even though not all the ions are mobile, as indicated by the conductivity (Table 1), it is strong enough to prevent the release of the counterions from the polymers, or to replace the released counterions by ion-exchange. Since the solubility of polycations in ILs is in general lower than polyanions, the strong interaction of polyelectrolyte with the bulky cations in ILs favors dissolution. Since the interaction between polyelectrolyte and ILs is strong, ion-containing polymers, including most of the natural polymers, should be easier to find suitable ILs for dissolution. Note that conductivity of ILs also affects the solubility and the conformation of polyelectrolytes in ILs by screening the electrostatic interactions and ion-dipole interactions. Higher conductivity generally suggests stronger ionic strength, and consequently lower Debye length. As indicated in Table 1, the conductivity of [BMIM][COOH] at 25 °C is more than 10 times higher than that of [AMIM][Cl] at 50 °C, this is probably the reason that the chain conformation is more condensed in [BMIM][COOH].

#### 4. Cellulose in ILs

The solubility of cellulose in ILs has been widely investigated by experimental studies and computer simulations [43–49]. It is generally accepted that the anions of ILs form hydrogen bonds with the carbohydrate hydroxyl protons during the dissolution process [14,45]. The solubility of cellulose, therefore, is determined by the hydrogen bond basicity of ILs, and strong basicity is necessary to weaken the inter- and intra-molecular hydrogen bonds of the cellulose chains [47]. The dissolution capacity of cellulose is also influenced by the melting temperature and the viscosity of ILs [50]. In spite of the tremendous studies on the solubility of celluloses, the conformation of cellulose in ILs is rarely reported.



Cellulose with  $DP = 2400$  is only swollen in [BMIM][COOH] even after being heated to  $80\text{ }^\circ\text{C}$ , but it quickly dissolves in [AMIM][Cl] at  $80\text{ }^\circ\text{C}$ . The solution is transparent after being cooled to room temperature. As shown in Fig. 8A, cellulose exhibits one single relaxation in [AMIM][Cl] at  $50\text{ }^\circ\text{C}$ , in agreement with the findings from Wan et al. [48] Interestingly, the plot of  $\Gamma$  vs  $q^2$  is linear but does not pass through the origin (Fig. 8B), suggesting that the relaxation mode of cellulose in [AMIM][Cl] is not diffusive.  $^{13}\text{C}$  and  $^{35/37}\text{Cl}$  NMR relaxation study has demonstrated the formation of hydrogen bond between hydroxyl protons in cellulose and chloride in ILs. [45] Therefore, the relaxation of cellulose is coupled with that of ILs. Besides the thermal fluctuation induced Brownian motion (diffusion), cellulose could also undergo an extra motion caused by solvent molecules. Under such conditions, the  $\Gamma/q^2$  (or the mutual diffusion coefficient) increases with decreasing scattering angle (Fig. S5), similar to that of the coupled diffusion of single polyelectrolyte with counterions in low or free salt solutions [51]. Since cellulose in [AMIM][Cl] is not diffusive, the Stokes–Einstein equation does not apply here. Otherwise, the hydrodynamic radius  $R_h$  of 12 nm will be obtained at zero scattering angle. The value is too small for the size of cellulose with  $DP = 2400$ .

Fig. 9 shows the Zimm plot of cellulose in [AMIM][Cl] at  $50\text{ }^\circ\text{C}$ .  $R_g$  is determined to be 75 nm.  $A_2$  is positive,  $2.0 \times 10^{-4}\text{ mol mL/g}^2$ . With  $\rho$  being 1.56, the corresponding  $\chi$  is determined to be 0.432, indicating that [AMIM][Cl] is a good solvent for cellulose. The refractive index is calculated to be  $\sim 0.028\text{ mL/g}$ ,  $M_w = 7.9 \times 10^5\text{ g/mol}$ , close to that of cellulose with  $DP = 2400$ , is obtained from Fig. 9. With the measured  $M_w$  and  $R_g$ , the overlap concentration ( $\approx M_w/(4/3\pi R_g^3)$ ) of cellulose in [AMIM][Cl] is calculated to be  $\sim 1\text{ mg/mL}$ , in the same order of the concentrations used for Zimm plot. This might bring a few percent of errors on the determined values, but the characterization is still valid. The flexibility of cellulose in [AMIM][Cl] could

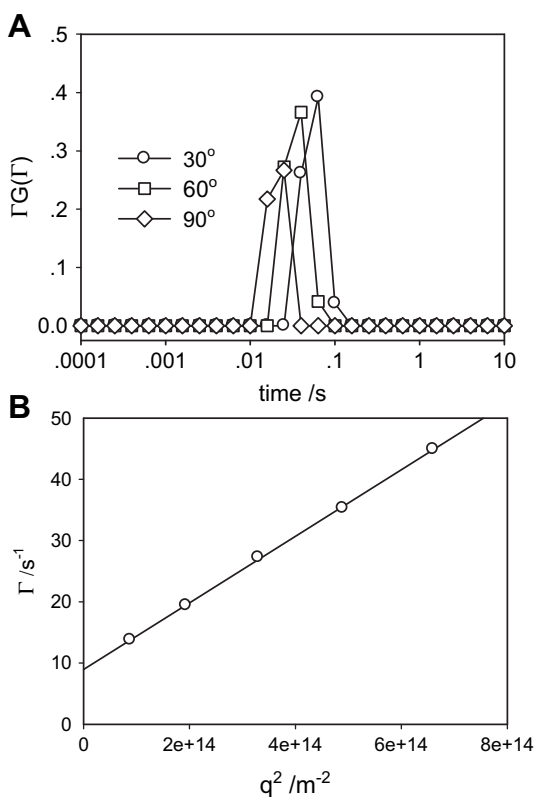


Fig. 8. Relaxation of cellulose in [AMIM][Cl] at  $50\text{ }^\circ\text{C}$ . (A) Angular dependence at  $4.0\text{ mg/mL}$ ; (B) plot of  $\Gamma$  vs  $q^2$ .

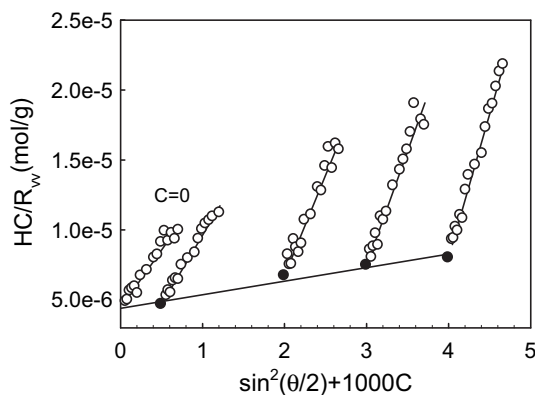


Fig. 9. Zimm plot of cellulose ( $DP = 2400$ ) in [AMIM][Cl] at  $50\text{ }^\circ\text{C}$ .

be estimated from the persistence length  $\rho$ , which is calculated according to Benoit–Doty equation [52]

$$R_g^2 = \rho^2 \left[ \frac{L}{3\rho} - 1 + \frac{2\rho}{L} - \frac{2\rho^2}{L^2} (1 - e^{-L/\rho}) \right] \quad (4)$$

where  $L$  is the contour length of the chain. With the length of one glucoside being  $0.515\text{ nm}$ , the persistence length of cellulose in [AMIM][Cl] is estimated to be  $14\text{ nm}$  by Eq. (4). This value is in the same order as that of cellulose in other solvents, but much larger than that of flexible polymer chains. The characteristic ratio  $C_\infty$ , which is also generally used to represent the chain flexibility, could be determined according to

$$C_\infty = \frac{\langle R_0^2 \rangle}{nl^2} \quad (5)$$

with  $\langle R_0^2 \rangle$ ,  $n$ , and  $l$  being the unperturbed mean square end-to-end distance, the number of main-chain bonds, and the bond length, respectively. As we know  $\langle R_0^2 \rangle = 6 R_{g,0}^2$ , and the radius of gyration in the unperturbed state  $R_{g,0}$  is related with  $R_g$  as  $R_{g,0} = R_g/\alpha_s$ . The linear expansion factor  $\alpha_s$  can be obtained from  $M_w$ ,  $A_2$ , and  $R_g$  by a penetration function  $\psi$  derived from the Kurata–Fukatsu–Sotobayashi–Yamakawa theory (KFSY) [53]

$$\psi = zh_0(z) = (0.746 \times 10^{-25}) A_2 M^2 / R_g^3 \quad (6)$$

where  $h_0(z) = 1 - (1 + 3.903z)^{-0.468} / 1.828$ , and  $\alpha_s = 1 + 1.78z$ . The expansion factor  $\alpha_s$  of cellulose in [AMIM][Cl] is determined to be 1.03, and  $C_\infty$  is about 51.6. As reported in literature, the  $C_\infty$  values of cellulose in Cd-tren [54], cuoxam [55], LiOH/Urea [56], 9%LiCl/DMAc [57], are 24.7, 25.0, 20.8, 91.9, respectively. Therefore, the conformation of cellulose in [AMIM][Cl] is semi-rigid or worm-like, which is also confirmed by rheological measurement [58].

Importantly, a mobility of  $-0.11 \pm 0.02\text{ }\mu\text{m s}^{-1}\text{V}^{-1}$  is obtained from the zeta potential measurement on cellulose in [AMIM][Cl] at  $2.0\text{ mg/mL}$  at  $50\text{ }^\circ\text{C}$ , suggesting that cellulose carries negative charges in [AMIM][Cl]. Since only chloride bears negative charge in the system, and the carbohydrate hydroxyl groups are difficult to ionize by themselves, the charges carried by cellulose in [AMIM][Cl] must be caused by the attachment of chlorides. However, for other polymers containing hydroxyl protons, such as PVA (Fig. 2) and hydroxyethylcellulose (data not shown), their solubility in [AMIM][Cl] is not as good as that of cellulose, and no effective charge is detected. The strong binding of chloride on cellulose instead of on PVA or HEC is probably due to the conformation and configuration of cellulose. The distribution of carbohydrate hydroxyl groups along cellulose backbone not only facilitates the intra- and inter-chain

hydrogen bonding, but also causes a regulation of chloride upon forming hydrogen bonds. The formation of dynamic polyelectrolyte is able to explain the solubility of cellulose in ILs: the electrostatic repulsion is stronger than hydrogen-bonding, cellulose quickly dissolves in chloride-containing ILs. Since the electrostatic repulsion of polyelectrolyte is determined by the concentration and property of the counterions [59], the cations in ILs also involves in the dissolution of cellulose [32]. Note that the conductivity of [AMIM][Cl] is only  $1.35 \text{ mS cm}^{-1}$ , corresponding to that of  $0.01 \text{ M}$  KCl. Therefore, the ionic strength of [AMIM][Cl] is not strong enough to screen the electrostatic interactions.

#### 4.1. Solubility of polymers in ILs

The above results suggested that the solubility of polymers in ILs is far more complicate than that in molecular solvents (including water). Compared with molecular solvents, ILs are composed of two parts: an anion and a flexible cation containing hydrophobic alkyl chains. The size of one IL molecule (anion/cation pair) is much larger than that of molecular solvents. Moreover, the alkyl chains, depending on the length and property, associate together to form spatial heterogeneity (Fig. 1), which further increases the effective size of IL molecules. According to the lattice model and Flory–Huggins equation [60], the molar entropy of mixing  $\Delta S_m$  is

$$\Delta S_m = n_a \Delta S_a + n_b \Delta S_b = -k(n_a \ln \phi_a + n_b \ln \phi_b) \quad (7)$$

in which  $n_a$  and  $n_b$  are the numbers of molecules of polymer and solvent,  $\Delta S_a$  and  $\Delta S_b$  are the corresponding molecular entropy of mixing,  $\phi_a$  and  $\phi_b$  are the volume fractions and defined by:  $\phi_a = n_a N_a / N$ ,  $\phi_b = n_b N_b / N$ , ( $N_a$  and  $N_b$  are the numbers of lattice sites occupied by each polymer chain,  $N$  is the total numbers of lattice sites in the mixed system). Therefore, per lattice site entropy of mixing:

$$\Delta \bar{S}_m = \frac{\Delta S_m}{N} = -k \left( \frac{\phi_a}{N_a} \ln \phi_a + \frac{\phi_b}{N_b} \ln \phi_b \right) \quad (8)$$

For polymer a in molecular solvent b,  $N_a$  equals to the degree of polymerization of polymer a, and  $N_b = 1$ . However,  $N_b$  is much larger than 1 in ILs, which results in a decrease in entropy. Since entropy favors mixing in binary system, the solubility of polymers in ILs is more difficult than that in molecular solvents.

The Flory interaction parameter,  $\chi$ , is able to qualitatively account for the short range interactions between polymer and solvent. For polymers dissolved in molecular solvents, only one  $\chi$  is applied. However, polymer/ILs should be treated as a ternary mixture: polymer, large cations, and anions. Thus, three  $\chi$ 's are needed for polymers dissolved in ILs, i.e., polymer–anion, polymer–cation, and cation–anion (no long-range interaction considered) interactions. This approach has been applied by Aerov et al. [61] to treat the salvation of molecular solute in ILs, and should be suitable to treat neutral polymers dissolved in ILs.

For non-polar polymers in ILs, the dispersion force between polymers, and the interactions between the cation and anion are strongly attractive. The  $\chi$  values of polymer–anion and polymer–cation are positive, but that of anion–cation is negative. Since all  $\chi$  values do not favor mixing, non-polar polymers, such as polyethylene, are not soluble in most of ILs. Even for polar polymers, such as PVA and PSA in our case, if the attractive force between polymer and anions or cations in ILs cannot counterbalance the attraction between cation and anion, aggregation or precipitation of polymers commonly occurs.

For polyelectrolytes, the suppression of ion disassociation rules out the long-range electrostatic interactions. Polar–polar interaction prevails and plays a key role for dissolution. For polyelectrolyte

carrying negative charges, such as DNA and PSS (Figs. 5–7), the interaction with the bulky cations alleviates the spatial heterogeneity in ILs, and facilitates dissolution. However, for positive polyelectrolyte, such as P4VP, the interaction between polymers and anions (whose size is small) in ILs, does not favor mixing. The coupling of the polyelectrolyte with cations or anions in ILs increases the diffusion rate of polymers, leading to a smaller  $R_h$  value.

The solubility of cellulose in ILs should be treated as a special case. Cellulose is a neutral polymer, and it forms aggregates in many molecular solvents [62–65]. The strong binding of chloride in ILs renders cellulose the behavior of transient polyelectrolytes, and dissolution in molecular level is thus achieved. The hydrogen bonding between cellulose and ILs also explains the non-diffusion of cellulose in ILs (Fig. 8). The relaxation of polyelectrolyte in solvent of low ionic strength is usually accompanied with an extraordinary slow relaxation mode [51,66], whose relaxation time is two or more orders slower than that of the single polymer chain. The disappearance of the slow mode in ILs is probably caused by the binding frequency of anion. When the binding rate is faster than the relaxation time of the slow mode, the slow mode would not show up.

## 5. Conclusions

LLS study yielded essential information on the solubility of polymers in ILs. The polymer/IL should be treated as a ternary system rather than binary system. Therefore, a variety of mutual interactions, some of which were polymer specific, worked together to control the solubility and conformation of polymers in ILs. Even though it was difficult to work out the exact rules governing the dissolution of polymers in ILs, our preliminary study indicated that, to achieve dissolution at molecular level, polymers should be able to strongly interact the bulky cations in ILs, while not resulted in a decrease in entropy.

## Acknowledgments

This work was financially supported by the National Natural Science Foundation of China (20774004, 50873025), Shanghai Science and Technology Commission (09JC1400800), Shanghai Municipal Education Commission (08GG11), and the innovation funds for Ph.D students (Ye Chen) of Donghua University.

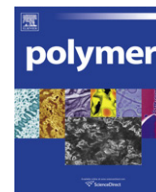
## Appendix. Supplementary material

Supplementary data related to this article can be found online at doi:10.1016/j.polymer.2010.11.034.

## References

- [1] Seddon KR, Stark A, Torres MJ. *Pure Appl Chem* 2000;72:2275–87.
- [2] Krossing I, Slattery JM, Daguene C, Dyson PJ, Oleinikova A, Weingartner H. *J Am Chem Soc* 2006;128:13427–34.
- [3] Rebelo LPN, Lopes JNC, Esperanca J, Guedes HJR, Lachwa J, Najdanovic-Visak V, et al. *Acc Chem Res* 2007;40:1114–21.
- [4] Welton T. *Chem Rev* 1999;99:2071–83.
- [5] Dupont J, de Souza RF, Suarez PAZ. *Chem Rev* 2002;102:3667–91.
- [6] Visser AE, Swatloski RP, Rogers RD. *Green Chem* 2000;2:1–4.
- [7] Arce A, Earle MJ, Rodriguez H, Seddon KR. *J Phys Chem B* 2007;111:4732–6.
- [8] Holbrey JD, Reichert WM, Nieuwenhuizen M, Johnston S, Seddon KR, Rogers RD. *Chem Commun*; 2003:1636–7.
- [9] Macfarlane DR, Forsyth M, Howlett PC, Pringle JM, Sun J, Annat G, et al. *Acc Chem Res* 2007;40:1165–73.
- [10] Earle MJ, Seddon KR. *Pure Appl Chem* 2000;72:1391–8.
- [11] Rogers RD, Seddon KR. *Science* 2003;302:792–3.
- [12] Kubisa P. *Prog Polym Sci* 2004;29:3–12.
- [13] Barth J, Buback M, Schmidt-Naake G, Woelch I. *Polymer* 2009;50:5708–12.
- [14] Swatloski RP, Spear SK, Holbrey JD, Rogers RD. *J Am Chem Soc* 2002;124:4974–5.
- [15] Wu Y, Sasaki T, Irie S, Sakurai K. *Polymer* 2008;49:2321–7.
- [16] El Seoud OA, Koschella A, Fidale LC, Dorn S, Heinze T. *Biomacromolecules* 2007;8:2629–47.

- [17] Phillips DM, Drummy LF, Conrady DG, Fox DM, Naik RR, Stone MO, et al. *J Am Chem Soc* 2004;126:14350–1.
- [18] Xie HB, Li SH, Zhang SB. *Green Chem* 2005;7:606–8.
- [19] Triolo A, Russina O, Keiderling U, Kohlbrecher J. *J Phys Chem B* 2006;110:1513–5.
- [20] Kawauchi T, Kumaki J, Okoshi K, Yashima E. *Macromolecules* 2005;38:9155–60.
- [21] Liu WW, Cheng LY, Zhang HY, Zhang YM, Wang HP, Yu MF. *Int J Mol Sci* 2007;8:180–8.
- [22] Zhao TT, Wang HP, Wang B, Tu XP, Zhang YM, Jiang JM. *Polym Bull* 2006;57:369–75.
- [23] Tu XP, Zhang YM, Zhao TT, Wang HP. *J Macromol Sci Phys* 2006;45:665–9.
- [24] Ueki T, Watanabe M. *Chem Lett* 2006;35:964–5.
- [25] He YY, Li ZB, Simone P, Lodge TP. *J Am Chem Soc* 2006;128:2745–50.
- [26] He YY, Lodge TP. *J Am Chem Soc* 2006;128:12666–7.
- [27] Susan MA, Kaneko T, Noda A, Watanabe M. *J Am Chem Soc* 2005;127:4976–83.
- [28] Marcilla R, Blazquez JA, Rodriguez J, Pomposo JA, Mecerreyes D. *J Polym Sci Pol Chem* 2004;42:208–12.
- [29] Snedden P, Cooper AI, Scott K, Winterton N. *Macromolecules* 2003;36:4549–56.
- [30] Fukushima T, Kosaka A, Ishimura Y, Yamamoto T, Takigawa T, Ishii N, et al. *Science* 2003;300:2072–4.
- [31] Winterton N. *J Mater Chem* 2006;16:4281–93.
- [32] Zhang H, Wu J, Zhang J, He JS. *Macromolecules* 2005;38:8272–7.
- [33] Huglin MB. *Light scattering from polymer solutions*. London and New York: Academic Press; 1972.
- [34] Provencher SW. *Comput Phys Commun* 1982;27:229–42.
- [35] Urahata SM, Ribeiro MCC. *J Chem Phys* 2004;120:1855–63.
- [36] Wang YT, Voth GA. *J Am Chem Soc* 2005;127:12192–3.
- [37] Padua AAH, Gomes MF, Lopes JNAC. *Acc Chem Res* 2007;40:1087–96.
- [38] Budhlall BM, Landfester K, Sudol ED, Dimonie VL, Klein A, El-Aasser MS. *Macromolecules* 2003;36:9477–84.
- [39] Triolo A, Russina O, Bleif HJ, Di Cola E. *J Phys Chem B* 2007;111:4641–4.
- [40] Nagarajan R, Ganesh K. *Macromolecules* 1989;22:4312–25.
- [41] Brown W. *Light scattering: principles and development*. New York: Oxford University Press; 1996. 439–476.
- [42] Sedlak M. *J Chem Phys* 1996;105:10123–33.
- [43] Barthel S, Heinze T. *Green Chem* 2006;8:301–6.
- [44] Moulthrop JS, Swatloski RP, Moyna G, Rogers RD. *Chem Commun*; 2005:1557–9.
- [45] Remsing RC, Swatloski RP, Rogers RD, Moyna G. *Chem Commun*; 2006:1271–3.
- [46] Youngs TGA, Holbrey JD, Deetlefs M, Nieuwenhuyzen M, Gomes MFC, Hardacre C. *Chemphyschem* 2006;7:2279–81.
- [47] Fukaya Y, Sugimoto A, Ohno H. *Biomacromolecules* 2006;7:3295–7.
- [48] Wan ZZ, Li L, Cui SX. *Biopolymers* 2008;89:1170–3.
- [49] Zhang JM, Zhang H, Wu J, Zhang J, He JS, Xiang JF. *Phys Chem Chem Phys* 2010;12:1941–7.
- [50] Pinkert A, Marsh KN, Pang SS, Staiger MP. *Chem Rev* 2009;109:6712–28.
- [51] Forster S, Schmidt M. *Adv Polym Sci* 1995;120:51–133.
- [52] Benoit H, Doty P. *J Phys Chem* 1954;57:958–63.
- [53] Kurata M, Fukatsu M, Sotobayashi H, Yamakawa H. *J Chem Phys* 1964;41:139–49.
- [54] Saalwachter K, Burchard W, Klufers P, Kettenbach G, Mayer P, Klemm D, et al. *Macromolecules* 2000;33:4094–107.
- [55] Seger B, Burchard W. *Macromol Symp* 1994;83:291–310.
- [56] Cai J, Liu YT, Zhang LN. *J Polym Sci Pol Phys* 2006;44:3093–101.
- [57] McCormick CL, Callais PA, Hutchinson BH. *Macromolecules* 1985;18:2394–401.
- [58] Kuang QL, Zhao JC, Niu YH, Zhang J, Wang ZG. *J Phys Chem B* 2008;112:10234–40.
- [59] Israelachvili JN. *Intermolecular and surface forces*. 2nd ed. London: Academic Press; 1992.
- [60] Flory PJ. *Principles of polymer chemistry*. Ithaca, NY: Cornell University Press; 1953.
- [61] Aerov AA, Khokhlov AR, Potemkin II. *J Phys Chem B* 2006;110:16205–7.
- [62] Morgenstern B, Kammer HW. *Polymer* 1999;40:1299–304.
- [63] Schulz L, Seger B, Burchard W. *Macromol Chem Phys* 2000;201:2008–22.
- [64] Roder T, Morgenstern B. *Polymer* 1999;40:4143–7.
- [65] Cai J, Zhang L, Liu SL, Liu YT, Xu XJ, Chen XM, et al. *Macromolecules* 2008;41:9345–51.
- [66] Schmitz KS. *An introduction to dynamic light scattering by macromolecules*. New York: Academic Press; 1999.



# In situ optical microscopy observation of the growth and rearrangement behavior of surface holes in the breath figure process

Hengyu Ma, Ye Tian, Xiaolin Wang\*

State Key Laboratory of Chemical Engineering, Department of Chemical Engineering, Tsinghua University, Beijing 100084, China

## ARTICLE INFO

### Article history:

Received 21 September 2010

Received in revised form

18 November 2010

Accepted 20 November 2010

Available online 27 November 2010

### Keywords:

Honeycomb films

In situ optical microscope observation

Formation of BF pattern

## ABSTRACT

Using in situ optical microscope observations of the surface of polyphenylene oxide (PPO)/chloroform solution in the breath figure (BF) process, the detailed formation phenomenon of surface of the BF pattern was obtained. This phenomenon directly supports the “bursting hypothesis”. Based on the “bursting hypothesis” and additional experimental data, the mechanism for the late BF process of the PPO/chloroform system is discussed. Moreover, the formation process of defects on the film surface was also directly observed, and the defect formation mechanism of the system is discussed. This work can help to further understand the formation of patterns and defects on the surface of BF films.

© 2010 Elsevier Ltd. All rights reserved.

## 1. Introduction

Microporous films with honeycomb structures have received great interest in recent years because of their wide applications in chemical sensors [1], optical apparatus [2], scaffold for nanostructures [3], biology [4–6], micrographics [7], membrane separation [8,9], etc. The breath figure (BF) method, first reported by Francois et al. [10], is a facile and versatile approach to produce such structures. In brief, the procedure of the BF method is to dissolve the polymer in a highly volatile and water immiscible solvent and cast the solution on a substrate under high humidity. When the solvent completely evaporates, a honeycomb-patterned polymer film is obtained. The BF process occurs when the local low temperature on the solution surface, which results from the rapid evaporation of solvent, causes the condensation of water droplets. Droplets with equal diameters form a honeycomb-patterned array, and the array is surrounded by the polymer solution. When the solvent and water droplets completely evaporate, a honeycomb-patterned polymer film (the contrary copy of the droplet array) forms. By using the BF method, a variety of materials, such as polymers [11–13], inorganic materials [14,15] and nano particles [16,17], have been made into honeycomb-patterned, microporous films.

The applicability of the BF film is affected by its surface geometrical properties. Of these properties, the diameters of the surface holes (SHs) and defects (irregular SHs) are significant [18,19]. The empirical relationship between the two properties and conventional

parameters that affect the BF process, including the material system, temperature & humidity of the environment and solution concentration, have been studied, suggesting that the properties can be locally controlled by adjusting these parameters [20–23]. To further understand the mechanism of BF and to control the surface geometrical properties of the BF film more effectively, the formation processes of SHs and defects are worthy of study.

Pitois et al. [24] proposed a “bursting hypothesis” for SH formation. According to this hypothesis, droplets are completely encapsulated by a polymer layer after condensation. When most of the solvent evaporates, the temperature near the surface of the solution increases to reach the ambient temperature again. Water contained inside the droplets evaporates and bursts the top of the polymer layer, leading to the formation of SHs. Indirect evidence has been reported, such as the surface tension and spreading behavior of polymer solution droplets floating on water [24] and the encapsulation behavior of millimeter sized water droplets deposited on a polymer solution [25]. However, this hypothesis has not been widely accepted because of the lack of in situ direct evidence for the BF process [26–32].

Peng et al. [29] and Xu et al. [33] studied the defects of SH loss and grain boundaries, respectively. The proposed formation mechanisms of the defects were speculated from the resulting film morphology and the probable mechanism for the BF process. Direct observations of the processes were not reported.

In situ observations by optical microscopy (OM) have been employed [24,34,35] to record the phenomenon on the solution surface during the BF process. Only relative macroscopic results [35,36] were derived from these observations because either

\* Corresponding author. Tel.: +86 10 62794741; fax: +86 10 62794742.

E-mail address: [xl-wang@mail.tsinghua.edu.cn](mailto:xl-wang@mail.tsinghua.edu.cn) (X. Wang).

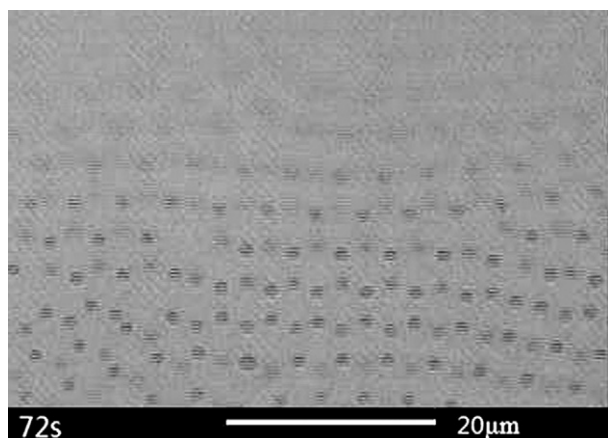


Fig. 1. OM photograph of SHs at 72 s. The time shown at bottom is the time after casting (same as below).

low magnification or short observation time (about 200 ms) was employed.

In this work, the surface of a polyphenylene oxide (PPO)/chloroform solution was observed in situ using OM at high magnification during the entire BF process. The “bursting hypothesis” was strongly supported in the PPO/chloroform system by the direct evidence obtained. Based on this hypothesis and additional experimental data, a three-stage mechanism for the late BF process of the PPO/chloroform system is proposed here. Moreover, by observing the rearrangement behavior of the SHs, the formation processes of several typical kinds of defects were obtained. The formation mechanisms for these kinds of defects in the PPO/chloroform system are discussed.

## 2. Experimental section

### 2.1. Materials

PPO/chloroform system was chosen for its convenience, i.e., it requires no surfactant [37] and has sufficient formation time for the BF process (which is more than 2 min). The polymer solution with PPO (Mw = 30K, Aldrich) and chloroform (spectroscopy

grade, Beijing Chemical Corporation) was prepared. Water was purified by a Millipore system (Milli-Q, Millipore).

### 2.2. Preparation of honeycomb films and pincushion structures

The honeycomb films were directly prepared by casting a PPO solution (200  $\mu\text{L}$  at a time) of 10 g/L on glass substrates in the observation cell, which was attached to the hot stage (THMS600, Linkam) at a temperature of 25  $^{\circ}\text{C}$  and relative humidity (RH) of 70% (In the results and discussion part, when different temperatures, RH or concentrations were employed, it would be depicted particularly). The temperature and RH in the cell were controlled by the hot stage and the flow of a proper quantity of moist argon through the pipe, respectively. The pincushion structures of films were prepared by peeling off the tops of the honeycomb films using scotch tape [38].

### 2.3. Instruments and measurements

OM images with resolution of  $768 \times 636$  (width by height) were recorded every 0.2 s with an Olympus optical microscope (BX51) in reflection mode with a CCD camera (TK-C1481BEC, JVC) attachment. The magnification of the OM images was 1000 (the ocular lens was  $10\times$  and the objective lens was  $100\times$ ). No filter was applied except to increase the contrast of images to make them clearer. The OM figures shown in the article are local parts of the OM images where particular phenomenon occurred. As the solvent evaporated, the solution height decreased from about 500  $\mu\text{m}$  to about 10  $\mu\text{m}$  in about 160 s. Thus, the height of solution decreased at a speed of about 3  $\mu\text{m/s}$ , i.e., 30  $\mu\text{m}/10$  s. The position of the objective lens was decreased 10  $\mu\text{m}$  by rotating the fine adjustment knob. To effectively focus on the sample, the fine adjustment knob was rotated by hand at a speed of about 3 circles per 10 s. The morphology of the films was characterized by scanning electron microscopy (SEM, JSM7401, JEOL, 1 kV). Prior to imaging with SEM, the samples were sputtered with a thin layer of gold.

### 2.4. Calculation of SHs' diameter and moving speed

The diameters and positions of SHs in images were detected using the image processing function in the Linkam software

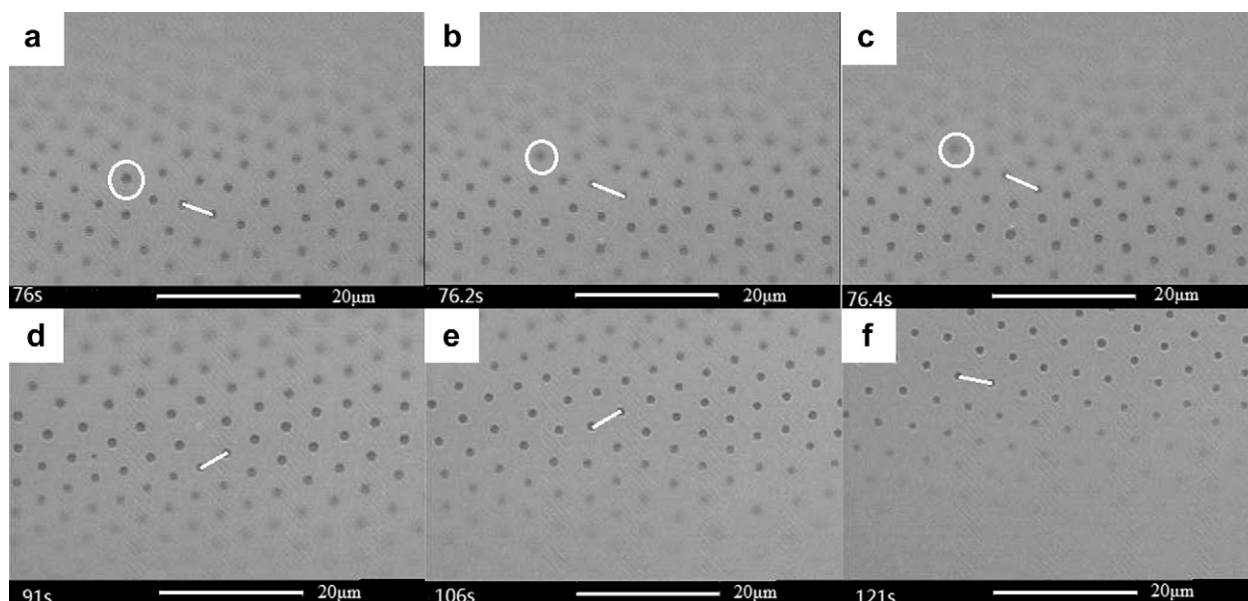


Fig. 2. OM photographs of the pattern of SHs at (a–c) 76 s–76.4 s and (d–f) 91 s–121 s.

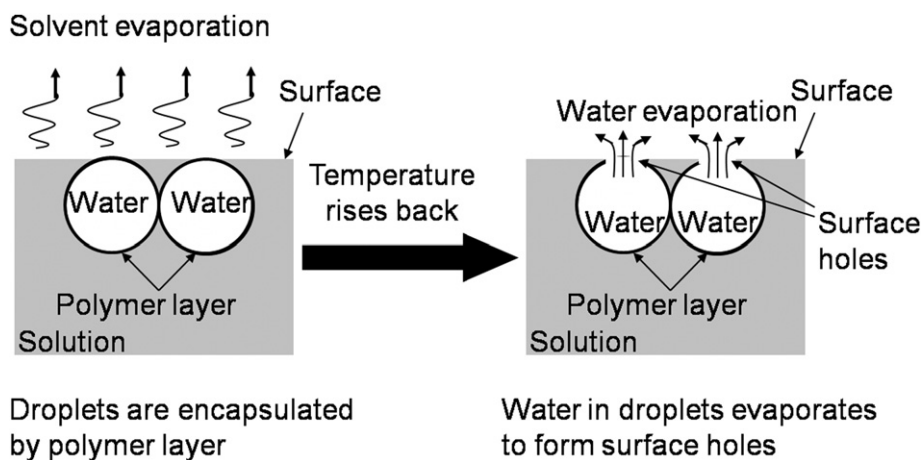


Fig. 3. Schematic diagram of the formation process of SHs from the side view as assumed by the “bursting hypothesis”.

system. The diameter at the specific time was calculated by the average diameter of three randomly selected SHs in the image. The moving speed of the SHs at the specific time was calculated by dividing the position difference between the same SHs in the image and in the next image by the time difference (0.2 s). To ensure that the same SHs were chosen in the sequential images, odd spots, i.e., irregular SHs, were used as references. Other SHs were detected by their position relative to the odd spots.

### 3. Results and discussion

#### 3.1. The appearance of SHs and the support for the “bursting hypothesis”

Immediately after the casting of the PPO solution, the CCD camera was focused on the surface of the solution, and the time was recorded. The observed BF process could be divided into several stages with characteristic features. The starting times for each stage varied in different experiments, though the controllable parameters were fixed. The parameters that determined these times might be complicated, and they are under further investigation. However, identical stages with identical features were shared by each experiment. In the following text, the times of one specific experiment were chosen to discuss the stages and features of the BF process in the PPO/chloroform system.

Similar to the work proposed by Karthaus et al. [36], shortly after the casting of the PPO solution, a turbid top layer on the

polymer solution could be seen. This top layer indicated the formation of water droplets. The diffraction of light, caused by the difference in the refractive index between the water and PPO/chloroform solution, induced the opacity.

As shown in Fig. 1, SHs did not appear until 72 s. The SHs had small diameters compared with the distances between them. They moved so fast relative to the field of view that there are double images on the graph.

At 76 s, SHs began to move slowly enough to be clearly recorded. Fig. 2 shows the pattern of SHs during the BF process. Fig. 2a–c show that, over a short time (0.4 s), the distance (from center to center, the same below) between a specific pair of adjacent SHs remained 4.7  $\mu\text{m}$  when the SHs moved at a speed of 20.1  $\mu\text{m}/\text{s}$  (The method of calculation is in Section 2.4 of this article. The white circle marks an odd spot, which was bigger. A specific pair of adjacent SHs marked by the white band was confirmed by using the odd spot as reference.) The speed was fast compared to the diameter. Fig. 2d–f show that the distances between most adjacent SHs remained 4.7  $\mu\text{m}$ , and the diameters of the SHs remained nearly the same over 30 s when the SHs were moving.

Two features of the appearance and movement of SHs can be summarized as follows: (1) SHs appeared later than the formation of droplets. (2) Their diameters and the distances between adjacent SHs remained almost the same over a relatively long time when the SHs were moving.

The following two features are consistent with the “bursting hypothesis”. (1) In the early stage of the BF process, the solvent is

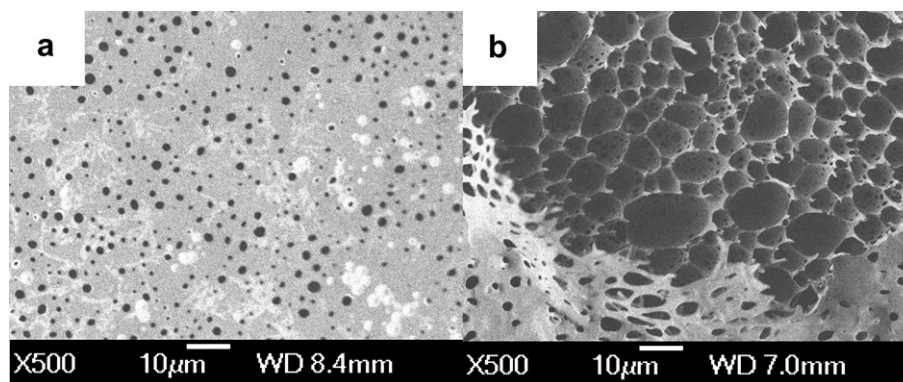


Fig. 4. SEM photographs of the surface morphology of the PPO film (a) with top and (b) without top. The casting conditions were a concentration of 100 g/L, a temperature of 25 °C and an RH of 95%.

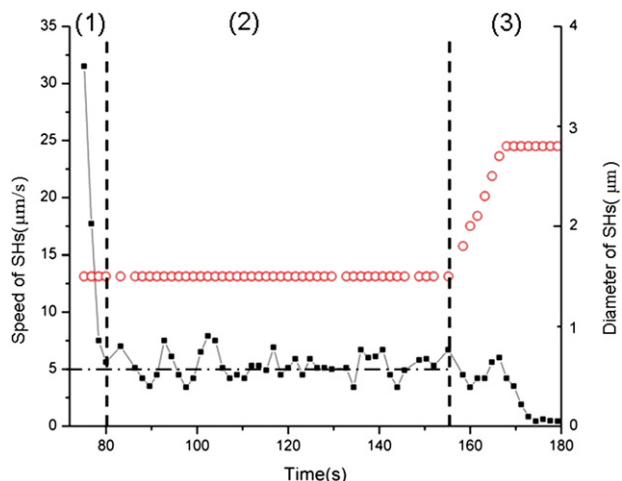


Fig. 5. Graph of the diameter and speed of SHs versus time. The squares indicate the speed, and the circles indicate the diameter.

evaporated so fast that the temperature of the solution is low enough to prevent the evaporation of water droplets. As a result, the polymer layer encapsulating the droplets is not burst, and SHs do not appear. (2) The compact packing array of droplets forms before the appearance of SHs. SHs then appear as emerged parts of droplets, as shown in Fig. 3. Because the distance between adjacent droplets is fixed by the compact packing array, the distance between them cannot be changed. Thus, in situ direct evidence for the “bursting hypothesis” was obtained.

Moreover, new indirect evidence for the “bursting hypothesis” was also found in this work. A concentrated PPO solution of 100 g/L was cast at a temperature of 25 °C and RH of 95%. Fig. 4a shows that there were fewer SHs on this film. Without regard to the “bursting hypothesis”, it can be speculated that fewer droplets formed, leading to fewer SHs on the surface. However, as shown in Fig. 4b, by peeling off the top of the film, pits that were packed and extruded with one another were found in the film. These pits indicate that there were droplets packed under the solution surface during the BF process. Why were there fewer SHs? One explanation is that the high viscosity of the solution made the encapsulating polymer layer difficult to burst. Consequently, the special experimental conditions preserved the condition when the droplets were completely encapsulated by the polymer layer, and, thus, the key factor of the “bursting hypothesis” was supported in the PPO/chloroform system.

### 3.2. The growth of SHs and the mechanism for the late BF process in the PPO/chloroform system

After the appearance of SHs, they grew and moved until the solution was cured. The direction of movement was observed mainly toward the edge of the solution, i.e., the solution–air–substrate three-phase line. This phenomenon is consistent with the mechanism proposed by Shimomura et al. [39].

Detailed data of the diameter and speed versus time are shown in Fig. 5. Points in the figure indicate average values of the diameters and speeds in image groups. An image group consisted of 8 sequential images, and there were 67 groups formed by the 536 images from 72 s to 180 s. Among the 67 groups, 7 groups were removed for their exceptional speed values. Generally, the diameter increased and the speed decreased with time.

By further investigating the data in Fig. 5, a three-stage growth history of the SHs from their appearance to the curing of the solution is proposed.

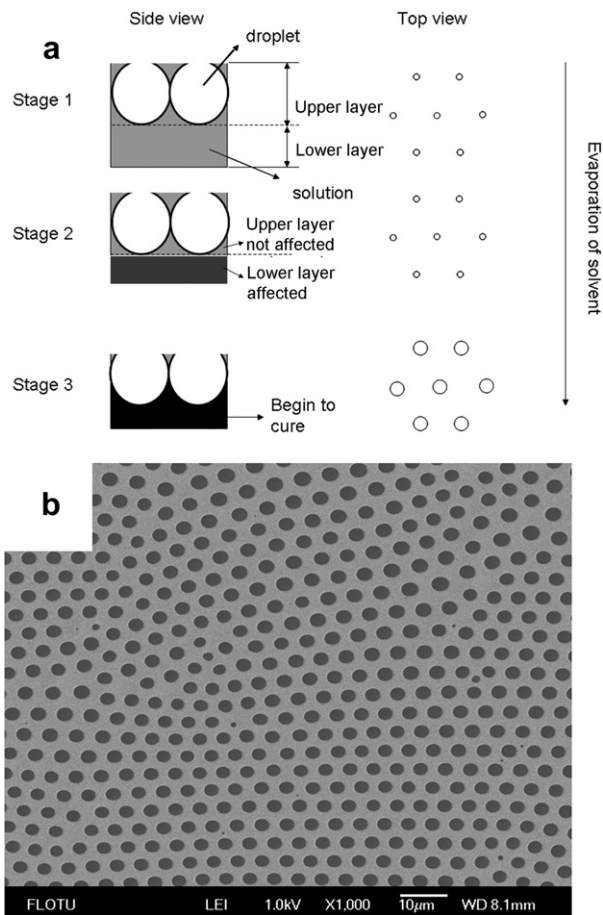


Fig. 6. Schematic diagram of the mechanism for the late BF process of the PPO/chloroform system (a) and an SEM photograph of the resulting surface morphology (b).

- (1) From 72 s to 80 s, the diameter of the SHs was 1.5 μm, and their speed decreased rapidly from more than 30 μm/s to about 5 μm/s.
- (2) From 80.2 s to 156 s, the diameter of the SHs remained 1.5 μm, and their speed fluctuated around 5 μm/s.
- (3) From 156.2 s to 180 s, the diameter of the SHs increased to 2.8 μm in the early part of this stage and remained at this value subsequently. Their speed decreased from 5 μm/s to 0 after the last fluctuation.

The detailed mechanism for the three stages is illustrated in Fig. 6a.

Stage 1 is the stage following the bursting behavior of the droplets. The appearance of SHs indicates that most of the solvent has evaporated, and the temperature of the solution is returning to the ambient temperature. With the evaporation of most of the solvent, the viscosity of the solution increases. The driving force of the Marangoni effect [10] decreases in conjunction with the decrease of the temperature gradient. Because of these two factors, the speed of the SHs rapidly drops.

Stage 2 shows features of relative equilibrium for both the diameter and speed of SHs. To explain these features, the solution is divided into the two layers in the direction vertical to the substrate shown in Fig. 6a, called the upper layer, which is around the droplets, and the lower layer, which is under the droplets. Because most of the solvent has evaporated, the solution is saturated in Stage 2. The lower layer is affected by further evaporation, but the upper layer is not. As a result, the diameter and speed of SHs show features of relative equilibrium during this stage.

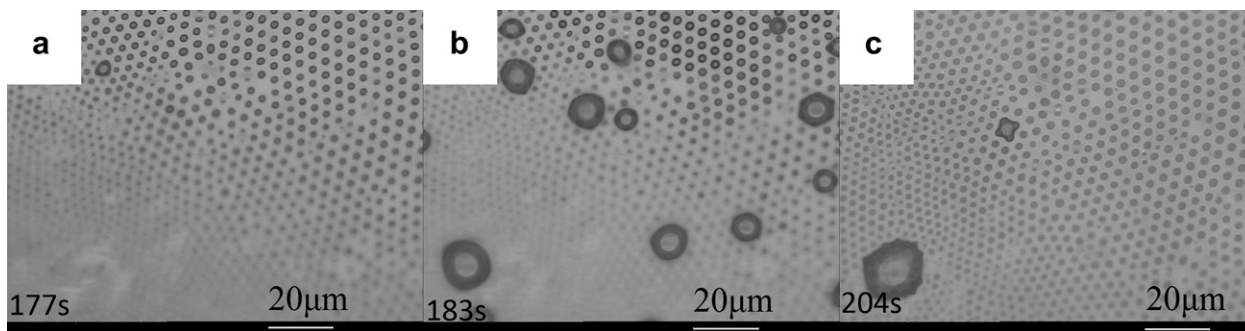


Fig. 7. OM photographs of the seeping phenomenon on the surface of a solidifying film at (a) 177 s (b) 183 s and (c) 204 s.

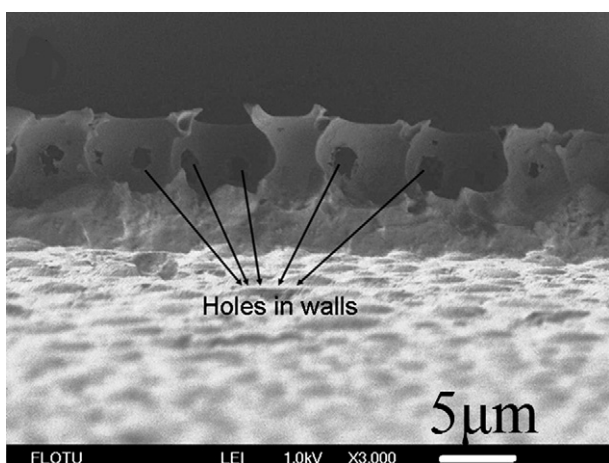


Fig. 8. SEM photograph of the resulting cross sectional morphology.

Stage 3 is close to the complete curing of the solution. Further evaporation causes the decrease of the thickness of the upper layer. A greater volume of the droplets emerges, leading to the growth of SHs. In the late part of this stage, the upper layer starts to cure, leading to the decrease of the speed of the SHs and the fixing of their diameter.

Finally, a PPO film with a honeycomb structure, as shown in Fig. 6b, forms.

At the time, during the solidification of film, some water under the film surface was observed to seep out through the SHs, as shown in Fig. 7. The seeping phenomenon lasted for about 30 s, indicating that the curing of the upper layer and the solidifying of film reduced the volume of pits under the SHs, which drew water out of the pits and is consistent with the assumption in Stage 3, Fig. 6a. Fig. 7a–c shows the beginning, duration and end of the phenomenon. The SEM photograph of a film cross section in Fig. 8 shows that the pits are connected to each other by holes in the walls between them. Water in a group of adjacent pits might concentrate in one pit through the wall holes and seep out through the SH corresponding to the concentrated pit.

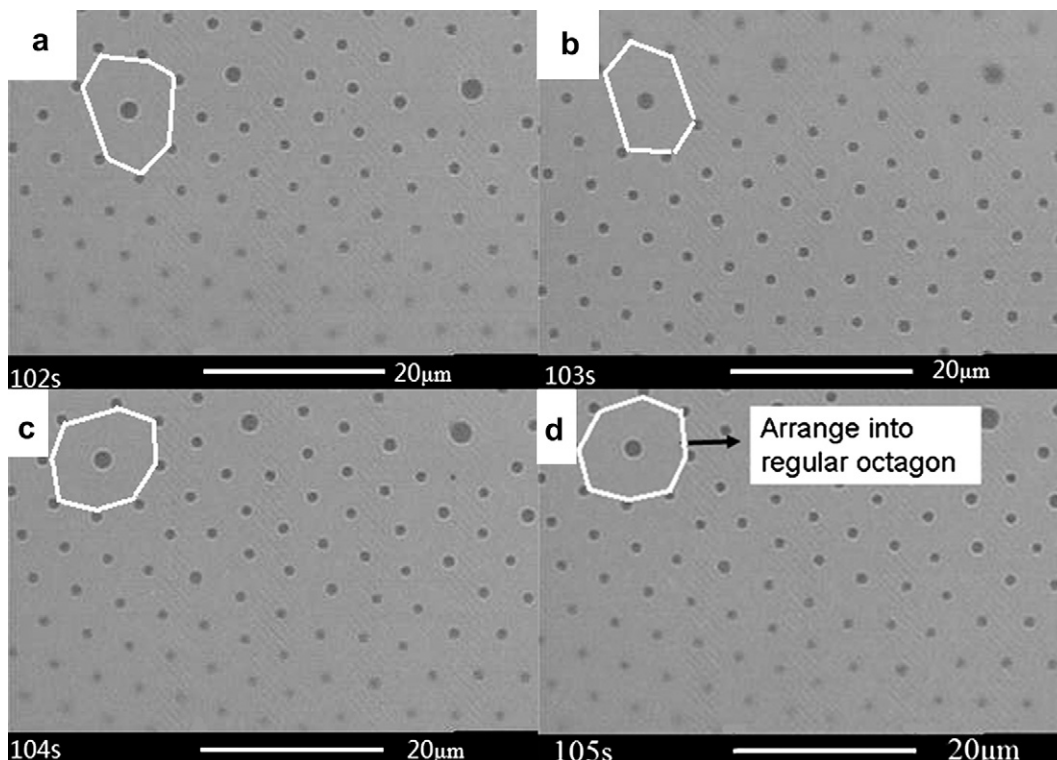


Fig. 9. OM photographs of the rearrangement of SHs around a bigger SH at (a) 102 s (b) 103 s (c) 104 s and (d) 105 s.



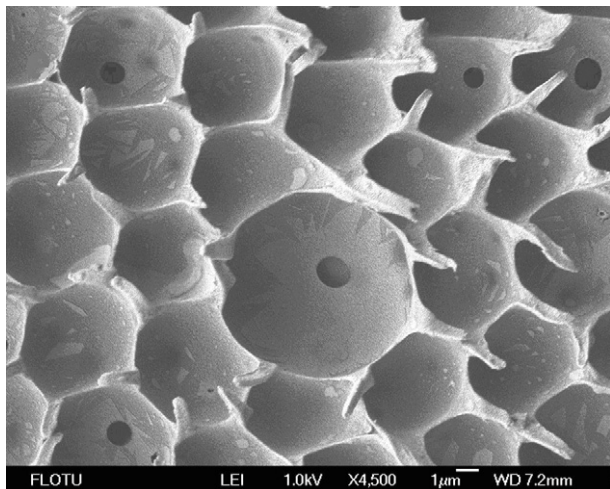


Fig. 10. SEM photograph of the morphology of a bigger pit, whose corresponding SH might be a bigger SH.

### 3.3. The rearrangement of SHs and the formation mechanism of defects

Defects are irregular SHs that are not surrounded evenly by 6 equal-diameter SHs. The formation processes of several typical kinds of defects, including bigger SHs, grain boundaries and points without SHs, were observed by tracking the rearrangement of the moving SHs.

Fig. 9 shows the rearrangement of SHs around a bigger SH. The polygon composed of the adjacent SHs around the bigger SH changed from an irregular polygon to a regular octagon in 3 s, indicating that adjacent SHs tend to rearrange evenly around the bigger SH. With regard to the “bursting hypothesis”, it can be speculated that there were 8 equal-diameter droplets packed around a bigger droplet, and it led to the structure where 8 equal-diameter pits were packed around a big pit. The speculation is consistent with the SEM photograph of the film with its top peeled off, as shown in Fig. 10. In all the images obtained, no SH with normal size was observed to grow into an SH bigger than normal ones. Consequently, in the PPO/chloroform system, the formation of bigger droplets might occur in the early BF stage, before the appearance of SHs.

Fig. 11 shows the collision of two blocks (divided by two straight lines) with SHs packed in different directions. The change of the pentagon in Fig. 11a–c indicates that the five SHs on the edge of two blocks were rearranged from different directions to the same direction in less than 1 s.

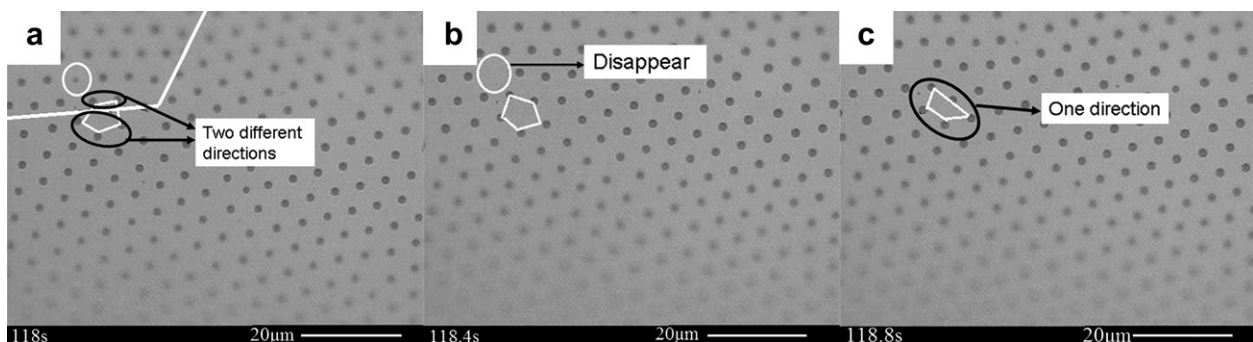


Fig. 11. OM photographs of a collision between SH blocks at (a) 118 s (b) 118.4 s and (c) 118.8 s.

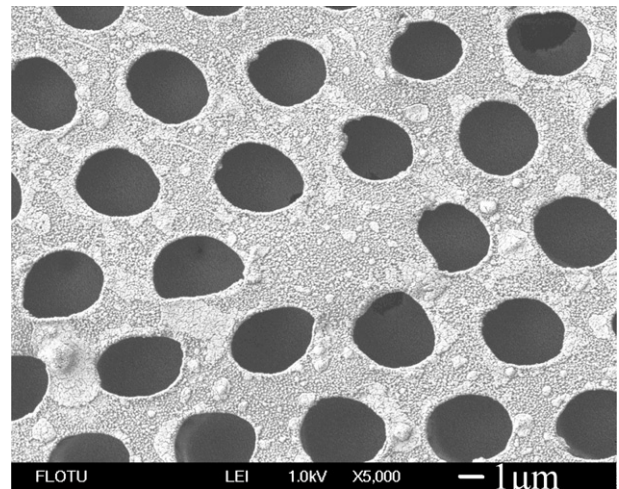


Fig. 12. SEM photograph of the morphology of a point without SH.

Xu et al. [33] proposed that defects in grain boundaries could arise because of the collision between blocks. In this work, the collision data was observed to support Xu’s hypothesis. Furthermore, it was found that the two blocks colliding with each other tended to rearrange into one direction. In the PPO/chloroform system, the factor that essentially causes grain boundaries might be the insufficient rearrangement of SHs during the collision, i.e., the driving force for the movement of droplets decreases, or the solution cures before the completion of the rearrangement.

Another interesting phenomenon occurring during the collision was that, in Fig. 11b, an SH on the edge of the two blocks marked by the circle vanished at 118.4 s. This phenomenon might lead to the defect without SH, as shown in Fig. 12.

Peng et al. [29] proposed that this kind of defect may arise from the loss of water droplets, i.e., water droplets condensing to these points are carried away by the evaporating solvent vapor. According to this hypothesis, there should be no droplets under the points without SHs. In the PPO/chloroform system, this hypothesis was not consistent with the experimental phenomena. As indicated by Fig. 4b, the droplets were closely packed under the surface with no SHs.

To further investigate the formation of defects without SHs, the iterative disappearance of SH shown in Fig. 13 is worth studying. An odd SH with more adjacent SHs was marked by a polygon composed of its adjacent SHs. By using this SH as reference, SHs could be detected. In Fig. 13a (96 s) to Fig. 13c (97 s), an SH marked by the circle became smaller and then disappeared. Although it reappeared in Fig. 13d (97.4 s), it disappeared again in Fig. 13e (97.8 s).

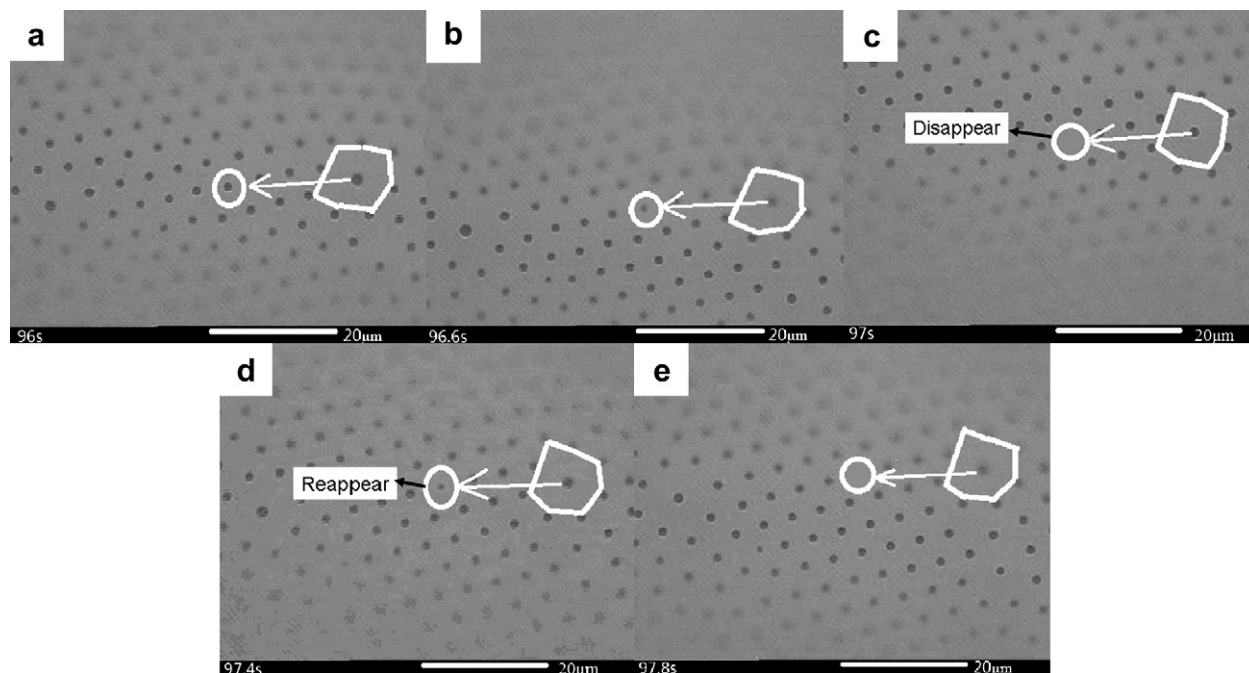


Fig. 13. OM photographs of the reappearance phenomenon of an SH at (a) 96 s (b) 96.6 s (c) 97 s (d) 97.4 s and (e) 97.8 s.

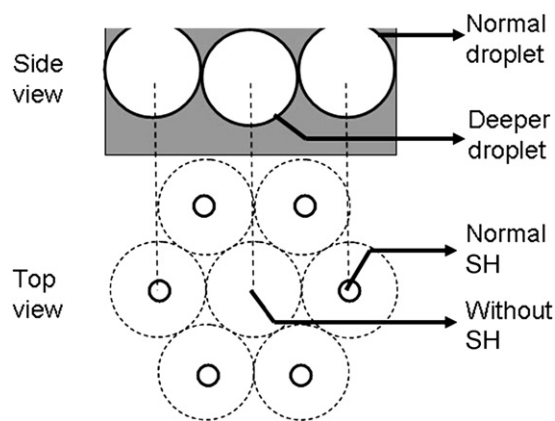


Fig. 14. Schematic diagram of the mechanism for the formation of a defect without an SH.

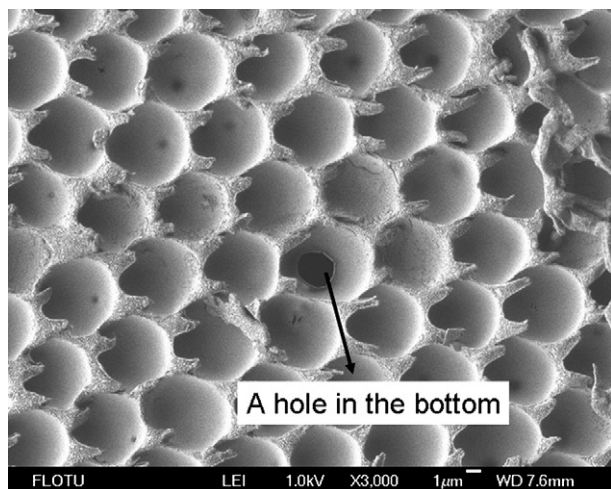


Fig. 15. SEM photograph of a hole in the bottom of a pit.

Peng's hypothesis is also inconsistent with the reappearance phenomenon. The SH cannot reappear if the droplet has been carried away. With regard to the "bursting hypothesis", a mechanism consistent with the reappearance phenomenon is proposed for the PPO/chloroform system. When SHs are rearranging, some droplets are extruded more deeply by others. The polymer layer consequently encapsulates these deeper droplets again, as illustrated in Fig. 14, leading to the defects without SHs. The water in a deeper droplet may evaporate away through other passages, such as the holes in walls to adjacent SHs, as shown in Fig. 8, or the hole in the bottom, as shown in Fig. 15.

The rearrangement of SHs, which plays an important role in the formation of defects, is a surface phenomenon caused by the rearrangement of droplets in solution. Controlling the movement and rearrangement of droplets may help to reduce defects.

#### 4. Conclusion

The growth and rearrangement behavior of SHs on the surface of a PPO solution, in conjunction with the formation phenomenon of defects during BF process, were observed in situ under OM. In the PPO/chloroform system, SHs appeared later than the condensation of droplets. The "bursting hypothesis" was directly supported by the appearance and movement of SHs and indirectly supported by the inner structure of the film with fewer SHs. The late BF process of the PPO/chloroform system after the appearance of SHs can be divided into 3 stages according to the diameter and speed of the SHs. In Stage 1, SHs appear, and their speed rapidly drops because most of the solvent has evaporated. In Stage 2, their diameter and speed show features of relative equilibrium. The reason may be that the upper layer of the solution that surrounds the droplets has been saturated and is almost unaffected by further evaporation of the solvent until Stage 3. In Stage 3, their diameter increases to the maximum value as their speed decreases to 0 because a greater volume of the droplets emerge and the solution cures with the completion of the evaporation of the solvent. Moreover, the formation process of defects was observed. The mechanisms for the

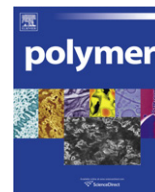
formation of grain boundaries and defects without SHs in the PPO/chloroform system were discussed. The grain boundaries might arise from the collision between SH blocks and insufficient rearrangement. The cause of defects without SHs could be that the droplets under these points are deeper, and the polymer layer encapsulating these droplets does not burst.

### Acknowledgment

This work was supported by the National Basic Research Program of China (973 Program) (2009CB623404), the National High Technology Research and Development Program of China (863 Program) (2009AA062901) and the Major Program of Beijing Municipal Natural Science Foundation (2100001).

### References

- [1] Xu XX, Zhuang J, Wang X. *Journal of the American Chemical Society* 2008;130(37):12527–35.
- [2] Chari K, Lander CW, Sudol RJ. *Applied Physics Letters* 2008;92(11).
- [3] Nurmawati MH, Ajikumar PK, Renu R, Valiyaveetil S. *Advanced Functional Materials* 2008;18(20):3213–8.
- [4] Fukuhira Y, Kitazono E, Hayashi T, Kaneko H, Tanaka M, Shimomura M, et al. *Biomaterials* 2006;27(9):1797–802.
- [5] Tanaka M, Nishikawa K, Okubo H, Kamachi H, Kawai T, Matsushita M, et al. *Colloids and Surfaces A - Physicochemical and Engineering Aspects* 2006;284:464–9.
- [6] Chaudhuri JB, Davidson MG, Ellis MJ, Jones MD, Wu XJ. *Macromolecular Symposia* 2008;272:52–7.
- [7] Vohra V, Yunus S, Attout A, Giovannella U, Scavia G, Tubino R, et al. *Soft Matter* 2009;5(8):1656–61.
- [8] Gugliuzza A, Aceto MC, Macedonio F, Drioli E. *Journal of Physical Chemistry B* 2008;112(34):10483–96.
- [9] Bormashenko E, Schechter A, Stanevsky O, Stein T, Balter S, Musin A, et al. *Macromolecular Materials and Engineering* 2008;293(11):872–7.
- [10] Widawski G, Rawiso M, Francois B. *Nature* 1994;369(6479):387–9.
- [11] Hayakawa T, Horiuchi S. *Angewandte Chemie-International Edition* 2003;42(20):2285–9.
- [12] Dong WY, Zhou YF, Yan DY, Mai YY, He L, Jin CY. *Langmuir* 2009;25(1):173–8.
- [13] de Boer B, Stalmach U, van Hutten PF, Melzer C, Krasnikov VV, Hadziioannou G. *Polymer* 2001;42(21):9097–109.
- [14] Zhao HJ, Shen YM, Zhang SQ, Zhang HM. *Langmuir* 2009;25(18):11032–7.
- [15] Karthaus O, Cieren X, Maruyama N, Shimomura M. *Materials Science & Engineering C - Biomimetic and Supramolecular Systems* 1999;10(1–2):103–6.
- [16] Xu XX, Wang X, Nisar A, Liang X, Zhuang J, Hu S, et al. *Advanced Materials* 2008;20(19):3702–8.
- [17] Korgel BA, Fullam S, Connolly S, Fitzmaurice D. *Journal of Physical Chemistry B* 1998;102(43):8379–88.
- [18] Stenzel MH, Barner-Kowollik C, Davis TP. *Journal of Polymer Science Part A - Polymer Chemistry* 2006;44(8):2363–75.
- [19] Bunz UHF. *Advanced Materials* 2006;18(8):973–89.
- [20] Connal LA, Vestberg R, Hawker CJ, Qiao GG. *Advanced Functional Materials* 2008;18(22):3706–14.
- [21] Tian Y, Ding HY, Jiao QZ, Shi YQ. *Macromolecular Chemistry and Physics* 2006;207(5):545–53.
- [22] Liu WY, Liu RG, Li YX, Wang W, Ma L, Wu M, et al. *Polymer* 2009;50(12):2716–26.
- [23] Peng J, Han YC, Yang YM, Li BY. *Polymer* 2004;45(2):447–52.
- [24] Pitois O, Francois B. *European Physical Journal B* 1999;8(2):225–31.
- [25] Bormashenko E, Musin A, Bormashenko Y, Whyman G, Pogreb R, Gendelman O. *Macromolecular Chemistry and Physics* 2007;208(7):702–9.
- [26] Srinivasarao M, Collings D, Philips A, Patel S. *Science* 2001;292(5514):79–83.
- [27] Song L, Bly RK, Wilson JN, Bakbak S, Park JO, Srinivasarao M, et al. *Advanced Materials* 2004;16(2):115–8.
- [28] Li J, Cheng JT, Zhang Y, Gopalakrishnakone P. *Colloid and Polymer Science* 2009;287(1):29–36.
- [29] Peng J, Han YC, Fu J, Yang YM, Li BY. *Macromolecular Chemistry and Physics* 2003;204(1):125–30.
- [30] Billon L, Manguian M, Pellerin V, Joubert M, Etteradossi O, Garay H. *Macromolecules* 2009;42(1):345–56.
- [31] Kojima M, Hirai Y, Yabu H, Shimomura M. *Polymer Journal* 2009;41(8):667–71.
- [32] Park JS, Lee SH, Han TH, Kim SO. *Advanced Functional Materials* 2007;17:2315–20.
- [33] Xu Y, Zhu BK, Xu YY. *Polymer* 2005;46(3):713–7.
- [34] Barrow MS, Jones RL, Park JO, Srinivasarao M, Williams PR, Wright CJ. *Spectroscopy - An International Journal* 2004;18(4):577–85.
- [35] Maruyama N, Karthaus O, Ijiro K, Shimomura M, Koito T, Nishimura S, et al. *Supramolecular Science* 1998;5(3–4):331–6.
- [36] Karthaus O, Maruyama N, Cieren X, Shimomura M, Hasegawa H, Hashimoto T. *Langmuir* 2000;16(15):6071–6.
- [37] Tian Y, Jiao QZ, Ding HY, Shi YQ, Liu BQ. *Polymer* 2006;47(11):3866–73.
- [38] Yabu H, Takebayashi M, Tanaka M, Shimomura M. *Langmuir* 2005;21(8):3235–7.
- [39] Maruyama N, Koito T, Nishida J, Sawadaishi T, Cieren X, Ijiro K, et al. *Thin Solid Film* 1998;327:854–6.



## Interface-tuned epoxy/clay nanocomposites

Izzuddin Zaman<sup>a,b</sup>, Quyen-Huyen Le<sup>a</sup>, Hsu-Chiang Kuan<sup>c</sup>, Nobuyuki Kawashima<sup>d</sup>, Lee Luong<sup>a</sup>, Andrea Gerson<sup>d</sup>, Jun Ma<sup>a,\*</sup>

<sup>a</sup>School of Advanced Manufacturing and Mechanical Engineering, University of South Australia, Mawson Lakes, SA 5095, Australia

<sup>b</sup>Faculty of Mechanical Engineering and Manufacturing, University of Tun Hussein Onn Malaysia, 68400 Batu Pahat, Malaysia

<sup>c</sup>Department of Energy Application Engineering, Far East University, Tainan County 744, Taiwan, ROC

<sup>d</sup>Applied Centre for Structural and Synchrotron Studies, University of South Australia, SA 5095, Australia

### ARTICLE INFO

#### Article history:

Received 29 September 2010

Accepted 3 December 2010

Available online 10 December 2010

#### Keywords:

Interface

Nanocomposites

Clay

### ABSTRACT

Though interface has been known for a critical role in determining the properties of conventional composites, its role in polymer nanocomposites is still fragmented and in its infancy. This study synthesized a series of epoxy/clay nanocomposites with different interface strength by using three types of modifiers: ethanolamine (denoted ETH), Jeffamine<sup>®</sup> M2070 (M27) and Jeffamine<sup>®</sup> XTJ502 (XTJ). XTJ created a strong interface between clay layers and matrix because it bridged the layers with matrix by a chemical reaction as proved by Fourier transform infrared spectroscopy; M27 produced an intermediate interface strength due to the molecular entanglement between grafted M27 chains and matrix molecules; the interface made by ETH was weak because neither chemical bridging nor molecular entanglement was involved. The studies of mechanical and thermal properties and morphology at a wide range of magnification show that the strong interface promoted the highest level of exfoliation and dispersion of clay layers, and achieved the most increment in Young's modulus, fracture toughness and glass transition temperature ( $T_g$ ) of matrix. With  $\sim 1.3$  wt% clay, the critical strain energy release rate  $G_{Ic}$  of neat epoxy improved from 179.0 to 384.7 J/m, 115% improvement and  $T_g$  enhanced from 93.7 to 99.7 °C, 6.4% improvement.

© 2010 Elsevier Ltd. All rights reserved.

### 1. Introduction

The interface of composites is a well-known factor posing a significant effect on the composite properties due to its role of transferring stress or electrons across matrix and filler. Polymer nanocomposites offer significant improvements in material properties, such as modulus, strength, toughness, scratch resistance, optical properties, electrical conductivity, gas and solvent transport, with much lower fractions of nanoparticles than the conventional composites. Despite the large volume of nanocomposite research published over the past 15 years, the understanding of the role of interface in morphology and properties remains in its infancy. This is mainly due to the lack of reliable experimental data from a series of comparable nanocomposites of tailored interface strength.

Of thermosets, epoxy has been widely used across industries owing to its high chemical resistance against severe corrosive

conditions, good thermal and mechanical properties, excellent adhesion to a wide range of materials and easy processability. However, it is inherently brittle and thus attracted increasingly more interest from both industries and universities for toughening. Essentially, there are two common approaches to toughen brittle epoxy resin: to modify epoxy structure [1–3] and to introduce toughening agents [4–6]. The latter has been the focus, in specific using nanoparticles in recent years as the tougheners because of significantly improved fracture toughness with no loss of other desired properties at low fractions [7–11]. Nanocomposites are generally classified by the geometries of the nanoparticles—particulate (e.g. silica), layered (silicate layers), and fibrous geometries (nanotubes)—of which layered polymer nanocomposites have shown the greatest mechanical and barrier properties, and attracted the most extensive research and development due to the fillers' high specific surface area, functionality and cost-effective fabrication [12–15].

Based on the arrangement of silicate layers in polymer matrixes, two types of morphology are formed in nanocomposites: intercalated or exfoliated. The exfoliated morphology is always preferred because it produces better performance, despite the fact that exfoliation is difficult to achieve. Three key factors to achieve exfoliation

\* Corresponding author. Tel.: +61 8 8302 5117; fax: +61 8 8302 3380.  
E-mail addresses: [abcjunma@hotmail.com](mailto:abcjunma@hotmail.com), [jun.ma@unisa.edu.au](mailto:jun.ma@unisa.edu.au) (J. Ma).  
URL: <http://people.unisa.edu.au/jun.ma>

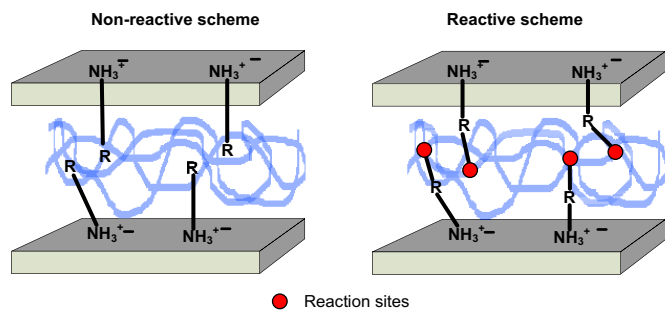


Fig. 1. Schematic of two routes to polymer/clay nanocomposites.

include: increase in the silicate interlayer spacing through suspension in solvent/water or polymerization prior to compounding with polymers [16]; the adoption of reactive modifier bridging the layers with polymer matrix [17,18]; and the creation of physical entanglement between silicate modifier and matrix [19]. Epoxy/clay nanocomposite research was pioneered by Messersmith and Giannelis [20] who produced merely intercalated nanocomposites. Curing was then proved helpful to promote the exfoliation layers [21,22]. A few studies justified the ameliorated mechanical properties by the highly exfoliated, uniformly dispersed silicate layers in epoxy matrix based upon just one or two high magnification micrographs, rather than observation made on low magnification TEM micrographs [18,20–23]. In fact, clusters of silicate layers were found at low magnification [24,25], an important factor in studying epoxy/clay nanocomposites since phase separation often occurs during fabrication.

A recent trend is to adopt reactive surfactants to modify silicate which subsequently bridged to matrix molecules [18,23]. Cheng-Yang et al. adopted an epoxide-containing surfactant to modify silicate layers which was then mixed with epoxy and hardener; during curing, the epoxide groups reacted with hardeners to produce links between silicate layers and matrix. Since an epoxy of low modulus was chosen as matrix, no fracture toughness measurement was made. Although the silicate layers obviously improved modulus and strength, the nanocomposites showed reduced glass transition temperatures ( $T_g$ s) [23].

In spite of these extensive studies on epoxy/clay nanocomposites, it is still not clear the effect of interface on the morphology, mechanical properties, fracture toughness and thermal mechanical properties of these materials. This research attempts to

synthesize epoxy/clay nanocomposites with three levels of interface strength by adapting the following routes: (1) Molecular entanglement. Matrix molecules physically entangle with surfactants that are grafted into silicate layer surface via ion exchange; and (2) Chemical reaction. The surfactant used for clay contains two end-amine groups: one grafting into the silicate surface via ion exchange and the other reacting with epoxy molecule. Fig. 1 illustrates the proposed routes for improving the interaction between epoxy and silicate. We then investigate the effect of interface on the morphology, mechanical properties, fracture toughness and thermal mechanical properties of these materials. Through this work, an understanding of the interface effect on layered polymer nanocomposites is obtained.

## 2. Experimental parts

### 2.1. Materials

Epoxy resin, diglycidyl ether of bisphenol A (DGEBA, Araldite-F) with epoxide equivalent weight 182–196 g/equiv, was purchased from Ciba-Geigy, Australia. Hardener polyoxypropylene (Jeffamine® J230) was provided by Huntsman. Sodium montmorillonite was provided by Southern Clay Products with a cation exchange capacity (CEC) of 85 mequiv/100 g. Ethanolamine was purchased from APS Specialty Chemicals; surfactants Jeffamine® M2070 and Jeffamine® XTJ502 were provided by Huntsman. The chemical structures and molecular weight of these surfactants are shown in Table 1.

### 2.2. Modification of clay surface

10 g clay was dispersed in 2 kg boiling deionized water through 10 min vigorous stirring using a mechanical mixer. Stoichiometric amount of ethanolamine or M27 or XTJ was dissolved in 200 g water, followed by adding 10 g of hydrochloric acid solution (0.83 mol/L). The mixture was stirred by a glass rod and then added slowly to the clay suspension, followed by 10 min vigorous stirring at 90 °C. The resulting clay was condensed using a rotary vacuum evaporator for 30 min at 80–90 °C and then separated using a centrifuge. The precipitate was repeatedly washed three times with acetone using a magnetic mixer, an ultrasonic bath and the centrifuge. The final precipitate was suspended in 500 ml acetone to form clay/acetone slurry, which were denoted as *eth*-clay or *m27*-clay or *xtj*-clay depending on the type of surfactant used.

Table 1  
Surfactants used to modify raw clay.

Modifiers	ABBR.	$M_w^a$	Formulae
Ethanolamine	ETH	61	$\text{HO}-\text{CH}_2-\text{CH}_2-\text{NH}_2$
JEFFAMINE M2070 monoamine	M27	~2000	$\text{H}_3\text{C}-\text{O}-\left[\text{CH}_2-\text{CH}_2-\text{O}\right]_{29.2}-\left[\text{CH}_2-\underset{\text{CH}_3}{\text{CH}}-\text{O}\right]_{12.5}-\text{CH}_2-\underset{\text{CH}_3}{\text{CH}}-\text{NH}_2$
XTJ502 (JEFFAMINE ED-2003)	XTJ	~2000	$\text{H}_2\text{N}-\underset{\text{CH}_3}{\text{CH}}-\text{CH}_2-\left[\text{O}-\underset{\text{CH}_3}{\text{CH}}-\text{CH}_2\right]_a-\left[\text{O}-\text{CH}_2-\text{CH}_2\right]_{39.5}-\left[\text{O}-\text{CH}_2-\underset{\text{CH}_3}{\text{CH}}\right]_c-\text{NH}_2$ <p style="text-align: center;">with <math>a + c = 5</math></p>

<sup>a</sup> Molecular weight of grafted surfactant.

### 2.3. Preparation of epoxy/clay nanocomposite

An *in situ* reaction was used, taking advantage of the increased layer spacing in a solvent—a key factor to achieve exfoliation [16]. DGEBA was mixed with a desired amount of the modified clay slurry for 1 h at 55 °C using a mechanical mixer at 400 rpm in a round-bottom flask with a condenser. The mixture was then transferred into a beaker followed by mixing and heating at 300 rpm and 120 °C for 1 h to evaporate acetone, followed by degassing in a vacuum oven at 120 °C. A stoichiometric amount of curing agent J230 (3.3:1 weight ratio of DGEBA to J230) was added to the mixture and mixed for ~2 min at 50 °C. The resultant mixture was highly degassed in a vacuum oven for ~5 min to remove trapped bubbles, followed by pouring into a rubber mould and curing at 80 °C for 3 h and at 120 °C for 12 h.

### 2.4. Chemical characterization

A Nicolet Avatar 320 Fourier transform infrared spectroscopy (FTIR) was employed to analyze the bonding between matrix and nanoparticles, by recording the spectra of neat epoxy and the nanocomposites from 4000 to 700  $\text{cm}^{-1}$  at 2  $\text{cm}^{-1}$  using a minimum of 32 scans. The FTIR samples were prepared by a solution-casting method on the KBr plate.

### 2.5. Morphological observation

Transmission electron microscopy (TEM) was performed to provide two dimensional images of internal structure of the nanocomposites. Ultrathin sections of 50 nm were microtomed from bulk samples using Leica Ultracut S microtome equipped with a diamond knife and collected on 200-mesh copper grids. These sections were examined with a Philips CM200 transmission electron microscope at 200 kV accelerating voltage.

X-ray diffraction (XRD) was conducted at room temperature using a Mini-Materials Analyzer (MMA). The diffractometer was equipped with a curved graphite monochromator, tuned to Cu K radiation, which was applied at a tube voltage of 35 kV and an X-ray power of 1 kW. The diffraction patterns were then collected in reflection mode geometry between  $2\theta = 1.5\text{--}12^\circ$  at a scanning rate of  $1^\circ/\text{min}$ .

### 2.6. Mechanical measurement

Tensile test was performed on dumb-bell samples of gauge length 100 mm at 0.5 mm/min according to the ASTM D-638 to determine the elastic modulus, ultimate stress, and ultimate strain of neat epoxy and nanocomposites, by using Instron 5567 testing system with a 30 kN load cell and an extensometer. The average values of all the properties were taken from five repetitions of each test; Young's moduli were calculated at a strain range 0.05–0.15%.

Fracture toughness measurement requests great care to produce an instantly propagated crack [26]. In comparison with compact tension (CT) or double cantilever beam (DCB), single edge notch bending (SENB) just needs the least volume of materials but it is the most difficult to produce an instantly propagated crack due to its limited cross section area. Therefore, this study tested fracture toughness according to ASTM D-5045 using the compact tension (CT) of ~30 mm in width and ~5 mm in thickness. An instantly propagated crack was produced for each CT by tapping a razor blade to the samples as it is the most cost-effective way to produce a sufficiently sharp crack [26]. It was then tested using the Instron equipped with a 2 kN load cell at 0.5 mm/min. The fracture toughness properties were expressed as stress intensity factor,  $K_{IC}$

and critical strain energy release rate,  $G_{IC}$ . The fracture toughness was calculated using Eqs. (1) and (2).

$$K_{IC} = \frac{P_Q f(x)}{BW^{1/2}} \quad (1)$$

$$G_{IC} = \frac{K_{IC}^2}{E(1-\nu^2)} \quad (2)$$

where

$$f(x) = \frac{(2+x)(0.866 + 4.64x - 13.32x^2 + 14.72x^3 - 5.6x^4)}{(1-x)^{3/2}}$$

and ( $0.2 < x < 0.8$ ):

$$x = \frac{a}{W}$$

where  $P_Q$  is the maximum load,  $B$  is the thickness,  $W$  is the width,  $E$  is Young's modulus and  $\nu$  is Poisson's ratio 3.4.

### 2.7. Dynamic mechanical measurement

Dynamic Mechanical Analyzer 2980 (TA Instruments, Inc., USA) was utilized at 1 Hz to determine the glass transition temperatures of neat epoxy and its nanocomposites. A single cantilever clamp with a supporting span of 20 mm and torque of 1 Nm was used to clamp rectangular specimens of  $3.0 \times 6.0 \times 40.0$  mm which were scanned from 50 to 120 °C and recorded at 2 s/point.

## 3. Results and discussion

### 3.1. Reactions for interface

Fourier transform infrared spectroscopy (FTIR) was employed to analyze the interaction and bonding between silicate surface and epoxy molecules during fabrication. Fig. 2 shows the FTIR spectra of epoxy, raw clay, the clay modified by ethanolamine (*eth*-clay), and the washed mixture of epoxy/*eth*-clay. The dominant absorption from 991  $\text{cm}^{-1}$  to 1045  $\text{cm}^{-1}$  is ascribed to the Si–O band in-plane stretching of clay [27,28]. The absorption of raw clay at 1636  $\text{cm}^{-1}$  is due to the O–H deformation of entrapped water and the absorption at 3620  $\text{cm}^{-1}$  is created by the O–H stretching of structural

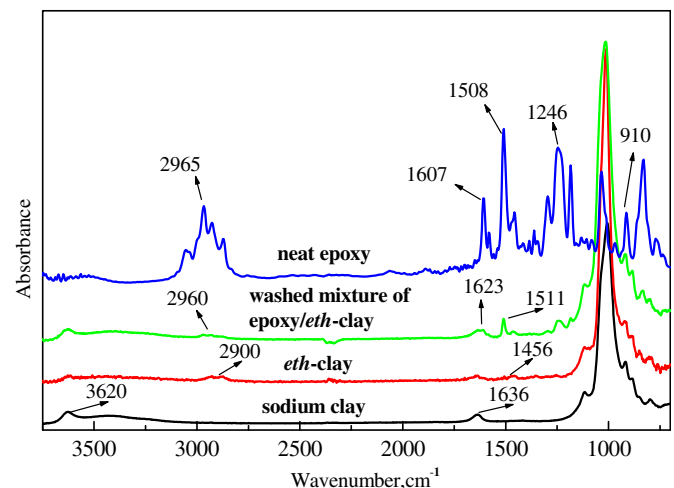


Fig. 2. FTIR spectra of sodium clay, *eth*-clay, the washed mixture of epoxy/*eth*-clay and neat epoxy (Graphs are vertically shifted for clarity).

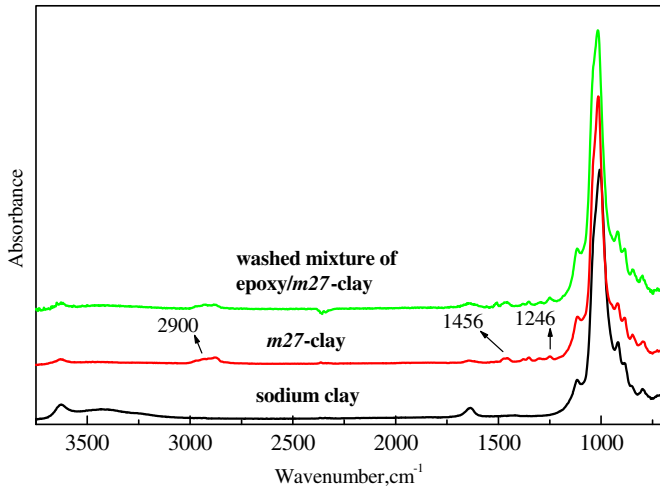


Fig. 3. FTIR spectra of sodium clay, *m27*-clay, and the washed mixture of epoxy/*m27*-clay.

hydroxyl group of the clay. Upon modification with ethanolamine (ETH), new absorption bands are expected in FTIR. Actually, absorption at  $1456\text{ cm}^{-1}$  and  $2900\text{ cm}^{-1}$  are observed due to the presence of  $-\text{CH}_2-$  groups [29] and  $-\text{CH}-$  groups [30], and this confirms the graft of ethanolamine into the clay layer surface. For epoxy, the absorption from  $1450\text{ cm}^{-1}$  to  $1600\text{ cm}^{-1}$  corresponds to the benzyl groups; the C–H band stretching of SP2 is observed at  $3048\text{ cm}^{-1}$ , the C–H band stretching of SP3 at  $2965\text{ cm}^{-1}$ ,  $2927\text{ cm}^{-1}$  and  $2873\text{ cm}^{-1}$ , C–O band stretching  $1246\text{ cm}^{-1}$ , and the existence of epoxide groups at  $910\text{ cm}^{-1}$  [31]. After *eth*-clay was mixed with epoxy followed by thoroughly washing using acetone as shown in Section 2.2, absorption bands for epoxy should be observed if epoxy molecules react or attract to the grafted ethanolamine. Indeed, there is just little characteristic bands of epoxy observed (at  $910\text{ cm}^{-1}$ ), indicating traces of epoxy molecules between the clay layers, which is caused by the incomplete removal of epoxy during washing due to the interaction between the hydroxide group of ETH and that of epoxy.

In Fig. 3, new absorption bands are found for the clay modified by M27 (*m27*-clay): the absorption at  $1456\text{ cm}^{-1}$  is contributed by the  $-\text{CH}_2-$  groups [29] and the absorption at  $2900\text{ cm}^{-1}$  by the  $-\text{CH}-$  groups of the M27 molecules [30], and C–O band stretching

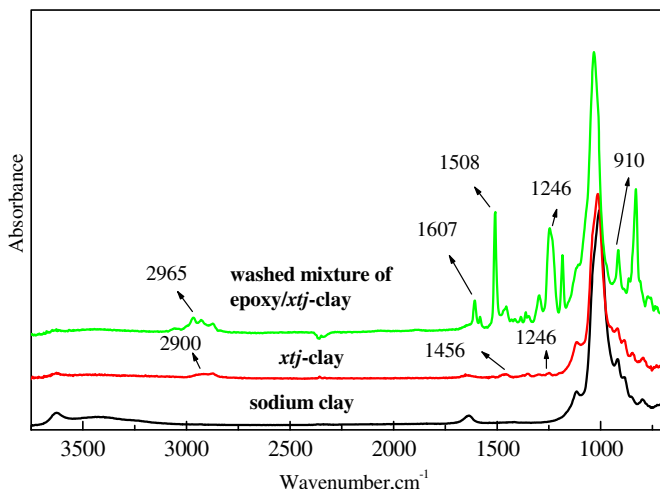


Fig. 4. FTIR spectra of sodium clay, *xtj*-clay, and the washed mixture of epoxy/*xtj*-clay.

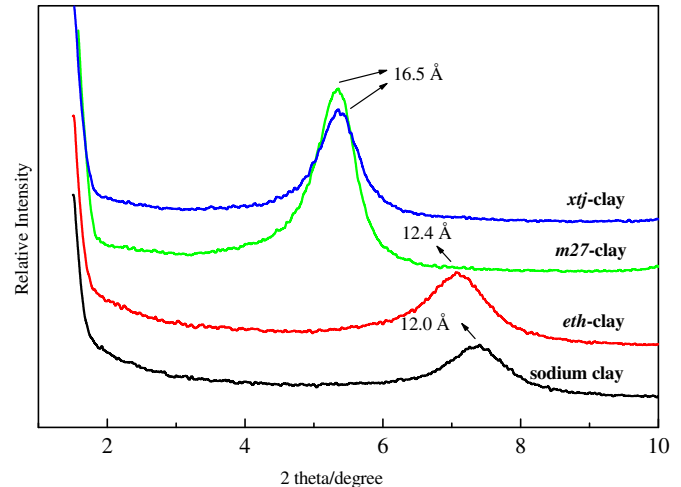


Fig. 5. XRD spectra of sodium clay, *eth*-clay, *m27*-clay and *xtj*-clay.

is found  $1246\text{ cm}^{-1}$ , all of which confirms the graft of M27 into the clay layers. The washed mixture of epoxy/*m27*-clay shows a similar spectrum to the *m27*-clay, indicating that neither chemical reaction nor strong physical interaction combines epoxy molecules with *m27*-clay.

The spectra of the *xtj*-clay and its washed mixture are shown in Fig. 4. The spectrum of *xtj*-clay shows a similar feature to M27 in Fig. 3, indicating the graft of XTJ chains into the clay layers as XTJ has similar chemical composition to M27 except the number of end-amine groups as shown in Table 1. Upon mixing with epoxy followed by thoroughly washing as shown in Section 2.2, the mixture shows intensive characteristic absorption which is similar to neat epoxy in Fig. 2, and this confirms the reaction of epoxy molecules with the grafted XTJ chains. The absorption at  $910\text{ cm}^{-1}$  corresponds to epoxide groups, implying that only one of the two end-groups of each epoxy molecule between the layers reacted with the grafted XTJ chains. When *xtj*-clay was further mixed and cured, the free end-group  $\text{NH}_2$  of a grafted XTJ chain reacted with hardener J230, building up a bridge linking the clay layers with matrix to produce a strong interface.

In summary, the interface strength between clay layers and epoxy increases in the order of raw clay < *eth*-clay < *m27*-clay < *xtj*-clay, based on the interaction of the surfactants with epoxy molecules.

### 3.2. Morphology

The structure analysis of these nanocomposites were performed not only using the XRD, but TEM as it is the only method to identify the distribution of individual silicate layers in matrix [32].

#### 3.2.1. XRD spectra

Fig. 5 presents the XRD patterns of raw clay and the modified clay in  $2\theta = 1.5\text{--}10^\circ$ . A diffraction peak assigned to the [001] lattice spacing of raw clay at  $2\theta = 7.36^\circ$ , corresponds to a d-spacing of

Table 2  
Interlayer distance of various types of clay system.

Type of clay systems	(2 $\theta$ ) Peak angle, (deg)	(001) Basal spacing, (Å)
Sodium clay	7.36	12.0
<i>eth</i> -clay	7.10	12.4
<i>m27</i> -clay	5.36	16.5
<i>xtj</i> -clay	5.36	16.5

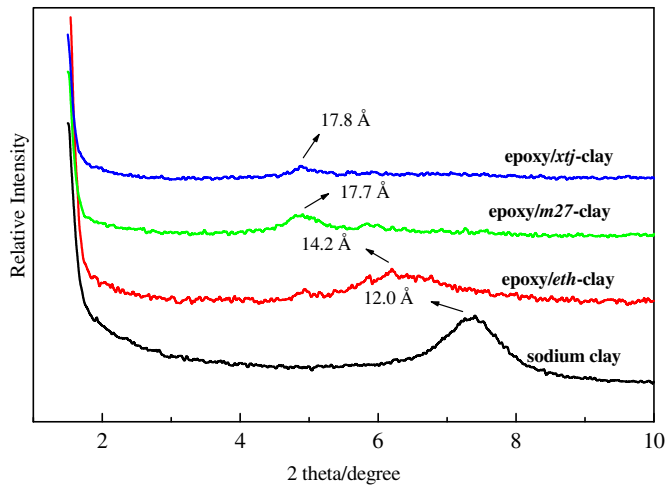


**Fig. 6.** XRD spectra of sodium clay and the epoxy/*eth*-clay, epoxy/*m27*-clay and epoxy/*xtj*-clay nanocomposite (nominal clay content 2.5 wt%).

12.0 Å. Upon modification, the diffraction shifts left to lower angles, revealing an increase in the layers' spacing. This result confirms the grafting of the surfactant into the layers through cationic exchange between layers and surfactants as supported by FTIR analysis in Figs. 2–4.

Table 2 contains the peak angles and interlayer distance for each type of clay. *eth*-clay shows the lowest value of spacing due to its short chain length. When clay is modified with the long-chain surfactants XTJ and M27, the diffraction peak moves to lower angle, corresponding to a layer spacing of 1.65 nm. *xtj*-clay and *m27*-clay show similar diffraction pattern and the same basal spacing because of their similar chain length.

The XRD patterns of the nanocomposites containing nominal 2.5 wt% clay are presented in Fig. 6. In comparison with Fig. 5, the diffraction moves to lower angles and all diffraction intensity reduces, indicating the expansion of layer spacing due to the

intercalation of epoxy molecules into the clay gallery. Epoxy/*eth*-clay nanocomposite shows a broad peak at  $2\theta = 6.2^\circ$  relative to 14.2 Å layer spacing. By contrast, the diffraction of epoxy/*m27*-clay nanocomposite appears at  $2\theta = 4.98^\circ$ , corresponding to a layer spacing 17.7 Å; the diffraction intensity is much smaller. This indicates that the layer spacing of *m27*-clay is further increased and most layers may have exfoliated as more epoxy molecules migrate into the clay interlayer space through compounding with epoxy. The chain length of M27 is over 40 fold longer than that of ETH, and thus the grafted M27 molecules are much more effective in entangling with and migrating epoxy molecules into the interlayer space of clay. Although *m27*-clay and *xtj*-clay were modified by similar molecular weight surfactants, epoxy/*xtj*-clay nanocomposite demonstrates a lower angle diffraction with much smaller intensity than the epoxy/*m27*-clay. This is caused by the reactivity of the graphed XTJ chains, each of which has two amine end-groups: one grafting into clay layers and the other reacting with epoxy molecules as discussed in FTIR, thus creating a strong interface between layers and matrix. The reaction of XTJ with epoxy brought a great amount of epoxy molecules into the interlayer space, significantly increasing the layer spacing and probably causing a higher level of exfoliation than the epoxy/*m27*-epoxy. This explains why *xtj*-clay is of the best capacity for exfoliation. Therefore, the three types of clay follow the following sequence to exfoliate in epoxy: *eth*-clay < *m27*-clay < *xtj*-clay.

### 3.2.2. TEM micrograph

The exfoliation and dispersion of clay layers are two critical factors determining the mechanical and functional properties of polymer/clay nanocomposite. While exfoliation is proved by XRD and high magnification TEM micrographs, the uniformly dispersion of clay layers can only be certified by low magnification TEM micrographs, although a number of research claimed a homogeneous nanostructure of epoxy-clay without sufficient TEM evidence [23,33].

Figs. 7–9 present the TEM micrographs of these nanocomposites at magnification 500–50000 $\times$ . At the lowest magnification micrographs “a” in these figures, all types of clay form clusters of 2–10  $\mu\text{m}$  in

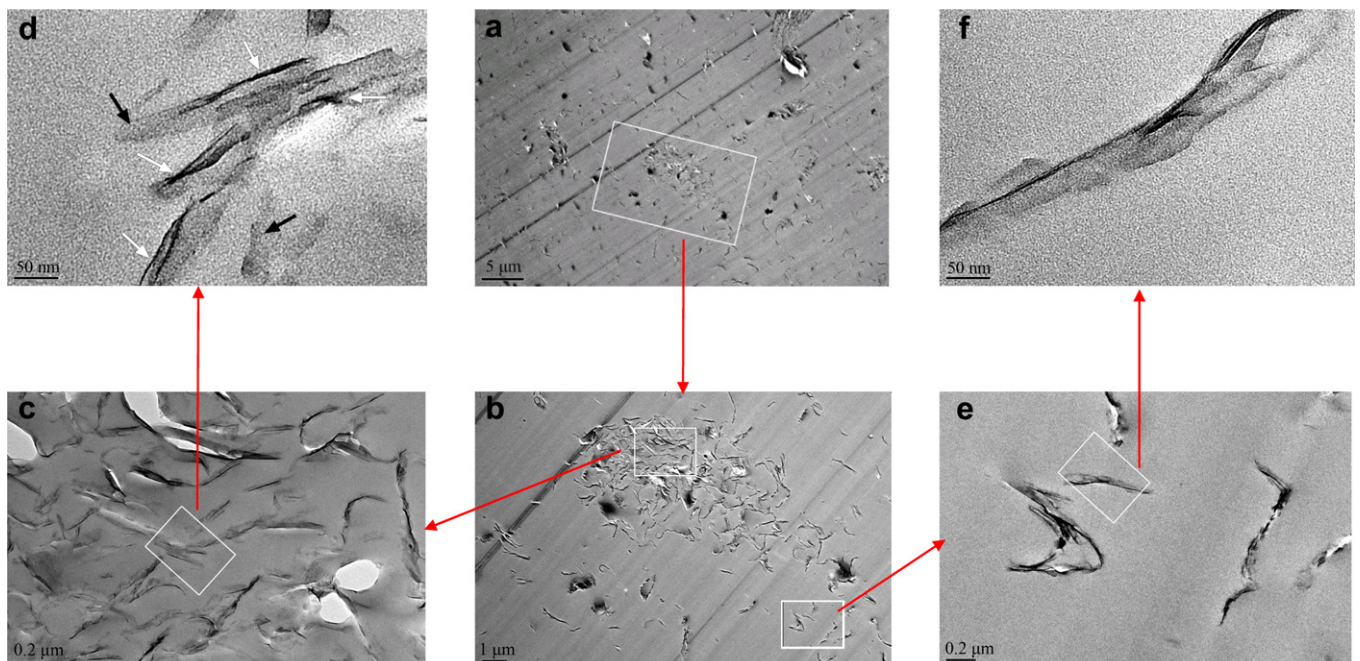


**Fig. 7.** TEM micrographs of epoxy/*eth*-clay nanocomposite (absolute clay content ~2.4 wt%).



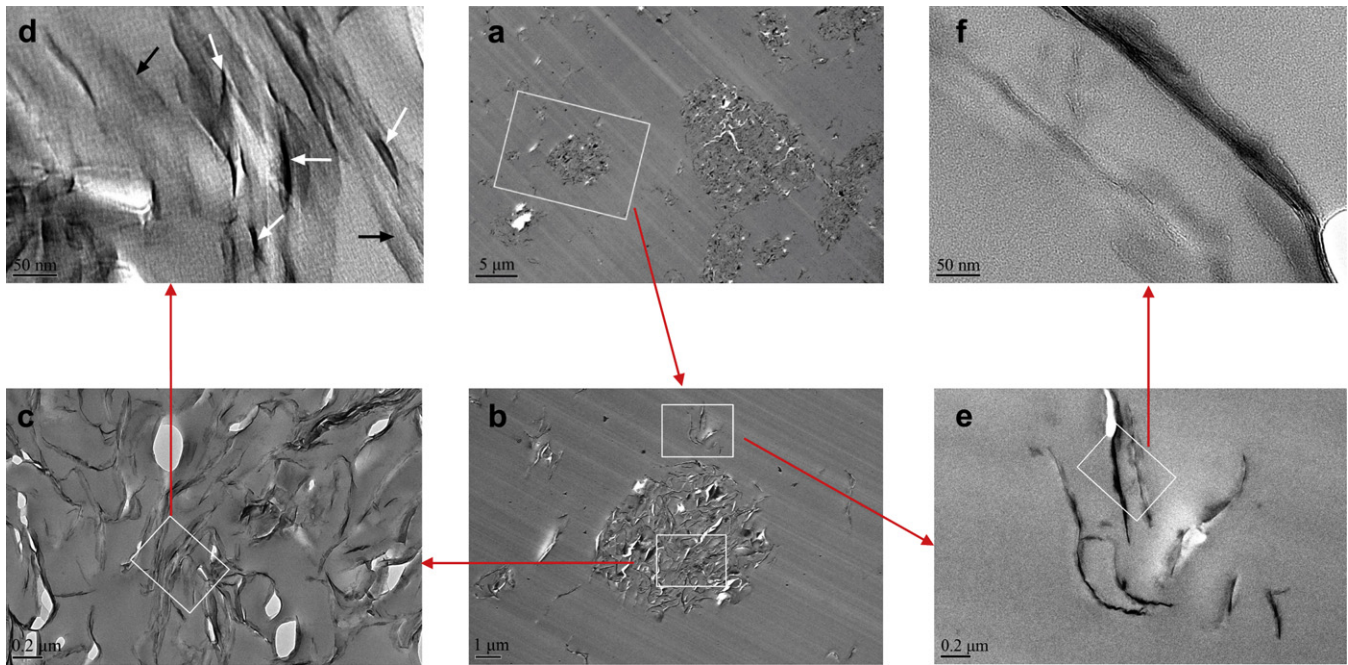


Fig. 8. TEM micrographs of epoxy/m27-clay nanocomposite (absolute clay content  $\sim 1.4$  wt%).

diameter in the matrix. The dark lines consist of the single or multiple layers of inorganic clay, while the organic matrix appears light. From XRD analysis, the clay exfoliation follows the sequence: *eth*-clay < *m27*-clay < *xtj*-clay, leading to a prediction that *eth*-clay should have the lowest degree of dispersion. However, epoxy/*eth*-clay nanocomposite shows many clay layers dispersed separately in addition to the clusters in Fig. 7a and by contrast, this is not the case for the other two nanocomposites. The contradiction is explained in light of phase separation and compatibility. The surfactant ETH grafted on the clay layer surface is  $\sim 0.5$  nm in length, while the chains of the

surfactants M27 and XTJ are as long as  $\sim 20$  nm. During curing, the long-chain surfactant molecules just phase-separated, a phenomenon similar to liquid rubber-toughened epoxy where rubber molecules phase-separate to create micron-sized particles [34]. By comparing Fig. 9a with Fig. 8a, smaller clusters' size is found for epoxy/*xtj*-clay nanocomposite than the epoxy/*m27*-clay, and this is caused by the cluster composition: epoxy molecules were combined with clay layers by the reaction between grafted XTJ and matrix, which improved the compatibility between clay and matrix and thus reduced the cluster size and produced more separated layers in matrix.

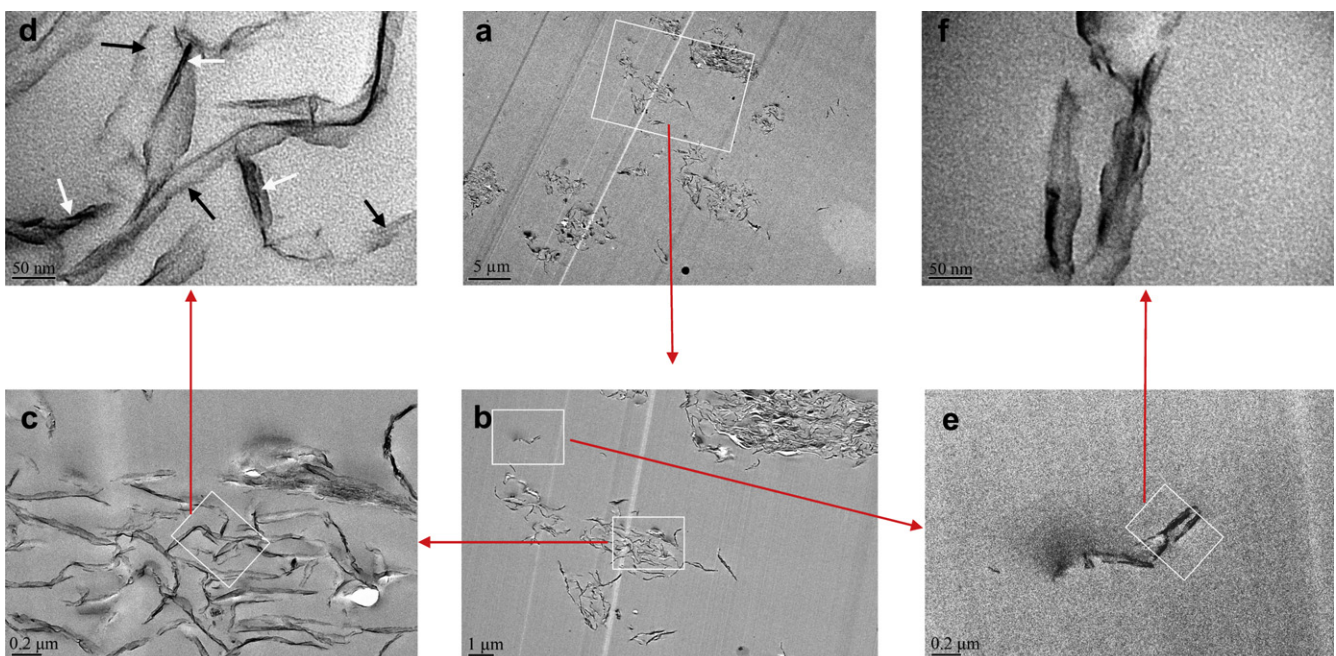


Fig. 9. TEM micrographs of epoxy/*xtj*-clay nanocomposite (absolute clay content  $\sim 1.3$  wt%).

**Table 3**  
Mechanical properties of neat epoxy and nanocomposites cured by J230.

Materials	Nominal clay content (wt%)	Absolute clay content (wt%) <sup>a</sup>	Young's modulus, GPa	Tensile strength, MPa	Plane-strain fracture toughness, $K_{Ic}$ , MPa m <sup>1/2</sup>	Critical strain energy release rate, $G_{Ic}$ , J/m
Neat epoxy	0	0	2.693 ± 0.130	64.0 ± 2.1	0.653 ± 0.034	179.0 ± 10.0
Epoxy/eth-clay, 2.5 wt%	2.5	~2.4	2.901 ± 0.078	40.6 ± 0.8	0.791 ± 0.028	243.9 ± 11.4
Epoxy/m27-clay, 2.5 wt%	2.5	~1.4	2.952 ± 0.099	52.6 ± 3.0	0.942 ± 0.030	339.9 ± 10.3
Epoxy/xtj-clay, 2.5 wt%	2.5	~1.3	3.136 ± 0.059	59.0 ± 1.0	1.033 ± 0.044	384.7 ± 37.1

<sup>a</sup> Tested by heating specimens at 700 °C for 1 h.

In Figs. 7–9, representative zones in micrographs “a” are magnified in micrographs “b” which typically contain a cluster and a few separately dispersed silicate layers; each cluster is then magnified in micrographs “c” and further in “d”; the separately dispersed layers are magnified in micrographs “e” and further in “f”. The micrographs “a–c” in Figs. 7 and 8 all show a number of voids which occurs at the interface between layers and matrix. The voids were produced by a diamond knife during microtoming, indicating a weak interface. The micrographs “a–c” in Fig. 9 show less quantity of voids in comparison, possibly indicating an improved interface strength by the grafted XTG chains which bridge the clay layers with the matrix. In Fig. 7d, white arrows indicate intercalated layers while black arrows refer to exfoliated arrows; most layers remain intercalated. In Fig. 8d, most layers are orderly exfoliated; that is, the layer spacing is too large to be detected by XRD but the layers still remain stacked. In contrast, most layers in Fig. 9d are disorderly exfoliated. In spite of the co-existence of intercalation and exfoliation for these nanocomposites, an exfoliation degree is sequenced from these micrographs: eth-clay < m27-clay < xtj-clay, which is in agreement with XRD analysis.

Regarding the clay layers separately dispersed in matrix, similar exfoliation degree sequence can be reached by comparing micrographs “e” and “f” through Figs. 7–9. The incomplete exfoliation of xtj-clay is attributed by either the inconsistent of clay layers charge varied from layer to layer or the inadequacy of alkylammonium ions in the clay galleries, as supported by Chen [35] and Kornmann [36].

### 3.3. Mechanical analysis

#### 3.3.1. Mechanical properties

The mechanical properties of neat epoxy and its nanocomposites are shown in Table 3. Young's modulus of neat epoxy significantly increases with the clay addition, whereas the tensile strength drops. The significant improvement of stiffness is explained as the inorganic clay layers share a portion of load and restrict the polymer chain mobility through transferring stress and creating shear deformation.

Since the values of Young's moduli are determined and affected by testing speed and the initial strain range chosen for calculation, we hereby compare the moduli of the nanocomposites with that of neat epoxy, rather than with previous data. Of these nanocomposites, epoxy/xtj-clay nanocomposite demonstrates the most significant increase of Young's modulus and the least reduction of tensile strength followed by the epoxy/m27-clay and the epoxy/eth-clay. This is explained in light of the interface modification. ETH grafted on the clay layers is short in length and thus cannot interact effectively with matrix molecules, while M27 is a long-chain molecule surfactant which entangles with matrix molecules and thus produces a high level of interface strength. As a result, the ~1.4 wt% (absolute fraction) epoxy/m27-clay nanocomposite demonstrates higher increment in modulus and lower reduction in strength than the ~2.4 wt% epoxy/eth-clay. With a similar chain length to M27, XTJ molecules that grafted on the clay layers reacted with matrix molecules, bridging nanolayers with matrix—creating

the strongest interface of these nanocomposites. This explained why the 1.3 wt% epoxy/xtj-clay nanocomposite achieved the most significant modulus increment with the least loss of strength.

#### 3.3.2. Fracture toughness

The fracture toughness and critical energy release rate listed in Table 3 were obtained in the presence of an instantly propagated crack as described in Section 2.6. Overall, the fracture toughness of epoxy improves obviously upon the addition of the modified clay. Epoxy/xtj-clay nanocomposite shows the most significant toughness improvement, 58% for  $K_{Ic}$  and 115% for  $G_{Ic}$ , followed by the epoxy/m27-clay and the epoxy/eth-clay. It is worth to note that the fracture toughness improvement by ~1.3 wt% of xtj-clay surpasses all the previous effort [37,38] in the condition that the toughness measurement was conducted with the presence of a sufficiently sharp crack because the crack sharpness poses a huge effect on the toughness values for stiff materials [26,37]. Interface debonding is generally accepted as the major toughening mechanisms for epoxy/clay nanocomposites [37]. As aforementioned, xtj-clay obtained the highest interface strength and m27-clay had the lowest upon compounding with epoxy. When loaded, the xtj-clay layers are able to carry and transfer the highest portion of stress to relieve stress concentration on the crack and absorb fracture energy. This is in agreement with the TEM analysis—the least quantity of voids in Figs. 7–9 is found for the epoxy/xtj-clay. The chain length of M27 is ~40 times longer than that of ETH and thus the M27 chains entangle with matrix molecules, providing a thicker and more flexible interface than ETH, and this explains why epoxy/m27-clay nanocomposite shows a higher fracture toughness than the epoxy/eth-clay.

### 3.4. Thermal dynamic analysis

The glass transition temperature ( $T_g$ ) of a thermosetting polymer—a temperature at which crosslinked chains start vibrating to

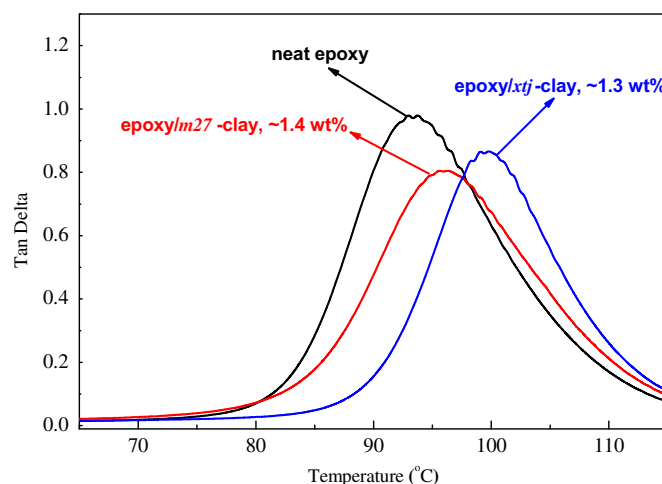


**Fig. 10.** Thermal dynamic properties of neat epoxy and its nanocomposites.

rearrange themselves—is the most important thermal parameter indicating the upper temperature limit for its application. The rate of rearrangement or relaxation process is determined by matrix chain stiffness, crosslink density, reinforcement particles and the interface between particles and matrix. Since matrix chain stiffness and crosslink density are not variable in this study, the change of  $T_g$ s must be caused by reinforcement particles and the interface between particles and matrix.

Fig. 10 shows the damping behaviour of neat epoxy and the epoxy/*m27*-clay and epoxy/*xtj*-clay nanocomposites at the absolute fraction of 1.3–1.4 wt% clay. Determined from the midpoints of the corresponding glass transition regions, the  $T_g$ s for these materials are 93.7 °C, 96.2 °C and 99.7 °C, respectively. While both nanocomposites show improved  $T_g$ s, the epoxy/*xtj*-clay shows a higher value. This is explained by the interface modification. M27 molecules grafted on the clay layer surface have a  $M_w$  of ~2000 with a chain length ~20 nm, and thus they are able to entangle with matrix molecules to increase the layer spacing and cause exfoliation, leading to the presence of matrix molecules between the layers; these 1 nm thick layers of extremely high specific surface area poses barriers to the vibration of matrix molecules through the  $T_g$  region and thus causes longer relaxation time, implying higher  $T_g$ . This is supported by previous research [8,24]. XTJ molecules grafted on the layers are of similar chain length to M27, but they build up a strong interface with matrix by reacting with matrix molecules during curing; this creates more significant barriers to the movement of matrix molecules, causing a longer relaxation time and a higher  $T_g$ . In conclusion, higher interface strength means higher  $T_g$  for epoxy/clay nanocomposites.

We have recently showed a number of improved  $T_g$ s due to the barrier provided by 55 nm rubber particles that are less stiff than matrix [9]. In contrast, clay is a stiff, 1-nm thick layer which produces a significantly restricting effect on the matrix chain movement, leading to improved  $T_g$ s. However, previous studies regarding the improvement of  $T_g$ s of epoxy/clay nanocomposites are inconsistent. With addition of clay, some reported an increment of  $T_g$ s [39–41], while there are reports of reduced [42–44] or no change of  $T_g$ s [45,46]. This may be caused by inappropriate ratio of epoxy to hardener, variations of curing condition and excessive surfactants left by modification.

#### 4. Conclusion

Although it was proved that polymer nanocomposites demonstrated a significantly higher level of performance compared to conventional composites, no clear understanding has yet emerged regarding the effect of interface on the various properties of polymer nanocomposites. In this study, we designed three levels of interface strength by adopting ethanolamine (denoted ETH), Jeffamine® M2070 (M27) and Jeffamine® XTJ502 (XTJ) to modify clay. It was remarkable to see how the adopted systems had produced significant outcomes, which demonstrated the effects of different interface strength on the morphology, mechanical properties, fracture toughness and thermal dynamic behaviour of epoxy. The chemical reaction of *xtj*-clay with epoxy created a strong interface, resulting in the best dispersion of clay layers and the most increment of Young's modulus, fracture toughness and thermal property. Upon compounding with ~1.3 wt% clay, the fracture toughness and fracture energy of epoxy were improved at 58% and 115%, respectively. Although no chemical bonding was employed to produce the interface for epoxy/*m27* nanocomposite, the long chain of M27 entangled with matrix molecules and thus produced an intermediate interface which explained for relatively good

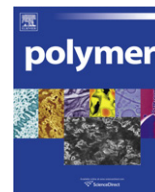
dispersion of clay layers and the moderate improvement of modulus, fracture toughness and thermal property. *eth*-clay produced a weak interface for epoxy/*eth*-clay nanocomposite, because neither chemical bonding nor molecular entanglement occurred between *eth*-clay and matrix.

#### Acknowledgments

J.M. thanks the Australian Research Council for the award of an Australian Postdoctoral Fellowship, tenable at the University of South Australia. He also thanks UniSA for the awards of ResearchSA Fellowship, New Appointee Start-up Grant and TRGGS Grant. Jeffamine was kindly provided courtesy of Huntsman (Melbourne). The authors thank B. Wade, L. Waterhouse and J. Terlet for technical support at Adelaide Microscopy. I.Z. appreciates assistance and help from Ly Truc Bao La, Sanjay Stephen and Ahmad Aliff.

#### References

- [1] Zubeldia A, Larranaga M, Remiro P, Mondragon I. *J Polym Sci B Polym Phys* 2004;42:3920.
- [2] Francis B, Rao VL, Poel GV, Posada F, Groeninckx G, Ramaswamy R, et al. *Polymer* 2006;47:5411.
- [3] Yang JP, Chen ZK, Yang G, Fu SY, Ye L. *Polymer* 2008;49:3168.
- [4] Balakrishnan S, Start PR, Raghavan D, Hudson SD. *Polymer* 2005;46:11255.
- [5] Ye Y, Chen H, Wu J, Ye L. *Polymer* 2007;48:6426.
- [6] Wang K, Chen Y, Zhang Y. *Polymer* 2008;49:3301.
- [7] Liu W, Hoa SV, Pugh M. *Compos Sci Technol* 2005;65:307.
- [8] Ma J, Mo MS, Du XS, Rosso P, Friedrich K, Kuan HC. *Polymer* 2008;49:3510.
- [9] Le QH, Kuan HC, Dai JB, Zaman I, Luong L, Ma J. *Polymer* 2010;51:4867.
- [10] Kinloch A, Mohammed RD, Taylor AC, Eager C, Sprenger S, Egan D. *J Mater Sci* 2006;41:1293.
- [11] Thompson ZJ, Hillmyer MA, Liu J, Sue HJ, Dettloff M, Bates FS. *Macromolecules* 2009;42:2333.
- [12] Zeng QH, Yu AB, Lu GQ, Paul DR. *J Nanosci Nanotechnol* 2005;5:1574.
- [13] Goettler LA, Lee KY, Thakkar H. *Polym Rev* 2007;47:291.
- [14] Podsiadlo P, Kaushik AK, Arruda EM, Waas AM, Shim BS, Xu J, et al. *Science* 2007;318:80.
- [15] Paul DR, Robeson LM. *Polymer* 2008;49:3187.
- [16] Ma J, Xu J, Ren JH, Yu ZZ, Mai YW. *Polymer* 2003;44:4619.
- [17] Ma J, Xiang P, Mai YW, Zhang LQ. *Macromol Rapid Commun* 2004;25:1692.
- [18] Ma J, Yu ZZ, Zhang QX, Xie XL, Mai YW, Luck I. *Chem Mater* 2004;16:757.
- [19] Ma J, Yu ZZ, Kuan HC, Dasari A, Mai YW. *Macromol Rapid Commun* 2005;26:830.
- [20] Messersmith PB, Giannelis EP. *Chem Mater* 1994;6:1719.
- [21] Kornmann X, Lindberg H, Berglund LA. *Polymer* 2001;42:4493.
- [22] Yasmin A, Abot JL, Daniel IM. *Scr Mater* 2003;49:81.
- [23] Wang WS, Chen HS, Wu YW, Tsai TY, Chen-Yang YW. *Polymer* 2008;49:4826.
- [24] Pluart LL, Duchet J, Sautereau H. *Polymer* 2005;46:12267.
- [25] Langat J, Bellayer S, Hudriik P, Hudriik A, Maupin PH, Gilman Sr JW, et al. *Polymer* 2006;47:6698.
- [26] Ma J, Qi Q, Bayley J, Du XS, Mo MS, Zhang LQ. *Polym Test* 2007;26:445.
- [27] Katti KS, Sikdar D, Katti DR, Ghosh P, Verma D. *Polymer* 2006;47:403.
- [28] Madejova J. *Vib Spectrosc* 2003;31:1.
- [29] Malucelli G, Bongiovanni R, Sangermano M, Ronchetti S, Priola A. *Polymer* 2007;48:7000.
- [30] McMurry J. *Organic Chemistry*. 7th ed.: Thomson; 2008.
- [31] Lee KY, Kim KY, Hwang IR, Choi YS, Hong CH. *Polym Test* 2009;29:139.
- [32] Becker O, Simon GP. *Adv Polym Sci* 2005;179:29.
- [33] Park SJ, Kim BJ, Seo DI, Rhee KY, Lyu YY. *Mater Sci Eng A* 2009;526:74.
- [34] Paul DR, Bucknall CB, editors. *Polymer blends*. New York: John Wiley & Sons; 2000.
- [35] Chen B, Liu J, Chen H, Wu J. *Chem Mater* 2004;16:4864.
- [36] Kornmann X, Lindberg H, Berglund LA. *Polymer* 2001;42:1303.
- [37] Wang K, Chen L, Wu J, Toh ML, He C, Yee AF. *Macromolecules* 2005;38:788.
- [38] Dean K, Krstina J, Tian W, Varley RJ. *Macromol Mater Eng* 2007;292:415.
- [39] Koerner H, Misra D, Tan A, Drummy L, Mirau P, Vaia R. *Polymer* 2006;47:3426.
- [40] Guo B, Ouyang X, Cai C, Jia D. *J Polym Sci B Polym Phys* 2004;42:1192.
- [41] Lu H, Nutt S. *Macromolecules* 2003;36:4010.
- [42] Triantafyllidis KS, Xidas PI, Pinnavaia TJ. *Macromol Symp* 2008;267:41.
- [43] Ayad MM, Salahuddin N, Ali M. *Polym Compos* 2009;30:467.
- [44] Kornmann X, Thomann R, Mulhaupt R, Finter J, Berglund LA. *J Appl Polym Sci* 2002;86:2643.
- [45] Wang K, Wang L, Wu J, Chen L, He C. *Langmuir* 2005;21:3613.
- [46] Wang K, Chen L, Kotaki M, He C. *Compos Part A Appl Sci Manuf* 2007;38:192.



## Free volume distribution at the Teflon AF<sup>®</sup>/silicon interfaces probed by a slow positron beam

Stephan Harms<sup>a</sup>, Klaus Rätzke<sup>a,\*</sup>, Vladimir Zaporojtchenko<sup>a</sup>, Franz Faupel<sup>a</sup>, Werner Egger<sup>b</sup>, Luca Ravelli<sup>b</sup>

<sup>a</sup> Institut für Materialwissenschaft – Materialverbunde, Technische Fakultät, Christian-Albrechts Universität zu Kiel, 24143 Kiel, Germany

<sup>b</sup> Institut für Angewandte Physik und Messtechnik, Universität der Bundeswehr München Werner Heisenberg-Weg 39, 85577 Neubiberg, Germany

### ARTICLE INFO

#### Article history:

Received 6 October 2010

Received in revised form

20 November 2010

Accepted 22 November 2010

Available online 29 November 2010

#### Keywords:

Free volume

Positron annihilation

Interphase

### ABSTRACT

We performed positron annihilation lifetime spectroscopy experiments at Teflon AF<sup>®</sup>/silicon interfaces as function of the positron implantation energy to determine the free volume hole size distribution in the interfacial region and to investigate the width of the interphase. While no interphase was detected in very short chained solvent-free, thermally evaporated Teflon AF<sup>®</sup>, an interphase of some tens of nm in extension was observed for high molecular weight spin-coated Teflon AF<sup>®</sup> films. Influences of the native oxide layer on the data evaluation could be ruled out.

© 2010 Elsevier Ltd. All rights reserved.

### 1. Introduction

It is well known that the polymer properties may deviate significantly from those of the polymer bulk in the interfacial region between a polymer and a solid [1]. Confinement effects or chemical interaction between the polymer chains and the solid can lead to different rearrangement of the chains near the polymer–solid interface. The reported width of this so-called interphase ranges from some nm for weakly interacting thermoplastics [2] to beyond 10  $\mu\text{m}$  for crosslinked polymers [3]. This effect is of particular concern for nanocomposites, where the nanoparticles, due to their large interface to volume ratio, give rise to a large contribution of the interphase to the polymer. This can affect, e.g., the mechanical properties drastically [4].

Several investigations have been reported on nanocomposites [5–8], however, investigations of interphase effects on planar interfaces are scarce. Measuring the surface glass transition temperatures, Ellison and Torkelson [9,10] also studied the interfacial properties of different polymer–solid systems at different depths by means of fluorescence spectroscopy. Whereas the glass transition temperature was found not to deviate from the bulk value, the relaxation times increased by several orders of magnitude near the interface in the systems under investigation, which

was attributed to different polymer dynamics. However, no correlation to intrinsic properties like the free volume was made.

The hole free volume, i.e. the unoccupied space between polymer chains is a key quantity for many properties like viscosity, diffusion, and mechanical properties. It can be determined by positron annihilation lifetime spectroscopy (PALS) and other techniques. Nowadays, PALS is the technique of choice for investigating free volume in polymers [8,11–14] because of the well established relationship between ortho-positronium (o-Ps) lifetime and average free volume size.

Once injected into polymers, positrons recombine with electrons in the polymer matrix and have different decay possibilities; either they decay as free positrons, or they form – in most polymers – hydrogen-like positronium (Ps) states. The para-positronium (singlet state) can easily decay, whereas ortho-Positronium (o-Ps, triplet state) with parallel spin can only decay via a pick-off processes and is hence the longest of the usually three lifetimes considered. Positronium preferentially resides in free volume holes, and the pick-off lifetime of an ortho-positronium, (generally termed  $\tau_3$ ), is well correlated to the free-volume hole size in polymers. A quantum mechanical model for the calculation of free volume hole sizes has been developed by Tao [15]. In this model, the positronium is assumed to be confined in a spherical potential well with infinite wall height. Furthermore, the model postulates an electron layer at the pore wall, with which the ortho-positronium can interact and decay. Calculation of the overlap integral of the positronium

\* Corresponding author. Tel.: +49 431 880 6227; fax: +49 431 880 6229.  
E-mail address: [kr@tf.uni-kiel.de](mailto:kr@tf.uni-kiel.de) (K. Rätzke).

probability density function with this electron layer yields a direct relation between the positronium lifetime and the hole radius:

$$1/\tau_3 = \lambda_0 \left[ 1 - \frac{R_h}{R_h + \Delta R} + \frac{1}{2\pi} \sin \left( \frac{2\pi R_h}{R_h + \Delta R} \right) \right] \quad (1)$$

This formula includes the reciprocal ortho-positronium decay rate  $\tau_3$ , the spin averaged decay rate in the electron layer  $\lambda_0$ , the hole radius  $R_h$ , and the thickness of the electron layer  $\Delta R$ , which has been calibrated using substances with known pore sizes [16]. Since hole sizes in amorphous polymers exhibit a relatively broad distribution, the discrete  $\tau_3$  values obtained from fits to lifetime spectra and the resulting hole radius have to be regarded as average values [17].

In contrast to the o-Ps lifetime  $\tau_3$ , the interpretation of the o-Ps intensity  $I_3$ , which has often been used as a measure for the hole concentration, is much less straightforward, as the intensity is, to a first approximation, the product of hole concentration and positronium formation probability. The latter decreases for higher energies in the present experiments due to increasing fraction of positrons implanted into the silicon substrate, where no positronium is formed. This effect will be modeled in the present paper by integrating the implantation profile of the positrons in the polymer.

Positron annihilation lifetime spectroscopy in bulk polymers is well established [18,19], whereas thin film investigations are relatively scarce [20]. The main reason is that conventional (radioactive) positron sources emit the positron with rather high energies; hence complete absorption of positrons requires large sample thickness and does not allow depth sensitive experiments. Depth resolved positron annihilation spectroscopy has only been becoming increasingly relevant since the availability of slow positron beams with tunable energy [21]. Continuous positron beams are easier to operate, however, only Doppler spectroscopy is possible, which does not allow to separate the three different decay possibilities discussed above. Positron annihilation lifetime spectroscopy became available after the development of a timing structure for beams which made lifetime measurements possible. This and many more requirements are fulfilled for the reactor based pulsed-low-energy-positron-system (PLEPS) at the FRM II in Munich [22], which has already been used successfully for various applications [12,23,24].

When positrons with elevated energy penetrate matter, they lose their energy by various scattering processes. As this is a statistical process, the depth profile is broadened as a function of the respective energy [25,26]. The usual description is by a Markov equation:

$$P(z, E) = \frac{mz^{m-1}}{z_0^m(E)} \exp \left[ - \left( \frac{z}{z_0(E)} \right)^m \right]; \quad (2)$$

$$z_0(E) = z_{1/2}(E) [\ln(2)]^{-1/m}$$

The median penetration depth  $z_{1/2}$  is dependent on the beam energy  $E$  (in keV) and the sample density  $\rho$ :

$$z_{1/2} = \frac{A}{\rho} E^n \quad (3)$$

Algers et al. [26] found the best description of implantation of positrons into polymers setting the exponents  $m = 2$  and  $n = 1.71$ , and the factor  $A = 2.81$  ( $\mu\text{g}/\text{cm}^2$ ).

Many investigations on moderated positron annihilation spectroscopy have been centered around surface effects [27,28], where changes in  $T_g$  [27] and density gradients [28] were detected or interfacial polymerisation in polymers was investigated [29]. During the discussion on thickness dependence of the glass transition in thin supported and free standing films, DeMaggio et al. [30]

performed temperature dependent PALS beam measurements on polystyrene films of varying thickness on hydrogen passivated substrates at fixed penetration depth. They observed a decrease in  $T_g$  and the coefficient of thermal expansion with decreasing film thickness and fitted this to a two or three layer model including surface and interface similar to the approach described by Forrest et al. [2]. In a very recent paper by Ata et al. [31] the changes in free volume were investigated for thin spin-cast films. Distinct deviations from bulk polystyrene in thermal expansion of the free volume holes and the glass transition temperature associated with the free volume properties were observed for the thinnest film with 22 nm thickness, indicating a higher chain mobility. Comparison of the polystyrene concentration in the precursor solution around the overlap concentration suggests that the high chain mobility is due to less entangled chains caused by rapid removal of the solvent from the very diluted solution required to prepare the very thin film. In another series on positron annihilation spectroscopy measurements with a moderated beam the group of Y. Jean [32,33] used Doppler broadening and the VEPFIT program [34] to model the depth profile. However, at least the Doppler data have to be treated with caution because the density at the interface, calculated from the data is  $0.4 \text{ g}/\text{cm}^3$ , which is less than half of the bulk density, and the resulting total layer thickness deviates by more than 50% from the measured values. The corresponding lifetime experiments are similar to the ones reported here. For an 80 nm thick polystyrene film on Si the measured depth dependent PALS spectra resemble our results (see below). One has to mention that there are several papers on characterizing the interaction between solid and polymers, e.g. for shape memory performance an interesting paper just appeared [35] unfortunately, there no depth profiling is performed.

In the present investigation we used the Teflon AF<sup>®</sup>/silicon system as a model system to investigate polymer/solid interfaces and to determine the width of the interphase. Teflon AF<sup>®</sup> is a polymer with high free volume fraction [36] and was chosen, because it can be thermally evaporated as a very short chained thin film [37] and spin-coated from solution with very high molecular weight. Thus it is an ideal system for studying the influence of the molecular weight on the extension of the interphase region. Moreover, due to the high free volume fraction, the o-Ps lifetime is high allowing a clear separation between polymer and substrate lifetime. While no interphase was detected in very short chained evaporated Teflon AF<sup>®</sup>, an interphase of some tens of nm in extension was observed for high molecular weight spin-coated Teflon AF<sup>®</sup> films.

## 2. Experimental

Amorphous Teflon AF 2400<sup>®</sup> is a random copolymer of tetrafluoroethylene and 2,2-bis(trifluoromethyl)-4,5-difluoro-1,3-dioxole with the mole content of  $-\text{C}_2\text{F}_4-$  units of 13%.

It was obtained from DuPont in solid form (order code: AF2400) for the evaporated samples and as a 1% resin (order code: 400S2-100-1) in FC-40 solution (3M Company) for spin coating.

The substrates used for our investigations were Si wafers in (100) orientation with low n-doping. Cutting of the wafer was done prior to film preparation. Solvent free thermal evaporation of Teflon AF<sup>®</sup> onto Silicon-wafer was performed as described in detail in Refs. [37,38] at a base pressure of  $10^{-7}$  mbar and a rate of some nm/min, which was controlled by a quartz balance. Samples were analyzed by XPS afterwards to proof the stoichiometry. The wafer used for spin coating was rinsed in acetone and flushed with isopropanol before performing an ionic RCA clean (5:1:1  $\text{H}_2\text{O}:\text{NH}_3:\text{H}_2\text{O}_2$  at  $75^\circ\text{C}$  for 15 min). The concentration of the Teflon AF 2400<sup>®</sup> resin used for spin coating was 0.5% and 1%. Spin coating was performed at maximum speeds from  $1000 \text{ min}^{-1}$  to  $2000 \text{ min}^{-1}$  for 60 s. For

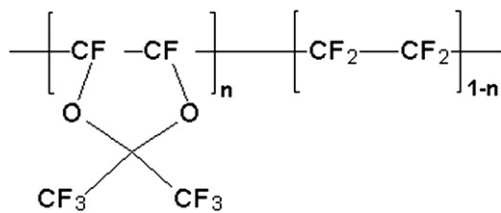


Fig. 1. Repeat units of the Teflon AF<sup>®</sup> copolymer.

evaporating the FC-40 solvent all samples were annealed at 250 °C, i.e. well above  $T_g$  in a vacuum furnace for at least 1 h at a pressure  $\leq 10^{-5}$  mbar. The thickness of the films was determined with a standard profilometer (DEKTA 8000) and for selected samples reference measurements by ellipsometry. The results agreed within the error bar of the respective techniques.

Free volume measurements were performed employing positron annihilation lifetime spectroscopy (PALS) in conjunction with the pulsed low-energy positron beam at the Garching nuclear research reactor FMR II [22]. For the present studies the beam energy was varied between 0.5 keV and 18 keV. The positron implantation energy can be converted to an implantation profile according to a well established procedure [26]. For low energy the mean implantation depth can be calculated from eq. (3) within the Teflon AF<sup>®</sup> film (eg.  $E = 2$  keV corresponds to  $z_{1/2} = 54$  nm). At beam energies  $E \geq 8$  keV most of the positrons are implanted into the substrate. However, the Markov implantation profile has to be taken into account when modeling the intensity profile to get relevant information from the broader implantation profile for higher energies. Lifetime spectra of  $3.6 \times 10^6$ – $3.9 \times 10^6$  counts were taken at a count rate of 5500–6000 cps. The peak to background ratio was approx. 10000–1. Data evaluation with the program LT 9.0 was identical for all samples. The resolution function, which depends on the implantation energy, was obtained from spectra of a SiC reference sample and fitted by a sum of three Gaussians. Typical values determined from the fits at 2 keV are: FWHM<sub>1</sub>: 297ps (75%), FWHM<sub>2</sub>: 229ps (23%, shift 4.3 ch), FWHM<sub>3</sub>: 134ps (2%, shift -7.8 ch). The spectra of our thin film samples were split into three lifetime components  $\tau_{1-3}$  with its associated intensities  $I_{1-3}$  without fixing any parameter except the resolution function. The fit variance  $\chi^2$  was typically  $\leq 1.1$ .

Here it has to be mentioned that there is an intrinsic problem with the evaluation of the data for acceleration voltages where the implantation is into the polymer and the substrate. The resulting spectra are sums of the relative contributions of polymer Teflon AF<sup>®</sup> and the substrate Si incl. native SiO<sub>2</sub> layer, the former with three lifetimes, the latter with at least two lifetimes (Si) and three lifetimes (SiO<sub>2</sub>) plus presumably interface states, in analogy to surface states for low energy. However, it is not possible to separate the contributions from the two materials for the short lifetimes as, e.g., the lifetime of the free positron in the polymer ( $\sim 400$  ps) and the lifetime in the bulk of the Si ( $\sim 385$  ps) do overlap. Fortunately, the free volume information comes from the longest lifetimes of  $\sim 6.5$  ns for Teflon AF<sup>®</sup> which can be discriminated from the 1.6 ns for SiO<sub>2</sub>, thus a detailed analysis can be made (Fig. 1).

### 3. Results and discussion

The discussion is organized as follows. We will first present the data for the short chained evaporated Teflon AF<sup>®</sup> in Fig. 2, where no interphase is expected. This allows us to test the evaluation procedure for modeling the intensity, which is presented in Fig. 3. From the results we can conclude that we have an interphase width of less than a few nm and that the thin native SiO<sub>2</sub> layer (some nm)

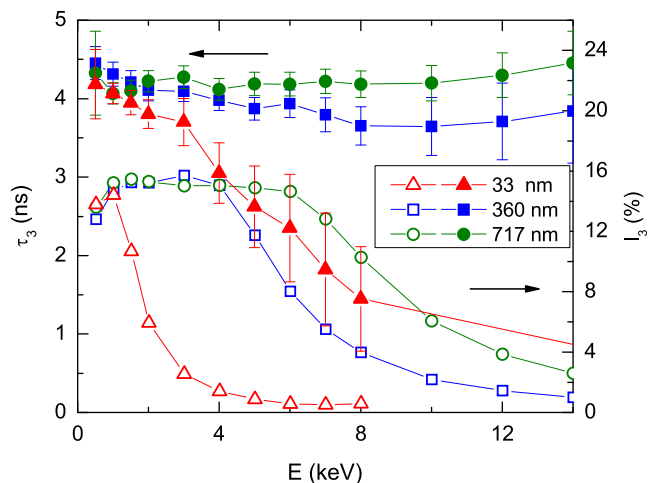


Fig. 2. o-Ps lifetime (filled symbols, left axis) and o-Ps intensity (open symbols, right axis) as function of implantation energy for three thermally evaporated Teflon AF<sup>®</sup> film with thickness as indicated. Lines between data are only to guide the eye.

does not influence the analysis. In contrast, a thick thermal SiO<sub>2</sub> layer, has a significant influence on the positronium formation probability, as shown in Fig. 5, and hence complicates the analysis. In the last part we will then present the data for the spin-coated high molecular weight films, where a clear interphase effect is seen and where we can estimate the interphase width.

In Fig. 2, the results for the evaporated films are depicted. o-Ps lifetime (filled symbols) as a measure for average hole size and o-Ps intensity (open symbols) are plotted as function of the primary positron acceleration voltage, which is a measure of the implantation depth (eq. (3)).  $\tau_3$  at intermediate voltages, i.e. in the bulk of the film, is approx. 4 ns, much smaller than the bulk value for high molecular weight samples [36] and for high molecular weight spin-coated films (Fig. 4). This is to be expected due to the fact that the film is evaporated, hence a short chained film with high packing density is created.

The o-Ps lifetime  $\tau_3$  decreases only for the 33 nm film at high energies, where most of the positrons are implanted into the silicon-wafer. Hence, the intensity of o-Ps becomes rather low ( $I_3 < 2\%$ ), and the evaluation of lifetime spectra much less accurate,

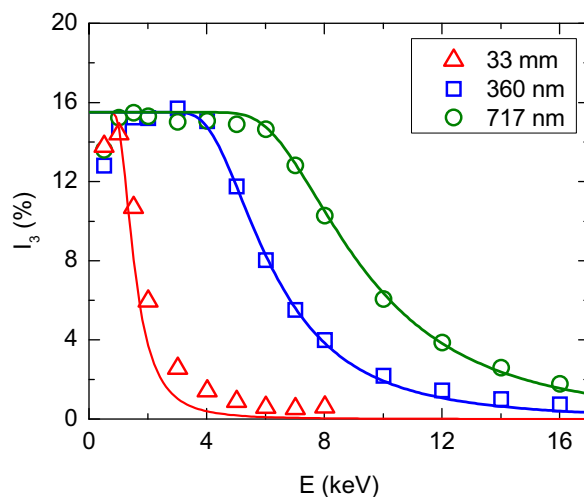
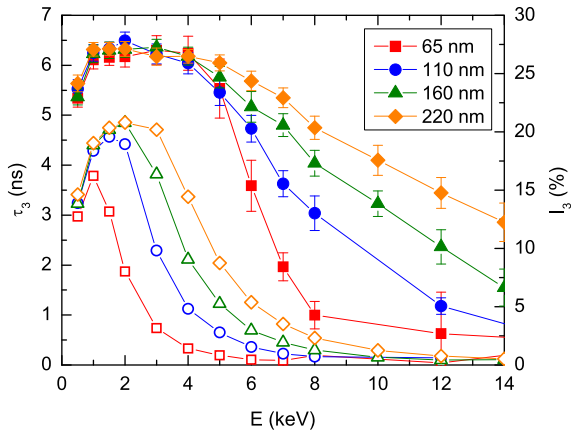


Fig. 3. o-Ps intensity as function of positron implantation energy for the three evaporated Teflon AF<sup>®</sup> samples and the fit according to the simple model explained in the text.



**Fig. 4.** o-Ps lifetime (filled symbols) and o-Ps intensity (open symbols) as function of implantation energy for spin-coated Teflon AF<sup>®</sup> film with thickness as indicated. Lines between data are only to guide the eye. Note that the o-Ps lifetime of 7 ns at  $E = 1$  keV–2 keV is in the expected range for the bulk [36].

which is reflected in the larger error bars. However, this constancy of the o-Ps lifetimes is a first hint that the interphase thickness is very small, although the influence of the positron diffusion in silicon has to be further investigated (see below).

The decrease in o-Ps intensity at higher energies, as already stated, is due to increased implantation of positrons into the Si, where no o-Ps is formed. The simplest approach to model this intensity decrease is to use the Markov implantation profile at the corresponding energy, reflecting a certain implantation depth and to integrate the part, which belongs to the polymer, assuming the constant intensity of 15.5% in the bulk. The corresponding fits for the intensity as function of implantation energy are depicted in Fig. 3. Due to the good description of the experimental data by these fit it can be concluded, that the positronium formation probability is not a function of film depth but constant throughout the films.

In Fig. 4, the analogous data to Fig. 2 are depicted, but now for high molecular weight spin-coated films. Here the decrease in o-Ps lifetime occurs much earlier, i.e. at lower implantation depth, although a modeling of the intensity decrease similar to Fig. 3 shows that the samples are homogeneous with respect to positronium formation probability (fit not shown).

In order to rule out effects from the native SiO<sub>2</sub> layer on the positronium formation probability we compared two Teflon AF<sup>®</sup> films of equal thickness (160 nm) but one on a Si wafer with native SiO<sub>2</sub> layer (~some nm), the other one on a thick (300 nm) thermally

grown SiO<sub>2</sub>. The structure of the Teflon film should be equal, only the influence of the o-Ps from the SiO<sub>2</sub> layer should be larger for the thicker SiO<sub>2</sub> layer. Fig. 5 (a) shows the PALS results. Both sets of data were evaluated as discussed above, i.e. in terms of three lifetimes. One notes that for the thermally grown thick oxide the intensity increases for energies higher than 4 keV, whereas the intensity for the thin oxide layer decreases. This is expected for a significant implantation into the substrate. The increase in intensity in case of the thick thermal oxide layer is due to the fact that positronium also forms in SiO<sub>2</sub> but not in Si. Positronium formation in the very thin native SiO<sub>2</sub> layer is apparently negligible. For both samples the longest lifetime decreases, but for the thick oxide layer sample it saturates at 1.6 ns, the o-Ps lifetime of the SiO<sub>2</sub> substrate layer. Hence it is not clear, whether the decrease in o-Ps lifetime can be attributed to increased substrate contributions or is really due to the finite interphase width. Hence we reevaluated both sets of data with a fourth lifetime, fixed to 1.6 ns and attributed to the positronium decay in the SiO<sub>2</sub> layer. The corresponding results are depicted in Fig. 5 (b). The scatter, reflected in the error bar becomes higher, but the following things are obvious.

For both samples the longest o-Ps lifetime, attributed to the decay in the polymer, is slightly higher, as expected due to the subtraction of a smaller contribution of 1.6 ns from the SiO<sub>2</sub>, but the o-Ps lifetime still decreases with increasing acceleration voltage. For the thin SiO<sub>2</sub> layer the corresponding intensity, reflecting the decay probability in the SiO<sub>2</sub> layer, is below 1.5%, hence it is acceptable, to ignore this contribution. (Please note, 1.5% absolute intensity means 10% relative intensity of the total o-Ps decays). For the thick oxide layer, the intensity of o-Ps decay in the polymer decreases as expected and the contribution of the substrate increases with increasing implantation depth. However, the key point is that, although we properly took into account the contribution of the SiO<sub>2</sub> layer to the positron decay (which is small for the native layer anyhow) we still get a decrease in o-Ps lifetime from the polymer with increasing depth, reflecting a finite interface width with smaller average hole free volume. The whole arguments show that the decrease in lifetime is not an artifact of the decay in the substrate and that the limit of detection is of the order of the thickness of the native SiO<sub>2</sub> layer.

Further clear evidence that the decrease in the hole free volume observed for the high molecular weight spin-coated Teflon AF<sup>®</sup> is an interphase property and not an artifact from positron decay in the substrate is provided by comparison with the results for the very short chained evaporated Teflon AF<sup>®</sup> in Fig. 2, which was evaporated on an identical substrate. From comparison of the o-Ps lifetimes in Figs. 2 and 4 it is clear that there is significant

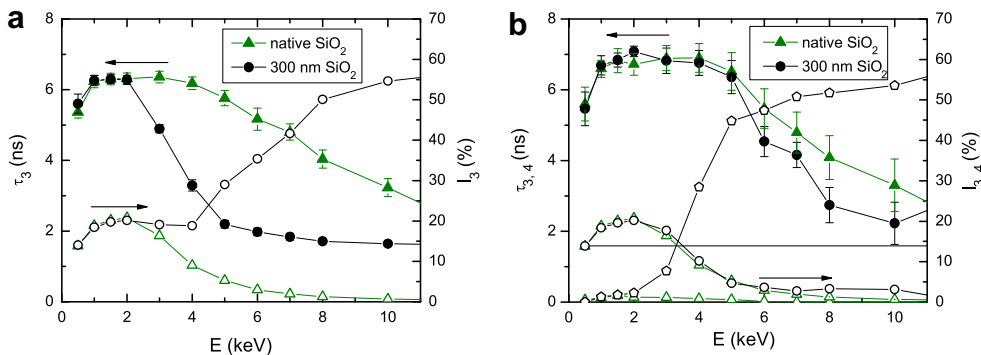


**Fig. 5.** PALS beam implantation profile into 160 nm Teflon AF<sup>®</sup> on two different substrates, one with native SiO<sub>2</sub> (~some nm) on Si (triangles) the other one with 300 nm, thermally grown SiO<sub>2</sub> on Si (circles). Filled symbols display lifetimes, open symbols intensities. (a) left hand side: evaluation with three lifetimes, as before (b) right hand side: evaluation with four lifetimes, one fixed contribution from the respective SiO<sub>2</sub> layer. Note the decrease of the o-Ps lifetime attributed to the polymer for higher acceleration voltages, reflecting finite interface width.

interphase width, because the lifetime decreases much earlier to lower values in Fig. 4 compared to Fig. 2, if one takes into account the different thicknesses.

A first estimate of the interphase width can be obtained in the following way. For the thinnest sample (65 nm thickness) at an acceleration voltage of 1 keV, corresponding to an average penetration depth of 20 nm we see bulk value of the o-Ps lifetime of approx. 6.5 ns. This shows that the interface width is much smaller than this. On the other hand, as stated above, the detection limit of the present technique is about 3 nm. So, this simple estimate shows that the interface width is of the order of some tens of nm.

#### 4. Conclusions

In order to obtain information on the free volume distribution and the interphase width at the polymer–substrate interface, positron annihilation lifetime spectroscopy experiments as function of depth were performed on Teflon AF<sup>®</sup> films of various thicknesses on silicon. Evaporated very short chained Teflon AF<sup>®</sup> samples on Silicon showing no interphase were compared with high molecular weight spin-coated samples on Si wafers with native and thermally grown oxide. The o-Ps lifetime and intensity for the spin-cast samples are in the expected range of literature values [36]. The lifetimes for the evaporated films are much shorter as a consequence of the deposition by evaporation which generates much shorter chains with a higher packing density corresponding to lower free volume. The positronium formation probability is constant throughout the film for all samples as indicated by fitting the decrease of intensity  $I_3$  with increasing acceleration by a simple model. The detection limit of the present technique is of the order of the thickness of the native oxide layer (~some nm). As can be seen from the comparison of films of spin-coated films on thin native silicon dioxide vs thick thermally grown silicon oxide. For evaporated films, within experimental resolution no interphase could be detected, whereas for spin-coated films, the width of the interface is estimated to be of the order of some ten nm indicating an interface with higher chain packing.

#### Acknowledgements

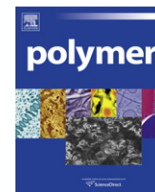
Financial support by the German Research Society (DFG) within the priority program SPP 1369 Interfaces and Interphases, Project Ra-796/5-1 is gratefully acknowledged. We thank Isabell Jonas (Kiel) for assistance in sample preparation and Juliane Bunk (IPP Dresden) for independent thickness measurements.

#### References

- [1] Possart W, editor. Adhesion – Current research and applications. Weinheim: Wiley-VCH; 2005.
- [2] Forrest JA, Dalnoki-Veress K. Adv Colloid Interface Sci 2001;94:167.

- [3] Munz M, Chung J, Kalinka G. Mapping epoxy interphases. In: Possart W, editor. Adhesion – Current research and applications. Weinheim: Wiley-VCH; 2005. p. 103–23.
- [4] Montes H, Chaussée T, Papon A, Lequeux F, Guy L. Eur Phys J 2010;31(3): 263–9.
- [5] Putz KW, Palmeri MJ, Cohn RB, Andrews R, Brinson LC. Macromolecules 2008;41(18):6752–6.
- [6] Ciprari D, Jacob K, Tannenbaum R. Macromolecules 2006;39:6565.
- [7] Winberg P, Eldrup M, Pedersen NP, van Es MA, Maurer FHJ. Polymer 2005;46:8239–49.
- [8] Dlubek G. Positron annihilation spectroscopy. In: Seidel A, editor. Encyclopedia of polymer science and technology. Hoboken: John Wiley & Sons; 2008.
- [9] Ellison C, Torkelson J. Nat Mater 2003;2:695.
- [10] Priestley R, Ellison C, Bradbeld L, Torkelson J. Science 2005;309:456.
- [11] Wang SJ, Chen ZQ, Wang B, Jean YC. Positron and positronium chemistry. Zurich: Tran Tech Pub; 2009.
- [12] Faupel F, Kanzow J, Günther-Schade K, Nagel C, Sperr P, Kögel G. Mat Sci Forum 2004;445–446:219.
- [13] Kanzow J, Faupel F, Egger W, Sperr P, Kögel G, Wehlack C, et al. Current research and applications. In: Possart W, editor. Adhesion. Wiley-VCH; 2005. p. 465–77.
- [14] Rätzke K, Shaikh MQ, Faupel F, Noeske PL. Int J Adhes Adhes 2010;30:105–10.
- [15] Tao JC, Sandler SI, Ganzi GC. J Chem Phys 1972;56:378.
- [16] Jean YC. Microchem J 1990;42:72–102.
- [17] Nagel C, Schmidtke E, Günther-Schade K, Fritsch D, Strunskus T, Faupel F. Macromolecules 2000;35:2242.
- [18] Mogensen OE. Positron annihilation in chemistry. Springer; 1995.
- [19] Yampolskii YP. Materials science of membranes for gas and vapor separation. Wiley; 2007.
- [20] Jean YC, Mallon PE, Schrader DS, editors. Principles and applications of positron & positronium chemistry. River Edge, NJ: World Scientific, <http://kiopc4.ub.uni-kiel.de:8080/DB=1/SET=4/TTL=1/MAT=/NOMAT=T/CLK?IKT=1008&TRM=World+Scientific>; 2003.
- [21] Coleman P. Positron beams and their applications. Singapore: World Scientific, <http://kiopc4.ub.uni-kiel.de:8080/DB=1/SET=1/TTL=87/MAT=/NOMAT=T/CLK?IKT=1008&TRM=World+Scientific>; 2000.
- [22] Sperr P, Egger W, Kögel G, Dollinger G, Hugenschmidt C, Repper R, et al. Appl Surf Sci 2008;255:35.
- [23] Harms S, Rätzke K, Faupel F, Egger W, Ravello L, Laschewsky A, et al. Macromol Rapid Comm 2010;31(15):1364.
- [24] Rätzke K, Wiegemann M, Shaikh MQ, Harms S, Adeling R, Egger W, et al. Acta Biomater 2010;6:2690–4.
- [25] Schulz PJ, Lynn KG. Rev Mod Phys 1988;60:701.
- [26] Algers J, Sperr P, Egger W, Kögel G, Maurer FHJ. Phys Rev B 2003;67(12):125404.
- [27] Jean YC, Zhang R, Cao H, Yuan JP, Huang CM, Nielsen B, et al. Phys Rev B 1997; 56(14):8459–62.
- [28] Algers J, Suzuki R, Ohdaira T, Maurer FHJ. Polymer 2004;45(13):4533–9.
- [29] Jean YC, Hung WS, Lo CH, Chen H, Liu G, Chakka L, et al. Desalination 2008; 234:89–98.
- [30] DeMaggio GB, Frieze W, Gidley DW, Zhu M, Hristov H, Yee A. Phys Rev Lett 1997;78:1524–7.
- [31] Ata S, Muramatsu M, Takeda J, Ohdaira T, Suzuki R, Ito K, et al. Polymer 2009; 50:3343.
- [32] Zhang J, Chen H, Zhang R, Li Y, Suzuki R, Ohdaira T, et al. Mat Sci Forum 2004; 445–446:367–9.
- [33] Zhang J, Chen H, Zhang R, Li Y, Suzuki R, Ohdaira T, et al. Rad Phys Chem 2007; 76:172.
- [34] Van Veen A, Schut H, de Vries J, Hakvoort RA, Ijpma MR. AIO Conf Proc 1990; 218:171.
- [35] Gunes IS, Perez-Bolivar C, Cao F, Jimenez GA, Anzenbacher P, Jana SC. J Mat Chem 2010;20:3467–74.
- [36] Rudel M, Kruse J, Rätzke K, Faupel F, Yampolskii YP, Shantarovich VP, et al. Macromolecules 2008;41:788.
- [37] Biswas A, Márton Z, Kanzow J, Kruse J, Zaporojtchenko V, Strunskus T, et al. Solid State Phenom 2003;94:285.
- [38] Ding SJ, Zaporojtchenko V, Kruse J, Zekonyte J, Faupel F. Appl Phys A 2003;76(5):851–6.





## Toughening vinyl ester networks with polypropylene meso-fibers: Interface modification and composite properties

Y. Liang<sup>a</sup>, R.E. Jensen<sup>b</sup>, D.D. Pappas<sup>b</sup>, G.R. Palmese<sup>a,\*</sup>

<sup>a</sup>Department of Chemical and Biological Engineering, Drexel University, Philadelphia, PA 19104, USA

<sup>b</sup>U.S. Army Research Laboratory, Aberdeen Proving Ground, MD 21005, USA

### ARTICLE INFO

#### Article history:

Received 9 September 2010

Received in revised form

29 November 2010

Accepted 1 December 2010

Available online 9 December 2010

#### Keywords:

Toughening

Surface treatments

Mechanical properties

### ABSTRACT

Polymer–polymer composites comprised of vinyl ester matrices (VE) and polypropylene (PP) fiber meshes were fabricated and tested in this investigation. Results indicated that PP fibers greatly enhanced fracture toughness; however, strength of the VE was significantly reduced as voids were observed at the interface of the PP and VE. A two-step surface modification, oxygen plasma treatment followed by grafting vinyltrimethoxysilane (VTMS), was conducted on PP fibers in an effort to improve interfacial strength. Interfacial discontinuities of composites were improved after surface modification of PP. The oxygen plasma treatment added hydrophilic functional groups but caused surface roughness. Surface treatment of PP slightly increased fracture toughness of the PP-VE composite by enhancing energy absorption capacity at the interface. However, mechanical strength and modulus did not significantly increase for the composite using VTMS grafted PP fibers due to the weak fiber material. Small PP fibers with higher strength may attain the expected improvement in mechanical properties after surface treatment.

© 2010 Elsevier Ltd. All rights reserved.

### 1. Introduction

Polymer–polymer nano/meso composites are being investigated to develop tough materials with enhanced energy absorbing capability through the unique combination of distinct polymeric phases that possess chemical, structural, and geometric attributes tailorable at the nano/meso scales. Vinyl ester resins (VE) are a class of thermoset polymers that possess high chemical and corrosion resistance, good thermal and mechanical properties, and are relatively easy to process. However, VE resins are brittle, thus limiting their use in high performance composite materials. Liquid rubber modifiers, such as carboxyl-terminated butadiene nitrile (CTBN), vinyl terminated butadiene-acrylonitrile (VTBN) and epoxy terminated butadiene-acrylonitrile (ETBN), have been used to toughen epoxy resins [1–3] and VE resins [4,5]. In these systems a suitable liquid rubber is usually dissolved in the uncured resin to form a one phase system that phase separates upon reaction to form rubber domains within a continuous hard matrix. Good phase separation obtained by controlling the polymerization reaction can limit plasticization and add energy dissipating mechanisms to improve fracture toughness [2]. However, poor compatibility of liquid

rubbers with the resin monomers can hinder their application in VE systems [5]. In contrast, toughening using preformed particles [6–9] and fibers [10] does not require phase separation and has been developed for thermosetting resins.

Compared to common particulate rubber fillers, polymeric fibers, because of their continuous nature, offer potentially distinct toughening mechanisms while providing good physical properties. Unfortunately, the low surface energy of polyolefinic fibers normally results in poor wettability and weak bonding at the interface. It is also known that discontinuities and void formation limit the interfacial strength and load transfer from the matrix to the toughening fibers. This can occur when the fibers are not easily wetted by the matrix resin. Surface treatments play an important role in improving interfacial bonding and preventing such discontinuities.

Chemical functional groups have been added to the surface of polymeric fibers by techniques such as plasma treatment [11–13], UV/Ozone [14] and the use of coupling agents [15,16]. Such functional groups interact with the polymer matrix to enhance interfacial adhesion and mechanical properties of polymer–polymer composites. Gas plasma treatment is a commonly used technique because it has a relatively low operation cost, it is a fast process, and it affects the surface properties of the exposed material without altering its bulk. Chemical functional groups and minor surface etching are created during plasma treatment. The improved wettability through chemical bonding and mechanical interlocking

\* Corresponding author. Tel.: +1 215 895 5814; fax: +1 215 895 5837.

E-mail address: [palmese@coe.drexel.edu](mailto:palmese@coe.drexel.edu) (G.R. Palmese).

due to the rough surface are believed to be important in improving interfacial adhesion of polyethylene fiber-VE composites, with mechanical interlocking providing a greater contribution to increased adhesion [11]. Plasma generated functional groups tend to reorganize in order to lower the surface energy during storage [17], which may explain the less pronounced contribution of chemical bonding in aged samples. However, a rough surface created through oxygen and nitrogen plasma treatment on polypropylene (PP) was reported to have negative contribution on adhesion of polymer coatings due to the weak bond of the surface layer to the bulk [18]. Our previous study also showed that oxygen/helium plasma treated PP fibers failed to improve interfacial and mechanical properties of PP-VE composites [20]. Therefore, stable functional groups grafted through coupling agents are preferred when an immediate follow-up process is unrealistic.

In this work a commercial vinyl ester resin, Derakane<sup>®</sup> 411-350 (Ashland) was used. PP fiber meshes were encapsulated in VE resins via vacuum assisted resin transfer molding (VARTM). PP is a tough, semi-crystalline thermoplastic with a melting temperature of 161 °C. In addition to the toughening properties of the PP fibers the phase transition associated with melting could provide a new energy absorption mechanism. Surface treatment using silane coupling agents after applying oxygen plasma to fibrous mats was performed to graft siloxane linkages with vinyl groups to PP, which could react with VE monomers during curing. Those chemical bonds were expected to enhance the interfacial interaction between the PP fibers and VE resin. Surface treatment on PP fiber meshes was evaluated using X-Ray photoelectron spectroscopy (XPS), contact angle measurements, thermogravimetric analysis (TGA), environmental scanning electron microscopy (ESEM), and differential scanning calorimetry (DSC). PP-VE composites were evaluated using standard thermal and thermomechanical analysis techniques as well as mechanical characterization which included fracture toughness, tensile and flexural property measurement.

## 2. Experimental

### 2.1. Materials

The commercial vinyl ester (VE) resin used in this work was Derakane<sup>®</sup> 411-350 Epoxy VE Resin (Ashland Specialty Chemical Co), which contains approximately 45% styrene as a reactive diluent. Commercial polypropylene (PP) fibers with diameters of 1–2 μm were obtained from Hills Inc. These fibers were melt-blown using ExxonMobil PP3746G granular homopolymer with a melt flow index (MFI) of 1500. The fiber mats are composed of randomly oriented PP fibers with an average aerial density of 26 g/m<sup>2</sup>. The free radical initiator used was Trigonox 239A (Akzo Nobel Polymer Chemicals). This initiator contains 45 wt.% cumyl hydroperoxide, 45 wt.% carboxylic ester and 10 wt.% cumyl acid, as specified by the manufacturer. Cobalt Napthenate (CoNap) (OMG Americas) containing 6 wt.% cobalt was used as an accelerator to enable room temperature cure. Vinyltrimethoxysilane (VTMS) (Aldrich) was used as a silane coupling agent in this study.

### 2.2. Surface modification of PP fibers

A planar Dielectric Barrier Discharge (DBD) plasma system was used for the surface treatment with desired gases. The distance between the electrodes was 3 mm and the power output during plasma treatment was approximately 0.1 W/cm<sup>2</sup> with a frequency of 165 Hz. The area of each electrode was approximately 225 cm<sup>2</sup>. Oxygen (O<sub>2</sub>) was used as the desired treatment gas to increase the hydrophilicity of the surface [17–19]. A flow rate of 1 L/min pure O<sub>2</sub> was injected into the space between two electrodes at atmospheric

pressure for more than 2 min before discharge to allow a uniform glow discharge. Treatment time varied from 15 to 180 s and both sides of PP fiber meshes were exposed to oxygen plasma for the same period. VTMS, a silane coupling agent with a vinyl functional group, was dissolved in deionized water to make a 0.3 wt.% solution. Its pH was then adjusted to 3.5 by drop-wise addition of acetic acid [21]. The solution was prepared 1 h prior to use to allow complete hydrolysis and used within 2 h to limit condensation in the solution. Within 1 h after oxygen plasma treatment, PP meshes were soaked in the VTMS solution for 10 min and then dried in a vacuum oven at 60 °C for at least 40 h to allow for condensation of the siloxane linkages and subsequent removal of water. The reaction mechanism is described by Rahmathullah et al. [22]. The suggested VTMS polycondensation temperature of 125 °C was decreased to 60 °C because plasma treated PP was found to degrade during polycondensation of silane coupling agents at 125 °C. Interestingly, PP without plasma treatment exhibited resistance to degradation during silane treatment at 125 °C.

### 2.3. Fiber characterization

Element compositions and chemical functional groups on the fiber surface were analyzed by X-Ray photoelectron spectroscopy (XPS). XPS spectra were obtained using a Kratos Axis Ultra 165 spectrometer equipped with a hemispherical analyzer. The X-ray was generated with an Aluminum K $\alpha$  (1486.7 eV) monochromatic source energized at 20 kV and 100 W, and irradiated at a 1 mm × 0.5 mm area. The takeoff angle was adjusted to 90° with respect to the sample surface. The pressure in the analysis chamber was <10<sup>-9</sup> mbar. Surface charge effects were neutralized by using a flood gun. A value of 285.0 eV for the hydrocarbon C1s core level was used as the calibration energy for the binding energy scale.

While XPS functional group analyses provide information from a surface layer about 10 nm in depth, contact angle measurement can give true surface information [17]. Static contact angle measurements using the sessile drop method were performed on a modular CAM200 Optical Contact Angle and Surface Tension Meter (KSV Instruments, Ltd., Finland), by dispensing a drop of deionized water with known volume from a microliter syringe onto the sample surface at ambient conditions. A monochromatic LED light source was used to image the water drops and the images captured were used to measure contact angles ( $\theta$ ) using Young–Laplace curve fitting. At least ten measurements were made for each sample.

The amount of VTMS grafted on PP fibers was determined by heating the treated PP fiber mats to 800 °C in N<sub>2</sub> flow at a rate of 10 °C/min using a TA Instruments TGA Q50 thermogravimetric analyzer. Since crosslinked siloxanes are stable at temperatures as high as 800 °C but PP decomposes at a much lower temperature, the weight remaining at 800 °C was taken as the weight of grafted VTMS. Samples weighing approximately 20 mg were used.

A TA Instruments DSC Q2000 differential scanning calorimeter (DSC) was used to determine the melting temperature ( $T_m$ ) and heat of melting ( $\Delta H_m$ ) of untreated and treated PP fibers under N<sub>2</sub> flow. Sample sizes were about 3 mg. Temperature scans were performed from -70 °C to 200 °C at a heating/cooling rate of 10 °C/min.

Fiber surface morphologies were studied using an environmental field emission scanning electron microscope (ESEM), Model XL30 ESE FEG, with an acceleration voltage of 3 keV in high vacuum mode. Samples were sputter-coated with platinum for 30 s prior to ESEM evaluation.

### 2.4. Resin and composite fabrication

Neat VE resin test plaques were fabricated in a metal mold. VE monomer was degassed in a Thinky planetary centrifugal mixer

ARE-250 for 15 min at a speed of 1500 rpm. Trigonox 239A, cobalt Napthenate and VE monomers were mixed at a weight proportion of 1:0.12:100 to control the gel time to 1.5 h. The mixture was degassed for another 4 min, poured into a mold, and then sealed. After being precured at ambient temperature for 24 h, the mold was placed in an oven and allowed to postcure at 125 °C for 3 h.

PP-VE composites were fabricated via vacuum assisted resin transfer molding (VARTM). PP fiber meshes were cut into 150 mm × 150 mm squares and stacked to desired thickness. After being weighed, the stacked meshes were covered by release cloth and a distributing layer and then sealed in a vacuum bag. VE was mixed with Trigonox 239A and cobalt Napthenate at the same proportion as used in the preparation of neat VE resin test plaques. Once infiltration was complete, the inlet and outlet were sealed. The composites were precured in the vacuum bag at ambient temperature for 24 h, and then postcured at 125 °C for 3 h. The resulting composites contained approximately 20 volume percent PP fibers due to the relatively low aerial density of the PP mats.

### 2.5. Composite characterization

Densities of composites were measured based on Archimedes' principle. Weight in air and weight in a heptane bath were measured for each sample. Density was calculated from weights of the sample and density of heptane. The equation for the density calculation is as follows:

$$\rho(\text{sample}) = \frac{\rho(\text{heptane}) \times W(\text{sample})_{\text{in-air}}}{W(\text{sample})_{\text{in-air}} - W(\text{sample})_{\text{in-hep tane}}}$$

Volume fractions of PP, VE and air were calculated based on density and weight of each component in the composite.

Dynamic mechanical analysis was performed on a TA Instruments DMA 2980 dynamic mechanical analyzer (DMA) with a dual cantilever clamp frame. Loss and storage moduli were recorded from 30 °C to 180 °C at a heating rate of 2 °C/min and an oscillation frequency of 1 Hz. The glass transition temperature ( $T_g$ ) of each VE system was taken as the temperature corresponding to the peak of the loss modulus curve. The activation energies of  $\alpha$  and  $\beta$  transitions were calculated from multiple frequency sweeps (0.1, 0.3, 1, 3, 10 and 30 Hz) at 3 °C isothermal steps from –50 °C to 180 °C. Arrhenius activation energy is defined by the following equation [23]:

$$\log f = \frac{-E_a}{2.303R} \left( \frac{1}{T} \right)$$

where  $E_a$  is Arrhenius activation energy,  $f$  is frequency, and  $T$  is corresponding transition temperature at the frequency. The slope in the plot of  $\log f$  vs.  $1/T$  is used to calculate the activation energy, giving

$$E_a = -2.303R \times \text{slope}$$

All samples were tested at an oscillatory-displacement amplitude of 15  $\mu\text{m}$ . Typical sample dimensions in the DMA were 35 mm in length, 12.75 mm in width, and 3.15 mm in thickness.  $T_g$  and  $T_m$  of each VE system was also determined via DSC using the procedure described above.

Mechanical properties were obtained using an Instron 8872 universal testing instrument. Three-point single-edge notch bend (SENB) specimens were used for plane-strain fracture toughness measurements. ASTM 5045-99 [24] specifies sample dimensions of 50.84 mm (span) × 12.71 mm (width) × 6.35 mm (thickness) to assure plain strain conditions. An initial crack was made by first sawing a notch with length half the sample width, and then using a sharp razor blade to initiate a crack at the base of the notch.

The samples were tested in flexural mode at a crosshead speed of 10 mm/min. Three-point bend specimens were used to measure flexural strength and modulus of elasticity in bending. Typical specimen dimensions were 50.84 mm (span) × 12.71 mm (width) × 3.17 mm (thickness) specified according to ASTM 790-03 [25] standard. The samples were tested in flexural mode at a crosshead speed of 1.3 mm/min. Tests were stopped when samples were broken. Tensile strength and modulus of elasticity were measured according to ASTM D638-03 [26]. Dog-bone shaped specimens were machined according to dimensions of specimen type V. An extensometer was used to indicate the strain with the initial gage length set at 12.5 mm. Samples were tested to failure at a crosshead speed of 1 mm/min. All tests were performed at ambient conditions. Fracture surfaces of composites were examined with ESEM using an acceleration voltage of 10 keV.

## 3. Results and discussion

### 3.1. Surface modification

The surface treatment followed in this study involved a two-step process. Theoretically, plasma treatment with  $\text{O}_2$  can add functional groups such as hydroxyl, ether, carbonyl, and carboxyl groups to the surface [17–19]. Silane coupling agents covalently graft to the polymer surface via functional groups such as hydroxyl groups and polymerize by condensation reactions to form a cross-linked network [21,22]. Generally a shorter plasma treatment time is favored for adding functional groups to the surface. In our study, we used treatment times ranging from 15 s to 180 s in an attempt to determine the optimal treatment time. Oxygen plasma treated PP ( $\text{O}_2$ -PP) and VTMS grafted PP (VTMS-PP) fibers were analyzed using untreated PP fibers as a control.

The XPS survey spectrum of VTMS-PP in the range of 0–1200 eV given in Fig. 1 clearly shows peaks corresponding to C at 285 eV, O at 532.5 eV, and Si at 153.5 and 102.6 eV. Also in Fig. 1, the XPS survey spectrum of  $\text{O}_2$ -PP shows two peaks corresponding to C and O while untreated PP only has one peak at 285 eV corresponding to C. Atomic ratios of O:C and Si:C for  $\text{O}_2$ -PP, VTMS-PP and untreated PP are compared as a function of the treatment time in Fig. 2. It is clear that 30 s and 180 s plasma treatment gave the highest Si:C ratio, while 15 s plasma treatment resulted in the lowest O:C and Si:C ratios. Oxygen concentration of  $\text{O}_2$ -PP increased with longer treatment times, but the plasma-induced hydrophilic functional groups reached equilibrium at an O:C ratio of approximately 0.3 as seen from the VTMS-PP samples in Fig. 2, which was also reported

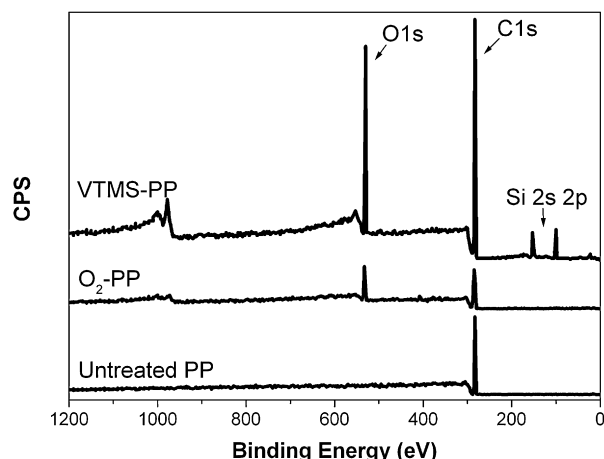


Fig. 1. XPS survey spectra of untreated PP,  $\text{O}_2$ -PP and VTMS-PP.

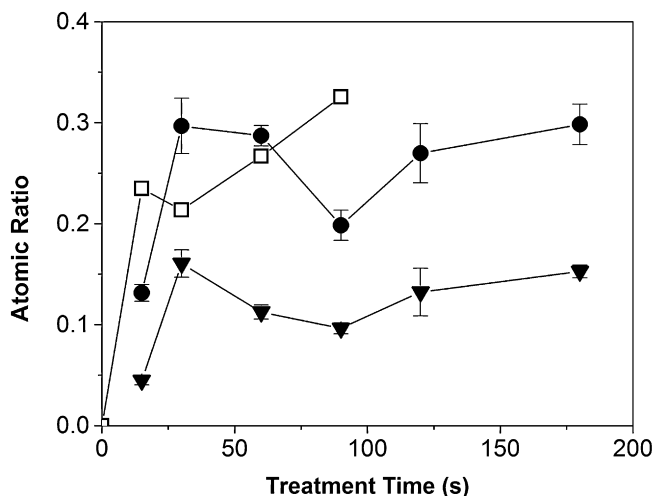


Fig. 2. Atomic concentration ratios obtained from XPS analysis for ● - O:C of VTMS-PP, ▼ - Si:C of VTMS-PP, □ - O:C of O<sub>2</sub>-PP after 24 h delay.

by Cui and Brown [17]. They explained that the methyl groups on the polymer chains oxidized during plasma treatment so that the backbone carbons remained relatively unaffected. Therefore the oxidation reached equilibrium when 1/3 of the surface carbons, i.e. those from methyl groups, were oxidized. The XPS results for O<sub>2</sub>-PP

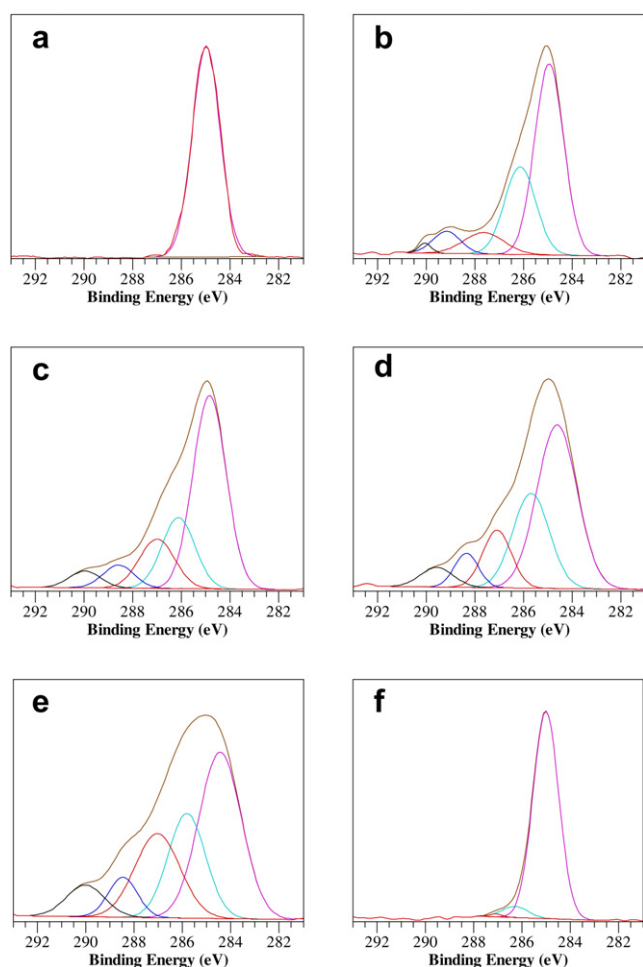


Fig. 3. High resolution XPS carbon spectrum of untreated and surface treated PP fibers. (a) Untreated; (b) 15 s, (c) 30 s, (d) 60 s and (e) 90 s in O<sub>2</sub> plasma; (f) VTMS after 30 s O<sub>2</sub> plasma.

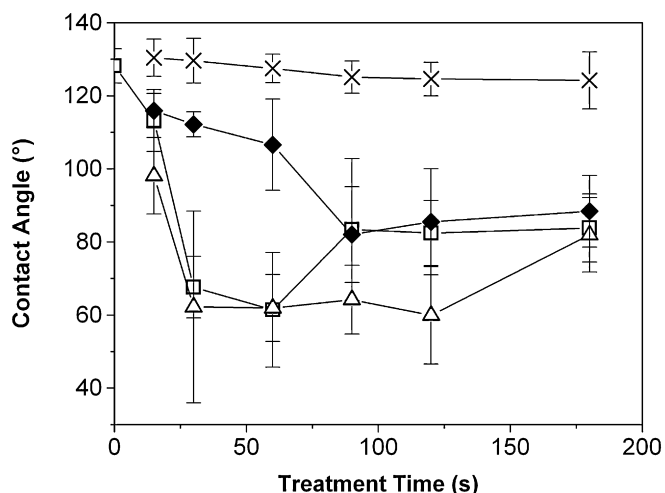
were obtained one day after the treatment. However, Cui and Brown discovered that plasma treated PP films did not show significant changes in surface composition obtained from XPS after being stored in air at room temperature for eight days [17].

Fig. 3 shows the high resolution XPS carbon (C1s) spectrum of the PP fiber surface before and after processing for 15–90 s in the oxygen plasma, as well as after VTMS grafting. Chemical components and their concentrations of the C1s peak can be obtained by deconvolution using Gaussian–Lorentzian fit, and the peak positions and the types of functional groups are based on literature values [17,19,27]. C1s spectrum of untreated PP can be well-fitted with one peak at binding energy  $E_b = 285$  eV, which represents the hydrocarbons [–(C–C)–] and [–(C–H)–]. After plasma treatment, the C1s peak broadened towards higher energy values in the form of a long tail extending up to 292 eV. This indicates that oxidized carbon species at higher binding energy appeared. C1s spectrum of oxidized PP can be well-fitted by introducing four oxidized carbon peaks, i.e. alcohol [–(C–O–H)–] and/or ether [–(C–O–C)–] at 286.3 eV, carbonyl [–(C=O)–] and/or acetal [–(O–C–O)–] at 287.2 eV, carboxyl [–(C=O)–O–] at 288.7 eV, and carbonate [–O–(C=O)–O–] at 290.1 eV. Following VTMS treatment, the C1s peak became narrower and the tail shortened to 287.5 eV. C1s spectrum of VTMS-PP can be deconvoluted with three peaks associated with hydrocarbon, alcohol/ether, and carbonyl/acetal, respectively. Since all high resolution C1s spectra of VTMS-PP samples were found to be similar, only the results of VTMS-PP after 30 s oxygen plasma treatment are shown in Fig. 3. The atomic concentration of each component for all samples discussed above is listed in Table 1. It is clear that the concentration of the hydrocarbon component decreased with increasing plasma treatment time. C–OH or C–O–C was formed at a short treatment time, but the concentration decreased as further oxidation occurred. The atomic concentrations of more oxidized carbon species increased as the treatment time increased, except for (C=O)–O concentration that underwent almost no change. We can assume that the alcohol or ether group is created as soon as enough discharge energy is applied. As the discharge energy increases, the oxidized carbon species oxidize further and more hydrocarbon bonds are oxidized, until the oxidation process reaches equilibrium. After VTMS treatment, the concentration of hydrocarbon greatly increased, as only 5% alcohol/ether carbon and less than 1% carbonyl/acetal carbon were present. This may be attributed to the fact that –OH groups reacted with VTMS and highly oxidized carbon species were fully oxidized to CO<sub>2</sub> during the VTMS grafting process. It is worth mentioning that a takeoff angle of 90° was used on the fibers to obtain higher intensity at the expense of a larger penetration depth. This may have resulted in an altered distribution of carbon functional groups from a more precise distribution obtained using angle resolved XPS, which can provide depth distribution of chemical composition on a smooth surface [28,29].

Water contact angle (CA) measurements were used to evaluate the influence of time delay between plasma conditioning and the subsequent silane treatment. The changes to surface chemistry

Table 1  
High resolution XPS carbon (C1s) peak deconvolution results.

$E_b$ (eV)	Functional groups	Atom%					
		Untreated	15 s	30 s	60 s	90 s	VTMS + 30 s
285.0	C–H, C–C	100	56.23	54.86	50.70	41.36	94.30
286.3	C–OH, C–O–C	–	27.68	20.09	26.28	22.85	5.00
287.2	C=O, O–C–O	–	8.68	14.84	12.55	22.06	0.60
288.7	O–C=O	–	6.14	6.07	6.22	6.72	–
290.1	O–(C=O)–O	–	1.26	4.12	4.88	7.02	–



**Fig. 4.** Contact angles of PP at various treatment conditions: -□- 10 min delay after O<sub>2</sub> plasma treatment, -△- 30 min delay after O<sub>2</sub> plasma treatment, -◆- 24 h delay after O<sub>2</sub> plasma treatment, and -×- after VTMS treatment.

after the plasma treatment are potentially complex as the hydrophilic functional groups can reorganize to reduce surface energy while, conversely, free radicals can continue to create additional hydrophilic surface functionality through further reaction with atmospheric oxygen. Contact angles as a function of both treatment time and delay time are compared in Fig. 4. The significant standard deviation of contact angle measurements of O<sub>2</sub>-PP mats indicates that the surface treatment was not uniform. In general oxygen plasma treatment can reduce the water contact angle. Nevertheless, a slight decrease of CA for treatment times of 15 s, 90 s and 120 s was observed but almost no change for treatment times of 30 s, 60 s and 180 s after a delay time of approximately 30 min. After 24 h, CA for treatment times of 15 s, 90 s, 120 s and 180 s approached values found immediately after treatment, but CA for 30 s and 60 s treatments significantly increased. This indicates that reorganization and generation of hydrophilic groups were in equilibrium during short delay time for 30 s and 60 s plasma treatment, while for treatment times of 15 s, 90 s and 120 s, a net increase of hydrophilic ether, carbonyl, and carboxyl functional groups might contribute to the decreased CA observed during short delay times. After a 24 h delay, plasma treatment times of 15–60 s

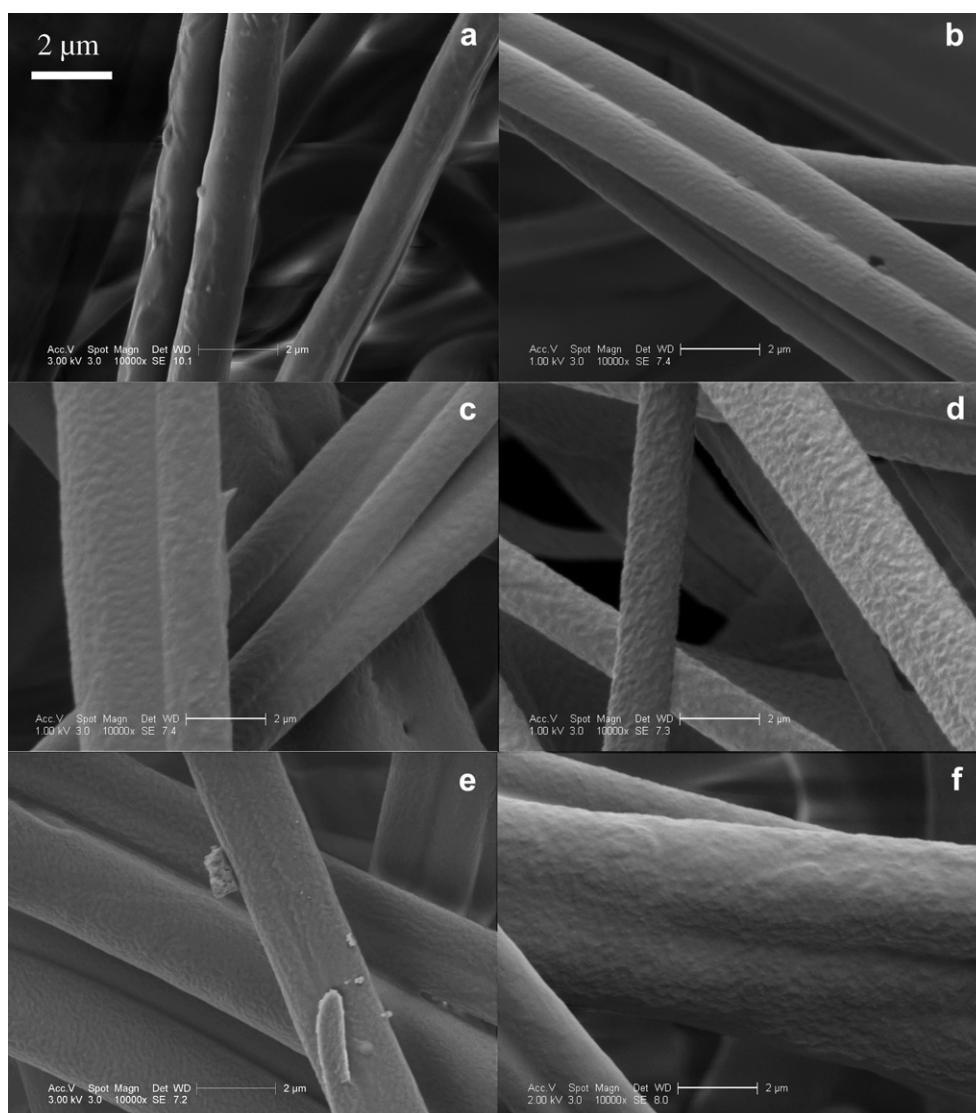


**Fig. 5.** ESEM micrographs showing difference in surface roughness of PP fibers (a) before treatment, after (b) 30 s, (c) 90 s and (d) 180 s plasma treatment in O<sub>2</sub>, and after VTMS treatment following (e) 30 s and (f) 180 s O<sub>2</sub> plasma treatment.

showed large recovery of CA. However, the 180 s treatment did not seem to be affected by delay time. After VTMS grafting, the CA was significantly increased in comparison to the O<sub>2</sub>-PP, and became very close to untreated PP. ESEM micrographs of treated and untreated fiber surfaces are given in Fig. 5 and clearly show that treated fibers possessed rougher surfaces than untreated fibers and that roughness increased with treatment time. After the VTMS was crosslinked on the surface, the surface was still rougher than that of untreated PP. These results suggest that 15 s of plasma exposure is too short to greatly oxidize the methyl groups of PP, while more than 60 s of plasma exposure significantly etches the polymer surface. Based on both XPS and CA results, we selected 30 s as the optimal treatment time and it was used as the baseline for this study. TGA results indicated approximately 1 wt.% VTMS grafted onto PP after 30 s plasma treatment. This corresponds to a grafted layer about 2 nm in thickness if it is assumed that the crosslinked VTMS covers the fiber surface uniformly.

Although ESEM analysis showed clear signs of surface degradation, no appreciable differences in the melting transition temperature and heat of melting ( $\Delta H_m$ ) were observed in DSC thermograms for treated and untreated fibers as shown by Fig. 6.  $T_m$  for all untreated and treated PP was about 161 °C and  $\Delta H_m$  at the corresponding melting transition was approximately 90 J/g. The typical DSC thermogram of PP has two melting peaks because of the

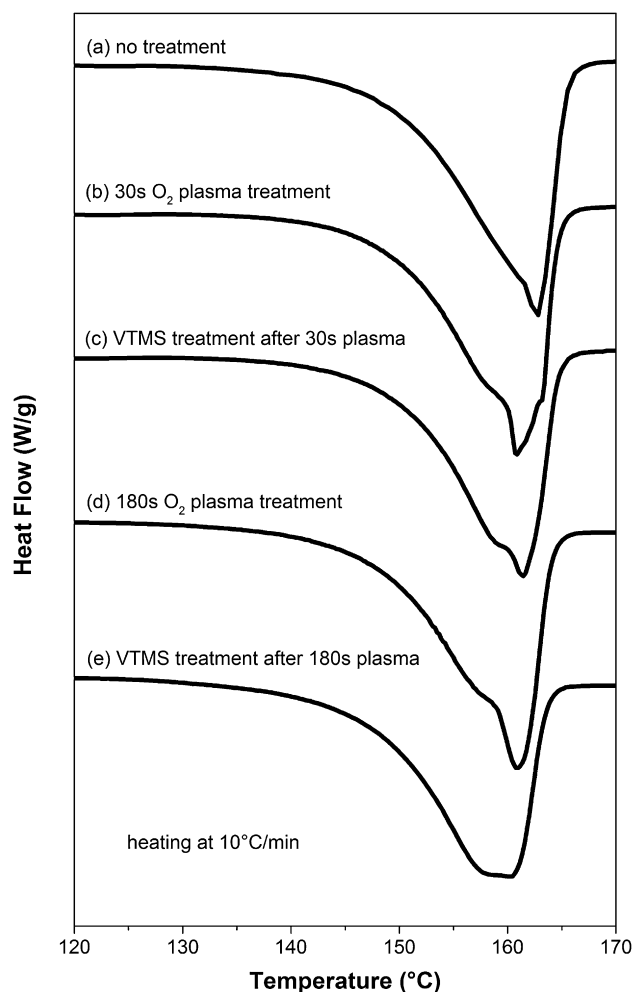


Fig. 6. DSC thermograms of untreated PP, O<sub>2</sub> plasma treated PP and VTMS grafted PP showed similar melting transitions during the first heating ramp at a heating rate of 10 °C/min.

Table 2  
Densities and volume fractions of VE systems.

	Density (g/cm <sup>3</sup> )	Volume fraction of PP	Volume fraction of air
VE	1.142 ± 0.003	–	0.0059 ± 0.0025
PP-VE	1.096 ± 0.007	0.197 ± 0.019	0.0031 ± 0.0005
VPP-VE	1.097 ± 0.005	0.196 ± 0.021	0.0029 ± 0.0003

semi-crystalline nature of PP. At most processing conditions, crystallites formed during cooling are not perfect. Therefore the melting process is accompanied by recrystallization and crystal reorientation. The overall peak is superimposed with melting of original crystallites, reorientation of imperfect structures, recrystallization, and melting of newly formed crystallites [30]. The peak at the higher melting temperature represents the melting of crystallites formed through recrystallization during melting. Slow cooling or crystallizing isothermally at higher temperature will reduce the imperfection so we will not see noticeable recrystallization peaks in the DSC thermogram, as this may be the case for the as-received PP fiber which only showed a small shoulder at 160 °C on the melting peak without obvious split.

### 3.2. Composite properties

The density of PP-VE composite samples fabricated by VARTM was found to be about 1.1 g/cm<sup>3</sup>. Since the density of PP is about 0.90 g/cm<sup>3</sup> and the density of cured VE resin was found to be 1.148 g/cm<sup>3</sup>, the measured composite density is reasonable. For PP-VE composites using untreated PP (PP-VE) or VTMS-treated PP (VPP-VE), the calculated volume fractions of PP fibers and air were 20% and 0.3%, respectively. The densities and volume fractions for VE systems discussed in this work are listed in Table 2.

PP used in this work has a melting temperature of 161 °C and a flexural modulus of 2 GPa. In comparison, the amorphous VE thermoset has a modulus of 3.3 GPa and a  $T_g$  of ~115 °C. Therefore, incorporation of PP fibers is expected to influence modulus and softening behavior. Plasma treatment roughens the PP fiber surface and the VTMS functional groups are expected to react with VE, so the modulus and softening behavior may also be affected by PP surface treatment.

Fig. 7 shows storage modulus ( $E'$ ) as a function of temperature as measured by DMA for VE, PP-VE and VPP-VE systems. It was observed that neat VE polymer possessed a higher storage modulus

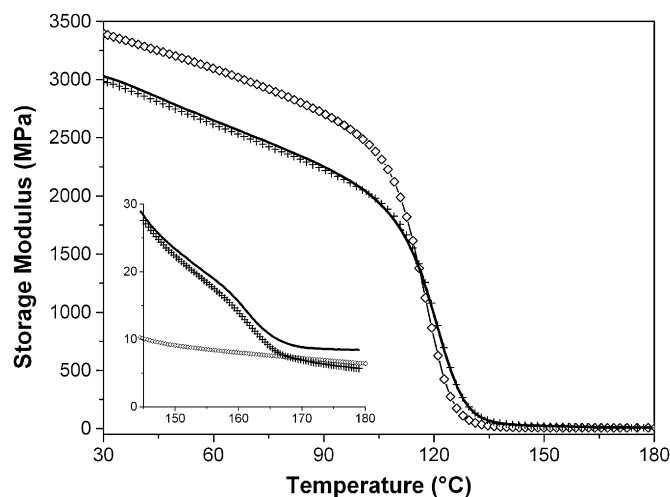
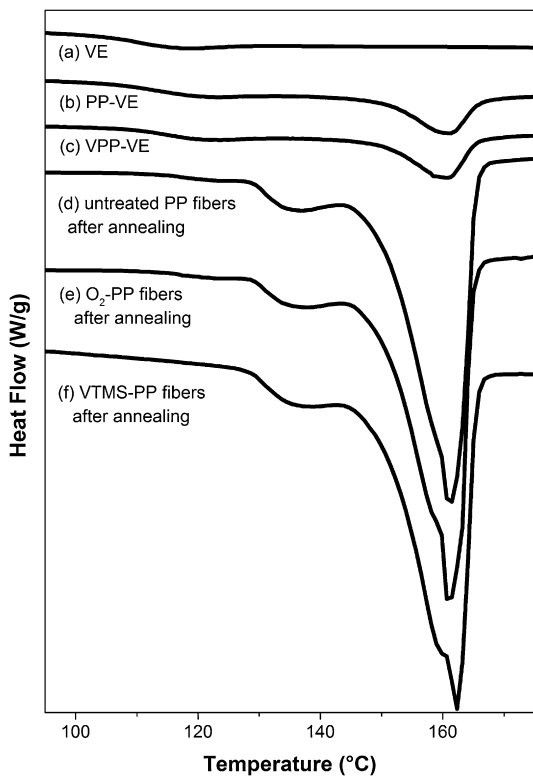


Fig. 7. DMA temperature scan of storage modulus for neat VE resin and VE composites.  $\diamond$  - VE,  $\blacksquare$  - PP-VE,  $\circ$  - VPP-VE.



**Fig. 8.** DSC thermograms during the first heating ramp for (a) neat VE resin, (b) PP-VE and (c) VPP-VE composites, and (d) untreated PP fibers, (e) O<sub>2</sub>-PP fibers and (f) VTMS-PP fibers after isothermal annealing at 125 °C under N<sub>2</sub> flow for 3 h.

**Table 3**

Thermal and thermomechanical properties of neat VE resin, PP-VE and VPP-VE composites.

	DMA		DSC (first ramp)		
	E' at 35 °C GPa	T <sub>g</sub> °C	T <sub>g</sub> °C	T <sub>m</sub> °C	ΔH <sub>m</sub> J/g
VE	3.35	118	111	–	–
PP-VE	2.93	121	114	161	9.7
VPP-VE	2.97	121	114	161	9.5

than PP-VE and VPP-VE below the T<sub>g</sub> of the VE resin. At temperatures between the T<sub>g</sub> of VE resin and T<sub>m</sub> of PP, PP-VE and VPP-VE displayed higher storage moduli than the VE resin. This indicates that PP could increase the modulus of softened VE below its

melting temperature. Above the melting temperature of PP, VE and PP-VE had similar storage moduli. However, VPP-VE showed slightly higher storage modulus than PP-VE below 105 °C and above 150 °C. The higher modulus may be a result of covalent bonds between PP and VE introduced by VTMS, while the lower modulus near the melting transition of PP may be related to surface damage of PP as observed by ESEM. The T<sub>g</sub>s of neat VE and composites were taken as the peak of the curves graphing loss modulus (E'') as a function of temperature at a frequency of 1 Hz. For comparison T<sub>g</sub> was also measured using DSC as shown in Fig. 8a–c. These data are included in Table 3 and show that the composites possessed slightly higher T<sub>g</sub> using both measurement methods. The T<sub>g</sub> of PP-VE composite was 3 °C higher than that of VE resin, and surface treatment did not affect T<sub>g</sub>. These changes were most likely associated with the reinforcing nature of PP fibers. DSC scans also showed a melting peak at 161 °C associated with PP for composites, and the heat of melting was about 9.7 J/g in the first ramp. Given that 20 v% (about 16 wt.%) PP was in the composites, the equivalent ΔH<sub>m</sub> of PP inside VE is 60 J/g, which is lower than that of PP before being embedded in VE. In an attempt to distinguish the annealing effect on PP fibers during post-curing of composites from potential interfacial effects, DSC scans were taken for PP fibers (virgin and treated) after isothermal conditioning at 125 °C under N<sub>2</sub> flow for 3 h to mimic composite cure conditions. The results are shown in Fig. 8d–f. An annealing peak is observed around 130–140 °C for all PP fibers in the first ramp. Otherwise, the melting transition and the heat of melting were similar to the controls (no annealing) shown in Fig. 6a–c.

The shape of the melting peaks of PP fibers confined by VE were found to be slightly different than observed for free PP fiber mats in the first ramp. It is possible that reorientation and recrystallization behaviors are affected by imposing predefined submicron structure. The heterogeneous interface could also be responsible for orienting crystallite growth [30].

All PP fibers and VE composites after being tested in DSC were examined using ESEM. Representative micrographs are given in Fig. 9. The fibers inside the VE matrix during DSC testing maintained a fibrous morphology even at a heating rate as low as 2 °C/min although fibers on the DSC specimen surface lost their original morphology.

Loss modulus curves as a function of temperature and frequency were obtained as described in the experimental section and shown in Fig. 10. These data were used to determine the activation energy (E<sub>a</sub>) associated with major transitions. VE showed one large transition around 114 °C (1 Hz) and the corresponding activation energy was 604 kJ/mol, which indicates it is the α-transition of VE. PP-VE and VPP-VE showed a large transition at about 116 °C (1 Hz) and

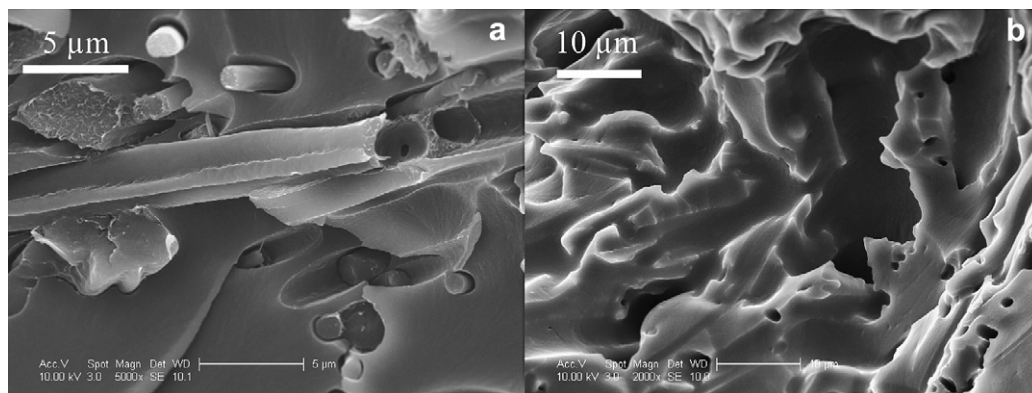


**Fig. 9.** ESEM micrographs of PP-VE composites after heating to 200 °C at 2 °C/min during DSC testing. (a) PP fibers inside VE matrix maintained fibrous morphology, and (b) PP completely lost fibrous morphology outside VE matrix.

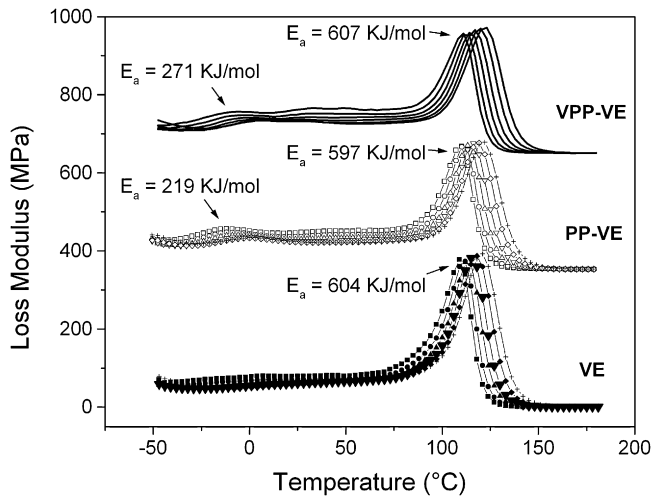


**Fig. 10.** Multiple frequency sweep of VE, PP-VE and VPP-VE. For each material, curves shift from left to right when frequency increases from 0.1 Hz to 30 Hz.

**Table 4**  
Mechanical properties of neat VE resin, PP-VE and VPP-VE composites.

	fracture Toughness		flexural Properties		tensile Properties	
	$G_{IC}$	$K_{IC}$	$\sigma_{fM}$	$E_B$	$\sigma_M$	$E$
	J/m <sup>2</sup>	MPa·m <sup>1/2</sup>	MPa	GPa	MPa	GPa
VE	231 ± 41	1.08 ± 0.15	130 ± 2	3.22 ± 0.07	89 ± 2	3.44 ± 0.13
PP-VE	596 ± 27	1.77 ± 0.06	71 ± 4	2.92 ± 0.07	47 ± 3	3.25 ± 0.16
VPP-VE	651 ± 22	1.81 ± 0.12	66 ± 4	3.06 ± 0.11	48 ± 3	3.23 ± 0.17

a small transition near  $-5^\circ\text{C}$  (1 Hz).  $E_a$  for the major transition was 597 kJ/mol and that for the minor transition was 219 kJ/mol for PP-VE. Following VTMS treatment of PP,  $E_a$  of the major transition increased slightly to 607 kJ/mol and  $E_a$  of the minor transition at  $1^\circ\text{C}$  (1 Hz) increased to 271 kJ/mol. The major transition for the composites is attributed to the  $T_g$  of the VE matrix.  $E_a$  for the minor transitions observed for the composites are higher than 100 kJ/mol, which means that they are  $\alpha$ -transitions of PP instead of  $\beta$ -transitions of VE [23]. This is consistent with the  $T_g$  of PP reported to be in the range of  $-10$ – $0^\circ\text{C}$ . Surface modified PP-VE composites had higher activation energy than untreated PP-VE composites, possibly because of interfacial bonding between PP and the VE matrix via the VTMS.

The fracture toughness, tensile properties and flexural properties of VE resin, PP-VE and VPP-VE composites were obtained. Critical stress intensity factor ( $K_{IC}$ ), critical strain energy release rate ( $G_{IC}$ ) at fracture initiation, tensile strength ( $\sigma_M$ ), modulus of elasticity ( $E$ ), flexural strength ( $\sigma_{fM}$ ), and modulus of elasticity in bending ( $E_B$ ) are given in Table 4. The critical stress intensity factor for PP-VE composite was about 1.6 times that of VE resin, while the critical strain energy release rate for PP-VE composite was more than twice that of VE resin. Thus, fracture toughness is improved significantly by encapsulating PP fibrous mats in VE resin. After VTMS grafting on PP surface, a further increase in fracture toughness was observed. The difference between PP-VE and VPP-VE may be attributed to the greater interfacial strength created by covalent bonds between VTMS-modified PP and VE resin. This better interface improved stress/energy transfer between fibers and matrix, and added a distinct energy absorption mechanism at the interface. The fracture morphology is discussed in the next section. Neat VE resin had higher flexural strength and modulus of elasticity than PP-VE composites, with almost double the flexural strength of the

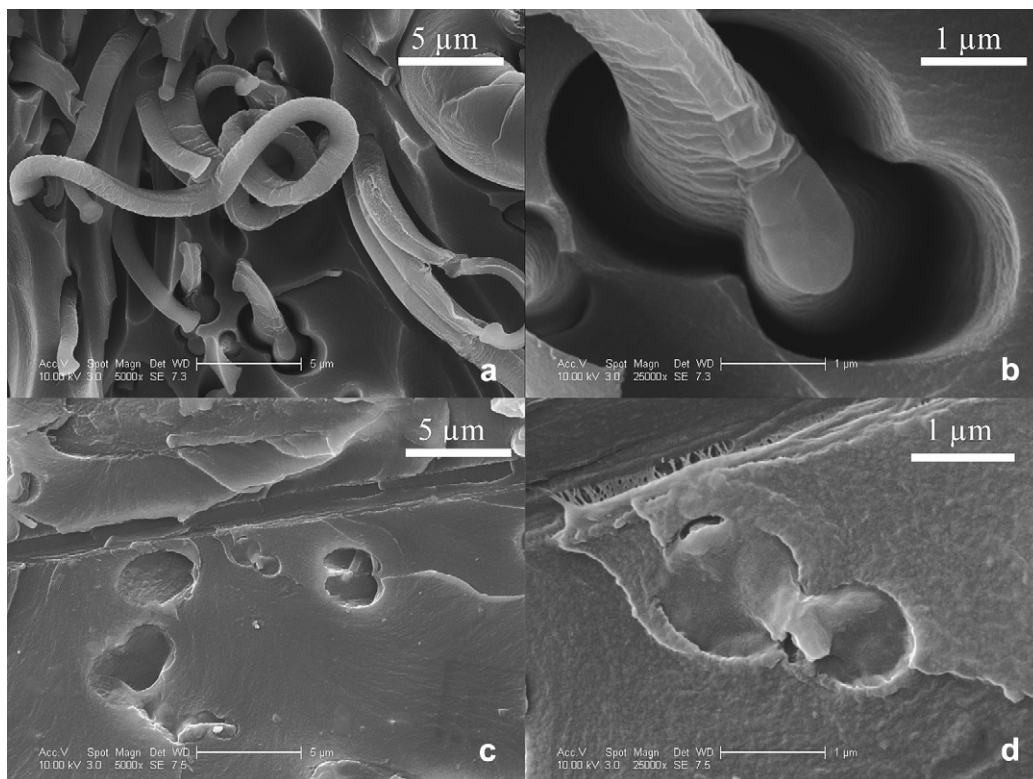


**Fig. 11.** ESEM micrographs of fracture surface of (a, b) PP-VE and (c, d) VPP-VE.



composites (Table 4). The experimentally measured flexural modulus of the PP-VE was approximately 2.92 GPa in comparison to 3.22 GPa for the neat VE matrix, which was very close to a predicted modulus of 2.99 GPa based on the Voigt model (upper bound) [31]. This indicated that the upper bound model of the combining rule could fit the PP-VE system reasonably well. The upper bound model could be applied because the moduli of both components were of similar magnitude, i.e. 3.22 GPa for the VE and 2 GPa for the PP, and the stiffer phase occupied over 80 v% in the composites [31]. The predicted modulus of 2.99 GPa for VPP-VE using the same model also closely matched the measured flexural modulus of 3.06 GPa. Nevertheless, VPP-VE composites did not show a significant difference in flexural properties compared to PP-VE composites, possibly because of the weak nature of PP itself – PP fibers broke before the enhanced interfacial strength could contribute to the measured flexural strength and modulus. The use of higher strength PP fibers may attain the expected improvement in flexural properties after surface treatment. The tensile testing results match flexural properties well.

### 3.3. Fracture morphology

ESEM micrographs of composite fracture surfaces were used to gauge interface integrity and to analyze the dominant failure mode. Analysis of the fracture morphologies showed obvious interfacial discontinuities between PP fibers and the VE resin as seen in Fig. 11a–b. By contrast Fig. 11c–d shows that such discontinuities were reduced substantially in composites with VTMS grafted PP fibrous mats. Fiber pullout, fiber breakage and matrix cracking were the dominant failure modes for the composite using untreated PP. The weak interface led to relatively easy fiber pullout at small loads. Energy absorption was mainly from fiber breakage, matrix cracking and voids. While for surface treated PP, fiber breakage and matrix cracking were the dominant failure modes because the strong bonding at the fiber–matrix interface restrained the fiber pullout. Energy absorption mechanisms included fiber breakage, matrix cracking and interfacial interaction. Stronger interfacial interactions provided increased load-bearing capability by transferring load from the brittle matrix to the thermoplastic fiber. In addition, mechanical interlocking resulting from the rougher fiber surface might also contribute to improved fracture toughness. However, the PP fiber used in this work has weak tensile properties due to the low molecular weight (high melt flow index). This curtailed the ability of the thermoplastic phase to absorb energy through deformation mechanisms and limited the contribution from enhanced interfacial interaction. The use of small PP fibers with higher strength would probably result in a significant increase in fracture toughness after enhancing the interfacial interaction.

## 4. Conclusions

Composites containing micron-sized PP fiber mats and VE matrices were fabricated using VARTM. PP fibers showed good wetting characteristics in VE monomer, but void discontinuities were generated at the interface of VE and PP fibers during cure. DMA showed the predicted negative contribution of the PP fiber phase on storage modulus, and a minor positive effect on the softening transition. Fracture toughness was greatly improved, but flexural strength was substantially decreased upon encapsulation of the PP fibrous phase. The loss in strength was partly due to the

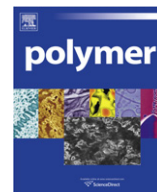
poor interface between the PP fibers and the VE matrix. A two-step surface modification on PP using silane coupling agents improved interfacial discontinuities by forming covalent bonds between matrix and fibers. The oxygen plasma treatment caused surface roughness but did not degrade the bulk polymer. Fracture toughness of the composite was slightly increased after surface treatment of PP, which might be attributed to enhanced energy absorption capacity via chemical bonding and mechanical interlocking at the interface. Because of the weak fiber material, mechanical strength and modulus did not show significant increases for the VPP-VE composite. Small PP fibers with higher strength may attain the expected improvement in mechanical properties after surface treatment.

## Acknowledgements

The authors from Drexel University wish to acknowledge the U. S. Army Research Laboratory for financial support under the Army Materials Center of Excellence Program, contract W911NF-06-2-0013.

## References

- [1] Yee AF, Pearson RA. *J Mater Sci* 1986;21:2462–74.
- [2] Kinloch AJ, Shaw SJ, Tod DA, Hunston DL. *Polymer* 1983;24:1341–54.
- [3] Frigione ME, Mascia L, Acierio D. *Eur Polym J* 1995;31(11):1021–9.
- [4] Robinette EJ, Ziaee S, Palmese GR. *Polymer* 2004;45:6143–54.
- [5] Ullett JS, Chartoff RP. *Polym Eng Sci* 1995;35(13):1086–97.
- [6] Groleau MR, Shi Y-B, Bertram JL, Sue HJ, Yang PC. *Compos Sci Technol* 1996;56:1223–40.
- [7] Gilbert EN, Hayes BS, Seferis JC. *Compos Part A Appl Sci Manuf* 2003;34:245–52.
- [8] Johnsen BB, Kinloch AJ, Mohammed RD, Taylor AC, Sprenger S. *Polymer* 2007;48:530–41.
- [9] Yun NG, Won YG, Kim SC. *Polym Bull* 2004;52:365–72.
- [10] Hogg PJ. *Mater Sci Eng A* 2005;412:97–103.
- [11] Moon SI, Jang J. *J Mater Sci* 1998;33:3419–25.
- [12] Lin SP, Han JL, Yeh JT, Chang FC, Hsieh KH. *J Appl Polym Sci* 2007;104:655–65.
- [13] Brown JR, Mathys Z. *J Mater Sci* 1997;32:2599–604.
- [14] Khanchaitit P, Aht-Ong D. *Polym Compos* 2006;27:484–90.
- [15] Lu J, Askeland P, Drzal LT. *Polymer* 2008;49:1285–96.
- [16] Hashemi SA, Arabi H, Mirzaeyan N. *Polym Compos* 2007;28:713–21.
- [17] Cui NY, Brown NMD. *Appl Surf Sci* 2002;189:31–8.
- [18] Harth K, Hibst H. *Surf Coat Technol* 1993;59:350–5.
- [19] Wang C, He X. *Surf Coat Technol* 2006;201:3377–84.
- [20] Liang Y, Pappas DD, Yim J, Rahmathullah AM, Jensen RE, Palmese GR. Encapsulated nano- and meso-fiber mesh composites. Society for the Advancement of Material and Process Engineering conference proceedings. Baltimore, Maryland, USA; June 2007.
- [21] Almanza-Workman AM, Raghavan S, Deymier P, Monk DJ, Roop R. *Colloids Surf A Physicochem Eng Asp* 2004;232:67–75.
- [22] Rahmathullah AM, Robinette EJ, Chen H, Elabd YA, Palmese GR. *Nucl Instrum Methods Phys Res B* 2007;265:23–30.
- [23] Ferry JD. *Viscoelastic properties of polymers*. 2nd ed. New York: Wiley; 1970.
- [24] Standard test methods for plane-strain fracture toughness and strain energy release rate of plastic materials. Annual book of ASTM standards, designation: D 5045–5099. ASTM International; June 1999.
- [25] Standard test methods for flexural properties of unreinforced and reinforced plastics and electrical insulating materials. Annual book of ASTM standards, designation: D 790–03. ASTM International; April 2003.
- [26] Standard test method for tensile properties of plastics. Annual book of ASTM standards, designation: D 638–03. ASTM International; January 2004.
- [27] Borgia G, Chiper A, Rusu I. *Plasma Sources Sci Technol* 2006;15:849–57.
- [28] Gries WH. *Appl Surf Sci* 1996;100/101:41–6.
- [29] Hamamura N, Yumoto M, Sakai T. 1998 International symposium on electrical insulating materials conference proceedings: IEEE Xplore. Toyohashi, Japan; 1998. p. 163–8.
- [30] Karger-Kocsis J. Polypropylene: structure, blends and composites. In: *Structure and morphology*, vol. 1. London: Chapman & Hall; 1995.
- [31] Whitney JM, McCullough RL. Delaware composites design encyclopedia. In: *Micromechanical materials modeling*, vol. 2. Pennsylvania: Technomic; 1990.



# Investigation of post-spinning stretching process on morphological, structural, and mechanical properties of electrospun polyacrylonitrile copolymer nanofibers

Chuilin Lai<sup>a</sup>, Ganji Zhong<sup>b</sup>, Zhongren Yue<sup>c</sup>, Gui Chen<sup>d</sup>, Lifeng Zhang<sup>a</sup>, Ahmad Vakili<sup>c</sup>, Ying Wang<sup>d</sup>, Lei Zhu<sup>b,\*</sup>, Jie Liu<sup>d,\*\*</sup>, Hao Fong<sup>a,\*\*\*</sup>

<sup>a</sup> Department of Chemistry, South Dakota School of Mines and Technology, Rapid City, SD 57701, USA

<sup>b</sup> Department of Macromolecular Science and Engineering, Case Western Reserve University, Cleveland, OH 44106, USA

<sup>c</sup> Department of Materials Science and Engineering, University of Tennessee Space Institute, Tullahoma, TN 37388, USA

<sup>d</sup> Key Laboratory of Carbon Fiber and Functional Polymers, Ministry of Education, Beijing University of Chemical Technology, Chao-Yang District, Beijing 100029, China

## ARTICLE INFO

### Article history:

Received 29 September 2010

Received in revised form

22 November 2010

Accepted 25 November 2010

Available online 2 December 2010

### Keywords:

Electrospinning  
Carbon nanofibers  
Polyacrylonitrile

## ABSTRACT

Electrospun polyacrylonitrile (PAN) copolymer nanofibers with diameters of  $\sim 0.3 \mu\text{m}$  were prepared as highly aligned bundles. The as-electrospun nanofiber bundles were then stretched in steam at  $\sim 100^\circ\text{C}$  into 2, 3, and 4 times of the original lengths. Subsequently, characterizations and evaluations were carried out to understand morphological, structural, and mechanical properties using SEM, 2D WAXD, polarized FT-IR, DSC, and mechanical tester; and the results were compared to those of conventional PAN copolymer microfibers. The study revealed that: (1) the macromolecules in as-electrospun nanofibers were loosely oriented along fiber axes; although such an orientation was not high, a small extent of stretching could effectively improve the orientation and increase the crystallinity; (2) most of macromolecules in the crystalline phase of as-electrospun and stretched nanofibers possessed the zig-zag conformation instead of the helical conformation; and (3) the post-spinning stretching process could substantially improve mechanical properties of the nanofiber bundles. To the best of our knowledge, this study represented the first successful attempt to stretch electrospun nanofibers; and we envisioned that the highly aligned and stretched electrospun PAN copolymer nanofibers could be an innovative type of precursor for the development of continuous nano-scale carbon fibers with superior mechanical strength.

© 2010 Elsevier Ltd. All rights reserved.

## 1. Introduction

Carbon fibers with high mechanical strength are prepared from polyacrylonitrile (PAN) precursor fibers through the thermal treatments of stabilization and carbonization; the excellent strength-to-weight ratio combined with superior stiffness has made the PAN-based carbon fibers the material of choice for the development of large load-bearing composites [1]. Shortly after the discovery of how to produce PAN-based carbon fibers approximately half a century ago, the tensile strength of the T300 carbon fibers produced by the Toray Industries, Inc. in Japan quickly reached  $\sim 3 \text{ GPa}$ . The maximal tensile strength of carbon fibers, however, is estimated over  $180 \text{ GPa}$  [1,2]. After many years of

research, the strongest carbon fibers that can be produced presently (*i.e.*, the T1000 carbon fibers) have the tensile strength of merely  $\sim 7 \text{ GPa}$ . Numerous research efforts have indicated that (1) the amount, size, and distribution of structural imperfections determine the mechanical strength of carbon fibers; and (2) many types of structural imperfections in the precursor fibers are likely to retain in the resulting carbon fibers [3–6]. Thus, the fundamental approach for further improving the mechanical strength of carbon fibers is to reduce the amounts of structural imperfections (including surface and bulk defects) as well as structural inhomogeneity such as sheath-core structures [7–9].

The production of PAN-based carbon fibers involves the synthesis of PAN precursors, the spinning of PAN precursor fibers, and the thermal treatments (*i.e.*, stabilization and carbonization) of precursor fibers. The PAN homopolymer contains highly polar nitrile groups, hindering the alignment of macromolecular chains during spinning (particularly during stretching of as-spun fibers); additionally, the oxidative stabilization of PAN homopolymer occurs at relatively high temperature, and the reaction is difficult to

\* Corresponding author. Tel.: +1 216 368 5861; fax: +1 216 368 4202.

\*\* Corresponding author. Tel.: +86 10 64438724; fax: +86 10 64420710.

\*\*\* Corresponding author. Tel.: +1 605 394 1229; fax: +1 605 394 1232.

E-mail addresses: [lxz121@case.edu](mailto:lxz121@case.edu) (L. Zhu), [liuj@mail.buct.edu.cn](mailto:liuj@mail.buct.edu.cn) (J. Liu), [Hao.Fong@sdsmt.edu](mailto:Hao.Fong@sdsmt.edu) (H. Fong).

control due to a sudden and rapid evolution of heat. This surge of heat can cause the scission of macromolecular chains and make the resulting carbon fibers mechanically weak. Carbon fibers with the highest mechanical strength have been produced exclusively from PAN copolymer precursors. The co-monomer content usually ranges from 0.5 to 8 wt.%; typical co-monomers include itaconic acid, methyl acrylate, and others [1]. The inclusion of co-monomer (s) mitigates the nitrile–nitrile interactions, renders the copolymer higher solubility in spinning solvent(s), allows better macromolecular orientation in precursor fibers, and makes the stabilized and carbonized fibers more structurally homogeneous.

The wet spinning and air-gap spinning (also known as “dry-jet wet spinning”) are the commonly adopted spinning methods for producing PAN precursor fibers [1]. In wet spinning, a spinneret with 40–80  $\mu\text{m}$  diameter orifices is immersed in a coagulation bath (*i.e.*, an aqueous solution), and a spin dope (*i.e.*, a 15–20 wt.% PAN copolymer solution using appropriate solvents such as *N,N*-dimethylformamide) is extruded directly into the bath to form filaments. In air-gap spinning, the spinneret is positioned several millimeters above a coagulation bath, and filaments are extruded vertically into the bath. The method of air-gap spinning permits the spin dope and the coagulation bath to be at different temperatures, thus avoids the high stress caused by coagulation of spin dope on the surface of filaments. In addition, the filaments partially gel before entering the bath; therefore, the air-gap spun fibers are generally smoother with probably fewer surface defects than the wet spun fibers [1]. No matter which spinning method is adopted, the rapid removal of solvent(s) from large diameter filaments in coagulation bath can introduce various types and large amounts of structural defects (*e.g.*, sub-micron scaled voids/flaws). Although post-spinning stretching can substantially improve the macromolecular orientation, the reduction of these structural defects is limited. Consequently, voids/flaws with sizes being tens of nanometers are commonly observed in the precursor fibers and the resulting carbon fibers. The existence of these defects is an important reason that the mechanical strength of the current carbon fibers only reaches a small percentage of the theoretically predicted value. Additionally, the large diameter of precursor fibers is responsible for the formation of structural inhomogeneity (particularly sheath-core structures) during stabilization and carbonization. The presence of structural inhomogeneity in the current carbon fibers is another important reason accounted for low mechanical strength. For example, stabilization occurs in an oxidative environment such as in air, and it is a diffusion-controlled process [10–12]. The large fiber diameter hinders the diffusion of molecules including oxygen and stabilization by-products; often the results are that the outer region of the precursor fibers has been well-stabilized while the inner region has not. Such a condition leads to the formation of sheath-core structures, and the stabilized fibers are therefore structurally inhomogeneous; this further leads to the resulting carbon fibers being mechanically weak. Previous research has revealed that the mechanical strength of carbon fibers increases as the diameter of precursor fibers decreases when produced under comparable conditions; *i.e.*, a smaller diameter allows for a higher fraction of the theoretically predicted strength to be reached [13]. This is well-known as the “size effect”. For example, the T1000 carbon fibers have the diameter of  $\sim 5 \mu\text{m}$  and the tensile strength of  $\sim 7 \text{ GPa}$ ; and their precursor fibers are produced by reducing the size of orifices in the spinneret from  $\sim 70$  to  $\sim 40 \mu\text{m}$ . Nonetheless, the conventional spinning methods are difficult, if not impossible, to prepare precursor fibers with diameters that are orders of magnitude smaller than  $10 \mu\text{m}$ .

The technique of electrospinning provides a unique approach to prepare PAN precursor fibers with diameters of  $\sim 0.3 \mu\text{m}$ , which are  $\sim 30$  times thinner than those of conventional PAN precursor fibers

[14–18]. During electrospinning, a spin dope (*e.g.*, a PAN copolymer solution) is placed in a spinneret. High DC voltage, usually in the range from 5 to 40 kV, is applied to the spin dope through an electrode (*e.g.*, a thin metal rod). An electrically grounded collector is placed at a distance (known as “gap distance”) away from the spinneret. The gap distance usually ranges from a few centimeters to 1 m. When the applied voltage reaches a critical value and the electric force overcomes the surface tension and the viscoelastic force, a jet ejects and travels straight for a certain distance. The jet then starts to bend, forming helical loops. This phenomenon has been termed as “bending instability” [18]; typically, the bending instability causes the length of an electrospinning jet to elongate up to 10,000 times in a very short time period of 50 ms or less. Thus, the elongation (draw) rate during bending instability is extremely large [16], which can effectively stretch the macromolecules and closely align them along the fiber axis. Additionally, the solvent evaporation during electrospinning is very fast; over 99% of solvent(s) in the electrospinning jet/filament can be removed during or shortly after bending instability [16,18], so that the macromolecular orientation introduced through bending instability is likely to retain in electrospun nanofibers. Furthermore, since the solvent is removed through evaporation while no coagulation bath is involved during nanofiber formation, the surface of electrospun nanofibers can be even smoother and presumably the surface defects can be even fewer than those of the air-gap spun fibers. Nonetheless, the rapid elongation/drawing of electrospinning jet/filament occurs in solution or gel state; although extended macromolecular chains are expected to exist during electrospinning (particularly during bending instability), these chains can relax afterwards, especially if the collected nanofibers still contain trace amounts of solvent(s) which would allow the relaxation of macromolecules.

It is noteworthy that the process of electrospinning can produce a single, very long (*i.e.*, continuous) nanofiber [8,18]. By judiciously designing the spinneret and carefully selecting electrospinning conditions (*e.g.*, spin dope properties, processing and environmental conditions), the process can be extremely stable with a visually steady jet running continuously without breaking. The mat deposited on the electrically grounded collector is thus made of a single nanofiber. If the collector is a fast-moving belt (or water flow) and hundreds to thousands of spinnerets are placed above it, a continuous bundle made of loosely oriented nanofibers that possess desired morphological and structural properties could be obtained. After the nanofibers in the bundle are straightened and stretched, a highly aligned nanofiber bundle can be prepared for the subsequent stabilization and carbonization.

In this study, instead of using the fast-moving belt (or water flow) and many spinnerets, a U-shaped metal device with the distance between two legs being  $\sim 25 \text{ mm}$  was used for the collection of highly aligned electrospun PAN nanofiber bundles [19]. By manually moving the electrically grounded device back and forth for several times between the spinneret and the electrically grounded metal plate during electrospinning, tens of aligned nanofibers could be collected between the metal legs. These nanofibers were then transferred to a slightly smaller U-shaped metal device, and the process was repeated for  $\sim 50$  times to collect a bundle with highly aligned nanofibers. The obtained PAN copolymer nanofiber bundle was then stretched in an oven at  $\sim 100 \text{ }^\circ\text{C}$ , and a pan of boiling water was maintained during the stretching process [1]. The stretched nanofiber bundles with final lengths being 2, 3, and 4 times of original lengths of the bundles were acquired. Subsequently, characterizations and evaluations were carried out to understand the morphological, structural, and mechanical properties of the nanofibers before and after the post-spinning stretching using SEM, two-dimensional (2D) WAXD, polarized FT–IR, DSC, and mechanical tester; and the results were

compared to those of the conventional PAN precursor microfibers that were used as the starting materials for making electrospun nanofibers.

## 2. Experimental

### 2.1. Materials

The PAN used in this study were the Special Acrylic Fibers (SAF 3K fibers) provided by the Courtaulds, Ltd in the UK. The SAF 3K fibers were made of the PAN copolymer with 92.8 wt.% of acrylonitrile, 1.2 wt.% of itaconic acid, and 6.0 wt.% of methyl acrylate, and they were in the form of bundle with 3000 fibers. *N,N*-dimethylformamide (DMF) and acetone were purchased from the Sigma–Aldrich Co. (Milwaukee, WI). The chemicals were used without further purification.

### 2.2. Electrospinning

The SAF 3K fibers were first immersed in acetone to remove the surface oil; the fibers were then dissolved in DMF to prepare a 15 wt.% solution. Subsequently, the solution was pushed through a glass fiber filter with pore size of 2  $\mu\text{m}$  to remove gel particles, if there were any, to obtain the spin dope. DMF was selected because it is a good solvent for the PAN copolymer; additionally, DMF is also suitable for conducting electrospinning due to its high dielectric constant and appropriate volatility [16,17]. A specially designed spinneret was utilized for electrospinning inside a fume hood at  $\sim 25^\circ\text{C}$ . The spinneret consisted of a polypropylene tube with the inner diameter of 1.0 inch, and a stainless steel hemispherical head which had an orifice with the diameter of 0.4 mm at the center. The electrospinning setup also consisted of a high voltage power supply (model number: ES30P) purchased from the Gamma High Voltage Research, Inc. (Ormond Beach, FL). During electrospinning, a positive voltage of 25 kV was applied through a thin metal rod to the spin dope held inside the spinneret. Electrospun nanofibers were deposited on an electrically grounded metal plate covered with aluminum foil. The distance between the spinneret and the metal plate was set at 40 cm. In this manner, the process was extremely stable; and the electrospinning jet could run continuously without breaking for many hours. To collect highly aligned electrospun PAN precursor nanofiber bundles, a U-shaped metal device with the distance between two legs being  $\sim 25$  mm was used [19]. By manually moving the electrically grounded device back and forth for several times between the spinneret and the electrically grounded metal plate during electrospinning, tens of aligned nanofibers were collected between the metal legs. This U-shaped device functioned like a traverse guide in a conventional wind-up, and a skein of aligned nanofibers could be formed on the device. These nanofibers were then transferred to a slightly smaller U-shaped metal device, and the process was repeated for  $\sim 50$  times to collect a bundle with highly aligned PAN precursor nanofibers.

### 2.3. Stretching

Prior to stretching, both ends of an as-electrospun nanofiber bundle (containing  $\sim 2000$ – $5000$  highly aligned PAN precursor nanofibers) were first attached on the opposite sides of a square plastic frame with the inside dimension being  $2.0 \times 2.0$  cm; subsequently, one side of the frame was tied with a metal hook inside an oven, while the other side was tied with a device that could apply varied amounts of tension; finally, the two sides of the plastic frame (without the attachment of nanofiber bundle) were cut and the PAN copolymer nanofiber bundle was then stretched in the oven at  $\sim 100^\circ\text{C}$ . It is noteworthy that a pan of boiling water

was maintained during the stretching process [1]. The stretched nanofiber bundles with the final lengths being 2, 3, and 4 times of original lengths of the bundles were prepared for the morphological, structural, and mechanical characterizations and evaluations.

### 2.4. Characterization and evaluation

A Zeiss Supra 40VP field-emission SEM was employed to examine the fiber morphologies. Prior to SEM examinations, the specimens were sputter-coated with gold to avoid charge accumulations. DSC experiments were carried out in dry nitrogen using a TA Q-100 DSC instrument. Less than 1.0 mg of sample was used for the DSC studies to avoid the possible thermal lag. The DSC curves were recorded from 50 to  $350^\circ\text{C}$ , and the scanning rate was set at  $10^\circ\text{C}/\text{min}$ . The experiments of 2D WAXD were carried out using a rotating anode X-ray generator (RU 300, 12 kW, Rigaku, Woodlands, TX) operating at 40 kV and 90 mA with the Cu  $K\alpha$  radiation (wavelength  $\lambda = 0.154$  nm). The patterns were collected with a Bruker AXS (Madison, WI) HI-STAR area detector. The sample-to-detector distance was set at 74 mm. FT–IR spectra were acquired using a Bruker Tensor-27 FT–IR spectrometer equipped with a polarizer; the samples were prepared by pressing the aligned nanofibers with potassium bromide, and the FT–IR spectra were acquired by scanning the samples (64 scans) from 600 to  $4000\text{ cm}^{-1}$  with the resolution of  $4\text{ cm}^{-1}$ . The tensile properties of nanofiber bundles were measured with a Diastron Limited FDAS 765 fiber analyzer that consisted of a high resolution tensile tester (LEX810) with a force resolution of 50  $\mu\text{N}$  and a Mitutoyo LSM-500 Laser Scan Micrometer with a positional repeatability of 0.1  $\mu\text{m}$ .

## 3. Results and discussion

### 3.1. Scanning electron microscopy (SEM)

The SEM images in Fig. 1 showed representative morphologies of as-electrospun PAN copolymer nanofiber bundle (image “A”) and the stretched nanofiber bundles with the final lengths being 2 (image “B”), 3 (image “C”), and 4 (image “D”) times of the original lengths; for comparison, the representative morphology of the conventional SAF 3K microfiber bundle was also shown in the figure (image “E”). The diameters of as-electrospun nanofibers were  $\sim 0.3\text{ }\mu\text{m}$ , and the surface of nanofibers appeared to be smooth. In contrast, the conventional PAN copolymer microfibers had diameters of  $\sim 10\text{ }\mu\text{m}$ ; and the fibers had relatively rough surfaces with nicks, cracks, and diametrical bulges. When examining the as-electrospun nanofibers under a polarized optical microscope, the birefringence characteristic could be readily detected by rotating the nanofibers between two crossed polarizers, suggesting that the macromolecules in the crystalline and possibly the amorphous phases in the nanofibers were oriented. Additionally, the PAN copolymer nanofibers in the as-electrospun bundle contained no microscopically identifiable beads and/or beaded-nanofibers [20], and they were uniform with relatively small variation in diameters.

By measuring diameters of the nanofibers (in each image of Fig. 1) at 50 randomly selected locations using the image-analysis software affiliated with the SEM, average diameters and the associated one standard deviations were acquired as  $300 \pm 57$ ,  $239 \pm 37$ ,  $221 \pm 38$ , and  $222 \pm 47$  nm for the nanofibers in the as-electrospun bundle and the 2-, 3-, and 4-time stretched bundles, respectively. It is noteworthy that, if a nanofiber with diameter of 300 nm could be uniformly stretched into 2, 3, and 4 time longer, the final diameters would be 212, 173, and 150 nm, respectively. This indicated that there might be segments/sections of nanofibers that were not well aligned in the as-electrospun bundle, and the stretching process

would straighten these segments/sections first. It was also evident that the reduction of fiber diameters from the as-electrospun bundle to the 2-time stretched bundle was quite substantial, suggesting the macromolecular orientation in amorphous and/or crystalline phases in the as-electrospun nanofibers was relatively low. Nonetheless, further stretching (especially from the 3-time stretched bundle to the 4-time stretched bundle) did not reduce the diameters of nanofibers appreciably. This was probably due to the reason that the macromolecular orientations in amorphous and/or crystalline phases in the stretched nanofiber bundles were considerably high, even if the extent of stretching was small. Therefore, the further stretching could not effectively elongate the nanofibers and thus could not reduce the diameters; instead, some nanofibers in the bundle broke into shorter ones. It is noteworthy that, through post-spinning stretching process, conventional as-spun PAN copolymer microfibrils could be stretched uniformly into 8–10 times longer; while it appeared that the as-electrospun PAN copolymer nanofibers could only be stretched into 2–3 times longer.

This might indicate that, unlike the macromolecules in the conventional as-spun microfibrils that had almost no preferred orientation, the macromolecules in the as-electrospun nanofibers were loosely oriented along fiber axes; although such an orientation was not high, a small extent of stretching could effectively improve the macromolecular orientation and probably increase the crystallinity. Additionally, some nanofibers in the stretched bundles appeared to form film- and/or rod-like structures with tens to hundreds of nanofibers tightly stacked together; such structures were attributed to hydrophobic interactions among the nanofibers, similar to those observed in carbon nanotubes. Continuing research efforts have been devoted to mitigate the formation of such structures through surface sizing the nanofibers with mineral oils.

### 3.2. Two-dimensional wide-angle X-ray diffraction (2D WAXD)

The crystalline and macromolecular structures and orientations of the PAN copolymer in the as-electrospun nanofiber bundle,

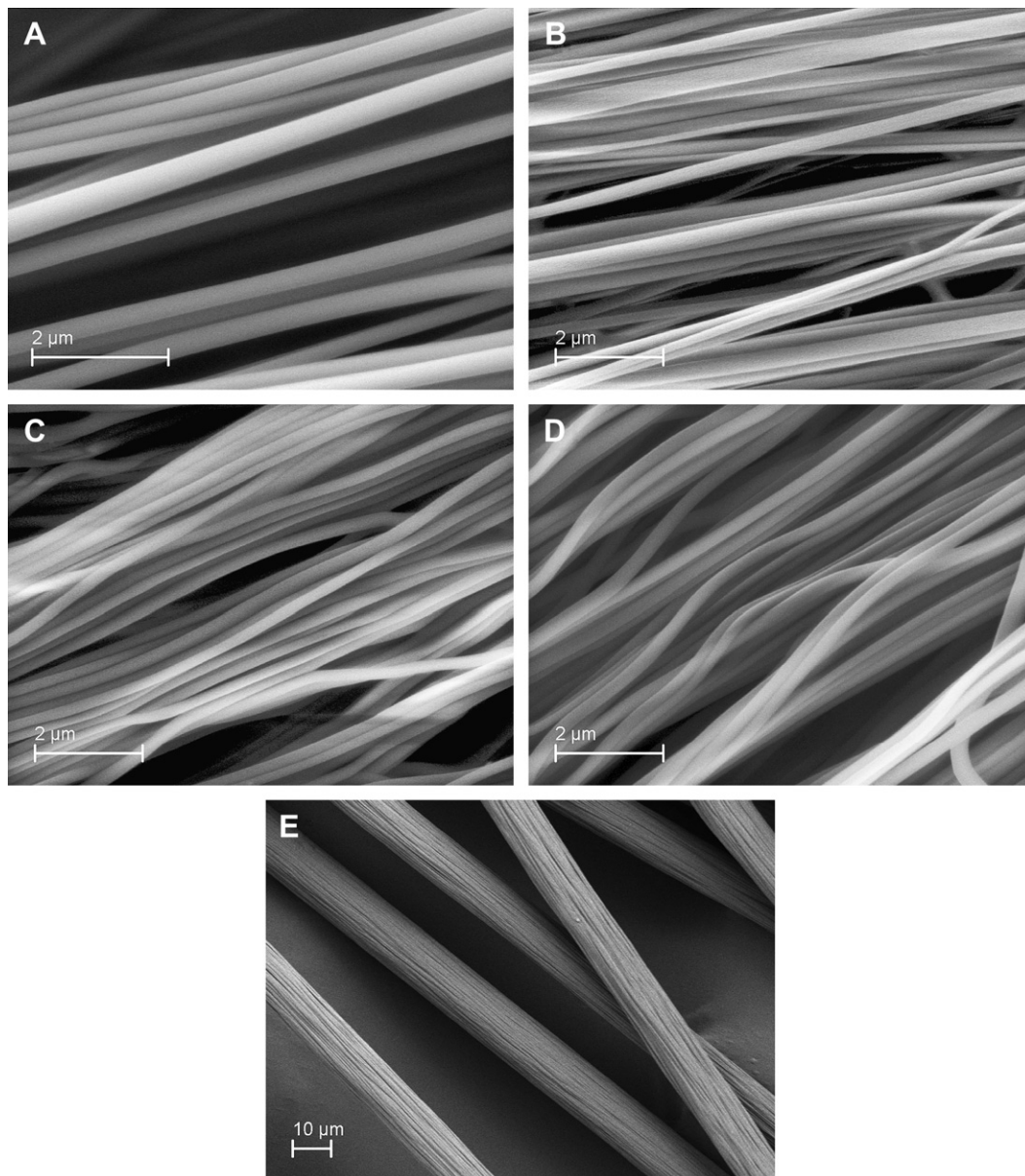


**Fig. 1.** SEM images showing representative morphologies of the as-electrospun PAN copolymer nanofiber bundle (A), the stretched nanofiber bundles with the final lengths being 2 (B), 3 (C), and 4 (D) times of original lengths of the bundles, as well as the conventional SAF 3K microfibril bundle.

stretched nanofiber bundles, as well as the conventional microfiber bundle were further investigated by 2D WAXD experiments, and results were shown in Fig. 2. All types of fibers showed a strong diffraction centered at the  $2\theta$  angle of  $\sim 16.7^\circ$  and a weak diffraction centered at the  $2\theta$  angle of  $\sim 29.0^\circ$ ; these were characteristic (100) and (110) reflections for the PAN hexagonal lattice [1,9].

The above 2D WAXD patterns were converted into 1D XRD curves through integrating the diffraction intensities versus  $2\theta$  angles, and the obtained profiles were shown in the left panel of Fig. 3. The average interplanar spacing  $d$  was determined using the Bragg equation, while the average crystallite size parameter  $D_{(100)}$  was determined using the Scherrer equation [21,22]. It appeared that the average  $d$ -spacing of the as-electrospun nanofibers was similar to those of the stretched nanofibers and the microfibers, because the diffraction peaks were all centered at the same  $2\theta$  angle of  $\sim 16.7^\circ$ . However, the average crystallite size in the as-electrospun nanofibers was much smaller than those in the stretched nanofibers and the microfibers, because the width of the (100) reflection peak at its half height was considerably broader; while the sharpness of the peaks for stretched nanofibers was similar to that for the microfibers, even though the microfibers were stretched uniformly for 8 times from their as-spun fibers. It was noteworthy that the average diameter of 2-time stretched nanofibers was  $\sim 239$  nm, while that of as-electrospun nanofibers was  $\sim 300$  nm. This indicated that the effective stretching (from the as-electrospun bundle to 2-time stretched bundle) was merely  $\sim 20\%$ ; nonetheless, such a small extent of stretching substantially improved the crystallinity and orientation. This further supported the previous discussion that the macromolecules in the as-electrospun nanofibers were loosely oriented along fiber axes. The crystallinity for each sample was also obtained as shown in the left panel of Fig. 3. It was evident that, with increasing the draw ratio,

the crystallinity also increased; while the crystallinity in the conventional SAF 3K microfiber bundle was similar to that in the as-electrospun nanofibers, despite its peak appeared much sharper.

Additionally, the azimuthal-scan profiles were acquired through integrating the diffraction intensities azimuthally at a fixed  $2\theta$  angle, and the results were shown in the right panel of Fig. 3. It was evident that the degree of crystalline orientation in the as-electrospun nanofibers was considerably lower than those in the stretched nanofibers and the conventional microfibers, as evidenced by the Herman's orientation function shown in the right panel of Fig. 3. As described in the Introduction section, the rapid elongation (drawing) of an electrospinning jet/filament occurs in solution or gel state. Although extended macromolecular chains are expected to exist during electrospinning (particularly during bending instability), these chains can relax afterwards, especially if the collected nanofibers still contain a trace amount of solvent(s) which would allow the relaxation of macromolecules. Therefore, most of macromolecules in the as-electrospun nanofibers were loosely oriented along the fiber axes and the crystallite size was small. After 2 times stretching of the as-electrospun nanofibers (e.g., from curves "A" to "B" in Fig. 3 with nanofiber diameters being reduced from  $\sim 300$  nm to  $\sim 239$  nm), the azimuthal peaks centered at the angles of  $90^\circ$  and  $270^\circ$  in the right panel of Fig. 3 became much sharper. As described above, the conventional SAF 3K microfibers used in this study have been effectively stretched for 8 times to the original length of their as-spun fibers. However, the sharpness of curve "E" was not higher than that of curve "B" in the left spectra of Fig. 3, while the Herman's orientation function of curve "E" (0.68) appeared to be much lower than that (0.87) of curve "B" in the right spectra of Fig. 3. This suggested that the crystallinity and orientation of the stretched nanofiber bundle with the final length being 2 times of original lengths were higher than

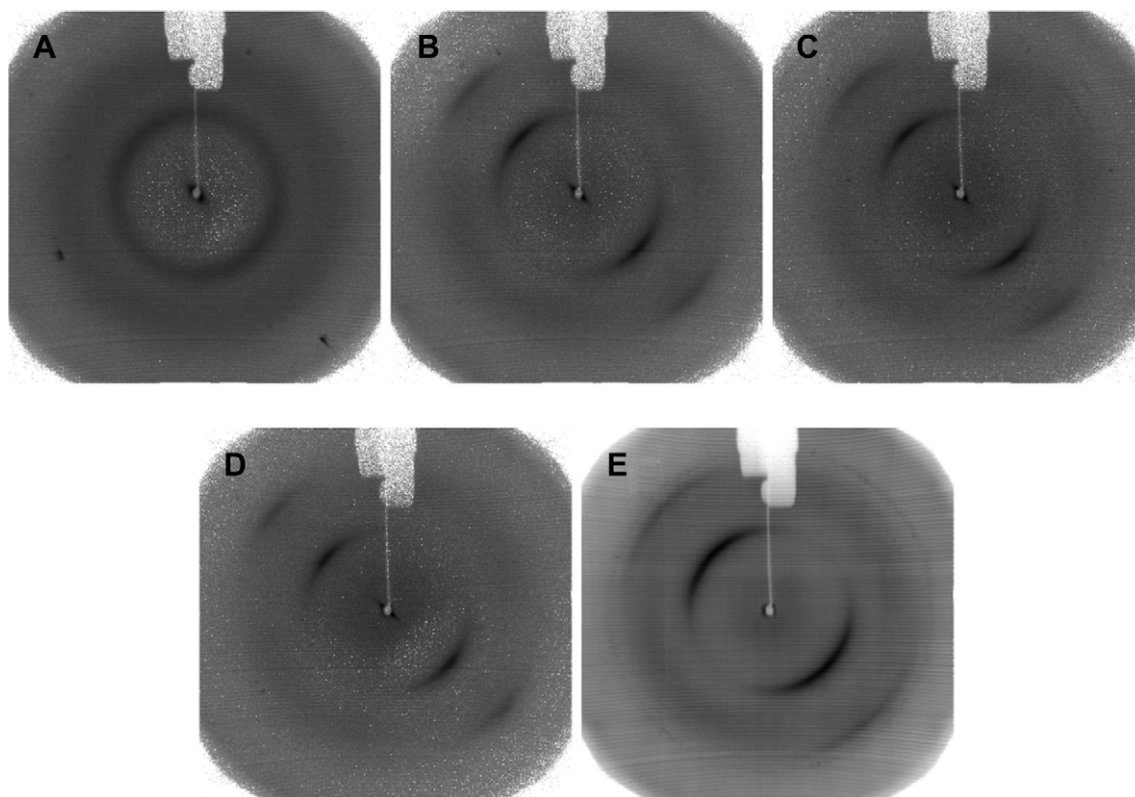


**Fig. 2.** 2D WAXD patterns for as-electrospun PAN copolymer nanofiber bundle (A), and the stretched nanofiber bundles with the final lengths being 2 (B), 3 (C), and 4 (D) times of original lengths of the bundles, as well as the conventional SAF 3K microfiber bundle (E).

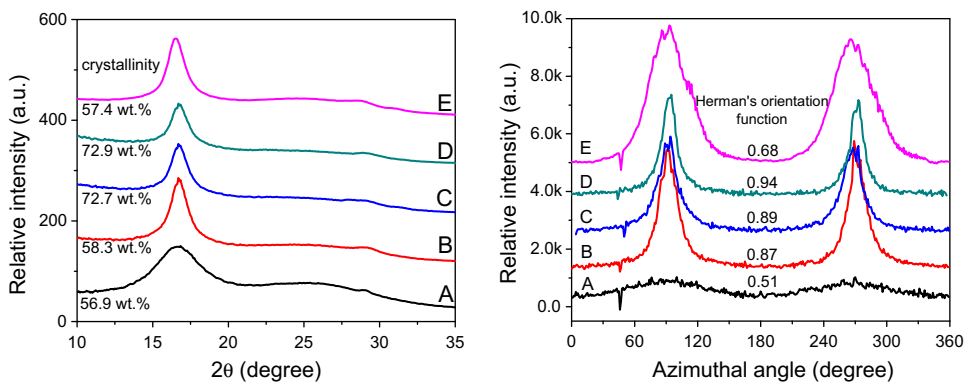


**Fig. 3.** 1D XRD curves (left) and azimuthal-scan profiles for the (100) reflections (right) of the as-electrospun PAN copolymer nanofiber bundle (A), and the stretched nanofiber bundles with the final lengths being 2 (B), 3 (C), and 4 (D) times of original lengths of the bundles, as well as the conventional SAF 3K microfiber bundle (E). The profiles were offset for clarity.

those of the conventional SAF 3K microfibers. Further stretching of the 2-time stretched bundle to 3 and 4 times of the original length improved the crystallinity to 72.7 and 72.9 wt.% and macromolecular orientation with the Herman's orientation function being 0.89 and 0.94, respectively.

### 3.3. Differential scanning calorimetry (DSC)

Thermo-chemical behaviors of the PAN copolymer in the as-electrospun nanofiber bundle and the stretched nanofiber bundles were characterized by DSC, and the results were shown in Fig. 4. The exothermic peaks for all types of nanofibers appeared around  $\sim 280$  °C, indicating the same thermo-chemical reaction occurred for the PAN copolymer in the as-electrospun nanofibers as well as in the stretched nanofibers. The previously reported research indicated that such a thermo-chemical reaction at 280 °C was likely associated with the intra-molecular cyclization of nitrile groups in the PAN macromolecules with extended (instead of helical) chain conformations [9]. Note that different from running the DSC in air, these experiments were conducted in nitrogen atmosphere. Therefore, the oxidative reaction seen at 310 °C disappeared [9]. Additionally, the exothermal peak increased from 528.8 to 557.7, 599.2, and 595.5 J/g for the as-electrospun nanofibers, the 2-, 3-, and 4-time stretched nanofibers, respectively; this once again supported the previous discussion that the macromolecules in the as-electrospun nanofibers were loosely aligned along the fiber axes, while a small extent of stretching could effectively improve the molecular orientation.

### 3.4. Fourier transform infrared spectroscopy (FT-IR)

An FT-IR equipped with a polarizer was employed to further examine the molecular orientation in the as-electrospun nanofiber bundle and the stretched nanofiber bundles. It was revealed that the characteristic nitrile absorption of PAN ( $\nu_{\text{C}\equiv\text{N}}$  at  $\sim 2250$   $\text{cm}^{-1}$ ) was sensitive to the polarization angle of incident beam (*i.e.*, the angle between the polarized infrared beam and the axes of the aligned nanofibers). Polarized FT-IR spectra of the as-electrospun nanofiber bundle and the stretched nanofiber bundles with the final lengths being 2, 3, and 4 times of the original lengths were shown in Fig. 5. From bottom to top in each sample, seven spectra were collected at the polarization angles of 0°, 30°, 60°, 90°, 120°, 150°, and 180°, respectively. With the increase of the angle from 0° (perpendicular to the direction of the bundles) to 90° (parallel to the direction of the bundles), the area and/or height of nitrile band gradually increased; while with further increasing the angle from

90° to 180°, the area and/or height of nitrile band gradually decreased. In contrast, the areas and/or heights of both the CJO band (from the itaconic acid component) centered at  $\sim 1725$   $\text{cm}^{-1}$  and the C-H band centered at  $\sim 1450$   $\text{cm}^{-1}$  appeared to be the same regardless of the polarization angle. The plots in Fig. 6 depicted the area or height ratios between the bands of  $\text{C}\equiv\text{N}$  ( $\sim 2250$   $\text{cm}^{-1}$ ) and  $\text{C}=\text{O}$  ( $\sim 1725$   $\text{cm}^{-1}$ ) or C-H ( $\sim 1450$   $\text{cm}^{-1}$ ) at varied polarization angles of infrared beam. It was evident that (1) both area and height ratios had the maximum value at the polarization angle of 90°, (2) the variation of ratios for the as-electrospun bundle was considerably less than the stretched nanofiber bundles, and (3) the variation of ratios for the 2-, 3-, and 4-time stretched nanofiber bundles were similar. This also supported the previous discussion that the macromolecules in the as-electrospun nanofibers were loosely aligned along the fiber axes, while a small extent of stretching could effectively improve the molecular orientation.

The following are the explanations on the dependence of nitrile band with respect to the polarization angle. At the angle of 0°, the axes of the aligned nanofibers are perpendicular to the direction of the electric field of the polarized incoming IR beam. Assuming the conformation of PAN macromolecules is zig-zag instead of helical, the nitrile groups would be perpendicular to the fiber axis (90° to the fiber axis). Thus, the absorption of incoming IR beam by the  $\text{C}\equiv\text{N}$  bonds is minimal at 0°. When the fiber axis is parallel to the incident beam at the polarization angle of 90°, the  $\text{C}\equiv\text{N}$  absorption reaches a maximal as a result of the resonance between the nitrile

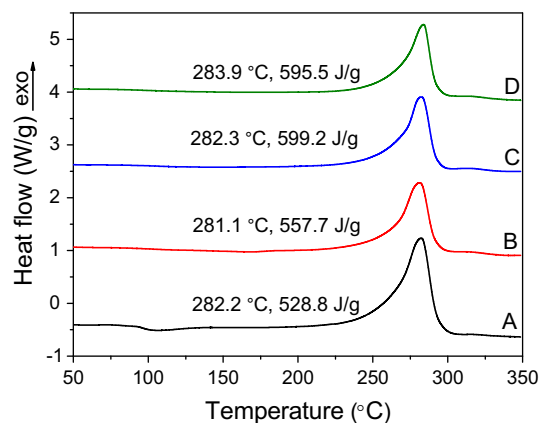


**Fig. 4.** DSC curves of the as-electrospun PAN copolymer nanofiber bundle (A), and the stretched nanofiber bundles with the final lengths being 2 (B), 3 (C), and 4 (D) times of original lengths of the bundles. The profiles were offset for clarity.

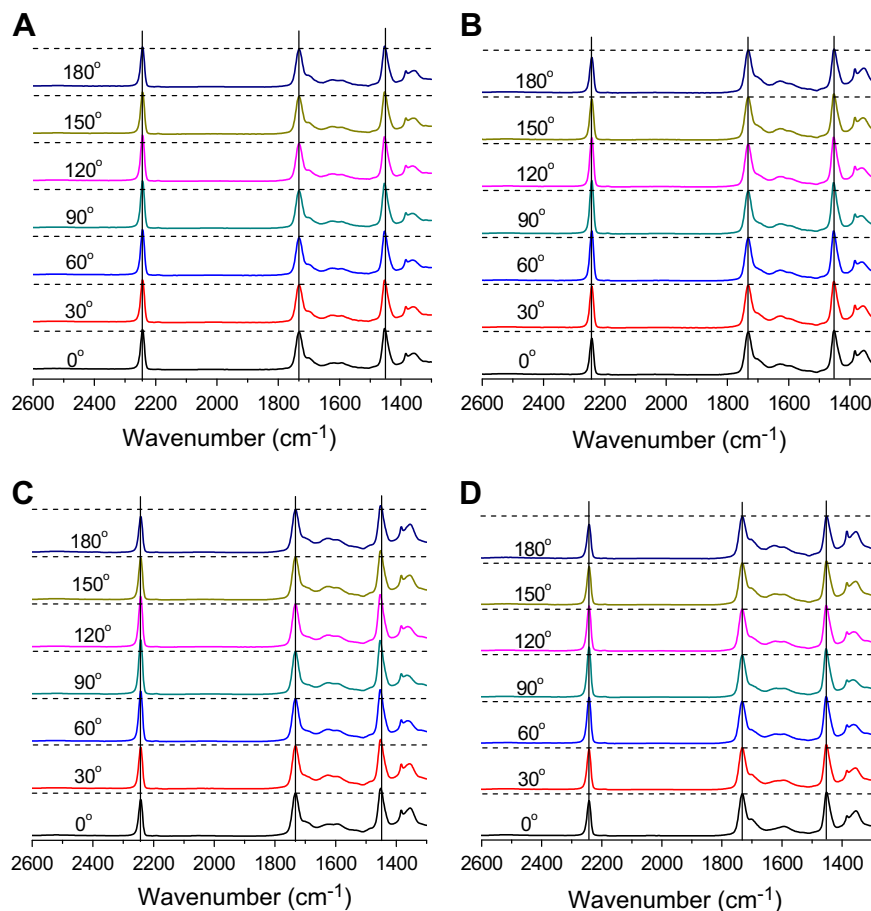


**Fig. 5.** Polarized FT-IR spectra of the as-electrospun PAN copolymer nanofiber bundle (A), and the stretched nanofiber bundles with the final lengths being 2 (B), 3 (C), and 4 (D) times of original lengths of the bundles. The spectra were offset for clarity.

stretching and the electric field of the polarized incoming IR beam [23]. On the other hand, the orientations of both C=O groups (in the itaconic acid component) at  $\sim 1725\text{ cm}^{-1}$  and C-H groups at  $\sim 1450\text{ cm}^{-1}$  are random in the nanofiber bundles; therefore, their absorptions would not be affected by the polarization angle [23].

It is noteworthy that both crystalline and amorphous PAN macromolecules contribute to the nitrile band in FT-IR spectrum; the substantial absorption change at different polarization angles suggested that a significant amount of amorphous PAN macromolecules might also adopt more or less parallel orientation along fiber axes due to rapid elongation rate followed by vitrification during (or shortly after) electrospinning. Furthermore, it is likely that most macromolecules in the electrospun nanofiber bundles (both as-electrospun and stretched) possess the zig-zag conformation (Fig. 7A) instead of the helical conformation (Fig. 7B [1,24]). This is also consistent with previous report that conventional PAN fibers contained zig-zag crystalline conformation with kink defects [25].

### 3.5. Mechanical properties

The tensile properties of nanofiber bundles were measured with a Diastron Limited FDAS 765 fiber analyzer that consisted of a high resolution tensile tester (LEX810) with a force resolution of  $50\text{ }\mu\text{N}$  and a Mitutoyo LSM-500 Laser Scan Micrometer with a positional repeatability of  $0.1\text{ }\mu\text{m}$ . The FDAS 765 laser micrometer automatically performed diameter (or cross-sectional area) measurements at several longitudinal points, recorded the elongation, and calculated various parameters related to tensile fracture. Prior to the testing,

the nanofiber bundles were carefully mounted on sample supports using specially designed plastic mounting tabs that were inserted into slotted rows on a plastic loading tray. The tray was spaced at the same distance as the sample length at  $10\text{ mm}$ . The inner edge of each tab contained a well for securing the nanofiber bundles with wax. The sample was attached in the inner well of one tab and stretched across the tray to the inner well of the second tab. Notches in the center of each well helped for aligning the nanofiber bundles during mounting as they were stretched between the two tabs.

A vital part of determining the tensile strength of a nanofiber bundle was to obtain the cross-sectional area of the bundle. The FDAS 765 laser micrometer secured the bundle in place for measurement of cross-sectional area using a mechanized holder. The holder rotated and moved horizontally so that measurements could be taken along the length of bundle as well as at different points around the circumference of bundle. Taking multiple data points produced a more accurate cross-sectional area than taking readings at a single point or angle since irregularities in shape such as bulges or asymmetrical cross-sections of a nanofiber bundle could be averaged out. Readings were taken along the length of bundle at points referred to as "slices." At each slice, the measurements of cross-sectional area were taken around the bundle as it was rotated at  $20$  azimuthal angles, incrementally to  $180^\circ$ . The cross-sectional areas for each angle of each slice were then averaged to give the mean cross-sectional area of the bundle. In this study, 10 slices were scanned for each nanofiber bundle with the length of  $\sim 10\text{ mm}$ . The minimum cross-sectional area among the 10 slices was used for the tensile calculation. A factor of fiber



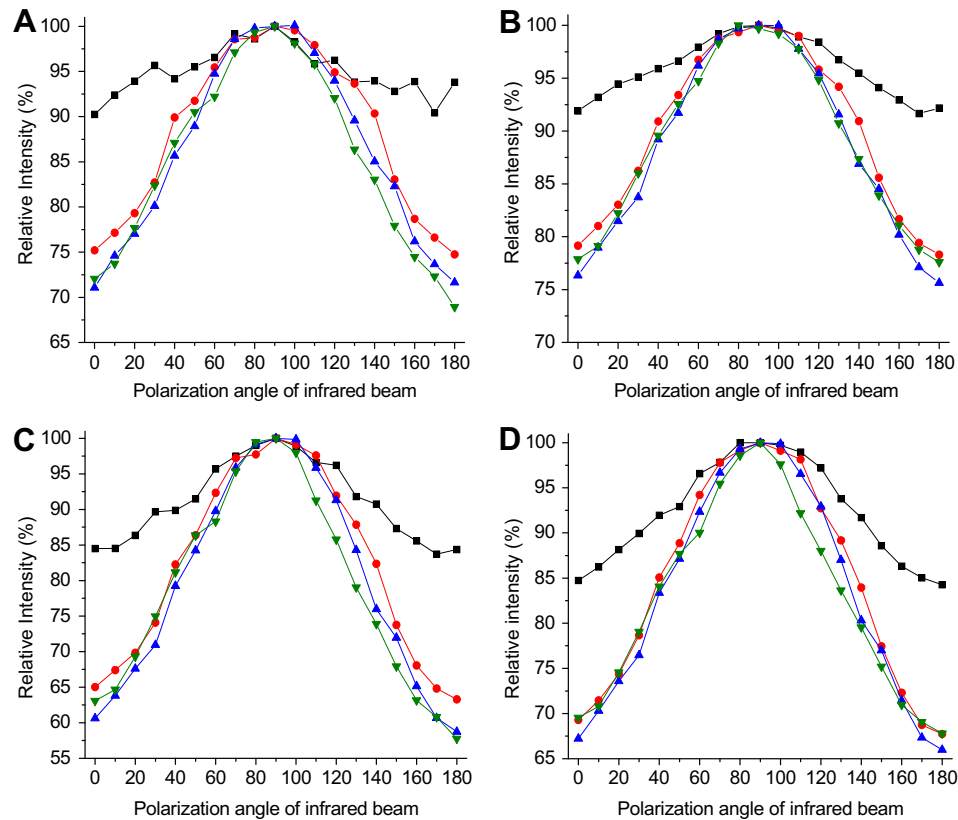


**Fig. 6.** (A) Area ratios and (B) height ratios between the bands of C≡N ( $\sim 2250\text{ cm}^{-1}$ ) and C=O ( $\sim 1725\text{ cm}^{-1}$ ), (C) area ratios and (D) height ratios between the bands of C≡N ( $\sim 2250\text{ cm}^{-1}$ ) and C-H ( $\sim 1450\text{ cm}^{-1}$ ), at varied polarization angle of infrared beam. (—■—: as-electrospun nanofiber bundle, —●—: 1-time stretched nanofiber bundle, —▲—: 2-time stretched nanofiber bundle, —▼—: 3-time stretched nanofiber bundle).

volume at 0.9069 (*i.e.*, the free space in the bundle was 0.0931) was used to calibrate the cross-sectional area assuming that the nanofibers in the bundle had the round shape and the same diameter, and the nanofibers were closely packed.

It is noteworthy that the LEX810 High Resolution Tensile Tester used a DC micrometer motor to extend the sample. A Sensotec semi-conductor strain gauge load cell measured the tension applied to the sample. It had a reported positional repeatability of 0.1  $\mu\text{m}$  and a range of 50 mm with the speed being 0.05 mm/min. For each sample tested, at least six specimens were prepared for the

measurement of cross-sectional area and tensile properties. Stress-strain curves were plotted for each sample, and the average tensile properties (strength, Young's modulus, and elongation at break) were calculated.

The tensile strengths and Young's moduli of the as-electrospun nanofiber bundle, as well as the 2-, 3-, and 4-time stretched nanofiber bundles were shown in Fig. 8. It was evident that the values of both tensile strength and Young's modulus were appreciably increased with the stretching of the nanofiber bundles. The tensile strength and Young's modulus for the as-electrospun nanofiber bundle (mean  $\pm$  standard deviation,  $n = 6$ ) were ( $15 \pm 11$ ) MPa and ( $275 \pm 140$ ) MPa, respectively. For the 4-time stretched bundle, the tensile strength and Young's modulus were increased to ( $65 \pm 26$ ) MPa and ( $1412 \pm 461$ ) MPa, respectively. Thus, the tensile strength was improved by 333%, and the Young's modulus was improved by 413%.

The representative stress-strain curves of nanofiber bundles were shown in Fig. 9. The curve of the as-electrospun bundle had several places of sudden decrease, indicating the breakage of nanofibers in the bundle; additionally, the elongation at break of the bundle was substantially larger than that of the stretched bundles. This was consistent with the SEM results, supporting the previous speculation that there might be segments/sections of nanofibers that were not well aligned in the as-electrospun bundle. It was important to note that the mechanical properties of the bundles could not be directly interpreted as those of individual nanofibers in the bundles. Generally speaking, mechanical properties of the nanofiber bundles were attributed to two factors including (1) the mechanical properties of individual nanofibers in the bundles, and (2) the alignment and morphological structure of

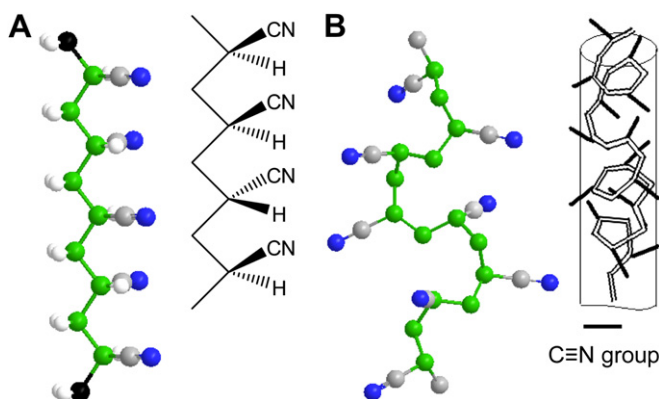


**Fig. 7.** Schematic representations showing (A) the zig-zag conformation of PAN macromolecules with the angle between C≡N groups and macromolecular axis being  $90^\circ$ , and (B) the helical conformation of PAN macromolecules with the angle between C≡N groups and macromolecular axis being  $\sim 30^\circ$  [24].

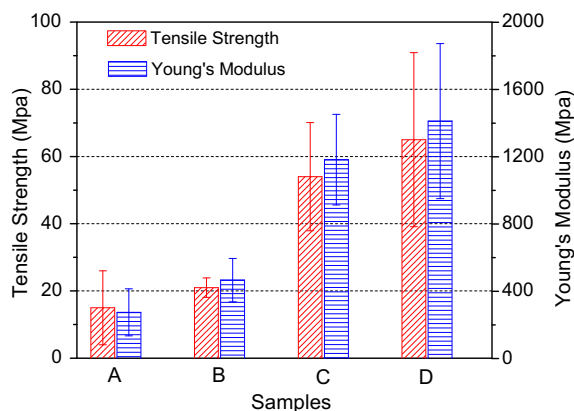


**Fig. 8.** Tensile strengths and Young's moduli of the as-electrospun PAN copolymer nanofiber bundle (A), and the stretched nanofiber bundles with the final lengths being 2 (B), 3 (C), and 4 (D) times of original lengths of the bundles. Each datum was the mean value of six measurements with error bar representing one standard deviation.

nanofibers in the bundles. Therefore, we believed that it was inappropriate to directly compare the mechanical properties of the nanofiber bundles with those of the conventional SAF 3K microfibers, which had the strength, modulus, and elongation at break of 664 MPa, 6.53 GPa, and 9.94%, respectively. In order to measure mechanical properties of individual nanofibers, the testing methods for measuring mechanical properties of carbon nanotubes might be appropriate. Nonetheless, to the best of our knowledge, this research effort represented the first successful attempt to stretch the electrospun nanofibers, despite the effectiveness of stretching and the precise measurement of individual nanofibers were upon further investigations.

### 3.6. Uniqueness and advantages

The crucial factors determining the mechanical strength of carbon fibers include the following properties and/or characteristics of precursor fibers: (1) the diameter, (2) the amount, size, and distribution of structural defects (including both surface and bulk defects), (3) the macromolecular orientation and crystalline structure, and (4) the morphological and structural homogeneity. The highly aligned and stretched electrospun PAN copolymer nanofibers can be an innovative type of precursors for the further development of continuous, nano-scaled, and extremely strong carbon fibers due to the following three reasons: (1) the diameters

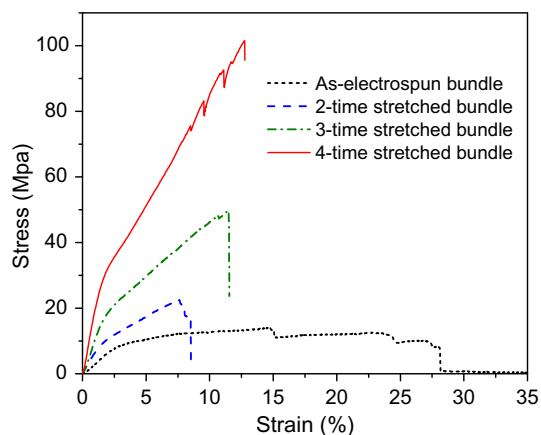


**Fig. 9.** The representative stress-strain curves of the as-electrospun nanofiber bundle, as well as the 2-, 3-, and 4-time stretched nanofiber bundles.

of the as-electrospun nanofibers are  $\sim 0.3 \mu\text{m}$ , whereas the diameters of as-spun (before stretching) conventional fibers are tens of microns. Fewer amounts of structural defects (such as sub-micron scaled voids/flaws) would be formed during the removal of solvent (s) from much smaller diameter electrospinning jets than that from much larger diameter conventional spinning filaments. Furthermore, solvents are removed through evaporation in electrospinning, whereas they are removed through coagulation in the conventional spinning methods (including both wet spinning and air-gap spinning). Compared to coagulation, evaporation results in much fewer structural defects. (2) Before stretching, the conventional fibers have almost no preferred macromolecular orientation; whereas in the as-electrospun nanofibers, the macromolecular chains are oriented due to the huge elongation (draw) rate involved in the electrospinning process, particularly during bending instability. Therefore, after undergoing the post-spinning stretching process, the stretched electrospun nanofibers can possess a higher degree of macromolecular orientation than their conventional counterparts. (3) The stretched electrospun PAN copolymer nanofibers have diameters of  $\sim 100 \text{ nm}$ , while their conventional counterparts have diameters of  $\sim 10 \mu\text{m}$ . The nanofibers are two orders of magnitude thinner, and are much less likely to form structural inhomogeneity (particularly sheath-core structures) during the thermal treatments of stabilization and carbonization.

Since the diameters of as-electrospun PAN copolymer nanofibers are  $\sim 0.3 \mu\text{m}$ , after these nanofibers undergo stretching (which reduces the fiber diameter) as well as stabilization and carbonization (which further reduce the fiber diameter by  $\sim 1.5$  times, based on the fact that the carbon yield of PAN copolymer precursors is typically 50–60 wt.% [1]), the resulting nano-scaled carbon fibers could have diameters in tens of nanometers, which are in the same order of magnitude as diameters of multi-wall carbon nanotubes. But unlike carbon nanotubes, which are produced by bottom-up methods, the nano-scaled carbon fibers are produced through a top-down nano-manufacturing process, which results in low-cost, and more importantly, continuous nanofibers that do not require further expensive purification; and they are also easy to align, assemble, and process into applications.

## 4. Summary

In this study, uniform PAN copolymer nanofibers with diameters of  $\sim 300 \text{ nm}$  were prepared by the electrospinning technique; and the nanofibers were collected as highly aligned bundles using a U-shaped metal device. The electrospun nanofibers contained no microscopically identifiable beads and/or beaded-nanofibers, and the surface of the nanofibers appeared to be smooth. The as-electrospun nanofiber bundles were then stretched in an oven at  $\sim 100 \text{ }^\circ\text{C}$ , and a pan of boiling water was maintained during the stretching process; the stretched nanofiber bundles with final lengths being 2, 3, and 4 times of original lengths of the bundles were acquired. Subsequently, characterizations and evaluations were carried out to understand the morphological, structural, and mechanical properties of the nanofibers before and after the post-spinning stretching using SEM, 2D WAXD, polarized FT-IR, DSC, and mechanical tester; and the results were compared to those of the conventional SAF 3K microfibers that were used as the starting materials for making electrospun nanofibers. The study revealed that: (1) the macromolecules in the as-electrospun nanofibers were loosely oriented along fiber axes; although such an orientation was not high, a small extent of stretching could effectively improve the macromolecular orientation and probably increase the crystallinity; (2) it was likely that most macromolecules in crystalline phase of both as-electrospun and stretched electrospun nanofiber bundles possessed the zig-zag conformation instead of the helical

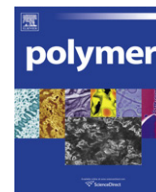
conformation; and (3) the post-spinning stretching process could substantially improve the mechanical properties of the nanofiber bundles. To the best of our knowledge, this research effort represented the first successful attempt to stretch the electrospun nanofibers, despite the effectiveness of stretching and the precise measurement of individual nanofibers were upon further investigations. We envisioned that the highly aligned and stretched electrospun PAN nanofibers could be an innovative type of precursor for the development of continuous nano-scale carbon fibers with superior mechanical strength.

### Acknowledgements

JL thanks the supports from the National Natural Science Foundation of China (Grant No.: 51073011 and 50673011), the National High Technology Research and Development Program of China (“863 Program”, Grant No.: 2006AA06Z382), and the National Basic Research Program of China (“973 Program”, Grant No.: 2006CB605304). HF thanks the supports from the National Aeronautics and Space Administration of the United States (Grant No.: NNX07AT52A), the Department of Energy in the United States (Grant No.: DE-FG02-08ER64624), and the National Science Foundation of the United States (Grant No. CBET-0827844).

### References

- [1] Morgan PE. Carbon fibers and their composites. Boca Raton, FL: CRC Press; 2005. pp. 185–267.
- [2] Donnet JB, Wang TK, Peng JC, Rebouillat S. Carbon fibers. New York, NY: Marcel Dekker; 1998. pp. 231–309.
- [3] Johnson JW, Thorne DJ. Effect of internal polymer flaws on strength of carbon fibers prepared from an acrylic precursor. *Carbon* 1969;7(6):659–60.
- [4] Watt W. Production and properties of high modulus carbon fibers. *Proceedings of the Royal Society of London, Series A, Mathematical and Physical Sciences* 1970;319(1536):5–15.
- [5] Thorne DJ. Carbon-fibers with large breaking strain. *Nature* 1974;248(5451):754–6.
- [6] Moreton R, Watt W. Spinning of polyacrylonitrile fibers in clean room conditions for production of carbon fibers. *Carbon* 1974;12(5):543–54.
- [7] Zhang W, Liu J, Wu G. Evolution of structure and properties of PAN precursors during their conversion to carbon fibers. *Carbon* 2003;41(14):2805–12.
- [8] Liu J, Yue Z, Fong H. Continuous nano-scaled carbon fibers with superior mechanical strength. *Small* 2009;5(5):536–42.
- [9] Liu J, Zhou P, Zhang L, Ma Z, Liang J, Fong H. Thermo-chemical reactions occurring during the oxidative stabilization of electrospun polyacrylonitrile precursor nanofibers and the resulting structural conversions. *Carbon* 2009;47(4):1087–95.
- [10] Fitzer E, Müller DJ. The influence of oxygen on the chemical reactions during stabilization of PAN as carbon fiber precursor. *Carbon* 1975;13(1):63–9.
- [11] Warner SB, Peebles LH, Uhlmann DR. Oxidative stabilization of acrylic fibers. *Journal of Materials Science* 1979;14(3):565–72.
- [12] Jain MK, Balasubramanian M, Desai P, Abhiraman AS. Conversion of acrylonitrile-based precursor fibers to carbon fibers, Part 2 Precursor morphology and thermooxidative stabilization. *Journal of Materials Science* 1987;22(1):301–12.
- [13] Fitzer E. PAN-based carbon fibers – present state and trend of the technology from the viewpoint of possibilities and limits to influence and to control the fiber properties by the process parameters. *Carbon* 1989;27(5):621–45.
- [14] Reneker DH, Chun I. Nanometer diameter fibers of polymer, produced by electrospinning. *Nanotechnology* 1996;7(3):216–23.
- [15] Dzenis Y. Spinning continuous fibers for nanotechnology. *Science* 2004;304(5679):1917–9.
- [16] Fong H. Electrospun polymer, ceramic, carbon/graphite nanofibers and their applications. In: Nalwa HS, editor. *Polymeric nanostructures and their applications*, vol. 2. Stevenson Ranch, CA: American Scientific Publishers; 2007. p. 451–74.
- [17] Greiner A, Wendorff JH. A fascinating method for the preparation of ultrathin fibers. *Angewandte Chemie International Edition* 2007;46(30):5670–703.
- [18] Reneker DH, Yarin AL, Fong H, Koombhongse S. Bending instability of electrically charged liquid jets of polymer solutions in electrospinning. *Journal of Applied Physics* 2000;87(9):4531–47.
- [19] Liu Y, Cui L, Guan F, Gao Y, Hedin NE, Zhu L, et al. Crystalline morphology and polymorphic phase transitions in electrospun nylon-6 nanofibers. *Macromolecules* 2007;40(17):6283–90.
- [20] Fong H, Chun I, Reneker DH. Beaded nanofibers formed during electrospinning. *Polymer* 1999;40(16):4585–92.
- [21] Mittal J, Bahl OP, Mathur RB. Single step carbonization and graphitization of highly stabilized PAN fibers. *Carbon* 1997;35(8):1196–7.
- [22] Iwashita N, Park CR, Fujimoto H, Shiraishi M, Inagaki M. Specification for a standard procedure of X-ray diffraction measurements on carbon materials. *Carbon* 2004;42(4):701–14.
- [23] Liang CY, Krimm S. Infrared spectra of high polymers. VII. Polyacrylonitrile. *Journal of Polymer Science* 1958;31(123):513–22.
- [24] Henrici-Olive G, Olive S. Molecular interactions and macroscopic properties of polyacrylonitrile and model substances. *Advances in Polymer Science* 1979;32:123–52.
- [25] Liu XD, Ruland W. X-ray studies on the structures of polyacrylonitrile fibers. *Macromolecules* 1993;26:3030–6.



## Biaxial elastic–viscoplastic behavior of Nafion membranes

Meredith N. Silberstein, Priam V. Pillai, Mary C. Boyce\*

MIT Department of Mechanical Engineering, 77 Massachusetts Avenue, Cambridge, MA 02139, USA

### ARTICLE INFO

#### Article history:

Received 28 September 2010

Received in revised form

16 November 2010

Accepted 20 November 2010

Available online 3 December 2010

#### Keywords:

Polymer mechanics

Nafion

Biaxial

### ABSTRACT

Durability is a major limitation of current proton exchange membrane fuel cells. Mechanical stress due to hygro-thermal cycling is one failure mechanism of the polymer electrolyte membrane (PEM). In a fuel cell the PEM is highly constrained in the membrane plane and relatively unconstrained in the through-thickness direction, leading to primarily biaxial loading upon hygro-thermal cycling. The rate, temperature, and hydration dependent elastic–viscoplastic mechanical behavior of Nafion, the benchmark PEM, has been extensively investigated in uniaxial tension in prior work which also served as a data basis for a three dimensional constitutive model. Here, the important effects of the biaxiality of the loading conditions on the elastic–viscoplastic Nafion stress–strain behavior are investigated for the first time via experiments and simulation. Biaxial stress–strain behaviors were shown to exhibit similar features to uniaxial behavior including linear elasticity followed by a highly non-linear transition to yield followed by post-yield strain hardening with highly non-linear unloading and reloading; these features were each quantitatively dependent on the biaxiality of the loading conditions. The constitutive model was found to successfully quantitatively predict the loading behavior and its dependence on biaxiality. The constitutive model was also found to predict the magnitude of the yield shoulder during unloading and reloading, but to underestimate the gradual nature of both the forward and reverse plastic deformation processes as well as the strain recovery at zero load. These errors are consistent with those seen in the uniaxial model indicating that the framework used to incorporate the uniaxial behavior into a three dimensional model is capable of predicting the biaxial deformation response of the membrane.

© 2010 Elsevier Ltd. All rights reserved.

### 1. Background

The proton exchange membrane fuel cell (PEMFC) is a promising clean technology for converting chemical energy into electrical energy, particularly for transportation. Insufficient durability is one of the major factors inhibiting the widespread distribution of this technology. In particular, the membrane electrode assembly (MEA), which consists of a selectively permeable polymer electrolyte membrane (PEM) with a catalyst layer and porous carbon electrode support on each side, is known to fail under the cyclic operating conditions of automobiles. The PEM is responsible for conducting protons while preventing hydrogen and oxygen gas crossover. Until recently, durability research has focused on preventing degradation due to chemical attacks, however, with progress against chemical attacks focus has shifted to the increasingly significant mechanical degradation modes [1]. Cyclic mechanical loading results from water content driven swelling and deswelling of the membrane within the partially constrained environment of the fuel cell. Since

the membrane in a fuel cell is highly constrained in the membrane plane and relatively unconstrained in the through-thickness direction, this cyclic loading will be primarily biaxial in nature. Biaxial loading also has relevance for polymeric membranes more generally given their increasing use in separation and transport applications.

In our prior work [2], the uniaxial tensile behavior of Nafion was characterized under both monotonic and cyclic loading as a function of rate, temperature, and hydration. This data provided the foundation for the development of a constitutive model to describe the hygro-thermal elastic–viscoplastic stress–strain behavior of Nafion. The model was shown to capture the stress–strain behavior of Nafion over a wide range of uniaxial loadings histories. Here we assess the biaxial behavior of Nafion experimentally under different biaxiality ratios and then use the data to further validate the aforementioned constitutive model. Previous biaxial testing on Nafion has been reported for pressure loaded blister cells [3,4] which create an equibiaxial tensile stress at the center of the specimen, aimed at determining the stress at which gas leaks occur across the membrane. Biaxial testing has been conducted on a variety of other polymers such as poly(ethylene terephthalate) [5–8], polypropylene [9,10], polystyrene [11], polyethylene [12],

\* Corresponding author.

E-mail addresses: [meri.silberstein@gmail.com](mailto:meri.silberstein@gmail.com) (M.N. Silberstein), [mboyce@mit.edu](mailto:mboyce@mit.edu) (M.C. Boyce).

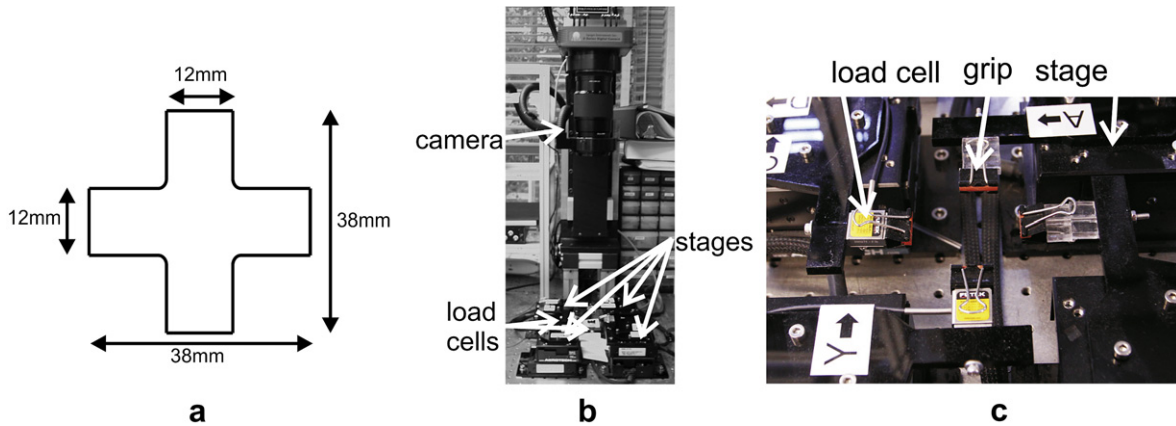


Fig. 1. Experimental setup for biaxial tensile tests (a) specimen shape (b) thin film multi-axial tensile machine (c) close up of stages from thin film multi-axial tensile machine.

and polyamide [12] for which biaxial draw is an important part of the manufacturing process. Most of these biaxial characterizations were conducted via in-plane extension devices which consist of many grips along each edge of a square specimen that can move independently in the two principal directions. With appropriate slitting or specimen design this can provide a close to homogeneous deformation with control over the degree of imposed biaxiality. In characterizing the biaxial behavior of metals, it is typical to use cruciform specimens with a single grip on each edge (i.e. Refs. [13–15]). The thickness in the central region of the specimen is reduced to ensure that the deformation is localized and slits are introduced in the legs for stress relief. In this paper, the cruciform configuration is used with a single grip on each edge of a uniform thickness specimen. This in-plane biaxial method also allows the desired control of the degree of biaxiality. The thickness reduction and slitting is not practical for the thin Nafion membrane ( $t = 27 \mu\text{m}$ ), consequently the homogeneity of the resulting stress field will be discussed in depth in the results section.

## 2. Experimental methods

### 2.1. Materials

Commercially available dispersion cast NRE211 films (thickness  $t = 27 \mu\text{m}$ , Dupont, Ion Power Inc) and NRE212 films (thickness  $t = 54 \mu\text{m}$ , Dupont, Ion Power Inc) were used for the experimental characterization of Nafion. NRE211 and NRE212 are identical in chemical composition and processing, differing only in thickness. The films were stored in a desiccator cabinet upon removal from the initial packaging to minimize variability in data from aging and humidity effects.

### 2.2. Uniaxial tension

Uniaxial tension tests were conducted on Nafion NRE212 under monotonic, cyclic, stress relaxation, and creep histories, at constant engineering strain rates from  $0.001 \text{ s}^{-1}$  to  $0.1 \text{ s}^{-1}$ , at temperatures from  $25 \text{ }^\circ\text{C}$  to  $100 \text{ }^\circ\text{C}$ , and at various water contents. The uniaxial results are presented in terms of time, true strain, and true stress as applicable. For full information on the uniaxial testing procedure and data reduction see Silberstein and Boyce [2].

### 2.3. Biaxial tension

Biaxial tests were performed on Nafion NRE211 laser cut into the cruciform shape shown in Fig. 1a. This particular cruciform geometry

is chosen as a compromise between achieving a uniform stress field at the center of the specimen and reaching a reasonably large strain within the range of motion of the experimental setup. Biaxial tests were conducted on the thin film multi-axial tensile machine developed in the Bio-instrumentation lab at MIT (Fig. 1b) modified from the design of A. Herrmann in his master's thesis [16]. The film was gripped by rubber padded spring loaded clips. Each grip is mounted to an Aerotech ATS125 leadscrew-actuated stage and all actuators are moved such that the membrane center remains in place. For all tests the grips are initially 29 mm apart. Two of the grips are mounted to FUTEK LSB200 force sensors. The force and stage location are recorded at 1 s intervals. The deformation is monitored by an Apogee Alta U10 camera. A frame is recorded roughly every 10 s as limited by the capabilities of the acquisition system. The stage motion and data acquisition is controlled by a custom LabView code. The image frames are post-processed using the Vic2D strain analysis software to find local displacement values. The force-displacement and processed videos are then converted to the engineering stress components  $\bar{\sigma}_{11}$  and  $\bar{\sigma}_{22}$  using the initial cross-sectional area of the edge of the central square region ( $12 \text{ mm} \times 27 \mu\text{m}$ ) and engineering strain values  $\bar{\epsilon}_{11}$  and  $\bar{\epsilon}_{22}$  in the biaxial region based on the markers near the edge of the region.

Monotonic experiments consist of grip displacement at a constant rate until reaching a preset displacement value. Cyclic experiments consist of grip displacement at a constant rate until reaching a preset displacement value, followed by grip displacement at the same constant rate in the opposite direction until the grips

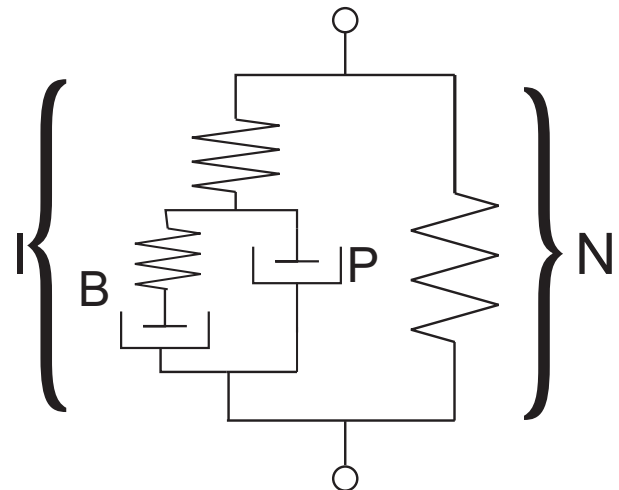
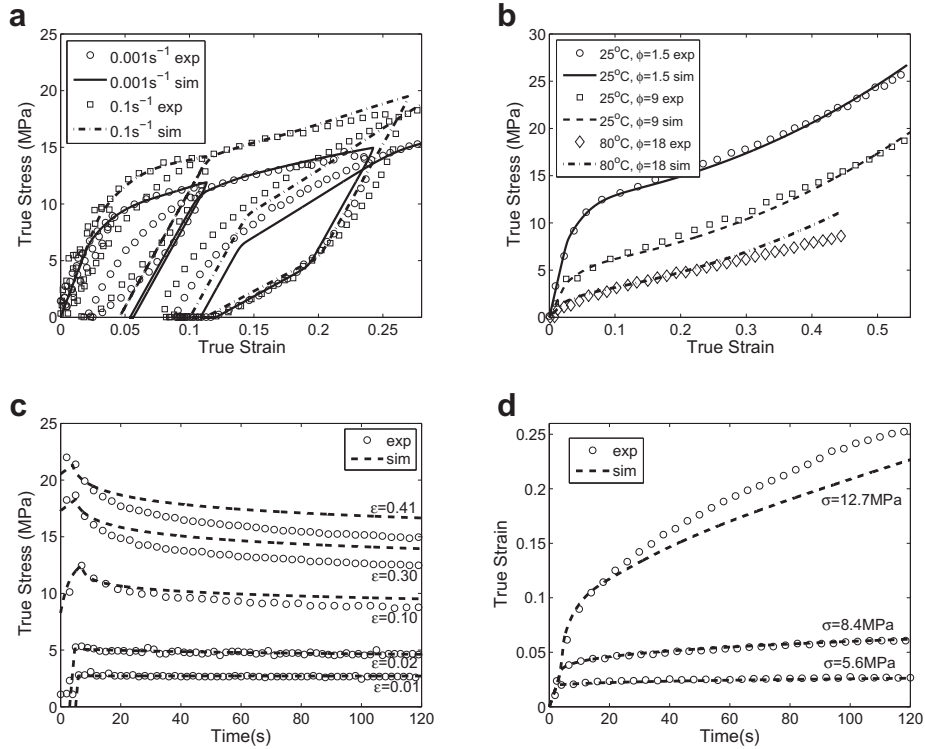


Fig. 2. Rheological depiction of Nafion constitutive model.



**Fig. 3.** Comparison of constitutive model predictions with experimental data for uniaxial tensile loading (a) cyclic rate dependence at ambient conditions ( $\phi = 1.5$ ) (b) temperature and hydration dependence at  $0.01 \text{ s}^{-1}$  (c) stress relaxation at ambient conditions ( $\phi = 1.5$ ) (d) creep at ambient conditions ( $\phi = 1.5$ ).

return to their original location; this process is then repeated. It is typical for the specimens to buckle during the unloading process resulting in a near zero force. During this period the video extensometer continues to track the strain, however, due to the three dimensional nature of the deformation it does not indicate a local material strain.

**3. Constitutive model review**

In prior work of the authors a three dimensional constitutive model for Nafion was developed and implemented as a user

material subroutine in the finite element program Abaqus [2]. Monotonic and cyclic uniaxial tension experiments over a range in strain rates and environmental conditions were used to fit and validate the model. This model and the experimentally observed uniaxial behavior will be briefly reviewed here to facilitate understanding of the results.

The elastic–viscoplastic constitutive model is depicted rheologically in Fig. 2, it consists of an intermolecular deformation mechanism (Mechanism I) acting in parallel with a molecular network alignment mechanism (Mechanism N). A summary of the model formulation is provided in the Appendix. The intermolecular

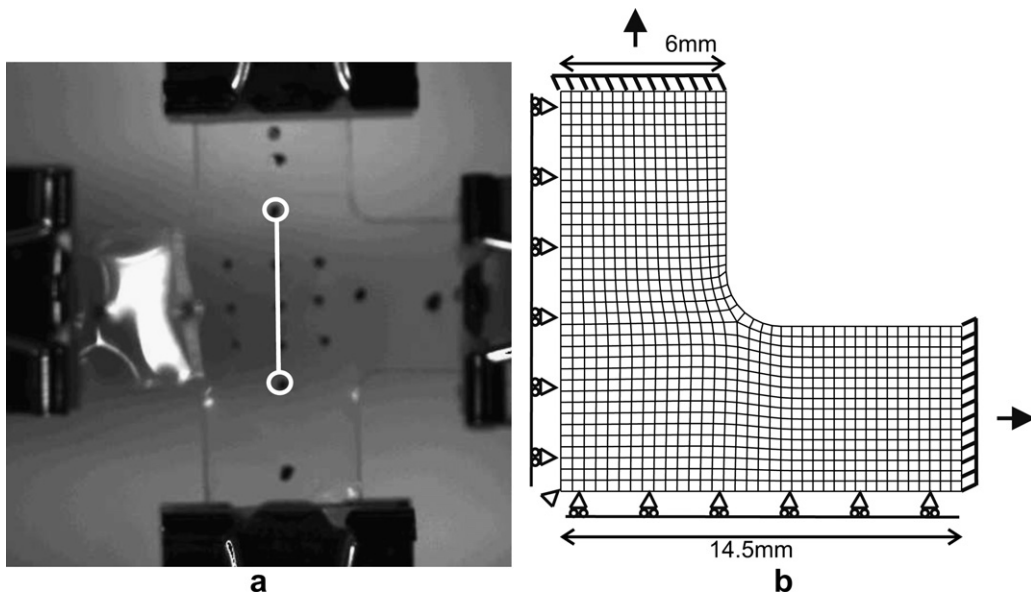


**Fig. 4.** (a) Specimen with line indicating location of points used for local strain measure of biaxial experiments. (b) Geometry and boundary constraints of biaxial simulation.

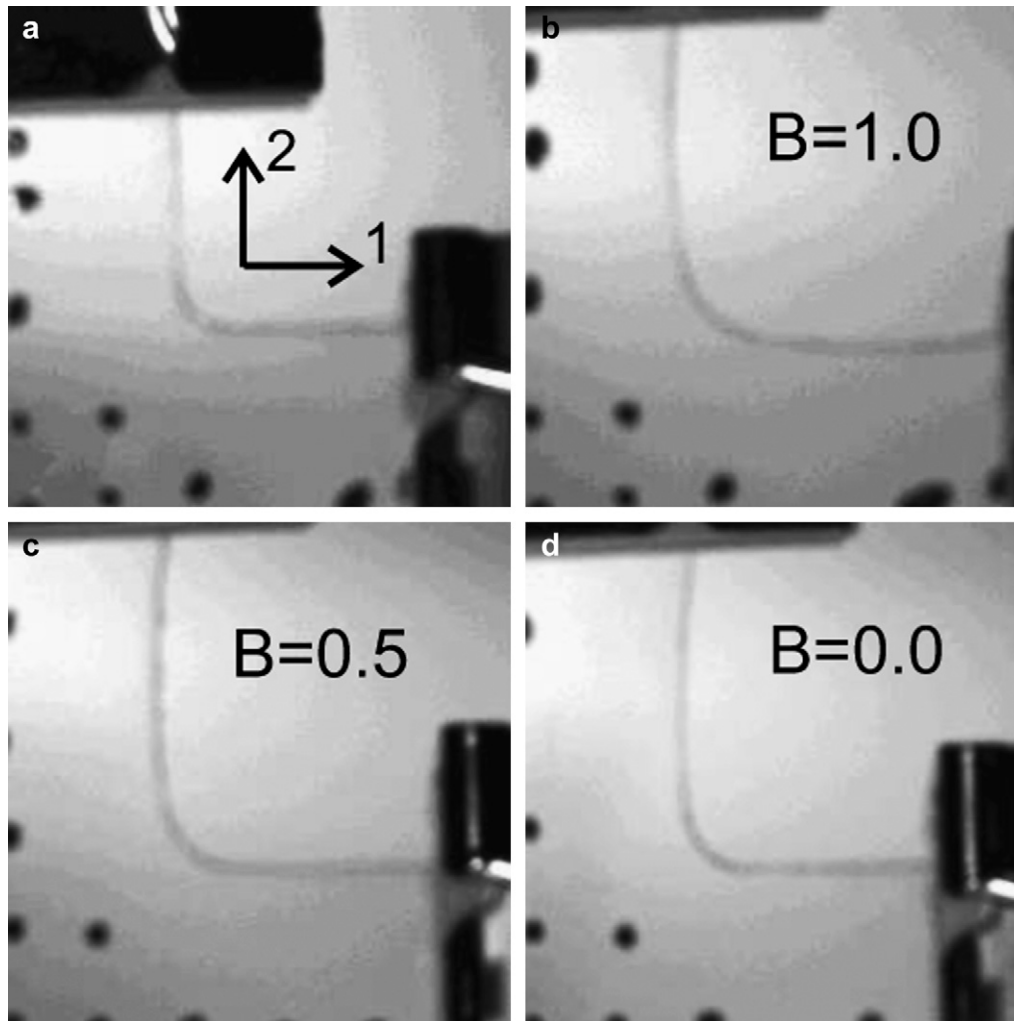


**Fig. 5.** Images of top right quarter of experimental biaxial specimens (a) typical specimen prior to deformation ( $\bar{\epsilon}_{22} = 0$ ) (b)  $B = 1.0$  specimen at 2-direction grip displacement = 2.5 mm ( $\bar{\epsilon}_{22} = 0.05$ ) (c)  $B = 0.5$  specimen at 2-direction grip displacement = 2.5 mm ( $\bar{\epsilon}_{22} = 0.06$ ) (d)  $B = 0.0$  specimen at 2-direction grip displacement = 2.5 mm ( $\bar{\epsilon}_{22} = 0.08$ ).

mechanism, rheologically depicted as an elastic spring in series with a viscoplastic dashpot (P), represents the resistance to deformation due to the intermolecular interactions where the spring captures the stiffness of these interactions and the non-linear dashpot captures the yielding of these interactions. The intermolecular mechanism has a back stress (B) on the viscoplastic element which develops during loading to assist inelastic recovery. This back stress captures the inherent inhomogeneity of the local inelastic processes in polymers where a back stress builds around locally sheared domains; the existence of such stored energy which drives recovery has been experimentally found in calorimetry measurements (e.g. Refs. [17,18]) and modeled as a back stress in Ref. [19] and also more recently in Ref. [20]. The network mechanism is a non-linear spring which captures the resistance due to the stretching and orientation of the molecular network. The intermolecular resistance is strongly dependent on temperature and hydration, decreasing significantly when the polymer goes from the glassy state into the glass–rubber transition regime ( $\sim 60^\circ\text{C}–120^\circ\text{C}$ ). Hydration in the model is quantified as moles of water per mole of sulfonic acid group as is the custom in the Nafion literature (i.e. Ref. [21]). This quantity is given the symbol  $\varphi$  and varies from  $\sim 1.5$  at  $25^\circ\text{C}$ , 30% relative humidity to  $\sim 22$  at  $90^\circ\text{C}$  and soaked in water. The model is presented in detail in Silberstein and Boyce [2].

A summary of results from this model compared with uniaxial tensile experimental data is shown in Fig. 3. The model is able to capture the linear-elastic response, the rate dependent distributed yield event, and the non-linear strain hardening under monotonic and cyclic tensile loading. Additionally it is able to capture the non-linear unloading and reloading observed to be characteristic of cyclic loading both as a function of strain and as a function of strain rate. The linear superposition of the effects of temperature and water content is seen to work well. The evolution of stress relaxation and creep through yield are also well predicted by the model.

#### 4. Biaxial experiments: results and discussion

Cruciform specimens were subjected to three different biaxial loading conditions where the biaxiality ratio is described as the ratio of the stretching rates in the 1- and 2-directions ( $B = \dot{\lambda}_1/\dot{\lambda}_2$ ).  $B = 1.0$  corresponds to grips in both directions displaced at the same rate ( $14\ \mu\text{m s}^{-1}$ ),  $B = 0.5$  corresponds to the 1-direction grips displaced at one-half the rate ( $7\ \mu\text{m s}^{-1}$ ) as the 2-direction grips ( $14\ \mu\text{m s}^{-1}$ ), and  $B = 0.0$  corresponds to the 1-direction grips held fixed while the 2-direction grips are displaced ( $14\ \mu\text{m s}^{-1}$ ). The biaxial stress–strain response is determined from the strain in the central biaxial region calculated using the video extensometer points in the central square region of the specimen as indicated in

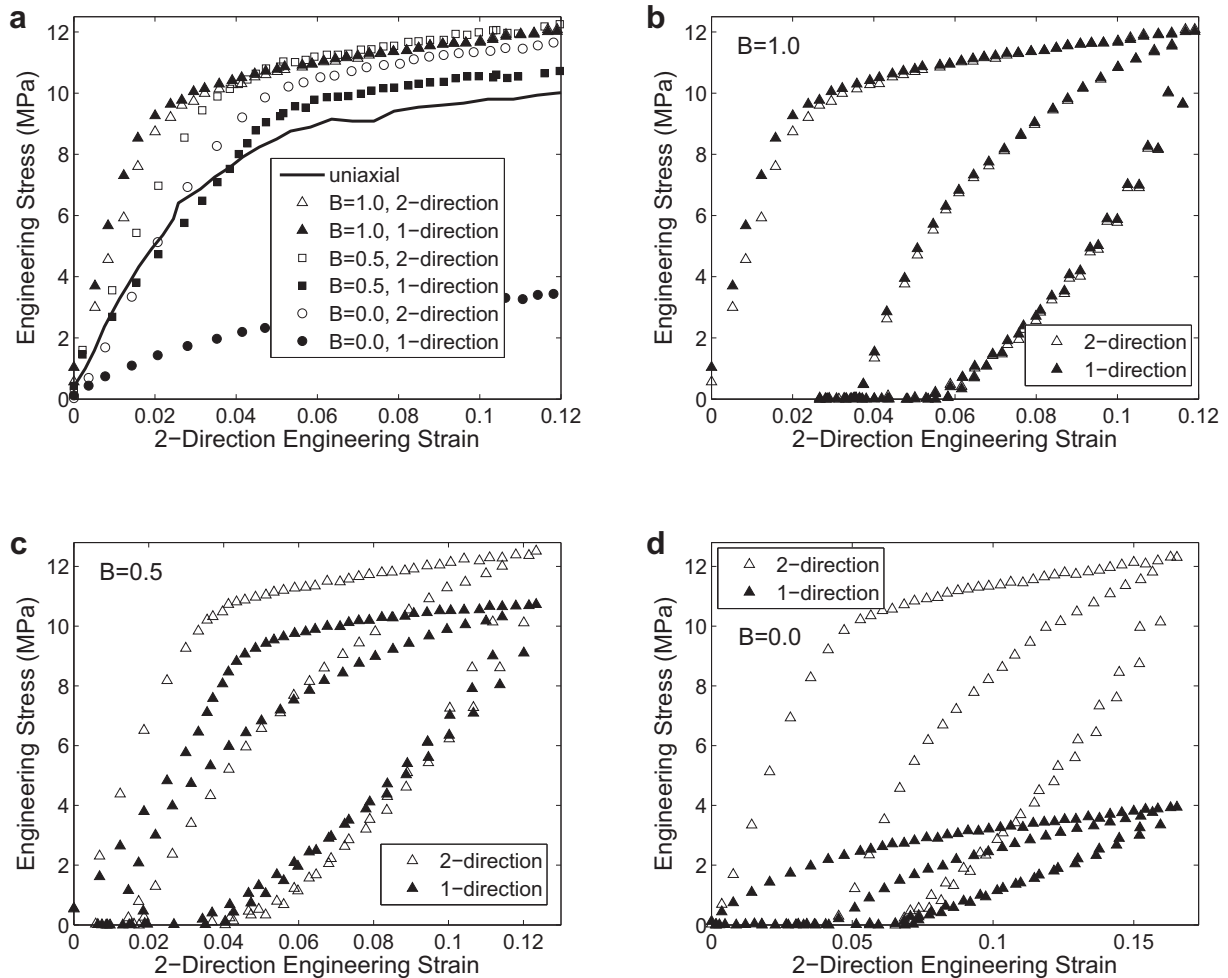


**Fig. 6.** Biaxial experimental data ( $\varphi = 2$ ) (a) comparison of different degrees of biaxiality under monotonic loading (uniaxial data at  $\varphi = 1.5$ ) (b) cyclic loading with 1- and 2-direction grips displaced at  $14 \mu\text{m s}^{-1}$  ( $B = 1.0$ ) (c) cyclic loading with 2-direction grips displaced at  $14 \mu\text{m s}^{-1}$  and 1-direction grips displaced at  $7 \mu\text{m s}^{-1}$  ( $B = 0.5$ ) (d) cyclic loading with 2-direction grips displaced at  $14 \mu\text{m s}^{-1}$  and 1-direction grips held fixed ( $B = 0.0$ ).

**Fig. 4a.** The stress–strain behavior will be reported in terms of engineering stress versus engineering strain.

Images of the deformed specimen for all three cases are shown in **Fig. 5**; only the top right quarter is displayed in order to better correlate with the simulation images which will be shown subsequently. The character of the deformed shapes is most prominent in the legs of the cruciform since that is where the strain is largest. There is a distinct concave curvature between the grip and the central region in the 2-direction leg for all three cases and in the 1-direction leg for  $B = 1.0$ ; this curvature is clearly absent in the 1-direction leg for  $B = 0.0$ .

**Fig. 6a** shows the monotonic biaxial engineering stress–strain response of all three cases compared to the uniaxial tensile behavior. In all cases the stress–strain behavior exhibits an elastic–plastic response with features similar to the uniaxial behavior. The biaxial effect on the stress–strain response is apparent. For the case of equibiaxial ( $B = 1.0$ ) loading, the initial elastic stiffness is greater than the uniaxial stiffness, as expected (recall, the biaxial modulus is  $E/(1 - \nu)$  compared to the uniaxial modulus  $E$ ). The yield stress level required for biaxial yielding is also greater than for uniaxial yielding which is unexpected; the biaxial stress components at yield for equibiaxial tension would be expected to be equal to the uniaxial yield following a Mises or Tresca yield criterion (they would be expected to be lower if there were a pressure dependence). The unexpected disparity in yield stress between the uniaxial and

equibiaxial experiments is a result of: (1) the inhomogeneous stress distribution in the central region of the cruciform which produces a sharper yield transition in the reduced data; and (2) the rollover nature of the yield event which occurs more rapidly with biaxial loading as compared to uniaxial loading. Thus even though yield is technically initiating at the same value for equibiaxial as for uniaxial loading, this very initial yielding cannot be observed directly by this experiment. The specimen geometry effect will be discussed further in Section 5. There is also a minor strain rate effect since the effective rate driving yield is larger for the equibiaxial case than the uniaxial case, but this is negligible in comparison to the effects of either geometry or rollover yield evolution.

The  $B = 0.5$  and the  $B = 0.0$  results also reveal the effect of biaxiality on initial stiffness, the yield, and post-yield behavior as well as the dramatically different  $\sigma_{11}$  and  $\sigma_{22}$  histories for these non-equibiaxial conditions. In the 2-direction the  $B = 0.5$  and the  $B = 0.0$  responses follow the trend of the  $B = 1.0$  and uniaxial ( $B \sim -0.5$ ) responses with the initial stiffness, yield stress, and post-yield hardening decreasing monotonically from  $B = 1.0$  to  $B = -0.5$ . The stress response in the 1-direction decreases as expected going from  $B = 1.0$  to  $B = 0.5$  to  $B = 0.0$  since there is less strain applied in that direction. The cyclic behavior is shown in **Fig. 6b–d** for the  $B = 1.0$ ,  $B = 0.5$ , and  $B = 0.0$  cases, respectively. In each case for both the 1- and 2-directions there is a non-linear unloading and reloading with a reduced yield upon reloading,



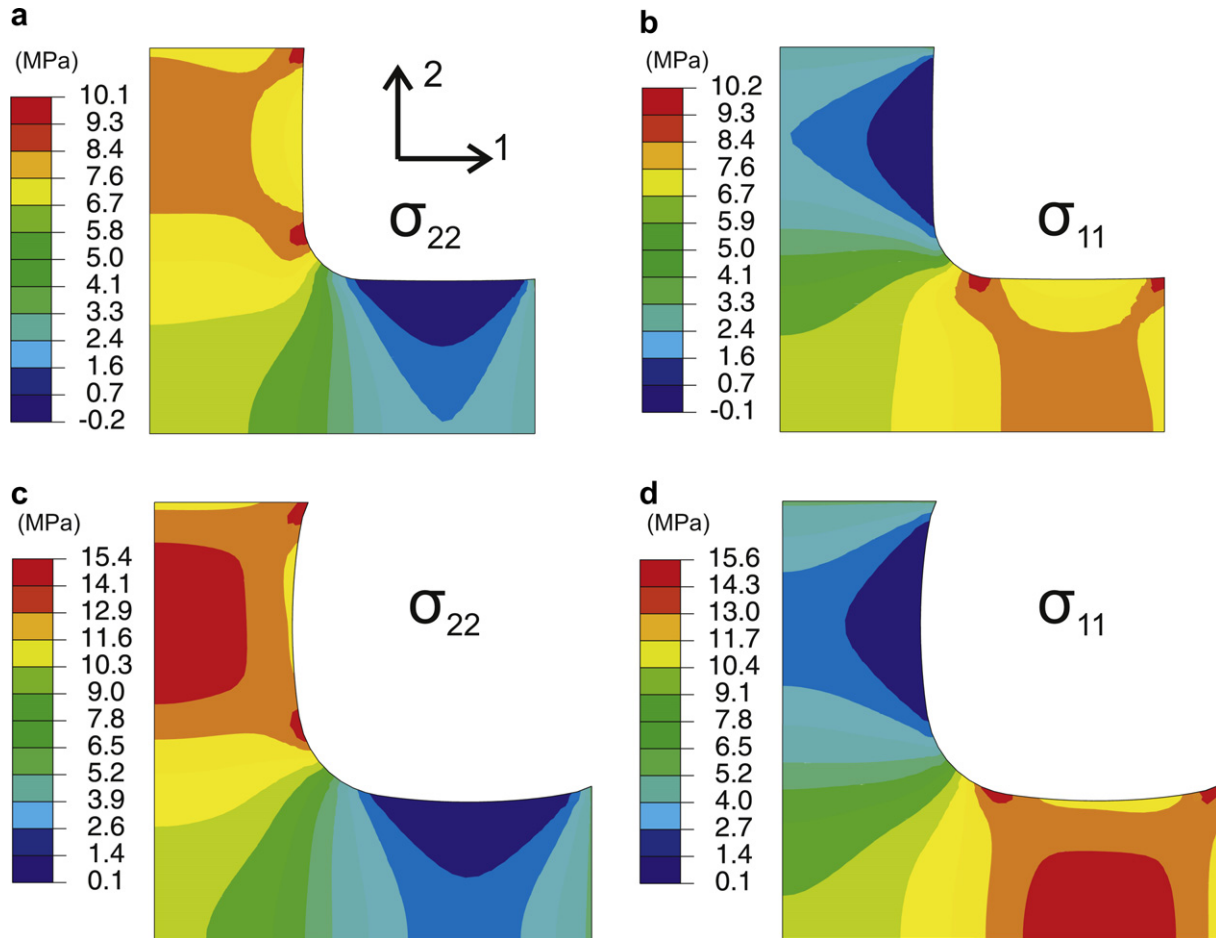


**Fig. 7.** Stress contours from simulated equibiaxial tensile loading ( $B = 1.0$ ) for the 1- and 2-direction grips extended at  $14 \mu\text{m s}^{-1}$ : prior to yield (2-direction grip displacement = 0.42 mm) (a)  $\sigma_{22}$  ( $\bar{\sigma}_{22} = 8.0$ ) (b)  $\sigma_{11}$  ( $\bar{\sigma}_{11} = 8.0$ ) and just after yield (2-direction grip displacement = 2.5 mm) (c)  $\sigma_{22}$  ( $\bar{\sigma}_{22} = 10.7$ ) (d)  $\sigma_{11}$  ( $\bar{\sigma}_{11} = 10.7$ ).

much as observed earlier in uniaxial tension. The specimens buckle during the process of returning the grips to their initial locations. Further strain recovery is seen to occur in the buckled state, resulting in reloading initiating from a lower strain than that at which zero strain was reached during unloading.

## 5. Biaxial modeling: results and discussion

Finite element simulations of each of the biaxial loading tests are conducted. The symmetry of the tests enables a one-fourth model of the specimen with appropriate boundary conditions as shown in Fig. 4b; a mesh convergence study was conducted to assess the quality of the mesh. The material behavior is modeled using the constitutive model with the properties determined from uniaxial tests obtained in Silberstein and Boyce [2]. Contours of ( $\sigma_{11}$ ) and ( $\sigma_{22}$ ) in the elastic regime and just past yield are shown for the  $B = 1.0$ ,  $B = 0.5$ , and  $B = 0.0$  cases in Figs. 7–9, respectively. First, we note that the deformed shape just past yield for each of these figures matches well with the corresponding experimental images taken at the same grip displacement. As in the experiments, there is a distinct concave curvature between the grip and the central region in the 2-direction leg for all three cases and the 1-direction leg for  $B = 1.0$  and this curvature is clearly absent in the 1-direction for  $B = 0.0$ . Second, even though the cruciform specimen shape was chosen to achieve a uniform biaxial stress state at the central region, it is clear from these simulations that this is not the case. The stress varies by approximately 25% across this central region. It

is therefore critical that the finite element results are reduced to biaxial stress–strain results in the same manner as the experimental results for any direct comparison: the reaction forces are measured at the grips and strains are measured from the displacement of points just outside the central square biaxial region. The model results are found to well predict the loading portion of the experimental results in all three cases (Fig. 10). The simulations capture the initial stiffness, the yield, and the post-yield behavior as observed for ( $\bar{\sigma}_{11}$ ) and ( $\bar{\sigma}_{22}$ ) histories for all three biaxial conditions, indicating high accuracy of the model in predicting biaxial loading. The unloading and reloading slopes in the model appear to be stiffer than in the experiments. Interestingly, the unload and reload yield shoulders occur at the same stress as in the experiments. This model therefore seems to underestimate the gradual nature of both the forward and reverse plastic deformation processes. The model also underpredicts the strain recovery of the specimen in the buckled state prior to reloading. The magnitude of the uncaptured strain recovery is similar in all cases ( $\bar{\epsilon} \sim 0.015$ ). While the origin of this disparity is not known at this time, it does not appear to be specific to multi-axial loading. We can see that the framework used to incorporate the uniaxial behavior into a three dimensional model is in fact capable of predicting the multi-axial deformation response of the membrane.

As discussed above, this particular geometry does not provide a perfect homogeneous biaxial stress distribution within the central region. In order to understand the biaxial test itself better and the accuracy of the data for providing the material

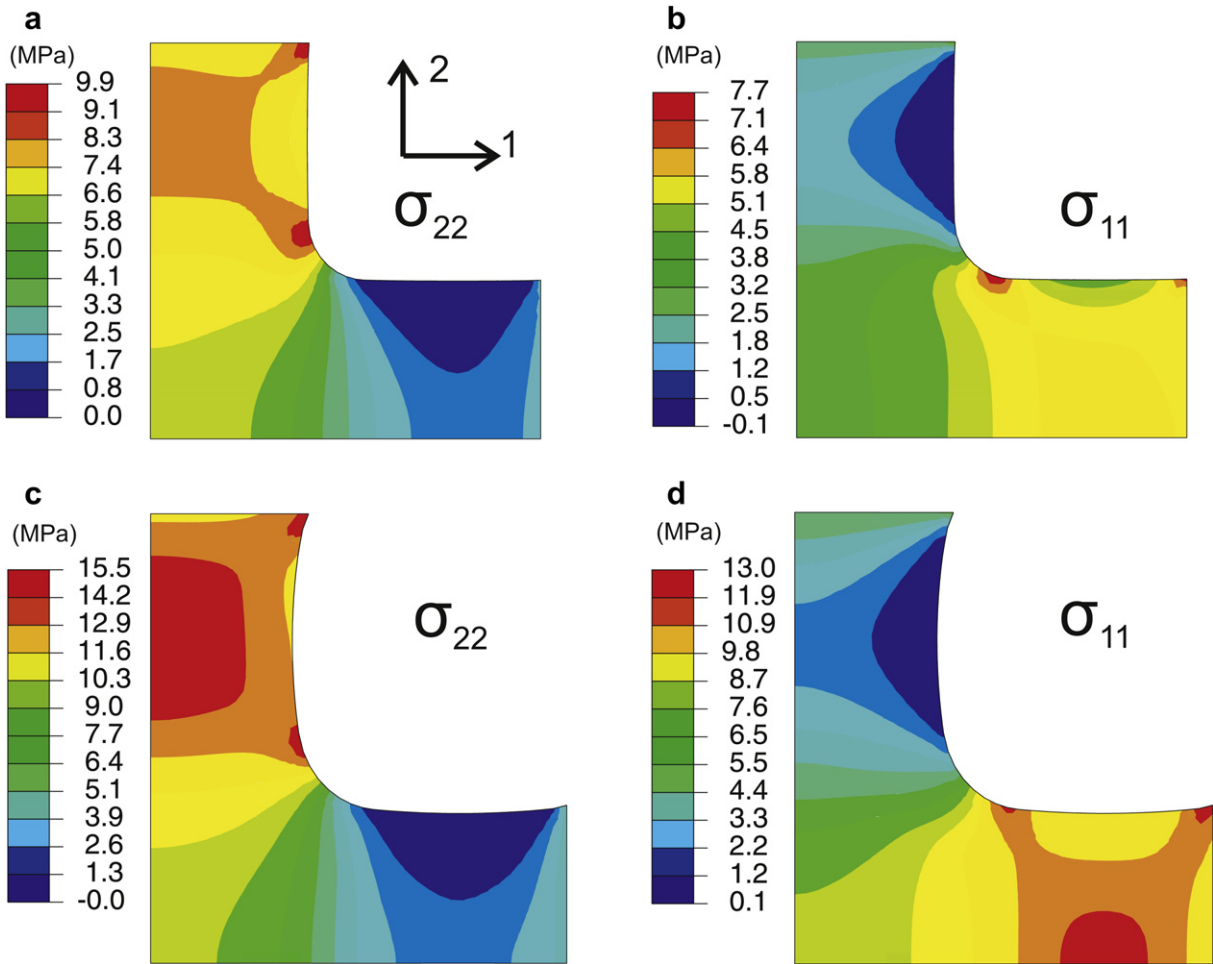


**Fig. 8.** Stress contours from simulated biaxial tensile loading ( $B = 0.5$ ) for the 2-direction grips extended at  $14 \mu\text{m s}^{-1}$  and 1-direction grips extended at  $7 \mu\text{m s}^{-1}$ ; prior to yield (2-direction grip displacement =  $0.42 \text{ mm}$ ) (a)  $\sigma_{22}$  ( $\bar{\sigma}_{22} = 7.8$ ) (b)  $\sigma_{11}$  ( $\bar{\sigma}_{11} = 5.4$ ) and just after yield (2-direction grip displacement =  $2.5 \text{ mm}$ ) (c)  $\sigma_{22}$  ( $\bar{\sigma}_{22} = 10.7$ ) (d)  $\sigma_{11}$  ( $\bar{\sigma}_{11} = 9.6$ ).

stress–strain response under different biaxial histories, we compare the stress–strain histories reduced from the test simulation with the model predictions of the corresponding pure homogeneous strain histories (Fig. 11). The homogeneous simulations are run with the 2-direction strain rate matched to the initial  $\bar{\epsilon}_{22}$  rate of the cruciform. The strain rate variation in  $\bar{\epsilon}_{22}$  which never exceeds a factor of three was neglected. Looking first at  $\sigma_{22}$  (Fig. 11a), it is evident that the cruciform specimen provides an accurate measure of the elastic regime. However, the yield event occurs in a sharper manner and at a higher stress as compared to the homogeneous response indicating that reduction of the cruciform data loses some of the details of the distributed yield event. The cruciform specimen also results in an exaggerated difference in the stress response of  $B = 1.0$ ,  $B = 0.5$ , and  $B = 0.0$  around the yield event. An increase in the magnitude and sharpness of yield is also evident in each of the ( $\sigma_{11}$ ) responses (Fig. 11b–d). For completeness we also include the simulated uniaxial response at a strain rate matching the 2-direction rate of the homogeneous biaxial simulations. Comparing the homogeneous equibiaxial stress–strain response to the uniaxial stress–strain response, it is evident that yield initiates at roughly the same stress for these two loading histories, but the hardening evolves more rapidly for the equibiaxial case, initially as a result of the greater effective strain rate (and hence the greater effective strain at any given axial strain where the yield stress evolves with effective strain) and then as a result of the network stretch. These simulation results indicate that while the experimental data is

generally capturing the biaxial material response, it would not be appropriate for direct evaluation of the biaxial yield stress or post-yield tangent modulus. Conversely, this method is quite appropriate for model validation since it requires the model to capture not only the homogeneous biaxial response but also the effects of stress and strain distributions.

## 6. Conclusions

The behavior of Nafion was experimentally explored under tensile biaxial loading conditions varying the degree of biaxiality. Biaxial testing was conducted via in-plane tensile testing of cruciform shaped specimens. A video extensometer system was used to enable determination of the local biaxial response in the central region. The biaxial response was qualitatively similar to the uniaxial response with the stiffness and strength in a given direction dependent on the degree of biaxiality. A three dimensional hygro-thermal elastic–viscoplastic constitutive model developed for Nafion based on uniaxial tensile data was used to simulate these experiments via a finite element implementation. These simulations revealed that the stress distribution is not completely uniform in the central “biaxial” region of the specimen. The cruciform specimens result in a greater and sharper yield event as compared to the pure homogeneous biaxial response. Nonetheless, the constitutive model was shown to well predict this complex multi-axial deformation response when the model is implemented in the

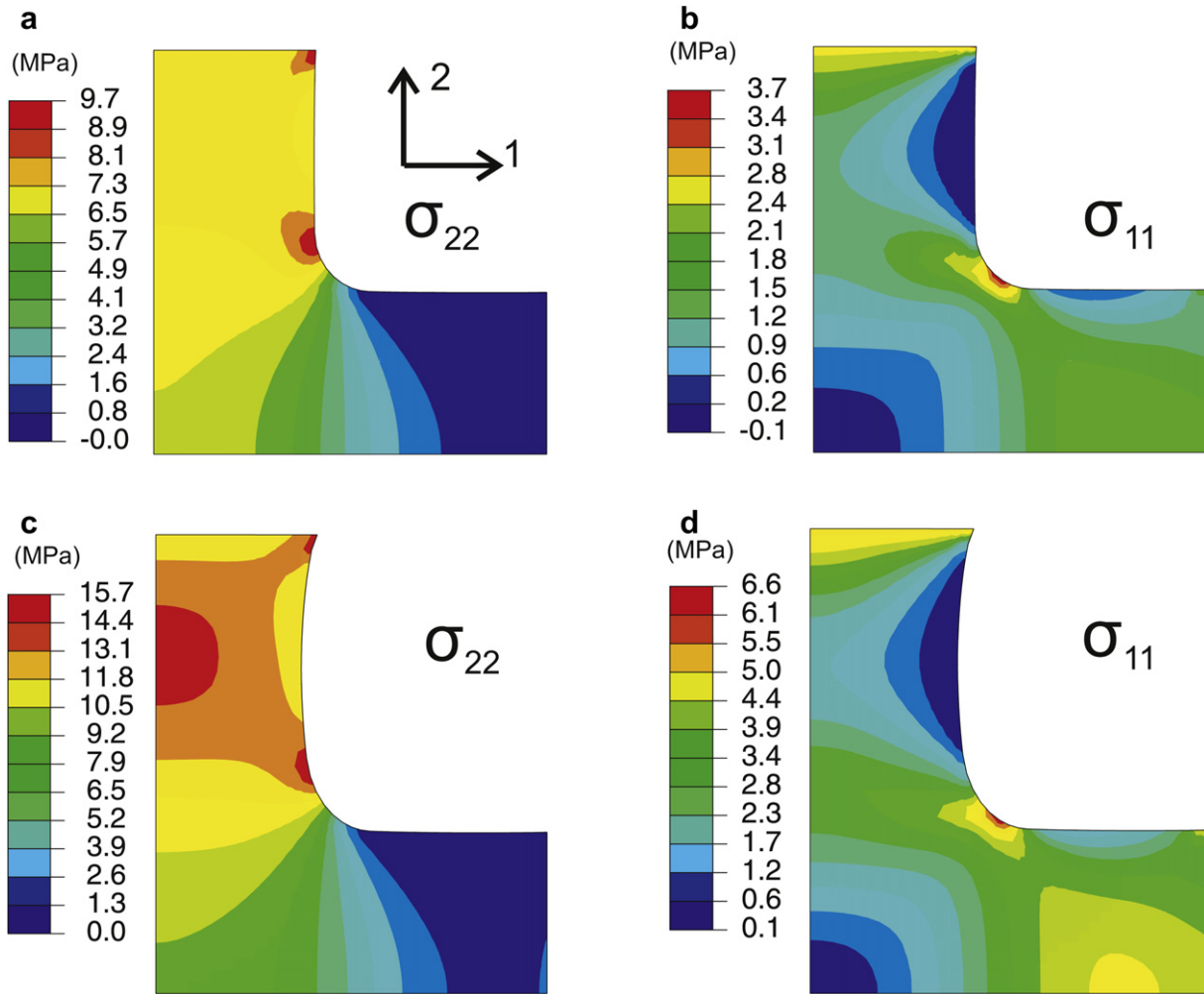


**Fig. 9.** Stress contours from simulated biaxial tensile loading ( $B = 0.0$ ) for the 2-direction grips extended at  $14 \mu\text{m s}^{-1}$  and 1-direction grips held fixed: prior to yield (2-direction grip displacement =  $0.42 \text{ mm}$ ) (a)  $\sigma_{22}$  ( $\bar{\sigma}_{22} = 7.3$ ) (b)  $\sigma_{11}$  ( $\bar{\sigma}_{11} = 1.6$ ) and just after yield (2-direction grip displacement =  $2.5 \text{ mm}$ ) (c)  $\sigma_{22}$  ( $\bar{\sigma}_{22} = 10.6$ ) (d)  $\sigma_{11}$  ( $\bar{\sigma}_{11} = 3.6$ ).

experimental geometry and reduced by the same methods as the experimental results. These results also indicated that while the initial yield under equibiaxial and uniaxial loading conditions are the same, the evolution in strength with strain (the rollover nature of yield) gives the appearance of a greater yield stress during biaxial loading compared to uniaxial loading – an effect captured by the model. It should be noted that no material parameters were modified to fit the biaxial data, the success therefore demonstrates the truly predictive capability of the model. The biaxial testing method and predictive constitutive modeling have broad relevance to polymeric membranes, especially considering the need for robustness to biaxial loading for polymer membranes in a wide range of separation and transport processes.

#### Acknowledgements

Funding for this work was provided by the Institute for Soldier Nanotechnologies, NSF grant CMMI-0700414, and the Masdar Institute.

#### Appendix. Constitutive model at constant temperature and hydration

A rheological schematic of the elastic–viscoplastic constitutive model for Nafion is shown in Fig. 2 in the main body of the text. A

fundamental assumption in the model structure is that the stress response of a material can be decomposed into multiple mechanisms. In this case two mechanisms are needed to model the material behavior: Mechanism I, rheologically depicted as an elastic spring in series with a viscoplastic dashpot, represents the resistance to deformation due to the intermolecular interactions where the spring captures the stiffness of these interactions and the non-linear dashpot captures the yielding of these interactions; Mechanism N is a non-linear spring which represents a resistance due to the stretching and orientation of the molecular network.

The model is fully three dimensional but will be expressed in principal stretch space for simplicity. Throughout this discussion  $i = 1, 2, 3$  are taken to indicate the three principal stretch directions with no sum on repeated  $i$  unless otherwise noted. The macroscopic deformation is given by the principal stretches  $\lambda_i$ . Each mechanism is taken to experience the same deformation and the total stress acting on the system is equal to the sum of the contributions from each mechanism:

$$\lambda_{Ii} = \lambda_{Ni} = \lambda_i \quad (1)$$

$$T_i = T_{Ii} + T_{Ni} \quad (2)$$

where  $\lambda_{Ii}$  and  $\lambda_{Ni}$  are the principal stretches of the intermolecular (I) and network (N) mechanisms, respectively, and  $T_{Ii}$  and  $T_{Ni}$  are the Cauchy (true) stress contributions of the intermolecular and

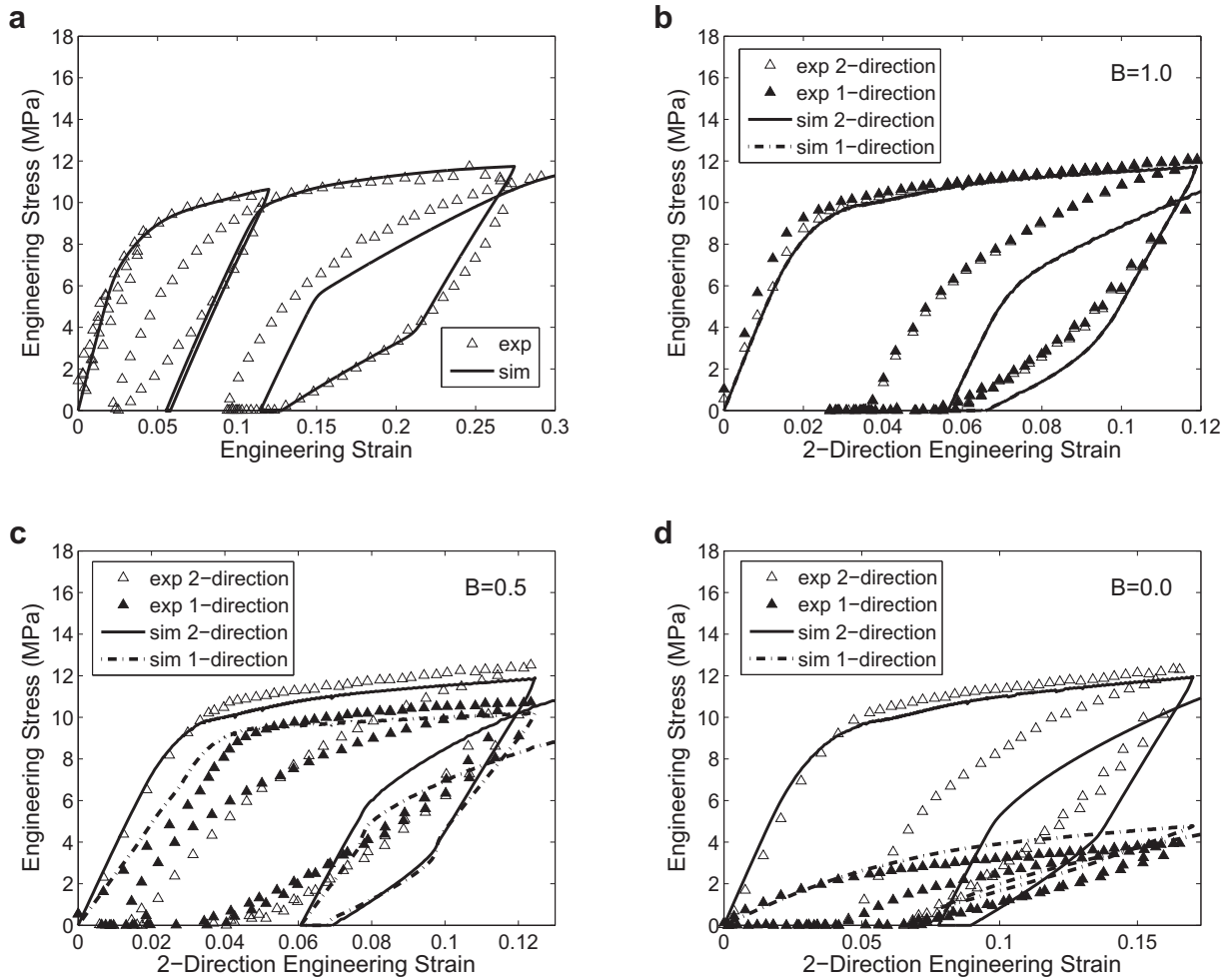


**Fig. 10.** Model compared to experimental data for biaxial tensile loading using video extensometer equivalent strain measure (a) uniaxial behavior for reference ( $\phi = 1.5$ ) (b) 1- and 2-direction grips displaced at  $14 \mu\text{m s}^{-1}$  ( $B = 1.0$ ,  $\phi = 2$ ) (c) 2-direction grips displaced at  $14 \mu\text{m s}^{-1}$  and 1-direction grips displaced at  $7 \mu\text{m s}^{-1}$  ( $B = 0.5$ ,  $\phi = 2$ ) (d) 2-direction grips displaced at  $14 \mu\text{m s}^{-1}$  and 1-direction grips held fixed ( $B = 0.0$ ,  $\phi = 2$ ).

network mechanisms, respectively. The governing equations for each mechanism are given below followed by a table listing the values used for the material parameters (Table 1).

**Mechanism N:** The stress arising from the network resistance to deformation ( $T_{Ni}$ ) is taken to be deviatoric and is derived from the resistance to stretching and orientation of the molecular network; here we use the Neo-Hookean model:

$$T_{Ni} = \frac{1}{J} \mu_N B'_{Ni} \quad (3)$$

where  $J = \lambda_1 \lambda_2 \lambda_3$  is the volume ratio,  $\mu_N$  is the rubbery shear modulus, and  $B'_{Ni}$  is the deviatoric part of the Cauchy Green

tensor given by  $B'_{Ni} = \lambda_{Ni}^2 - \lambda_{\text{chain}}^2 \cdot \lambda_{\text{chain}} = \sqrt{(\lambda_1^2 + \lambda_2^2 + \lambda_3^2)}/3$  is a measure of network stretch.

**Mechanism I:** At ambient temperatures, the intermolecular mechanism provides an initially relatively stiff response followed by yielding and post-yield flow. To capture the elastic–plastic nature of the deformation, the stretch is decomposed into elastic and plastic components using the Kröner–Lee multiplicative decomposition  $\lambda_{ii} = \lambda_{ii}^e \lambda_{ii}^p$  where  $\lambda_{ii}^e$  are the elastic stretches and  $\lambda_{ii}^p$  are the plastic stretches. The plastic deformation is taken to be isochoric giving the plastic volume ratio  $J^p = \lambda_1^p \lambda_2^p \lambda_3^p = 1$ . The intermolecular contribution to the Cauchy (true) stress is found from a generalized Hookean relationship:

$$T_{ii} = \frac{1}{J^e} \left[ 2\mu (\ln \lambda_{ii}^e)' + \kappa \ln J^e \right] \quad (4)$$

where  $J^e = \lambda_{i1}^e \lambda_{i2}^e \lambda_{i3}^e$  is the elastic mechanical volume ratio,  $\mu$  is the shear modulus, and  $\kappa$  is the bulk modulus.

**Plastic Flow:** To obtain the decomposition of  $\lambda_{ii}$  into  $\lambda_{ii}^e$  and  $\lambda_{ii}^p$ , the rate kinematics are needed where the velocity gradient is given by

$$D_{ii} = \dot{\lambda}_{ii} \lambda_{ii}^{-1} \quad (5)$$

$D_{ii}$  is further decomposed into elastic and plastic quantities

$$D_{ii} = D_{ii}^e + D_{ii}^p \quad (6)$$

where  $D_{ii}^e$  is the elastic velocity gradient and  $D_{ii}^p$  is the plastic velocity gradient.  $D_{ii}^p$  is constitutively prescribed below. Initially, plastic flow is driven by the deviator of the stress  $T_{ii}$ . Once plastic flow ensues, a back stress  $T_{Bi}$  develops around locally deforming sites; this back stress drives reverse plasticity and the corresponding highly non-linear unloading. Therefore, the driving stress for plastic flow is the deviator of the stress difference ( $T_{ii} - T_{Bi}$ ). Hence,  $D_{ii}^p$  is constitutively defined to follow a thermally activated flow process driven by  $T_{ii} - T_{Bi}$ .

$$D_{ii}^p = \dot{\gamma}_I^p \frac{T'_{Pi}}{\sqrt{2}\tau_p} \quad (7)$$

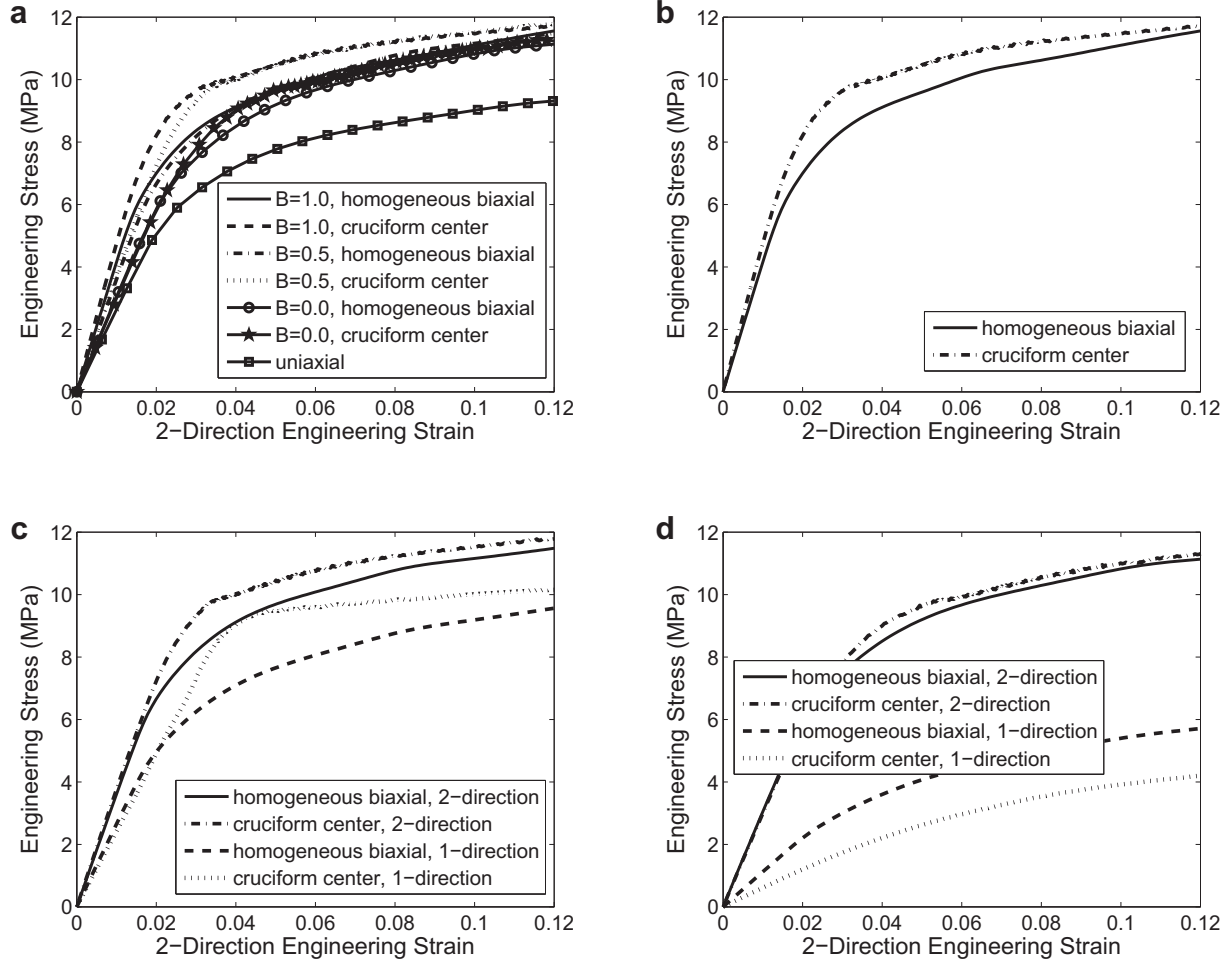


**Fig. 11.** Comparison of simulation result for pure homogeneous biaxial deformation with simulation result for biaxial deformation as conducted experimentally with the cruciform specimen ( $\phi = 2$ ) (a)  $\bar{\sigma}_{22}$  for all three degrees of biaxiality (b) 1- and 2-direction grips displaced at  $14 \mu\text{m s}^{-1}$  ( $B = 1.0$ ) (c) 2-direction grips displaced at  $14 \mu\text{m s}^{-1}$  and 1-direction grips displaced at  $7 \mu\text{m s}^{-1}$  ( $B = 0.5$ ) (d) 2-direction grips displaced at  $14 \mu\text{m s}^{-1}$  and 1-direction grips held fixed ( $B = 0.0$ ).

$$\dot{\gamma}_I^p = \dot{\gamma}^o \exp \left[ \frac{-\Delta G}{k_b \theta} \right] \sin h \left[ \frac{\Delta G}{k_b \theta} \frac{\tau_p}{s} \right] \quad (8)$$

$$T'_{Pi} = (T_{li} - T_{Bi})' \quad (9)$$

$$T'_{Bi} = \frac{1}{j} 2 \mu_B \ln \lambda_{Bi}^e \quad (10)$$

**Table 1**  
Material parameters for Nafion constitutive model.

Model component	Material parameter	Value
Elastic	$\kappa$	$3.3 \times 10^8 \text{ Pa}$
	$\mu_o$	$1.1 \times 10^8 \text{ Pa}$
Elastic evolution	$\bar{h}$	$4.7 \times 10^9 \text{ Pa}$
	$\mu_{sat}$	$7.0 \times 10^7 \text{ Pa}$
Rate dependent yield	$\dot{\gamma}^o$	$6.72 \text{ s}^{-1}$
	$\Delta G$	$8.98 \times 10^{-20} \text{ J}$
	$\bar{s}_o$	$6.5 \times 10^6 \text{ Pa}$
Distributed yield	$\bar{h}$	$1.2 \times 10^9 \text{ Pa}$
	$\bar{s}_{sat}$	$9.6 \times 10^6 \text{ Pa}$
	$\bar{h}$	$7.5 \times 10^7 \text{ Pa}$
	$\bar{s}_{sat}$	$6.5 \times 10^6 \text{ Pa}$
Isotropic hardening	$\bar{h}$	$2.6 \times 10^7 \text{ Pa}$
	$\bar{n}$	1
Back stress	$\mu_B$	$2.65 \times 10^7 \text{ Pa}$
	$S_{Bo}$	$4.3 \times 10^6 \text{ Pa}$
	$h_B$	$2.3 \times 10^8 \text{ Pa}$
	$S_{Bsat}$	$7.7 \times 10^6 \text{ Pa}$
Network	$\mu_N$	$3.3 \times 10^6 \text{ Pa}$

where  $\dot{\gamma}_I^p$  is the magnitude of the plastic velocity gradient,  $\tau_p = \sqrt{1/2(T_{p1}^2 + T_{p2}^2 + T_{p3}^2)}$  is the scalar equivalent shear stress,  $\dot{\gamma}^o$  is a pre-exponential factor proportional to the attempt frequency,  $\Delta G$  is the activation energy,  $s$  is the isotropic shear resistance,  $k_b$  is Boltzmann's constant,  $\theta$  is the absolute temperature,  $\mu_B$  is the back stress shear modulus, and  $\lambda_{Bi}^e$  is the elastic portion of the back stress stretch to be discussed shortly.

The plastic stretch is found by integrating  $\dot{\lambda}_{li}^p = D_{li}^p \lambda_{li}^p$ . The elastic stretch is then calculated by  $\lambda_{li}^e = \lambda_{li}^p (\lambda_{li}^p)^{-1}$ .

**Distributed yield event:** The yield process is observed to be a distributed event as evident by the gradual rollover nature of yielding. This distributed aspect of yield could be captured by numerous dashpots of different energy barriers in parallel; however, for simplicity, this is captured by an evolution in strength  $s$  with plastic flow.  $s$  evolves throughout the deformation process, with an initial increase during yield ( $\bar{s}$ ), a softening with further plasticity ( $\tilde{s}$ ), and an increase with network alignment ( $\bar{s}$ ). The initial shear resistance  $\bar{s}_o$  is taken to increase with  $\dot{\gamma}_I^p$  until reaching a saturated state during plastic deformation reflecting the distributed nature of yield.

$$\dot{s} = \bar{h} \left( 1 - \frac{\tilde{s}}{\bar{s}_{sat}} \right) \dot{\gamma}_I^p \quad (11)$$

where  $\tilde{h}$  controls the rate of approach of  $\tilde{s}$  to its saturation value  $\tilde{s}_{sat}$ . To capture a softening that occurs upon percolation,  $s_o = 0$ , which is subtracted from  $\tilde{s}$ , is taken to increase with  $\dot{\gamma}_I^p$  at a slower rate than  $\tilde{s}$ , to its saturated value  $\tilde{s}_{sat}$ .

$$\hat{s} = h \left( 1 - \frac{\tilde{s}}{\tilde{s}_{sat}} \right) \dot{\gamma}_I^p \quad (12)$$

where  $h$  controls the rate of approach of  $\hat{s}$  from its initial value of 0 to its saturation value  $\tilde{s}_{sat}$ .

*Post-yield isotropic hardening:* Molecular alignment provides an additional increase to the intermolecular shear resistance captured by the contribution  $\tilde{s}$ .

$$\bar{s} = \bar{h} (\lambda_{chain}^{\bar{n}} - 1) \quad (13)$$

where  $\bar{h}$  controls the initial slope and  $\bar{n}$  controls the nonlinearity. The strength ( $s$ ) is then given by:

$$s = \tilde{s} - \hat{s} + \bar{s}. \quad (14)$$

*Saturation of the intermolecular back stress:* The back stress is observed to saturate as evident by the nonlinearity of the unloading curves and as also found in calorimetry measurements on other polymers [17]. This is captured by the dashpot on the back stress element. The back stretch  $\lambda_{Bi}$  is therefore separated into elastic and plastic components using the Kroner-Lee multiplicative decomposition  $\lambda_{Bi} = \lambda_{Bi}^e \lambda_{Bi}^p$  where  $\lambda_{Bi}^e$  are the elastic stretches and  $\lambda_{Bi}^p$  are the plastic stretches. The rate kinematics are needed where the velocity gradient is given by

$$D_{Bi} = \dot{\lambda}_{Bi} \lambda_{Bi}^{-1} \quad (15)$$

$D_{Bi}$  is further decomposed into elastic and plastic quantities

$$D_{Bi} = D_{Bi}^e + D_{Bi}^p \quad (16)$$

where  $D_{Bi}^e$  is the elastic velocity gradient and  $D_{Bi}^p$  is the plastic velocity gradient. The back stress saturation dashpot is prescribed to evolve according to:

$$D_{Bi}^p = \dot{\gamma}_B^p \frac{T'_{Bi}}{\sqrt{2}\tau_B} \quad (17)$$

$$\dot{\gamma}_B^p = \dot{\gamma}^o \exp \left[ -\frac{\Delta G}{k_b \theta} \right] \sin h \left[ \frac{\Delta G}{k_b \theta} \frac{\tau_B}{s_B} \right] \quad (18)$$

where  $\tau_B = \sqrt{1/2(T_{B1}^2 + T_{B2}^2 + T_{B3}^2)}$  is the corresponding equivalent shear stress and  $s_B$  is the isotropic back stress saturation strength.  $\dot{\gamma}^o$  and  $\Delta G$  are the same constants as for the intermolecular plastic deformation since the rate dependence of unloading is similar to that of loading.  $s_B$  is taken to evolve to a maximum with  $\dot{\gamma}_B^p$  such that the saturation of the back stress occurs gradually.

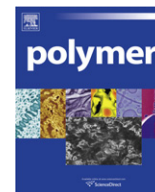
$$\dot{s}_B = h_B \left( 1 - \frac{s_B}{s_{Bsat}} \right) \dot{\gamma}_B^p \quad (19)$$

where  $h_B$  controls the evolution with shear and  $s_{Bsat}$  is the saturation value.

The plastic back stretch is found by integrating  $\dot{\lambda}_{Bi}^p = D_{Bi}^p \lambda_{Bi}^p$ . The elastic back stretch is then calculated by  $\lambda_{Bi}^e = \lambda_{Bi}^p (\lambda_{Bi}^p)^{-1}$ .

## References

- [1] Borup R, Meyers J, Pivovar B, Kim YS, Mukundan R, Garland N, et al. Chemical Reviews 2007;107:3904–51.
- [2] Silberstein MN, Boyce MC. Journal of Power Sources 2010;195:5692–706.
- [3] Dillard DA, Li YQ, Grohs JR, Case SW, Ellis MW, Lai YH, et al. Journal of Fuel Cell Science and Technology 2009;6:031014-1–031014-8.
- [4] Li YQ, Dillard DA, Case SW, Ellis MW, Lai YH, Gittleman CS, et al. Journal of Power Sources 2009;194:873–9.
- [5] Matthews RG, Duckett RA, Ward IM, Jones DP. Polymer 1997;38:4795–802.
- [6] Adams AM, Buckley CP, Jones DP. Polymer 1998;39:5761–3.
- [7] Gerlach C, Buckley CP, Jones DP. Chemical Engineering Research and Design 1998;76:38–44.
- [8] Adams AM, Buckley CP, Jones DP. Polymer 2000;41:771–86.
- [9] Sweeney J, Collins TLD, Coates PD, Ward IM. Polymer 1997;38:5991–9.
- [10] Sweeney J, Spares R, Woodhead M. Polymer Engineering and Science 2009;49:1902–8.
- [11] Zhang XM, Aiji A. Journal of Applied Polymer Science 2003;89:487–96.
- [12] Zeng FF, Le Grogne P, Lacrampe MF, Krawczak P. Mechanics of Materials 2010;42:686–97.
- [13] Makinde A, Thibodeau L, Neale KW. Experimental Mechanics 1992;32:138–44.
- [14] Demmerle S, Boehler JP. Journal of Mechanics and Physics of Solids 1993;41:143–81.
- [15] Hannon A, Tiernan P. Journal of Materials Processing Technology 2008;198:1–13.
- [16] Herrmann AM, MS thesis, Cambridge, MA: Massachusetts Institute of Technology; February 2006.
- [17] Hasan OA, Boyce MC. Polymer 1993;34:5085–92.
- [18] Salamantina OB, Rudnev SN, Voennyi VV, Oleynik EF. Journal of Thermal Analysis 1992;38:1271–81.
- [19] Hasan OA, Boyce MC. Polymer and Engineering Science 1995;35:331–44.
- [20] Anand L, Ames NM, Srivastava V, Chester SA. International Journal of Plasticity 2009;25:1474–94.
- [21] Kusoglu A, Karlsson AM, Santare MH. Polymer 2010;51:1457–64.



# Charge dynamics and bending actuation in Aquivion membrane swelled with ionic liquids

Junhong Lin<sup>a,b</sup>, Yang Liu<sup>b,c,\*</sup>, Q.M. Zhang<sup>a,b,c</sup>

<sup>a</sup> Department of Materials Science and Engineering, The Pennsylvania State University, University Park, PA 16802, USA

<sup>b</sup> Materials Research Institute, The Pennsylvania State University, University Park, PA 16802, USA

<sup>c</sup> Department of Electrical Engineering, The Pennsylvania State University, University Park, PA 16802, USA

## ARTICLE INFO

### Article history:

Received 4 October 2010

Received in revised form

18 November 2010

Accepted 20 November 2010

Available online 27 November 2010

### Keywords:

Ionic electroactive polymer actuator

Ionic liquids

Poisson–Nernst–Planck equations

## ABSTRACT

The actuation strain and speed of ionic electroactive polymer (EAP) actuators are mainly determined by the charge transport through the actuators and excess ion storage near the electrodes. We employ a recently developed theory on ion transport and storage to investigate the charge dynamics of short side chain Aquivion<sup>®</sup> (Hyflon<sup>®</sup>) membranes with different uptakes of ionic liquid (IL) 1-ethyl-3-methylimidazolium trifluoromethanesulfonate (EMI-Tf). The results reveal the existence of a critical uptake of ionic liquids above which the membrane exhibits a high ionic conductivity ( $\sigma > 5 \times 10^{-2}$  mS/cm). Especially, we investigate the charge dynamics under voltages which are in the range for practical device operation ( $\sim 1$  V and higher). The results show that the ionic conductivity, ionic mobility, and mobile ion concentration do not change with the applied voltage below 1 V (and for  $\sigma$  below 4 V). The results also show that bending actuation of the Aquivion membrane with 40wt% EMI-Tf is much larger than that of Nafion, indicating that the shorter flexible side chains improve the electromechanical coupling between the excess ions and the membrane backbones, while not affecting the actuation speed.

© 2010 Elsevier Ltd. All rights reserved.

## 1. Introduction

Ion transport and storage in ionomer membranes are of great interest for electroactive polymer (EAP) devices, such as actuators, sensors, energy harvesting devices, and supercapacitors [1–3]. Ionic liquids (ILs), which are a class of salt in liquid form that contain both ions and neutral molecules, possess many interesting properties that make them very attractive to be employed as electrolytes in electroactive polymer devices [4–11]. For example, the vapor pressure of ionic liquids is negligibly low and as a result they will not evaporate out of the EAP devices when operated in ambient condition. It has been demonstrated that comparing to water the use of ILs as solvent for EAP actuators can dramatically increase the lifetime of transducer [12,13]. Their high mobility leads to the potential of fast response of EAP devices while the wide electrochemical window allows for higher applied voltages [13–19].

This paper investigates charge dynamics of room temperature ionic liquid 1-ethyl-3-methylimidazolium trifluoromethanesulfonate (EMI-Tf) in Aquivion<sup>®</sup> (Hyflon<sup>®</sup>) membranes swelled with different

uptakes of ILs and the actuations of the membranes swelled with ILs above the critical uptake. EMI-Tf served in this study due to its comparably high conductivity (8.6 mS/cm), low viscosity (45 cP at 25 °C) and larger electrochemical window (4.1 V) [17]. Hyflon<sup>®</sup> is known in the literature as short side chain ionomer (in comparison to Nafion<sup>®</sup> that is indicated as long side chain ionomer) and was originally developed by Dow Chemicals Company at the beginning of the '80 but now named Aquivion<sup>®</sup> by Solvay Solexis [22–25]. These perfluorosulfonate ionomers consist of a polytetrafluoroethylene (PTFE) backbone and double ether perfluoro side chains terminating in a sulfonic acid group as illustrated in Fig. 1(a). The backbone provides the mechanical support and the flexible side chains facilitate the aggregation of a hydrophilic clusters (Fig. 1(b)). When swelled with ILs the clusters expand. Above a certain IL uptake (critical uptake), these clusters will be connected with narrow channels forming percolation pathways for easy ion conduction, resulting in a high conductivity in the ionomer membrane [20–25]. Although in the literature, most ionic EAPs employ Nafion as the polymer matrix, [14–17] the short flexible side chains in Aquivion may provide better mechanical coupling between the ions and membrane backbones and, consequently, more efficient electromechanical transducers.

In this study, we investigate the charge transport and storage in Aquivion EAP membranes as schematically illustrated in Fig. 2(a), where the Aquivion membrane is coated with Au electrodes on two

\* Corresponding author. Department of Electrical Engineering, Pennsylvania State University, University Park, PA 16802, USA. Tel.: +1 814 863 9558; fax: +1 814 863 7846. E-mail address: [yul165@psu.edu](mailto:yul165@psu.edu) (Y. Liu).

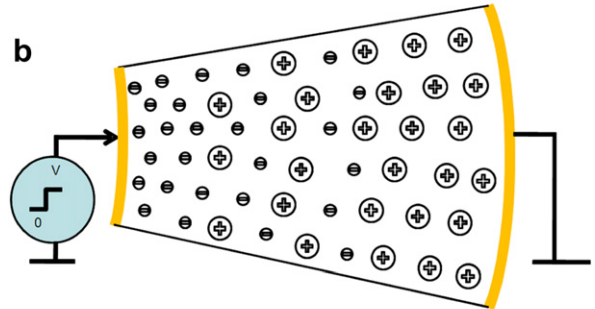
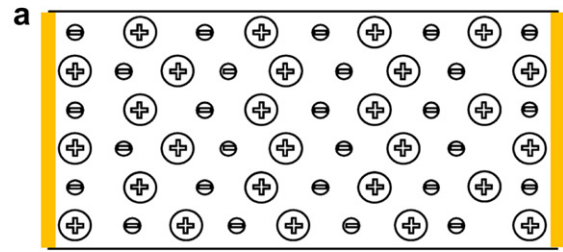
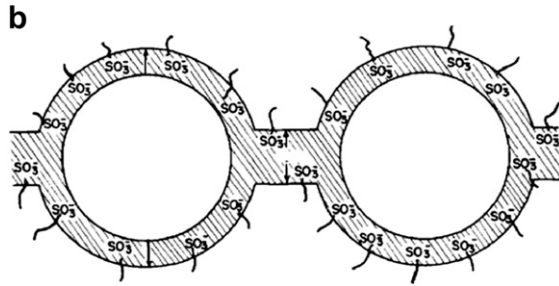
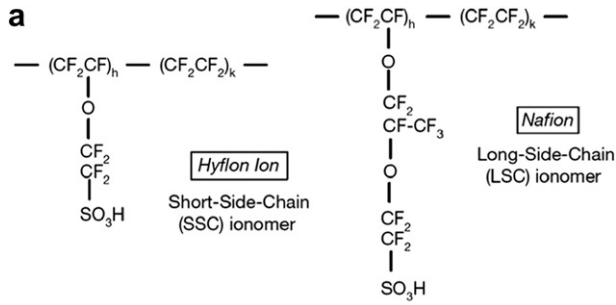


**Fig. 1.** (a) Is the molecular structure of short side chain Aquivion and long side chain Nafion (b) the cluster network morphology modeled by Gierke et al [20,21].

surfaces and swelled with a given amount of EMI-Tf. Under applied voltage, anions and cations migrate towards the anode and cathode, and form electric double layers and diffusion layers as illustrated in Fig. 2(b). Moreover, the excess ions at the two electrodes cause strains in the membranes, and as a result, generate bending (actuation) of the membrane as shown in Fig. 2(c). Therefore, these ionomer membranes are attractive for ionic polymer actuators and transducers operated under low voltage (1–4 V).

In general, charge transport is a result of drift and diffusion and can be described by Poisson–Nernst–Planck equations,

$$\varepsilon\varepsilon_0 \frac{\partial E}{\partial x} = \rho \quad (1)$$

$$\psi_{\pm} = \pm \mu n_{\pm} E - D \frac{\partial n_{\pm}}{\partial x} \quad (2)$$

where  $\rho$  is the charge concentration,  $\varepsilon$  the dielectric constant of the medium,  $\varepsilon_0$  the vacuum permittivity,  $\psi$  is the ion flux density (current density  $J = q\psi$ ),  $\mu$  is the ion mobility,  $n$  is the ion concentration (the subscripts + and - indicate positive and negative charges,  $E$  electric field,  $D$  diffusion coefficient. For the ionic liquids studied here, we assume  $n_+ = n_-$ .  $\mu$  and  $D$  are related by the Einstein equation,  $D = \mu kT/q$  [26,27].

For the ionomer membrane in Fig. 2(a) under a step voltage (from 0 at  $t < 0$  to  $V$  volts at  $t > 0$ ), the initial current density before the screening of electric field occurs is  $I_0 = \sigma VS/d$ , where  $\sigma (=qn\mu)$  is the conductivity,  $d$  is the membrane thickness, and  $S$  is the electrode area. When the applied voltage is not high (in the order of  $10 kT$ , where  $k$  is the Boltzmann's constant), the initial transient current follows the charging of an electric double layer capacitor  $C_D$  in series with a bulk resistor  $R$  [28–31],

$$I(t) = I_0 \exp(-t/\tau_{DL}) \quad (3)$$

where  $\tau_{DL} = d \lambda_{DL}/2D = RC_D$ , describes the typical charging time for the electric double layer which has a thickness  $\lambda_{DL}$ , the Debye length,

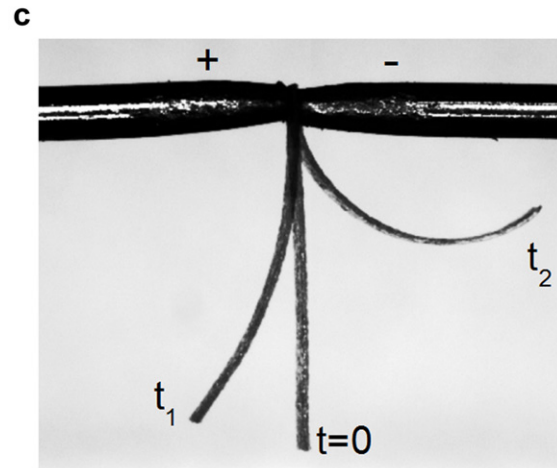


**Fig. 2.** Charge distribution (a) before and (b) after an applied step voltage in ionomer. (c) Bending actuation of 62um thick Aquivion membrane when a voltage step from 0 V to 4 V is applied.

$$\lambda_{DL} = \left( \varepsilon\varepsilon_0 kT / Z^2 q^2 n \right)^{1/2} \quad (4)$$

where  $Z$  is the mobile ion charge ( $=1$  for EMI-Tf), and  $q = e$ , electron charge. It was further shown that at longer time, the charge diffusion from the bulk to the double layer region leads to a power law decay of the diffusion current (see Fig. 3, in which the initial current fits well by Eq. (3), followed by a power law decay of the diffusion current, having a typical time constant  $\tau \sim d^2/(4D)$ ). Therefore, by fitting experimental transient current  $I(t)$  with Eq. (3), as illustrated in Fig. 3,  $\sigma$ ,  $n$ , and  $\mu$  can be obtained if  $\varepsilon$  of the ionomer membrane (with ILs) is known, [28–31]

$$\sigma = \frac{I_0 d}{VS} \quad \mu = \frac{qV S \varepsilon \varepsilon_0 d}{4kT \tau_{DL}^2 I_0} \quad n = \frac{4kT I_0^2 \tau_{DL}^2}{\varepsilon \varepsilon_0 q^2 V^2 S^2}$$

Impedance spectroscopy is employed to determine  $\varepsilon$ . Besides  $\varepsilon$ ,  $\sigma (=d/(SR))$ , where  $d$  is the thickness and  $S$  the surface area of the



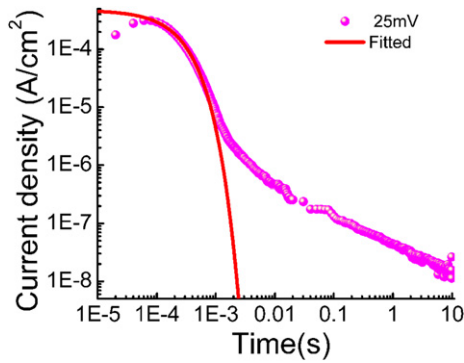


Fig. 3. The transient current of Aquivion membrane with 40wt% uptake of EMI-Tf when a voltage step from 0 V to 25 mV is applied.

membrane), can also be determined from the Nyquist plot as shown in Fig. 4.

## 2. Experimental

Aquivion (EW790) membrane and EMI-Tf was purchased from Solvay Solexis and Aldrich, respectively. All the materials were dried in vacuum at 80 °C to remove moisture before processing. Aquivion membranes swollen with various EMI-Tf uptakes were prepared by varying the soaking time for the Aquivion membrane in EMI-Tf at 80 °C to approach the target values. 50 nm thick of gold foils (L.A.Gold Leaf) were hot-pressed on both side of the membrane to serve as the electrodes. The uptake of ionic liquid within Aquivion membrane was calculated by measuring the weight gain after swelling. In this study, membranes with 9, 17, 29 and 40wt% uptake of EMI-Tf were prepared (or 11.5, 19.7, 29.6, 36.7 vol%) and their thicknesses are 55, 57, 59, 62  $\mu\text{m}$  after the swelled with ILS, respectively. Nafion with 40wt% uptake was prepared with

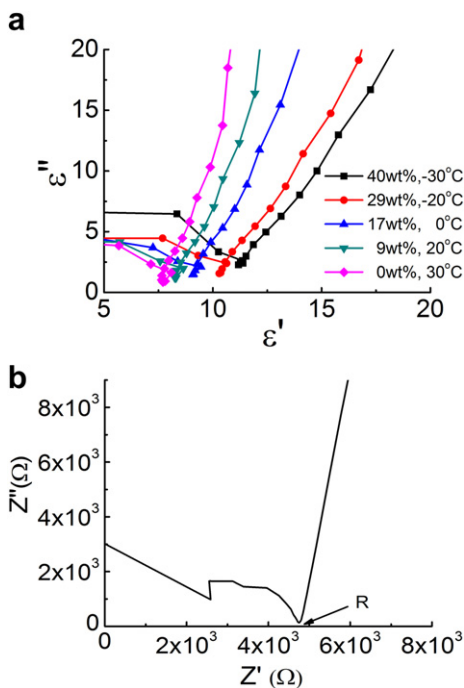


Fig. 4. (a) The cole–cole plot of Aquivion (AQ) membrane with various EMI-Tf uptakes under various temperatures (b) Nyquist plot of Aquivion membrane with 17wt% uptake of EMI-Tf.

the same procedure and its thickness is 63  $\mu\text{m}$ . Samples were held at an elevated temperature ( $\sim 80$  °C) for more than 12 h to enhance the uniform dispersion of ionic liquids inside the membranes. This is especially important for films with low uptakes of ionic liquids.

The electrical measurement was carried out in a sealed metal box with desiccant inside to prevent the absorption of moisture and equipped with a thermal couple to monitor the temperature during the measurement. The impedance spectroscopy was measured by a potentiostat Princeton 2237. The dc conductivity was calculated by  $\sigma = d/RS$ , where  $R$  is the impedance curve intersection on the  $Z'$  axis of Nyquist plot. To obtain the dielectric constant  $\epsilon$  of the membranes, the samples were cooled down in an environment chamber (Versa Tenn III) to shift the dielectric spectrum to the measurable frequency window of the set-up which is below 1 MHz (so that the dielectric constant before the screening of the applied field occurs can be measured, at frequencies  $\gg 1/\tau_{DL}$ ,  $\sigma$  decreases with temperature while in comparison dielectric constant is very weakly temperature dependent) [32–34]. The transient current vs. time was collected by a potentiostat Princeton 2237 which output was connected to a high sampling rate oscilloscope to collect data during the fast charging process ( $<1$   $\mu\text{s}$ ). The accumulation of blocked charges on sample electrode interface and the charge imbalance in the membrane may affect the electrical measurement. Therefore, several cycles of Cyclic Voltammetry (CV) scan with a low voltage and high scan rate were performed to help cleaning the electrode surface then the samples were shorted for at least 30 min to ensure that the charges redistribute to the equilibrium state as possible [35].

The time-dependent bending actuations of the actuators under applied voltage were recorded using a probe station (Cascade Microtech M150) equipped with a Leica microscope. A DC step voltage was applied to the actuator and images of bending actuation as a function of time were recorded using a CCD camera (Pulnix 6740CL). Radii of curvature of the bending actuators were determined using image-processing software.

## 3. Results and discussion

### 3.1. Charge transport behavior of Aquivion membranes swelled with EMI-Tf

The current responses for Aquivion with 40wt% of EMI-Tf under various step voltages are presented in Fig. 5. From these curves, conductivity  $\sigma$  under different applied voltages can be determined from  $I_0$  (up to 4 V in the experiment). On the other hand, the data shows that fitting to Eq. (3) can be performed only for  $I(t)$  at  $V \leq 1$  V. Beyond that, there is no distinctive crossover region in the  $I(t)$  curve between the exponential decay of the drifting current and the power law decay of the diffusion current.

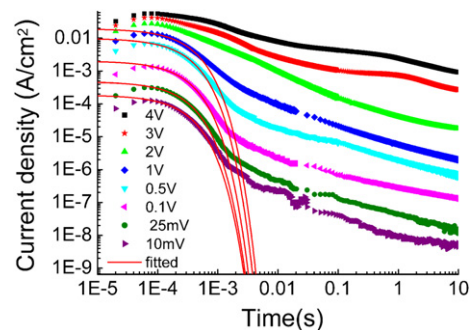
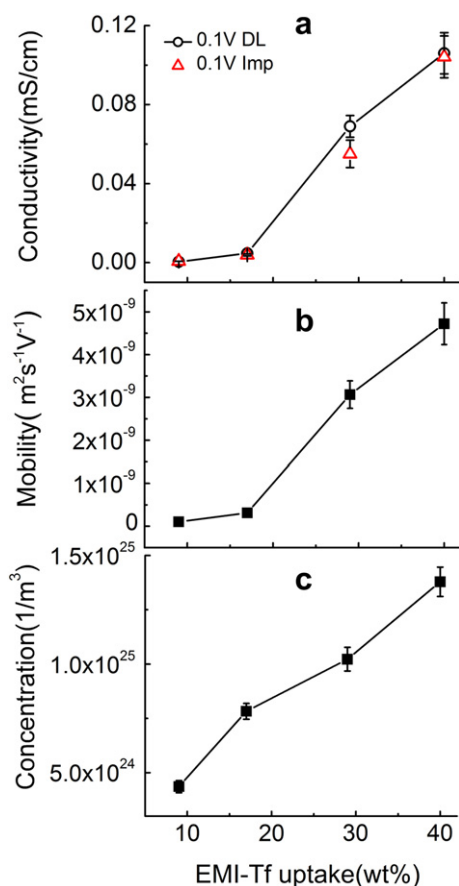


Fig. 5. The transient current and numerical fitting for Aquivion membrane with 40wt% EMI-Tf uptake when a voltage step from 0 V to 8 different voltages is applied.



**Fig. 6.** (a) Conductivity (b) mobility and (c) mobile charge concentration as a function of EMI-Tf uptake in Aquivion membrane when a voltage step from 0 V to 100 mV is applied.

Results for the conductivity  $\sigma$ , free charge concentration  $n$  and mobility  $\mu$  as a function of IL uptake are presented in Fig. 6. The data reveals that the mobile ion concentration increases almost linearly with the IL uptake. In contrast, the conductivity and mobility display abrupt changes with the increase of IL uptake, revealing a critical uptake of EMI-Tf in the Aquivion (EW790) membrane  $\sim 29$  wt% (0.88 mol EMI-Tf/mol of  $\text{SO}_3^-$ ) above which the conductivity and mobility dramatically increase. In the study of IL uptake in Nafion membranes, Leo et al. found that the critical uptake is closely related to the minimum amount of IL required to displace the counter ions away from the exchange sites [17]. Above the critical uptake, the ionomers form percolation pathways for charges to transport and also there are more mobile ions that do not strongly interact with exchange sites. Therefore, with the increase of IL content the mobile charge concentration increase and the mobility and conductivity are enhanced. It is noted that the critical uptake of EMI-Tf in Aquivion is higher than that of EMI-Tf in Nafion membrane (23 wt%,  $\sim 1$  mol of EMI-Tf/mol of  $\text{SO}_3^-$ ), which may be due to that Aquivion (EW790) has a higher side chain density than Nafion (EW1100). With 40wt% of EMI-Tf uptake, at which a substantial actuation is observed in both Aquivion and Nafion membranes, the conductivities of Aquivion and Nafion membranes are close to each other (Aquivion 0.11 mS/cm, Nafion 0.21 mS/cm).

In Fig. 6(a),  $\sigma$  determined from the ac impedance curve (Nyquist plot, Fig. 4) under 0.1 V is also shown. The two methods yield nearly identical values of  $\sigma$ , indicating that both methods can be used to determine  $\sigma$  at low voltage. On the other hand, at high voltage, the ac electric impedance method to determine  $\sigma$  may become difficult

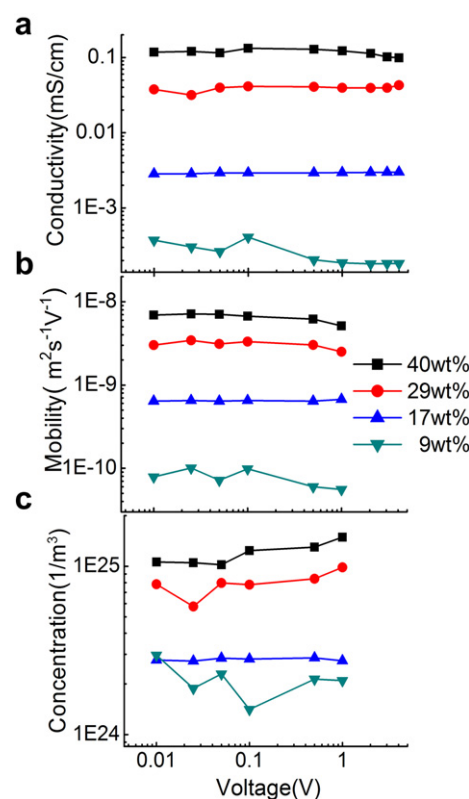


**Fig. 7.** (a) Conductivity (b) mobility (c) mobile charge concentration of Aquivion membrane with different uptake under different applied voltage step.

due to non-linear electric response and even possible heating in the samples.

Fig. 7(a) presents the conductivity  $\sigma$  of Aquivion membrane with different EMI-Tf uptake as a function of voltage, up to 4 V. The data shows that within the experimental error ( $\pm 10\%$ ),  $\sigma$  does not change with applied voltage for all EMI-Tf uptakes. Fig. 7(b) and (c) are the mobility and mobile ion concentration vs. applied voltage, measured up to 1 V, and within the experimental error, no systematical variation with applied voltage was observed. These results indicate that the double layer charging time  $\tau_{\text{DL}}$  as well as the overall charge dynamics do not change much with voltage, below 1 V. At voltages higher than 1 V, the data shown in Fig. 5 reveal that overall charging process becomes slower. This might be caused by the increased dissociation of ion clusters in EMI-Tf at high voltages.

In Table 1, we summarize the mobile ion concentration in Fig. 7 (c) and compare them with the total ion concentration from the EMI-Tf. As can be seen, only about 0.5%–0.55% of EMI-Tf is dissociated for all the ILs uptakes below 1 V. This low dissociation ratio of ionic liquid may due to the fact that the Bjerrum length of EMI-Tf is larger than the ion pair distance and hence the Coulomb force dominates [36,37].

**Table 1**

The measured mobile charge concentration, the calculated total charges and dissociation ratio for different uptake of EMI-Tf.

wt%	Measured charges ( $1/\text{m}^3$ )	Total charges ( $1/\text{m}^3$ )	Dissociation ratio
40	$1.37\text{E} + 25$	$2.48\text{E} + 27$	$5.55\text{E} - 03$
29	$1.03\text{E} + 25$	$2.04\text{E} + 27$	$5.04\text{E} - 03$
17	$7.82\text{E} + 24$	$1.43\text{E} + 27$	$5.47\text{E} - 03$
9	$4.35\text{E} + 24$	$8.58\text{E} + 26$	$5.08\text{E} - 03$

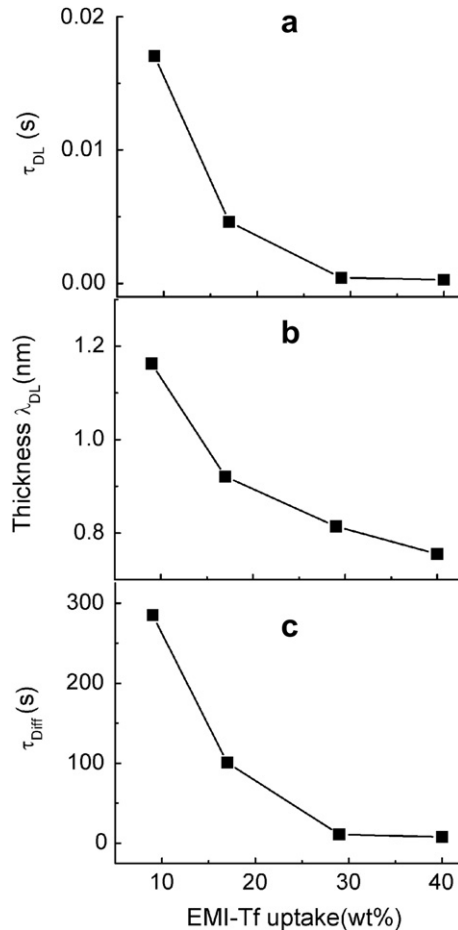


**Fig. 8.** Double layer (a) time constant (b) thickness and (c) diffusion time constant as a function of EMI-Tf uptake when a voltage step from 0 V to 100 mV is applied.

### 3.2. Charge storage in and electromechanical actuation of Aquivion membranes swelled with of EMI-Tf

Fig. 8 presents  $\tau_{DL}$  (Fig. 8(a)),  $\lambda_{DL}$  (Fig. 8(b)), and  $\tau = d^2/(4D)$  (Fig. 8(c)) vs. ILs uptakes. The high conductivity in the membrane above the critical uptake results in a very fast charging time of the double layer,  $\tau_{DL} < 0.5$  ms. The Debye length  $\lambda_{DL}$  is  $\sim 1$  nm due to the high free ion concentration and becomes small with increasing EMI-Tf uptake. On the other hand, the bulk diffusion time constant  $\tau_D = d^2/(4D)$ , which is the time needed for charges to diffuse from bulk to diffuse layer, is still around  $\sim 10$  s even above the critical uptake. As will be shown later, for the membrane bending actuators, the actuation is mainly determined by the diffusion charges that stored near the electrodes. Hence by reducing  $d$ , the membrane thickness, the bending action time can be reduced significantly.

In Fig. 9(a), we present the charge stored vs. time in the Aquivion membrane which has 40 wt% of EMI-Tf uptake under different step voltages and shows a substantial bending actuation at  $>3$  V (see Fig. 1(c)). From the data and using the  $\tau_{DL}$  and  $\tau_D$  determined at voltages below 1 V, we plot in Fig. 9(b) the charge stored at the time  $\tau_{DL}$  and  $\tau_D$  as a function of applied voltage. The data shows that the charge stored at  $\tau_{DL}$  increases linearly with applied voltage. In other words, the ratio between charge stored and V, which is the overall capacitance, does not change with applied step voltage, or the differential capacitance, defined as  $\Delta Q/\Delta V$ , for the electric double layer here does not change with applied voltage up to the

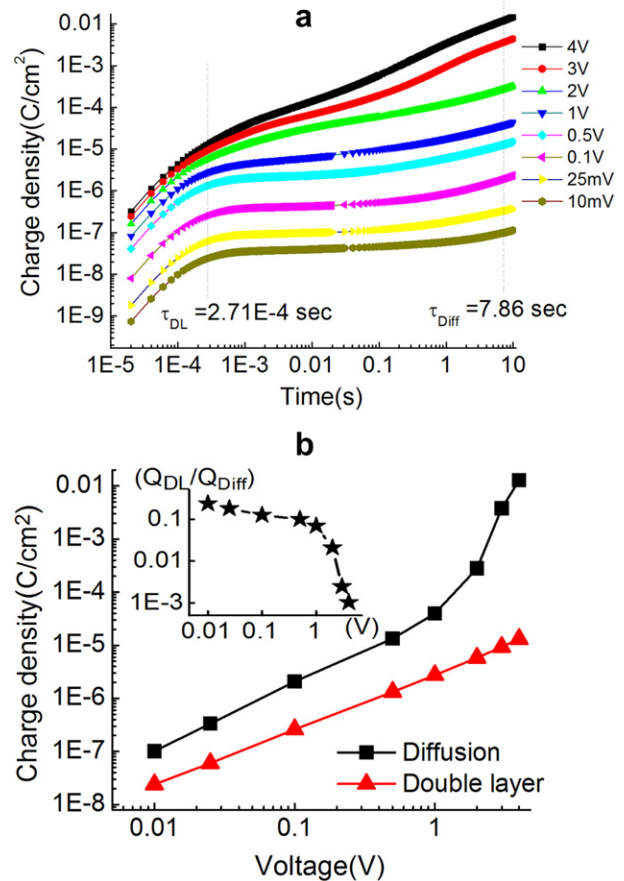


**Fig. 9.** (a) Charge storage with time (40wt% uptake) under different applied voltage step (10 mV to 4 V). (b) storage of double layer charge and diffusion charge under different applied voltage step. The inset graph is the charge ratio ( $Q_{DL}/Q_{Diff}$ ) as a function of applied voltage step.

highest voltage measured (4 V). On the other hand, the charge stored at  $t = \tau_D$  increases linearly with voltage up to 1 V. Beyond that, a much faster (non-linear) increases with applied voltage is observed, which causes a seemingly slowdown of the charge process in Fig. 9(a). This may be caused by the charge dissociation at high voltage, which leads to high leakage current.

Fig. 10 is the charge stored in the Aquivion membrane with different EMI-Tf uptake vs. time after the application of a 4 V step

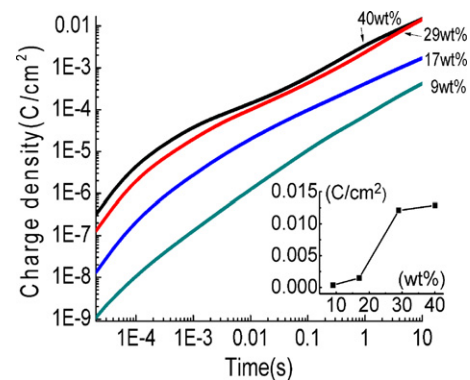


**Fig. 10.** Charge storage as a function of time for Aquivion membranes with four different uptakes when a voltage step from 0 to 4 V is applied. The inset shows the charge storage at 7.8 s (diffusion time of 40wt% uptake) for different uptakes.

voltage (at  $t = 0$ ). The data shows that the stored charge increases with ILs uptake up to the critical uptake (29wt%). Above that, the rate of increase of the stored charge with ILs uptake becomes much smaller. This is also true for the diffusion time  $\tau_D$ , which does not show much change with the ILs uptake above the critical uptake. Hence, above the critical uptake, further increase in the ILs uptake will not cause marked increase in the charging speed, charge storage, and, consequently, the bending actuation of the Aquivion membranes.

The electromechanical response of the Aquivion membrane was measured (see Fig. 2(c)) and compared with that of the Nafion membrane with the same 40 wt% of EMI-Tf uptake, far above the critical uptake in both ionomers. The measured conductivities of these two membranes are similar (Aquivion 0.11 mS/cm, Nafion 0.21 mS/cm). The slightly larger  $\sigma$  in Nafion membrane indicates an easier ion transport path resulting from less coupling between ions and polymer matrix. Presented in Fig. 11(a) is the curvature ( $1/R$  where  $R$  is the radius) of the bending membrane actuators vs. time after the application of a step voltage of 4 V. The strain near the two electrodes (anode and cathode) is proportional to the curvature ( $1/R$ ) [14]. The data reveals several interesting features: (i) the initial slope of the curvatures of the two ionomers is nearly the same, indicating similar actuation speed of the two membranes; (ii) the maximum positive curvature of the Aquivion membrane is higher than that of the Nafion, indicating higher strain generated by the positive charges; (iii) the maximum negative curvature of the Aquivion is also much larger than that of Nafion (higher negative strain generated by negative charges in Aquivion). As shown in earlier publications, the presence of both cations and anions in the membrane may cause cancellation in bending actuation [14]. For example, in Fig. 2(b), if positive charges at the cathode and negative charges at the anode generate same value of strain at the same time, there will be no bending actuation. Due to different effective

sizes of the positive charges and negative charges (cations and anions may form clusters rather than bare ions in the processes of ion transport and storage), the strains generated by the positive and negative charges are different, causing bending actuation as we observed here. The results in Fig. 11(a) indicate that the ions in Aquivion can generate much more bending strain, compared with that of Nafion membrane. Moreover, the transient strain response data also reveals that the transport time for positive charges and negative charges in the Aquivion is different (negative charges are slower), causing observed time-dependent bending actuation [14].

Fig. 11(b) shows the charge stored in the two membranes under the same electric conditions as in Fig. 11(a). Combining the data in the two figures indicates that the bending strain generated per charge is much large in Aquivion than that in Nafion. The difference in the strain generation is likely caused by the weaker elastic coupling of the excess ions to the membrane backbones in Nafion, due to longer flexible side chains, compared with that of Aquivion. As shown in Kreuer's study [25], from the SAXS, the average width of hydrophilic channels of Aquivion is smaller and did not increase as much as that of Nafion with the increasing of water uptake. This implies that by reducing these soft side chain lengths, the excess ions in the ionomers will couple more effectively with the backbones to generate strain of the membranes.

#### 4. Conclusion

In conclusion, a time domain approach is applied to study the charge dynamics in an ionomer membrane (Aquivion) swelled with ILs which, when combined with recently developed theoretical works, allows quantitative analysis of the membrane performance under real device working voltages ( $>1$  V). A critical uptake (29wt%) of EMI-Tf in Aquivion membrane is observed, above which the charge mobility and mobile charge concentration increase markedly. It is also observed that the dissociation ratio of the swollen EMI-Tf remains at 0.5% for all IL uptakes. The experimental results reveal that the charge transport behavior does not change with applied voltage. Furthermore, it was found that the actuation of the ionic polymer membrane actuator is dominated by slow diffusion charges, which time constant scales with square of the membrane thickness. Therefore, by reducing the membrane thickness, the actuation speed can be increased. A comparison of the actuation strain shows that the short side chain Aquivion exhibits a better electromechanical coupling with ions than that of the long side chain Nafion, while the actuation speeds of the two membranes under same electrical stimulus are the same. Therefore, short side chain ionomers are preferred for ionic polymer actuator applications.

This material is based upon work supported in part by the U.S. Army Research Office under Grant No. W911NF-07-1-0452 Ionic Liquids in Electro-Active Devices (ILEAD) MURI, by NSF under Grant No. CMMI 0709333, and by NIH under Grant No. R01-EY018387-02. The authors thank Ralph Colby and Sheng Liu for many stimulating discussions.

#### References

- [1] Lu W, Fadeev AG, Qi BH, Smela E, Mattes BR, Ding J, et al. *Science* 2002;297(5583):983–7.
- [2] McEwen AB, Ngo HL, LeCompte K, Goldman JL. *Journal of the Electrochemical Society* 1999;146(5):1687–95.
- [3] Ue M, Takeda M, Toriumi A, Kominato A, Hagiwara R, Ito Y. *Journal of the Electrochemical Society* 2003;150(4):A499–502.
- [4] Fukumoto K, Yoshizawa M, Ohno H. *Journal of the American Chemical Society* 2005;127(8):2398–9.
- [5] Huddleston JG, Visser AE, Reichert WM, Willauer HD, Broker GA, Rogers RD. *Green Chemistry* 2001;3(4):156–64.
- [6] Tokuda H, Hayamizu K, Ishii K, Abu Bin Hasan Susan M, Watanabe M. *Journal of Physical Chemistry B* 2004;108(42):16593–600.

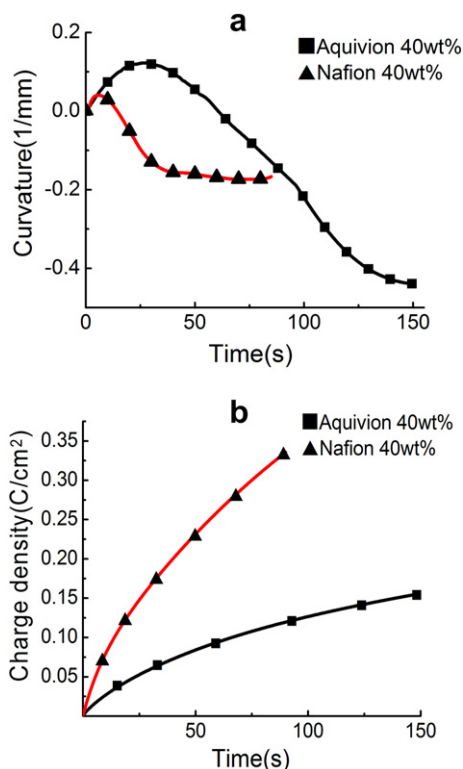
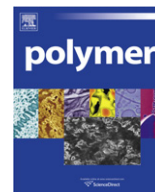


Fig. 11. (a) The curvature change with time (b) the accumulated charge/area of a 62μm thick of Aquivion and Nafion membrane when a voltage step from 0 V to 4 V is applied.

- [7] Tokuda H, Hayamizu K, Ishii K, Susan MABH, Watanabe M. *Journal of Physical Chemistry B* 2005;109(13):6103–10.
- [8] Tokuda H, Ishii K, Susan MABH, Tsuzuki S, Hayamizu K, Watanabe M. *Journal of Physical Chemistry B* 2006;110(6):2833–9.
- [9] Galinski M, Lewandowski A, Stepniak I. *Electrochimica Acta* 2006;51(26):5567–80.
- [10] Ono S, Seki S, Hirahara R, Tominari Y, Takeya J. *Applied Physics Letters* 2008;92(10).
- [11] Bar-Cohen Y, Zhang QM. *Mrs Bulletin* 2008;33(3):173–81.
- [12] Kim D, Kim KJ, Tak Y. *Applied Physics Letters* 2007;90(18).
- [13] Bennett MD, Leo DJ. *Sensors and Actuators A-Physical* 2004;115(1):79–90.
- [14] Liu Y, Liu S, Lin JH, Wang D, Jain V, Montazami R, et al. *Applied Physics Letters* 2010;96(22).
- [15] Liu S, Liu WJ, Liu Y, Lin JH, Zhou X, Janik MJ, et al. *Polymer International* 2010;59(3):321–8.
- [16] Akle BJ, Leo DJ, Hickner MA, McGrath JE. *Journal of Materials Science* 2005;40(14):3715–24.
- [17] Bennett MD, Leo DJ, Wilkes GL, Beyer FL, Pechar TW. *Polymer* 2006;47(19):6782–96.
- [18] Watanabe M, Shirai H, Hirai T. *Journal of Applied Physics* 2001;90(12):6316–20.
- [19] Watanabe M, Shirai H, Hirai T. *Journal of Applied Physics* 2002;92(8):4631–7.
- [20] Mauritz KA, Moore RB. *Chemical Reviews* 2004;104(10):4535–85.
- [21] Hsu WY, Gierke TD. *Journal of Membrane Science* 1983;13(3):307–26.
- [22] Ghielmi A, Vaccarano P, Troglia C, Arcella V. *Journal of Power Sources* 2005;145(2):108–15.
- [23] Jalani NH, Datta R. *Journal of Membrane Science* 2005;264(1–2):167–75.
- [24] Halim J, Buchi FN, Haas O, Stamm M, Scherer GG. *Electrochimica Acta* 1994;39(8–9):1303–7.
- [25] Kreuer KD, Schuster M, Obliers B, Diat O, Traub U, Fuchs A, et al. *Journal of Power Sources* 2008;178(2):499–509.
- [26] Bazant MZ, Thornton K, Ajdari A. *Physical Review E* 2004;70(2).
- [27] Kilic MS, Bazant MZ, Ajdari A. *Physical Review E* 2007;75(2).
- [28] Beunis F, Strubbe F, Marescaux M, Beeckman J, Neyts K, Verschueren ARM. *Physical Review E* 2008;78(1).
- [29] Strubbe F, Verschueren ARM, Schlangen LJM, Beunis F, Neyts K. *Journal of Colloid and Interface Science* 2006;300(1):396–403.
- [30] Beunis F, Strubbe F, Neyts K, Verschueren ARM. *Applied Physics Letters* 2007;90(18).
- [31] Marescaux M, Beunis F, Strubbe F, Verboven B, Neyts K. *Physical Review E* 2009;79(1).
- [32] Wakai C, Oleinikova A, Ott M, Weingartner H. *Journal of Physical Chemistry B* 2005;109(36):17028–30.
- [33] Serghei A, Tress M, Sangoro JR, Kremer F. *Physical Review B* 2009;80(18).
- [34] Krause C, Sangoro JR, Iacob C, Kremer F. *Journal of Physical Chemistry B* 2010;114(1):382–6.
- [35] Lockett V, Sedev R, Ralston J, Horne M, Rodopoulos T. *Journal of Physical Chemistry C* 2008;112(19):7486–95.
- [36] Klein RJ, Zhang SH, Dou S, Jones BH, Colby RH, Runt J. *Journal of Chemical Physics* 2006;124(14).
- [37] Fragiadakis D, Dou S, Colby RH, Runt J. *Journal of Chemical Physics* 2009;130(6).



# Anaerobic biodegradation of the microbial copolymer poly(3-hydroxybutyrate-co-3-hydroxyhexanoate): Effects of comonomer content, processing history, and semi-crystalline morphology

Margaret-Catherine Morse<sup>a,1</sup>, Qi Liao<sup>b,1</sup>, Craig S. Criddle<sup>a,\*</sup>, Curtis W. Frank<sup>b,\*\*</sup>

<sup>a</sup> Department of Civil and Environmental Engineering, Stanford University, Stanford, CA 94305, USA

<sup>b</sup> Department of Chemical Engineering, Stanford University, Stanford, CA 94305, USA

## ARTICLE INFO

### Article history:

Received 6 August 2010  
Received in revised form  
8 November 2010  
Accepted 13 November 2010  
Available online 23 November 2010

### Keywords:

Biodegradable polymer  
Polyhydroxyalkanoates  
Polymer morphology

## ABSTRACT

Films of poly(3-hydroxybutyrate-co-3-hydroxyhexanoate) (P3HB-co-3HHx) containing 3.8–10 mol% of 3-hydroxyhexanoate (3HHx) comonomer were subjected to anaerobic biodegradation to explore the effects of copolymer composition, crystallinity, and morphology on biodegradation. As biodegradation proceeded, samples with higher HHx fraction tended to have faster weight loss; on Day 7 of the degradation experiment, P3HB-co-10 mol%-3HHx lost 80% of its original weight, while P3HB-co-3.8 mol%-3HHx lost only 28%. Scanning electron microscopy (SEM) images revealed that the anaerobic biodegradation proceeded at the surface of the samples, with preferential erosion of the amorphous regions, exposing the crystalline spherulites formed inside the copolymer films. It was observed that copolymers with higher HHx fraction had smaller diameter spherulites, ranging from roughly 40 μm for P3HB-co-3.8 mol%-3HHx to 10 μm for P3HB-co-10 mol%-3HHx. A banded spherulite morphology was observed for P3HB-co-6.9 mol%-3HHx and P3HB-co-10 mol%-3HHx, with much wider band spacing (2 μm) for the former than the latter (0.3 μm). Different thermal history seemed to affect the morphological properties and, thus, the biodegradability of the P3HB-co-3HHx samples as well. When comparing copolymers with the same copolymer composition, P3HB-co-3HHx annealed at 70 °C had 5–30% more weight loss after the same duration of incubation in active sludge compared to the quenched samples. We suggest that annealing of P3HB-co-3HHx likely induces void formation in the semi-crystalline structure, facilitating the movement of water or perhaps enzymes to a higher degree of penetration into the sample and subsequently enhancing microbial degradation.

© 2010 Elsevier Ltd. All rights reserved.

## 1. Introduction

Poly(3-hydroxybutyrate) (P3HB), a microbially synthesized and completely biodegradable polymer, is one possible “green” alternative for petroleum-based plastics. Previous studies have confirmed its biodegradability under aerobic conditions in salt-water, freshwater, canal water, and household compost [1]; soil [2]; earthworm compost [3]; and by *Comamonas* sp. and *P. lemoignei* [4]. Anaerobic biodegradation studies have also been conducted with anaerobic digester sludge [5], [6] and *PHB depolymerase* [7].

Because homopolymer P3HB is brittle [10], comonomers are often incorporated to obtain copolymers that may exhibit improved processability and performance. The biodegradability of these copolymers has been compared to that of the homopolymer. For instance, copolymers of 3-hydroxybutyrate (3HB) with 3-hydroxyvalerate (3HV), P3HB-co-3HV, were found to degrade faster in soil than the homopolymer [2], and there was more biofilm growth on P3HB-co-3HV exposed to garden soil compared to P3HB [8].

More recently, new PHA copolymers have been developed that consist mainly of 3HB and a small fraction of randomly distributed comonomer 3-hydroxyhexanoate (3HHx). It was found that, if incorporated as a comonomer with 3HB, 3HHx is much more effective than 3HV in reducing the melting temperature and enhancing the ductility of the material [9,10]. Copolymers of 3HB with 3HHx, P3HB-co-3HHx, appear more flexible than P3HB or P3HB-co-3HV, exhibiting improved elongation at break [10] and effective processing at lower temperatures [11]. With respect to its

\* Corresponding author. Tel.: +1 650 723 9032.

\*\* Corresponding author. Tel.: +1 650 723 4573; fax: +1 650 723 9780.

E-mail addresses: [crriddle@stanford.edu](mailto:crcriddle@stanford.edu) (C.S. Criddle), [curt.frank@stanford.edu](mailto:curt.frank@stanford.edu) (C.W. Frank).

<sup>1</sup> These authors contributed equally to this work.

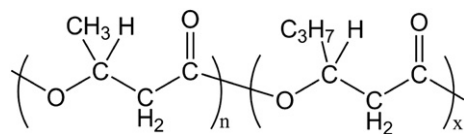


Fig. 1. Molecular structure of P3HB-co-3HHx copolymer.

biodegradability, P3HB-co-3HHx was found to have faster weight loss upon exposure to *PHB depolymerase*, but the relationship between the erosion rate and the copolymer composition was still unclear. Moreover, a systematic study of the biodegradation of P3HB-co-3HHx copolymers in a microbially active environment that mimics the natural environment, e.g., activated sludge, is still missing. We believe that before its use can become widespread, additional information is needed on the relationship between biodegradation characteristics of P3HB-co-3HHx and the semi-crystalline morphology.

In this paper, we have investigated the anaerobic biodegradation of P3HB-co-3HHx with varying fraction of HHx in activated sludge. We studied the effects of copolymer composition and thermal processing history on solid-state properties, such as thermal transitions and morphology, and their subsequent influence on the biodegradability. We also evaluated the surface morphological characteristics of P3HB-co-3HHx samples that are partially degraded. We observed that microbial activity tends to preferentially excavate amorphous regions, thus revealing the more degradation-resistant morphological features in the semi-crystalline spherulites.

## 2. Experimental

### 2.1. Materials

The poly(3-hydroxybutyrate-co-3-hydroxyhexanoate) copolymers (P3HB-co-3HHx) used in this work were provided by the Procter & Gamble Company. These biodegradable random copolymers consisted primarily of 3-hydroxybutyrate (3HB) with a small fraction of randomly distributed 3-hydroxyhexanoate (3HHx), as shown in Fig. 1.

Samples with biomass contamination were purified by dissolution in hot chloroform, followed by separation of the insoluble impurities and precipitation in ethanol. The resulting white polymer precipitant was filtered and dried under vacuum for at least 72 h prior to use. Weight-average molecular weight,  $M_w$ , and number-average molecular weight,  $M_n$ , of the P3HB-co-3HHx copolymers were measured by gel permeation chromatography (GPC) on a Viscotek GPCMax system equipped with refractive index detector. Tetrahydrofuran (THF) was used as a solvent. All experiments were carried out at room temperature at a flow rate of 1 ml/min. The measured refractive index versus the elution volume was transformed to molecular weight data using a polystyrene standard for calibration. Table 1 summarizes the P3HB-co-3HHx materials evaluated in this study, including the molecular weight and the polydispersity index ( $M_w/M_n$ ) [12].

### 2.2. Preparation of biodegradable P3HB-co-3HHx films

Powders of P3HB-co-3HHx were pressed into thin film specimens of approximately 0.3 mm thickness using a Carver hydraulic hot-press. Roughly 4 g of powder were placed between the aluminum plates of the Carver press, which had been preheated to 155 °C. The lower plate was raised until the powder just touched the bottom of the upper plate, and the polymer was allowed to melt freely for 0.5 min. The plates were then brought closer together so as to achieve a pressure of 200 kPa across the plates. Samples were held at this pressure for 2 min, removed from the hot-press, and quenched between two cold aluminum plates at room temperature (in air). The resulting films were allowed to crystallize under a slight pressure at room temperature for three days prior to their use in biodegradation studies. To obtain P3HB-co-3HHx films of the same chemical composition but different thermal processing history, some hot-pressed samples were placed immediately in an oven set at 70 °C for 7 days for thermal annealing [13].

### 2.3. Thermal and morphological properties of degraded film specimens

Thermal transitions and heat flow from P3HB-co-3HHx films were recorded with a TA Instruments Q100 Modulated Differential Scanning Calorimeter at a nitrogen flow of 50 mL/min. Samples at different degradation stages were cut and sealed in aluminum pans and heated from –50 to 185 °C at a heating rate of 10 °C/min. The change in heat capacity during the glass transition,  $\Delta C_p$ , was taken as the height of the step on the heat flow curve. The glass transition temperature,  $T_g$ , was taken as the midpoint temperature of this heat capacity change. The melting temperature,  $T_m$ , and enthalpy of fusion,  $\Delta H_m$ , were determined from the endothermic peaks.

SAXS experiments were performed on beamline 1–4 of the Stanford Synchrotron Radiation Lightsource (SSRL), which has a spot size of approximately  $0.25 \times 1 \text{ mm}^2$ . The wavelength of the incident X-ray beam is 0.149 nm, and the scattering wave vector ranges from  $0.1 \text{ nm}^{-1}$  to  $1.2 \text{ nm}^{-1}$ . Background and parasitic scattering were determined by separate measurements on an empty holder and were later subtracted from the scattering data of the samples. The exposure time was 5 min for all P3HB-co-3HHx samples.

### 2.4. Anaerobic biodegradation assays

Anaerobic biodegradation experiments were performed in simple, visually monitored microcosms containing anaerobic biosolids from an anaerobic digester at the City of San Jose wastewater treatment plant. The method is described in detail elsewhere [14]. Briefly, test microcosms were prepared by weighing out small rectangular pieces (approximately 0.07 g) of thin P3HB-co-3HHx films (approximately 0.3 mm thick), placing each piece in a glass graduated cylinder (50 mL, Fisher 20040), then filling all of the test cylinders with biosolids (diluted 1:1 with warm tap water). Control microcosms were prepared with diluted biosolids only. Each filled cylinder was capped with a one-hole rubber stopper (Fisher 14-135G size 5), inverted in a cup of water, and incubated in a constant temperature chamber at 37 °C. During incubation, biogas

Table 1  
Name and molecular compositions of PHA materials used [12].

Sample name	Polymer	$M_w (\times 10^3)$	$M_w/M_n$
P3HB-co-3HHx3.8	Poly(3-hydroxybutyrate-co-3.8mol% 3-hydroxyhexanoate)	659	2.99
P3HB-co-3HHx4.6	Poly(3-hydroxybutyrate-co-4.6mol% 3-hydroxyhexanoate)	658	2.87
P3HB-co-3HHx6.9	Poly(3-hydroxybutyrate-co-6.9mol% 3-hydroxyhexanoate)	723	2.55
P3HB-co-3HHx10	Poly(3-hydroxybutyrate-co-10mol% 3-hydroxyhexanoate)	312	2.30

accumulated at the top of the cylinders, displacing anaerobic fluid out the hole in the stopper. Markings on the graduated cylinder enabled quantitative monitoring of biogas production.

Biogas production was monitored daily for 12 days. One sample of each copolymer was removed at 10 different time points to assess changes in physical properties. These samples were collected (Tyler Standard Sieve 9 meshes to the inch), rinsed with deionized water and dried under vacuum at room temperature until the weights stabilized (24 h). Weight loss was computed as the percentage decrease from the initial sample weight:

$$\%wt \text{ Loss} = \left[ \frac{(wt_{\text{initial}} - wt_{\text{biodegraded}})}{wt_{\text{initial}}} \right] \times 100\% \quad (1)$$

After being collected, dried and weighed, subsamples of degraded specimens were cut for microscopic investigation. Excised samples were attached to an SEM specimen mount with hot glue and coated with Au<sub>60</sub>Pt<sub>40</sub> alloy using a Gressington sputter coater operated at a current of 20 mA for 30 s. The surface topology was then examined using a Scanning Electron Microscope (SEM) (FEI XL30 Sirion with FEG source, EDX detector).

### 3. Results

#### 3.1. Thermal properties and semi-crystalline morphology of P3HB-co-3HHx and their dependence on composition and thermal history

Fig. 2 illustrates the melting behavior of P3HB-co-3HHx films, as evaluated with DSC at a constant heating rate of 10 °C/min. All P3HB-co-3HHx samples displayed multiple endothermic melting peaks over a broad temperature range. The isothermally crystallized samples (b, d, f, and h in Fig. 2) have three endothermic peaks, denoted as I, II, and III in the sequence of increasing temperature. Endotherm I, which is only observed for annealed samples and is seen as a “shoulder” on the heat scan curves, is a pseudo-crystalline phase [13]. It is believed that Endotherm II corresponds to the melting of the crystals formed during the crystallization of P3HB-co-3HHx that recrystallize during the heating scan and subsequently

**Table 2**  
Melting and Crystallization Properties of P3HB-co-3HHx Films.

Prep. method	Polymer	T <sub>I</sub>	T <sub>II</sub>	T <sub>III</sub>	χ <sub>c</sub>	l (nm)
Quenched	P3HB-co-3HHx3.8	–	138.0	151.4	0.432	7.6
	P3HB-co-3HHx4.6	–	133.7	149.0	0.406	7.1
	P3HB-co-3HHx6.9	–	123.0	139.5	0.350	6.8
	P3HB-co-3HHx10	–	108.5	129.9	0.291	6.8
Annealed	P3HB-co-3HHx3.8	94.6	141.7	152.0	0.481	7.7
	P3HB-co-3HHx4.6	92.1	138.0	149.2	0.446	7.9
	P3HB-co-3HHx6.9	88.5	131.0	143.9	0.436	8.2
	P3HB-co-3HHx10	90.4	125.2	136.9	0.338	8.9

remelt to give Endotherm III [15]. Similar multiple melting behavior of P3HB-co-3HHx has been observed and reported by other researchers [16,17]. Table 2 summarizes T<sub>I</sub>, the onset temperature of the “shoulder” in the endothermic heat flow, as well as T<sub>II</sub> and T<sub>III</sub>, the highest points of the endothermic peaks II and III. Also included in Table 2 is the overall degree of crystallization (χ<sub>c</sub>) for each sample. Crystallinity of the P3HB-co-3HHx is calculated by dividing the enthalpy of fusion of the copolymer by the thermodynamic melting enthalpy of homopolymer P3HB [10,18,19], since the 3HHx was found to not crystallize together with 3HB segments [13]:

$$\chi_c = \Delta H_m(\text{PHA}) / \Delta H_m^0(\text{P3HB}) \quad (2)$$

where ΔH<sub>m</sub><sup>0</sup>(P3HB) is the thermodynamic melting enthalpy per gram of P3HB (146.6 J/g).

In general, nearly all of the endothermic peaks shift to lower temperatures as the 3HHx content increases, but T<sub>I</sub> varies the least among the four annealed P3HB-co-3HHxs, remaining 18–25 °C above the annealing temperature (70 °C). Hu et al. [13] previously reported that if the annealing temperature is increased, T<sub>I</sub> tends to increase accordingly. Thus, it was concluded that T<sub>I</sub> is an annealing peak, which is an endothermic relaxation of the crystal/amorphous region interface during annealing [20]. T<sub>II</sub> and T<sub>III</sub>, on the other hand, decrease significantly and monotonically with increasing 3HHx content. It is also seen that χ<sub>c</sub> decreases for these copolymers with increasing content of 3HHx, as expected.

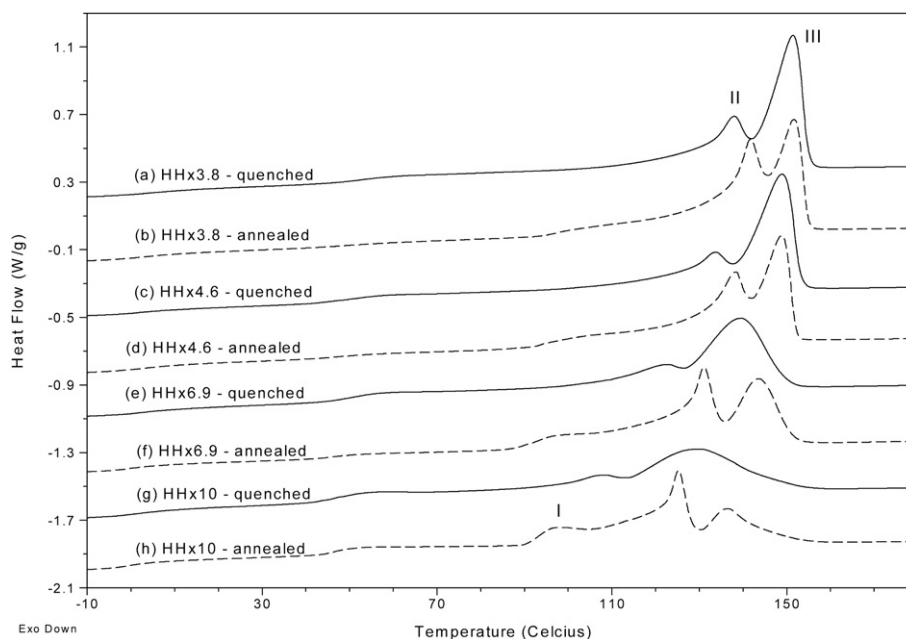


**Fig. 2.** Melting curves for P3HB-co-3HHx films: solid lines, samples quenched from molten state to room temperature: (a) P3HB-co-3HHx3.8, (c) P3HB-co-3HHx4.6, (e) P3HB-co-3HHx 6.9, and (g) P3HB-co-3HHx10; dashed lines, samples thermally annealed for 7 days at 70 °C: (b) P3HB-co-3HHx3.8, (d) P3HB-co-3HHx4.6, (f) P3HBco-3HHx 6.9, and (h) P3HB-co-3HHx10. I, II, and III are the respective multiple melting peaks in the sequence of increasing temperature.



The thermal processing history also influenced the melting characteristics of samples. Endotherm I was not found for quenched samples, so no value was assigned to  $T_i$ .  $T_{II}$  increased notably for annealed samples compared to quenched samples with the same 3HHx content, while  $T_{III}$  was nearly the same, annealed versus quenched, for P3HB-co-3HHx3.8 and 4.6, and increased only slightly for the 6.9 and 10 samples. Moreover, the peak area under Endotherm II increased, while that of Endotherm III decreased with annealing. The overall crystallinity also increased after annealing. These observations suggest that after thermal annealing P3HB-co-3HHx polymer chains obtain more ordered packing and the fraction of imperfect crystalline domains is decreased, which is well-known behavior for semi-crystalline polymers [21].

In addition to the bulk crystallinity measurement, morphology of P3HB-co-3HHx films was investigated on micro-length scales using small angle X-ray scattering (SAXS). Fig. 3 shows the SAXS data of different P3HB-co-3HHx, especially comparing the scattering profile of the annealed sample to the respective quenched sample. A scattering intensity peak, although close to the cut-off of the scattering vector magnitude,  $q$ , of the SAXS measurement, was found for each P3HB-co-3HHx sample. The average repeat distance in the semi-crystalline structure, referred to as the long period,  $l$ , corresponding to the spacing between crystalline lamellae, was calculated from the peak in the SAXS profile using Bragg's law:

$$l = \lambda / 2 \sin \theta = 2\pi / q_{\text{peak}} \quad (3)$$

where  $\theta$  is half the scattering angle,  $\lambda$  is the X-ray wavelength, and  $q_{\text{peak}}$  is the scattering vector magnitude at the intensity peak. The long periods of each P3HB-co-3HHx sample, quenched or annealed, are listed and compared in Table 2. Samples annealed at 70 °C have longer periods than the quenched samples, indicating the occurrence of lamellar thickening during annealing [22,23].

In summary, the thermal properties, crystallinity, and microscale morphology for P3HB-co-3HHx are highly dependent on the copolymer composition and thermal processing history. Decreases in melting temperature and overall crystallinity occur with increase in 3HHx content. Given the same copolymer composition, the annealed P3HB-co-3HHx sample has higher crystallinity compared to the quenched counterpart. In addition, higher  $T_m$  and narrower temperature range of melting DSC endotherms of the annealed compared to the quenched P3HB-co-3HHx suggests an increase in lamellar thickness and uniformity. Moreover, SAXS results confirmed an increase in lamellar thickness after thermal annealing for the P3HB-co-3HHx sample with the same copolymer composition.

### 3.2. Biodegradation of P3HB-co-3HHx and the surface morphology of the degraded sample

The biodegradation rate of PHAs is known to be influenced by the crystallinity and thickness of the crystalline lamellae [15]. Hence, anaerobic biodegradation of P3HB-co-3HHx having different degree of crystallinity and lamellar thickness was expected to show

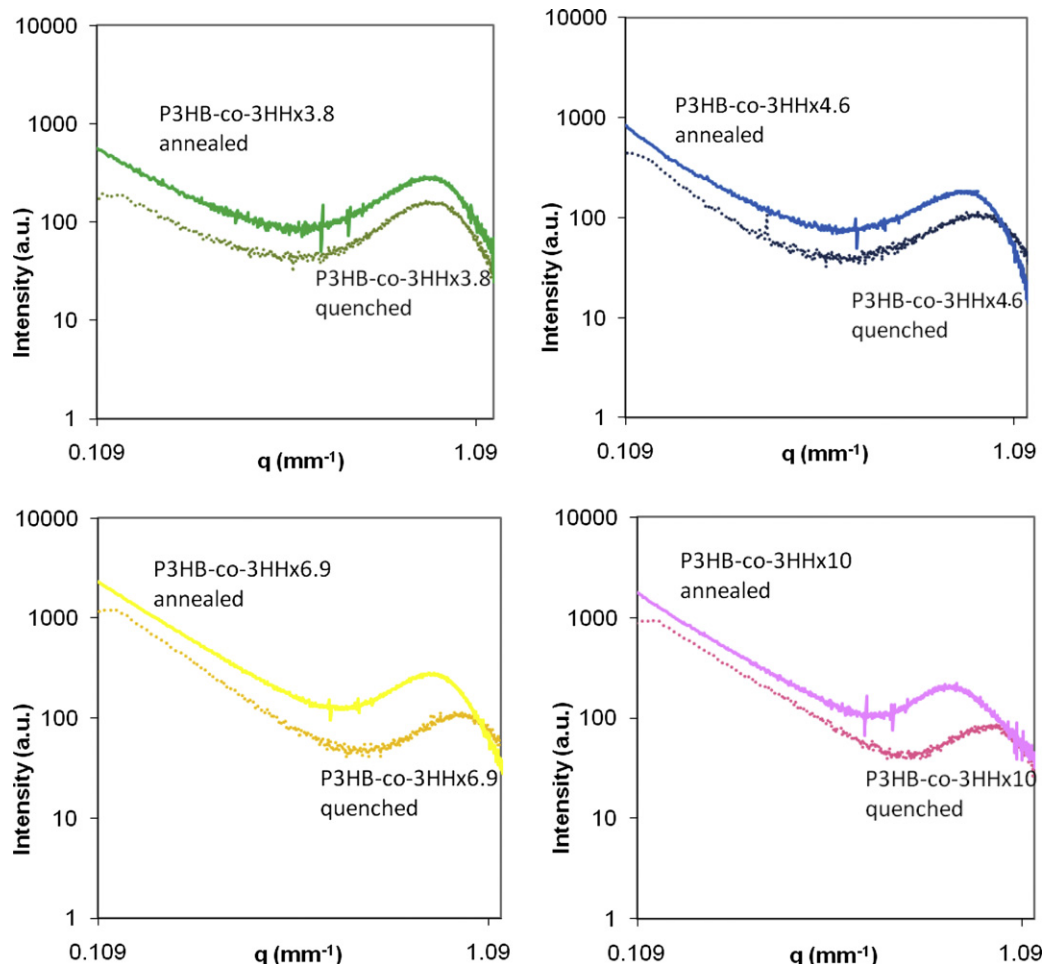


Fig. 3. Small-angle X-ray scattering patterns of P3HB-co-3HHx samples, comparing annealed and quenched samples of the same copolymer composition.

dependence of the biodegradation rate on the copolymer composition and processing history. It was found that samples with higher 3HHx fraction biodegraded at a faster rate than samples with lower 3HHx content (Fig. 4). Thin films made of P3HB-co-3HHx10 biodegraded the fastest, followed by P3HB-co-3HHx6.9, P3HB-co-3HHx4.6 and finally P3HB-co-3HHx3.8. On Day 7, P3HB-co-3HHx10 had lost 80% of the original weight compared to 63%, 46%, and 28% for P3HB-co-3HHx6.9, P3HB-co-3HHx4.6, and P3HB-co-3HHx3.8, respectively. Other researchers have reported a similar pattern for composting of the P3HB-co-3HV copolymer, with the biodegradation rate increasing as 3HV content increased [24].

The approximate three-day delay for the onset of weight loss observed for all P3HB-co-3HHx samples (Fig. 4) is believed to be due to the time requirement for microbes to first attach to the sample surface. It is generally understood that adhesion of microbes to a surface is essential for the development of microbial activity and the release of active enzyme [25,26]. As supporting evidence, we have previously obtained SEM images of adhered microbes on the surface of P3HB-co-3HHx and found that the attachment was developed over time [27]. The presence of bacterial extracellular polymeric substance (EPS) [27] further confirmed the microbial attachment since EPS is generally thought to help keep the microbes attached and the enzyme localized [28]. By contrast, in cases where microbial attachment was not a prerequisite, e.g., degradation of PHAs in the aqueous solution of *PHB depolymerase*, samples lost weight in the first few hours and the rates of weight loss were linear functions of time [29].

In addition, the biodegradation of PHAs seems to be closely related to the semi-crystalline morphology. Specifically, the enzymatic degradation seems to first occur in the amorphous regions and then spread to the crystalline regions [15,30,31]. Microbial degradation of the P3HB-co-3HHx polymer films, as a result, may provide a contrast mechanism to observe their underlying morphology. Our SEM results on the surface morphology of partially degraded P3HB-co-3HHx samples confirmed this hypothesis. Fig. 5 illustrates the progressive morphological changes in P3HB-co-3HHx10 for Days 0, 3, and 7. As biodegradation progressed, the polymer became blemished. Comparing images of samples not exposed to the microbial action with images after degradation, it is clear that biodegradation exposed the underlying semi-crystalline morphology of the polymer. Such exposed surface semi-crystalline morphology due to biodegradation is similar to the morphological features observed in polarized optical micrographs for intact thin film P3HB-co-HHx [32,33], supporting the occurrence of differential rate of erosion between the amorphous and crystalline regions for P3HB-co-HHx.

We may hence compare P3HB-co-3HHx copolymers with different HHx after they have been partially degraded under anaerobic conditions. Fig. 6 shows the SEM images of the four types of P3HB-co-3HHx samples incubated for 7 days. It is worth noting

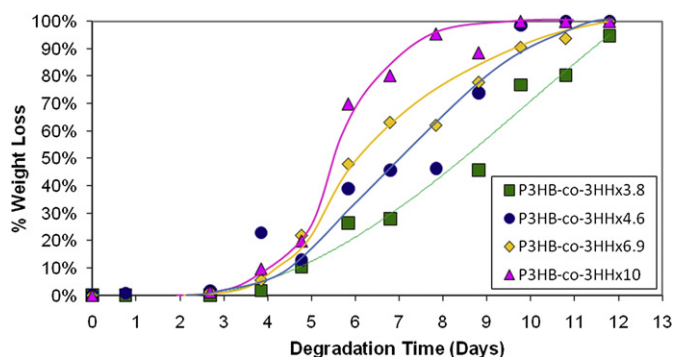


Fig. 4. Anaerobic biodegradation of P3HB-co-3HHx samples.

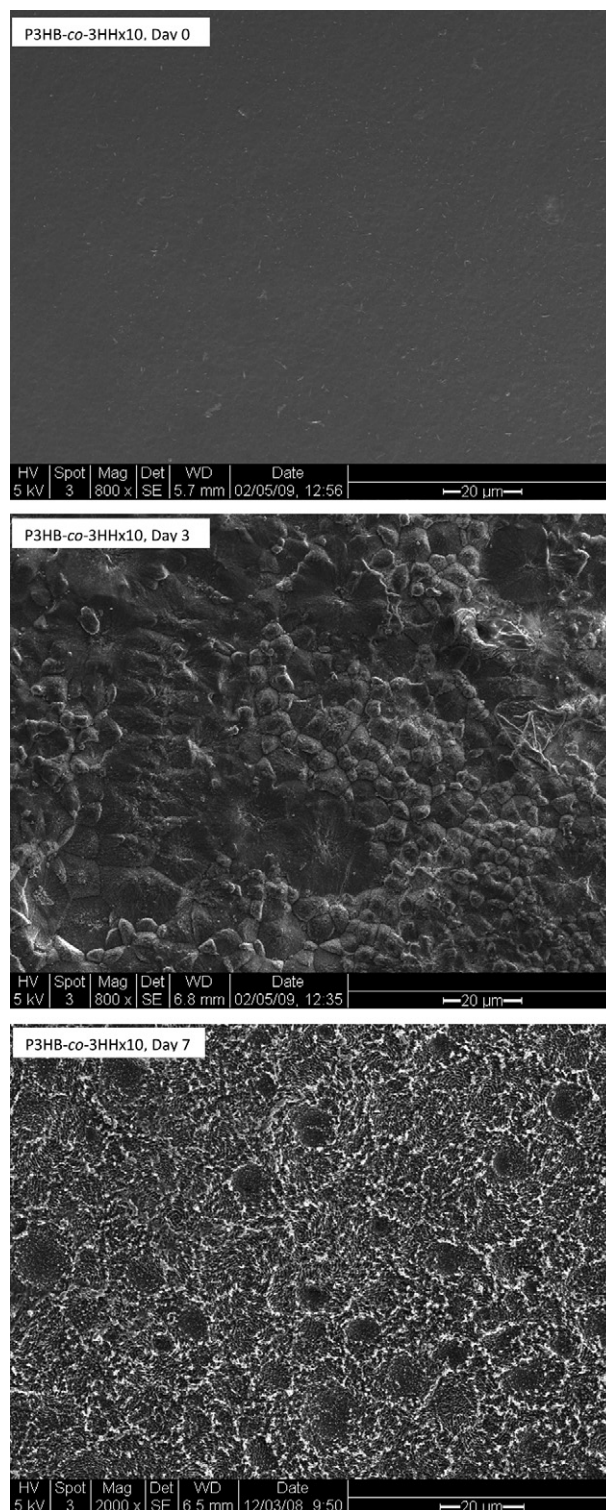


Fig. 5. P3HB-co-3HHx10 samples biodegraded for 0 days, 3 days and 7 days.

that due to the difference in biodegradation rate, as shown in Fig. 4, the mass loss of different copolymer samples differed significantly at Day 7. P3HB-co-3HHx10 lost 80% of its original mass, P3HB-co-3HHx6.9 lost 63%, P3HB-co-3HHx4.6 lost 46%, and P3HB-co-3HHx3.8 lost 28%. For all samples, spherulitic structures are clearly observed. With increasing HHx content, the spherulite diameter seems to decrease, from being roughly 40 µm for P3HB-co-3HHx3.8 down to approximately 10 µm for P3HB-co-3HHx10.

In addition, while the P3HB-*co*-3HHx3.8 and P3HB-*co*-3HHx4.6 samples appear to display normal morphology, with lamellar ribbons growing radially outwards from the nucleated center of the spherulite, HHx 6.9 and HHx 10 show banded morphology. Such banding often stems from the twisting of the crystallographic orientation in the crystalline lamellae about the radial axis along which the lamellar ribbon grows. It has been observed for a wide variety of semi-crystalline polymers, such as polyethylene and poly(vinylidene fluoride), but its mechanism is unclear [34]. It has also been observed previously with atomic force microscopy and microbeam X-ray diffraction for P3HB-*co*-3HHx with 8 mol% HHx [35] and 17 mol% HHx [36].

In particular, partially biodegraded P3HB-*co*-3HHx10 samples clearly revealed densely packed banded patterns (Fig. 6d). The spiral morphology may result from the molecular chirality (*R*-3-hydroxybutyrate and *R*-3-hydroxyhexanoate) [37]. The band spacing for P3HB-*co*-3HHx6.9 (2  $\mu\text{m}$ ) is significantly larger than that of P3HB-*co*-3HHx10 (0.3  $\mu\text{m}$ ). Although a banded pattern is not observed for P3HB-*co*-3HHx4.6 and P3HB-*co*-3HHx3.8, it is possible that the periodic twisting of crystalline lamellae still exists in these copolymers, but the band spacing may be further increased. Supporting evidence for lower HHx comonomer leading to larger band spacing can be found in the literature. The band spacing for P3HB was reported to be 100  $\mu\text{m}$ , five times of that of P3HB-*co*-3HHx with 8 mol% HHx prepared under the same condition [35].

### 3.3. Effect of thermal annealing on biodegradation of P3HB-*co*-3HHx

As DSC and SAXS data have already shown, solid-state properties such as crystallinity and lamellar thickness changed if the P3HB-*co*-3HHx copolymer of the same copolymer composition was

annealed at 70 °C compared to being quenched. Hence, it was also expected that annealed samples would have different biodegradation behavior compared to the corresponding quenched samples.

Fig. 7 shows the comparison of the rate of weight loss in anaerobic environment for the quenched P3HB-*co*-3HHx samples relative to the annealed ones. In general, the annealed P3HB-*co*-3HHx tends to have higher initial rate of biodegradation, i.e., the annealed sample has higher degree of weight loss over the first several days. However, the quenched samples tend to have lower long-term extent of degradation. The rate of weight loss for quenched samples seems to surpass the annealed samples when the accumulative weight loss has reached 60%, e.g., P3HB-*co*-3HHx3.8 on Day 7–8 and P3HB-*co*-3HHx10 on Day 6–7. Since the enzymatic degradation of PHAs was found to erode the amorphous regions much faster than the crystalline regions [15,30,31], it is understandable that the rate of long-term weight loss will depend on the overall fraction of the amorphous region and the thickness of the crystalline lamellae [15]. Given that quenched samples have lower crystallinity than the annealed counterparts, greater extent of weight loss is expected to be seen for quenched samples within the experiment duration. However, the initial higher rate of weight loss for the annealed samples was unexpected and, given that annealed samples have higher crystallinity and thicker crystalline lamellae (Table 2), is contrary to the common argument where higher crystalline and thicker lamellae are generally believed to lead to slower degradation [15]. To account for these contradictions, we propose that the annealed P3HB-*co*-3HHx samples biodegrade faster because of a particular change in morphology during thermal annealing – void formation in the crystal lamellae. These voids then act to facilitate diffusion of the microbial enzymes inwards, resulting in faster erosion. A more detailed discussion will be provided in the Discussion.

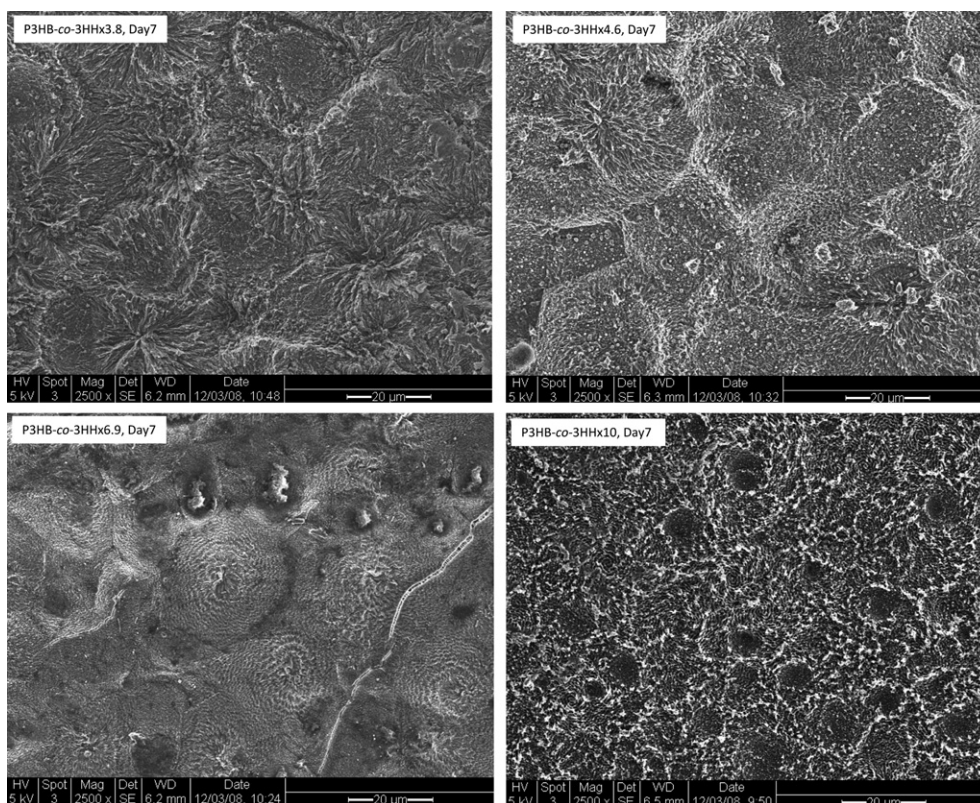


Fig. 6. P3HB-*co*-3HHx samples on Day 7 of biodegradation. (a) P3HB-*co*-3HHx3.8, 28% weight loss; (b) P3HB-*co*-3HHx4.6, 46% weight loss; (c) P3HB-*co*-3HHx6.9, 63% weight loss; (d) P3HB-*co*-3HHx10, 80% weight loss.

Biodegraded, annealed P3HB-co-3HHx samples were also imaged by SEM and compared to biodegraded, quenched samples (Fig. 8), where all samples have roughly the same degree of weight loss (lost 80% of the original weight). The annealed samples revealed spherulites that were more distinct, with clearer boundaries, than those of the quenched samples. P3HB-co-3HHx3.8 and P3HB-co-3HHx4.6 still show normal spherulites similar to those seen in the quenched samples. Surprisingly, the annealed P3HB-co-3HHx6.9 images seem to lack the banded pattern (Fig. 8f). In the case of P3HB-co-3HHx10, banded spherulites are still observed, but the band spacing is much larger for the annealed sample (3  $\mu\text{m}$ ) than the quenched counterpart (0.3  $\mu\text{m}$ ). This is consistent with previous findings that increased crystallization temperature reduces lamellar twisting and thus increases the band spacing in P3HB-co-3HHx [36]. The disappearance of banded patterns for P3HB-co-3HHx6.9, hence, may arguably be a result of an increase in band spacing that makes the banded pattern difficult to see visually.

The exposed underlying semi-crystalline morphology in annealed P3HB-co-3HHx shows a clear persistence of lamellar ribbons under anaerobic conditions (Fig. 8) confirming a faster erosion of the amorphous region, as previously proposed [38]. In addition to the erosion of the amorphous regions, evidence of degradation of the lamellae was also observed, which was shown as holes at the center of the spherulites, as shown in Fig. 8f, g, and h. Such phenomenon was previously reported for P3HB that was degraded by *PHB depolymerase* [39] or by *Alcaligenes paradoxus* and *C. testosteroni* [38], and was explained as a result of lamellae packing imperfection near the nucleation center, which led to preferential enzymatic attack at the center, resulting in a hole. As the degradation continues, this hole will spread and penetrate through the film, leaving behind only crystalline remnants (Fig. 9), which suggests that the central part of the spherulite is eroded

most rapidly. These ring-shaped remnants have also been reported for aerobically degraded samples of pure P3HB [38].

#### 4. Discussion

The biodegradation rate of PHAs has long been found to be highly dependent on the molecular composition, the overall crystallinity, and the semi-crystalline morphology. Kumagai et al. [30] reported that the rate of enzymatic degradation of P3HB in the aqueous solution of *PHB depolymerase* and phosphate buffer (weight loss in 19 h, ranging from 20 to 80%) decreased with an increase in crystallinity and was not sensitive to the spherulite size. Shimamura et al. [40] studied the enzymatic biodegradation of poly (3-hydroxybutyrate-co-3-hydroxypropionate) (P3HB-co-3HP) in an aqueous solution of *PHB depolymerase* as well and found that the rate of erosion (weight loss in 2 h, ranging from 5 to 30%) was increased by the incorporation of 3HP units up to 20 mol%. Koyama et al. [29] and Abe et al. [15] studied the enzymatic degradation of PHA copolymers in addition to the homopolymer P3HB in an aqueous solution of *PHB depolymerase*, including P3HB-co-3HV with 6, 7, 16, and 22 mol% HV content, as well as P3HB-co-3HHx with 4, 8, and 11 mol% of HHx. Although these copolymers prepared under the same melt crystallization condition were found to degrade several times faster than the homopolymer P3HB, no particular trends were found for the dependence of rates of enzymatic degradation on the comonomer content, the degree of crystallinity with the same polymer composition, or the crystal sizes obtained from X-ray diffraction.

In the present study, instead of aqueous solutions of *PHB depolymerase*, we used activated sludge that contained a mixed microbe colony to anaerobically degrade P3HB-co-3HHx samples. Instead of a constant rate of weight loss, which was usually the case

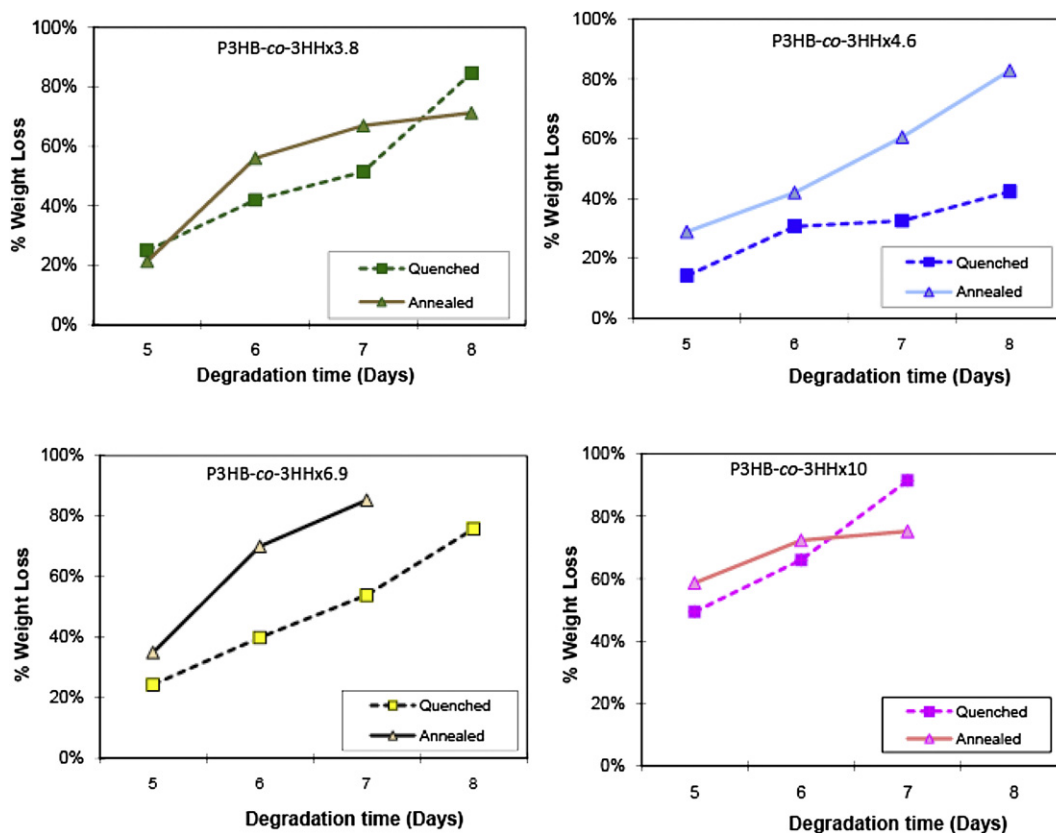
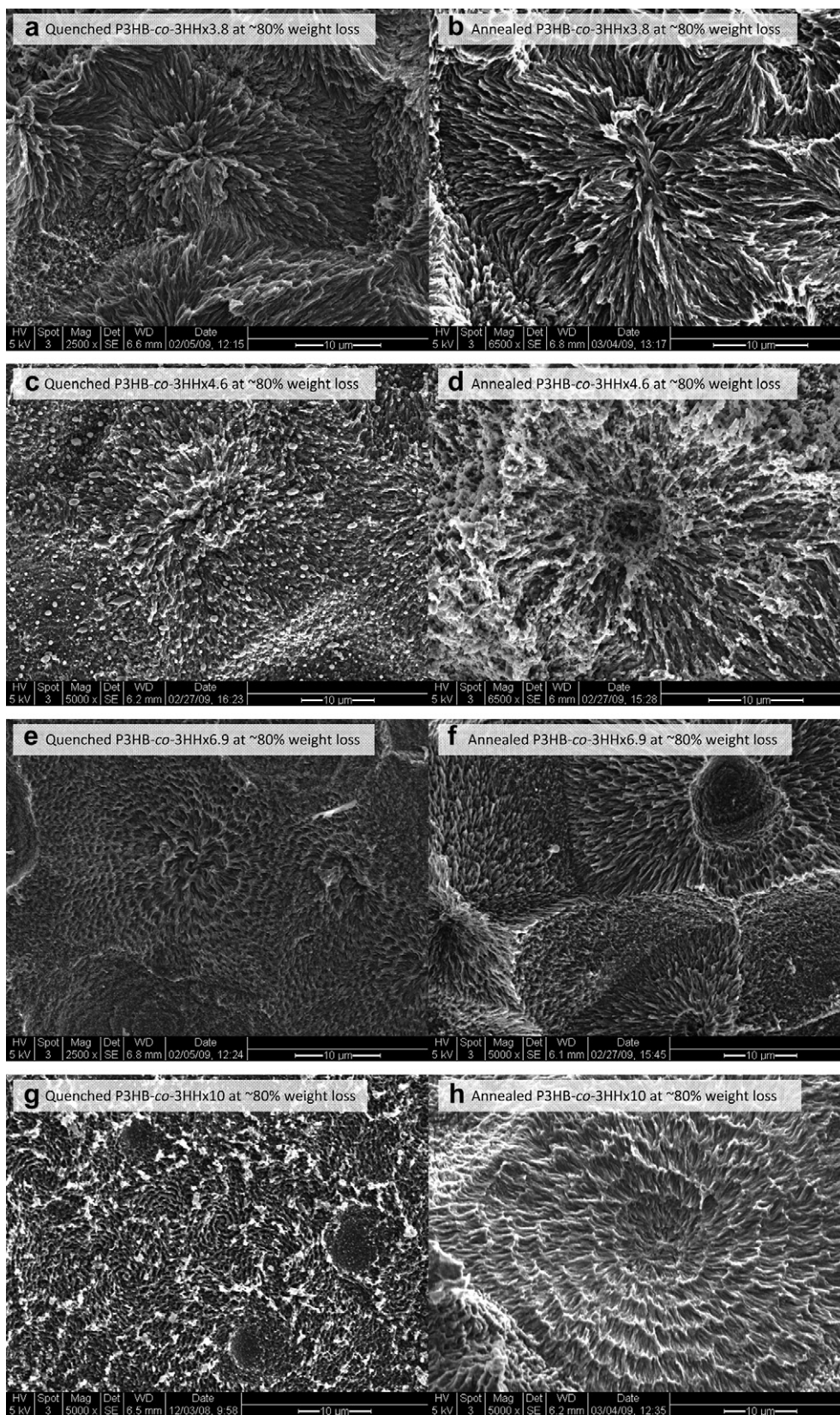
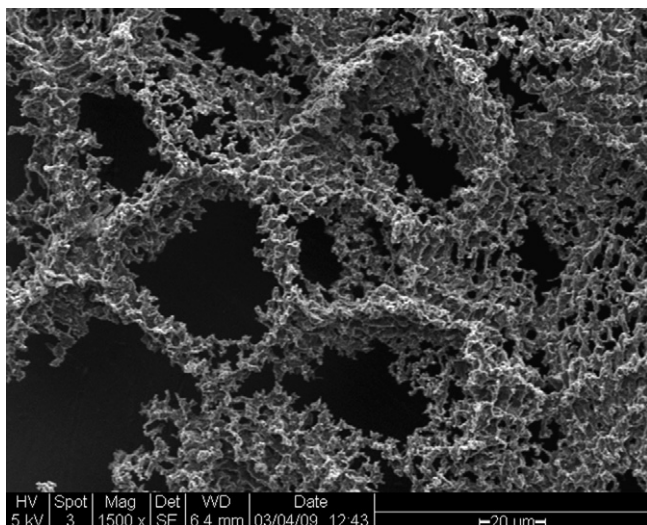


Fig. 7. Anaerobic biodegradation of quenched P3HB-co-3HHx samples compared to annealed counterparts.



**Fig. 8.** P3HB-co-3HHx samples with weight loss of approximately 80%: (a) quenched P3HB-co-3HHx3.8, Day 11; (b) annealed P3HB-co-3HHx3.8, Day 11; (c) quenched P3HB-co-3HHx4.6, Day 9; (d) annealed P3HB-co-3HHx4.6, Day 8; (e) quenched P3HB-co-3HHx6.9, Day 9; (f) annealed P3HB-co-3HHx6.9, Day 9; (g) quenched P3HB-co-3HHx10, Day 7; (h) annealed P3HB-co-3HHx10, Day 7.



**Fig. 9.** Remnant of the annealed P3HB-*co*-3HHx10 sample that is highly degraded (7 day incubation).

if PHB depolymerase solution was used [29], there was a roughly three-day delay before any weight loss could be observed. As the weight loss began, the rate of sample erosion increased if the copolymer contained higher 3HHx content. Since there was an expected decrease in crystallinity and a decrease in the thickness of the crystalline lamellae with the increase in 3HHx content (Table 2), the increased rate of degradation could be explained as a result of higher enzymatic activity of depolymerase on the amorphous region compared to the crystalline region, where lower crystallinity leads to faster erosion [15,29,38].

However, we found that the crystallinity and the thickness of crystalline lamellae were not the only factors influencing the biodegradation rate of P3HB-*co*-3HHx. After the same quenched P3HB-*co*-3HHx sample was annealed at elevated temperature (70 °C), crystallinity was increased after annealing (Table 2), but the rate of degradation, opposite to what would be expected, also increased (Fig. 5). The result indicates that the semi-crystalline morphologies affected by the thermal processing history can become the controlling factors for biodegradation.

We hypothesize that the increase in biodegradation rate after thermal annealing is due to a change in the semi-crystalline morphology of P3HB-*co*-3HHx films during thermal processing. In particular, we propose that voids are formed within and at the boundaries of crystal lamella. Our reasoning begins from the well-known spherulitic morphology, which consists of crystalline lamellae bundles growing radially from nucleation center as well as amorphous regions in between the crystalline lamellae. Annealing at elevated temperature usually results in some reorganization of the polymeric chain configuration and, subsequently, alterations in the morphology. One common effect of such reorganization is lamellar thickening [22,41], where the thickness of the crystalline lamellae increases. Our results confirmed the occurrence of such phenomenon for P3HB-*co*-3HHx during the annealing; higher  $T_m$  and narrower melting peaks of annealed samples as measured by DSC suggest thicker and more uniformly sized crystalline lamellae. Moreover, SAXS results revealed an increase in the long period, which is a well-established measure of lamellar thickening [42].

The thickening process is believed to occur through solid-state diffusion where additional molecular sequences are pulled into the crystalline lamellae. Under circumstances where a chain end is pulled completely into a crystalline lamella, microvoids or even vacancy rows are formed inside the lamella, as has been observed

for polyethylene [43,44] and polypropylene [45]. In other cases, the lamellar thickening often involves molecular segments migrating from the adjacent amorphous region, causing an overall increase in the void content in the amorphous phase through diffusion and relaxation [46]. We believe that formation of these defects in the annealed sample accounts for the increased biodegradation rate. Water and other solutes associated with the microbial degradation of the P3HB-*co*-3HHx sample should more easily penetrate through the voids induced by annealing and enhance the etch rate of the samples. A similar phenomenon was observed for gas transport in semi-crystalline polymers. Michaels et al. reported increased helium solubility in polyethylene after annealing [44], while Holden et al. reported similar results that the oxygen barrier property of polyethylene decreased after annealing [47]. Moreover, Vieth et al. found that gas diffusivities showed significant enhancement for annealed polypropylene despite increased crystallinity [45]. These results were attributed to the formation of intra-lamellar defects in the crystalline domains, which provided easy access for gas permeation.

## 5. Conclusion

The microbial biodegradation rate of P3HB-*co*-3HHx depends on the copolymer composition and processing history. Increasing the 3HHx fraction in P3HB-*co*-3HHx resulted in increased rates of biodegradation that are likely due to the decreased crystallinity. However, a P3HB-*co*-3HHx sample that had been annealed biodegraded faster than the corresponding annealed sample with the same composition, despite the higher crystallinity. We hypothesize that this is due to an increase in void content in the sample as a result of thermal annealing, which could provide easier access for diffusion of water and enzymes into the sample, thus enhancing the microbial biodegradation rate. Finally, we note that biodegradation exposed the underlying morphological details of the polymer. Some P3HB-*co*-3HHx samples displayed normal spherulitic morphology while others showed banded structures. The simple assay used to assess anaerobic biodegradability may thus also be used to explore underlying polymer characteristics.

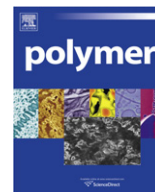
## Acknowledgments

The authors would like to thank the Procter & Gamble Company, especially Dr. Isao Noda, for providing the copolymer materials used in this study. The authors are grateful to the Center on Polymer Interfaces and Macromolecular Assemblies (CPIMA) - an NSF-Materials Research Science and Engineering Center, the Stanford Woods Institute for the Environment, and the Precourt Energy Efficiency Center (PEEC) for funding support. The X-ray experiments were carried out at the Stanford Synchrotron Radiation Lightsource (SSRL), a national user facility operated by Stanford University on behalf of the US Department of Energy, Office of Basic Energy Sciences. SAXS measurements were carried out with the kind assistance from Dr. Masaki Yanagioka. This work was also supported in part by the California EPA Department of Toxic Substances Control, Sponsor Ref. No. 07T3451.

## References

- [1] Mergaert J, Anderson C, Wouters A, Swings J, Kersters KFEMS. *Microbiology Letters* 1992;103(2–4):317–21.
- [2] Mergaert J, Anderson C, Wouters A, Swings J. *Journal of Polymers and the Environment* 1994;2(3):177–83.
- [3] Miyazaki SS, Yep AR, Kolton F, Hermida EB, Povolo F, Fernandes EG, Chiellini E. *Macromolecular Symposia* 2003;197:57–64.
- [4] Molitoris HP, Moss ST, De Koning GJM, Jendrossek D. *Applied Microbiology and Biotechnology* 1996;46(5):570–9.

- [5] Abou-Zeid D. Anaerobic biodegradation of natural and synthetic polyesters. Dissertation. Germany: Technische Universität Carolo-Wilhelmina zu Braunschweig, <http://opus.tu-bs.de/opus/volltexte/2001/246>; 2001.
- [6] Budwill K, Fedorak PM, Page WJ. Applied and Environmental Microbiology 1992;58(4):1398–401.
- [7] Abe H, Doi Y. International Journal of Biological Macromolecules 1999;25(1–3):185–92.
- [8] Woolnough CA, Charlton T, Yee LH, Sarris M, Foster LJR. Polymer International 2008;57(9):1042–51.
- [9] Asrar J, Valentin HE, Berger PA, Tran M, Padgett SR, Garbow JR. Biomacromolecules 2002;3(5):1006–12.
- [10] Doi Y, Kitamura S, Abe H. Macromolecules 1995;28(14):4822–8.
- [11] Hong SG, Lin YC, Lin CH. Journal of Applied Polymer Science 2008;110(5):2718–26.
- [12] Liao Q, Noda I, Frank CW. Polymer 2009;50(25):6139–48.
- [13] Hu Y, Zhang JM, Sato H, Noda I, Ozaki Y. Polymer 2007;48(16):4777–85.
- [14] Morse MC, McCarty PL, Billington SL, Criddle CS. Journal of Chemical Education; submitted for publication.
- [15] Abe H, Doi Y, Aoki H, Akehata T. Macromolecules 1998;31(6):1791–7.
- [16] Chen C, Cheung MK, Yu PHF. Polymer International 2005;54(7):1055–64.
- [17] Asrar J, Valentin HE, Berger PA, Tran M, Padgett SR, Garbow JR. Biomacromolecules 2002;3(5):1006–12.
- [18] He Y, Masuda T, Cao A, Yoshie N, Doi Y, Inoue Y. Polymer J 1999;34(2):184–92.
- [19] Zheng Z, Bei FF, Tian HL, Chen GQ. Biomaterials 2005;26(17):3537–48.
- [20] Bonnet M, Rogausch KD, Petermann J. Colloid and Polymer Science 1999;277(6):513–8.
- [21] Fontaine F, Ledent J, Groeninckx G, Reynaers H. Polymer 1982;23(2):185–91.
- [22] Mitomo H, Doi Y. International Journal of Biological Macromolecules 1999;25(1–3):201–5.
- [23] Hurrell S, Cameron RE. Biomaterials 2002;23(11):2401–9.
- [24] Mergaert J, Webb A, Anderson C, Wouters A, Swings J. Appl. Environ. Microbiol. 1993;59(10):3233–8.
- [25] Grossart HP, Tang KW, Kiorboe T, Ploug H. Fems Microbiology Letters 2007;266(2):194–200.
- [26] Geoghegan M, Andrews JS, Biggs CA, Eboigbodin KE, Elliott DR, Rolfe S, et al. Faraday Discussions 2008;139:85–103.
- [27] Morse M. PhD thesis, Stanford University; 2009.
- [28] Flemming HC, Wingender J. Water Science and Technology 2001;43(6):1–8.
- [29] Koyama N, Doi Y. Macromolecules 1997;30(4):826–32.
- [30] Kumagai Y, Kanesawa Y, Doi Y. Makromolekulare Chemie-Macromolecular Chemistry and Physics 1992;193(1):53–7.
- [31] Tomasi G, Scandola M, Briese BH, Jendrossek D. Macromolecules 1996;29(14):5056.
- [32] Pan PJ, Liang ZC, Nakamura N, Miyagawa T, Inoue Y. Macromolecular Bioscience 2009;9(6):585–95.
- [33] Cai HY, Qiu ZB. Physical Chemistry Chemical Physics 2009;11(41):9569–77.
- [34] Keith HD, Padden FJ. Macromolecules 1996;29(24):7776–86.
- [35] Tanaka T, Fujita M, Takeuchi A, Suzuki Y, Uesugi K, Doi Y, Iwata T. Polymer 2005;46(15):5673–9.
- [36] Xu J, Guo BH, Zhang ZM, Zhou JJ, Jiang Y, Yan S, et al. Macromolecules 2004;37(11):4118–23.
- [37] Singfield KL, Hobbs JK, Keller A. Journal of Crystal Growth 1998;183(4):683–9.
- [38] Nishida H, Tokiwa Y. Journal of Polymers and the Environment 1993;1(1):65–80.
- [39] Tomasi G, Scandola M, Briese BH, Jendrossek D. Macromolecules 1996;29(2):507–13.
- [40] Shimamura E, Scandola M, Doi Y. Macromolecules; 1994:4429–35.
- [41] Sawayanagi T, Tanaka T, Iwata T, Abe H, Doi Y, Ito K, et al. Macromolecules 2006;39(6):2201–8.
- [42] Fischer EW. Pure and Applied Chemistry 1972;31:113–31.
- [43] Keller A. Polymer 1962;3(3):393–421.
- [44] Michaels AS, Bixler HJ, Fein HL. Journal of Applied Physics 1964;35(11):3165–78.
- [45] Vieth W, Wuerth WF. Journal of Applied Polymer Science 1969;13(4):685–712.
- [46] Shen SY, Lou JH, Cheng JX, Hong KL, Zhu QG, Zhou XY. Physica Status Solidi A - Applied Research 1995;147(2):447–52.
- [47] Holden PS, Orchard GAJ, Ward IM. Journal of Polymer Science Part B-Polymer Physics 1985;23(11):2295–306.



## Microstructure of two polypropylene homopolymers with improved impact properties

Yandi Fan, Chunyu Zhang, Yanhu Xue, Xuequan Zhang, Xiangling Ji\*, Shuqin Bo\*

State Key Laboratory of Polymer Physics and Chemistry, Changchun Institute of Applied Chemistry, Chinese Academy of Sciences, Changchun 130022, PR China

### ARTICLE INFO

#### Article history:

Received 20 June 2010

Received in revised form

1 October 2010

Accepted 5 December 2010

Available online 10 December 2010

#### Keywords:

Polypropylene

Fractionation

Microstructure

### ABSTRACT

Two polypropylene homopolymers, samples A and B, synthesized with heterogeneous Ziegler–Natta catalysts, are studied in this work. Both samples show improved impact properties at low temperature than isotactic PP. Particularly, sample B exhibits better toughness, higher molecular weight and slight lower flexural properties than sample A. Then, these two samples were fractionated into six fractions via temperature rising dissolution fractionation, respectively. Both samples are mainly composed of fractions 4, 5 and 6, which were collected above 100 °C and have high isotacticity. On the one hand, the fractions of sample B have higher molecular weight than the corresponding fractions of sample A collected at the same temperatures. On the other hand, <sup>13</sup>C NMR and DSC analyses of the fractions indicate clearly that fractions of sample B have lower isotacticity and crystallinity than the corresponding fractions of sample A. The above difference in microstructure between samples A and B should be the key factors resulting in their difference in mechanical properties finally. Both polypropylene homopolymers possibly become new type of impact PP.

© 2010 Elsevier Ltd. All rights reserved.

### 1. Introduction

It is well recognized that heterogeneous Ziegler–Natta catalysts contain multiple active sites, which produce polypropylene (PP) with varying degree of stereoregularity [1–4]. Actually, Ziegler–Natta catalysts have evolved considerably from the low active, low stereospecific catalysts to the highly active, highly stereospecific catalysts used in modern polyolefin manufacturing plants. Today, highly efficient Ziegler–Natta catalysts and new processing technologies lead to products applied in a very broad range. For example, polypropylene can now span the full range of polymeric properties from soft elastomers to hard thermoplastics [5–12]. These differences in properties arise largely from differences in molecular structure, *i.e.* molecular weight distribution and stereostructure distribution of the chain [4].

The influence of the type of catalyst and polymerization process on microstructures of industrial Ziegler–Natta polypropylenes has been studied by many investigators [11–20]. Viville et al. [11] reported that the change in the mechanical properties of PP is not only due to differences in the average isotacticity but also in the

way tacticity is distributed between the chains. In order to get a complete description of the molecular microstructure, some fractionation methods described in literatures have been employed to separate Ziegler–Natta polypropylenes, including temperature rising elution fractionation (TREF) [11–15], solvent gradient extraction [16–20] and successive self-nucleation and annealing (SSA) [18–20]. TREF and solvent gradient extraction, such techniques that fractionate semicrystalline polymers according to their solubility–temperature relationship, led to fractions of increasing isotacticity, and these results clearly indicated a nonuniform interchain composition of stereodefects. In our previous work [12], the molecular weights of TREF fractions tend to increase with elution temperature, while the crystallinity of fractions do not increase monotonically with elution temperature. There is a maximum in the plot of crystallinity versus elution temperature, indicating the fractionation is based on the longest crystallizable sequences in a chain. SSA is based on the sequential application of self-nucleation and annealing steps to a polymer sample. After thermal conditioning a final DSC heating run reveals the distribution of melting points induced by the SSA treatment as a result of the heterogeneous nature of the chain structure of the polymer under analysis [21]. Virkkunen and coworkers [18,19] applied SSA measurement and analytical TREF for study of isotacticity distribution in polypropylene fractions with variable isotacticity. The polypropylene fractions have clearly been separated according to

\* Corresponding authors. Tel.: +86 431 8526 2876; fax: +86 431 8568 5653.

E-mail addresses: [xlji@ciac.jl.cn](mailto:xlji@ciac.jl.cn) (X. Ji), [sqbo@ciac.jl.cn](mailto:sqbo@ciac.jl.cn) (S. Bo).



the longest crystallizable sequences; however, they contain a broad intra-molecular distribution of tacticity defects since the distribution of melting points varies widely from fraction to fraction. They also found the good correspondence between melting scans after SSA fractionation and TREF fractionation profile.

In this paper, two Ziegler–Natta polypropylenes with improved impact properties at low temperatures were fractionated into six fractions via temperature rising dissolution fractionation (TRDF), respectively. GPC,  $^{13}\text{C}$  NMR and DSC techniques are exploited to investigate the tacticity distribution in the molecules and the relationship between microstructure and mechanical properties of the whole samples.

## 2. Experimental

### 2.1. Materials

Two samples used in this study were synthesized in our institute and coded as samples A and B, respectively. The mechanical properties of the samples are listed in Table 1. The impact strength at 23 °C of the samples A and B is 19.9 and 39.5 kJ/m<sup>2</sup>, and much higher than that of isotactic PP (iPP) of 4.4 kJ/m<sup>2</sup>. Interestingly, the impact strength at –20 °C of the samples A and B is 3.8 and 4.4 kJ/m<sup>2</sup>, and close to the impact strength at 23 °C of iPP (4.4 kJ/m<sup>2</sup>). Meanwhile, the flexural moduli of the samples are 1.30 and 1.07 GPa for sample A and B, which are lower than that of iPP of 1.40 GPa.

### 2.2. Temperature rising dissolution fractionation

About 10 g of polymer was placed into a 2 L flask and 1 L of xylene was added to get 1% solution (w/v) at 135 °C.  $1 \times 10^{-3}$  g/mL 2, 6-di-*tert*-butyl-4-methylphenol (BHT) was added to xylene as antioxidant. The mixture was heated for about 3 h at 135 °C, and then the solution was cooled to room temperature at a rate of 2 °C/h. The solution was kept at room temperature for 24 h and finally was separated into two phases: the concentrated phase and the dilute phase. The concentrated phase was filtered and washed with xylene. Fraction 1 was obtained after concentrating the dilute phase, precipitating the polymer, and washing with acetone, then drying the fractions in vacuum. The concentrated phase was placed in the cylindrical container made by nickel net; it was then put into a similar cylindrical glass tube, and about 250 mL of xylene was added. This glass tube was maintained at 80 °C for 24 h. After 12 h, the solution in the tube was removed and was replaced with hot xylene. Finally, the net with insoluble polymer was taken out and washed with hot xylene (80 °C). The solutions collected twice in this step were mixed together, cooled, precipitated with double volume of acetone, and filtered. The obtained polymer, named as fraction 2, was then dried in vacuum. The fraction 3, 4 and 5, soluble at 100 °C, 110 and 118 °C respectively, were obtained through the same procedure like fraction 2. The polymer insoluble at 118 °C, named as fraction 6, was washed by acetone and dried in vacuum.

**Table 1**  
The mechanical properties of samples A and B.

Sample	Flexural Strength (MPa)	Flexural Modulus (GPa)	Notched Izod Impact Strength (kJ/m <sup>2</sup> )	
			23 °C	–20 °C
A	38.9	1.30	19.9	3.8
B	32.0	1.07	39.5	4.4

### 2.3. Molecular weight and molecular weight distribution

The molecular weight and molecular weight distribution (MWD) of the samples and their fractions were determined by a PL-GPC 220 high-temperature gel permeation chromatography (Polymer Laboratories Ltd) at 150 °C. The columns used were three PLgel 10- $\mu\text{m}$  mixed-B LS columns (300 mm  $\times$  7.5 mm). The eluent was 1,2,4-trichlorobenzene stabilized with  $5 \times 10^{-4}$  g/mL BHT and was filtered with a 0.2  $\mu\text{m}$  pore size membrane before use. The injection volume was 200  $\mu\text{L}$ , and the flow rate was 1.0 mL/min. Calibration was made by polystyrene standard EasiCal PS-1 (PL Ltd.).

### 2.4. Nuclear magnetic resonance (NMR)

$^{13}\text{C}$  NMR was measured at 130 °C on a Varian Unity 400 MHz NMR spectrometer. Polymer solution was prepared with 70–75 mg of polymer in 0.5 mL of deuterated *o*-dichlorobenzene at 130 °C.

### 2.5. Differential scanning calorimetry (DSC)

Differential scanning calorimetry (DSC) scans were recorded on a TA Instrument model DSC Q100. About 5 mg of sample was sealed in aluminum sample pan and were firstly heated from 50 to 200 °C at a rate of 10 °C/min, held at 200 °C for 5 min to remove thermal history, then cooled from 200 to 50 °C at 10 °C/min, held at 50 °C for 1 min, and finally heated again to 200 °C at 10 °C/min. Temperature calibration was performed using indium. The melting temperature  $T_m$  and heat of fusion  $\Delta H_m$  were measured during reheating experiments. The degree of crystallinity was calculated by comparison with heat of fusion of a perfectly crystalline polypropylene, i.e., 209 J/g.

The SSA (successive self-nucleation and annealing) method used was presented in the original paper by Müller et al. [22]. The annealing time was kept at 5 min; heating and cooling were done at a rate of 10 °C/min. In all the measurements, the first  $T_s$  temperature was chosen from predetermined values (168 °C, 164 °C, 159 °C, 155 °C) based on the final melting temperature from DSC curve. This ensures that all the steps (peaks in the melting curve) will coincide in the different measurements and the comparison of the measurements is easier. In all cases, the first  $T_s$  is in domain II as defined by Fillon et al. [23], which is essential for the self-nucleation process. The melting temperature of the SSA measurement was taken from the largest peak in the melting curve.

## 3. Results and discussion

### 3.1. Characterization of the whole samples

The molecular weight data, meso triads distribution and thermal properties of samples A and B are summarized in Table 2. Sample B has higher weight-average molecular weight ( $M_w$ ) of 452000 g/mol and a little narrower molecular weight distribution (MWD) of 9.74 than sample A ( $M_w = 330000$  g/mol, MWD = 9.91). Definitely, both samples have broad MWD due to the presence of several types of active site on these heterogeneous Ziegler–Natta

**Table 2**  
The molecular weight data, meso triads distribution and thermal properties of samples A and B.

Sample	$M_w$ ( $10^{-4}$ )	$M_w/M_n$	$mm$	$mr$	$rr$	$n_m$	$n_r$	$T_m$ (°C)	Cryst. (%)
A	33.0	9.91	0.863	0.064	0.073	28.0	3.28	162.9	38.9
B	45.2	9.74	0.817	0.081	0.102	21.2	3.52	160.0	37.1

catalysts.  $^{13}\text{C}$  NMR measurements of the meso triads have shown that sample B has a lower isotacticity ( $mm$ ) of 0.817 than sample A of 0.863, and the  $mr$  and  $rr$  triads of sample B are higher than that of sample A ( $mr$ : 0.063, 0.070 for samples A and B,  $rr$ : 0.074, 0.104 for samples A and B), respectively. The average sequence lengths ( $n_m$  and  $n_r$ ) calculated from the  $^{13}\text{C}$  NMR data are also summarized in Table 2. The average sequence lengths of meso ( $n_m$ ) and racemic ( $n_r$ ) was defined as:

$$n_m = \frac{mm + \frac{1}{2}mr}{\frac{1}{2}mr} \quad (1)$$

$$n_r = \frac{rr + \frac{1}{2}mr}{\frac{1}{2}mr} \quad (2)$$

Sample B has shorter  $n_m$  and longer  $n_r$  than sample A. The DSC results show that sample B has lower melting temperature ( $T_m$ ) at 160.0 °C and lower crystallinity of 37.1% than sample A ( $T_m$ : 162.9 °C, Cryst.: 38.9%), this indicates that sample B has lower ability to crystallize as the result of its lower isotacticity.

The above data exhibit the average values on microstructure for whole samples, but it is not sufficient to elucidate completely the relationship between the chain microstructure and the mechanical properties of the resins. Thus, an intensive understanding to chain structure can be acquired via the determination of the differences of tacticity distribution of these two polypropylenes. The related information can be obtained via fractionation and subsequent characterization of fractions by GPC,  $^{13}\text{C}$  NMR and DSC.

### 3.2. Fractionation results

Samples A and B are fractionated into six fractions, respectively, according to a procedure stated in experimental part (fraction 1 to fraction 6). Table 3 lists the fractionation results and meso triads distribution of the fractions from  $^{13}\text{C}$  NMR results. The weight fractions of the fractions are shown in Fig. 1. For both samples, the major parts, i.e. fractions 4, 5 and 6, are collected above 100 °C. Sample B has lower content of fractions above 100 °C (77.7 wt%) than 80.9 wt% for sample A. We noticed that fraction at 118 °C, i.e. A5 is 41.1 wt% while fraction above 118 °C B6 is 48.1 wt%.

As shown in Table 3, isotacticities and  $n_m$  of the fractions increase with the elution temperature for both samples. It should be mentioned that the isotacticities and  $n_m$  of the fractions from sample B are lower than the corresponding fractions from sample A, the tacticity differences between the corresponding fractions of samples A and B indicate that the longest crystallizable sequences have determined the fractionation.

**Table 3**  
The fractionation results and meso triads distribution of the fractions.

Sample	Temp. (°C)	Fraction	wt%	$mm$	$mr$	$rr$	$n_m$	$n_r$
A	RT	A1	6.1	0.299	0.282	0.419	3.12	3.97
	80	A2	5.3	0.628	0.138	0.234	10.1	4.39
	100	A3	7.7	0.872	0.073	0.055	24.9	2.51
	110	A4	16.4	0.943	0.039	0.018	49.4	1.92
	118	A5	41.1	0.965	0.025	0.010	78.2	1.80
	140	A6	23.4	0.986	0.011	0.003	180	1.55
B	RT	B1	6.4	0.248	0.299	0.453	2.66	4.03
	80	B2	6.3	0.476	0.168	0.356	6.67	5.24
	100	B3	9.6	0.844	0.078	0.076	22.6	2.95
	110	B4	20.5	0.917	0.052	0.031	36.3	2.19
	118	B5	9.1	0.933	0.046	0.021	41.6	1.91
	140	B6	48.1	0.974	0.016	0.010	123	2.25

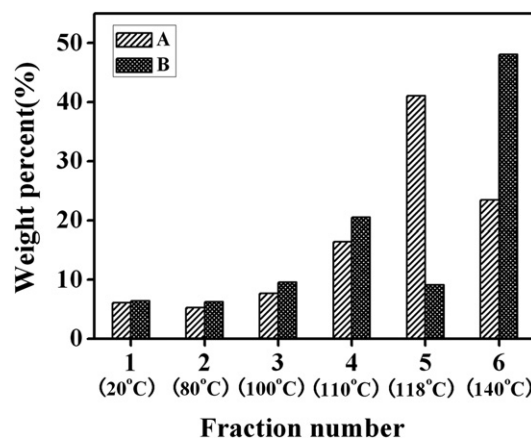


**Fig. 1.** Weight percent (%) of the fractions of samples A and B.

The observed pentad tacticities of the fractions are listed in Table 4. The  $[mmmm]$  of A1 and B1 is 0.172 and 0.125, respectively. The distribution of pentad tacticities in A1 and B1 are relatively homogeneous, these results imply that both A1 and B1 are atactic PP. The  $[mmmm]$  of fraction 2 is higher than that of fraction 1, but still lower than 0.5. Both A6 and B6 contain highly isotactic PP determined from  $[mmmm]$  (A6: 0.973, B6: 0.951) and small amount of other pentads, such as  $mmmr$ ,  $mmrr$  and  $mrrm$ , which fit a three-site model [24,25], describing each fraction as a mixture of highly isotactic, weakly isotactic and syndiotactic sequences. According to such model, the fractions of samples A and B comprise the same three components and differ merely in their relative amounts. Fraction 1 has high content of weakly isotactic and syndiotactic sequences and low content of highly isotactic sequences. From fraction 1 to fraction 6, the content of highly isotactic sequences increases meanwhile the content of weakly isotactic and syndiotactic sequences becomes lower.

Different fractions have different chain microstructures. The fractions 1 and 2 with low isotacticity act as softening agent and occupy 11.4 wt% and 12.7 wt% for samples A and B, respectively, which definitely contribute to the toughness and lead to higher impact strength than iPP. Fraction 3 (collected at 100 °C) has a medium isotacticity (~0.85). Fractions 4, 5 and 6 (collected above 100 °C) have higher isotacticity, the higher isotactic polypropylene reveals higher flexural strength and flexural modulus due to the higher crystallinity [26–28].

B1 and B2 has lower  $[mm]$  and  $n_m$  than A1 and A2, respectively, indicating that B1 and B2 contain more stereo-irregular sequences distribution; and the content of B1 and B2 is higher than that of A1 and A2, respectively, which contributes to the higher impact strength and lower flexural strength and flexural modulus of sample B. In addition, sample B has lower content of 77.7 wt% for above 100 °C fractions (B4, B5 and B6) than sample A of 80.9 wt% (A4, A5 and A6), the isotacticities and  $n_m$  of B4, B5 and B6 are lower than the corresponding fractions from sample A, which should be a key factor resulting in a lower flexural strength and flexural modulus of sample B.

Fig. 2 shows the weight percent of fractions as a function of isotacticity for samples A and B. It can be seen that both samples exhibit different isotacticity distribution. Sample A has a unimodal isotacticity distribution, and A5 ( $[mm] = 0.965$ ) has the highest weight percent; there are two maximums in isotacticity distribution of sample B, and B6 with highest isotacticity ( $[mm] = 0.974$ ) has the highest weight percent. The tacticity distribution in sample B is more heterogeneous than that in sample A, which should be another key factor resulting in higher impact strength in sample B.

**Table 4**  
Observed pentad tacticities of the fractions.

Fraction	<i>mmmm</i>	<i>mmmr</i>	<i>rmmr</i>	<i>mmnr</i>	<i>mmrm + rmrr</i>	<i>rmrm</i>	<i>rrrr</i>	<i>rrrm</i>	<i>mrrm</i>
A1	0.172	0.093	0.034	0.117	0.130	0.035	0.220	0.109	0.090
A2	0.482	0.119	0.027	0.078	0.044	0.016	0.134	0.049	0.051
A3	0.767	0.086	0.019	0.051	0.015	0.007	0.019	0.013	0.023
A4	0.879	0.050	0.014	0.028	0.008	0.003	0.005	0.005	0.008
A5	0.908	0.047	0.010	0.017	0.005	0.003	0.002	0.002	0.006
A6	0.973	0.013	–	0.007	0.004	–	–	–	0.003
B1	0.125	0.087	0.036	0.115	0.136	0.048	0.244	0.123	0.086
B2	0.361	0.091	0.024	0.083	0.060	0.025	0.238	0.070	0.048
B3	0.736	0.088	0.020	0.049	0.022	0.007	0.037	0.019	0.022
B4	0.808	0.072	0.037	0.027	0.018	0.007	0.012	0.007	0.012
B5	0.875	0.049	0.009	0.026	0.014	0.006	0.006	0.005	0.010
B6	0.932	0.019	0.023	0.016	–	–	–	–	0.010

### 3.3. GPC analysis

Fig. 3 shows the original samples along with the weight normalization GPC curves of the fractions and their sums, distribution of the smaller fraction (A1–A3 and B1–B3) are shown on the right with a magnified scale. Table 5 lists the related molecular weight data of the fractions. In Fig. 3, the sum of GPC curves of the fractions is in good agreement with the GPC curves of unfractionated samples, which suggests that the fractionation method used in this work is definitely efficient. As shown in Fig. 3, the low isotactic fractions have very broad MWD, such as fractions 2 and 3 have a bimodal MWD. For the high isotactic fractions, the MWD become narrower, but for the last fraction (A6 and B6), the values are still close to 4 (Table 5). The broad molecular weight distribution of the fractions of samples A and B indicate that all fractions contain composition produced by different site types.

The  $M_w$  values of the fractions are shown in Fig. 4. It should be mentioned that the fraction labeled as 140 °C is fraction 6, actually it is insoluble fraction at 118 °C but soluble at 140 °C. For both samples,  $M_w$  firstly decreases with increasing fractionation temperature and the fraction at 100 °C (fraction 3) has the lowest  $M_w$ , then  $M_w$  increases with increasing fractionation temperature and the fraction at 140 °C (fraction 6) has the highest  $M_w$ . It is clearly shown that these fractions are not separated according to molar mass, only depending on their crystallization ability. The fractions of sample B have higher  $M_w$  than the corresponding fractions of sample A collected at the same temperature. For the propylene homopolymer, increasing molecular weight offer enhanced mechanical properties, particularly in toughness [29]. Increasing the molecular weight of the polymer causes a larger amount of entanglements in the inter-lamellar and inter-spherulitic regions. This leads to the tendency of an enhanced stabilization

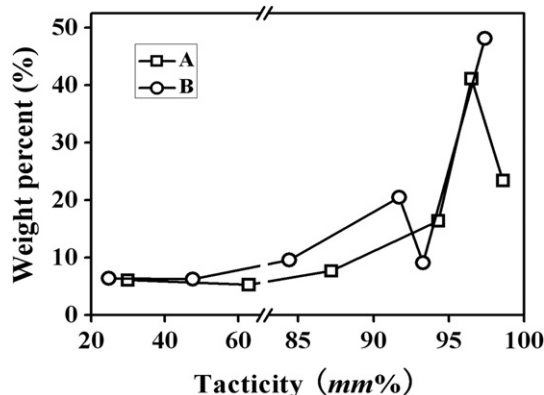


Fig. 2. Weight percent (%) as a function of tacticity (*mm%*) for samples A and B.

and extension of a crazed network with increasing molecular weight, resulting in higher toughness [30]. Except for the isotacticity distribution, the higher molecular weight of both sample B and its fractions should be another key factor resulting in higher impact strength in sample B finally.

### 3.4. DSC analysis and thermal fractionation

Table 6, Fig. 5 and Fig. 6 show the results of the thermal analysis of the fractions. Fig. 5 shows that the melting temperatures of fractions from samples A and B rise gradually with increasing fractionation temperature. This indicates an increase of isotacticity and length of isotactic sequences. The fractions of sample B have lower  $T_m$  than the corresponding fractions of sample A collected at the

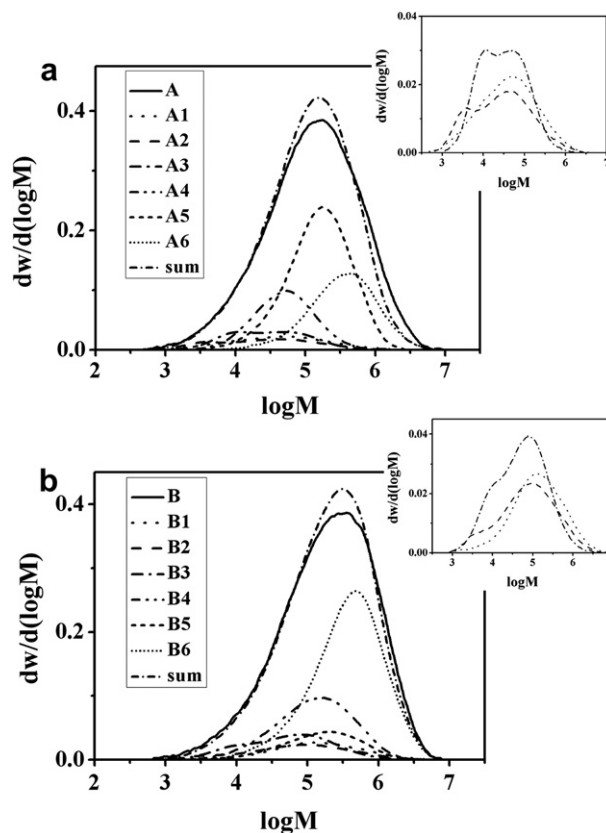


Fig. 3. Molecular weight distribution profiles of samples A (a) and B (b) with the weighted distributions of the fractions and their sums. Distribution of the smaller fraction (A1–A3 and B1–B3) are shown on the right with a magnified scale.

**Table 5**  
The molecular weight data of the fractions.

Sample	Fraction	Temp.(°C)	$M_w (10^{-4})$	$M_n (10^{-4})$	$M_w/M_n$
A	A1	RT	12.1	1.22	9.90
	A2	80	9.63	0.861	11.2
	A3	100	6.50	1.42	4.58
	A4	110	8.03	3.05	2.63
	A5	118	24.7	7.96	3.11
	A6	140	59.1	16.6	3.56
B	B1	RT	32.0	3.78	8.48
	B2	80	22.0	1.94	11.3
	B3	100	12.9	1.90	6.78
	B4	110	23.7	5.47	4.35
	B5	118	29.2	6.28	4.66
	B6	140	62.8	15.8	3.96

same fractionation temperature, indicating a lower isotacticity of fractions from sample B, which was in accordance with  $^{13}\text{C}$  NMR results.

In Fig. 6, the crystallinity of the fractions does not show a monotonical increase with fractionation temperature, there is a maximum in each plot. Definitely, the above result is very similar to that obtained in TREF, which separates macromolecules according to the longest crystallizable sequences [11,31–33]. The crystallizable sequences in PP chains are the isotactic sequences. For fractions of sample A collected at 110, 118, 140 °C (A4–A6) and fractions of sample B collected at 118, 140 °C (B5 and B6), their melting temperature of fractions increase slightly with fractionation temperature, but the molecular weight of fractions increases drastically. The decrease of crystallinity for these high molecular weight fractions possibly comes from imperfection of crystallization due to restricted mobility of very long chains in these fractions. Fig. 6 also show that fractions of sample B show a lower crystallinity than the corresponding fractions of sample A, resulting from lower isotactic degrees and shorter isotactic sequence for sample B fractions. B4, B5 and B6 with the higher isotacticity, have lower crystallinity than the corresponding fractions of sample A, resulting in a lower flexural strength and flexural modulus of sample B finally.

The SSA melting curves of the fractions of samples A and B are presented in Fig. 7, except fraction 1 due to atactic PP without detectable thermogram. Both fractions 2 and 3 show broad thermograms with multiple melting peaks (the main melting peaks for A2 locate at 121.6, 126.4, 131.6, 135.8 °C, and 121.7, 126.7, 131.1, 136.1 °C for B2; 144.9, 148.0, 152.5, 157.3 °C for A3, 141.6, 147.4, 152.7, 158.0 °C for B3), reflecting the fractions crystallized in successive steps of SSA. The chains in one fraction can still contain a broad intra-molecular crystallizable sequence distribution, which explains the presence of multiple melting peaks. The broad melting

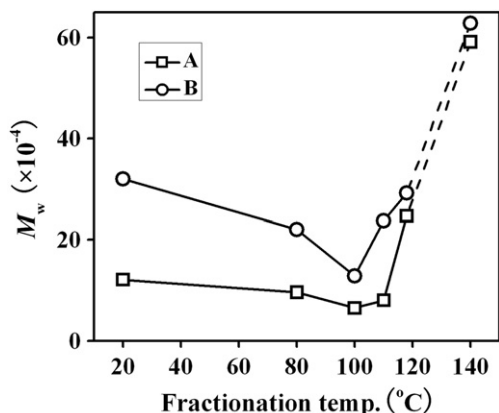


Fig. 4. Change of  $M_w$  of the fractions with fractionation temperatures.

**Table 6**  
DSC results from the fractions.

A			B		
Fraction	$T_m(°C)$	Cryst. (%)	Fraction	$T_m(°C)$	Cryst. (%)
A1	—	—	B1	—	—
A2	125.3	24.5	B2	121.7	17.0
A3	145.9	38.7	B3	143.8	34.0
A4	158.2	45.3	B4	158.1	39.4
A5	164.0	42.8	B5	160.6	40.7
A6	165.5	41.2	B6	164.1	39.7

curves also indicate that temperature rising dissolution fractionation (TRDF) used in this work separated the fractions according to the longest crystallizable sequences. The high isotactic fractions, i.e., fraction 4, 5 and 6, show narrower thermograms which contains only one or two clear peaks. For example, the main melting peaks of A4, A5, A6, B4, B5, B6 locate at 168.9, 174.6, 175.4, 170.5, 170.7, 174.8 °C, respectively. The above narrow melting peaks of the high isotactic fractions indicate that these fractions have more homogeneous crystallizable sequence distribution.

Although the  $[mm]$  of A3 and B3 are higher than 0.8, their SSA melting curves still show broad thermograms with multiple melting peaks. The main melting peaks for A3 locate at 144.9, 148.0, 152.5, 157.3 °C for A3, 141.6, 147.4, 152.7, 158.0 °C for B3. This means that A3 and B3 have relatively longer crystallizable sequences, but the crystallizable sequences are irregular interrupted by the stereoirregular sequences. It had been found that the chains of intermediate crystallinity which melt at lower temperature possibly act as tie molecules and help in holding together the crystallites in different regions. Removing this material might result in a crystallinity increase, however, on application of a tensile load the energy absorption mechanisms are not as strong as when fraction with intermediate crystallinity is present [34–36]. Thus, A3 and B3 can act as tie molecules that connect the crystal lamellae to improve the toughness of samples.

The three-dimensional wire surface plots of the TRDF-GPC cross-fractionation of samples A and B are shown in Fig. 8. Each region on the surface gives the relative amount of species with a given molecular weight and composition. Although only six fractions are collected here, it still clearly shows the great heterogeneity and difference in the microstructure distribution of the samples in both composition and molecular weight. Both samples contain approximately 11–13 wt% fractions with low isotacticity, so there is a tiny peak in the low temperature region (below 100 °C). Definitely, low isotacticity contents improve the impact properties

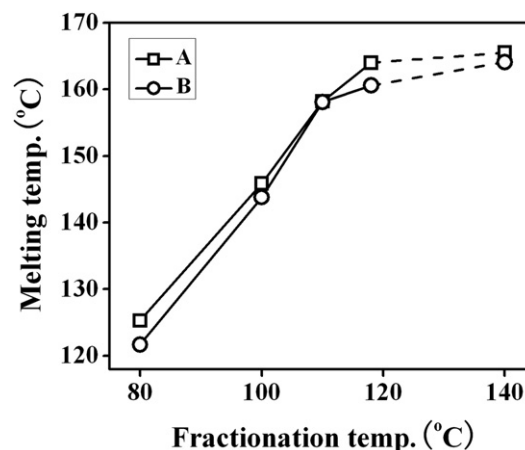


Fig. 5. Change of melting temperatures of the fractions with fractionation temperatures.

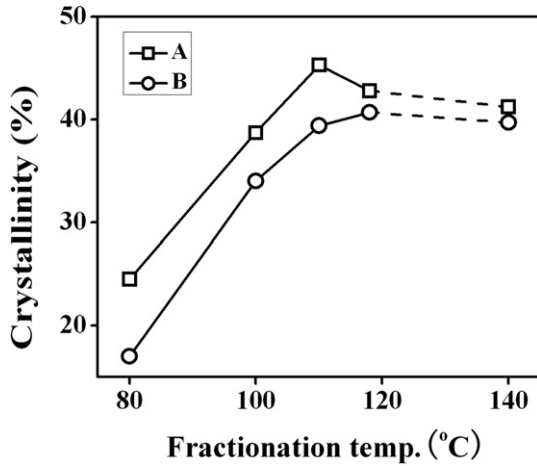


Fig. 6. Change of crystallinity of the fractions with fractionation temperatures.

of both sample A and B as shown in Table 1. As shown in Fig. 8, the main differences in microstructure distribution are caused by fraction 5 (118 °C) and fraction 6 (above 118 °C). The weight percent of A5 is 41.1%, which is almost five times higher than that B5 of 9.1%. The weight percent of B6 is 48.1%, which is almost twice than A6 of 23.4%. As a result, sample B exhibits three peaks clearly. GPC results have shown that the fractions of sample B have higher  $M_w$  than the corresponding fractions of sample A collected at the same temperature. These results indicate that heterogeneous isotacticity distribution accompanied with high molecular weight contributes to the better toughness of sample B.

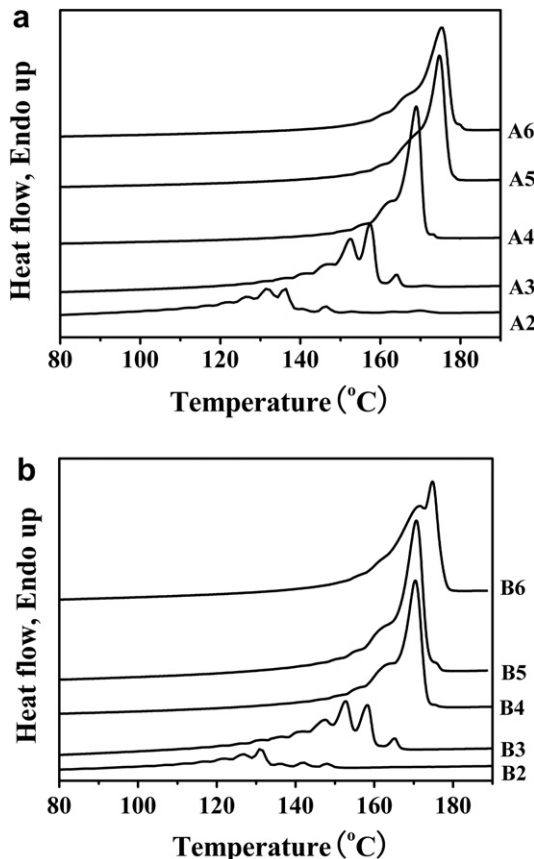


Fig. 7. SSA melting curves of the fractions of samples A(a) and B (b).

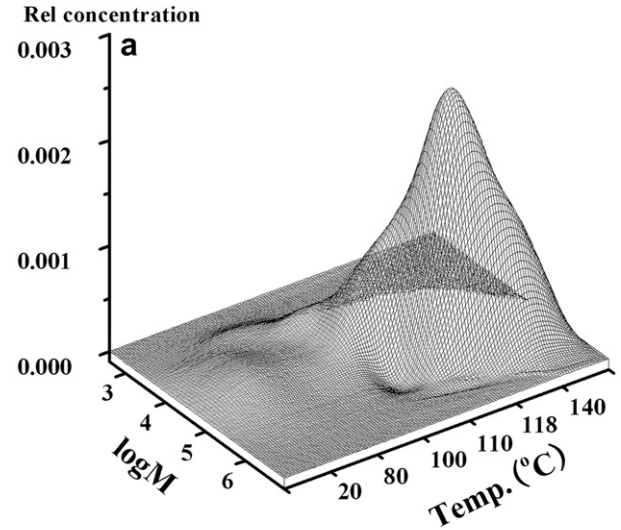


Fig. 8. The 3D Wire Surface plots of the fractionation-GPC analysis of samples A (a) and B (b).

#### 4. Conclusions

Two polypropylene homopolymers, samples A and B, synthesized with heterogeneous Ziegler–Natta catalysts, exhibit good impact properties at low temperature, particularly sample B has better performance. These two samples were fractionated into six fractions via a simple fractionation method, i.e. temperature rising dissolution fractionation (TRDF), respectively. Definitely, the TRDF used in this work fractionates the polypropylene samples according to the longest crystallizable sequence length similar to temperature rising elution fractionation (TREF).

Fraction 1 (room-temperature fraction) is atactic PP, which is approximately to be random ethylene–propylene copolymer (EPR) in PP/EPR in-reactor alloys. Fraction 2 (fraction at 80 °C) has low isotacticity. Increasing fractionation temperature leads to a high isotacticity. Absolutely, fraction 1 and 2 with 11–13 wt% serve as toughening agent like EPR or elastomers in resins and lead to higher impact strength than iPP. Fraction 3 (collected at 100 °C) has a medium isotacticity (~0.85), which can act as tie molecules that connect the crystal lamellae to improve the toughness of samples. Fractions 4, 5 and 6 (collected above 100 °C) have higher

isotacticity, the higher isotactic polypropylene contributes to higher flexural strength and flexural modulus due to the higher crystallinity.

On the other hand, two samples exhibit some difference. <sup>13</sup>C NMR and DSC analysis of the fractions has clearly shown that fractions of sample B have lower isotacticity and crystallinity than the corresponding fractions of sample A. The lower isotacticity and crystallinity of fractions in sample B should be one key factor resulting in better toughness. On the other side, the fractions of sample B have higher molecular weight than the corresponding fractions of sample A collected at the same temperature, which should be another key factor leading to better toughness of sample B.

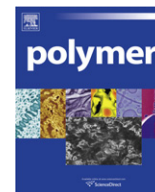
Definitely, both higher molecular weight and heterogeneity of inter- and intra- molecular isotacticity distribution are helpful to improve the toughness of polypropylene homopolymer with high isotacticity and adjust the balance between the stiffness and toughness finally in the resins. Possibly, it provides another approach to get impact polypropylene resins.

### Acknowledgments

This work was subsidized by the National Natural Science Foundation of China (Key Project: 20734006, Innovation Group: 50921062), National Basic Research Program of China (2005CB623806).

### References

- [1] Kakugo M, Miyatake T, Naito Y, Mizunuma K. *Macromolecules* 1988;21:314.
- [2] Soares JBP, Hamielec AE. *Polymer* 1996;37:4607.
- [3] Xu JT, Feng LX. *Eur Polym J* 2000;36:867.
- [4] Paukkeri R, Vaananen T, Lehtinen A. *Polymer* 1993;34:2488.
- [5] Natta G. *J Polym Sci* 1959;34:531.
- [6] Collette JW, Ovenall DW, Buck WH, Ferguson RC. *Macromolecules* 1989;22:3858.
- [7] Viville P, Daoust D, Jonas AM, Nysten B, Legras R, Dupire M, et al. *Polymer* 1953;2001:42.
- [8] Liu YG, Bo SQ. *Int J Polym Anal Char* 2003;8:225.
- [9] Thomassin JM, Huynen I, Jerome R, Detrembleur C. *Polymer* 2010;51:115.
- [10] Yu HO, Jiang ZW, Gilman JW, Kashiwagi T, Liu J, Song RJ, et al. *Polymer* 2009;50:6252.
- [11] Farzi G, Akbar S, Beyou E, Cassagnau P, Melis F. *Polymer* 2009;50:5901.
- [12] Li SZ, Xiao MM, Wei DF, Xiao HN, Hu FZ, Zheng AN. *Polymer* 2009;50:6121.
- [13] Morini G, Albizzati E, Balbontin G, Mingizzi I, Sacchi MC, Forlini F, et al. *Macromolecules* 1996;29:5770.
- [14] Xu JT, Yang Y, Feng LX, Kong X, Yang S. *J Appl Polym Sci* 1996;62:727.
- [15] Paukkeri R, Iiskola E, Lehtinen A, Salminen H. *Polymer* 1994;35:2636.
- [16] Alamo RG, Blanco JA, Agarwal PK, Randall JC. *Macromolecules* 2003;36:1559.
- [17] De Rosa C, Auriemma F, Spera C, Talarico G, Tarallo O. *Macromolecules* 2004;37:1441.
- [18] Virkkunen V, Laari P, Pitkänen P, Sundholm F. *Polymer* 2004;45:3091.
- [19] Virkkunen V, Laari P, Pitkänen P, Sundholm F. *Polymer* 2004;45:4623.
- [20] Kravchenko RL, Sauer BB, McLean RS, Keating MY, Cotts PM, Kim YH. *Macromolecules* 2000;33:11.
- [21] Müller AJ, Arnal ML. *Prog Polym Sci* 2005;30:559.
- [22] Müller AJ, Hernandez ZH, Arnal ML, Sanchez JJ. *Polym Bull* 2007;39:465.
- [23] Fillon B, Wittmann JC, Lotz B, Thierry A. *J Polym Sci Polym Phys Ed* 1993;31:1383.
- [24] Busico V, Cipullo R, Monaco G, Talarico G, Vacatello M, Chadwick JC, et al. *Macromolecules* 1999;32:4273.
- [25] Garoff T, Virkkunen V, Jaaskelainen P, Vestberg T. *Eur Polym J* 1679:39.
- [26] Spieckermann F, Wilhelm H, Kerber M, Schafner E, Polt G, Bernstorff S, et al. *Polymer* 2010;51:4195.
- [27] Androsch R, Di Lorenzo ML, Schick C, Wunderlich B. *Polymer* 2010;51:4639.
- [28] White HM, Bassett DC, Jääskeläinen P. *Polymer* 2009;50:5559.
- [29] Fayolle B, Tcharkhtchi A, Verdu J. *Polymer Testing* 2004;23:939.
- [30] Patel RM, Sehanobish K, Knight GW. *J Appl Polym Sci* 1996;60:749.
- [31] Zhang M, Lynch DT, Wanke SE. *J Appl Polym Sci* 2000;75:960.
- [32] Elicabe G, Cordon C, Carella J. *J Polym Sci Part B Polym Phys* 1996;34:1147.
- [33] Bonner JG, Frye CJ, Capaccio G. *Polymer* 1993;34:3532.
- [34] Stagnaro P, Boragno L, Canetti M, Forlini F, Azzurri F, Alfonso GC. *Polymer* 2009;50:5242.
- [35] Zhang CH, Shangquan YG, Chen RF, Wu YZ, Chen F, Zheng Q, et al. *Polymer* 2010;51:4969.
- [36] Balta Calleja FJ. *Adv Polym Sci* 1985;66:117.



# Fracture behavior of bimodal polyethylene: Effect of molecular weight distribution characteristics

Xin Sun, Hongwang Shen, Banghu Xie\*, Wei Yang, Mingbo Yang

College of Polymer Science and Engineering, Sichuan University, State Key Laboratory of Polymer Materials Engineering, Chengdu 610065, Sichuan, China

## ARTICLE INFO

### Article history:

Received 30 July 2010

Received in revised form

21 October 2010

Accepted 5 December 2010

Available online 10 December 2010

### Keywords:

Bimodal polyethylene (BPE)

Molecular weight distribution (MWD)

Essential work of fracture (EWF)

## ABSTRACT

A series of bimodal polyethylenes with different molecular weight distribution characteristics were prepared by melt blending, and the fracture behavior of these bimodal polyethylenes was studied by the method of essential work of fracture. The results show that specific essential work of fracture,  $w_e$ , increases obviously with the molecular weight distribution characteristic,  $A_{L/U}$ , indicating the improvement of the resistance to crack propagation. By means of successive self-nucleation and annealing analysis, obvious variations in the crystal structures of bimodal polyethylenes with increasing  $A_{L/U}$  have been found. That is, the crystal size and the amount of relatively thick lamellas increase with  $A_{L/U}$ , but no large variation of crystallinities has been observed. So, the influence of  $A_{L/U}$  is mainly on the crystal perfection, the improvement of which produces an enhancement of fracture toughness since more energy would be dissipated in the superior network structure constructed from crystalline zones and amorphous zones.

© 2010 Elsevier Ltd. All rights reserved.

## 1. Introduction

Since the application of polyethylene (PE) in pipes over 40 years ago, more and more attention has been paid to reach even higher performance standards. Numerous novel polymerization technologies have been developed in order to tailor the architecture of PE to obtain materials with higher properties [1,2]. It is well known that the mechanical properties of PE are usually influenced by molecular weight (Mw) and molecular weight distribution (MWD), as well as other microstructural features, such as the comonomer type, comonomer content, short chain branch (SCB) and its length etc. [3–7].

As for Mw, unimodal polyethylenes made by traditional catalysts have conflicts between their mechanical properties and processing behaviors, that is, improving mechanical performances by increasing Mw usually deteriorates the processing properties owing to high melt viscosity. Recently, based on metallocene catalysts, some novel synthetic techniques have been developed to produce bimodal polyethylene (BPE) with particular double peaks in the MWD curve. The bimodal material consisted of both high molecular weight fraction and low molecular weight fraction provides more balanced performances to processing and mechanical behaviors, because the high molecular weight fraction brings

excellent mechanical properties and the low molecular weight fraction allows the melt to flow easily.

The BPEs with different MWD characteristics (such as peak position and peak height) show great variations in their properties, which are controlled by both the catalysts and the process [8–12]. Obviously, the understanding of the relationship between MWD and properties of BPE has great value and significance for its preparation and application. Some researchers [7,13,14] have already studied the melting behaviors and crystallization kinetics of BPE with different Mw and Mw/Mn. DesLauriers et al. [10] used some BPE pipe resins with different Mw and Mw/Mn to compare their yielding stress, tensile strength and rheology parameters. However, there are few reports particularly focusing on how the fracture behaviors of BPE are influenced by the MWD characteristic.

Usually single stage process, two stage cascade polymerization process and melt mixing are used to produce BPE, and in essence, two kinds of polyethylenes with different Mw and MWDs are mixed together using these methods [15,16]. Some literatures [2,7,17] have reported that the high molecular weight fraction of BPE usually consists of  $\alpha$ -olefin copolymers and the low molecular weight fraction is generally homopolymer. For the benefits of preparing BPE samples with desired MWDs, we used melt blending method to prepare samples due to the difficulty in obtaining BPEs with regular variable MWDs from commercial channels. So a homo-polyethylene was used to blend with a commercial BPE. The samples made by this procedure have the same double peak positions but different peak heights in their MWD curves. In this

\* Corresponding author. Tel./fax: +86 28 8540 5324.

E-mail address: [xiebangh@tom.com](mailto:xiebangh@tom.com) (B. Xie).

study the influences of bimodal characteristic on the fracture behaviors of BPE will be discussed.

In the industrial practice, after a long period of service, brittle fracture can be observed for many PEs although under loads well below their yield stress [18,19]. Usually common PEs used for pressure pipes have defects such as low environmental stress cracking resistance and lack of the ability to stop the crack effectively, which may cause severe economic and environmental losses by leakage. Considerable efforts have been paid to study the influences of structural factors, including Mw, SCB content, length of SCB and distribution of SCB, on the fracture behaviors and long term properties of materials [20–28]. Undoubtedly, evaluation of the cracking resistance of BPE is especially important for its application as pressure pipes. In this article, one available method, namely essential work of fracture (EWF) has been used to assess the BPEs' fracture toughness. This method has been developed greatly and become much attractive in evaluating the fracture behavior of ductile polymers, particularly due to its validity and ease of implementation [29–37]. Meanwhile, based on the successive self-nucleation and annealing analysis (SSA), the reason for the varied fracture behaviors of BPEs with different bimodal characteristics was discussed and the underlying mechanism was elucidated reasonably.

## 2. Experimental

### 2.1. Materials and sample preparation

Two kinds of parent polymers named bimodal PE100 (Shanghai Petrochemical Co.;  $\rho = 0.949 \text{ g/cm}^3$ ,  $M_w = 5.9 \times 10^5 \text{ g/mol}$ ) and unimodal PE2911 (Fushun Petrochemical Co.;  $\rho = 0.960 \text{ g/cm}^3$ ;  $M_w = 1.7 \times 10^5 \text{ g/mol}$ ,  $\overline{M}_w/\overline{M}_n = 4.18$ ) were used in this paper. The samples were prepared by blending PE100 and PE2911 with the mass ratio of 100/0, 92/8 and 84/16 in a TSSJ-25 co-rotating twin screw extruder twice,  $L/D = 33$ . and they were labeled as  $S_1$ ,  $S_2$  and  $S_3$ , respectively. The temperature profiles were 130 °C, 160 °C, 180 °C, 210 °C, 210 °C, 205 °C for the feed zone, the compression zone, the metering zone, the exhaust zone and the pumping zone, respectively.

### 2.2. GPC

The MWD curves of all samples were obtained by GPC (Model PL-GPC 220, UK) using 1,2,4-trichlorobenzene (TCB) as a solvent at 160 °C. The calibration of the data was conducted using standard polystyrene samples.

### 2.3. Dynamic rheological test

The samples were melt-pressed at 200 °C into 25 mm × 1 mm circular disks. Dynamic frequency sweeps were performed over the 0.01–100 Hz at 220 °C and 1% strain, using Rheometer System Gemini 200 with the parallel mode.

### 2.4. EWF tests

The pellets were compression-molded into sheets about 0.5 mm thickness at 220 °C and 10 MPa, and then DENT specimens (length × width = 100 mm × 35 mm) were cut from the sheets. The sharp pre-cracks on both sides of the specimens were made perpendicularly to the tensile direction with a fresh razor blade. The ligament lengths and the thickness were measured using a microscope and a vernier caliper before the tensile tests. At least 20 DENT specimens with different ligament lengths were needed for each sample. The EWF tests were conducted on an Instron 4302

universal testing machine equipped with a 500 N load cell at a crosshead speed of 5 mm/min, and the test temperature was  $23 \pm 2 \text{ °C}$ . The load–displacement curves were recorded and the total absorbed energy was calculated by computer integration of the loading curves.

### 2.5. Differential scanning calorimetry (DSC) experiments

The calorimetric experiments were performed in TA Q20 DSC calibrated with indium. All the following DSC scans were conducted in a nitrogen atmosphere with both cooling rate and heating rate of 10 °C/min. Samples of about 5 mg were used for the tests.

*Common DSC tests:* The samples were first melted at 160 °C for 5 min to erase previous thermal history, then cooled to 40 °C to obtain cooling curves and heated to 160 °C again to record the melting curves.

*SSA thermal fractionation:* After melting the samples at 160 °C for 5 min to erase previous thermal history, a “standard” thermal history was created by cooling them down to 40 °C; then heating the samples to the first self-nucleation temperature 132 °C and holding 5 min for isothermal crystallization. After that, the samples were cooled down to 40 °C, and were heated once again to the second self-nucleation temperature 127 °C and after 5 min isothermal procedure cooling the samples down to 40 °C. This cyclic procedure was repeated 6 times, and each self-nucleation annealing temperature was 5 °C lower than the previous one. Finally, SSA fractionation curves were obtained by melting the samples to 160 °C at 10 °C/min.

## 3. Results and discussion

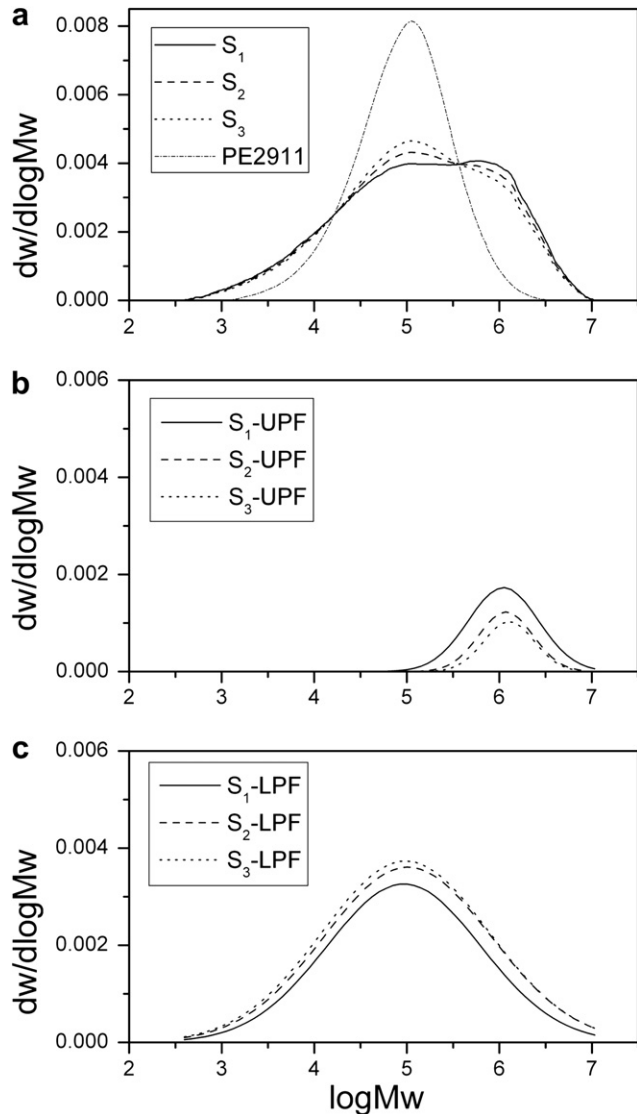
### 3.1. MWD characteristic and compatibility

Fig. 1a presents the MWD curves of BPE samples  $S_1$ – $S_3$  prepared by blending unimodal PE2911 and bimodal PE100. As can be seen, the relative intensities of the two peaks in the GPC MWD curves vary regularly. The average molecular weight,  $\overline{M}_w$ , and molecular weight distribution width,  $\overline{M}_w/\overline{M}_n$ , are listed in Table 1. It is seen that the  $\overline{M}_w$  does not show obvious variation and the decrease of  $\overline{M}_w/\overline{M}_n$  is also slight. The main differences exist in the intensities of the upper (the high molecular weight fraction) and lower (the low molecular weight fraction) peaks. The upper peaks descend and the lower peaks ascend regularly from the sample  $S_1$  to  $S_3$ , while their positions in transverse axis almost keep the same. So, by using Gaussian Fit Multi-peaks, each of these MWD curves in Fig. 1a can be fitted by a superposition of two normal distributed Gaussian components, both of which are distinct unimodal curves (Fig. 1b and c). The peaks of MWD curves in Fig. 1b and c are respectively located in  $\log M_w = 6.05$  and  $\log M_w = 4.97$ . For these BPEs, the curves in Fig. 1b reflect the change of the content of upper peak fraction (UPF, the high molecular weight fraction) and the curves in Fig. 1c are related to the lower peak fraction (LPF, the low molecular weight fraction) correspondingly.

As also can be indicated from Fig. 1, the content of UPF (area under corresponding curves in Fig. 1b) decreases but the content of LPF (area under corresponding curves in Fig. 1c) increases in sequence from  $S_1$  to  $S_3$ . Obviously, for the BPEs prepared in this work, the ratio of the content of LPF and UPF, shown as the ratio of the area under corresponding unimodal curves (marked as  $A_{L/U}$ ), can be regarded as the characteristic value of bimodal distribution. The results of  $A_{L/U}$  are also listed in Table 1 in order to conveniently discuss the influences of bimodal characteristic values on the properties of BPE in the following sections.

Before other studies, it is necessary to verify the compatibility of the prepared blends. Usually, there are many ways to estimate the





**Fig. 1.** MWD curves of BPE samples. a, the experimental MWD curves of BPEs; b and c, the upper and lower MWD curves after peak division process by Gaussian Fit Multi-peaks.

compatibility of PE blends, such as rheological behaviors (Cole–Cole curve, Han curve and additivity law of viscosity, etc.) and thermodynamic properties [3,38–40]. In this work, we give the dynamic rheological results to show the compatibility of the prepared BPE blends. In Fig. 2, the complex viscosity ( $\eta^*$ ) values versus weight fraction of PE2911 in the blends are plotted at different frequencies for BPEs. For partially miscible or immiscible blends,  $\eta^*$  versus composition curve may exhibit positive or negative deviation from linearity owing to phase separation [41,42]. Fig. 2 indicates that  $\eta^*$  of the BPEs shows good linearity with the increase of PE2911 at different frequencies, and the values are very close to those calculated viscosities according to the additivity law,

**Table 1**  
The molecular weight parameters and characteristic values of BPE samples.

Sample	$\bar{M}_w$ (g/mol)	$\bar{M}_w/\bar{M}_n$	$A_{L/U}$
S <sub>1</sub>	589,000	28.2	4.15
S <sub>2</sub>	550,000	25.5	8.48
S <sub>3</sub>	525,000	23.0	11.14

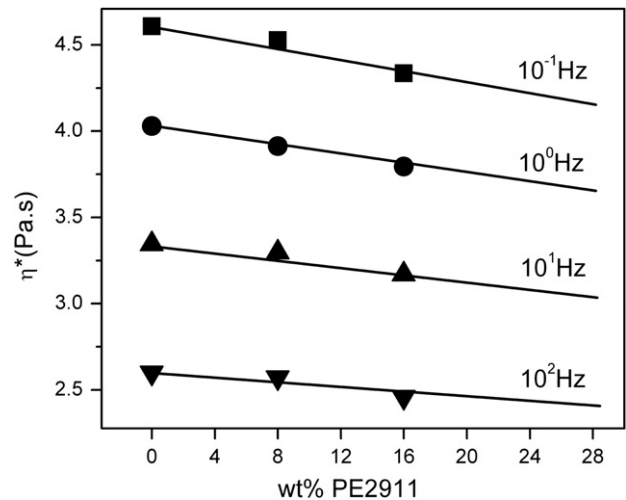


**Fig. 2.** The composition dependence of complex viscosity  $\eta^*$  for the BPEs at different frequency. (The solid lines represent the additive  $\eta^*$  of S<sub>1</sub> and PE2911 according to the additivity law).

demonstrating the good miscibility of the BPE blends. Additional discussion on the crystallization behaviors related to miscibility will also be involved in Section. 3.3.

### 3.2. Fracture behavior

According to the essential work of fracture (EWF) theory, the total work of fracture ( $W_f$ ) is composed of the essential work required to fracture the polymer in its process zone ( $W_e$ ) and the plastic work consumed by various deformation mechanisms in the plastic zone ( $W_p$ ).  $W_e$  is surface-related, whereas  $W_p$  is volume-related.  $W_f$  can be written by the related specific work terms:

$$W_f = W_e + W_p = w_e t l + \beta w_p t l^2 \quad (1)$$

$$w_f = W_f/tl = w_e + \beta w_p l \quad (2)$$

where  $w_f$ ,  $w_e$  and  $w_p$  represent the specific total work of fracture, specific essential work and specific non-essential or plastic work respectively, and  $l$  is the ligament length,  $t$  thickness of the specimen and  $\beta$  a shape factor related to the form of the plastic zone. Provided that  $\beta w_p$  is a constant independent of  $l$ ,  $w_e$  and  $\beta w_p$  can be easily determined respectively by reading the ordinate intercept and the slope of the linear plot  $w_f$  vs  $l$ .

The load–displacement curves of DENT specimens for the three BPEs with different ligament lengths are presented in Fig. 3. We could see that all curves showed good self-similarity and the slight increase of load in the beginning caused the fast increase of displacement, the procedure of which was called linear elastic zone. With continuing rise of the load, the materials reached yielding point, afterwards the load decreased suddenly and the ligaments yielded and began necking. After the complete necking, cracks emerged and started to grow stably until the DENT specimens were destroyed. From the appearance and the phenomena during the whole fracture process, all fracture tests met the prerequisites of EWF tests [30,32,43,44].

The linear relationships between  $w_f$  and  $l$  of different BPEs are shown in Fig. 4. For these samples, the  $w_f$ – $l$  linear relationships are very good and the linear regression coefficients,  $R^2$ , are all over 0.97.  $w_e$  is obtained by extrapolating the  $w_f$ – $l$  curve to  $l = 0$  and  $\beta w_p$  is determined by the slope of the line. The values of  $w_e$  and  $\beta w_p$  of all BPEs are listed in Table 2.

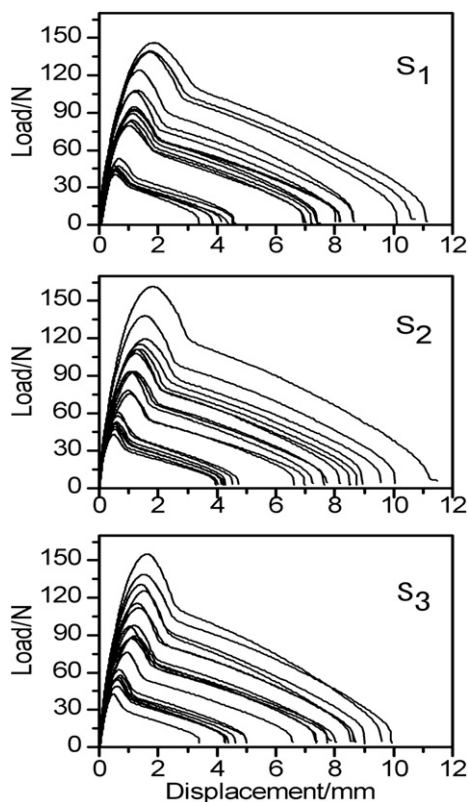


Fig. 3. Load–displacement curves of different BPEs in EWF tests.

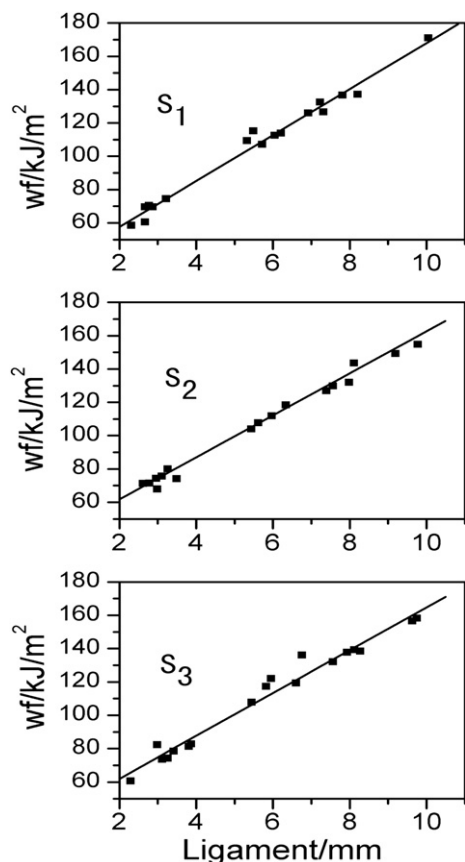


Fig. 4.  $W_f$ – $l$  curves of different BPEs.

Table 2

Fracture parameters of different BPEs obtained from EWF tests.

Sample	$A_{L/U}$	$w_e$ (kJ/m <sup>2</sup> )	$\beta w_p$ (kJ/m <sup>3</sup> )	$R^2$
S <sub>1</sub>	4.15	28.62	14.13	0.984
S <sub>2</sub>	8.48	35.41	12.88	0.971
S <sub>3</sub>	11.14	36.23	12.81	0.978

As can be seen from Table 2, the specific essential work of fracture,  $w_e$ , is the least when  $A_{L/U}$  is 4.15, revealing that S<sub>1</sub> has smaller fracture toughness or lower ability to resist crack propagation. With the increases of  $A_{L/U}$ ,  $w_e$  gets larger gradually and the largest increasing extent is near 27%. When  $A_{L/U}$  increases from 4.15 to 8.48,  $w_e$  of S<sub>2</sub> is much larger than that of S<sub>1</sub>, and the increasing range is close to 25%, indicating that the resistance of crack propagation increases significantly. Although  $w_e$  increases further until  $A_{L/U}$  reaches 11.14, the range of increase becomes smaller (only about 1 kJ/m<sup>2</sup>). This phenomenon probably indicates that the trend of improved resistance to crack propagation might be weakened gradually with increasing  $A_{L/U}$ .

For the specific plastic work, S<sub>1</sub> has relatively large  $\beta w_p$ . With increasing  $A_{L/U}$ , the  $\beta w_p$  values of BPEs decrease for a certain degree, which implies that the ability of resisting plastic deformation decreases. However, the decreased trend of  $\beta w_p$  is not obvious when the  $A_{L/U}$  increases gradually to 11.14. This decrease from S<sub>2</sub> to S<sub>3</sub> is so slight that the work consumed in plastic deformation can be considered practically unchanged.

These two EWF parameters ( $w_e$  and  $\beta w_p$ ) usually display different or even opposite varying tendencies, that is to say, one of them increases and the other will decrease. As has been declared in some literatures [45,46],  $w_e$  is the energy necessary to create new surfaces, and it is actually the work done to separate physically the material into two parts.  $\beta w_p$  includes a sum of plastic deformation mechanisms that occur around the fracture path (but out of it). In all, the influence of  $A_{L/U}$  on  $\beta w_p$  is not significant, whereas the effect of  $A_{L/U}$  on  $w_e$  is great. So the improvement in  $w_e$  owing to the increased  $A_{L/U}$  has great significance for BPE materials to enhance the resistance of crack propagation.

Some literatures [33,47] have reported that  $w_e$  of materials increases with Mw, which is generally recognized as the increase of entanglements among the molecular chains. However, what surprises us is that the increase in the content of LPF causes the reduction of Mw (see Table 1) while a great increase in fracture toughness, although the average molecular weight of LPF is not very low. Actually, the crack propagation in BPE could be intimately related to the morphology evolution during the sample preparation, which determines the crystal size, the relative fractions between crystalline and amorphous zones, as well as the amount of tie molecules between crystal lamellas. In this regard, the variation in the phase structures of different BPEs will show difference in their thermal behaviors, from which we may get the fundamental difference of BPEs to find the relationship between fracture toughness and phase structures.

### 3.3. Crystallization behavior

#### 3.3.1. Common DSC analysis

In common DSC tests, each BPE sample shows a single melting peak in the heating scan, and the corresponding parameters are listed in Table 3. In the range of these MWDs, the melting peak temperatures ( $T_m$ ) have a small upward trend with the increased  $A_{L/U}$  values. The  $T_m$  of S<sub>3</sub> with the largest  $A_{L/U}$  is only about 1 °C higher than that of S<sub>1</sub>; meanwhile the half peak width ( $\Delta W_m$ ) of the melting peaks also displays a slight increase with  $A_{L/U}$ . With more

**Table 3**  
The crystallization parameters of BPEs in common DSC tests.

Sample	$T_m$ (°C)	$\Delta W_m$ (°C)	$X_c$
S <sub>1</sub>	130.31	7.17	0.5932
S <sub>2</sub>	130.59	7.23	0.6038
S <sub>3</sub>	131.38	8.49	0.6259

LPF, in addition, a certain extent of increase can be found in the crystallinity ( $X_c$ ), the maximum increase of which is about 0.03 (the corresponding increasing percentage is near 5%).

In a word, increasing  $A_{L/U}$  shows small amplitude of variation in the melting behaviors of BPEs, which is not obvious enough to explain the improvement of fracture toughness. In order to thoroughly explore the reason for improved fracture toughness with  $A_{L/U}$ , more in-depth analyses are required.

### 3.3.2. Successive self-nucleation annealing (SSA) analysis

The aggregated structures of semi-crystallized polymers, such as PE and PP, directly determine the service performances. So, investigation on the morphology of semi-crystalline polymers is propitious to understand and control the changes in properties. Successive self-nucleation and annealing (SSA) method, developed by Fillon et al [48–50], has been widely used in analyzing the chain structures of semi-crystalline polymers. The SSA approach enhances the molecular fractionation which can occur during crystallization at each stage of the process, meanwhile encourages annealing of the unmelted crystals, so that small thermal effects can be magnified after SSA treatments [48,51].

The basic principle of SSA thermal fractionation is that crystallization temperature of the chain segment relies on the methylene sequence length (MSL) since longer methylene chain segments will easily arrange themselves into crystal lattice to form thicker lamellas at higher temperatures. That is to say, the presence of branched or cross-linked points destroys the regularity of methylene sequences and makes the crystals have less perfection. Thus the formation of thick lamellar becomes difficult. After SSA thermal fractionation, the lamellas with different thickness will develop a distribution of melting peaks in the final DSC heating scan, from which plenty of information about the structure of materials may be known. Compared with other fractionation techniques, such as temperature rising elution fractionation (TREF), crystallization analysis fractionation (CRYSTAF) and step crystallization (SC), SSA exhibits a leading advantage that is performed with non-solvent, higher resolution and shorter experimental time [52–55].

Fig. 5 is the typical DSC heating curve of BPE after SSA thermal fractionation ( $S_2$  as an example). We can see that there are six separate melting peaks located at the corresponding annealing temperatures. The method ‘Gaussian fitting multi-peaks’ is applied to separate the curve to six distinct peaks (the dot lines), from which the thickness and the content of different lamella fractionations can be calculated by the peak temperatures and the area under corresponding curves, respectively [48,52,56].

The SSA fractionation curves of all BPEs as well as PE2911 are presented in Fig. 6a. As can be seen, the most important difference is that PE2911 has only one melting peak after the same SSA procedures compared with BPEs. Moreover, the peak temperature (about 135 °C) of PE2911 is much higher than that of other samples. This is related to the chain structure of homopolymer PE2911 (having longer and more successive methylene chain segments with negligible branching). The SSA results of PE100 ( $S_1$ ), PE2911 and their theoretical blends (named ‘unmixed’ blends that constructed from the weighted mathematical average of the DSC scans of the parent polymers) are shown in Fig. 6b. For the theoretical weighted curves, each peak temperature corresponding to that of  $S_1$  shows no

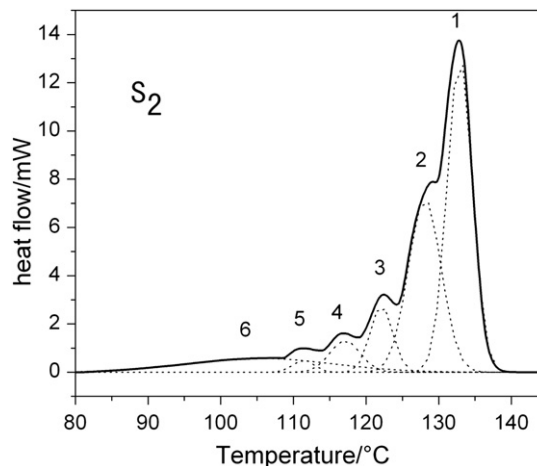


**Fig. 5.** DSC melting curve of  $S_2$  after SSA thermal fractionation. (The solid curve — original DSC melting curve. The dot curves — separated fractionations obtained from peak division process by Gaussian Fit Multi-peaks).

variation, as clearly demonstrated by the vertical dot lines connecting the peaks. However, an obvious bulge around 135 °C (higher than the highest peak temperature of  $S_1$ ) appears and tends to be more evident with the increase of PE2911 in the theoretical curves. The superfluous peaks indicate the separate crystallization of PE2911 and PE100 in the theoretical blends. But the practical SSA fractionation curves in Fig. 6a have no superfluous peaks around 135 °C, which implies PE2911 co-crystallizes with PE100 by way of increasing LPF. This similar co-crystallization behavior has been reported by Arnal et al. [40] in the study of LLDPE/HDPE (ethylene-1-butene copolymer) blend system. Another evident phenomenon in Fig. 6a is that, for  $S_2$  and  $S_3$ , each endothermic peak corresponding to that of  $S_1$  shifts to a higher temperature with increasing  $A_{L/H}$ , particularly for the highest peaks (shown by the dot line). Thereby, it is clear that the addition of PE2911 significantly has changed the crystalline morphology of materials.

The fractionated samples clearly exhibit a series of melting peaks that correspond to the melting of crystallites with different lamellar thickness. For better comparison and analysis of the effects of increasing  $A_{L/U}$  on the crystalline structures of BPEs, Thomson–Gibbs equation [54,57] can be used to establish a correlation between melting temperature and lamellar thickness as given in the following equation:

$$L = 2\sigma T_m^0 / \Delta H_v (T_m^0 - T_m) \quad (3)$$

According to this equation, higher melting temperature represents the formation of thicker crystal lamellas. Each peak temperature  $T_{mi}$  in the SSA results can be transformed to lamellar thickness  $L_i$  via this equation. As reported by Starck [57], the values of the constants in Eq. (3) are the followings:  $\sigma$ , lamellar surface free energy ( $0.07 \text{ J m}^{-2}$ ),  $\Delta H_v$ , melting enthalpy of the lamella with infinite thickness ( $288 \times 10^6 \text{ J m}^{-3}$ ),  $T_m^0$ , equilibrium melting point (414.5 K).

We list the crystal lamellar thickness ( $L_i$ ) corresponding to the six melting peak temperatures ( $T_{mi}$ ) for the samples in Table 4. Obviously, for all BPE samples, the lamellar thickness corresponding to the lower  $T_{mi}$  of SSA curves in Fig. 6a shows almost no difference (peak 3–6).

Actually, the lamellar thickness corresponding to peak 2,  $L_2$ , increases only over 1 nm from  $S_1$  to  $S_3$ , while  $L_1$  increases remarkably with  $A_{L/U}$  and the increasing percentage of which is as large as 30%. This increasing trend is nearly in proportion to  $A_{L/U}$ .

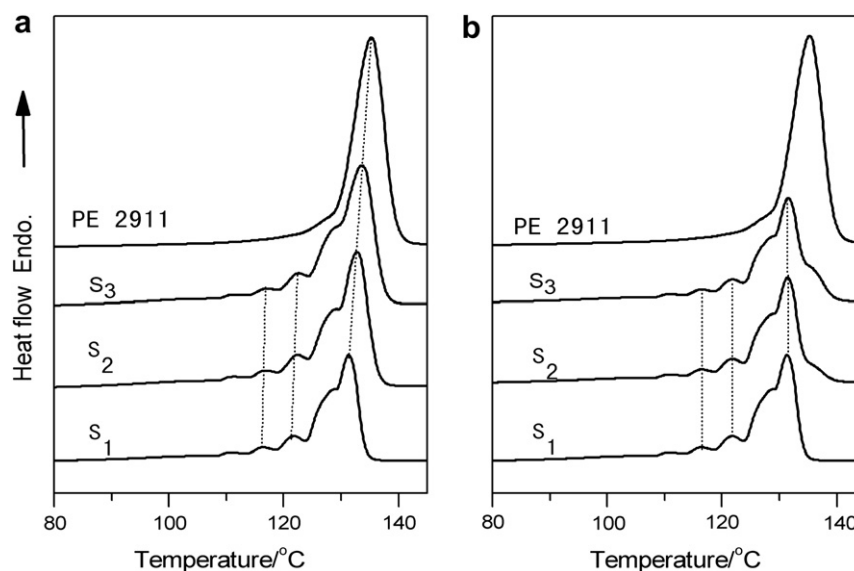


Fig. 6. DSC heating curves of BPEs and PE2911 after SSA thermal fractionation: (a) practical melt mixed sample; (b) theoretical 'unmixed sample'.

So it may be concluded that the obvious increase in the thickness of the lamellas corresponding to peak 1 and peak 2 (lamellas with the thickness over 12 nm, called *thick lamellas* here) is the main variation in aggregated structures, which has positive effects on the fracture toughness of BPEs.

In addition, from the area (enthalpy) under each peak, the crystallinity of corresponding crystal lamella fractionation in the whole material can be calculated. The total crystallinity and the 6 crystallinities corresponding to each melting peaks under SSA curves are listed in Table 5. Compared with the results from common DSC tests, the total crystallinity of each BPE sample after SSA is larger (about 0.032), although the increasing extent from  $S_1$  to  $S_3$  is almost the same (5%). This similar varying trend in crystallinity indicates that both of the two tests show similar results in evaluating the crystallinity of materials. From Table 5, it can also be found that the crystallinity corresponding to lamellas under peak 3 changes a little with increasing  $A_{L/U}$ , and almost no significant variation in crystallinity corresponding to lamellas under peak 4 to peak 6 is observed. All these four parts of lamellas only contribute to about 1/4 of the total crystallinity of each BPE sample, revealing that these thin crystal lamellas have no obvious influence on the properties of BPEs with increasing  $A_{L/U}$ . However, for the *thick lamellas* corresponding to lamellas at peak 1 and peak 2, their contribution to the total crystallinity is about 3/4. The crystallinity increases obviously (more than 11%, almost two times of the changing extent of total crystallinity) with the content of PE2911 in the blends or  $A_{L/U}$ , although the crystallinity of *thick lamellas* changes differently and irregularly. This change is resulted from the slight decrease of the small quantity of thin crystal lamellas and the increase of total crystallinity.

Combining both Tables 4 and 5, it can be seen that the larger  $A_{L/U}$  value (or content of LPF) is, the thicker and larger amount of *thick*

lamellas will form in BPEs after the same SSA thermal treatments. This is because the addition of homopolymer PE2911 facilitates the formation of *thick lamellas* when the longer methylene chain segments in PE2911 co-crystallize with the molecular chains of  $S_1$ . During this co-crystallization, the more regular chain segments in PE2911 drive more chains into crystal lattice to form thicker lamellas. This apparent variation in the crystalline structure would affect the properties of BPE samples greatly.

There may be a doubt that the crystallization conditions in SSA treatments are different from those used to prepare specimens for EWF test, which will induce different crystal parameters for samples under both conditions. However, from the results of SSA, the tendency or ability of crystallization can be reflected definitely for the BPE samples. The superior crystalline ability of BPEs with larger  $A_{L/U}$  implies that more thick lamellas will also form during the preparation of DENT specimens. A certain amount of increase in  $T_m$  and  $X_c$  (see Table 3) also reflects this tendency although the conditions for sample preparation are not sufficient enough to form more perfect crystals as those in the SSA treatments. As a matter of fact, these phenomena reveal the nature of material. So the improvement of fracture toughness,  $w_e$ , with increasing  $A_{L/U}$  is probably caused by the formation of the thicker and larger amount of *thick lamellas*.

Generally, the mechanical behaviors of semi-crystalline polymers are dependent upon both the amorphous and crystalline phases and their interactions [58]. To reveal the effect of amorphous and crystalline phases on the fracture behaviors of semi-crystalline polymers, the method of annealing to vary their crystallinity visibly was generally adopted. For instance, Viana et al. [58] used heat

Table 4  
The lamellar thickness ( $L_i$ ) corresponding to  $T_{mi}$  of different crystal fractions of BPEs after SSA fractionation.

Sample	$L_1$ (nm)	$L_2$ (nm)	$L_3$ (nm)	$L_4$ (nm)	$L_5$ (nm)	$L_6$ (nm)
$S_1$	20.21	16.00	10.11	7.98	6.51	5.58
$S_2$	23.59	15.93	10.42	8.10	6.61	5.61
$S_3$	26.24	17.15	10.48	8.10	6.61	5.59

Table 5  
The crystallinity  $X_c$  of each corresponding melting peak after SSA treatment for all BPEs.

	$X_{c1}^a$	$X_{c2}^a$	$X_{c3}^a$	$X_{c4}^a$	$X_{c5}^a$	$X_{c6}^a$	Total $X_c$	$X_c$ of all lamellas <12 nm	$X_c$ of all lamellas >12 nm
$S_1$	0.188	0.272	0.050	0.036	0.010	0.070	0.625	0.165	0.460
$S_2$	0.276	0.197	0.052	0.032	0.009	0.070	0.636	0.163	0.473
$S_3$	0.273	0.239	0.037	0.037	0.008	0.066	0.659	0.147	0.512

<sup>a</sup>  $X_{ci}$  means the crystallinity of the melting peak of number  $i$  corresponding to Fig. 5.

shrinkable films as a model to study the influence of annealing on the mechanical properties including fracture behaviors. Ferrer-Balas et al. [46] studied the fracture behavior of iPP films suffered annealing at different temperatures and reported that an increase of  $w_e$  accompanying a decrease of  $\beta w_p$  was induced by higher annealing temperatures as the crystal perfection (crystallinity) improved a lot. Mouzakis et al. [59] used three types of elastomeric polypropylene (ELPP) with different length of stereoregular chain segments to study the variation of EWF parameters, and found that  $w_e$  increased with crystallinity, whereas in respect to  $\beta w_p$  an opposite tendency was found. All of these results can be reasonably explained by the viewpoint proposed by Karger-Kocsis [60], that is, the toughness of semi-crystalline polymers depends on the crystallinity. On the one hand, the crystal perfection (including the crystallinity, lamellar size, etc.) increases, the toughness of the bulk crystals improves because destroying these crystals needs more energy consumption; on the other hand, however, an increase in the crystal perfection by raising the crystallinity may reducing the number of tie molecules, which act as stress-transfer units between the crystalline zones. It has been elucidated that the toughness of materials decreased obviously when the crystallinity overcome a threshold due to the lack of tie molecules [46].

It should be noted that, compared with the highly improved crystallinity in their results, the improvement in crystallinity of our BPE samples is not so great. So, in our samples, the amorphous zones decrease little and we may speculate that the number of tie molecules does not vary greatly. Based on these analyses, a reasonable explanation for the greatly improved fracture toughness is as follows. Increasing  $A_{L/U}$  of the BPE samples causes a remarkable increase in thickness and amount of *thick lamellas*, which induces the materials to be fractured with more energy consumption, whereas the contribution of amorphous zones (including tie molecules) has no obvious change. In a word, improvement of crystal perfection can increase the dissipative work of BPE samples during the ductile fracture. This indicates the increase in resistance of crack propagation. presented as the improved  $w_e$ , though this range of increase probably exists a limit when  $A_{L/U}$  reaches a certain extent.

#### 4. Conclusion

It has been demonstrated that the MWD characteristic parameter ( $A_{L/U}$ , the ratio of LFP to UPF) effectively influences the properties of BPE materials, especially the fracture toughness. Increasing the value of  $A_{L/U}$  leads to obvious improvement of the fracture toughness  $w_e$ , namely, the enhancement of resistance to crack propagation.

As verified by SSA fractionation, the crystal perfection of BPEs is intensely affected by  $A_{L/U}$ . With  $A_{L/U}$  increasing, the thickness and amount of *thick lamellas* increase while the total crystallinity of the BPEs does not vary greatly. This improvement in crystal perfection produces an enhancement of fracture toughness since more energy will be dissipated in the superior network structure constructed by thick lamellas and tie molecules when the material is suffered fracture deformation.

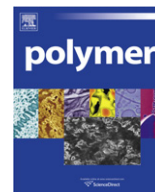
#### Acknowledgements

We gratefully acknowledge the financial support from the National Natural Science Foundation of China (50873068, 51073109 and 20734005).

#### References

[1] Alt FP, Böhm LL, Enderle HF, Berthold J. *Macromol Symp* 2001;163:135–43.

- [2] Böhm LL, Berthold J, Enderle HF, Fleissner M. In: Kaminsky W, editor. *Metallorganic catalysts for synthesis and polymerization*, vol. 1. Berlin: Springer-Verlag; 1999. p. 3.
- [3] Shan CLP, Soares JBP, Penlidis A. *Polymer* 2003;44(1):177–85.
- [4] Wood-Adams PM, Dealy deGroot JM, deGroot AW, Redwine OD. *Macromolecules* 2000;33(20):7489–99.
- [5] Kim YS, Chung CI, Lai SY, Hyun KS. *J Appl Polym Sci* 1996;59(1):125–37.
- [6] Gupta P, Wilkes GL, Sukhadia AM, Krishnaswamy RK, Lamborn MJ, Wharry SM, et al. *Polymer* 2005;46(20):8819–37.
- [7] Hubert L, David L, Seguela R, Vigier G, Degoulet C, Germain Y. *Polymer* 2001;42(20):8425–34.
- [8] Barabanov AA, Semikolenova NV, Matsko MA, Echevskaya LG, Zakharov VA. *Polymer* 2010;51(15):3354–9.
- [9] Knuutila H, Lehtinen A, Nummila-Pakarinen A. *Adv Polym Sci* 2004;169:13–28.
- [10] DesLauriers PJ, McDaniel MP, Rohlffing DC, Krishnaswamy RK, Secora SJ, Benham EA, et al. *Polym Eng Sci* 2005;45(9):1203–13.
- [11] Chen XL, Liu DB, Wang HT. *Macromol React Eng* 2010;4(5):342–6.
- [12] Wang SB, Liu DB, Xu RW, Mao BQ. *Chin Sci Bull* 2006;51(1):115–6.
- [13] Krumme A, Lehtinen A, Viikna A. *Eur Polym J* 2004;40(2):359–69.
- [14] Krumme A, Lehtinen A, Viikna A. *Eur Polym J* 2004;40(2):371–8.
- [15] Heidemeyer P, Pfeiffer J. *Macromol Symp* 2002;181:167–76.
- [16] Verlag V. In: Brömstrup H, editor. *PE 100 Pipe Systems*. Essen: German National Bibliography; 2004.
- [17] Böhm LL, Enderle HF, Fleissner M. *Adv Mater* 1992;4:231–8.
- [18] Peres FM, Schon CG. *J Mater Sci* 2008;43(6):1844–50.
- [19] Tsui S-W, Duckett RA, Ward IM. *J Mater Sci* 1992;27:2799–806.
- [20] Ting SKM, Williams JG, Ivankovic A. *Polym Eng Sci* 2006;46(6):792–8.
- [21] Chen HB, Karger-Kocsis J, Wu JS. *Polymer* 2004;45(18):6375–82.
- [22] Channell AD, Clutton EQ. *Polymer* 1992;33(19):4108–12.
- [23] Wang HC, Sung CM, Hamilton J. *J Mater Sci Lett* 1998;17(1):41–3.
- [24] Nunes RW, Martin JR, Johnson JF. *Polym Eng Sci* 2004;22(4):205–28.
- [25] Li B, Gong G, Xie BH, Yang W, Yang MB. *J Appl Polym Sci* 2008;109(2):1161–7.
- [26] Shah A, Stepanov EV, Capaccio G, Hiltner A, Baer E. *J Polym Sci B Polym Phys* 1998;36(13):2355–69.
- [27] Krishnaswamy RK, Yang Q, Fernandez-Ballester L, Kornfield JA. *Macromolecules* 2008;41(5):1693–704.
- [28] Kim YM, Park JK. *J Appl Polym Sci* 1996;61(13):2315–24.
- [29] Karger-Kocsis J, Moskala EJ. *Polymer* 2000;41(16):6301–10.
- [30] Kwon HJ, Jar RYB. *Polym Eng Sci* 2007;47(9):1327–37.
- [31] Lach R, Schneider K, Weidisch R, Janke A, Knoll K. *Eur Polym J* 2005;41(2):383–92.
- [32] Wu JS, Mai YW. *Polym Eng Sci* 1996;36(18):2275–88.
- [33] Wang XL, Li RKY, Cao YX, Meng YZ. *Polym Test* 2005;24(16):699–703.
- [34] Yang W, Xie BH, Shi W, Li ZM, Liu ZY, Chen J, et al. *J Appl Polym Sci* 2006;99(4):1781–7.
- [35] Fasce L, Bernal C, Frontini P, Mai YW. *Polym Eng Sci* 2001;41(1):1–14.
- [36] Fayolle B, Verdu J. *Polym Eng Sci* 2005;45(3):424–31.
- [37] Choi BH, Demirors M, Patel deGroot RM, deGroot AW, Anderson KW, Juarez V. *Polymer* 2010;51(12):2732–9.
- [38] Hussein IA, Hameed T, Sharkh BFA, Mezghani K. *Polymer* 2003;44(16):4665–72.
- [39] Lee LT, Woo EM, Hou SS, Förster S. *Polymer* 2006;47(25):8350–9.
- [40] Arnal ML, Sanchez JJ, Müller AJ. *Polymer* 2001;42(16):6877–90.
- [41] Cho KC, Lee BH, Hwang KM, Lee HS, Choe SJ. *Polym Eng Sci* 1998;38(12):1969–1975.
- [42] Xanthos M, Tan V, Ponnusamy A. *Polym Eng Sci* 1997;37(6):1102–12.
- [43] Williams JG, Rink M. *Eng Fract Mech* 2007;74(7):1009–17.
- [44] Pegoretti A, Castellani L, Franchini L, Mariani P, Penati A. *Eng Fract Mech* 2009;76(18):2788–98.
- [45] Chen HB, Wu JS. *Macromolecules* 2007;40(12):4322–6.
- [46] Ferrer-Balas D, MasPOCH ML, Martinez AB, Santana OO. *Polymer* 2001;42(4):1697–705.
- [47] Sheng BR, Li B, Xie BH, Yang W, Feng HM, Yang MB. *Polym Degrad Stab* 2008;93(1):225–32.
- [48] Müller AJ, Arnal ML. *Prog Polym Sci* 2005;30(5):559–603.
- [49] Lorenzo AT, Arnal ML, Sanchez JJ, Müller AJ. *J Polym Sci B Polym Phys* 2006;44(12):1738–50.
- [50] Fillon B, Wittmann JC, Lotz B, Thierry AJ. *Polym Sci B Polym Phys* 1993;31(10):1383–93.
- [51] Song SJ, Wu PY, Ye MX, Feng JC, Yang YL. *Polymer* 2008;49(12):2964–73.
- [52] Perez CJ, Villarreal N, Pastor JM, Failla MD, Valles EM, Carella JM. *Polym Degrad Stab* 2009;94(10):1639–45.
- [53] Perez CJ, Carella JM. *Polym Degrad Stab* 2007;92(7):1213–8.
- [54] Müller AJ, Hernandez ZH, Arnal ML, Sanchez JJ. *Polym Bull* 1997;39(4):465–72.
- [55] Song SJ, Wu PY, Feng JC, Ye MX, Yang YL. *Polymer* 2009;50(1):286–95.
- [56] Chau J, Teh J. *J Therm Anal Calorim* 2005;81(1):217–23.
- [57] Starck P. *Polym. Int* 1996;40(2):111–22.
- [58] Viana JC, Cunha EM. *Mater Sci Forum* 2006;514–516:1186–90.
- [59] Mouzakis DE, Gahleitner M, Karger-Kocsis J. *J Appl Polym Sci* 1998;70(5):873–81.
- [60] Karger-Kocsis J. In: Cunha AM, Fakirov S, editors. *Structure development during polymer processing*. NATO-ASI Series. Dordrecht: Kluwer Academic; 2000.



## Semicrystalline ordering in polymeric systems simulated by Bond Fluctuation Model

J. Molina-Mateo<sup>a,\*</sup>, M. Arnoult<sup>b</sup>, J.M. Saiter<sup>c</sup>, J.M. Meseguer-Dueñas<sup>a</sup>, J.L. Gómez-Ribelles<sup>a</sup>

<sup>a</sup> Universidad Politécnica de Valencia, Center for Biomaterials and Tissue Engineering, Camino de Vera s/n, 46022 Valencia, Spain

<sup>b</sup> University of Nebraska-Lincoln, Department of Engineering Mechanics, W316 Nebraska Hall, Lincoln, NE 68588-0526, USA

<sup>c</sup> Laboratoire d'Etude et Caractérisation des Amorphes et des Polymères, Université de Rouen, Rouen, France

### ARTICLE INFO

#### Article history:

Received 8 October 2010  
Received in revised form  
30 November 2010  
Accepted 1 December 2010  
Available online 9 December 2010

#### Keywords:

Glass transition  
Bond Fluctuation Model  
Dynamically accessible volume

### ABSTRACT

Arresting of segmental mobility in polymer systems on cooling from the melt was simulated by means of the Bond Fluctuation Model. In order to represent the behaviour of the system, three potentials were included: a Lennard–Jones potential, a bond length potential and a bond angle potential. The effect of the bond angle and bond length potential combination is to stretch the chains, while the Lennard–Jones potential leads to a lack of free volume which appears when temperature decreases. So, when a cooling ramp is applied, depending on the balance of these potentials, the system shows a transition in which molecules densely pack or, on the contrary, remains amorphous. Therefore, the choice in the weighting of these three potentials is a key point to simulate a physical system by using the Bond Fluctuation Model.

© 2010 Elsevier Ltd. All rights reserved.

### 1. Introduction

Polymer chains adopt at a high temperature random coil conformations in an equilibrium liquid state characterized with a high segmental mobility. On cooling, chains may order in a crystal lattice provided they are regular enough to allow crystal packing. Only a part of the polymer mass crystallizes from the melt, and the term semicrystalline is normally used to refer to the situation in which polymer crystals coexist with amorphous or liquid-like chains which retain the conformational mobility characteristic of the liquid state. Crystallization takes place with a certain undercooling with respect to equilibrium melting temperature due to the thermodynamic requirements for the formation of stable crystal nuclei that allow further crystal growth. Nucleation and crystal growth are kinetic-controlled processes and, as a consequence, process parameters such as cooling rate or annealing times or temperatures determine crystal size distribution or crystal fraction. The non-crystallized or amorphous fraction vitrifies on further cooling when glass transition takes place yielding an out of equilibrium glass with arrested segmental mobility at low temperatures. Nevertheless the amorphous glass, even with restricted

mobility, continuously evolves at temperatures below the glass transition reducing specific volume, enthalpy or entropy approaching an equilibrium state in a process that has been called structural relaxation or physical ageing.

In previous papers [1,2], we have studied the simulation of this complex behaviour using Bond Fluctuation Model (BFM) [3]. Computer simulation using a coarse grained model can help understanding the importance of physical factors such as chain connectivity, flexibility or inter and intra-molecular interactions on the competition between crystallization and vitrification in polymer systems, independently of the details of the chemical structure of the polymer. The dynamics of BFM can be governed by an inter-molecular Lennard–Jones potential and intra-molecular bond angle and bond length potentials while temperature appears through the Metropolis criterium that determines the probability of accepting a segmental motion that implies an increase in the energy of the system [4]. In this work we focus on the role of bond angle potential in the tendency of polymer chains to pack in a crystal order. The hypothesis is that the combination of a low energy of bond angles corresponding to the fully extended chain and a Lennard–Jones inter-molecular potential could yield crystal packing similar to that of n-alkanes, with extended parallel chains. The question that arises is if molecular mobility at the crystallization temperatures will be enough to allow chain extension in a polymer in bulk.

\* Corresponding author. Tel.: +34 963877007; fax: +34 963879896.  
E-mail address: [jmmateo@fis.upv.es](mailto:jmmateo@fis.upv.es) (J. Molina-Mateo).

## 2. Simulations

The Bond Fluctuation Model is one of the most widely employed Monte Carlo models to simulate polymeric materials [3–8]. It consists of a cubic lattice where each monomeric group (representing three to five carbon atoms of the polymeric chain) occupies eight cells forming a cube. The length of the bonds between monomeric groups can fluctuate between 2 and  $\sqrt{10}$  (distance  $\sqrt{8}$  is not allowed in order to avoid bond crossing [5,9]).

The simulation steps consist of choosing randomly a monomeric group and one of the six possible directions of movement. If the resulting distances for the involved bonds are allowed by the model and the volume exclusion is respected then the movement is considered as geometrically viable. Finally the movement is performed with the probability of the Metropolis criterion [5]:

$$P = \min \left[ 1, \exp \left( \frac{-\Delta E}{k_B T} \right) \right] \quad (1)$$

In this expression  $\Delta E$  is the increase of energy caused by the evaluated movement,  $k_B$  is Boltzmann's constant and  $k_B T$  is the temperature of the system.

In this work we have employed three different potentials. First, a Lennard–Jones potential calculated up to a distance of four lattice units [4]. It was calculated between all non-bonded monomers:

$$U_{LJ} = 4\epsilon \left[ \left( \frac{\sigma}{r} \right)^{12} - \left( \frac{\sigma}{r} \right)^6 \right] \quad (2)$$

where  $\sigma$  was 2.0, in order to be coherent with the excluded volume imposed by the lattice conditions of the Bond Fluctuation Model. A bond length potential [4]:

$$U(l) = U_0(l - l_0)^2 \quad (3)$$

where the minimal energy distance was given by  $l_0 = 3.0$  lattice units. And a bond angle potential [4]:

$$V(\theta) = V_0(\cos\theta - \cos\theta_0)^2 \quad (4)$$

where the minimal energy angle  $\theta_0$  corresponded to  $180^\circ$ .

The simulation parameters consisted of a three dimensional simulation box ( $L = 40$ ) with boundary conditions. This system was occupied by 400 chains, formed by 10 monomeric groups, so we had a density  $\varphi = 0.5$ . The simulations began with an initial equilibration period of  $10^5$  Monte Carlo Steps (MCS) at high temperature  $k_B T = 5$ , followed by a cooling ramp at a constant rate of  $-0.1$  units of temperature every 1000 MCS until  $k_B T = 0.01$ . On the other hand the time evolution of the different systems was analyzed during annealing at different temperatures, with a duration of  $10^7$  MCS, starting in the state attained by the cooling ramp.

The dependence of structure and segmental mobility of the system with time and temperature was characterized with a series of parameters. Total energy of the lattice was evaluated and used to monitor the evolution of the state of the system.

As a measure of segmental mobility we use the Dynamically Accessible Volume (DAV) [10–12] modified to characterize thermal systems [13]. DAV measures the number of empty cells, which can be occupied in one Monte Carlo Step, contributing to the diffusion of the system:

$$DAV = \frac{1}{L^3} \sum_{j=1}^{L^3} \left\{ \min \left[ 1, \sum_{i=1}^{nn} \exp \left( \frac{-\Delta E_{ij}}{k_B T} \right) \right] \right\} \quad (5)$$

where  $L$  is the box simulation size,  $nn$  is the number of first neighbours of a cell and  $\Delta E_{ij}$  is the variation in the energy of the system caused by a monomeric jump from the cell  $i$  to the cell  $j$ . This

parameter gives a landscape of the free space of the system that contributes to diffusion.

The squared radius of gyration was calculated too [4]:

$$\langle R_G^2(N) \rangle = \frac{1}{N} \left\langle \sum_{i=1}^N |\vec{r}_i - \vec{r}_{cm}|^2 \right\rangle \quad (6)$$

where  $N$  is the number of monomeric groups of the chains,  $\vec{r}_{cm}$  is the position of the centre of mass of the chain and  $\vec{r}_i$  is the position of every group of the chain.

In order to analyze the structure of the system the pair correlation function of the system was calculated [14]:

$$g(r) = \frac{2L^3 H(r)}{(NP)^2 h(r)} \quad (7)$$

where  $H(r)$  represents the histogram that counts the number of times the allowed distance  $r$  occurs,  $h(r)$  the number of possible  $r$ -vectors for a given distance  $r$  in the lattice,  $L$  is the box simulation size and  $NP$  is the total number of particles.

A bond correlation function was calculated too in order to study the orientation of the bonds of the model [15]:

$$M(j) = \langle \cos\theta_{i,i+j} \rangle \quad (8)$$

where  $\theta_{i,i+j}$  was the angle between the  $i$ th bond and the  $(i + j)$ th bond within the same chain.

Finally, in order to characterize the bond alignment, we calculated a bond order parameter based on the 2nd Legendre polynomial of the scalar product [2]:

$$P_2(r) = \frac{1}{2} \langle 3(\vec{u}_i \cdot \vec{u}_j)^2 - 1 \rangle \quad (9)$$

$u_i$  and  $u_j$  are the normalized vectors corresponding to every pair of vectors  $ij$  whose centre of mass is at the distance  $r$ .

One of the key issues of this work was the balance of the three potentials in order to define a semicrystalline system exhibiting both crystallization and glass transition. It has been shown that a strong inter-molecular energy potential is able to induce some degree of molecular order in Bond Fluctuation Model systems [4]. In fact in our previous works [1,2], we studied polymer systems with inter and intra-molecular interactions described with a Lennard–Jones potential and the bond length potential, respectively. Appropriate values of  $\epsilon$  and  $U_0$  parameters yielded the formation on cooling of structures in which chains densely packed and that could be interpreted as a semicrystalline structure of the polymers, but these systems showed no bond ordering in the Legendre's function (equation (9)), as expected for polymer crystallization. We hypothesize that considering a bond angle potential chain extension and even chain folding can be induced so better

**Table 1**

Energy parameters used for simulations. In systems A–F, the bond angle potential was increased while the value of  $U_0$  was kept 9 times higher than that of  $\epsilon$ . In systems G–I, the Lennard–Jones potential was increased while the bond angle one was kept constant. The sum of the three parameters was always kept constant at 1. The combinations were labelled in order to reference them easily.

System	$\epsilon$	$U_0$	$V_0$
A	0.1	0.9	0.0
B	0.09	0.81	0.1
C	0.08	0.72	0.2
D	0.07	0.63	0.3
E	0.06	0.54	0.4
F	0.05	0.45	0.5
G	0.10	0.50	0.4
H	0.15	0.45	0.4
I	0.30	0.30	0.4

reproducing the molecular order found experimentally in polymeric systems. Crystallization and glass transition temperature intervals are further analyzed following energy, free volume and structure parameters evolution during isothermal annealing in a broad temperature range. The energy values tested are summarized in Table 1. In order to maintain a relatively constant temperature scale, the sum of the three parameters  $\varepsilon$ ,  $U_0$  and  $V_0$  was always 1. A first series of simulations begun with a value of  $V_0 = 0$ , to start with a known system, and then  $V_0$  was increased while the value of  $U_0$  was kept 9 times higher than that of  $\varepsilon$  (systems A–F in Table 1). In systems G–I, the Lennard–Jones potential was increased while the bond angle one was kept constant in a high value.

### 3. Results and discussion

#### 3.1. The cooling ramps

In order to understand the role of the bond angle potential on the behaviour of the simulated configuration, different ratios between the three potentials were tested according to Table 1. For each of these systems, the response to cooling ramps from  $k_B T = 5$  to  $k_B T = 0.01$  was simulated using four different cooling rates:  $-0.1 k_B T$  per 1000 Monte Carlo Steps (MCS),  $-0.1 k_B T$  per 10,000 MCS,  $-0.1 k_B T$  per 100,000 MCS and  $-0.1 k_B T$  per 1,000,000 MCS. The energy versus temperature profile, monitored during these cooling ramps, shows two qualitatively different behaviours depending on the values of the energy potentials used to define the system.

Fig. 1 corresponds to the cooling scans of the system H but it is representative of systems A–G as well. This figure exhibits the expected cooling scans of a glass former: at high temperatures, energy linearly decreases with increasing  $1/k_B T$  as the system is in the equilibrated liquid state [1,2,13]. The cooling ramp has been simulated with a series of  $k_B T = 0.1$  steps followed by isothermal periods to give the desired average cooling rate. On cooling, around  $1/k_B T = 3$  the energy curve start deviating from the equilibrium line. Each point represented in the plot corresponds to the final state attained at the end of the isothermal stage and clearly the time allowed after each temperature step start being insufficient to attain the equilibrium energy value. As cooling rate decreases the system is able to go closer to equilibrium in each temperature

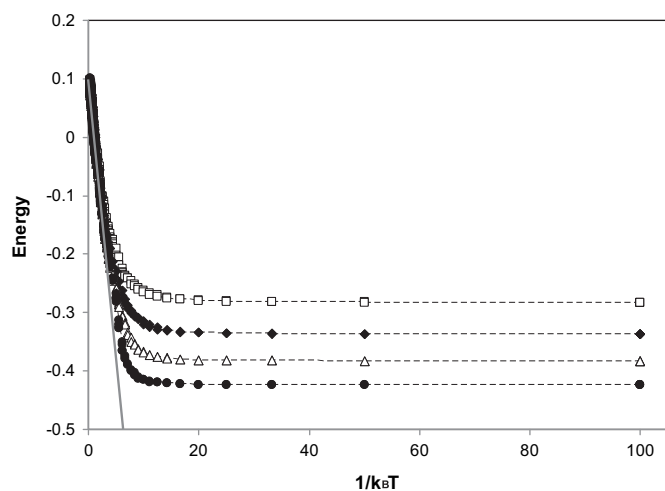


Fig. 1. Energy profile in cooling ramps simulated for system H (see Table 1) for different cooling rates:  $-0.1 k_B T$  units per 1000 MCS ( $\square$ ),  $-0.1 k_B T$  units per 10,000 MCS ( $\blacklozenge$ ),  $-0.1 k_B T$  units per 100,000 MCS ( $\triangle$ ) and  $-0.1 k_B T$  units per 1,000,000 MCS ( $\bullet$ ). The extrapolated equilibrium line has been represented as a solid line.

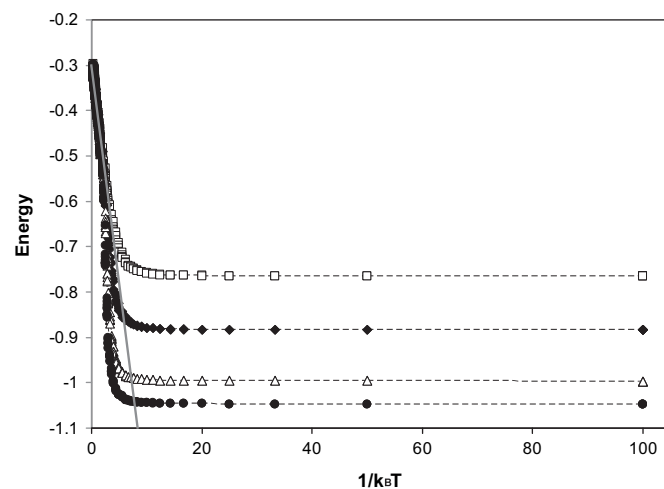


Fig. 2. Energy profile in cooling ramps simulated for system I (see Table 1), showing a phase transition where the energy goes below the equilibrium line. Cooling rates:  $-0.1 k_B T$  units per 1000 MCS ( $\square$ ),  $-0.1 k_B T$  units per 10,000 MCS ( $\blacklozenge$ ),  $-0.1 k_B T$  units per 100,000 MCS ( $\triangle$ ) and  $-0.1 k_B T$  units per 1,000,000 MCS ( $\bullet$ ). The extrapolated equilibrium line has been represented as a solid line.

step. The glass transition yields a system with nearly no segmental mobility at temperatures below  $k_B T = 0.05$  ( $1/k_B T = 20$ ), which implies that the energy line becomes horizontal. This corresponds to the behaviour of a glass with a frozen conformational mobility.

The explanation in the former paragraph is incompatible with energy values below the equilibrium line as shown in Fig. 2 which corresponds to system I in which the influence of the Lennard–Jones potential has been increased. In this system, a fast cooling rate also leads to a glass transition as explained for systems A–H. Nevertheless, slow cooling produces a sharp energy loss at a temperature of around  $k_B T = 0.35$  ( $1/k_B T = 2.85$ ) independently of cooling rate. After this energy drop, mobility is completely arrested and on further cooling the energy curve becomes horizontal. This behaviour can be associated to a first order transition which is supported by the fact that the Lennard–Jones potential is well known to create order.

Fig. 3 describes the variations of the average squared radius of gyration as a function of reciprocal temperature for systems A–F. This figure helps understanding the influence of the bond angle potential on chain folding in each glassy system. As this potential is set to be minimum at an angle of  $180^\circ$ , it is expected that the higher

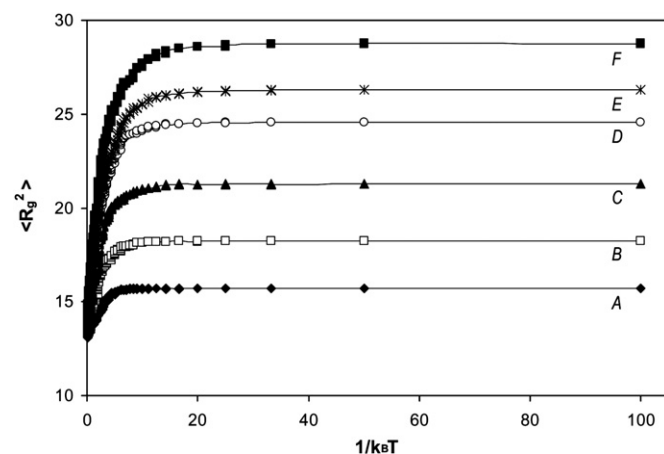
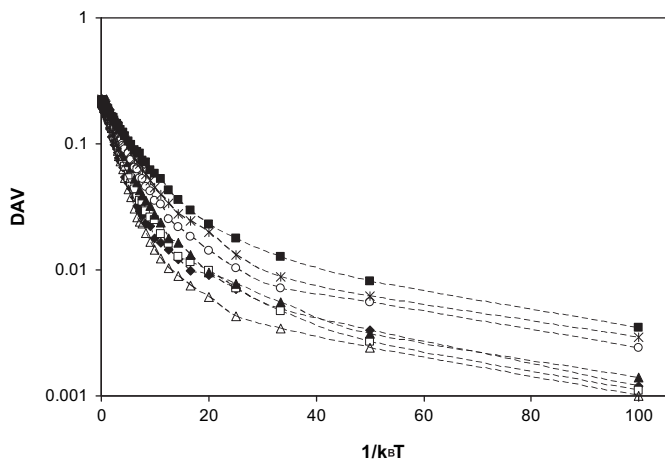


Fig. 3. Evolution of the squared radius of gyration during the cooling ramps. The radius of gyration increases as the bond angle potential increases from system A to system F.





**Fig. 4.** DAV during cooling ramps showing the effect of increasing the bond angle potential for systems A(◆), B(□), C(▲), D(○), E(\*), F(■) and I(Δ). Cooling rate was  $-0.1$  units of temperature every 1000 MCS.

is the bond angle potential, the higher the value of the radius of gyration should be. This chain unfolding tendency is confirmed by Fig. 3 which shows that  $\langle R_g^2 \rangle$  varies from 16 to 28 squared lattice units when the parameter defining the bond angle potential varies from 0 to 0.5.

A deeper insight in the system behaviour can be obtained from the temperature dependence of dynamic accessible volume (DAV), representing the number of empty cells accessible in one MCS. Fig. 4 displays the evolution of the DAV during the cooling ramp at  $-0.1 k_B T$  per 1000 MCS for systems A–F. The glass transition appears in these plots as a change of slope in the DAV versus  $1/k_B T$ . In these diagrams it can be observed that arresting of conformational mobility at the glass transition is not complete and the polymer chains maintain certain capacity of rearrangement in the glassy state as observed in real amorphous polymers. Furthermore, this figure clearly shows the effect of the increasing bond angle on the system. An increase of bond angle potential increases free volume in the system both in equilibrium liquid and in the glassy state. In addition the glass transition broadens, covering a larger temperature interval.

### 3.2. Isothermal annealing

In order to analyze the segmental mobility in the glassy state, long isothermal annealing periods were computer simulated at several temperatures, starting in the state attained from a fast cooling ramp, and thus starting with an amorphous system. These simulations aim to prove the capacity of the polymer chains to order in crystalline-like structures pack at least in a given temperature window as should be expected for a semicrystalline polymer. Fig. 5 shows the energy of the system as a function of temperature before and after an isothermal stage of  $10^7$  MCS. The behaviour of system B (Fig. 5a) is expected for a glass, annealing at temperatures below or in the range of the glass transition produces a decrease of the energy of the system approaching the equilibrium state at the annealing temperature. The increase of the bond angle parameter does not change qualitatively this behaviour as shown in Fig. 5b for system E. It is necessary to increase Lennard–Jones potential to observe in a narrow temperature range a decrease of the energy below that of the equilibrium liquid that can be associated to a crystallization (Fig. 5c).

Both physical ageing or structural relaxation of an amorphous glass and crystallization produce a decrease in the energy of the system during isothermal annealing. To probe the development of

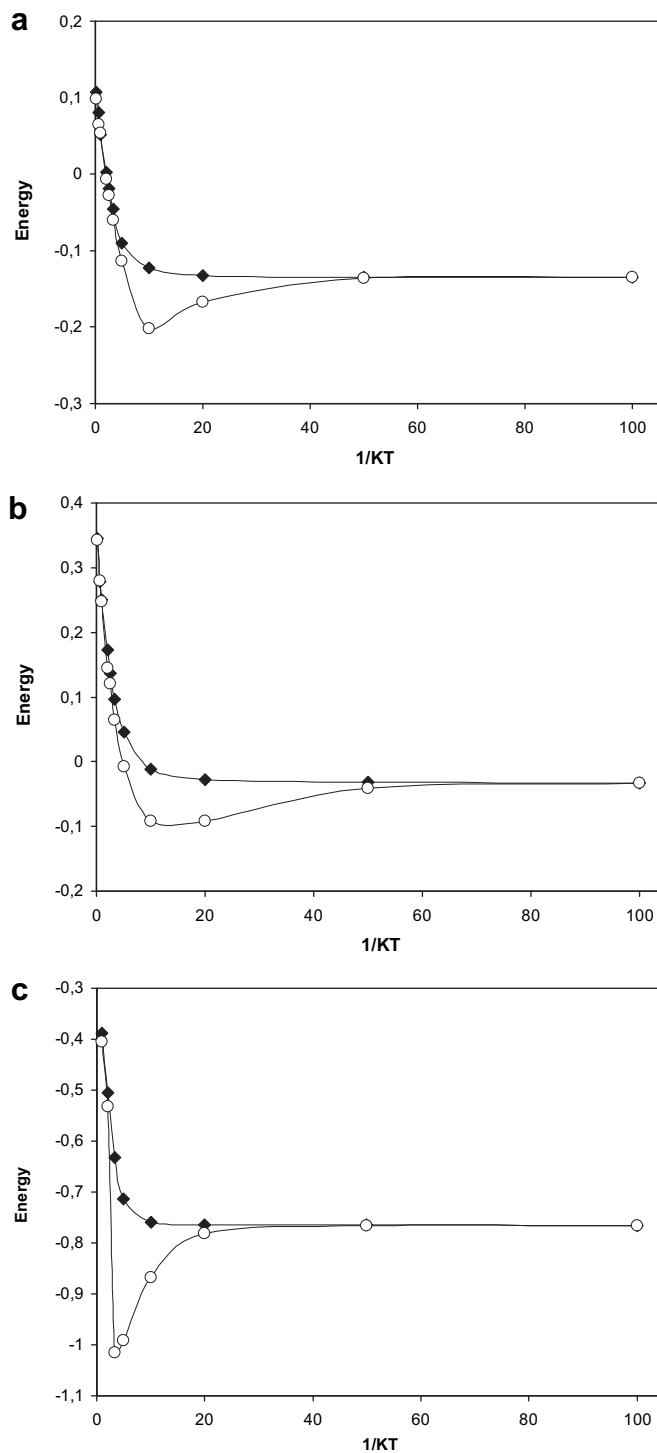


**Fig. 5.** Changes on energy before (◆) and after annealing (○) at different temperatures are similar for low bond angle potential (system B) (a), high bond angle potential (system E) (b) and high Lennard–Jones potential (system I) (c). Only when Lennard–Jones potential is strong enough, the energy goes below the equilibrium line extrapolation. Lines are employed only as a guideline for the eye.

crystalline order in the polymeric system we compare the values of the parameters that probe structural order before and after the isotherm. Pair correlation function (Figs. 6 and 7) probes the spatial order of monomeric units, bond correlation function (Fig. 8) characterizes chain stretching while Legendre's polynomial analysis (Fig. 9) probes spatial correlation of bond orientation.

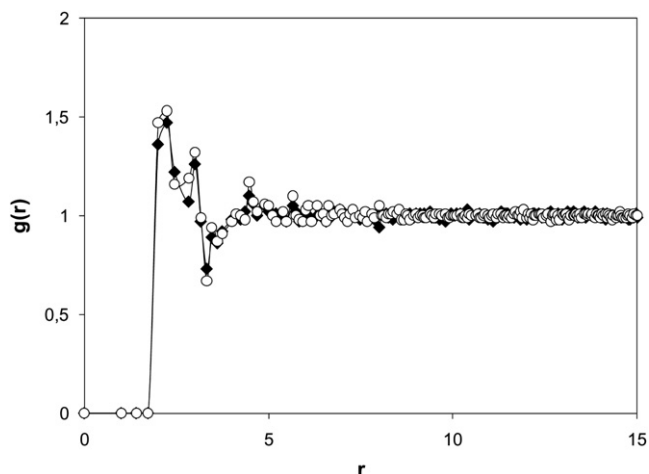


**Fig. 6.** The pair correlation function indicated that most of the systems were amorphous with no dependence on the potential. This is an example of system E at temperature  $k_B T = 0.1$  before ( $\blacklozenge$ ) and after ( $\circ$ ) annealing.

Fig. 6 shows the pair correlation function of system E at the initial state of annealing, after a fast cooling from the liquid state, and is representative of all systems at all temperatures. It is not significantly different from that of the equilibrium liquid as has

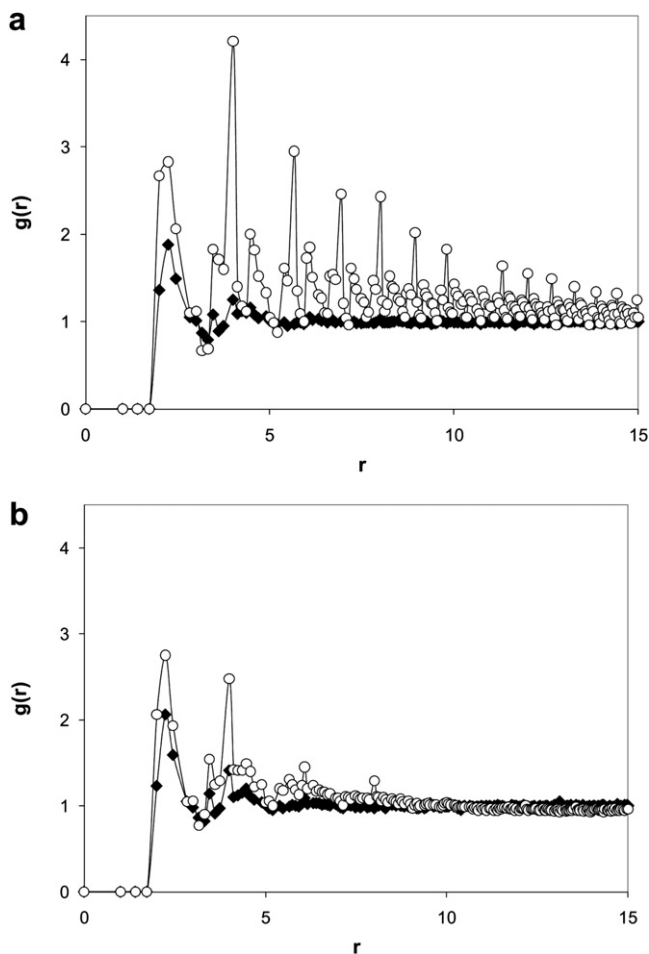


**Fig. 7.** Development of the spatial order of monomeric units shown by the comparison of the pair correlation function before ( $\blacklozenge$ ) and after ( $\circ$ ) annealing in system I at  $k_B T = 0.3$  when the Lennard–Jones potential took the highest value (a). At only slightly different temperatures, for example at  $k_B T = 0.2$ , the evolution is not so clear (b).

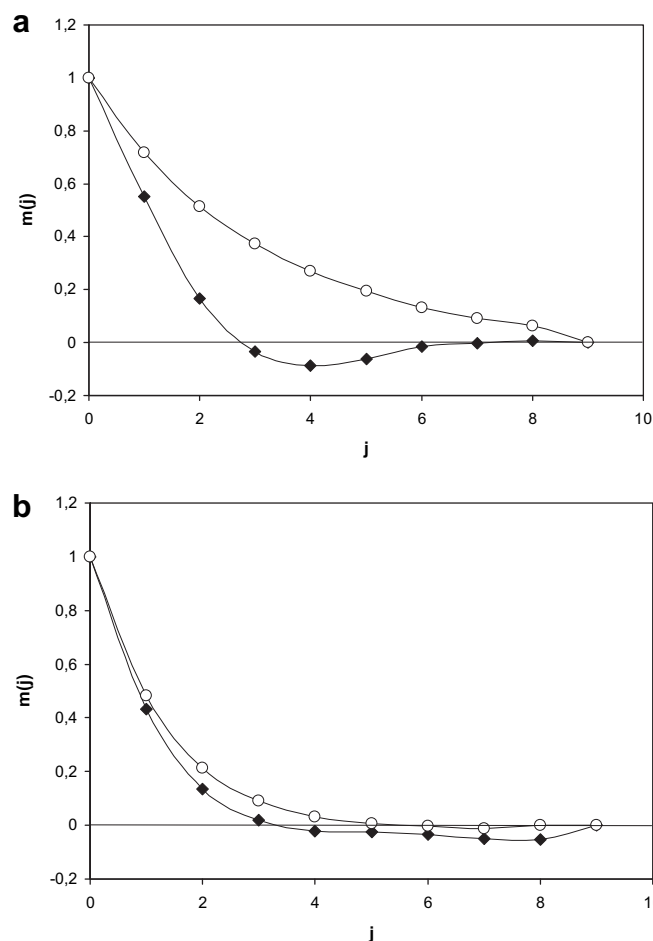


**Fig. 8.** Chain stretching during annealing of system E at  $k_B T = 0.1$  probed by comparing bond correlation parameter  $M(j)$  before ( $\blacklozenge$ ) and after annealing ( $\circ$ ) (a). A high Lennard–Jones potential (system I at  $k_B T = 0.3$ ) hinders chain stretching during crystallization (b).

already been discussed in Refs. [1,2] and corresponds to an amorphous glass. In most of the systems, annealing did not modify this structure of the system. While structural relaxation takes place, energy (Fig. 5) and DAV (results not shown) continuously diminishes but not as a consequence of development of any form of order in the sample. In the case of high values of bond angle potential, chains significantly stretch during this process as shown in Fig. 8a by an important change in  $M(j)$  (equation (8)) that shows that while no correlation can be found for more than 2 bonds along the same polymer chain, significant correlation up to 6 bonds is found at the end of the annealing process. Nevertheless, no spatial order is shown by the monomeric units and no bond angle correlations are found by Legendre analysis (Fig. 9).

Interestingly enough, system I clearly changes from an amorphous liquid to a long range ordered material when annealed at  $k_B T = 0.3$  as reveals the pair correlation function (Fig. 7a), nevertheless the situation is completely different if annealed at  $k_B T = 0.2$  when no spatial order was developed (Fig. 7b). No situation similar to that shown in Fig. 7a was found for any other system at any temperature. This is the situation one must expect for the semi-crystalline polymer. Crystallization takes place in a narrow temperature interval and once the sample is undercooled on fast cooling below this temperature range crystallization is no longer possible and a glass is formed whose segmental mobility is not enough to facilitate the reorganization needed to form a crystal. But the structure of the ordered system is far from that experimentally

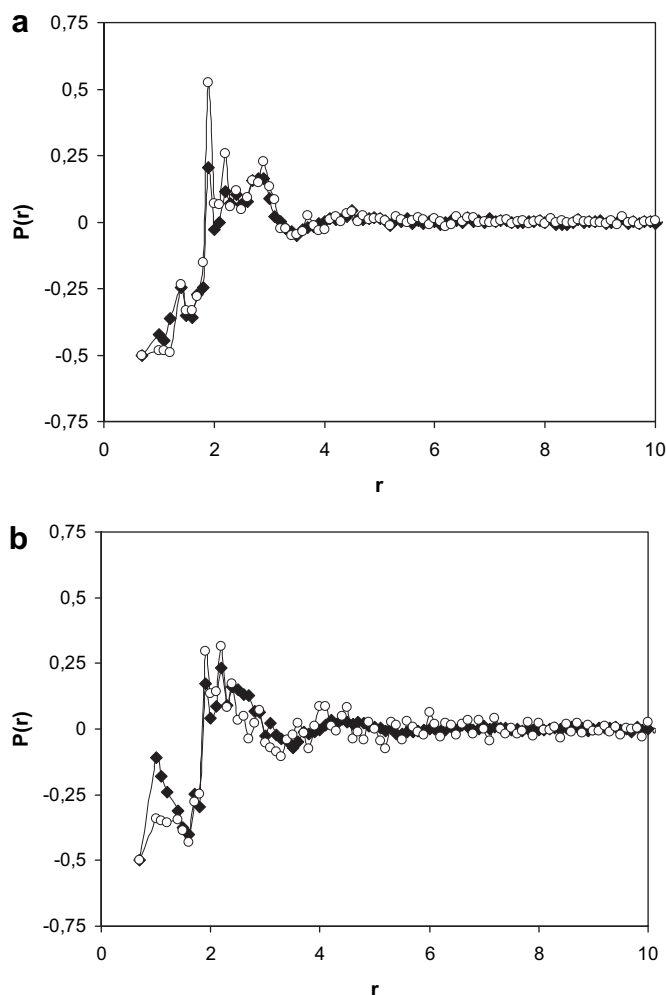


**Fig. 9.** Legendre calculations show no bond orientation order for most of the systems even with high bond angle parameter. The comparison of systems before ( $\blacklozenge$ ) and after ( $\circ$ ) annealing in system E at temperature  $k_B T = 0.1$  is shown in (a). Even for system I at temperature  $k_B T = 0.3$  (b), no clear special bond orientation order was developed during annealing.

observed in physical systems. Stretching of the polymer chains do not take place on annealing of system I during ordering. As shown in Fig. 8b no correlation of bond angles along a polymer chain is detected. Spatial correlation of bonds is neither observed (Fig. 9). This means that spatial order of monomeric units is not accomplished by obtaining elongated conformations of the polymer chains and further ordering of them parallel to each other. It seems that the rearrangements needed to minimize Lennard–Jones contribution to the energy of the whole lattice involve the motion of a relatively small number of polymer chain segments and can be accomplished in the crystallization window. Nevertheless, the large reorganization that the system needs to elongate the polymer chains from a disordered initial situation is hindered by the

monomeric order that forms faster. It is interesting to note that this elongation of the chains can perform in the case of system E which is always amorphous even at quite low temperatures (Fig. 8). A continuous evolution from the behaviour described for system E to that of system I was found with intermediate situation in systems G and H defined by intermediate strength of Lennard–Jones potential.

#### 4. Conclusions

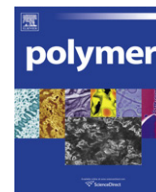
Crystallization of polymer from the melt involves conformational rearrangements of polymer chains to adopt an extended configuration and then ordering of the extended polymer chains. Simulation of this phenomena using Bond Fluctuation Model requires a high bond angle potential to drive chain extension and high Lennard–Jones potential to induce inter-molecular order. Nevertheless spatial order of monomeric units induced by Lennard–Jones potential hinders chain extension. In this way the result is that the behaviour of a semicrystalline polymer is reproduced in the sense that crystallization can be observed in a narrow temperature interval, at temperatures immediately below this range segmental mobility is arrested and no further ordering is possible. Nevertheless, chain conformations and the lack of spatial correlation of bond angles are not as complete as it could be expected.

#### Acknowledgements

The authors would like to acknowledge the support provided by the Conselleria d'Educació of the Generalitat Valenciana through the GV/2009/033 project. This work was supported by the computer-time grant (No. 2003014) of the Centre de Ressources Informatiques de Haute Normandie (CRIHAN).

#### References

- [1] Molina-Mateo J, Meseguer-Dueñas JM, Gómez-Ribelles JL. *Polymer* 2005;46:7463.
- [2] Arnoult M, Saiter JM, Pareige C, Meseguer-Dueñas JM, Gómez-Ribelles JL, Molina-Mateo J. *Journal of Chemical Physics* 2009;130:214905.
- [3] Carmesin I, Kremer K. *Macromolecules* 1988;21:2819.
- [4] Binder K. *Monte Carlo and molecular dynamics simulations in polymer science*. Oxford: Oxford University Press; 1995.
- [5] Deutsch H, Binder K. *Journal of Chemical Physics* 1990;94:2294.
- [6] Paul W, Binder K, Heermann D, Kremer K. *Journal of Chemical Physics* 1991;95(10):7726.
- [7] Lobe B, Baschnagel J, Binder K. *Macromolecules* 1994;27:3658.
- [8] Di Cecca A, Freire JJ. *Macromolecules* 2002;35:2851.
- [9] Trautenberg HL, Hölzl T, Göritz D. *Computational and Theoretical Polymer Science* 1996;6:135.
- [10] Dawson KA, Lawlor A, McCullagh GD, Zaccarelli E, Tartaglia P. *Physica A* 2002;316:115.
- [11] Dawson KA, Lawlor A, DeGregorio P, McCullagh GD, Zaccarelli E, Fo G, et al. *Faraday Discussions* 2003;123:13.
- [12] Lawlor A, Reagan D, McCullagh GD, De Gregorio P, Tartaglia P, Dawson K. *Physical Review Letters* 2002;89(24):245503.
- [13] Molina-Mateo J, Meseguer-Dueñas JM, Gómez-Ribelles JL. *Macromolecular Theory and Simulations* 2006;15:32.
- [14] Baschnagel J, Binder K. *Physica A* 1994;204:47.
- [15] Xu G, Mattice WL. *Computational and Theoretical Polymer Science* 2001;11:405.



## Modeling initial stage of phenolic pyrolysis: Graphitic precursor formation and interfacial effects

Tapan G. Desai<sup>a,\*</sup>, John W. Lawson<sup>b</sup>, Pawel Keblinski<sup>c</sup>

<sup>a</sup>Advanced Cooling Technologies, Inc., Lancaster, PA 17601, USA

<sup>b</sup>Thermal Protection Materials Branch, NASA Ames Research Center, Moffett Field, California 94035, USA

<sup>c</sup>Department of Materials Science and Engineering, Rensselaer Polytechnic Institute, Troy, NY 12180, USA

### ARTICLE INFO

#### Article history:

Received 29 September 2010

Received in revised form

9 November 2010

Accepted 10 November 2010

Available online 18 November 2010

#### Keywords:

Reactive molecular dynamics simulation

Polymer pyrolysis

Carbonization

### ABSTRACT

Reactive molecular dynamics simulations are used to study the initial stage of pyrolysis of phenolic polymers with carbon nanotube and carbon fiber. The products formed are characterized and water is found to be the primary product in all cases. The water formation mechanisms are analyzed and the value of the activation energy for water formation is estimated. A detailed study of graphitic precursor formation reveals the presence of two temperature zones. In the lower temperature zone (<2000 K) polymerization occurs resulting in the formation of large, stable graphitic precursors, while in the high temperature zone (>2000 K) polymer scission results in formation of short polymer chains/molecules. Simulations performed in the high temperature zone of the phenolic resin (with carbon nanotubes and carbon fibers) show that the presence of interfaces does not have a substantial effect on the chain scission rate or the activation energy value for water formation.

© 2010 Elsevier Ltd. All rights reserved.

### 1. Introduction

Ablative materials are thermal insulators used in hypersonic space vehicles. They are typically carbon reinforced composites with a phenolic resin matrix, which absorb heat in part through endothermic, pyrolysis of the matrix. The char produced as a result of these reactive processes yields a thermally insulating and protective layer at the material surface. Mechanical strength of the char layer is required to prevent premature flaking and subsequent exposure of the virgin material underneath. The amount of material should be enough to compensate for any part of the char layer that might be ablated away during the re-entry. However, the weight of the material should be kept to a minimum. Optimization of the thermal protection system requires accurate prediction of the pyrolysis process and the evolution of char morphology. The pyrolytic processes are important for other applications as well, including carbonization of polymers, development of fire retardants, etc.

One recently developed ablative material is “phenolic impregnated carbon ablator” (PICA). This low-density material is a good choice due to its low thermal conductivity and efficient ablation properties. Phenolic resins have a high char yield under pyrolytic

conditions. These reactions involve a complex sequence of reactions, and further development of these materials will require fundamental understanding of these molecular processes, and subsequent char evolution under transient conditions. Computational modeling of the resin-to-char process using atomistic-level simulation technique such as Molecular Dynamics (MD) with reactive force field can provide insights into the involved reaction barriers and pathways.

Recently, De-en Jiang *et al.*, [1] performed MD simulations with the reactive force field, ReaxFF, to simulate the initial stages of phenolic resin pyrolysis. Results from these simulations are benchmarks for the studies presented in this paper. The time scale accessible for routine MD simulations is limited to the nanosecond range, which allows study of only the initial stage of pyrolysis. Lawson and Srivastava [2] developed a high temperature, pyrolytic MD simulation method for polyethylene, based on the gradual removal of free Hydrogen atoms from the system. With their method, they were able to run the reactions to completion, however because of the approximations involved, accurate information about reaction kinetics was difficult to obtain.

In an effort to improve the mechanical properties of the char layer, NASA Ames Research Center has recently explored the effect of adding of carbon nanotubes (CNT) to PICA. Tensile test results showed a 35% increase in strength with the addition of 0.4 wt% functionalized CNTs in PICA, without any change in insulation properties [3]. This increase

\* Corresponding author. Tel.: +1 518 331 7704.

E-mail addresses: [tapandesai06@gmail.com](mailto:tapandesai06@gmail.com), [tapan.desai@1-act.com](mailto:tapan.desai@1-act.com) (T.G. Desai).

in strength at low concentrations is possible because the percolation threshold for CNT composites is very low, on the order of 0.1 vol %. The CNT–polymer interface is expected to play a major role in maintaining the insulation properties by limiting the effective thermal conductivity of CNTs in the composite due to a large interfacial thermal resistance [4]. Thus, without an appreciable increase in the weight or thermal conductivity, CNT addition can provide large mechanical reinforcement to the composite. In addition, the char morphology is known to change due to the addition of CNTs, as the char strongly adheres to the CNT yielding a cigar-like structure [5].

Furthermore, addition of CNT in flame retardant materials has been recently explored. Research has shown that the addition of only 0.5 wt% concentration of single-walled CNT (SWCNT) resulted in formation of a crack-free network-structured protective residual layer in PMMA composites and also reduced the rate of heat release [6]. Formation of this crack-free protective layer is essential to prevent exposure of virgin ablative material underneath. However, in both the cases (ablation and flame retardant), the role of CNTs in altering the (already) complex pyrolysis reaction is not known.

In this paper, we attempt to understand the role of CNT and carbon fibers on the initial stage of pyrolysis. We performed detailed simulations with the ReaxFF method to characterize the products involved and the kinetics of pyrolysis. For the pristine phenolic resin case, (i.e., without carbon fillers) we also performed simulations to determine the conditions and processes involved in the formation of graphitic precursors. Two temperature zones were found to be important: in the lower temperature zone (<2000 K) polymerization occurred resulting in formation of stable graphitic precursors, and in the high temperature zone (>2000 K), disintegration resulted in the formation of short polymer chains/molecules. The effect of two fillers, carbon fibers and CNT, on the initial stage of pyrolysis was also studied. No substantial effect was found due to filler addition on the product (water) formation rate or polymer disintegration rate in the high temperature zone. The paper is organized as follows: Section 2 describes the simulation method and details; results are presented in Section 3; and Section 4 provides a summary and conclusion of this work.

## 2. Method

MD simulations were performed with the LAMMPS molecular dynamics code [7]. The reactive force field, ReaxFF [8], was employed to perform pyrolysis simulations. ReaxFF uses an empirical relationship between bond orders and bond lengths to allow smooth bond formation and breaking. This method has been quite successfully applied to a variety of chemical problems, including thermal degradation of polymers [9]. Different ReaxFF parameter sets have appeared in the literature and in general we expect our results will depend on the particular choice of potential. To be consistent with previous work [1], we use the version of ReaxFF given by Chenoweth et al. [10]. Further optimization of the potentials may be required in future work.

Simulations were performed on a non cross-linked phenolic formaldehyde resin (Fig. 1: top panel) in which two, neighboring phenol moieties are connected by a methylene group. The simulation cell, shown in Fig. 1: bottom panel, consisted of 16 phenol formaldehyde chains with 8 repeating units each in the ortho–ortho sequence and a methyl group termination. The 16 polymer chains were randomly placed in the simulation cell by using the software Xenoview [11], which uses a Monte Carlo algorithm to build the amorphous structure. The simulation box size was adjusted to  $2.62 \text{ nm} \times 2.62 \text{ nm} \times 2.62 \text{ nm}$  to yield the experimental resin density of 1.25 gm/cc at 300 K. The polymer, simulation cell size and density are similar to the work performed by De-en Jiang et al. [1]. The time step used to perform the simulation was 0.25 femtosecond (fs).

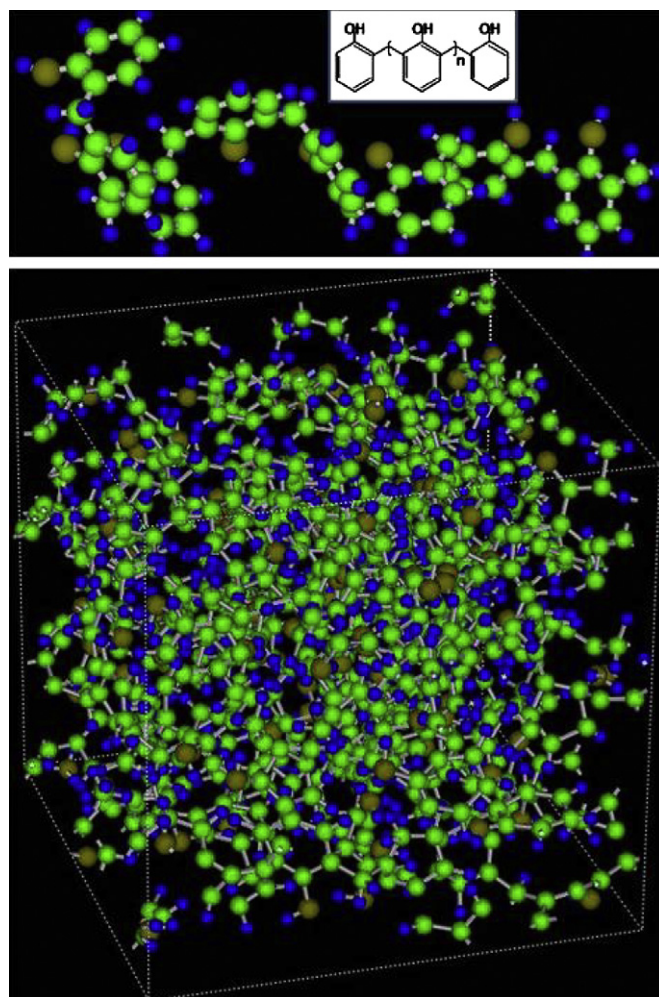


**Fig. 1.** Top Panel – Snapshot of a single phenol formaldehyde polymer chain with 8 repeating units and terminated with a methyl group on one end; color code: Carbon – green, Hydrogen – blue, Oxygen – brown. Bottom Panel – Snapshot of the simulation cell containing 16 phenol formaldehyde polymer chains equilibrated at 300 K after annealing. (For interpretation of the references to colour in this figure legend, the reader is referred to the web version of this article).

Periodic boundary conditions were applied in all the directions of the simulation cell. A Berendsen thermostat [12] with a temperature damping constant of 100 fs was used to maintain constant temperature of the simulation cell.

For composite systems, we chose to model two fillers – CNT and carbon fibers. Two CNT composite systems with two different single-walled CNT chirality, (5,5) and (10,10) were studied. The radius of (5,5) and (10,10) CNT was 3.5 and 7.0 Å, respectively. In both systems, the CNT was 27 Å long and uncapped (or open) as shown in the inset in Fig. 2a. The phenolic resin structure was similar to the pristine case. The phenolic resin chains were introduced randomly around the CNT. Periodic boundary conditions were applied in all the directions of the simulation cell. The size of the simulation cell was adjusted such that the resin density was 1.25 gm/cc. The excluded volume due to the van der Waal's distance between the CNT and resin was also accounted during this adjustment. Our simulations indicate that the van der Waal's distance between the resin and CNT is 3.4 Å, similar to the work published by Wei and Srivastava for CNT–polyethylene composite modeled with a Tersoff–Brenner potential and united atom model potential [13].

Currently, the ablation materials employed on space vehicle are made of phenolic resin impregnated within carbon fibers. Owing to

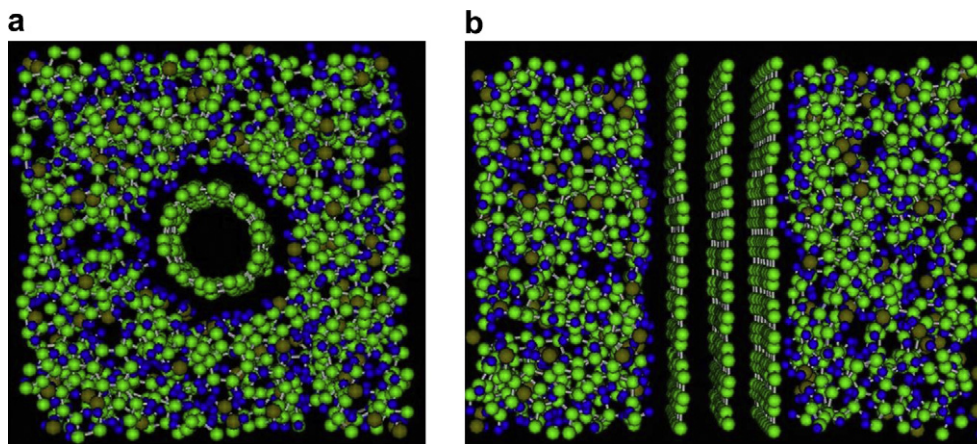


**Fig. 2.** (a) Snapshot of equilibrated resin composite structure with CNT (5,5) at the center of the simulation cell; (b) Snapshot of equilibrated resin composite structure with a graphite block (containing 3 graphene layers in A–B–A stacking sequence) at the center of the simulation cell. The color code for both snapshots is: Carbon – green, Hydrogen – blue, Oxygen – brown. (For interpretation of the references to colour in this figure legend, the reader is referred to the web version of this article).

the nanometer length-scale of the present study, the carbon fibers were simulated as surfaces with zero curvature, i.e., planar graphite sheets. As shown in the snapshot in Fig. 2b, the graphite block had 3 graphene sheets in the A–B–A stacking sequence. The surface area parallel to the sheet had the dimensions,  $25.56 \times 24.6 \text{ \AA}^2$ . The value of the surface area for the graphite block was selected to match the surface area of CNT (10,10). This was intended to provide insights on the effects introduced by the presence of tube curvature. The phenolic resin structure was similar to the pristine and the CNT-filled systems. The phenolic resin chains were introduced randomly on both sides of the graphite sheet. Periodic boundary conditions were applied in all the directions of the simulation cell and the size of the simulation cell was adjusted such that the resin density was  $1.25 \text{ gm/cc}$ .

The equilibration procedure for all systems (pristine and composite) involved (i) equilibration at 0.1 K with an NVT-MD simulation for 40 ps (ps), followed by, (ii) thermal annealing procedure – heating the system with a ramp rate of  $0.02 \text{ K/fs}$  to 1000 K, equilibrating at 1000 K for 20 ps and then cooling to 300 K with the same ramp rate. This annealing procedure was performed twice followed by an equilibration at 2000 K for 200 ps. Our in-house code was used to examine and identify the new molecules that were produced during the pyrolysis simulations. Our analysis confirmed that no reactions took place during the 200 ps equilibration run.

Pyrolysis simulations were performed at 5 different temperatures – 2750, 2875, 3000, 3125 and 3250 K to obtain reaction rates and activation energy. To improve the statistical accuracy and provide error bars for the reaction rate values, all simulations were performed with 4 different starting structures at each temperature.

### 3. Results and discussions

This section is divided into two sub-sections – pristine phenolic resin and phenolic resin composites.

#### 3.1. Pristine phenolic resin

Under this subsection, first the product evolution is discussed including the associated reaction rates and activation energies. Then, the details on graphitic precursor formation are presented.

##### 3.1.1. Evolution of products

A detailed structural analysis on the equilibrated phenol formaldehyde resin is performed to analyze the accuracy of the structure yielded by the relatively new ReaxFF potential. NPT simulation performed to estimate the resin density at 300 K indicates that the resin density is only 4.5% lower than the experimental resin density

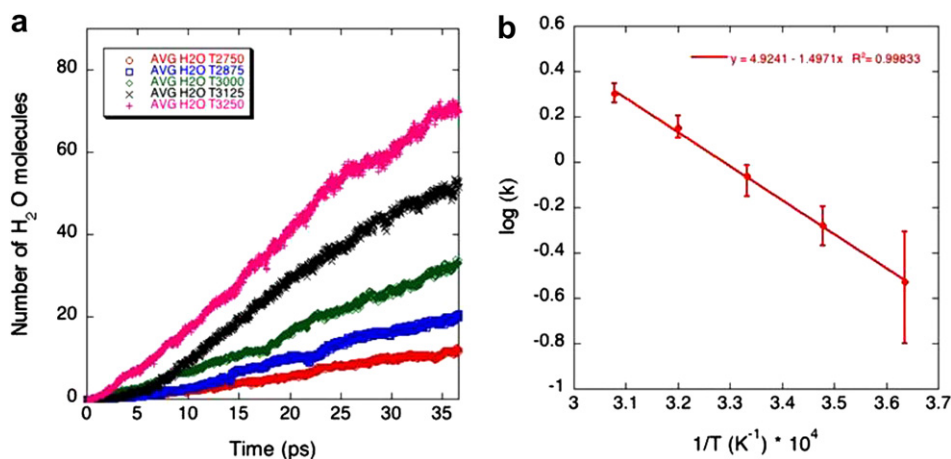


**Fig. 3.** (a) Number of water molecules (averaged over 4 different simulation runs) plotted against time for 5 different temperatures – 2750 K (red), 2875 K (blue), 3000 K (green), 3125 K (black) and 3250 K (magenta). (b) Arrhenius plot of the logarithm of the water formation rate ( $k$ ) vs. temperature gives an activation energy of  $124 \pm 20 \text{ kJ/mol}$ . This value matches well with Ref. [1]. (For interpretation of the references to colour in this figure legend, the reader is referred to the web version of this article).

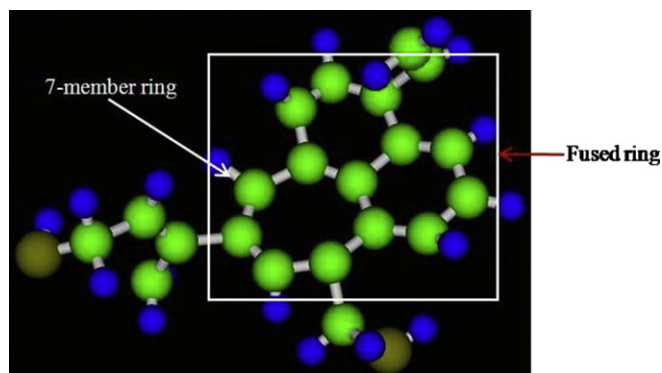


**Fig. 4.** Snapshot of a small graphitic precursor molecule containing 3 fused rings out of which one is a 7-membered ring. The molecule was found after a 40 ps run at 3250 K. The atoms that form this molecule come from 4 different chains. Color code: Carbon – green, Hydrogen – blue, Oxygen – brown. (For interpretation of the references to colour in this figure legend, the reader is referred to the web version of this article).

of the commercially available Bakelite novolac. However, in all the simulations the polymeric resin density was maintained at 1.25 gm/cc to directly compare the pyrolysis results with Jiang's [1] work. Schürmann and Vogel [14] performed simulations on a similar phenol formaldehyde resin containing 8 repeat units with 57% in ortho–para and 43% in ortho–ortho sequence at 300 K and resin density of 1.25 gm/cc with the force field – pcff. The radial distribution function (rdf) plots generated by ReaxFF at 300 K averaged over a 40 ps trajectory from the amorphous phenol formaldehyde resin structure matched qualitatively with the rdf plot in Fig. 3 of Ref. [14]. They both show the length of the short-range order (due to the amorphous nature of the structure) as 0.6 nm. Quantitatively, compared to the polymer consistent force field (pcff), the peaks indicating the C–C, C–H, C–O and O–H bonds are higher and less broad for systems with the ReaxFF potential. Further estimation of the fidelity of the ReaxFF method to simulate phenol formaldehyde resin is performed by comparing the rdf from ReaxFF with *ab-initio*

MD simulations at 300 K (see Fig. 12). A good agreement was seen which validates the ReaxFF potential at room temperature. The details on this comparison are provided in Appendix A.

High temperature simulations at 5 different temperatures in the range of 2750–3250 K are performed on 4 different equilibrated structures. Water is the primary product in all these simulations. The second most abundant product is hydrogen gas. The number of water molecules formed (averaged over 4 different starting structures) is plotted as a function of time in Fig. 3a. The rate of water formation (i.e., the slope) increases with temperature, suggesting a thermally activated reaction process. At each temperature, the value of the water formation rate is calculated from a least-square fit of the data sets and plotted in Fig. 3b. The error bars in Fig. 3b indicate the difference between the maximum (minimum) rate from the different starting structures and the average rate. Using the Arrhenius equation, a value of  $124 \pm 20$  kJ/mol is obtained for the activation energy for water formation. This value matches well with the value of  $144 \pm 28$  kJ/mol published by Jiang et al. [1].

Additionally, simulations are performed for an equilibrated structure at three different temperatures, 2750, 3000 and 3250 K with simulation time extended to 200 ps to reach completion of reactions. Initially the water formation rate depends on the temperature. At all temperatures, the total number of water molecules formed reaches a plateau after a certain time and converges to a value of  $\sim 100$ . The simulation cell contains 128 oxygen atoms, which indicates a yield (defined as the ratio of actual product formed to the theoretical) of  $\sim 78\%$ . The different mechanisms involved in water formation (including the transition states) are analyzed and presented in Appendix B. The remaining oxygen atoms are consumed during formation of CO, CO<sub>2</sub>, and, small amounts of aldehydes, ketones and alcohols.

### 3.1.2. Graphitic precursor formation

The ablation process during the re-entry of the space vehicles involves carbonization of the phenolic resin under an inert atmosphere at high temperatures ranging from 1500 to 2000 K that leads to

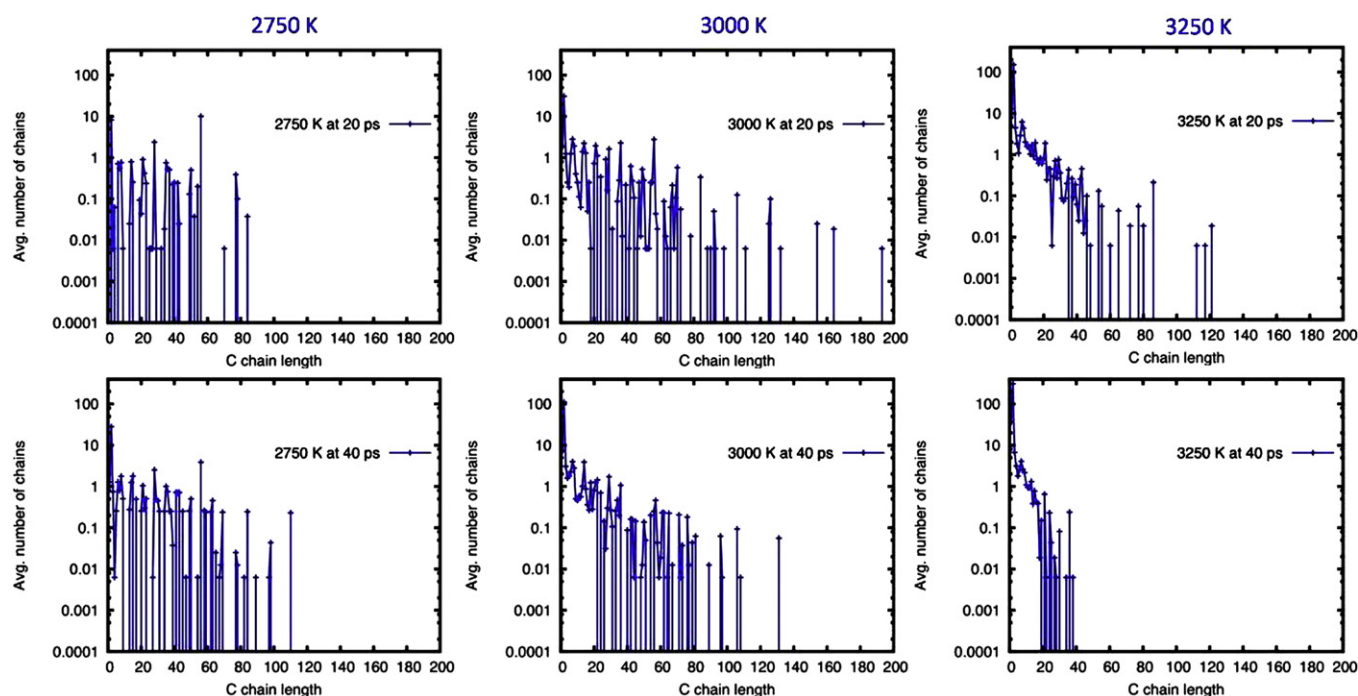


**Fig. 5.** Average number of chains as a function of carbon chain length on a semi-log scale at 3 different temperatures, 2750, 3000 and 3250 K and at two different times, 20 ps (top panel) and 40 ps (bottom panel). Disintegration of polymer chains to form small molecules is prominent at all temperatures.

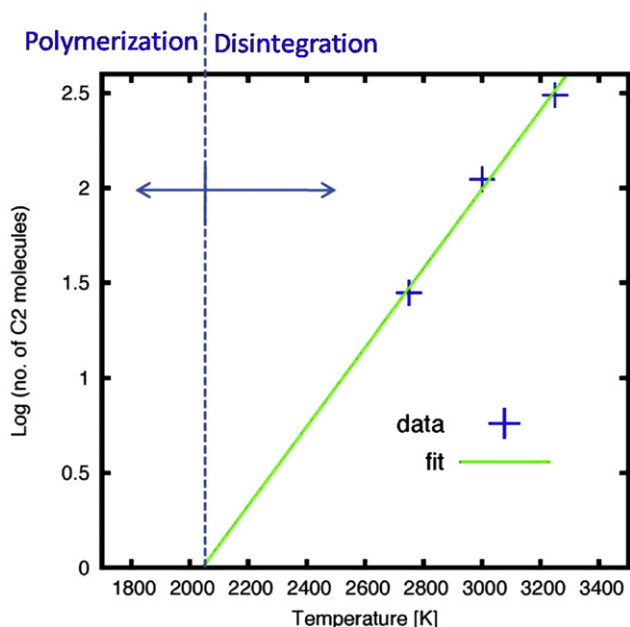


**Fig. 6.** The number of C2 molecules formed after 40 ps (averaged over 4 different starting structures) is plotted as a function of temperature on a semi-log scale. On extrapolating the slope, it intersects on the x-axis at 2050 K, suggesting the existence of two temperature zones, disintegration and polymerization.

formation of glassy carbon with large graphene fragments. Shown in Fig. 4 is a snapshot of a small graphitic precursor molecule containing 3 fused rings (two 6-membered rings and one 7-membered ring) formed after a 40 ps run at 3250 K. A commonly proposed reaction pathway [15] is that an open benzene ring and a closed benzene ring combine to form fused ring. However, our simulations illustrate that alkyl-like fragments from four different chains break, rearrange themselves and combine to form the fused ring fragment. Thus, it reveals another complex reaction pathway for graphitic precursor formation. This fused-ring structure is unstable at longer times, possibly due to the extremely high temperatures, and fragments into smaller carbon molecules.

To identify a temperature zone where the graphitic precursors would be stable, detailed chain disintegration analysis is performed. In Fig. 5, the number of chains as a function of chain length (averaged over 4 different starting structures and a simulation time of 2 ps) is plotted on a semi-log scale for two different times – 20 ps (top panel) and 40 ps (bottom panel) and 3 different temperatures – 2750, 3000 and 3250 K. At the start of the simulation run, the equilibrated structures have 16 chains with a carbon chain length of 56. At all temperatures after 20 ps, polymerization occurs between polymer chains resulting in longer chains of carbon chain length up to 120 at 3250 K and 190 at 3000 K. However, at longer times, all the long chains break to form smaller, shorter chains. This fragmentation into smaller chain occurs for other temperatures (2750 and 3000 K) at simulation times longer than 40 ps. The number of C2 molecules (C2 stands for molecule which has two carbon atoms) is seen to increase. Included in the number of C2 molecules are a large amount of  $C_2H_2$ ,  $C_2H$  radicals and  $C_2$  gas molecules. This increase in C2 molecules with time is seen at all three temperatures. The fragmentation indicates that the temperatures are too high to polymerize and form large graphitic molecules.

The results from Fig. 5 suggest that pyrolysis kinetics can be divided into two temperature zones. The high temperature (fragmentation) zone involves breaking of polymers into smaller molecules and the low temperature (polymerization) zone promotes bonding between polymers to form large connected graphitic

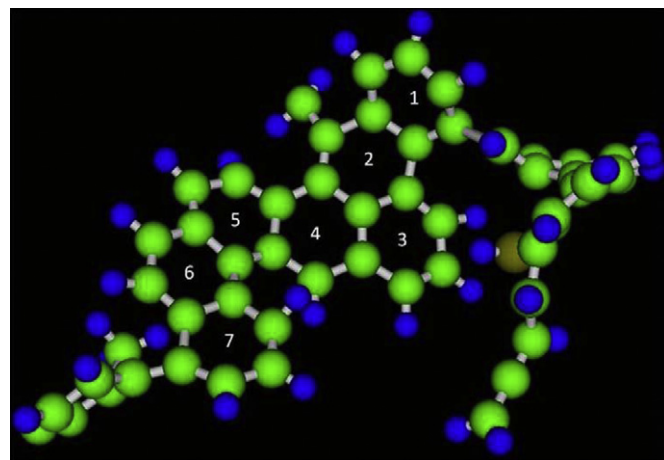


**Fig. 7.** Snapshot of a large graphitic precursor structure formed after a simulation run time of 12 ns at 1750 K. Lower temperatures (<2000 K) are necessary to capture the formation and growth of graphitic precursors. Color code: Carbon – green, Hydrogen – blue, Oxygen – brown. (For interpretation of the references to colour in this figure legend, the reader is referred to the web version of this article).

network. In order to estimate a temperature range for these zones, in Fig. 6, the total number of C2 molecules formed after 40 ps is plotted as a function of temperature on a semi-log scale. The slope through the data points is extrapolated to intersect the x-axis (temperature-axis). The intersection occurs at 2050 K signifying a higher probability of graphitization at temperatures below 2000 K.

To capture large (stable) graphitic precursor formation a simulation was performed at 1750 K. Since, no pyrolysis reactions are observed at 2000 K during the equilibration run for 250 ps, it can be expected that the time scale to observe any chemical reaction at 1750 K would go beyond the time scale accessible by MD simulations. Hence, to capture pyrolysis at 1750 K, a partially pyrolyzed structure from a 2750 K run after 40 ps was chosen as an input structure. In this structure more than 60% of the chains were intact. A reaction generally proceeds in 3 stages: initiation, propagation and termination. By using a partially pyrolyzed structure, the initiation stage is drastically reduced. In addition, after every 1.25 ns, stable molecules such as  $H_2O$  and  $CO_2$  are removed from the simulation cell. These stable gases interfere during the graphitization process preventing formation of large graphene precursors. At the end of a 12 ns simulation run two large graphitic structures are found, one containing 7 fused rings as shown in Fig. 7 and other containing 5 fused rings. The precursor starts with 2 fused rings and grows over the 12 ns simulation run. This indicates that the reaction kinetics is different in the two temperature zones and it is necessary to perform the MD simulations at the temperature of experimental interest for accurate representation of the reaction behavior rather than merely increasing the MD simulation temperature to capture the reactions on the MD time scale.

### 3.2. Phenolic resin composites

Under this subsection, the effect of addition of CNT and carbon fibers on the initial stage of pyrolysis is discussed.

#### 3.2.1. CNT-Phenolic resin composite

Pyrolysis simulations are performed at three different temperatures 2750, 3000 and 3250 K, on two composites containing CNT with (5,5) and (10,10) chirality. The CNT with two different chirality, is chosen to evaluate the effect of diameter on the pyrolysis simulation. In Fig. 8, the evolution of the primary product, water, is plotted as a function of time at three different temperatures, for



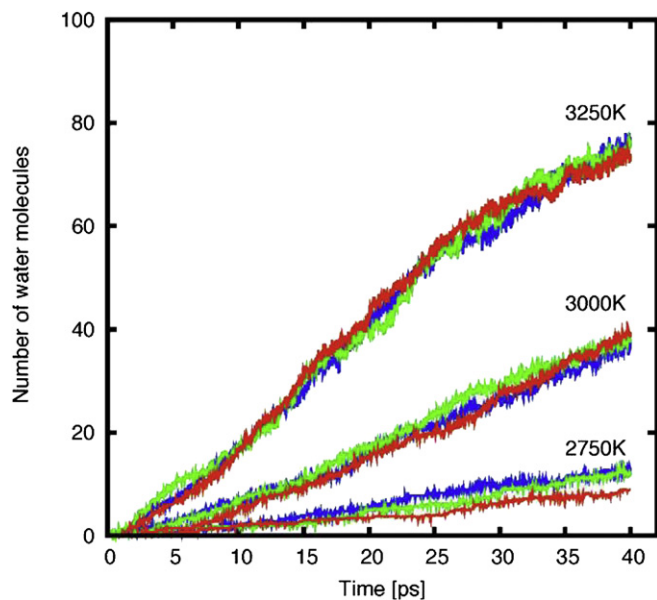


**Fig. 8.** Number of water molecules produced (averaged over 4 different starting structures) as a function of time for 3 different cases: pristine, CNT (5,5) composite and CNT (10,10) composite at 2750, 3000 and 3250 K. The pristine case is represented in blue, CNT (5,5) composite in green and CNT (10,10) in red. No effect of CNT filler on water production rate is seen. (For interpretation of the references to colour in this figure legend, the reader is referred to the web version of this article).

CNT composites and compared with the pristine phenolic resin case. For all cases, the data is averaged over 4 different starting structures to improve the statistical accuracy. The addition of fillers did not change the water production rate. The activation energy for water formation for the two types of CNT composites and the pristine case is same,  $124 \pm 20$  kJ/mol. Thus, the chemical reactions in the initial stages of the pyrolysis are not affected by the presence of CNT, even at very high weight loading of 19% and 38% for CNT (5,5) and (10,10), respectively.

Detailed analysis on the structure of CNT (5,5) after a simulation run of 40 ps for 4 different starting structures is performed. As shown in the various snapshots in Fig. 9, different starting structures yield a different number of chemically adsorbed molecules on the CNT surface. Hence, it is important for statistical purposes to perform 4 to 5 different simulation runs at each temperature of interest. Fig. 9a, suggests that a CNT can play host to a wide range of molecules from a single hydrogen atoms to a 5-membered ring to large polymer chains. Even at 3000 K, the CNT is still stable after 40 ps and chemical adsorption of polymers. At 3250 K, in Fig. 9c, CNT is distorted for 2 different starting structures, but it is found to be stable for other two starting structures after 40 ps. Separate

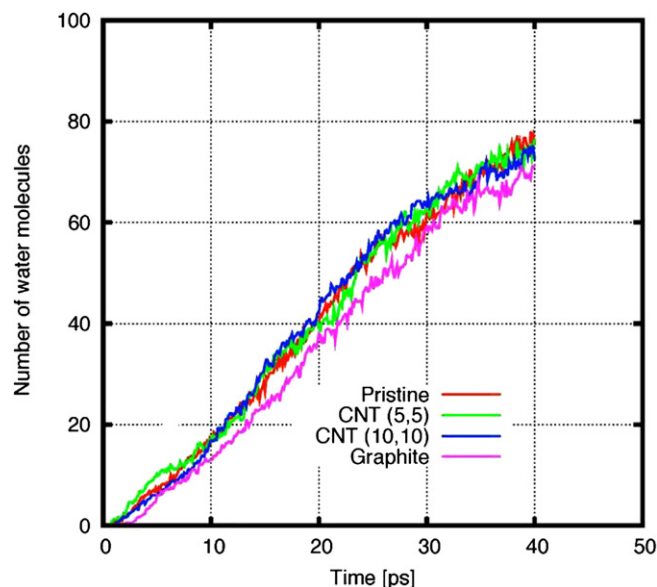


**Fig. 10.** Comparison of the number of water molecules formed (averaged over 4 different starting structures) against time at 3250 K for the pristine, CNT (5,5), CNT (10,10) and graphite case. No substantial effect of filler addition is seen on water formation rate.

simulations were performed on CNT without the phenolic resin at 3250 K to test the stability of CNT at this high temperature with ReaxFF potential. The CNT was stable at 3250 K during a 40 ps simulation run implying that the distortion of CNT is caused due to the physical and chemical interactions with the phenolic resin.

### 3.2.2. Carbon fiber-phenolic resin composite

As mentioned in Section 2, the carbon fiber is modeled as a block of graphite at the nanometer length-scale. Pyrolysis simulation results are performed at 3250 K and averaged over 4 different starting structures. The number of water molecules formed is plotted against time and compared with the results from the pristine, CNT (5,5) and CNT (10,10) composite case in Fig. 10. A strong overlap of the water formation rate with no appreciable difference is seen in all cases. Similar overlap was seen at lower temperatures (2750 and 3000 K). Thus, it can be concluded that the presence of fillers such as CNT and carbon fibers do not play a catalytic role in the dehydration stage of the pyrolysis of the phenolic resin, even under high loading conditions.

Even at 3250 K, for all the 4 structures studied, the graphite block is found to be stable during the simulation run of 50 ps. At the end of the simulation run, small molecules such as methyl, ethyl

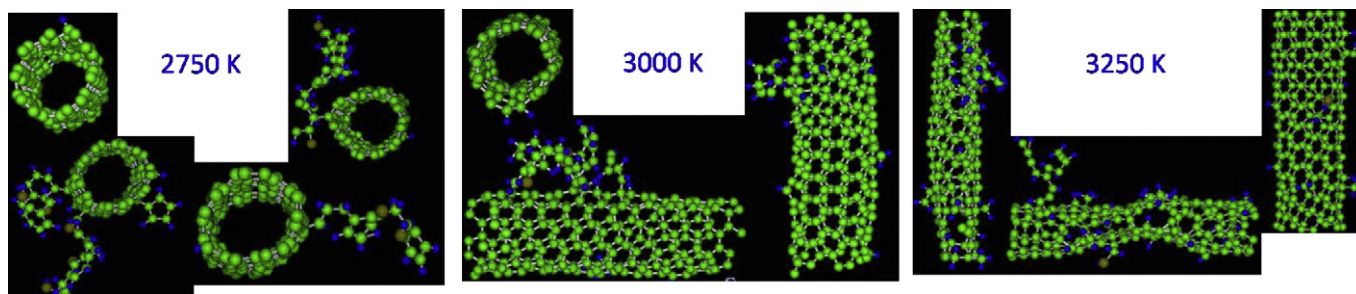


**Fig. 9.** Snapshot of CNT (5,5) after a simulation run of 40 ps for 4 different starting structures at 3 different temperatures, 2750, 3000 and 3250 K. At 3250 K, the CNT is found to be distorted for 2 different starting structures. The distortion results from physical and chemical interactions with the resin. Color code: Carbon – green, Hydrogen – blue, Oxygen – brown. (For interpretation of the references to colour in this figure legend, the reader is referred to the web version of this article).

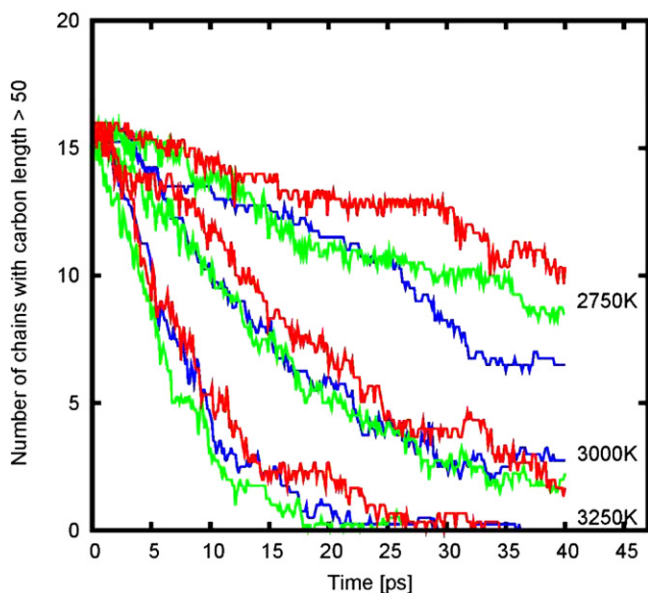


**Fig. 11.** Number of phenolic resin chains with carbon chain length greater than 50 (averaged over 4 different starting structures) is plotted as a function of time for 3 different cases: pristine, CNT (5,5) composite and graphite composite at 2750, 3000 and 3250 K. The pristine case is represented in blue, CNT (5,5) composite in green and graphite composite in red. This shows the disintegration rate of the polymer chains. (For interpretation of the references to colour in this figure legend, the reader is referred to the web version of this article).

group are bounded to the graphite layer. For the lowest pyrolysis simulation temperature studied at 2750 K no molecules were bounded to graphite (in contrast to CNT, see Fig. 9a). For a simulation run at 3000 K, similar to other two temperatures for the fiber-resin composite, no large molecules were found bounded to the graphite. Thus, in comparison to carbon fiber, a stronger covalent binding occurs in the case of CNT filler addition.

The dehydration rate does not represent the entire kinetics of the phenolic resin pyrolysis and therefore it is unjustifiable to claim that the filler addition does not have any effect on the pyrolysis process. However, disintegration of polymer chains to form shorter molecules encompasses a large part of the overall pyrolysis process. Hence, in Fig. 11, we track the number of polymer chains with carbon chain length greater than 50 as a function of time for 4 different starting structures and at 3 different temperatures. The

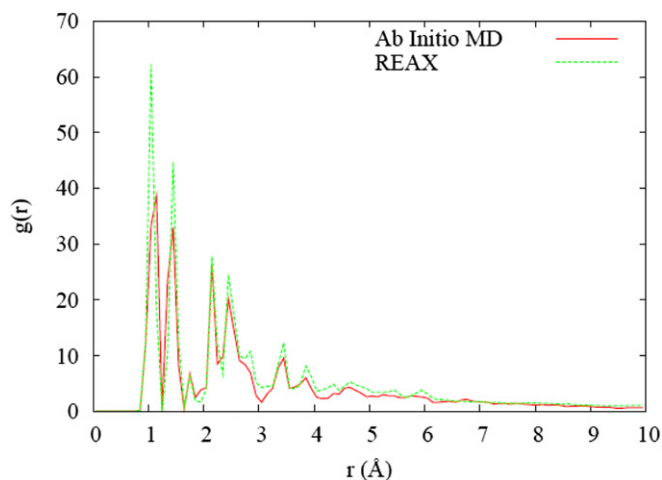


**Fig. 12.** RDF for a short, four unit phenolic chain comparing the force field, ReaxFF vs. *ab-initio* molecular dynamics at 300 K.

original carbon chain length of the phenolic resin in the starting structure is 56. The value of 50 during the disintegration analysis is used for statistical purposes to prevent any chain end effects. At 3000 and 3250 K, the disintegration rate for the pristine case (in blue) overlaps the CNT case (in green) and the graphite case (in red). At 2750 K, there is a slight discrepancy between the disintegration rates for simulation times greater than 20 ps. However, to confirm the effect of fillers, the simulations need to be performed in the low temperature zone (<2000 K). Experimentally, it has been observed the addition of CNT produced cigar-like structures where the char strongly adheres to the CNT.

#### 4. Conclusion

The primary objective of this paper was to model the effect of filler materials such as CNT and carbon fibers on the initial stage of the phenolic resin pyrolysis. Water was found to be the primary product for all the cases. There was no major effect of the filler addition on the water formation rate or the polymer disintegration rate. The evolution of graphitic precursors was studied rigorously. Two temperature zones were identified: the high temperature zone (>2000 K) involved fragmentation leading to non-graphitic structures and the low temperature zone (<2000 K) involved polymerization leading to predominantly graphitic structures. Formation of stable large (7 fused rings) graphitic precursors was captured at 1750 K during a simulation run of 12 ns. Thus, running the simulations at low temperatures was identified as the key to study the formation and growth of graphitic precursors. In the high temperature zone, no effect of fillers was observed on the graphitic precursor formation. To capture the cigar-like structures observed at 1000 K experimentally for the CNT-resin composites, the simulations need to be performed in the low temperature reaction zone.

The dehydration observed in our simulations is also found to be prominent in experiments during the curing stage of the resin which involves crosslinking of polymer chains to improve the mechanical properties of resin. However, the curing occurs at lower temperatures ~450–550 K. Jiang and coworkers showed that the simulation results for activation energy falls within the experimental range of 74–199 kJ/mol for low mass-loss peaks [16]. The experiments were performed by Trick and Saliba on a cured sample of carbon-phenolic resin composite, where the pyrolysis kinetics was calculated from thermo-gravimetric analysis. It is difficult to compare our MD simulation results with such experiments because: (i) experiments are performed on a composite structure with carbon fibers as filler material; (ii) the phenolic resin is cured at 450 K in experiments, where most of the dehydration takes place resulting in crosslinking of polymer chains; (iii) for pyrolysis experiments, the heating rate is 1 °C/min in the temperature range of 573–1173 K, whereas simulations are performed with a step-change in temperature in the range of 2750–3250 K. Thus, in addition to a different starting structure, an additional assumption is needed that the reaction kinetics in the experimental temperature range of 573–1173 K is same as the kinetics in the simulation temperature range of 2750–3250 K. According to our knowledge, there are no experiments to which we can directly compare our simulation results.

The reactive MD simulations are definitely an important tool to provide insights on the involved reaction pathways and energy barriers. However, corresponding experiments are needed to validate these simulations. The experiments should include high heating rates to reach high temperatures (within a nanosecond time scale) such that the kinetics are monitored on the time scale accessible to MD simulations. State-of-the-art laser heating of polymer samples couple with spectroscopy is an option. In addition, the MD time scale needs to be increased from nanosecond to

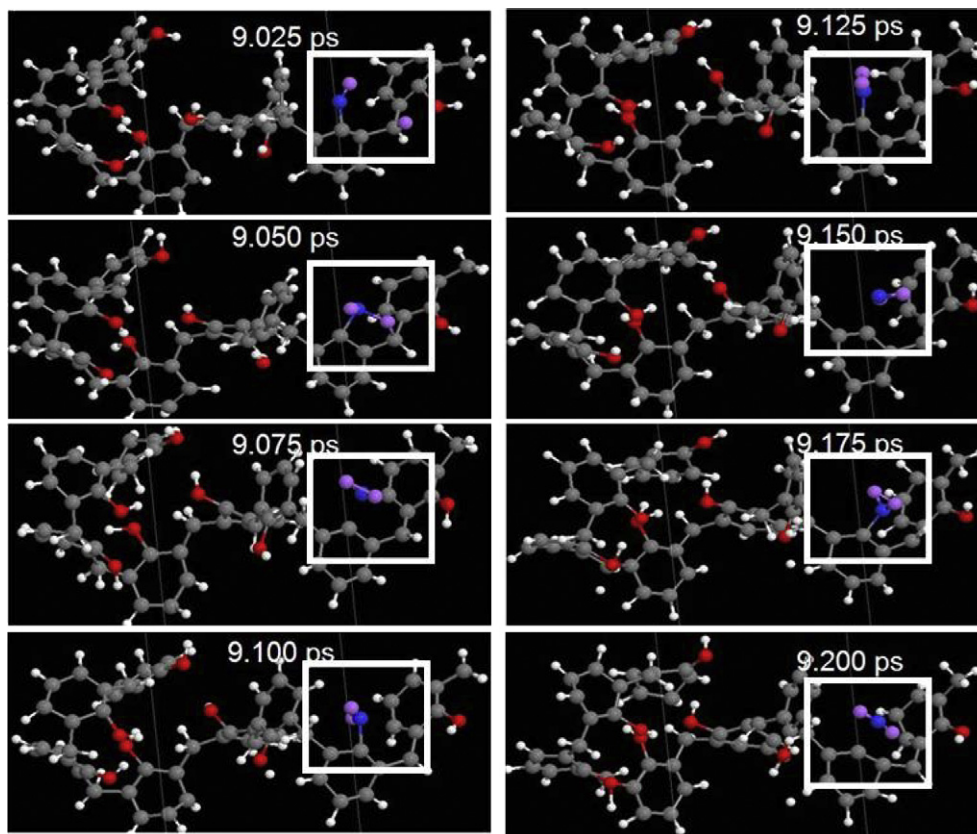


**Fig. 13.** Temporal snapshot of intramolecular dehydration mechanism between –OH group on phenol and hydrogen from adjacent methyl group. The polymer chain stays intact during the reaction period. Color code: Carbon – gray, Hydrogen – white, Oxygen – red (for atoms involved in reactions, Oxygen – blue, Hydrogen – magenta). The region of interest is highlighted by a square white box. (For interpretation of the references to colour in this figure legend, the reader is referred to the web version of this article).

micro-seconds in order to perform simulations at temperature of interest (1500–2000 K) without losing the atomistic information. This increase in MD time scale can be achieved by applying appropriate accelerated MD techniques [17]. Nevertheless, the results serve as a good model to provide insights on reaction mechanisms with caution while direct comparison with experiments.

#### Acknowledgement

The work was supported by the NASA Small Business Innovation Research Grant (SBIR), under Contract No. NNX10CC69P. We thank Dr. Howard Pearlman from Advanced Cooling Technologies, Inc. for his input during the project.

#### Appendix A. Comparison of radial distribution function – ReaxFF vs. *ab-initio* calculations

Since ReaxFF is a relatively new force field, we tested its reliability for this specific application by comparing the radial distribution function (rdf) obtained from ReaxFF against results from *ab-initio* based MD simulations. In particular, we performed simulations for a single phenolic chain with four repeating units at  $T = 300$  K and confined in a periodic box of size 20 Å on a side. The *ab-initio* simulations were performed with the code VASP within the context of density functional theory (DFT). Note that unlike other implements of *ab-initio* MD, VASP evolves the electronic and ionic degrees of freedom separately: forces obtained from DFT are converged first, and then used to advance the ionic positions. The GGA of Perdew and Wang was used with a cutoff of 300 eV and

computations were done using the Projected Augmented Wave (PAW) potentials. Results are shown in Fig. 12. As can be seen the agreement is very good. Various bond lengths identified by peaks on the rdf agree very well although there is some variation in the peak heights. It should not be concluded that this represents a definitive test of ReaxFF. However, DFT is very good at describing bonded interactions, but is well known to have difficulties with weaker, long-ranged interactions that are common to polymer systems and are in principle included in ReaxFF.

#### Appendix B. Water formation mechanisms

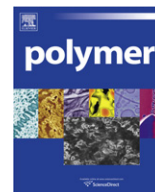
Several dehydration mechanisms were observed during the different simulation runs. Similar to observations by Ref. [1], the dehydration mechanisms involved were: (i) between two –OH groups on phenols, (ii) a disassociated H and –OH group on a phenol, (iii) H from a benzene ring and –OH group from a phenol, and (iv) H from the methyl group (between two benzene rings) and –OH group on a phenol. For these four mechanisms, both intermolecular and intramolecular reactions took place.

Shown in Fig. 13 is the temporal snapshot of a single polymer chain (for the pristine case) undergoing the fourth mechanism during intramolecular dehydration. The single polymer chain is isolated from the rest of the 15 polymer chains in the simulation cell for clarity. The simulation temperature is 2750 K and the simulation time is in the range of 9.025–9.2 ps. After 9.05 ps, the first transition state involves bonding between the –OH group from a phenol and hydrogen atom in the adjacent methyl group. At 9.075 ps, the –OH group breaks from the phenol, however, at 9.1 ps, the water molecule

reattaches to the benzene ring. After 9.2 ps, the water molecule breaks free of the polymer and diffuses away from the parent phenolic resin chain. During this period, the polymer chain is intact without undergoing any substantial disintegration (except thermal dissociation of couple of hydrogen atoms). Thus, Fig. 13 provides an atomistic picture of the transition states involved during a particular water formation mechanism for a thermally stable polymer chain. This process can be adopted to develop reaction pathways and extract associated chemical kinetic information to build highly detailed atomistically-informed chemical kinetic models.

## References

- [1] Jiang D, van Duin ACT, Goddard WA, Dai S. *J Phys Chem A* 2009;113(25):6891–4.
- [2] Lawson JW, Srivastava D. *Phys Rev B* 2008;77(14):144209-1–144209-6.
- [3] NASA biennial report, <http://research.jsc.nasa.gov/BiennialResearchReport/PDF/Eng-14.pdf>; 2007.
- [4] Shenogin S, Xue L, Ozisik R, Koblinski P, Cahill DG. *J Appl Phys* 2004;95(12):8136–45.
- [5] Fan W. Private communication; 2010.
- [6] Kashiwagi T, Du F, Douglas JF, Winey KI, Harris RH, Shields JR. *Nat Mater* 2005;4(12):928–33.
- [7] Plimpton S. *J Comput Phys* 1995;117(1):1–19, <http://lammps.sandia.gov>.
- [8] van Duin ACT, Dasgupta S, Lorant F, Goddard WA. *J Phys Chem A* 2001;105(41):9396–409.
- [9] Chenoweth K, Cheung S, van Duin ACT, Goddard WA, Kober EM. *J Am Chem Soc* 2005;127(19):7192–202.
- [10] Chenoweth K, van Duin ACT, Goddard WA. *J Phys Chem A* 2008;112(5):1040–53.
- [11] Shenogin S, Ozisik R. Xenoview: visualization for atomistic simulations, <http://www.rpi.edu/~shenos3/xenoview.html>; 2007.
- [12] Berendsen HJC, Postma JPM, van Gunsteren WF, Dinola A, Haak JR. *J Chem Phys* 1984;81(8):3684–91.
- [13] Wei C, Srivastava D. *Nano Lett* 2004;4(10):1949–52.
- [14] Schürmann BL, Vogel L. *J Mater Sci* 1996;31(13):3435–40.
- [15] Eyfe CA, McKinnon MS, Rudin A, Tchir WJ. *Macromolecules* 1983;16(7):1216–9.
- [16] Trick KA, Saliba TE. *Carbon* 1995;33(11):1509–15.
- [17] Voter A, Montalenti F, Germann T. *Annu Rev Mater Res* 2002;32(1):321–46.



# Hetero-structure of ABC triblock copolymer thin film on polymer-coated substrate

Rong Wang\*, Shanning Zhang, Yudong Qiu

Department of Polymer Science and Engineering, State Key Laboratory of Coordination Chemistry, Nanjing National Laboratory of Microstructures, School of Chemistry and Chemical Engineering, Nanjing University, Nanjing 210093, China

## ARTICLE INFO

### Article history:

Received 7 July 2010

Received in revised form

15 November 2010

Accepted 20 November 2010

Available online 27 November 2010

### Keywords:

ABC triblock copolymer

Film thickness

Grafting density

## ABSTRACT

The morphology and the phase diagram of the ABC block copolymer on the polymer-coated substrate were studied by using the self-consistent field theory. Due to the asymmetric surfaces for the block copolymer thin film, the rich hetero-structures occur, which are the combination of two different microstructures, such as perforated lamellar and lamellar phase (PL + L), cylindrical and lamellar phase (C + L). The phase diagrams were constructed for the identical interaction parameters case and the non-frustrated case. The effect of the film thickness is also considered at the fixed grafting density. Comparing the results, we found that the essence of the variation of the grafting density is the change of the effective film thickness in most cases. The relationship between the grafting density and the film thickness is constructed. Our results offer another way to tailor the phase behavior of the block copolymer thin film and obtain the hetero-structures on nanoscale.

© 2010 Elsevier Ltd. All rights reserved.

## 1. Introduction

Block copolymers can microphase separate to form a variety of ordered nanoscale morphologies [1,2]. Self-assembly and phase separation in diblock copolymers have been well studied and characterized both theoretically and experimentally in the last few decades [3–10]. Recently, there has been a great interest in studying the thin film of block copolymers experimentally and theoretically. The function of the thin film is very important for its application besides the perfect nanopattern of the film. In thin films, incompatibility between different polymer components and the thin film thickness creates frustration, the effect of which can be probed by surface-induced effect. The presence of a surface or interface can strongly influence the microdomain morphologies and the kinetics of microdomain ordering.

The phase behavior of diblock copolymers melts confined in a parallel slit or in a thin film has been extensively studied [3,11–15]. Comparing with two-component systems (*i.e.* AB diblock copolymers), the phase behavior of ABC triblock terpolymers is much more complex, and a much larger number of simulation parameters is needed to describe thin films: the film thickness ( $H$ ), the volume fractions of the components  $f_A$ ,  $f_B$  and  $f_C$  ( $1 - f_A - f_B$ ), three mutual interaction parameters between the components  $\chi_{AB}$ ,

$\chi_{AC}$ ,  $\chi_{BC}$ , and interaction parameters between the interfaces and the three components ( $\chi_{AS}$ ,  $\chi_{BS}$ , and  $\chi_{CS}$ , and  $S$  representing the surface). The phase behavior of ABC triblock copolymer thin film is widely studied since the prediction of morphologies, especially certain valuable morphologies of the thin film is of great importance. SCFT predicts that the phase behavior of ABC triblock copolymer in bulk is controlled by two independent volume fractions, and the products of the chain length with three different Flory–Huggins parameters,  $\chi N$  [16,17]. However, the phase behavior of block copolymer thin film is also controlled by surface effect and confined spatial nature, especially the thickness of thin film [3,18,19]. Pickett and Balazs have used the self-consistent field theory to probe the preferential orientation of lamellae formed by an ABC triblock terpolymer confined between two walls attracting the middle block [20]. They found that an orientation of the lamellae perpendicular to the plane of the film orientation is highly favored, indicating that triblock terpolymers possess distinct advantages over diblocks in technological applications. Monte Carlo simulations by Feng and Ruckenstein for ABC melts in thin films show that the microdomain morphology can be very complicated and is affected by the composition, the interactions [21] and even the geometry of the confinement. Chen and Fredrickson have applied the self-consistent field theory and strong segregation limit studies (SSL) to investigate the films of linear ABC triblock terpolymer melts [22] for the particular case where A and C blocks are in equal size, the interaction parameters are identical, and both walls have identical chemical properties. Self-consistent Field Theory (SCFT) [19] and dynamic density functional field theory [23]

\* Corresponding author. Tel.: +86 25 83596802; fax: +86 25 83317761.  
E-mail address: [rong\\_wang73@hotmail.com](mailto:rong_wang73@hotmail.com) (R. Wang).

are also used to study symmetric ABC triblock copolymer thin film. The above results show that the morphology of block copolymer thin film depends on the film thickness, the surface-polymer interaction, and the incompatibility between different blocks of the copolymer, which is usually characterized by a Flory–Huggins parameter.

Therefore, we can tailor surface fields, film thicknesses and even the geometry of the confinement to manipulate the microdomain structure, shape, and orientation. For example, to induce phase transitions of block copolymer thin film there are two ways: varying surface conditions as changing the grafting density of confined substrates and changing the thickness of thin film. Both two methods are widely used to predict different morphologies and get phase diagrams. Ludwigs et al. did both experimental and theoretical study on the phase behavior of ABC triblock copolymer thin film when increasing the thickness of thin film [19]. Tang et al. studied the self-assembly of star ABC triblock copolymer thin film by changing the thin film thickness and the surface field [24]. Zhou and Ma studied the phase behavior of copolymer films confined between two-grafted surfaces by changing the grafting numbers and positions [25]. However, the relationship between these two methods was rarely studied.

In practice, besides using pure (silicon) substrates, the hydrophobic or hydrophilic substrates are prepared by chemically grafting self-assembled monolayer onto (silicon) substrate [26], which form so-called “polymer brush” to provide a simple way of modifying surface properties, such as adhesion, lubrication and wetting behavior. Ma and his group members [27,28] observed the structure transformation of the AB diblock copolymer thin film by tailoring the grafting density of the coated surface or the concentration of the copolymer. The phase transitions of the block copolymer thin film are based on the double brush-coated substrate in order to obtain the symmetric structures [25,27,28]. In fact, the single brush-coated substrate is used and the other surface is the hard surface or the free air surface. Therefore, we choose to study the block copolymer on the single brush-coated substrate. Under this condition, the asymmetric structure can be obtained and is very helpful for designing the hetero structures.

We use the real space self-consistent field theory (SCFT) [16,29] to search the equilibrium microphases of ABC linear triblock copolymers with short end block confined between the polymer brush-coated surface and the flat impenetrable surface in three dimensions (3D). We chose two types of ABC triblock copolymers: the copolymer with three identical Flory–Huggins parameters and non-frustrated copolymer [17]. Polymer films on brush-coated substrate are mimicked as a polymer melt confined between the brush-coated surface and a hard surface. With a certain thickness, the ABC triblock copolymer thin films are simulated on two neutral substrates with one of them grafted having different brush density. To discover the relationship between changing the grafting density and increasing the thickness of ABC triblock copolymer thin film, we also simulated the ABC triblock copolymer thin film with varying the film thickness at the fixed brush density.

## 2. The model

We assume the ABC triblock copolymer is confined between the polymer-grafted substrate and the flat impenetrable surface (hard surface) with a distance  $L_z$  along the  $z$ -axis. There are  $n_c$  ABC triblock copolymers with polymerization  $N$  and  $n_g$  polymer with polymerization  $P$  (here, we take  $P = N$ ) grafting on the substrate. Each copolymer chain consists of  $N$  segments with

compositions (average volume fractions)  $f_A$  and  $f_B$  ( $f_C = 1 - f_A - f_B$ ), respectively. The monomers of the ABC triblock copolymer and the grafted polymers are assumed to be flexible with a statistical length  $a$  and the mixture is incompressible with each polymer segment occupying a fixed volume  $\rho_0^{-1}$ . The substrate coated by the polymers is horizontally placed on the  $xy$ -plane at  $z = 0$  and the hard free surface is placed at  $z = L_z + 1$ . The volume of the system is  $V = L_x L_y L_z$ , where  $L_x$  and  $L_y$  are the lateral lengths of the substrate and the flat impenetrable surface along the  $xy$ -plane and  $L_z$  is the film thickness. The grafting density is defined as  $\sigma = n_g a^2 / L_x L_y$ . The average volume fractions of the grafted chains and copolymers are  $\phi_g = n_g N / \rho_0 V$  and  $\phi_c = n_c N / \rho_0 V$ , respectively.

In the SCFT one considers the statistics of a single copolymer chain in a set of effective external fields  $w_i$ , where  $i$  represents block species A, B, C or grafted polymers. These external fields, which represent the actual interactions between different components, are conjugated to the segment density fields,  $w_i$ , of different species  $i$ . Hence, the free energy (in unit of  $k_B T$ ) of the system is given by,

$$F = -\phi_c \ln(Q_c / \phi_c V) - \phi_g \ln(Q_g / \phi_g V) - 1/V \int d\mathbf{r} \left[ \sum_i w_i \phi_i + \xi \left( 1 - \sum_i \phi_i \right) \right] + 1/V \int d\mathbf{r} \left[ \frac{1}{2} \sum_{i \neq j} \chi_{ij} N \phi_i \phi_j + \sum_i \chi_{iS} N \phi_i \delta_{\mathbf{r}, \mathbf{r}_s} \right] \quad (1)$$

where  $\chi_{ij}$  is the Flory–Huggins interaction parameter between species  $i$  and  $j$ ,  $\xi$  is the Lagrange multiplier (as a pressure),  $\chi_{iS}$  is the interaction parameter between the species  $i$  and the free hard surface  $S$ .  $\mathbf{r}_s$  is the position of the free hard surface.  $Q_c = \int d\mathbf{r} q_c(\mathbf{r}, 1)$  is the partition function of a single copolymer chain in the effective external fields  $w_A$ ,  $w_B$  and  $w_C$ , and  $Q_g = \int d\mathbf{r} q_g(\mathbf{r}, 1)$  is the partition function of a grafted polymer chain in the external field  $w_g$ . The fundamental quantity to be calculated in mean-field studies is the polymer segment probability distribution function,  $q(\mathbf{r}, s)$ , representing the probability of finding segment  $s$  at position  $\mathbf{r}$ . It satisfies a modified diffusion equation using a flexible Gaussian chain model,

$$\frac{\partial}{\partial s} q(\mathbf{r}, s) = \frac{Na^2}{6} \nabla^2 q(\mathbf{r}, s) - w q(\mathbf{r}, s) \quad (2)$$

where  $w$  is  $w_A$  when  $0 < s < f_A$ ,  $w_B$  when  $f_A < s < f_A + f_B$ ,  $w_C$  when  $f_A + f_B < s < 1$  for ABC triblock copolymer and  $w_g$  for the grafted polymer. The initial condition of Eq. (2) satisfies  $q_c(\mathbf{r}, 0) = 1$  for ABC triblock copolymer. Because the two ends of the block copolymer are different, a second distribution function  $q_c^+(\mathbf{r}, s)$  is needed which satisfies Eq. (2) but with the right-hand side multiplied by  $-1$  and the initial condition  $q_c^+(\mathbf{r}, 1) = 1$ . The initial condition of  $q_g(\mathbf{r}, s)$  for grafted polymer is  $q_g(\mathbf{r} = \mathbf{r}_z, 0) = 1$  and  $q_g(\mathbf{r} \neq \mathbf{r}_z, 0) = 0$ , where  $\mathbf{r}_z$  presents the position of the substrate at  $z = 0$ , and that of  $q_g^+(\mathbf{r}, s)$  is  $q_g^+(\mathbf{r}, 1) = 1$ . The periodic boundary condition is used for  $q_c(\mathbf{r}, s)$ ,  $q_c^+(\mathbf{r}, s)$ ,  $q_g(\mathbf{r}, s)$ , and  $q_g^+(\mathbf{r}, s)$  along  $x$ -direction when  $z \in [0, L_z]$ .  $q_c(\mathbf{r}, s)$ ,  $q_c^+(\mathbf{r}, s)$ ,  $q_g(\mathbf{r}, s)$ , and  $q_g^+(\mathbf{r}, s)$  are equal to zero when  $z < 0$  or  $z > L_z$ .

Minimization of the free energy with respect to density, pressure, and fields,  $\delta F / \delta \phi = \delta F / \delta \xi = \delta F / \delta w = 0$ , leads to the following equations.

$$w_A(\mathbf{r}) = \sum_{i \neq A} \chi_{Ai} N \phi_i(\mathbf{r}) + \xi(\mathbf{r}) + \chi_{AS} N \delta_{\mathbf{r}, \mathbf{r}_s} \quad (3)$$

$$w_B(\mathbf{r}) = \sum_{i \neq B} \chi_{Bi} N \phi_i(\mathbf{r}) + \xi(\mathbf{r}) + \chi_{BS} N \delta_{\mathbf{r}, \mathbf{r}_s} \quad (4)$$

$$w_C(\mathbf{r}) = \sum_{i \neq C} \chi_{Ci} N \phi_i(\mathbf{r}) + \xi(\mathbf{r}) + \chi_{CS} N \delta_{\mathbf{r}, \mathbf{r}_s} \quad (5)$$

$$w_g(\mathbf{r}) = \sum_{i \neq g} \chi_{gi} N \phi_i(\mathbf{r}) + \xi(\mathbf{r}) + \chi_{gS} N \delta_{\mathbf{r}, \mathbf{r}_s} \quad (6)$$

$$\phi_A(\mathbf{r}) + \phi_B(\mathbf{r}) + \phi_C(\mathbf{r}) + \phi_g(\mathbf{r}) = 1 \quad (7)$$

$$\phi_A(\mathbf{r}) = \frac{\varphi_c V}{Q_c} \int_0^{f_A} ds q_c(\mathbf{r}, s) q_c^+(\mathbf{r}, s) \quad (8)$$

$$\phi_B(\mathbf{r}) = \frac{\varphi_c V}{Q_c} \int_{f_A}^{f_A+f_B} ds q_c(\mathbf{r}, s) q_c^+(\mathbf{r}, s) \quad (9)$$

$$\phi_C(\mathbf{r}) = \frac{\varphi_c V}{Q_c} \int_{f_A+f_B}^1 ds q_c(\mathbf{r}, s) q_c^+(\mathbf{r}, s) \quad (10)$$

$$\phi_g(\mathbf{r}) = \frac{\varphi_g V}{Q_g} \int_0^1 ds q_g(r, s) q_g^+(r, s) \quad (11)$$

Eqs. (3–11) form a close set of self-consistent equations, which are numerically implemented by a combinatorial screening algorithm proposed by Drolet and Fredrickson [16,29]. The Crank-Nicolson scheme and the Douglas-Gunn scheme are used to make the solution unconditionally stable [30]. The algorithm consists of randomly generating the initial values of the fields  $w_i(\mathbf{r})$ . Then the diffusion equations are then integrated to obtain  $q$  and  $q^+$ , for  $0 < s < 1$ . The right-hand sides of Eqs. (8–11) are evaluated to obtain new values for the volume fractions of blocks A, B, C, and grafted polymers. The simulation is carried out until the phase patterns are stable.

The simulations are performed on a three-dimensional cubic box  $L_x \times L_y \times L_z$  with periodic boundary conditions in the  $x$ - and  $y$ -directions. The walls are presented as planes at  $z = 0$  (substrate) and  $L_z + 1$  (hard surface). The  $L_x$  and  $L_y$  are varied between 40 and 45 (in unit of  $a$ ) along  $xy$ -plane. The film thickness is  $L_z = 40$ . And we can vary the brush density  $\sigma$  to tailor the morphology of the ABC block copolymer thin film. It should be noted that the resulting microphases largely depend on the initial conditions. Therefore, all the simulations are repeated at least 10–20 times using different random states to guarantee the structure is not occasionally observed. Also the simulation box in the  $x$ - and  $y$ -directions is varied to find the final stable phase. We should note that this method will not influence the final morphologies of the system according to comparing the free energy to determine the stable and metastable morphologies. We only address the thin films of ABC triblock copolymer on the densely polymer-grafted substrate and the grafted polymers are assumed to be identical with the middle block B. The grafting density of the grafted chains is changed from  $\sigma = 0.15$  to 0.6 to insure that the polymer brush is in the dry brush regime ( $\sigma N^{1/2} > 1$ ) and the pattern of the ABC triblock copolymer film is perfect. The polymerization of ABC triblock copolymer is  $N = 60$  and that of the grafted chains is same with the copolymers, i.e.,  $P = N = 60$ . The core-shell hexagonal phase with compositions  $f_A = 0.1$ ,  $f_B = 0.2$  and  $f_C = 0.7$  in melts [31] is studied, which is equivalent to the short block A adding to

the diblock copolymer AB. It is very important in nanolithography [32], photoelectric applications [33]. In this work, we studied two cases: 1) identical interaction parameter  $\chi_{ij} N = 35$ , and 2) non-frustrated state  $\chi_{AB} N = \chi_{BC} N = 13$  and  $\chi_{AC} N = 35$  based on Jung's [32] and Tyler's work [17].

### 3. Results and discussion

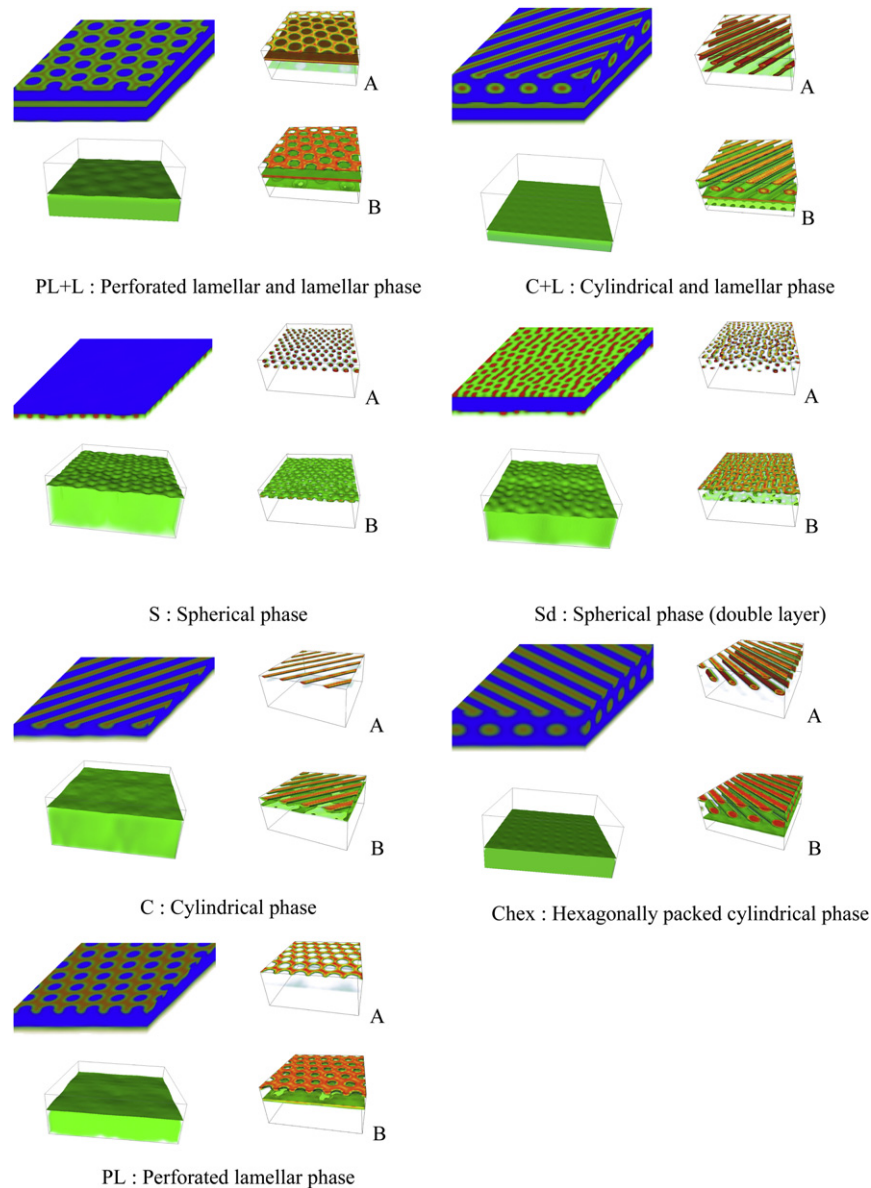
#### 3.1. Morphology

Fig. 1 shows the morphologies of the ABC block copolymer by varying the brush density with the neutral hard surface. The microphase patterns, displayed in the form of density, are the red, green and blue, assigned to blocks A, B and C, respectively. For a clear presentation of the final pattern, the linear dimensions of the unit cell are replicated 2 times in  $x$ - and  $y$ -direction. In the large icons of each group, the final color plotted at each point is the mixture of three colors, in which the concentration of each color is proportional to the local volume fraction of an individual block. The patterns of the polymer brush and the single block (block A or block B) are shown with the small icons in each group. Seven ordered microphases are found with  $f_A = 0.1$ ,  $f_B = 0.2$  and  $f_C = 0.7$  at  $L_z = 40$  by varying the brush density from  $\sigma = 0.1$  to 0.6: Perforated lamellar and lamellar phase (PL + L), Cylindrical and lamellar phase (C + L), Spherical phase (S), Spherical phase (double layer) (Sd), Cylindrical phase (C), Hexagonally packed cylindrical phase (Chex), Perforated lamellar phase (PL). The morphology is asymmetric along  $z$ -direction, which is due to the different confining surfaces (one is the brush-coated surface and the other is the free hard surface). The final structure is the combination of the different morphology, such as C + L, PL + L. In the work, we observed the severely uneven distribution of the grafted brushes like our previous work ( $f_A = 0.18$ ,  $f_B = 0.39$  and  $f_C = 0.43$ ) [4]. Only when the brush density is very high, the interface between the brushes and the block copolymer shows some pattern. This is due to the different composition here,  $f_A = 0.1$ ,  $f_B = 0.2$  and  $f_C = 0.7$ . The relative short middle blocks B can easily overcome the bending energy between them and the short end blocks A. Here, the polymer brushes act as the soft surface to make the good morphology of the ABC triblock copolymer with the middle block tending to aggregate at the surface. From Fig. 1, we can see three main kinds of morphologies: cylinders, perforated lamellae and spheres (Fig. 2).

- Cylinders:** In the cylinders, block A forms the core, block B forms the shell of the core, and the matrix is the block C. The phases related with cylinders are cylindrical and lamellar phase (C + L), hexagonally packed cylindrical phase (Chex), and cylindrical phase (C), where, the C + L phase is due to the minority of blocks A and B, which cannot separate from each other.
- Perforated lamellae:** There are two perforated lamellar phases. One is the perforated lamellar phase (PL) and the other is the perforated lamellar phase (PL) combined with lamellar phase with single layer (PL + L).
- Spheres:** Spherical phases include single layer spheres (S) and double spheres (Sd) depending on the brush density. The block A forms the 'core' and the block B forms the 'shell' of the 'core', and the matrix is the block C. In this case, there are not enough block copolymer to form the cylinders or perforated lamellae.

#### 3.2. Phase diagram by varying the brush density

By continuously changing the brush density (we start the brush density  $\sigma$  from 0.1 here), the phase diagrams are constructed for the



**Fig. 1.** Morphologies of the ABC block copolymer by varying the brush density at  $f_A = 0.1$ ,  $f_B = 0.2$  and  $f_C = 0.7$ ,  $L_z = 40$ . The microphase patterns, displayed in the form of density, are the red, green and blue, assigned to A, B and C, respectively. The isosurfaces of polymer brush (below the morphology of ABC triblock copolymer) and the single block (block A or block B) are also shown with the small icons in each group (for interpretation of the references to colour in this figure legend, the reader is referred to the web version of this article).

two cases: identical interaction parameter  $\chi_{ij}N = 35$ , and non-frustrated state  $\chi_{AB}N = \chi_{BC}N = 13$  and  $\chi_{AC}N = 35$ . The phase diagram as a function of the brush density is shown in Fig. 2. The left column is for  $\chi_{AB}N = \chi_{BC}N = \chi_{AC}N = 35$  and the right column is for  $\chi_{AB}N = \chi_{BC}N = 13, \chi_{AC}N = 35$ . There are six phases for the case of the identical interaction parameters  $\chi_{AB}N = \chi_{BC}N = \chi_{AC}N = 35$ . When the brush density is between 0.10 and 0.20, the stable phase of the block copolymer is the mixture of cylinders and lamellae (C + L). When the brush density increases to 0.20–0.28, the perforated lamellar and lamellar phase forms. Blocks A and B form one phase in this case. At the interface, there are not enough short blocks A and B to form the lamellar phase, then the perforated phase occurs at the interface. When further increasing the brush density, the cylindrical and lamellar phase occurs again. The lamellae are near the brush-coated substrate and the cylinders are near the other free surface. This is due to the difference of the two surfaces (one is the brush-coated surface and the other the free hard surface). When the brush density increases to 0.36–0.40, the

stable phase is the cylindrical phase. The thickness of the block copolymer thin film decreases when the brush density increases, so the phase becomes simple. When further increasing the brush density, the spherical phase occurs, which is due to that there is not enough block copolymer to form cylinders or lamellae. When the brush density is very high, such as larger than 0.56, the disordered phase is stable because the block copolymer is the minority compared to the brush, so the blocks cannot separate from each other. The phase transition with changing the brush density is similar to that of the ABA block copolymer on the B polymer brush-coated substrate by changing the film thickness [34]. Although the condition (chain blocks and composition) is not fully identical, the phase transition from the cylinder to perforated phase to cylinder and last to disordered phase. This means that there is some correspondence between the coated brush density and the film thickness. We will give the comparison in Section 3.3.

For the non-frustrated case,  $\chi_{AB}N = \chi_{BC}N = 13$ ,  $\chi_{AC}N = 35$ , only four phases are found: Chex, PL, C and Dis. The repulsive interaction



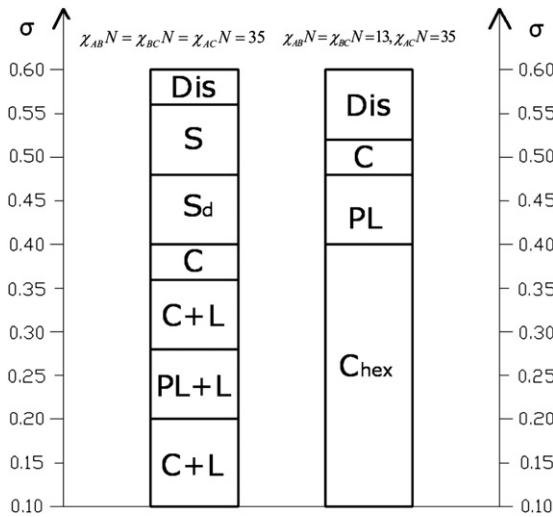


**Fig. 2.** Phase diagram of the ABC block copolymer thin film confined between the brush-coated substrates when increasing the grafting density  $\sigma$  of the brush at  $f_A = 0.1$ ,  $f_B = 0.2$  and  $f_C = 0.7$ ,  $L_z = 40$ . The left column is for  $\chi_{AB}N = \chi_{BC}N = \chi_{AC}N = 35$  and the right column is for  $\chi_{AB}N = \chi_{BC}N = 13$ ,  $\chi_{AC}N = 35$ .

between the end blocks A and C is the largest in the three interaction parameters. It is a favorable case. The block A forms the “core”, the block B forms the “shell” and the core-shell structure is inserted in the matrix composed of the block C when the brush

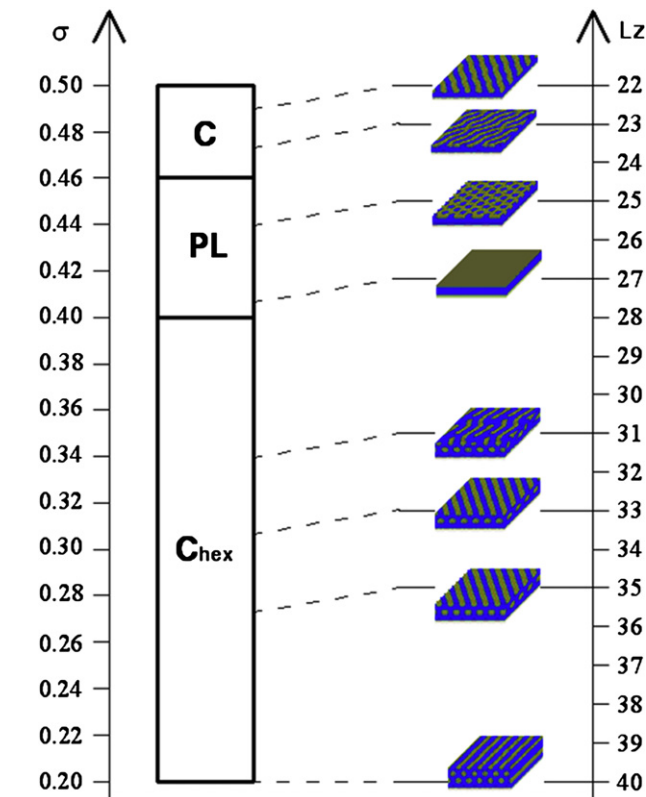


**Fig. 3.** Comparison of ABC triblock copolymer thin film phase behaviour between varying the grafting density and changing the thickness when the volume fractions of A and B are 0.10 and 0.20 respectively and the interaction parameters are  $\chi_{AB}N = \chi_{BC}N = 13$ ,  $\chi_{AC}N = 35$ . The left column is the phase behaviour of the ABC triblock copolymer thin film by varying the grafting density with  $f_A = 0.1$ ,  $f_B = 0.2$  and  $f_C = 0.7$ ,  $L_z = 40$ . The right column is the phase behaviour of the ABC triblock copolymer thin film by varying the film thickness with the fixed brush density  $\sigma = 0.2$ , where the effective film thickness is  $L_z^{\text{eff}} = L_z - h = L_z - \sigma P = L_z - 12$ . The effective film thickness of the ABC triblock copolymer by varying the brush density is  $L_z^{\text{eff}} = L_z - h = 40 - \sigma P = 40 - 60\sigma$ .

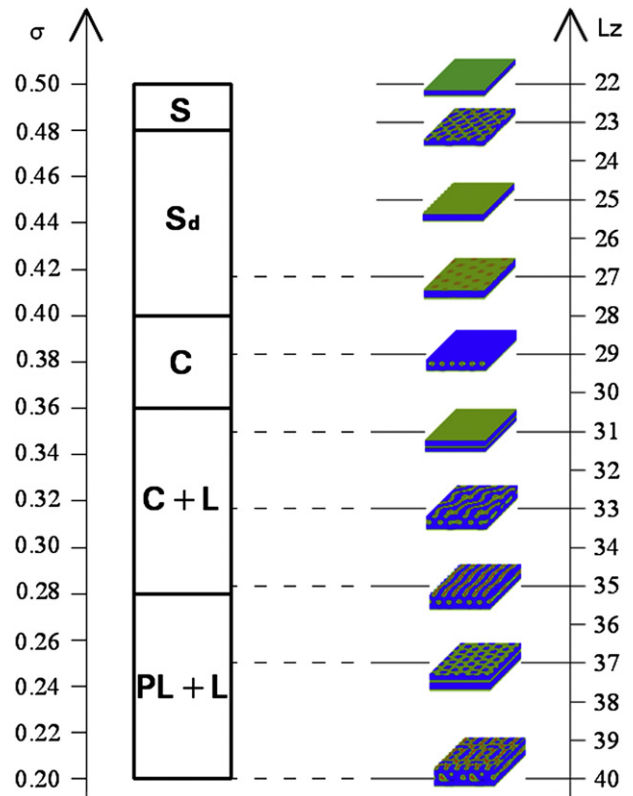


**Fig. 4.** Comparison of ABC triblock copolymer thin film phase behaviour between varying the grafting density and changing the thickness when the volume fractions of A and B are 0.10 and 0.20 respectively and the interaction parameters are  $\chi_{AB}N = \chi_{BC}N = \chi_{AC}N = 35$ . The left column is the phase behaviour of the ABC triblock copolymer thin film by varying the grafting density with  $f_A = 0.1$ ,  $f_B = 0.2$  and  $f_C = 0.7$ ,  $L_z = 40$ . The right column is the phase behaviour of the ABC triblock copolymer thin film by varying the film thickness with the fixed brush density  $\sigma = 0.2$ .

density is small relatively. When the brush density increases to 0.4, the effective film thickness is small, so the perforated lamellar phase occurs. When further increasing the brush density, the cylindrical phase is stable, which is equivalent to the Chex phase with a single layer.

From the phase diagrams, we can see that there are only four phases when the brush density is varied from 0.1 to 0.6 for  $\chi_{AB}N = \chi_{BC}N = 13$ ,  $\chi_{AC}N = 35$ , while six phases for  $\chi_{AB}N = \chi_{BC}N = \chi_{AC}N = 35$ . It is energetically favourable for  $\chi_{AB}N = \chi_{BC}N = 13$ ,  $\chi_{AC}N = 35$  because it does not need to overcome the bending energy to avoid the contact between the blocks A and B. Then there is a large region for the hexagonally packed cylindrical phase (Chex). But for the case for  $\chi_{AB}N = \chi_{BC}N = \chi_{AC}N = 35$ , it exists the energy competition between the blocks A and B, B and C, A and C, so the phase behavior is more complex.

### 3.3. Effective thickness of the ABC triblock copolymer thin film

#### 3.3.1. $\chi_{AB}N = \chi_{BC}N = 13$ , $\chi_{AC}N = 35$

From the above results, we can see that the effective film thickness changes with increasing the brush density. In order to relate the brush density with the effective film thickness. We also consider the ABC thin film with different film thicknesses at the brush density  $\sigma = 0.20$ . In this part, we also consider the cases for the identical interaction parameter and the non-frustrated state.

Due to the higher grafting density of the coated polymer, the brush height is  $h = \sigma P a$  [35], therefore, the effective thickness of the ABC block copolymer is only about  $L_z^{\text{eff}} = L_z - h$ . Fig. 3 gives the comparison of the non-frustrated case  $\chi_{AB}N = \chi_{BC}N = 13$ ,  $\chi_{AC}N = 35$ .

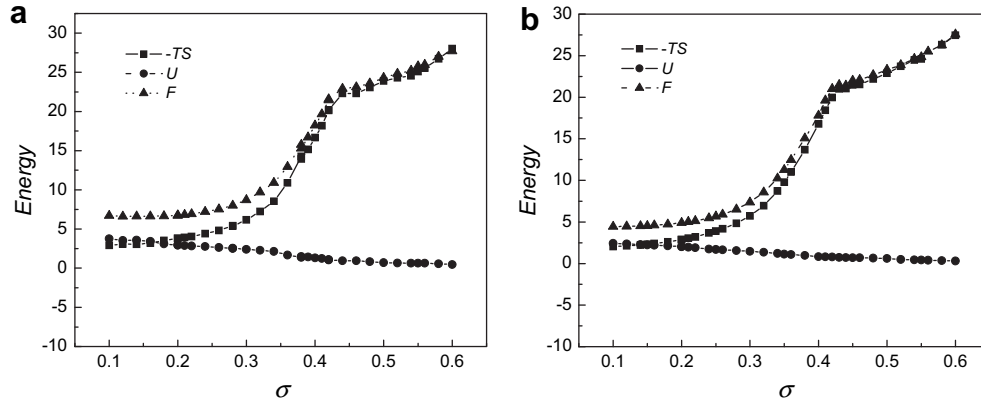


**Fig. 5.** Entropic free energy  $-TS$  (squares), enthalpic free energy  $U$  (spheres), and total free energy  $F$  (triangles) of the system for  $f_A = 0.1$ ,  $f_B = 0.2$  and  $f_C = 0.7$  at (a)  $\chi_{AB}N = \chi_{AC}N = \chi_{BC}N = 35$  and (b)  $\chi_{AB}N = \chi_{BC}N = 13$ ,  $\chi_{AC}N = 35$ .

The left column shows the phase diagram when varying the brush density with the fixed film thickness  $L_z = 40$ . The right is the morphology of the block copolymer by varying the film thickness  $L_z = 22 - 40$  at the fixed brush density  $\sigma = 0.2$ . The dash lines show the correspondence. From the figure, we can see that there is a good correspondence between the two cases, which satisfies the relation  $L_z^{\text{eff}} = L_z - h$ . The effective film thickness of the ABC triblock copolymer by varying the brush density is  $L_z^{\text{eff}(1)} = L_z - h = 40 - \sigma P = 40 - 60\sigma$ . The effective film thickness of the ABC triblock copolymer thin film by varying the film thickness with the fixed brush density  $\sigma = 0.2$  is  $L_z^{\text{eff}(2)} = L_z - h = L_z - \sigma P = L_z - 12$ . In the present case, the phase behavior of the ABC triblock copolymer shows the good agreement. The good correspondence is also due to the favourable interaction between different blocks. It is easily understandable, the effective film thickness decreases with the increase of the brush density. As for these two cases for the change of the film thickness and the change of brush density, the interface A/C cannot easily form, so the microstructure of block B around the minority block A is stable.

### 3.3.2. $\chi_{AB}N = \chi_{BC}N = \chi_{AC}N = 35$

Fig. 4 gives the comparison of  $\chi_{AB}N = \chi_{BC}N = \chi_{AC}N = 35$ . The left column is the phase diagram when varying the brush density with the fixed film thickness. The morphologies of ABC block copolymer at different film thickness with fixed brush density are shown in the right column. From the figure, we can see that there is good correspondence when the brush density is relatively low, such as  $\sigma = 0.2 - 0.42$ . The dash lines in Fig. 4 show the correspondence. But when the brush density is very high, which means the effective film thickness is very small, the morphology does not well related. This phenomena is different from the non-frustrated case  $\chi_{AB}N = \chi_{BC}N = 13$ ,  $\chi_{AC}N = 35$ . As for the case of  $\chi_{AB}N = \chi_{BC}N = \chi_{AC}N = 35$ , the morphology at different film thickness shows some periodicity, which is similar with our previous work [4]. The ordered periodicity decreases when the film thickness decreases along  $z$ -direction. The interfacial effect and the special effect have strong influence to the morphology due to the identical interaction between the three different blocks. The energy competition is strong between different blocks comparing with the non-frustrated case. But for the present case for changing the brush density, the substrate will have more compatibility with the block B of ABC triblock copolymer. The block B will stay near to the polymer brush-coated substrate, therefore, the structure of block B around the block A easily forms. It is more favorable in energy than that the blocks A and B forms one phase, that is to say, blocks A and B cannot separate from each other.

### 3.4. Energy analysis

In the following, we provide insight into the entropic and the enthalpic free energies of the system, where  $-TS = -\phi_c \ln(Q_c/\phi_c V) - \phi_g \ln(Q_g/\phi_g V) - 1/V \int \mathbf{dr} \sum_i w_i \phi_i$ , and  $U = 1/V \int \mathbf{dr} [\frac{1}{2} \sum_{i \neq j} \chi_{ij} N \phi_i \phi_j + \sum_i \chi_{is} N \phi_i \delta_{\mathbf{r}, \mathbf{r}_s}]$ . Fig. 5 shows the entropic free energy  $-TS$  (squares), enthalpic free energy  $U$  (spheres), and total free energy  $F$  (triangles) ( $F = U - TS$ ) of the system as a function of the brush density  $\sigma$ . With the brush density increasing, the entropic free energy increases and the enthalpic free energy decreases a little. We can see that the entropic free energy contributes the phase transition of the ABC triblock copolymer. When the brush density increases from 0.1 to 0.3, the entropic free energy almost does not change, which is reasonable because the effective film thickness is large enough. When the brush density is 0.3–0.45, the entropic free energy increases because the film goes into the thin film regime and the confinement effect dominates. Due to the grafted polymer serving as a hydrophilic part (identical with the block B) of the block copolymer, the large energy fluctuation is suppressed in our system as compared with the block copolymer confined in the film only by hard surfaces. Comparing with the two components ( $-TS$ ,  $U$ ) of the free energy, we can clearly see that the entropic free energy contributes more to the hetero-structure formation.

### 4. Conclusions

In this paper, the morphology and the phase diagram of the ABC block copolymer on the polymer-coated substrate were studied by using the self-consistent field theory (SCFT) in three dimensions. By continuously changing the grafting density with the fixed film thickness, seven ordered morphologies were found for the block copolymer thin film with the composition  $f_A = 0.1$ ,  $f_B = 0.2$  and  $f_C = 0.7$ : perforated lamellar and lamellar phase (PL + L), cylindrical and lamellar phase (C + L), spherical phase (S), spherical phase (double layer) (Sd), cylindrical phase (C), hexagonally packed cylindrical phase (Chex), perforated lamellar phase (PL). Due to the asymmetric surfaces for the block copolymer thin film, the rich hetero-structures occur, which is the combination of two different microstructures, such as PL + L phase, C + L phase. They can be separated into three kinds: cylinders, perforated lamellae and spheres. The phase diagrams were constructed for the identical interaction parameters case and the non-frustrated case. We can clearly see the phase transitions with the increase of the brush

density. The transition includes complex lamellar phase to cylindrical phase to spherical phase and last to disordered phase for the case  $\chi_{AB}N = \chi_{BC}N = \chi_{AC}N = 35$ . The phase transition is simple for the non-frustrated case  $\chi_{AB}N = \chi_{BC}N = 13$ ,  $\chi_{AC}N = 35$ . The effect of the film thickness is also considered at the fixed grafting density  $\sigma = 0.2$ . Comparing the results, we found that there is a correspondence between the thin film thickness and the brush density, which shows that the essence of the variation of the grafting density is the change of the effective film thickness in most cases. The relationship between the grafting density and the film thickness is constructed. Actually, the change of the brush density tailors the surface confinement effect, that is to say, the film thickness changes. Our results offer another way to tailor the phase behavior of the block copolymer thin film and obtain the hetero-structures.

### Acknowledgment

We gratefully acknowledge financial support from National Natural Science Foundation of China (Nos. 20674035, 20874046 and 21074053) and National Basic Research Program of China (Grant no. 2010CB923303).

### References

- [1] Hamley IW. The physics of block copolymers. New York: Oxford University Press; 1998.
- [2] Balsamo V, Collins S, Hamley IW. *Polymer* 2002;43:4207.
- [3] Matsen MW. *Journal of Chemical Physics* 1998;108:785.
- [4] Jiang ZB, Wang R, Xue G. *Chinese Journal of Polymer Science* 2009;27:583.
- [5] Srinivas G, Discher DE, Klein ML. *Nature Materials* 2004;3:638.
- [6] Srinivas G, Shelley JC, Nielsen SO, Discher DE, Klein ML. *Journal of Physical Chemistry B* 2004;108:8153.
- [7] Glass R, Moller M, Spatz JP. *Nanotechnology* 2003;14:1153.
- [8] Sun RG, Wang YZ, Wang DK, Zheng QB, Kyllö EM, Gustafson TL, et al. *Synthetic Metals* 2000;111:595.
- [9] Wurlitzer A, Politsch E, Huebner S, Kruger P, Weygand M, Kjaer K, et al. *Macromolecules* 2001;34:1334.
- [10] Muthukumar M. *Current Opinion in Colloid & Interface Science* 1998;3:48.
- [11] Morkved TL, Jaeger HM. *Europhysics Letters* 1997;40:643.
- [12] Geisinger T, Muller M, Binder K. *Journal of Chemical Physics* 1999;111:5251.
- [13] Huinink HP, Brokken-Zijp JCM, van Dijk MA, Sevink GJA. *Journal of Chemical Physics* 2000;112:2452.
- [14] Spontak RJ, Shankar R, Bowman MK, Krishnan AS, Hamersky MW, Samseth J, et al. *Nano Letters* 2006;6:2115.
- [15] Niihara KI, Sugimori H, Matsuwaki U, Hirato F, Morita H, Doi M, et al. *Macromolecules* 2008;41:9318.
- [16] Drolet F, Fredrickson GH. *Macromolecules* 2001;34:5317.
- [17] Tyler CA, Qin J, Bates FS, Morse DC. *Macromolecules* 2007;40:4654.
- [18] Binder K. Phase transitions of polymer blends and block copolymer melts in thin films. In: *Advances in polymer science; polymers in confined environments*. Springer-Verlag; Springer-Verlag New York, Inc.; 1999. p. 1.
- [19] Ludwigs S, Krausch G, Magerle R, Zvelindovsky AV, Sevink GJA. *Macromolecules* 2005;38:1859.
- [20] Pickett GT, Balazs AC. *Macromolecular Theory and Simulations* 1998;7:249.
- [21] Feng J, Ruckenstein E. *Polymer* 2002;43:5775.
- [22] Chen HY, Fredrickson GH. *Journal of Chemical Physics* 2002;116:1137.
- [23] Knoll A, Lyakhova KS, Horvat A, Krausch G, Sevink GJA, Zvelindovsky AV, et al. *Nature Materials* 2004;3:886.
- [24] Han WC, Tang P, Li X, Qiu F, Zhang HD, Yang YL. *Journal of Physical Chemistry B* 2008;112:13738.
- [25] Zhou L, Ma YQ. *Journal of Physics-Condensed Matter* 2008;20.
- [26] Fukunaga K, Hashimoto T, Elbs H, Krausch G. *Macromolecules* 2002;35:4406.
- [27] Ren CL, Ma YQ. *Physical Review E* 2005;72:051804.
- [28] Ren CL, Chen K, Ma YQ. *Journal of Chemical Physics* 2005;122:154904.
- [29] Drolet F, Fredrickson GH. *Physical Review Letters* 1999;83:4317.
- [30] Thomas JW. *Numerical partial differential equations*. New York: Springer-Verlag; 1995.
- [31] Tang WH. *Macromolecules* 2000;33:1370.
- [32] Jung YS, Jung W, Tuller HL, Ross CA. *Nano Letters* 2008;8:3776.
- [33] Register RA, Angelescu DE, Pelletier V, Asakawa K, Wu MW, Adamson DH, et al. *Journal of Photopolymer Science and Technology* 2007;20:493.
- [34] Knoll A, Horvat A, Lyakhova KS, Krausch G, Sevink GJA, Zvelindovsky AV, et al. *Physical Review Letters* 2002;89.
- [35] Aubouy M, Fredrickson GH, Pincus P, Raphael E. *Macromolecules* 1995;28:2979.